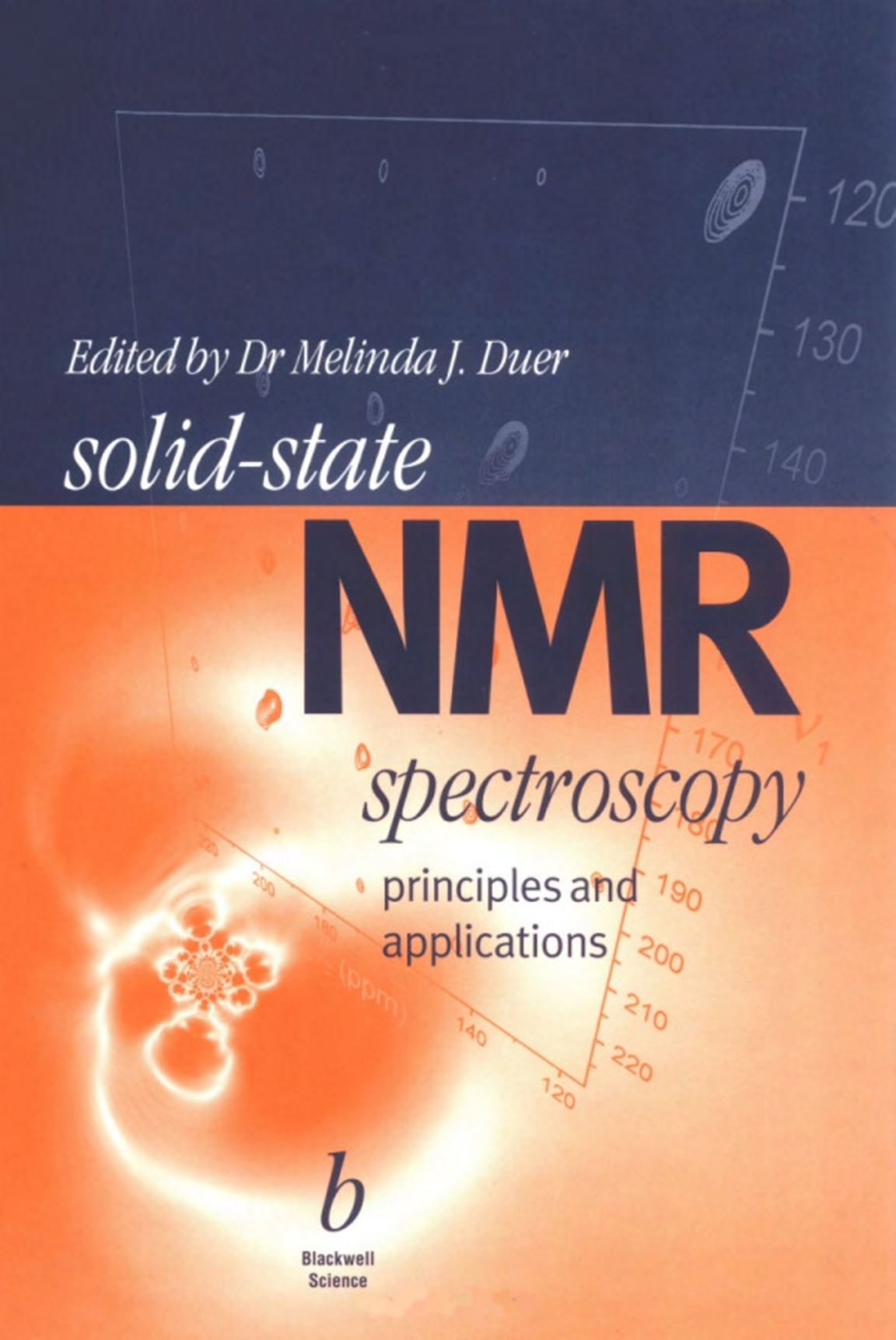

Edited by Dr Melinda J. Duer

solid-state NMR *spectroscopy*

principles and applications

b
Blackwell
Science

Solid-State NMR Spectroscopy

Principles and Applications

Solid-State NMR Spectroscopy
Principles and Applications

EDITED BY

Melinda J. Duer
Department of Chemistry
University of Cambridge
Lensfield Road
Cambridge
CB2 1EW

Blackwell
Science

© 2002 by
Blackwell Science Ltd
Editorial Offices:
Osney Mead, Oxford OX2 0EL
25 John Street, London WC1N 2BS
23 Ainslie Place, Edinburgh EH3 6AJ
350 Main Street, Malden
MA 02148 5018, USA
54 University Street, Carlton
Victoria 3053, Australia
10, rue Casimir Delavigne
75006 Paris, France

Other Editorial Offices:

Blackwell Wissenschafts-Verlag GmbH
Kurfürstendamm 57
10707 Berlin, Germany

Blackwell Science KK
MG Kodenmacho Building
7–10 Kodenmacho Nihombashi
Chuo-ku, Tokyo 104, Japan

Iowa State University Press
A Blackwell Science Company
2121 S. State Avenue
Ames, Iowa 50014-8300, USA

The right of the Author to be identified as the Author of this Work has been asserted in accordance with the Copyright, Designs and Patents Act 1988.

All rights reserved. No part of this publication may be reproduced, stored in a retrieval system, or transmitted, in any form or by any means, electronic, mechanical, photocopying, recording or otherwise, except as permitted by the UK Copyright, Designs and Patents Act 1988, without the prior permission of the publisher.

First published 2002

Set by Best-set Typesetter Ltd., Hong Kong
Printed and bound in Great Britain by
MPG Books Ltd, Bodmin Cornwall

The Blackwell Science logo is a trade mark of Blackwell Science Ltd, registered at the United Kingdom Trade Marks Registry

DISTRIBUTORS

Marston Book Services Ltd
PO Box 269
Abingdon
Oxon OX14 4YN
(*Orders*: Tel: 01235 465500
Fax: 01235 465555)

USA
Blackwell Science, Inc.
Commerce Place
350 Main Street
Malden, MA 02148 5018
(*Orders*: Tel: 800 759 6102
781 388 8250
Fax: 781 388 8255)

Canada
Login Brothers Book Company
324 Saulteaux Crescent
Winnipeg, Manitoba R3J 3T2
(*Orders*: Tel: 204 837-3987
Fax: 204 837-3116)

Australia
Blackwell Science Pty Ltd
54 University Street
Carlton, Victoria 3053
(*Orders*: Tel: 03 9347 0300
Fax: 03 9347 5001)

A catalogue record for this title
is available from the British Library

ISBN 0-632-05351-8

Library of Congress
Cataloging-in-Publication Data

Solid-State NMR Spectroscopy : principles and applications/edited by Melinda J. Duer.
p. cm.
Includes bibliographical references and index.
ISBN 0-632-05351-8 (alk. paper)
1. Nuclear magnetic resonance spectroscopy.
2. Solid state chemistry. I. Duer, Melinda J.

QD96.N8 S63 2002
543′.0877 – dc21 2001035179

For further information on
Blackwell Science, visit our website:
www.blackwell-science.com

List of Contributors

Oleg N. Antzutkin *Division of Inorganic Chemistry, Luleå University of Technology, S-971 87 Luleå, Sweden*

Melinda J. Duer *Department of Chemistry, University of Cambridge, Lensfield Road, Cambridge CB2 1EW, UK*

James W. Emsley *Department of Chemistry, University of Southampton, Southampton, Hants SO17 1BJ, UK*

Ian Farnan *Department of Earth Sciences, University of Cambridge, Downing Street, Cambridge CB2 3EQ, UK*

Jacek Klinowski *Department of Chemistry, University of Cambridge, Lensfield Road, Cambridge CB2 1EW, UK*

Ulrich Scheler *Institüt für Polymerforschung Dresden, Hohe Strasse 6, D-01069 Dresden, Germany*

Jonathan F. Stebbins *Department of Geology and Environmental Science, Stanford University, Stanford, CA 94305, USA*

Contents

List of Contributors, v
Preface, xv
Acknowledgements, xviii

PART I: THE THEORY OF SOLID-STATE NMR AND ITS EXPERIMENTS, 1

1 The Basics of Solid-State NMR, 3
Melinda J. Duer

1.1 The vector model of pulsed NMR, 3
1.1.1 Nuclei in a static, uniform magnetic field, 3
1.1.2 The effect of rf pulses, 5
1.2 The quantum mechanical picture: hamiltonians and the Schrödinger equation, 7
Box 1.1 *Quantum mechanics and NMR*, 8
1.2.1 Nuclei in a static, uniform field, 13
1.2.2 The effect of rf pulses, 16
Box 1.2 *Exponential operators, rotation operators and rotations*, 20
1.3 The density matrix representation and coherences, 29
1.3.1 Coherences and populations, 30
1.3.2 The density operator at thermal equilibrium, 33
1.3.3 Time evolution of the density matrix, 33
1.4 Nuclear spin interactions, 36
1.4.1 The chemical shift and chemical shift anisotropy, 38
1.4.2 Dipole–dipole coupling, 46
Box 1.3 *Basis sets for multispin systems*, 51

1.4.3 Quadrupolar coupling, 56
1.5 Calculating NMR powder patterns, 59
1.6 General features of NMR experiments, 61
1.6.1 Multidimensional NMR, 61
1.6.2 Phase cycling, 63
1.6.3 Quadrature detection, 66
Box 1.4 *The NMR spectrometer*, 70

References, 72

2 Essential Techniques for Spin-$\frac{1}{2}$ Nuclei, 73
Melinda J. Duer

2.1 Introduction, 73
2.2 Magic-angle spinning (MAS), 73
2.2.1 Spinning sidebands, 75
2.2.2 Rotor or rotational echoes, 79
2.2.3 Removing spinning sidebands, 80
2.2.4 Magic-angle spinning for homonuclear dipolar couplings, 83
2.3 High-power decoupling, 85
2.4 Multiple pulse decoupling sequences, 86
Box 2.1 *Average hamiltonian theory and the toggling frame*, 88
2.5 Cross-polarization, 97
2.5.1 Theory, 98
2.5.2 Experimental details, 102
Box 2.2 *Cross-polarization and magic-angle spinning*, 104
2.6 Solid or quadrupole echo pulse sequence, 108

References, 109

3 Dipolar Coupling: Its Measurement and Uses, 111
Melinda J. Duer

3.1 Introduction, 111
Box 3.1 *The dipolar hamiltonian in terms of spherical tensor operators*, 113
3.2 Techniques for measuring homonuclear dipolar couplings, 122
3.2.1 Recoupling pulse sequences, 122
Box 3.2 *Analysis of the DRAMA pulse sequence*, 126

3.2.2 Double-quantum filtered experiments, 132
3.2.3 Rotational resonance, 135
Box 3.3 *Excitation of double-quantum coherence under magic-angle spinning*, 138
3.3 Techniques for measuring heteronuclear dipolar couplings, 144
Box 3.4 *Analysis of the C7 pulse sequence for exciting double-quantum coherence in dipolar-coupled spin pairs*, 145
3.3.1 Spin-echo double resonance, 148
Box 3.5 *Theory of rotational resonance*, 149
3.3.2 Rotational-echo double resonance, 154
Box 3.6 *Analysis of the REDOR experiment*, 156
3.4 Techniques for dipolar-coupled quadrupolar (spin-$\frac{1}{2}$) pairs, 160
3.4.1 Transfer of population in double resonance, 161
3.4.2 Rotational echo, adiabatic passage, double resonance, 164
3.5 Techniques for measuring dipolar couplings between quadrupolar nuclei, 165
3.6 Correlation experiments, 166
3.6.1 Homonuclear correlation experiments for spin-$\frac{1}{2}$ systems, 166
3.6.2 Homonuclear correlation experiments for quadrupolar spin systems, 169
3.6.3 Heteronuclear correlation experiments for spin-$\frac{1}{2}$, 171
3.7 Spin-counting experiments, 171
3.7.1 The formation of multiple-quantum coherences, 172
3.7.2 Implementation of spin-counting experiments, 175

References, 177

4 Quadrupole Coupling: Its Measurement and Uses, 179
Melinda J. Duer and Ian Farnan

4.1 Theory, 179
4.1.1 The quadrupole hamiltonian, 179
4.1.2 The effect of rf pulses, 184
4.2 High-resolution NMR experiments for half-integer quadrupolar nuclei, 188
4.2.1 Magic-angle spinning, 189
4.2.2 Double rotation, 191
4.2.3 Dynamic-angle spinning, 193
4.2.4 Multiple-quantum magic-angle spinning, 195

4.2.5 Recording two-dimensional datasets for DAS and MQMAS, 200
4.3 Other techniques for half-integer quadrupolar nuclei, 205
4.3.1 Quadrupole nutation, 206
4.3.2 Cross-polarization, 209

References, 214

5 Shielding and Chemical Shift, 216
Melinda J. Duer

5.1 The relationship between the shielding tensor and electronic structure, 216
5.2 Measuring chemical shift anisotropies, 222
5.2.1 Magic-angle spinning with recoupling pulse sequences, 222
5.2.2 Variable angle spinning experiments, 225
5.2.3 Magic-angle turning, 228
5.2.4 Two-dimensional separation of spinning sideband patterns, 231

References, 235

PART II: APLICATIONS OF SOLID-STATE NMR, 237

6 NMR Techniques for Studying Molecular Motion in Solids, 239
Melinda J. Duer

6.1 Introduction, 239
6.2 Powder lineshape analysis, 242
6.2.1 Simulating powder pattern lineshapes, 243
6.2.2 Resolving powder patterns, 250
6.2.3 Using homonuclear dipolar coupling lineshapes: the WISE experiment, 256
6.3 Relaxation time studies, 258
6.4 Exchange experiments, 261
6.4.1 Achieving pure absorption lineshapes in exchange spectra, 263
6.4.2 Interpreting two-dimensional exchange spectra, 266
6.5 ^{2}H NMR, 267
6.5.1 Measuring ^{2}H NMR spectra, 268
6.5.2 ^{2}H lineshape simulations, 273
6.5.3 Relaxation time studies, 274

6.5.4 ^{2}H exchange experiments, 275
6.5.5 Resolving ^{2}H powder patterns, 276

References, 279

7 Molecular Structure Determination: Applications in Biology, 280
Oleg N. Antzutkin

7.1 Introduction, 280
7.1.1 Useful nuclei in biological solid-state NMR, 281
7.1.2 An overview of nuclear spin interactions encountered in biological samples, 285
7.2 Chemical shifts, 288
7.2.1 Is a protein in a disordered or in the native well-structured form? 288
7.2.2 Chemical shift anisotropy, 293
7.3 Interspin distance measurements, 303
7.3.1 Heteronuclear distance measurements: the REDOR experiment, 303
7.3.2 Homonuclear distance measurements: rotational resonance, 308
7.3.3 Homonuclear distance measurements: DRAWS, RFDR, (fp)-RFDR, 311
7.4 Torsion angle measurements, 319
7.4.1 Chemical shift–chemical shift tensor correlation experiments, 322
7.4.2 Dipolar–chemical shift tensor correlation experiments, 338
7.4.3 Experiments correlating two dipole–dipole coupling tensors, 350
7.5 ^{13}C multiple-quantum NMR spectroscopy, 371

References, 384

8 NMR Studies of Oxide Glass Structure, 391
Jonathan F. Stebbins

8.1 Introduction, 391
8.1.1 The 'structure' of a glass, 392
8.1.2 The extent of disorder, 394
8.1.3 Liquids vs. glasses, 395
8.2 NMR techniques for studying glass structure, 395
8.2.1 Static samples, 395
8.2.2 Simple MAS spectra, 398

8.2.3 Techniques for observing ^{1}H and ^{19}F in glasses, 405
8.2.4 Cross-polarization techniques, 406
8.2.5 Other double resonance experiments, 407
8.2.6 Two-dimensional correlation experiments, 409
8.2.7 Techniques that eliminate second-order quadrupolar broadening (DOR, DAS, MQMAS), 411
8.2.8 Spin-lattice relaxation and structure, 414
8.3 Applications to specific glass systems, 415
8.3.1 Boron-containing oxide glasses, 416
8.3.2 Silicate, aluminosilicate and germanate glasses, 421
8.3.3 Hydrogen-containing species in oxide glasses, 425
8.3.4 Phosphate glasses, 426
8.3.5 Thermal history effects, 428
8.3.6 Long-range structural anisotropy, 430

References, 431

9 Porous Materials, 437
Jacek Klinowski

9.1 Introduction, 437
9.2 Zeolites, 437
9.3 Aluminophosphate molecular sieves, 438
9.4 Mesoporous molecular sieves, 440
9.5 Spectroscopic considerations, 441
9.6 Monitoring the composition of the aluminosilicate framework of zeolites, 442
9.7 Ordering of atoms in tetrahedral frameworks, 443
9.8 Resolving crystallographically inequivalent tetrahedral sites, 445
9.9 Spectral resolution, lineshape and relaxation, 448
9.10 Dealumination and realumination of zeolites, 450
9.11 NMR studies of Brønsted acid sites, 455
9.12 Chemical status of guest organics in the intracrystalline space, 457
9.13 *In situ* studies of catalytic reactions, 459
9.14 Direct observation of shape selectivity, 463
9.15 Aluminophosphate molecular sieves, 464
9.16 Multinuclear studies of sorbed species, 469
9.17 ^{129}Xe NMR, 471
9.18 New NMR techniques for the study of molecular sieves, 475
9.19 Conclusions, 478

References, 478

10 Solid Polymers, 483
Ulrich Scheler

10.1 Introduction, 483
10.2 Structure of polymers, 485
10.3 Polymer dynamics, 488
10.3.1 NMR methods for studying polymer dynamics, 489
10.4 Phase separation of polymers, 494
10.5 Oriented polymers, 502
10.6 Fluoropolymers, 506

References, 510

11 Liquid-Crystalline Materials, 512
James W. Emsley

11.1 The liquid-crystalline state, 513
11.2 Orientational order, 514
11.2.1 Phase symmetry, 515
11.2.2 Molecular orientational order, 515
11.3 The general, time-independent NMR hamiltonian for liquid-crystalline samples, 516
11.4 Molecular order parameters, 518
11.4.1 Different representations of the order parameters, 519
11.4.2 Molecular order parameters and the symmetry of rigid molecules, 520
11.5 Director alignment, 521
11.6 Dipolar couplings between nuclei in rigid molecules in liquid-crystalline phases, 523
11.6.1 Geometry of rigid molecules from dipolar couplings, 524
11.7 Deuterium quadrupolar splittings for rigid molecules in liquid-crystalline phases, 525
11.7.1 Signs of quadrupolar splittings, 527
11.8 Chemical shift anisotropy for rigid molecules in liquid-crystalline phases, 527
11.9 Electron-mediated spin–spin coupling in liquid-crystalline samples, 529
11.9.1 The determination of the structure, orientational order and conformations of flexible molecules in liquid-crystalline samples, 531
11.9.2 Molecular orientational order for flexible molecules, 531
11.9.3 Conformationally dependent order parameters, 534

11.10 Determination of the conformationally dependent orientational order parameters and the conformational distributions of molecules in liquid-crystalline phases from NMR parameters, 535
11.10.1 Theoretical models for $P_{LC}(\beta_{md}, \gamma_{md}, (\varphi_l))$, 536
11.11 NMR experiments for liquid-crystalline samples, 540
11.11.1 Simplification of proton spectra by partial deuteriation plus deuterium decoupling, 540
11.11.2 Multiple-quantum spectra, 542
11.11.3 Symmetry selection by multiple-quantum filtering, 544
11.11.4 Rotation of liquid-crystalline samples, 548
11.11.5 Liquid-crystalline mixed solvents consisting of two components of opposite sign of the anisotropy in their magnetic susceptibility, 551
11.11.6 The separated local field experiment, 554
11.12 Spectra of chiral and prochiral molecules in chiral liquid-crystalline phases, 558

References, 561

Index, 563

Preface

In the 50 or so years since NMR was first invented, solid-state NMR has seen a steady increase in popularity, until the 1980s when its expansion was rapid. Its initial lack of use relative to solution-state NMR was because of the inherent lack of resolution in solid-state NMR spectra (if nothing is done to deliberately improve it). The sudden increase in its popularity went hand-in-hand with the invention of new techniques that enabled high resolution to be achieved even in the solid state.

This latter development was to a large extent driven by increasing numbers of chemical problems for which solid-state NMR promised great utility if higher resolution could be obtained, and which could not be solved by other techniques. The chemical problems to which solid-state NMR has been applied since then are very diverse indeed. The vast majority can be divided into one of two areas: molecular structure determination, studies of which are now virtually routine for determining molecular structures and intermolecular packing. For those solids which do not form suitable single crystals, powder XRD can give useful information, but refinement of the structures relies on very high-resolution XRD patterns; currently structures for molecules with up to 20 or so atoms can be refined, but no bigger. Solid-state NMR can provide useful information on the number of molecules in the asymmetric unit and on the site symmetry of the molecule in the lattice to assist in the refinement of powder XRD data. Alternatively, it can be used to measure internuclear distances directly, and often with great accuracy. For amorphous and disordered solids, such as inorganic glasses and organic polymers, solid-state NMR has provided, and continues to provide, invaluable structural information which, as yet, *cannot be obtained by any other technique*. For instance, ranges of Si–O–Si bond angles in silicate glasses have been obtained by correlating chemical shifts with these angles.

While diffraction techniques are very good at determining static molecular structure on suitable samples, they often give a poor overall picture of a material, because they indicate little about the dynamics in the system. Even relatively simple organic molecules undergo continuous conformational exchange in the solid state at ambient

temperature. To ignore this feature of a material is to ignore a major determinant of its properties. The motional degrees of freedom in solids determine, for instance, their brittleness and flexiblity. They also determine the entropy of the phase and, through this, contribute to the phase diagram for the material. There have been many studies of molecular dynamics in polymers using solid-state NMR, and these are discussed in Chapter 10. These are not the only areas for molecular dynamics studies however, and solid-state NMR has played a major role in studies on glasses, which is discussed in Chapter 8. As more sophisticated techniques become available to study more complex motions and sequences of motions, this area can be expected to find yet further applications. Biopolymers and oriented proteins, such as membrane proteins, are one new area currently being explored (Chapter 7).

Solution and solid-state NMR are both excellent methods of determining chemical composition. The chemical shift allows different chemical sites to be distinguished and intensities of NMR lines are (at least in principle) directly proportional to the number of each site in the sample. A further feature of solid-state NMR is its ability to distinguish different polymorphs. This is especially valuable to the pharmaceutical industry, for instance, as frequently it is only one particular polymorph of a compound that is the active drug they require; furthermore, other polymorphs may actually be harmful. In order to license the drug, pharmaceutical companies must demonstrate that they are manufacturing the right polymorph and no other, and solid-state NMR is one of the few techniques that allow unequivocal identification of polymorphs.

All of these applications of solid-state NMR require that (as in solution-state NMR) the signals from different chemical sites can be resolved from each other in some way. As intimated above, solid-state NMR spectra are characteristically composed of broad lines. The linebroadening arises from the various interactions which act on the nuclear spins: anisotropic chemical shielding, dipole–dipole coupling between magnetic nuclear dipoles and, for nuclei with spin I greater than $\frac{1}{2}$, quadrupole coupling. All of these are discussed in subsequent chapters. In solution, rapid random tumbling of the molecules averages each of these interactions to zero, so that their direct effects are rarely seen in the NMR spectrum.[1] Removing the effects of these interactions from solid-state NMR spectra has received, and indeed continues to receive, much attention and is discussed extensively in Chapter 2. However, we should not be too quick to remove the effects of these interactions without trace. They all depend on details of molecular and/or electronic structure, and so, by inference, we can in principle gain information on these factors from studying these interactions through solid-state NMR spectra. In practice, dipole–dipole coupling is being used very successfully to measure internuclear distances. The chemical shielding interaction is relatively easily used to the extent of observing empirical correlations between shielding values and geometric factors such as bond angles in molecules. Only recently, however, have *ab initio* calculations of shielding and quadrupole-coupling interactions become good enough to extract

information from experimentally observed values by comparing them with calculated ones for different molecular geometries. As *ab initio* calculations improve still further and become more routine for the chemist, this application is expected to increase.

The first part of this book deals with what I call the basics of solid-state NMR; what the spectra look like under the influence of the various nuclear spin interactions, how to record spectra and how to interpret them. These chapters, while reviewing current work in the respective areas of each chapter are not intended to be exhaustive reviews. Rather, they concentrate on what are currently considered to be the most useful or widely applicable experiments, and therefore on those which someone new to solid-state NMR might venture into. The references cited also reflect this approach. Obviously I have referenced work where I have used it, but, in addition, I have added those references that I think will be the most useful starting points for new solid-state NMR spectroscopists.

The second part of the book deals with specific areas of science where solid-state NMR has played a major part in recent years, and these chapters provide extensive reviews of the chosen areas. That is not to say that solid-state NMR has not made big impacts elsewhere, or will not in the future, but we had to stop somewhere! In essence, NMR provides an excellent *local* probe of solids. It is invaluable in cases where other structural techniques are found wanting.

Note

1. They do however continue to affect relaxation times. In addition, larger molecules may not tumble at rates high enough to average the interaction on the NMR timescale; this leads to linebroadening in ^{13}C and ^{1}H spectra of large proteins in solution. The NMR timescale in this instance refers to the linewidth caused by the interaction in the absence of molecular motion; rates of motion which are large compared to the linewidth cause effective averaging. Molecules in liquid-crystalline solvents do not tumble isotropically, so some residual vestige of the nuclear interactions remains and influences the NMR spectrum.

Acknowledgements

I am very grateful to all the authors who have contributed to this book for writing chapters which demonstrate the huge scope of solid-state NMR and point forward to many more applications in the future. There are, however, many more people who have contributed to this book and one of those, who deserves special thanks, is friend and colleague, Dr James Keeler, who in the last ten years has done his best to teach me something about NMR. He has also been invaluable in the production of this book by his insightful comments and awkward questions. Professor Cynthia Jameson and Dr Oleg Antzutkin have both contributed hugely by their respective comments on various parts of the book

Nicky McDougal, Niko Loening and Matthew Jones have done painstaking work in proof-reading and gently pointing out the more incomprehensible sentences. My husband, Dr Neil Piercy, has kept my computer working, dealt with awkward graphics, and many times has stepped in to rescue the printer, when for the umpteenth time, it decided to give up the ghost part way through printing out a chapter. More importantly, he has kept me supplied with chocolate and tea during the more hectic parts of the writing.

A large part of this book was written while on sabbatical leave from Cambridge University and I am very grateful to Professor Brian Johnson for allowing me to have this valuable period of leave. However, I still could not have produced this book without the peace and quiet afforded by an old farmhouse on Garrow Tor in the middle of Bodmin Moor, Cornwall, England. This was made possible by Julie Mansfield and Rio, the horse who provided transport while I was there.

Finally, there are a number of other people who each played a valuable part: John and Rose Duer, Annie Burton and Jane Moore.

Melinda Duer

Solid-State NMR Spectroscopy Principles and Applications
Edited by Melinda J. Duer
Copyright © 2002 by Blackwell Science Ltd

Part I

The Theory of Solid-State NMR and its Experiments

Solid-State NMR Spectroscopy Principles and Applications
Edited by Melinda J. Duer
Copyright © 2002 by Blackwell Science Ltd

Chapter 1
The Basics of Solid-State NMR

Melinda J. Duer

This chapter is concerned with the basics of how to describe nuclear spin systems in NMR experiments. To this end, we first consider the classical vector model, which in many cases, provides a sufficient description of an uncoupled spin system. As soon as there are interactions between the spins, such as dipolar or quadrupolar coupling, we must use a quantum mechanical model to describe the dynamics of the spin system. We will use the *density operator* approach, which combines a quantum mechanical modelling of individual spins or sets of coupled spins with an ensemble averaging over all the spins (or sets of spins) in the sample.

The latter sections of the chapter deal with the various internal nuclear spin interactions, (chemical shielding, dipole–dipole coupling and quadrupole coupling), their quantum mechanical description and their effect on an NMR spectrum.

1.1 The vector model of pulsed NMR

In the semi-classical model of NMR, only the net magnetization arising from the nuclei in the sample and its behaviour in magnetic fields is considered. It is a suitable model with which to consider the NMR properties of isolated spin-$\frac{1}{2}$ nuclei, i.e. those which are not coupled to other nuclei. This model also provides a convenient picture of the effects of radiofrequency pulses on such a system. Only a brief description is given here in order to define the terms and concepts that will be used throughout this book.

1.1.1 Nuclei in a static, uniform magnetic field

The net magnetization (which is equivalent to a bulk magnetic moment) arising from the nuclei in a sample is **M** and is the vectorial sum of all the individual magnetic moments associated with all the nuclei (Fig. 1.1):

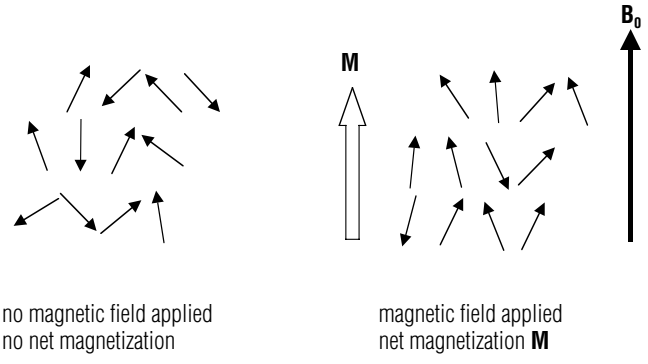

Fig. 1.1 The classical model of the formation of net nuclear magnetization in a sample. In the absence of a magnetic field, the individual nuclear magnetic moments (represented by vector arrows here) have random orientation so that there is no net magnetization. In the presence of an applied magnetic field, however, the nuclear magnetic moments are aligned preferentially with the applied field, except that thermal effects cause a distribution of orientations rather than perfect alignment. Nevertheless, there is in this case, a net nuclear magnetization.

$$\mathbf{M} = \sum_i \mu_i \tag{1.1}$$

where μ_i is the magnetic moment associated with the ith nucleus. In turn, each nuclear magnetic moment is related to the *nuclear spin* $\mathbf{I}_i$ of the nucleus by

$$\mu_i = \gamma \mathbf{I}_i \tag{1.2}$$

γ is the magnetogyric ratio, a constant for a given type of nucleus. Thus we can write the net magnetization of the sample as

$$\mathbf{M} = \gamma \mathbf{J} \tag{1.3}$$

where **J** is the net spin angular momentum of the sample giving rise to the magnetization **M**. If the nuclei are placed in a uniform magnetic field **B** as in the NMR experiment, a torque **T** is exerted on the magnetization vector:

$$\mathbf{T} = \frac{\mathrm{d}}{\mathrm{d}t}\mathbf{J} \tag{1.4}$$

In turn, the torque in this situation is given by

$$\mathbf{T} = \mathbf{M} \times \mathbf{B} \tag{1.5}$$

Combining Equations (1.3) to (1.5), we can write,

$$\frac{\mathrm{d}\mathbf{M}}{\mathrm{d}t} = \gamma \mathbf{M} \times \mathbf{B} \tag{1.6}$$

which describes the motion of the magnetization vector **M** in the field **B**. It can be shown that Equation (1.6) predicts that **M** precesses about a fixed **B** at a constant rate $\omega = \gamma B$.

In NMR, the applied magnetic field is generally labelled $\mathbf{B}_0$ and is taken to be along z, i.e. $\mathbf{B} = (0,0,B_0)$ in the above equations. The frequency with which the magnetization precesses about this field is defined as ω_0, the *Larmor frequency*:

$$\omega_0 = \gamma B_0 \tag{1.7}$$

1.1.2 The effect of rf pulses

An electromagnetic wave, such as a radiofrequency (rf) wave, has associated with it an oscillating magnetic field, and it is this field which interacts with the nuclei in addition to the static field in the NMR experiment. The rf wave is arranged in the NMR experiment so that its magnetic field oscillates along a direction perpendicular to z and the $\mathbf{B}_0$ field. Such an oscillating field can be thought of as a vector which can be written as the sum of two components rotating about $\mathbf{B}_0$ in opposite directions. The frequencies of these two components can be written as $\pm\omega_{rf}$, where ω_{rf} is the frequency of the rf pulse. Furthermore, it can be shown that only the component which rotates in the same sense as the precession of the magnetization vector $\mathbf{M}$ about $\mathbf{B}_0$ has any significant effect on $\mathbf{M}$; we will henceforth label this component $\mathbf{B}_1(t)$. The effect of this field is most easily seen by transforming the whole problem into a rotating frame of reference which rotates at frequency ω_{rf} around $\mathbf{B}_0$; in this frame $\mathbf{B}_1$ appears static, i.e. its time dependence is removed. We can see what happens to the $\mathbf{B}_0$ field in this frame by examining the effect of a similar rotating frame in the absence of an rf pulse, i.e. in the case of the static, uniform magnetic field considered previously. We concluded that in the presence of a field $\mathbf{B}_0$ only that the magnetization vector $\mathbf{M}$, would precess around $\mathbf{B}_0$ at frequency ω_0. If the pulse is *on resonance*, i.e. $\omega_0 = \omega_{rf}$, then the magnetization vector appears stationary in the rotating frame. In effect, the $\mathbf{B}_0$ field is removed in this frame; the effective static field parallel to z is zero. So, in the presence of a pulse, the only field remaining in the rotating frame is the $\mathbf{B}_1$ field. As in the case of the magnetization experiencing the static field $\mathbf{B}_0$ in the laboratory frame, the result of this interaction is that the magnetization vector $\mathbf{M}$ precesses about the resultant field, which is now $\mathbf{B}_1$, at frequency γB_1. We define this *nutation frequency* γB_1 as ω_1.

The direction of the magnetic field due to the rf pulse can be anywhere in the xy plane. The *phase* of a pulse, ϕ_{rf}, is defined as the angle $\mathbf{B}_1$ makes to the x axis in the rotating frame. The pulse does not have to be applied on resonance; indeed there will be many, many cases in solid-state NMR experiments when the pulse will be off resonance at least for part of the total spectrum available. In a frame rotating at ω_{rf} about $\mathbf{B}_0$, in the absence of a pulse, the Larmor precession frequency is reduced from ω_0 to $\omega_0 - \omega_{rf}$ about $\mathbf{B}_0$. We can infer from this that there is an effective static field along z in this frame of $(\omega_0 - \omega_{rf})/\gamma$, rather

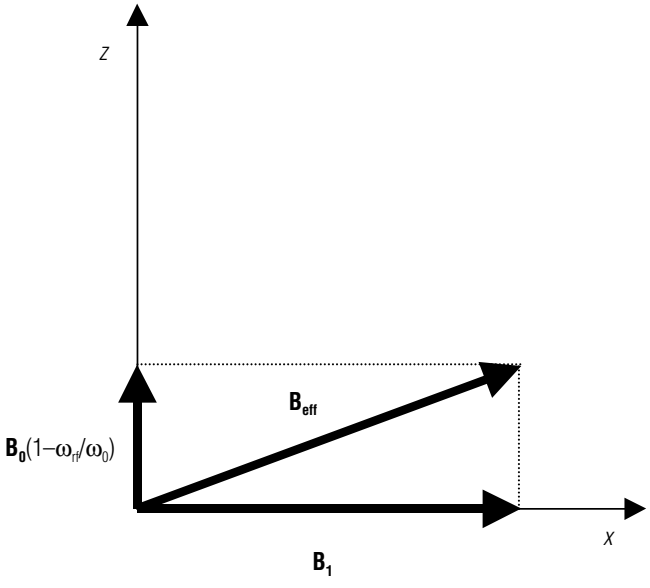

Fig. 1.2 The magnetic fields present in the rotating frame of reference. The rotating frame rotates about *z* at the frequency of the rf pulse, ω_{rf}. The pulse is applied along *x*. The field due to the pulse appears static in the rotating frame, and the static field $\mathbf{B}_0$ appears to be reduced by a factor of ω_{rf}/ω_0, where ω_0 is the Larmor frequency, $\omega_0 = \gamma B_0$. The net effective field in the rotating frame is the vectorial sum of the components along *x* and *z*, $\mathbf{B}_{eff}$. It is this field that the nuclear spin magnetization precesses around.

than zero, as in the on-resonance case. The magnetic fields present in the rotating frame are then those shown in Fig. 1.2; there is a field of magnitude $(\omega_0 - \omega_{rf})/\gamma$ along *z* and B_1 along *x* (for a pulse with phase 0°). The magnetization precesses around the resultant field $\mathbf{B}_{eff}$ shown in Fig. 1.2.

NMR spectroscopists talk generally of an rf pulse 'flipping' the magnetization. The flip angle, θ_{rf}, of an on-resonance pulse is the angle that the pulse field $\mathbf{B}_1$ turns the magnetization during time τ_{rf}:

$$\theta_{rf} = \omega_1 \tau_{rf} = \gamma B_1 \tau_{rf} \tag{1.8}$$

Thus, a 90° pulse is simply one which has a flip angle of $\theta_{rf} = \pi/2$ radians or 90°. The corresponding pulse length is referred to as the 90° pulse length. RF pulses along *x* in the rotating frame are referred to as '*x* pulses', those along *y* as '*y* pulses', and so on.

By definition, positive rotations are anticlockwise about the given axis. So, after a 90° *x* pulse (for shorthand labelled $90°_x$), nuclear magnetization **M** which started along *z*, is left lying along $-y$ (Fig. 1.3). From the point at which the rf pulse is turned off, the magnetization acts under the only magnetic field remaining, which is the effective field along *z*, of magnitude $(\omega_0 - \omega_{rf})/\gamma$, i.e. zero if the rotating frame frequency ω_{rf} is the same as the Larmor frequency, ω_0. If the effective field along *z* is zero, then the magnetization is stationary in the rotating frame after the pulse is switched off; if non-zero, the magnetization precesses around *z* from the position it was in at the end of the pulse at frequency $\omega_0 - \omega_{rf}$.

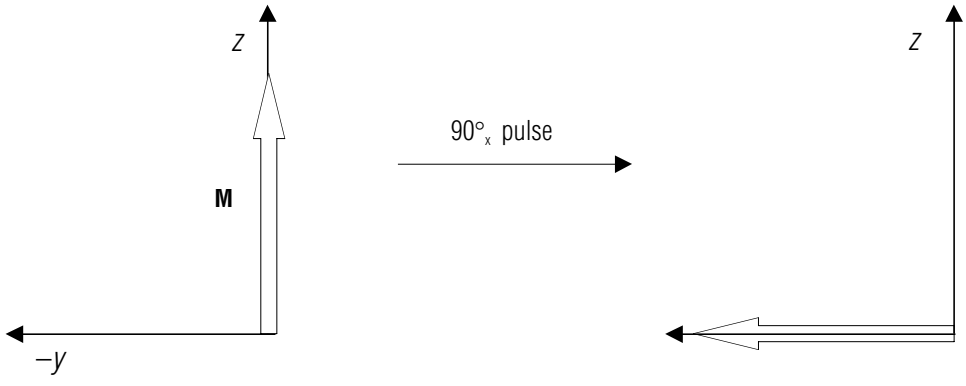

Fig. 1.3 The effect of a $90°_x$ on-resonance pulse on equilibrium magnetization in the rotating frame. The equilibrium magnetization rotates by 90° about *x* and ends up along −*y*.

1.2 The quantum mechanical picture: hamiltonians and the Schrödinger equation

In the quantum mechanical picture, we start from a consideration of individual nuclei and from this generate a picture for the whole collection of nuclei in a sample. This is called the *ensemble average*. We will often refer to the *spin system* by which we mean a nuclear spin or collection of interacting nuclear spins, in a specified environment, such as a static magnetic field along *z*, for instance. We will find that the state of a spin system at equilibrium is in one of a number of possible states or *eigenstates*, whose specific form depends on the nature of the spin system. In an NMR experiment, we have a sample which is composed of many identical spin systems. For instance, if each spin in the sample is isolated from other nuclei (so that there are no interactions between nuclei) and in the same chemical environment, then the spin system is a single nuclear spin subjected to whatever magnetic fields are present in the NMR experiment. The sample contains many such (identical) spin systems, the state of each being one of the possible eigenstates of the spin system. The proportion of the spin systems in the sample in any one eigenstate is given by a Boltzmann distribution for a sample which is at thermal equilibrium. In an NMR experiment, we measure the behaviour of the whole sample, not of individual spin systems. From the preceding discussion, it is clear that the behaviour of the sample depends not only on the nature of the possible eigenstates of the spin systems in the sample, but also on the population of each eigenstate over the sample as a whole. This will lead us to describe the state of each spin system in the sample as a superposition of the possible eigenstates for the spin system. The superposition state is the same for all identical spin systems and takes into account the probability of occurrence of each eigenstate, so leading to a proper description of the behaviour of the whole sample of spin systems.

Box 1.1 Quantum mechanics and NMR

In this box, we describe the key concepts in quantum mechanics which are used when discussing NMR and define the terms which will be used throughout this book.

Wavefunctions

In quantum mechanics, the state of a system, such as a nuclear spin or collection of spins in some specified environment, is described by a wavefunction, a mathematical function which depends on the spatial and spin coordinates of the nuclei in the system. We shall denote wavefunctions by the symbol ψ or Ψ. The wavefunctions themselves can often be specified by a set of *quantum numbers*, which in turn determine the values of the physical observables for the system.

Operators, physical observables and expectation values

We actually determine the value of any physical observable for the system by using the appropriate *operator* corresponding to the observable. An operator is simply something which acts on a function to produce another function, e.g. multiply by y, d/dx and so on. Throughout this work, we shall denote operators by '$\wedge$', to distinguish them from functions, etc.

The value of a physical observable in a state described by ψ is equal to the *expectation value* of the corresponding operator. For an operator $\hat{A}$, the expectation value $\langle A \rangle$ is

$$\langle A \rangle = \frac{\int \psi * \hat{A} \psi \ \mathrm{d}\tau}{\int \psi * \psi \ \mathrm{d}\tau} \qquad \text{(i)}$$

where the integrals are over all the spatial and spin coordinates of the wavefunction ψ.

Schrödinger's equation, eigenfunctions and eigenvalues

The wavefunction for a nuclear spin system in which all interactions are time invariant is the solution of the time-independent Schrödinger equation:

$$\hat{H} \psi = E \psi \qquad \text{(ii)}$$

$\hat{H}$ is the energy operator for the system, called the *hamiltonian*. The form of the hamiltonian varies from system to system and depends on the interactions in

the spin system. The quantity E is the energy of the system. Equation (ii) is that of an *eigenvalue* equation; the general form of such an equation for an operator $\hat{A}$ is

$$\hat{A}f = af \tag{iii}$$

where f is an eigenfunction of the operator $\hat{A}$ and a is the eigenvalue of $\hat{A}$ corresponding to the eigenfunction f. Thus the problem of finding the wavefunction for a system is one of finding the eigenfunctions of the relevant hamiltonian operator. In general, there are a set of eigenfunctions which solve (iii) for any given operator. The set of all the functions which solve (iii) is called a *complete set*. That is, any other function can be written as some linear combination of this complete set.

If the spin system is subject to a time-dependent interaction (as will often be the case in NMR experiments), then the wavefunction describing the state of the system is necessarily time dependent. We must then solve the time-dependent Schrödinger equation:

$$\hat{H}(t)\psi(t) = i\hbar\frac{\partial\psi(t)}{\partial t} \tag{iv}$$

where the time-dependent interaction is represented by a time-dependent hamiltonian.

Spin operators and spin states

The total nuclear wavefunction Ψ, can be approximately factorized into a spatial and a spin part:

$$\Psi = \psi_{\text{spin}}\psi_{\text{space}} \tag{v}$$

where ψ_{spin} is a function, the *nuclear spin wavefunction* describing the spin state of the nucleus, which depends only on the nuclear spin coordinates and ψ_{space} is a function depending only on the spatial coordinates of the nucleus. We shall be dealing almost exclusively with the wavefunctions describing the *spin states* of nuclei. Fortunately, the spin and spatial parts of a nuclear wavefunction are largely uncoupled; that is, the spatial position of a nucleus is largely unaffected by its spin coordinates and *vice versa*.[1]*

Continued on p. 10

* Notes are given on p. 71.

Box 1.1 *Cont.*

To determine the spin properties of a nucleus, we operate on the nuclear spin wavefunction with *spin operators*, i.e. operators which act only on the spin coordinates of the nuclear wavefunction.

For a single spin, a consistent set of spin operators which allow all possible spin properties of a nucleus to be determined are: $\hat{I}^2$, the operator for the magnitude of the nuclear spin squared, $\hat{I}_x$, $\hat{I}_y$ and $\hat{I}_z$, which are the operators for the x, y and z components of nuclear spin respectively. These are *single spin operators*, i.e. they act only on wavefunctions describing one spin. These are related via

$$\hat{I}^2 = \hat{I}_x^2 + \hat{I}_y^2 + \hat{I}_z^2 \tag{vi}$$

If two operators commute, it can be shown that they have identical eigenfunctions. The *commutator* of two operators $\hat{A}$ and $\hat{B}$, $\lfloor \hat{A}, \hat{B} \rfloor$ is defined as

$$[\hat{A}, \hat{B}] = \hat{A}\hat{B} - \hat{B}\hat{A} \tag{vii}$$

Now $\hat{I}^2$ commutes with $\hat{I}_z$. Hence, $\hat{I}^2$ and $\hat{I}_z$ have identical eigenfunctions; they are specified by the quantum numbers I and m and are denoted ψ_{Im}. The eigenfunctions of $\hat{I}_z$ for $I = \frac{1}{2}$ are often denoted α ($m = \frac{1}{2}$) and β ($m = -\frac{1}{2}$). The quantum number I can take the values 0, $\frac{1}{2}$, 1, $\frac{3}{2}$, 2, . . . , etc. and m, the values I, $I - 1$, . . . , $-I$. Hence, we talk of ^{1}H being a 'spin-$\frac{1}{2}$' nucleus, i.e. $I = \frac{1}{2}$, ^{23}Na, a spin-$\frac{3}{2}$ nucleus ($I = \frac{3}{2}$) and so on.

The eigenvalues corresponding to the ψ_{Im} are defined by the eigenvalue equations:

$$\begin{aligned} \hat{I}^2\psi_{Im} &= I(I+1)\hbar\psi_{Im} \\ \hat{I}_z\psi_{Im} &= m\hbar\psi_{Im} \end{aligned} \tag{viii}$$

However, in NMR, the factor of $\hbar$ in these eigenvalues is commonly ignored, and included instead as part of the operator, i.e.

$$\begin{aligned} \hat{I}^2\psi_{Im} &= I(I+1)\psi_{Im} \\ \hat{I}_z\psi_{Im} &= m\psi_{Im} \end{aligned} \tag{ix}$$

or

$$\begin{aligned} \hbar\hat{I}^2\psi_{Im} &= I(I+1)\hbar\psi_{Im} \\ \hbar\hat{I}_z\psi_{Im} &= m\hbar\psi_{Im} \end{aligned} \tag{x}$$

We shall adopt this latter convention also. The expectation values of $\hat{I}^2$ and $\hat{I}_z$ (see Equation (i)), i.e. the magnitude of the nuclear spin angular momentum squared and the z component of the nuclear spin angular momentum respectively, when the wavefunction describing the system is an eigenfunction of $\hat{I}^2$ and $\hat{I}_z$ are given by:

$$\langle I^2 \rangle = \frac{\int \psi_{Im} * \hat{I}^2 \psi_{Im} d\tau}{\int \psi_{Im} * \psi_{Im} d\tau}$$
$$= I(I+1) \frac{\int \psi_{Im} * \psi_{Im} d\tau}{\int \psi_{Im} * \psi_{Im} d\tau}$$
$$= I(I+1) \quad \text{(xi)}$$

and

$$\langle I_z \rangle = \frac{\int \psi_{Im} * \hat{I}_z \psi_{Im} d\tau}{\int \psi_{Im} * \psi_{Im} d\tau} = m \quad \text{(xii)}$$

That is, the expectation values of $\hat{I}^2$ and $\hat{I}_z$ when the spin state is described by one of their eigenfunctions, are simply the eigenvalues of the respective operators.

If the hamiltonian for a spin system can be described entirely in terms of $\hat{I}^2$ and $\hat{I}_z$ operators only, then the spin wavefunctions of the system are eigenfunctions of $\hat{I}^2$ and $\hat{I}_z$, i.e. ψ_{Im}. If not, providing the spin system consists of non-interacting nuclei so that the hamiltonian only involves single spin operators, we can describe the spin wavefunction, Ψ as a linear combination of the ψ_{Im} functions, i.e.

$$\Psi = \sum_m c_m \psi_{Im} \quad \text{(xiii)}$$

where the c_m are the combination coefficients in the eigenfunction Ψ of the system. The ψ_{Im} are said to be the *basis* or *basis set* for the expansion of Ψ. Substituting Equation (xiii) for Ψ into the time-independent Schrödinger equation, we have

$$\hat{H}\Psi = E\Psi$$
$$\Rightarrow \hat{H}\left(\sum_m c_m \psi_{Im} \right) = E \sum_m c_m \psi_{Im}$$
$$\Rightarrow \sum_m c_m \hat{H} \psi_{Im} = E \sum_m c_m \psi_{Im} \quad \text{(xiv)}$$

We find the combination coefficients $\{c_m\}$ by multiplying from the left by each possible ψ^*_{Im} in turn and integrating over all spin space, so generating $(2I + 1)$ simultaneous equations. Each equation so generated has the form

$$\sum_m c_m \int \psi_{Im'} * \hat{H} \psi_{Im} d\tau = E \sum_m c_m \int \psi_{Im'} * \psi_{Im} d\tau$$
$$\Rightarrow \sum_m c_m \int \psi_{Im'} * \hat{H} \psi_{Im} d\tau - E c_{m'} = 0 \quad \text{(xv)}$$

Continued on p. 12

Box 1.1 *Cont.*

where in the final step we have used the fact that the ψ_{Im} are orthogonal and normalized, i.e. $\int \psi_{Im'} * \psi_{Im} d\tau = \delta_{m'm}$. Equation (xv) can be rewritten in matrix form:

$$(\mathbf{H} - E\mathbf{1}) \cdot \mathbf{c} = 0 \tag{xvi}$$

where the elements of the matrix **H** are

$$H_{m'm} = \int \psi_{Im'} * \hat{H} \psi_{Im} d\tau \tag{xvii}$$

and the vector **c** contains the combination coefficients, c_m; **1** is a (diagonal) unit matrix. The $(2I + 1)$ simultaneous equations represented by Equation (xvi) can be solved by setting

$$\det | \mathbf{H} - E\mathbf{1} | = 0 \tag{xviii}$$

and finding the $(2I + 1)$ values of E. Substituting any one of these back into the Equations (xv) allows the c_m coefficients to be determined for the wavefunction corresponding to that value of E.

Dirac's bra-ket notation

When dealing with integrals of the form in Equation (xv), it is often easier to use Dirac's bra-ket notation, and we will use this notation throughout this book. In the notation, the integral in Equation (xv) is written

$$\int \psi_{Im'} * \hat{H} \psi_{Im} d\tau = \langle I, m' | \hat{H} | I, m \rangle \tag{xix}$$

where, the *bra* is

$$\langle I, m' | = \psi_{Im'} * \tag{xx}$$

and the *ket* is

$$| I, m \rangle = \psi_{Im} \tag{xxi}$$

Note that $\langle I, m|$ is the complex conjugate of $|I, m\rangle$ and that the presence of a ket and bra implies integration over all variables in ψ_{Im}.

Matrices

The matrix representations of operators such as hamiltonians (Equation (xvii)) are frequently needed in NMR. The ψ_{Im} functions involved in the integrals in each matrix element in Equation (xvii) for instance are the *basis functions* for

the representation. Below, for future use, are the matrices of the $\hat{I}^2$, $\hat{I}_x$, $\hat{I}_y$, $\hat{I}_z$ operators in the spin-$\frac{1}{2}$ basis, $\psi_{\frac{1}{2},\frac{1}{2}}$ and $\psi_{\frac{1}{2},-\frac{1}{2}}$, otherwise denoted α and β.

$$\begin{aligned} \mathbf{I}^2 &= \frac{3}{4}\begin{pmatrix} 1 & 0 \\ 0 & 1 \end{pmatrix} \qquad \mathbf{I}_x = \frac{1}{2}\begin{pmatrix} 0 & 1 \\ 1 & 0 \end{pmatrix} \\ \mathbf{I}_y &= -\frac{i}{2}\begin{pmatrix} 0 & -1 \\ 1 & 0 \end{pmatrix} \quad \mathbf{I}_z = \frac{1}{2}\begin{pmatrix} 1 & 0 \\ 0 & -1 \end{pmatrix} \end{aligned} \tag{xxii}$$

where each matrix is

$$\mathbf{A} = \begin{pmatrix} \langle \alpha|\hat{A}|\alpha\rangle & \langle \alpha|\hat{A}|\beta\rangle \\ \langle \beta|\hat{A}|\alpha\rangle & \langle \beta|\hat{A}|\beta\rangle \end{pmatrix} \tag{xxiii}$$

The matrix elements of $\hat{I}_x$ and $\hat{I}_y$ are evaluated using the *raising* and *lowering* operators, which are defined as

$$\hat{I}_{\pm} = \hat{I}_x \pm \hat{I}_y \tag{xxiv}$$

such that

$$\hat{I}_x = \frac{1}{2}(\hat{I}_+ + \hat{I}_-) \qquad \hat{I}_y = -\frac{i}{2}(\hat{I}_+ - \hat{I}_-) \tag{xxv}$$

The action of these operators on a function ψ_{Im} is

$$\begin{aligned} \hat{I}_+|I,m\rangle &= (I(I+1) - m(m+1))^{\frac{1}{2}}|I,m+1\rangle \\ \hat{I}_-|I,m\rangle &= (I(I+1) - m(m-1))^{\frac{1}{2}}|I,m-1\rangle \end{aligned} \tag{xxvi}$$

In other words, $\hat{I}_+$ creates a new wavefunction with the quantum number m raised by 1, whilst $\hat{I}_-$ creates one with m lowered by 1. Note that if $\hat{I}_+$ operates on a wavefunction with the maximum value of m (for a given I), the result is zero, and similarly for $\hat{I}_-$ operating on a wavefunction with minimum m, i.e.

$$\hat{I}_+|I,I\rangle = 0 \qquad \hat{I}_-|I,-I\rangle = 0 \tag{xxvii}$$

1.2.1 Nuclei in a static, uniform field

The simplest spin system is that consisting of an isolated spin in the static, uniform magnetic field of the NMR experiment, with no other interactions present. The hamiltonian $\hat{H}$ for a nuclear spin in a static field is

$$\hat{H} = -\hat{\boldsymbol{\mu}} \cdot \mathbf{B}_0 \tag{1.9}$$

where $\hat{\boldsymbol{\mu}}$ is the nuclear magnetic moment operator and $\mathbf{B}_0$ is the magnetic field applied in the NMR experiment. This hamiltonian is often referred to as the *Zeeman hamiltonian*. In turn, $\hat{\boldsymbol{\mu}}$ can be written in terms of the nuclear spin operator $\hat{\mathbf{I}}$:[2]

$$\hat{\boldsymbol{\mu}} = \gamma\hbar\hat{\mathbf{I}} \tag{1.10}$$

The applied field is taken to be along z, so combining Equations (1.9) and (1.10), we have

$$\hat{H} = -\gamma\hbar\hat{I}_z B_0 \tag{1.11}$$

The *eigenfunctions* of $\hat{H}$ are the wavefunctions describing the possible states of the spin system in the $\mathbf{B}_0$ field. Since $\hat{H}$ is proportional to the operator $\hat{I}_z$ in this case, the eigenfunctions of $\hat{H}$ are the eigenfunctions of $\hat{I}_z$, which are simply written as $|I,m\rangle$ in *bra-ket* notation, or alternatively as ψ_{Im}, where I is the nuclear spin quantum number. The quantum number m can take $2I + 1$ values: I, $I - 1$, $I - 2$, . . . , $-I$. The *eigenvalues* of $\hat{H}$ are the energies associated with the different possible states of the spin. The eigenvalues are obtained by operating with $\hat{H}$ on the spin wavefunctions:

$$\hat{H}|I,m\rangle = E_{I,m}|I,m\rangle \tag{1.12}$$

where $E_{I,m}$ is the energy of the eigenstate $|I,m\rangle$. Substituting Equation (1.11) for $\hat{H}$ in Equation (1.12) yields

$$\hat{H}|I,m\rangle = -(\gamma\hbar B_0)\hat{I}_z|I,m\rangle = -(\gamma\hbar B_0)m|I,m\rangle \tag{1.13}$$

since $|I,m\rangle$ is an eigenfunction of $\hat{I}_z$, with eigenvalue m, i.e.

$$\hat{I}_z|I,m\rangle = m|I,m\rangle \tag{1.14}$$

The energies of the eigenstates are obtained from comparing Equations (1.12) and (1.13):

$$E_{I,m} = -\gamma\hbar B_0 m \tag{1.15}$$

For a spin with $I = \frac{1}{2}$, $m = \pm\frac{1}{2}$ so there are two possible eigenstates with energies $E_{\frac{1}{2},\pm\frac{1}{2}} = \mp\frac{1}{2}\gamma\hbar B_0$ (Fig. 1.4). These states are frequently referred to as the *Zeeman states*. The transition energy ΔE between the spin states is $\gamma\hbar B_0$. In frequency units, this corresponds to ω_0 ($= \gamma B_0$), the Larmor frequency in the vector model. Note however, that the Larmor frequency in the vector model corresponds to a rotation of the net nuclear magnetization vector about $\mathbf{B}_0$ and not to a transition.

So in a sample of non-interacting spin-$\frac{1}{2}$ nuclei, each spin system can exist in one of two possible eigenstates. At equilibrium, there is a Boltzmann distribution of nuclear spins over these two states, the population of each eigenstate ψ, being p_ψ given by

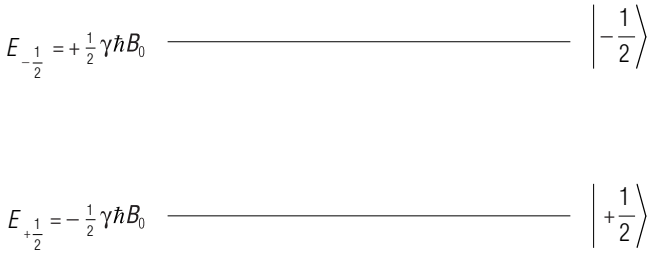

Fig. 1.4 The energy levels for a spin-$\frac{1}{2}$ nucleus in an applied magnetic field $\mathbf{B}_0$ (positive γ). The levels are labelled according to their magnetic quantum number, *m*.

$$p_\psi = \frac{\exp(-E_\psi/kT)}{\sum_{\psi'}\exp(-E_{\psi'}/kT)} \tag{1.16}$$

where E_ψ is the energy of the ψ eigenstate. For spin-$\frac{1}{2}$ nuclei, $\Sigma_{m=\pm\frac{1}{2}}\exp(-E_m/kT) \approx 2$.

The nature of the eigenstates and their respective populations determines all the properties of the ensemble of spin systems in the sample and hence determine the outcome of any NMR experiment on the sample. For instance, the expectation value of the *z* magnetization for the sample is given by a sum of contributions from each possible eigenstate, scaled by the population of each eigenstate. We call this the *ensemble average* of the *z* magnetization, and denote it by a bar over the appropriate quantities, i.e. those which are averaged over the sample:

$$\overline{\langle\hat{\mu}_z\rangle} = \gamma\hbar\overline{\langle\hat{I}_z\rangle} = \gamma\hbar\sum_\psi p_\psi\langle\psi|\hat{I}_z|\psi\rangle \tag{1.17}$$

where $\gamma\hbar\langle\psi|\hat{I}_z|\psi\rangle$ is the expectation value of the *z* magnetization for a spin in eigenstate ψ.

In this picture of the spin ensemble, each spin system is in one of the possible eigenstates of the hamiltonian describing a single spin, the probability of it being in the ψ eigenstate is p_ψ. Alternatively, we can describe each spin system as being in the same superposition state, Ψ, where

$$\Psi = \sum_\psi \sqrt{p_\psi}\,|\psi\rangle \tag{1.18}$$

This is a completely equivalent approach, as identical spin systems in the sample cannot be distinguished nor their individual spin states observed in the NMR experiment. All we can observe is the ensemble average, and whether we choose to describe the spin systems of the sample as being distributed over a set of eigenstates or in some superposition state, the same ensemble properties are calculated. For instance, if we use the superposition state Ψ to calculate the expectation value of *z* magnetization, we obtain

$$\overline{\langle\hat{\mu}_z\rangle} = \gamma\hbar\langle\Psi|\hat{I}_z|\Psi\rangle = \gamma\hbar\sum_\psi p_\psi\langle\psi|\hat{I}_z|\psi\rangle \tag{1.19}$$

which is the same expression obtained previously (Equation (1.17)) by considering the distribution of spins over the possible eigenstates for each spin.

Expanding Equation (1.17) or equivalently (1.19) for the two-level system corresponding to isolated spin-$\frac{1}{2}$ nuclei in the $\mathbf{B}_0$ field, we have

$$\begin{aligned}\overline{\langle\hat{\mu}_z\rangle} &= \gamma\hbar\left(p_{\frac{1}{2}}\left\langle\frac{1}{2},\frac{1}{2}\middle|\hat{I}_z\middle|\frac{1}{2},\frac{1}{2}\right\rangle + p_{-\frac{1}{2}}\left\langle\frac{1}{2},-\frac{1}{2}\middle|\hat{I}_z\middle|\frac{1}{2},-\frac{1}{2}\right\rangle\right)\\ &= \gamma\hbar\left(\frac{1}{2}p_{\frac{1}{2}} - \frac{1}{2}p_{-\frac{1}{2}}\right)\\ &= \frac{1}{2}\gamma\hbar\left(p_{\frac{1}{2}} - p_{-\frac{1}{2}}\right)\end{aligned} \tag{1.20}$$

where $p_{\pm\frac{1}{2}}$ are the populations of the respective spin states. In other words, the z magnetization corresponds to the population difference between the two spin states.

1.2.2 The effect of rf pulses

An rf pulse introduces an oscillating magnetic field, $\mathbf{B}_1(t)$ into the spin system. The time-dependence of the magnetic field in this case means that both the eigenstates of the spin systems and their energies are time-dependent, in contrast to the previous case considered of the nuclei in the static field $\mathbf{B}_0$. We will find that the eigenstates of the hamiltonian describing the spin systems in this case are time-dependent, linear combinations of the Zeeman states found previously, i.e. the eigenstates for spins in a static field, $\mathbf{B}_0$. Thus, we say that the oscillating field $\mathbf{B}_1(t)$ *mixes* the Zeeman states. The hamiltonian, $\hat{H}$, describing a single spin in this situation must now include the interaction of the nuclear spin with both the static $\mathbf{B}_0$ field along z and the oscillating $\mathbf{B}_1(t)$ field, which will be taken to oscillate along x. The total field felt by the nucleus is then

$$\mathbf{B}_{\text{total}}(t) = \mathbf{i}B_1\cos(\omega_{\text{rf}}t) + \mathbf{k}B_0 \tag{1.21}$$

where $\mathbf{i}$ and $\mathbf{k}$ are unit vectors along x and z respectively. Bearing in mind that the general form for a hamiltonian describing the interaction of a nuclear spin $\mathbf{I}$ with a field $\mathbf{B}$ is

$$\hat{H} = -\hat{\boldsymbol{\mu}}\cdot\mathbf{B} = -\gamma\hbar\,\hat{\mathbf{I}}\cdot\mathbf{B} \tag{1.22}$$

the hamiltonian for the current case is then

$$\hat{H} = -\gamma\hbar\left(\hat{I}_z B_0 + \hat{I}_x B_1\cos(\omega_{\text{rf}}t)\right) \tag{1.23}$$

As in the vector model, the oscillating $\mathbf{B}_1$ vector can be written as two counter-rotating components. It can be shown that only one of these components has any significant effect on the spin system, allowing the hamiltonian of Equation (1.23) to be re-written as (see Box 1.2 for details)

$$\hat{H} = -\gamma\hbar\left(\hat{I}_z B_0 + B_1 e^{-i\omega_{rf}t\hat{I}_z}\hat{I}_x e^{+i\omega_{rf}t\hat{I}_z}\right) \tag{1.24}$$

Ultimately, we want to find the (time-dependent) wavefunctions Ψ corresponding to $\hat{H}$ in Equation (1.23). We are thus obliged to use the *time-dependent Schrödinger equation* to find the spin system eigenfunctions, rather than the time-independent Schrödinger equation of (1.11). The time-dependent Schrödinger equation is

$$-\frac{\hbar}{i}\frac{\partial\psi(t)}{\partial t} = \hat{H}(t)\psi(t) \tag{1.25}$$

where $\psi(t)$ are the (time-dependent) wavefunctions describing the spin system. To proceed, we need to remove the time-dependence of the hamiltonian (Equation (1.23)) by transforming into a rotating frame identical to that used in the vector model previously, i.e. one rotating about $\mathbf{B}_0$ at rate ω_{rf}. The hamiltonian in this frame becomes $\hat{H}'$ where

$$\hat{H}' = -\hbar\left((\gamma B_0 - \omega_{rf})\hat{I}_z + \gamma B_1\hat{I}_x\right) \tag{1.26}$$

and the wavefunction ψ becomes

$$\psi' = e^{-i\psi_{rf}t\,\hat{I}_z}\,\Psi \tag{1.27}$$

in the new rotating frame where the operator $e^{-i\psi_{rf}t\hat{I}_z}$ is the rotation operator required to *rotate the (spin coordinate) axis frame* in which the spin wavefunction is defined about the axis frame z by angle $\omega_{rf}t$ (see Box 1.2 for details). Using these in the time-dependent Schrödinger equation (Equation (1.25)) we obtain

$$-\frac{\hbar}{i}\frac{\partial\psi'}{\partial t} = -\hbar\left((\gamma B_0 - \omega_{rf})\hat{I}_z + \gamma B_1\hat{I}_x\right)\psi' \tag{1.28}$$

where the time-dependence has been removed by transforming the whole problem to the rotating frame.

We will solve the differential Equation (1.28) for the specific case of a spin system consisting of an isolated spin-$\frac{1}{2}$ nuclei. In the following discussion, we will use the eigenfunctions of the spin operator $\hat{I}_z$, $|\frac{1}{2},\frac{1}{2}\rangle$ and $|\frac{1}{2},-\frac{1}{2}\rangle$, i.e. the Zeeman states, which we shall abbreviate to $|\frac{1}{2}\rangle$ and $|-\frac{1}{2}\rangle$ depicting only the m spin quantum number for clarity. These functions form a complete set for a spin-$\frac{1}{2}$ nucleus, and so any state of a spin-$\frac{1}{2}$ nucleus can be expressed as some linear combination of them, albeit with time-dependent combination coefficients as will be the case here. So we write the eigenfunctions of Equation (1.28) that we seek as

$$\Psi'(t) = c_{\frac{1}{2}}\left(t\right)\left|\frac{1}{2}\right\rangle + c_{-\frac{1}{2}}\left(t\right)\left|-\frac{1}{2}\right\rangle \tag{1.29}$$

Substituting this into Equation (1.28) we obtain

$$\frac{\hbar}{i}\left(\left|\frac{1}{2}\right\rangle\frac{\mathrm{d}c_{\frac{1}{2}}}{\mathrm{d}t}+\left|-\frac{1}{2}\right\rangle\frac{\mathrm{d}c_{-\frac{1}{2}}}{\mathrm{d}t}\right)=(\gamma B_1\hat{I}_x)\left(c_{\frac{1}{2}}\left|\frac{1}{2}\right\rangle+c_{-\frac{1}{2}}\left|-\frac{1}{2}\right\rangle\right) \tag{1.30}$$

By multiplying this equation from the left by $\langle\frac{1}{2}|$, integrating over all spin space and using the orthonormality of $|+\frac{1}{2}\rangle$ and $|-\frac{1}{2}\rangle$ we obtain

$$\frac{\hbar}{i}\frac{\mathrm{d}c_{\frac{1}{2}}}{\mathrm{d}t}=\frac{1}{2}\gamma\hbar B_1 c_{-\frac{1}{2}} \tag{1.31}$$

where we have evaluated the matrix elements of $\hat{I}_x$ using Equations (xxii) in Box 1.1. Now multiplying Equation (1.30) from the left by $\langle-\frac{1}{2}|$ instead, we obtain a second equation:

$$\frac{\hbar}{i}\frac{\mathrm{d}c_{-\frac{1}{2}}}{\mathrm{d}t}=\frac{1}{2}\gamma\hbar B_1 c_{\frac{1}{2}} \tag{1.32}$$

Equations (1.31) and (1.32) are simultaneous equations which we can easily solve to find expressions for $c_{\pm\frac{1}{2}}$, the combination coefficients in Equation (1.29):

$$\begin{aligned} c_{\frac{1}{2}}(t)&=c_{\frac{1}{2}}(0)\cos\left(\frac{1}{2}\omega_1 t\right)-ic_{-\frac{1}{2}}(0)\,\sin\left(\frac{1}{2}\omega_1 t\right)\\ c_{-\frac{1}{2}}(t)&=c_{-\frac{1}{2}}(0)\cos\left(\frac{1}{2}\omega_1 t\right)+ic_{\frac{1}{2}}(0)\,\sin\left(\frac{1}{2}\omega_1 t\right)\end{aligned} \tag{1.33}$$

where $\omega_1=\gamma B_1$ as usual and $c_{\pm\frac{1}{2}}(0)$ are the combination coefficients at time $t=0$, i.e. at the start of the pulse. For any given spin system in the sample, the $c_{\pm\frac{1}{2}}(0)$ are simply 1 or 0 depending on which of the two possible initial states, $|\pm\frac{1}{2}\rangle$, the spin system is in at the start of the pulse. Equations (1.33) with the $c_{\pm\frac{1}{2}}(0)$ coefficients set to 1 and 0 or vice versa then describe the two possible time-dependent states of that one spin system. The population of each of these states over the sample as a whole is determined by the populations of the initial starting states, $|\pm\frac{1}{2}\rangle$.

Alternatively, we can find the superposition state (Equation (1.18)) which effectively describes each spin system in the sample by using the superposition state at $t=0$, i.e. in the absence of the pulse, to determine the coefficients $c_{\pm\frac{1}{2}}(0)$. We have already seen that in the absence of a pulse, each spin system can be described by a single superposition state of the form:

$$\Psi(0)=\sqrt{p_{\frac{1}{2}}}\left|\frac{1}{2}\right\rangle+\sqrt{p_{-\frac{1}{2}}}\left|-\frac{1}{2}\right\rangle \tag{1.34}$$

where $\sqrt{p_{\pm\frac{1}{2}}}$ are the square roots of the populations of the Zeeman states for the spin system $|\pm\frac{1}{2}\rangle$; these can be substituted for the $c_{\pm\frac{1}{2}}(0)$ coefficients in Equations (1.33) to find the $c_{\pm\frac{1}{2}}(t)$ coefficients which define the time-dependent superposition state

describing each of the spin systems during the rf pulse. As in Equation (1.34), these coefficients then correspond to the square roots of the 'populations' of the $|\pm\frac{1}{2}\rangle$ functions. In making this statement however, we must recognize that the eigenstates of the spin system during an rf pulse are time-dependent mixtures of these functions and not the $|\pm\frac{1}{2}\rangle$ states themselves.

There are a couple of interesting points to note about Equations (1.33). If a 90° pulse is applied, i.e. $\omega_1 t = \pi/2$, then at the end of the pulse, $t = \pi/(2\omega_1) = t_p$, the average spin state coefficients are

$$\begin{aligned} c_{\frac{1}{2}}(t_p) &= \sqrt{p_{\frac{1}{2}}(0)}\cos(\pi/4) - i\sqrt{p_{-\frac{1}{2}}(0)}\sin(\pi/4) \\ c_{-\frac{1}{2}}(t_p) &= \sqrt{p_{-\frac{1}{2}}(0)}\cos(\pi/4) + i\sqrt{p_{\frac{1}{2}}(0)}\sin(\pi/4) \end{aligned} \tag{1.35}$$

so that the populations $p_{\pm\frac{1}{2}}(t_p) = c_{\pm\frac{1}{2}}(t_p) * c_{\pm\frac{1}{2}}(t_p)$ are simply

$$\begin{aligned} p_{\frac{1}{2}}(t_p) &= \frac{1}{2}\left(p_{\frac{1}{2}}(0) + p_{-\frac{1}{2}}(0)\right) \\ p_{-\frac{1}{2}}(t_p) &= \frac{1}{2}\left(p_{-\frac{1}{2}}(0) + p_{\frac{1}{2}}(0)\right) \end{aligned} \tag{1.36}$$

since $\cos(\pi/4) = \sin(\pi/4) = \frac{1}{\sqrt{2}}$. In other words, the populations of the $|\pm\frac{1}{2}\rangle$ functions are equal after a 90° pulse. A similar analysis for a 180° pulse shows that the populations of the $|\pm\frac{1}{2}\rangle$ functions are inverted at the end of a 180° pulse, i.e.

$$p_{\frac{1}{2}}(t_p) = p_{-\frac{1}{2}}(0) \qquad p_{-\frac{1}{2}}(t_p) = p_{\frac{1}{2}}(0) \tag{1.37}$$

Finally, we know from the vector model that an x pulse creates y magnetization in the rotating frame. To calculate the expectation value of y magnetization in the rotating frame in the quantum mechanical model, we use the definition of expectation value (Equation (i) in Box 1.1 above) with Equations (1.29) and (1.33) for the rotating frame eigenfunctions Ψ':

$$\begin{aligned} \langle\hat{\mu}_y(t)\rangle &= \gamma\hbar\langle\hat{I}_y(t)\rangle = \gamma\hbar\langle\Psi'(t)|\hat{I}_y|\Psi'(t)\rangle \\ &= \gamma\hbar\left(c_{-\frac{1}{2}}(t) * c_{\frac{1}{2}}(t)\left\langle -\frac{1}{2}\middle|\hat{I}_y\middle|\frac{1}{2}\right\rangle + c_{\frac{1}{2}}(t) * c_{-\frac{1}{2}}(t)\left\langle\frac{1}{2}\middle|\hat{I}_y\middle|-\frac{1}{2}\right\rangle\right) \\ &= -\frac{1}{2}\gamma\hbar\left(c_{\frac{1}{2}}(0)^2 - c_{-\frac{1}{2}}(0)^2\right)\sin(\omega_1 t) \end{aligned} \tag{1.38}$$

where we have substituted Ψ' (and the coefficients $c_{\pm\frac{1}{2}}(t)$ within Ψ') and evaluated the matrix elements of $\hat{I}_y$, $\langle\pm\frac{1}{2}|\hat{I}_y|\mp\frac{1}{2}\rangle$. The y magnetization in Equation (1.38) can be re-written in terms of the populations of the $|\pm\frac{1}{2}\rangle$ functions:

$$\langle \hat{\mu}_y(t) \rangle = -\frac{1}{2}\gamma\hbar\left(p_{\frac{1}{2}}(0) - p_{-\frac{1}{2}}(0) \right)\sin(\omega_1 t) \tag{1.39}$$

Comparing this with Equation (1.20) for the z magnetization in the $\mathbf{B}_0$ field prior to the rf pulse, we see that the y magnetization is equal to the initial z magnetization multiplied by a factor $-\sin(\omega_1 t)$, which is the same result that the vector model gave us.

Box 1.2 Exponential operators, rotation operators and rotations

In NMR, we frequently use *exponential operators* which have the form $e^{\hat{A}}$ where $\hat{A}$ itself is an operator. An exponential operator is defined through the series expansion for an exponential:

$$e^{\hat{A}} = 1 + \hat{A} + \frac{\hat{A}^2}{2!} + \frac{\hat{A}^3}{3!} + \ldots \tag{i}$$

One of the properties of exponential operators which we will use from time to time is that $e^{(\hat{A}+\hat{B})} = e^{\hat{A}} e^{\hat{B}}$ only if the operators $\hat{A}$ and $\hat{B}$ commute (see Box 1.1 for definition of commutation).

Rotation of vectors, wavefunctions and operators (active rotations)

A special class of exponential operators are the *rotation operators* which have the form $e^{-i\phi \hat{L}_\alpha}$ where $\hat{L}_\alpha$ is the operator for the α component of angular momentum. As we will show below, $e^{-i\phi \hat{L}_\alpha}$ is an operator for a rotation about the axis α by angle ϕ. Rotation operators can be used for rotating axis frames, vectors, functions, such as wavefunctions and operators. Rotation of an object within an axis frame is called an *active rotation*; in such an operation, the axis frame remains unchanged, but the orientation of the object with respect to the frame changes. Perhaps the simplest such rotation operation is the rotation of a Cartesian vector, $\mathbf{v}$ within the axis frame within which the vector is defined. The rotated vector $\mathbf{v}'$ is given by

$$\mathbf{v}' = \hat{R}\mathbf{v} \tag{ii}$$

where $\hat{R}$ is the rotation operator. In this book, we are primarily interested in the rotation of wavefunctions and operators within their defining axis frames. The transformation required to rotate a wavefunction ψ (or indeed any other type of function defined with respect to a Cartesian axis frame) is

$$\psi' = \hat{R}\psi \tag{iii}$$

where ψ' is the rotated wavefunction.

We can easily demonstrate that $e^{-i\phi \hat{L}\alpha}$ represents a rotation operator for rotation of an object about axis α by angle ϕ by considering a specific example. Consider the rotation of a function $f(x,y,z) = x$ (i.e. the value of the function at all points in space is simply the value of the x coordinate) by angle ϕ about z. The rotated function, $f'(x,y,z)$ is given by

$$f'(x,y,z) = \hat{R}_z(\phi)f(x,y,z) = e^{-i\phi\hat{L}_z}x \tag{iv}$$

Now, we can use the series expansion of Equation (i) to expand $e^{-i\phi \hat{L}_z}$ in Equation (iv):

$$e^{-i\phi\hat{L}_z}x = x - i\phi\hat{L}_z x - \frac{\phi^2}{2}\hat{L}_z^2 x + \ldots \tag{v}$$

We can then use the definition of the angular momentum operator $e^{-i\phi \hat{L}_z}$ to find how $e^{-i\phi \hat{L}_z}$ operates on x. The definition of $e^{-i\phi \hat{L}_z}$ is[3]

$$\hat{L}_z = \frac{1}{i}\left(\hat{x}\frac{\partial}{\partial y} - \hat{y}\frac{\partial}{\partial x}\right) \tag{vi}$$

where $\hat{x}$, $\hat{y}$ are the operators for position along x and y respectively and whose operations are multiplied by x and y respectively. Using this definition in Equation (v), we obtain

$$e^{-i\phi\hat{L}_z}x = x + y\phi - \frac{\phi^2}{2}x + \ldots \tag{vii}$$

which can be rewritten as

$$e^{-i\phi\hat{L}_z}x = x\cos\phi + y\sin\phi = f'(x,y,z) \tag{viii}$$

where we have used the series expansions for sine and cosine:

$$\cos\phi = 1 - \frac{\phi^2}{2} + \ldots \quad \sin\phi = \phi - i\frac{\phi^3}{6} + \ldots \tag{ix}$$

That Equation (viii) represents the rotated function $f'(x,y,z)$ can be easily seen as follows. Consider a line of points along the x axis, i.e. points with coordinates $(x,0,0)$ and their corresponding values of $f(x,y,z)$ (the original function before rotation). The values of f for these points are of course just x, for a function

Continued on p. 22

Box 1.2 *Cont.*

$f(x,y,z) = x$, i.e. the value of the function is the distance from the origin along this line of points. Now consider the rotation of f by angle ϕ about z. The part of the function that lay along x now lies along a line in the x–y plane which is oriented an angle ϕ from the x axis. The coordinates of points along this line are $(r\cos\phi, r\sin\phi, 0)$ where r is the distance along the line from the origin. If we use these coordinates in the rotated function $f'(x,y,z)$ of Equation (viii), to obtain the values of the rotated function along this line, we get $f'(r\cos\phi, r\sin\phi, 0) = r\cos^2\phi + r\sin^2\phi = r$, i.e. the value of the function is equal to the distance from the origin along this new line. The rotated function at points along this line is thus equal to the original unrotated function at points along x, as it should be.

To rotate an operator within its defining axis frame, we must perform a transformation of the form

$$\hat{B}' = \hat{R}\,\hat{B}\,\hat{R}^{-1} \tag{x}$$

where $\hat{R}$ is the rotation operator, $\hat{B}$ the operator being rotated and $\hat{B}'$ the operator after rotation, i.e. the rotated operator.

In NMR, we frequently come across exponential operators of the form $e^{-i\phi\hat{I}_\alpha}$ which have a similar form to a rotation operator with the angular momentum operator replaced with a spin angular momentum operator. Indeed, it can be shown that $e^{-i\phi\hat{I}_\alpha}$ represents a rotation operator which acts on spin coordinates (rather than spatial coordinates as in the example above), because, of course, $\hat{I}_\alpha$ acts only on spin coordinates. We can demonstrate this with an example, using the transformation of Equation (x) to rotate a spin operator, $\hat{I}_x$, with $\hat{R}_z(\phi) = e^{-i\phi\hat{I}_z}$:

$$\begin{aligned}\hat{R}_z(\phi)\hat{I}_x\hat{R}_z(\phi)^{-1} &= e^{-i\phi\hat{I}_z}\hat{I}_x\,e^{+i\phi\hat{I}_z}\\ &= \left(1 - i\phi\hat{I}_z - \frac{\phi^2}{2}\hat{I}_z^2 + \ldots\right)\hat{I}_x\left(1 + i\phi\hat{I}_z - \frac{\phi^2}{2}\hat{I}_z^2 + \ldots\right)\\ &= \hat{I}_x - i\phi[\hat{I}_z,\hat{I}_x] - \frac{\phi^2}{2}[\hat{I}_z,[\hat{I}_z,\hat{I}_x]]\\ &\quad + \frac{i\phi^3}{6}[\hat{I}_z,[\hat{I}_z,[\hat{I}_z,\hat{I}_x,]]] + \ldots\end{aligned} \tag{xi}$$

using the series expansion of the exponential operators (Equation (i)). To proceed further, we need to simplify the commutators in Equation (xi). The Cartesian spin operators do not commute among themselves, but the following commutation relation exists

$$\lfloor\hat{I}_x,\hat{I}_y\rfloor = i\hat{I}_z \tag{xii}$$

and all cyclic permutations of this, i.e.

$$\lfloor \hat{I}_z, \hat{I}_x \rfloor = i\hat{I}_y \quad \lfloor \hat{I}_y, \hat{I}_z \rfloor = i\hat{I}_x \tag{xiii}$$

Using the commutation relations of Equations (xii) and (xiii), we can simplify equation (xi) quite considerably:

$$\begin{aligned}
&\hat{I}_x - i\phi[\hat{I}_z, \hat{I}_x] - \frac{\phi^2}{2}[\hat{I}_z, [\hat{I}_z, \hat{I}_x]] + \frac{i\phi^3}{6}[\hat{I}_z, [\hat{I}_z, [\hat{I}_z, \hat{I}_x]]] + \ldots \\
&= \hat{I}_x + \phi\hat{I}_y - \frac{\phi^2}{2}\hat{I}_x - \frac{i\phi^3}{6}\hat{I}_y + \ldots \\
&= \hat{I}_x\left(1 - \frac{\phi^2}{2} + \ldots\right) + \hat{I}_y\left(\phi - \frac{i\phi^3}{6} + \ldots\right) \\
&= \hat{I}_x \cos\phi + \hat{I}_y \sin\phi
\end{aligned} \tag{xiv}$$

where we have used the series expansions for $\cos\phi$ and $\sin\phi$ (Equation (ix)) in the last step.

So the transformation has transformed $\hat{I}_x$ into $\hat{I}_x\cos\phi + \hat{I}_y\sin\phi$. Figure B1.2.1, in which the Cartesian spin operators are represented as vectors along the appropriate axes, shows that this represents a rotation of $\hat{I}_x$ by an angle ϕ about z.

We can generalize this result: if two operators have the commutation relation,

$$[\hat{A}, \hat{B}] = i\hat{C} \tag{xv}$$

then the following transformation exists

$$e^{-i\phi\hat{A}}\,\hat{B}\,e^{+i\phi\hat{A}} = \hat{B}\cos\phi + \hat{C}\sin\phi \tag{xvi}$$

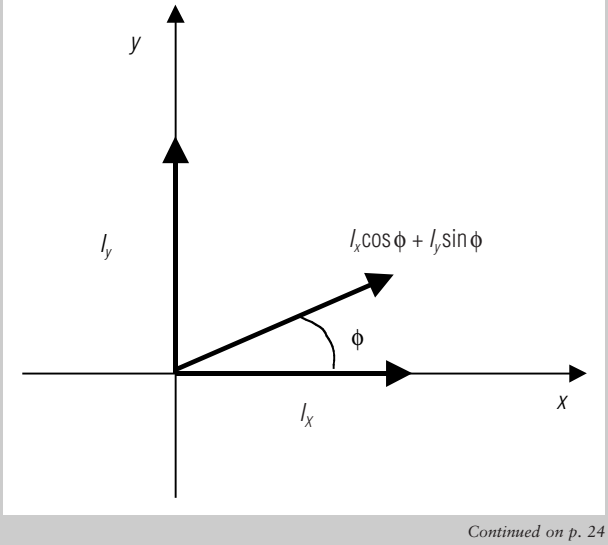

Fig. B1.2.1 The result of rotating I_x by an angle ϕ about the z axis.

Continued on p. 24

Box 1.2 *Cont.*

In Equation (1.24), we need to represent a rotating magnetic field, specifically one of magnitude B_1 which is rotating at frequency ω_{rf} about the z axis, the field lying along the x axis at time $t = 0$. From the above discussion, it is clear that the field a time t into the rotation is given by

$$B_1 e^{-i\omega_{rf}t\hat{I}_z}\hat{I}_x e^{+i\omega_{rf}t\hat{I}_z}$$

as used in Equation (1.24).

Rotation of axis frames

So far we have considered *active* rotations of operators and wavefunctions within their defining axis frames. Often, we will want to rotate an axis frame, and then re-express an operator or wavefunction in the new axis frame, a so-called *passive* rotation; the operator or wavefunction stays still while the axis frame moves (Fig. B1.2.2).

The relationship between a wavefunction ψ, expressed in the '*old*' frame and the same wavefunction expressed with respect to the '*new*' frame is

$$\psi^{new} = \hat{R}^{-1}\psi^{old} \qquad \text{(xvii)}$$

where $\hat{R}$ is the rotation operator which transforms the *old* axis frame into the *new* axis frame, i.e.

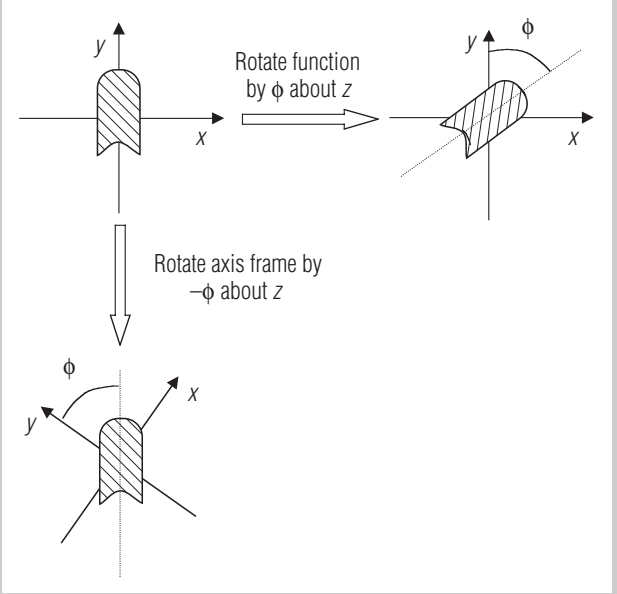

Fig. B1.2.2 Demonstrating that rotating a function by an angle ϕ about an axis is equivalent to rotating the axis frame by $-\phi$ about the same axis. The relationship between the function and the axis frame is the same in both cases.

$$\hat{R}(x^{\text{old}}, y^{\text{old}}, z^{\text{old}}) = (x^{\text{new}}, y^{\text{new}}, z^{\text{new}}) \quad \text{(xviii)}$$

The relationship between an operator $\hat{A}$ expressed with respect to its original frame ('*old*') and the same operator expressed in a rotated frame ('*new*') is

$$\hat{A}^{\text{new}} = \hat{R}^{-1}\hat{A}^{\text{old}}\hat{R} \quad \text{(xix)}$$

The rotation operators in all cases have the same form as those used in the active rotation of wavefunctions and operators, i.e. $\hat{R} = e^{-i\phi\hat{I}\alpha}$, but remember that here $\hat{R}$ describes the rotation of the axis frame from the old frame into the new frame. It is worth comparing the equations for rotation of operators and wavefunctions (active rotations) with those expressing the effect of a rotation of axis frame on operators and wavefunctions (passive rotations), i.e. Equations (iii) and (x) and Equations (xvii) and (xix). Clearly, they have a very similar form, but the operator $\hat{R}$ in the active rotation equations is replaced by $\hat{R}^{-1}$ in the passive rotation equations and $\hat{R}^{-1}$ by $\hat{R}$. Figure B1.2.2 illustrates the reason for this: a rotation of a function (or operator) by an angle ϕ about a given axis (leaving the axis frame unchanged) leads to the same result as leaving the function alone and rotating the axis frame in which the function is defined by $-\phi$ about the same axis, i.e. rotating a function is equivalent to performing the *inverse rotation* on the axis frame in which the function is defined.

Euler angles

In NMR, we often define rotation operators in terms of the *Euler angles* between the two frames, (X, Y, Z) and (x, y, z) in this case. Euler angles are generally labelled (α, β, γ) and are defined as follows:

Euler angles The transformation of frame (X, Y, Z) into (x, y, z) is described by a rotation of (X, Y, Z) by angle α about Z. This takes the (X, Y, Z) frame into (X_2, Y_2, Z_2). There then follows a rotation of angle β about the Y_2 axis that resulted from the previous rotation, taking the (X_2, Y_2, Z_2) frame into (X_3, Y_3, Z_3). Finally, there is a rotation of angle γ about the Z_3 axis that has resulted from the previous two coordinate rotations. This takes (X_3, Y_3, Z_3) into the (x, y, z) frame.

A completely equivalent definition of Euler angles expresses all rotations with respect to a single axis frame (rather than one which moves with the axis frame being rotated). This feature often makes this definition easier to deal with. It is:

Continued on p. 26

Box 1.2 *Cont.*

Euler angles The transformation of (X, Y, Z) into (x, y, z) is described by a rotation of a frame coincident with (X, Y, Z) by γ about Z, taking this frame into (X_2, Y_2, Z_2). There then follows a rotation of (X_2, Y_2, Z_2) by β about Y, i.e. the original axis frame Y axis, taking the (X_2, Y_2, Z_2) frame into (X_3, Y_3, Z_3). Finally, a rotation of α about Z, i.e. the original axis frame Z axis, takes (X_3, Y_3, Z_3) into (x, y, z). The frame being rotated in this case (the one initially coincident with (X, Y, Z)) acts like an object being rotated within the axis frame (X, Y, Z) in this definition of Euler angles. This definition thus employs *active* rotations, while the previous definition used passive rotations.

We employ the definition throughout that a positive rotation is that defined by the right-hand thumb rule, i.e. the direction of a positive rotation is the direction of the curl of the fingers when the right-hand thumb is pointed along the positive direction of the required axis.

It is not always easy to identify the Euler angles relating two frames! Polar angles are often easier to visualize; fortunately it is relatively easy to derive Euler angles from some polar angles as follows:

- (α, β) are the polar angles (θ, ϕ) of the z axis in the (X, Y, Z) frame.
- $(\beta, 180° - \gamma)$ are the polar angles of the Z axis in the (x, y, z) frame.

Rotations with Euler angles

With the definition of the Euler angles, we can now derive an expression for a rotation operator, $\hat{R}(\alpha, \beta, \gamma)$ which performs the rotation of an axis frame (x, y, z) by the Euler angles (α, β, γ). We imagine this (x, y, z) frame to be attached to an object which is located within an axis frame (X, Y, Z) such that (x, y, z) is initially coincident with (X, Y, Z). $\hat{R}(\alpha, \beta, \gamma)$ is then the operator which performs a rotation of the object and its axis frame by an angle γ about Z, then β about Y and finally α about Z. The operator $\hat{R}(\alpha, \beta, \gamma)$ can be broken down into its constituent rotations as

$$\hat{R}(\alpha, \beta, \gamma) = \hat{R}_Z(\gamma)\hat{R}_Y(\beta)\hat{R}_Z(\alpha) \qquad \text{(xx)}$$

where $\hat{R}_Z(\alpha)$ for instance is a rotation of angle α about the Z axis. It has already been shown that the operator for a rotation of an object by angle θ about an axis a is

$$\hat{R}_a(\theta) = \exp\left(-i\theta\hat{L}_a\right) \qquad \text{(xxi)}$$

where $\hat{L}_a$ is the operator for angular momentum (or spin) about axis *a*. So, we can now write down the expression for the operator $\hat{R}(\alpha,\beta,\gamma)$:

$$\hat{R}(\alpha,\beta,\gamma) = \exp(-i\gamma\hat{L}_Z)\exp(-i\beta\hat{L}_Y)\exp(-i\alpha\hat{L}_Z) \qquad \text{(xxii)}$$

Rotation of Cartesian axis frames

It is simple to derive a rotation matrix **R**, the matrix equivalent of the operator $\hat{R}$ above, which describes how to rotate an axis frame (x,y,z) fixed on an object within a frame (X,Y,Z) (and so rotate the object in the process). Consider first the rotation of γ about Z. Figure B1.2.3 illustrates how this moves the (x,y,z) object-fixed frame.

The rotation matrix which performs this transformation is:

$$\mathbf{R}_Z(\gamma) = \begin{pmatrix} \cos\gamma & -\sin\gamma & 0 \\ \sin\gamma & \cos\gamma & 0 \\ 0 & 0 & 1 \end{pmatrix} \qquad \text{(xxiii)}$$

This can be verified by taking unit vectors along each of the (X,Y,Z) axes, $\mathbf{n}_X$, $\mathbf{n}_Y$, $\mathbf{n}_Z$ which are coparallel with the initial orientation of (x,y,z) and performing the transformation $\mathbf{R}_Z(\gamma)\mathbf{n}_\alpha$ on each of these, where $\alpha = X, Y, Z$. The resultant in each case will be a new unit vector along the appropriate axis of the rotated (x,y,z).

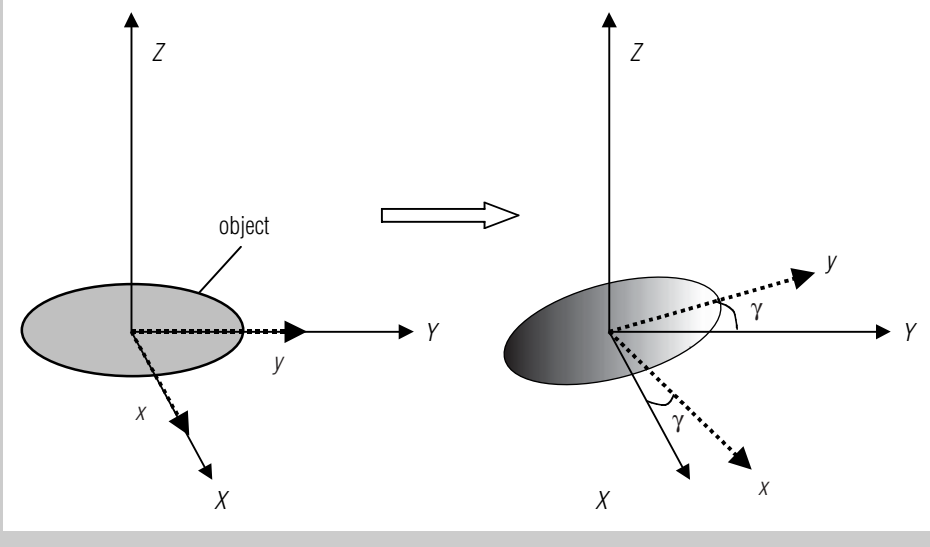

Fig. B1.2.3 The rotation of an object-fixed axis frame (x,y,z) by γ about Z.

Continued on p. 28

Box 1.2 *Cont.*

We can then go on to the rotation of β about *Y*. The rotation matrix describing this rotation is:

$$\mathbf{R}_Y(\beta) = \begin{pmatrix} \cos\beta & 0 & \sin\beta \\ 0 & 1 & 0 \\ -\sin\beta & 0 & \cos\beta \end{pmatrix} \tag{xxiv}$$

which can be verified in the same way as the previous rotation matrix. Finally, the last rotation of α about *Z* is described by:

$$\mathbf{R}_Z(\alpha) = \begin{pmatrix} \cos\alpha & -\sin\alpha & 0 \\ \sin\alpha & \cos\alpha & 0 \\ 0 & 0 & 1 \end{pmatrix} \tag{xxv}$$

Now we can produce the required transformation matrix, $\mathbf{R}(\alpha,\beta,\gamma)$ to go from (X,Y,Z) to the final orientation of (x,y,z) using Equation (xx) (in which rotation matrices can be substituted for rotation operators) and Equations (xxiii), (xxiv) and (xxv):

$$\begin{aligned} \mathbf{R}(\alpha,\beta,\gamma) &= \mathbf{R}_Z(\alpha)\mathbf{R}_Y(\beta)\mathbf{R}_Z(\gamma) \\ &= \begin{pmatrix} \cos\alpha & -\sin\alpha & 0 \\ \sin\alpha & \cos\alpha & 0 \\ 0 & 0 & 1 \end{pmatrix} \begin{pmatrix} \cos\beta & 0 & \sin\beta \\ 0 & 1 & 0 \\ -\sin\beta & 0 & \cos\beta \end{pmatrix} \begin{pmatrix} \cos\gamma & -\sin\gamma & 0 \\ \sin\gamma & \cos\gamma & 0 \\ 0 & 0 & 1 \end{pmatrix} \end{aligned} \tag{xxvi}$$

which altogether gives:

$$\mathbf{R}(\alpha,\beta,\gamma) = \begin{pmatrix} \cos\alpha\cos\beta\cos\gamma & -\cos\alpha\cos\beta\sin\gamma & \cos\alpha\sin\beta \\ -\sin\alpha\sin\gamma & -\sin\alpha\cos\gamma & \\ \sin\alpha\cos\beta\cos\gamma & -\sin\alpha\cos\beta\sin\gamma & \sin\alpha\sin\beta \\ +\cos\alpha\sin\gamma & +\cos\alpha\cos\gamma & \\ -\sin\beta\cos\gamma & \sin\beta\sin\gamma & \cos\beta \end{pmatrix} \tag{xxvii}$$

Often, we will want to transform a Cartesian tensor **T** describing a physical quantity from being expressed in frame (X,Y,Z) to being expressed in a frame (x,y,z) (a passive rotation). The appropriate transformation in these circumstances is:

$$\mathbf{T}(x,y,z) = \mathbf{R}^{-1}\,\mathbf{T}(X,Y,Z)\mathbf{R} \tag{xxviii}$$

where **R** is the rotation matrix derived above which rotates a frame initially coparallel with (X,Y,Z) into a frame (x,y,z).

1.3 The density matrix representation and coherences

The quantum mechanical description given in the previous section examines spin systems in a sample of many spin systems through a superposition state. This approach is revealing, but time consuming.

A completely equivalent approach is to describe the spin system through a *density operator* or *density matrix*. Our discussion of the density operator which follows, uses the ideas behind the superposition state introduced in Section 1.2. However, whereas our previous discussion of the superposition state used the specific example of identical spin-$\frac{1}{2}$ nuclei in various environments, here we keep the discussion completely general.

We start by imagining a collection of identical spin systems (the concept of a spin system was defined previously at the beginning of Section 1.2), each of which can be in any one of N states we label ψ. We do not know which state each individual spin system is in, only the probability p_ψ of it being in a particular state, ψ. This was what led us to describe the state of each spin system with a single superposition state, Ψ, where $\Psi = \Sigma_\psi p_\psi \psi$. The expectation value of a quantity A with corresponding operator $\hat{A}$ over the sample is given by (see Box 1.1 for definition of expectation value):

$$\overline{\langle \hat{A} \rangle} = \langle \Psi | \hat{A} | \Psi \rangle = \sum_\psi p_\psi \langle \psi | \hat{A} | \psi \rangle \tag{1.40}$$

where the summation is over all the possible states for each spin system, and where we have assumed that the wavefunction ψ is normalized. Now let us write the state of the system in a general form as a sum over functions ϕ_i taken from a complete set of functions; we call this complete set the *basis set* for expressing the states of spin system. We did this in Section 1.2 when finding the wavefunctions for a system consisting of a single spin under the effects of an rf pulse. In practice, the basis set is some convenient complete set, often the eigenfunctions of the Zeeman hamiltonian for the spin system, as in Section 1.2. So, we can write the possible states of each spin system in general as

$$\psi = \sum_i c_{\psi i} \phi_i \tag{1.41}$$

Substituting this in Equation (1.40) we have

$$\overline{\langle \hat{A} \rangle} = \sum_\psi p_\psi \sum_{i,j} c_{\psi j} * c_{\psi j} \langle \phi_i | \hat{A} | \phi_j \rangle \tag{1.42}$$

The advantage of this approach is that the matrix elements of $\hat{A}$ in this basis, i.e. $\langle \phi_i | \hat{A} | \phi_j \rangle$, are the same whichever state ψ we are dealing with. If we now define $\Sigma_\psi p_\psi c_{\psi j} c_{\psi i}{}^*$ to be the jith element of another matrix ρ, then we can see that Equation (1.42) for the expectation value of $\hat{A}$ can be rewritten as

$$\langle \hat{A} \rangle = Tr(\mathbf{A}\rho) = \sum_i (\mathbf{A}\rho)_{ii} = \sum_i \sum_j A_{ij}\rho_{ji} \tag{1.43}$$

where **A** is the matrix of operator $\hat{A}$ in the $\{\phi_i\}$ basis whose *ij*th element is $\langle \phi_i | \hat{A} | \phi_j \rangle$. The matrix ρ, called the *density matrix*, has a corresponding operator which can be deduced by inspecting its matrix elements, i.e. $\rho_{ji} = \langle j | \hat{\rho} | i \rangle = \Sigma_\psi p_\psi c_{\psi j} c_{\psi i}^*$:

$$\hat{\rho} = \sum_\psi p_\psi |\psi\rangle\langle\psi| \tag{1.44}$$

For further details and discussion of the density matrix, the reader is referred to the excellent text by Goldman [**1**].

1.3.1 Coherences and populations

Let us examine some of the properties of the density operator and its matrix representation. First, the diagonal elements are equal to

$$\rho_{ii} = \sum_\psi p_\psi c_{\psi i} * c_{\psi i} = \overline{c_{\psi i} * c_{\psi i}} \tag{1.45}$$

The bar here simply means 'average over all the spins' or *ensemble average* which is what the weighted sum over all possible states for the spin system, ψ in Equation (1.45), represents. We can see from Equation (1.45) that ρ_{ii} is simply the average population of the ϕ_i basis function over the sample, as $c_i * c_i$ is the population of the *i*th basis function. Secondly, consider an off-diagonal element of the density matrix:

$$\rho_{ij} = \sum_\psi p_\psi c_{\psi i} * c_{\psi j} = \overline{c_{\psi i} * c_{\psi j}} \tag{1.46}$$

Consider first a sample where all the spin systems in the sample are in the same state, ψ′. Then the diagonal elements of the corresponding density matrix are

$$\rho_{ii} = c_{\psi' i} * c_{\psi' i} \qquad \rho_{jj} = c_{\psi' j} * c_{\psi' j} \tag{1.47}$$

and the off-diagonal elements are

$$\rho_{ij} = c_{\psi' i} * c_{\psi' j} \tag{1.48}$$

The diagonal elements represent the populations of the basis functions in the state, ψ′. A non-zero off-diagonal element signifies that both $c_{\psi' i}$ and $c_{\psi' j}$ are non-zero and therefore that the state ψ′ contains (possibly among other things) a mixture of ϕ_i and ϕ_j basis functions.

Now consider a sample in which there is a distribution of spin systems among all possible states. Then, the averaging over states which occurs in Equation (1.46) may well cause the off-diagonal elements of the density matrix to vanish. Indeed, the

off-diagonal elements will vanish if there is no *correlation over time* between the basis functions from which the spin system states are derived. However, if there is some correlation between the basis functions, the average in Equation (1.46) no longer vanishes, and off-diagonal elements of the density matrix representing the sample will be non-zero. We say in this case that there is a *coherence* between the ϕ_i and ϕ_j functions in the superposition state Ψ, which describes the spin system. An example will help to clarify this; consider the situation dealt with in Section 1.2, where the spin system consisted of a single isolated spin. Let us take as our basis set of functions to describe the possible states of this system in any environment, the Zeeman states for this spin system, i.e. $|+\frac{1}{2}\rangle$ and $|-\frac{1}{2}\rangle$. In the absence of any rf pulses, the two possible states of the system are simply $|+\frac{1}{2}\rangle$ and $|-\frac{1}{2}\rangle$, i.e.

$$\psi_1 = \left|+\frac{1}{2}\right\rangle \quad \psi_2 = \left|-\frac{1}{2}\right\rangle \tag{1.49}$$

We now form the density matrix for this spin system, using Equations (1.45) and (1.46) for the diagonal and off-diagonal matrix elements respectively. The summation in these two equations is over the states ψ_1 and ψ_2. So, for instance,

$$\rho_{\frac{1}{2},\frac{1}{2}} = p_{\frac{1}{2}}(1\times 1) + P_{-\frac{1}{2}}(0\times 0) \tag{1.50}$$

The complete density matrix so formed is calculated to be (where the basis functions forming the elements are arranged horizontally and vertically in the order $|+\frac{1}{2}\rangle$, $|-\frac{1}{2}\rangle$)

$$\rho = \begin{pmatrix} p_{+\frac{1}{2}} & 0 \\ 0 & p_{-\frac{1}{2}} \end{pmatrix} \tag{1.51}$$

So, there are no coherences associated with this spin system, only populations of the basis functions.

Now consider the same spin system but subjected to an rf pulse. The wavefunctions describing the possible states of this spin system are given by Equations (1.29) and (1.33). The two possible wavefunctions are now

$$\begin{aligned} \psi_1 &= \cos\left(\frac{1}{2}\omega_1 t\right)\left|+\frac{1}{2}\right\rangle + i\sin\left(\frac{1}{2}\omega_1 t\right)\left|-\frac{1}{2}\right\rangle \\ \psi_2 &= -i\sin\left(\frac{1}{2}\omega_1 t\right)\left|+\frac{1}{2}\right\rangle + \cos\left(\frac{1}{2}\omega_1 t\right)\left|-\frac{1}{2}\right\rangle \end{aligned} \tag{1.52}$$

which are found by setting $c_{+\frac{1}{2}}(0) = 1$; $c_{-\frac{1}{2}}(0) = 0$ for ψ_1, i.e. initial state of the spin system at the start of the pulse ($t = 0$) is $|+\frac{1}{2}\rangle$ and $c_{+\frac{1}{2}}(0) = 0$; $c_{-\frac{1}{2}}(0) = 1$ for ψ_2, i.e. initial state is $|-\frac{1}{2}\rangle$. The density matrix is then calculated for this situation to be

$$\rho = \begin{pmatrix} P_+ & i\sin(w_1 t) \\ -i\sin(\omega_1 t) & P_- \end{pmatrix} \tag{1.53}$$

where

$$\begin{aligned} P_+ &= p_1 \cos^2\left(\frac{1}{2}\omega_1 t\right) + p_2 \sin^2\left(\frac{1}{2}\omega_1 t\right) \\ P_- &= p_1 \sin^2\left(\frac{1}{2}\omega_1 t\right) + p_2 \cos^2\left(\frac{1}{2}\omega_1 t\right) \end{aligned} \tag{1.54}$$

Here, then, there is a coherence between the $|+\frac{1}{2}\rangle$ and $|+\frac{1}{2}\rangle$ basis functions, as well as populations of both functions. In essence, the coherence is an expression of the fact that the wavefunctions describing the spin system in this situation contain mixtures of the $|+\frac{1}{2}\rangle$ and $|-\frac{1}{2}\rangle$ basis functions. Looking at the form of the wavefunctions for this case (Equation (1.51)), we see that over time the ψ_1 wavefunction oscillates between $\psi_1 = |+\frac{1}{2}\rangle$ and $\psi_1 = |-\frac{1}{2}\rangle$ while the ψ_2 wavefunction oscillates in the opposite sense, i.e. between $\psi_2 = |-\frac{1}{2}\rangle$ and $\psi_2 = |+\frac{1}{2}\rangle$. The oscillations of the two wavefunctions ψ_1 and ψ_2 are *coherent* in the sense that as the amount of $|+\frac{1}{2}\rangle$ function (say) increases in one wavefunction over time, so the amount of $|+\frac{1}{2}\rangle$ function in the other wavefunction decreases at the same rate.

To complete this illustration, we use Equation (1.43) to calculate the expectation value of *y* magnetization for this situation of isolated spins subjected to an rf pulse. Following Equation (1.42)

$$\langle \hat{\mu}_y \rangle = \mathrm{Tr}(\mu_y \rho) = \gamma\hbar\,\mathrm{Tr}(\mathbf{I}_y \rho) \tag{1.55}$$

The matrix of $\hat{I}_y$ in the basis set of $|\pm\frac{1}{2}\rangle$ functions is given in Equation (xx) in Box 1.1 previously. Using this and the density matrix of Equation (1.53), we find that

$$\langle \hat{\mu}_y \rangle = -\frac{1}{2}\gamma\hbar(p_1 - p_2)\sin(\omega_1 t) \tag{1.56}$$

For short *t*, the populations p_1 and p_2 of the wavefunctions, ψ_1 and ψ_2, are the same as the populations of the initial wavefunctions the ψ_1 and ψ_2 wavefunctions started from at $t = 0$, i.e. the $|\pm\frac{1}{2}\rangle$ states, as there has been insufficient time for thermal equilibration to take place. So Equation (1.56) can be rewritten as

$$\langle \hat{\mu}_y \rangle = -\frac{1}{2}\gamma\hbar\left(p_{+\frac{1}{2}}(0) - p_{-\frac{1}{2}}(0)\right)\sin(\omega_1 t) \tag{1.57}$$

which is the same as Equation (1.39) obtained previously using the superposition state approach.

If the set of basis functions $\{\phi\}$ is the Zeeman basis, the *coherence order* of a density matrix element ρ_{ij} is given by $m_j - m_i$, the difference between the *z* spin quantum numbers for the *i* and *j* basis functions which are mixed in the coherence.

The terms coherence and coherence order are used widely and should be understood in the context of the density matrix representation. In the previous example of a spin under the influence of an rf pulse, if we compare the density matrix before the pulse (Equation (1.51)) with that during the pulse (Equation (1.53)), we see that the effect of the pulse is to create ±1- order coherences.

1.3.2 The density operator at thermal equilibrium

Given the description of the density operator and matrix given above, it is relatively easy to show that the density operator for a spin system at thermal equilibrium (i.e. obeying the Boltzmann distribution) and in which individual spin systems are described by a hamiltonian $\hat{H}$ is

$$\hat{\rho}_{eq} = \frac{1}{Z} e^{-\hat{H}/kT} \tag{1.58}$$

where

$$Z = \mathrm{Tr}\left(e^{-\hat{H}/kT}\right) \tag{1.59}$$

Equation (1.58) involves the exponential of an operator, which is defined in Equation (i) in Box 1.2. If the basis functions chosen to form the density matrix from the density operator in Equation (1.58) are the eigenfunctions of $\hat{H}$, then the equilibrium density matrix is diagonal with elements equal to the populations of the corresponding eigenstates of $\hat{H}$, as predicted by the Boltzmann distribution.

1.3.3 Time evolution of the density matrix

Nuclei in a static, uniform field

Taking the simplest case of a spin in a uniform magnetic field $\mathbf{B}_0$, the hamiltonian in question is, as before

$$\hat{H} = -\gamma\hbar\hat{I}_z B_0 = -\hbar\omega_0\hat{I}_z \tag{1.60}$$

as previously. Using this hamiltonian, we can approximate ρ_{eq} as

$$\hat{\rho}_{eq} \approx \frac{1}{Z}\left(1 + \frac{\hbar\omega_0}{kT}\hat{I}_z\right) \tag{1.61}$$

neglecting the higher terms in the expansion of $e^{-\hat{H}/kT}$. This approximation is valid for the typical magnetic fields $\mathbf{B}_0$ and temperatures used in NMR experiments. As discussed above, we can think of the density operator as describing a superposition state of a spin system. Any new interaction in the spin system will of course change its state and also the density operator describing it. An interaction in a spin system

is described by a hamiltonian and the change it causes on the density operator is given by

$$\frac{\mathrm{d}\hat{\rho}}{\mathrm{d}t} = -i[\hat{H}, \hat{\rho}] \tag{1.62}$$

This equation is derived from the time-dependent Schrödinger equation (Equation (1.25)). The solution of Equation (1.62) for a time-independent hamiltonian is

$$\hat{\rho}(t) = \mathrm{e}^{-i\hat{H}t}\hat{\rho}(0)\,\mathrm{e}^{i\hat{H}t} \tag{1.63}$$

where $\hat{\rho}(t)$ is the density operator at time t and $\hat{\rho}(0)$ that at time $t = 0$, i.e. immediately prior to the new interaction described by $\hat{H}$. The term $\mathrm{e}^{-i\hat{H}t}$ is often referred to as the *propagator*. In the case of a time-dependent hamiltonian, Equation (1.63) becomes

$$\hat{\rho}(t) = \hat{T}\,\mathrm{e}^{-i\int_0^t \hat{H}(t')\mathrm{d}t'}\hat{\rho}(t)\mathrm{e}^{i\int_0^t \hat{H}(t')\mathrm{d}t'} \tag{1.64}$$

where $\hat{T}$ is the Dyson time-ordering operator. This operator is necessary when $\hat{H}(t)$ does not commute with itself at different times t. The exponential $\mathrm{e}^{i\int_0^t \hat{H}(t')\mathrm{d}t'}$ can be written as a product

$$\mathrm{e}^{i\int_0^t \hat{H}(t')\mathrm{d}t'} = \prod_{\substack{n=0 \\ \lim \Delta t \to 0}}^{n=t/\Delta t} \mathrm{e}^{i\hat{H}(t_n)\Delta t} \tag{1.65}$$

where $\hat{H}(t_n)$ is the hamiltonian at the nth time interval Δt. The Dyson time-ordering operator ensures that the $\mathrm{e}^{i\hat{H}(t_n)\Delta t}$ operators in the series are placed in strict chronological sequence, with the earliest one placed on the right-hand side.

The same approach is used if the hamiltonian describing the spin system is *piecewise constant*; that is, it is $\hat{H}_1$ for a period of time t_1, $\hat{H}_2$ for a period t_2 and so on. This might be the case, for instance, for a pulse sequence, where there are periods during which the rf pulse is switched on and periods in between where other interactions are present. The hamiltonians describing the spin system during each period depend on the interactions present, and so vary through the pulse sequence. In these circumstances, the density operator at the end of the pulse sequence is given by

$$\hat{\rho}(t_1 + t_2 + \ldots + t_n) = \mathrm{e}^{-i\hat{H}_n t_n} \ldots \mathrm{e}^{-i\hat{H}_2 t_2}\,\mathrm{e}^{-i\hat{H}_1 t_1}\,\hat{\rho}(0)\,\mathrm{e}^{i\hat{H}_1 t_1}\,\mathrm{e}^{i\hat{H}_2 t_2} \ldots \mathrm{e}^{i\hat{H}_n t_n} \tag{1.66}$$

The effect of rf pulses

We will now consider a specific example, that of an x pulse acting on a spin system which starts at equilibrium in a uniform magnetic field $\mathbf{B}_0$. We can then compare

the results obtained using the density matrix approach with those obtained in Section 1.2.

In the rotating frame, the hamiltonian describing the interaction of the on-resonance rf x pulse with the spin system is (as shown in Section 1.2 and Box 1.2)

$$\hat{H}_{\mathrm{rf}} = -\hbar\omega_1 \hat{I}_x \tag{1.67}$$

with $\omega_1 = \gamma B_1$, where B_1 is the magnetic field associated with the rf pulse. Then using Equation (1.63), the density operator $\hat{\rho}(t)$ during the rf pulse is

$$\hat{\rho}(t) = \mathrm{e}^{i\omega_1 \hat{I}_x t}\, \hat{\rho}(0)\, \mathrm{e}^{-i\omega_1 \hat{I}_x t} \tag{1.68}$$

where $\hat{\rho}(0)$ is the density operator at the start of the pulse. Substituting $\hat{\rho}_{\mathrm{eq}}$ (Equation (1.61)), the density operator at equilibrium, for $\hat{\rho}(0)$ we have

$$\begin{aligned}\hat{\rho}(t) &= \mathrm{e}^{i\omega_1 \hat{I}_x t}\left(1 - \frac{1}{Z}\frac{\hbar\omega_0}{kT}\hat{I}_z\right)\mathrm{e}^{-i\omega_1 \hat{I}_x t} \\ &= 1 - \frac{1}{Z}\frac{\hbar\omega_0}{kT}\,\mathrm{e}^{i\omega_1 \hat{I}_x t}\hat{I}_z\,\mathrm{e}^{-i\omega_1 \hat{I}_x t}\end{aligned} \tag{1.69}$$

The term $\mathrm{e}^{i\omega_1 \hat{I}_x t}\hat{I}_z \mathrm{e}^{-i\omega_1 \hat{I}_x t}$ represents a rotation of the operator $\hat{I}_z$ about x by angle $\omega_1 t$ (see Box 1.2); thus we have

$$\mathrm{e}^{i\omega_1 \hat{I}_x t}\hat{I}_z \mathrm{e}^{-i\omega_1 \hat{I}_x t} = \hat{I}_z \cos\omega_1 t + \hat{I}_y \sin\omega_1 t \tag{1.70}$$

Substituting this in Equation (1.69) for the density operator $\hat{\rho}(t)$

$$\hat{\rho}(t) = 1 - \frac{1}{Z}\frac{\hbar\omega_0}{kT}\left(\hat{I}_z \cos\omega_1 t + \hat{I}_y \sin\omega_1 t\right) \tag{1.71}$$

The y magnetization is then given by

$$\begin{aligned}\langle \mu_y(t)\rangle &= \mathrm{Tr}(\hat{\rho}(t)\hat{\mu}_y) = \gamma\hbar\,\mathrm{Tr}(\hat{\rho}(t)\hat{I}_y) \\ &= \gamma\hbar\,\mathrm{Tr}(\mathbf{1}\cdot\mathbf{I}_y) - \gamma\hbar\frac{1}{Z}\frac{\hbar\omega_0}{kT}\,\mathrm{Tr}(\mathbf{I}_z\mathbf{I}_y\cos\omega_1 t + \mathbf{I}_y^2 \sin\omega_1 t) \\ &= -\frac{1}{2}\gamma\hbar\left(\frac{1}{Z}\frac{\hbar\omega_0}{kT}\right)\sin\omega_1 t\end{aligned} \tag{1.72}$$

In the final step in Equation (1.72), we have used the $\mathbf{I}_y$ and $\mathbf{I}_z$ matrices in the Zeeman basis as given in Box 1.1. Comparing this with Equation (1.39) for the y magnetization derived from the quantum mechanical picture

$$\langle \hat{\mu}_y(t)\rangle = -\frac{1}{2}\gamma\hbar\left(p_{\frac{1}{2}}(0) - p_{-\frac{1}{2}}(0)\right)\sin(\omega_1 t) \tag{1.39}$$

If we write the spin level populations as $p_{\pm\frac{1}{2}}(0) = \dfrac{1}{z}\exp\left(\mp\dfrac{1}{2}(\hbar\omega_0/kT)\right)$ and

approximate the exponentials as $\exp\left(\mp\frac{1}{2}(\hbar\omega_0/kT)\right)\approx 1\mp\left(\mp\frac{1}{2}(\hbar\omega_0/kT)\right)$, as was done in deriving the density operator, Equations (1.39) and (1.72) are identical.

1.4 Nuclear spin interactions

So far the only interactions we have considered on the nuclear spin system are those with externally applied magnetic fields, the static, uniform field $\mathbf{B}_0$ in the NMR experiment and that due to rf pulses, $\mathbf{B}_1$. However, there are sources of magnetic fields internal to the sample which also affect the nuclear spin system and which for solid samples can cause extensive linebroadening. Here, we consider the hamiltonian operators which describe the most important of these interactions, chemical shielding, dipole coupling and quadrupole coupling, and briefly consider the effects of each interaction on the NMR spectrum. More detailed discussion of each interaction is to be found in later chapters.

In the NMR experiment, the applied static field $\mathbf{B}_0$ is, in general, orders of magnitude larger than any local fields arising within the sample as a result of other nuclear magnetic dipoles and chemical shielding. As a result, $\mathbf{B}_0$ remains as the quantization axis for the nuclear spins in the sample and many of these local fields have a negligible effect on the spin states (at equilibrium). The only components of local fields which have any significant effect on the spin states are

(i) components parallel or antiparallel to the applied field $\mathbf{B}_0$ and
(ii) components precessing in the plane perpendicular to the applied field $\mathbf{B}_0$ at a frequency at or near the Larmor frequency (or other resonance frequencies of the spin system).

Components parallel (or antiparallel) to $\mathbf{B}_0$ add to (or subtract from) $\mathbf{B}_0$ and therefore alter the energies of the spin states which are determined by the total field strength parallel to $\mathbf{B}_0$, the quantization axis.

Components perpendicular to $\mathbf{B}_0$ precessing near the Larmor frequency are akin to the rf x pulse considered in Section 1.3. As seen there, such fields mix the Zeeman spin states which exist in the $\mathbf{B}_0$ field alone.

The hamiltonian describing the interaction between any local field $\mathbf{B}_{\text{loc}}$ and a nuclear spin $\mathbf{I}$ takes the usual form:

$$\begin{aligned}\hat{H}_{\text{loc}} &= -\gamma\hbar\hat{\mathbf{I}}\cdot\mathbf{B}_{\text{loc}} \\ &= -\gamma\hbar\left(\hat{I}_x B_x^{\text{loc}} + \hat{I}_y B_y^{\text{loc}} + \hat{I}_z B_z^{\text{loc}}\right)\end{aligned} \tag{1.73}$$

When we consider specific nuclear spin interactions in the following pages, we will find that we can always express the local magnetic field $\mathbf{B}_{\text{loc}}$ in the interaction as

$$\mathbf{B}_{\text{loc}} = \mathbf{A}_{\text{loc}} \cdot \mathbf{J} \tag{1.74}$$

where $\mathbf{A}_{\text{loc}}$ is a second-rank tensor, often referred to as the *coupling tensor*, which describes the nuclear spin interaction and its orientation dependence. The vector $\mathbf{J}$ is the ultimate source of the $\mathbf{B}_{\text{loc}}$ magnetic field at the nucleus, e.g. another nuclear spin in the case of dipole–dipole coupling, or the $\mathbf{B}_0$ field itself in the case of chemical shielding. Hence, we can write a general contribution to the nuclear spin hamiltonian from an interaction by reference to Equations (1.73) and (1.74) as

$$\hat{H}_i = -\gamma\hbar\mathbf{I} \cdot \mathbf{B}_{\text{loc}} = -\gamma\hbar\mathbf{I} \cdot \mathbf{A}_{\text{loc}} \cdot \mathbf{J} \tag{1.75}$$

The relevance of the vector $\mathbf{J}$ and the tensor $\mathbf{A}_{\text{loc}}$ will become clear as we consider some examples.

An alternative way of assessing the effect of a nuclear spin interaction uses *perturbation theory*. The Zeeman interaction for the spin system in question, i.e. interaction of the spin system (whatever that might be) with the applied field, $\mathbf{B}_0$ is considered to be the dominant interaction in the system and is described by the hamiltonian $\hat{H}_0$. The nuclear spin interaction, described by a hamiltonian, $\hat{H}_1$, is then considered as a perturbation on the spin system, so that the total hamiltonian $\hat{H}$ for the spin system is given by

$$\hat{H} = \hat{H}_0 + \hat{H}_1 \tag{1.76}$$

Now perturbation theory shows that if we are interested in the energy of the perturbed system to first order, we need to consider the wavefunctions of the perturbed system to *zeroth order*. The wavefunctions of a perturbed system described by $\hat{H}$ are, to zeroth order, simply the eigenfunctions of the dominant interaction hamiltonian, $\hat{H}_0$. These eigenfunctions are of course just the Zeeman states for the spin system, $\psi_{I,m}$ (where I denotes the total spin for the system, and m its component along $\mathbf{B}_0$). The parts of $\hat{H}_1$ which affect the spin system wavefunctions to zeroth order must also have eigenfunctions $\psi_{I,m}$, i.e. must have the same eigenfunctions as $\hat{H}_0$. As discussed in Box 1.1, two operators can only have the same eigenfunctions if they commute. Thus, the only parts of $\hat{H}_1$ which affect the spin system to zeroth order (and so its energy levels to first order) are those parts which commute with $\hat{H}_0$.[4] That is not to say that an interaction hamiltonian, $\hat{H}_1$, which does *not* commute with $\hat{H}_0$ may not cause higher-order energy corrections. However, these higher-order energy corrections are unlikely to be important in determining the energy levels of the spin system, and therefore in determining the NMR spectrum, unless the interaction has a large amplitude relative to the Zeeman interaction. Hamiltonians describing nuclear spin interactions within a spin system which commute with the Zeeman hamiltonian for that spin system are said to be *secular*.

1.4.1 The chemical shift and chemical shift anisotropy

The electrons that surround a nucleus are not impassive in the magnetic field used in the NMR experiment, but react to produce a secondary field. This secondary field contributes to the total field felt at the nucleus, and therefore has the potential to change the resonance frequency of the nucleus. This interaction of the secondary field produced by the electrons with the nucleus is the *shielding interaction*. The frequency shift that this interaction causes in an NMR spectrum is the *chemical shift*. The shielding interaction may be considered as being composed of two components:

1. The external magnetic field causes all electrons to circulate around it. This produces a secondary field which opposes the applied field at the centre of motion. Hence, this field tends to shield the nucleus. This is known as the *diamagnetic* contribution to the shielding. This contribution varies as $\frac{1}{r_i^3}$ where r_i is the distance of the ith electron from the nucleus. Hence, it arises principally from the core electrons. This means that the diamagnetic shielding arising from an atom in a molecule is fairly constant for a given atom type, whatever its environment. However, it should be noted that all atoms surrounding the atom in question also generate diamagnetic electron currents, and so also contribute to the total diamagnetic field felt at the nucleus.
2. The external magnetic field may also mix excited electronic states that possess paramagnetic properties with the ground state, creating a small amount of paramagnetism in the ground state of the molecule while it is in the magnetic field. This creates a field which supports the applied field at the nucleus, and so tends to deshield the nucleus. This is known as the *paramagnetic* contribution and varies considerably with the nuclear environment. The degree of mixing of the excited paramagnetic states with the ground state depends on the energy difference between the mixed states, and is known as Temperature Independent Paramagnetism (TIP).

Shielding anisotropy

The chemical shielding hamiltonian acting on a spin **I** is

$$\hat{H}_{\mathrm{cs}} = -\gamma\hbar\ \hat{\mathbf{I}}\cdot\boldsymbol{\sigma}\cdot\mathbf{B}_0 \tag{1.77}$$

which has the general form proposed in Equation (1.75). $\mathbf{B}_0$ is the applied field, the equivalent of **A** in Equation (1.75); $\mathbf{B}_0$ is the ultimate source of the shielding magnetic field as it is $\mathbf{B}_0$ that generates the electron current which in turn generates the shielding magnetic field. The term $\boldsymbol{\sigma}$ is a second-rank tensor, called the chemical shielding tensor, and is the quantity that we now discuss in some detail.

In general, the electron distribution around a nucleus in a molecule is not spherically symmetric. Therefore, the size of electron current around the field, and hence

the size of the shielding, will depend on the orientation of the molecule within the applied field $\mathbf{B}_0$.

The shielding property associated with a nucleus cannot therefore be described by a single number, but must be described by a second-rank tensor. The shielding tensor describes how the size of shielding varies with molecular orientation.

In general, a Cartesian tensor, such as the shielding tensor $\boldsymbol{\sigma}$, is represented by a 3×3 matrix:

$$\boldsymbol{\sigma} = \begin{pmatrix} \sigma_{xx} & \sigma_{xy} & \sigma_{xz} \\ \sigma_{yx} & \sigma_{yy} & \sigma_{yz} \\ \sigma_{zx} & \sigma_{zy} & \sigma_{zz} \end{pmatrix} \tag{1.78}$$

where x, y, z is some, as yet unspecified, axis frame. The meaning of the shielding tensor becomes clearer when we express the shielding tensor in the laboratory frame (which is defined by $\mathbf{B}_0$ being along z). The local magnetic field $\mathbf{B}_{\text{loc}}$ at a nucleus with a shielding tensor $\boldsymbol{\sigma}^{\text{lab}}$, i.e. shielding tensor expressed within the laboratory frame, is

$$\mathbf{B}_{\text{loc}} = \boldsymbol{\sigma}^{\text{lab}} \cdot \mathbf{B}_0 \tag{1.79}$$

for an applied field $\mathbf{B}_0$. So, for instance, $\boldsymbol{\sigma}_{xz}^{\text{lab}} B_0$ is the local shielding field in the x direction, when $\mathbf{B}_0$ is applied along z.

It is useful at this point to decompose the shielding tensor into a *symmetric* ($\boldsymbol{\sigma}^{\text{s}}$) and *antisymmetric* ($\boldsymbol{\sigma}^{\text{as}}$) component:

$$\boldsymbol{\sigma} = \boldsymbol{\sigma}^{\text{s}} + \boldsymbol{\sigma}^{\text{as}} \tag{1.80}$$

where

$$\begin{aligned} \boldsymbol{\sigma}^{\text{s}} &= \begin{pmatrix} \sigma_{xx} & \frac{1}{2}(\sigma_{xy} + \sigma_{yx}) & \frac{1}{2}(\sigma_{xz} + \sigma_{zx}) \\ \frac{1}{2}(\sigma_{xy} + \sigma_{yx}) & \sigma_{yy} & \frac{1}{2}(\sigma_{yz} + \sigma_{zy}) \\ \frac{1}{2}(\sigma_{xz} + \sigma_{zx}) & \frac{1}{2}(\sigma_{yz} + \sigma_{zy}) & \sigma_{zz} \end{pmatrix} \\ \boldsymbol{\sigma}^{\text{as}} &= \begin{pmatrix} 0 & \frac{1}{2}(\sigma_{xy} - \sigma_{yx}) & \frac{1}{2}(\sigma_{xz} - \sigma_{zx}) \\ \frac{1}{2}(\sigma_{yx} - \sigma_{xy}) & 0 & \frac{1}{2}(\sigma_{yz} - \sigma_{zy}) \\ \frac{1}{2}(\sigma_{zx} - \sigma_{xz}) & \frac{1}{2}(\sigma_{zy} - \sigma_{yz}) & 0 \end{pmatrix} \end{aligned} \tag{1.81}$$

The reason for this decomposition is that only the symmetric part of the shielding tensor, $\boldsymbol{\sigma}^{\text{s}}$, turns out to affect the NMR spectrum to any great extent[5]; this will become clear as we examine how the shielding interaction affects the NMR spectrum in the next section. Henceforth, we will only concern ourselves with

the symmetric part of the shielding tensor, and 'σ' should be taken to mean the symmetric part of the shielding tensor in what follows.

It is possible to chose the axis frame that σ is defined with respect to so that shielding tensor is diagonal. This axis frame is the *principal axis frame*, designated 'PAF', or x^{PAF}, y^{PAF}, z^{PAF}. The numbers along the resulting diagonal of σ^{PAF} are the *principal values* of the shielding tensor, so for instance, $\sigma_{xx}^{\mathrm{PAF}}$ is the principal value associated with the principal frame x axis. The orientation of the principal axis frame is determined by the electronic structure of the molecule that contains the nucleus in question and is fixed with respect to the molecule. We can picture the shielding tensor as being represented by an ellipsoid fixed within the molecule and centred on the nucleus it applies to. The principal axes of the ellipse coincide with the principal axis frame of the shielding tensor, and the length of each principal axis of the ellipsoid is proportional to the principal value of the shielding tensor associated with that principal axis. If the molecular orientation in the laboratory frame changes, then so does the orientation of the shielding tensor, as illustrated in Fig. 1.5. If the nucleus is at a crystallographic site of symmetry, then the shielding tensor reflects this symmetry. For instance, the shielding tensor for a nucleus at a site of axial symmetry has a principal axis frame in which the z^{PAF} axis coincides with the symmetry axis and the principal values are such that $\sigma_{xx}^{\mathrm{PAF}} = \sigma_{yy}^{\mathrm{PAF}} \neq \sigma_{zz}^{\mathrm{PAF}}$.

The three principal values of the shielding tensor $\sigma_{\alpha\alpha}^{\mathrm{PAF}}$ are frequently expressed instead as the isotropic value σ_{iso}, the anisotropy Δ, and the asymmetry η. These quantities are defined from the principal values as follows:

$$\begin{aligned} \sigma_{\mathrm{iso}} &= \frac{1}{3}\left(\sigma_{xx}^{\mathrm{PAF}} + \sigma_{yy}^{\mathrm{PAF}} + \sigma_{zz}^{\mathrm{PAF}}\right) \\ \Delta &= \sigma_{zz}^{\mathrm{PAF}} - \sigma_{\mathrm{iso}} \\ \eta &= \left(\sigma_{xx}^{\mathrm{PAF}} - \sigma_{yy}^{\mathrm{PAF}}\right)\Big/\sigma_{zz}^{\mathrm{PAF}} \end{aligned} \tag{1.82}$$

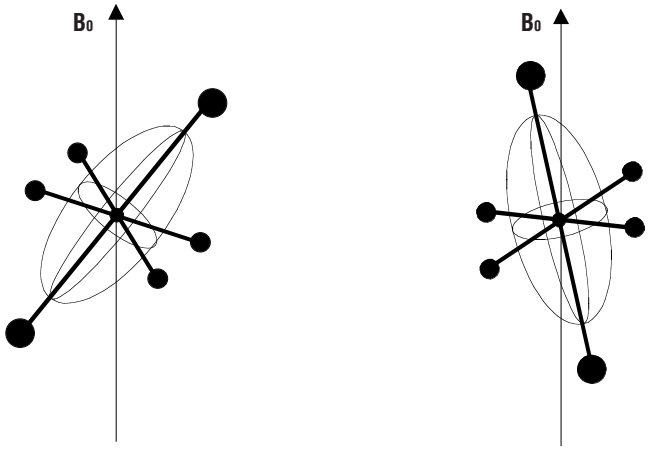

Fig. 1.5 Illustrating the ellipsoid representation of the shielding tensor. The principal axes of the ellipsoid coincide with the shielding tensor principal axis frame, which in turn, is fixed in orientation with respect to the molecule.

If the applied field $\mathbf{B}_0$ is along z, then the shielding interaction hamiltonian in Equation (1.77) becomes

$$\hat{H}_{cs} = -\gamma\hbar\hat{I}_z\sigma_{zz}^{lab}B_0 \tag{1.83}$$

where the z is the laboratory frame z axis. Note that only the zz component of the shielding tensor is required, i.e. that which governs the shielding field in the direction of the applied field $\mathbf{B}_0$, and the quantization axis for the spins. The shielding interaction generates no oscillating fields perpendicular to $\mathbf{B}_0$ which could also influence the spin system as discussed in the previous section (in the absence of molecular motion). It is therefore an *inhomogeneous* interaction; it is time-independent. The question of how to generate the laboratory frame-shielding tensor, σ^{lab}, from that expressed in its principal axis frame, σ^{PAF}, is discussed in the next section.

Experimental manifestations of the shielding tensor

The shielding anisotropy has its most important consequences for powder samples, although, of course, it influences the frequencies of the resonances observed for single crystal samples too.

The effect of the shielding hamiltonian of Equation (1.83) is found by applying $\hat{H}_{cs}$ to the spin levels described by $|I, m\rangle$, in order to find the first-order energy shift on these levels. The first-order contribution to the energy of the spin levels from chemical shielding, E_{cs} is

$$\begin{aligned} E_{cs} &= -\gamma\hbar\sigma_{zz}^{lab}B_0\langle I,m|\hat{I}_z|I,m\rangle \\ &= -\gamma\hbar\sigma_{zz}^{lab}B_0 m \end{aligned} \tag{1.84}$$

The NMR spectral frequency (in absolute units) corresponds to the transition energy between the $|+\tfrac{1}{2}\rangle$ and $|-\tfrac{1}{2}\rangle$ energy levels, in frequency units. The contribution to this frequency from the chemical shielding ω_{cs}, is easily found from Equation (1.84) to be

$$\omega_{cs} = -\gamma\sigma_{zz}^{lab}B_0 = -\omega_0\sigma_{zz}^{lab} \tag{1.85}$$

To examine ω_{cs} further, we need to rewrite the σ_{zz}^{lab} term in terms of the principal values of the shielding tensor and the orientation of its principal axis frame in the laboratory frame. We find σ_{zz}^{lab} from

$$\sigma_{zz}^{lab} = (0 \quad 0 \quad 1)\,\sigma^{lab}\begin{pmatrix}0\\0\\1\end{pmatrix} \tag{1.86}$$

where the unit vector along z (laboratory frame) (0 0 1) ensures that it is the zz component of σ^{lab} which is projected out in Equation (1.86).[6] If the shielding tensor is expressed in some other axis frame f, the equivalent expression is

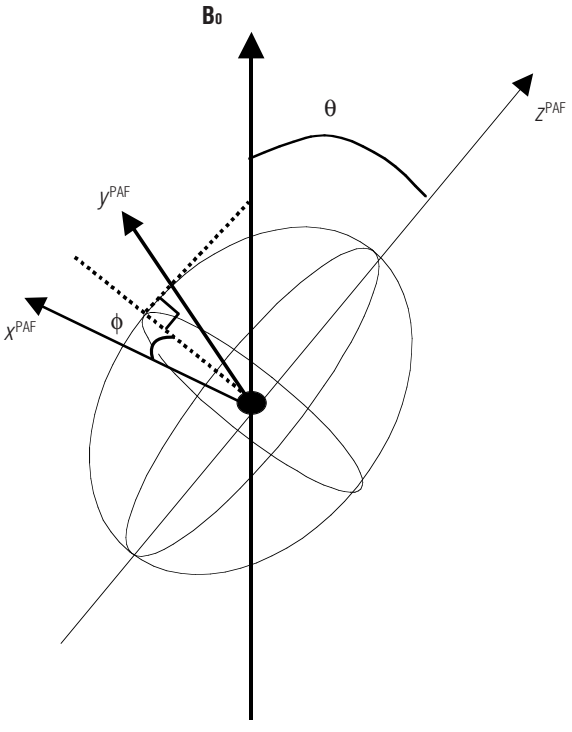

Fig. 1.6 Definitions of the angles θ and ϕ, which are the polar angles defining the orientation of the $\mathbf{B}_0$ field in the $(x^{PAF}, y^{PAF}, z^{PAF})$ axis frame, the principal axis frame of the shielding tensor.

$$\sigma_{zz}^{\text{lab}} = \mathbf{b}_0^f \boldsymbol{\sigma}^f \mathbf{b}_0^f \tag{1.87}$$

where $\mathbf{b}_0^f$ is the unit vector in the direction of $\mathbf{B}_0$ in the frame f and $\boldsymbol{\sigma}^f$ is the shielding tensor in the same frame. Thus combining Equations (1.85) and (1.87), we have for the chemical shift contribution to the spectral frequency,

$$\omega_{\text{cs}} = -\omega_0 \mathbf{b}_0^f \boldsymbol{\sigma}^f \mathbf{b}_0^f \tag{1.88}$$

If the direction of $\mathbf{B}_0$ in the shielding tensor principal axis frame, $\mathbf{b}_0^{\text{PAF}}$, is described by the polar angles (θ, ϕ) then (see Fig. 1.6 for definitions of these angles)

$$\mathbf{b}_0^{\text{PAF}} = (\sin\theta\cos\phi, \sin\theta\sin\phi, \cos\theta) \tag{1.89}$$

Using Equation (1.89) in Equation (1.88) for ω_{cs} we find

$$\omega_{\text{cs}}(\theta,\phi) = -\omega_0(\sigma_{xx}^{\text{PAF}} \sin^2\theta\cos^2\phi + \sigma_{yy}^{\text{PAF}} \sin^2\theta\sin^2\phi + \sigma_{zz}^{\text{PAF}} \cos^2\theta) \tag{1.90}$$

For a shielding tensor with axial symmetry, $\sigma_{xx}^{\text{PAF}} = \sigma_{yy}^{\text{PAF}}$, and so this equation simplifies to

$$\omega_{cs}(\theta) = -\omega_0 \sigma_{zz}^{PAF} \frac{1}{2}(3\cos^2\theta - 1) \tag{1.91}$$

Often we define the shielding tensor relative to the isotropic shielding. The isotropic shielding, σ_{iso} is simply the average of the diagonal elements of the shielding tensor (in any frame since the trace of a tensor is invariant to rotation of the axis frame defining the tensor). Thus

$$\sigma_{iso} = \frac{1}{3}(\sigma_{xx}^f + \sigma_{yy}^f + \sigma_{zz}^f) \tag{1.92}$$

The *anisotropic* part of the shielding tensor, when the shielding tensor is expressed in frame *f*, is then

$$\sigma_{aniso}^f = \sigma^f - \mathbf{1}\cdot\sigma_{iso} \tag{1.93}$$

and the anisotropic part of the chemical shift frequency, for an axially symmetric shielding tensor is

$$\omega_{cs}^{aniso}(\theta) = -\omega_0(\sigma_{zz}^{PAF} - \sigma_{iso})\frac{1}{2}(3\cos^2\theta - 1) \tag{1.94}$$

Alternatively, the chemical shift frequency can be expressed in terms of the isotropic component (ω_{iso}), shielding anisotropy (Δ) and asymmetry (η) (see Equation (1.82) for their definition):

$$\omega_{cs}(\theta,\phi) = -\omega_0\sigma_{iso} - \frac{1}{2}\omega_0\Delta\{3\cos^2\theta - 1 + \eta\sin^2\theta\cos 2\phi\} \tag{1.95}$$

where the quantity $-\omega_0\sigma_{iso} = \omega_{iso}$ is the isotropic chemical shift frequency, relative to the bare nucleus.

So what are the implications of Equations (1.91) and (1.95) for the chemical shift frequency? In a *powder* sample, all molecular orientations are present. Remembering that the shielding principal axis frame is fixed in the molecule, this means that in a powder sample all values of the angle θ (and ϕ in non-axial symmetry) are possible. Each different molecular orientation implies a different orientation of principal axis frame with respect to the applied field, $\mathbf{B}_0$, and so has a different chemical shift associated with it, from Equation (1.95). The spectrum will therefore take the form of a *powder pattern* with lines from the different molecular orientations covering a range of frequencies. The lines from the different orientations overlap and form a continuous lineshape. As can be seen from Equation (1.95), some molecular orientations yield the same chemical shift, and so there may be a number of lines at the same chemical shift. The resultant intensity at any given frequency in the powder pattern is therefore proportional to the number of molecular orientations that have that particular chemical shift. This means that the powder pattern lineshape is very distinctive, which depends on the symmetry of the shielding tensor,

which in turn, depends on the site symmetry at the nucleus, as we have already seen (Fig. 1.7).

The discontinuities in the lineshapes give the principal values of the shielding tensor, which may be thus read directly off the spectrum. The directions of the principal axes have no effect on a powder spectrum, providing there is true random distribution of molecular orientations in the sample. The isotropic frequency ω_{iso} is at the centre of 'mass' of the powder pattern, i.e. one-third of the way between $\omega_\perp$ and $\omega_\parallel$ in this case.

In the axial symmetry case in Fig. 1.7, the frequencies of the discontinuities are given by (again, in absolute frequency units)

$$\begin{aligned} \omega_\perp &= \omega_0 - \omega_0(\sigma_{xx}^{PAF} - \sigma_{iso}) = \omega_0 - \omega_0(\sigma_{yy}^{PAF} - \sigma_{iso}) \\ \omega_\parallel &= \omega_0 - \omega_0(\sigma_{zz}^{PAF} - \sigma_{iso}) \end{aligned} \tag{1.96}$$

i.e. the Larmor frequency (spectral frequency of the bare nucleus) plus the chemical shift contribution.

The lineshape in this case has a much larger intensity at the frequency $\omega_\perp$ than at $\omega_\parallel$, reflecting the larger number of molecular orientations which contribute to the lineshape at this frequency; all molecules oriented so that the x^{PAF}–y^{PAF} plane is parallel to $\mathbf{B}_0$ contribute to the lineshape at $\omega_\perp$, while those oriented so that z^{PAF} is parallel to $\mathbf{B}_0$ contribute to the lineshape at $\omega_\parallel$. There are an infinite number of molecular orientations with the x^{PAF}–y^{PAF} plane is parallel to $\mathbf{B}_0$, but only one with z^{PAF} is parallel to $\mathbf{B}_0$.

For the less than axial symmetry case, ω_{11}, ω_{22} and ω_{33} correspond to principal values of the shielding tensor in a similar manner to $\omega_\perp$ and $\omega_\parallel$ in the axial symmetry case, i.e.

$$\omega_{ii} = \omega_0 - \omega_0(\sigma_{\alpha\alpha}^{PAF} - \sigma_{iso}) \tag{1.97}$$

but we cannot tell from the powder pattern which axis of the principal axis frame each value corresponds to.

Definition of the chemical shift

The total spectral frequency in absolute units is the Larmor frequency plus the chemical shift contribution, i.e.

$$\omega = \omega_0 + \omega_{cs}(\theta, \phi) \tag{1.98}$$

When performing NMR experiments, absolute frequencies, such as ω in Equation (1.98), are not measured; a reference substance is used and frequencies of lines are measured relative to a specific line in the spectrum of the reference substance and quoted as *chemical shifts with respect to that substance* or *offset frequencies*. The chemical shift δ_{iso} is defined in Equation (1.99):

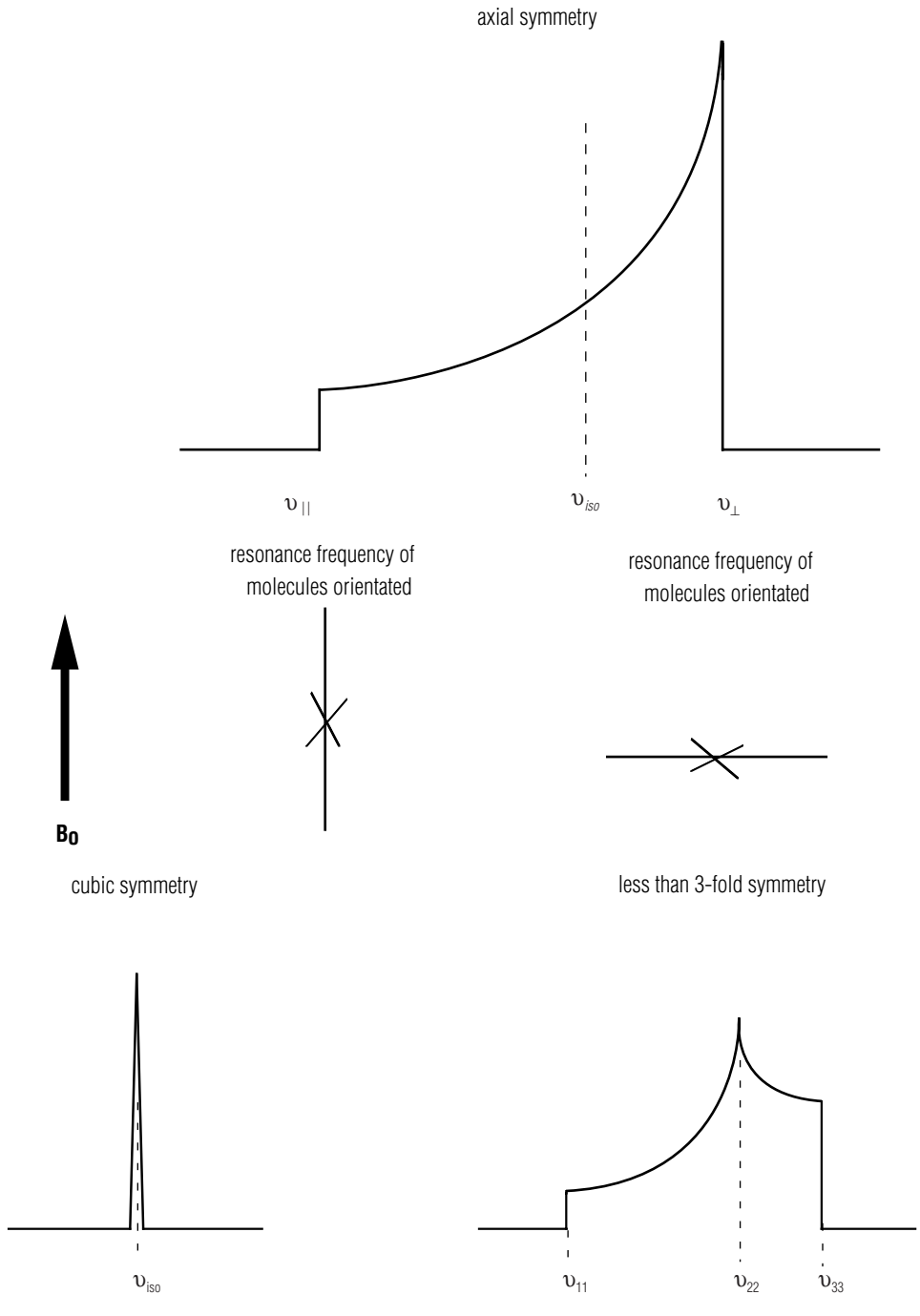

Fig. 1.7 Chemical shift anisotropy powder patterns. Powder patterns arise from samples where there are many crystallites randomly oriented, so that all possible molecular orientations are present with random distribution. Powder patterns arise because each different molecular orientation with respect to $\mathbf{B}_0$ has its own spectral frequency. Each different orientation thus gives rise to its own (sharp) spectral line; the lines from different orientations overlap continuously giving rise to the observed powder pattern. These powder lineshapes are thus *inhomogeneous*; they may be considered as made up of many independent contributions from different parts of the sample.

$$\delta = \frac{\nu - \nu_{\text{ref}}}{\nu_{\text{ref}}} = \frac{\sigma_{zz}^{\text{lab}}(\text{ref}) - \sigma_{zz}^{\text{lab}}}{1 - \sigma_{zz}^{\text{lab}}(\text{ref})} \tag{1.99}$$

where ν is the spectral frequency of the signal for the spin of interest (in its given chemical site) and ν_{ref} is the resonance frequency of the same spin in some reference compound. In the case where $1 >> \sigma_{zz}^{\text{lab}}(\text{ref})$, this reduces to

$$\delta \approx \sigma_{zz}^{\text{lab}}(\text{ref}) - \sigma_{zz}^{\text{lab}} \tag{1.100}$$

The corresponding *chemical shift tensor* has elements

$$\delta_{\alpha\beta} = \frac{\sigma_{\alpha\beta}(\text{ref}) - \sigma_{\alpha\beta}}{1 - \sigma_{\alpha\beta}} \tag{1.101}$$

where $\sigma_{\alpha\beta}$ is the $\alpha\beta$ element of the shielding tensor for the spin of interest in some axis frame, and $\delta_{\alpha\beta}$ is the corresponding element of the chemical shift tensor for that spin in the same frame. The chemical shift anisotropy and asymmetry are defined in an analogous manner to the shielding anisotropy and asymmetry of Equation (1.82). Often however, the principal values of the chemical shift tensor are known, but not its principal axis frame. The principal values are then labelled by convention as δ_{11}^{PAF}, δ_{22}^{PAF}, δ_{33}^{PAF}, where $\delta_{11}^{\text{PAF}} \geq \delta_{22}^{\text{PAF}} \geq \delta_{33}^{\text{PAF}}$. The *chemical shift* anisotropy (Δ_{cs}) and asymmetry (η_{cs}) and are defined from these as

$$\begin{aligned} \Delta_{\text{cs}} &= \delta_{11}^{\text{PAF}} - \delta_{\text{iso}} \\ \eta_{\text{cs}} &= \frac{\delta_{33}^{\text{PAF}} - \delta_{22}^{\text{PAF}}}{\delta_{11}^{\text{PAF}}} \end{aligned} \tag{1.102}$$

Observed chemical shifts are related to the chemical shift tensor through

$$\delta = \delta_{\text{iso}} + \frac{1}{2}\Delta_{\text{cs}}\{3\cos^2\theta - 1 + \eta_{\text{cs}}\sin^2\theta\cos 2\phi\}$$

where the isotropic chemical shift, δ_{iso}, is

$$\begin{aligned} \delta_{\text{iso}} &= \frac{\sigma_{\text{iso}}(\text{ref}) - \sigma_{\text{iso}}}{1 - \sigma_{\text{iso}}(\text{ref})} \\ &\approx \sigma_{\text{iso}}(\text{ref}) - \sigma_{\text{iso}} \\ &= \frac{1}{3}(\delta_{11}^{\text{PAF}} + \delta_{22}^{\text{PAF}} + \delta_{33}^{\text{PAF}}) \end{aligned} \tag{1.103}$$

1.4.2 Dipole–dipole coupling

Theory

Each nuclear spin possesses a magnetic moment and these interact through space; this is dipole–dipole or dipolar coupling. Note that this is distinct from scalar (J) coupling, which is an indirect coupling of the nuclear spins mediated by electrons.

In solution, the dipole–dipole interaction is averaged to its isotropic value, zero, by molecular tumbling. This is not the case in solids where this interaction is a major cause of linebroadening.

Classically, the energy of interaction between two point-magnetic dipoles $\boldsymbol{\mu}_1$ and $\boldsymbol{\mu}_2$ separated by a distance r is:

$$U = \left\{ \frac{\boldsymbol{\mu}_1 \cdot \boldsymbol{\mu}_2}{r^3} - 3\frac{(\boldsymbol{\mu}_1 \cdot \mathbf{r})(\boldsymbol{\mu}_2 \cdot \mathbf{r})}{r^5} \right\} \frac{\mu_0}{4\pi} \tag{1.104}$$

where $\mathbf{r}$ is the vector between point-magnetic dipoles.

Quantum mechanically, the magnetic moment operator $\hat{\boldsymbol{\mu}}$, is given by:

$$\hat{\mu} = \gamma \hbar \, \hat{\mathbf{I}} \tag{1.105}$$

for a spin I.

Substituting this operator in the classical expression for energy of interaction, we obtain the interaction hamiltonian for dipolar coupling between two spins I and S in angular frequency units (rad s^{-1}):

$$\hat{H}_{\mathrm{dd}} = -\left(\frac{\mu_0}{4\pi}\right)\gamma_I \gamma_S \hbar \left(\frac{\mathbf{I} \cdot \mathbf{S}}{r^3} - 3\frac{(\mathbf{I} \cdot \mathbf{r})(\mathbf{S} \cdot \mathbf{r})}{r^5} \right) \tag{1.106}$$

Expressing Equation (1.106) in spherical polar coordinates, and expanding the scalar products, we obtain after some considerable rearrangement (and again, in angular frequency units),

$$\hat{H}_{\mathrm{dd}} = -\left(\frac{\mu_0}{4\pi}\right)\frac{\gamma_I \gamma_S \hbar}{r^3}[A + B + C + D + E + F] \tag{1.107}$$

where:

$$\begin{aligned}
A &= \hat{I}_z \hat{S}_z (3\cos^2\theta - 1) \\
B &= -\frac{1}{4}[\hat{I}_+ \hat{S}_- + \hat{I}_- \hat{S}_+](3\cos^2\theta - 1) \\
C &= -\frac{3}{2}[\hat{I}_z \hat{S}_+ + \hat{I}_+ \hat{S}_z]\sin\theta\cos\theta\, e^{-i\phi} \\
D &= -\frac{3}{2}[\hat{I}_z \hat{S}_- + \hat{I}_- \hat{S}_z]\sin\theta\cos\theta\, e^{+i\phi} \\
E &= -\frac{3}{4}[\hat{I}_+ \hat{S}_+]\sin^2\theta\, e^{-2i\phi} \\
F &= -\frac{3}{4}[\hat{I}_- \hat{S}_-]\sin^2\theta\, e^{+2i\phi}
\end{aligned} \tag{1.108}$$

$\hat{I}_+$, $\hat{S}_+$ and $\hat{I}_-$, $\hat{S}_-$ are the raising and lowering operators respectively acting on spins I and S (defined in Box 1.2, and the polar angles θ and ϕ are defined in Fig. 1.8 below.

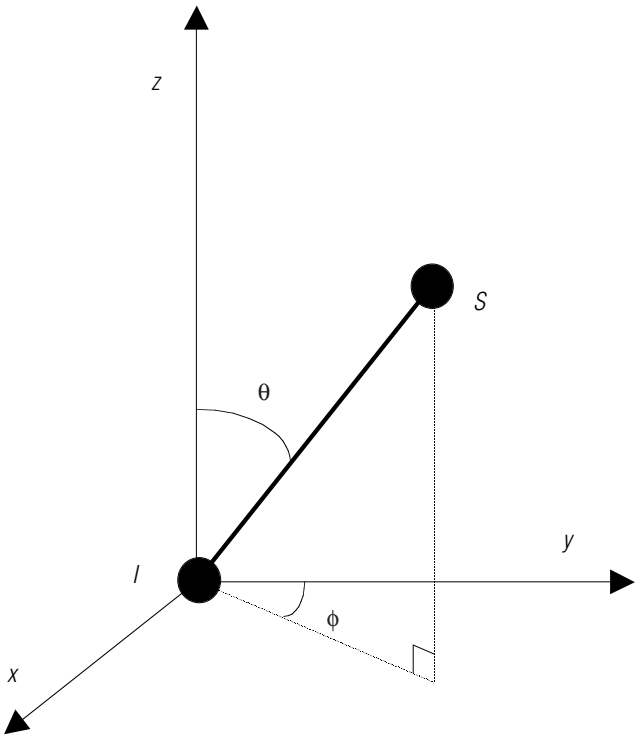

Fig. 1.8 Definition of the polar angles θ and ϕ specifying the orientation of the *I–S* internuclear vector with respect to the $\mathbf{B}_0$ field which is along the laboratory frame *z* axis.

Alternatively, we may express the dipolar hamiltonian (in angular frequency units) in the tensorial form

$$\hat{H}_{\mathrm{dd}} = -2\,\hat{\mathbf{I}} \cdot \mathbf{D} \cdot \hat{\mathbf{S}} \tag{1.109}$$

The spin *S* is the equivalent of vector **A** in Equation (1.75) and it is the spin *S* which is the ultimate source of local field at spin *I*. The term **D** is the dipolar-coupling tensor, with principal values of $-d/2$, $-d/2$, $+d$ where d is given by

$$d = \hbar\left(\frac{\mu_0}{4\pi}\right)\frac{1}{r^3}\gamma_I\gamma_S \tag{1.110}$$

and is known as the *dipolar-coupling constant* (in units of rad s^{-1}). The dipolar-coupling tensor **D** describes how the field due to spin *S* varies with the orientation of the *I–S* internuclear vector in the applied field. The spin angular momenta of *I* and *S* determines the local magnetic field they each give rise to. In turn, these angular momenta are quantized, with $\mathbf{B}_0$ defining the quantization axis for both. Thus the local field that each spin gives rise to depends on the direction of $\mathbf{B}_0$ (and the spin state, i.e. component of spin parallel to $\mathbf{B}_0$). The strength of field at spin *I* due to spin *S* thus depends on the relative orientation of the *I–S* vector in the applied field, $\mathbf{B}_0$.

It should be noted that the dipolar-coupling tensor is *traceless*, i.e. there is no isotropic component. Thus, when the dipole coupling is averaged by molecular

motion in liquid samples, it is averaged to zero and there is no direct effect of the dipolar coupling on the NMR spectrum. The dipolar-coupling tensor **D** is always axially symmetric in its principal axis frame, with the unique axis of the principal axis frame lying along the *I*–*S* vector – see Section 1.4.1 for further discussion of tensors and their principal axis frames.

We now consider two possible cases of dipolar coupling, *homonuclear dipolar coupling* where spins *I* and *S* are the same species, and *heteronuclear dipolar coupling* where spins *I* and *S* are different.

Homonuclear dipolar coupling

If we are considering interactions of a spin *I* with its environment, we know that only certain terms of the form $-\gamma\hbar(\hat{I}_x B_x^{\text{loc}}(t) + \hat{I}_y B_y^{\text{loc}}(t) + \hat{I}_z B_z^{\text{loc}})$ are likely to have a significant effect on the spin system at equilibrium, as explained in Section 1.4. To recap briefly, the term B_z^{loc} represents a static field parallel to the applied field $\mathbf{B}_0$, which affects the energy gap between the nuclear spin levels. The term $(B_x^{\text{loc}}(t), B_y^{\text{loc}}(t))$ represents a magnetic field in the transverse plane: this field has a significant effect on the spin system only if it precesses around $\mathbf{B}_0$ at a frequency close to the resonance frequency (Larmor frequency) of the spin. Now consider the interaction hamiltonian representing the dipolar interaction between two spins *I* and *S* as written in Equation (1.107), the sum of six terms, *A*, *B*, *C*, *D*, *E* and *F*.

As we will now show, a term *A* + *B* corresponds to the general form

$$-\gamma\hbar\left(\hat{I}_x B_x^{\text{loc}}(t) + \hat{I}_y B_y^{\text{loc}}(t) + \hat{I}_z B_z^{\text{loc}}\right).$$

The terms *A* and *B* are given by

$$A = \hat{I}_z\hat{S}_z(3\cos^2\theta - 1)$$
$$B = -\frac{1}{2}[\hat{I}_x\hat{S}_x + \hat{I}_y\hat{S}_y](3\cos^2\theta - 1)$$

expressing *B* in terms of Cartesian operators rather than the raising and lowering operators of Equation (1.108). Classically, a spin angular momentum **S** gives rise to a magnetic dipole moment $\boldsymbol{\mu}_S$ with components

$$\begin{aligned}\mu_x^S &= \gamma S_x\\ \mu_y^S &= \gamma S_y\\ \mu_z^S &= \gamma S_z\end{aligned} \tag{1.111}$$

which gives a local magnetic field $\mathbf{B}^{\text{loc}}$

$$\begin{aligned}\mathbf{B}^{\text{loc}} &= \left(\frac{\mu_0}{4\pi}\right)\frac{1}{r^3}(3\cos^2\theta - 1)\boldsymbol{\mu}_S\\ &= \left(\frac{\mu_0}{4\pi}\right)\frac{\gamma_S}{r^3}(3\cos^2\theta - 1)(\mathbf{i}S_x + \mathbf{j}S_y + \mathbf{k}S_z)\end{aligned} \tag{1.112}$$

a distance r away along a vector oriented at an angle θ to the magnetic dipole moment $\boldsymbol{\mu}_S$; **i**, **j**, **k** are the unit Cartesian vectors. The term $A + B$ can then be rewritten as

$$(A+B)\hbar^2\left(\frac{\mu_0}{4\pi}\right)\frac{\gamma_I\gamma_S}{r^3} = \left(\frac{\mu_0}{4\pi}\right)\frac{\gamma_I\gamma_S\hbar^2}{r^3}(3\cos^2\theta - 1)\left[\hat{I}_z\hat{S}_z - \frac{1}{2}(\hat{I}_x\hat{S}_x + \hat{I}_y\hat{S}_y)\right]$$
$$= \gamma_I\hbar\left[\hat{I}_z\hat{B}_z^{\text{loc}} - \frac{1}{2}(\hat{I}_xB_x^{\text{loc}} + \hat{I}_y\hat{B}_y^{\text{loc}})\right] \qquad (1.113)$$

where $\hat{\mathbf{B}}^{\text{loc}}$ is the operator for the local field produced by spin S and is given by Equation (1.112) with all physical quantities replaced by the appropriate operator, i.e.

$$\hat{B}_\alpha^{\text{loc}} = \left(\frac{\mu_0}{4\pi}\right)\frac{\gamma_s}{r^3}(3\cos^2\theta - 1)\hbar\hat{S}_\alpha$$

The transverse term $\gamma_I\hbar(\hat{I}_x\hat{B}_x^{\text{loc}} + \hat{I}_y\hat{B}_y^{\text{loc}})$ only has a significant effect if the local magnetic field arising from spin S, $\mathbf{B}^{\text{loc}}$, precesses about $\mathbf{B}_0$ at roughly the Larmor frequency of spin I. The transverse components of spin S (S_x and S_y) precess about $\mathbf{B}_0$ at the Larmor frequency for spin S, γ_SB_0 (see Section 1.1) and so the field arising from them (B_x^{loc},B_y^{loc}) will do likewise. If spin I and S are the same species, i.e. $\gamma_S = \gamma_I$, then the Larmor frequencies of spins I and S are the same, so the field arising from spin S necessarily precesses about $\mathbf{B}_0$ at near the Larmor frequency of spin I. Then the $\gamma_I\hbar(\hat{I}_x\hat{B}_x^{\text{loc}} + \hat{I}_y\hat{B}_y^{\text{loc}})$ term in Equation (1.113) has a significant effect on spin I. Note that this situation only arises for homonuclear dipolar coupling, where spins I and S are the same.

A similar analysis shows that we may discard terms C, D, E and F as they do not have the general form $-\gamma\hbar(\hat{I}_xB_x^{\text{loc}}(t) + \hat{I}_yB_y^{\text{loc}}(t) + \hat{I}_zB_z^{\text{loc}})$. They therefore make an insignificant contribution to the energy of the spin system (although they may be important in relaxation processes for instance). The same conclusions may be deduced by examining which components of $\hat{H}_{\text{dd}}$ commute with the Zeeman hamiltonian for the I–S spin system. As discussed in the introduction to Section 1.4, only those terms which commute with the Zeeman hamiltonian have a first-order energy contribution to the energy levels of the spin system.

In summary, then, the homonuclear dipolar hamiltonian may be truncated to

$$\hat{H}_{\text{dd}}^{\text{homo}} = -\left(\frac{\mu_0}{4\pi}\right)\frac{\gamma_I\gamma_S\hbar}{r^3}(3\cos^2\theta - 1)\left[\underbrace{\hat{I}_z\hat{S}_z}_{\text{Term }A} - \frac{1}{2}\underbrace{(\hat{I}_x\hat{S}_x + \hat{I}_y\hat{S}_y)}_{\text{Term }B}\right] \qquad (1.114)$$

for the calculation of energies of nuclear spin levels. Equation (1.114) is often written more succinctly as

$$\hat{H}_{\text{dd}}^{\text{homo}} = -d\cdot\frac{1}{2}(3\cos^2\theta - 1)[3\hat{I}_z\hat{S}_z - \hat{\mathbf{I}}\cdot\hat{\mathbf{S}}] \qquad (1.115)$$

where d is the dipolar coupling constant defined previously (Equation (1.110)) and where we have used the fact that $\hat{\mathbf{I}}\cdot\hat{\mathbf{S}} = \hat{I}_x\hat{S}_x + \hat{I}_y\hat{S}_y + \hat{I}_z\hat{S}_z$.

Box 1.3 Basis sets for multispin systems

Consider a spin system with N uncoupled spin in the static magnetic field of an NMR experiment. The hamiltonian describing this spin system is simply the sum of the operators for the energy of each individual spin in the field, i.e.

$$\hat{H}_0 = -\gamma \sum_j^N \hat{I}_z^j B_0 \tag{i}$$

where j denotes the nucleus and the operator $\hat{I}_z^j$ only acts on the spin coordinates of the spin j. The eigenfunctions of the $\hat{I}_z^j$ operators are $|I_j m_j\rangle$ or $\Psi_{I_j m_j}$ depending on the notation being used (see Box 1.1). The eigenfunctions Ψ of the $\hat{H}_0$ hamiltonian must then be products of the $\Psi_{I_j m_j}$ functions:

$$\Psi = \psi_{I_1 m_1} \psi_{I_2 m_2} \ldots \psi_{I_N m_N} \tag{ii}$$

so that

$$\begin{aligned} \hat{H}_0 \Psi &= -\gamma\hbar \sum_j^N \hat{I}_z^j B_0 |I_1 m_1; I_2 m_2; \ldots I_N m_N\rangle \\ &= -\gamma\hbar B_0 (m_1 + m_2 + \ldots m_N) |I_1 m_1; I_2 m_2; \ldots I_N m_N\rangle \end{aligned} \tag{iii}$$

which has the general form of the eigenfunction/eigenvalue equation given in Box 1.1. The eigenvalue, i.e. the energy of the spin system, E_0, is by inspection of (iii),

$$E_0 = -\gamma\hbar B_0 (m_1 + m_2 + \ldots m_N) \tag{iv}$$

The product wavefunctions/eigenfunctions of Equation (ii) constitute a complete set for an N spin system, from which any other function describing the system can be formed. These product wavefunctions are thus a good basis set with which to describe the spin system under more complex interactions on the spin system, such as dipole–dipole coupling.

The effect of homonuclear dipolar coupling on a spin system

In order to see what effect the dipole–dipole coupling operator has on a homonuclear spin system, consider the simple two-spin system which before dipolar-coupling effects are taken into account may be represented by the product spin states illustrated in Fig. 1.9.

We now need to consider what effect the operator $\hat{H}_{\mathrm{dd}}$ has on the energies and wavefunctions of these states. Consider the effects of each term in the dipole–dipole operator in turn.

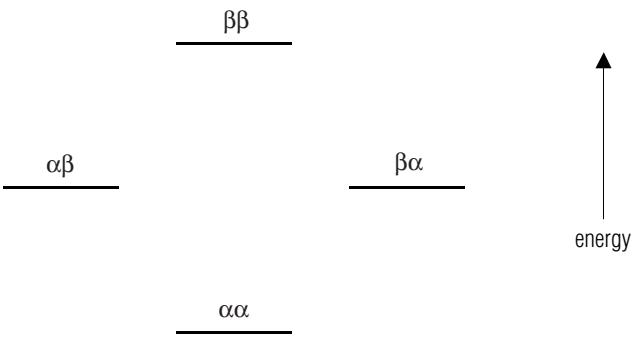

Fig. 1.9 The energy levels and wavefunctions in a homonuclear two-spin system, before dipolar coupling is considered, i.e. the Zeeman states. The αβ and βα levels are degenerate in a homonuclear spin system and are mixed by dipolar coupling.

1. Term *A*: this term contains the spin operator $\hat{I}_z\hat{S}_z$. This has the effect of giving a first-order change in energy to all the states of, for example,

$$-\left(\frac{\mu_0}{4\pi}\right)\frac{\gamma_I\gamma_S\hbar^2}{r^3}(3\cos^2\theta-1)\langle\alpha\alpha|\hat{I}_z\hat{S}_z|\alpha\alpha\rangle$$

   for the αα spin state. The eigenfunctions of this operator are simply the product Zeeman states, αα, αβ, βα, ββ. This can be verified by operating with the *A* operator on each of these functions in turn, and seeing that the result is the original function, multiplied by a constant, i.e. $\hat{I}_z\hat{S}_z|\alpha\alpha\rangle = \frac{1}{4}|\alpha\alpha\rangle$.
2. Term *B*: this term contains the $[\hat{I}_+\hat{S}_- + \hat{I}_-\hat{S}_+]$ spin operator term. Therefore, in the matrix representation of this operator, there will be non-zero elements between the αβ and βα basis functions, i.e.

$$\mathbf{B} = -\frac{1}{2}(3\cos^2\theta-1)\begin{pmatrix}0&0&0&0\\0&0&1&0\\0&1&0&0\\0&0&0&0\end{pmatrix} \tag{1.116}$$

   where the basis functions in this representation are in the order αα, αβ, βα, ββ. We say that *B mixes* the αβ and βα functions. Hence, the eigenfunctions of *B* include two linear combinations of the αβ and βα functions. The other eigenfunctions are simply αα and ββ, since these are not mixed with any other functions by the *B* term.

Now look more closely at the homonuclear dipolar hamiltonian. The two terms, *A* and *B*, do not commute. As explained in Box 1.2 previously, two operators that do not commute cannot have the same eigenfunctions. Thus the terms *A* and *B* in the dipolar hamiltonian do not, in general, have common eigenfunctions, so there can be no eigensolution for the homonuclear dipolar hamiltonian. The one excep-

tion to this is when the two spins, I and S, are degenerate. In this case, the product Zeeman states, $\alpha\alpha$, $\alpha\beta$, $\beta\alpha$, $\beta\beta$, are not the only eigenfunctions of the A term; since the $\alpha\beta$ and $\beta\alpha$ states are degenerate, any linear combination of them is also an eigenfunction of the A term. Now, we have already seen that the eigenfunctions of the B term are $\alpha\alpha$, $\beta\beta$ and two linear combinations of $\alpha\beta$ and $\beta\alpha$.[7] Hence, the eigenfunctions of B are also eigenfunctions of A in this case. These eigenfunctions constitute the eigenfunctions of the truncated homonuclear dipolar hamiltonian also of course; their corresponding eigenvalues are the energies of the possible states of the two-spin system. These are *stationary states*, i.e. they are constant with time, by virtue of the fact that the wavefunctions which describe them are eigenfunctions of the hamiltonian for the system.

Now consider a three-spin system. The dipolar hamiltonian for such a system is

$$\begin{aligned}\hat{H}_{\mathrm{dd}}^{\mathrm{homo}} = &-d_{12}\cdot\frac{1}{2}(3\cos^2\theta_{12}-1)\left[2\hat{I}_{1Z}\hat{I}_{2z}-\frac{1}{2}(\hat{I}_{1+}\hat{I}_{2-}+\hat{I}_{1-}\hat{I}_{2+})\right]\\ &-d_{23}\cdot\frac{1}{2}(3\cos^2\theta_{23}-1)\left[2\hat{I}_{2Z}\hat{I}_{3z}-\frac{1}{2}(\hat{I}_{2+}\hat{I}_{3-}+\hat{I}_{2-}\hat{I}_{3+})\right]\\ &-d_{13}\cdot\frac{1}{2}(3\cos^2\theta_{13}-1)\left[2\hat{I}_{1Z}\hat{I}_{3z}-\frac{1}{2}(\hat{I}_{1+}\hat{I}_{3-}+\hat{I}_{1-}\hat{I}_{3+})\right]\end{aligned} \qquad (1.117)$$

where 1, 2, 3 label the three spins, and d_{ij} is the dipolar-coupling constant associated with the coupling between spins i and j. The angle θ_{ij} is the angle between the i–j internuclear vector and the applied field $\mathbf{B}_0$. It is easy to show that the Zeeman states $\alpha\alpha\alpha$ and $\beta\beta\beta$ are eigenfunctions of this hamiltonian. However, the remaining possible states of the system (which will be linear combinations of the remaining Zeeman functions, among which there are several degeneracies) are less easy to find. None of the operator terms in Equation (1.117) commutes with any other; in particular, none of the B-type terms, $(\hat{I}_{i+}\hat{I}_{j-} + \hat{I}_{i-}\hat{I}_{j+})$ commute with another. Thus, although it is possible to form linear combinations of degenerate Zeeman functions, $\alpha\beta\alpha$ and $\beta\alpha\alpha$ (or $\alpha\beta\beta$ and $\beta\alpha\beta$), which are eigenfunctions of $(\hat{I}_{1+}\hat{I}_{2-} + \hat{I}_{1-}\hat{I}_{2+})$, for instance, we will require a different linear combination for each of the other $(\hat{I}_{i+}\hat{I}_{j-} + \hat{I}_{i-}\hat{I}_{j+})$ terms.

The result is that these remaining possible states of the spin system change with time or *evolve* under the influence of the dipolar coupling. We can describe the dipolar-coupled multispin system in terms of time-dependent wavefunctions which are solutions to the time-dependent Schrödinger equation. Each of the wavefunctions will be a time-dependent mixture of degenerate Zeeman functions for the spin system (degenerate, that is, in the absence of dipolar coupling). The fluctuation of these over time makes it *look as though* each spin described by such a wavefunction is constantly changing its spin function, $\alpha \leftrightarrow \beta$. This is tantamount to saying that there is continual exchange of longitudinal magnetization between the spins of the dipolar-coupled system. Only the total z component of spin, M, for the whole spin system is conserved, where M is given by

$$M = m_1 + m_2 + m_3 + \ldots + m_N \tag{1.118}$$

for an N spin system, where m_i is the z compnent of spin for spin i in the absence of dipolar coupling. The effects of the homonuclear dipolar-coupling hamiltonian are summarized in Fig. 1.10.

The time-dependence of the state of the multispin system under homonuclear dipolar coupling is the reason for the huge linebroadening seen in the NMR spectra of dipolar-coupled spin systems (Fig. 1.11).

Heteronuclear dipolar coupling

The dipolar interaction hamiltonian for a homonuclear two-spin system is (from the previous section)

$$\hat{H}_{\mathrm{dd}}^{\mathrm{homo}} = -\left(\frac{\mu_0}{4\pi}\right)\frac{\gamma_I\gamma_S\hbar}{r^3}(3\cos^2\theta - 1)\Bigg[\underbrace{\hat{I}_z\hat{S}_z}_{\text{Term } A} - \frac{1}{2}\underbrace{(\hat{I}_x\hat{S}_x + \hat{I}_y\hat{S}_y)}_{\text{Term } B}\Bigg] \tag{1.119}$$

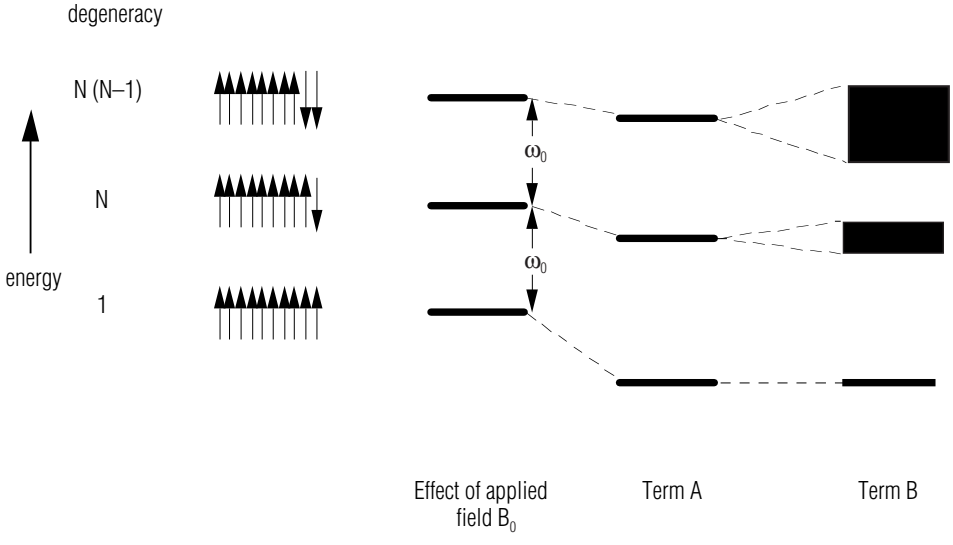

Fig. 1.10 In an N-spin, homonuclear, system, there may be many Zeeman levels with the same M quantum number ($M = m_1 + m_2 + \ldots + m_N$); these are degenerate in the absence of dipolar coupling. Dipolar coupling has the effect of mixing these degenerate states and splitting their energy.

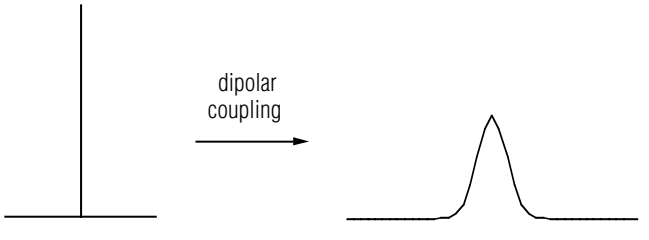

Fig. 1.11 The effect of homonuclear dipolar coupling in a multispin system is to broaden the resonance line, the lineshape tending to gaussian for a sufficiently large number of spins. For this reason, the ^{1}H linewidth in organic solids is frequently several tens of kHz wide.

in angular frequency units. However, we also noted that the transverse term, term *B*, is only significant if the magnetic field associated with spin *S* precesses at or near the resonance frequency of spin *I*. This is only the case if spin *I* and *S* are the same nuclide (with similar chemical shifts). So in a heteronuclear spin system, the dipolar hamiltonian is further truncated so that it only contains term *A*:

$$\hat{H}_{\mathrm{dd}}^{\mathrm{hetero}} = -\left(\frac{\mu_0}{4\pi}\right)\frac{\gamma_I\gamma_S\hbar}{r^3}(3\cos^2\theta - 1)\hat{I}_z\hat{S}_z \tag{1.120}$$

or

$$\hat{H}_{\mathrm{dd}}^{\mathrm{hetero}} = -d(3\cos^2\theta - 1)\hat{I}_z\hat{S}_z \tag{1.121}$$

in angular frequency units, where d is the dipolar coupling constant.

The effect of heteronuclear dipolar coupling on the spin system

This has the same form as the more familiar *J* or scalar coupling. The linebroadening effects of term *B* are now absent. The effect on the spectrum is much simpler than for homonuclear dipolar coupling. As seen above, the term *A* simply shifts the energies of the nuclear spin levels, much in the same way as (first-order) scalar coupling. The form of the spin states is unchanged from the original basis, i.e. there is no mixing of the spin states under heteronuclear dipolar coupling, so the simple product basis functions

$$\psi_{I,m_I}\psi_{S,m_S} = |I,m_I\rangle|S,m_S\rangle = |I,m_I;S,m_S\rangle \tag{1.122}$$

are the eigenfunctions of the heteronuclear dipolar hamiltonian. The resulting dipolar contribution to the energy levels of the *I*–*S* spin system are therefore

$$\begin{aligned} E_{\mathrm{dd}}^{\mathrm{hetero}} &= \langle Im_I;Sm_S|\hat{H}_{\mathrm{dd}}^{\mathrm{hetero}}|Im_I;Sm_S\rangle \\ &= -d\hbar(3\cos^2\theta - 1)m_Im_S \end{aligned} \tag{1.123}$$

where m_I and m_S are the z components of spin for spin *I* and *S*. Using the selection rule $\Delta m_I = \pm 1$ for the *I* spin spectrum and $\Delta m_S = \pm 1$ for the *S* spin spectrum, we can now establish the transition frequencies for the *I* and *S* spins in the dipolar-coupled *I*–*S* spin system.

For the *I* spin they are:

$$\omega_{\mathrm{dd}}^I(0) = \omega_0^I \pm \frac{1}{2}d(3\cos^2\theta - 1) \tag{1.124}$$

where ω_0^I is the transition frequency in the absence of dipolar coupling between *I* and *S*.

If *I* and *S* are both spin-$\frac{1}{2}$ nuclei, there are two *I* spin (and two *S* spin) transitions (as shown in Fig. 1.12), each with a $(3\cos^2\theta - 1)$ dependence, and so for powder

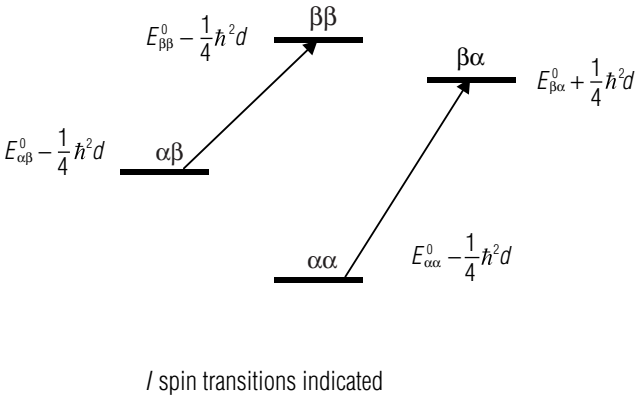

Fig. 1.12 The *I* spin transitions in a two-spin heteronuclear spin system (*I–S*). The form of the spectrum for spin *I* in a powder sample is shown in Fig. 1.13. The $E^0_{\alpha\alpha}$, etc., are the energies of the spin levels in the absence of dipolar coupling between *I* and *S*.

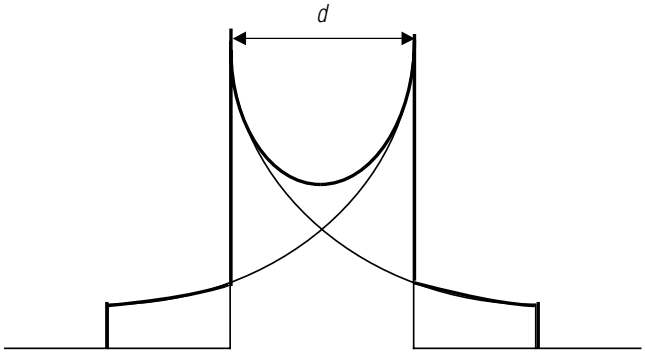

Fig. 1.13 The powder lineshape for the *I* spin in a heteronuclear two-spin system. The splitting of the 'horns' is equal to the dipolar coupling constant *d*. The horns are created by crystallites in which the *I–S* internuclear vector is perpendicular to the applied field $\mathbf{B}_0$.

samples each gives rise to the typical powder pattern seen for axial chemical shift anisotropy. However, one transition has a $+(3\cos^2\theta - 1)$ dependence, while the other has a $-(3\cos^2\theta - 1)$ dependence, so the powder pattern arising from one transition is the mirror image of that arising from the other. Both transitions have the same isotropic frequency, $\nu^I_{\rm iso}$ however. The general form of the lineshape is found to be that shown in Fig. 1.13.

1.4.3 Quadrupolar coupling

What is a quadrupolar nucleus?

A distribution of charge, such as protons in a nucleus, cannot be adequately described by simply specifying the total charge. In general, a proper description requires expanding the charge distribution function as a series of *multipoles*. The total charge is the zeroth-order multipole; the electric dipole moment is the first-order multipole in the expansion. The next highest term is the electric *quadrupole moment*, which has the distribution of charge illustrated in Fig. 1.14.

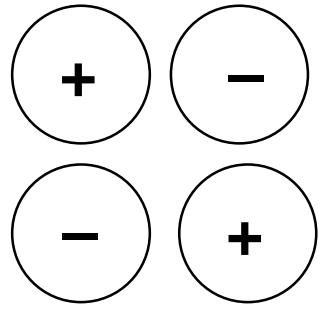

Fig. 1.14 The distribution of charge which gives rise to an electric quadrupole moment.

All nuclei with a spin greater than $\frac{1}{2}$ necessarily possess an electric quadrupole moment in addition to the magnetic dipole moment possessed by spin-$\frac{1}{2}$ nuclei. Electric quadrupoles interact with electric field gradients. Thus, a nucleus with a spin greater than $\frac{1}{2}$ not only interacts with the applied magnetic field and all local magnetic fields, but also with any electric field gradients present at the nucleus. This interaction affects the nuclear spin energy levels in addition to the other magnetic interactions already described.

The strength of the interaction depends upon the magnitude of the nuclear quadrupole moment and the strength of the electric field gradient. The electric quadrupole moment of a nucleus is generally given as eQ, where e is the proton charge: eQ is constant for a given nuclear species, and does not change with the chemical environment of the nucleus for instance.

It is important to realize that in a strong applied field $\mathbf{B}_0$, the applied field acts as the quantization axis for the nuclear spin levels, which are thus still able to be described by specifying I and m, the total spin, and the component directed along the applied field respectively. If however, the strength of interaction of the nucleus with the applied field is of similar order of magnitude to the strength of its interaction with a local field gradient, then the applied field can no longer be considered as the quantization axis. This situation arises for nuclear species with large quadrupole moments, such as ^{87}Rb and ^{14}N at sites of low symmetry, which necessarily have large electric field gradients associated with them.

The quadrupole coupling hamiltonian

The quadrupole interaction hamiltonian is formed in the same way as all previous interaction hamiltonians, by substituting quantum mechanical operators for the physical quantities in the classical expression for the energy of interaction of an electric quadrupole in an electric field gradient. We will not go through that process here, but go straight to the result; further details are given in Chapter 4. The quadrupolar hamiltonian for a spin I, in the case where the interaction with the applied field $\mathbf{B}_0$ outweighs the quadrupolar term, can be written in tensorial form as:

$$\hat{H}_Q = \frac{eQ}{6I(2I-1)\hbar}\mathbf{I}\cdot e\mathbf{q}\cdot\mathbf{I} \tag{1.125}$$

The tensor $e\mathbf{q}$ describes the electric field gradient; a component $eq_{\alpha\beta}$; $\alpha, \beta = x, y, z$, is the gradient of the α component of an electric field (E_x, E_y, E_z) in direction β. The electric field gradient tensor $e\mathbf{q}$ is traceless, i.e. it has no isotropic component. Two parameters, the *quadrupole coupling constant*, χ, and the *asymmetry parameter*, η_Q, are defined from the principal values of the electric field gradient tensor when it is expressed in its principal axis frame, i.e. q_{xx}^{PAF}, q_{yy}^{PAF}, q_{zz}^{PAF} (see Section 1.4.1 for a discussion of tensors, their principal axis frames and values):

$$\chi = \frac{e^2 q_{zz}^{\mathrm{PAF}} Q}{\hbar} \tag{1.126}$$

$$\eta_Q = \frac{q_{xx}^{\mathrm{PAF}} - q_{yy}^{\mathrm{PAF}}}{q_{zz}^{\mathrm{PAF}}} \tag{1.127}$$

The quadrupole interaction is dealt with in much more detail in Chapter 4, where the effect on the NMR spectra of quadrupolar nuclei is also considered. Here, for completeness, we state results from Chapter 4 without proof.

In the case where the electric field gradient tensor has axial symmetry, i.e. $q_{xx}^{\mathrm{PAF}} = q_{yy}^{\mathrm{PAF}} \neq q_{zz}^{\mathrm{PAF}}$, the quadrupolar hamiltonian in Equation (1.125) may be expressed to first order in the applied field $\mathbf{B}_0$ as

$$\hat{H}_Q = \frac{3\chi}{8I(2I-1)}(3\cos^2\theta - 1)(3\hat{I}_z^2 - \hat{I}^2) \tag{1.128}$$

where θ is the angle between the principal z axis of the electric-field gradient tensor (the unique axis in axial symmetry) and the quantization axis of the nuclear spin, the applied field $\mathbf{B}_0$. In the absence of axial symmetry, i.e. $q_{xx}^{\mathrm{PAF}} \neq q_{yy}^{\mathrm{PAF}} \neq q_{zz}^{\mathrm{PAF}}$, the equivalent expression, again to first order, is

$$\hat{H}_Q = \frac{3\chi}{8I(2I-1)}\left(3\cos^2\theta - 1 + \frac{1}{2}\eta\sin^2\theta\cos 2\phi\right)(3\hat{I}_z^2 - \hat{I}^2) \tag{1.129}$$

where θ and ϕ are the polar angles defining the orientation of the applied field $\mathbf{B}_0$ in the principal axis frame of the electric field gradient tensor. These equations are suitable when the quadrupole coupling constant is much less than the Larmor frequency. In cases where the quadrupole coupling constant is approximately one-tenth of the Larmor frequency or more, Equations (1.128) and (1.129) are inadequate, and second-order or even higher-order terms must be included. This is discussed much more in Chapter 4.

Experimental manifestations of quadrupole coupling

We can use the quadrupolar hamiltonians defined in Equations (1.128) and (1.129) acting within a basis of $|I,m\rangle$ states to find the transition frequencies expected for a quadrupolar nucleus in a strong magnetic field. These are given by

$$\omega_Q(\theta) = \omega_0 - \frac{3}{8}\left(\frac{2m-1}{I(2I-1)}\right)\chi(3\cos^2\theta - 1) \qquad (1.130)$$

for axial symmetry, for instance, where ω_0 is the transition frequency in the absence of quadrupole coupling; the second term describes the modulation of the transition frequency by the quadrupole coupling. The term m is the z component of spin in the initial spin level of a transition, and so can take values between I and $-I + 1$ for a spin-I nucleus. There are thus $2I$ transitions that must be considered. The familiar $(3\cos^2\theta - 1)$ dependence of the transition frequencies means that each transition gives rise to a lineshape of the form seen when discussing chemical shift anisotropy and dipole–dipole coupling.

For a spin-1 nucleus, the $m = 1 - m = 0$ transition has a $+(3\cos^2\theta - 1)$ dependence, while the $m = 0 - m = -1$ transition has a $-(3\cos^2\theta - 1)$ dependence. Thus, the form of spectrum expected for a spin-1 species in axial symmetry is that shown in Fig. 1.15.

The lineshape associated with any half-integer quadrupolar nucleus has a special feature: the $m = +\frac{1}{2} - m = -\frac{1}{2}$ transition has no θ dependence, as can be seen from Equation (1.130). This transition thus gives rise to a sharp line at the centre of the spectrum. The form of the spectrum for a spin-$\frac{3}{2}$ species thus has the form shown in Fig. 1.16.

1.5 Calculating NMR powder patterns

As already seen, the total hamiltonian governing the nuclear spin energy levels is a sum of contributions from several nuclear interactions in general:

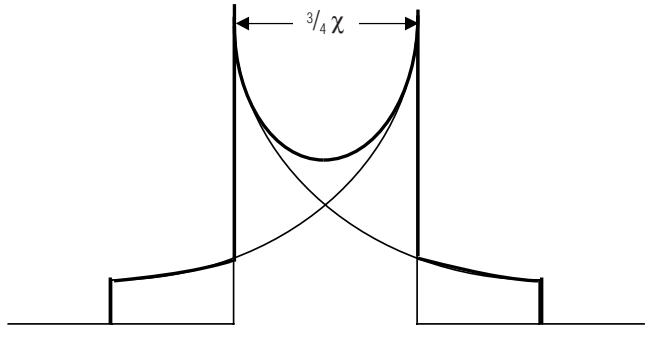

Fig. 1.15 The quadrupolar powder lineshape for a spin-1 nucleus at a site of axial symmetry. There are two possible transitions for a spin-1 nucleus ($m = +1$ to $m = 0$ and $m = 0$ to $m = -1$), which give rise to mirror image lineshapes. The splitting of the 'horns' in the pattern is equal to $\frac{3}{4}\chi$, where χ is the quadrupole coupling constant. The horns are created by crystallites in which the principal z axis of the quadrupolar coupling tensor is perpendicular to the applied field $\mathbf{B}_0$.

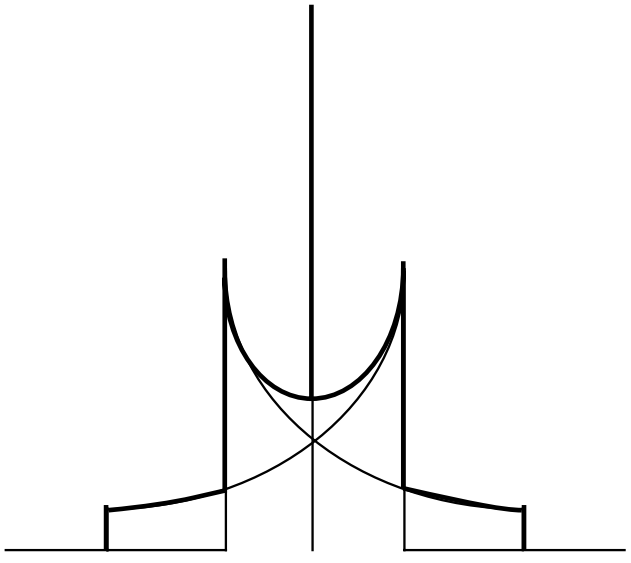

Fig. 1.16 The powder lineshape for a spin-$\frac{3}{2}$ nucleus at a site of axial symmetry, and suffering quadrupole coupling. There are three possible $\Delta m = \pm 1$ transitions for a spin-$\frac{3}{2}$ nucleus. The so-called *satellite transitions*, $m = +\frac{3}{2}$ to $m = +\frac{1}{2}$ and $m = -\frac{1}{2}$ to $m = -\frac{3}{2}$, give rise to mirror image lineshapes. The central transition, $m = +\frac{1}{2}$ to $m = -\frac{1}{2}$, has no orientation dependence (to first order in the applied field $\mathbf{B}_0$) and so gives a sharp signal.

$$\hat{H} = \hat{H}_0 + \hat{H}_{cs} + \hat{H}_{dd} + \hat{H}_Q \tag{1.131}$$

where $\hat{H}_0$ is the Zeeman term; $\hat{H}_{cs}$ is the chemical shift term; $\hat{H}_{dd}$ is the dipole–dipole coupling term, which includes both homonuclear and heteronuclear interactions; and $\hat{H}_Q$ is the quadrupolar term, which is only non-zero for nuclei with spins greater than $\frac{1}{2}$. In the solid state, the latter three terms $\hat{H}_{cs}$, $\hat{H}_{dd}$ and $\hat{H}_Q$ are anisotropic, and are each described by separate interaction tensors. We have seen how each term individually affects the NMR spectrum of a powder sample: the NMR spectrum with all these anisotropic interactions present is generally considerably more complicated, because the different interaction tensors in general have different principal axis frames (PAF) relative to the molecular axis frame. Fortunately however, the powder patterns due to these interactions are relatively easily calculated, except in the case of homonuclear coupling between more than three or four nuclei. For this latter case, the principles involved in the calculation are simple enough, but the computational effort required is highly prohibitive.

The simplest way to calculate a powder pattern is actually to calculate it in the time domain, i.e. to calculate the FID. It is then a simple matter to Fourier transform the calculated FID to obtain the frequency spectrum.

In the following, we consider only inhomogeneous interactions, i.e. time-independent interactions, such as the chemical shielding, heteronuclear dipolar coupling and quadrupolar coupling. The FID, $g(t)$, describes the evolution of the transverse magnetization in an NMR experiment and for a powder sample is given by

$$g(t) = \frac{1}{8\pi^2}\int_0^{2\pi}\int_0^{\pi} \exp\left(i\sum_A \omega_A(\theta,\phi)t\right)\sin\theta\,d\theta\,d\phi \tag{1.132}$$

where $\omega_A(\theta,\phi)$ is the contribution to the spectral or evolution frequency from interaction A when the applied field $\mathbf{B}_0$ is oriented by the polar angles (θ,ϕ) with respect to the interaction tensor principal axis frame (PAF). The integrals over θ and ϕ sum the individual FIDs from all the different molecular/crystallite orientations in the powder samples. These integrals can be performed numerically by approximating them as a finite sum. Values for $\omega_A(\theta,\phi)$ for the orientations (θ,ϕ) chosen in the summation are simply evaluated using the equation appropriate to each interaction given in the previous sections. Note that in the case of axial symmetry, the interactions depend only on the angle θ and only the integral over θ is required in Equation (1.132).

Calculating powder patterns for homonuclear dipolar coupling involving more than two spins is not dealt with in detail here. Suffice to say that in order to find the energy levels in a homonuclear, multispin system, mixing between degenerate levels has to be taken into account, as discussed in Section 1.4.2. This makes the whole calculation computationally very intensive.

1.6 General features of NMR experiments

One of the most important features of the NMR experiment is that we do not measure absolute spectral frequencies, but measure all frequencies relative to some carrier or spectral frequency, as outlined in Box 1.4 below, which is constant for a given nuclear species. We refer to the frequency relative to the spectral frequency as the *frequency offset*. We may then reference all signals in the spectrum relative to a specific signal given by a standard or reference compound, in order to quote the positions of the signals in our spectrum as *chemical shifts* (see Section 1.4.1), which are dimensionless quantities. We shall often refer to frequency offsets throughout this book, and they should be understood in terms of the concept outlined above and detailed in Box 1.4.

1.6.1 Multidimensional NMR

As the preceding sections have hinted, what we observe in an (FT) NMR experiment are not transitions between energy levels as we do in other forms of spectroscopy. Rather, we observe the evolution over time of the ensemble average state or superposition state of the spin system, having first created a non-equilibrium (ensemble average) state in order to force the spin system to change with time; an equilibrium state is of course stationary. The evolution of the spin system in its non-equilibrium state takes place at characteristic frequencies determined by the various interactions in the spin system discussed in Section 1.4, and it is these frequencies which we hope to extract from our observations of the spin system.

So, for instance, in the absence of any rf pulses or other interactions, nuclear spins feel only the applied field $\mathbf{B}_0$, and the ensemble average spin state is described by a linear combination of the Zeeman spin states, with combination coefficients determined by the Boltzmann populations of these levels (providing the spin system is at equilibrium). This is the equilibrium spin state for this situation. If we then apply an rf pulse, the Zeeman functions are mixed as described in Section 1.2. After the pulse, the situation of the spin system returns to that before the pulse, i.e. interaction with the $\mathbf{B}_0$ field only. However, the superposition state describing the spin system at this point is some new linear combination of the Zeeman functions determined by the rf pulse as well as the Boltzmann population distribution before the pulse and is (in general) a non-equilibrium state for the spin system in this environment.

Another way of putting this is to say that, in NMR, we observe the time evolution of coherences between the Zeeman functions of the spin system. As we saw in Section 1.3, the idea of a coherence arises directly from the density matrix description of the state of a spin system; this is the reason for the immense importance of the density matrix in NMR. The time evolution of coherences takes a simple form when the Zeeman functions for the spin system are the eigenfunctions of the hamiltonian describing the spin system. This will be the case if the hamiltonian commutes with the Zeeman hamiltonian for the spin system (see Box 1.1). In these circumstances, we can show that the ijth element of a density matrix in the Zeeman basis, i.e. the coherence between Zeeman levels i and j, evolves according to $\exp(-i\omega_{ij}t)$, where ω_{ij} is the energy gap between the i and j energy levels of the spin system in frequency units, i.e. eigenvalues of the hamiltonian for the spin system in frequency units. The only coherence we can observe directly is coherence of order –1, i.e. evolution of coherent superpositions of Zeeman functions whose magnetic quantum numbers m differ by –1. The transverse magnetization of the classical vector model of NMR is equivalent to such coherences. The Fourier transform of $\exp(-i\omega_{ij}t)$ is a δ function at frequency ω_{ij}. Thus, if we can measure the $\exp(-\omega_{ij}t)$ evolution over time of the desired coherence, Fourier transformation of the resulting time domain series will produce a frequency spectrum of that coherence. This in turn, contains signals at frequencies which correspond to the energy gaps between energy levels in the system.

Although we can only observe –1-order coherence, we can create many other orders and observe their evolution too, providing we do it indirectly. This is the idea behind two-dimensional (or in general multidimensional) NMR experiments. Consider the pulse sequence in Fig. 1.17. An initial sequence of rf pulses (the *preparation sequence*) creates a non-equilibrium spin state. In the subsequent period t_1, the desired coherence of order n is allowed to evolve. In practice, selecting the desired coherence order is performed using phase cycling (see below for details). The mixing or transfer pulse sequence at the end of t_1 transforms the selected n-order coherence into observable –1 coherence for observation during t_2. The signal in t_2 has either its amplitude or phase or both modulated according to the evolution in t_1. Thus by repeating the experiment for successive different values of t_1, we end up with a two-dimensional time-

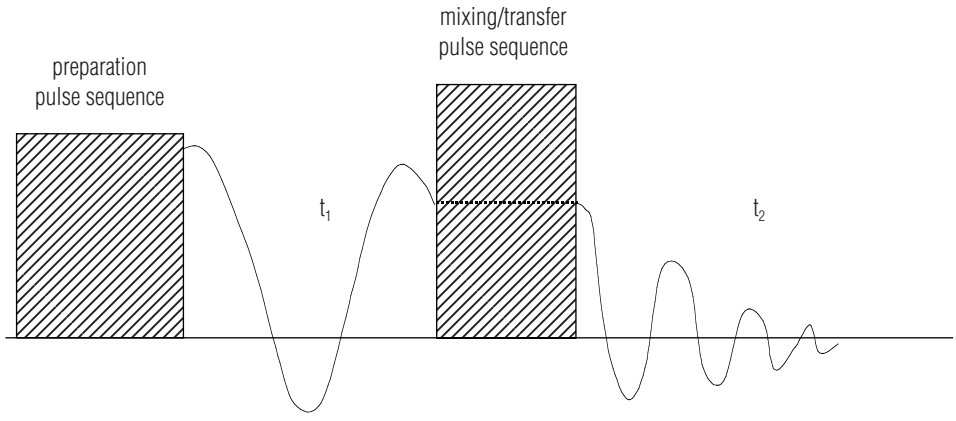

Fig. 1.17 The general form of a two-dimensional NMR pulse sequence. Selected coherences evolve at frequency ω_1 during t_1 and at ω_2 during t_2.

domain dataset which contains, in the t_2 dimension, information on the evolution of the –1-order coherence and, in the t_1 dimension, information on the evolution of the *n*-order coherence. The experiment can also be arranged so that –1-order coherence is monitored in both dimensions. This is the case in exchange experiments where, during the mixing period, the frequency of evolution of the t_1 – 1-order coherence changes as a result of chemical or spin exchange, the new frequency then being recorded in t_2.

Whatever the coherences involved, the result and interpretation of the final spectrum is the same. The two-dimensional time-domain dataset can be transformed to the frequency domain (usually by Fourier transformation) to produce a two-dimensional frequency spectrum, in which the f_1 dimension contains the characteristic evolution frequencies of the *n*-order coherences in t_1, and the f_2 dimension contains those of the –1-order coherences present in t_2. The two-dimensional spectrum is then a correlation map in which a peak in the two-dimensional spectrum at (ω_1, ω_2) indicates that, in t_1, there was *n*-order coherence evolving at frequency ω_1 which was then transformed by the mixing period into –1-order coherence with frequency ω_2.

In order to obtain this two-dimensional frequency spectrum, we need to understand how to use phase cycling to select our desired coherences and how to transform from a time-domain dataset to a frequency spectrum containing pure absorption lineshapes. This latter part comes down to being able to record the two time dimensions in *quadrature*. Both of these features are discussed in the following sections.

1.6.2 Phase cycling

A typical pulse sequence is shown in Fig. 1.18. It consists of three pulses, with phases ϕ_1, ϕ_2 and ϕ_3 respectively. Also shown in Fig. 1.18 is the desired *coherence order pathway*, the sequence of coherence orders required at each stage during the pulse sequence. The desired coherence order pathway in Fig. 1.18 is $0 \rightarrow +2 \rightarrow +1 \rightarrow -1$.

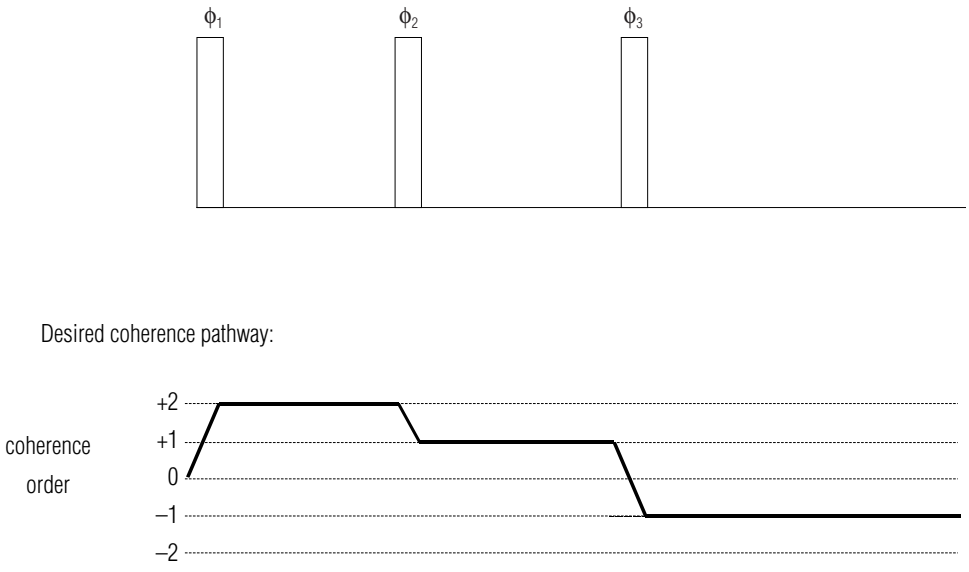

Fig. 1.18 A typical pulse sequence with pulse phases ϕ_1, ϕ_2 and ϕ_3. Each pulse causes a change in coherence order; the coherences evolve in the periods between the pulses. The desired coherence orders at each stage of the pulse sequence are shown in the diagram at the bottom. Selection of this pathway is achieved with phase cycling as discussed in the text.

We use rf pulses to change the order of coherence present at the different stages in a pulse sequence, with each of the three pulses endeavouring to execute the three changes in coherence order. We will label the change in coherence order caused by a pulse as Δp.

The key rule we use in phase cycling is the following [**2**]

If the phase of a pulse is changed by ϕ, a coherence undergoing a change in coherence level of Δp acquires a phase shift of $-\Delta p \cdot \phi$.

Thus the overall phase acquired by the desired coherence pathway in Fig. 1.18 is $-2\phi_1 + \phi_2 + 2\phi_3$, since the change in coherence order at the first pulse (phase ϕ_1) is +2, at the second (phase ϕ_2) is –1, and at the third (phase ϕ_3) is –2. We now have to arrange a phase cycle of the pulses in the sequence, while always setting the receiver phase to follow the overall phase acquired by the desired coherence order pathway, so that the signal due to this pathway adds up over the phase cycle. The phase cycle of N steps needs to be arranged so that the signals due to unwanted pathways arrive at the receiver with phases such that the signals exactly cancel over the cycle. In order to achieve this, the following rules can be employed [2]:

If a phase cycle uses steps of $360/N$ degrees, then in addition to the pathway with change in coherence order Δp, pathways with $\Delta p \pm nN$, where $n = 1, 2, 3, \ldots$ are also selected. If a particular value of Δp is to be selected from m consecutive values, then N must be at least m.

In order to derive an effective phase cycle, we must know the other pathways and coherence orders that are likely to be present in addition to the one we want, so that we know what we must aim to exclude. The phase cycle can be simplified by noting that, as we can only observe −1-order coherence in the final observation, there is no need to deliberately select −1-order coherence in the final step of the pulse sequence; the experiment is already self-selecting in this respect.

An example will suffice to show how a suitable phase cycle may be constructed. Suppose, in the example in Fig. 1.18, another unwanted coherence pathway $0 \rightarrow -1$ (rather than +2) $\rightarrow +1 \rightarrow -1$ can occur in addition to the desired pathway. We can exclude this pathway by phase cycling the first pulse so as to select only $\Delta p = +2$ at this step. We need to select +2 from possible −1, 0 and +1 coherence order changes at this step. Actually, we do not know if the 0 and +1 coherence order changes can occur, but we do know −1 can, so we include all the other coherence order changes between that and the desired one. So, we need to select the Δp from four consectutive values of a possible Δp. Thus the number of steps in the phase cycle, N, needs to be at least four. Table 1.1 follows what happens to the overall phase of coherence along the desired pathway and the unwanted pathway. We assume that the phases of pulses 2 and 3 remain constant through out the cycles; we have set them to zero so that they do not contribute to the overall phase of the coherence at the end of the sequence, but this does not affect the outcome of the phase cycle. The unwanted signal has a different relative phase at the receiver on

Table 1.1 The effects of phase cycling on the pulse sequence shown in Fig. 1.6.

The first pulse only is cycled in four steps. The phases of the other two pulses are assumed to be zero. The phases shown in brackets are the equivalent phase angles between 0° and 360°. The receiver is stepped to follow the phase of the desired coherence throughout the cycle, so that the signal from this coherence adds throughout the cycle.

Desired pathway $0 \rightarrow +2 \rightarrow +1 \rightarrow -1$

Cycle step	Pulse phase (pulse 1)	Phase of coherence after pulse $\Delta p = +2$	Receiver phase (following desired coherence)	Phase of final coherence relative to receiver
1	0°	0°	0°	0°
2	90°	−180° (180°)	180°	0°
3	180°	−360° (0°)	0°	0°
4	270°	−540° (180°)	180°	0°

Unwanted pathway $0 \rightarrow -1 \rightarrow +1 \rightarrow -1$

Cycle step	Pulse phase (pulse 1)	Phase of coherence after pulse $\Delta p = -1$	Receiver phase (following desired coherence)	Phase of final coherence relative to receiver
1	0°	0°	0°	0°
2	90°	90°	180°	90°
3	180°	180°	0°	180°
4	270°	270°	180°	270°

each step of the phase cycle; and adding these four signals, which have a 90° phase shift between each of them, gives a net signal of zero. Thus as required, the unwanted signal cancels over the phase cycle, while the desired one adds. In general, a signal cancels exactly if, in an N-step phase cycle, its phase relative to the receiver acquires each of the possible values $360/N$ over the phase cycle.

1.6.3 Quadrature detection

In NMR, we measure all time-evolving signals relative to the rotating frame of reference rotating at the *carrrier frequency*, which is normally the same as the frequency of the rf pulse. Any coherence evolves in general according to $C\exp(i\omega t)$ where ω is the evolution frequency offset in the rotating frame, and C is the overall amplitude of the coherence, which may be time-dependent, for example, due to the loss of the coherence through relaxation. $C\exp(i\omega t)$ can be rewritten in terms of its real and imaginary components:

$$C\exp(i\omega t) = C\cos(\omega t) + iC\sin(i\omega t) \tag{1.133}$$

Both the real and imaginary components of the evolution must be measured if Fourier transformation of the time-domain signal is to produce an unambiguous frequency spectrum, as illustrated in Fig. 1.7. The measurement of these two components is known as *quadrature detection*.

We should also consider the decay of the coherence. The effect of decay is shown in Fig. 1.19. If the amplitude of the coherence is multiplied by a decaying function $\exp(-t/T_2)$, there are two principal effects we should note. (1) The lines in the frequency spectrum acquire a linewidth rather than being δ functions, and (2) the imaginary part of the frequency spectrum is no longer zero (although its net integral is zero).

Fourier transformation of $C\exp(i\omega t)$, where C includes a decaying term $\exp(-t/T_2)$, results in a complex frequency spectrum $A + iD$, as described in Fig. 1.20. The real part of this frequency spectrum, A, is a pure absorption lineshape, and is what spectroscopists usually refer to as 'the spectrum'. The imaginary part is a purely dispersive lineshape (Fig. 1.20).

Quadrature detection is performed in practice using the scheme outline in Box 1.2. The two time-domain signals arising from quadrature detection, S_1 and S_2, should be directly proportional to the real ($F_{Re} = C\cos(\omega t)$) and imaginary ($F_{Im} = C\sin(\omega t)$) parts of the coherence evolution in Equation (1.133). However, there may by a phase offset (determined by the *receiver phase*) between S_1/S_2 and F_{Re}/F_{Im}, such that they are in fact related by (ignoring the proportionality constant between S_1/S_2 and F_{Re}/F_{Im} for convenience):

$$\begin{aligned} F_{Re} &= S_1\sin\phi + S_2\cos\phi \\ F_{Im} &= -S_1\cos\phi - S_2\sin\phi \end{aligned} \tag{1.134}$$

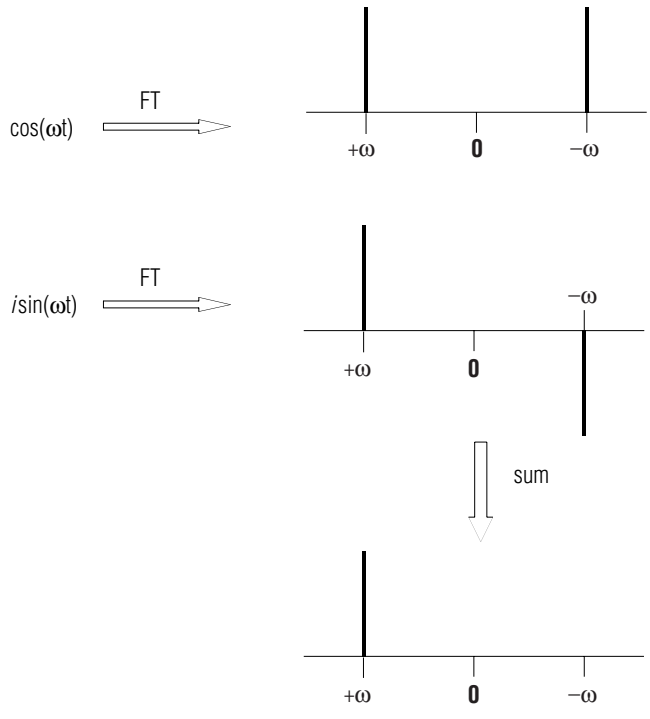

Fig. 1.19 The Fourier transformation of $\exp(i\omega t) = \cos(\omega t) + i\sin(\omega t)$.

Fourier transformation of $S_1 + iS_2$ (i.e. treating S_1/S_2 as F_{Re}/F_{Im}) with no phase correction results in a *phase-distorted* lineshape:

$$S_1 + iS_2 \xrightarrow{\text{FT}} (A\cos\phi + D\sin\phi) + (-A\sin\phi + D\cos\phi) \tag{1.135}$$

where the real part of the frequency spectrum is now a mixture of absorptive (A) and dispersive (D) lineshapes, $A\cos\phi + D\sin\phi$. This can be corrected according to Equation (1.134) in either the time or frequency domains; this is the so-called *phasing* of the spectrum. The phase factor ϕ is adjusted until the real part of the frequency spectrum is purely absorptive, and the imaginary part purely dispersive.

In a two-dimensional NMR experiment, as well as recording separately the $\sin(\omega_2 t_2)$ and $\cos(\omega_2 t_2)$ signals arising in t_2, we must also arrange that the sin/cos components arising in t_1 are recorded separately. If we do not do this, but acquire a signal of the form $\exp(i\omega_1 t_1)\exp(i\omega_2 t_2)$, subsequent Fourier transformation in t_1 and t_2 has the following effect:

$$\begin{aligned}\exp(i\omega_1 t_1)\exp(i\omega_2 t_2) &\xrightarrow{\text{FT}} (A_1 + iD_1)(A_2 + iD_2)\\ &= (A_1A_2 - D_1D_2) + i(A_1D_2 + D_1A_2)\end{aligned} \tag{1.136}$$

The real part of the resulting frequency spectrum contains a mixture of absorptive and dispersive signal being of the form $(A_1A_2–D_1D_2)$, which is a *phase-twisted lineshape*.

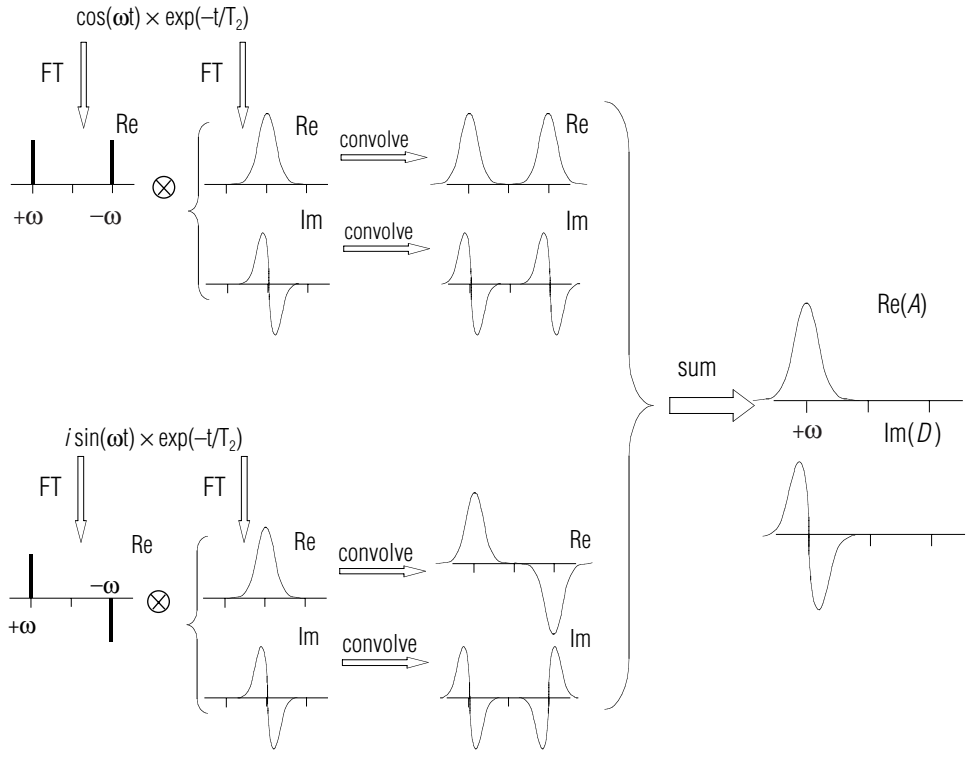

Fig. 1.20 The effects of multiplying a time domain signal exp($i\omega t$) by a decaying function exp($-t/T_2$) on the frequency spectrum. The frequency spectrum is found by Fourier transforming the product function, exp($i\omega t$) exp($-t/T_2$), which is the process shown above. The Fourier transforms of the sine and cosine components of exp($i\omega t$) (= cos(ωt) + i sin(ωt)) are shown in Fig. 1.19. The Fourier transform of exp($-t/T_2$) is shown above; the real part is an absorption mode lorenzian of linewidth $2/T_2$ at half height and the imaginary part is a dispersive mode lorenzian. The frequency spectrum of exp($i\omega t$) exp($-t/T_2$) is found by convolving the frequency spectra of exp($i\omega t$) and exp($-t/T_2$). The final frequency spectrum has real and imaginary parts. The real part is a pure absorption spectrum, denoted as A, and the imaginary part is a pure dispersive spectrum, denoted D. It is worth noting that in the absence of the decaying function, the Fourier transform of exp($i\omega t$) alone has no imaginary part. The non-zero imaginary (and dispersive) part of the frequency spectrum arises from the decaying function, exp($-t/T_2$).

A method of producing purely absorptive lineshapes in two-dimensional frequency spectra is to perform two experiments, with their respective preparation pulse sequences phase shifted so that the desired coherences in t_1 have a 90° phase shift between the two experiments. This is done by shifting the phases of all the preparation pulses by $90°/(n_0 - n)$, where n_0 is the initial coherence order present at the start of the preparation pulse sequence (usually 0) and n is the desired coherence order in t_1. The experiments must be arranged so that $+n$ and $-n$ coherences are both selected in t_1, with equal amplitude. The evolution frequency of the $-n$-order coherence is minus that of the $+n$-order coherence, so the $+n$-order coherence evolves according to $\exp(i\omega_n t_1)$ and the $-n$-order coherence according to $\exp(-i\omega_n t_1)$. The signals arising in the two experiments are then

1. $[\exp(i\omega_n t_1) + \exp(-i\omega_n t_1)]\ \exp(i\omega_2 t_2) = 2\cos\omega_n t_1 \cdot \exp(i\omega_2 t_2)$
2. $[\exp(i\pi/2)\ \exp(i\omega_n t_1) + \exp(-i\pi/2)\ \exp(-i\omega_n t_1)]\ \exp(-i\omega_2 t_2) = 2i\sin\omega_n t_1 \cdot \exp(i\omega_2 t_2)$

where in signal 2 a phase shift of $\pi/2$ has been applied to the t_1 signal. These two datasets are then processed as shown in Fig. 1.21, and result in a purely absorptive two-dimensional frequency spectrum.

This technique relies on the $+n$- and $-n$-order coherence pathways being selected with the same amplitude; sometimes this is not achieved, and so phase-twisted lineshapes are still observed in the spectrum. What prevents their amplitude being equal is usually that the final mixing steps $\pm n \rightarrow -1$ which cause the transformation to observable coherence do not occur with equal efficiency. One way around this is to amend the pulse sequence so that the coherence order pathway is $\pm n \rightarrow 0 \rightarrow -1$. The symmetrical routes $\pm n \rightarrow 0$ should occur with equal efficiencies. This procedure is often called a *z filter* as coherence order zero also corresponds to a state with spin polarization along z.

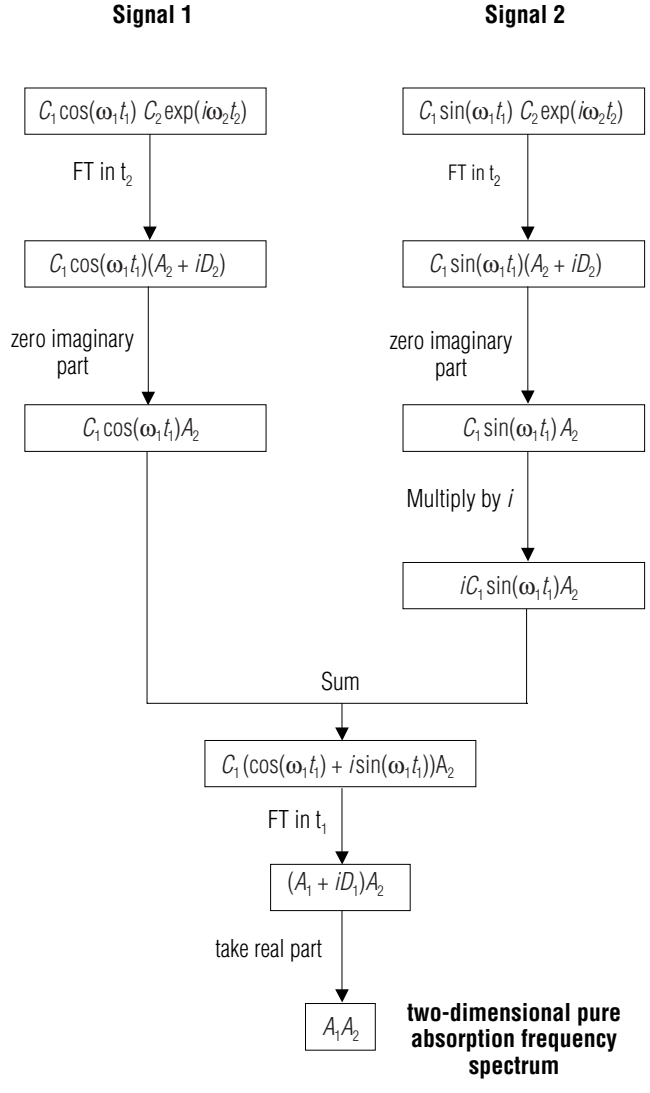

Fig. 1.21 Processing of the two signals from a two-dimensional NMR experiment so as to produce pure absorption lineshapes in the two-dimensional frequency spectrum. The two signals are produced in two separate experiments and have the forms indicated at the top of the diagram (see text for details). The C_1 and C_2 coefficients in the signals are the amplitudes of the signals during the t_1 and t_2 periods of the experiment respectively, and normally contain decay terms which are functions of time. A_1 and A_2 are the amplitudes of the real parts of the frequency spectra arising from Fourier transformation (FT) of the t_1 and t_2 time domain signals and D_1 and D_2 are their imaginary counterparts. The A terms correspond to absorption mode lineshapes, while the D terms correspond to dispersive mode lineshapes.

Box 1.4 The NMR spectrometer

A schematic diagram of an NMR spectrometer is given in Fig. 1.22. The signal coming from the NMR probehead (detected by the coil in the probe) is of the form $2c\exp(i(\omega_0 + \Delta\omega)t)$, where $2c$ is the amplitude of the signal, ω_0 is the *carrier* or *spectral frequency* and $\Delta\omega$ is the offset, which may include chemical shift as well as the effects of other nuclear spin interactions. The first step in the recording of this signal is to amplify the whole signal (which also has the effect of amplifying any noise present); the *pre-amplifier* which performs this step may be tuned to the approximate frequency expected for the signal beforehand. In the next

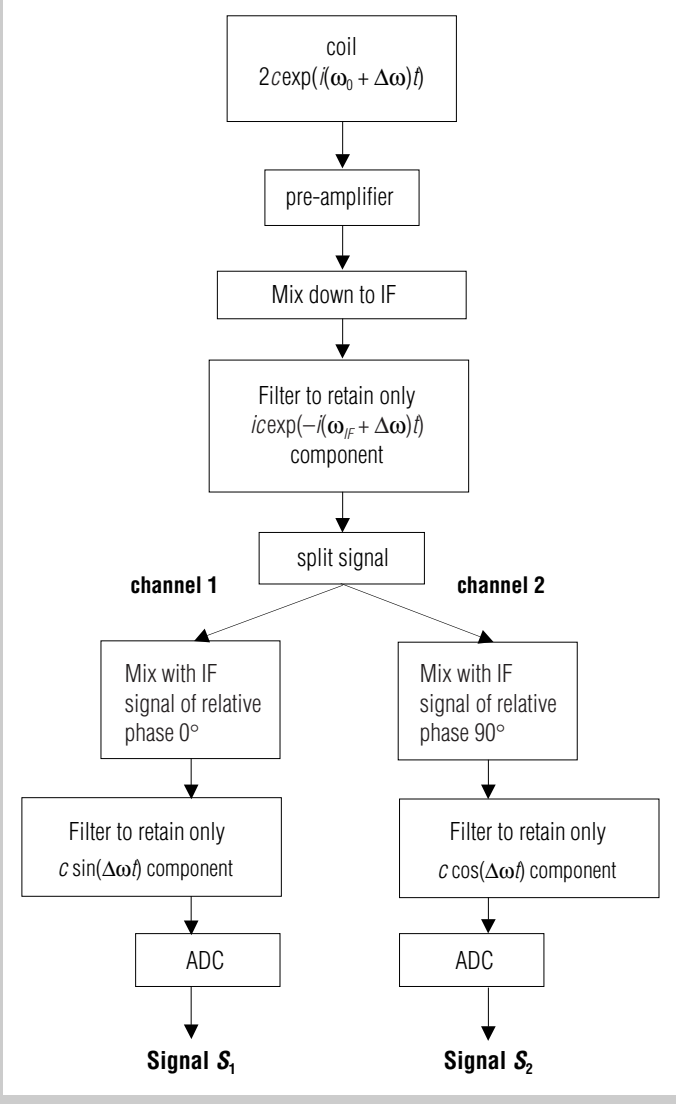

Fig. 1.22 A schematic diagram of an (FT) NMR spectrometer. See text for details.

step, the signal is mixed down to an *intermediate frequency* or *IF* so that the signal now has frequency $\omega_{IF} + \Delta\omega$. The same IF is used whatever nucleus is being studied, and therefore, whatever the initial spectral frequency might have been. The reason for performing this step is that the spectrometer now has only to deal with frequencies around ω_{IF}, a relatively small range, no matter what nucleus is being studied. Thus, constant frequency filters, etc., can be used in the subsequent steps, which has tremendous advantages over variable frequency filtration, which would have to be used otherwise. The frequency of the IF is chosen to minimize noise and optimize frequency accuracy and phase stability. The mixing-down step is actually performed by multiplying the incoming signal with a spectrometer-generated signal of frequency $\omega_0 - \omega_{IF} = \omega_{mix}$. This produces a signal whose time variation is of the form

$$\begin{aligned} & 2c\exp(i(\omega_0 + \Delta\omega)t)\sin(\omega_{mix}t) \\ & \quad = 2c[\cos((\omega_0 + \Delta\omega)t) + i\sin((\omega_0 + \Delta\omega)t)]\sin(\omega_{mix}t) \\ & \quad = 2c[\cos((\omega_0 + \Delta\omega)t)\sin(\omega_{mix}t) + i\sin((\omega_0 + \Delta\omega)t)\sin(\omega_{mix}t)] \\ & \quad = ci[\exp(i(\omega_0 + \omega_{mix} + \Delta\omega)t) - \exp(-i(\omega_{IF} + \Delta\omega)t)] \end{aligned}$$

Filtering the resulting signal with a narrow band filter then selects the component oscillating around ω_{IF}. The form of the signal at this point is then $ic\exp(-i(\omega_{IF} + \Delta\omega)t)$. The next step is to separate the $\sin(\omega_{IF} + \Delta\omega)$ (real) and $\cos(\omega_{IF} + \Delta\omega)$ (imaginary) components of this complex signal. This is done as follows. The signal is first divided into two. The two halves are routed through different channels (1 and 2) and are each mixed down with a spectrometer-generated signal at the IF frequency, one of which differs in phase by 90° relative to the other. Filters are applied to both channels so that only the difference frequency between the input signal and the IF, i.e. $\Delta\omega$, remains, in a similar manner to the mixing down from the spectral frequency to the IF. The signal is now said to be at *baseband*. The signal in channel 1 mixed with the reference IF signal, generates a $\sin(\Delta\omega t)$, or *in-phase*, component, while the signal in channel 2 mixed with the signal 90° phase-shifted from the reference IF generates a $\cos(\Delta\omega t)$, or *quadrature*, component. The final step is to put the baseband signals from both channels through analogue-to-digital converters (ADCs) to produce digitized signals from the analogue waveforms. These digitized signals can then be stored in a computer for subsequent processing to the frequency domain.

Notes

1. As implied, there is a small coupling between the spatial and spin coordinates of the nuclear wavefunction and this becomes important when considering nuclear spin relaxation.
2. Note that here we are using the definition that the operator for the nuclear spin angular momentum is $\hbar\hat{\mathbf{I}}$ – see Box 1.1 for more details.

3. The definition of $\hat{L}z$ comes from the classical expression for angular momentum about z and replacing all the terms in that expression with the corresponding quantum mechanical operators.
4. It is worth noting for later use that the first-order energy correction to the energy of a Zeeman state due to a perturbation described by an hamiltonian $\hat{H}_1$, is from perturbation theory $E_m^{(1)} = \langle \Psi_{I,m} | \hat{H}_1 | \Psi_{I,m} \rangle$.
5. This is only true when the Zeeman interaction is significantly larger than any other interaction on the spin system, and so the applied field $\mathbf{B}_0$ provides the quantization axis for the spin system.
6. Equation (1.86) implicitly uses the symmetric part of the shielding tensor as σ^{lab}. If the antisymmetric part of the shielding tensor were used as σ^{lab} in Equation (1.86), the result for σ_{zz}^{lab} would be zero. Thus the antisymmetric part of the shielding tensor makes no contribution to the chemical shift frequency of Equation (1.85) as previously stated. This will be the case as long as the chemical shift frequency depends only on the σ_{zz}^{lab} component of the laboratory frame shielding tensor, which it does if the Zeeman interaction provided by $\mathbf{B}_0$ is the dominant interaction on the spin system.
7. In fact, the particular linear combinations which are eigenfunctions of the B term for a degenerate two-spin system are $\frac{1}{\sqrt{2}}(\alpha\beta \pm \beta\alpha)$.

References

1. M. Goldman, *Quantum Description of High-Resolution NMR in Liquids*, Clarendon Press, Oxford (1988).
2. J.H. Keeler, *Multinuclear Magnetic Resonance in Liquids and Solids – Chemical Applications*, NATO ASI Series C, **322** (1988) 103 (Eds. P. Granger and R.K. Harris).

Solid-State NMR Spectroscopy Principles and Applications
Edited by Melinda J. Duer
Copyright © 2002 by Blackwell Science Ltd

Chapter 2
Essential Techniques for Spin-$\frac{1}{2}$ Nuclei

Melinda J. Duer

2.1 Introduction

In solid-state NMR, we generally deal with *powder samples*; that is, samples consisting of many crystallites with random orientations. The nuclear spin interactions discussed in Chapter 1 are all dependent on the crystallite orientation; they are said to be *anisotropic*. As a result of this, the NMR spectrum of a powder sample contains broad lines, or *powder patterns*, as all the different molecular orientations present in the sample give rise to different spectral frequencies. As outlined in Chapter 1, studying nuclear interactions through their NMR spectra can give useful information on a chemical system. However, when there are several inequivalent nuclear sites in a sample, the powder patterns from each may overlap. The consequent lack of resolution in the NMR spectrum obscures any information that the spectrum might contain.

Hence, it is necessary in solid-state NMR to apply techniques to achieve high resolution in spectra. So in this chapter, we will first discuss how to achieve high-resolution NMR spectra and then go on to examine two further techniques, cross polarization and echo pulse sequences, which are both commonly used in solid-state NMR, either on their own, or as part of more complicated pulse sequences.

2.2 Magic-angle spinning

Magic-angle spinning (MAS) is used routinely in the vast majority of solid-state NMR experiments, where its primary task is to remove the effects of chemical shift anisotropy and to assist in the removal of heteronuclear dipolar-coupling effects. It is also used to narrow lines from quadrupolar nuclei and is increasingly the method of choice for removing the effects of homonuclear dipolar coupling from NMR spectra. This latter application requires very high spinning speeds however, and so is not yet routine in all laboratories.

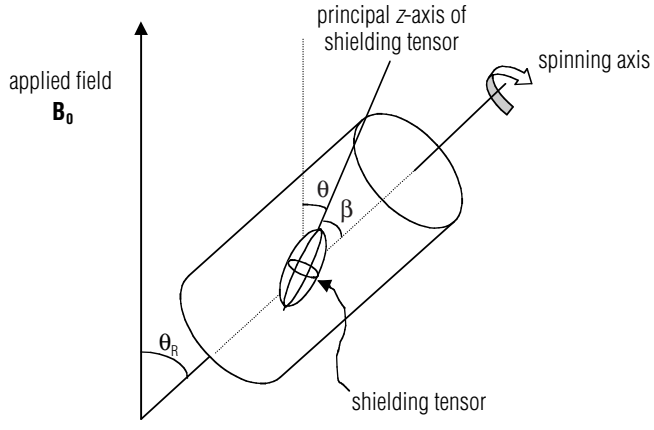

Fig. 2.1 The magic-angle spinning experiment. The sample is spun rapidly in a cylindrical *rotor* about a spinning axis oriented at the magic angle (β = 54.74°) with respect to the applied magnetic field $\mathbf{B}_0$. Magic-angle spinning removes the effects of chemical shielding anisotropy and heteronuclear dipolar coupling. The chemical shielding tensor is represented here by an ellipsoid; it is fixed in the molecule to which it applies and so rotates with the sample. The angle θ is the angle between $\mathbf{B}_0$ and the principal *z*-axis of the shielding tensor; χ is the angle between the *z*-axis of the shielding tensor principal axis frame and the spinning axis.

In solution NMR spectra, effects of chemical shift anisotropy, dipolar coupling, etc., are rarely observed. This is because the rapid tumbling of the molecules in a solution means that the angle θ (or in general, θ and ϕ) describing the orientation of the shielding/dipolar tensor with respect to the applied field $\mathbf{B}_0$ is rapidly averaged over all possible values. This averages the $(3\cos^2\theta - 1)$ dependence of the transition frequencies (see Section 1.4 for details) to zero on the NMR timescale, i.e. rate of change of molecular orientation is fast relative to the chemical shift anisotropy, dipole–dipole coupling, etc.

Magic-angle spinning achieves the same result for solids. Consider the following experimental setup in Fig. 2.1.

If we spin the sample about an axis inclined at an angle θ_R to the applied field, then θ, the angle describing the orientation of the interaction tensor fixed in a molecule within the sample, varies with time as the molecule rotates with the sample. The average of $(3\cos^2\theta - 1)$ in these circumstances can be shown to be

$$\langle 3\cos^2\theta - 1\rangle = \frac{1}{2}(3\cos^2\theta_R - 1)(3\cos^2\beta - 1) \qquad (2.1)$$

where the angles β and θ_R are defined in Fig. 2.1. The angle β is between the principal *z*-axis of the shielding tensor and the spinning axis; θ_R is the angle between the applied field and the spinning axis; θ is the angle between the principal *z*-axis of the interaction tensor and the applied field $\mathbf{B}_0$. The angle β is obviously fixed for a given nucleus in a rigid solid, but like θ it takes on all possible values in a powder sample. The angle θ_R is under the control of the experimenter however.

If θ_R is set to 54.74°, then $(3\cos^2\theta_R - 1) = 0$, and so the average, $\langle 3\cos^2\theta - 1\rangle$ is zero also. Therefore, provided that the spinning rate is fast so that θ is averaged rapidly compared with the anisotropy of the interaction, the interaction anisotropy averages to zero.

This technique averages the anisotropy associated with *any* interaction which causes a shift in the energies of the Zeeman spin functions, such as chemical shift anisotropy, heteronuclear dipolar coupling, but no mixing between Zeeman functions (to first order). However, it also has an effect on secular interactions which mix Zeeman functions, i.e. homonuclear dipolar coupling. This topic is discussed in Section 2.2.4.

2.2.1 Spinning sidebands

In order for magic-angle spinning to reduce a powder pattern to a single line at the isotropic chemical shift, the rate of the sample spinning must be fast in comparison to the anisotropy of the interaction being spun out. 'Fast' in this context means around a factor of 3 or 4 greater than the anisotropy.

Slower spinning produces a set of *spinning sidebands* in addition to the line at the isotropic chemical shift (Fig. 2.2). The spinning sidebands are sharp lines, set at the spinning speed apart and radiate out from the line at isotropic chemical shift. Note that the line at the isotropic chemical shift is *not* necessarily the most intense line. The only characteristic feature of the isotropic chemical shift line is that it is the only line that does not change position with spinning speed; this feature is the only reliable way of identifying it. At the time of writing, spinning speeds of up to 50 kHz are achievable, with 20 kHz being routine on a modern spectrometer. For example, at this spinning speed, there will rarely be more than one or two small spinning sidebands in the spectrum for ^{13}C, ^{15}N and ^{31}P. However, nuclei which have large numbers of associated electrons, such as ^{195}Pt, ^{207}Pb $^{117,119}Sn$, can have very large chemical shift anisotropies, so that even at very high spinning speeds many spinning sidebands are still observed. It is worth noting at this point that the chemical shift anisotropy (in frequency units) is proportional to B_0, and as the trend towards ever larger magnetic fields increases, these nuclei are likely to become more difficult to deal with, rather than less.

However, as we shall see, spinning sidebands can be very useful. They can be used to determine details of the anisotropic interactions which are being averaged by the magic-angle spinning. In order to do this we must first describe a mathematical analysis of these spinning sidebands.

Fortunately, a mathematical description of magic-angle spinning is easily given. Consider the case of chemical shielding, where the shielding tensor is expressed with respect to an axis frame fixed on the rotor (the 'rotor axis frame') and is labelled $\boldsymbol{\sigma}^R$, for a given crystallite orientation with respect to the rotor axis frame (Fig. 2.3).

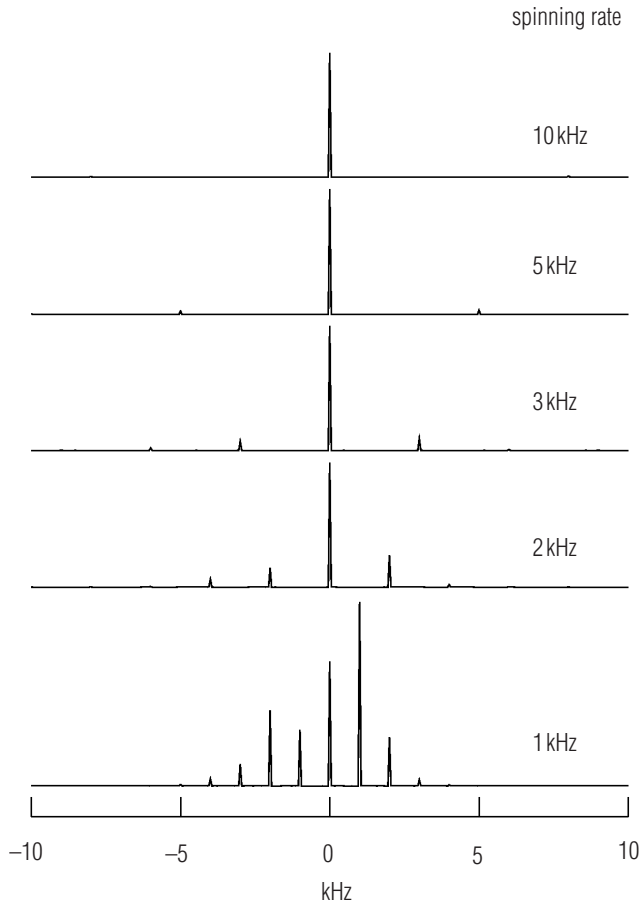

Fig. 2.2 The effect of slow speed magic-angle spinning. A set of spinning sidebands appears, with a centreband at the isotropic chemical shift and further lines spaced at the spinning frequency. The intensities of the sidebands change with spinning speed, with higher-order sidebands (i.e. those further away from the centreband) becoming less intense as the spinning speed increases. The chemical shift parameters used in the calculation of these sideband patterns are: isotropic chemical shift offset, 0 Hz; chemical shift anisotropy, 5 kHz; asymmetry, 0.

As shown in Chapter 1, the spectral frequency, i.e. chemical shift due to the shielding interaction, is

$$\omega = -\omega_0 \mathbf{b}_0^R \boldsymbol{\sigma}^R \mathbf{b}_0^R \tag{2.2}$$

where $\mathbf{b}_0^R$ is the unit vector in the direction of $\mathbf{B}_0$ in the rotor axis frame R. In turn, $\mathbf{b}_0^R$ is given by

$$\mathbf{b}_0^R = (\sin\theta_R \cos\omega_R t, \sin\theta_R \sin\omega_R t, \cos\theta_R) \tag{2.3}$$

where θ_R is the angle of the rotor axis frame z-axis with respect to $\mathbf{B}_0$ and ω_R is the spinning speed. (θ_R, $\omega_R t$) are the polar angles which describe the orientation of $\mathbf{B}_0$

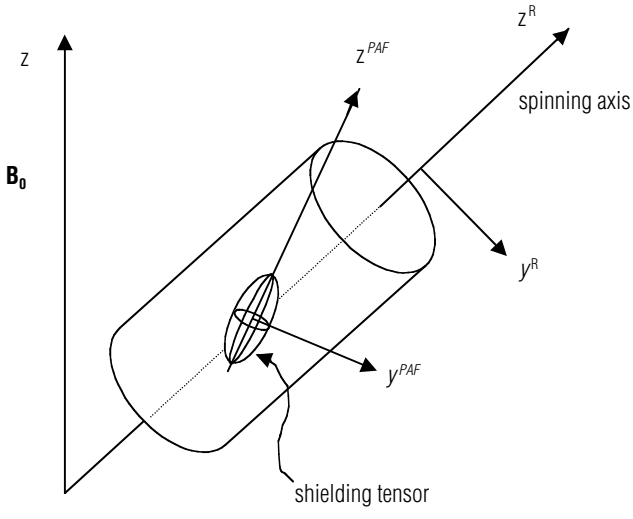

Fig. 2.3 Illustrating the axis frames used in the discussion of magic-angle spinning. Shown here is the so-called *laboratory frame* whose *z* axis defines the direction of $\mathbf{B}_0$, the *rotor frame* (superscript R) whose z^R axis is parallel to the spinning axis and the *principal axis frame* (superscript PAF), the frame in which the shielding tensor is diagonal. The shielding tensor is represented here by an ellipsoid.

in the rotor axis frame *R*. Substituting for $\mathbf{b}_0^R$ in Equation (2.2) for the spectral frequency and, after some (considerable) rearrangement, using trigonometric identities, we obtain [1, 2]

$$\begin{aligned}\omega = -\omega_0 \Big\{ & \sigma_{iso} + \frac{1}{2}(3\cos^2\theta_R - 1)(\sigma_{zz}^R - \sigma_{iso}) \\ & + \sin^2\theta_R \left[\frac{1}{2}(\sigma_{xx}^R - \sigma_{yy}^R)\cos(2\omega_R t) + \sigma_{xy}^R \sin(2\omega_R t) \right] \\ & + 2\sin\theta_R \cos\theta_R [\sigma_{xz}^R \cos(\omega_R t) + \sigma_{yz}^R \sin(\omega_R t)] \Big\} \end{aligned} \tag{2.4}$$

where σ_{iso} is the isotropic shielding defined by:

$$\sigma_{iso} = \frac{1}{3}(\sigma_{xx} + \sigma_{yy} + \sigma_{zz}) \tag{2.5}$$

In this definition of isotropic shielding, $\boldsymbol{\sigma}$ can be measured in any frame, as the trace of a tensor is invariant to rotation of the defining axis frame.

Now, $\boldsymbol{\sigma}^R$ can be written in terms of $\boldsymbol{\sigma}^{PAF}$, the shielding tensor expressed in the principal axis frame as

$$\boldsymbol{\sigma}^R = \mathbf{R}^{-1}(\alpha, \beta, \gamma) \begin{pmatrix} \sigma_{xx}^{PAF} & 0 & 0 \\ 0 & \sigma_{yy}^{PAF} & 0 \\ 0 & 0 & \sigma_{zz}^{PAF} \end{pmatrix} \mathbf{R}(\alpha, \beta, \gamma) \tag{2.6}$$

where $\mathbf{R}(\alpha, \beta, \gamma)$ is the rotation matrix corresponding to the rotation operator which rotates the *PAF* into the rotor axis frame via Euler angles α, β and γ. Euler angles are defined in Box 1.2 (Chapter 1), as is the effect of frame rotation on tensor quantities. Using this definition of $\boldsymbol{\sigma}^{R}$ and the fact that $\theta_R = 54.74°$ (so that $(3\cos^2\theta - 1) = 0$), after much rearrangement we find

$$\begin{aligned}\omega = -\omega_0\{\sigma_{iso} + [A_1\cos(\omega_R t + \gamma) + B_1\sin(\omega_R t + \gamma)] \\ + [A_2\cos(2\omega_R t + 2\gamma) + B_2\sin(2\omega_R t + 2\gamma)]\}\end{aligned} \tag{2.7}$$

with

$$\begin{aligned}A_1 &= \frac{2}{3}\sqrt{2}\sin\beta\cos\beta[\cos^2\alpha(\sigma_{xx}^{PAF} - \sigma_{zz}^{PAF}) + \sin^2\alpha(\sigma_{yy}^{PAF} - \sigma_{zz}^{PAF})] \\ B_1 &= \frac{2}{3}\sqrt{2}\sin\alpha\cos\alpha\sin\beta(\sigma_{xx}^{PAF} - \sigma_{zz}^{PAF}) \\ A_2 &= \frac{1}{3}((\cos^2\beta\cos^2\alpha - \sin^2\alpha)(\sigma_{xx}^{PAF} - \sigma_{zz}^{PAF}) \\ &\quad + (\cos^2\beta\sin^2\alpha - \cos^2\alpha)(\sigma_{yy}^{PAF} - \sigma_{zz}^{PAF})) \\ B_2 &= -\frac{2}{3}\sin\alpha\cos\alpha\cos\beta(\sigma_{xx}^{PAF} - \sigma_{yy}^{PAF})\end{aligned} \tag{2.8}$$

The first term in Equation (2.7) is obviously just the isotropic term. The remaining terms however, oscillate at frequencies ω_R and $2\omega_R$ respectively. When the spinning speed ω_R is much greater than the chemical shift anisotropy Δ_{cs} (see Section 1.4.1, Equation (1.102) for definition) these terms have a negligible effect on the NMR spectrum. However, when $\omega_R \leq \Delta_{cs}$, these terms create the spinning sidebands.

It is a simple matter to calculate the spinning sideband pattern using Equation (2.7). The free induction decay (FID) $g(t)$ in an NMR experiment where the evolution frequency of the observed coherence/magnetization is time-dependent is

$$g(t) = \frac{1}{8\pi^2}\int_0^{2\pi}\int_0^{\pi}\int_0^{2\pi}\exp\left(i\int_0^t \omega(\alpha, \beta, \gamma; t)\,dt\right)\sin\beta\,d\alpha\,d\beta\,d\gamma \tag{2.9}$$

for a powder sample, where the integrals over α, β and γ sum the FIDs from all possible molecular/crystallite orientations in the powder sample. The Euler angles (α, β, γ) define the orientation of the molecule-fixed principal frame (*PAF*) relative to the rotor frame. $\omega(\alpha, \beta, \gamma; t)$ is the spectral or evolution frequency of the observed coherence/magnetization for the molecular orientation defined by (α, β, γ). Substituting Equation (2.7) for $\omega(\alpha, \beta, \gamma; t)$ in Equation (2.9) and performing the integrations over molecular orientation numerically allows the full FID for the sample to be calculated. From that, it is a simple matter to obtain the frequency spectrum by Fourier transformation.

The chemical shift anisotropy and asymmetry (see Section 1.4.1, Equation (1.102)) for definitions) can be obtained from an experimentally observed spinning sideband pattern by calculating the expected spectrum for different anisotropy and asymmetry values until reasonable agreement with the experimental pattern is obtained [**1, 2**]. Spinning sideband patterns of the type described here can be produced from heteronuclear dipolar coupling and quadrupolar coupling as well as chemical shielding. By substituting the relevant interaction tensor in Equations (2.7) and (2.8), the spinning sideband patterns arising from them can be calculated. There is a small modification in the case of dipolar coupling. If we consider the dipolar coupling between two spins I and S for instance, the FID arising from spin I, $g^I(t)$, is as in Equation (2.9) but in addition must be summed over the $(2S + 1)$ possible I-spin transitions that can occur, each corresponding to a different possible S-spin z magnetization.

2.2.2 Rotor or rotational echoes

Solid-state NMR literature often refers to *rotational echoes* in association with magic-angle spinning. These are simply explained as follows. Consider a component of magnetization in the x–y plane of the rotating frame (resulting from a 90° pulse for instance); the evolution of this magnetization is what is recorded in the FID in the NMR experiment. This magnetization has an evolution frequency determined by the applied field $\mathbf{B}_0$ and chemical shielding. Suppose this component arises from a principal axis frame of orientation (α, β, γ) with respect to the rotor axis frame and that the whole sample is spun at the magic angle. As the sample spins, the evolution frequency (as recorded in the FID) varies, because the crystallite orientation changes with respect to the $\mathbf{B}_0$ field as the sample rotates, and so the chemical shielding changes also. However, when the sample returns to its starting position, the evolution frequency returns to its starting value and then goes through the same cycle of values again. Thus, the FID corresponding to the magnetization component consists of a sequence of repeated 'sub-FIDs', or *rotational echoes* (Fig. 2.4).

Summing over all the magnetization components arising from the whole sample gives a similar result. Fourier transformation of any one of the rotor echoes results in a powder pattern identical to that from a non-spinning sample. This is because rotating the sample alters the γ angle for each crystallite, but as one crystallite moves from $\gamma \rightarrow \gamma + \Delta\gamma$ due to the sample rotation, so another moves from $\gamma - \Delta\gamma \rightarrow \gamma$, so that the distribution of crystallites over the γ at any point during the rotor cycle is as it would be in a static sample (assuming the sample has cylindrical symmetry).

If a new time series is made up of the rotational echo maxima (the dots in Fig. 2.4) and Fourier transformed, a purely isotropic spectrum free of spinning sidebands is obtained as explained below.

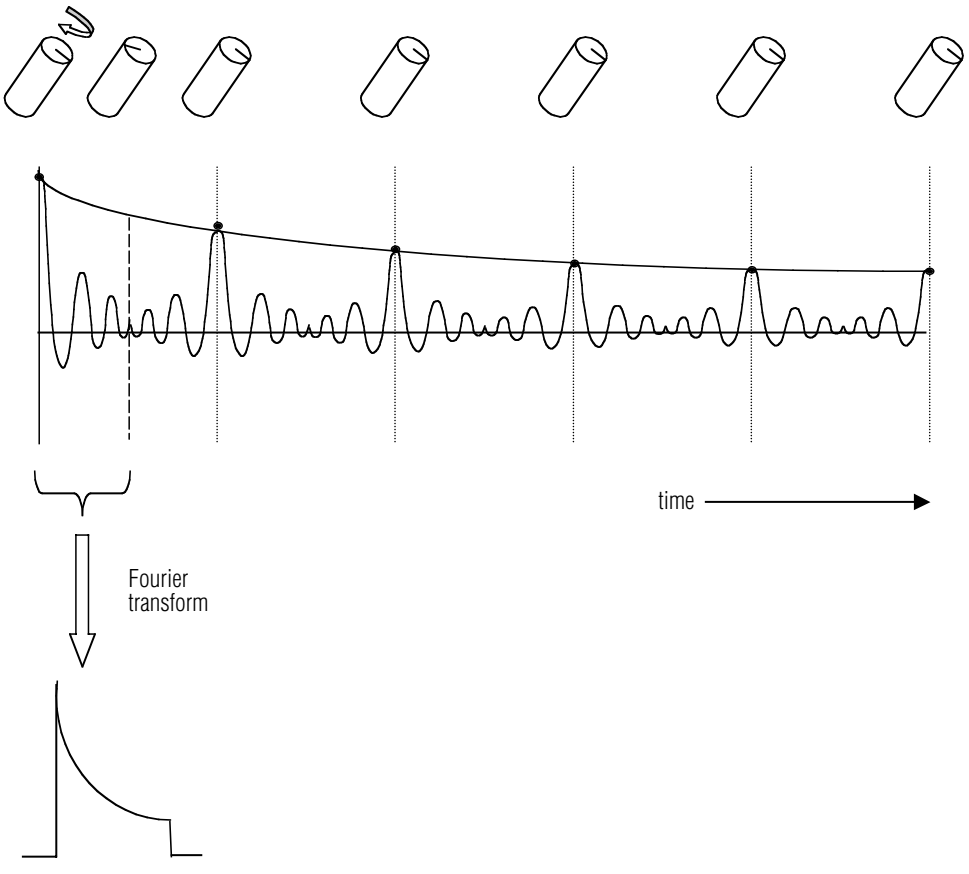

Fig. 2.4 The formation of rotor echoes. The FID shown is that formed under magic-angle spinning (on resonance); essentially the FID repeats every rotor period (marked with dotted lines) and within each rotor period, is symmetric about the half period point. Fourier transformation of one half of a single rotor period gives the powder pattern that would be formed in the absence of magic-angle spinning. Fourier transformation of the echo maxima (denoted by the black dots) gives a single line at the isotropic chemical shift. Fourier transformation of the entire FID gives a line at the isotropic chemical shift flanked by spinning sidebands as described in the text. The rotor echoes arise as a result of the orientation dependence of the chemical shift (or other time-independent interaction); the chemical shift of a given crystallite changes as the rotor changes position during spinning. As the rotor returns to its original position at the end of each rotor period, so the chemical shift returns to its original value and an echo forms in the FID.

2.2.3 Removing spinning sidebands

Although spinning sidebands are very useful for determining anisotropies and asymmetries of nuclear spin interactions, they can obscure other signals in the spectrum. Several sets of overlapping spinning sidebands can also result in a very confusing spectrum. Therefore, we need some way of removing spinning sidebands.

One of the best ways of removing spinning sidebands is simply to spin the sample faster! At the time of writing, speeds of 50 kHz are achievable with rotors of 2 mm external diameter. Where this is still not fast enough, or not possible, there are two

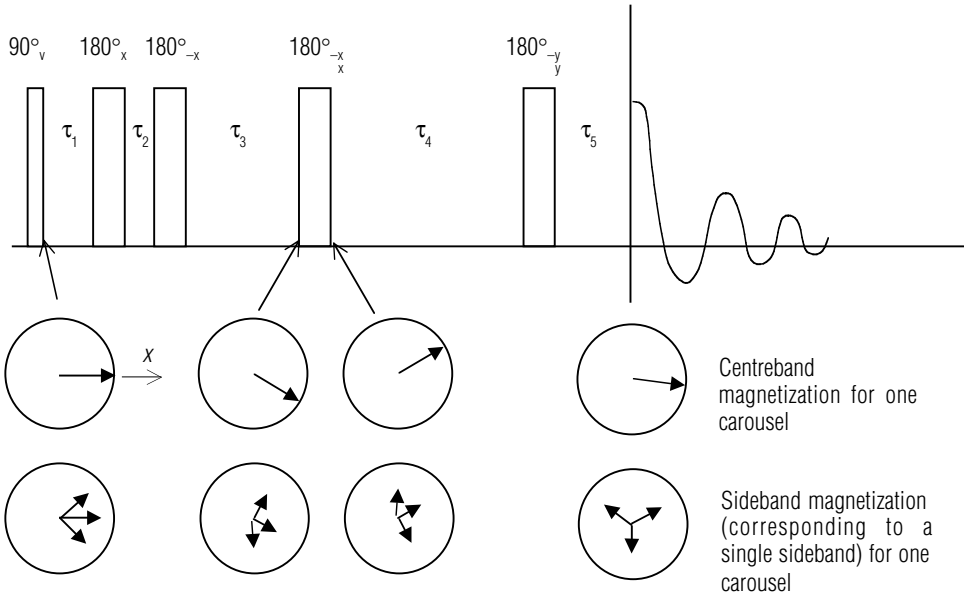

Fig. 2.5 The TOSS pulse sequence (total suppression of spinning sidebands) consists of four 180° pulses in a period prior to acquisition. The phase cycling of the 180° pulses shown compensates for pulse imperfections. The initial 90° pulse simply generates transverse magnetization. An example of the pulse spacings is $\tau_1 = 0.1885\tau_R$, $\tau_2 = 0.0412\tau_R$, $\tau_3 = 0.5818\tau_R$, $\tau_4 = 0.9588\tau_R$, $\tau_5 = 0.2297\tau_R$, where τ_R is the rotor period. The schematics below the pulse sequence indicate the precessional motion of the centreband magnetization and a single sideband magnetization for one carousel of crystallite orientations (see text for details). At the end of the TOSS sequence, the phases of the sideband magnetization components from the different crystallite orientations within the carousel are random, so that there is no net sideband magnetization.

other options. The first is to record the FID synchronously with the sample spinning, i.e. set the FID dwell time equal to the rotor period or, equivalently, spectral width equal to rotor spinning speed. This works because all the anisotropic components of $\omega(\alpha, \beta, \gamma; t)$ in Equation (2.9) for the FID, $g(t)$, integrate over complete rotor periods to zero, leaving only the isotropic component at the sampling points $t = n\tau_R$, where n is an integer and τ_R is the rotor period. This is equivalent to sampling at the points indicated by dots in Fig. 2.4. This method, however, is not often used as it requires the use of what is often a restrictively small spectral width (which leads to problems with folding if it results in part of the spectrum falling outside the spectral width).

The preferred method is to use a special pulse sequence known as Total Suppression of Spinning Sidebands (TOSS) [3]. This method applies a series of 180° pulses at precisely placed points in a period *prior* to acquisition. Usually four 180° pulses are used with phase cycling to compensate for pulse imperfections. The pulse sequence is shown in Fig. 2.5. Finite 180° pulse lengths reduce the efficiency of this technique, so sometimes composite 180° pulses are used to compensate. The technique assumes that the sample has cylindrical symmetry, which is normally the case, providing the crystallites in the sample are small and truly randomly distributed.

If there are many spinning sidebands, TOSS does not work well and small residual spinning sidebands (which may show phase distortions) are observed. It is worth noting that the isotropic signal intensity under TOSS is different from the isotropic signal intensity in the sideband pattern and that in general, TOSS signals are not quantitative. The original TOSS sequence [**3**] as shown in Fig. 2.5 involves two 180° particularly close together. At high spinning speeds these two pulses can become so close that they merge, in which case the pulse sequence is ineffective. For this reason, there has been some effort towards producing improved TOSS sequences [**4**], although all work on the same principles.

The way a TOSS pulse sequence works can be understood qualitatively as follows. An initial 90°_y pulse creates transverse magnetization along x. The transverse magnetization associated with each different crystallite orientation in the sample begins to precess about the applied field $\mathbf{B}_0$. Before we look at the TOSS sequence in detail, we need to first describe further the transverse magnetization components from each crystallite orientation. The precession frequency of each such component will change with time as the rotor rotates and the crystallites change orientation with respect to the applied field. The *phase* of a magnetization component is the angle between it and the x-axis of the transverse plane (Fig. 2.5). The spectrum associated with the transverse magnetization of each crystallite consists of a centreband at the isotropic chemical shift and a series of spinning sidebands radiating out from the centreband, as we have already seen. Thus we can decompose the time-varying transverse magnetization for each crystallite into a component precessing at the isotropic chemical shift frequency, plus a series of other components precessing at the sideband frequencies, i.e. $\omega_{iso} + m\omega_R$, where m is an integer (positive or negative). We will refer to these components as centreband magnetization and sideband magnetization respectively, with mth-order sideband magnetization being that associated with the mth spinning sideband. The initial phase (i.e. at time $t = 0$) and the amplitude of each sideband and centreband magnetization component depends on crystallite orientation. The sum of centreband and sideband magnetization components for a single crystallite orientation will be oriented along x however, representing the initial transverse magnetization after a 90°_y pulse. This is a useful picture from which to understand the mechanism of the TOSS experiment.

We then need to define the concept of a *carousel* of crystallite orientations. A crystallite orientation with respect to a rotor-fixed axis frame is defined by the set of Euler angles (α, β, γ), as in Section 2.2.1 previously. A carousel of crystallite orientations is the set of crystallite orientations with the same α and β angles, but different γ, with all γ values from 0 to 2π being in the set. The significance of this is that a crystallite in one orientation within the carousel will visit all other orientations in the carousel during the course of one rotor cycle. This in turn means that the transverse magnetization associated with all crystallite orientations

within the carousel go through the same precessional frequencies during one rotor cycle, albeit at different times. The initial phase of the *m*th-order sideband magnetization within a carousel depends on γ, while the initial phase of the centreband magnetization is independent of γ, and thus constant within a carousel of orientations.

A TOSS pulse sequence makes the phases of the *m*th-order sideband magnetizations for the crystallite orientations within one carousel, random at the end of the pulse sequence. Thus, the net *m*th-order sideband magnetization when summed over all the orientations of the carousel is zero at the end of the TOSS pulse sequence, i.e. at the start of the FID whose acquisition follows the TOSS sequence (Fig. 2.5). At the same time, the phases of the centreband magnetizations within the carousel are arranged to be all the same, and so the centreband magnetizations add constructively, and are present at the end of the TOSS sequence with the intensity that would be expected in the absence of the TOSS preparation sequence.

The reason that for a powder sample the intensity of the centrebands tends to be reduced after a TOSS preparation sequence (in comparison to the centreband intensity in the absence of TOSS) is that most TOSS sequences result in the centrebands having a phase which is carousel-dependent. In a powder sample, the centreband signal is summed over all possible carousels, and so there is inevitably some destructive interference between signals from different carousels.

The phases acquired by the sideband and centreband magnetizations are determined by the 180° pulses in the TOSS sequence and their positions in time. The effect of a 180°_{α} pulse on transverse magnetization is to rotate all magnetization components by 180° about the pulse axis, α, as illustrated in Fig. 2.5. In between the 180° pulse of the TOSS sequence, the transverse magnetization components continue to precess at their sideband and centreband frequencies respectively. Thus the net phase acquired by a magnetization component by the end of the pulse sequence depends on their precessional frequency and the number and timing of the 180° pulses. We will not go into the details of how to determine a suitable series of pulses here; suffice to say that solutions can be found, one of which is shown in Fig. 2.5. Details of how to generate other solutions can be found in reference [**4**].

2.2.4 Magic-angle spinning for homonuclear dipolar couplings

As mentioned at the beginning of this section, magic-angle spinning can be used for removing the effects of homonuclear dipolar-coupling providing the spinning speed is high enough. The dipolar-coupling hamiltonian for a homonuclear-coupled spin pair, *I* and *S*, was shown in Chapter 1 to be (in angular frequency units):

$$\hat{H}_{\mathrm{dd}}^{\mathrm{homo}} = -d \cdot \frac{1}{2}(3\cos^2\theta - 1)\left[3\hat{I}_z\hat{S}_z - \hat{\mathbf{I}}\cdot\hat{\mathbf{S}}\right] \tag{2.10}$$

with $d = \left(\frac{\mu_0}{4\pi}\right)\frac{\gamma_I\gamma_S\hbar}{r^3}$, the dipolar-coupling constant.

For a general multispin system, the corresponding hamiltonian is simply

$$\hat{H}_{\mathrm{dd}}^{\mathrm{homo}} = -\sum_{i>j} d_{ij} \cdot \frac{1}{2}(3\cos^2\theta_{ij} - 1)\left[3\hat{I}_z^i\hat{S}_z^j - \hat{\mathbf{I}}^i \cdot \hat{\mathbf{I}}^j\right] \tag{2.11}$$

where i and j label the spins, so that $d_{ij} = \left(\frac{\mu_0}{4\pi}\right)\frac{\gamma_i\gamma_j\hbar}{r_{ij}^3}$, where r_{ij} is the internuclear distance between spins i and j, and θ_{ij} is the angle between the i–j internuclear vector and the applied magnetic field $\mathbf{B}_0$.

From Equations (2.10) and (2.11), the homonuclear dipolar coupling quite clearly depends on the geometric factor $(3\cos^2\theta - 1)$, and so is averaged to zero by magic-angle spinning (see Section 2.2 for details of magic-angle spinning), if the rate of spinning is fast compared to the homonuclear dipolar-coupling linewidth. Nowadays, spinning rates of 30–50 kHz can be achieved on commercially available probes. This is fast enough to produce high-resolution spectra for ^{1}H in many organic solids for instance, where otherwise homonuclear dipolar linebroadening (linewidth at half maximum height) would be of the order of 20–50 kHz.

At spinning speeds much less than the dipolar linewidth, magic-angle spinning has very little effect on the NMR spectrum, and the broad dipolar line that would be observed in the absence of spinning is little altered.

At intermediate spinning rates (rates around a quarter to a half of the dipolar linewidth), spinning sidebands appear, but these spinning sidebands are very different in character to those arising from incompletely spun-out chemical shift anisotropy or heteronuclear dipolar coupling (Fig. 2.6). The spinning sidebands associated with chemical shift anisotropy and heteronuclear dipolar coupling are all sharp lines. Those associated with homonuclear dipolar coupling are usually broad. It is difficult to describe this regime in a rigorously quantitative fashion. The behaviour can, however, be understood qualitatively at least, as follows. The term B in the homonuclear dipolar-coupling hamiltonian mixes the degenerate Zeeman functions associated with the collection of spins in the spin system. As shown in Chapter 1, this mixing is time-dependent if there are more than two spins in the system, so that the wavefunctions describing the spin system are time-dependent linear combinations of the Zeeman functions. To average an interaction to zero through magic-angle spinning, the state of the spin system needs to be constant over the time for one period of the sample rotation. However, in the case of homonuclear dipolar coupling, the state of the spin system is changing on the timescale of the sample rotation, for intermediate sample rotation rates. This prevents the complete averaging of the dipolar interaction in the spin system.

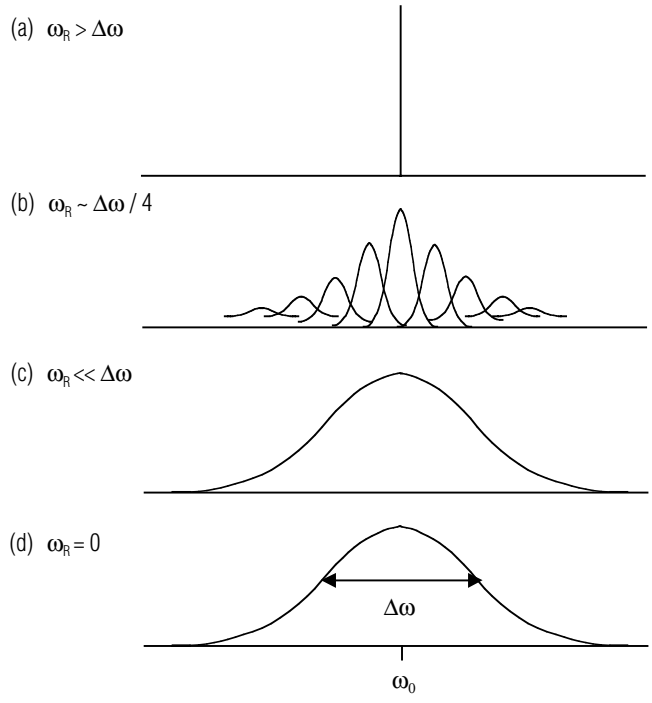

Fig. 2.6 The effects of magic-angle spinning on homonuclear dipole–dipole coupling. (a) The broad line which arises in the NMR spectrum (shown in (d)) from this interaction is only narrowed by magic-angle spinning for spinning rates of the order of the linewidth or greater. (b) For slower speeds, broad spinning sidebands appear, and (c) at still slower speeds, there is little effect on the spectrum at all.

At lower spinning rates, however, the rate at which the state of the system changes is rapid compared to the sample spinning. In this case, then, the spinning does not have a chance to alter the time-dependent state of the spin system; hence the NMR spectrum of the system is unaffected by the spinning. This does not happen in heteronuclear spin systems, as there are no degenerate spin levels in such a system.

2.3 High-power decoupling

When observing a dilute spin, e.g. ^{13}C with 1.1% abundance, with ^{1}H or other abundant spins nearby, broadening due to heteronuclear dipolar coupling often causes a serious problem to an already weak spectrum. High-power decoupling is a simple technique which removes the effects of heteronuclear coupling in such cases.

Consider the case of dipolar-coupled ^{1}H and ^{13}C spins, where the ^{13}C spins are to be observed. The method (Fig. 2.7) consists of applying a continuous irradiation of very high power (100–1000 watts) at the frequency of the proton resonance. The required pulse sequence for the ^{13}C nuclei is then applied, and the ^{13}C FID measured while continuing the ^{1}H irradiation.

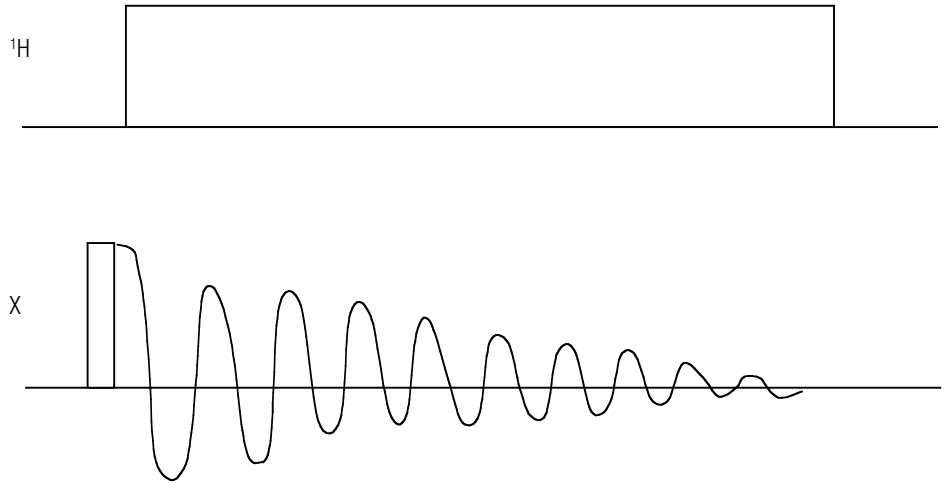

Fig. 2.7 High-power decoupling. This removes the effects of ^{1}H dipolar coupling from the NMR spectrum of X in this case; it can of course be applied to any abundant spin in place of ^{1}H in the same manner. High-power irradiation is simply applied to the ^{1}H spins during the acquisition of the X spin spectrum. Here a single pulse is used to generate the X transverse magnetization; this can of course be replaced with a more complicated preparation sequence. ^{1}H decoupling can also be used in the preparation sequence if necessary.

It is worth noting that the pulses used for decoupling ^{1}H in samples with abundant ^{1}H spins do not need to be particularly broad banded, i.e. do not need to cover a wide frequency range. Because of the homonuclear dipolar coupling between the ^{1}H nuclei in such samples, the effects of an rf pulse applied to any part of the ^{1}H spectrum are transmitted among all coupled ^{1}H. This is because the rf irradiation applied to the ^{1}H spins affects the z-component of spin of each ^{1}H nucleus which is close to resonance with the irradiation. The z-component of spin of any one ^{1}H spin affects that of all nearby ^{1}H spins through the $\hat{I}_{i+}\hat{I}_{j-} + \hat{I}_{i-}\hat{I}_{j+}$ terms in the homonuclear dipolar-coupling hamiltonian (see Section 1.4.2 for details). The close-to-resonance spins which are affected by the rf irradiation then affect the z-component of spin of all their neighbours, and so on, so that the effect of rf irradiation on just one ^{1}H spin is transmitted throughout the ^{1}H dipolar-coupled network.

Any proper explanation of how high-power decoupling in solids works requires the uses of *average hamiltonian theory* which is described in Box 2.1 below.

2.4 Multiple pulse decoupling sequences

As described in Section 2.2.4, magic-angle spinning can be used to remove the effects of homonuclear dipolar coupling from NMR spectra, providing the rate of sample spinning is fast relative to the homonuclear dipolar linewidth. Where this is not achievable, the effects of homonuclear dipolar coupling may be removed instead by special pulse sequences. Many such are known, and are collectively referred to as *multiple pulse sequences*.

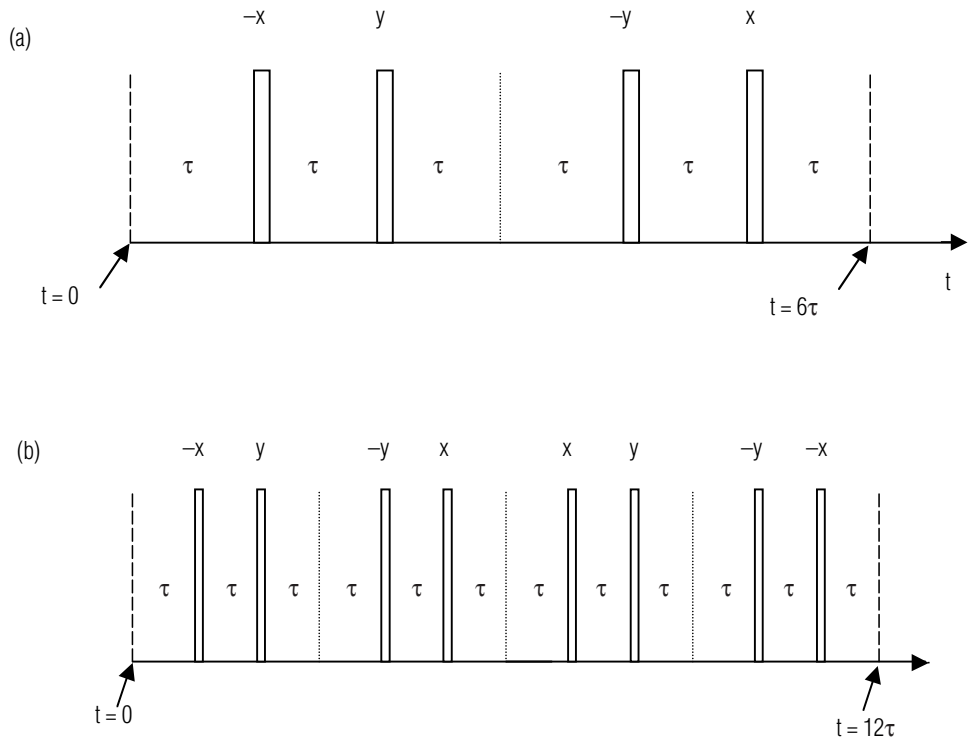

Fig. 2.8 Multiple pulse sequences for removing the effects of homonuclear dipolar coupling from the NMR spectrum. All pulses are 90° pulses with the phase indicated. (a) WAHUHA sequence and (b) MREV-8 sequence. The sequences are repeated throughout acquisition, with FID points being collected at the end of each cycle, indicated by an arrow in each case. The MREV-8 sequence is in fact two phase-cycled WAHUHA sequences and has the effect of zeroing higher-order terms in the average hamiltonian.

Most multiple pulse sequences are arranged in such a way that, at certain windows within the pulses sequence, the effect of the dipolar hamiltonian on the nuclear magnetization is zero. If the nuclear magnetization is detected only at these points, the effects of dipolar coupling are removed from the spectrum. There are many useful sequences in the literature. The first, and one of the simplest, is the WAHUHA sequence, shown in Fig. 2.8 [**5**]. The MREV-8 sequence [**6**] is also widely used (also shown in Fig. 2.8). There is a whole host of other sequences which have been devised since the pioneering WAHUHA sequence, which all aim to achieve the same type of result (see, for instance, reference [7]). In all, the pulsing continues in cycles throughout the period of the free induction decay, with one detection point per cycle at the appropriate point until the magnetization has decayed completely from the *x*–*y* plane. Rather than average the geometrical parts of $\hat{H}_{\mathrm{dd}}^{\mathrm{homo}}$ to zero in the way that magic-angle spinning does, these pulse sequences average the spin factors of $\hat{H}_{\mathrm{dd}}^{\mathrm{homo}}$ to zero. Any explanation of these sequences needs the application of average hamiltonian theory; this and its application to the analysis of the WAHUHA pulse sequence is outlined in Box 2.1.

Box 2.1 Average hamiltonian theory and the toggling frame

Average hamiltonian theory

As shown in Chapter 1, we can calculate the density operator describing a spin system at time t, $\hat{\rho}(t)$ from that at time 0 via the equation

$$\hat{\rho}(t) = \hat{U}(t)\hat{\rho}(0)\hat{U}(t)^{-1} \quad \text{(i)}$$

where the so-called propagator $\hat{U}(t)$ is given by

$$\hat{U}(t) = \exp(-i\hat{H}t) \quad \text{(ii)}$$

in which $\hat{H}$ is the hamiltonian operator which describes the spin system between 0 and t. This formulation of the propagator assumes that the hamiltonian is constant over the time period. Frequently, however, this is not the case. For instance, in the WAHUHA pulse sequence (Fig. 2.8) described above, the hamiltonian changes when rf pulses are applied from that which operates during the time gaps τ between pulses. In these circumstances, Equation (ii) for the propagator becomes

$$\hat{U}(t) = \exp(-i\hat{H}_n t_n) \ldots \exp(-i\hat{H}_1 t_1) \quad \text{(iii)}$$

where the hamiltonian which operates in the first time period t_1 is $\hat{H}_1$ and so on. Note that the hamiltonians in Equation (iii) appear in strict chrononlogical order. In cases like this, it would be much more convenient to replace the series of exponential functions in Equation (iii) for the propagator with a single exponential relying on some *average hamiltonian* $\overline{H}$ which has the same effect as the series of hamiltonians $\hat{H}_1 \ldots \hat{H}_n$ (Fig. B2.1.1), i.e.

$$\hat{U}(t) = \exp(-i\hat{H}_n t_n) \ldots \exp(-i\hat{H}_1 t_1) = \exp(-i\overline{H}t)$$

Of course, this is always possible, but not unfortunately, always useful, as in general, the appropriate average hamiltonian $\overline{H}$ will depend on t, the time at which we wish to know the propagator.

However, in the case where the hamiltonian (or series of hamiltonians) describing the spin system is *periodic* in time, and we only wish to know about the state of the spin system at specific time points spaced by the period of the hamiltonian, we can always calculate a single average hamiltonian which correctly describes the behaviour of the spin system at these points.

One way of calculating this average hamiltonian, a rather 'brute force' approach, is to calculate the propagator $\hat{U}(t)$ by simply evaluating the series

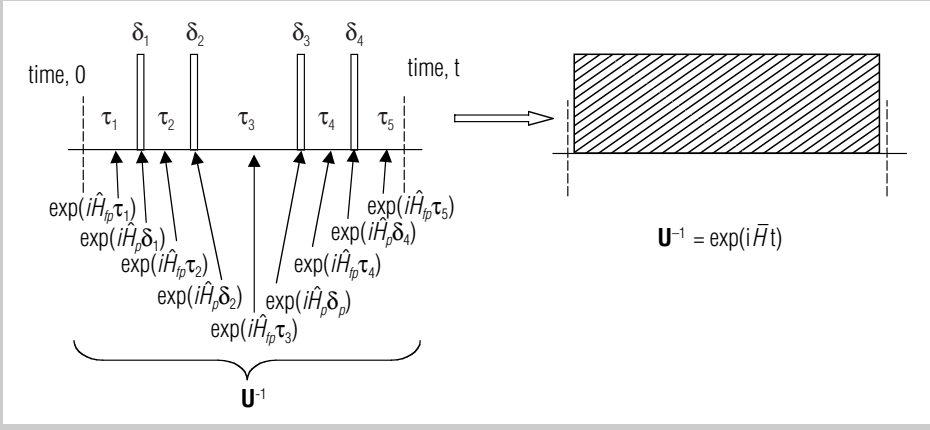

Fig. B2.1.1 The idea behind average hamiltonian theory. The propagator **U** which describes a pulse sequence consists of a series of exponentials, $\exp(-i\hat{H}_i\tau_i)$ and $\exp(-i\hat{H}_i\delta_i)$ where the hamiltonian $\hat{H}_i$ describes the spin system during the period τ_i and δ_i respectively. In this diagram, the hamiltonian $\hat{H}_{fp}$ operates during periods of free precession between the pulses and $\hat{H}_p$ operates during the pulses. The lengths of the pulses are given by δ_i for the *i*th pulse and the lengths of the periods of free precession by τ_i. In average hamiltonian theory, the series of exponentials is replaced by a single exponential $\exp(-i\bar{H}t)$ employing an *average hamiltonian* $\bar{H}$ which describes the net effect of the pulse sequence at its end. $\bar{H}$ can be envisaged as a 'black box' which accounts for the effects of the whole pulse sequence but does not allow us to see what happens at points during the pulse sequence.

of exponentials in Equation (iii) appropriate to the particular periodic hamiltonian of interest. This then equates to $\exp(-i\overline{H}t)$ $(= \hat{U}(t))$, so that $\overline{H}$ may be found by diagonalizing the matrix $\mathbf{U}(t)$ formed from $\hat{U}(t)$ in some appropriate basis. The eigenvalues resulting from this process are then $\exp(-i\overline{H}_{jj}t)$ for the *j*th eigenvalue, where $\overline{H}_{jj}$ is the matrix element of $\overline{H}$ in the eigenvector basis arising from the diagonalization. However, this process rarely leads to much physical insight.

An alternative approach evaluates the series of exponential operators in Equation (iii) using the Magnus expansion:

$$e^{\hat{A}}e^{\hat{B}} = \exp\left\{\hat{A}+\hat{B}+\frac{1}{2!}[\hat{A},\hat{B}]+\frac{1}{3!}([\hat{A},[\hat{A},\hat{B}]]+[[\hat{A},\hat{B}],\hat{B}])+\ldots\right\} \qquad \text{(iv)}$$

If this is applied to the series of exponential operators in Equation (iii) for a periodic hamiltonian of period t_p, i.e. $t_1 + t_2 + \ldots + t_n = t_p$ to evaluate $\hat{U}(t_p)$ and we then equate

$$\hat{U}(t_p) = \exp(-i\overline{H}t_p) \qquad \text{(v)}$$

we find that

$$\overline{H}(t_p) = \overline{H}^{(0)} + \overline{H}^{(1)} + \overline{H}^{(2)} + \ldots \qquad \text{(vi)}$$

where

Continued on p. 90

Box 2.1 *Cont.*

$$\begin{aligned}
\overline{H}^{(0)} &= \frac{1}{t_{\mathrm{p}}}\{\hat{H}_1 t_1 + \hat{H}_2 t_2 + \ldots + \hat{H}_n t_n\} \\
\overline{H}^{(1)} &= -\frac{i}{2t_{\mathrm{p}}}\{[\hat{H}_2 t_2, \hat{H}_1 t_1] + [\hat{H}_3 t_3, \hat{H}_1 t_1] + [\hat{H}_2 t_2, \hat{H}_3 t_3] + \ldots\} \\
\overline{H}^{(2)} &= -\frac{1}{6t_{\mathrm{p}}}\{[\hat{H}_3 t_3, [\hat{H}_2 t_2, \hat{H}_1 t_1]] + [[\hat{H}_3 t_3, \hat{H}_2 t_2], \hat{H}_1 t_1] \\
&\quad + \frac{1}{2}[\hat{H}_2 t_2, [\hat{H}_2 t_2, \hat{H}_1 t_1]] + \frac{1}{2}[[\hat{H}_2 t_2, \hat{H}_1 t_1], \hat{H}_1 t_1] + \ldots\}
\end{aligned} \tag{vii}$$

Equations (vi) and (vii) are not as daunting as they at first appear; the first-order term $\overline{H}^{(0)}$ (first order in the hamiltonian) is simply the average of the piecewise hamiltonians $\hat{H}_1$, $\hat{H}_2, \ldots, \hat{H}_n$ which operate during one period. In the case where these hamiltonians all commute with each other, or nearly so, all higher-order terms can be neglected and the first-order term is a good description of the average hamiltonian. Clearly if this is the case, the analytic form of the approximate average hamiltonian is easily determined and can often give useful physical insight into how a pulse sequence works.

In cases where the hamiltonians which operate over the time period do not commute with each other, it is often possible to transform them into a new frame, the so-called *toggling frame*, in which non-commuting terms disappear. It is then possible to approximate the average hamiltonian in this frame by the first-order term of Equation (vi).

As we shall see shortly, the WAHUHA pulse sequence creates an average hamiltonian which to first order, i.e. for $\overline{H} = \overline{H}^{(0)}$, has no contribution from homonuclear dipolar coupling. The other pulse sequences for the removal of homonuclear dipolar-coupling effects (see reference [7] for instance) create average hamiltonians for which this is the case to higher orders of $\overline{H}^{(j)}$ in $\overline{H}$.

The toggling frame and the WAHUHA pulse sequence

The WAHUHA pulse sequence in Fig. 2.8 is a typical series of rf pulses with gaps between them (of length τ) where whatever coherences present are simply allowed to evolve under the effects of whatever internal spin interactions are present – in this case, homonuclear dipolar coupling.

We will assume all pulses are of negligible length compared to τ, the gaps between them, and are strong compared to the dipolar coupling, so that we can ignore the coupling during the pulse. We also assume that the pulses are all on

resonance and are defined with respect to the rotating frame, so that throughout the pulse sequence, the effect of the $\mathbf{B}_0$ field apparently vanishes, i.e. the Zeeman term in the hamiltonian in this frame is zero. Then the hamiltonian for the system (in angular frequency units) during a pulse is then simply

$$\hat{H}^{\phi}_{\text{pulse}} = -\omega_1(\hat{I}_x \cos\phi + \hat{I}_y \sin\phi) \tag{viii}$$

where ϕ is the phase of the pulse and

$$\hat{I}_x = \sum_i \hat{I}^i_x \quad \text{and} \quad \hat{I}_y = \sum_i \hat{I}^i_y,$$

with $\hat{I}^i_x$, $\hat{I}^i_y$ being the single spin operators, i.e. $\hat{I}_x$, $\hat{I}_y$ are the sums over the single spin operators for all spins of interest. The hamiltonian during the periods of free evolution is simply that due to the homonuclear dipolar coupling, in the absence of other interactions (we will consider the effects of chemical shift and other inhomogeneous interactions at the end), namely (in angular frequency units)

$$\hat{H}_{\text{fe}} = \sum_{i>j} B_{ij}(3\hat{I}^i_z\hat{I}^j_z - \hat{\mathbf{I}}^i\cdot\hat{\mathbf{I}}^j) \tag{ix}$$

where

$$B_{ij} = -\left(\frac{\mu_0}{4\pi}\right)\frac{\gamma_i\gamma_j}{r^3_{ij}}\hbar\cdot\frac{1}{2}(3\cos^2\theta - 1) \tag{x}$$

In all these hamiltonians, x, y and z refer to the rotating frame axes. Now, the hamiltonians describing the pulses and those describing the periods of free precession do not commute with each other, so the first-order term in the average hamiltonian is *not* a good approximation to the full average hamiltonian. In particular, the pulse hamiltonians are a problem, as they do not commute among each other, that is, $\hat{I}_x$ in an x-pulse operator does not commute with $\hat{I}_y$ in a y-pulse operator, and the WAHUHA sequence employs both x and y pulses. We need to transform to a new frame where the terms in the hamiltonian due to the pulses disappear and the remaining dipolar terms still commute with each other. The average hamiltonian in this new frame is then simply the first-order term of Equation (vi), which is easy to calculate.

In order to find this new frame, we start by asking: What is the effect of a pulse on the density operator describing this spin system? Consider a situation, in the rotating frame, of an on-resonance x pulse, with no other interactions present, so that the hamiltonian is simply

$$\hat{H} = \hat{H}^x_{\text{pulse}} = -\omega_1\hat{I}_x \tag{xi}$$

Continued on p. 92

Box 2.1 *Cont.*

The density operator after time t is given by the usual expression:

$$\hat{\rho}(t) = \exp(-i\hat{H}t)\hat{\rho}(0)\exp(i\hat{H}t) = \exp(i\omega_1\hat{I}_x t)\hat{\rho}(0)\exp(-i\omega_1\hat{I}_x t) \qquad \text{(xii)}$$

Previous discussion of exponential operators (Chapter 1, Box 1.2) explained that an expression of the form $\exp(i\theta\hat{I}_x)\,\hat{O}\exp(-i\theta\hat{I}_x)$, where $\hat{O}$ is an operator is simply a rotation of the operator $\hat{O}$ by θ about x. As shown in the diagram below (Fig. B2.1.2), rotating an operator (or function) by θ about a given axis is equivalent to leaving the operator (or function) where it is and instead, rotating the axis frame in which the operator is defined by –θ about the same axis.

So the effect of the on-resonance x pulse is to rotate the density operator by $+\omega_1 t$ about x, or, equivalently, to rotate the axis frame that the density operator $\hat{\rho}$ is defined in by $-\omega_1 t$ about x, where x in every case refers to the normal, rotating frame axis. Thus, when considering the effect of a pulse sequence, every time we get to a pulse, rather than rotate the density operator according to the pulse, we can instead rotate the axis frame in which the density operator is defined. A rotation of the axis frame by $-\omega_1 t$ about the pulse axis creates the same effect as rotating the density operator by $+\omega_1 t$ about the pulse axis.

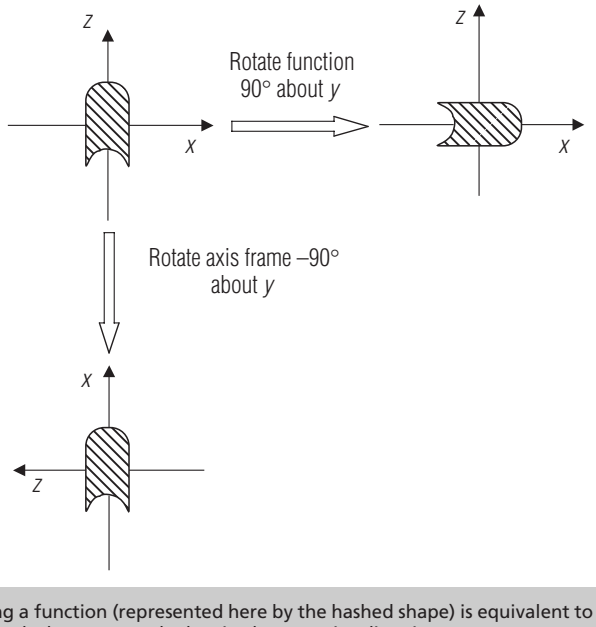

Fig. B2.1.2 Rotating a function (represented here by the hashed shape) is equivalent to rotating the defining axis frame through the same angle, but in the opposite direction.

We call the new, transformed frame, the *toggling frame*. Expressing the density operator in this way, in a frame which moves with the effect of a pulse, is often called the *interaction representation*.

The hamiltonian $\hat{H}^*(t)$ after a time t in such a toggling frame is in general

$$\hat{H}^*(t) = \hat{R}_x^{-1}\hat{H}\hat{R}_x + \omega_1\hat{I}_x \qquad \text{(xiii)}$$

where $\hat{R}_x = \exp(-i\omega_1\hat{I}_x t)$ represents the rotation operator for rotation of the original axis frame by $\omega_1 t$ about the rotating frame x axis, and $\hat{H}$ is the hamiltonian in the rotating frame. See Box 1.2 in Chapter 1 for further discussion of frame transformations.

The form of Equation (xiii) is found by insisting that the time-dependent Schrödinger equation (see Box 1.1 in Chapter 1) is invariant to the frame transformation, as we shall now show.

The time-dependent Schrödinger equation is $-i(\mathrm{d}\psi/\mathrm{d}t) = \hat{H}\psi$, expressed in angular frequency units, where ψ is the wavefunction describing the spin system. The time-dependent Schrödinger equation in the toggling frame must be invariant to the frame transformation and so is simply

$$-i\frac{\mathrm{d}\psi^{\mathrm{tog}}}{\mathrm{d}t} = \hat{H}^{\mathrm{tog}}\psi^{\mathrm{tog}} \qquad \text{(xiv)}$$

where all quantities are referred to the toggling frame. Under the frame transformation described by the rotation operator $\hat{R}_x$, the wavefunction ψ becomes ψ^{tog} in the toggling frame, where

$$\psi^{\mathrm{tog}} = \hat{R}_x^{-1}\psi = \exp\left(+i\omega_1\hat{I}_x t\right)\psi \qquad \text{(xv)}$$

Thus $\mathrm{d}\psi^{\mathrm{tog}}/\mathrm{d}t$ is given by

$$\begin{aligned}\frac{\mathrm{d}\psi^{\mathrm{tog}}}{\mathrm{d}t} &= \exp\left(+i\omega_1\hat{I}_x t\right)\frac{\mathrm{d}\psi}{\mathrm{d}t} + i\omega_1\hat{I}_x\exp\left(+i\omega_1\hat{I}_x t\right)\psi \\ &= \exp\left(+i\omega_1\hat{I}_x t\right)\frac{\mathrm{d}\psi}{\mathrm{d}t} + i\omega_1\hat{I}_x\psi^{\mathrm{tog}} \\ &= \hat{R}_x^{-1}\frac{\mathrm{d}\psi}{\mathrm{d}t} + i\omega_1\hat{I}_x\psi^{\mathrm{tog}} \qquad \text{(xvi)}\end{aligned}$$

where all quantities are expressed with respect to the toggling frame. Substituting for $\mathrm{d}\psi^{\mathrm{tog}}/\mathrm{d}t$ in Equation (xiv) gives

$$-i\left(\hat{R}_x^{-1}\frac{\mathrm{d}\psi}{\mathrm{d}t} + \left(i\omega_1\hat{I}_x\right)\psi^{\mathrm{tog}}\right) = H^{\mathrm{tog}}\psi^{\mathrm{tog}} \qquad \text{(xvii)}$$

We then use the fact that $-i(\mathrm{d}\psi/\mathrm{d}t) = \hat{H}\psi$ and $\psi = \hat{R}_x\psi^{\mathrm{tog}}$ to rewrite the left-hand side of this equation as

$$\hat{R}_x^{-1}\hat{H}\hat{R}_x\psi^{\mathrm{tog}} - i\left(i\omega_1\hat{I}_x\right)\psi^{\mathrm{tog}} = \hat{H}^{\mathrm{tog}}\psi^{\mathrm{tog}} \qquad \text{(xviii)}$$

By comparing the left- and right-hand sides of this equation, we see that $\hat{H}^{\mathrm{tog}}$, the hamiltonian in the rotating frame, is

$$\hat{H}^{\mathrm{tog}} = \hat{R}_x^{-1}\hat{H}\hat{R}_x + \omega_1\hat{I}_x \qquad \text{(xix)}$$

Continued on p. 94

Box 2.1 *Cont.*

So, in the case where $\hat{H} = \hat{H}^x_{\text{pulse}} = -\omega_1 \hat{I}_x$, the toggling frame hamiltonian is simply

$$\hat{H}*(t) = -\omega_1 \hat{R}_x^{-1} \hat{I}_x \hat{R}_x + \omega_1 \hat{I}_x; \quad R_x = \exp(-i\omega_1 \hat{I}_x t) \tag{xx}$$

The first term represents a rotation of the operator $\hat{I}_x$ about x, which of course leaves the x direction, and so $\hat{I}_x$, unchanged. Thus $\hat{H}^*(t)$ becomes

$$\hat{H}*(t) = -\omega_1 \hat{I}_x + \omega_1 \hat{I}_x = 0 \tag{xxi}$$

As expected, in this toggling frame, the effect of the rf pulse is nulled. The same frame transformation on the density operator takes account of the pulse effects.

Now suppose we have a hamiltonian in the rotating frame

$$\hat{H} = \hat{H}_{\text{int}} + \hat{H}^x_{\text{pulse}} \tag{xxii}$$

where $\hat{H}_{\text{int}}$ describes some spin interaction and $\hat{H}^x_{\text{pulse}}$ describes an x pulse. Transforming this hamiltonian to the toggling frame again using Equation (xiii):

$$\begin{aligned} \hat{H}*(t) &= \hat{R}_x^{-1} \hat{H} \hat{R}_x + \omega_1 \hat{I}_x \\ &= \hat{R}_x^{-1} (\hat{H}_{\text{int}} + \hat{H}^x_{\text{pulse}}) \hat{R}_x + \omega_1 \hat{I}_x \\ &= \hat{R}_x^{-1} \hat{H}_{\text{int}} \hat{R}_x + \hat{R}_x^{-1} \hat{H}^x_{\text{pulse}} \hat{R}_x + \omega_1 \hat{I}_x \\ &= \hat{R}_x^{1} \hat{H}_{\text{int}} \hat{R}_x \end{aligned} \tag{xxiii}$$

since

$$\hat{R}_x^{-1} \hat{H}^x_{\text{pulse}} \hat{R}_x = -\omega_1 \exp(i\omega_1 \hat{I}_x t) \hat{I}_x \exp(-i\omega_1 \hat{I}_x t) = -\omega_1 \hat{I}_x$$

as before. In other words, the toggling frame hamiltonian depends only on the spin interaction hamiltonian $\hat{H}_{\text{int}}$ and not on the pulse part.

$\hat{H}^*$ can then be used to calculate $\hat{\rho}^*$, the toggling frame density operator using an equivalent expression to that in Equation (xii):

$$\hat{\rho}*(t) = \exp(-i\hat{H}*t) \hat{\rho}*(0) \exp(i\hat{H}*t) \tag{xxiv}$$

where $\hat{\rho}^*(0)$ is the initial density operator at time $t = 0$ in the toggling frame. Calculating the average hamiltonian within the toggling frame truncates the expression (vi) for the average hamiltonian to the first-order term $\overline{H}_0$ only, providing that the toggling frame hamiltonians which occur at different times in the time period considered, commute with each other in this frame. The toggling frame density operator calculated in this way is completely equivalent to the more usual rotating frame density operator, but simply expressed with respect to a different frame.

So, we now apply the principle of the toggling frame to the particular sequence at hand for the calculation of $\hat{H}^{(0)}$. At the start of the pulse sequence, there is a period of free evolution where the system evolves under the dipolar coupling with the usual hamiltonian:

$$\hat{H}(0\rightarrow\tau)_{\text{fe}} = \sum_{i>j} B_{ij}\left(3\hat{I}_z^i\hat{I}_z^j - \hat{\mathbf{I}}^i\cdot\hat{\mathbf{I}}^j\right) = \hat{H}_{zz} \qquad \text{(xxv)}$$

Next, we have a $90°_{-x}$ pulse (see Fig. B2.1.3).

So, we first transform to a new toggling frame which is rotated about $-x$ by 90°. Now we can ignore the pulse and continue on. Next is another period of free evolution under the dipolar coupling. We must transform the hamiltonian for this period to the new toggling frame we are in, or equivalently rotate the hamiltonian within the original rotating frame. To follow this latter route, we must rotate the operator $\hat{H}_{\text{fe}} = \Sigma_{i>j}B_{ij}(3\,\hat{I}_z^i\hat{I}_z^j - \hat{\mathbf{I}}^i\cdot\hat{\mathbf{I}}^j)$ by rotating it –90° about $-x$.[1]* As the B_{ij}'s are just numbers, they do not need to be transformed, and as $\hat{\mathbf{I}}^i\cdot\hat{\mathbf{I}}^j$ are scalar products, rotation has no effect on them. So we only have to consider the $\hat{I}_z^i\hat{I}_z^j$ terms. Rotating $\hat{I}_z^i$ by –90° about $-x$ gives $\hat{I}_y^i$, where y refers to the rotating frame y axis. Thus, the transformed dipolar hamiltonian which describes the system in the second τ period is

$$\hat{H}(\tau\rightarrow 2\tau)_{\text{fe}} = \sum_{i>j} B_{ij}\left(3\hat{I}_y^i\hat{I}_y^j - \hat{\mathbf{I}}^i\cdot\mathbf{I}^j\right) \equiv \hat{H}_{yy} \qquad \text{(xxvi)}$$

The next pulse requires a toggling frame which is rotated by 90° about y of the original rotating frame. We have to accumulate the effects of the frame changes on the dipolar hamiltonian in the τ period which follows subsequently, so we must rotate $\hat{H}_{yy}$, the dipolar hamiltonian in the previous frame, by –90° about y, which gives $\hat{H}_{xx}$ (where x again refers to the rotating frame x axis) which has an analogous definition to $\hat{H}_{yy}$ and $\hat{H}_{zz}$.

We continue in this fashion through the entire pulse sequence and end up with the average first-order hamiltonian (first order in the hamiltonian):

$$\overline{H}^{(0)} = \frac{\hat{H}_{zz}\tau + \hat{H}_{yy}\tau + 2\hat{H}_{xx}\tau + \hat{H}_{yy}\tau + \hat{H}_{zz}\tau}{6\tau} \qquad \text{(xxvii)}$$

Now

$$\begin{aligned}\hat{H}_{xx} + \hat{H}_{yy} + \hat{H}_{zz} \\ = \sum_{i>j} B_{ij}\left\lfloor\left(3\hat{I}_x^i\hat{I}_x^j - \hat{\mathbf{I}}^i\cdot\hat{\mathbf{I}}^j\right) + \left(3\hat{I}_y^i\hat{I}_y^j - \hat{\mathbf{I}}^i\cdot\hat{\mathbf{I}}^j\right) + \left(3\hat{I}_z^i\hat{I}_z^j - \hat{\mathbf{I}}^i\cdot\hat{\mathbf{I}}^j\right)\right\rfloor \equiv 0\end{aligned} \qquad \text{(xxviii)}$$

Continued on p. 96

* Note 1 is given on page 109.

Box 2.1 *Cont.*

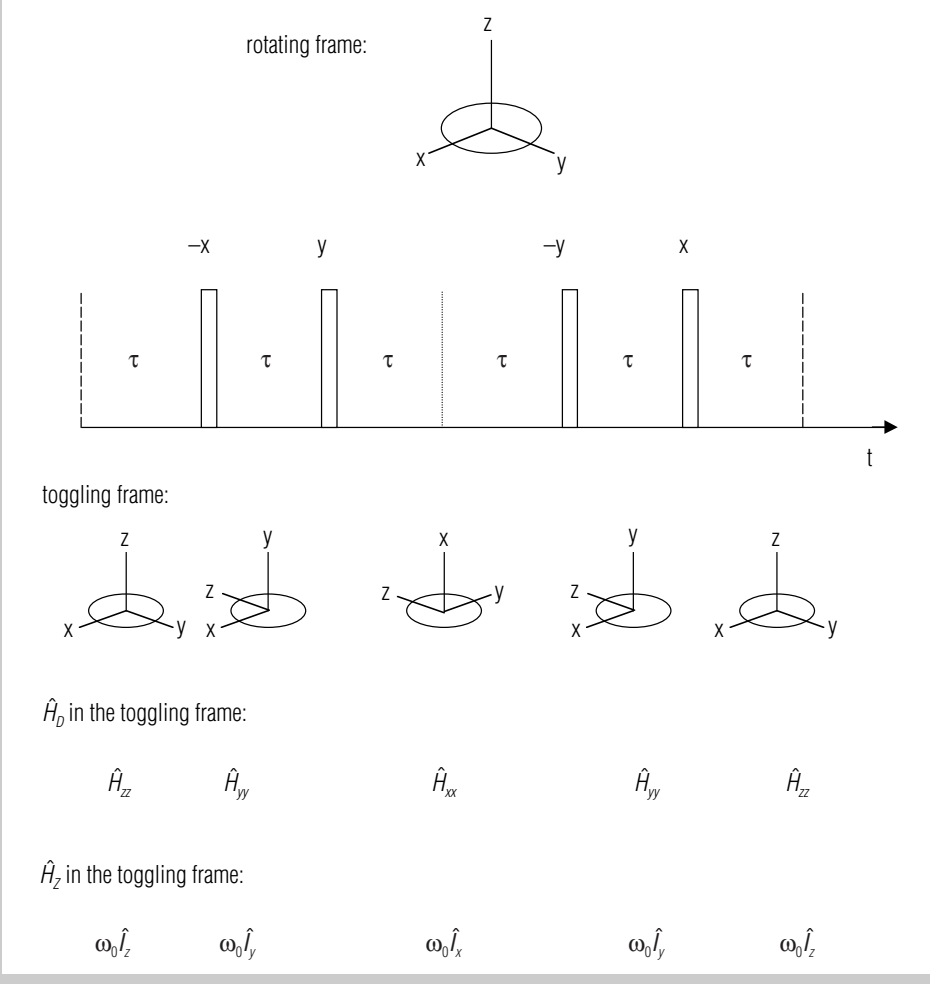

Fig. B2.1.3 The toggling frame for the WAHUHA pulse sequence. The pulse phases in the sequence are referred to the rotating frame indicated. The frame in which the homonuclear dipolar coupling is considered is the toggling frame. The toggling frame is determined by the phase of the rf pulse before each τ period. The dipolar hamiltonian $\hat{H}_{dd}$ and Zeeman hamiltonian H_z in the toggling frame are given in the diagram.

using

$$\hat{\mathbf{I}}^i \cdot \hat{\mathbf{I}}^j = \hat{I}_x^i \hat{I}_x^j + \hat{I}_y^i \hat{I}_y^j + \hat{I}_z^i \hat{I}_z^j \qquad \text{(xxix)}$$

In other words, there is no net interaction acting on the spin system at the end of the pulse sequence to first order in the dipolar coupling; the effects of the dipolar coupling have been averaged to zero to first order. Note that throughout this analysis, the toggling frame hamiltonian has been expressed in terms of

operators defined with respect to the usual rotating frame. This allows the summation of hamiltonians from different toggling frames (as in Equation (xxviii)). Furthermore, the toggling frame density operator calculated from the final average hamiltonian analysed in this way, is then expressed in terms of rotating frame operators and is therefore identical to the rotating frame density operator.

It is interesting to determine what happens to any chemical shift terms under the WAHUHA pulse sequence. The hamiltonian describing the chemical shift is the usual

$$\hat{H}_{cs} = -\omega_{cs}\hat{I}_z \qquad \text{(xxx)}$$

where ω_{cs} is the chemical shift and $\hat{I}_z = \Sigma_i \hat{I}_z^i$. Going through the same toggling frame sequence described above for the WAHUHA pulse sequence (and shown in Fig. B2.1.3), we obtain the first-order average hamiltonian for the chemical shift interaction as

$$\overline{H}_{cs}^{(0)} = -\omega_{cs}\left(\frac{\hat{I}_z\tau + \hat{I}_y\tau + 2\hat{I}_x\tau + \hat{I}_y\tau + \hat{I}_z\tau}{6\tau}\right) = -\frac{1}{3}\omega_{cs}(\hat{I}_x + \hat{I}_y + \hat{I}_z) \qquad \text{(xxxi)}$$

The chemical shift hamiltonian has the general form $-\gamma\mathbf{B}_{eff}\cdot\hat{\mathbf{I}}$ with a characteristic frequency $\omega = \gamma B_{eff}$. Comparing this with the last line of Equation (xxxi), we see that $\mathbf{B}_{eff}$ must lie in the direction (1, 1, 1) of the (x, y, z) rotating frame (in which $\hat{I}_x$, etc., are defined). The characteristic frequency ω is $(1/\sqrt{3})\omega_{cs}$ (bearing in mind that a unit vector in the direction (1, 1, 1) is in fact $(1/\sqrt{3})(1, 1, 1)$. Thus, all I-spin chemical shifts in a spectrum recorded while using WAHUHA are scaled by a factor of $1/\sqrt{3}$. Indeed, the size of any interaction linear in $\hat{I}_z$ will be scaled by this same factor, and this includes any heteronuclear dipolar couplings acting on the I-spins. All the pulse sequences designed to average away the effects of homonuclear dipolar-coupling scale chemical shifts, though the particular scaling factor depends on the particular pulse sequence. When finite length pulses are used, these change the first-order-average hamiltonian from that derived using infinitely sharp pulses, and so the scaling factor is changed. It is not always easy to predict the true scaling factor in a real multiple pulse experiment where finite length pulses are used.

2.5 Cross-polarization

Cross-polarization is usually used to assist in observing dilute spins, such as ^{13}C, though it can also be used to perform some spectral editing, and to obtain information on which spins are close in space. Observing dilute spins such as ^{13}C presents a number of problems including:

1. The low abundance of the nuclei means that the signal-to-noise ratio is inevitably poor.
2. The relaxation times of low abundance nuclei tend to be very long. This is because strong homonuclear dipolar interactions which can stimulate relaxation transitions are largely absent. Only much weaker heteronuclear dipolar interactions are present. The long relaxation times means that long gaps must be left between scans, often of the order of minutes. When several thousand scans are required to lower the noise to a suitable level, the spectra can take a very long time to collect!

Both problems can be solved with the pulse sequence in Fig. 2.9 in which the dilute nucleus, X, derives its magnetization from a nearby network of abundant spins, in this case assumed to be ^{1}H, though it can be any abundant spin-$\frac{1}{2}$ nucleus. Abundant quadrupolar nuclei can also be used although the experiment is slightly different in these cases.

2.5.1 Theory

A proper explanation of cross-polarization involves the use of average hamiltonian theory and is described in Box 2.2 below. Fortunately however, it is rarely necessary to know the details of the explanation for the everyday practice of the technique. There are, however, several important points to note, most particularly that the cross-polarization transfer is mediated by the dipolar interaction between ^{1}H and X spins. The following is a simplistic explanation of the polarization transfer, but it does serve to highlight the main important features of the experiment. It relies on a transformation of the whole problem to a *doubly rotating frame*, that is, one in which the ^{1}H spins are considered in a frame in which all the magnetic fields due to ^{1}H pulses appear static, and the X spins are considered in a frame in which all the fields due to X likewise appear static. We shall also simplify the procedure slightly by assuming that all the pulses are exactly on resonance for the spins to which they are applied.[2]

An initial ^{1}H 90°_x pulse creates ^{1}H magnetization along $-y$ in the ^{1}H rotating frame (Fig. 2.10). An on-resonance, $-y$ ^{1}H *contact pulse* is then applied. The field due to this pulse (along $-y$) is known as the *spin-lock field* and is labelled $\mathbf{B}_1(^1\mathrm{H})$. It acts on the rotating frame ^{1}H magnetization in the same way as $\mathbf{B}_0$ does in the laboratory frame on the equilibrium ^{1}H magnetization in the absence of rf pulses. Thus it acts to maintain, to some extent, the ^{1}H magnetization along $-y$. $\mathbf{B}_1(^1\mathrm{H})$ is the only field acting on the ^{1}H spins in the ^{1}H rotating frame, since we consider the contact pulse it arises from to be on resonance, so the effects of the $\mathbf{B}_0$ field vanish. $\mathbf{B}_1(^1\mathrm{H})$ thus acts as a quantization axis for the ^{1}H spins in the rotating frame during the contact pulse. We can then describe the ^{1}H spin states in the rotating frame during the pulse as α^*_H and β^*_H where α^*_H corresponds to a state with a quantized spin

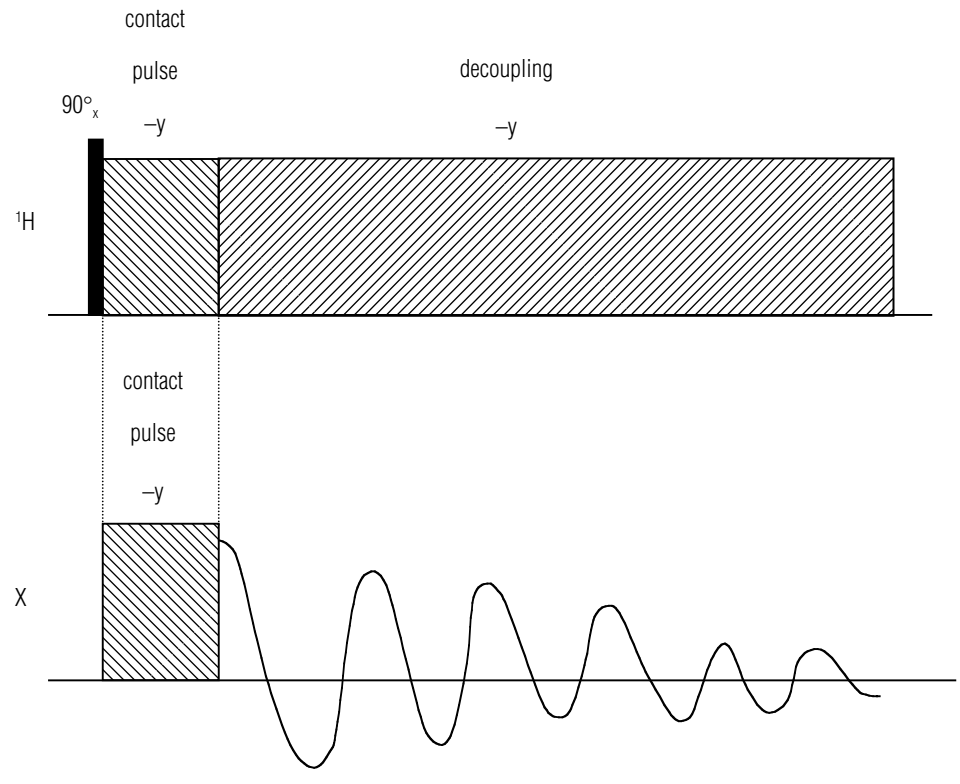

Fig. 2.9 The cross-polarization pulse sequence. The effect of the sequence is to transfer magnetization from the abundant ^{1}H spins in the sample to the X spin via the agency of the dipolar coupling between ^{1}H and X spins.

component parallel to $\mathbf{B}_1(^1\mathrm{H})$ and β^*_H corresponds to a state with a quantized spin component antiparallel to $\mathbf{B}_1(^1\mathrm{H})$. We include the primes on the spin states simply to remind us that they are rotating frame spin states.

We then consider the X spins during the simultaneous X contact pulse (with concomitant spin-lock field $\mathbf{B}_1(\mathrm{X})$) in a rotating frame rotating at the X rf pulse frequency. In a similar manner, the $\mathbf{B}_1(\mathrm{X})$ field provides the quantization axis for the X spins in the rotating frame during the X contact pulse; the X spin states in the rotating frame are α^*_X and β^*_X in analogy with the ^{1}H spin states, but defined now with respect to the $\mathbf{B}_1(\mathrm{X})$ field.

Now, the amplitudes of the two contact pulses in the cross-polarization experiment have to be carefully set so as to achieve the Hartmann–Hahn matching condition:

$$\gamma_\mathrm{H} B_1(^1\mathrm{H}) = \gamma_\mathrm{X} B_1(\mathrm{X}) \tag{2.12}$$

In this simplistic approach, this sets the energy gaps between the respective rotating frame spin states of ^{1}H and X spins to be equal. Now we need to consider the

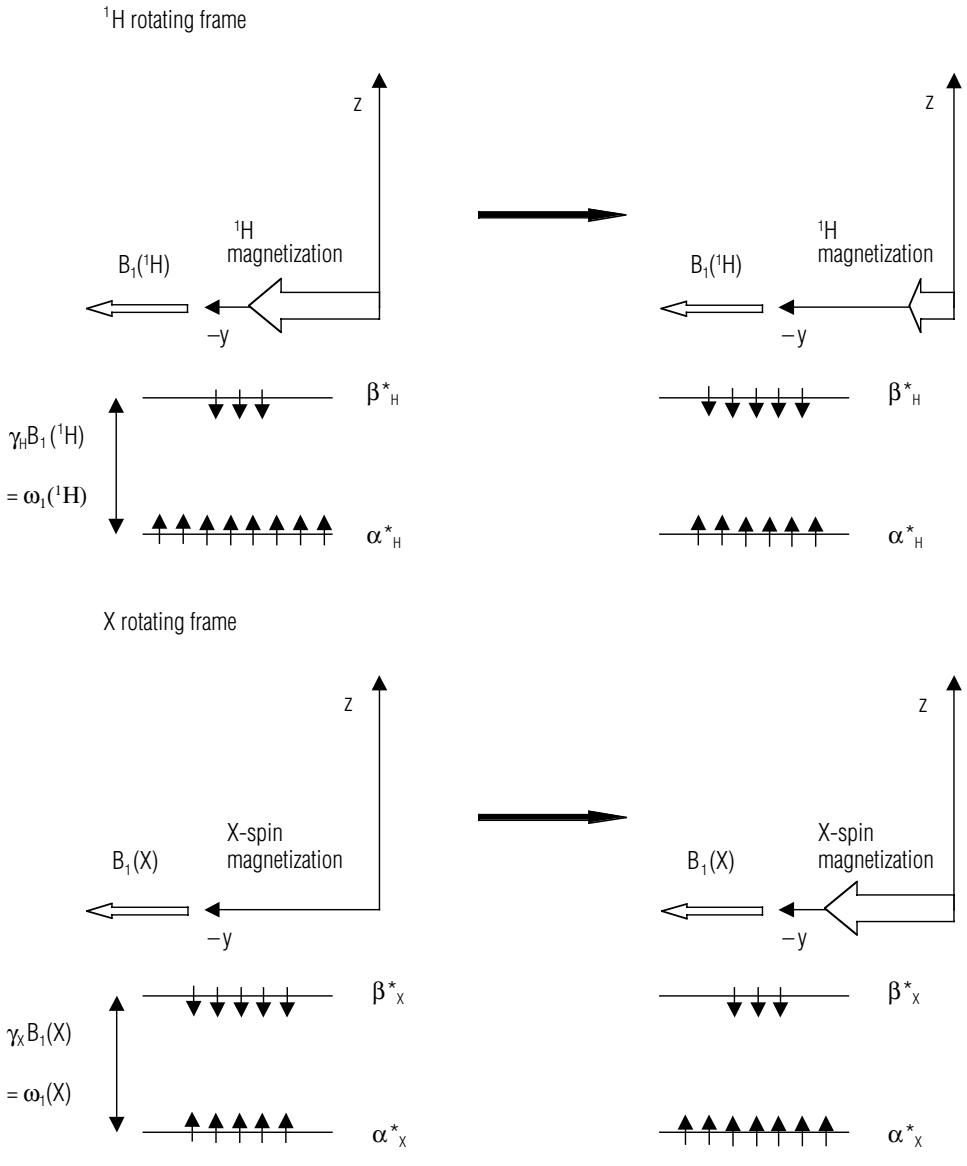

Fig. 2.10 Explanation of the cross-polarization experiment. In this experiment, ^{1}H magnetization is transferred to the X spins via the dipolar coupling between ^{1}H and X during a contact pulse applied simultaneously to both spin types after an initial 90°_x pulse to the ^{1}H spins. The figure here deals with what happens to the spins during the contact pulse. We consider a doubly rotating frame of reference such that the pulses applied to both spins appear stationary along *–y*. The pulses are on resonance for the spins they are applied to, so the only magnetic fields present in the rotating frames are those due to the respective pulses. These fields constitute the quantization axes for the spins in the rotating frame. Also shown in the figure are the spin polarizations, again in their respective rotating frames. Note that at the start of the contact pulse, there is no X-spin polarization in this frame. The α^* and β^* states are the spin states of the spins in their respective rotating frames in the absence of any other interactions. The dipolar coupling between ^{1}H and X spins depends on operators like $\hat{I}^H_{zi}\hat{I}^X_{zk}$ which act in a direction perpendicular to the quantization axes of the spins. Thus, the effects of this operator cannot change the *net* spin polarization along the quantization axes, nor can it change the net energy of the combined ^{1}H, X spin system. Thus, for every ^{1}H spin which flips, an X spin must flip in the opposite sense, but this should be a zero-energy process. When the Hartmann–Hahn condition is met, i.e. $\gamma_H B_1(^1H) = \gamma_X B_1(X)$, the energy gaps between the rotating frames ^{1}H and X spin states are the same, so the flipping process results in no net energy change as required.

effect of dipolar coupling between the ^{1}H and X spins. The dipolar-coupling operator which describes this interactions has the usual form for a heteronuclear dipolar interaction (in angular frequency units) (Section 1.4.2):

$$H_{\mathrm{HX}} = -\sum_{i>k} d_{ik} \cdot \frac{1}{2}(3\cos^2\theta_{ik} - 1) \cdot \hat{I}_{iz}^{\mathrm{H}} \hat{I}_{kz}^{X} \tag{2.13}$$

where d_{ik} is the dipolar-coupling constant for the coupling between the ith ^{1}H and kth X spin. This operator is unaffected by transformation to the doubly rotating frame, as it only contains $\hat{I}_z$ operators, which are obviously unaltered by rotations about z (of the laboratory frame). Now, in their respective rotating frames, both the ^{1}H and X spins are quantized in directions which are perpendicular to z; thus the dipole–dipole coupling operator cannot affect the net energy of the spin system in the rotating frame, as the energy of the spin system is determined by fields (and thus operators) which are parallel to the spins' quantization axes, which in turn are in the x–y plane of the rotating frame. For a similar reason, the dipole–dipole coupling operator cannot alter the net magnetization (sum of ^{1}H and X magnetizations) parallel to the quantization axis. So the dipole–dipole coupling operator, which from its form, clearly couples the ^{1}H and X spins, has to act in such a way as to conserve both the energy and the angular momentum of the total spin system. When the Hartmann–Hahn condition is met, the energy gaps between ^{1}H and X rotating frame spin states are equal, so a transition requiring energy on a ^{1}H spin for instance, can be exactly compensated by a transition releasing energy on an X spin. In these circumstances, the dipolar coupling between ^{1}H and X can allow a redistribution of energy between ^{1}H and X spins while maintaining the total energy of the system as a constant, as required. Because every transition on a ^{1}H spin is compensated for by a transition in the opposite direction on an X spin, the net magnetization of the system is also necessarily preserved, as required. The nature of the redistribution of energy in the spin system is determined by the initial distribution of spins over the rotating frame states. The initial magnitude of ^{1}H magnetization in the direction of the spin-lock field $\mathbf{B}_1(^1\mathrm{H})$ is the same as that in the laboratory frame parallel to $\mathbf{B}_0$, since it was produced by a 90° rotation of the $\mathbf{B}_0$-generated ^{1}H magnetization. It is thus too big to be sustained by the much smaller $\mathbf{B}_1(^1\mathrm{H})$ field. The ^{1}H magnetization thus reduces by $\alpha^* \rightarrow \beta^*$ rotating frame spin state transitions, while at the same time X spin $\beta^* \rightarrow \alpha^*$ transitions occur to conserve energy and lead ultimately to a large X magnetization in the direction of the $\mathbf{B}_1(\mathrm{X})$ field in the rotating frame.

The only thing this analysis does not consider explicitly is the effect of dipolar coupling between ^{1}H spins (we assume that between the rare X nuclei to be negligible, because of the unlikelihood of finding two X spins in close spatial proximity). Clearly ^{1}H–^{1}H dipolar coupling cannot be ignored and in fact acts to redistribute energy within the ^{1}H network. This has important implications in the

cross-polarization experiment, as it means that as the ^{1}H magnetization is transferred to X, the ^{1}H magnetization itself adjusts to the new circumstances.

2.5.2 Experimental details

The setting of the Hartmann–Hahn match is critical to the success of the experiment, i.e. setting the contact pulse amplitudes so that $\gamma_H B_1(^1H) = \gamma_X B_1(X)$. This is generally done by fixing the amplitude of the pulse for one of the spins, then slowly varying the amplitude of the other until a signal is seen. The phase cycling employed in the cross-polarization experiment is normally such that no signal will arise from direct excitation of the X spins, so any signal observed arises via cross-polarization from ^{1}H. The amplitudes are then adjusted until maximum signal is achieved; this should then be the Hartmann–Hahn match, although complications can arise when the experiment is conducted under magic-angle spinning (see below).

The detailed dynamics of cross-polarization are complicated. Experiment and calculations show that at very short contact times ($\tau_{contact} < d_{ij}^{-1}$ for cross-polarization between i and j), the initial cross-polarization transfer to X is from the closest ^{1}H only. As the contact time increases, the magnetization from the other ^{1}H spins redistributes and 'tops up' the closest ^{1}H so that the transfer continues. An extra complication is the fact that the spin-locked ^{1}H magnetization relaxes during the contact pulses, with a characteristic time $T_{1\rho}$. This arises because the spin-locking field is too small to support the initially large ^{1}H magnetization, and has the effect of reducing the degree of cross-polarization transfer. In simple cases, the cross-polarization dynamics can be described by [8]:

$$\frac{S(t)}{S_0} = \left(\frac{1}{1-(T_{CP}/T_{1\rho})}\right)\left[1-\exp\left(-\frac{(1-T_{CP}/T_{1\rho})t}{T_{CP}}\right)\exp\left(-\frac{t}{T_{1\rho}}\right)\right] \qquad (2.14)$$

where T_{CP} is the time constant describing the cross-polarization transfer, $S(t)$ is the signal intensity at time t and S_0 is the theoretical maximum signal. Experiments are sometimes performed with varying contact time so as to study the cross-polarization dynamics. $T_{1\rho}$ can be determined in a separate set of experiments, then allowing T_{CP} to be calculated by analysing the data according to Equation (2.14). T_{CP}, in turn, can give useful information on the ^{1}H–X spin system.

In experiments where cross-polarization is simply being used to increase signal intensity, the contact times should be varied until maximum signal intensity is achieved. For ^{1}H–^{13}C cross-polarization in organic solids, contact times of a few milliseconds are usually optimal. Generally speaking, there will be very little signal if the contact time in these cases is less than about 0.5 ms, due to lack of polarization transfer or more than around 20 ms, because of $T_{1\rho}$ relaxation. The rate of magnetization transfer in a cross-polarization experiment depends on the strength of the dipolar coupling between ^{1}H and X – the stronger the coupling, the faster the rate

of transfer. The coupling, in turn, gets stronger with shorter internuclear distances and larger γ for the nuclei concerned. Anything which disrupts the dipolar coupling, also disrupts cross-polarization transfer. So, for instance, molecular motion which averages the dipolar coupling to a smaller value reduces the rate of the cross-polarization transfer. Likewise, magic-angle spinning, which averages the dipolar to zero if it is fast enough, severely disrupts cross-polarization transfer. Variable amplitude contact pulses on one of the spins can be used to increase the cross-polarization efficiency under magic-angle spinning [**9**, **10**]. The pulse sequences using these are shown in Fig. 2.11. Related to this is the fact that magic-angle spinning with cross-polarization complicates the Hartmann–Hahn matching condition [**11**]. This is discussed in more detail in Box 2.2.

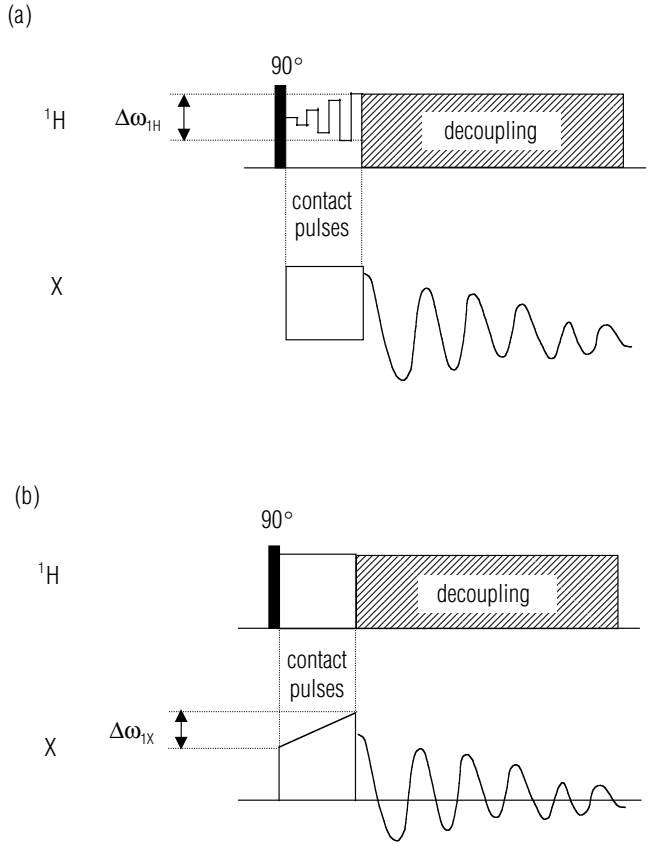

Fig. 2.11 Pulse sequences for cross-polarization under rapid magic-angle spinning. (a) Variable amplitude cross-polarization (VACP) [**9**]. The 'contact pulse' on the ^{1}H spins consists of a series of pulses of different amplitude (but same phase). There is a fixed step size in amplitude between the pulses. The overall amplitude variation, $\Delta\omega_{1H}$, is generally of the order of $2\omega_R$. (b) Ramped-amplitude cross-polarization [**10**]. The contact pulse on one of the spins (it can be either) is steadily increased in amplitude over the contact period. The size of the amplitude increase, $\Delta\omega_{1C}$, is generally of the order of ~2–3ω_R. For both experiments, the total length of the contact time is of the order of a few milliseconds; the pulse sequence parameters depend on the nature of the sample.

Box 2.2 Cross-polarization and magic-angle spinning

During the contact pulses of the cross-polarization experiment, the hamiltonian acting on the ^{1}H–X spin system is (in angular frequency units) [8]:

$$\hat{H} = \hat{H}_Z + \hat{H}_{HH} + \hat{H}_{HX} + \hat{H}^x_{pulse} \tag{i}$$

with

$$\hat{H}_Z = -\omega_0^H \hat{I}_z^H - \omega_0^X \hat{I}_z^X \tag{ii}$$

$$\hat{H}_{HH} = -\sum_{i>j} B_{ij}^{HH}\left(3\hat{I}_{iz}^H \hat{I}_{jz}^H - \hat{\mathbf{I}}_i^H \cdot \hat{\mathbf{I}}_j^H\right) \tag{iii}$$

$$\hat{H}_{HX} = -2\sum_k \sum_i B_{ik}^{HX}\left(\hat{I}_{iz}^H \hat{I}_{kz}^X\right) \tag{iv}$$

$$\hat{H}^x_{pulse} = -2\omega_1^H \hat{I}_x^H \cos\omega_0^H t - 2\omega_1^X \hat{I}_x^X \cos\omega_0^X t \tag{v}$$

and

$$B_{ij}^{HH} = \left(\frac{\mu_0}{4\pi}\right)\frac{\gamma_H^2}{\gamma_{ij}^3}\frac{1}{2}(3\cos^2\theta_{ij} - 1) \tag{vi}$$

$$B_{ik}^{HX} = \left(\frac{\mu_0}{4\pi}\right)\frac{\gamma_{1_H}\gamma_X}{r_{ik}^3}\frac{1}{2}(3\cos^2\theta_{ik} - 1) \tag{vii}$$

where $\hat{H}_Z$ represents the Zeeman terms of both ^{1}H and X spins; $\hat{H}_{HH}$ represents the dipolar coupling between the abundant ^{1}H spins and $\hat{H}_{HX}$ represents the dipolar coupling between the ^{1}H and X spins. We assume that the X spins are low in abundance so that we can ignore dipolar coupling between the X spins. $\hat{H}^x_{pulse}$ describes the effects of the contact pulse applied to each spin; these pulses are assumed to be on resonance for the spins they are applied to. The operators $\hat{I}_x^H$, $\hat{I}_x^X$, etc., are sums over the individual spins of the appropriate species, i.e.

$$\hat{I}_x^H = \sum_i \hat{I}_{ix}^H \qquad \hat{I}_x^X = \sum_k \hat{I}_{kx}^X \tag{viii}$$

ω_1^H and ω_1^X are the amplitudes of the ^{1}H and X contact pulses respectively, and ω_0^H and ω_0^X are their frequencies.

Now we perform a series of transformations to remove the effects of the contact pulses, so that we are left with a hamiltonian in some new frame which only contains terms that relate to the various dipolar couplings. It is then much easier to assess the whole cross-polarization process. A similar procedure was

adopted in the discussion of the WAHUHA pulse sequence in Box 2.1. First we transform the hamiltonian to a doubly-rotating frame, so that the frame precesses about z ($\mathbf{B}_0$) at ω_0^{H} for the ^{1}H spins and at ω_0^{X} for the X spins, the rf pulse frequencies for each spin. Mathematically, this is accomplished by the transformation

$$\hat{H}^{\mathrm{rot}} = \hat{R}_0^{-1}\hat{H}\hat{R}_0 + \omega_0^{\mathrm{H}}\hat{I}_z^{\mathrm{H}} + \omega_0^{\mathrm{X}}\hat{I}_z^{\mathrm{X}} \qquad \text{(ix)}$$

where $\hat{H}^{\mathrm{rot}}$ is the hamiltonian in the doubly rotating frame and the rotation operator $\hat{R}_0$ is given by

$$\hat{R}_0 = \exp(-i\omega_0^{\mathrm{H}}\hat{I}_z^{\mathrm{H}}t)\exp(-i\omega_0^{\mathrm{X}}\hat{I}_z^{\mathrm{X}}t)$$

In this rotation operator, the first term necessarily acts only on the ^{1}H spins and the second on the X spins. The form of Equation (ix) is found by insisting that the time-dependent Schrödinger equation (see Box 1.1 in Chapter 1) is invariant to the frame transformation, as we shall now show (a similar procedure was used in Box 2.1 earlier in this chapter).

The time-dependent Schrödinger equation is $-i(\mathrm{d}\psi/\mathrm{d}t) = \hat{H}\psi$ expressed in frequency units, where ψ is the wavefunction describing the spin system. The time-dependent Schrödinger equation in the rotating frame is invariant to the frame transformation and so is simply

$$-i\,\mathrm{d}\psi^{\mathrm{rot}}/\mathrm{d}t = \hat{H}^{\mathrm{rot}}\psi^{\mathrm{rot}} \qquad \text{(x)}$$

where all quantities are referred to the rotating frame. Under the frame transformation described by the rotation operator $\hat{R}_0$, the wavefunction ψ becomes ψ^{rot} in the rotating frame, where

$$\psi^{\mathrm{rot}} = \hat{R}_0^{-1}\psi = \exp\left(+i\omega_0^{\mathrm{H}}\hat{I}_z^{\mathrm{H}}t\right)\exp\left(+i\omega_0^{\mathrm{X}}\hat{I}_z^{\mathrm{X}}t\right)\psi \qquad \text{(xi)}$$

Thus $\mathrm{d}\psi^{\mathrm{rot}}/\mathrm{d}t$ is given by

$$\begin{aligned}\frac{\mathrm{d}\psi^{\mathrm{rot}}}{\mathrm{d}t} &= \exp\left(+i\omega_0^{\mathrm{H}}\hat{I}_z^{\mathrm{H}}t\right)\exp\left(+i\omega_0^{\mathrm{X}}\hat{I}_z^{\mathrm{X}}t\right)\frac{\mathrm{d}\psi}{\mathrm{d}t} \\ &\quad + i\omega_0^{\mathrm{X}}\hat{I}_z^{\mathrm{X}}\exp\left(+i\omega_0^{\mathrm{H}}\hat{I}_z^{\mathrm{H}}t\right)\exp\left(+i\omega_0^{\mathrm{X}}\hat{I}_z^{\mathrm{X}}t\right)\psi \\ &\quad + i\omega_0^{\mathrm{H}}\hat{I}_z^{\mathrm{H}}\exp\left(+i\omega_0^{\mathrm{H}}\hat{I}_z^{\mathrm{H}}t\right)\exp\left(+i\omega_0^{\mathrm{X}}\hat{I}_z^{\mathrm{X}}t\right)\psi \\ &= \exp\left(+i\omega_0^{\mathrm{H}}\hat{I}_z^{\mathrm{H}}t\right)\exp\left(+i\omega_0^{\mathrm{X}}\hat{I}_z^{\mathrm{X}}t\right)\frac{\mathrm{d}\psi}{\mathrm{d}t} + \left(i\omega_0^{\mathrm{X}}\hat{I}_z^{\mathrm{X}} + i\omega_0^{\mathrm{H}}\hat{I}_z^{\mathrm{H}}\right)\psi^{\mathrm{rot}} \\ &= \hat{R}_0^{-1}\frac{\mathrm{d}\psi}{\mathrm{d}t} + \left(i\omega_0^{\mathrm{X}}\hat{I}_z^{\mathrm{X}} + i\omega_0^{\mathrm{H}}\hat{I}_z^{\mathrm{H}}\right)\psi^{\mathrm{rot}} \qquad \text{(xii)}\end{aligned}$$

where all quantities are expressed with respect to the rotating frame. Substituting for $\mathrm{d}\psi^{\mathrm{rot}}/\mathrm{d}t$ gives

$$-i\left(\hat{R}_0^{-1}\frac{\mathrm{d}\psi}{\mathrm{d}t} + \left(i\omega_0^{\mathrm{X}}\hat{I}_z^{\mathrm{X}} + i\omega_0^{\mathrm{H}}\hat{I}_z^{\mathrm{H}}\right)\psi^{\mathrm{rot}}\right) = H^{\mathrm{rot}}\psi^{\mathrm{rot}} \qquad \text{(xiii)}$$

We then use the fact that $-i(\mathrm{d}\psi/\mathrm{d}t) = \hat{H}\psi$ and $\psi = \hat{R}_0\psi^{\mathrm{rot}}$ to rewrite the left-hand side of this equation as

Continued on p. 106

Box 2.2 *Cont.*

$$\hat{R}_0^{-1}\hat{H}\hat{R}_0\psi^{\text{rot}} - i\left(i\omega_0^{\text{X}}\hat{I}_z^{\text{X}} + i\omega_0^{\text{H}}\hat{I}_z^{\text{H}}\right)\psi^{\text{rot}} = \hat{H}^{\text{rot}}\psi^{\text{rot}} \tag{xiv}$$

By comparing the left- and right-hand sides of this equation, we see that $\hat{H}^{\text{rot}}$, the hamiltonian in the rotating frame, is

$$\hat{H}^{\text{rot}} = \hat{R}_0^{-1}\hat{H}\hat{R}_0 + \omega_0^{\text{X}}\hat{I}_z^{\text{X}} + \omega_0^{\text{H}}\hat{I}_z^{\text{H}} \tag{xv}$$

Substituting Equation (i) for $\hat{H}$ into Equation (xv) for the rotating frame hamiltonian, we obtain

$$\hat{H}_{\text{rot}} = \hat{H}_{\text{HH}} + \hat{H}_{\text{HX}} + \hat{H}^{x}_{\text{pulse,rot}} \tag{xvi}$$

with

$$\hat{H}^{x}_{\text{pulse,rot}} = -\omega_1^{\text{H}}\hat{I}_x^{\text{H}} - \omega_1^{\text{X}}\hat{I}_x^{\text{X}} \tag{xvii}$$

Now we transform $\hat{H}^{\text{rot}}$ further into a toggling frame as described in Box 2.1. The toggling frame, in effect, follows the effects of the contact pulses so as to null the hamiltonians describing them. As shown in Box 2.1, the toggling frame which nulls the terms in the rotating frame hamiltonian due to ^{1}H and X pulses is one which rotates the ^{1}H spins' frame of reference about the x-axis (the direction of the ^{1}H contact pulse) at rate ω_1^{H} and the X spin frame of reference about x at rate ω_1^{X}. This transforms $\hat{H}^{\text{rot}}$ into $\hat{H}^*$ in a similar manner to the rotating frame transformation described previously:

$$\hat{H}^*(t) = \hat{R}_1^{-1}\hat{H}^{\text{rot}}\hat{R}_1 + \omega_1^{\text{H}}\hat{I}_x^{\text{H}} + \omega_1^{\text{X}}\hat{I}_x^{\text{X}} \tag{xviii}$$

with $\hat{R}_1 = \exp(-i\omega_1^{\text{H}}\hat{I}_x^{\text{H}}t)\exp(-i\omega_1^{\text{X}}\hat{I}_x^{\text{X}}t)$, the rotation operator required to transform to the toggling frame (cf. $\hat{R}_0$ above). The resulting toggling frame hamiltonian $\hat{H}^*(t)$ is

$$\hat{H}^*(t) = \hat{H}^*_{\text{HH}} + \hat{H}^*_{\text{HX}} \tag{xix}$$

where

$$\hat{H}^*_{\text{HH}} = -\frac{1}{2}\sum_{i>j} B_{ij}^{\text{HH}}\left(\hat{\mathbf{I}}_i^{\text{H}}\cdot\hat{\mathbf{I}}_j^{\text{H}} - 3\hat{I}_{ix}^{\text{H}}\hat{I}_{jx}^{\text{H}}\right) \tag{xx}$$

$$\hat{H}^{*}_{\mathrm{HX}} = -\frac{3}{2}\sum_{k}\sum_{i} B^{\mathrm{HX}}_{ik}\left[\left(\hat{I}^{\mathrm{H}}_{iz}\hat{I}^{\mathrm{X}}_{kz} + \hat{I}^{\mathrm{H}}_{iy}\hat{I}^{\mathrm{X}}_{ky}\right)\cos(\omega^{\mathrm{H}}_{1} - \omega^{\mathrm{X}}_{1})t + \left(\hat{I}^{\mathrm{H}}_{iz}\hat{I}^{\mathrm{X}}_{ky} + \hat{I}^{\mathrm{H}}_{iy}\hat{I}^{\mathrm{X}}_{kz}\right)\sin(\omega^{\mathrm{H}}_{1} - \omega^{\mathrm{X}}_{1})t\right] \qquad \text{(xxi)}$$

The expression for $\hat{H}^{*}(t)$ in Equation (xix) ignores any terms which are non-secular or which oscillate at ω^{H}_{1} or ω^{X}_{1}, as these are assumed to average to zero over the time of the contact pulses. $\hat{H}^{*}_{\mathrm{HH}}$ only affects the ^{1}H spins and is a constant. When $\omega^{\mathrm{H}}_{1} \neq \omega^{\mathrm{X}}_{1}$, the term $\hat{H}^{*}_{\mathrm{HX}}$ has little effect on the spin system as it contains oscillating terms which average to zero over the contact pulse. However, when $\omega^{\mathrm{H}}_{1} \cong \omega^{\mathrm{X}}_{1}$ (the Hartmann–Hahn match), the oscillating terms (largely) disappear and $\hat{H}^{*}_{\mathrm{HX}}$ becomes important in causing a double resonance effect between the ^{1}H and X spins. In particular, the $\hat{I}^{\mathrm{H}}_{iy}\hat{I}^{\mathrm{X}}_{ky}$ term contains terms of the form $\hat{I}^{\mathrm{H}}_{i+}\hat{I}^{\mathrm{X}}_{k-}$ and $\hat{I}^{\mathrm{H}}_{i-}\hat{I}^{\mathrm{X}}_{k+}$ which cause magnetization transfer between the ^{1}H and X spins. It is important to appreciate that these terms arise ultimately from the $\hat{I}^{\mathrm{H}}_{iz}\hat{I}^{\mathrm{X}}_{kz}$ term in the ^{1}H–X dipolar-coupling hamiltonian, the *A*-type terms, and not the *B*-type terms as is often mistakenly thought.

Now we must consider the effect of magic-angle spinning on the experiment. Magic-angle spinning has the effect of introducing time-dependence into the dipolar coupling. This appears in the toggling frame (or other frame) hamiltonian via the B^{HH}_{ij} and B^{HX}_{ik} terms which contain the geometric terms describing the dipolar coupling between ^{1}H spins and between ^{1}H and X spins respectively. Section 2.2.1 describes magic-angle spinning and the time-dependence it induces in nuclear spin interactions. In essence, the strength of an interaction under magic-angle spinning is described by terms which oscillate at $\pm\omega_{\mathrm{R}}$ and $\pm 2\omega_{\mathrm{R}}$, where ω_{R} is the spinning rate. For dipolar coupling, there is no isotropic (constant) term which remains under magic-angle spinning (though there is for the chemical shift). It is the $\hat{H}^{*}_{\mathrm{HX}}$ term which induces cross-polarization between the ^{1}H and X spins. However, under magic-angle spinning the B^{HX}_{ik} terms in $\hat{H}^{*}_{\mathrm{HX}}$ are no longer constant, but oscillate at $\pm\omega_{\mathrm{R}}$ and $\pm 2\omega_{\mathrm{R}}$. This means that at the normal Hartmann–Hahn match, $\omega^{\mathrm{H}}_{1} \cong \omega^{\mathrm{X}}_{1}$, the net cross-polarization term in the hamiltonian averages to zero, or at least a small value, over the time of the contact pulse [**11**]. However, $\hat{H}^{*}_{\mathrm{HX}}$ contains other oscillatory terms; $\cos(\omega^{\mathrm{H}}_{1} - \omega^{\mathrm{X}}_{1})t$ and $\sin(\omega^{\mathrm{H}}_{1} - \omega^{\mathrm{X}}_{1})t$. The net oscillatory behaviour of the $\hat{H}^{*}_{\mathrm{HX}}$ term under magic-angle spinning can be cancelled by matching $(\omega^{\mathrm{H}}_{1} - \omega^{\mathrm{X}}_{1})$ to $\pm\omega_{\mathrm{R}}$ or $\pm 2\omega_{\mathrm{R}}$.

Thus the match condition under magic-angle spinning is $(\omega^{\mathrm{H}}_{1} - \omega^{\mathrm{X}}_{1}) = \pm\omega_{\mathrm{R}}$ or $\pm 2\omega_{\mathrm{R}}$, the so-called *sideband match conditions*. Cross-polarization intensity is found at the normal Hartmann–Hahn match, $(\omega^{\mathrm{H}}_{1} - \omega^{\mathrm{X}}_{1}) = 0$, but, as explained above, this decreases as the spinning speed is increased and the dipole coupling is more effectively averaged.

2.6 Solid or quadrupole echo pulse sequence

Broad lines, such as those arising from chemical shift anisotropy, dipolar coupling, etc., have rapidly decaying FIDs. 'Ringing' in the coil which is used to measure the FID, prevents measurement of the signal until a short time (the *dead time*) after a pulse. This delay means that a significant part of the rapidly decaying FID is not recorded.

This loss leads to severely distorted lineshapes after Fourier transformation in the case where the FID decays rapidly, i.e. the NMR resonances are broad. The effect is small in solution NMR, since there the FID signals decay much more slowly, so the proportion of the total FID lost in the dead time is only very small. In solid-state NMR, the problem is overcome by use of the spin-echo pulse sequence

$$90^\circ_x\text{–}\tau\text{–}180^\circ_y\text{–}\tau\text{–}\textit{acquire}$$

for lines broadened by chemical shift anisotropy or heteronuclear dipole–dipole coupling, i.e. for any interaction linear in the observed spin operators, and the *solid-* or *quadrupole-echo pulse sequence:*

$$90^\circ_x\text{–}\tau\text{–}90^\circ_y\text{–}\tau\text{–}\textit{acquire}$$

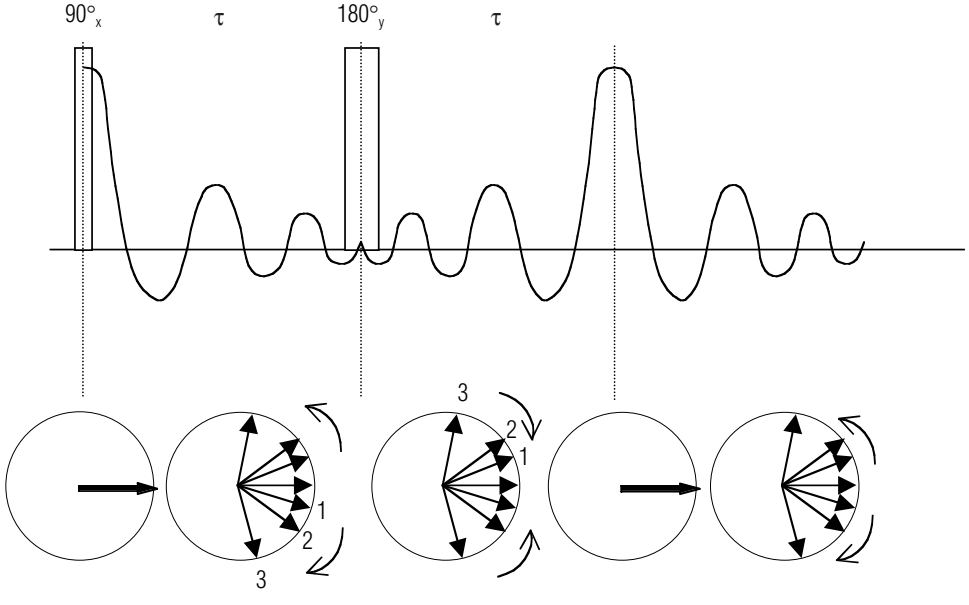

Fig. 2.12 The spin–echo pulse sequence. The behaviour of the transverse magnetization components is shown. Magnetization components dephase under the effects of chemical shift anisotropy or heteronuclear dipolar coupling during the first τ period. The subsequent 180° pulse rotates the magnetization components 180° about the pulse axis (*y* in this case) so that the components refocus after a further τ period. The τ delay is chosen to be long enough to include the dead time for the probe. Then the FID can be completely recorded from the true echo maximum. If the FID were simply recorded after a single 90° pulse, a significant part of the FID would be lost due to the dead time required before recording can begin.

for lines broadened by quadrupole coupling or homonuclear dipole–dipole coupling, i.e. any interaction bilinear in the observed spin operators.

This latter pulse sequence operates in a similar fashion to the spin-echo pulse sequence (Fig. 2.12) in that it refocuses the dispersing transverse magnetization components a time τ after the refocusing pulse. Note that the refocusing pulse in the solid-echo pulse sequence is a 90° pulse rather than the 180° pulse in the spin-echo sequence. Using the above sequence, acquisition of the FID signal necessarily begins at time τ after the last pulse in the sequence, and hence, no signal is lost due to a dead time delay.

In more complicated pulse sequences which generate broad lines, an 'echo' sequence, τ–180°–τ– or τ–90°–τ– as appropriate, is often added to the end of the sequence to circumvent dead time problems. It should be noted that if the experiment is being recorded with magic-angle spinning, then the echo delay τ should be an integral number of rotor periods, as the sample spinning induces rotor echoes (see Section 2.2.2) which refocus every rotor period.

Notes

1. The advantage of rotating the hamiltonian operator rather than transforming its frame of reference is that we end up with an operator that is expressed with respect to the original rotating frame. When we come to sum operators expressed with respect to different toggling frames (for instance, when forming the first-order component of the average hamiltonian), this is a distinct advantage. In essence, we are expressing the dipolar hamiltonian in a toggling frame in terms of operators defined with respect to the rotating frame.
2. Transformation to a singly rotating frame in the quantum mechanical picture was discussed in Section 1.3. The transformation to a doubly rotating frame required here is achieved in a similar manner to that used in Section 1.2. Now however, the wavefunction describing the spin system is transformed by $\Psi' = \exp(i\omega_{1_H} \hat{I}_{Hz} t)\ \exp(i\omega_X \hat{I}_{Xz} t)\Psi$, where ω_{1_H} and ω_X are the frequencies of the ^{1}H and X rf pulses respectively; $\hat{I}_{Hz}$ and $\hat{I}_{Xz}$ are sums of $\hat{I}_z$ operators over the ^{1}H and X spins respectively, and only operate on these spins respectively. Hence, it appears as though the ^{1}H spins are in a frame which rotates at the ^{1}H Larmor frequency, while the X spins rotate in one which rotates at their Larmor frequency.

References

1. M.M. Maricq and J.S. Waugh, *J. Chem. Phys.* **70** (1979) 3300.
2. J. Herzfeld and A.E. Berger, *J. Chem. Phys.* **73** (1980) 6021.
3. W.T. Dixon, *J. Chem. Phys.* **77** (1982) 1800.
4. O.N. Antzutkin, Z. Song, X. Feng and M.H. Levitt, *J. Chem. Phys.* **100** (1994) 130.
5. U. Haeberlen and J.S. Waugh, *Phys. Rev.* **175** (1968) 453.
6. W.-K. Rhim, D.D. Elleman and R.W. Vaughan, *J. Chem. Phys.* **59** (1973) 3740.
7. D.P. Burum and W.-K. Rhim, *J. Chem. Phys.* **71** (1979) 944.

8. S.R. Hartmann and E.L. Hahn, *Phys. Rev.* **128** (1962) 2042.
9. O.B. Peersen, X. Wu, I. Kustanovich and S.O. Smith, *J. Magn. Reson.* **A104** (1993) 334.
10. G. Metz, X. Wu and S.O. Smith, *J. Magn. Reson.* **A110** (1994) 219.
11. E.O. Stejskal, J. Schaefer and J.S. Waugh, *J. Magn. Reson.* **28** (1977) 105.

Solid-State NMR Spectroscopy Principles and Applications
Edited by Melinda J. Duer
Copyright © 2002 by Blackwell Science Ltd

Chapter 3
Dipolar Coupling: Its Measurement and Uses

Melinda J. Duer

3.1 Introduction

The essential elements of dipolar coupling were introduced in Chapter 1. There it was shown that the hamiltonian describing the magnetic dipolar coupling between pairs of homonuclear, or like nuclear spins could be truncated to

$$\hat{H}_{\mathrm{dd}} = -\sum_{i>j} C_{ij}\left(3\hat{I}_z^i\hat{I}_z^j - \hat{\mathbf{I}}^i\cdot\hat{\mathbf{I}}^j\right) \tag{3.1}$$

where $\hat{H}_{\mathrm{dd}}$ is expressed in units of angular frequency (rad s^{-1}) or, alternatively,

$$\begin{aligned}\hat{H}_{\mathrm{dd}} &= -2\sum_{i>j} C_{ij}\left[\hat{I}_z^i\hat{I}_z^j - \frac{1}{2}\left(\hat{I}_x^i\hat{I}_x^j + \hat{I}_y^i\hat{I}_y^j\right)\right] \\ &= -2\sum_{i>j} C_{ij}\left[\underbrace{\hat{I}_z^i\hat{I}_z^j}_{\text{Term A}} - \frac{1}{4}\left(\hat{I}_+^i\hat{I}_-^j + \underbrace{\hat{I}_-^i\hat{I}_+^j}_{\text{Term B}}\right)\right]\end{aligned} \tag{3.2}$$

where:

$$C_{ij} = \left(\frac{\mu_0}{4\pi}\right)\frac{\gamma_i\gamma_j}{r_{ij}^3}\hbar\cdot\frac{1}{2}\left(3\cos^2\theta_{ij} - 1\right) \tag{3.3}$$

where r_{ij} is the distance between the i and j spins and θ_{ij} is the angle between the internuclear axis and the applied field, $\mathbf{B}_0$ (Fig. 3.1). For heteronuclear spins, the hamiltonian is truncated still further to

$$\hat{H}_{\mathrm{dd}} = -2\sum_{i>j} C_{ij}\hat{I}_z^i\hat{I}_z^j \tag{3.4}$$

The dipolar-coupling hamiltonian is often described using spherical tensor operators, rather than the Cartesian spin operators of Equations (3.1), (3.2) and (3.4). This manner of describing the dipolar-coupling interaction is detailed in Box 3.1.

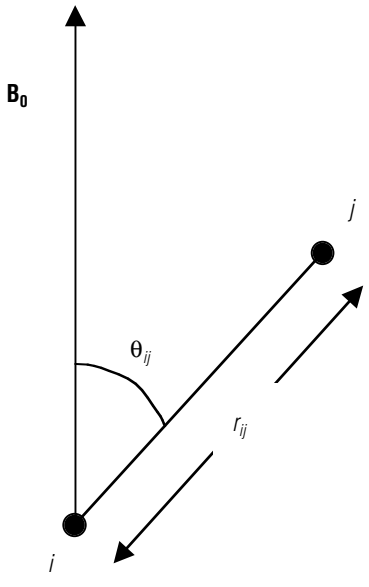

Fig. 3.1 The dipolar interaction between two spins *i* and *j*. The strength of the interaction depends upon the geometry of the spin pair in the applied magnetic field, as defined by the internuclear distance, r_{ij} and the angle between the internuclear axis and the applied magnetic field $\mathbf{B}_0$, θ_{ij}.

The dipolar-coupling interaction can cause huge linebroadening as described in Chapter 1; even where it is not huge, it still causes significant loss of resolution. Thus to the spectroscopist, dipolar coupling is often more of a problem than anything else. Chapter 2 deals with schemes for removing the effects of both homonuclear and heteronuclear dipolar coupling from NMR spectra. However, to the chemist and material scientist, dipolar coupling probably represents the single most important spin interaction, and one which we would very much like to be able to measure. This is because of the direct dependence of its magnitude on the distance, r_{ij}, between the two spins *i* and *j*. The dipolar coupling is then the one spin interaction which can provide a means of determining internuclear distances and from these, the geometry and conformation of molecules. Of course, this sort of structure determination is the traditional domain of diffraction techniques. However, there are many types of material which do not lend themselves readily to diffraction techniques. Many compounds of interest – for instance, biopolymers such as proteins – have an inherent degree of disorder and so do not form single crystals. Thus, any diffraction study can only produce rather limited information. This is not to say that there are not clear structural features in such materials; most have well-defined secondary and tertiary structures, albeit along with some molecular degrees of freedom which confer a dynamic disorder on the overall structure. Other important materials, such as zeolites, are highly crystalline, but only form microcrystals, too small for single crystal diffraction studies. So-called amorphous materials always have some structure, despite their name, but the lack of regular repeating units (translational symmetry) means that, once again, diffraction techniques have only limited use. Nevertheless, it is possible to pick out common structural units in most such materials. Moreover, a knowledge

Box 3.1 The dipolar hamiltonian in terms of spherical tensor operators

The dipolar hamiltonian consists of a so-called *spin part*, consisting of spin operators and a *spatial part* which consists of geometrical functions describing the crystallite-orientation dependence of the strength of the interaction. All nuclear spin interactions can be broken down in this way. In this box, we show how the spin part of the dipolar hamiltonian can be written in terms of entities called *spherical tensor operators* [**1**, **2**] and the space part in terms of *spherical tensor functions*. We then use this representation of the dipolar-coupling hamiltonian to derive the form of the hamiltonian under magic-angle spinning.

Spherical tensor operators

In this book, we have for the most part expressed hamiltonians and density operators in terms of the Cartesian spin operators, $\hat{I}_x$, $\hat{I}_y$, $\hat{I}_z$, etc. and products of these. Conceptually, these certainly provide a convenient way of describing spin interactions. However, we do not *have* to express spin hamiltonians and spin density operators in this way; there are other sets of operators that we might use equally well, and spherical tensor operators are one such set. Where we use these and where we use Cartesian operators is largely a matter of choice, but it is certainly true to say that for every situation, one set of operators will prove more convenient than another. Spherical tensor operators have specific symmetry properties with respect to rotations in three-dimensional space, and this makes their manipulation under such rotations much more straightforward than, for instance, that of products of Cartesian spin operators [**1**, **2**]. Furthermore, we have seen elsewhere in this book how analysis of pulse sequences involves the use of a toggling frame, which in turn necessitates the rotation of the hamiltonian operator currently appropriate to the spin system. Clearly, in these circumstances, spherical tensor operators are likely to be a more convenient basis set for writing the hamiltonian than are other possible basis sets.

So-called *irreducible spherical tensor operators* transform according to the irreducible representations of the three-dimensional rotation point group [**1**, **2**], also called the full rotation point group. An irreducible tensor operator is labelled in the following by $\hat{T}_{kq}$, where k is the *rank* of the operator. For a given k, there are $2k + 1$ different irreducible tensor operators, each with a different *order*, q; the possible values of q are k, $k - 1, \ldots, -k$. The set of $\{\hat{T}_{kk}, \hat{T}_{kk-1}, \ldots, \hat{T}_{k-k}\}$, i.e. irreducible tensor operators for a given k, transform under rotations like the kth irreducible representation of the full rotation point group. The q can

Continued on p. 114

Box 3.1 *Cont.*

therefore be thought of as designating different components of a set. It is this feature which makes these *tensor* operators. A useful analogy can be drawn between irreducible spherical tensor operators and atomic orbitals. Atomic orbitals also transform like the irreducible representations of the full rotation group, though clearly atomic orbitals are functions rather than operators. An *s*-orbital for instance has the same symmetry as the $\hat{T}_{00}$ irreducible operator, i.e. operator with $k = 0$ and (therefore) $q = 0$. A set of *p*-orbitals, i.e. three of them, transform like the set of operators with rank 1, i.e. $\hat{T}_{11}$, $\hat{T}_{10}$, $\hat{T}_{1-1}$.

A specific symmetry property of irreducible tensor operators is that, under a rotation, their rank does not change. This can be seen in the analogy with atomic orbitals; if you rotate a *p*-orbital, the result is another *p*-orbital, or more generally a linear combination of *p*-orbitals. Under a rotation of the axis frame in which the tensor is defined, from $(x^{\text{old}}, y^{\text{old}}, z^{\text{old}})$ to $(x^{\text{new}}, y^{\text{new}}, z^{\text{new}})$, the $\hat{T}_{kq}$ tensor operators transform as follows:

$$\begin{aligned}\hat{T}_{kq}(\text{new}) &= \hat{R}^{-1}(\alpha, \beta, \gamma)\hat{T}_{kq}(\text{old})R(\alpha, \beta, \gamma) \\ &= \sum_{q'} \hat{T}_{kq'}(\text{old})D^{k}_{q'q}(\alpha, \beta, \gamma) \qquad \text{(i)}\end{aligned}$$

where $\hat{T}_{kq}$ (new) is the tensor element in the new frame, and $\hat{T}_{kq}$ (old) the tensor element in the old frame. $\hat{R}(\alpha, \beta, \gamma)$ is the rotation operator described in Box 1.2, Chapter 1 and (α, β, γ) are the Euler angles which rotate the old frame $(x^{\text{old}}, y^{\text{old}}, z^{\text{old}})$ into the new frame $(x^{\text{new}}, y^{\text{new}}, z^{\text{new}})$, i.e. rotation of a frame initially coincident with $(x^{\text{old}}, y^{\text{old}}, z^{\text{old}})$ by γ about z^{old}, followed by rotation of β about y^{old}, then rotation by α about z^{old} takes this frame into $(x^{\text{new}}, y^{\text{new}}, z^{\text{new}})$. The $D^{k}_{q'q}(\alpha, \beta, \gamma)$ are elements of a matrix, the *Wigner rotation matrix* [**1**, **2**], which can be decomposed into

$$D^{k}_{q'q}(\alpha,\beta,\gamma) = \exp(-i\alpha q')\exp(-i\gamma q)\mathrm{d}^{k}_{q'q}(\beta) \qquad \text{(ii)}$$

where $\mathrm{d}^{k}_{q'q}(\beta)$ is a *reduced Wigner function*.

So, in essence, rotating the axis frame about any axis simply transforms an irreducible tensor operator into a linear combination of irreducible tensor operators of the same rank.

Using this rotation property, we can find linear combinations of Cartesian spin operators and products of spin operators which behave as irreducible tensor operators of different ranks k and orders q. For instance, if we use only single spin operators

$\hat{T}_{00} = \dfrac{1}{\sqrt{2}}$ i.e. a scalar

$$\hat{T}_{10} = \sqrt{2}\hat{I}_z \qquad \hat{T}_{1\pm1} = \mp(\hat{I}_x \pm i\hat{I}_y)$$
$$\hat{T}_{20} = \sqrt{\frac{2}{3}}(3\hat{I}_z^2 - \hat{\mathbf{I}}\cdot\hat{\mathbf{I}}) \qquad \hat{T}_{2\pm1} = \mp(\hat{I}_\pm\hat{I}_z + \hat{I}_z\hat{I}_\pm) \qquad \hat{T}_{2\pm2} = \hat{I}_\pm^2 \tag{iii}$$

are the appropriate combinations of spin operators. If we have spin operators associated with two spins available, i.e. $\hat{I}_{1x}$, $\hat{I}_{1y}$, $\hat{I}_{1z}$ and $\hat{I}_{2x}$, $\hat{I}_{2y}$, $\hat{I}_{2z}$, then we can generate more irreducible tensor operators:

$$\hat{T}_{00}^{(12)} = -\frac{2}{\sqrt{3}}\left(\hat{I}_{1z}\hat{I}_{2z} + \frac{1}{2}(\hat{I}_{1+}\hat{I}_{2-} + \hat{I}_{1-}\hat{I}_{2+})\right)$$
$$\hat{T}_{10}^{(12)} = \frac{1}{\sqrt{2}}(\hat{I}_{1-}\hat{I}_{2+} - \hat{I}_{1+}\hat{I}_{2-}) \qquad \hat{T}_{1\pm1}^{(12)} = (-\hat{I}_{1\pm}\hat{I}_{2z} + \hat{I}_{1z}\hat{I}_{2\pm}) \tag{iv}$$
$$\hat{T}_{20}^{(12)} = \sqrt{\frac{2}{3}}(3\hat{I}_{1z}\hat{I}_{2z} - \hat{\mathbf{I}}_1\cdot\hat{\mathbf{I}}_2) \qquad \hat{T}_{2\pm1}^{(12)} = \mp(\hat{I}_{1\pm}\hat{I}_{2z} + \hat{I}_{1z}\hat{I}_{2\pm}) \qquad \hat{T}_{2\pm2}^{(12)} = \hat{I}_{1\pm}\hat{I}_{2\pm}$$

where the (12) superscripts on the tensor operators simply show which spins are involved in each.

Interaction tensors

In Chapter 1, we introduced the idea that nuclear spin interactions, such as dipolar coupling, could be expressed in terms of Cartesian tensors, $\mathbf{D}^{ij}$ in the case of dipolar coupling, which expressed the orientation dependence of the interaction. We can equally well describe the orientation dependence of spin interactions in terms of *spherical tensors*. Note here that we are talking about tensors whose components are numbers or functions rather than operators as above. There is a link between these two, however, which is that both spherical tensor operators and the spherical tensors describing the orientation dependence of spin interactions transform as irreducible representations of the spherical point group. Before we can usefully write the dipolar hamiltonian in terms of spherical tensor operators, we will need to express the orientation dependence of the dipolar interaction in terms of spherical tensor components also.

The transformation of spherical tensors under axis frame rotations are, not surprisingly, described in the same way as for tensor operators above, i.e. under a rotation of the axis frame described by Euler angles (α, β, γ), a numerical spherical tensor component Λ_{lm}, becomes

$$\hat{R}^{-1}(\alpha,\beta,\gamma)\Lambda_{lm}\hat{R}(\alpha,\beta,\gamma) = \sum_{m'}\Lambda_{lm'}D^l_{m'm}(\alpha,\beta,\gamma) \tag{v}$$

where the $D^l_{m'm}(\alpha, \beta, \gamma)$ are once again elements of a Wigner rotation matrix. The effect of rotating the defining axis frame on a Cartesian tensor, such as the dipolar tensor $\mathbf{D}^{ij}$, is described in Box 1.2, Chapter 1.

Continued on p. 116

Box 3.1 *Cont.*

The homonuclear dipolar hamiltonian under static and MAS conditions

In Chapter 1 we stated that spin interaction hamiltonians could always be written in the form

$$\hat{H}_{\text{int}} = \hat{\mathbf{I}} \cdot \mathbf{A}_{\text{loc}} \cdot \hat{\mathbf{J}} \tag{vi}$$

where $\mathbf{A}_{\text{loc}}$ is a second-rank Cartesian tensor which describes the strength and orientation dependence of the local spin interaction, and $\hat{\mathbf{J}}$ is a vector operator, whose exact nature depends on the particular spin interaction. For dipolar coupling between two spins, I and S, the hamiltonian expressed in this form is

$$\hat{H}_{\text{dd}} = -2\hbar\hat{\mathbf{I}} \cdot \mathbf{D} \cdot \hat{\mathbf{S}} \tag{vii}$$

The Cartesian tensor **D** contains the information on the spatial dependence of the interaction. Now, it can be shown (though not here) that an equation of the form of Equation (vi) or (vii) is equivalent to the scalar product of a spherical tensor operator (replacing the spin operators in Equations (vi) and (vii)) and a spherical tensor function, replacing the Cartesian tensor [**3**], i.e.

$$\hat{H}_{\text{int}} = \hat{\mathbf{I}} \cdot \mathbf{A}_{\text{loc}} \cdot \hat{\mathbf{J}} \equiv -\sum_{k=0}^{2} \sum_{q=-k}^{+k} (-1)^q \Lambda_{k-q} \hat{T}_{kq} \tag{viii}$$

where Λ_{k-q} is a component of a spherical tensor and $\hat{T}_{kq}$ is a component of a spherical tensor operator. The combination of a $+q$ component of Λ and $-q$ component of $\hat{T}_k$ in Equation (viii) ensures that the result of the product is a scalar, as it must be since the hamiltonian operator is itself a scalar operator (as it is the operator for energy, which is a scalar quantity). The summation over k goes up to $k = 2$ which takes account of the fact that Equations (vi) and (vii) are *bilinear* in Cartesian vector operators; a glance at Equation (iv) shows that the $k = 2$ operators also have this form. We now seek to find an expression of this form for the homonuclear dipolar hamiltonian.

The homonuclear dipolar hamiltonian in *Cartesian* form in the laboratory frame of reference (z parallel to $\mathbf{B}_0$) is

$$\hat{H}_{\text{dd}} = -\sum_{i>j} C_{ij} \left(3\hat{I}_z^i \hat{I}_z^j - \hat{\mathbf{I}}^i \cdot \hat{\mathbf{I}}^j\right) \tag{ix}$$

for a static, i.e. non-spinning, sample. The spin part of this hamiltonian can clearly be identified with the spherical tensor operator, $\hat{T}_{20}^{ij}$. Thus the summation in Equation (viii) reduces to a single term with $k = 2$ and $q = 0$,

$$\hat{H}_{\mathrm{dd}} = -\sum_{i>j} \Lambda_{20}^{ij} \hat{T}_{20}^{ij} \tag{x}$$

where Λ_{20}^{ij} can be found by comparing Equations (ix) and (x) to be

$$\Lambda_{20}^{ij} = C_{ij} = d_{ij} \cdot \frac{1}{2}(3\cos^2\theta_{ij} - 1) \tag{xi}$$

in which θ_{ij} is the angle between the dipolar tensor principal z axis (z^{PAF}) and the laboratory frame z axis (parallel to $\mathbf{B}_0$). The ij superscipt on the spherical tensor component Λ_{20} simply designates the particular spin pair. d_{ij} is the dipolar coupling constant for the ij spin pair. The tensor operator $\hat{T}_{20}^{ij}$ is defined in Equation (iv) in terms of Cartesian spin operators defined with respect to the laboratory frame.

We can equally well derive Λ_{20}^{ij} from the dipolar-coupling tensor in spherical tensor form expressed in its principal axis frame. The dipolar-coupling tensor in its principal axis frame (PAF) for a spin pair ij, is denoted λ^{ij} in spherical tensor form. The PAF is simply the axis frame in which the dipolar-coupling tensor is diagonal; this depends on molecular structure. The only non-zero component of λ^{ij} is in fact $\lambda_{20}^{ij} = \sqrt{\frac{3}{2}} d_{ij}$ so that the dipolar-coupling hamiltonian when the molecular orientation is such that the dipolar-coupling principal axis frame coincides with the laboratory frame, i.e. internuclear axis of the dipolar-coupled spin pair (z^{PAF}) is parallel to $\mathbf{B}_0$ (z in the laboratory frame), is

$$\hat{H}_{\mathrm{dd}}^{\mathrm{PAF}} = -\sum_{i>j} \lambda_{20}^{ij} \hat{T}_{20}^{ij} = -d_{ij}\left(3\hat{I}_z^i \hat{I}_z^j - \hat{\mathbf{I}}^i \cdot \hat{\mathbf{I}}^j\right) \tag{xii}$$

as it should be. Of course in general, the PAF does not coincide with the laboratory frame. It is fixed to the molecule, and so varies with molecular orientation. Different PAF orientations with respect to the laboratory frame (see Fig. B3.1.1) reflect different strengths of dipolar coupling for different molecular orientations. More generally, the PAF will be oriented by the Euler angles (α, β, γ) with respect to the laboratory frame, where (α, β, γ) are the Euler angles which rotate the PAF into the laboratory frame. To find the strength of dipolar coupling for some arbitrary orientation of the PAF (i.e. arbitrary molecular orientation), we need to express the dipolar-coupling tensor $\boldsymbol{\lambda}^{ij}$ in the laboratory frame, where we label it $\boldsymbol{\Lambda}^{ij}$.

The dipolar-coupling tensor in the laboratory and PAF frames is related via (see Equation (v))

Continued on p. 118

Box 3.1 *Cont.*

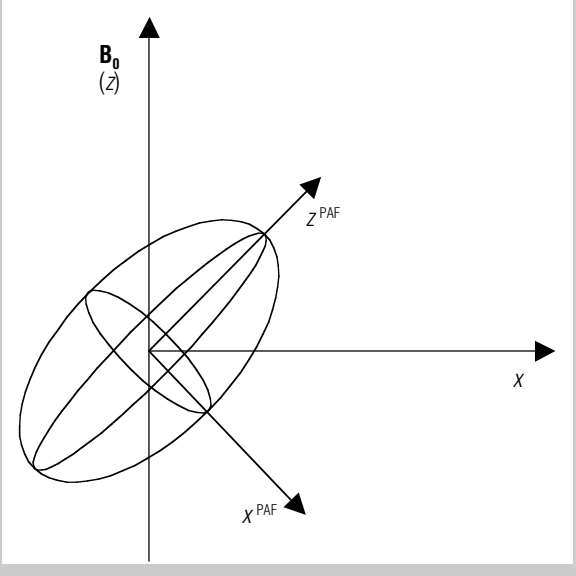

Fig. B3.1.1 The relationship between the laboratory frame (*x*, *y*, *z*) and dipolar-coupling tensor principal axis frame (PAF). The applied field $\mathbf{B}_0$ defines the *z* axis of the laboratory frame. The dipolar-coupling tensor PAF *z* axis is defined by the internuclear axis of the dipolar-coupled spin pair. The tensor is represented in this diagram by an ellipsoid whose principal axes are in the directions of the PAF; the radius of the ellipsoid in the direction of $\mathbf{B}_0$ is proportional to the strength of dipolar coupling for that orientation of PAF.

$$\Lambda^{ij}_{2m} = \sum_{m'=-2}^{+2} D^2_{m'm}(\alpha, \beta, \gamma)\lambda^{ij}_{2m'} = D^2_{0m}(\alpha, \beta, \gamma)\lambda^{ij}_{20} \qquad \text{(xiii)}$$

where we have used the fact that λ^{ij}_{20} is the only non-zero component of λ^{ij} and where $D^2_{0m}(\alpha, \beta, \gamma)$ is a Wigner rotation matrix element, defined in Equation (ii). For the truncated dipolar hamiltonian of Equation (x), we are only interested in the Λ^{ij}_{20} component. The other components of Λ^{ij} are only relevant for the higher-order terms in the dipolar-coupling hamiltonian (see Section 1.4.2 for details of these higher-order terms). So we have for Λ^{ij}_{20} from Equation (xiii)

$$\Lambda^{ij}_{20} = D^2_{00}(\alpha, \beta, \gamma)\lambda^{ij}_{20} = \frac{1}{2}(3\cos^2\beta - 1)\lambda^{ij}_{20} \qquad \text{(xiv)}$$

where we have substituted for the Wigner rotation matrix element $D^2_{00}(\alpha, \beta, \gamma)$ in the last line of Equation (xiv).

We now need to consider the effects of magic-angle spinning. To do this, we need to describe an extra axis frame, the rotor frame, which we designate (x^R, y^R, z^R). This frame is fixed to the rotor. A molecule inside the rotor changes its orientation as the rotor spins, and so the orientation of the PAFs associated with all spins in that molecule also change. As in the static case, we need to express the dipolar-coupling tensor in the laboratory frame to find the strength of dipolar coupling for different PAF orientations. In the case of magic-angle spinning, we do this in two steps, first finding the dipolar-coupling tensor with respect to the

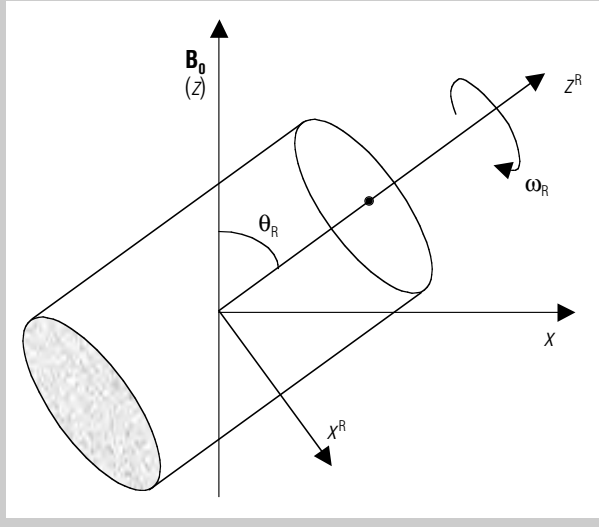

Fig. B3.1.2 The relationship between the laboratory frame and the rotor frame (R). The applied field $\mathbf{B}_0$ defines the *z* axis of the laboratory frame. The rotor frame is fixed to the rotor and so spins with it under magic-angle spinning. θ_R is the angle between the rotor spinning axis and $\mathbf{B}_0$; ω_R is the spinning rate. Thus the rotor turns through an angle $\omega_R t$ after a time *t*. The rotor frame is shown at time $t = 0$.

rotor axis frame and then relating the tensor in that frame to the laboratory frame. The PAF remains fixed in orientation relative to the rotor-fixed frame; the Euler angles (α, β, γ) now relate the PAF to the rotor frame, *R*. The dipolar-coupling tensor in the rotor frame, $\mathbf{\Lambda}^{ij}(R)$, is then given by an equation of the same form as Equation (xiii) previously, i.e.

$$\Lambda^{ij}_{2m}(R) = \sum_{m'=-2}^{+2} D^2_{m'm}(\alpha, \beta, \gamma)\lambda^{ij}_{2m'} \qquad \text{(xv)}$$

where λ^{ij} is the dipolar-coupling tensor in its PAF as before.

The dipolar tensor in the laboratory frame, $\mathbf{\Lambda}^{ij}(\text{lab})$ is then found from $\Lambda^{ij}(R)$ in a similar manner:

$$\begin{aligned}\Lambda^{ij}_{2m}(\text{lab}) &= \sum_{m'=-2}^{+2} D^2_{m'm}(-\omega_R t, \theta_R, 0)\Lambda^{ij}_{2m'}(R) \\ &= \sum_{m'=-2}^{+2} D^2_{m'm}(-\omega_R t, \theta_R, 0)D^2_{0m'}(\alpha, \beta, \gamma)\lambda^{ij}_{20} \qquad \text{(xvi)}\end{aligned}$$

where the rotor frame is related to the laboratory frame by the Euler angles $(-\omega_R t, \theta_R, 0)$ when the rotor has been spinning at angle θ_R, and rate ω_R for time *t* and where the *y* axes of the rotor and laboratory frame are parallel at time $t = 0$ (see Fig. B3.1.2). In the last line of Equation (xvi), we have used the fact that λ^{ij}_{20} is the only non-zero component of λ^{ij}, the dipolar tensor in its PAF.

We require the $\Lambda^{ij}_{20}(\text{lab})$ component of the laboratory frame dipolar-coupling tensor for the truncated dipolar hamiltonian of Equation (x). From Equation (xvi), this is given by

Continued on p. 120

Box 3.1 *Cont.*

$$\Lambda_{20}^{ij}(\text{lab}) = \sum_{m=-2}^{+2} D_{m0}^{2}(-\omega_R t, \theta_R, 0) D_{0m}^{2}(\alpha, \beta, \gamma) \lambda_{20}^{ij} \tag{xvii}$$

Expanding the Wigner rotation matrix elements (Equation (ii)) relating the rotor to the laboratory frame in this expression then gives

$$\begin{aligned} \Lambda_{20}^{ij}(\text{lab}) &= \sum_{m=-2}^{+2} \exp(im\omega_R t) d_{m0}^{2}(\theta_R) D_{0m}^{2}(\alpha, \beta, \gamma) \lambda_{20}^{ij} \\ &= \sum_{m=-2}^{+2} \exp(im\omega_R t) \omega_{ij}^{(m)} \end{aligned} \tag{xviii}$$

where

$$\omega_{ij}^{(m)} = \sum_{m=-2}^{+2} d_{m0}^{2}(\theta_R) D_{0m}^{2}(\alpha, \beta, \gamma) \lambda_{20}^{ij} \tag{xix}$$

Thus the homonuclear dipolar hamiltonian under magic-angle spinning in spherical tensor form is

$$\hat{H}_{dd}(t) = -\sum_{i>j} \hat{T}_{20}^{ij} \sum_{m=-2}^{+2} \exp(im\omega_R t) \omega_{ij}^{(m)} \tag{xx}$$

of these structural units is essential to our understanding of the material's physical properties. Solid-state NMR gives the hope of structural information on all these types of material, via measurement of dipolar couplings.

A more qualitative use for dipolar coupling is in correlation spectroscopy (Fig. 3.2). Techniques such as COSY are common in solution-state NMR, where the scalar or J coupling is used to determine which spins are linked by chemical bonds. A two-dimensional COSY spectrum showing a signal at (f_1, f_2) in the two-dimensional plane, indicates that the spins giving rise to the signals at f_1 and f_2 are close together in the bonding network of the molecule under study. In solid-state NMR, dipolar coupling between spins can be used in a similar way to indicate which spins are close in space.

Another use of dipolar coupling is in spin counting, which is the determination of the number of spins in close proximity (Fig. 3.3). As shown in Chapter 1 (Box 1.3), in a homonuclear, many-spin system, the eigenstates (or coupled spin states) of the system are described by the total nuclear spin in the laboratory z direction, M

$$M = m_1 + m_2 + m_3 + \ldots + m_N \tag{3.5}$$

where N is the number of coupled spins and m_i is the spin state of spin i. Remembering that the strength of dipolar coupling drops off as $1/r^3$, only those spins in close

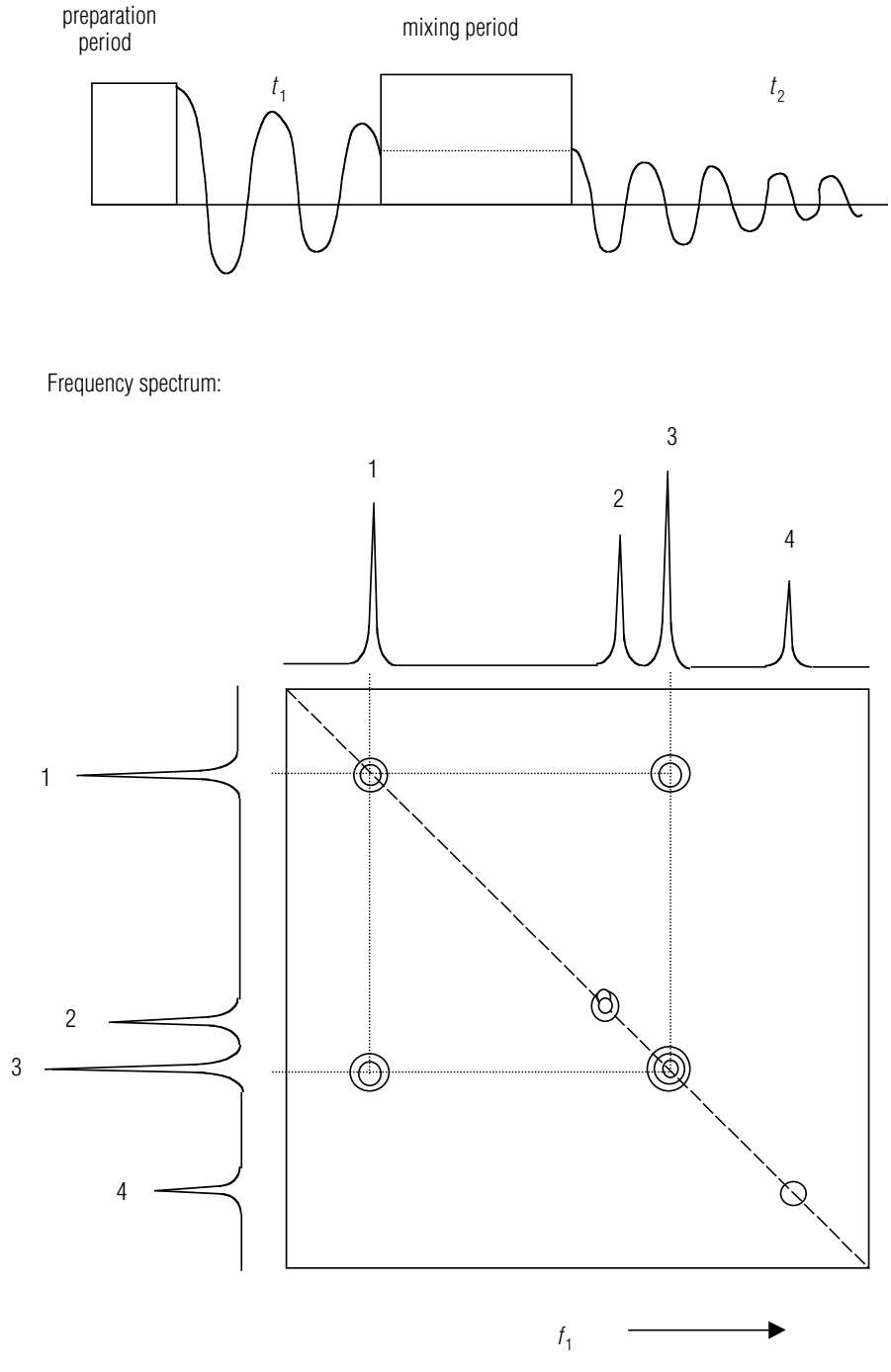

Fig. 3.2 The form of a homonuclear correlation experiment and spectrum. In the experiment, spins are allowed to evolve at their characteristic frequency during t_1 and t_2. During the mixing period between t_1 and t_2 magnetization is transferred between spins via the dipolar coupling or scalar coupling between them. A two-dimensional dataset is collected as a function of t_1 and t_2. Two-dimensional Fourier transformation of this time domain dataset then produces a two-dimensional frequency spectrum, with frequency axes labelled f_1 and f_2 (corresponding to the t_1 and t_2 time domain axes, respectively). Signals along the $f_1 = f_2$ diagonal are *autocorrelation* peaks and arise from magnetization that did not transfer between spins during the mixing period (as well as possibly magnetization that transferred between like spins). This particular two-dimensional spectrum shows an off-diagonal peak between signals from spins 1 and 3, which in turn shows that magnetization has transferred between spins 1 and 3 during the mixing period. If the mixing period relied on dipolar-coupling effects for magnetization transfer, then this demonstrates that these spins are close in space. If the mixing period relied on the scalar or *J* coupling, then 1 and 3 are close together in the bonding network.

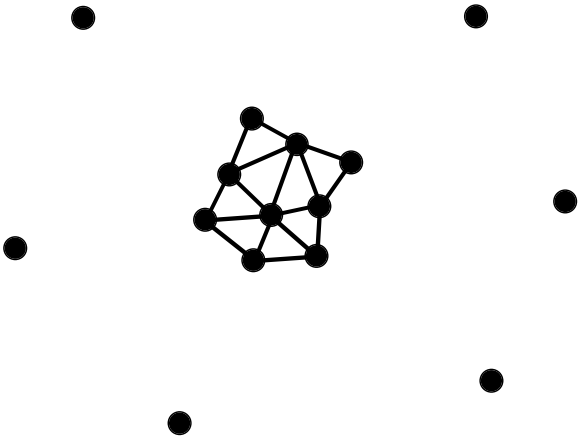

Fig. 3.3 Illustrating the concept of a *spin cluster*. Spins in close proximity are all dipole-coupled together. The states describing such a spin system are product spin states involving all N spins in the cluster and are characterized by a quantum number representing the total nuclear spin in the laboratory z direction, M, where M is given by $M = m_1 + m_2 + \ldots + m_N$, i.e. the sum of the components provided by the N individual spins.

proximity will contribute to the coupled spin state. N is thus the number of spins in close proximity, or in a cluster. There are many M states for a given cluster of N spins, and multiple-quantum coherences of order ΔM can be excited between them, where $\Delta M = M_a - M_b$ with a and b denoting the M states involved in the coherence. The maximum order of coherence which can be excited for a given spin cluster is N for a spin-$\frac{1}{2}$ system (since the minimum M is $-\frac{1}{2} + -\frac{1}{2} + \ldots + -\frac{1}{2} = -\frac{1}{2}N$ and maximum M is $\frac{1}{2} + \frac{1}{2} + \ldots + \frac{1}{2} = \frac{1}{2}N$) and this gives a means of measuring N by investigating the orders of coherence which can be excited and their relative amplitudes.

In this chapter, we first discuss how to measure dipolar couplings for both homonuclear and heteronuclear spin-$\frac{1}{2}$ and quadrupolar spin systems. In any NMR experiment, one of the first requirements is that of resolution. In a system where there are dipolar couplings, the requirements of resolution generally means removing the effects of these couplings, which otherwise cause a high degree of linebroadening. However, this defeats the object of an experiment designed to measure those same couplings. The ingenuity of spectroscopists in devising experiments to measure dipolar couplings has been in dealing with these two somewhat contrary features.

3.2 Techniques for measuring homonuclear dipolar couplings

3.2.1 Recoupling pulse sequences

As already highlighted, a primary requirement for any NMR experiment is to produce sufficient resolution to separate signals from different chemical sites. The linebroadening caused by dipolar coupling generally prevents this, and so its effects need to be removed from any part of the NMR experiment requiring high resolution. Magic-angle spinning is one of the simplest and most effective ways of removing the effects of dipolar coupling (see Chapter 2), and has the added bonus of also

removing the effects of chemical shift anisotropy. Having effectively removed the dipolar coupling with magic-angle spinning, it can then be reintroduced for selected periods of the experiment by carefully designed pulse sequences, known as *recoupling sequences*.

In practice, dipolar couplings are measured using such pulse sequences as part of a two-dimensional experiment (Fig. 3.4). After initial excitation of transverse magnetization, a recoupling sequence is applied synchronously with the sample spinning in t_1. Thus, t_1 must be an integral number of rotor periods. An FID is then recorded as usual in t_2. Appropriate processing of the two-dimensional time domain data (recorded as a function of t_1 and t_2) then results in a two-dimensional frequency spectrum, with a high resolution, magic-angle spinning spectrum in f_2 correlated in f_1 with spectra which represent the homonuclear dipolar coupling associated with each of the sites represented in the f_2 spectrum. For powder samples, the spectra in f_1 are generally some sort of powder pattern, though different from the powder patterns that would be expected in a conventional one-dimensional spectrum for a static sample.

The dipolar-coupling constants $\left(d_{ij} = \left(\frac{\mu_0}{4\pi}\right)\frac{\gamma_i\gamma_j}{r_{ij}^3}\hbar\right)$ associated with each f_1 lineshape are extracted by simulating the f_1 lineshapes for different d_{ij} until good agreement with the experimental lineshapes in achieved. Often, the t_1 time domain datasets are simulated rather than the frequency domain powder patterns; the two processes are equivalent. Recoupling pulse sequences generally reintroduce *all* the homonuclear dipolar couplings associated with the irradiated spin type; clearly if more than two or three spins are coupled together, the corresponding spectra in f_1 are likely to be rather broad and featureless lineshapes which cannot be simulated unambiguously. Accordingly, these types of experiment are generally carried out on samples in which there are discrete spin pairs, often arranged through site-specific isotopic labelling of, e.g., ^{13}C.

The first dipolar-recoupling pulse sequence was the DRAMA (Dipolar Recovery at the Magic Angle) sequence, invented by Tycko and Dabbagh [**4**]. This sequence is shown in Fig. 3.5 and consists of two 90° pulses symmetrically placed in each

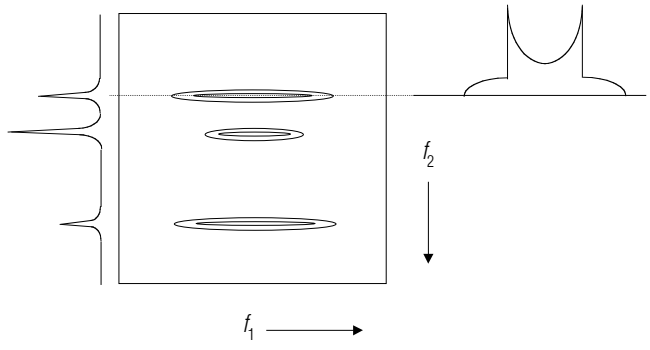

Fig. 3.4 A schematic illustration of the two-dimensional experiments used to measure homonuclear dipolar couplings. The experiment separates a high-resolution spectrum of isotropic chemical shifts in the f_2 spectral dimension from powder patterns representing the dipolar-coupling interaction for each resolved site, in the f_1 spectral dimension.

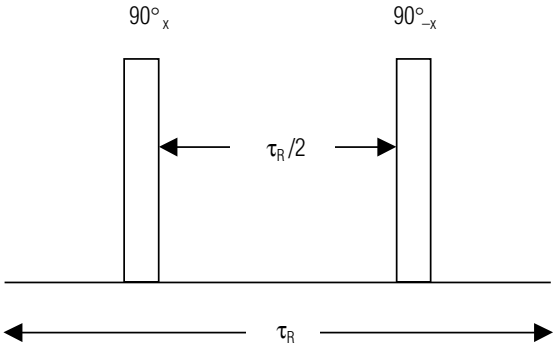

Fig. 3.5 The DRAMA (Dipolar Recovery at the Magic-Angle) pulse sequence [**4**]. This pulse sequence has the effect of preventing the averaging to zero of homonuclear dipolar-coupling interactions under magic-angle spinning. The two 90° pulses are placed symmetrically within each rotor period (τ_R) for which dipolar evolution is required.

(a)

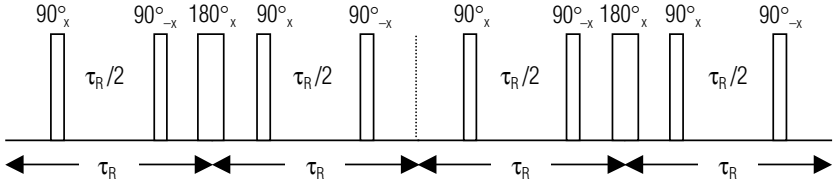

(b)

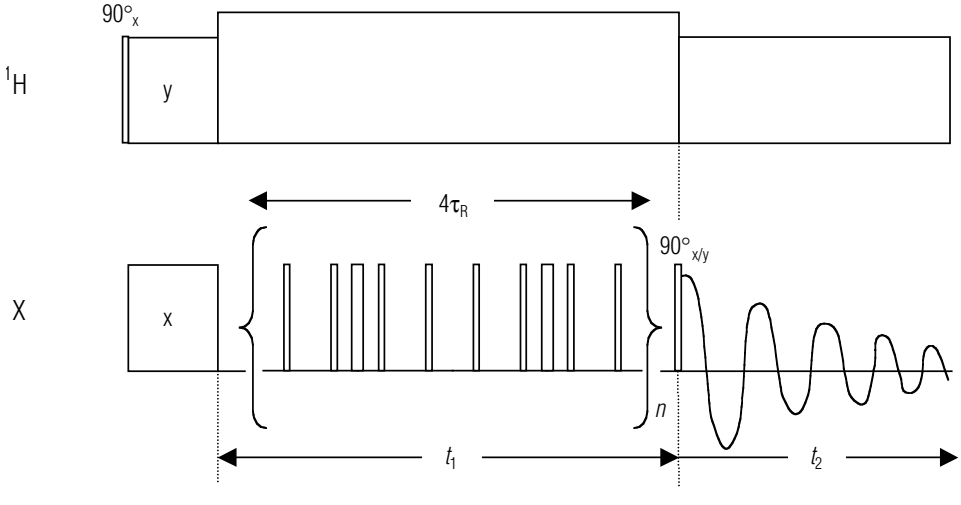

Fig. 3.6 (a) The modified form of the DRAMA pulse sequence which refocuses chemical shift anisotropies, while still preventing the averaging to zero of homonuclear dipolar couplings. (b) The two-dimensional NMR experiment which is used with the DRAMA sequence to obtain dipolar powder patterns for the X nucleus in f_1, correlated with a high-resolution magic-angle spinning spectrum in f_2. In this particular pulse sequence, cross-polarization from ^{1}H is used to generate the initial X transverse magnetization. The sequence in (a) then runs during t_1 of the experiment for $4n$ rotor cycles (τ_R). The ^{1}H decoupling power is increased during t_1 so that the ^{1}H and X rf powers no longer satisfy the Hartmann–Hahn condition; this ensures that ^{1}H-X dipolar is effective decoupling.

rotor period. Analysis of this pulse sequence requires the use of average hamiltonian theory and a toggling frame of reference as described in Box 3.2 below. This pulse sequence, like most other dipolar-recoupling sequences, has the effect of also reintroducing any chemical shift anisotropy associated with the observed spins. This would give rise to powder lineshapes in f_1 which were determined by both the chemical shift anisotropy and dipolar coupling, and would complicate their analysis. Accordingly, the DRAMA sequence is usually used in the modified form [**4**] in Fig. 3.6, where the addition of 180° pulses in every second rotor period has the effect of refocusing chemical shift anisotropy and isotropic chemical shift offsets during the period of the pulse sequence in t_1. However, since the 180° pulses are rather sparse, high spinning frequencies (>5 kHz) are recommended for a better performance of DRAMA. Even so, DRAMA performs badly for ^{31}P systems for instance, because of the large chemical shift anisotropies associated with ^{31}P sites, which have a substantial effect on the spin evolution between the DRAMA 90° pulses.

In practice, two datasets are recorded, one using the pulse sequence in Fig. 3.6 with a $90°_x$ pulse at the end, and the other with a $90°_y$ pulse at the end. Dataset 1 then is modulated by the x component of the transverse magnetization present in t_1, while dataset 2 is modulated by the y component, i.e. the x and y components of the t_1 magnetization are effectively recorded in separate experiments. This then allows pure absorption lineshapes to be obtained in the final two-dimensional frequency spectrum, if the processing scheme in Fig. 3.7 is followed. Similar processing can be applied to experiments employing other recoupling pulse sequences, but note that the final Fourier transformation in t_1 is often omitted, and the t_1 data is simulated rather than the Fourier transformed f_1 spectra.

Recoupling pulse sequences need to be robust to large chemical shift anisotropies, isotropic chemical shift offsets, chemical shift differences between recoupled spins and rf inhomogeneities. Large chemical shift anisotropies and offsets mean that the spins to be recoupled can have quite different frequencies, which is a problem in itself. However, an equally important problem arises in this situation if polycrystalline samples are being examined, as it means that the full chemical shift range of the sample is large, and so the recoupling sequence must be effective over this whole range. This is often referred to as the recoupling sequence needing a large bandwidth. Since the DRAMA experiment first appeared in the literature, many other sequences have been designed to perform better in one respect or another. The DRAMA pulse sequence is not robust to large chemical shift anisotropies and offsets; however, both features have been addressed in new pulse sequences based on the DRAMA experiment [**5**, **6**]. The MELODRAMA experiment [**7**] is a reasonably robust sequence that uses rotor-synchronized spin-locking to recouple homonuclear dipolar coupling. The RFDR (Radio-Frequency Driven Recoupling) experiment [**8**] uses one 180° pulse per rotor period, and shows efficient recoupling for a wide range of chemical shift offsets.

Box 3.2 Analysis of the DRAMA pulse sequence

This analysis of the DRAMA pulse sequence aims to show that this pulse sequence does indeed prevent the averaging to zero of the dipolar coupling by magic-angle spinning. It employs average hamiltonian theory and use of a toggling frame of reference for the hamiltonian describing the spin system and, accordingly, follows a similar path to the analysis of the WAHUHA pulse sequence in Box 2.1, chapter 2. The reader is referred to this earlier section for details concerning the operation of average hamiltonian theory and the toggling frame.

We refer to the basic DRAMA pulse sequence [**4**] in Fig. 3.5 and assume that the pulse amplitude is sufficiently large that all other interactions may be ignored during the pulse. We further assume that chemical shift offsets are zero in order to simplify the analysis, but still retain its salient features. The hamiltonian in the rotating frame during the pulses is then simply that due to the pulse,

$$\hat{H}_{\text{pulse}} = -\omega_1 \hat{I}_x \tag{i}$$

for an x pulse for instance, where ω_1 is the rf amplitude. During periods of free precession between the pulses, we assume that the only spin interaction present is homonuclear dipolar coupling. We restrict ourselves to considering a spin system consisting of a single pair of spins as this leads to no loss of generality. The hamiltonian during the periods of free precession between the rf pulses (in the rotating frame) is then simply

$$\hat{H}_{\text{dd}} = -C_{ij}(t)\left(3\hat{I}_z^i\hat{I}_z^j - \hat{\mathbf{I}}^i \cdot \hat{\mathbf{I}}^j\right) \equiv \hat{H}_{zz}(t) \tag{ii}$$

where $C_{ij}(t)$ is the strength of the dipolar coupling interaction, time-dependent due to magic-angle spinning. The form of $C_{ij}(t)$ is discussed later.

We then form the average hamiltonian over one rotor period, all subsequent rotor periods in the pulse train in Fig. 3.5 being effectively identical. As discussed in Box 2.1, Chapter 2, the average hamiltonian over a period of time t_{p} is given by a sum of contributions

$$\overline{H}(t_{\text{p}}) = \overline{H}^{(0)} + \overline{H}^{(1)} + \overline{H}^{(2)} + \ldots \tag{iii}$$

where the successive terms are given by

$$\overline{H}^{(0)} = \frac{1}{t_{\text{p}}}\left\{\hat{H}_1 t_1 + \hat{H}_2 t_2 + \ldots + \hat{H}_n t_n\right\}$$

$$\overline{H}^{(1)} = -\frac{i}{2t_p}\{[\hat{H}_2 t_2, \hat{H}_1 t_1] + [\hat{H}_3 t_3, \hat{H}_1 t_1] + [\hat{H}_2 t_2, \hat{H}_3 t_3] + \dots\}$$

$$\overline{H}^{(2)} = -\frac{1}{6t_p}\Big\{[\hat{H}_3 t_3, [\hat{H}_2 t_2, \hat{H}_1 t_1]] + [[\hat{H}_3 t_3, \hat{H}_2 t_2], \hat{H}_1 t_1] + \frac{1}{2}[\hat{H}_2 t_2, [\hat{H}_2 t_2, \hat{H}_1 t_1]] + \frac{1}{2}[[\hat{H}_2 t_2, \hat{H}_1 t_1], \hat{H}_1 t_1] + \dots\Big\} \quad \text{(iv)}$$

in which $\hat{H}_i$ is the hamiltonian describing the interactions in the spin system during the time period t_i. Now, as explained in Box 2.1, the pulse hamiltonian (Equation (i)) and dipolar hamiltonian (Equation (ii)) do not commute with each other. In other words, hamiltonians $\hat{H}_i$ at different time periods t_i in the rotor period in the DRAMA pulse sequence do not commute with each other, so the higher-order terms in the average hamiltonian, $\overline{H}^{(1)}$, $\overline{H}^{(2)}$, etc. are decidedly non-zero and may contribute significantly to the average hamiltonian. This makes the average hamiltonian tricky to calculate. To get around this, at the point of each pulse in the sequence, we transform the hamiltonian to a new frame, the so-called *toggling frame*, in which the pulse term in the hamiltonian vanishes. Then the hamiltonians describing the spin system throughout the rotor period all commute with one another, so that the $\overline{H}^{(0)}$ term of Equation (iii) alone is a good approximation to the average hamiltonian.[1]* A hamiltonian described in the toggling frame is said to be in the *interaction representation*. The act of performing these frame transformations takes account of the rf pulse effects as far as the density operator is concerned, i.e. if we calculate the density operator in the toggling frame at any point, we obtain the density operator with the effects of the rf pulses included, as shown in Box 2.1.

During the period of free precession which follows a pulse, the spin system simply evolves under the dipolar-coupling hamiltonian expressed in the current toggling frame. Thus, during the first $\tau_R/4$ period of the pulse sequence, the system evolves according to the usual rotating frame[2] hamiltonian for dipolar coupling between spins I^i and I^j

$$\hat{H}(0 \rightarrow \tau_R/4) = -C_{ij}(t)(3\hat{I}_z^i\hat{I}_z^j - \hat{\mathbf{I}}^i \cdot \hat{\mathbf{I}}^j) \equiv \hat{H}_{zz}(t) \quad \text{(v)}$$

The first $90°_x$ pulse of the DRAMA sequence then requires us to transform to a new toggling frame which is one rotated by –90° about the rotating frame x axis from the original (rotating) frame. This frame transformation has taken account of the rf pulse as far as the density operator is concerned. The dipolar hamiltonian in this new frame is equivalent to the original dipolar hamiltonian rotated by + 90° about the same axis and leaving the axis frame unchanged (see Box 1.2 in Chapter 1 for a detailed discussion of this). The advantage of rotating the

Continued on p. 128

* Notes are given on p. 177.

Box 3.2 *Cont.*

hamiltonian rather than the axis frame in which it is defined is that the transformed hamiltonian is expressed in terms of rotating frame spin operators. When we come to sum hamiltonians expressed in different toggling frames, it is much easier if they are all in terms of spin operators defined in a single frame. The rotated dipolar hamiltonian in this case is:

$$\hat{H}(\tau_R/4 \rightarrow 3\tau_R/4) = -C_{ij}(t)\left(3\hat{I}_y^i\hat{I}_y^j - \hat{\mathbf{I}}^i \cdot \hat{\mathbf{I}}^j\right) \equiv \hat{H}_{yy}(t) \qquad \text{(vi)}$$

where y refers to the rotating frame spin operators. At the next $90°_{-x}$ pulse, we transform to another toggling frame, which is rotated from the previous toggling frame by $-90°$, this time about the rotating frame $-x$ axis. The effect on the dipolar hamiltonian $\hat{H}_{yy}(t)$ is equivalent to a $+90°$ rotation of this operator about the rotating frame $-x$ axis. This produces

$$\hat{H}(3\tau_R/4 \rightarrow \tau_R) = -C_{ij}(t)\left(3\hat{I}_z^i\hat{I}_z^j - \hat{\mathbf{I}}^i \cdot \hat{\mathbf{I}}^j\right) \equiv \hat{H}_{zz}(t) \qquad \text{(vii)}$$

where again z refers to rotating frame spin operators. The average hamiltonian $\overline{H}$ over the rotor period is then found by summing the hamiltonians which describe the spin system at the various points through the pulse sequence. The hamiltonians due to the pulses are zero with the toggling frames used, so we simply have to sum the hamiltonians from the periods of free precession:

$$\overline{H} = \frac{1}{\tau_R}\left(\int_0^{\tau_R/4} \hat{H}_{zz}(t)\,\mathrm{d}t + \int_{\tau_R/4}^{3\tau_R/4} \hat{H}_{yy}(t)\,\mathrm{d}t + \int_{3\tau_R/4}^{\tau_R} \hat{H}_{zz}(t)\,\mathrm{d}t\right) \qquad \text{(viii)}$$

To proceed further, we now need to explore the form of the time-dependence of the dipolar coupling under magic-angle spinning. This was done in Box 3.1 previously for a dipolar-coupling strength written in terms of spherical tensor functions. Here we perform an equivalent derivation for the dipolar-coupling strength written in terms of the Cartesian dipolar tensor, $\mathbf{D}_{ij}$.

The time-dependence of the dipolar-coupling interaction under magic-angle spinning arises, of course, due to the molecular orientation dependence of the dipolar interaction. For a static sample, the geometric part of the dipolar coupling is

$$C_{ij} = \left(\frac{\mu_0}{4\pi}\right)\frac{\gamma_i\gamma_j}{r_{ij}^3}\hbar \cdot \frac{1}{2}(3\cos^2\theta_{ij} - 1) \qquad \text{(ix)}$$

An alternative way of writing the dipolar hamiltonian is as

$$\hat{H}_{dd} = -2\hbar\mathbf{I}^i \cdot \mathbf{D}^{ij} \cdot \mathbf{I}^j \qquad \text{(x)}$$

where the Cartesian dipolar-coupling tensor $\mathbf{D}^{ij}$ is expressed in the laboratory frame. Expanding this and comparing the result with Equation (ii) for the dipolar hamiltonian leads to the identity:

$$C_{ij} = D_{zz}^{ij} \tag{xi}$$

where D_{zz}^{ij} is a component of the dipolar-coupling tensor, z referring to the laboratory frame z axis.

Under magic-angle spinning, the dipolar tensor $\mathbf{D}^{ij}$ acquires a time-dependence in exactly the same way as the shielding tensor described in Section 2.2.1. There, Equations (2.2)–(2.8) derive the time-dependence of the chemical shift frequency, ω_{cs} which is equal to $-\omega_0 \sigma_{zz}$, where σ_{zz} is the shielding tensor equivalent of D_{zz}^{ij}. We can therefore use these equations to derive an expression for D_{zz}^{ij} by substituting components of $\mathbf{D}^{ij}$ for those of $\boldsymbol{\sigma}$ in Equations (2.2) to (2.8). Doing this and using the fact that the dipolar tensor is always axial with principal values $-d_{ij}/2, -d_{ij}/2, +d_{ij}$, where d_{ij} is the dipolar-coupling constant $\left(d_{ij} = \left(\frac{\mu_0}{4\pi}\right)\frac{\gamma_i\gamma_j}{r_{ij}^3}\hbar\right)$, we obtain

$$D_{zz}^{ij}(t) = d_{ij}\left(-\frac{1}{\sqrt{2}}\sin 2\beta\cos(\omega_R t + \gamma) + \frac{1}{2}\sin^2\beta\cos(2\omega_R t + 2\gamma)\right) \tag{xii}$$

where β and γ are Euler angles describing the rotation of the dipolar tensor principal axis frame into the rotor-fixed frame, R, and ω_R is the spinning rate. The integrals in Equation (viii) can now be evaluated:

$$\begin{aligned}
\int_{\tau_1}^{\tau_2} \hat{H}_{\alpha\alpha}(t)\mathrm{d}t &= \int_{\tau_1}^{\tau_2} -D_{zz}^{ij}(t)\left[3\hat{I}_\alpha^i\hat{I}_\alpha^j - \hat{\mathbf{I}}^i\cdot\hat{\mathbf{I}}^j\right]\mathrm{d}t \\
&= -d_{ij}\left[3\hat{I}_\alpha^i\hat{I}_\alpha^j - \hat{\mathbf{I}}^i\cdot\hat{\mathbf{I}}^j\right]\left(-\frac{1}{\sqrt{2}}\sin 2\beta\int_{\tau_1}^{\tau_2}\cos(\omega_R t + \gamma)\,\mathrm{d}t\right. \\
&\quad \left. + \frac{1}{2}\sin^2\beta\int_{\tau_1}^{\tau_2}\cos(2\omega_R t + 2\gamma)\mathrm{d}t\right) \\
&= -d_{ij}\hat{T}_{\alpha\alpha}\left(-\frac{1}{\omega_R\sqrt{2}}\sin 2\beta[\sin(\omega_R\tau_2 + \gamma) - \sin(\omega_R\tau_1 + \gamma)]\right. \\
&\quad \left. + \frac{1}{4\omega_R}\sin^2\beta[\sin(2\omega_R\tau_2 + 2\gamma) - \sin(2\omega_R\tau_1 + 2\gamma)]\right)
\end{aligned} \tag{xiii}$$

where

$$\hat{T}_{\alpha\alpha} = 3\hat{I}_\alpha^i\hat{I}_\alpha^j - \hat{\mathbf{I}}^i\cdot\hat{\mathbf{I}}^j \tag{xiv}$$

and from Equation (xiii) we can easily derive the average hamiltonian over a rotor period by substituting this expression for the integral in Equation (viii):

Continued on p. 130

Box 3.2 *Cont.*

$$\overline{H} = \frac{1}{\sqrt{2}\pi} d_{ij} \sin 2\beta \cos\gamma\left(\hat{T}_{zz} - \hat{T}_{yy}\right) \quad \text{(xv)}$$

This is the effective hamiltonian under which the spin system evolves over one rotor period. Without the DRAMA pulse sequence, the average hamiltonian over one rotor period would be zero (in the absence of chemical shift offsets). This is clearly not the case here and, moreover, the spin system evolution depends on the dipolar coupling, as required. The evolution is also dependent on the orientation of the crystallites in the rotor-fixed frame (through β and γ), and so we can expect some kind of powder pattern in the spectrum arising from using the DRAMA pulse sequence. However, the orientation dependence is different from that for a normal, static sample.

Simulating powder patterns from the DRAMA experiment

In order to simulate the dipolar powder patterns which arise from a DRAMA pulse sequence, we use Equation (xv) for the average hamiltonian over one rotor period of the DRAMA sequence, and use this to calculate the density operator at the end of the pulse sequence using

$$\hat{\rho}(t) = \exp(-i\overline{H}_t)\hat{\rho}(0)\exp(+i\overline{H}t) \quad \text{(xvi)}$$

where $\hat{\rho}(0)$ is the density operator at the start of the experiment (spin system at equilibrium, so $\hat{\rho}(0) = \hat{I}_z$, where $\hat{I}_z = \hat{I}_z^i + \hat{I}_z^j$ for the two-spin system); t is the length of time for which the DRAMA sequence runs (an integral number of rotor periods). This is done in practice by forming the matrix representations of $\hat{\rho}(0)$ and $\overline{H}$ in the two-spin product basis (i.e. $\alpha\alpha$, $\alpha\beta$, $\beta\alpha$, $\beta\beta$). The exponentials in Equation (xvi) are then evaluated by performing an eigenvalue/eigenvector analysis on the matrix of $\overline{H}$. The exponentials are then given by

$$\exp(i\overline{\mathbf{H}}t) = \mathbf{V}^{-1}\exp(\mathbf{E})\mathbf{V} \quad \text{(xvii)}$$

where $\mathbf{V}$ is the eigenvector matrix and $\mathbf{E}$ is the (diagonal) matrix of eigenvalues with elements (eigenvalues) E_k. Exp($\mathbf{E}$) is simply a diagonal matrix with elements $\exp(E_k)$.

Having calculated the matrix representation of $\hat{\rho}(t)$, we can use this to calculate the expectation value of the x magnetization at time t using

$$\langle \hat{I}_x(t) \rangle = \mathrm{Tr}(\hat{I}_x\hat{\rho}(t)) \quad \text{(xviii)}$$

where $\hat{I}_x = \hat{I}_x^i + \hat{I}_x^i$. The trace in Equation (xviii) is evaluated from the matrices of the $\hat{I}_x$ and $\hat{\rho}(t)$ operators in the two-spin product basis.

$\langle \hat{I}_x(t) \rangle$ needs to be calculated as a function of t (the t_1 values used in the experiment) for a given value of d_{ij}, the dipolar-coupling constant which appears in the expression for $\overline{H}$ and summed over a representative sample of crystallite orientations (β, γ) (on which $\overline{H}$ also depends) to produce a simulation of the t_1 time domain data for a powder sample. This same basic procedure can be used to simulate the data arising from any recoupling pulse sequence; all that changes is the form of the average hamiltonian, $\overline{H}$.

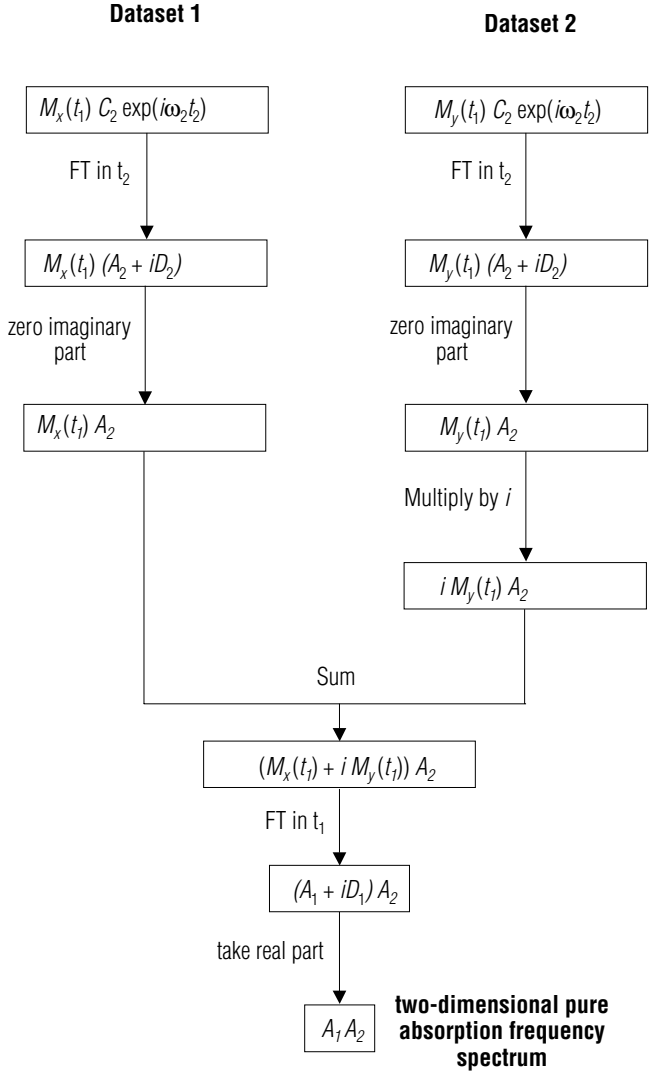

Fig. 3.7 The processing scheme for the two-dimensional time domain datasets arising from the experiment of Fig. 3.4, which uses a recoupling pulse sequence, such as the DRAMA pulse sequence (Figs 3.5 and 3.6) during t_1 of the experiment. The two datasets are produced in two separate experiments and have the forms indicated at the top of the diagram (see text for details). $M_x(t_1)$ and $M_y(t_1)$ are the x and y components of the X spin transverse magnetization in the t_1 period of the experiment. $C_2 \exp(i\omega_2 t_2)$ is the form of the signal recorded in t_2. The C_2 coefficient is the amplitude of the signal during the t_2 period of the experiment; it normally contains a decay term which is a function of time (i.e. accounts for transverse relaxation of the transverse magnetization in t_2). A_1 and A_2 are the real parts of the frequency spectra arising from Fourier transformation (FT) of the t_1 and t_2 time domain signals and D_1 and D_2 are their imaginary counterparts. The A terms correspond to absorption mode lineshapes, while the D terms correspond to dispersive mode lineshapes.

3.2.2 Double-quantum filtered experiments

In any system with strongly dipolar-coupled spin pairs, it is in principle possible to excite double-quantum coherences involving the pairs of coupled spins (see Fig. 3.8). This feature can be and is used to measure the dipolar couplings between the spins in a spin pair system. The experiments rely on the fact that excitation efficiency for the double-quantum coherence depends upon the strength of the dipolar coupling. Another way of saying this is that the nutation rate of the double-quantum coherence during its excitation depends on the dipolar coupling between the spins involved in the double-quantum coherence. Thus, if we can follow the amplitude of double-quantum coherence produced as a function of excitation time, we should be able to analyse this data to extract the dipolar-coupling constant for the pairs of spins associated with the double-quantum coherence. The analysis will depend on the way in which the double-quantum coherence was excited. Now, we cannot of course observe double-quantum coherences directly, so we must first convert any double-quantum coherence the experiment has excited into observable, single-quantum coherence and measure that, hence the expression double-quantum *filtered* experiments. In practice, then, we measure the intensity of the double-quantum filtered signal intensity as a function of double-quantum excitation time, and analyse the resulting data to extract dipolar-coupling constants. The format of the experiment is depicted in Fig. 3.9.

Double-quantum coherence can be easily excited with a simple 90°–τ–90° pulse sequence, where single-quantum coherence (corresponding to transverse magnetization) is excited by the first 90° pulse, allowed to evolve under the dipolar coupling during τ, creating terms in the density operator which the second 90° pulse then converts into double-quantum terms. However, most double-quantum filtered experiments need to be run under magic-angle spinning for the sake of resolution in the final spectrum. As magic-angle spinning averages all dipolar couplings to zero,

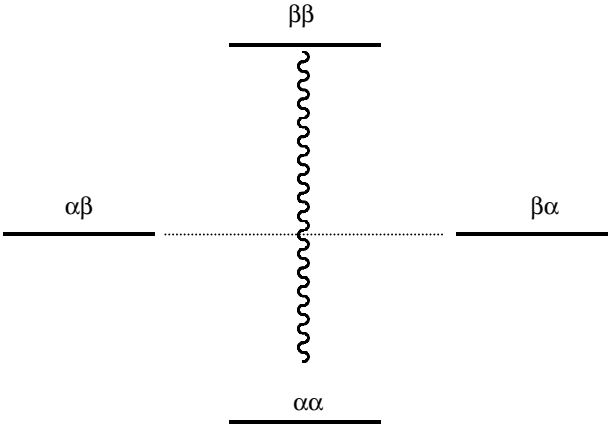

Fig. 3.8 The spin states in a dipolar-coupled spin pair. Double-quantum coherence can be excited between the αα and ββ states ($\Delta M = \pm 2$), while zero-quantum coherence can be generated between αβ and βα ($\Delta M = 0$).

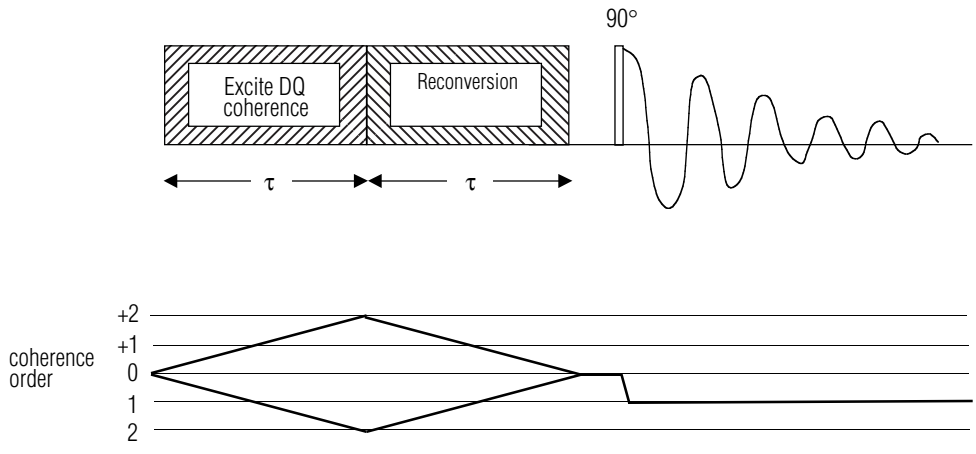

Fig. 3.9 The format of double-quantum filtered experiments for the measurement of dipolar couplings in homonuclear spin systems. Double-quantum coherence is excited then converted via longitudinal magnetization to observable single-quantum coherence. The amount of double-quantum coherence generated for a given spin pair depends on the strength of dipolar coupling between the pair. The experiment is repeated for different lengths of excitation time, τ and the final signal intensity monitored as a function of τ.

if we wish to excite double-quantum coherences, we have to first reintroduce the dipolar coupling between the spins of interest. Section 3.2.1 discussed rf pulse sequences which reintroduce dipolar couplings under conditions of magic-angle spinning. Although these were first introduced with the aim of measuring dipolar couplings directly, these same pulse sequences can all be used to reintroduce dipolar couplings for the purpose of exciting multiple-quantum coherences in correlation experiments. Pulse sequences such as DRAMA can be readily used in this fashion [**9**]. Figure 3.10 shows a pulse sequence which uses DRAMA to excite double-quantum coherence. Box 3.3 describes the theory of their use in such applications. The conversion of multiple-quantum coherences to observable single-quantum coherence takes place in two steps. In the first step, the multiple-quantum coherence is reconverted to zero-quantum coherence (longitudinal magnetization). This is done by a reversal of the process by which multiple-quantum coherence was first excited from longitudinal magnetization [**10**]; this requires using the same pulse sequence as for the excitation, but with all the pulse phases shifted by 90°, as explained in Box 3.3. In the second step, single-quantum coherence is finally produced from the longitudinal magnetization by the simple application of a 90° pulse in the usual fashion.

More recently, the C7 sequence [**11**] and related R14 sequence [**12**] have been introduced by Levitt et al. for the explicit purpose of exciting double-quantum coherences under magic-angle spinning. These are members of general families of pulse sequences denoted C_n^N and R_n^N whose purpose is to recouple (under magic-angle spinning) any spin interaction of choice. Thus their applicability extends well beyond homonuclear dipolar recoupling, although that is the use we discuss here.

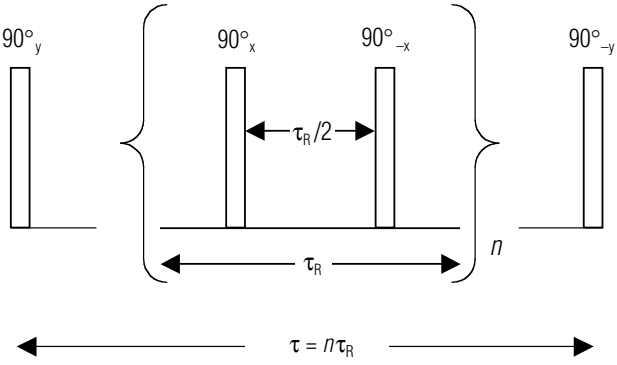

Fig. 3.10 The pulse sequence used to excite double-quantum coherence under magic-angle spinning for the analysis in Box 3.3. The sequence consists of a basic 90°–τ–90° pulse sequence, with a recoupling pulse sequence operating n times during the τ period to prevent the magic-angle spinning from averaging the dipolar coupling (which is ultimately responsible for the double-quantum coherence) to zero. The recoupling pulse sequence in this case is the DRAMA sequence (Fig. 3.5), but any dipolar-recoupling pulse sequence can in principle be used.

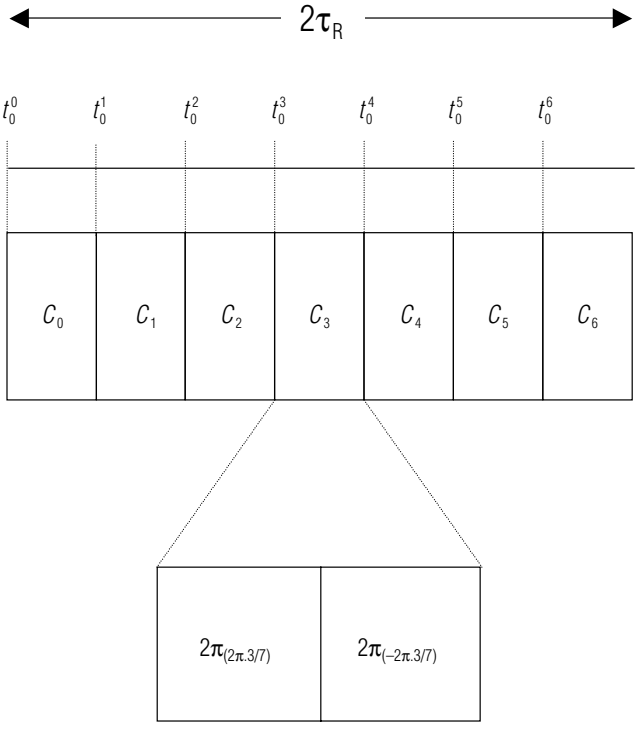

Fig. 3.11 The form of the C_n^N pulse sequences. The sequences consist of a series of $n(2\pi_\phi\ 2\pi_{-\phi})$ pulse cycles, each labelled C_p, timed so that they fit continuously into N rotor periods of sample spinning at the magic angle. The phase ϕ of the 2π pulses changes between each set so that for the pth cycle of pulses, $\phi = 2\pi\ p/n$. The whole sequence is generally run M times, where M is an integer. The particular pulse sequence shown here is the C_7^2 sequence. Also shown are the start timings of each cycle t_0^p.

The *C* sequences [**11**] (Fig. 3.11) consist of a series of $n(2\pi_\phi\, 2\pi_{-\phi})$ pulses sets with the rf amplitude adjusted so that they fit continuously into *N* rotor periods of sample spinning at the magic angle. The phase ϕ of the 2π pulses changes between each set so that for the *j*th set of pulses, $\phi = 2\pi j/n$. The sequence is generally run for $M \times N$ rotor periods, where *M* is an integer, i.e. for several complete cycles of the pulse sequence (note, however, that the C7 pulse sequence works even with fractions of one rotor period). For the *R* sequences, the nomenclature is the same except that the $2\pi_\phi\, 2\pi_{-\phi}$ sets are replaced by $\pi_\phi\, \pi_{-\phi}$. By adjusting *N* and *n*, the particular spin interaction which is recoupled can be changed [**11**]. The simplest sequence which recouples homonuclear dipolar coupling is the C_7^2 or simply, C7 sequence [**11**]. The advantage of this sequence over those previously discussed is that it is much less sensitive to rf pulse amplitude errors and chemical shift offsets, in addition to having a higher recoupling efficiency.

The beauty of the C_n^N and R_n^N pulse sequences is the way they may be manipulated to remove those components of spin interactions we do not want and to keep those we do. The theory behind the operation of these sequences is well explained in reference [**11**], and outlined in Box 3.4 below for the C7 sequence.

3.2.3 Rotational resonance

We saw in Chapter 1 that in *degenerate* homonuclear spin systems, the *B* term in the dipolar hamiltonian (see Equation (3.2)) mixes degenerate Zeeman levels of the spin system and so causes exchange of longitudinal magnetization between the spins (see Section 1.4.2 for details). This is the ultimate cause of linebroadening in dipolar-coupled, homonuclear spin systems. In a homonuclear spin system where two spins *I* and *S* have a chemical shift difference, the operation of the *B* term in the dipolar hamiltonian is rendered ineffective because of the lack of degeneracy between the *I* and *S* spin states. However, under magic-angle spinning and under the condition known as *rotational resonance*, this situation can be altered [**14**]. The rotational resonance condition is that the chemical shift difference between the two spins, $\Delta\omega_I - \Delta\omega_S$ is equal to $n\omega_R$, where $n = \pm 1, \pm 2$ and ω_R is the sample spinning rate. Under this condition, the effect of the *B* term in the dipolar-coupling hamiltonian is reintroduced, but just between spins *I* and *S* for which the rotational resonance condition has been set. This feature can then be used to measure the dipolar coupling between spins *I* and *S*. This is usually done using one of the pulse sequences in Fig. 3.12 or similar [**14**]. Spin *I* (say) is selectively inverted. The rotational resonance condition is then applied for a time τ (equal to an integral number of rotor periods) to allow exchange of magnetization between spins *I* and *S*, after which a spectrum of *I* and *S* is recorded. The experiment is repeated for many τ; the form of spectra which arise as a function of τ is depicted in Fig. 3.13. For very short τ, the *I* spin signal appears at maximum intensity, but inverted (because of the initial selective inversion of the *I* spins), and the *S* spin signal is close to its maximum, positive

(a)

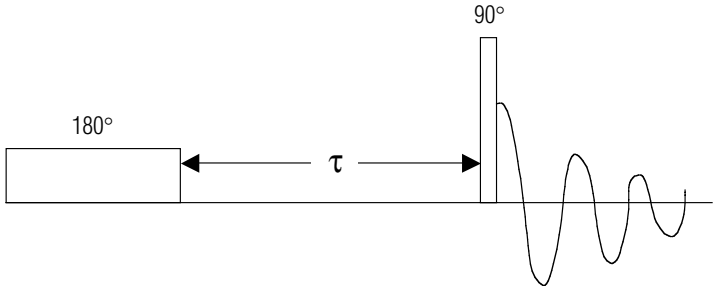

(b)

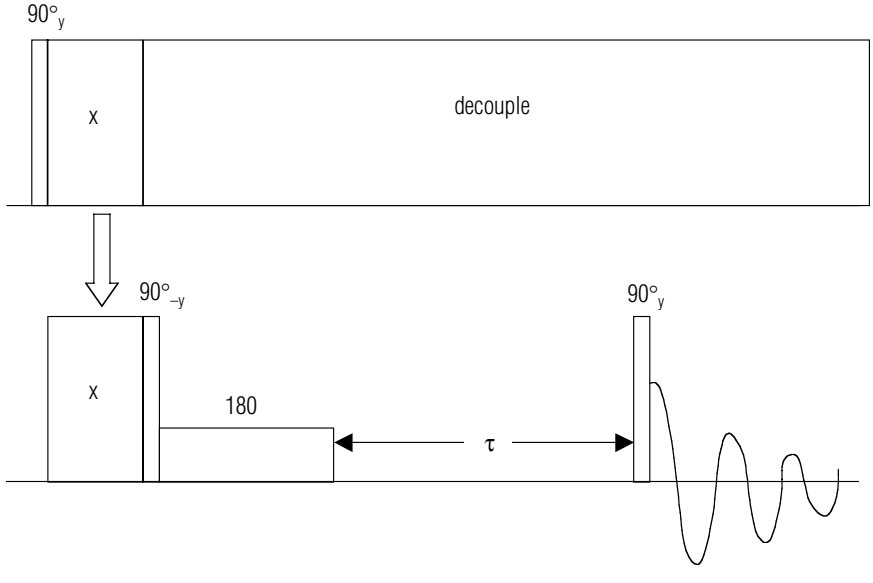

Fig. 3.12 (a) The pulse sequence used in the rotational resonance experiment described in the text. A rotational resonance experiment aims to measure the dipolar coupling between two non-degenerate homonuclear spins, labelled *I* and *S*. The pulse sequence selectively inverts one of the spins, using a low power (and therefore long) 180° pulse centred on the resonance frequency of that spin. (The bandwidth of a pulse is inversely proportional to its length, so by using a long pulse, we ensure a small bandwidth of rf irradiation.) The rotational resonance condition (the sample spinning rate is set so that $n\omega_R$ is equal to the difference in isotropic chemical shift between spins *I* and *S*) is then applied for a period τ, during which time, magnetization exchanges between *I* and *S*. Finally a non-selective 90° pulse is applied to monitor the state of magnetization on both spins. (b) Cross-polarization can be used in a rotational resonance experiment to generate initial transverse magnetization on both spins *I* and *S*. A 90° pulse then converts this back to longitudinal magnetization, but of much greater magnitude than that which exists at equilibrium. The rotational resonance experiment then proceeds as for (a), with a selective inversion of one of the spins, a period τ under the rotational resonance condition followed by a non-selective 90° pulse to monitor both spins.

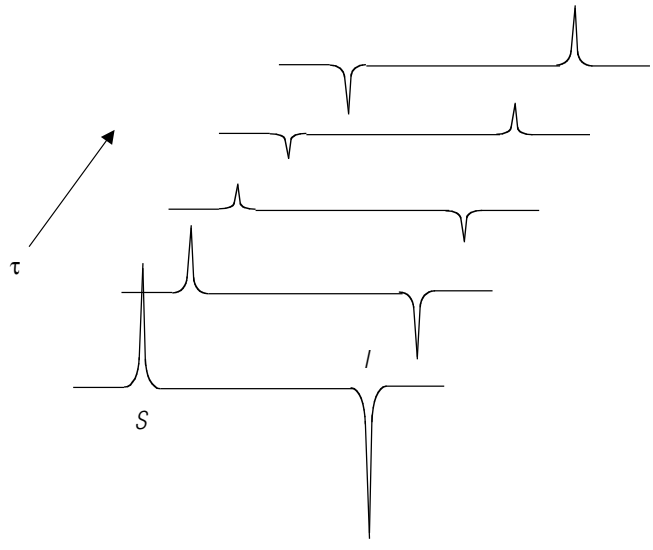

Fig. 3.13 The form of data resulting from a rotational resonance experiment. The experiment uses the pulse sequence of Fig. 3.12 to record NMR spectra of a two-spin system (*I* and *S*) as a function of τ. Spin *I* is the spin which is initially inverted in the experiment (see Fig. 3.12 for details). The signal intensities continue to oscillate as τ increases further (though with damping due to relaxation effects). In addition to changes of intensity with τ, the lineshapes of the *I* and *S* resonances are also affected by the rotational resonance condition, being split into asymmetric doublets [**14**].

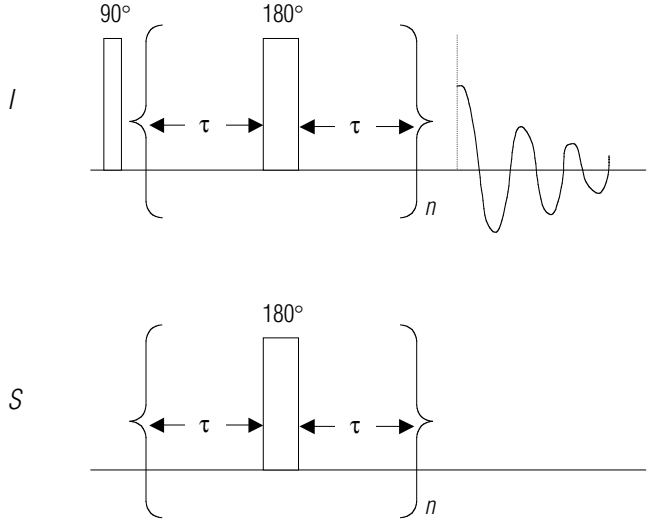

Fig. 3.14 The spin-echo double resonance (SEDOR) pulse sequence. This sequence is used to measure heteronuclear dipolar couplings in non-spinning samples. Two experiments have to be performed, a reference experiment in which refocusing pulses (refocusing the heteronuclear dipolar coupling) only are applied, and only to one spin, *I* in this case. In a second experiment, the refocusing of the *I* spin magnetization is interrupted by pulses applied to the *S* spin. The degree to which the *S* spin pulses prevent the refocusing of the *I* spin magnetization is a measure of the dipolar coupling between spins *I* and *S*. *I* spin spectra are collected as a function of *n*, the number of *I* spin echoes, from $n = 1$ until the *I* spin signal is lost through relaxation.

Box 3.3 Excitation of double-quantum coherence under magic-angle spinning

As mentioned above, any of the pulse sequences discussed in Section 3.2.1 for the reintroduction of dipolar couplings under magic-angle spinning can be used (at least in principle) in the excitation of dipolar-coupling mediated, double-quantum coherence. Here, we shall use the example of the DRAMA pulse sequence [**4**, **9**], as that was extensively analysed in Box 3.2. The sequence used to excite double-quantum coherence is the DRAMA sequence (or N cycles of it) sandwiched between two 90° pulses, whose phases are shifted by 90° from those of the DRAMA sequence (Fig. 3.10).

We use average hamiltonian theory to assess the effect of this complete sequence, and in doing so, follow much of the analysis of the DRAMA sequence in Box 3.3. We calculate the zeroth-order term in the average hamiltonian, $\overline{H}^{(0)}$, as providing we use the interaction representation, this is a good approximation to the total average hamiltonian. As in the analysis of the DRAMA sequence, we consider a two-spin system, I^i and I^j, and assume that we can neglect all other spin interactions other than that with the rf pulse field during a pulse. For simplicity here, we further assume that between pulses, the spin system evolves under the dipolar coupling between the two spins i and j only, i.e. we do not take account of chemical shift offsets, etc. The hamiltonian describing this interaction is

$$\hat{H}_{\mathrm{dd}} = -C_{ij}(t)(3\hat{I}_z^i\hat{I}_z^j - \hat{\mathbf{I}}^i \cdot \hat{\mathbf{I}}^j) \equiv \hat{H}_{zz}(t) \qquad \text{(i)}$$

where the strength of the interaction is described by $C_{ij}(t)$ whose form is derived in Box 3.2.

In forming the zeroth-order average hamiltonian, we use the interaction representation; that is, we transform to a new, toggling frame each time we get to a pulse in the pulse sequence, the new frame being such as to null the hamiltonian describing the effects of the pulse. We then have to transform the dipolar hamiltonian describing the evolution of the spin system after the pulse into the new frame. Equivalent to transforming the frame of reference is to rotate the dipolar hamiltonian instead; if the new frame is rotated by θ about axis α from the original rotating frame, then the equivalent rotation of the hamiltonian is by -0 about axis α.

So in the analysis of the excitation sequence of Fig. 3.10, we first transform to a toggling frame rotated by –90° about y of the rotating frame, to take account of the first $90°_y$ pulse. For the period of evolution (τ_1) which follows, we must transform the dipolar hamiltonian (Equation (i)) to this new frame, which is equivalent to rotating the dipolar hamiltonian +90° about y (of the rotating frame). This transforms $\hat{H}_{zz}(t)$ (Equation (i)) to $\hat{H}_{xx}(t)$ where x refers to the rotating frame x axis and $\hat{H}_{\alpha\alpha}(t)$, $\alpha = x, y, z$, is given by

$$\hat{H}_{\alpha\alpha}(t) = -C_{ij}(t)(3\hat{I}^i_\alpha \hat{I}^j_\alpha - \hat{\mathbf{I}}^i \cdot \hat{\mathbf{I}}^j) \qquad \text{(ii)}$$

The system then evolves under $\hat{H}_{xx}(t)$ for a time $\tau_R/4$. Then there is a $90°_x$ pulse, so we switch to a new toggling frame rotated by –90° about the rotating frame x axis. The dipolar hamiltonian in this new frame is $\hat{H}_{yy}(t)$ (with y being the rotating frame y axis) and the system evolves under this for a time $\tau_R/2$. Finally, the last $90°_{-x}$ pulse demands a toggling frame transformation in which the dipolar hamiltonian is transformed to $\hat{H}_{xx}(t)$, and evolution under this occurs for $\tau_R/4$. The zeroth-order average hamiltonian for one rotor period is then simply the time average of the hamiltonians occurring over one rotor period:

$$\overline{H}^{(0)}(\tau_R) = \frac{1}{\tau_R}\left(\int_0^{\tau_R/4} \hat{H}_{xx}(t)\,dt + \int_{\tau_R/4}^{3\tau_R/4} \hat{H}_{yy}(t)\,dt + \int_{3\tau_R/4}^{\tau_R} \hat{H}_{xx}(t)\,dt\right) \qquad \text{(iii)}$$

The symmetric nature of the time dependence of the dipolar hamiltonian, with respect to the rotor period means that the first and last integrals in Equation (iii) are equal. The form of the integrals in Equation (iii) has been derived previously (Equation (xiii) in Box 3.2). Using this, we can simplify Equation (iii) to

$$\overline{H}^{(0)}(\tau_R) = \frac{3}{\sqrt{2}\pi} d_{ij} \sin 2\beta \cos\gamma(\hat{I}^i_x \hat{I}^j_x - \hat{I}^i_y \hat{I}^j_y) \qquad \text{(iv)}$$

where d_{ij} is the dipolar-coupling constant and (β, γ) are two of the Euler angles which rotate the dipolar tensor PAF into a rotor-fixed frame (R) as in Box 3.2 and x and y refer to the rotating axis frame.

Note that we can achieve the same result by taking the average hamiltonian already derived for the DRAMA pulse sequence (Equation (xv) in Box 3.2) as the appropriate hamiltonian for the DRAMA sequence in the τ_R period after the first $90°_y$ pulse of the double-quantum excitation sequence. So, we only need the first toggling frame transformation of –90° about y to account for the first $90°_y$ pulse of the sequence. We then transform the average hamiltonian of Equation (xv) in Box 3.2 into this same frame by rotating this average hamiltonian by +90° about the rotating frame y axis, which gives Equation (iv) above for the average hamiltonian over one rotor period of the double-quantum excitation sequence.

The form of the reconversion pulse sequence: the need for time reversal symmetry

In this section we assess how the form of the reconversion part of the pulse sequence in Fig. 3.9 can affect the strength of the final signal in a two-dimensional double-quantum experiment. We will see how sensible choice of

Continued on p. 140

Box 3.3 *Cont.*

this sequence, namely a so-called *time-reversed* sequence [**13**] (relative to the excitation sequence) leads to good signal intensities.

Many different double-quantum coherences associated with different pairs of spins and/or different molecular orientations in the sample, can be excited during the double-quantum excitation period of a double-quantum experiment. Each of these different double-quantum coherences is in general formed with a different *phase*. This is because the nutation rate for the double quantum coherence depends upon the magnitude of the average hamiltonian which governs the excitation period. Now, Equation (iv) above shows that the excitation average hamiltonian depends on the dipolar-coupling constant between the pair of spins in question (d_{ij}) and the particular molecular orientation (β, γ). In other words, the double-quantum coherence nutation angle, and so the phase of the double-quantum coherence formed, depends upon which spin pair the coherence is associated with and the orientation of the molecule. During the reconversion from double-quantum coherence back to longitudinal magnetization, a further phase shift is added to all the components of longitudinal magnetization arising from each component of double-quantum coherence. The net result is that the components of the longitudinal magnetization from different molecules in the sample, different spin pairs, etc., destructively interfere and partially cancel, so that the net signal at the end of the pulse sequence may be very small indeed. This can be expressed more formally as follows [**13**].

We take a general case where an average hamiltonian $\overline{H}_{ex}$ acting for a time τ governs the double-quantum excitation, and $\overline{H}_{recon}$ acting for a time τ' governs the reconversion (see Figure B3.3.1).

The density operator at the end of the reconversion period, $\hat{\rho}(\tau + t_1 + \tau')$ can be derived from the equilibrium density operator at time 0 and is given by (see Chapter 1 for details of the time-dependence of the density operator)

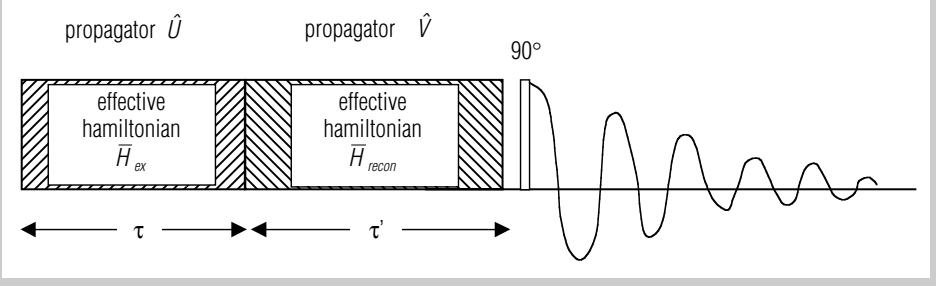

Fig. B3.3.1 The form of the general pulse sequence for multiple-quantum excitation – reconversion.

$$\begin{aligned}\hat{\rho}(\tau + t_1 + \tau') &= \exp(-i\overline{H}_{\text{recon}}\tau')\exp(-i\hat{H}_{\text{int}}t_1)\exp(-i\overline{H}_{\text{ex}}\tau)\hat{I}_z \\ &\quad \exp(i\overline{H}_{\text{ex}}\tau)\exp(i\hat{H}_{\text{int}}t_1)\exp(i\overline{H}_{\text{recon}}\tau') \\ &= \hat{V}(\tau')\exp(-i\hat{H}_{\text{int}}t_1)\hat{U}(\tau)\hat{I}_z\hat{U}^*(\tau)\exp(i\hat{H}_{\text{int}}t_1)\hat{V}^*(\tau') \qquad \text{(v)}\end{aligned}$$

where $\hat{I}_z$ (= $I_z^i + I_z^j$ for a two-spin system) is the equilibrium density operator ($\hat{\rho}(0)$) at time 0, and $\hat{H}_{\text{int}}$ is the hamiltonian describing the internal spin interactions that govern the evolution of the density operator during the t_1 period of the experiment. For convenience, we have written the propagators $\exp(-i\overline{H}_{\text{ex}}\tau)$ and $\exp(-i\overline{H}_{\text{recon}}\tau')$ in Equation (v) as

$$\exp(-i\overline{H}_{\text{ex}}\tau) = \hat{U} \qquad \exp(-i\overline{H}_{\text{recon}}\tau') = \hat{V} \qquad \text{(vi)}$$

Note that if we wish to calculate the density matrix which arises after double-quantum coherence *only* has been excited in the excitation period, we should only retain those terms which correspond to double-quantum coherence in the density matrix at time τ, i.e. the end of the double-quantum excitation. The density operator at this point is $\hat{\rho}(\tau) = \hat{U}(\tau)\hat{I}_z\hat{U}^*(\tau)$.

Now, we wish to know the longitudinal magnetization which remains at the end of the pulse sequence, i.e. at $t = \tau + t_1 + \tau'$. The expectation value of any observable A at time t can be found from the density operator at time t via (see Chapter 1 for details)

$$\langle A \rangle = \text{Tr}(\hat{A}\hat{\rho}(t)) \qquad \text{(vii)}$$

where $\hat{A}$ is the operator corresponding to the observable A. The expectation value of the longitudinal magnetization is proportional to $\langle \hat{I}_z \rangle$, which, at the end of the sequence is then given by

$$\begin{aligned}< \hat{I}_z(\tau + t_1 + \tau') > &= \text{Tr}(\hat{I}_z\hat{\rho}(\tau + t_1 + \tau')) \\ &= \text{Tr}(\hat{I}_z\hat{V}(\tau')\exp(-i\hat{H}_{\text{int}}t_1)\hat{U}(\tau)\hat{I}_z\hat{U}^*(\tau) \\ &\quad \exp(i\hat{H}_{\text{int}}t_1)\hat{V}^*(\tau')) \\ &= \sum_{a,b}\langle a|\hat{U}\hat{I}_z\hat{U}^*|b\rangle\langle b|\hat{V}^*\hat{I}_z\hat{V}|a\rangle\exp(-i(\omega_a - \omega_b)t_1) \qquad \text{(viii)}\end{aligned}$$

where we have substituted Equation (v) for $\hat{\rho}(\tau + t_1 + \tau')$. Calculating the trace in Equation (viii) requires us to form the matrices of $\hat{I}_z$ and $\hat{\rho}(\tau + t_1 + \tau')$ in some basis. In Equation (viii) we have formed the matrices of these operators in terms of basis functions a, b, etc., which are eigenfunctions of the internal spin interaction hamiltonian $\hat{H}_{\text{int}}$, with eigenvalues (energies) ω_a and ω_b respectively (see Box 1.1, Chapter 1, for more discussion of the matrix representation of operators). Having formed the matrices of these operators, it is then comparatively simple to evaluate the trace required in Equation (viii) for the expectation value

Continued on p. 142

Box 3.3 *Cont.*

of the longitudinal magnetization. It is the complex matrix elements, $\langle a|\hat{U}\hat{I}_z\hat{U}^*|b\rangle$ and $\langle b|\hat{V}^*\hat{I}_z\hat{V}|a\rangle$ which contain the phases of the components of longitudinal magnetization supplied by the excitation and reconversion periods respectively. The eigenfunctions a and b can be written as linear combinations of product Zeeman functions involving all the spins in the spin system (two in the case we have been considering). The summation over these in Equation (viii) plus the further summation over different molecular orientations in a powder sample (not shown in Equation (viii), but $\hat{U}$, $\hat{V}$ and $\hat{H}_{\text{int}}$ all depend on molecular orientation) leads to destructive interference between contributions from different pairs of functions a, b. This phenomenon has sometimes been referred to as dipolar dephasing.

The way to avoid this process and consequent loss of signal is to make the propagator $\hat{V}$ which describes the reconversion, equal to $\hat{U}^*$, where $\hat{U}$ is the excitation propagator. Then, the expectation value for the longitudinal magnetization reduces to:

$$< \hat{I}_z(\tau + t_1 + \tau') >= \sum_{a,b} \left|\langle a|\hat{U}\,\hat{I}_z\,\hat{U}^*|b\rangle\right|^2 \exp(-i(\omega_a - \omega_b)t_1) \qquad \text{(ix)}$$

So the expectation value for the longitudinal magnetization at the end of the pulse sequence in Figure B3.3.1 now depends on the *squared modulus* of the complex matrix elements $\langle a|\hat{U}^*\hat{I}_z\hat{U}|b\rangle$, so all the terms in the summation of Equation (ix) add constructively.

The only remaining question is how do we make $\hat{V} = \hat{U}^*$ in practice? Since $\exp(-i\overline{H}_{\text{ex}}\tau) = \hat{U}$, setting $\hat{V}$ equal to $\hat{U}^*$ gives,

$$\hat{V} = \hat{U}^* = \exp(+i\overline{H}_{\text{ex}}\,\tau) \qquad \text{(x)}$$

Now rewriting $\hat{V}$ in the form $\exp(-i\hat{H}t)$, the usual form for a propagator, where $\hat{H}$ is the hamiltonian acting during the period of the propagator, we have for $\hat{V}$

$$\hat{V} = \exp(-i(-\overline{H}_{\text{ex}})\tau) \qquad \text{(xi)}$$

In other words, the average hamiltonian which must act during the reconversion period is *minus* the average hamiltonian we used in the excitation of double-quantum coherence, and it must act for the same length of time, τ, as the original excitation period. Such an average hamiltonian is commonly called *time reversed*; this is somewhat of a misnomer, because of course it is impossible to reverse time. However, it is the terminology in common usage.

So now we return to the use of the DRAMA sequence in double-quantum excitation/reconversion and examine how to achieve a time-reversed hamiltonian for the reconversion period. We want to use a pulse sequence which produces *minus* the average hamiltonian we used in the excitation of multiple-quantum coher-

ence, $\overline{H}^{(0)}$ of Equation (iv) above. The pulse sequence which creates such an effective hamiltonian is the same excitation sequence but with all the pulses shifted in phase by 90°, i.e. an initial $90°_{-x}$ pulse followed by a $90°_{y}$ pulse at $\tau_R/4$, $90°_{-y}$ at $3\tau_R/4$ (and in each subsequent rotor period for which the reconversion is applied) with a final $90°_{x}$ pulse at the end of the sequence. Following the analysis of the exciation sequence above, this then leads to the operator $\hat{H}_{yy}$ acting during $t = 0$ to $t = \tau_R/4$, then $\hat{H}_{xx}$ for $\tau_R/4 < t \leq 3\tau_R/4$ and finally, $\hat{H}_{yy}$ for $3\tau_R/4 < t \leq \tau_R$. Thus, we end up with an effective hamiltonian (equivalent to Equation (iii) above) of

$$\overline{H}^{(0)}(\tau_R) = \frac{1}{\tau_R}\left(\int_0^{\tau_R/4} \hat{H}_{yy}(t)\,dt + \int_{\tau_R/4}^{3\tau_R/4} \hat{H}_{xx}(t)\,dt + \int_{3\tau_R/4}^{\tau_R} \hat{H}_{yy}(t)\,dt\right) \qquad \text{(xii)}$$

Evaluating the integrals in Equation (vii) using Equation (xiii) of Box 3.2 yields

$$\overline{H}^{(0)}(\tau_R) = -\frac{3}{\sqrt{2}\pi} d_{ij} \sin 2\beta \cos\gamma (\hat{I}_x^i \hat{I}_x^j - \hat{I}_y^i \hat{I}_y^j) \qquad \text{(xiii)}$$

which is indeed minus the average hamiltonian for the excitation period, as required.

Analysis of the double-quantum filtered data

In a double-quantum filtered experiment, we measure the double-quantum filtered signal intensity as a function of double-quantum excitation time. We then wish to extract the dipolar-coupling constant, d_{ij}, for the dipolar coupling between the spins i and j giving rise to the double-quantum coherence. The double-quantum filtered signal intensity is proportional to the expectation value of the longitudinal magnetization at the end of the time-reversed reconversion period, assuming the subsequent conversion to transverse magnetization is done with a hard (non-selective) rf pulse. Equation (ix) above gives an expression for the expectation value of the longitudinal magnetization. It consists of a sum of matrix elements over all states for the spin system. The matrix elements involved in $\langle \hat{I}_z \rangle$ further depend on the propagator $\hat{U}$, where

$$\begin{aligned} \hat{U} &= \exp(-i\overline{H}_{ex}\tau) \\ &= \exp(-i\overline{H}^{(0)}\tau) \\ &= \exp\left(-\frac{3i}{\sqrt{2}\pi} d_{ij} \sin 2\beta \cos\gamma [\hat{I}_x^i \hat{I}_x^j - \hat{I}_y^i \hat{I}_y^j]\tau\right) \end{aligned} \qquad \text{(xiv)}$$

Continued on p. 144

Box 3.3 *Cont.*

The matrix elements of Equation (ix) are then readily calculated (using Equation (xiv) for the propagator $\hat{U}$) for given values of d_{ij} (the dipolar-coupling constant) and the molecular orientation angles β and γ, as the matrix elements $\langle a|\hat{U}\hat{I}_z\hat{U}^*|b\rangle$ in Equation (ix) are simply the elements of the matrix **A**, where **A** is

$$\mathbf{A} = \mathbf{U}^*\mathbf{I}_z\mathbf{U} \qquad \text{(xv)}$$

$\langle \hat{I}_z \rangle$ in Equation (ix) also depends on the energies ω_a, etc., of the states of the spin system. These energies are the eigenvalues of $\hat{H}_{\text{int}}$, which describes all the spin interactions which are present during t_1 of the experiment. They may be evaluated by simply diagonalizing the corresponding matrix $\mathbf{H}_{\text{int}}$ of $\hat{H}_{\text{int}}$ in the Zeeman basis for the spin system.

With these components, it is then a relatively straightforward matter to calculate $\langle \hat{I}_z \rangle$ for given values of d_{ij}, β and γ. For powder samples, $\langle \hat{I}_z \rangle$ needs to be summed over a distribution of β and γ angles representing the crystallite orientations of the powder. The result can then be compared with the experimentally measured signal intensity. The form of the propagator $\hat{U}$ (Equation (xiv)) contained in the expression for $\langle \hat{I}_z \rangle$ (Equation (ix)) means that the signal intensity (which is proportional to $\langle \hat{I}_z \rangle$) is expected to oscillate with frequency determined by d_{ij} and the powder average of $\sin 2\beta \cos\gamma$.

intensity. As τ increases, so the *I* signal becomes less negative, and the *S* signal smaller as longitudinal magnetization is transferred between the *I* and *S* spins during the period of rotational resonance in the experiment. At still longer τ, the *I* signal becomes positive and the *S* signal negative and the signal intensities begin to oscillate at a frequency characteristic of the dipolar coupling between the *I* and *S* spins. For quantitative analysis, a plot of the *I* signal intensity minus the *S* signal intensity as a function of τ is constructed. Simulation of this plot allows determination of the dipolar-coupling constant for coupling between *I* and *S* and hence, the *I*–*S* spin internuclear distance. One complication is that the rate of magnetization exchange between the two spins also depends on the *I* and *S* spin chemical shift anisotropies and the relative orientation of their shielding tensors and so a knowledge of these is required for the analysis of the data.

3.3 Techniques for measuring heteronuclear dipolar couplings

All of the techniques for measuring heteronuclear dipolar couplings have a similar form. All are based on some sort of *echo* experiment, in which the heteronuclear dipolar couplings would normally be refocused. However, complete refocusing can

Box 3.4 Analysis of the C7 pulse sequence for exciting double-quantum coherence in dipolar-coupled spin pairs

We consider a general pulse sequence of the C_n^N form [**11**] shown in Fig. 3.11 in which a sequence of n rf pulse cycles C, is timed to fit into N periods of the sample rotation exactly. Each rf pulse cycle consists of $(2\pi_{\phi_p}\ 2\pi_{-\phi_p}$ where the phase ϕ_p is given by $\phi_p = 2\pi p/n (p = 0, 1, 2, \ldots, n-1)$ and the length of each cycle is $\tau_C = N\tau_R/n$. For simplicity, we consider that the rf pulses are on-resonance (no chemical shift offsets) and ignore chemical shift anisotropy, so that the only interactions are the dipolar coupling and interactions with the rf pulse field. Here, we are *not* using hard rf pulses as in the DRAMA sequence, but relatively low amplitude rf pulses. Therefore, at each point in the pulse sequence, the hamiltonian appropriate to the spin system is the sum of a term due to the rf pulse and a term due to the dipolar coupling; the size of the dipolar interaction is no longer negligible compared with the interaction with the rf pulse.

We use the form of the dipolar hamiltonian under magic-angle spinning derived in Box 3.1, in terms of spherical tensor operators and spherical tensor functions to describe the orientation dependence:

$$\hat{H}_{dd}(t) = -\sum_{i>j} \hat{T}_{20}^{ij} \sum_{m=-2}^{+2} \exp(im\omega_R t)\ \omega_{ij}^{(m)} \qquad \text{(i)}$$

where the $\omega_{ij}^{(m)}$ describe the orientation dependence of the dipolar interaction (defined in Box 3.1) and the $\hat{T}_{20}^{ij}$ are spherical tensor operators (also defined in Box 3.1). As in the analysis of the DRAMA pulse sequence, we wish to form the average hamiltonian over the whole pulse sequence of n cycles. We begin by finding the average hamiltonian over one cycle C_p in which the rf phase ϕ_p is $2\pi p/n$.

If the pulse sequence starts at time 0, and the pulse cycle C_p starts at time t_p^0, then a time τ into the cycle, the dipolar hamiltonian is given by

$$\begin{aligned}
\hat{H}_{dd}(t_p^0 + \tau) &= -\sum_{i>j} \hat{T}_{20}^{ij} \sum_{m=-2}^{+2} \exp(im\omega_R (t_p^0 + \tau))\ \omega_{ij}^{m} \\
&= \sum_{i>j} \hat{T}_{20}^{ij} \sum_{m=-2}^{+2} \exp(im\omega_R Np\tau_R/n) \exp(im\omega_R \tau)\ \omega_{ij}^{(m)} \\
&= \sum_{i>j} \hat{T}_{20}^{ij} \sum_{m=-2}^{+2} \exp(i2\pi mNp/n) \exp(im\omega_R \tau)\ \omega_{ij}^{(m)} \qquad \text{(ii)}
\end{aligned}$$

where we have used $t_p^0 = Np\tau_R/n$, since each cycle is of length $N\tau_R/n$.

We now follow the same procedure as for the DRAMA sequence in Box 3.2. During the pulse cycle, we transform the hamiltonian describing the spin system to a toggling frame in which the effect of the rf pulse is null. This frame is one

Continued on p. 146

Box 3.4 *Cont.*

which is rotated from the normal rotating frame by $-\beta_{rf}(\tau)$ about the axis of the pulse, where β_{rf} is the nutation angle of the pulse, $\omega_1\tau$. The nutation angle of the rf pulse is the angle through which the rf pulse has turned the equilibrium magnetization in time t. The axis of the pulse is in the x–y plane of the rotating frame, an angle ϕ_p from the x axis. The rotating frame is therefore rotated into the toggling frame by the Euler angles $(-(\pi/2 - \phi_p), -\beta_{rf}(\tau), (\pi/2 - \phi_p))$, i.e. rotate a frame coincident with the rotating frame by $(\pi/2 - \phi_p)$ about the rotating frame z axis, then by $-\beta_{rf}(\tau)$ about the rotating frame y axis, then by $-(\pi/2 - \phi_p)$ about the rotating frame z axis (see Figure B3.4.1 below).

In transforming the dipolar hamiltonian of Equation (ii) to this new frame, we need to re-express all axis-specific terms with respect to the new frame. The axis-specific term in the spin hamiltonian is the spin operator,

$$\hat{T}_{20}^{(ij)} = \sqrt{\frac{2}{3}}(3\hat{I}_z^i\hat{I}_z^j - \hat{\mathbf{I}}^i \cdot \hat{\mathbf{I}}^j).$$

The other elements of the dipolar hamiltonian in Equation (ii) are components of the dipolar-coupling tensor which describe the strength of the dipolar-coupling

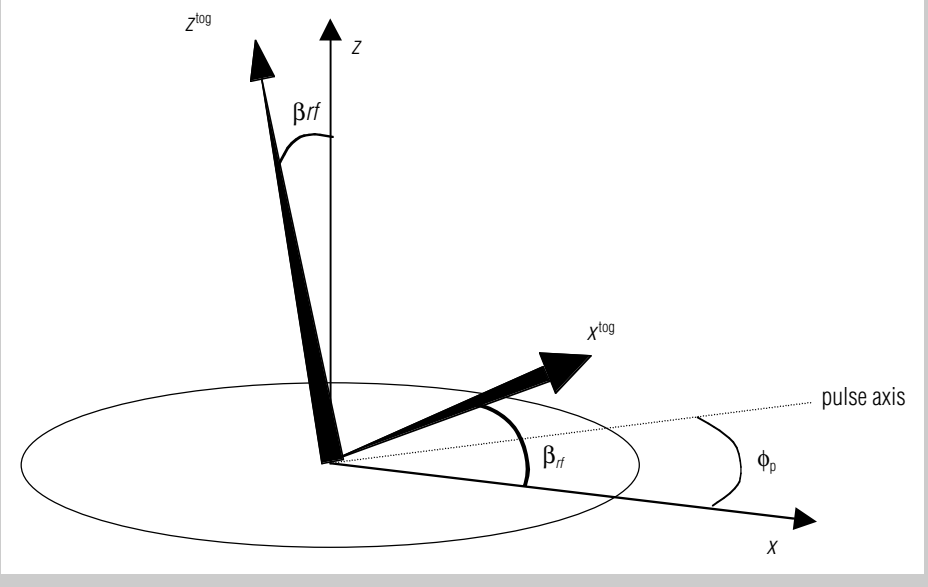

Fig. B3.4.1 The relationship between the rotating frame (x, y, z) and the toggling frame (x^{tog}, y^{tog}, z^{tog}) employed in the analysis of the C7 pulse sequence. A rotation of $-(\pi/2 - \phi_p)$ about z brings y into coincidence with the pulse axis in the rotating frame. We will call this intermediate frame (x_2, y_2, z_2). A rotation of $-\beta_{rf}$ about the y_2 axis (pulse axis) brings the z_2 into coincidence with the z^{tog} of the toggling frame. This new intermediate frame is (x_3, y_3, z_3). Finally, a rotation of $+(\pi/2 + \phi_p)$ about z_3 (z^{tog}) brings the intermediate frame x_3 and y_3 axes into coincidence with the x^{tog} and y^{tog} axes of the toggling frame.

interaction. The strength of the interaction does not change with the frame of reference.

The dipolar hamiltonian, a time τ into the pulse cycle, expressed in the new toggling frame is $\hat{H}^*(t_p^0 + \tau)$, given by

$$\begin{aligned}\hat{H}^*(t_p^0 + \tau) &= \hat{R}^{-1}(-(\pi/2 - \phi_p), -\beta_{rf}(\tau), (\pi/2 - \phi_p))\hat{H}_{dd}(t_p^0 + \tau) \\ &\quad \times \hat{R}(-(\pi/2 - \phi_p), -\beta_{rf}(\tau), (\pi/2 - \phi_p)) \qquad \text{(iii)}\end{aligned}$$

in which the pulse part of the hamiltonian has vanished because of the frame rotation. The rotation operator $\hat{R}$ is the operator which rotates the rotating frame into the toggling frame. It acts on the spin operators of the dipolar hamiltonian, i.e. $\hat{T}_{20}^{ij}$. Box 3.1 gives the transformation of spherical tensor operators under rotations; for this case

$$\begin{aligned}\hat{R}^{-1}\hat{T}_{20}^{ij}\hat{R} &= \sum_{q=-2}^{+2} D_{q0}^2(-(\pi/2 - \phi_p), -\beta_{rf}(\tau), (\pi/2 - \phi_p))\hat{T}_{2q}^{ij} \\ &= \sum_{q=-2}^{+2} \exp(iq(\pi/2 - \phi_p)) d_{q0}^2(-\beta_{rf}(\tau))\hat{T}_{2q}^{ij} \\ &= \sum_{q=-2}^{+2} \exp(iq\pi/2)\exp(-iq2\pi p/n) d_{q0}^2(-\beta_{rf}(\tau))\hat{T}_{2q}^{ij} \\ &= \sum_{q=-2}^{+2} i^q \exp(-iq2\pi p/n) d_{q0}^2(-\beta_{rf}(\tau))\hat{T}_{2q}^{ij} \qquad \text{(iv)}\end{aligned}$$

Thus, the hamiltonian in the toggling frame can be rewritten as

$$\begin{aligned}\hat{H}^*(t_p^0 + \tau) &= \sum_{i>j}\sum_{q=-2}^{+2}\sum_{m=-2}^{+2} i^q \exp(i2\pi mNp/n + im\omega_R\tau) \\ &\quad \exp(-iq2\pi p/n) d_{q0}^2(-\beta_{rf}(\tau))\omega_{ij}^{(m)}\hat{T}_{2q}^{ij} \\ &= \sum_{i>j}\sum_{q=-2}^{+2}\sum_{m=-2}^{+2} i^q \exp(i2\pi(Nm - q)p/n) \\ &\quad \exp(im\omega_R\tau) d_{q0}^2(-\beta_{rf}(\tau))\omega_{ij}^{(m)}\hat{T}_{2q}^{ij} \\ &= \sum_{i>j}\sum_{q=-2}^{+2}\sum_{m=-2}^{+2} \exp(i2\pi(Nm - q)p/n)\,\Omega_{qm}^{ij}(\tau)\hat{T}_{2q}^{ij} \qquad \text{(v)}\end{aligned}$$

where Ω_{qm}^{ij} is given by

$$\Omega_{qm}^{ij} = i^q \exp(im\omega_R\tau) d_{q0}^2(-\beta_{rf}(\tau))\omega_{ij}^{(m)} \qquad \text{(vi)}$$

The average hamiltonian to first order over the pth pulse cycle can now be formed by taking the average of $\hat{H}^*$ in Equation (v) over the period of the pulse cycle:

$$H_p^{(0)} = \sum_{i>j}\sum_{q=-2}^{+2}\sum_{m=-2}^{+2} \exp(i2\pi(Nm - q)p/n)\overline{\Omega}_{qm}^{ij}\hat{T}_{2q}^{ij} \qquad \text{(vii)}$$

Continued on p. 148

Box 3.4 *Cont.*

where

$$\overline{\Omega}_{qm}^{ij} = \frac{1}{\tau_C}\int_0^{\tau_C} \Omega_{qm}^{ij}(\tau)\,\mathrm{d}t \qquad \text{(viii)}$$

where τ_C is the length of the pulse cycle. The average hamiltonian over the whole pulse sequence is then found by summing Equation (vii) over all the n cycles in the pulse sequence:

$$\begin{aligned}\hat{H}^{(0)} &= \frac{1}{n}\sum_p \hat{H}_p^{(0)} \\ &= \frac{1}{n}\sum_p \sum_{i>j} \sum_{q=-2}^{+2} \sum_{m=-2}^{+2} \exp(i2\pi(Nm-q)\,p/n)\,\overline{\Omega}_{qm}^{ij}\hat{T}_{2q}^{ij}\end{aligned} \qquad \text{(ix)}$$

where p labels the pulse cycles, C_p. The oscillating (exponential) term in this average hamiltonian means that in general the average hamiltonian sums to zero when the sum over p is performed. The only exception to this is if $(Nm - q)p/n$ = integer, when the exponential term simply becomes unity.

We wish to excite double-quantum coherence with the C_n^N pulse sequence; for that we need to retain $\hat{T}_{2\pm2}^{ij}$ terms in the average hamiltonian of Equation (ix), i.e. terms with $q = \pm2$. If we also make a condition that we wish to suppress in the average hamiltonian, other terms arising from the dipolar hamiltonian, i.e. $q = \pm1$ (and chemical shift terms which we have not considered here), then it turns out that the simplest sequence which satisfies the $(Nm - q)p/n$ = integer condition for $q = \pm2$ (but not $q = \pm1$) is that with $n = 7$ and $N = 2$. The C_7^2 sequence therefore generates double-quantum coherence in a dipolar-coupled spin pair.

be prevented, for instance, by applying rf pulses to one of the two coupled spins. The aim of the experiments is then to examine to what extent the perturbing rf pulses prevent refocusing, as this is a measure of the dipolar-coupling strength. Many such experiments have and continue to appear in the literature; however, all are based on the spin-echo double resonance (SEDOR) and rotational-echo double resonance (REDOR) experiments which are described in detail here.

3.3.1 Spin-echo double resonance

Spin-echo double resonance [SEDOR; **15**] typifies the general scheme of experiments designed to measure heteronuclear dipolar couplings. It is performed on static

Box 3.5 Theory of rotational resonance

Consider a two-spin system in a sample undergoing magic-angle spinning. The hamiltonian governing this system, expressed in the rotating frame (rotating at the *I*, *S* spin Larmor frequency) and ignoring for the moment chemical shift anisotropy effects, is

$$\hat{H}(t) = \hat{H}_0 + \hat{H}_{\mathrm{dd}}(t) \tag{i}$$

where

$$\begin{aligned}\hat{H}_0 &= -\omega_{\mathrm{iso}}^I \hat{I}_z - \omega_{\mathrm{iso}}^S \hat{S}_z \\ \hat{H}_{\mathrm{dd}}(t) &= -2C_{IS}(t)\Big[\underbrace{\hat{I}_z\hat{S}_z}_{\text{Term A}} - \frac{1}{4}\underbrace{(\hat{I}_+\hat{S}_- + \hat{I}_-\hat{S}_+)}_{\text{Term B}}\Big]\end{aligned} \tag{ii}$$

The term $\hat{H}_0$ accounts for the *I* and *S* spin isotropic chemical shift offsets and $\hat{H}_{\mathrm{dd}}(t)$ describes the dipolar coupling between *I* and *S*. This latter term is time-dependent because of the sample spinning at the magic angle.

We want to form an average hamiltonian over one rotor period, much as we did for the DRAMA pulse sequence in Box 3.2 previously, so that we can see the effect of the rotational resonance condition. The average hamiltonian consists of a sum of terms (see Box 2.2, Chapter 2 for details)

$$\overline{H}(t_{\mathrm{p}}) = \overline{H}^{(0)} + \overline{H}^{(1)} + \overline{H}^{(2)} + \ldots \tag{iii}$$

where

$$\begin{aligned}\overline{H}^{(0)} &= \frac{1}{t_{\mathrm{p}}}\{\hat{H}_1 t_1 + \hat{H}_2 t_2 + \ldots + \hat{H}_n t_n\} \\ \overline{H}^{(1)} &= -\frac{i}{2t_{\mathrm{p}}}\{[\hat{H}_2 t_2, \hat{H}_1 t_1] + [\hat{H}_3 t_3, \hat{H}_1 t_1] + [\hat{H}_2 t_2, \hat{H}_3 t_3] + \ldots\} \\ \overline{H}^{(2)} &= -\frac{1}{6t_{\mathrm{p}}}\{[\hat{H}_3 t_3, [\hat{H}_2 t_2, \hat{H}_1 t_1]] + [[\hat{H}_3 t_3, \hat{H}_2 t_2], \hat{H}_1 t_1] \\ &\quad + \frac{1}{2}[\hat{H}_2 t_2, [\hat{H}_2 t_2, \hat{H}_1 t_1]] + \frac{1}{2}[[\hat{H}_2 t_2, \hat{H}_1 t_1], \hat{H}_1 t_1] + \ldots\end{aligned} \tag{iv}$$

in which $\hat{H}_i$ is the hamiltonian during time period t_i. Now, the hamiltonian in Equation (i) does not commute with itself at different times *t* during the rotor period. That this is so can be seen by forming the matrix representation of the hamiltonian in the coupled spin basis, i.e. $m_I m_S$, and calculating the commutator

$$[\mathbf{H}_1 t_1, \mathbf{H}_2 t_2] = (\mathbf{H}_1\mathbf{H}_2 - \mathbf{H}_2\mathbf{H}_1) t_1 t_2$$

Continued on p. 150

Box 3.5 *Cont.*

for two arbitrary times t_1 and t_2. Clearly then, the higher-order terms, $\overline{H}^{(1)}$, $\overline{H}^{(2)}$, etc., in the average hamiltonian in Equation (iii) are non-zero, as the commutators they contain are non-zero. This makes the average hamiltonian very difficult to calculate, as we must calculate many higher-order terms to obtain a reasonable approximation to the average hamiltonian. It is the combination of the $\hat{H}_0$ and $\hat{H}_{\mathrm{dd}}(t)$ terms which prevents the hamiltonian in Equation (i) from commuting with itself at different times; $\hat{H}_{\mathrm{dd}}(t)$ alone commutes with itself at different times. So, in order to construct the average hamiltonian, we transform to a new frame of reference, a frame in which the $\hat{H}_0$ term in the total hamiltonian is effectively removed and in which the remaining hamiltonian commutes with itself at all times. The average hamiltonian (in the new frame) is then simply the first-order term of Equation (iii), all higher-order terms being zero (within the approximations made in the analysis). This first-order term is easily found by integrating the hamiltonian in the new frame over a rotor period.

The new or toggling frame is found as follows (and this argument follows exactly the same form as that discussion surrounding the toggling frame in Box 2.1, Chapter 2). The state of the spin system is described at any point in time by a density operator, which can in general be expressed as some linear combination of I and S spin operators. The density operator a further time t later is given by

$$\hat{\rho}(t) = \exp(-i\hat{H}t)\hat{\rho}(0)\exp(+i\hat{H}t) \qquad \text{(v)}$$

where $\hat{\rho}(0)$ is the initial density operator and $\hat{H}$ is the hamiltonian governing the evolution of the system during t. In our case, $\hat{H}$ is given by Equation (i) and is a sum of $\hat{H}_0$ and $\hat{H}_{\mathrm{dd}}$. We want to change to a new frame of reference in which the effect of $\hat{H}_0$ (on the density operator) is removed. As we shall see shortly, the effect of $\hat{H}_0$ on the density operator is to rotate the I and S spin terms in the density operator about z, where z refers to the rotating frame z axis. Thus if we transform to a frame of reference in which the I and S spin operators are rotated by the appropriate amounts about z, the frame transformation itself has taken on the effect of the $\hat{H}_0$ term. $\hat{H}_0$ can then be ignored in the new frame.

Effect of $\hat{H}_0$ term on the density operator

The $\hat{H}_0$ term acting for a time t gives a new density operator of

$$\begin{aligned}\hat{\rho}(t) &= \exp(-i\hat{H}_0 t)\hat{\rho}(0)\exp(+i\hat{H}_0)\\ &= \exp\left(i\left[\omega^I_{\mathrm{iso}}\hat{I}_z + \omega^S_{\mathrm{iso}}\hat{S}_z\right]t\right)\hat{\rho}(0)\exp\left(-i\left[\omega^I_{\mathrm{iso}}\hat{I}_z + \omega^S_{\mathrm{iso}}\hat{S}_z\right]t\right)\\ &= \exp\left(i\omega^I_{\mathrm{iso}}\hat{I}_z t\right)\exp\left(i\omega^S_{\mathrm{iso}}\hat{S}_z t\right)\hat{\rho}(0)\exp\left(-i\omega^S_{\mathrm{iso}}\hat{S}_z t\right)\exp\left(-i\omega^I_{\mathrm{iso}}\hat{I}_z t\right) \qquad \text{(vi)}\end{aligned}$$

where we have used the general Equation (v) for $\hat{\rho}(t)$. The term

$$\exp(i\omega_{iso}^{S}\hat{S}_z t)\hat{\rho}(0)\exp(-i\omega_{iso}^{S}\hat{S}_z t)$$

in Equation (vi) for the density operator at time t has the effect of rotating any S spin operators in the initial density operator, $\hat{\rho}(0)$, by $\omega_{iso}^{S}t$ about z and the equivalent term for the I spin rotates any I spin operators by $\omega_{iso}^{I}t$ about z. This is equivalent to transforming to a new frame of reference where the I spin axis frame is rotated by $-\omega_{iso}^{I}t$ about its z axis and the S spin axis frame by $-\omega_{iso}^{S}t$ about its z axis. By the I spin axis frame, we mean the frame in which the I spin operators are defined, and throughout, z refers to the Larmor rotating frame z axis.

The hamiltonian in the new rotated frame

The hamiltonian in this new frame of reference is denoted $\hat{H}^*(t)$ and is given by (see Box 2.2, Chapter 2 for details)

$$\hat{H}^*(t) = \hat{R}^{-1}\hat{H}(t)\hat{R} + \omega_{iso}^{I}\hat{I}_z + \omega_{iso}^{S}\hat{S}_z \qquad \text{(vii)}$$

where the rotation operator $\hat{R}$ is

$$\hat{R} = \exp(-i(\omega_{iso}^{I}\hat{I}_z + \omega_{iso}^{S}\hat{S}_z)t) \qquad \text{(viii)}$$

Now substituting Equation (i) for $\hat{H}(t)$ in Equation (vii), we see immediately that the $\hat{H}_0$ term of $\hat{H}(t)$ is unaffected by the $\hat{R}$ rotation, as $\hat{R}$ describes a rotation about the I and S spin z axes, and the $\hat{H}_0$ term contains only the operators $\hat{I}_z$ and $\hat{S}_z$ which are unaffected by z rotations. The effect of the frame rotation on $\hat{H}_{dd}(t)$ can be found by considering this operator in the Cartesian form in Equation (3.2) and remembering that a frame rotation by angle θ about an axis is completely equivalent to rotating the operator $\hat{H}_{dd}(t)$ by $-\theta$ about the same axis within the original frame, i.e. rotating $\hat{I}_{x,y}$ by $\omega_{iso}^{I}t$ about z and rotating $\hat{S}_{x,y}$ by $\omega_{iso}^{S}t$ also about z, where z refers to the Larmor rotating frame z axis. Doing this and after some rearrangement, we obtain

$$\hat{H}^*(t) = C_{IS}(t)\left[\hat{I}_z\hat{S}_z - \frac{1}{4}(\hat{I}_+\hat{S}_-\exp(-i[\omega_{iso}^{I} - \omega_{iso}^{S}]t) + \hat{I}_-\hat{S}_+\exp(+i[\omega_{iso}^{I} - \omega_{iso}^{S}]t))\right] \qquad \text{(ix)}$$

Note that the $\hat{H}_0$ term has vanished in this toggling frame hamiltonian, cancelling as it does with the last two terms of Equation (vii). Thus, as promised at the outset, the effect of the $\hat{H}_0$ term has been removed by an appropriate choice of axis frame.

Continued on p. 152

Box 3.5 *Cont.*

The average hamiltonian

We can now form the average hamiltonian over a rotor period in the toggling frame by integrating Equation (ix) over one rotor period so as to form the $\overline{H}^{(0)}$ term of the average hamiltonian. The time dependence of the term $C_{IS}(t)$ under magic-angle spinning was described in Box 3.2 and was shown to be:

$$C_{IS}(t) = \sum_{m=-2}^{+2} \omega_{IS}^{(m)} \exp(im\omega_R t) \qquad \text{(x)}$$

The oscillating terms in $C_{IS}(t)$ means that it integrates over a rotor period to zero and, therefore, does the part of the average hamiltonian deriving from the $\hat{I}_z \hat{S}_z$ term in Equation (ix), which has no other time dependence. If we now impose the rotational resonance condition, $\omega_{iso}^I - \omega_{iso}^S = n\omega_R$, then Equation (ix) takes on the form

$$\hat{H}^*(t) = -\frac{1}{4} \sum_{m=-2}^{+2} \omega_{IS}^{(m)} \exp(im\omega_R t)\left[\left(\hat{I}_+ \hat{S}_- \exp(-in\omega_R t) + \hat{I}_- \hat{S}_+ \exp(+in\omega_R t)\right)\right] \qquad \text{(xi)}$$

ignoring that part we know to integrate to zero over a rotor period. When $n = 1, 2$, this hamiltonian contains time-*independent* terms as the $\exp(im\omega_R t)$ terms cancel with the $\exp(\pm in\omega_R t)$ terms. Thus, for $n = 1, 2$, $\hat{H}^*(t)$ integrates to a non-zero value over one rotor period, i.e. the average hamiltonian is non-zero. The final average hamiltonian over one rotor period therefore contains terms in $\hat{I}_+ \hat{S}_-$ and $\hat{I}_- \hat{S}_+$, which ultimately arise from the B term in the dipolar-coupling operator. Like the B term in the normal dipolar coupling hamiltonian, these terms in the average hamiltonian drive the exchange of longitudinal magnetization between the I and S spins.

In summary, setting the rotational resonance condition prevents averaging of the dipolar coupling to zero under magic-angle spinning and, moreover, reintroduces a part of the dipolar coupling, term B, which otherwise would be ineffective in a non-degenerate, homonuclear spin system.

In practice, the I and S spins probably both have chemical shift anisotropies associated with them. This means that the isotropic chemical shift offsets ω_{iso}^I and ω_{iso}^S terms in the original hamiltonian (Equation (i)) should be replaced by chemical shift offsets $\omega_{cs}^I(t)$ and $\omega_{cs}^S(t)$, time-dependent due to the effect of magic-angle spinning on the (anisotropic) chemical shifts of spin I and S. In turn, this means that the $\exp(\pm i[\omega_{iso}^I - \omega_{iso}^S]t)$ terms of Equation (ix) for the toggling frame hamiltonian should be replaced by

$$\exp\left(\pm i \int_0^t [\omega_{cs}^I(t') - \omega_{cs}^S(t')]\,dt'\right).$$

This term is simply the time-domain difference spectrum between spins I and S, in effect the 'FID' for the spin I signal minus that for the spin S signal. Both the I and S spin signals, under conditions of magic-angle spinning and non-zero chemical shift anisotropies, consist of a set of spinning sidebands, set at the spinning speed apart and radiating out from their respective isotropic chemical shift.

Thus the term $\exp\left(\pm i\int_0^t [\omega_{cs}^I(t') - \omega_{cs}^S(t')]\,dt'\right)$ takes the form

$$\exp\left(\pm i\int_0^t [\omega_{cs}^I(t') - \omega_{cs}^S(t')]\,dt'\right) = \sum_{k=-\infty}^{\infty} a_\Delta^{(k)} \exp(\pm i(k\omega_R + \Delta\omega_{iso})t) \qquad \text{(xii)}$$

where $a_\Delta^{(k)}$ is the difference in intensity of the kth spinning sidebands for each spin, which occur at frequency $k\omega_R + \omega_{iso}$, and $\Delta\omega_{iso}$ is the difference between the I and S spin isotropic shifts. Setting the rotational resonance condition, $\Delta\omega_{iso} = n\omega_R$ then gives

$$\exp\left(\pm i\int_0^t [\omega_{cs}^I(t') - \omega_{cs}^S(t')]\,dt'\right) = \sum_{k=-\infty}^{\infty} a_\Delta^{(k)} \exp(\pm i(k+n)\omega_R t) \qquad \text{(xiii)}$$

and substituting this in Equation (ix) in place of the $\exp(\pm i[\omega_{iso}^I - \omega_{iso}^S]t)$ terms gives a toggling frame hamiltonian of

$$\hat{H}^*(t) = -\frac{1}{4}\sum_{k=-\infty}^{+\infty}\sum_{m=-2}^{+2} a_\Delta^{(k)}\omega_{IS}^{(m)} \exp(im\omega_R t) \times [(\hat{I}_+\hat{S}_- \exp(-i(k+n)\omega_R t) + \hat{I}_-\hat{S}_+ \exp(+i(k+n)\omega_R t))] \qquad \text{(xiv)}$$

again ignoring that term in $\hat{H}^*(t)$ known to average to zero when integrated over a rotor period. Now terms in this hamiltonian with $m = \pm(k+n)$ are time-independent, and so give non-zero contributions to the average hamiltonian over one rotor period. This is clearly a more wide-ranging condition than that previously derived. Equation (xiv) also shows that the average hamiltonian depends on the chemical shift anisotropies of the two spins through the terms $a_\Delta^{(k)}$. This dependence is stronger as n increases, i.e. for higher-order rotational resonance conditions.

samples, and so does not provide the resolution so often required, and consequently, is not often used nowadays. It is however, still instructive to examine its operation (Fig. 3.14). After initial excitation of transverse magnetization on one spin (spin I in Fig. 3.14), a series of 180° pulses with the spacings shown are applied to the I spin [**15**]. As explained in Section 2.6, these 180° pulses have the effect of refocusing any inhomogeneous interactions, such as heteronuclear dipolar coupling. To recap the results of Section 2.6 briefly, if transverse magnetization dephases under whatever inhomogeneous interactions are present for a time τ, and a 180° pulse applied, the dephased transverse magnetization is refocused a further time τ after the 180° pulse. The series of 180° pulses in Fig. 3.14 causes the dephasing due to

heteronuclear dipolar coupling to be refocused at times 2τ, 4τ, 6τ, etc. after the initial excitation of the I transverse magnetization. The echo intensities at these times are recorded as a reference data set. The only loss of intensity between the echoes is due to transverse relaxation. A second experiment is then performed in which 180° pulses are also applied to the S spin at times τ, 3τ, 5τ, etc. These have the effect of inverting the S spins at these points in time, and thus changing the sign of the strength of the dipolar-coupling interaction between I and S, as the hamiltonian describing the interaction is

$$\hat{H}_{\mathrm{dd}} = -2C_{IS}\hat{I}_z\hat{S}_z \tag{3.6}$$

where the constant C_{IS} is defined in Equation (3.3). This in turn prevents the complete refocusing of the I–S dipolar coupling at the echo points of 2τ, 4τ, 6τ, etc. The difference in intensity of the echo maxima between the two experiments depends on the dipolar-coupling strength, and the dipolar-coupling constant is then relatively easily extracted from the plots of echo intensity versus $n\tau$, $n = 2, 4, 6, \ldots$ for the case where I and S constitute an isolated spin pair.

3.3.2 Rotational-echo double resonance

The REDOR experiment [**16**] is very similar in its operation to the SEDOR experiment described in the previous section, except that the I spin echoes are now provided by magic-angle spinning. Under magic-angle spinning, any I spin transverse magnetization dephases under the I–S dipolar coupling during the first half of the rotor period and is then refocused during the second half. This is explained in more detail in Section 2.2.2, albeit for the case of dephasing under chemical shift anisotropy rather than heteronuclear dipolar coupling; however, the principles are exactly the same. The pulse sequence used in the REDOR experiment is shown in Fig. 3.15.

If 180° pulses are applied during the rotor period to the S spin, the I–S dipolar coupling is only partially refocused at the end of the rotor period for the same reason as the 180° pulses in the SEDOR experiment perturb the I spin echoes. The difference between the I spin intensity at the end of the rotor period between the experiment where no pulses are applied to the S spin (the normal, reference experiment, with intensity $I_0^{\mathrm{expt}}(\tau_{\mathrm{R}})$) and the I spin intensity in the experiment where 180° pulses are applied to the S spin ($I_f^{\mathrm{expt}}(\tau_{\mathrm{R}})$), depends quantitatively on the dipolar-coupling strength.

In practice, the extent of I spin dephasing resulting from incomplete refocusing of the rotational echoes is monitored as a function of the number of rotor periods for which the dephasing is allowed to occur; as the experiment extends to larger numbers of rotor periods, so the net I spin dephasing under S spin 180° pulses increases. An 180° pulse is also applied to the I spins in each experiment halfway through the dephasing period to refocus any I spin chemical shift offset, which would otherwise contribute to the net I spin dephasing. The S spin 180° pulse which would otherwise have occurred at this halfway point is omitted, as explained in

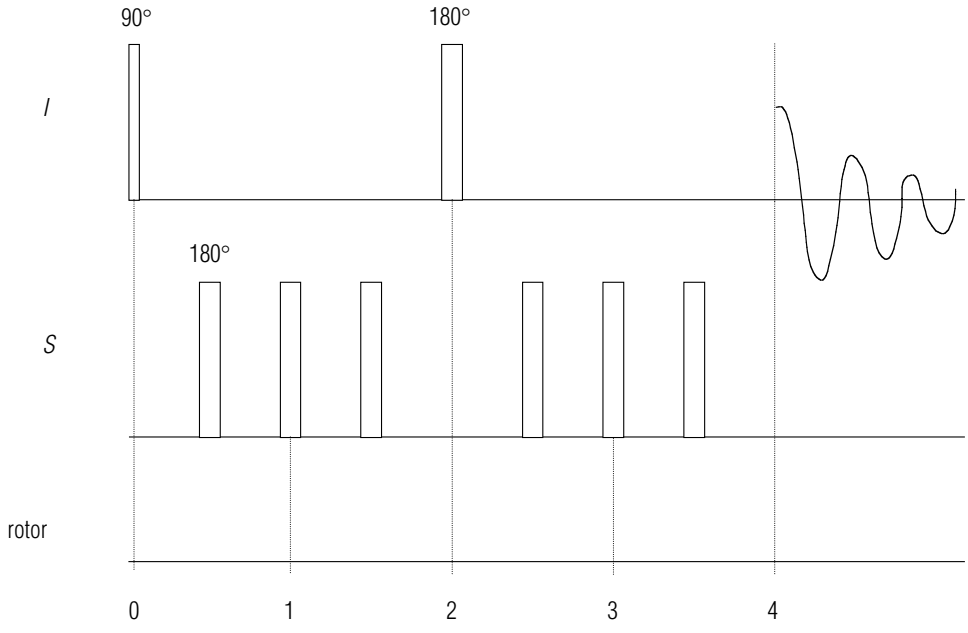

Fig. 3.15 The rotational-echo double resonance (REDOR) pulse sequence. As with the SEDOR sequence of Fig. 3.14, this pulse sequence is used to measure heteronuclear dipolar couplings, but this time on magic-angle spinning samples. Again, two experiments have to be performed with *I* as the observed spin in both cases. In the reference experiment, the dipolar coupling between the *IS* spin pair is refocused at the end of every rotor period, as normal under magic-angle spinning. In the second experiment, this refocusing of the dipolar coupling is prevented by a series of rotor-synchronized 180° pulses applied to one of the spins (*S* in this case). As with the SEDOR experiment, *I* spin spectra are collected for several different lengths of dephasing time, each of which is necessarily a multiple of $2\tau_R$, where τ_R is the rotor period. The initial *I* spin transverse magnetization is often generated via cross-polarization (from ^{1}H for example), rather than with a 90° pulse as shown here.

more detail in Box 3.6 below. A plot is then formed of $I_0^{expt}(N\tau_R) - I_f^{expt}(N\tau_R)$ as a function of number of rotor periods, N and this can be quantitatively analysed to determine the *IS* dipolar-coupling constant. Such an analysis is generally unambigous if *I*–*S* is an isolated spin pair. However, in the case where the *I* spin is coupled to several *S* spins, the data can often be fitted by many different sets of dipolar-coupling constants, and so is less useful.

This method is ideal for measuring dipolar-coupling constants of a few hundred to a few thousand Hertz. For very large dipolar couplings, the *I* spin transverse magnetization is completely dephased after only one or two rotor periods when 180° pulses are applied to the *S* spin. In these circumstances, the plot of $I_0^{expt}(N\tau_R) - I_f^{expt}(N\tau_R)$ versus the number of rotor periods does not contain enough data points for a good quantitative analysis. For very small dipolar couplings, the net dephasing when *S* spin 180° pulses are applied is just too small to be accurately measured by difference with the reference experiment. The net *I* spin dephasing depends on the rotor period of course, and is larger for slower spinning speeds, so it is worth while considering what spinning speed might be most suitable for the particular dipolar coupling constants to be measured.

Box 3.6 Analysis of the REDOR experiment

This analysis uses average hamiltonian theory to assess the effect of the pulse sequence in Fig. 3.15 [**17**], and as such follows much the same course as that for the DRAMA experiment in Box 3.2.

We deal with the case of a heteronuclear spin pair, *IS*. The hamiltonian in the rotating frame describing the dipolar interaction between these two is

$$\hat{H}_{\mathrm{dd}}(t) = -2C_{IS}(\beta, \gamma, t)\hat{I}_z\hat{S}_z \qquad \text{(i)}$$

where $C_{IS}(\beta, \gamma, t)$ is given by Equations (xi) and (xii) in Box 3.2. $C_{IS}(\beta, \gamma, t)$ describes the strength of the dipolar interaction for a given molecular orientation (β, γ) relative to the applied magnetic field and is time-dependent here due to the magic-angle spinning which takes place during the experiment. We assume that the 180° pulses in the experiment are of sufficiently high amplitude that, during the period of a pulse, the interaction with the pulse rf field is much stronger than any other interactions. We may then neglect all other interactions during the pulses; the hamiltonian during the pulses is then simply that due to the pulse, namely,

$$\hat{H}_{\mathrm{pulse}} = -\omega_1\hat{I}_x \qquad \text{(ii)}$$

for an x pulse for instance, where ω_1 is the rf pulse amplitude.

We then form the average hamiltonian over one rotor period, all subsequent rotor periods in the S spin 180° pulse train in Fig. 3.15 being effectively identical. The rotor period in which a 180° pulse is applied to the I spins rather than S is discussed later, and is shown to be equivalent to other rotor periods in the sequence. As discussed in Box 2.1 (Chapter 2), the average hamiltonian over a period of time t_{p} is given by

$$\overline{H}(t_{\mathrm{p}}) = \overline{H}^{(0)} + \overline{H}^{(1)} + \overline{H}^{(2)} + \ldots \qquad \text{(iii)}$$

where the higher order terms, $\overline{H}^{(1)}$, $\overline{H}^{(2)}$, depend on the commutators of the hamiltonians operating at different times in the t_{p} time period. Now, as explained in Box 3.2, the pulse hamiltonian (Equation (ii)) and dipolar hamiltonian (Equation (i)) do not commute with each other, so the higher-order terms, $\overline{H}^{(1)}$, $\overline{H}^{(2)}$, etc., are non-zero and contribute significantly to the total average hamiltonian. This makes the average hamiltonian difficult to calculate, as many higher-order terms may have to be considered. To get around this, at the point of each pulse in the sequence, we transform the hamiltonian to a new frame, the so-called *toggling frame*, in which the pulse hamiltonian vanishes. Then only the dipolar hamiltonian remains, which commutes with itself at all times, so that the $\overline{H}^{(0)}$ term of Equation (iii) alone is a good approximation to the average hamiltonian. In turn, $\overline{H}^{(0)}$ is simply the average of the hamiltonians which operate during

the rotor period, i.e. the sum of the hamiltonians which operate multiplied by the fraction of the rotor period for which they operate.

We can now proceed to calculate the average hamiltonian over a rotor period [**17**]. In the first half of the rotor period, the system simply evolves under the *IS* dipolar coupling, described by the hamiltonian, $\hat{H}_{dd}(t)$ as in Equation (i) above. At the first *S* spin 180° pulse (halfway through the rotor period), we transform the whole description of the spin system into a frame in which the pulse hamiltonian vanishes. The effect of an *S* spin 180° pulse is to rotate the parts of the density operator describing the *S* spin system by 180° about *x*. Thus, if we transform to a new *S* spin axis frame in which the *S* spin axis frame is rotated by –180° about the rotating frame *x* axis, we have emulated the effect of the pulse; the hamiltonian describing the effect of the pulse in this new representation must then be zero.

For the second half of the rotor period, the system again evolves under the *IS* dipolar coupling, but we must now transform the hamiltonian operator describing this interaction into the new toggling frame, in which the *S* spin axis frame is rotated by –180° about the rotating frame *x* axis. This is equivalent to rotating the dipolar hamiltonian itself by +180° about *x*, leaving the *S* spin axis frame alone. Rotating the *S* spin operators in the hamiltonian of Equation (i) above gives the new toggling frame hamiltonian as

$$\hat{H}^*(t) = 2C_{IS}\hat{I}_z(-\hat{S}_z) = -2C_{IS}\hat{I}_z\hat{S}_z = -\hat{H}_{dd} \qquad \text{(iv)}$$

where *z* refers to the rotating frame *z* axis. In the same manner, the *S* spin 180° pulse at the end of the rotor period then simply has the effect of transforming $-\hat{H}_{dd} \rightarrow \hat{H}_{dd}$, so that the hamiltonian describing the spin system at the beginning of the next rotor period is $\hat{H}_{dd}$ once again. The average hamiltonian over the rotor period is then simply

$$\overline{H}^{(0)} = \frac{1}{\tau_R}\left(\int_0^{\tau_R/2}\hat{H}_{dd}(t)\,dt - \int_{\tau_R/2}^{\tau_R}\hat{H}_{dd}(t)\,dt\right) \qquad \text{(v)}$$

The time dependence of $\hat{H}_{dd}$ is contained in the $C_{IS}(\beta, \gamma, t)$ term (Equation (i)) which was derived in Box 3.2 and is given by

$$C_{IS}(\beta, \gamma, t) = d_{IS}\left(-\frac{1}{\sqrt{2}}\sin 2\beta\cos(\omega_R t + \gamma) + \frac{1}{2}\sin^2\beta\cos(2\omega_R t + 2\gamma)\right) \qquad \text{(vi)}$$

where d_{IS} is the dipolar-coupling constant, $d_{IS} = \left(\frac{\mu_0}{4\pi}\right)\frac{\gamma_I\gamma_S}{r_{IS}^3}\hbar$ for the *IS* spin pair and (β, γ) are two of the Euler angles describing the rotation of the dipolar PAF of the current molecular orientation into a rotor-fixed frame. ω_R is the rotor spinning rate. Using this equation in Equation (v), it is easy to see that $\overline{H}^{(0)}$ is non-zero and, moreover, that $\overline{H}^{(0)}$ depends on the dipolar coupling between *I* and *S*. It is the *S* spin 180° pulse midway through the rotor period that prevents the

Continued on p. 158

Box 3.6 *Cont.*

average hamiltonian from being zero (and therefore prevents the *I*–*S* dipolar coupling from being refocused). In contrast, consider the situation without any *S* spin π pulses. The average hamiltonian over a rotor period then is

$$\overline{H}^{(0)} = \frac{1}{\tau_R}\left(\int_0^{\tau_R} \hat{H}_{dd}(t)\,dt\right) \qquad \text{(vii)}$$

which (using the periodic time dependence in Equation (vi)) is zero, as it should be under magic-angle spinning. Thus the application of an *S* spin 180° pulse, reverses the sign of the dipolar hamiltonian under which the spin system evolves and, in doing so, prevents the *IS* dipolar coupling from being refocused under magic-angle spinning, as it otherwise would be.

There is one rotor period in the pulse sequence of Fig. 3.15 in which a 180° pulse is applied to the *I* spins at the $\tau_R/2$ point (to refocus chemical shift offsets) and the pulse that would normally be applied to the *S* spins is omitted. Using a similar analysis to that above, it is easy to see that a single 180° pulse applied to either spin has the required effect of reversing the sign of the dipolar hamiltonian in the toggling frame, and so prevents the dipolar coupling from being refocused. 180° pulses applied to both spins simultaneously, however, leaves the dipolar hamiltonian unaltered, which is not what is required in this pulse sequence. Hence, the rotor period in which an *I* spin 180° pulse, but no *S* spin pulse, is applied is completely equivalent (in terms of average hamiltonian theory) to those rotor periods in which only *S* spin 180° pulses are applied.

We can then determine a quantitative expression for the loss of *I* spin signal intensity at the end of one rotor period resulting from the incomplete refocusing of the *I*–*S* dipolar coupling. The initial *I* spin transverse magnetization, prior to the *S* spin π pulse train, lies along a particular axis of the rotating frame. Any *I* spin magnetization at the end of the pulse sequence lying along this axis is effectively 'refocused' magnetization. Any *I* spin magnetization lying along an orthogonal axis arises from dephasing and does not contribute to the *I* spin signal intensity. We need to determine the amount of *I* spin magnetization lying along the initial axis at the end of the rotor period, as this is proportional to the *I* spin signal intensity. We do this by calculating the phase angle $\Delta\Phi$, acquired by the *I* spin transverse magnetization over the rotor period (see Fig. B3.6.1 below).

The *I* spin precession frequency in the rotating frame in the absence of chemical shift offsets is $\omega_{dd}^{I}(\beta, \gamma, t)$ for a given molecular orientation (time-dependent due to magic-angle spinning) and is given by

$$\omega_{dd}^{1}(\beta, \gamma, t) = \pm C_{IS}(\beta, \gamma, t) \qquad \text{(viii)}$$

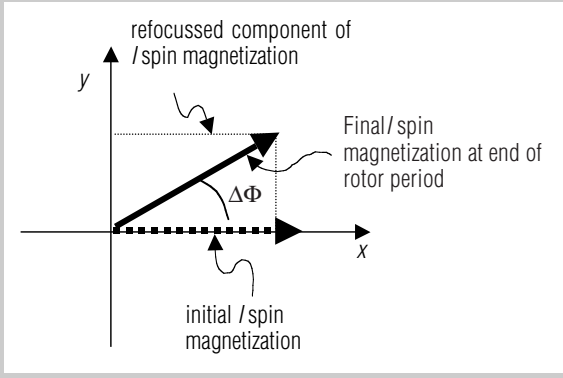

Fig. B3.6.1 Definition of the phase angle $\Delta\Phi$ acquired by *I* spin magnetization in the REDOR experiment (assuming no relaxation effect).

for a spin-$\frac{1}{2}$ nucleus, where we have used Equation (i) to determine the *I* spin precession frequency (which corresponds to the dipolar contribution to the *I* spin transition frequency for $m_I = +\frac{1}{2} \rightarrow m_I = -\frac{1}{2}$) assuming spins *I* and *S* are both spin-$\frac{1}{2}$ nuclei. Thus the *I* spin phase angle after one rotor period and the *S* spin 180° pulse sequence in Fig. 3.15 is given by

$$\Delta\Phi(\beta, \gamma, \tau_R) = \left(\int_0^{\tau_R/2} \omega_{dd}^I(\beta, \gamma, t)\,dt - \int_{\tau_R/2}^{\tau_R} \omega_{dd}^I(\beta, \gamma, t)\,dt \right) \qquad \text{(ix)}$$

The *I* spin signal intensity is proportional to $\cos\Delta\Phi(\beta, \gamma, \tau_R)$, i.e. the *x* component of the *I* spin transverse magnetization. Substituting for $\omega_{dd}^I(\beta, \gamma, t)$ in Equation (ix) from Equations (viii) and (vi), we obtain

$$\Delta\Phi(\beta, \gamma, \tau_R) = \pm 2\sqrt{2}\,\frac{d_{IS}}{\omega_R}\sin 2\beta \sin\gamma \qquad \text{(x)}$$

as the phase angle acquired by *I* spin magnetization for the molecular orientation described by Euler angles (β, γ). The *I* spin signal intensity for a powder sample at the end of the rotor period, $I_f(\tau_R)$, is then found by summing $\cos\Delta\Phi(\beta, \gamma, \tau_R)$ over all possible crystallite orientations. Overall then, we have for the *I* spin signal intensity:

$$I_f(\tau_R) = \frac{I_0(0)}{2\pi} \int_0^{\pi/2} \int_0^{2\pi} \cos(\Delta\Phi(\beta, \gamma, \tau_R)) \sin\beta\, d\gamma\, d\beta \qquad \text{(xi)}$$

where $I_0(0)$ is the signal intensity at time 0, i.e. immediately after the initial 90° pulse creating transverse magnetization.

The phase angle acquired after *N* rotor periods is simply $N\,\Delta\Phi(\beta, \gamma, \tau_R)$. Equation (xi) takes no account of relaxation effects. In practice, there is always a loss of signal intensity during the dephasing period due to relaxation in addition to any dephasing. As already mentioned, a reference experiment is recorded without

Continued on p. 160

Box 3.6 *Cont.*

any *S* spin 180° pulses during the dephasing period in order to be able to take account of this. The difference between $I_f^{\mathrm{expt}}(N\tau_R)$ and the reference spectrum intensity, $I_0^{\mathrm{expt}}(N\tau_R)$ then corresponds to

$$\frac{I_0^{\mathrm{expt}}(N\tau_R) - I_f^{\mathrm{expt}}(N\tau_R)}{I_0^{\mathrm{expt}}(0)} = 1 - \frac{1}{2\pi}\int_0^{\pi/2}\int_0^{2\pi} \cos(\Delta\Phi(\beta, \gamma, \tau_R))\sin\beta\, d\gamma\, d\beta \quad \text{(xii)}$$

from Equation (xi). $[I_0(N\tau_R)–I_f(N\tau_R)]/I_0(0)$ can be simulated for different values of the dipolar-coupling constant d_{IS} until good agreement is reached with the experimental plot. Analytical solutions for REDOR curves have been found by Mueller [18], and these can simplify the data analysis.

Since the introduction of the REDOR experiment several variants of it have appeared in the literature; however, the principles of these are largely the same as that just described.

3.4 Techniques for dipolar-coupled quadrupolar (spin-$\frac{1}{2}$) pairs

Many materials of interest contain quadrupolar ($I > \frac{1}{2}$) nuclei, so it is almost inevitable that, at times, we will want to measure dipolar couplings between quadrupolar and spin-$\frac{1}{2}$ nuclei, and indeed, between quadrupolar nuclei. Quadrupolar nuclei are discussed in detail in Chapter 4; however, it is appropriate to discuss dipolar-coupling measurements pertaining to them here.

Quadrupolar nuclei often suffer quadrupolar linebroadening of the order of MHz. This feature means that the techniques discussed in Section 3.3 for the measurement of heteronuclear dipolar couplings cannot in general be applied to quadrupolar–spin-$\frac{1}{2}$ pairs, as techniques like REDOR require hard 180° pulses (i.e. rf amplitude much greater than any other spin interaction) to be applied at some stage to both spins. Rf amplitudes of a few hundred kHz can be achieved, but not much more, and clearly this is a lot less than a quadrupole interaction strength of a few MHz. Consequently, the REDOR experiment described in Section 3.3 simply will not work if the *S* spin to which the train of 180° pulses is applied is a quadrupolar nucleus suffering moderate (or larger) quadrupole coupling). The 180° pulses in the REDOR experiment are required to invert the *S* spin populations, but with quadrupolar linebroadening of a few MHz, no achievable rf pulse can actually irradiate all the spins of a powder sample in order to do this.

Having said that, REDOR has been successfully applied in a number of quadrupolar–spin-$\frac{1}{2}$ pair cases, when the *S* spin to which the 180° pulse train is applied is the spin-$\frac{1}{2}$ nucleus rather than the quadrupolar one [**19**]. In these cases, the quadrupolar spin is always a half-integer spin and it is only the central transition ($+\frac{1}{2} \rightarrow -\frac{1}{2}$) that is observed. As mentioned in Section 3.3, it is important to refocus any dephasing of the observed spin that occurs by any means other than dipolar coupling to the *S* spin, for example by chemical shift offsets, or, in the case of a quadrupolar spin, by quadrupole coupling. In the case where the *I* spin is a spin-$\frac{1}{2}$, chemical shift offsets are refocused by a 180° pulse on the *I* spin in the middle of the *S* spin pulse train. Fortunately, it is relatively easy to refocus the dephasing of the central transition magnetization associated with the quadrupolar nucleus via a selective 180° pulse applied to the central transition of the quadrupolar spin in the middle of the *S* spin 180° pulse train. The dephasing here occurs due to quadrupole coupling as well as chemical shift effects. REDOR has also been used with MQMAS [**20**] (see Chapter 4) to improve the resolution in the experiment. However, these implementations of the REDOR experiment require that the spin-$\frac{1}{2}$ nucleus is abundant, otherwise the extent of dephasing by dipolar coupling on the quadrupolar spin magnetization is tiny. Moreover, they are only suitable for half-integer quadrupolar spins, and there are two potentially important integer quadrupolar spins, ^{14}N ($I = 1$) and ^{2}H ($I = 1$).

To this end, two experiments have been devised specifically to measure dipolar couplings between quadrupolar and spin-$\frac{1}{2}$ nuclei and which can be used with either half-integer or integer quadrupolar spins. These are the 'transfer of population in double resonance' (TRAPDOR) [**21**] and the 'rotational-echo, adiabatic passage, double resonance' (REAPDOR) [**22**] experiments.

3.4.1 Transfer of population in double resonance

The TRAPDOR experiment [**21**] is run under magic-angle spinning and is applied to quadrupolar–spin-$\frac{1}{2}$ pairs. The principle of the experiment is much the same as the REDOR experiment. One nucleus, *I* (the spin-$\frac{1}{2}$) is observed both with and without a perturbation being applied to the coupled nucleus, *S* (the quadrupolar one), the perturbation being designed to prevent the complete refocusing of the dipolar coupling between the pair under the magic-angle spinning. The experiment without any perturbation provides a reference dataset of signal intensities in the absence of any dipolar-coupling effects (just relaxation effects). The extent of the dephasing of the spin-$\frac{1}{2}$ transverse magnetization as a result of the incomplete refocusing in the second experiment is then a measure of the dipolar coupling between the spins. The experiment is repeated with the perturbation being applied for different lengths of time (the dephasing period) and a plot of the difference in signal intensity between the two experiments as a function of dephasing time is constructed. Analysis of this plot allows the determination of the dipolar coupling between the two spins.

In the REDOR experiment, the perturbation which prevents the complete refocusing of dipolar coupling is a series of rotor-synchronized 180° pulses applied to one of the spins. Pulses of 180° have the effect of inverting the spin populations among the levels of the particular spin type to which the pulses are applied. In turn, this has the effect of reversing the sign of the dipolar coupling interaction (which depends on the operator $\hat{I}_z \hat{S}_z$) part way through the rotor period, so that the average dipolar coupling over a rotor period is no longer zero.

The TRAPDOR experiment prevents complete refocusing of dipolar coupling between a spin pair in a similar way, namely by altering the strength of the dipolar coupling throughout the rotor period by changing the populations of the Zeeman spin levels of one of the spins. In the TRAPDOR experiment, it is the spin-$\frac{1}{2}$ nucleus which is observed and the populations of the quadrupolar spin levels which are changed through the rotor period. However, the method of changing the quadrupolar spin state populations is quite different to the method used in the REDOR experiment, and rather neat. Instead of a series of 180° pulses as in the REDOR experiment, a continuous rf pulse is applied to the quadrupolar spin for half the required dephasing period and nothing is applied in the second half of the dephasing period (Fig. 3.16). The effect of an rf pulse on quadrupolar spin states is discussed in detail in Chapter 4. Here, suffice to say that both the interaction with the rf field and the quadrupole coupling must be considered during the pulse, as the

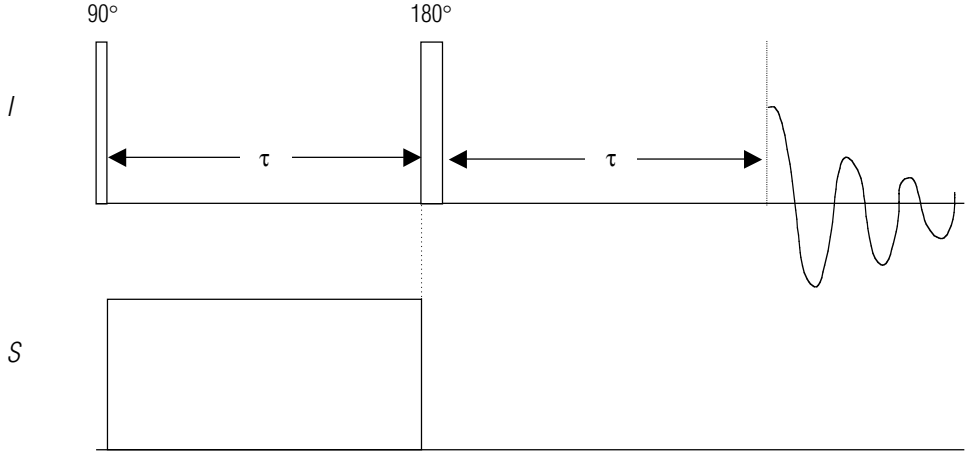

Fig. 3.16 The TRAPDOR pulse sequence, used for measuring dipolar couplings between quadrupolar (particularly $I = 1$) spins and spin-$\frac{1}{2}$ nuclei. The *I* spin sequence is run under magic-angle spinning both with and without (reference spectrum) the *S* spin irradiation. *I* spin spectra are collected for different values of τ from zero upwards, with the proviso that τ is always an integral number of rotor periods. In the absence of the *S* spin irradiation, the *I* spin magnetization is fully refocused at 2τ (except for any loss of signal due to relaxation). The *S* spin irradiation during the first τ period affects the *S* spin state, and so alters the dipolar coupling between *I* and *S* in this period. Switching off the *S* spin irradiation in the second τ period then ensures that the *I*–*S* dipolar coupling has a different time dependence in the second τ period from the first, so that the *I* spin magnetization is not fully refocused now at the end of the period. Cross-polarization from, for example, ^{1}H, is often used to generate the initial *I* spin transverse magnetization, rather than the 90° pulse shown here.

quadrupole coupling is generally large compared to the rf pulse amplitude, so cannot be ignored.

Different molecular orientations in a powder sample have different strengths of quadrupole coupling and so give rise to different energies of spin eigenstates during the pulse (and at other times too, of course). A plot of the energies of the three spin levels for a spin-1 nucleus as a function of quadrupole-coupling strength is shown in Fig. 3.17. Also shown on this plot are the forms of the spin levels at extreme values of the quadrupole coupling.

Now under magic-angle spinning, the molecular orientations are changing continuously, and so therefore does the quadrupole-coupling strength associated with any one crystallite. In effect, then, the nature and energy of the spin-1 eigenstates under magic-angle spinning oscillate between the two extremes on the horizontal axis during a rotor period. This means that the Zeeman level $|+1\rangle$ for instance which exists for large negative ω_Q becomes the Zeeman $|-1\rangle$ level as ω_Q becomes large and positive as a result of sample spinning. Providing the change between the two ω_Q values is done adiabatically, the result is that the population of the $|+1\rangle$ Zeeman level becomes that of the $|-1\rangle$ level, i.e. populations of these Zeeman levels are exchanged, as required in the TRAPDOR experiment. Further examination of Fig. 3.17 shows that, in addition, the $|-1\rangle$ Zeeman level becomes the $|0\rangle$ Zeeman level and $|0\rangle$ becomes $|+1\rangle$ as ω_Q goes from being large and negative to large and positive. Each time the rotor orientation changes such that ω_Q goes through zero (a so-called *zero crossing*), this change of spin levels and concomitant exchange of Zeeman level populations occurs. In turn, changing the nature of the quadrupolar spin eigenstates alters the dipolar coupling between this spin-1 nucleus and the dipolar-coupled spin-$\frac{1}{2}$ one. For instance, the change in eigenstate from $|+1\rangle$ to $|-1\rangle$, as ω_Q varies between large and positive and large and negative, changes the $\hat{S}_z$ eigenvalue from +1 to −1, which has a clear effect on the dipolar coupling which depends on $\hat{I}_z\hat{S}_z$. This then prevents the complete averaging of the dipolar

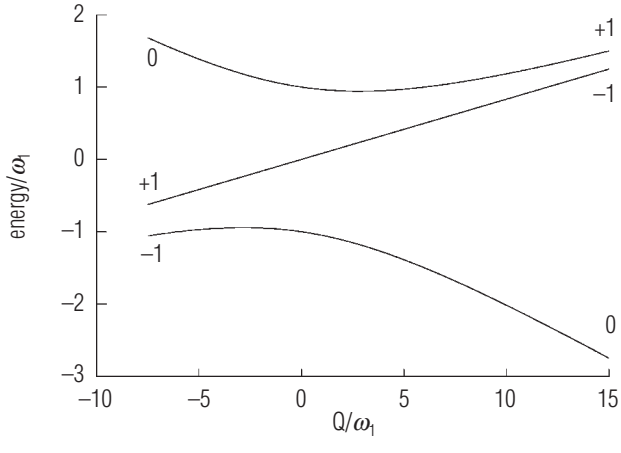

Fig. 3.17 The energies of the three spin levels of an $I = 1$ spin under rf irradiation, as a function of quadrupole-coupling strength. Shown on the plot are the nature of the spin states, Ms, at the extreme values of quadrupole-coupling strength.

coupling by the magic-angle spinning. Each molecular orientation in a powder sample experiences two or four zero crossings per rotor period, depending on the initial crystallite orientation; each zero crossing contributes to the net dephasing of the spin-$\frac{1}{2}$ transverse magnetization.

As already mentioned, this experiment requires the changes in the spin system to be adiabatic. The parameter which determines whether or not this is the case is the adiabaticity parameter, α, which has been determined to be [**21**]

$$\alpha = \frac{\omega_1^2}{\chi \omega_R} \tag{3.7}$$

where ω_1 is the rf pulse amplitude, χ is the *S* spin quadrupole-coupling constant (see Chapter 4 for more details) and ω_R is the sample spinning rate.

Analysis of the results from a TRAPDOR experiment involves calculating the number of zero crossings [**21**] which occur for each crystallite during the dephasing period of the experiment, and assuming that completely efficient transfer of populations occurs at each zero crossing, i.e. perfectly adiabatic passage occurs.

3.4.2 Rotational-echo, adiabatic passage, double resonance

The pulse sequence for the REAPDOR experiment [**22**] is shown in Fig. 3.18. Its operation is similar in principle to the TRAPDOR and REDOR experiments previously described (Sections 3.3.2 and 3.4.1). As in the TRAPDOR experiment, the spin-$\frac{1}{2}$ nucleus is observed. The 180° pulse train applied to the spin-$\frac{1}{2}$ nucleus is a REDOR-like sequence (see Section 3.3) designed to prevent the complete refocusing of the *IS* dipolar coupling under magic-angle spinning; the phases of the pulses shown in Fig. 3.18 ensure that chemical shift offsets however, are refocused as required. The missing 180° pulse in the middle of the spin-$\frac{1}{2}$ pulse train means that in the absence of any pulses on the coupled quadrupolar spin, any evolution under the dipolar coupling which takes place in the first half of the pulse train is refocused in the second half. This then constitutes the reference experiment in REDOR terms. In a second experiment, a transfer of populations between the spin states of the quadrupolar nucleus is effected in a similar way to the TRAPDOR experiment, via a continuous rf pulse applied to that nucleus. However, whereas in the TRAPDOR experiment, the quadrupole spin pulse is applied for half the total dephasing time required, in the REAPDOR experiment, it is always applied for a constant time, which is less than one rotor period.

The two experiments (reference and one with rf pulse on the quadrupolar nucleus) are repeated for different lengths of the spin-$\frac{1}{2}$ pulse train and the extent of dephasing monitored. The spin-$\frac{1}{2}$ pulse train must be incremented by blocks of 8 pulses being added to each half of the pulse train, so as to retain the property of refocusing chemical shift offsets.

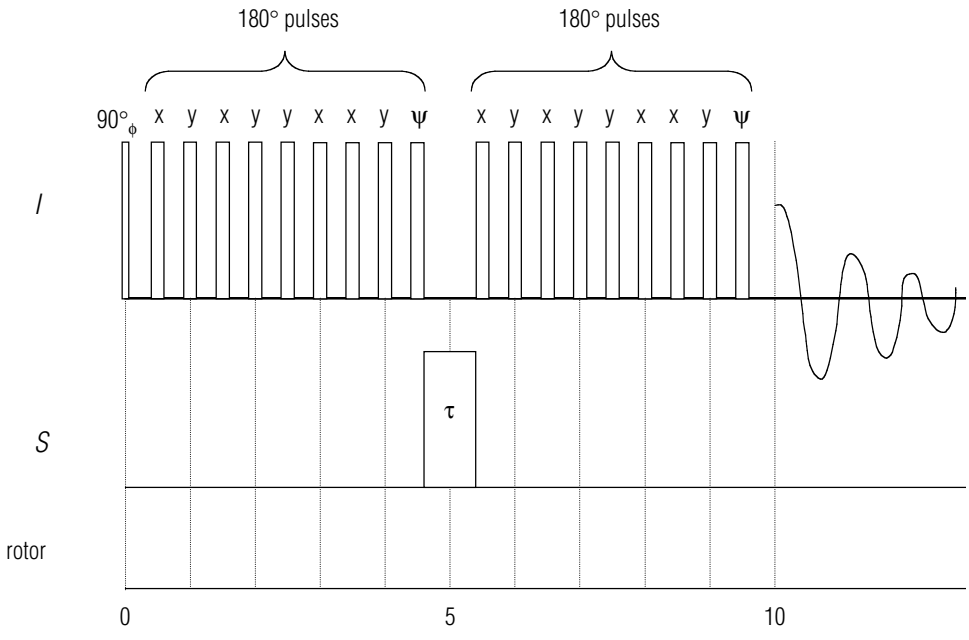

Fig. 3.18 The REAPDOR pulse sequence, used for measuring dipolar couplings between quadrupolar (particularly $I = 1$) spins and spin-$\frac{1}{2}$ nuclei. A reference experiment is recorded without any *S* spin irradiation. In this experiment, dipolar evolution occurs under the first series of *I* spin 180° pulses and is refocused (along with isotropic chemical shifts, chemical shift anisotropies) at the point at which acquisition starts. In the experiment with *S* spin irradiation, a pulse of length τ ($<\tau_R$) is applied to the *S* spin in the middle of the dipolar evolution period, which prevents the refocusing of the *I*–*S* dipolar coupling at the point of acquisition. The experiment is repeated for different dipolar evolution periods. The minimum dipolar evolution period is $8\tau_R$ (as in the illustrated sequence) and is incremented by $8\tau_R$ in successive experiments. As with the TRAPDOR experiment, the initial *I* spin magnetization can be derived from cross-polarization rather than a 90° pulse as shown here.

The advantage of the REAPDOR experiment over TRAPDOR [**22**] is that its analysis is less susceptible to error, if the condition of perfect adiabatic passage (see Section 3.4.1) is not met. Also, a much shorter pulse is required for the transfer of populations on the quadrupolar nucleus, which is technically less demanding. However, the REAPDOR experiment may be more susceptible to small errors in the spin-$\frac{1}{2}$ pulse train (amplitude and timing).

3.5 Techniques for measuring dipolar couplings between quadrupolar nuclei

As discussed in Section 3.4, the large quadrupole coupling suffered by many quadrupolar nuclei renders many of the techniques for measuring dipolar couplings discussed in Sections 3.2–3.4 well nigh useless for purely quadrupolar spin systems. Very few techniques exist for measuring dipolar couplings between quadrupolar spin pairs. Rotational resonance has been shown to be useful in cases where the central

transition (for half-integer quadrupolar nuclei) of the dipolar-coupled spins are well separated [**23**] (see Section 3.2.2 for a discussion of rotational resonance). Dipolar couplings between quadrupolar nuclei can be used in correlation experiments (see Section 3.7), which gives an indication of the spins that are close in space, but these do not give a quantitative measure of the dipolar-coupling constant.

3.6 Correlation experiments

Correlation spectroscopy is common in solution-state NMR, where the scalar or J coupling is most often used to correlate spins that are close together in the bonding network. Most techniques in the solid state utilize the dipolar coupling between spins to indicate which spins are close in space, although solution-like INADEQUATE-type experiments using the J or scalar coupling also exist [**24**]. All these experiments rely on the fact that multiple-quantum coherences can be excited in dipolar-coupled spin systems.

3.6.1 Homonuclear correlation experiments for spin-$\frac{1}{2}$ systems

There are two types of experiment that can be performed on homonuclear spin systems to establish spatial correlations of spins, both of which utilize mutliple-quantum coherences excited between dipolar-coupled spins. Most often, the experiments use the double-quantum coherence which can be excited between a spin-$\frac{1}{2}$ pair, but zero-quantum coherence is relevant in some experiments.

One type of two-dimensional correlation NMR experiment is shown in Fig. 3.19 in which double-quantum coherence is excited and then allowed to evolve in t_1 before being converted to single-quantum coherence to be observed in t_2 [**10**]. The resulting two-dimensional frequency spectrum correlates the double-quantum spectrum in f_1 with a double-quantum filtered single-quantum spectrum in f_2. The advantage of this type of experiment is that the final two-dimensional spectrum only shows signals arising from spin pairs where the two spins are moderately close in space. The intensity of each signal is dependent on the proximity of the two spins; in general, the closer the spins, the stronger the signal. Moreover, because the double-quantum spectrum is correlated with the single-quantum spectrum in this two-dimensional spectrum, we can identify *which* two spins contribute to each signal, and so identify the network of coupled spins (Fig. 3.20). Methods for exciting double-quantum coherence between spin pairs is discussed in Section 3.2.2.

The second type of two-dimensional correlation experiment is the more usual one which correlates two normal, single-quantum spectra, with cross-peaks occurring between signals from spins which are close in space. The general form of such experiments was shown in Fig. 3.2. After initial excitation, transverse magnetiza-

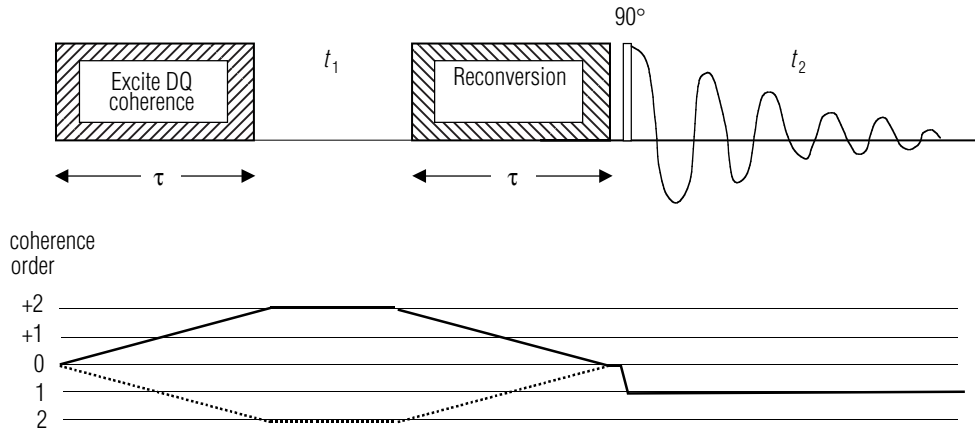

Fig. 3.19 Schematic illustration of a two-dimensional correlation experiment in which a double-quantum coherence spectrum, arising from dipolar-coupled spin pairs, is correlated with the normal single quantum spectrum. The experiments are generally performed under rapid magic-angle spinning so that the spectra in both dimensions are high resolution. Double-quantum coherence is initially excited with the aid of some type of recoupling pulse sequence (to counter the effect of magic-angle spinning which removes the dipolar couplings necessary for the generation of double-quantum coherences). The double-quantum coherence is then allowed to evolve in t_1 before being transferred back into longitudinal magnetization. A 90° pulse then generates observable transverse magnetization from this, for monitoring in t_2. Two separate experiments, employing the $+2 \rightarrow 0 \rightarrow -1$ and $-2 \rightarrow 0 \rightarrow -1$ pathways respectively, are generally performed, in order to produce pure absorption two-dimensional spectra.

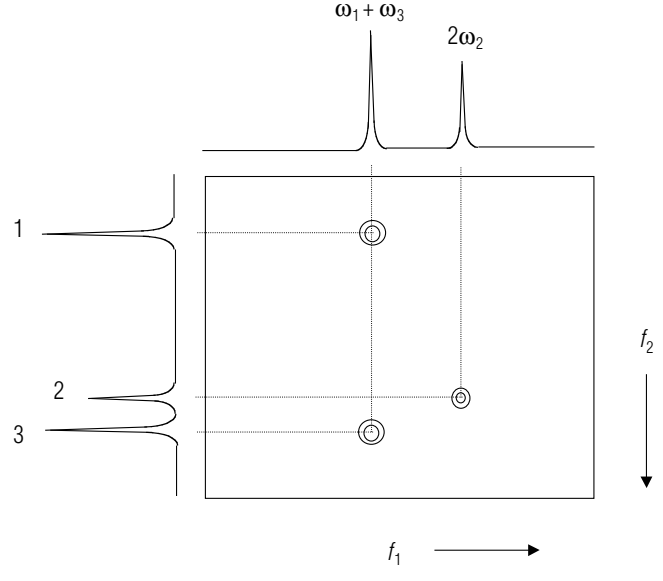

Fig. 3.20 The form of the two-dimensional frequency spectrum arising from the double/single-quantum correlation experiment of Fig. 3.19. The double-quantum spectrum appears in f_1 correlated with the single-quantum spectrum in f_2. A signal at $(\omega_i + \omega_j)$ in the double-quantum spectrum (correlated with signals at ω_i and ω_j in the single-quantum spectrum) indicates that the spins with frequencies ω_i and ω_j have a sufficiently large dipolar coupling between them to generate a significant double-quantum coherence, i.e. these spins are close in space. The spectrum shown indicates that spins 1 and 3 are close together and spins labelled 2 are also close to each other.

tion is allowed to evolve during t_1 at its characteristic frequency. There then follows a mixing period during which magnetization is exchanged or transferred between spins, before the transverse magnetization is regenerated and observed in t_2. The mixing period contains a pulse sequence designed to excite double and/or zero-quantum coherences between dipolar-coupled spin pairs, i.e. generate coherence involving spin pairs rather than the single-spin, single-quantum coherence present previously in t_1. When multiple-quantum coherences involving multiple spins is converted back to single-spin, single-quantum coherence, some coherence ends up on each of the spins involved in the multiple-quantum coherence, i.e. magnetization has in effect been transferred between the spins. Thus, if single-quantum coherence associated with spin 1 (say) in t_1 is converted to a double-quantum coherence between spin 1 and spin 2, the reconversion back to single-quantum coherence then results in single-quantum coherence on spins 1 *and* 2, which then evolves at their respective characteristic frequencies in t_2. A similar fate is suffered by single-quantum coherence associated with spin 2 in t_1. After processing, the resulting two-dimensional spectrum has signals from spins 1 and 2 in the f_1 and f_2 spectra (from the single-quantum coherences which evolve in t_1 and t_2). Moreover, it has cross-peaks between the spin 1 and spin 2 signals, because coherence which started on spin 1 in t_1 has ended up on spin 2 in t_2 (and vice versa).

For both types of experiment, magic-angle spinning is usually used for the sake of resolution in both dimensions of the experiment. This, of course, has the effect of averaging to zero any dipolar couplings on which the correlation experiments rely. Accordingly, the excitation of multiple-quantum coherences must involve some type of recoupling sequence, as discussed in detail in Section 3.2.2 on double-quantum filtering.

There is much interest in performing multiple-quantum correlation experiments in homonuclear spin systems, both in cases where the spin of interest is abundant, and where there are relatively isolated spin pairs. Abundant ^{1}H spin systems in particular have been investigated [**10**]. Generally speaking, the dipolar coupling between ^{1}H spins in systems where protons are abundant causes massive line-broadening, so resolution is a problem in any solid-state ^{1}H NMR spectroscopy. However, very fast magic-angle spinning is able to remove this broadening. The double-quantum/single-quantum correlation type of technique has been successfully applied in ^{1}H NMR to examine the spatial proximity of spins. Very fast magic-angle spinning (often in excess of 30 kHz) is needed to produce high resolution in the single-quantum ^{1}H dimension of the experiment. An example of such an experiment is shown in Fig. 3.21 [**10**].

The more traditional type of single-quantum/single-quantum two-dimensional correlation experiment as outlined above tends to be applied to systems with less abundant spins, particularly systems which have been partly isotopically labelled. An example of such use is shown in Fig. 3.22 on a uniformly labelled cytidine [**25**].

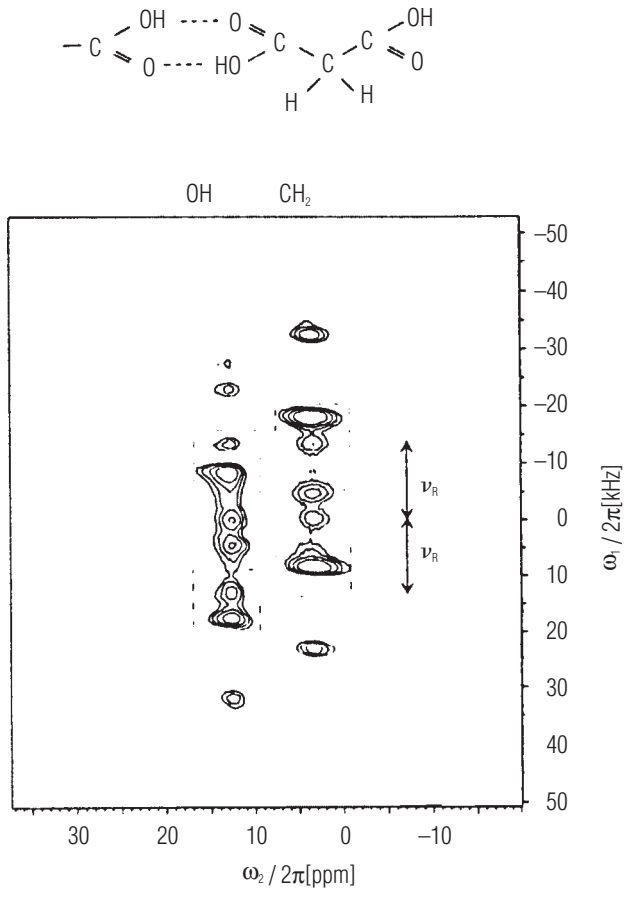

Fig. 3.21 A two-dimensional ^{1}H double-quantum/single-quantum correlation spectrum of malonic acid [**10**]. The experiment is conducted under very rapid magic-angle spinning to produce high-resolution spectra in both dimensions. Double-quantum coherences are generated between the two CH_2 protons and the two OH protons in close proximity and between each proton of the CH_2 and OH groups. Thus each double-quantum spectrum (in ω_1) consists of four lines plus spinning sidebands. (Taken from Gottwald, Demco, Graf *et al.* (1995).)

In this experiment, the RFDR recoupling pulse sequence [8] is used in the mixing period.

3.6.2 Homonuclear correlation experiments for quadrupolar spin systems

In principle, the same experiments that have been devised for spin-$\frac{1}{2}$ correlation experiments could be applied to quadrupolar spin systems, providing hard, non-selective pulses are used throughout (as for spin-$\frac{1}{2}$ systems). However, this latter proviso is rather harder to achieve for quadrupolar spins than for spin-$\frac{1}{2}$, because quadrupolar spins are generally subject to quadrupole coupling interactions which can broaden their respective NMR spectra by MHz. Given that rf pulses generate interactions which are at best a few hundred kHz in magnitude, it is clear that any rf pulse can only irradiate a small portion of the total spectrum. Accordingly, alternative methods must be found for generating multiple-quantum coherences between

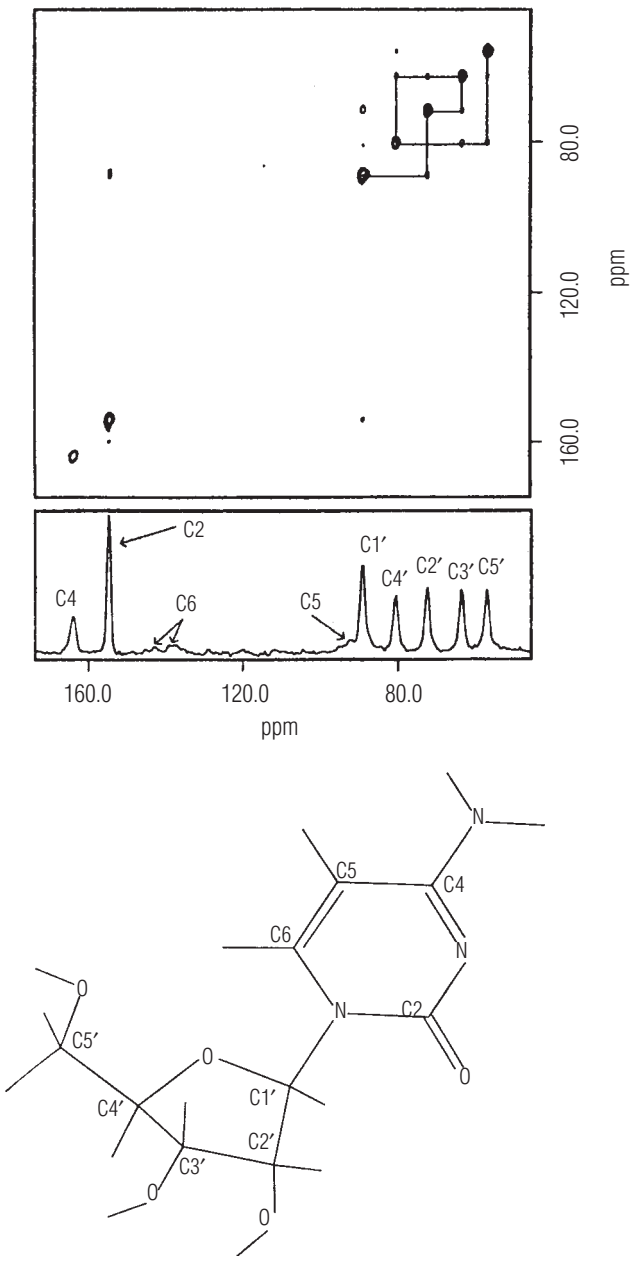

Fig. 3.22 Two-dimensional ^{13}C single-quantum/single-quantum correlation spectrum of cytidine–U–^{13}C–^{15}N [**25**]. The RFDR recoupling scheme [**8**] is used in the mixing period of the experiment to transfer polarization between ^{13}C spins which are close in space. (Taken from Kiihne, Geahigan, Oyler *et al.* (1999).)

quadrupolar spins, but only two methods have been reported in the literature so far. One experiment [**26**] generates 4*I*-quantum coherences between dipolar-coupled spin *I* pairs, where *I* is a half-integer spin. The 4*I*-quantum coherence is allowed to evolve in t_1 before being converted to observable single-quantum coherence for observation in t_2. The resulting 4*I*-quantum/single-quantum two-dimensional cor-

relation spectrum is equivalent to the double-quantum/single-quantum correlation spectrum for spin-$\frac{1}{2}$ nuclei discussed in Section 3.6.1. The second method is a single-quantum/single-quantum correlation technique [**27**] where a single, relatively long, but weak rf pulse is used in the mixing period to generate double-quantum coherence involving the central transitions of dipolar-coupled half-integer quadrupolar nuclei. By using a weak rf pulse, the averaging effect of magic-angle spinning on the dipolar coupling is disrupted [**27**]. An additional complication for quadrupolar spins is that it is quite possible to excite multiple-quantum coherences on a single spin, which do not of course depend on the dipolar coupling between spins at all. The advantage of the 4*I*-quantum correlation experiment is that 4*I*-quantum coherence can only arise from dipolar-coupled spins and not from a single spin [**26**].

3.6.3 Heteronuclear correlation experiments for spin-$\frac{1}{2}$

Single-quantum/single-quantum heteronuclear correlation experiments, similar to those described in Section 3.6.1 for homonuclear spin systems, are quite common in solid-state NMR. The form of the experiments is depicted in Fig. 3.23, and is very similar to that for homonuclear spin systems although the pulse sequence in the mixing period is often much simpler than that used in homonuclear spin systems. Most often, the mixing sequence used in heteronuclear correlation experiments to promote transfer of magnetization between heteronuclei is a simple cross-polarization step, with a properly adjusted contact pulse being applied to each nucleus (Fig. 3.23). Cross-polarization is discussed in detail in Section 2.5.

Magic-angle spinning is usually applied in such experiments, and clearly this can affect the efficiency of the cross-polarization step. Several methods have been used to circumvent this problem, such as using ramped contact pulses, as discussed in Section 2.5.

One frequently used heteronuclear correlation experiment is the WISE (WIdeline SpEctroscopy) experiment, which is particularly used in studies of molecular motion. This experiment is discussed in Chapter 6. A specific example of heteronuclear correlation for structural study is shown in Fig. 3.24 [**28**].

3.7 Spin-counting experiments

Dipolar coupling in extensive homonuclear spin systems allows spin-counting experiments to be performed. By spin counting, we mean the determination of the number of spins in close proximity (see Fig. 3.3). As shown in Chapter 1 (Box 1.4), in a homonuclear many-spin system, the eigenstates (or coupled spin states) of the system are described by the total nuclear spin in the laboratory z direction, M:

$$M = m_1 + m_2 + m_3 + \ldots + m_N \tag{3.5}$$

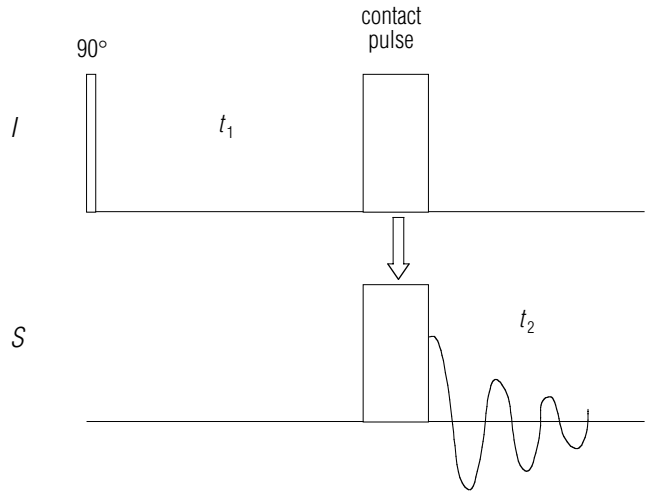

Fig. 3.23 The form of a heteronuclear correlation experiment. The experiment begins by exciting single-quantum coherence (transverse magnetization) on one of the spins (*I* in this case) and allows it to evolve at its characteristic frequency in t_1. Contact pulses applied to both spins at the end of t_1 result in cross-polarization from spin *I* to spin *S*, after which the resulting *S* spin transverse magnetization is observed in t_2. The resulting two-dimensional frequency spectrum displays a single-quantum *I* spin spectrum in f_1 and a single-quantum *S* spin spectrum in f_2, but only signals from *I* spins which are close to *S* spins appear, and vice versa. A peak in the two-dimensional spectrum at (ω_I, ω_S) indicates that the spins with spectral frequencies ω_I and ω_S are close in space.

where N is the number of coupled spins. As mentioned in the Introduction to this chapter (Section 3.1), multiple-quantum coherences of order ΔM can be excited between them, where $\Delta M = M_i - M_j$, with i and j being the M states involved in the coherence. By following the amplitude of different multiple-quantum coherences as a function of their excitation time, the value of N, the number of spins in the cluster, can be estimated.

Most spin-counting experiments have been performed on non-spinning samples [**29**], although experiments under magic-angle spinning are also possible [**30**]. The aim of the experiment is two-fold; firstly, to separate coherences of different order and then to examine their amplitudes as a function of the length of time for which the coherences are excited. By following the extent to which higher-order coherences are excited as a function of excitation time, detailed information on the size of spin clusters can be obtained.

3.7.1 The formation of multiple-quantum coherences

In Section 3.2.2, we showed how double-quantum coherences can be generated (albeit under magic-angle spinning). In fact, higher-order coherences can be excited with exactly the same pulse sequences that generate double quantum coherences [**13**]. To investigate this, we examine the simplest possible pulse sequence known to create double-quantum coherence, namely 90°–τ–90°. The density operator is a con-

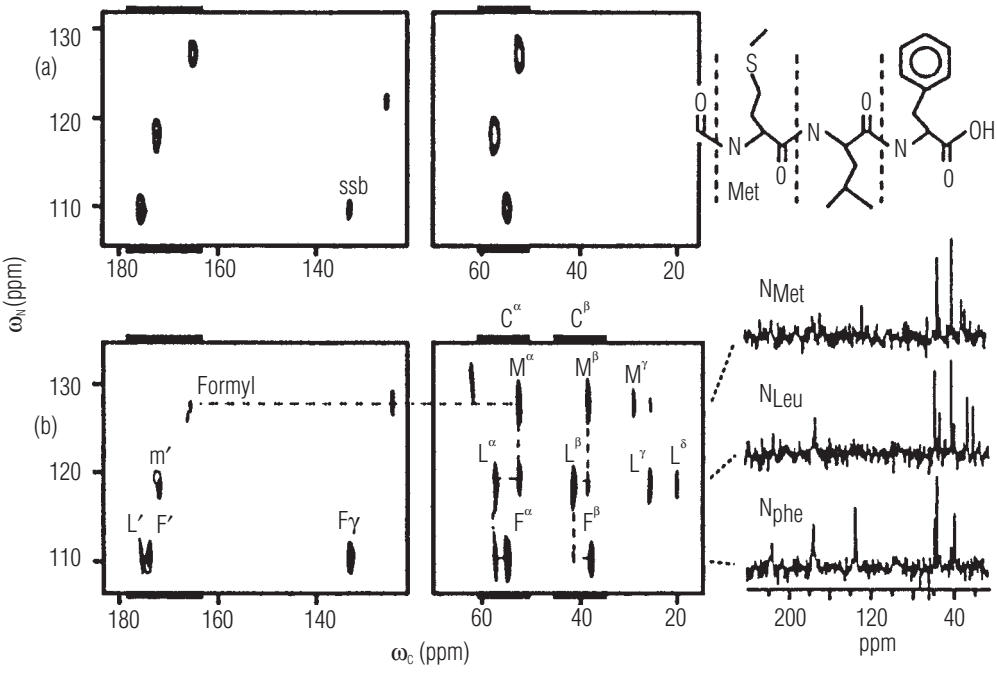

Fig. 3.24 Two-dimensional ^{15}N–^{13}C (single-quantum) correlation spectrum of the formyl–Met–Leu–Phe amino acid sequence shown in the figure. The experiment is conducted under magic-angle spinning and uses a REDOR sequence to recouple ^{13}C–^{15}N dipolar coupling during mixing periods. ^{13}C transverse magnetization is created initially by cross-polarization from ^{1}H. A REDOR-based polarization transfer from $^{13}C \rightarrow {}^{15}N$ then takes place during a mixing period τ_m, following which ^{15}N transverse magnetization is allowed to evolve for t_1. A similar REDOR mixing sequence is then applied for τ_m to transfer the remaining ^{15}N transverse magnetization back to ^{13}C. A ^{13}C FID is then collected in t_2. By this sequence of polarization transfer steps, only signals from ^{13}C and ^{15}N sites which are close in space are seen in the final spectrum. The longer the mixing time, the greater the distance between $^{13}C/^{15}N$ spins which contribute to the final spectrum. Two spectra are shown (a) mixing time $\tau_m = 614.4\,\mu s$ ($2\tau_R$) and (b) $\tau_m = 2.46\,ms$ ($8\tau_R$). (Taken from Hong and Griffiu (1998).)

venient means of studying the state of a spin system from our point of view, as the density operator formalism leads naturally to a description of the coherences that have been generated.

The equilibrium density operator before the 90°–τ–90° sequence is applied is proportional to $\hat{I}_z$, where $\hat{I}_z$ is given by

$$\hat{I}_z = \sum_i^N \hat{I}_z^i \tag{3.8}$$

where the sum is over all the spins in the cluster. The initial (hard) 90° pulse, of phase y for the sake of argument, transforms the density operator to $\hat{I}_x (\hat{I}_x = \Sigma_i^N \hat{I}_x^i)$. The density operator then evolves during τ under a hamiltonian, $\hat{H}_{\text{int}}$, which describes all the spin interactions present, namely chemical shifts and dipolar couplings between spins:

$$\hat{H}_{\text{int}} = \hat{H}_{\text{cs}} + \hat{H}_{\text{dd}} \tag{3.9}$$

where

$$\hat{H}_{\mathrm{cs}} = -\sum_i \omega_{\mathrm{cs},i}\hat{I}_z^i \qquad \hat{H}_{\mathrm{dd}} = -\sum_{i>j} C_{ij}(3\hat{I}_z^i\hat{I}_z^j - \hat{\mathrm{I}}^i \cdot \hat{\mathrm{I}}^j) \tag{3.10}$$

The density operator after a time t of this evolution is given by the usual expression (see Chapter 1)

$$\hat{\rho}(t) = \exp(-i\hat{H}_{\mathrm{int}}t)\hat{\rho}(0)\exp(i\hat{H}_{\mathrm{int}}t) \tag{3.11}$$

where $\hat{\rho}(0)$ is the density operator at the start of the evolution period, i.e. $\hat{I}_x$. Equation (3.11) can be expanded by use of the Magnus expansion (see Box 1.2, Chapter 1):

$$\hat{\rho}(t) = \hat{\rho}(0) + it[\hat{\rho}(0), \hat{H}_{\mathrm{int}}] - \frac{1}{2}t^2[[\hat{\rho}(0), \hat{H}_{\mathrm{int}}], \hat{H}_{\mathrm{int}}] + \ldots \tag{3.12}$$

Now, we examine what terms arise in the density operator at time t by virtue of Equation (3.12). The commutator $[\hat{\rho}(0), \hat{H}_{\mathrm{int}}]$ (= $\hat{\rho}(0)\hat{H}_{\mathrm{int}} - \hat{H}_{\mathrm{int}}\hat{\rho}(0)$) in Equation (3.12) for the density operator gives rise to spin operator terms such as

$$\begin{aligned}\hat{I}_{1x}\hat{I}_{1z}\hat{I}_{2z} - \hat{I}_{1z}\hat{I}_{2z}\hat{I}_{1x} &= (\hat{I}_{1x}\hat{I}_{1z} - \hat{I}_{1z}\hat{I}_{1x})\hat{I}_{2x} \\ &= [\hat{I}_{1x}, \hat{I}_{1z}]\hat{I}_{2z} \\ &= -i\hbar\hat{I}_{1y}\hat{I}_{2z}\end{aligned} \tag{3.13}$$

in the density operator $\hat{\rho}(t)$ when we substitute for $\hat{\rho}(0)$ and $\hat{H}_{\mathrm{int}}$ and where 1 and 2 label particular spins in the spin cluster. In generating (3.12), we have used the fact that spin operators associated with different spins all commute with one another. The term $[[\hat{\rho}(0), \hat{H}_{\mathrm{int}}], \hat{H}_{\mathrm{int}}]$ in Equation (3.12) then yields spin operator terms such as

$$\begin{aligned}\hat{I}_{1y}\hat{I}_{2z} \cdot \hat{I}_{1z}\hat{I}_{3z} - \hat{I}_{1z}\hat{I}_{3z} \cdot \hat{I}_{1y}\hat{I}_{2z} &= (\hat{I}_{1y}\hat{I}_{1z} - \hat{I}_{1z}\hat{I}_{1y})\hat{I}_{2z}\hat{I}_{3z} \\ &= [\hat{I}_{1y}, \hat{I}_{1z}]\hat{I}_{2z}\hat{I}_{3z} \\ &= i\hbar\hat{I}_{1x}\hat{I}_{2z}\hat{I}_{3z}\end{aligned} \tag{3.14}$$

in the density operator $\hat{\rho}(t)$, i.e. terms involving up to three spins. The higher-order terms (not shown explicitly in Equation (3.12)) have nested commutators which give rise to terms in the density operator involving progressively more and more spins, up to terms of the form $\hat{I}_{1x}\hat{I}_{2z}\hat{I}_{3z}\ldots\hat{I}_{(N-1)z}\hat{I}_{Nz}$ and all permutations of this.

A $90°_x$ pulse at the end of the τ period then converts a term $\hat{I}_{1x}\hat{I}_{2z}\hat{I}_{3z}$ (for instance) in the density operator into $\hat{I}_{1x}\hat{I}_{2y}\hat{I}_{3y}$ and terms like $\hat{I}_{1x}\hat{I}_{2z}\hat{I}_{3z}\ldots\hat{I}_{(N-1)z}\hat{I}_{Nz}$ into $\hat{I}_{1x}\hat{I}_{2y}\hat{I}_{3y}\ldots\hat{I}_{(N-1)y}\hat{I}_{Ny}$. If the $\hat{I}_x$ and $\hat{I}_y$ terms are rewritten in terms of the raising and lowering operators, $\hat{I}_+$ and $\hat{I}_-$ ($\hat{I}_x = (\hat{I}_+ + \hat{I}_-)/2$; $\hat{I}_y$ ($\hat{I}_+ - \hat{I}_-)/2i$) it then becomes apparent that $\hat{I}_{1x}\hat{I}_{2y}\hat{I}_{3y}$, for instance, consists of a sum of terms ranging from $\hat{I}_{1+}\hat{I}_{2+}\hat{I}_{3+}$, representing triple (+3) quantum coherence, through things like $\hat{I}_{1+}\hat{I}_{2+}\hat{I}_{3-}$ (+1 quantum coherence) to $\hat{I}_{1-}\hat{I}_{2-}\hat{I}_{3-}$ (−3 quantum coherence). In general, a term, $\hat{I}_{1x}\hat{I}_{2y}\hat{I}_{3y}\ldots$

$\hat{I}_{(N-1)y}\hat{I}_{Ny}$ represents all orders of coherence from the maximum $+N$ to the minimum $-N$ in steps of two.

It is clear then that high orders of coherence can be excited with this simple pulse sequence, the limit on the maximum order being which and how many pairs of spins appear in the dipolar coupling hamiltonian, $\hat{H}_{\mathrm{dd}}$ in Equation (3.10).

The next question is: What is the amplitude of each of these multiple quantum coherences? The amplitude of each coherence is its coefficient in the expression for the density operator, $\hat{\rho}(t)$. The term $\hat{I}_{1x}\hat{I}_{2y}\hat{I}_{3y}$, for instance, arising from the $[[\hat{\rho}(0), \hat{H}_{\mathrm{int}}], \hat{H}_{\mathrm{int}}]$ term in Equation (3.12) for the density operator, is multiplied by $\tau^2 d_{12}d_{13}$ where d_{12} is the dipolar-coupling constant for the dipolar coupling between spins 1 and 2 and d_{13} is that for spins 1 and 3; τ is the length of the evolution period between the 90° pulses in the excitation period.

In a similar manner, higher-order terms in Equation (3.12) give rise to terms in the density operator involving more spins and are multiplied by $\tau^n d_{12} \ldots d_{1n}$, where n is the order of the term in Equation (3.12). The terms arising from the nth-order terms of Equation (3.12) give rise to a maximum coherence order of $+(n + 1)$ in the density operator. Clearly, the amplitude of these coherences depends on the size of $\tau^n d_{12} \ldots d_{1n}$. If $\tau d_{ij} << 1$, then the higher-order terms of Equation (3.12) for the density operator are negligible and so the amplitude of higher-order coherences is very small. As τd_{ij} increases, however, the amplitude of the higher-order terms increases. Thus, as the τ delay in the pulse sequence is increased, so the amplitude of the higher-order coherences increases. The density operator, however, is always dominated by terms corresponding to the lower-order coherences, simply from the form of Equation (3.12) and the dependence of each term on a factor $\tau^n d_{12} \ldots d_{1n}$. It is worth noting that the amplitude of all coherences also depends on the various dipolar coupling constants between the spins involved in the coherence.

Finally, it is worth noting that a 90°–τ–90° sequence, where the two 90° pulses differ in phase by 90°, results in odd orders of coherence being excited (as in the above analysis), whereas when the two 90° pulses have the same phase, even orders of coherence are excited. That this is so can be easily seen by examining the above analysis for a $90°_y$–τ–$90°_y$ sequence. The final $90°_y$ pulse (rather than $90°_x$) transforms terms like $\hat{I}_{1x}\hat{I}_{2z}\hat{I}_{3z}$ into $-\hat{I}_{1z}\hat{I}_{2x}\hat{I}_{3x}$, which contains as its maximum quantum coherence $-\hat{I}_{1z}\hat{I}_{2+}\hat{I}_{3+}$, representing +2 coherence, and $-\hat{I}_{1z}\hat{I}_{2-}\hat{I}_{3-}$ (–2 quantum coherence) as its minimum quantum coherence, plus two other terms representing zero quantum coherence.

3.7.2 Implementation of spin-counting experiments

Although multiple-quantum coherences can be excited with a 90°–τ–90° pulse sequence, as illustrated in the previous section, it is only really effective at exciting the higher orders if the rf pulse power is very high, higher than can be achieved in

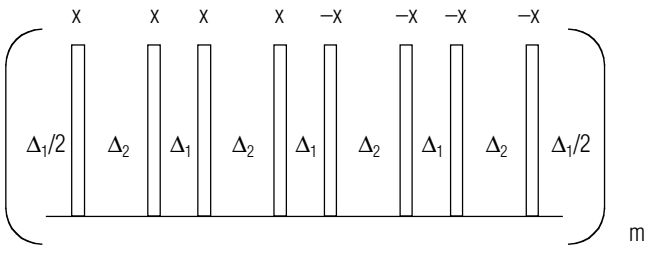

Fig. 3.25 The pulse sequence used for exciting multiple-quantum coherence orders in spin-counting experiments (static samples). All pulses are 90° pulses with the phases shown. The delays between pulses, Δ_1 and Δ_2 are such that $\Delta_2 = 2\Delta_1 + t_p$ where t_p is the 90° pulse length. In general, the longer the excitation sequence (i.e. the higher the value of m), the higher the orders of multiple-quantum coherences excited.

practice. Accordingly, other pulse sequences have been developed which are effective at moderate rf pulse powers [**13**]. The one which is commonly used is shown in Fig. 3.25. The experiments are generally carried out on non-spinning samples, so there is no need to counter the effect of magic-angle spinning during the multiple-quantum coherence excitation. The multiple-quantum coherences are then allowed to evolve during t_1 before being converted back to longitudinal magnetization. The reconversion step is achieved by a 'time-reversed' version of the excitation sequence. The need for 'time reversal' to prevent dipolar dephasing is discussed in Box 3.3. It is even more important here than in double-quantum experiments, because a given order of coherence, n, can arise from the nth-order term in Equation (3.12) for the density operator, *and from all higher-order terms greater than n* in Equation (3.12). Thus, there are potentially many contributions to a given order of coherence, which all in general have different phases (and therefore destructively interfere) unless the whole pulse sequence has so-called time-reversal symmetry.

After the reconversion to longitudinal magnetization, a period of a few milliseconds is allowed for unwanted coherences to dephase before a 90° pulse is applied to create transverse magnetization which is monitored in the subsequent t_2 period in the usual way. Two-dimensional Fourier transformation would then produce the normal single-quantum spectrum in f_2 and a spectrum in f_1 containing signals from all the multiple-quantum coherence orders excited in the experiment. Although signals from different multiple-quantum coherence orders have different frequencies, they may not be very different, and so there is a tendency for signals from different coherence orders to overlap. To separate the different coherence orders, the phases of the rf pulses in the reconversion step are shifted in concert with t_1. This results in a phase shift of all the components of longitudinal magnetization resulting from the reconversion, the phase shift being proportional to the order of coherence each component arose from. Thus the data acquired in t_2 behaves as though each coherence order in t_1 is phase shifted in proportion to the order of the coherence, i.e. appears to have evolved through an extra, order-dependent angle. Two-

dimensional Fourier transformation now results in well-separated signals for different coherence orders in f_1.

In general, the longer the excitation period in these experiments, the higher the maximum order of coherence excited, as discussed in the previous section. Much information about the size and geometry of spin clusters can be obtained by following the amplitude of different coherence orders as a function of excitation time [28].

Notes

1. The only remaining approximation is that the rf pulse amplitude is much larger than the dipolar coupling, i.e. the dipolar coupling can be ignored during a pulse.
2. The rotating frame here is the usual rotating frame that we first met in Chapter 1; the frame rotates about $\mathbf{B}_0$ at frequency ω_{rf}, the frequency of the rf pulse. In this frame, the time-dependence of the magnetic field due to the pulse is removed.

References

1. D.M. Brink and G.R. Satchler, *Angular Momentum*, Clarendon Press, Oxford.
2. R.N. Zare, *Angular Momentum*, Wiley.
3. H.W. Spiess, *Dynamic NMR Spectroscopy. NMR Basic Principles and Progress* **15** (1978) 55.
4. R. Tycko and G. Dabbagh, *Chem. Phys. Lett.* **173** (1990) 461.
5. R. Tycko and S.O. Smith, *J. Chem. Phys.* **98** (1993) 932.
6. C.A. Klug, W. Zhu, M.E. Merritt and J. Schaefer, *J. Magn. Reson.* **109** (1994) 134.
7. B.Q. Sun, P.R Costa, D. Kocisko, R.T. Lansbury and R.G. Griffin, *J. Chem. Phys.* **102** (1995) 702.
8. D.K. Sodrickson, M.H. Levitt, S. Vega and R.G. Griffin, *J. Chem. Phys.* **98** (1993) 6742.
9. R.Tycko and G. Dabbagh, *J. Am. Chem. Soc.* **113** (1991) 9444.
10. J. Gottwald, D.E. Demco, R. Graf and H.W. Spiess, *Chem. Phys. Lett.* **243** (1995) 314.
11. A. Brinkman, M. Eden and M.H. Levitt, *J. Chem. Phys.* **112** (2000) 8539.
12. M. Carravetta, M. Eden, X. Zhao, A. Brinkmann and M.H. Levitt, *Chem. Phys. Lett.* **321** (2000) 205.
13. J. Baum, M. Munowitz, A.N. Garroway and A. Pines, *J. Chem. Phys.* **83** (1985) 2015.
14. D.P. Raleigh, M.H. Levitt and R.G. Griffin, *Chem. Phys. Lett.* **146** (1988) 71.
15. S.E. Shore, J.P. Ansermet, C.P. Slichter and J.H. Sinfelt, *Phys. Rev. Lett.* **58** (1987) 953.
16. T. Gullion and J. Schaefer, *J. Magn. Reson.* **81** (1989) 196.
17. Y. Pan, T. Gullion and J. Schaefer, *J. Magn. Reson.* **90** (1990) 330.
18. K.T. Mueller, *J. Magn. Reson. A* **113** (1995) 81.
19. See, for instance, T.P. Jarvie, R.M. Wenslow and K.T. Mueller, *J. Am. Chem. Soc.* **117** (1995) 570.
20. C. Fernandez, D.P. Lang, J.P. Amoureux and M. Pruski, *J. Am. Chem. Soc.* **120** (1998) 2672; M. Pruski, A. Bailly, D.P. Lang, J.P. Amoureux and C. Fernandez, *Chem. Phys. Lett.* **307** (1999) 35.
21. C.P. Grey and W.S. Veeman, *Chem. Phys. Lett.* **192** (1992) 379.
22. T. Gullion, *Chem. Phys. Lett.* **246** (1995) 325.
23. M. Nijman, M. Ernst, A.P.M. Kentgens and B.H. Meier, *Molec. Phys.* **98** (2000) 161.
24. A. Lesage, D.C. Auger, S. Calderelli and L. Emsley, *J. Am. Chem. Soc.* **119** (1997) 7867; A. Lesage, D.D. Sakellariou, S. Steuernagel and L. Emsley, *J. Am. Chem. Soc.* **120** (1998) 13194.

25. S.R. Kiihne, K.B. Geahigan, N.A. Oyler, H. Zebroski, M.A. Mehta and G.P. Drobny, *J. Phys. Chem. A* **103** (1999) 3890.
26. M.J. Duer and A.J. Painter, *Chem. Phys. Lett.* **313** (1999) 763.
27. M. Baldus, D. Rovnyak and R.G. Griffin, *J. Chem. Phys.* **112** (2000) 5902.
28. M. Hong and R.G. Griffin, *J. Am. Chem. Soc.* **120** (1998) 7113.
29. J. Baum and A. Pines, *J. Am. Chem. Soc.* **108** (1986) 7447.
30. B.H. Meier and W.L. Earl, *J. Chem. Phys.* **85** (1986) 4905.

Solid-State NMR Spectroscopy Principles and Applications
Edited by Melinda J. Duer
Copyright © 2002 by Blackwell Science Ltd

Chapter 4
Quadrupole Coupling: Its Measurement and Uses

Melinda J. Duer and Ian Farnan

4.1 Theory

4.1.1 The quadrupole hamiltonian

Some 74% of NMR active nuclei have a spin greater than $\frac{1}{2}$, and so are quadrupolar. That is to say, they possess a nuclear electric quadrupole moment, which in turn is able to interact with any electric field gradient at the nucleus. Such gradients arise naturally in solids for all nuclei not at a site of cubic symmetry by virtue of the distribution of other nuclei and electrons in their vicinity. The basic form of the quadrupole hamiltonian, describing the interaction between a nuclear electric quadrupole moment and an electric field gradient is [**1**] (in angular frequency units):

$$\hat{H}_{\mathrm{Q}} = \frac{eQ}{6I(2I-1)\hbar}\hat{\mathbf{I}}\cdot e\mathbf{q}\cdot\hat{\mathbf{I}} \tag{4.1}$$

for a spin I, where $e\mathbf{q}$ is the electric field gradient at the nucleus (a second-rank tensor), $\hat{\mathbf{I}}$ is the nuclear spin vector and Q is the nuclear quadrupole moment. This can be simply rewritten in terms of the Cartesian components of $\hat{\mathbf{I}}$ and $e\mathbf{q}$ by expanding the tensor product in Equation (4.1):

$$\hat{H}_{\mathrm{Q}} = \frac{eQ}{6I(2I-1)\hbar}\sum_{\substack{\alpha,\beta= \\ x,y,z}} eq_{\alpha\beta}\left[\frac{3}{2}(\hat{I}_\alpha\hat{I}_\beta + \hat{I}_\beta\hat{I}_\alpha) - \delta_{\alpha\beta}\hat{I}^2\right] \tag{4.2}$$

It is then conventional to define the parameters,

$$eq = eq_{ZZ}^{\mathrm{PAF}} \quad \text{and} \quad \eta_{\mathrm{Q}} = \frac{q_{XX}^{\mathrm{PAF}} - q_{YY}^{\mathrm{PAF}}}{q_{ZZ}^{\mathrm{PAF}}} \tag{4.3}$$

where η_{Q} is known as the (*quadrupolar*) *asymmetry parameter* and the electric field gradient tensor is expressed in its principle axis frame (PAF) in which it is

diagonal; the elements of the tensor in this frame are labelled $eq_{\alpha\alpha}^{\mathrm{PAF}}$. The axes in this frame are labelled $x^{\mathrm{PAF}}, y^{\mathrm{PAF}}, z^{\mathrm{PAF}}$ to distinguish them from the laboratory frame (x, y, z). The orientation of the PAF is determined by the chemical structure around the nucleus. In the PAF frame, the quadrupole hamiltonian in (4.2) becomes simply (again, in angular frequency units):

$$\hat{H}_{\mathrm{Q}} = \frac{e^2qQ}{4I(2I-1)\hbar}\left[3\hat{I}^2_{z^{\mathrm{PAF}}} - \hat{I}^2 + \eta\left(\hat{I}^2_{x^{\mathrm{PAF}}} - \hat{I}^2_{y^{\mathrm{PAF}}}\right)\right] \tag{4.4}$$

The derivation of Equation (4.4) from Equation (4.2) uses the fact that the electric field gradient tensor is traceless (in any frame), i.e. $q_{xx} + q_{yy} + q_{zz} = 0$. If $\mathrm{Tr}(e\mathbf{q})$ were not zero, there would be a net force on the nucleus from the electric quadrupole interaction, and thus the nucleus would not be in equilibrium. The constant $e^2qQ/\hbar$ is known as the *quadrupole-coupling constant* and is given the symbol χ here (units rad s^{-1}). The quadrupole-coupling constant in units of Hz is often denoted C_{Q} $(= e^2qQ/h)$. The *quadrupole-coupling tensor* is also a term often used and is given by $\chi = (e^2qQ/\hbar)\mathbf{q}$.

The formulation of the quadrupole hamiltonian in Equation (4.4) is completely correct, but not very useful for dealing with NMR experiments. In the NMR experiment, the Zeeman interaction between applied magnetic field and nuclear spin is the dominant interaction. The hamiltonian describing this interaction is

$$\hat{H}_0 = -\omega_0\hat{I}_z \tag{4.5}$$

where ω_0 is the Larmor frequency and z is the direction of the applied magnetic field. Clearly we need to re-express Equation (4.4) in terms of the frame (x, y, z) (the laboratory frame) in which the Zeeman interaction is naturally described, rather than in terms of $(x^{\mathrm{PAF}}, y^{\mathrm{PAF}}, z^{\mathrm{PAF}})$, the principal axis frame for the quadrupole interaction. $\hat{I}_{x^{\mathrm{PAF}}}$, $\hat{I}_{y^{\mathrm{PAF}}}$, $\hat{I}_{z^{\mathrm{PAF}}}$ in Equation (4.4) are related to $\hat{I}_x$, $\hat{I}_y$, $\hat{I}_z$ through

$$\begin{pmatrix} \hat{I}_x \\ \hat{I}_y \\ \hat{I}_z \end{pmatrix} = \mathbf{R}(\theta, \phi)\begin{pmatrix} \hat{I}_{x^{\mathrm{PAF}}} \\ \hat{I}_{y^{\mathrm{PAF}}} \\ \hat{I}_{z^{\mathrm{PAF}}} \end{pmatrix} \tag{4.6}$$

where $\mathbf{R}(\theta, \phi)$ is the rotation matrix which rotates the principal axis frame $(x^{\mathrm{PAF}}, y^{\mathrm{PAF}}, z^{\mathrm{PAF}})$ into the laboratory frame (x, y, z) (see Box 1.2 in Chapter 1 for further discussion of rotations). The angles (θ, ϕ) are spherical polar angles describing the orientation of the laboratory frame z axis (as defined by $\mathbf{B}_0$) in the PAF; no third angle is needed to describe the relationship between the two frames, as the x and y axes of the laboratory frame are arbitrary. We can then write $\hat{H}_{\mathrm{Q}}$ in the laboratory frame (x, y, z), by substituting appropriate linear combinations of $\hat{I}_x$, $\hat{I}_y$, $\hat{I}_z$ in Equation (4.4) for $\hat{I}_{x^{\mathrm{PAF}}}$, $\hat{I}_{y^{\mathrm{PAF}}}$, $\hat{I}_{z^{\mathrm{PAF}}}$ with the aid of Equation (4.6) to find the linear combinations:

$$\begin{aligned}\hat{H}_{\mathrm{Q}} = {} & \frac{e^2qQ}{4I(2I-1)\hbar}\left\{\frac{1}{2}(3\cos^2\theta - 1)(3\hat{I}_z^2 - \hat{I}^2)\right. \\ & + \frac{3}{2}\sin\theta\cos\theta[\hat{I}_z(\hat{I}_+ + \hat{I}_-) + (\hat{I}_+ + \hat{I}_-)\hat{I}_z] \\ & \left. + \frac{3}{4}\sin^2\theta(\hat{I}_+^2 + \hat{I}_-^2)\right\} \\ & + \eta_{\mathrm{Q}}\frac{e^2qQ}{4I(2I-1)\hbar}\left\{\frac{1}{2}\cos 2\phi[(1-\cos^2\theta)(3\hat{I}_z^2 - \hat{I}^2)\right. \\ & + (\cos^2\theta + 1)(\hat{I}_+^2 + \hat{I}_-^2)] \\ & + \frac{1}{2}\sin\theta[(\cos\theta\cos 2\phi - i\sin 2\phi)(\hat{I}_+\hat{I}_z + \hat{I}_z\hat{I}_+) \\ & + (\cos\theta\cos 2\phi + i\sin 2\phi)(\hat{I}_-\hat{I}_z + \hat{I}_z\hat{I}_-)] \\ & \left. + (i/4)\sin 2\phi\cos\theta(\hat{I}_+^2 - \hat{I}_-^2)\right\} \end{aligned} \tag{4.7}$$

where x, y, z refer to the laboratory frame. θ and ϕ are determined by the orientation of the chemical structure containing the nucleus with respect to the applied field (along z). If the nucleus is part of a molecule, θ and ϕ are determined by the molecular orientation in the applied field. The operators $\hat{I}_+$ and $\hat{I}_-$ are defined in Box 1.1 in Chapter 1.

Clearly, in cases of an axially symmetric electric field gradient ($\eta = 0$), only the first term of Equation (4.7) is non-zero.

It is apparent from Equation (4.7) that the matrix of $\hat{H}_{\mathrm{Q}}$ in the Zeeman basis contains off-diagonal terms as well as diagonal terms. Thus, to find the exact energies of the spin levels under the quadrupole coupling, one would need to diagonalize the matrix of $\hat{H}_{\mathrm{Q}}$ in the Zeeman basis, to obtain the eigenstates (the new states of the spin system under $\hat{H}_{\mathrm{Q}}$; linear combinations of the Zeeman states) and corresponding eigenvalues (their energies). Clearly, this is a time-consuming process. If the Zeeman interaction is the dominant term in the hamiltonian for the spin system, then only the secular parts of $\hat{H}_{\mathrm{Q}}$ affect the energies of the states of the spin system. The non-secular parts of the matrix of $\hat{H}_{\mathrm{Q}}$ (in this case, the off-diagonal terms of the matrix in the Zeeman basis) are small compared with the diagonal terms provided by the Zeeman term in the total hamiltonian. Thus, they have little effect on the eigenvalues of the diagonalized matrix of the complete hamiltonian for the spin system $\hat{H}_0 + \hat{H}_{\mathrm{Q}}$ (where $\hat{H}_0$ is the Zeeman hamiltonian (Equation (4.5)). In these circumstances, the approximate energies of the spin system are found by recourse to perturbation theory. Corrections up to second order are generally sufficient for quadrupole interactions which cause splittings less than ~1/10 of the Zeeman splitting in the particular field used in the NMR experiment. The first- and second-order energy corrections to the energies of the Zeeman levels from quadrupole coupling from perturbation theory are [**2, 3**]:

$$E_m^{(1)} = \frac{e^2qQ}{4I(2I-1)}(I(I+1)-3m^2)\left[\frac{1}{2}(3\cos^2\theta-1)-\eta\cos 2\phi(\cos^2\theta-1)\right] \quad (4.8)$$

$$\begin{aligned} E_m^{(2)} = &-\left(\frac{e^2qQ}{4I(2I-1)}\right)^2\frac{m}{\omega_0} \\ &\left\{-\frac{1}{5}(I(I+1)-3m^2)(3+\eta_Q^2)\right. \\ &+\frac{1}{28}(8I(I+1)-12m^2-3)[(\eta_Q^2-3)(3\cos^2\theta-1)+6\eta_Q\sin^2\theta\cos 2\phi] \\ &+\frac{1}{8}(18I(I+1)-34m^2-5)\left[\frac{1}{140}(18+\eta^2)(35\cos^4\theta-30\cos^2\theta+3)\right. \\ &\left.\left.+\frac{3}{7}\eta_Q\sin^2\theta(7\cos^2\theta-1)\cos 2\phi+\frac{1}{4}\eta_Q^2\sin^4\theta\cos 4\phi\right]\right\} \end{aligned} \quad (4.9)$$

where m denotes the magnetic quantum number associated with the particular Zeeman level.

Several points arising from these equations are worth noting:

- The first term of Equation (4.9) for the second-order energy correction has no molecular/PAF orientation dependence; it is an isotropic term. This is very important as it means that the isotropic shift seen in any spectrum of a quadrupolar nucleus has a contribution from the quadrupole coupling as well as the usual chemical shift.
- The second-order term depends inversely on the Larmor frequency ($1/\omega_0$); thus the importance of this term diminishes with increasing field strength.

From these equations for the energy corrections due to the quadrupole interaction, we can derive effective operators describing the first- and second-order energy corrections arising from the quadrupole interaction, $\hat{H}_Q^{(1)}$ and $\hat{H}_Q^{(2)}$ respectively, by simply replacing m in Equations (4.8) and (4.9) with $\hat{I}_z$ and $I(I+1)$ with the operator $\hat{I}^2$. The nth-order energy corrections to the spin level m are then simply the (m, m) matrix elements of the $\hat{H}_Q^{(n)}$, i.e.

$$E_m^{(n)} = \langle m|H_Q^{(n)}|m\rangle \quad (4.10)$$

We may then replace $\hat{H}_Q$ of Equation (4.7) by $\hat{H}_Q^{(1)} + \hat{H}_Q^{(2)} = \hat{H}_Q^{\text{eff}}$ to give an effective quadrupolar hamiltonian, $\hat{H}_Q^{\text{eff}}$ which is correct to second order. This derivation of $\hat{H}_Q^{\text{eff}}$ is not merely an academic exercise. $\hat{H}_Q^{\text{eff}}$, is extremely useful if we wish to calculate the effect of the quadrupole interaction *plus* another non-commuting interaction, $\hat{H}_{nc}$, for instance, the interaction of an rf pulse with the quadrupole-coupled

spin system. Calculations using the full hamiltonian $\hat{H}_Q + \hat{H}_{nc}$ are likely to be very cumbersome. Calculations using $\hat{H}_Q^{eff} + \hat{H}_{nc}$ are correct to second order and since they only require the secular parts of the quadrupole interaction to be calculated, they are significantly faster. The effective hamiltonian $\hat{H}_Q^{eff}$ may also be derived from average hamiltonian theory (reference [**4**] and Box 2.1, Chapter 2).

$\hat{H}_Q^{(1)}$ and $\hat{H}_Q^{(2)}$ may be written in a more useful form, if in their derivation (a) the Cartesian operators $\hat{I}_x$, $\hat{I}_y$, $\hat{I}_z$ are replaced by spherical tensor operators $\{\hat{T}_{kq}\}$ (see Box 3.1, Chapter 3) and (b) the geometrical terms involving the spherical polar angles θ and ϕ are replaced by Wigner rotation matrix elements employing Euler angles (α, β, γ) which rotate the PAF $(x^{PAF}, y^{PAF}, z^{PAF})$ into the laboratory frame (x, y, z) [**5**] (see also Box 1.2, Chapter 1 for discussion of Euler angles). This results in the following equations for $\hat{H}_Q^{(1)}$ and $\hat{H}_Q^{(2)}$:

$$\hat{H}_Q^{(1)} = \frac{e^2qQ}{4I(2I-1)}\sqrt{6}V_{20}\hat{T}_{20} \tag{4.11}$$

$$\begin{aligned}\hat{H}_Q^{(2)} = -\left(\frac{e^2qQ}{4I(2I-1)}\right)^2 \frac{1}{\omega_0}\frac{2}{5} \\ \times \{[-3\sqrt{10}\hat{T}_{30} + \hat{T}_{10}(3-4I(I+1))]V_{00} \\ + [-12\sqrt{10}\hat{T}_{30} - \hat{T}_{10}(3-4I(I+1))]V_{20} \\ + [-34\sqrt{10}\hat{T}_{30} + 3\hat{T}_{10}(3-4I(I+1))]V_{40}\}\end{aligned} \tag{4.12}$$

where the spherical tensor operators are defined as follows:

$$\begin{aligned}\hat{T}_{10} &= \hat{I}_z \\ \hat{T}_{20} &= \sqrt{\frac{1}{6}}(3\hat{I}_z^2 - I(I+1)) \\ \hat{T}_{30} &= \sqrt{\frac{1}{10}}(5\hat{I}_z^2 - 3I(I+1)+1)\hat{I}_z\end{aligned} \tag{4.13}$$

and the V_{k0} parameters, which contain all the geometrical terms are [**6**]:

$$V_{k0} = \sum_n D_{n0}^k(\alpha, \beta, \gamma)A_{kn} \tag{4.14}$$

with

$$\begin{aligned}A_{00} &= -\frac{1}{5}(3+\eta_Q^2) \\ A_{20} &= \frac{1}{14}(\eta_Q^2 - 3) \qquad A_{2\pm2} = \frac{1}{7}\sqrt{\frac{3}{2}}\eta_Q\end{aligned} \tag{4.15}$$

$$A_{40} = \frac{1}{140}(18 + \eta_Q^2) \qquad A_{4\pm2} = \frac{3}{70}\sqrt{\frac{5}{2}}\eta_Q \qquad A_{4\pm4} = \frac{1}{4\sqrt{70}}\eta_Q^2$$

$D^k_{n0}(\alpha, \beta, \gamma)$ is a Wigner rotation matrix element, and α, β, γ are the Euler angles which rotate the quadrupole tensor principal axis frame into the laboratory frame (see Box 3.1, Chapter 3, for further details). The definitions of the Euler angles here follow the convention of Rose [7].

The form of the effective operators in Equations (4.11) and (4.12) is often very convenient: a change of axis frame is readily incorporated if the operator is defined in terms of spherical tensor operators. Under a rotation of axis frame through the Euler angles (α, β, γ), a spherical tensor operator $\hat{T}_{kq}$ (new) in the new frame simply becomes a linear combination of the $\{\hat{T}_{kq'}$ (old)$\}$ defined in the old frame (see Box 3.1, Chapter 3, for further details):

$$\hat{T}_{kq}(\text{new}) = \hat{R}^{-1}(\alpha, \beta, \gamma)\hat{T}_{kq}(\text{old})R(\alpha,\beta,\gamma) = \sum_{q'} \hat{T}_{kq'}(\text{old})D^k_{q'q}(\alpha, \beta, \gamma) \qquad (4.16)$$

The utility of this becomes apparent if we consider the case of quadrupole coupling under magic-angle spinning or other sample spinning. In such a case, we consider the principal axis frame (PAF) within a rotor-fixed frame (R), which is then referred to the laboratory frame. The new $\hat{H}_Q^{\text{eff}}$ has exactly the same form as that in Equations (4.11) and (4.12), but with the V_{k0} replaced by [6]:

$$V_{k0} = \sum_m D^k_{m0}(-\omega_R t, \theta_R, 0)\sum_n D^k_{nm}(\alpha, \beta, \gamma)A_{kn} \qquad (4.17)$$

where the Euler angles $(-\omega_R t, \theta_R, 0)$ describe the rotation of the rotor-fixed frame into the laboratory frame and the Euler angles (α, β, γ) describe the rotation of the PAF into that rotor-fixed frame. ω_R is the sample spinning rate, and θ_R the angle of the spinning axis with respect to the applied field.

4.1.2 The effect of rf pulses

For quadrupolar nuclei in many samples, the strength of the quadrupolar interaction can be larger than the strength of interaction with an rf pulse. Modern NMR spectrometers typically produce rf pulses with amplitudes of the order of 100 kHz, while quadrupole-coupling constants are often of the order of MHz. Thus the quadrupole interaction cannot be ignored during an rf pulse. It is not simply that the quadrupole coupling has some small effect which need only concern purists; in the majority of cases the quadrupole coupling has a drastic effect that dominates the whole experiment.

A large quadrupole coupling has a further effect if we are considering irradiation of the sample by rf pulses. If the rf pulse is applied at the Larmor frequency, only

the central transition is effectively irradiated. The satellite transitions (i.e. the other single-quantum transitions) are removed from the Larmor frequency by $(2m - 1)\omega_Q$ as a result of the quadrupole coupling where m is the initial (Zeeman) level involved in the transition and ω_Q, the *quadrupole splitting* is given by:

$$\omega_Q = \frac{3e^2qQ}{4I(2I-1)}\left[\frac{1}{2}(3\cos^2\theta - 1) - \eta_Q \cos 2\phi(\cos^2\theta - 1)\right] \tag{4.18}$$

Thus for most molecular (or PAF) orientations (defined by the spherical polar angles (θ, ϕ) relative to the laboratory frame), the satellite transitions are well off resonance.

During a pulse, the effective hamiltonian describing the spin system in the rotating frame is $\hat{H}_{\text{pulse}}$, where

$$\hat{H}_{\text{pulse}} = \hat{H}_{\text{cs}} + H_Q^{\text{eff}} + \hat{H}_{\text{rf}} + \hat{H}_\Delta \tag{4.19}$$

where $\hat{H}_{\text{cs}}$ is the chemical shift hamiltonian, and $\hat{H}_{\text{rf}}$ describes the effects of the rf pulse:

$$\hat{H}_{\text{cs}} = -\omega_{\text{cs}} I_z \tag{4.20}$$

$$\hat{H}_{\text{rf}} = \omega_1(\hat{I}_x \cos\phi + \hat{I}_y \sin\phi) = \frac{\omega_1}{\sqrt{2}}(\hat{T}_{1-1}\exp(+i\phi) - \hat{T}_{11}\exp(-i\phi)) \tag{4.21}$$

ω_{cs} is the chemical shift (see Section 1.4.1); ω_1 is the amplitude of the rf pulse and ϕ its phase. The tensor operators in $\hat{H}_{\text{rf}}$ are defined as

$$\hat{T}_{1\pm1} = \mp\sqrt{\frac{1}{2}}\hat{I}_\pm \tag{4.22}$$

The pulse may be applied at any frequency, ω, within the quadrupolar powder pattern. The rotating frame in which $\hat{H}_{\text{pulse}}$ is defined is then one which rotates at frequency ω about $\mathbf{B}_0$, so that the time-dependence of the rf magnetic field vanishes (see Section 1.2). The Zeeman term of the hamiltonian (Equation (4.5)) also vanishes in the rotating frame if the pulse is applied at the Larmor frequency. The term $\hat{H}_\Delta$ accounts for off-resonance effects [8, 9] if the pulse is applied at a frequency ω other than the Larmor frequency, ω_0, when the Zeeman term of the hamiltonian becomes

$$\hat{H}_\Delta = (\omega_0 - \omega)\hat{I}_z \tag{4.23}$$

In order to determine the effects of the rf pulse on the spin system, we need to use $\hat{H}_{\text{pulse}}$ to calculate the density matrix describing the spin system a time τ after the start of the pulse.

As described in Chapter 1, the density matrix ρ is usually calculated within the

Zeeman basis. At any given time τ may be calculated from that at time 0 using the solution to the Liouville–von Neumann equation:

$$\boldsymbol{\rho}(\tau) = \mathbf{U}^{-1}(\tau)\boldsymbol{\rho}(0)\mathbf{U}(\tau) \tag{4.24}$$

where the propagator matrix $\mathbf{U}(\tau)$ is

$$\mathbf{U}(\tau) = \hat{T}\exp\left(-i\int_0^{\tau}\mathbf{H}(t)\mathrm{d}t\right) \tag{4.25}$$

$\mathbf{H}(t)$ is the hamiltonian matrix in the Zeeman basis which describes the spin system at time t. The hamiltonian matrix does not commute with itself at different times t, so $\mathbf{U}(\tau)$ is calculated recursively using [**10**]:

$$\underset{\delta\tau\to 0}{\mathbf{U}}(\tau+\delta\tau) = \mathbf{V}^{-1}(\tau)\exp(\mathbf{E}(\tau)\delta\tau)\mathbf{V}(\tau)\mathbf{U}(\tau) \tag{4.26}$$

$\mathbf{E}(\tau)$ is a diagonal matrix of eigenvalues of $\mathbf{H}(\tau)$, and $\mathbf{V}(\tau)$ is the matrix of eigenvectors of $\mathbf{H}(\tau)$. Clearly, such a calculation is a time-consuming business.

However, we can get a general picture of the effects of the rf pulses by considering two limiting cases [**9**]. In the first, $\omega_1 >> \omega_Q$, so that we have non-selective excitation. All transitions are effectively on resonance, so that we can ignore $\hat{H}_\Delta$ as well as the quadrupole and chemical shift terms in Equation (4.19) for the hamiltonian describing the spin system. Thus we are left with just $\hat{H}_{\text{pulse}} \approx \hat{H}_{\text{rf}} = \omega_1\hat{I}_y$ for the case of a y pulse. This is just the same as for an isolated spin-$\frac{1}{2}$ system and was dealt with in detail in Section 1.3; as deduced there, a density matrix element $\rho_{m,m+1}(\tau)$ a time τ after the start of the pulse is simply given by

$$\begin{aligned}\frac{\rho_{m,m+1}(\tau)}{\left(\frac{1}{Z}\frac{\hbar\omega_0}{kT}\right)} &= \langle m|\hat{I}_y|m+1\rangle\sin(\omega_1\tau)\\ &= -\frac{i}{2}[I(I+1)-m(m+1)]^{\frac{1}{2}}\sin(\omega_1\tau)\end{aligned} \tag{4.27}$$

where $\langle m|\hat{I}_y|m+1\rangle$ is a matrix element of the $\hat{I}_y$ operator and is defined in Box 1.1 in Chapter 1. Z is defined in Equation (1.59).

In the limiting case of the quadrupole coupling being much larger than the interaction with the rf pulse [**9**], i.e. $\omega_Q >> \omega_1$, we necessarily have selective excitation of the transition on resonance, i.e. that at or near frequency ω. We assume no irradiation of any other transitions, so that we only need to consider the on-resonance transition, $m \to m+1$. Accordingly, we use the sub-matrix of $\hat{H}_{\text{pulse}}$ (Equation (4.19)) in the basis of $(m, m+1)$ in our calculations as though these were the only two spin levels which exist. The sub-matrix we require is then given by (again considering a y pulse)

$$\begin{aligned}\mathbf{H}_{\text{pulse}}^{m,m+1} &= \mathbf{H}_{\text{cs}}^{m,m+1} + \mathbf{H}_{\text{Q}}^{m,m+1} + \mathbf{H}_{\Delta}^{m,m+1} + \mathbf{H}_{\text{rf}}^{m,m+1} \\ &= \mathbf{H}_{\Sigma}^{m,m+1} + \mathbf{H}_{\text{rf}}^{m,m+1} \\ &= \begin{pmatrix} \langle m|\hat{H}_{\Sigma}|m\rangle & 0 \\ 0 & \langle m+1|\hat{H}_{\Sigma}|m+1\rangle \end{pmatrix} + \begin{pmatrix} 0 & (i/2)\omega_1 W_m \\ -(i/2)\omega_1 W_m & 0 \end{pmatrix} \end{aligned} \quad (4.28)$$

where $\mathbf{H}_{\Sigma}^{m,m+1} = \mathbf{H}_{\text{cs}}^{m,m+1} + \mathbf{H}_{\text{Q}}^{m,m+1} + \mathbf{H}_{\Delta}^{m,m+1}$ (and similarly $\hat{H}_{\Sigma} = \hat{H}_{\text{cs}} + \hat{H}_{\text{Q}}^{\text{eff}} + \hat{H}_{\Delta}$). The factor W_m arises from evaluating the $\hat{I}_y$ matrix elements in $\hat{H}_{\text{rf}}$ within the $(m, m+1)$ basis and is

$$W_m = [I(I+1) - m(m+1)]^{\frac{1}{2}} \quad (4.29)$$

We are only interested in the off-diagonal elements of the density matrix, as only these give rise to NMR signal. The $\mathbf{H}_{\Sigma}^{m,m+1}$ term in Equation (4.28) is diagonal and so does not contribute to the off-diagonal elements of the density matrix. Only the second term of Equation (4.28), $\hat{\mathbf{H}}_{\text{rf}}^{m,m+1}$, will contribute to off-diagonal elements of the density matrix. This term can then be used as the hamiltonian matrix for the purposes of calculating the $\rho_{m,m+1}$ term of the density matrix via Equation (4.24). This involves diagonalizing $\hat{\mathbf{H}}_{\text{rf}}^{m,m+1}$, but this is straightforward. The final result is [8, 9]:

$$\frac{\rho_{m,m+1}(\tau)}{\left(\frac{1}{Z}\frac{\hbar\omega_0}{kT}\right)} = i \cdot \frac{1}{2}\sin(W_m\omega_1\tau) \quad (4.30)$$

where W_m is defined in Equation (4.29). Thus, the effective rf field strength in this selective excitation is a factor $W_m = [I(I+1) - m(m+1)]^{\frac{1}{2}}$ larger than that for non-selective excitation. Thus the length τ of rf pulse which gives maximum signal intensity is in general shorter under selective excitation conditions. It is interesting to note that Equation (4.30) for the density matrix element under the condition of $\omega_Q >> \omega_1$ does not depend on the quadrupole coupling. The main effect of the very strong quadrupole coupling in this case is to ensure that only one transition, $m \rightarrow m+1$, is excited, in other words, to produce the selective excitation condition.

For values of ω_1 intermediate between the limits of selective and non-selective excitation, the density matrix elements, and thus the degree of excitation, in general depend upon both ω_1 and ω_Q. The dependence upon ω_Q which itself depends on molecular/crystallite orientation (Equation (4.18)) means that not only does the degree of excitation depend upon the quadrupole coupling constant, and therefore the chemical site of the quadrupolar nucleus, it also depends upon the molecular/crystallite orientation in the applied field. Thus in a powder sample, nuclei in equivalent chemical sites, but in different crystallites, experience

(potentially very) different excitation. These two factors result in distorted powder patterns, and intensities which are no longer proportional to the number of spins present.

The ω_Q-dependence of the rf excitation for quadrupolar nuclei is a perennial problem which has yet to be satisfactorily solved. The problem diminishes as the length of the rf pulse decreases and its power increases. Short ($\omega_1\tau < \pi/6$ radians), hard pulses are therefore commonly used in NMR studies of quadrupolar nuclei. In situations where the quadrupole coupling is very large, there is little option other than to use continuous wave-type experiments [**11**].

4.2 High-resolution NMR experiments for half-integer quadrupolar nuclei

In this chapter, we have been dealing with a general quadrupolar spin I. Now we make the distinction between integer and half-integer quadrupolar spins. Actually, the vast majority of quadrupolar spins are half integer. Of the integer quadrupolar spins, ^{2}H ($I = 1$) is the only one of major interest to chemists. This nucleus has a relatively small quadrupole moment, giving quadrupole around 160–190 kHz for ^{2}H in organic compounds for instance. It has been used extensively in studies of molecular dynamics and is discussed in detail in Chapter 6. ^{14}N ($I = 1$) is also potentially of interest to chemists. However, it has a sizeable quadrupole moment resulting in quadrupole coupling constants of MHz in many cases. Clearly such huge line broadening does not make this nucleus amenable to study and as yet, no good high-resolution techniques are available for spin-1 nuclei. However, its effects are used indirectly in the TRAPDOR and REAPDOR experiments described in Section 3.4. ^{6}Li ($I = 1$) has a very small value of Q and consequently behaves more or less as a spin-$\frac{1}{2}$ because the quadrupole splittings are not resolvable. A high-resolution ^{6}Li spectrum may thus be obtained using ^{6}Li rather than ^{7}Li, despite the very small chemical shift range of Li.

In contrast, there are now three feasible experiments for producing high-resolution spectra of half-integer quadrupolar nuclei. In addition to this, the central transition ($m = +\frac{1}{2} \rightarrow m = -\frac{1}{2}$) of half-integer quadrupolar nuclei is not broadened to first-order by quadrupole coupling (although it is to second order). The satellite transitions are, however, and this renders them largely unobservable in NMR experiments at the Larmor frequency, as they are too far off resonance. The lack of first-order broadening on the central transition makes it significantly easier to observe than the satellites, and so in this section we focus exclusively on the central transition. Although not broadened to first order, there still remain second- and higher-order contributions to the frequency of this transition which depend on molecular orientation and therefore cause linebroadening in powder samples, albeit rather less than would arise from first-order coupling. We shall only be dealing with powder samples in the subsequent discussion.

4.2.1 Magic-angle spinning

Magic-angle spinning (MAS) is an invaluable line-narrowing technique in solid-state NMR. As seen in Section 2.2, for inhomogeneous interactions which depend only on second-rank rotation matrix terms, the anisotropic parts of the interaction are averaged to zero, providing the rate of sample spinning is significantly larger than the anisotropic linewidth. Magic-angle spinning does have a line-narrowing effect on the central transition lineshape of half-integer quadrupolar nuclei; however, complete removal of the anisotropic quadrupolar effects by this technique is not possible. As Equation (4.12) shows, the second-order effects of quadrupole coupling depend on second- *and* fourth-rank rotation matrices. The former may be averaged to zero by sufficiently fast magic-angle spinning. The latter are averaged by magic-angle spinning too, but not to zero. Thus an anisotropic powder pattern remains even under conditions of very rapid magic-angle spinning. Figure 4.1 shows the effect of magic-angle spinning on central transitions of half-integer spins for different asymmetry parameters.

The frequency of the central transition to second order, under magic-angle spinning is easily derived from equations (4.11)–(4.15) and (4.17):

$$\omega_{\frac{1}{2}-\frac{1}{2}} = -\left(\frac{e^2qQ}{4I(2I-1)}\right)^2 \frac{1}{\omega_0}(3-4I(1+1))\left\{\frac{1}{2}V_{00} + 4V_{20} + 9V_{40}\right\} \tag{4.31}$$

where the V_{k0} parameters are given in Equation (4.17). The V_{k0} parameters depend on rotation matrices of rank k. Under the conditions of very rapid sample spinning, only the $D^k_{00}(\alpha, \beta, \gamma)$ terms involved in the respective V_{k0} parameters survive.

$$D^0_{00}(\alpha, \beta, \gamma) = 1 \tag{4.32}$$

$$D^2_{00}(\alpha, \beta, \gamma) = \frac{1}{2}(3\cos^2\beta - 1) \tag{4.33}$$

$$D^4_{00}(\alpha, \beta, \gamma) = \frac{1}{8}(35\cos^4\beta - 30\cos^2\beta + 3) \tag{4.34}$$

For *magic-angle* spinning, i.e. $\theta_R = 54.74°$, the D^2_{00} term averages to zero over one rotor cycle, removing the V_{20} term in the transition frequency (Equation (4.31)) as expected for a second-rank term under magic-angle spinning. Figure 4.2 shows the variation with angle of the terms D^2_{00} and D^4_{00} which are second and fourth order Legendre polynomials in $\cos\beta$, respectively. At the magic angle the D^4_{00} term is not zero but becomes a scaling factor (–0.389), and thus, the anisotropic V_{40} term, although reduced by magic-angle spinning, remains. In addition, there is an isotropic shift $\omega^{iso}_{\frac{1}{2},-\frac{1}{2}}$ (arising from the V_{00} term) of:

$$\omega^{iso}_{\frac{1}{2}-\frac{1}{2}} = \left(\frac{e^2qQ}{4I(2I-1)}\right)^2 \frac{1}{10\omega_0}(3-4I(I+1))\{3+\eta^2\} \tag{4.35}$$

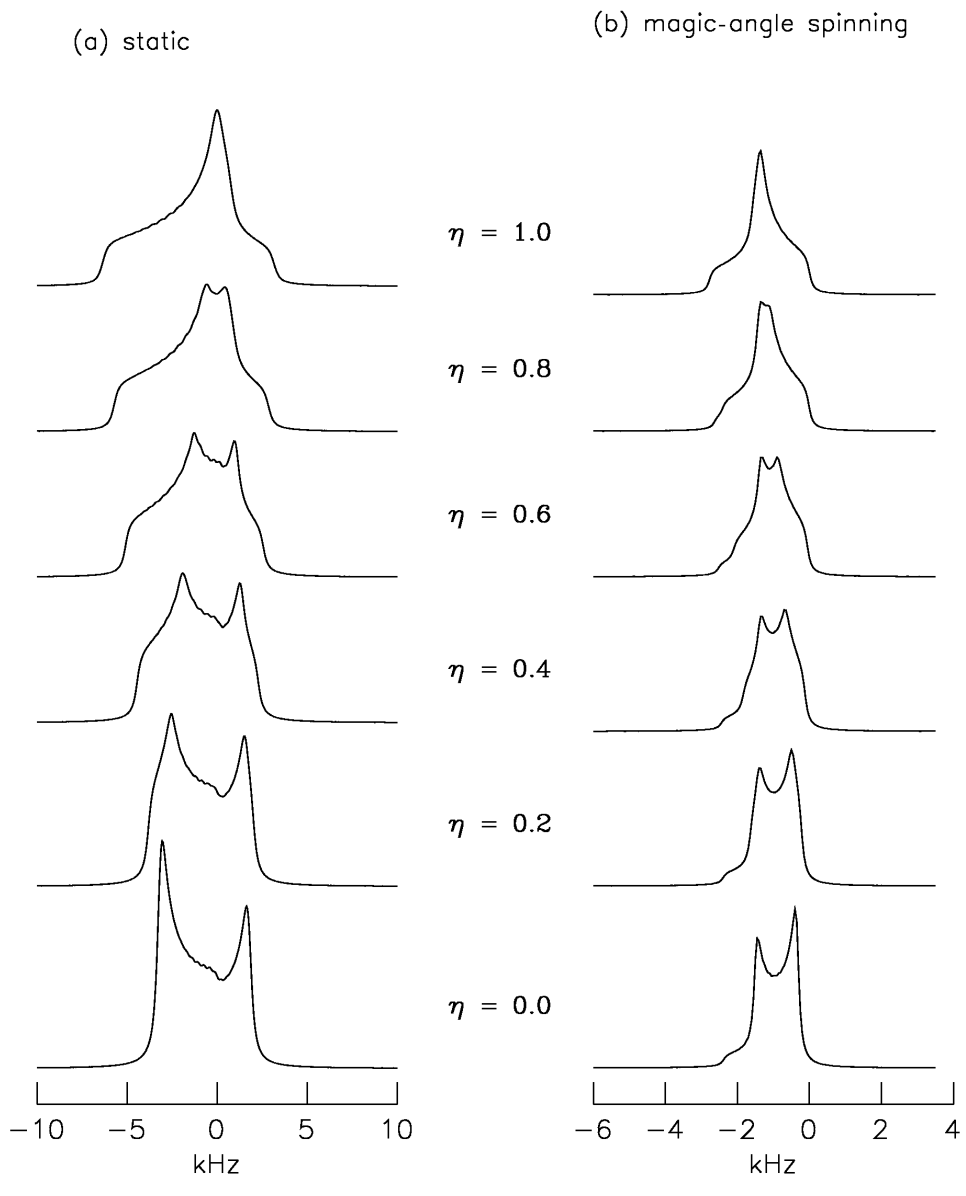

Fig. 4.1 The effect of magic-angle spinning on the central transition lineshape for a half-integer quadrupolar nucleus. Left: central transition lineshape under static, i.e. non-spinning conditions. Right: the same transition under magic angle spinning. The spectra are calculated for

$$X/\omega_0 = 0.02$$

The asymmetry parameter is given with each spectrum. The excitation pulses producing each spectrum are assumed to be ideal, i.e. $\omega_1 >> \omega_q$ where $\omega_q = \frac{3e^2Q}{2I(2I-1)}$. The spinning speed in the magic-angle spinning spectra is assumed to be much larger than ω_q.

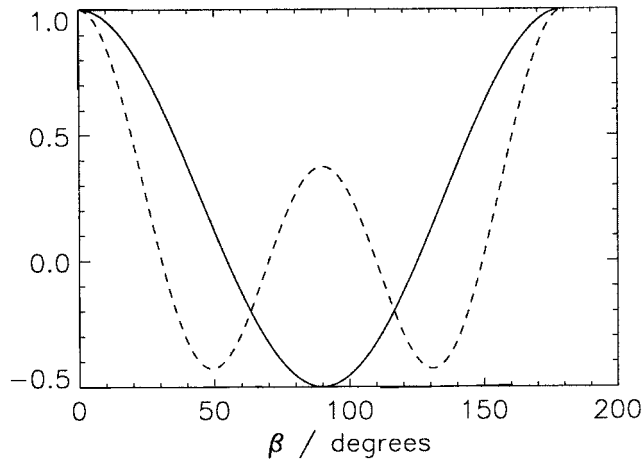

Fig. 4.2 Plots of the D^2_{00} (solid line) and D^4_{00} (dashed line) functions as a function of β. See equations (4.33) and (4.34) for definitions of these functions.

This shift is in addition to any chemical shift offset there might be and has no dependence on spinning speed, i.e. it also exists for static samples. It is important to bear in mind that the centre of gravity of the central transition powder patterns is the chemical shift *plus* the isotropic quadrupolar shift as defined in Equation (4.35). The quadrupolar shift, coupled with the orientation-dependent linebroadening of the central transition can make it very difficult to determine the true chemical shift accurately. One way around this is to use *satellite transition spectroscopy* [**12**]. This is particularly useful for higher spin numbers such as $\frac{5}{2}$, $\frac{7}{2}$, etc. In satellite transition spectroscopy [**12**], one simply observes the satellite transitions under magic-angle spinning. Under these conditions, satellite transition lineshapes (usually unobserved) are broken up into a series of spinning sidebands, albeit of relatively low intensity. However, it is much easier to find the centre of gravity of a satellite transition under magic-angle spinning than that of the central transition; it is simply the average of the positions of the $+N$- and $-N$-order spinning sidebands. Providing the quadrupole parameters are known, and the satellite transition correctly assigned, the isotropic quadrupolar shift associated with the transition can be calculated from the first term of Equation (4.9), and hence the chemical shift extracted from the satellite transition centre of gravity. When satellite transitions are observed, there is also a smaller V_{40} associated with the $m = \pm\frac{1}{2} \rightarrow \pm\frac{3}{2}$ and higher transitions than with the central transition. This results in an improvement in the resolution of overlapping V_{40} powder patterns in satellite bands [**13**] as shown in Fig. 4.3.

4.2.2 Double rotation

As already explained, second-order quadrupole effects mean that the frequency of the central transition is molecular orientation-dependent, being determined by both

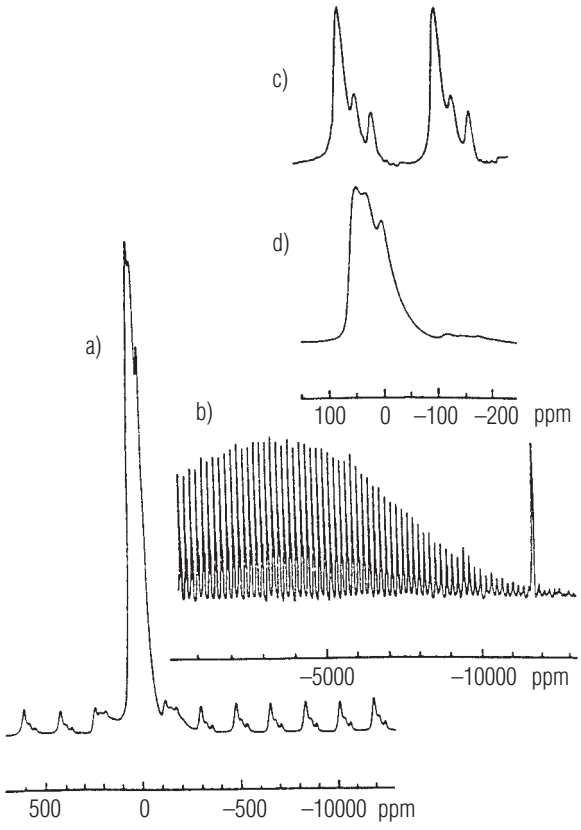

Fig. 4.3 (a) The ^{27}Al (I = 5/2) central transitions and part of the satellite transition manifold of a lead aluminoborate glass [13]. (b) The right hand part of the total satellite transition spinning sideband spectrum. (c) The third and fourth satellite transition sidebands, showing resolution of three signals corresponding to the four, five and six-coordinate aluminium sites. (d) The central transition centrebands, showing poor resolution of the three aluminium sites. Second-order broadening on the $\pm\frac{1}{2} \leftrightarrow \pm\frac{3}{2}$ transition for $I = \frac{5}{2}$ is $\frac{1}{8}$ that of the central $\frac{1}{2} \leftrightarrow -\frac{1}{2}$ transition. Therefore, there is much higher site resolution in the satellite transition sidebands, than in the central transition centrebands. (Taken from Jaeger, Mueller-Warmuth, Mundus *et al.* (1992).)

second- and fourth-rank rotation matrices, which express the molecular frame/PAF orientation with respect to the applied field. The double-rotation (DOR) technique [**14**, **15**] achieves high-resolution spectra of the central transitions by spinning the sample simultaneously at two angles. One angle is the magic-angle, and so averages the second-rank rotation matrix terms in Equation (4.31) to zero, while the other angle (30.6° or 70.1°) averages the fourth-rank terms to zero. This latter point may be determined from Fig. 4.2 or by putting $\langle\beta\rangle$ = 30.6° or 70.1° in Equation (4.34) for $D^4_{00}(\alpha, \beta, \gamma)$.

This conceptually simple technique is far from simple to implement however, and involves one rotor spinning inside another (Fig. 4.4) [**14**, **15**]. In order to achieve spectra free from spinning sidebands, it is necessary to spin each rotor at speeds of order of the anisotropic linewidth. Unfortunately, this is rarely achievable, and in some cases, spinning sidebands may obscure isotropic resonances. Nevertheless, the technique has been used with a great deal of success, and is likely to find many further applications as NMR experiments are performed at higher fields. At higher fields, the anisotropic quadrupolar linewidths are reduced (due to the dependence of the transition frequency on $1/\omega_0$), and so spinning sidebands are reduced in inten-

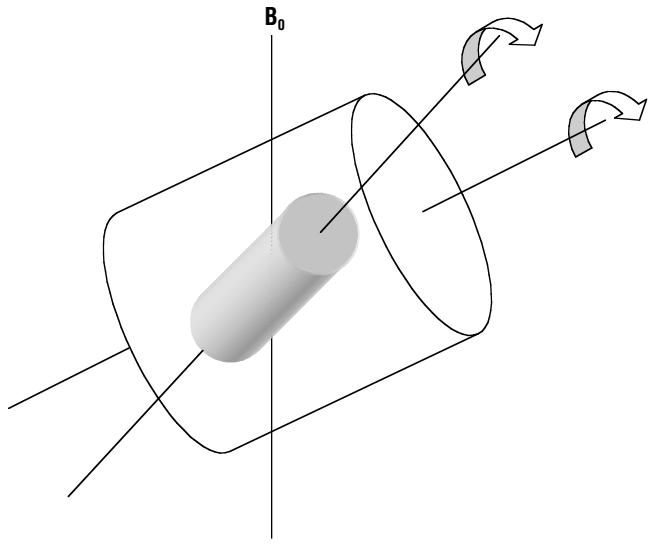

Fig. 4.4 Schematic diagram of the Double Rotation (DOR) experiment. There are two rotors, one spinning inside the other. The outer rotor spins about an axis inclined at 54.74° to the applied field $\mathbf{B}_0$, whilst the inner one spins about an axis inclined at 30.6° (or 70.1°).

sity for the same spinning speeds. An example of DOR at high field is shown in Fig. 4.5 [**16**].

4.2.3 Dynamic-angle spinning

Dynamic-angle spinning [DAS; **17**] is a two-dimensional NMR experiment which achieves isotropic signals in one dimension and quadrupolar-broadened, anisotropic powder patterns in the other.

The experiment takes advantage of the fact that the transition frequency (of the central transition and others) depends on the sample spinning angle, θ_R (Equations (4.12) and (4.17)), to perform a type of refocusing or echo experiment. Evolution under quadrupolar broadening during a first period of free precession is refocused during a second period by changing the transition or evolution frequency between the two periods, via a change in sample spinning angle. In detail (Fig. 4.6), initial coherence corresponding to the central transition is generated by a 90° pulse while the sample is spinning at the first angle, θ_1. Evolution under quadrupolar broadening, modified by spinning at θ_1, is then allowed to occur for a period t_1. At the end of t_1, the remaining coherence is stored along the applied magnetic field (using a selective 90° pulse) while the spinning angle is changed to θ_2. The central transition coherence is then regenerated (*via* another selective 90° pulse) and allowed to evolve for a further time kt_1 under quadrupole coupling while spinning at the new angle. The constant k is set (by prior calculation) so that the quadrupolar evolution in the first period t_1 is exactly undone by the subsequent evolution in kt_1. At the end of kt_1, a free induction decay is recorded during t_2 in the normal way. A two-dimensional dataset is collected by incrementing t_1; subsequent Fourier transformation in

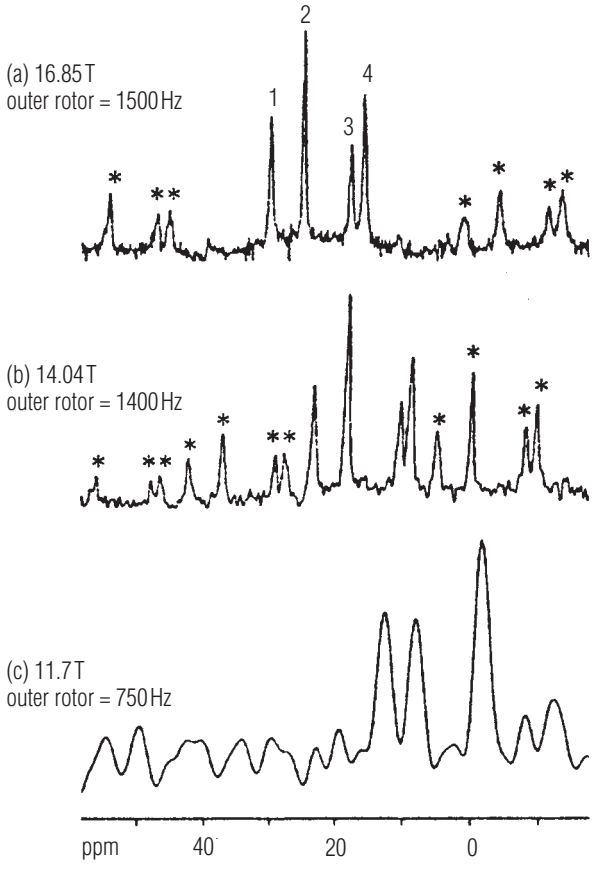

Fig. 4.5 ^{17}O DOR spectra of siliceous zeolite Y (faujasite) [16] at different field strengths. Four ^{17}O signals are clearly resolved at the higher field strengths. Spinning sidebands are marked with an asterix. The spinning rate of the outer rotor in the experiments is given with each spectrum. The spectra are referenced with respect to ^{17}O in H_2O (at 0 ppm). (Taken from Bull, Cheetham, Anupold *et al.* (1998).)

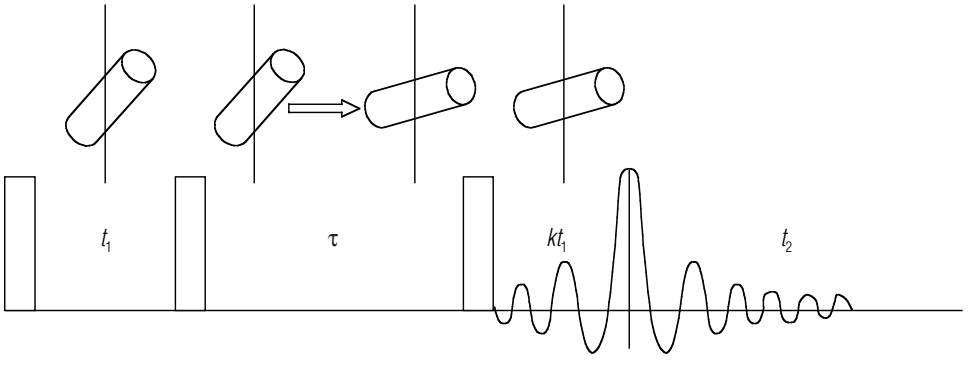

Fig. 4.6 Schematic illustration of the dynamic angle spinning (DAS) experiment. All the pulses are selective 90° pulses for the central transition of the quadrupolar spin in question. The sample is spun at angle θ_1 during t_1. At the end of t_1 a selective 90° pulse is used to store remaining magnetization along $\mathbf{B}_0$. During the subsequent τ delay, the spinning angle is changed to θ_2. Another 90° pulse restores the magnetization to the transverse plane. The evolution under the (second-order) quadrupole coupling during t_1 is refocused after a period kt_1 at the second spinning angle and an FID is then recorded in t_2. When $\theta_1 = 37.4°$ and $\theta_2 = 79.2°$, the constant $k = 1$. In practice, the selective 90° pulses are calibrated at each spinning angle required.

both dimensions yields in f_1 (corresponding to the transformed t_1 dimension) an isotropic spectrum from which the anisotropic effects of quadrupole coupling have been removed. As with DOR, the isotropic quadrupolar shift (Equation (4.35)) remains. Further discussion on recording and processing such spectra is given later.

There are many pairs of spinning angles [**17**] which allow this refocusing effect; for the combination $\theta_1 = 37.38°$, $\theta_2 = 79.19°$, $k = 1$, so that the refocusing period is equal in length to the initial evolution period. The advantage of this experiment over DOR is that only one spinning angle is required at a time, and so it is easier to implement in one sense. Furthermore, there is no difficulty in obtaining rapid spinning speeds in order to reduce the intensity of spinning sidebands. There may, however, be some difficulty in changing the spinning angle during the experiment, as the change must be perfomed in a much shorter time than the spin-lattice relaxation time for the signal, or the stored coherence relaxes back to equilibrium during the angle change. In addition, the storage step while the angle is changed results in the loss of half the signal compared with a single-pulse experiment, because only one component of the transverse magnetization (x or y) can be stored.

A further disadvantage compared to DOR is the fact that none of the DAS spinning angle pairs include the magic angle. Interactions such as the chemical shift anisotropy and dipole–dipole coupling are scaled at the DAS angles but *not* averaged out and so their effects remain in both dimensions of the two-dimensional spectrum. The 'best' angle pair in this respect is the $k = 5$ pair of 0°/63° with spectra acquired close to the magic angle at 63°. DAS spectra may be acquired without contributions from dipole–dipole or chemical shift anisotropy by the addition of an extra 'hop' to the magic angle before acquisition [**18**]. However, this results in a further loss of signal and the experiment will take 8 times as long to achieve the signal to noise equivalent of a single-pulse experiment. Figure 4.7(a) shows the overlapping magic-angle spinning pattern obtained for the ^{17}O spectrum of the SiO_2 polymorph coesite (5 oxygen sites) [**18**]. The advantage of the separation of the isotropic and anisotropic contributions to the spectrum afforded by DAS (Fig. 4.7 (b)) is very clear [**18**]. This two-dimensional spectrum was acquired with a final hop to the magic angle so that the anisotropic line shapes had no chemical shift anisotropy or dipole–dipole contributions.

4.2.4 Multiple-quantum magic-angle spinning

The MQMAS experiment was first proposed in the literature in 1995 [**19**] for achieving high-resolution spectra for half-integer quadrupolar nuclei while spinning the sample at just one angle, the magic angle, throughout the experiment. It is a two-dimensional experiment and achieves resolution in much the same way as the DAS experiment, via a refocusing of evolution during the t_1 period in a second period of free precession, kt_1. In order to do this, a change of transition frequency

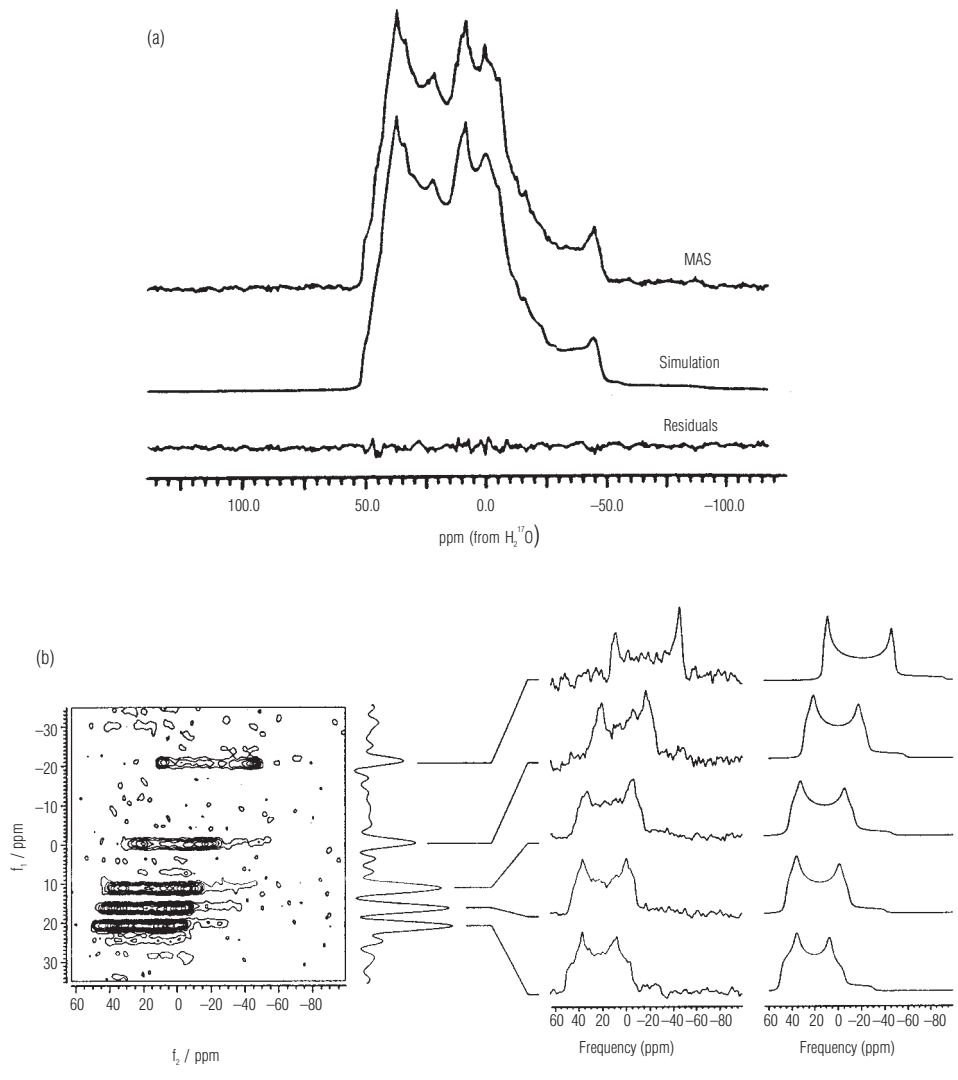

Fig. 4.7 (a) The ^{17}O magic-angle spinning spectrum of the silicate, coesite [18]. (b) The two-dimensional ^{17}O DAS spectrum of coesite [18]. The right hand side shows f_2 slices through the isotropic signals of the f_1 dimension. All spectra are recorded at 11.7 T. (Taken from Grandinetti, Baltisberger, Farnan *et al.* (1995).)

is needed between the two periods, which in the DAS experiment is done by changing the sample spinning angle. In the MQMAS experiment (Fig. 4.8), it is done by changing the order of the evolving coherence. In particular, a multiple-quantum coherence corresponding to a symmetric $+m \rightarrow -m$ transition evolves during t_1. This is then converted to (observable) single-quantum coherence, which evolves during kt_1.

The frequency of a $+m \rightarrow -m$ transition for a half-integer quadrupolar nucleus depends only on second-order terms and is given by:

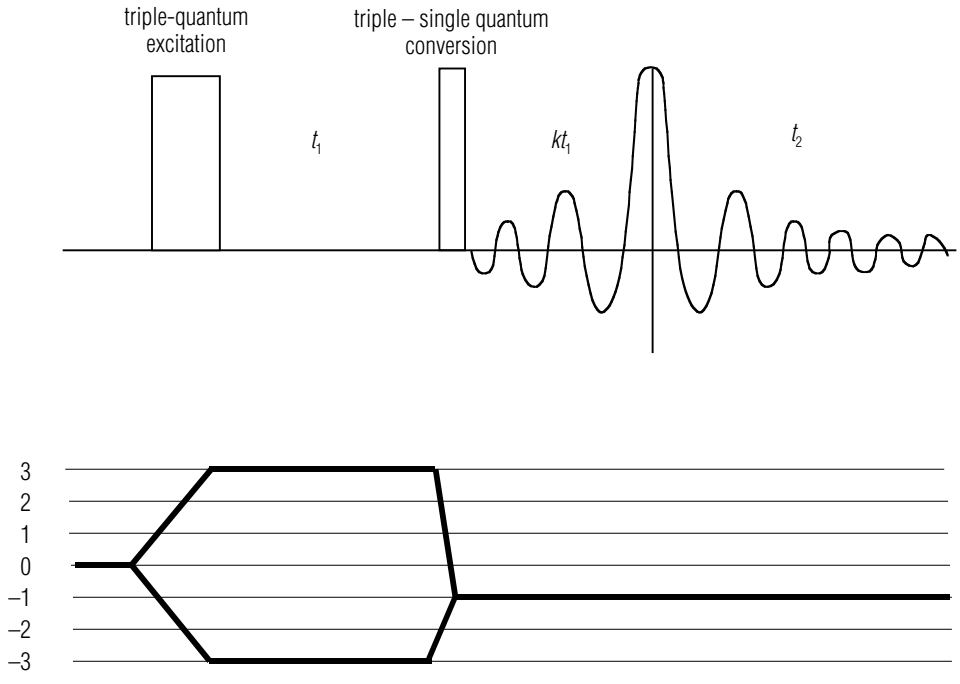

Fig. 4.8 Schematic illustration of the multiple-quantum magic-angle spinning (MQMAS) experiment for a spin-$\frac{3}{2}$. Both excitation and conversion pulses are optimized for each sample. The sample is spun at the magic angle throughout the experiment to remove the effects of second-rank terms of the quadrupole coupling (and chemical shift anisotropy and dipolar coupling). Triple-quantum coherence is excited initially and allowed to evolve during t_1. The remaining coherence is then transferred to single-quantum coherence. After a period kt_1 ($k = \frac{7}{9}$ for spin-$\frac{3}{2}$), evolution under the fourth-rank quadrupolar terms in t_1 is refocused and an FID is recorded in t_2.

$$\begin{aligned}\omega_{m,-m} = &\left(\frac{e^2qQ}{4I(2I-1)}\right)^2 \frac{4}{\omega_0} m \\ &\times [I(I+1) - 3m^2]V_{00} \\ &+ [8I(I+1) - 12m^2 - 3]V_{20} \\ &+ [18I(I+1) - 34m^2 - 5]V_{40}\end{aligned} \tag{4.36}$$

In the MQMAS experiment, multiple-quantum coherence of order $2m$ is first excited and allowed to evolve during t_1 at a rate given by Equation (4.36). The experiment is conducted under magic-angle spinning which may be assumed to average to zero the second-rank terms of V_{20} in this equation throughout the experiment. Thus, the only anisotropy in the evolution during t_1 arises from the V_{40} term. At the end of t_1, a second rf pulse transfers the remaining multiple-quantum coherence into a single-quantum (–1) coherence associated with the $+\frac{1}{2} \rightarrow -\frac{1}{2}$ transition. The new coherence has a frequency given by Equation (4.36) with $m = \frac{1}{2}$ (with V_{20} terms again averaged to zero by magic-angle spinning). The important point is that the evolution of the multiple-quantum coherence under the V_{40} term during t_1 is now

Table 4.1 The k values for the MQMAS experiment for different spin quantum numbers, I and different multiple-quantum transitions, $2m$

I	$2m$	k
$\frac{3}{2}$	3	–7/9
$\frac{5}{2}$	3	12/19
	5	–12/25
$\frac{7}{2}$	3	101/45
	5	11/9
	7	–161/45
$\frac{9}{2}$	3	91/36
	5	95/36
	7	7/18
	9	–31/6

'undone' by the evolution of the single-quantum coherence during kt_1 under the similar term. At the end of kt_1, a normal FID is collected. The values of k appropriate for different spin quantum numbers and m are given in Table 4.1. A two-dimensional dataset is collected in the same way as for DAS; in the MQMAS data, an echo analogous to the DAS echo is seen to shift in time with increasing t_1 values. Fourier transformation results in a two-dimensional frequency spectrum in which f_1 exhibits an isotropic spectrum and f_2 the anisotropic powder patterns associated with the central transitions (corresponding to the single-quantum coherence which evolves during t_2) of the different sites. The isotropic f_1 dimension exhibits signals at frequencies which are a combination of the single- and multiple-quantum isotropic shifts:

$$\omega_{f1}^{\text{iso}} = \frac{1}{k+1}(2m\omega_{\text{iso}} + \omega_{m,-m}^{\text{iso}}) + \frac{k}{k+1}\left(\omega_{\text{iso}} + \omega_{\frac{1}{2},-\frac{1}{2}}^{\text{iso}}\right) \tag{4.37}$$

where ω_{iso} is the isotropic chemical shift, $\omega_{\frac{1}{2},\frac{1}{2}}^{\text{iso}}$ is given by Equation (4.35) and

$$\omega_{m,-m}^{\text{iso}} = \left(\frac{e^2qQ}{4I(2I-1)}\right)^2 \frac{4}{\omega_0} m(I(I+1) - 3m^2) \tag{4.38}$$

The multiple-quantum coherence that evolves during t_1 can be excited in the conventional way for exciting multiple-quantum coherence in solution-state experiments with a 90°–τ–90° sequence, or with a single pulse [**19–22**]. Not surprisingly, the amplitude of multiple-quantum coherence generated depends on the strength of the quadrupole coupling. Vega and Naor [**22**] have shown that the amplitude of triple-quantum coherence for a spin-$\frac{3}{2}$ nucleus generated by a single pulse of length τ_{rf}, whose amplitude ω_1 is much less than the quadrupole splitting ω_{Q}, (defined in Equation (4.18)) is

$$c_{1,4} = \frac{3}{2}\frac{\omega_0}{kT}\sin\left(-\frac{3\omega_1^3}{8\omega_{\text{Q}}^2}\tau_{\text{rf}}\right) \tag{4.39}$$

where $c_{1,4}$ is the amplitude of the (1, 4) element of the density matrix (see Section 1.3), which corresponds to a triple-quantum coherence for a spin-$\frac{3}{2}$ when the density matrix is expressed in the basis of the Zeeman hamiltonian. The phase of this coherence is –90° out of phase with the pulse phase.

Practical considerations

Since the MQMAS experiment was first described, there have been numerous papers describing modifications of the experiment [**23–36**]. Most of these have concentrated on the optimal conditions for excitation of the multiple-quantum coherence and on its subsequent transformation to –1-quantum coherence.

The multiple-quantum coherence is selected *via* phase cycling, as described in Section 1.6.2. To select $\pm p$ quantum coherence, we need to phase cycle the excitation sequence (whatever it is) in $|p|$ steps of $360/|p|$ degrees (see Section 1.6.2). Specific phase-cycling schemes for MQMAS experiments are given in the next section.

- *Excitation conditions* If using a single excitation pulse, it has been shown from simulations that the optimal pulse length is around $0.8/\nu_1$ where ν_1 is the amplitude of the excitation pulse (in Hz) [**20**, **26**]. However, multiples of 360° pulses are often used, as these generate very little of the unwanted single-quantum coherence. If using a 90°–τ–90° sequence for excitation, the optimal conditions are for the two 90° pulses to differ in phase by 90° and for the τ delay to be $n\tau_R$, where $n = 0, 1, 2, \ldots$ and τ_R is the rotor period [**21**]. Whatever the scheme used, generally speaking, the higher the pulse power, the more efficient the excitation, at least until the pulse amplitude (in Hz) approaches the quadrupole-coupling constant in order of magnitude [**26**]. It is desirable to optimize the pulse lengths for the excitation on each sample to generate the maximum signal. It is worth noting that the excitation efficiency is highly dependent on the strength of quadrupole coupling. This means that the excitation efficiency is likely to vary considerably for different crystallite orientations. Moreover, there will be very large differences in excitation efficiency between different chemical sites with different quadrupole coupling constants; and at times these differences can be so profound that unless the excitation conditions are carefully chosen, some sites will not be represented at all in the final spectrum. In any case, the intensities will not be quantitative, and if information on site populations is required, it has to be obtained by simulation.
- *MQ → SQ conversion* It has been shown, again by simulation, that the optimal pulse length for the MQ → SQ conversion is around $0.2/\nu_1$ [**20**, **26**]. As with the excitation pulse, the higher the pulse power, the more efficient the conversion, up to the limit of the pulse amplitude being of the order of the

quadrupole-coupling constant. Fast amplitude-modulated pulses have also proved to be very successful for the MQ → SQ conversion [**36**].

For both the excitation and conversion steps, adiabatic transfer methods have been used, with very good results [**29**]. These require a little more care in the setup of the experiment, but have the advantage of giving quadrupolar powder patterns in the f_2 dimension which closely approximate the lineshapes that would arise in a simple one-dimensional experiment. For other excitation and conversion schemes, the lineshapes arising in f_2 can be very distorted relative to those from a one-dimensional experiment. Furthermore, adiabatic methods are less sensitive to the quadrupole coupling strength, so while intensites arising in the experiments are still not exactly quantitative, they are considerably more so than with other excitation schemes.

4.2.5 Recording two-dimensional datasets for DAS and MQMAS

General methods of producing pure absorption lineshapes in two-dimensional NMR spectra were discussed in Chapter 1. Both DAS or MQMAS experiments result in an echo being produced at kt_1, the decay of which in t_2 gives rise to the recorded signal. This echo formation allows different procedures to be used for achieving pure absorption lineshapes [**25**, **37**] from those detailed elsewhere in this book. Fourier transformation of the t_2 FID gives a frequency spectrum with dispersion-mode components. This is because, in effect, the dataset is only defined from $t_2 = 0$ (the top of the echo) to $t_2 \rightarrow \infty$. However, Fourier transformation involves an integral from $t_2 \rightarrow -\infty$ to $+\infty$. Thus the dataset appears to the Fourier transformation procedure as a step function (zero from t_2 , $-\infty$ to 0 and 1 thereafter) multiplied by the recorded data. The result in the frequency domain is therefore a convolution of the Fourier transform of the step function (a dispersive lineshape) and the Fourier transform of the recorded data (the required lineshape). In order to achieve pure absorption mode lineshapes information is needed about the signal prior to $t_2 = 0$. This can be obtained indirectly as in (i) below, or directly as in (ii). In both cases, the t_2 FID is generally recorded from immediately after the last pulse in the sequence rather than from the top of the echo maximum. With this definition of the t_2 dimension, the echo maximum appears at $t_2 = kt_1$. This shift of the time origin requires a phase correction as discussed below.

(i) Direct method

Record two two-dimensional datasets with a change in the rf phase in the excitation sequence between them such that the phase of the coherences in t_1 is shifted by 90° between the two experiments. Phase cycling is applied in both experiments so

that $+p$ and $-p$ of the appropriate coherence $|p|$ are selected in t_1 ($|1|$ for DAS; $|2m|$ for MQMAS). This results in echo formation at kt_1 from one of the components and a so-called *anti-echo* formation at $-kt_1$ from the other component [**25**]. It is the decay of the net sum of these two echo components which is recorded in t_2 (Fig. 4.9). Because data recording can only begin after the last pulse, the whole echo plus anti-echo cannot be recorded in one dataset. The true echo signal can however be reconstructed from the two datasets so obtained using the hypercomplex method [**25**]. The form of the signals in the two datasets was discussed in Section 1.6.3. From these, it can readily be seen that the echo and anti-echo signals are constructed from [**25**]:

$$\begin{aligned} S_{\mathrm{E}}(t_1, t_2) &= S_X(t_1, t_2) - iS_Y(t_1, t_2) \\ S_{\mathrm{A}}(t_1, t_2) &= S_X(t_1, t_2) - iS_Y(t_1, t_2) \end{aligned} \tag{4.40}$$

where S_X is the time domain dataset generated from t_1 coherence of relative phase 0° and S_Y is the time domain dataset generated from t_1 coherence of relative phase 90°. As illustrated in Fig. 4.9, the complete echo can then be reconstructed in the t_2 dimension by constructing a single new dataset with twice as many t_2 points as each individual dataset, and placing the anti-echo signal in the first half of the new dataset, and the echo signal in the latter half.

Fourier transformation in both dimensions results in a two-dimensional pure absorption mode spectrum which is symmetrical about $\omega_2 = 0$ (where ω_2 corresponds to the Fourier transformed t_2 domain); the two symmetric halves of the spectrum are identical and either half represents the required NMR spectrum. The two halves may be added to improve signal to noise.

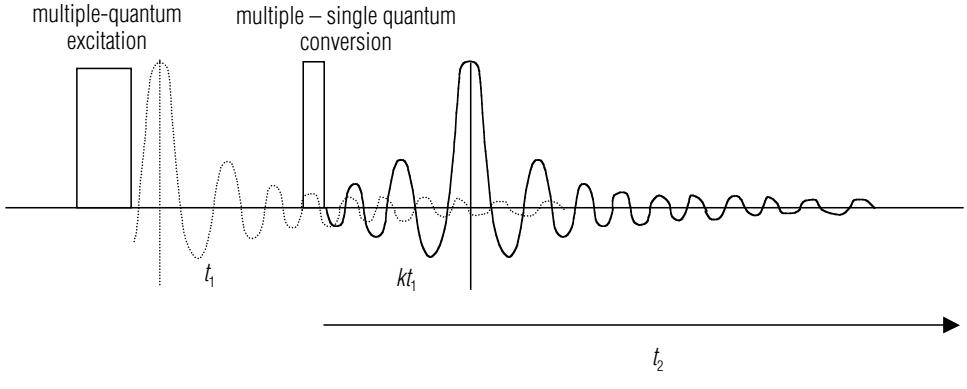

Fig. 4.9 Formation of the echo (solid line) and anti-echo (dashed line) in the MQMAS experiment. During t_1, both $+p$ and $-p$ multiple-quantum coherences are selected. One of these components leads to formation of the anti-echo at $-kt_1$ from the last pulse and the other, the formation of the echo at $+kt_1$ from the last pulse. For spin-$\frac{3}{2}$ and triple-quantum coherence, the -3 coherence leads to echo formation and $+3$ to anti-echo formation. The sum of the dashed and solid lines is recorded in the FID, which is generally recorded from the end of the last pulse.

An alternative and completely equivalent approach [**25**] is to Fourier transform S_E and S_A in t_2 and then in t_1. A first-order phase correction in the ω_2 dimension needs to be made after Fourier transformation in t_2. This is because the echo maximum in the experiment does not appear at the time origin, $t_2 = 0$, but is shifted in t_2 away from $t_2 = 0$ as a function of t_1. In fact, the echo maximum appears at $t_2 = kt_1$ in successive t_1 experiments, where k is a constant determined by the particular experiment. A Fourier transform theorem states that if a function $f(t)$ is displaced by Δt, i.e. $f(t) \rightarrow f(t + \Delta t)$, then its Fourier transform, $F(\omega)$, is multiplied by $\exp(-\omega\,\Delta t)$. This is simply a first-order phase shift, and to undo this phase shift in our two-dimensional experiment we must multiply the Fourier-transformed ω_2 dimension of the echo dataset by $\exp(i\omega_2 kt_1)$ and of the anti-echo dataset by $\exp(-i\omega_2 kt_1)$ in each t_1 slice.

The final pure absorption mode spectrum $S(\omega_1, \omega_2)$ is then produced by combining the individual Fourier-transformed and ω_2-phased datasets according to

$$S'(\omega_1, \omega_2) = S'_E(\omega_1, \omega_2) + S'_A(-\omega_1, \omega_2) \tag{4.41}$$

where the primes denote datasets that have received the ω_2 phase correction. An example phase-cycling scheme for this method for the triple-quantum MQMAS experiment for spin-$\frac{3}{2}$ is shown in Table 4.2 [**25**].

It is very important when using this technique that the two coherence pathways through $0 \rightarrow \pm p \rightarrow -1$ come through to the end of the sequence with the same amplitude. As illustrated in Fig. 4.8, the desired coherence pathways require simultaneous transformations $+p \rightarrow -1$ and $-p \rightarrow -1$; these transformations involve different changes in coherence order and unfortunately, they generally occur with different efficiency. This often leads to large spectral distortions. To avoid this, a *zero-quantum filter* or *z filter* can be applied [**27**]. As shown in Fig. 4.10, this involves an extra pulse in the sequence so that the coherence pathway becomes $\pm p \rightarrow 0 \rightarrow -1$. This now involves $+p \rightarrow 0$ and $-p \rightarrow 0$ transformations which have the same change in coherence order and so can be expected to have the same efficiencies. The mixing time during the z filter needs to be sufficiently long for unwanted coherences to dephase, generally around tens of microseconds for MQMAS and DAS experiments.

(ii) Indirect method

Record a single two-dimensional dataset using a *shifted-echo sequence* [**25**, **31**, **37**]. In this approach, a refocusing selective 180° pulse (selective for the central transition) is added a time τ after the end of the pulse sequence. This shifts the echo which arises from a DAS or MQMAS experiment a further time τ after the 180° pulse and allows the whole echo to be recorded. In this method, only one coherence ($+p$ or $-p$) is selected in t_1. The form of the signal is then $\exp(i\omega_1 t_1)\exp(i\omega_2 t_2)$

Table 4.2 The phase cycling scheme for the triple-quantum MQMAS experiment for $I = \frac{3}{2}$ using the hypercomplex method for producing pure absorption lineshapes in the two-dimensional frequency spectrum. (i) the *X*-dataset phase cycling; (ii) the *Y*-dataset phase cycling. Pulse phases are labelled according to the pulse sequence shown at the top of the tables; the coherence pathway is also shown.

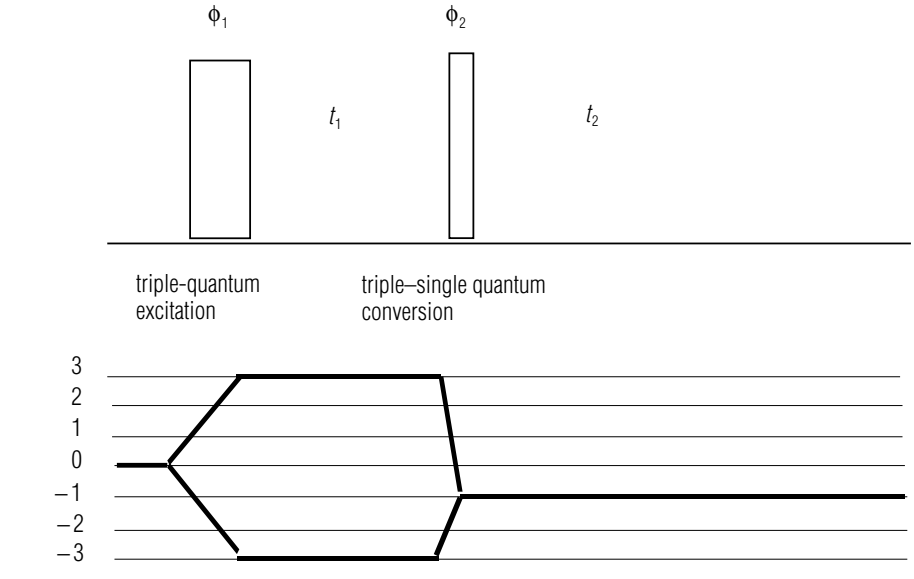

(i)	ϕ_1	0°	60°	120°	180°	240°	300°
	ϕ_2	0°					
	receiver phase	0°	180°	0°	180°	0°	180°
(ii)	ϕ_1	30°	90°	150°	210°	270°	330°
	ϕ_2	0°					
	receiver phase	0°	180°	0°	180°	0°	180°

with t_2 defined from $-\infty \rightarrow +\infty$ so that after Fourier transformation in t_2, the signal is $\exp(i\omega_1 t_1)A_2$ using the terminology in Section 1.6, after appropriate phasing as discussed below. Fourier transformation in t_2 gives only an absorptive part because the dataset is, in effect, defined for $t_2 = -\infty \rightarrow +\infty$. A dispersive (imaginary) part appears when the dataset is truncated to values for $t_2 = 0 \rightarrow +\infty$. After Fourier transformation in t_1, the final signal is (again after appropriate phase corrections) $(A_1 + iD_1)A_2 = A_1A_2 + iD_1A_2$ so that the real part of the final spectrum is purely absorptive.

As discussed in (i), a first-order phase correction is needed in ω_2 before Fourier transformation in t_1 to 'correct' for the fact that the echo maximum shifts in successive t_1 experiments; we need to multiply the ω_2 dimension by $\exp(i\omega_2 k t_1)$ in all

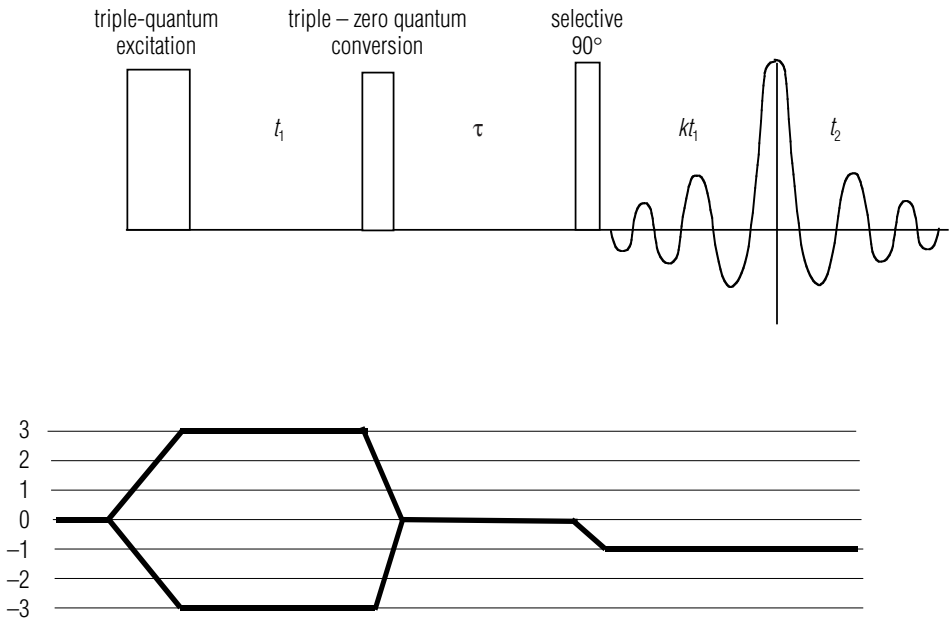

Fig. 4.10 The zero-quantum filtered MQMAS pulse sequence for a spin-$\frac{3}{2}$ nucleus. The two coherence pathways $0 \rightarrow -3 \rightarrow 0$ and $0 \rightarrow +3 \rightarrow 0$ have equal amplitudes because they are symmetric. In the basic MQMAS sequence the two pathways are $0 \rightarrow -3 \rightarrow -1$ and $0 \rightarrow +3 \rightarrow -1$. The final step in such an experiment involves coherence order changes of +2 and –4 respectively for the two coherence pathways. These different changes of coherence order generally have different efficiencies, which results in the two pathways giving different amplitudes to the final FID recorded in t_2. In turn, this leads to gross spectral distortions. The zero-quantum filtered sequence avoids this problem.

t_1 slices. In addition to this first-order phase correction, we must also perform a phase correction to correct for the fact that the echo maximum is shifted by a constant τ, the echo delay, in addition to the t_1-dependent shift in all t_1 experiments. This requires multiplication in the ω_2 dimension by $\exp(i\omega_2\tau)$ in all t_1 slices.

The shifted echo method is not appropriate for samples in which there is a significant homogeneous linebroadening, due to the loss of signal imposed by the echo delay (homogeneous linebroadening cannot be refocused by an rf pulse). When using this method, it is desirable to set the receiver phase so that the shifted echo appears as a symmetric echo with maximum intensity in the real part of the time domain. The experiment can be arranged so that the echo moves to increasing t_2 times as t_1 increases, or in the reverse direction. The phase-cycling schemes for these two alternatives are given in Table 4.3 for the triple-quantum MQMAS for spin-$\frac{3}{2}$ experiment [**25**].

Note that for both the DAS and MQMAS experiments, the spectral width in f_1 is $1/[(k + 1)\delta t_1]$, where δt_1 is the t_1 dwell time, for the definition of t_1 used here.

Table 4.3 The phase-cycling scheme for the triple-quantum MQMAS experiment for $I = \frac{3}{2}$ using the shifted echo method for producing pure absorption lineshapes in the two-dimensional frequency spectrum. Pulse phases are labelled according to the pulse sequence shown at the top of the tables. The coherence pathway is also shown; only one of the +3 or −3 coherences is selected. The phase cycle for the $+3 \rightarrow +1 \rightarrow -1$ pathway is given.

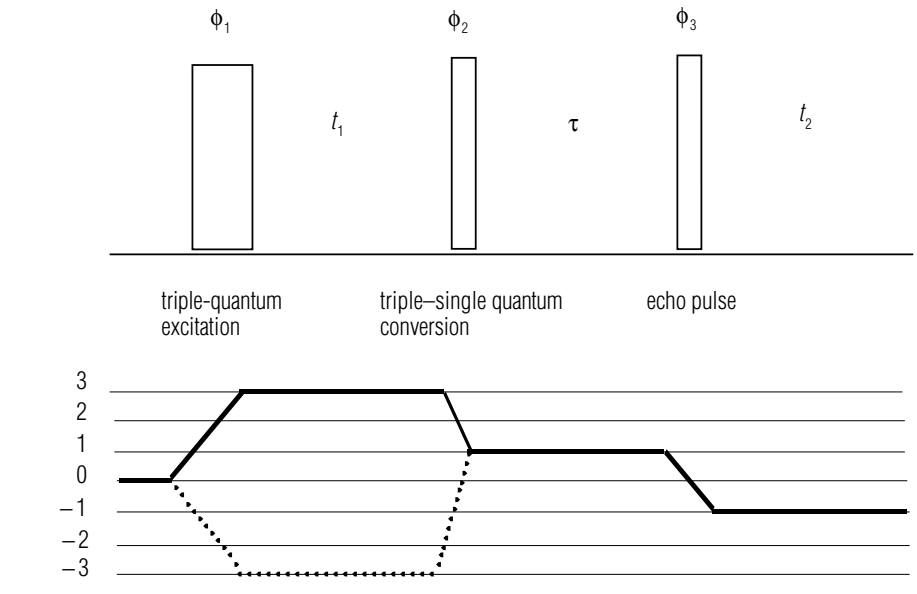

ϕ_1	0°	30°	60°	90°	120°	150°	180°	210°	240°	270°	300°	330°
ϕ_2	0°											
ϕ_3	0°	0°	0°	0°	0°	0°	0°	0°	0°	0°	0°	0°
	45°	45°	45°	45°	45°	45°	45°	45°	45°	45°	45°	45°
	90°	90°	90°	90°	90°	90°	90°	90°	90°	90°	90°	90°
	135°	135°	135°	135°	135°	135°	135°	135°	135°	135°	135°	135°
	180°	180°	180°	180°	180°	180°	180°	180°	180°	180°	180°	180°
	225°	225°	225°	225°	225°	225°	225°	225°	225°	225°	225°	225°
	270°	270°	270°	270°	270°	270°	270°	270°	270°	270°	270°	270°
	315°	315°	315°	315°	315°	315°	315°	315°	315°	315°	315°	315°
rec. phase	0°	270°	180°	90°	0°	270°	180°	90°	0°	270°	180°	90°
	90°	0°	270°	180°	90°	0°	270°	180°	90°	0°	270°	180°
	180°	90°	0°	270°	180°	90°	0°	270°	180°	90°	0°	180°
	270°	180°	90°	0°	270°	180°	90°	0°	270°	180°	90°	0°

4.3 Other techniques for half-integer quadrupolar nuclei

REDOR experiments employing spin-$\frac{1}{2}$–quadrupolar nuclei (half-integer) spin pairs have been developed [38–40] for the purposes of studying internuclear distances between quadrupolar nuclei. Some of these combine REDOR with MQMAS [38]. REDOR is discussed further in Section 3.3.2.

Very large quadrupole-coupling constants still cause problems, even for half-integer spins. For quadrupole-coupling constants which exceed an order 10 MHz,

even the central transition becomes excessively broad to observe. In these circumstances, the techniques described in Section 4.2 become considerably less useful, and one has to resort to quadrupole-echo detection of the central transition, usually under magic-angle spinning. More recently, a quadrupolar Carr–Purcell–Meiboom–Gill (CPMG) experiment has been developed which performs better than traditional quadrupole-echo experiments [**41**]. This is discussed further in Section 6.5.1.

There are, however, two further techniques applied to quadrupolar nuclei which should be mentioned: quadrupole nutation and cross-polarization. Quadrupole nutation is a simple experiment which has largely been superseded by MQMAS, which uses the same equipment and usually separates signals with different quadrupole-coupling constants more reliably. However, there is a great deal of beauty in the simplicity of the quadrupole nutation experiment, and it is included here because many papers in the literature in the pre-MQMAS era rely on it. Cross-polarization is not used extensively on quadrupolar nuclei, partly because it can be tricky to set up, but also because many quadrupolar nuclei of interest are highly abundant, and so cross-polarization is not needed to create signal intensity. However, it can be useful for judging which spins are close in space, and indeed this has been its primary use for quadrupolar nuclei to date. It has also been used in the MQMAS experiment [**42**].

4.3.1 Quadrupole nutation

The pulse sequence of the quadrupole nutation experiment is shown in Fig. 4.11 [**43–45**]. It is a two-dimensional experiment in which an irradiating rf pulse is applied for a period t_1 with subsequent detection of an FID during t_2. The purpose of the experiment is to study the evolution of the spin system in the rotating frame in the presence of the radiofrequency field $\mathbf{B}_1$ provided by the rf pulse in t_1. In the rotating frame, the effect of the $\mathbf{B}_0$ field is only very small, providing the rf pulse is close to resonance, so the principal field which the spins feel is the $\mathbf{B}_1$ field. Thus, the evolution during t_1 yields a low-frequency ($B_1 \sim 0.001B_0$) NMR spectrum, known as the *nutation spectrum*, while having the sensitivity of a high field experiment.

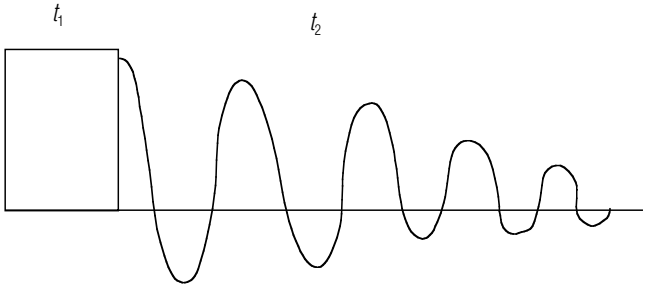

Fig. 4.11 The two-dimensional quadrupole nutation experiment. The length of the excitation pulse is increased step-wise in successive t_1 slices and the FID corresponding to the central transition of the half-integer quadrupolar nucleus under study is recorded in t_2.

Throughout this chapter we have considered the case where the Zeeman interaction is much larger than the quadrupole interaction, so that the eigenstates of the spin system are simply small perturbations of the Zeeman states. However, during the t_1 period, the Zeeman term in the rotating frame is very small in comparison to the other terms in the rotating frame hamiltonian describing the spin system in this period. The hamiltonian describing the spin system during the rf pulse irradiation in t_1 in the rotating frame is [**45**]

$$\begin{aligned}\hat{H}_{\text{pulse}} &= \hat{H}_{\text{rf}} + \hat{H}'_{\text{Q}} + \hat{H}_{\Delta} \\ &= -\omega_1 \hat{I}_y + \omega_{\text{Q}}(3\hat{I}_z^2 - \hat{I}^2) + (\omega_0 - \omega)\hat{I}_z \end{aligned} \tag{4.42}$$

where $\hat{H}_{\text{rf}}$ describes the effect of the rf pulse (taken to be a y pulse here), with the pulse amplitude, $\omega_1 = \gamma B_1$; $\hat{H}_{\text{Q}}$ describes the effects of the quadrupole coupling to first order; and $\hat{H}_{\Delta}$ describes off-resonance effects as detailed in Section 4.1.2. If we assume that the rf pulse is applied close to the Larmor frequency ($\hat{H}_{\Delta} \sim 0$), the eigenstates of the system during t_1 depend on the relative sizes of the two remaining terms in $\hat{H}_{\text{pulse}}$, namely $\hat{H}_{\text{rf}}$ and $\hat{H}_{\text{Q}}$. In other words, the eigenstates of the system depend on $\omega_1/\omega_{\text{Q}}$ (ω_{Q} is defined in Equation (4.18)), and while they may be described as linear combinations of the Zeeman spin functions (since these constitute a complete set for description of the state of the spin system), they are certainly not small perturbations of them.

During t_2, the $\mathbf{B}_1$ field, i.e. the rf pulse, is switched off and the hamiltonian governing the system becomes in the laboratory frame [**45**]

$$\hat{H}_2 = \hat{H}_0 + \hat{H}_{\text{cs}} + \hat{H}'_{\text{Q}} \tag{4.43}$$

where $\hat{H}_0$ is the Zeeman term (Equation (4.5)) and $\hat{H}_{\text{cs}}$ describes the effects of chemical shift. The eigenstates of the system now return to the usual Zeeman spin states. The FID due to coherence between the $+\frac{1}{2}$ and $-\frac{1}{2}$ spin levels, i.e. the central transition, is collected during t_2 (this is the on-resonance transition for rf irradiation near the Larmor frequency); as we have already seen in Section 4.1.1, this transition is only affected by $\hat{H}_{\text{Q}}$ in second order.

A two-dimensional dataset is collected by incrementing t_1, the length of the rf pulse during t_1. Two-dimensional Fourier transformation of this time-domain dataset yields a two-dimensional frequency spectrum with the normal central transition lineshape in f_2 and the nutation spectrum in f_1. As the nutation spectrum is principally governed by ω_1 and ω_{Q}, chemical shift effects are largely absent from this dimension.

In the extreme case of $\omega_1 >> \omega_{\text{Q}}$, $\hat{H}_{\text{pulse}}$ reduces to

$$\hat{H}_{\text{pulse}} \approx \hat{H}_{\text{rf}} = -\omega_1 \hat{I}_y \tag{4.44}$$

so the evolution (nutation) frequency of the spin system is clearly just ω_1, the rf pulse amplitude, as for any other case of an isolated (uncoupled) spin in the

presence of an on-resonance pulse. So, in this case, the nutation spectrum would just consist of a single line at frequency ω_1.

In the other extreme, $\omega_Q >> \omega_1$, $\hat{H}_{\text{pulse}}$ is simply

$$\hat{H}_{\text{pulse}} \approx \hat{H}'_Q = \omega_Q(3\hat{I}_z^2 - \hat{I}^2) \tag{4.45}$$

As shown previously in Section 4.1.2, such a case constitutes selective excitation of the transition which is on resonance. Assuming that the pulse frequency is on resonance for the central transition, the corresponding evolution or nutation frequency in this case is $(I + \frac{1}{2})\omega_1$. In this case, again, a single line is seen in the nutation spectrum, but this time at frequency $(I + \frac{1}{2})\omega_1$.

For intermediate cases, the nutation spectrum is quite complex, dependent on ω_1/ω_Q (remembering that ω_Q depends on molecular orientation) and, in general, consisting of several frequencies. Simulation of experimental nutation spectra in this regime allows quite accurate determination of the quadrupole coupling constant and asymmetry. Figure 4.12 shows the nutation spectrum calculated for a spin-$\frac{5}{2}$ nucleus in a powder sample for different χ/ω_1, where χ is the quadrupole coupling constant, including the limiting cases.

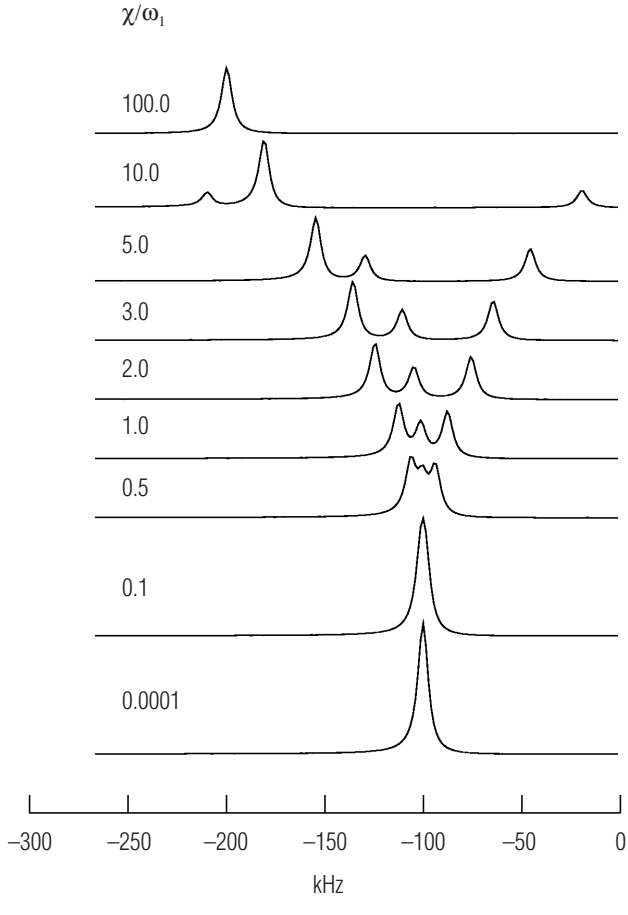

Fig. 4.12 Quadrupole nutation spectra (f_1 of the two-dimensional spectrum) for a spin-$\frac{5}{2}$ nucleus in a powder sample for various χ/ω_1 where ω_1 is the rf power used in the experiment and χ is the quadrupole coupling constant. Note the limiting cases when $\chi/\omega_1 << 1$, which gives a single line at $\omega = \omega_1$ and when $\chi/\omega_1 >> 1$, which gives a single line at $\omega = (I + \frac{1}{2})\omega_1$. $\omega_1/2\pi$ is 100 kHz in all the simulations.

4.3.2 Cross-polarization

Many quadrupolar nuclei that are studied are near to 100% abundant, so there is little need for cross-polarization in order to improve the signal-to-noise ratio. However, cross-polarization from spin-$\frac{1}{2}$ nuclei to half-integer quadrupolar nuclei is used from time to time in solid-state NMR in order to ascertain which spins are close in space.

The cross-polarization experiment for polarization transfer from spin-$\frac{1}{2}$ to quadrupolar nuclei takes much the same form as from the conventional spin-$\frac{1}{2}$–spin-$\frac{1}{2}$ experiment discussed in Section 2.4.1. The pulse sequence is shown again in Fig. 4.13 for convenience, where the cross-polarization is from the I spin-$\frac{1}{2}$ to the quadrupolar S spin.

The principal difference from the pure spin-$\frac{1}{2}$ case is in the Hartmann–Hahn match. For the spin-1/2–spin-$\frac{1}{2}$ cross-polarization case, the Hartmann–Hahn condition is simply $\omega_{1I} = \omega_{1S}$, where $\omega_{1I} = \gamma_I B_{1I}$ and $\omega_{1S} = \gamma_S B_{1S}$, the I and S spin amplitudes. When S is a quadrupolar nucleus, the Hartmann–Hahn condition is replaced by the more general condition that ω_{1I} should be equal to ω_{nut}, the nutation frequency of the S spin transition to which it is being cross-polarized. As seen in the previous section and in Section 4.1.2, the nutation behaviour of a quadrupolar spin depends on the relative magnitudes of the quadrupolar splitting, ω_Q (Equation (4.18)) and ω_{1S}. As we saw in the previous section, there are two limiting cases. When $\omega_{1S} >> \omega_Q$, the nutation frequency is not affected by the quadrupole coupling at all, so that the nutation frequency is just the usual $\omega_{\text{nut}} = \omega_{1S}$, as for any uncoupled spin system. When $\omega_{1S} << \omega_Q$, only a single transition is irradiated – the one that is on resonance. Primarily, we are interested in the central transition, for which the nutation frequency under these selective excitation conditions

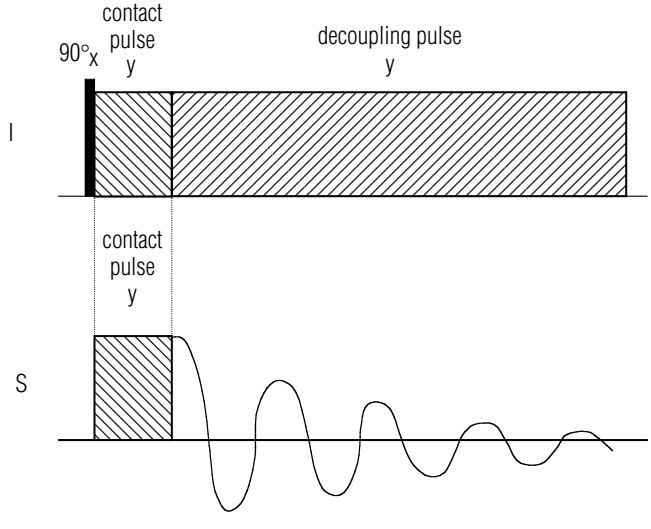

Fig. 4.13 The cross-polarization pulse sequence. This pulse sequence was introduced in chapter 2 for spin-$\frac{1}{2}$ nuclei. Here, I is a spin-$\frac{1}{2}$ nucleus and S a half-integer quadrupolar spin. Polarization is transferred from the spin-$\frac{1}{2}$ to one or more S spin transitions, depending on the size of the quadrupole coupling relative to the pulse amplitude – see text for details.

is $\omega_{nut} = (S + \frac{1}{2})\omega_{1S}$. Thus, for these two limiting cases, the appropriate matching conditions are:

$$\begin{aligned} \omega_{1S} >> \omega_Q: &\quad \omega_{1I} = \omega_{1S} \\ \omega_{1S} << \omega_Q: &\quad \omega_{1I} = \left(S + \frac{1}{2}\right)\omega_{1S} \end{aligned} \tag{4.46}$$

In the intermediate regime, $\omega_{1S} \sim \omega_Q$, the Hartmann–Hahn condition is not well defined. For a start, in this regime the nutation spectrum of the S spin has several frequencies as can be seen by looking at the nutation spectra in this regime in Fig. 4.12.

As well as cross-polarizing to the central transition of half-integer quadrupolar nuclei, it is also possible to cross-polarize to symmetric $+m \rightarrow -m$ multiple quantum transitions [**46**]. This has aroused interest recently in connection with the MQMAS experiment. Equation (4.36) gives the nutation frequency for the these multiple-quantum transitions, which can then be matched with ω_{1I} in the selective excitation limit, $\omega_{1S} << \omega_Q$ to cross-polarize to the particular multiple-quantum transition. A particularly good example of the use of cross-polarization involving quadrupolar nuclei is in the two-dimensional HETCOR (heteronuclear correlation) experiment shown in Fig. 4.14(a) [**47**]. A HETCOR spectrum shows spatial correlations between two heteronuclear spins. In the simplest version of this type of experiment, transverse magnetization is generated for one nuclear species, I (^{23}Na in the case shown in Fig. 4.14) and allowed to evolve at its characteristic frequency in t_1. The remaining magnetization is then transferred to the other nuclear species, S (^{31}P in Fig. 4.14) in a cross-polarization step, and an FID collected in t_2. Fourier transformation in t_1 and t_2 results in a two-dimensional frequency spectrum with cross peaks between I and S spin signals, indicating that cross-polarization took place between the corresponding spins, and therefore that these spins are close in space. Figure 4.14(b) shows another HETCOR spectrum of the same sample, but this time the experiment has been arranged so that a high-resolution MQMAS spectrum of the I spin (^{23}Na) appears in the f_1 dimension of the spectrum, rather than the standard magic-angle spinning spectrum of Fig. 4.14(a). This is done by using the usual MQMAS pulse sequence (Fig. 4.8) on the I spin (^{23}Na), then at the point of the MQMAS echo formation (at kt_1 after the mulitple-quantum $\rightarrow$ single-quantum transfer pulse), cross-polarization is used to transfer the I spin magnetization to the S spin (^{31}P). An S spin FID is then recorded in t_2 as in the simple HETCOR experiment.

Under static conditions, i.e. no sample spinning, cross-polarization to the central or symmetric multiple-quantum transition of a half-integer quadrupolar S spin is relatively straightforward. It only suffers the same difficulties as the cross-polarization between two spin-$\frac{1}{2}$ nuclei, with one exception. Only a fraction of the I spin magnetization (a half for spin-$\frac{3}{2}$ under selective excitation conditions for the

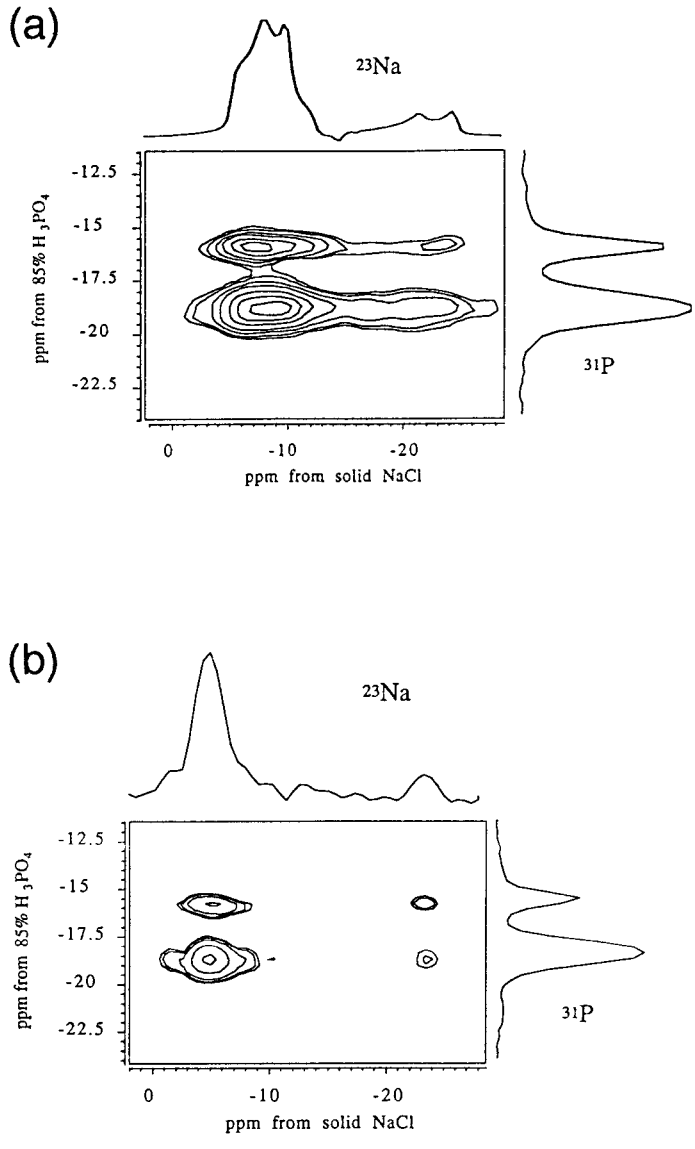

Fig. 4.14 A ^{23}Na($I = \frac{3}{2}$) – ^{31}P($I = \frac{1}{2}$) HETCOR (heteronuclear correlation) spectra of $Na_3P_3O_9$ [47]. (a) shows the HETCOR spectrum of $Na_3P_3O_9$ obtained with a 'standard' magic-angle spinning spectrum in the ^{23}Na dimension. (b) Shows a similar spectrum but this time, the experiment has been arranged so that a MQMAS ^{23}Na spectrum appears in the ^{23}Na dimension. (Taken from Wang, De Paul and Bull (1997).)

central transition for instance) participates in the polarization transfer process, the remaining I spin magnetization being associated with spin levels outside the central transition. In contrast, in cross-polarization between spin-$\frac{1}{2}$ nuclei, all the I spin magnetization is involved. However, there are key differences under magic-angle spinning, which principally relate to differences in spin locking a spin-$\frac{1}{2}$ and a quadrupolar spin system. As discussed in Section 2.5, during the contact pulses on both spins, both I and S spin systems are spin locked via their respective pulses and it is while in this situation that magnetization is transferred between the spins. The conditions for spin locking a quadrupolar spin system are discussed below.

Spin locking in half-integer quadrupolar spin systems under magic-angle spinning [48]

Spin locking was discussed briefly in Section 2.5. To elaborate, a spin system is considered to be spin locked if it can be described as a collection of populated eigenstates of the hamiltonian governing it. Such a system necessarily has a constant component of magnetization (in some direction) associated with it; this is what is required in spin locking. We shall consider whether or not this is the case for conditions of slow, intermediate and fast spinning rates relative to ω_Q.

The discussion which follows is in terms of eigenstates of the spin system and their populations rather than in terms of the density operator, as it is easier to define a spin-locked state in this way. We start therefore with the eigenstates of the system during a (spin-lock) rf pulse under static, i.e. no spinning, conditions.

The eigenstates in question are simply the eigenstates of a hamiltonian incorporating a term to describe the effects of the rf field, a quadrupolar term, and a term to take account of frequency offsets. Quadrupolar effects need only be considered to first order for this discussion. Thus the hamiltonian in question is

$$\begin{aligned}\hat{H}_{\text{pulse}} &= \hat{H}_{\text{rf}} + \hat{H}_{\text{Q}}^{(1)} + \hat{H}_{\Delta} \\ &= -\omega_{1S}\hat{S}_y + \omega_{\text{Q}}(3\hat{I}_z^2 - \hat{I}^2) + (\omega_0 - \omega)\hat{I}_z \end{aligned} \tag{4.47}$$

for a *y* pulse. The eigenvalues of this hamiltonian (calculated numerically) are shown in Fig 4.15 as a function of ω_Q/ω_1. The nature of the eigenstates these correspond to at extreme values of ω_Q/ω_1 is also indicated in this diagram, which simply shows that the nature of the eigenstate and its energy depend on ω_Q, which in turn depend on molecular/crystallite orientation within the applied field $\mathbf{B}_0$.

Now consider the effects of magic-angle spinning. Magic-angle spinning intro-

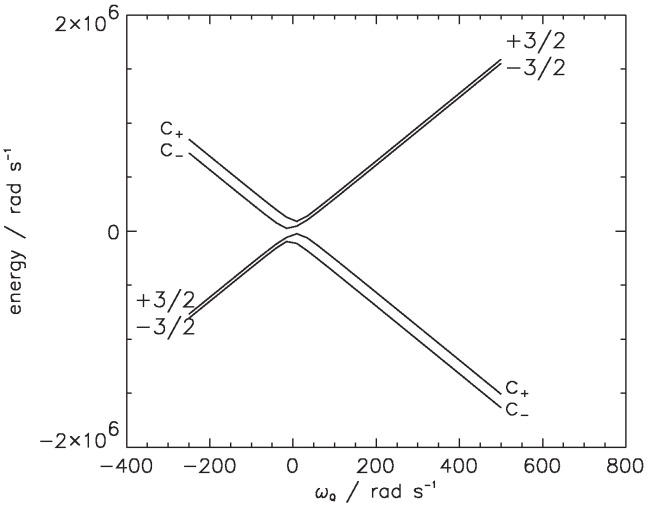

Fig. 4.15 The eigenstates of a spin-$\frac{3}{2}$ nucleus during an rf pulse.

duces time dependence into the system. Clearly as the sample rotates, each crystallite experiences a change in orientation and so ω_Q for each crystallite changes. However, when the speed of spinning is very slow ($\omega_{IS}^2/\omega_Q\omega_R >> 1$, where ω_R is the spinning rate), the change in spin state is slow enough to be adiabatic, i.e. the system remains in thermal equilibrium throughout the rotor cycle. Under these conditions, the eigenstates of the system at any point in the rotor cycle are simply those that would occur if the sample were static in that particular orientation. In other words, the eigenvalues and states of Fig. 4.15 apply. The system simply moves slowly along each of the lines in Fig. 4.15 as ω_Q changes during the spinning, with eigenstates changing smoothly between the extremes indicated. Because the system is constantly in thermal equilibrium, the eigenstates are populated according to a Boltzmann distribution. Thus, we can say that under conditions of slow speed spinning, the system can be spin locked; it is well described by a set of $2S + 1$ eigenstates with corresponding populations.

In the case of very rapid spinning, ($\omega_{IS}^2/\omega_Q\omega_R << 1$), the quadrupole interaction is being averaged rapidly relative to its size. We need only then consider the average quadrupole interaction over a rotor cycle (zero, in fact, if only first-order coupling is considered), which is a constant. In other words, the eigenstates of the system are effectively time-independent, and so therefore, are their populations. Hence, we can also say that under conditions of fast spinning, the system can be spin locked.

However, in the case of intermediate spinning speeds ($\omega_{IS}^2/\omega_Q\omega_R \approx 1$), the eigenstates of the spin system are rapidly time-dependent. The ensemble average spin state for the collection of spin systems in the sample can be described as a statistical linear combination of the eigenstates, but the combination coefficients here do not correspond to eigenstate populations. This point was discussed in Chapter 1 in Section 1.2 when examining the effect of an rf pulse on the state of a collection of isolated spin-$\frac{1}{2}$ nuclei. Therefore, the system cannot be described as spin locked. The time-dependence of the system means that there is no constant magnetization component in any direction.

Thus cross-polarization to the central transition of a half-integer quadrupolar spin can be conducted under slow speed (adiabatic) or very fast spinning, but not in the intermediate regime; in the latter, polarization formed in one part of the rotor cycle decays rapidly in another part.

In the adiabatic regime, it can be shown that all the I spin magnetization is involved in the polarization transfer process, in contrast to the static (non-spinning) case. Moreover, an S spin signal can arise from direct polarization under these conditions. This can be prevented by alternating the phase of the initial I spin 90° pulse along with phase alternation of the S spin signal detection, while keeping the spin-locking/contact pulses at the same phase.

Finally, it is interesting to enquire whether magic-angle spinning produces a sideband-modulated Hartmann–Hahn match as it does for spin-$\frac{1}{2}$–spin-$\frac{1}{2}$ cross-polarization. In particular, in the pure spin-$\frac{1}{2}$ case under rapid magic-angle spinning,

the Hartmann–Hahn match fails and is instead shifted by $\pm\omega_R$, $\pm 2\omega_R$ (see Section 2.5). The reason for this failure is that the net polarization transfer depends on the time integral of the *I–S* dipolar coupling interaction, which vanishes under rapid magic-angle spinning (or for time periods which are integral numbers of rotor periods). However, when cross-polarizing to a quadrupolar nucleus, the polarization transfer also depends on the strength of quadrupole coupling, which like the dipolar coupling, varies over the rotor period, but in a different manner. The net time integral of the dipolar interactions multiplied by the quadrupole coupling factor is no longer zero under magic-angle spinning. Thus, the Hartmann–Hahn match survives under magic-angle spinning, even if it is rapid compared to the dipolar-coupling strength, providing the spinning conditions are adiabatic with respect to the quadrupole coupling.

References

1. C.P. Slichter, *Principles of Magnetic Resonance*, Springer-Verlag, Berlin (1990).
2. A. Abragam, *The Principles of Nuclear Magnetism*, Clarendon Press, Oxford (1983), Ch. VII.
3. M.H. Cohen and F. Reif, *Solid-State Physics* **5** (1957) 321.
4. A. Samoson, E. Kundla and E. Lippmaa, *J. Magn. Reson.* **49** (1982) 350.
5. M.J. Duer and C. Stourton, *J. Magn. Reson.* **124** (1997) 189.
6. J.-P. Amoureux, *Solid-State NMR* **2** (1993) 83.
7. M.E. Rose, *Elementary Theory of Quantum Mechanics*, Wiley, New York (1957).
8. D. Fenzke, D. Freude, T. Fröhlich and J. Haase, *Chem. Phys. Lett.* **111** (1984) 171.
9. P.P. Man, J. Klinowski, A. Trokiner, H. Zanni and P. Papon, *Chem. Phys. Lett.* **151** (1988) 143.
10. N. Chr. Nielsen, H. Bildsøe and H.J. Jakobsen, *Chem. Phys. Lett.* **191** (1992) 205.
11. I.J.F. Poplett and M.E. Smith, accepted for publication in *Solid-State NMR* (1998).
12. A. Samoson, *Chem. Phys. Lett.* **119** (1985) 29.
13. C. Jaeger, W. Mueller-Warmuth, C. Mundus and L. van Wuellen, *J. Non-Cryst. Solids* **149** (1992) 209.
14. A. Samoson, E. Lippmaa and A. Pines, *Molec. Phys.* **65** (1988) 1013.
15. B.F. Chmelka, K.T. Mueller, A. Pines, J. Stebbins, Y. Wu and J.W. Zwanziger, *Nature* **339** (1989) 42.
16. L.M. Bull, A.K. Cheetham, T. Anupold, A. Reinhold, A. Samoson, J. Sauer, B. Bussemer, Y. Lee, S. Gann, J. Shore, A. Pines and R. Dupree, *J. Am. Chem. Soc.* **120** (1998) 3510.
17. K.T. Mueller, B.Q. Sun, G.C. Chingas, J.W. Zwanziger, T. Terao and A. Pines, *J. Magn. Reson.* **86** (1990) 470.
18. P.J. Grandinetti, J.H. Baltisberger, I. Farnan, J.F. Stebbins, U. Werner and A. Pines, *J. Phys. Chem.* **99** (1995) 12341.
19. L. Frydman and J.S. Harwood, *J. Am. Chem. Soc.* **117** (1995) 5367.
20. A. Medek, J.S. Harwood and L. Frydman, *J. Am. Chem. Soc.* **117** (1995) 12779.
21. M.J. Duer and C. Stourton, *J. Magn. Reson.* **124** (1997) 189.
22. S. Vega and Y. Naor, *J. Chem. Phys.* **75** (1981) 75.
23. C. Fernandez and J.-P. Amoureux, *Chem. Phys. Lett.* **242** (1995) 449.
24. G. Wu, D. Rovnyak, B. Sun and R.G. Griffin, *Chem. Phys. Lett.* **249** (1996) 210.
25. D. Massiot, B. Touzo, D. Trumeau, J.P. Coutures, J. Virlet, P. Florian and P.J. Grandinetti, *Solid-State NMR* **6** (1996) 73.
26. J.-P. Amoureux, C. Fernandez and L. Frydman, *Chem. Phys. Lett.* **259** (1996) 347.
27. J.-P. Amoureux, C. Fernandez and S. Steuernagel, *J. Magn. Reson.* **123** (1996) 116.

28. D. Massiot, *J. Magn. Reson.* **122A** (1996) 240.
29. G. Wu, D. Rovnyak and R.G. Griffin, *J. Am. Chem. Soc.* **118** (1996) 9326.
30. S. Ding and C.A. McDowell, *Chem. Phys. Lett.* **270** (1997) 81.
31. S.P. Brown and S. Wimperis, *J. Magn. Reson.* **124** (1997) 279.
32. M. Hanaya and R.K. Harris, *J. Phys. Chem.* **101A** (1997) 6903.
33. L. Marinelli, A. Medek and L. Frydman, *J. Magn. Reson.* **132** (1998) 88.
34. S. Ding and C.A. McDowell, *J. Magn. Reson.* **135** (1998) 61.
35. J-P. Amoureux and C. Fernandez, *Solid-State NMR* **10** (1998) 211.
36. P.K. Madhu, A. Goldbourt, L. Frydman and S. Vega, *Chem. Phys. Lett.* **307** (1999) 41.
37. P.J. Grandinetti, J.H. Baltisberger, A. Llor, Y.K. Lee, U. Werner, M.A. Eastman and A. Pines, *J. Magn. Reson.* **103A** (1993) 72.
38. C. Fernandez, D.P. Lang, J.P. Amoureux and M. Pruski, *J. Am. Chem. Soc.* **120** (1998) 2672; M. Pruski, A. Bailly, D.P. Lang, J.P. Amoureux and C. Fernandez, *Chem. Phys. Lett.* **307** (1999) 35.
39. C.A. Fyfe, K.T. Mueller, H. Grondey and K.C. Wongmoon, *J. Phys. Chem.* **97** (1993) 13484.
40. T.P. Jarvie, R.M. Wenslow and K.T. Mueller, *J. Am. Chem. Soc.* **117** (1995) 570.
41. F.H. Larsen, H.J. Jakobsen, P.D. Ellis and N. Chr. Nielsen, *Molec. Phys.* **95** (1998) 1185.
42. C. Fernandez, L. Delevoye, J.P. Amoureux, D.P. Lang and M. Pruski, *J. Am. Chem. Soc.* **119** (1997) 6858.
43. A. Samoson and E. Lippmaa, *Chem. Phys. Lett.* **100** (1983) 205.
44. A. Samoson and E. Lippmaa, *Phys. Rev.* **28B** (1983) 6567.
45. A.P.M. Kentgens, J.J.M. Lemmens, F.M.M. Geurts and W.S. Veeman, *J. Magn. Reson.* **71** (1987) 62.
46. S.E. Ashbrook and S. Wimperis, *Molec. Phys.* **98** (2000) 1.
47. S.H. Wang, S.M. De Paul and L.M. Bull, *J. Magn. Reson.* **125** (1997) 364.
48. A. Vega, *Solid-State NMR* **1** (1992) 17.

Solid-State NMR Spectroscopy Principles and Applications
Edited by Melinda J. Duer
Copyright © 2002 by Blackwell Science Ltd

Chapter 5
Shielding and Chemical Shift

Melinda J. Duer

5.1 The relationship between the shielding tensor and electronic structure

The nuclear magnetic shielding can be thought of as being composed of two components: (1) *the diamagnetic contribution* arises from the classical diamagnetic electronic current induced by the applied magnetic field. The circulating current in turn generates an induced magnetic field which opposes the applied field; (2) *the paramagnetic contribution* arises from the mixing of particular excited electronic states into the ground electronic state in the presence of a magnetic field (in the terminology used in perturbation theory). The net shielding tensor, $\boldsymbol{\sigma}$, is given by the sum of the diamagnetic and paramagnetic terms [**1**]:

$$\boldsymbol{\sigma} = \boldsymbol{\sigma}^{\mathrm{d}} + \boldsymbol{\sigma}^{\mathrm{p}} \tag{5.1}$$

where components of the constituent tensors are given by:

$$\sigma^{\mathrm{d}}_{\gamma\gamma} = \frac{\mu_0}{4\pi}\frac{e^2}{2m_{\mathrm{e}}}\left\langle \Psi_0 \left| \sum_i \frac{\alpha_i^2 + \beta_i^2}{r_i^3} \right| \Psi_0 \right\rangle \tag{5.2}$$

and

$$\sigma^{\mathrm{p}}_{\alpha\beta} = -\frac{\mu_0}{4\pi}\frac{e^2}{2m_{\mathrm{e}}}\sum_{k\neq 0}\left[\frac{\left\langle \Psi_0 \left| \sum_i \hat{l}_{i\alpha} \right| \Psi_k \right\rangle \left\langle \Psi_k \left| \sum_i \frac{\hat{l}_{i\beta}}{r_i^3} \right| \Psi_0 \right\rangle + \mathrm{c}\cdot\mathrm{c}}{E_k - E_0}\right] \tag{5.3}$$

when the gauge origin is at the nucleus in question. α, β, γ denote Cartesian axes. The Ψ are electronic wavefunctions; the suffix i denotes the ith electron. The ground electronic state is denoted 0 and an excited electronic state, by k. r_i is the distance of the ith electron from the nucleus, and α_i, β_i are its coordinates along the α and β directions respectively. $\hat{l}_{i\alpha}, \hat{l}_{i\beta}$ are components of the electronic orbital angular momentum operator, $\hat{\mathbf{l}}_i$ for the ith electron.

The diamagnetic term (Equation (5.2)) depends only on the ground electronic state. Furthermore, its dependence on r_i^{-3} means that it is very much a *local* contribution, arising largely from the core electrons surrounding the nucleus.

The paramagnetic term (Equation (5.3)) provides more of a commentary on bonding [**1**]. It depends on integrals involving components of the electronic orbital angular momentum operator, $\hat{l}_\alpha$, the ground electronic state and various excited electronic states. This equation can be written in a more tractable form with the following considerations. The electronic wavefunction, Ψ_0 is a product wavefunction involving all the occupied molecular orbitals in the ground electronic state and the excited states Ψ_k are similarly product wavefunctions, but involving electrons in molecular orbitals not occupied in the ground state. The integrals in Equation (5.3) over the excited states Ψ_k are only non-zero for Ψ_k with *one* of the electrons from a ground state occupied molecular orbital excited to an unoccupied orbital. Thus integrals between Ψ_0 and Ψ_k have the effect of mixing a ground state occupied molecular orbital with one that is unoccupied in the ground state, and indeed, we may rewrite Equation (5.3) so that only the two molecular orbitals which differ between the ground and excited state configurations appear in the integrals. The equation for $\sigma^{\mathrm{p}}_{\alpha\beta}$ then contains terms of the form

$$\frac{\left\langle \psi_{\mathrm{occ}} \left| \sum_i \hat{l}_{i\alpha} \right| \psi_{\mathrm{unocc}} \right\rangle \left\langle \psi_{\mathrm{unocc}} \left| \sum_i \frac{\hat{l}_{i\beta}}{r_i^3} \right| \psi_{\mathrm{occ}} \right\rangle + \mathrm{c \cdot c}}{\varepsilon_{\mathrm{unocc}} - \varepsilon_{\mathrm{occ}}} \tag{5.4}$$

where Ψ_{occ} is the molecular orbital which is occupied in the ground electronic state Ψ_0, but empty in the excited electronic state, Ψ_k; ψ_{unocc} is the molecular orbital which is unoccupied in the ground electronic state, but occupied in the excited electronic state Ψ_k. The $(E_k - E_0)$ energy factor has been replaced by $(\varepsilon_{\mathrm{unocc}} - \varepsilon_{\mathrm{occ}})$, the energy difference between the occupied and unoccupied molecular orbitals of (5.4) molecular orbitals, which is very approximately equal to $(E_k - E_0)$. This energy denominator means that the only important integrals in the sum of Equation (5.3) are those which involve high-lying occupied molecular orbitals and low-lying unoccupied molecular orbitals. The problem can be further broken down by approximating the molecular orbitals as linear combinations of atomic orbitals. The r_i^{-3} factor in Equation (5.3) means that only those electrons near the nucleus are important in determining $\boldsymbol{\sigma}^{\mathrm{p}}$. Therefore the only parts of the molecular orbitals which make a significant contribution to the integrals involving that factor are those which have significant contributions from atomic orbitals which are centred on the nucleus in question. Symmetry arguments allow further insight; the integrals in the expression of (5.4) are only non-zero if their integrands transform as the totally symmetric representation of the molecular point group. The orbital angular momentum operators $\hat{l}_\alpha$ transform as the rotation operators for rotation about axis α, so the requirement for non-zero integrals can be written as

$$\Gamma_{\text{occ}} \otimes \Gamma_{\hat{R}_\alpha} \otimes \Gamma_{\text{unocc}} \subset \Gamma_0 \tag{5.5}$$

where Γ_{occ} is the point group representation of the occupied molecular orbital of (5.4), Γ_{unocc} is that of the unoccupied molecular orbital, and $\Gamma_{\hat{R}_\alpha}$ is the symmetry of the $\hat{R}_\alpha$ rotation operator for rotation about axis α. An equivalent expression to (5.5) is

$$\Gamma_{\text{occ}} \otimes \Gamma_{\hat{R}_\alpha \psi_{\text{unocc}}} \subset \Gamma_0 \tag{5.6}$$

where $\Gamma_{\hat{R}_\alpha \psi_{\text{unocc}}}$ is the point group representation of $\hat{R}_\alpha \psi_{\text{unocc}}$, i.e. the ψ_{unocc} molecular orbital rotated about axis α. In other words, for the integrals in (5.4) to be non-zero, the occupied molecular orbital must have the same symmetry as (and significant overlap with) the unoccupied molecular orbital, *after it is rotated about axis* α.

The formulation in Equation (5.4), coupled with simple qualitative molecular orbital pictures describing the local bonding around a nucleus, allows a qualitative understanding of the shielding tensor in many compounds. From this basis, correlations between the bonding in different compounds can be made on the basis of simple chemical shift measurements. As an example consider the ^{13}C shielding tensor for ethene. Table 5.1 shows the principal shielding values determined by experiment [2]. The principal axes associated with these values are parallel to the molecular two-fold axes, as shown in Fig. 5.1.

Table 5.1 The principal values of the ^{13}C chemical shielding tensor and isotropic chemical shift (δ_i) relative to TMS for the C_2H_4 molecule and the C_2H_4 ligand in Zeise's salt. Note that in Zeise's salt, the two ethene carbons are inequivalent

	σ_{11} (ppm)	σ_{22} (ppm)	σ_{33}(ppm)	δ_i (ppm)	Ref.
Free C_2H_4	–234	–120	–24	123	[2]
C_2H_4 in Zeise's salt	–135	–67	10	63	[3]
	–133	–64	12	61	[3]

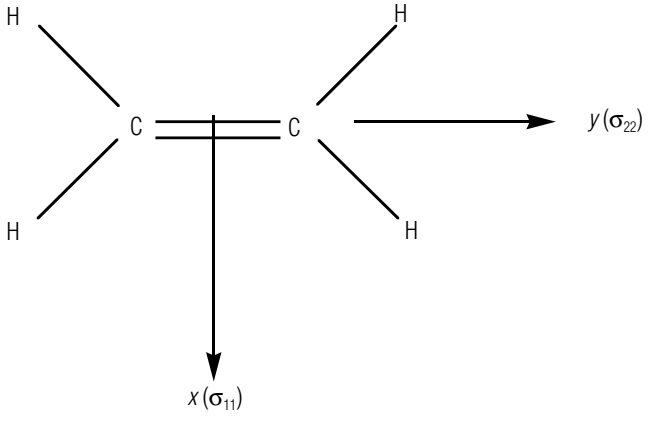

Fig. 5.1 The principal directions of the ^{13}C shielding tensor in ethene [2]. The σ_{33} (z) component is perpendicular to the plane of the molecule.

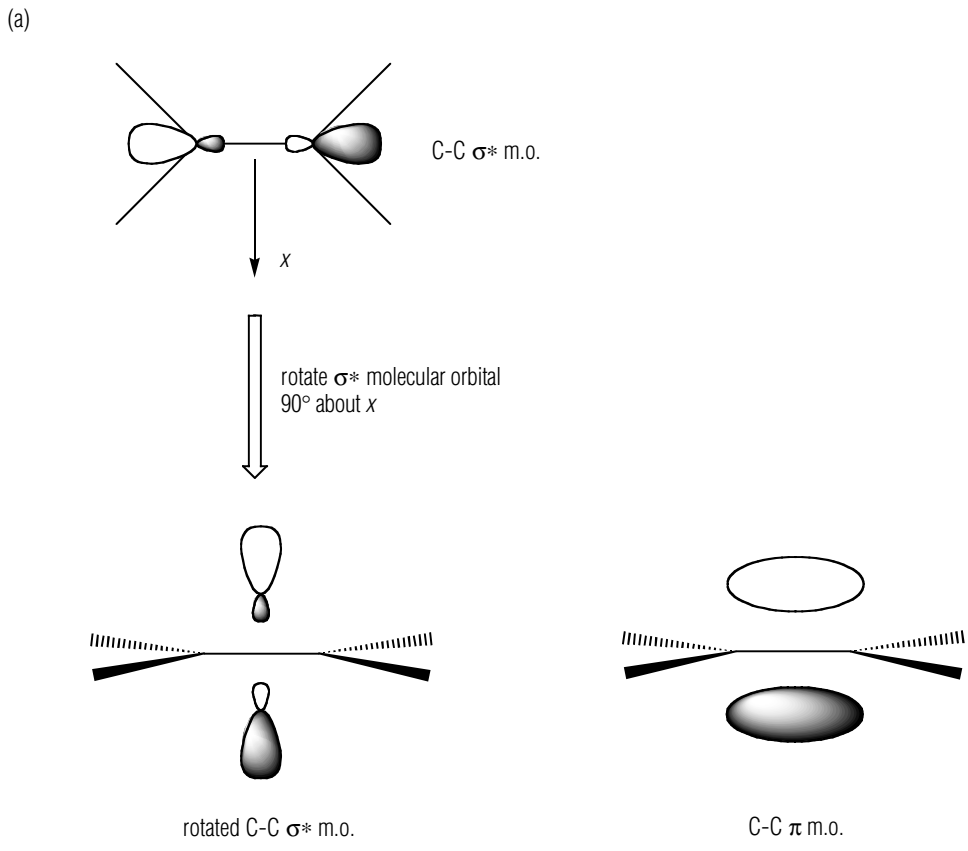

Fig. 5.2 (a) The charge rotation (C–C $\sigma^* \rightarrow$ C–C π) which contributes to the paramagnetic part of the σ_{11} component of the ^{13}C shielding tensor in ethene. The C–C π molecular orbital is also shown; there is clearly a non-zero overlap between this orbital and the rotated orbital. (b) The charge rotation (C–H $\sigma^* \rightarrow$ C–C π) which contributes to the paramagnetic part of the σ_{22} component of the ^{13}C shielding tensor in ethene. In the rotated orbital, the ethene molecule is shown end-on (viewed along the C–C bond), and only the parts of the rotated orbital close to the ^{13}C nuclei are shown. Again, the C–C π molecular orbital is shown. Once again, the rotated orbital has a non-zero overlap with this latter orbital.

The shielding component, σ_{11} is in the molecular plane; σ_{22} is parallel to the C=C bond, and σ_{33} is perpendicular to the molecular plane.

The contribution to the paramagnetic component of the shielding tensor, $\sigma^p_{\alpha\alpha}$ depends upon matrix elements of the form in expression (5.4). As Fig. 5.2(a) illustrates, rotating the C–C σ^* antibonding molecular orbital of the C_2H_4 molecule through 90° about the axis associated with the $\sigma_{11}(x)$ component transforms it into a new orbital which has a non-zero overlap with the C–C π bonding molecular orbital (Fig. 5.2(a)). Similarly, rotating C–C π^* about x gives an orbital that has a non-zero overlap with the C–C σ molecular orbital. These two interactions are the dominant contributions to the paramagnetic part of σ_{11}.

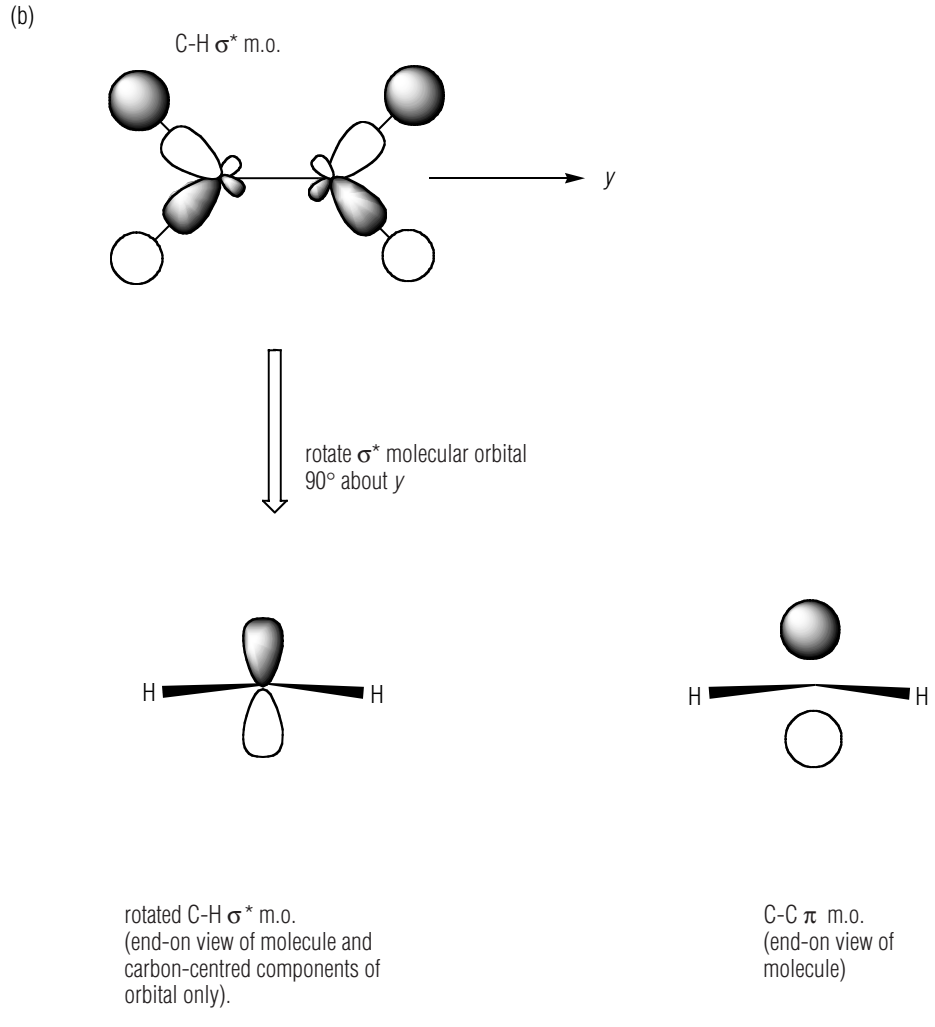

Fig. 5.2 *Continued*

Rotating the C–H σ* antibonding molecular orbitals about the axis associated with the σ_{22} component (y) transforms it into an orbital which has non-zero overlap with the C–C π bonding molecular orbital (Fig. 5.2(b)). Rotating C–C π* gives an orbital with a non-zero overlap with the C–H σ molecular orbital. These are the dominant contributions to the paramagnetic part of σ_{22}.

A similar analysis shows that only C–C σ* → C–H σ and C–H σ* → C–C σ molecular orbital interactions are important for the σ_{33} component of the shielding tensor.

To estimate the relative sizes of the shielding tensor principal values, we need to consider the relative sizes of the energy factors $(\varepsilon_{unocc} - \varepsilon_{occ})^{-1}$ involved for each shielding tensor component, and the relative sizes of the matrix elements in expression (5.4). The energy factors for the dominant terms in the σ_{11} component are $(\varepsilon_{C-C\,\sigma^*} - \varepsilon_{\pi})^{-1}$ and $(\varepsilon_{\pi^*} - \varepsilon_{C-C\,\sigma})^{-1}$; for the σ_{22} component they are $(\varepsilon_{C-H\,\sigma^*} - \varepsilon_{\pi})^{-1}$ and $(\varepsilon_{\pi^*} - \varepsilon_{C-H\,\sigma})^{-1}$ and for σ_{33} they are $(\varepsilon_{C-C\,\sigma^*} - \varepsilon_{C-H\,\sigma})^{-1}$ and $(\varepsilon_{C-H\,\sigma^*} - \varepsilon_{C-C\,\sigma})^{-1}$. The energy differences between the σ and σ^* molecular orbitals involved in σ_{33} are likely to be significantly larger than the π/σ^* or σ/π^* energy differences involved in σ_{11} and σ_{22}. This would render the paramagnetic part of the σ_{33} component much smaller than the paramagnetic parts of the other shielding tensor components. The net shielding is of course a sum of paramagnetic and diamagnetic parts, which contribute with opposite signs; the larger the paramagnetic part, the more negative the overall shielding. Thus a small paramagnetic contribution to σ_{33} for the ^{13}C in ethene results in the small negative value for σ_{33} value observed experimentally.

In comparing the values of σ_{11} and σ_{22}, we note that the paramagnetic part of σ_{11} depends on the mixing of the C–C σ^* molecular orbital after rotation about *x* and the C–C π molecular orbital and the mixing of the rotated C–C π^* and C–C σ molecular orbitals. The paramagnetic part of σ_{22} depends on the mixing of the C–H σ^* molecular orbital after rotation about *y* and the C–C π molecular orbital and of the rotated C–C π^* and C–H σ molecular orbitals). The mixing of the C–C σ^* and C–C π orbitals involved in σ_{11} is between molecular orbitals spanning the same two atoms, and so is likely to be larger than the mixing of the C–H σ^* and C–C π molecular orbitals involved in σ_{22}, which involves orbitals in relatively different regions of space. Hence, the largest paramagnetic contribution is likely to be in σ_{11}, which explains the very large negative value observed for this component experimentally.

Also shown in Table 5.1 are the ^{13}C shielding tensor principal values for ethene in Zeise's salt, $\{K[PtCl_3(\eta^2\text{-}C_2H_4)]\}$ [**3**]; the principal axes of the shielding tensor are assumed to be similar to those for the isolated ethene molecule. A comparison of the prinicpal values for the free ethene molecule and the ethene ligand shows that it is the σ_{11} and σ_{22} components which are most changed by the complexation to the Pt metral centre. From the above discussion, it is clear that these are the components which have significant contributions from the C–C π and π^* molecular orbitals of the ethene ligand. In turn, it is these orbitals which are chiefly involved in bonding to the Pt centre, so it is not surprising that the shielding components they contribute to are the most altered by the complexation.

The dependence of the shielding tensor on the electronic structure inevitably means that it depends on the geometry of bonds around the nucleus in question. This fact can be used to determine the molecular geometry, either through experimental correlations between chemical shift parameters and known bond angles or through *ab-initio* calculations of the shielding tensor for different molecular geometries and comparing these with experimentally derived shielding tensor principal values. Such applications are discussed extensively in Chapters 7 and 8 respectively.

Details of the spectroscopic features arising from chemical shift anisotropy and the hamiltonian which governs the shielding interaction are given in Section 1.4.1.

5.2 Measuring chemical shift anisotropies

Chemical shift anisotropies can be measured directly from simple one-dimensional NMR spectra of powder samples by observing the powder patterns in the spectra, providing that (i) only shielding effects contribute to the powder pattern, and not dipole–dipole or quadrupole coupling, and (ii) powder patterns from inequivalent nuclear sites are resolved. When either of these two conditions is not met, it is still possible to extract the anisotropic shielding parameters from the one-dimensional spectrum by simulating the spectrum for all nuclear sites involved and allowing contributions from all nuclear spin interactions. However, in such cases, it is highly likely that the experimental spectrum can be reproduced by more that one set of interaction parameters leading to unacceptable ambiguities. It is then necessary to resort to two-dimensional techniques to separate the signals from different sites. The following techniques all perform such separations. They are often combined with decoupling techniques to remove the effects of heteronuclear dipole coupling. For low-abundance nuclei, it is simple to use cross-polarization from a more abundant spin in the sample to generate initial transverse magnetization in the experiments. These techniques have to date only been performed on spin-$\frac{1}{2}$ nuclei; for spins with I greater than $\frac{1}{2}$, quadrupole-coupling effects tend to dominate any spectrum and render the observation of shielding effects difficult.

We deal mainly in these following sections with the principles of the techniques; when recording two-dimensional NMR spectra, it is important to arrange the experiment in such a way as to end up with pure absorption lineshapes in the final two-dimensional frequency spectrum. This is dealt with in Section 1.6.3, and is not explored further here.

5.2.1 Magic-angle spinning with recoupling pulse sequences

There are a whole family of techniques which use relatively fast magic-angle spinning to remove the effects of chemical shift anisotropy and which apply an rf pulse sequence during the t_1 interval of the two-dimensional experiment (Fig. 5.3(a)) to prevent the averaging of the chemical shift anisotropy by the magic-angle spinning during this period. To use current parlance, we refer to techniques which have the effect of *recoupling* the chemical shift anisotropy which would otherwise be averaged to zero by the magic-angle spinning.

Perhaps one of the best of these techniques is that due to Tycko et al. [**4**] which uses $(2n + 2)$ 180° pulses per rotor period during t_1, where n is 1, 2, 3, . . . These pulses are applied at specific times during the rotor period, the precise positions

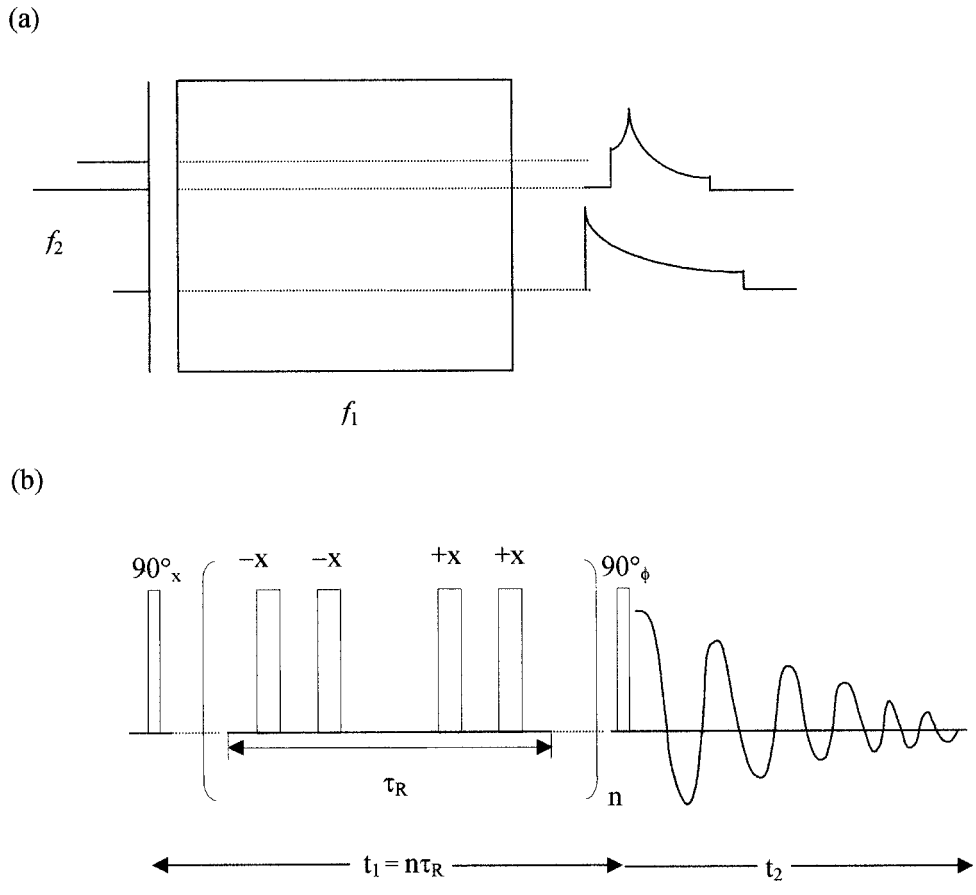

Fig. 5.3 Isotropic/anisotropic chemical shift separation experiment. (a) The form of the two-dimensional spectrum resulting from the pulse sequence due to Tycko et al. [**4**] shown in (b). The experiment is conducted under magic-angle spinning to produce an isotropic spectrum in f_2. An initial 90° pulse produces transverse magnetization in the usual manner. The series of four 180° pulses per rotor period during t_1 has the effect of preventing the averaging of the chemical shift anisotropy by magic-angle spinning during this period, so that powder patterns appear in f_1 of the two-dimensional experiment. To obtain the two-dimensional spectrum, two datasets are recorded; one in which the last 90° pulse in the sequence has the same phase ϕ as the first 90° pulse, and a second in which it has its phase shifted by 90°. In this way, the *x* and *y* components of the magnetization in t_1 are measured separately so that (with appropriate processing) a pure absorption two-dimensional spectrum can be obtained (see Section 1.6.3).

being determined by the analysis outlined below. t_1 is restricted to being an integral number of rotor periods and is generally incremented in steps of the rotor period. The initial transverse magnetization in the experiment is generated by an initial 90° pulse or cross-polarization from an abundant nucleus (Fig. 5.3(b)). In the rotating frame, this magnetization then precesses under the influence of the anisotropic chemical shift. The effect of the 180° pulses applied during the subsequent t_1 interval is to reverse the sense of the precession of the magnetization components. Thus we can write the precession frequency of the magnetization during t_1 as

$$\omega(\alpha, \beta, \gamma; t) = \omega_{cs}(\alpha, \beta, \gamma; t) f(t) \tag{5.7}$$

where $\omega_{cs}(\alpha, \beta, \gamma; t)$ is the precession frequency of the magnetization component arising from a molecular/crystallite orientation defined by the Euler angles (α, β, γ) relative to a rotor-fixed frame of reference; the time-dependence of this frequency is induced by the magic-angle spinning. The function $f(t)$ is simply a step function, stepping between the values of +1 and −1 as the 180° pulses are applied. The function $\omega_{cs}(\alpha, \beta, \gamma; t)$ was derived in Section 2.2.1 (Equation (2.7)):

$$\begin{aligned}\omega_{cs}(\alpha, \beta, \gamma; t) = -\omega_0 \{\sigma_{iso} &+ [A_1 \cos(\omega_R t + \gamma) + B_1 \sin(\omega_R t + \gamma)] \\ &+ [A_2 \cos(2\omega_R t + 2\gamma) + B_2 \sin(2\omega_R t + 2\gamma)]\}\end{aligned} \tag{5.8}$$

where A_1, etc., are functions of (α, β, γ) as defined in Equation (2.8). The precession frequency in a static experiment (no magic-angle spinning, so $\omega_R = 0$ in Equation (5.8)) by way of comparison is

$$\omega_{cs}(\alpha, \beta) = -\omega_0 \{\sigma_{iso} + A_1 + A_2\} \tag{5.9}$$

Our aim is to produce a form for the average resonance frequency over one rotor period in the spinning experiment, $\tilde{\omega}(\alpha, \beta, \gamma; t)$ which is proportional to that for the static experiment; if we can do this, the signal in t_1 of the experiment can be Fourier transformed to give a powder pattern which is simply a frequency-scaled version of the static powder pattern. The average resonance frequency over one rotor period is simply

$$\tilde{\omega}(\alpha, \beta, \gamma; t) = \int_0^{\tau_R} \omega(\alpha, \beta, \gamma; t)\, dt = \int_0^{\tau_R} \omega_{cs}(\alpha, \beta, \gamma; t) f(t)\, dt \tag{5.10}$$

Comparing Equations (5.8) (the precession frequency under magic-angle) and (5.9) (the precession frequency in a static experiment), we see that in Equation (5.10) we need the anisotropic terms A_1 and A_2 to be retained in equal amounts at the end of one rotor period, and the B_1 and B_2 terms to be averaged to zero over each rotor period (as they would normally be in a magic-angle spinning experiment with no rf pulses applied).

This is the case if the 180° pulses which define $f(t)$ are arranged such that

$$\int_0^{\tau_R} f(t) \cos(\omega_R t)\, dt = \int_0^{\tau_R} f(t) \cos(2\omega_R t)\, dt \tag{5.11}$$

If this condition is met, Equation (5.10) for the average precession frequency over the rotor period is just

$$\begin{aligned}\tilde{\omega}(\alpha, \beta, \gamma; t) &= \int_0^{\tau_R} \omega_{cs}(\alpha, \beta, \gamma; t) f(t)\, dt \\ &= -\omega_0 \Big\{ \sigma_{iso} \int_0^{\tau_R} f(t)\, dt + A_1 \int_0^{\tau_R} f(t) \cos(\omega_R t + \gamma)\, dt \\ &\quad + A_2 \int_0^{\tau_R} f(t) \cos(2\omega_R t + 2\gamma)\, dt + \int_0^{\tau_R} f(t) B_1 \sin(\omega_R t + \gamma)\, dt \\ &\quad + \int_0^{\tau_R} f(t) B_2 \sin(2\omega_R t + 2\gamma)\, dt \Big\}\end{aligned} \tag{5.12}$$

The last two integrals in Equation (5.12) are zero providing the step function $f(t)$ is even, so the average precession frequency reduces to

$$\tilde{\omega}(\alpha, \beta, \gamma; t) = -\omega_0\{\sigma_{iso}\delta + \chi(A_1 + A_2)\} \tag{5.13}$$

where the factors δ and χ are given by

$$\delta = \frac{1}{\tau_R}\int_0^{\tau_R} f(t)\,dt \quad \text{and} \quad \chi = \frac{1}{\tau_R}\int_0^{\tau_R} f(t)\cos(\omega_R t)\,dt \tag{5.14}$$

Equation (5.13) for the average precession frequency over a rotor period now has the form of the static precession frequency, but with the isotropic chemical shift scaled by δ and the chemical shift anisotropy by χ. All that remains is to choose step functions $f(t)$ to satisfy Equation (5.11). This is not detailed here, but may be found in reference [4]. Clearly, the scaling factors δ and χ depend on the step function $f(t)$. The spectral width in the f_1 dimension of the two-dimensional spectrum arising from this experiment is necessarily equal to the spinning speed, as the dwell time in the corresponding t_1 dimension is the rotor period. However, this does not provide too great a restriction on the experiment, as one of the strengths of this method is that the chemical shift anisotropy powder patterns (and isotropic chemical shifts) can be scaled to suit the chosen spectral width by selecting the appropriate 180° pulse timings in t_1.

Figure 5.4 shows the results from performing this experiment on ^{13}C in methyl-α-D-glucopyranoside [4].

5.2.2 Variable angle spinning experiments

These are experiments in which the sample is spun, but at several different angles, rather than just at the magic angle. To understand these experiments, we first need to consider how transition frequency varies as we spin at different angles. As we know, under magic-angle spinning, spectral frequencies become time-dependent according to Equation (2.4) derived in Section 2.2.1. So for a spin suffering anisotropic chemical shielding described by a shielding tensor $\boldsymbol{\sigma}^R$ in a rotor-fixed frame, the chemical shift frequency under magic-angle spinning is

$$\begin{aligned}\omega_{cs} = -\omega_0\Big\{&\sigma_{iso} + \frac{1}{2}(3\cos^2\theta_R - 1)(\sigma_{zz}^R - \sigma_{iso}) \\ &+ \sin^2\theta_R\left[\frac{1}{2}(\sigma_{xx}^R - \sigma_{yy}^R)\cos(2\omega_R t) + \sigma_{xy}^R\sin(2\omega_R t)\right] \\ &+ 2\sin\theta_R\cos\theta_R[\sigma_{zz}^R\cos(\omega_R t) + \sigma_{yz}^R\sin(\omega_R t)]\Big\}\end{aligned} \tag{5.15}$$

where ω_R is the spinning rate and θ_R is the spinning angle relative to B_0. If the rate of spinning is much greater than the chemical shift anisotropy, then the time-dependent parts of Equation (5.15) vanish, leaving just

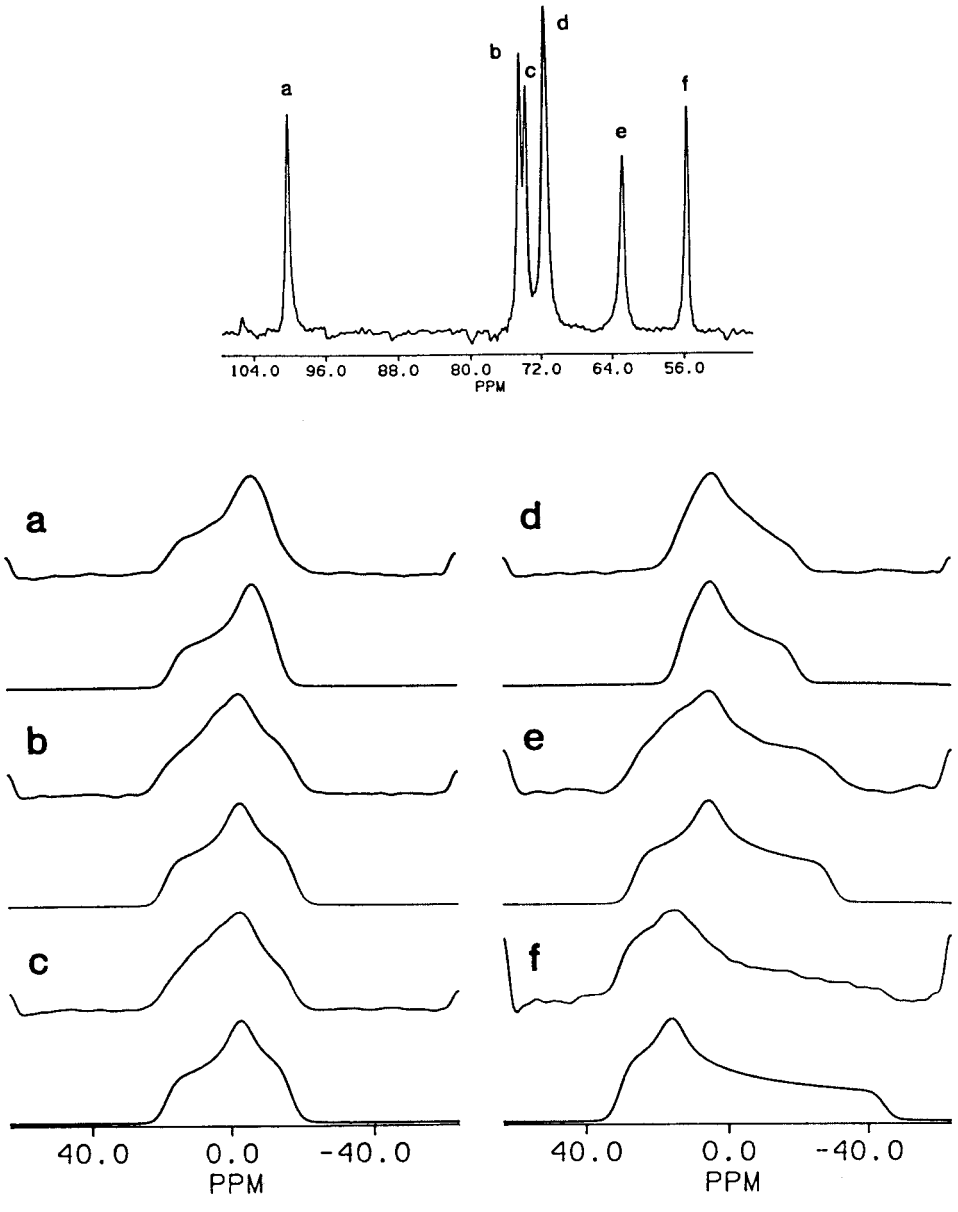

Fig. 5.4 Top: ^{13}C magic-angle spinning spectrum of methyl-α-D-glucopyranoside [**4**]. Below: ^{13}C chemical shift anisotropy powder patterns taken from the two-dimensional isotropic–anisotropic chemical shift separation experiment of the same compound [**4**] for the six ^{13}C sites. The top powder pattern in each case is the experimental one. Simulated powder patterns that best fit the experimental ones are shown below each powder pattern. (Taken from Tycho, Dabbagh and Mirau (1989).)

$$\omega_{cs} = -\omega_0\left\{\sigma_{iso} + \frac{1}{2}(3\cos^2\theta_R - 1)\,(\sigma_{zz}^R - \sigma_{iso})\right\} \tag{5.16}$$

At the magic-angle, the factor $(3\cos^2\theta_R - 1)$ is zero, leaving just the isotropic term as expected. However, consider what happens if the spinning angle is not the magic angle. In these circumstances, ω_{cs} consists of two terms, the usual isotropic term and a second anisotropic term scaled by $(3\cos^2\theta_R - 1)$. The anisotropic term can be rewritten in terms of the shielding tensor in its principal axis frame $\boldsymbol{\sigma}^{PAF}$ so that the chemical shift frequency ω_{cs}, becomes

$$\omega_{cs} = -\omega_0\left\{\sigma_{iso} + \frac{1}{2}(3\cos^2\theta_R - 1)(\sigma_{xx}^{PAF}\sin^2\beta\cos^2\alpha + \sigma_{yy}^{PAF}\sin^2\beta\sin^2\alpha + \sigma_{zz}^{PAF}\cos^2\beta - \sigma_{iso})\right\} \tag{5.17}$$

where α, β are Euler angles describing the rotation of the principal axis frame (PAF) into the rotor fixed frame (R). Equation (5.17) is exactly the same form as for a static sample, but with the anisotropic part of the shielding tensor scaled by a factor $(3\cos^2\theta_R - 1)$. In other words, the spectrum arising from sample spinning off the magic angle will be a static powder pattern, but with its chemical shift anisotropy scaled by $(3\cos^2\theta_R - 1)$. Thus one way of separating chemical shift anisotropy powder patterns is to perform a two-dimensional experiment in which during t_1 (say) the sample is spun at some angle other than the magic-angle and then the spinning angle is changed to the magic angle for the subsequent t_2 period. In practice, the angle flipping takes a finite length of time and the magnetization must be stored along $\mathbf{B}_0$ (effected by means of appropriately phased 90° pulses) during the change in spinning angle and then returned to the transverse plane at the start of the t_2 period after the angle adjustment. One problem with this experiment is the obvious one that considerable amounts of signal may be lost through relaxation during the angle-flipping process.

However, there is a much more ingenious way of using variable angle spinning to achieve isotropic/anisotropic separation, which has become known as Variable-Angle Correlation SpectroscopY or VACSY [5]. Equation (5.17) gives the chemical shift frequency under sample spinning at angle θ_R. The contribution to the FID signal arising from the chemical shift frequency is proportional to $\exp(i\omega_{cs}t)$, which can be rewritten by substituting for ω_{cs} from Equation (5.16):

$$\begin{aligned}\exp(i\omega_{cs}t) &= \exp\left(-i\omega_0\left[\sigma_{iso} + \frac{1}{2}(3\cos^2\theta_R - 1)\sigma_{aniso}\right]t\right)\\ &= \exp(-i\omega_0\sigma_{iso}t)\exp\left(-i\cdot\frac{1}{2}\omega_0(3\cos^2\theta_R - 1)\sigma_{aniso}t\right)\\ &= \exp(i\omega_{iso}t)\exp\left(i\cdot\frac{1}{2}(3\cos^2\theta_R - 1)\omega_{aniso}t\right)\end{aligned} \tag{5.18}$$

where

$$\sigma_{\text{aniso}} = \sigma_{xx}^{\text{PAF}} \sin^2\beta\cos^2\alpha + \sigma_{yy}^{\text{PAF}} \sin^2\beta\sin^2\alpha + \sigma_{zz}^{\text{PAF}} \cos^2\beta - \sigma_{\text{iso}} \tag{5.19}$$

and $\omega_{\text{iso}} = -\omega_0\sigma_{\text{iso}}$ and $\omega_{\text{aniso}} = -\omega_0\sigma_{\text{aniso}}$. In order to separate isotropic/anisotropic parts in a two-dimensional experiment, we need to obtain a signal of the form

$$\exp(i\omega_{\text{aniso}}t_1)\exp(i\omega_{\text{iso}}t_2) \tag{5.20}$$

from the experiment, i.e. precession at the isotropic frequency in t_2 and at the anisotropic part of the precession frequency in t_1. If we compare the last line of Equation (5.18) with (5.20), we see that, in fact, Equation (5.18) has the desired form if we set $t_2 = t$ and $t_1 = \frac{1}{2}(3\cos^2\theta_R - 1)t$. So we perform a two-dimensional experiment in which we first excite transverse magnetization and then record the FID during a period t_2 while spinning the sample at an angle θ_R. This is the first slice of the two-dimensional dataset. The next slice is obtained by incrementing t_1, which is achieved by changing the spinning angle θ_R, and recording the FID again. Continuing in this way gives a two-dimensional dataset, which after appropriate processing with respect to the t_1 and t_2 domains gives a two-dimensional frequency spectrum in which isotropic chemical shifts in f_2 are correlated with static-like powder patterns in f_1.

The increments in t_2 ($=\frac{1}{2}(3\cos^2\theta_R - 1)t$) are not necessarily linear (as they are generally arranged to be in a more conventional two-dimensional NMR experiment). Thus Fourier transformation cannot be used directly to transform from the t_1 domain to the corresponding frequency domain. However, there are other transformation procedures which can be used instead. Alternatively, the t_1 signal can be interpolated and a new t_1 dataset produced in which the samples points are at equal increments of t_1; this time series can then be Fourier transformed to produce the required frequency spectrum.

The great advantage of this experiment is that it gives lots of signal; each t_1 FID acquired is that resulting from a simple pulse-acquire experiment, albeit at a different spinning angle. There is no phase cycling (beyond the usual CYCLOPS), no rotor synchronization and no recoupling pulses. The changes in spinning angle take place between successive experiments, so there is no loss of signal through relaxation as in the previously described variable-angle spinning experiment.

Figure 5.5 shows a ^{13}C VACSY spectrum of *p*-anisic acid [5].

5.2.3 Magic-angle turning

Magic-angle turning [6] is a two-dimensional isotropic/anisotropic separation experiment conducted under very slow magic-angle spinning. Under very slow magic-angle spinning, the spectrum approximates to that of a static (non-spinning) experiment, and it is this feature which produces static-like powder patterns in the magic-angle turning experiment.

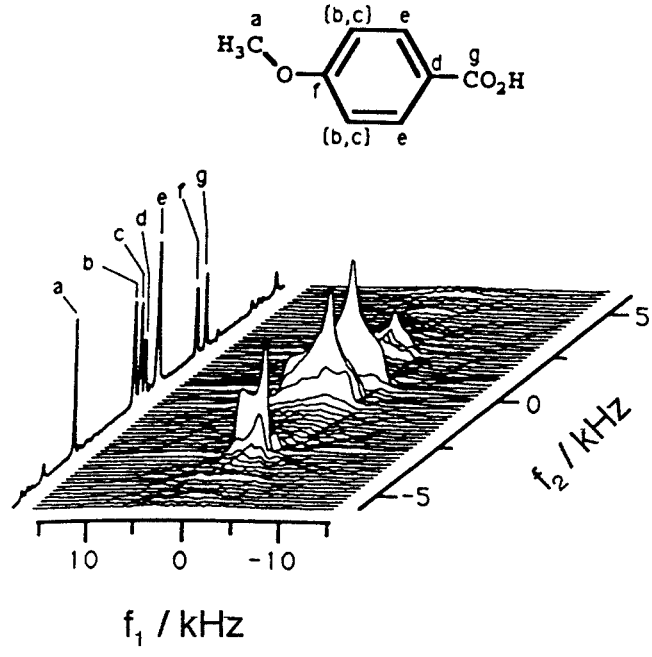

Fig. 5.5 Two-dimensional ^{13}C Variable-Angle Correlation (VACSY) spectrum of *p*-anisic acid. The isotropic ^{13}C spectrum is shown in f_2 and the powder lineshapes dependent on the chemical shift anisotropy and asymmetry for each site in f_1. (Taken from Frydman, Chingas, Lee *et al.* (1992).)

The isotropic spectrum in the other dimension of the experiment is produced as follows. Magic-angle spinning averages the anisotropic parts of the chemical shift anisotropy to zero by continuous rotation about a vector oriented at the magic angle with respect to $\mathbf{B}_0$. In fact, however, we do not need to use continuous rotation; we could use discrete hopping instead. Providing we hop the sample between a minimum of three equally-spaced angles about the magic angle, we achieve the same averaging of the anisotropic parts of the interaction. This is shown schematically in Fig. 5.6(a).[1]* In the magic-angle turning experiment, we assume that the magic-angle spinning rate is sufficiently slow compared to the precession of transverse magnetization under the chemical shift anisotropy that the sample is effectively stationary during any reasonably short time delay. The rf pulse sequence used in the magic-angle turning experiment is shown in Fig. 5.6(a). In the experiment, after initial excitation of transverse magnetization, the magnetization is allowed to evolve for a period $t_1/3$. During this period, the rotor is assumed static, at (say) position 1 in Fig. 5.6(a). The magnetization is then moved (by a 90° rf pulse) to z to be stored parallel to $\mathbf{B}_0$ until the rotor reaches position 2. At this point, another 90° pulse moves the stored magnetization back to the transverse plane where it is allowed to evolve for a further $t_1/3$. It is then stored along $z/\mathbf{B}_0$ again until the rotor reaches position 3, where the same process is repeated. Finally after the last $t_1/3$ period at position 3, an FID is recorded (as a function of t_2). This whole experiment is repeated

* Notes are given on page 234.

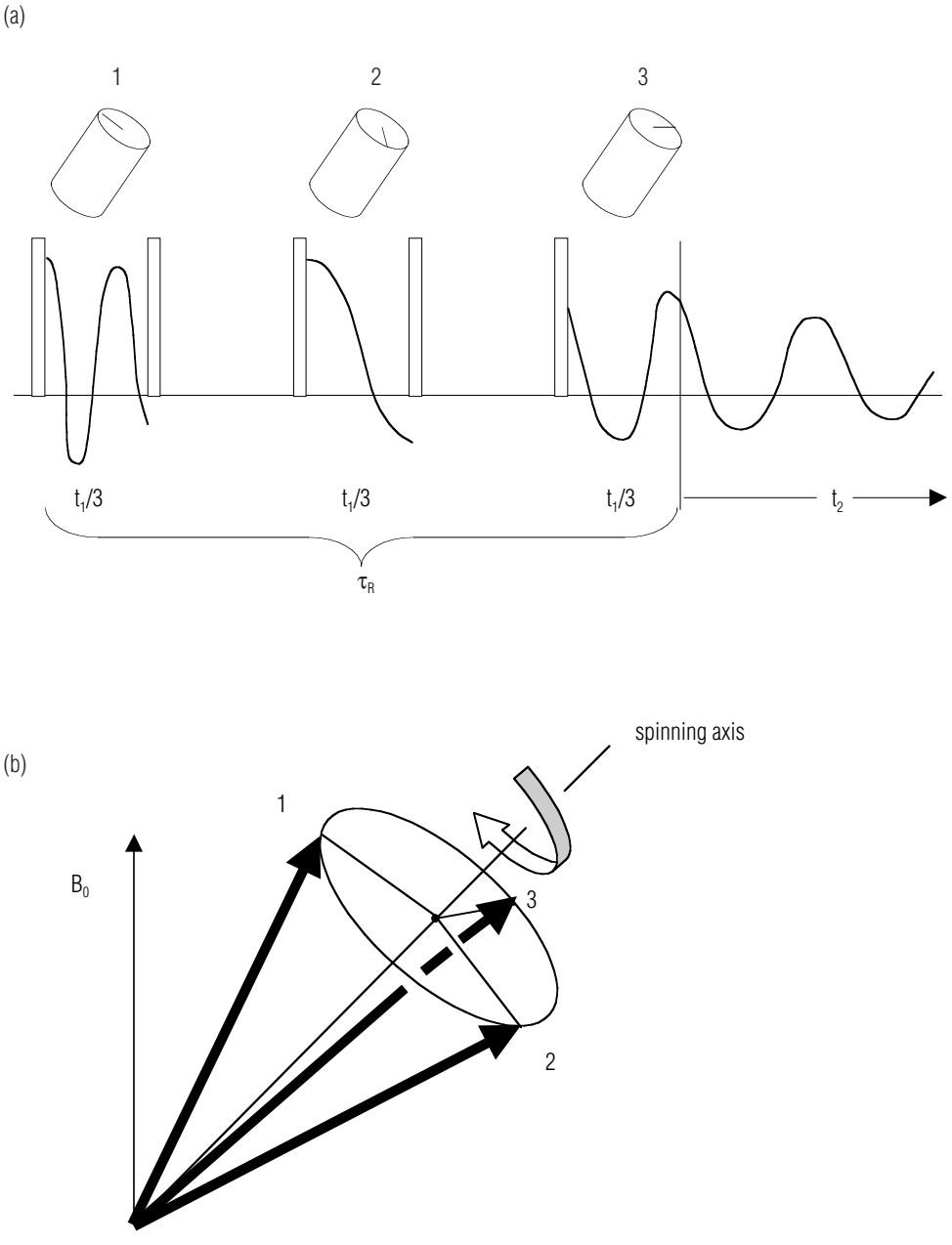

Fig. 5.6 The magic-angle turning experiment. The experiment is conducted under very slow magic angle-spinning, so that during the periods in which the t_1 magnetization is sampled, the rotor appears stationary at the positions 1, 2 and 3 labelled in (a). The pulse sequence used is also shown in (a). All pulses are 90° pulses. After each $t_1/3$ period, the magnetization is rotated to z ($\mathbf{B}_0$) by a 90° pulse of suitable phase and is stored while the sample rotates to the next position. The net evolution during the whole t_1 period is as if the spins suffered their isotropic chemical shift only; all anisotropic parts cancel identically. During t_2, the spinning is so slow that the spectrum is recorded as if the sample is static. (b) The position of the shielding tensor principal axis frame z axis for one molecular/crystallite orientation at the three rotor positions shown in (a). The average orientation for this axis is the sample spinning axis, which in turn, is oriented at the magic angle. For this average orientation, the anisotropic chemical shift contribution to the chemical shift frequency is zero. Thus the net evolution of the transverse magnetization in t_1 is governed by the isotropic chemical shift frequency only.

for many t_1 increments in the usual manner for a two-dimensional experiment; note, however, that the condition $t_1 << \tau_R$, where τ_R is the rotor period, must exist for all t_1 values. Fourier transformation in t_2 gives a static-like powder pattern (due to the ultra slow spinning). Fourier transformation with respect to t_1 produces an isotropic spectrum, as the net evolution during t_1 depends only on the isotopic chemical shift, the anisotropic parts averaging to zero between the three rotor orientations used in t_1.

The main problem with this experiment is that many modern magic-angle spinnning probes do not spin well (or at all!) at the very low rates required in this experiment (generally less than 50 Hz is required to produce quasi-static conditions). An example of a ^{13}C magic-angle turning experiment is shown in Fig. 5.7 for 1,4-dimethoxybenzene [**6**].

5.2.4 Two-dimensional separation of spinning sideband patterns

As explained in Section 2.2.1, magic-angle spinning at a rate which is less than the chemical shift anisotropy gives rise to spinning sidebands in the frequency spectrum. Analysis of the spinning sideband pattern can yield the chemical shift parameters in just the same way as analysis of the static chemical shift anisotropy powder pattern does. Indeed, analysis of spinning sidebands rather than static powder patterns can be preferable as the signal-to-noise ratio is generally better in the magic-angle spinning spectra, since all the spectral intensity is concentrated at a few discrete points in the frequency spectrum rather than being spread out over a powder pattern. Against this, however, is the fact that the simulations required in the analysis of a magic-angle spinning spectrum are more lengthy than those for a static powder pattern.

Often the resolution of different sideband patterns in a simple one-dimensional experiment is sufficient for a reliable analysis to be achieved. However, it is also possible to separate the spinning sideband patterns according to isotropic chemical shift. This can be done in two different ways. The first method separates spinning sideband patterns in f_2 according to the isotropic chemical shift of the pattern in f_1. The pulse sequence used is that in Fig. 5.8 [**7**]. After initial excitation of the transverse magnetization, the TOSS pulse sequence (see Section 2.2.1) is applied to remove the sideband components during the t_1 period. A 'de-TOSS' pulse sequence (reverse TOSS) is then applied to reintroduce the sideband components for the subsequent t_2 period in which the FID is recorded. Subsequent Fourier transformation of the two-dimensional dataset in both dimensions yields the sideband patterns in f_2 separated according to isotropic chemical shift in f_1.

One problem with this method is that many increments are required in t_1 to give the necessary resolution in the f_1 dimension to resolve all the isotropic signals properly, and this can lead to very long experiment times.[2] Furthermore, each peak in the two-dimensional spectrum has a mixed absorption/dispersion lineshape, which

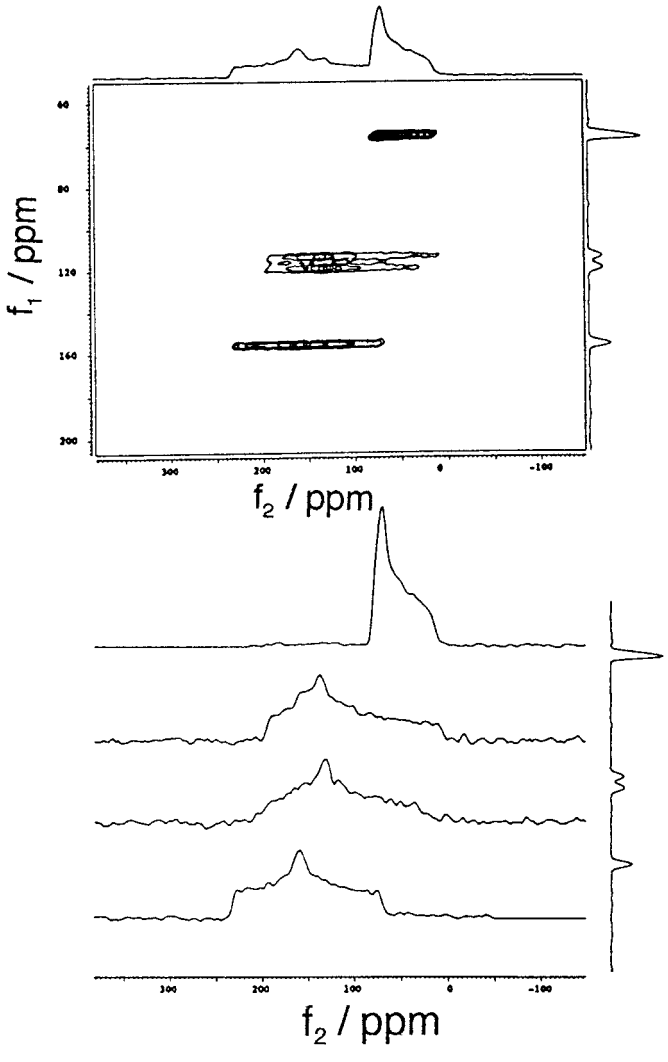

Fig. 5.7 Top: two-dimensional ^{13}C magic-angle turning spectrum (contour plot) of 1,4-dimethoxybenzene [**6**]. Below: the chemical shift anisotropy powder patterns in f_2 from the two-dimensional spectrum for each ^{13}C site [**6**]. (Taken from Gan (1992).)

can further complicate matters. Nevertheless, excellent results have been achieved using this method.

The second method of sideband separation results in a different sort of separation; each f_1 slice contains all the spinning sidebands of a given *order*, *m*, spread along the f_2 axis according to their offset frequency (see Fig. 5.9). The order of a sideband *m*, is its position in the sideband pattern radiating out from the isotropic chemical shift, where the offset frequencies of the sidebands are given by $\Delta\omega_{iso} + m\omega_R$, where $\Delta\omega_{iso}$ is the isotropic chemical shift offset and ω_R is the spinning rate. This method is known as the 2D-PASS (Phase Adjusted Spinning Sidebands) method [8]. The basic pulse sequence used is shown in Fig. 5.10. After initial excitation of

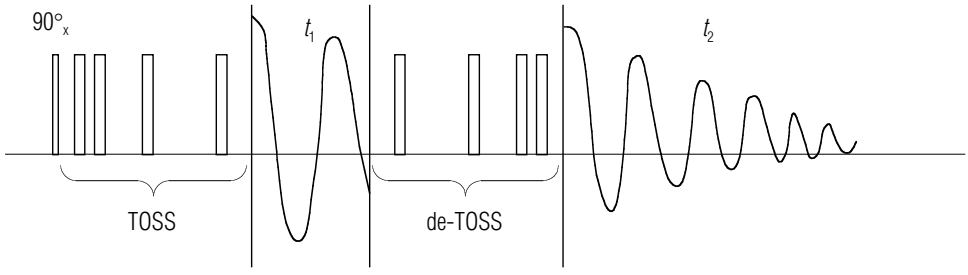

Fig. 5.8 The two-dimensional isotropic/spinning sideband separation experiment based on the TOSS pulse sequence. An initial 90° pulse creates transverse magnetization. The subsequent TOSS sequence, consisting of four 180° pulses, has the effect of removing the spinning sidebands in the variable t_1 period of the two-dimensional experiment. After t_1, a de-TOSS sequence (time-reversed TOSS), in effect, replaces the spinning sideband components for recording in t_2.

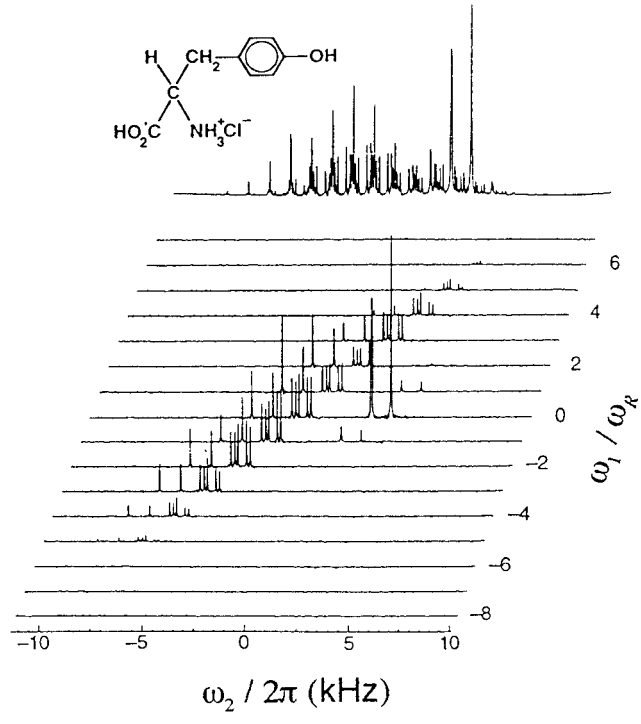

Fig. 5.9 Two-dimensional ^{13}C PASS spectrum of L-tyrosine hydrochloride (solid powder) [**8**]. The ω_1 slices are labelled with the order of the sideband. The ^{13}C magic-angle spinning spectrum for this sample at the same spinning speed (1030 Hz) is shown at the top. The overlap of spinning sidebands in this one-dimensional spectrum prevents their quantitative analysis. Once separated in two dimensions by sideband order, the spectra are comparatively easy to analyse. (Taken from Antzutzin, Shekar and Levitt (1995).)

transverse magnetization via a 90° pulse or cross-polarization, a five 180° pulse sequence (the 'PASS' sequence) is implemented, followed by recording of an FID in t_2. In successive experiments, rather than incrementing a t_1 time period as in a conventional two-dimensional experiment, the timings of the 180° pulses in the PASS sequence are altered. The purpose of the PASS sequence is to impart a specific phase shift to each sideband in the spectrum, that phase shift being dependent only on the

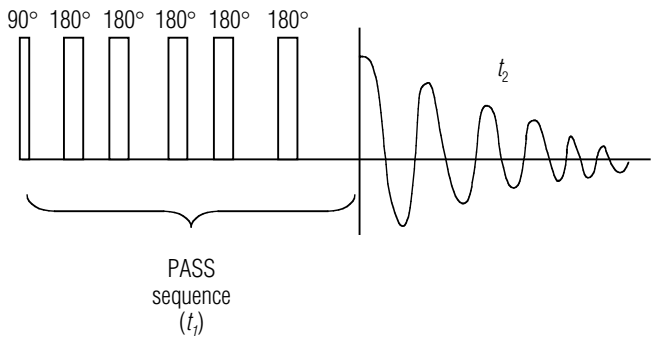

Fig. 5.10 The pulse sequence used in the 2D-PASS experiment. The positions of the five 180° pulses of the PASS part of the sequence are changed between successive t_1 increments of the two-dimensional experiment.

sideband order. The way it does this is similar in principle to the working of the TOSS sequence described in Section 2.2.3. The result is that in successive t_1 'increments' the phase of each order of sideband is shifted by an amount dependent only on the sideband order. Thus, the transverse magnetization associated with each sideband (in the terminology used in the discussion of the TOSS sequence in Section 2.2.3) appears to 'evolve' in t_1 at a 'frequency' dependent only on the sideband order. Subsequent Fourier transformation with respect to t_1 thus gives a spectrum of sideband orders as required.

The advantage of this experiment over the TOSS-based separation of sidebands is that very few t_1 'increments' are required. The corresponding f_1 dimension in the final two-dimensional spectrum needs only a sufficient number of points to represent each order of sideband visible in the complete NMR spectrum, i.e. the number of t_1 points needs only to be of the order of the number of sidebands in the most extensive sideband pattern in the spectrum.

Several applications of the 2D-PASS method are detailed in Chapter 7 on biomolecule applications of solid-state NMR.

Notes

1. The explanation of the magic-angle turning experiment in this figure is slightly simplistic as the chemical shielding interaction which determines the chemical shift and its anisotropy, is described by a second-rank tensor and not a single vector as implied by the diagram. We should look at what a second-rank tensor is averaged to when it is switched between these three orientations. A second-rank tensor can be represented by an ellipsoid whose principal axes (x, y, z) represent the principal axes of the tensor, and whose radius along each of the principal axes represents the tensors associated principal values. The diagram represents how the principal z axis only reorients under magic-angle turning. In fact a little thought shows that the (x, y) plane of the second rank tensor becomes isotropic under this three- (or higher) site hopping.
2. For this reason, it is usually better to arrange for the isotropic signal to be collected in the directly observed dimension, t_2 in any isotropic/anisotropic separation experiment.

References

1. C.J. Jameson and J. Mason, in The Chemical Shift in *Multinuclear NMR* (Ed J. Mason), Plenum Press, New York (1987), ch. 3, pp. 51–83.
2. H. Strub, A.J. Beeler, D.M. Grant, J. Michel, P.W. Cutts and K.W. Zilm, *J. Am. Chem. Soc.* **105** (1983) 3333.
3. Y. Huang, D.F.R. Gilson and I.S. Butler, *J. Chem. Soc. Dalton* (1992) 2881.
4. R. Tycko, G. Dabbagh and P.A. Mirau, *J. Magn. Reson.* **85** (1989) 265.
5. L. Frydman, G.C. Chingas, Y.K. Lee, P.J. Grandinetti, M.A. Eastman, G.A. Barrall and A. Pines, *J. Chem. Phys.* **97** (1992) 4800.
6. Z. Gan, *J. Am. Chem. Soc.* **114** (1992) 8307.
7. A.C. Kolbert and R.G. Griffin, *Chem. Phys. Lett.* **166** (1990) 87.
8. O.N. Antzutkin, S.C. Shekar and M.H. Levitt, *J. Magn. Reson.* **115** *A* (1995) 7.

Solid-State NMR Spectroscopy Principles and Applications
Edited by Melinda J. Duer
Copyright © 2002 by Blackwell Science Ltd

Part II
Applications of Solid-State NMR

Solid-State NMR Spectroscopy Principles and Applications
Edited by Melinda J. Duer
Copyright © 2002 by Blackwell Science Ltd

Chapter 6
NMR Techniques for Studying Molecular Motion in Solids

Melinda J. Duer

6.1 Introduction

There is a huge interest in molecular motions in solids. In part, this has arisen because of the realization that many bulk material properties are dependent on the flexibility and degrees of freedom of the underlying molecules. For instance, the flexibility of a bulk polymer ultimately rests with the flexibility of the constituent molecules. The ability of a material to withstand stress depends upon the molecular degrees of freedom which can absorb the energy of the stress imposed on the material. Most solid–solid phase transformations, including glass transitions of polymers, are accompanied by the onset (or quenching) of some molecular motion, and understanding how these motions arise can lead to an understanding of the occurrence of the phase transition itself. A more general reason for studying molecular motion in solids is that any observed motion is governed by the intermolecular potential which exists in the solid. Thus by studying the geometry and rate of the motions, as a function of temperature for instance, we can experimentally probe the intermolecular potential. This is crucial if we are to understand the structure and properties of any material.

NMR is an excellent method for studying dynamics of molecules in solids; all nuclear spin interactions are in general anisotropic, i.e. they depend on the molecular orientation within the applied magnetic field of the NMR experiment. Thus, as illustrated in Fig. 6.1, a change of molecular orientation is accompanied in general by a change in strength of the chemical shielding, any dipole–dipole coupling and, for $I > \frac{1}{2}$, the quadrupole coupling.

Molecular motions in solids are incoherent processes, and as such are best described by *autocorrelation functions*. If $f(t)$ describes the time-dependent position (orientation) of a molecule in a sample of many such molecules, the autocorrelation function, $G(\tau)$ is defined by

$$G(\tau) = \overline{f(t)\, f(t+\tau)} \tag{6.1}$$

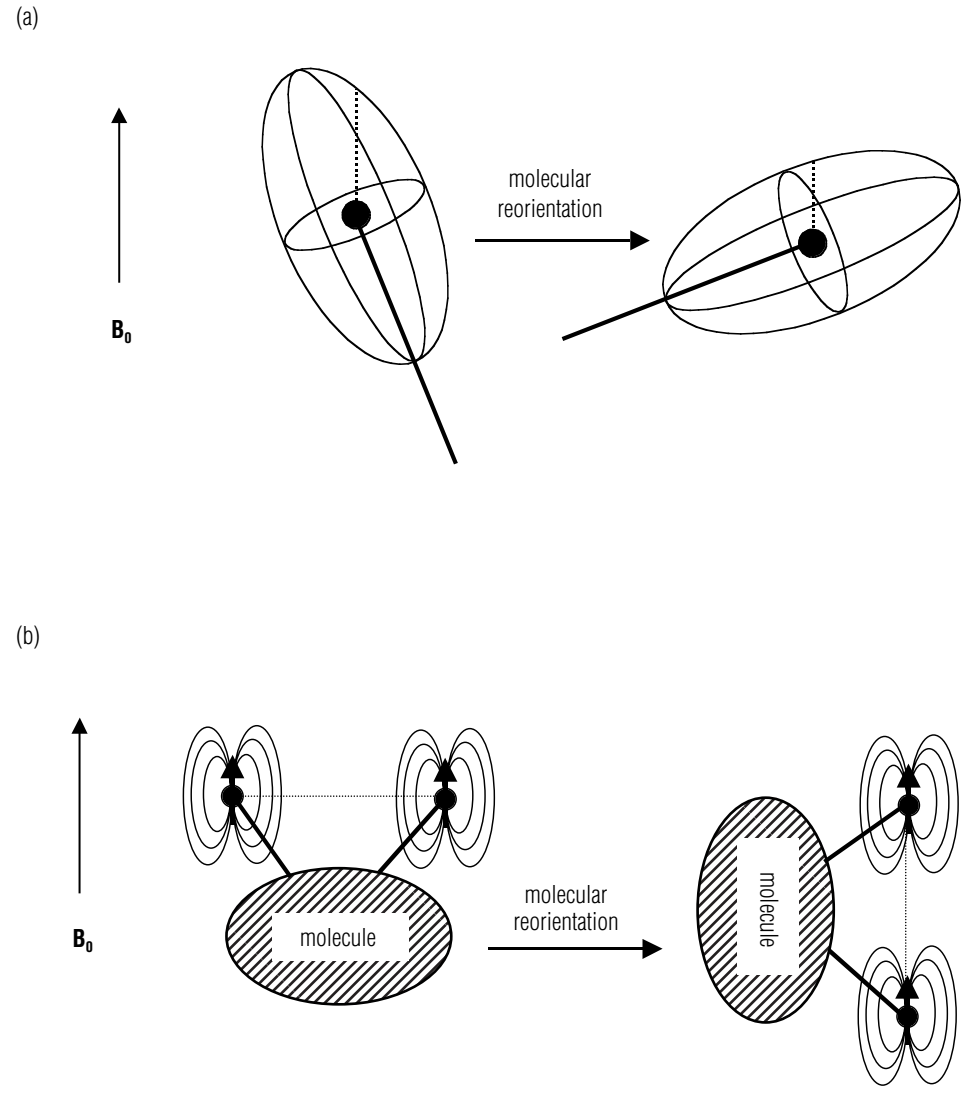

Fig. 6.1 The schematic illustration of effect of molecular reorientation on (a) chemical shift and (b) dipole–dipole coupling between two spins; the nuclei in (a) and (b) are represented by black dots. In (a), the shielding tensor is represented by an ellipsoid, whose principal axes represent the principal axis frame of the shielding tensor; the radius of the ellipsoid (dashed line) in the direction of the applied magnetic field ($\mathbf{B}_0$) is proportional to the value of the chemical shift for that molecular orientation. In (b), the strength of the dipole–dipole coupling depends on the orientation of the internuclear axis (dashed line) with respect to the applied magnetic field $\mathbf{B}_0$. The nuclear magnetic dipoles (represented by bold arrows) are oriented by the applied field. This means that the field each nuclear magnetic dipole presents to the other depends on their relative positions with respect to each other and $\mathbf{B}_0$.

where the bar indicates the ensemble average over all the molecules in the sample. $G(\tau)$ is a measure of the proportion of the molecules in the sample that have the same position at time $t + \tau$ as they did at time t. If most molecules have moved during the intervening period τ, and moved in many different directions, then there

will be a variety of different values for $f(t + \tau)$ describing all the new positions of the moved molecules. The sum of $f(t)\ f(t + \tau)$ over all the molecules in the sample then gives many cancellations between the values for different molecules, resulting in a small value for $G(\tau)$. If no molecules have moved in τ, then $f(t) = f(t + \tau)$ for all molecules, and so $G(\tau)$ is large. Clearly, $G(\tau)$ will decay with increasing τ; as the gap τ between measurement of molecular positions increases, more of the molecules in the sample will have moved, resulting in decreased values for $G(\tau)$. Often the decay is assumed to be exponential, i.e.

$$G(\tau) = \exp\left(-\frac{|\tau|}{\tau_c}\right) \tag{6.2}$$

where τ_c is the *correlation time* for the molecular motion. We use the concept of a correlation time to describe molecular motion extensively throughout this chapter. The correlation time essentially provides a monitor for the speed of the motion; the smaller the τ_c, the shorter the typical time between changes of molecular position.

Very slow motions ($\tau_c > 10^{-3}$s) may be studied via two-dimensional (or higher) exchange methods. In such techniques, the strength of a particular nuclear spin interaction is monitored during the t_1 period of a two-dimensional experiment. A mixing period then follows during which molecular reorientation may occur. Finally, the new strength of the nuclear spin interaction, resulting from the change of molecular orientation/chemical site is recorded in t_2. The final two-dimensional spectrum then correlates the strengths of the interaction during t_1 and t_2 and, from this, the angular reorientation involved in the motion can be inferred. Repeating the experiment for different mixing times allows the correlation time for the motion to be determined. These experiments are discussed in Section 6.4.

Motions with τ_c^{-1} of the order of the nuclear spin interaction anisotropy can be assessed via lineshape analysis. Here, the powder lineshape (for a powder sample) resulting from a specific nuclear spin interaction is analysed to reveal details of the molecular motion. The powder lineshapes are sensitive to motions with τ_c^{-1} of the order of the width of the powder pattern, i.e. the anisotropy of the nuclear spin interaction which causes the powder lineshape. These are generally motions with correlation times of 10^{-3} to 10^{-4}s for chemical shift and dipolar interactions, and smaller for quadrupolar interactions. The specific *dynamic range*, i.e. the motional correlation times to which the lineshapes are sensitive, will depend on the nucleus and its environment, and the interaction being observed. For τ_c^{-1} which are much less than the nuclear spin anisotropy, the powder pattern remains unaltered from a normal powder pattern for a static nucleus. Once the τ_c^{-1} for the motion is much greater (approximately a factor of 50 greater) than the nuclear spin interaction anisotropy, the motionally averaged powder pattern lineshape reaches a *fast motion limit*; further decreases in the correlation time have no effect on the lineshape. Lineshape analysis for studying molecular motion is dealt with in Section 6.2.

Motions with lower correlation times (10^{-6} to 10^{-9} s) which are out of the dynamic range for lineshape analysis can be examined by spin-lattice relaxation time studies. Spin-lattice relaxation (as other relaxation processes) relies on fluctuations in nuclear spin interactions induced by molecular motion. Thus in cases where relaxation is dominated by one particular nuclear spin interaction, the spin-lattice relaxation times can be calculated for different motions and compared with experimentally derived values to reveal motional details. Other relaxation processes can also be used to study molecular motion, as discussed in Section 6.3.

In general, quadrupolar nuclei are rarely used in molecular motion studies for several reasons. For integer-spin quadrupolar nuclei, the powder pattern linewidths are of the order of the quadrupole coupling constant, which can be of the order of MHz. Clearly, such broad lines are very difficult to observe at all, let alone use in detailed studies of molecular motion. For half-integer quadrupolar nuclei, the central transition ($+\frac{1}{2} \rightarrow -\frac{1}{2}$) is unaffected by quadrupole coupling to first order (see Chapter 4), and so is (usually) relatively easily observed. However, there is still the problem of resolving signals from different sites. The exception to all this is ^{2}H ($I = 1$) which has been and will probably continue to be used very extensively in molecular motion studies. This nucleus has a relatively small quadrupole moment and has quadrupole coupling constants in the region of 140–220 kHz in most organic compounds, for instance. This means that its powder patterns are relatively easily observed and, moreover, are sensitive to molecular motions with rates in the range 10^4–10^6 Hz. Its usage does not stop with lineshape studies, however. This nucleus has also been extensively used in relaxation time experiments and multidimensional exchange experiments for studying molecular motion. Accordingly, this nucleus is afforded its own section to discuss its use in molecular motion studies (Section 6.5).

6.2 Powder lineshape analysis

The orientation dependence of each nuclear spin interaction (see Chapter 1) means that, for powder samples, the NMR spectrum of a given nucleus consists of a broad powder pattern for each distinct chemical site for that nucleus. As discussed in Chapter 1, the powder pattern can be considered as being made up of an infinite number of sharp lines, one from each different molecular orientation present in the sample, the frequency of each line being determined by the molecular orientation itself. The lines from different orientations all overlap and result in the observed broad (but not featureless) line. Any molecular motion which changes a molecule's orientation, changes the spectral frequency associated with a nucleus in that molecule; the resonance line for that nucleus now moves to some other part of the powder pattern. If the motion has a τ_c^{-1} similar to the width of the powder pattern, then coalesence occurs between the lines corresponding to the different molecular orientations which arise during the course of the motion. This in turn causes dis-

tinctive distortions of the powder patterns, the distortions being dependent on both the correlation time and geometry of the molecular motion. As outlined below, powder pattern lineshapes can be simulated for likely models of the molecular motion and compared with experiment to reveal details of the molecular dynamics.

6.2.1 Simulating powder pattern lineshapes

In order to simulate any observable NMR spectrum, we must calculate the time evolution of the total transverse magnetization associated with the spins of interest; it is this which gives rise to the FID observed in the experiment. More precisely, the FID is proportional to the function $M^+(t)$ which describes the time evolution of the net transverse magnetization.

For the particular case of calculating a powder pattern lineshape under conditions of molecular motion, some kind of model must be assumed for the motion. It has become common practice to consider the motion as some kind of Markov process, that is, as a process involving exchange or hopping between N discrete sites, with the time taken to hop between sites being infinitesimally small compared to the residence time in each site. With this assumption, it is then straightforward to describe the time evolution of the transverse magnetization under the motional process as follows. In the *absence* of molecular motion, the time evolution of the (complex) transverse magnetization is simply given by

$$\frac{\mathrm{d}M^+(\theta, \phi; t)}{\mathrm{d}t} = M^+(\theta, \phi; t)(i\omega(\theta, \phi) + T_2) \tag{6.3}$$

which has the solution:

$$M^+(\theta, \phi; t) = M_0^+(\theta, \phi)\exp(i\omega(\theta, \phi)t + T_2) \tag{6.4}$$

θ and ϕ describe the molecular orientation in the applied field $\mathbf{B}_0$. More precisely, θ and ϕ are the polar angles describing the orientation of the applied field $\mathbf{B}_0$ in a molecule-fixed axis frame (see Fig. 6.2). T_2 is the transverse relaxation time for the spin. $\omega(\theta, \phi)$ is the resonance frequency of the spin in molecular orientation (θ, ϕ). $M_0^+(\theta, \phi; t)$ is the initial transverse magnetization associated with the particular molecular orientation. This is determined in general by the pulse sequence which generated the transverse magnetization in the experiment. $M_0^+(\theta, \phi; t)$ can most readily be calculated by calculating the density matrix through the pulse sequence (see Chapter 1) and then identifying the component or components of the density matrix which correspond to transverse magnetization at the end of the pulse sequence. If the transverse magnetization is generated by a single hard 90° pulse (i.e. a pulse whose amplitude, ω_1, is large compared to the nuclear spin interaction giving rise to the powder pattern), then the initial transverse magnetization $M_0^+(\theta, \phi; t)$ is the same for all molecular orientations, and may be nominally set to 1. The time evolution of the net transverse magnetization for the whole powder

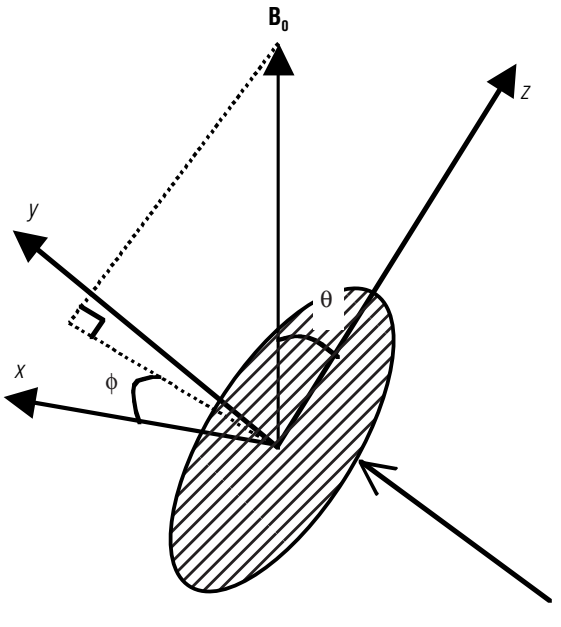

Fig. 6.2 Definition of the polar angles θ and ϕ which define the molecular orientation with respect to $\mathbf{B}_0$. The reference frame shown is a molecule-fixed frame.

sample, $M^+(t)$, is simply found from Equation (6.4) by integrating over all possible molecular orientations described by θ and ϕ:

$$M^+(t) = \frac{1}{8\pi^2}\int_0^{2\pi}\int_0^{\pi} M^+(\theta, \phi; t)\sin\theta \, d\theta \, d\phi$$
$$= \frac{1}{8\pi^2}\int_0^{2\pi}\int_0^{\pi} M_0^+(\theta, \phi)\exp(i\omega(\theta, \phi)t + T_2)\sin\theta \, d\theta \, d\phi \qquad (6.5)$$

To take account of molecular reorientations using a Markov model, Equation (6.3) is simply modified to [**1**]:

$$\frac{d\mathbf{M}^+(\theta, \phi; t)}{dt} = \mathbf{M}^+(\theta, \phi; t)(i\boldsymbol{\omega}(\theta, \phi) + \mathbf{T}_2 + \boldsymbol{\Pi}) \qquad (6.6)$$

$\mathbf{M}^+(\theta, \phi; t)$ is now an N-dimensional vector, each component being the complex transverse magnetization from one of the N sites involved in the motional process. $\boldsymbol{\omega}$ is an $N \times N$ diagonal matrix whose elements are the resonance frequencies associated with the N sites for a crystallite orientation (θ, ϕ). The matrix $\boldsymbol{\Pi}$ describes the exchange of magnetization between the N sites as a result of the molecular hopping process; it is also an $N \times N$ matrix whose elements Π_{ij} are given by

$$\Pi_{ij} = \Omega_{ij} p_j \quad \text{and} \quad \Pi_{ii} = -\sum_{j(\neq i)}^{N-1} \Pi_{ij} \qquad (6.7)$$

where Ω_{ij} is the inverse of the correlation time for hopping from site j to site i, i.e. $\tau_{c,ij}^{-1}$ and p_j is the population of site j. The solution to Equation (6.6) is analogous to

Equation (6.4). The net transverse magnetization summed over all the molecular orientations in the powder sample is then

$$\begin{aligned}\mathbf{M}^{+}(t) &= \frac{1}{8\pi^2}\int_0^{2\pi}\int_0^{\pi}\mathbf{M}_0^{+}(\theta,\phi)\exp(i\boldsymbol{\omega}(\theta,\phi)t + \mathbf{T}_2 + \boldsymbol{\Pi})\sin\theta\,\mathrm{d}\theta\,\mathrm{d}\phi \\ &= \frac{1}{8\pi^2}\int_0^{2\pi}\int_0^{\pi}\mathbf{M}_0^{+}(\theta,\phi)\mathbf{L}(\theta,\phi;t)\sin\theta\,\mathrm{d}\theta\,\mathrm{d}\phi \end{aligned} \tag{6.8}$$

where the propagator $\mathbf{L}(\theta, \phi; t)$ is

$$\mathbf{L}(\theta,\phi;t) = \exp(i\boldsymbol{\omega}(\theta,\phi)t + \mathbf{T}_2 + \boldsymbol{\Pi}) \tag{6.9}$$

The propagator $\mathbf{L}(\theta, \phi; t)$ is calculated by diagonalizing the matrix $(i\boldsymbol{\omega}(\theta, \phi)t + \mathbf{T}_2 + \boldsymbol{\Pi})$ to find its eigenvectors $\mathbf{V}$ and eigenvalues $\mathbf{A}$. The exponential in Equation (6.9) is then found from

$$\mathbf{L}(\theta,\phi;t) = \mathbf{V}^{-1}\exp(\mathbf{A})\mathbf{V} \tag{6.10}$$

As the eigenvalue matrix $\mathbf{A}$ is diagonal, $\exp(\mathbf{A})$ is also diagonal with elements $\exp(A_{ii})$.

Some comments on the calculation of the elements of ω, i.e. the resonance frequencies of the N sites for a molecular orientation (θ, ϕ), may be useful at this point. We consider the specific case of the chemical shift anisotropy powder pattern, but the same principles apply to all nuclear spin interactions. As shown in Chapter 1, the chemical shift contribution to the spectral frequency for a given molecular orientation is given by

$$\omega_{cs}(\theta,\phi) = -\omega_0\mathbf{b}_0^{\mathrm{PAF}}\boldsymbol{\sigma}^{\mathrm{PAF}}\mathbf{b}_0^{\mathrm{PAF}} \tag{6.11}$$

where $\boldsymbol{\sigma}^{\mathrm{PAF}}$ is the shielding tensor in its principal axis frame (PAF). The shielding tensor principal axis frame can be taken as the molecule-fixed frame which is used to describe molecular orientation. $\mathbf{b}_0^{\mathrm{PAF}}$ is the unit vector in the direction of $\mathbf{B}_0$ in the shielding tensor principal axis frame for the particular molecular orientation, $\mathbf{B}_0$ having an orientation in this frame given by the spherical polar angles (θ, ϕ) (see Fig. 6.2). Thus, $\mathbf{b}_0^{\mathrm{PAF}}$ is given by

$$\mathbf{b}_0^{\mathrm{PAF}} = (\sin\theta\cos\phi, \sin\theta\sin\phi, \cos\theta) \tag{6.12}$$

After a hop changing the molecular orientation by the Euler angles $(\alpha^{\mathrm{hop}}, \beta^{\mathrm{hop}}, \gamma^{\mathrm{hop}})$ (see Box 1.2, Chapter 1, for the definition of Euler angles), the new shielding tensor, expressed in the original principal axis frame is given by

$$\boldsymbol{\sigma}_{\mathrm{new}}^{\mathrm{PAF}} = \mathbf{R}(\alpha^{\mathrm{hop}}, \beta^{\mathrm{hop}}, \gamma^{\mathrm{hop}})\boldsymbol{\sigma}^{\mathrm{PAF}}\mathbf{R}^{-1}(\alpha^{\mathrm{hop}}, \beta^{\mathrm{hop}}, \gamma^{\mathrm{hop}}) \tag{6.13}$$

where $\mathbf{R}(\alpha^{\mathrm{hop}}, \beta^{\mathrm{hop}}, \gamma^{\mathrm{hop}})$ is the rotation matrix (see Box 1.2 in Chapter 1 for a discussion of rotations) describing the rotation of an object through the Euler angles $(\alpha^{\mathrm{hop}}, \beta^{\mathrm{hop}}, \gamma^{\mathrm{hop}})$. The new chemical shift contribution to the spectral frequency after the hop is

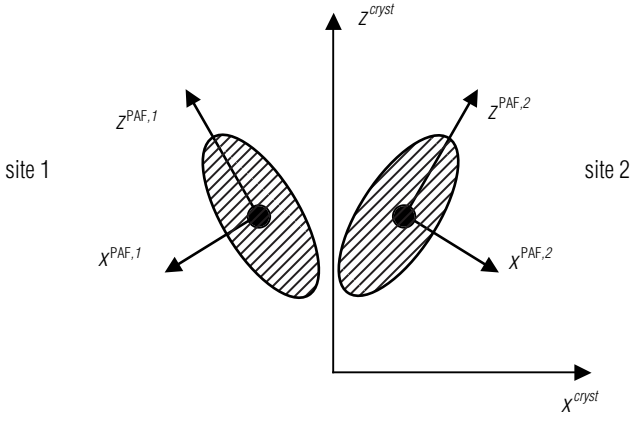

Fig. 6.3 Illustrating the crystallite-fixed frame of reference. The hashed shape represents a molecule (or part thereof) in which there is a nuclear spin (black dot). The molecule is involved in a motional process which means that it can exist in one of the two orientations or sites shown. The shielding tensor for the nucleus in each site has a principal axis frame labelled by PAF, *i*, where *i* denotes the particular site of the molecule.

$$\omega_{cs,new} = -\omega_0 \mathbf{b}_0^{PAF} \boldsymbol{\sigma}_{new}^{PAF} \mathbf{b}_0^{PAF} \tag{6.14}$$

Throughout this discussion, we have referred all quantities to the shielding tensor principal axis frame in the initial (before hop) molecular orientation. The principal axis frame is a molecule-fixed frame of reference, and so moves when the molecule hops. Often, however, it is more convenient to express all the shielding tensors associated with the N sites involved in the motional process with respect to some frame of reference fixed in the crystallite that the molecule is in, and so does not move when the molecule hops. We will label this frame '*cryst*' (Fig. 6.3). The shielding tensor for each site i expressed in this frame is simply

$$\boldsymbol{\sigma}_i^{cryst} = \mathbf{R}^{-1}(\alpha_i, \beta_i, \gamma_i) \boldsymbol{\sigma}_i^{PAF} \mathbf{R}(\alpha_i, \beta_i, \gamma_i) \tag{6.15}$$

where the Euler angles α_i, β_i, γ_i describe the rotation of the shielding tensor PAF in site i into the crystallite frame. $\boldsymbol{\sigma}_i^{PAF}$ is the shielding tensor in the principal axis frame for site i. The chemical shift contribution to the spectral frequency for each site is then

$$\omega_{cs,i}(\theta, \phi) = -\omega_0 \mathbf{b}_0^{cryst} \boldsymbol{\sigma}_i^{cryst} \mathbf{b}_0^{cryst} \tag{6.16}$$

where $\mathbf{b}_0^{cryst}$ is given by an equivalent expression to that in Equation (6.12), but where θ and ϕ now describe the orientation of $\mathbf{B}_0$ in the *crystallite* frame. If the molecular motion is a rotation about a given axis, then it is sensible to make the z axis of the crystallite frame coincide with the motion rotation axis. Then the Euler angles α_i, β_i correspond to the polar angles describing the orientation of the motion rotation axis in the (PAF, i) frame, while the third angle γ_i gives the angle of rotation about the molecular rotation axis. So, for instance, for an N site rotation about an axis inclined at an angle Θ to all the PAF z axes, the Euler angles defining the N sites are given by $\alpha_i = (i - 1)\ 360/N$; $\beta_i = \Theta$; $\gamma_i = 360 - (i - 1)\ 360/N$ (Fig. 6.4).

The final FID is proportional to the sum of the elements in the N-dimensional vector $\mathbf{M}^+(t)$ of Equation (6.8), each element being proportional to the FID at time

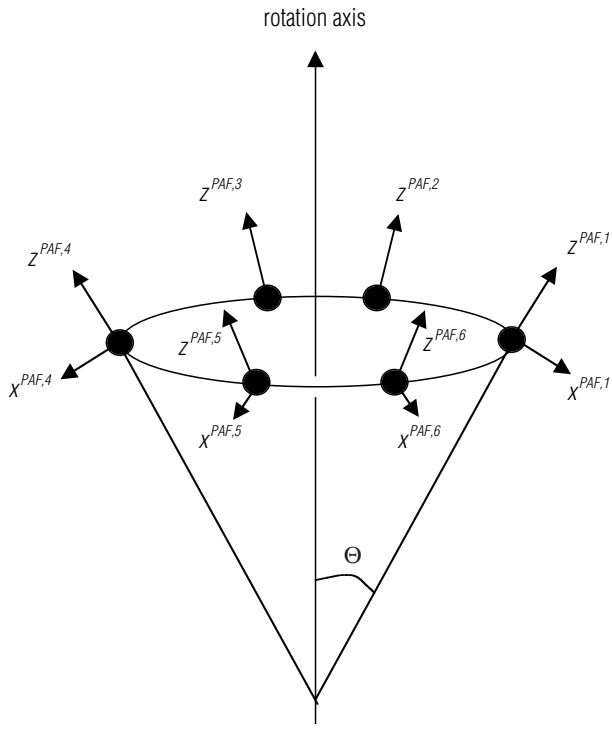

Fig. 6.4 Illustrating the relative orientations of the shielding tensor principal axis frames for the sites (in this case, six) involved in rotational motion about the axis indicated. If the rotation axis is taken as being the *z* axis of the crystallite-fixed frame of reference, the Euler angles describing the relative orientations of the principal axis frames to the crystallite-fixed frame are those given in the text.

t resulting from each of the *N* sites. Setting the proportionality constant between the FID, $F(t)$ and the time evolution of the transverse magnetization to be unity, the FID under conditions of a Markov motional process, is given by

$$F(t) = \sum_{i}^{N} \mathbf{M}_i^{+}(t) \tag{6.17}$$

where the sum is over the *N* sites involved in the motional process. In the limit where the transverse magnetization is produced by an ideally hard 90° pulse, as discussed above, Equations (6.8) and (6.17) combine to give

$$\begin{aligned} F(t) &= \frac{1}{8\pi^2} \int_0^{2\pi} \int_0^{\pi} \sum_{i}^{N} \sum_{j}^{N} \{p_i L(t)_{ji}\} \sin\theta \, d\theta \, d\theta \\ &= \frac{1}{8\pi^2} \int_0^{2\pi} \int_0^{\pi} \{\mathbf{p} \cdot \mathbf{L}(t) \cdot \mathbf{1}\} \sin\theta \, d\theta \, d\phi \end{aligned} \tag{6.18}$$

where $\mathbf{p}$ is an *N*-dimensional vector containing the populations p_i of each of the *N* sites in the motional process. θ and ϕ are the polar angles describing the orientation of $\mathbf{B}_0$ in whichever crystallite-fixed frame has been used as the frame of reference for calculating the *N* site spectral frequencies.

Some examples of chemical shift anisotropy powder lineshapes calculated using Equation (6.18) for a selection of different motional models are shown in Fig. 6.5. Also given with this figure are the $\mathbf{\Pi}$ matrices used in the calculations.

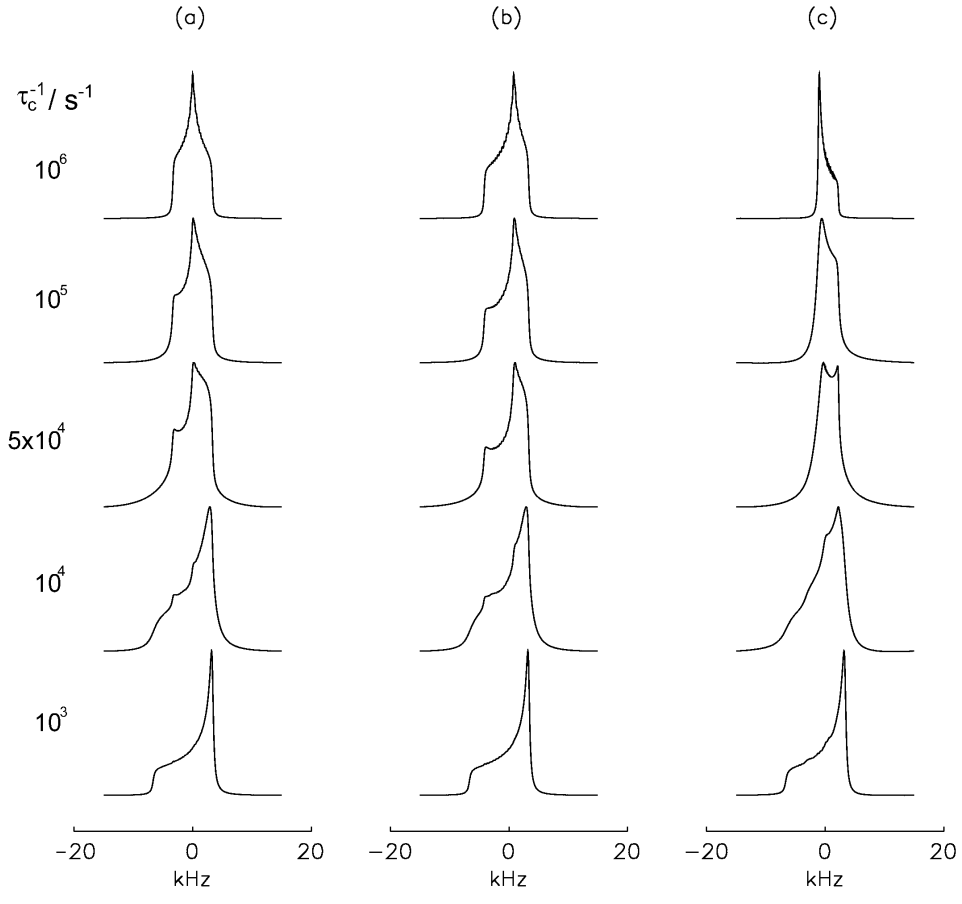

Fig. 6.5 Some chemical shift anisotropy lineshapes under conditions of molecular motion. Three different models of molecular motion are considered: (a) two-site hopping, chemical shift tensor principal *z* axis reorients by 109.5°; (b) two-site hopping, chemical shift tensor principal *z* axis reorients by 120°; and (c) three-site hopping about a rotation axis oriented at 70.5° to the chemical shift tensor principal *z* axis in each site. In all cases, the chemical shift tensor is axially symmetric and the populations of each site are equal. The $\tau_c^{-1}(\Omega)$ for each case are given with the spectra. The $\mathbf{\Pi}$ matrices used in the calculations are

$$\begin{bmatrix} -\frac{1}{2}\Omega & \frac{1}{2}\Omega \\ \frac{1}{2}\Omega & -\frac{1}{2}\Omega \end{bmatrix} \text{ for models (a) and (b) and } \begin{bmatrix} -\frac{2}{3}\Omega & \frac{1}{3}\Omega & \frac{1}{3}\Omega \\ \frac{1}{3}\Omega & -\frac{2}{3}\Omega & \frac{1}{3}\Omega \\ \frac{1}{3}\Omega & \frac{1}{3}\Omega & -\frac{2}{3}\Omega \end{bmatrix} \text{ for model (c).}$$

Note that the lineshapes show the greatest change with hopping rate when τ_c^{-1} is of the order of the chemical shift anisotropy (10 kHz for these simulations).

Lineshapes in the limit of fast motion

As intimated previously, once the rate of molecular reorientation is significantly faster than the width of the powder pattern, the motionally averaged powder pattern does not change with any further increases in the reorientation rate. It is particularly simple to calculate the fast-speed limit powder pattern within the limits of a Markov model for the molecular motion. The powder lineshape in this limit

is governed by a motionally-averaged interaction tensor which is simply the average interaction tensor over the N sites involved in the motional process. The simplest way to calculate this is to express the interaction tensors for each site with respect to a single crystallite-fixed axis frame, using Equation (6.15) above. The motionally-averaged interaction tensor in the crystallite frame is then just

$$\boldsymbol{\sigma}_{\text{avg}}^{\text{cryst}} = \sum_{i}^{N} p_i \boldsymbol{\sigma}_i^{\text{cryst}} \tag{6.19}$$

where p_i is the population of each site, i and σ_i^{cryst} is the interaction tensor for site i expressed in the crystallite-fixed frame. If the resulting interaction tensor is not diagonal in the chosen crystallite axis frame, it can always be diagonalized, yielding an effective principal axis frame for the motionally-averaged tensor and effective principal values, from which the effective (or motionally-averaged) interaction anisotropy and asymmetry may be determined.

A particularly simple case is that of axial reorientation about a single axis inclined at an angle Θ to the principal z axis of the interaction tensor in the static molecule (see Fig. 6.4). This results in an axially symmetric effective interaction tensor in the fast motion limit, with the unique axis of the effective tensor lying along the molecular rotation axis. The effective anisotropy, Δ_{eff} is given by

$$|\Delta_{\text{eff}}| = \Delta_0 \cdot \frac{1}{2}(3\cos^2\Theta - 1) \tag{6.20}$$

where Δ_0 is the interaction anisotropy in the static molecule.

Limitations of lineshape analysis

As with any kind of analysis which relies on fitting simulated to experimental data, one must always be aware that there are potentially several 'fits', i.e. different motional models which for some motional rates give equally good fits to the experimental data. In the absence of any other data, all these fits must be considered equally possible descriptions of the actual motional process. Often, it is possible to acquire other data, i.e. use a different nucleus or intrinsic knowledge of the nature of the molecular system to remove such ambiguities. However, it is still essential to search for all possible fits, and not to be content with the first one found.

In more complex systems, the motion may be composite, for instance involving rotations about several different axes at different rates simultaneously. In inhomogeneous systems, or glassy systems, such as polymers above the glass transition temperature, there is likely to be a distribution of correlation times and reorientation amplitudes. In either of these cases, it is likely that the lineshape is rather featureless over a wide temperature range. In these circumstances, it may not be possible

to extract unambiguous information on the motional components in the system from one-dimensional lineshape analysis; although all the information about the motion is contained in the lineshape, the information about different motional components is not resolved.

One of the problems with lineshape analysis for studying molecular motion is the model dependency of the analysis. There may well be cases where a Markov model does not describe the motional process well. Markov processes in effect, assume that the motion is a hopping between very sharp and very deep potential wells (the 'sites'). Hopping between broad, shallow potential wells goes against the main assumption of a Markov process, that the time taken for hopping is small compared with the residence time in a given site. Furthermore, broad potential wells allow diffusion within a well, so that each site is ill-defined. The diffusion process itself is not well described by a Markov model. This factor should always be borne in mind when analysing lineshapes with a Markov model.

The parameters arising from a Markov model – namely, the relative angular orientation of the sites involved in the dynamics process, the rate of hopping between sites, and the populations of those sites – are not always easy to interpret at a molecular level. To be more specific, the site orientation information that arises from a lineshape analysis using a Markov model is the relative angular orientation of the nuclear spin interaction principal axis frame in the N different sites involved in the motion. This information is only useful, however, if the orientation of the princpal axis frame is known relative to some molecular frame, as only then can the *molecular* motion (as opposed to the *principle axis frame* motion) be revealed.

Finally, it is important to understand that the vast majority (if not all) molecular motion processes that we are likely to study by NMR are *incoherent* processes. Thus, when we refer to, for instance, a three-site hopping process about a particular axis, we do not mean that there is a coherent rotation about the axis akin to magic-angle spinning. Such a process would give rise to sidebands in the NMR spectrum. Rather, we mean a more random process, where the correlation time describes the typical time between intersite hops.

6.2.2 Resolving powder patterns

For simple materials, where there is only one (or a few) chemical sites, powder patterns can be easily measured on static (i.e. non-spinning) samples in simple one-dimensional experiments. However, many materials of interest are complex with many different chemical sites for a given nuclear species. In a static experiment in such cases, powder patterns from different sites overlap and the concomitant lack of resolution prohibits analysis of the lineshapes. Consequently, much effort in recent years has been directed towards resolving powder patterns from different chemical sites, for the purposes of studying molecular motion.

Magic-angle spinning

One of the simplest methods is to use slow-speed magic-angle spinning. Magic-angle spinning has the effect of averaging second-rank terms in the nuclear spin hamiltonian to zero, and so removing the effects of chemical shift anisotropy, etc., from the NMR spectrum. This in itself would then remove the useful information on molecular reorientations which is contained in the anisotropic parts of the spectrum. However, under slow-speed spinning (spinning speed less than the powder pattern linewidth), spinning sidebands appear in the spectrum. For inhomogeneous nuclear spin interactions (chemical shift, heteronuclear dipole–dipole coupling and quadrupole coupling) the sidebands are sharp, and thus sideband patterns from different chemical sites are relatively easily resolved. The important point, however, is that the intensities of spinning sidebands are dependent on the anisotropic parts of the nuclear spin interaction and, thus, on any motional process in the sample; the linewidth of spinning sidebands is also affected by molecular motion. Thus, simulation of magic-angle spinning sideband patterns for particular models of molecular motion can yield information on molecular motions in much the same way as for static powder patterns. One interesting consequence of magic-angle spinning is that it affects the dynamic range of the experiment, i.e. the molecular motion correlation times to which the sideband pattern is sensitive. This is because the width of the sideband pattern which results from magic-angle spinning depends on the rate of spinning; faster spinning reduces the width of the sideband pattern, i.e. fewer sidebands. The motions to which spinning sideband patterns are sensitive are those of the order of the width of the sideband pattern, and thus are determined in part by the sample spinning rate as well as the nuclear spin interaction anisotropy.

The simulation of magic-angle spinning sideband patterns, resulting from chemical shift anisotropy for instance, is straightforward, if at times computationally intensive. The process is similar to that given above for the static, or non-spinning case. However, under magic-angle spinning, the spectral frequency ω_i for each site i, and crystallite orientation, is now periodically time-dependent, due to the time-dependent sample reorientation within the magnetic field, $\mathbf{B}_0$. This was discussed in detail in Section 2.2 for the example of chemical shift anisotropy. To recap the results from that section, the time-dependent chemical shift frequency for a site i involved in the motional process is given by

$$\omega_{cs,i}(t) = -\omega_0 \mathbf{b}_0^R \sigma_i^R \mathbf{b}_0^R \tag{6.21}$$

where $\mathbf{b}_0^R$ is the unit vector in the direction of $\mathbf{B}_0$ in a rotor-fixed axis frame R. In turn, $\mathbf{b}_0^R$ is given by

$$\mathbf{b}_0^R = (\sin\theta_R \cos\omega_R t, \sin\theta_R \sin\omega_R t, \cos\theta_R) \tag{6.22}$$

where θ_R is the sample spinning angle with respect to $\mathbf{B}_0$ and ω_R is the spinning rate in radians per second. The crystallite-orientation dependence of this resonance

frequency will become apparent shortly. σ_i^R is the shielding tensor expressed in the rotor axis frame for a spin in site *i*. In turn, σ_i^R can be found from the shielding tensor expressed in a crystallite-fixed frame (cryst) by:

$$\boldsymbol{\sigma}_i^R = \mathbf{R}^{-1}(\psi, \theta, \phi)\boldsymbol{\sigma}_i^{\text{cryst}}\mathbf{R}(\psi, \theta, \phi) \tag{6.23}$$

where the Euler angles (ψ, θ, ϕ) express the rotation of the crystallite frame into the rotor frame, and so describe the crystallite orientation (in the rotor axis frame). The reference frames involved in the calculation of the resonance frequency under magic-angle spinning are illustrated in Fig. 6.6.

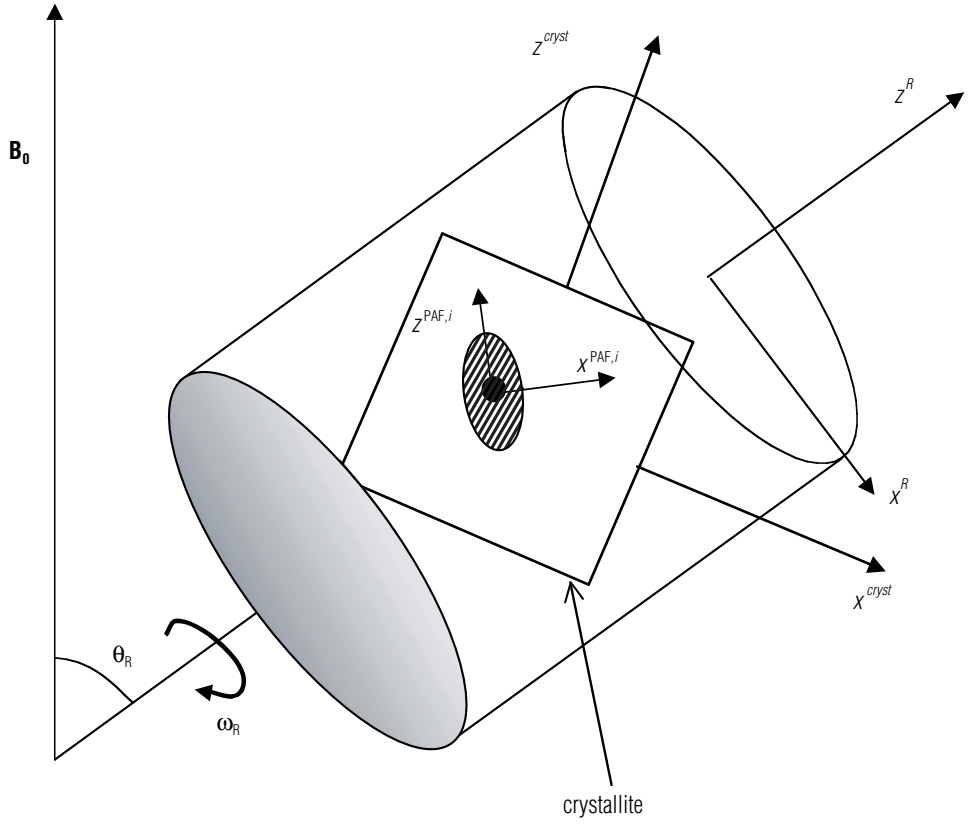

Fig. 6.6 The reference frames involved in the calculation of the resonance frequency under magic-angle spinning. One possible molecular orientation or site (labelled *i* in the text) within a single crystallite is shown; the molecule is represented by the hashed shape. In a motional process, the molecule changes orientation between *N* different sites. The shielding tensor for a nucleus (black dot) in the molecule has a principal axis frame labelled ($x^{PAF,\,i}$, $y^{PAF,\,i}$, $z^{PAF,\,i}$). Its orientation relative to a crystallite-fixed frame (x^{cryst}, y^{cryst}, z^{cryst}) is given by the Euler angles (α_i, β_i, γ_i). These Euler angles are clearly determined by the choice of crystallite-fixed frame, which can be any convenient frame. The orientation of the crystallite-fixed frame relative to a rotor-fixed frame (x^R, y^R, z^R) is given by the Euler angles (ψ, θ, ϕ); these angles vary with crystallite orientation, and so are summed over when calculating spectra for powder samples. The rotor-fixed frame conventionally has its *z* axis along the rotor spinning axis. Finally, the orientation of the rotor frame relative to the laboratory frame *z* axis ($\mathbf{B}_0$) is given by the Euler angles $(-\omega_R t, \theta_R, 0)$, where θ_R is the spinning angle (54.74° for magic-angle spinning), ω_R is the spinning rate (rad s^{-1}).

Note that in this magic-angle spinning case, three angles are required to describe the crystallite orientation, as compared to two (θ and ϕ) in the static, non-spinning case. This reduces to two (θ, ϕ) in the case of a shielding tensor with axial symmetry. Equation (6.15) above has already described how to determine σ_i^{cryst} from the shielding tensor in its principal axis frame. So we can determine the required chemical shift frequencies for the calculation of the time evolution of the transverse magnetization under magic-angle spinning conditions.

However, there are further considerations. The analytic integration of Equation (6.6) to provide a solution for the time-evolution of the transverse magnetization under molecular motion performed previously is only valid when the matrix of spectral frequencies for each site $\boldsymbol{\omega}(\theta, \phi)$ is time-independent. When $\boldsymbol{\omega}(\theta, \phi)$ is time-dependent, as it is under magic-angle spinning, the matrix $(i\boldsymbol{\omega}(t) + \mathbf{T}_2 + \Pi)$ does not commute with itself at different times t, so there is no analytical solution of the differential equation equivalent to Equation (6.6) in this case. Instead the integration must be performed numerically [**2**]. If we divide one rotor period into n equally spaced periods of $\Delta t = \tau_R/n$, we can say that the solution of

$$\frac{\mathrm{d}\mathbf{M}^+(t)}{\mathrm{d}t} = \mathbf{M}^+(t)(i\boldsymbol{\omega}(t) + \mathbf{T}_2 + \boldsymbol{\Pi}) \tag{6.24}$$

is

$$\mathbf{M}^+(t) = \mathbf{M}_0^+\mathbf{L}(t) \tag{6.25}$$

where $\mathbf{L}(t)$ is found iteratively from

$$\mathbf{L}(m\Delta t) = \exp(i\omega(t_m) + \mathbf{T}_2 + \boldsymbol{\Pi}) \cdot \mathbf{L}((m-1)\Delta t) \qquad \mathbf{L}(0) = \mathbf{1} \tag{6.26}$$

where t_m is the time point $t_m = (m - \frac{1}{2})\ \Delta t$ and m is an integer. The exponential of matrices in Equation (6.26) is found using Equation (6.10). Clearly, the number of time points n considered in this procedure needs to be adjusted until convergence is established. Once $\mathbf{L}(t)$ has been estimated for one rotor period, the values at all subsequent times may be derived from

$$\mathbf{L}(t + M\tau_R) = \mathbf{L}(\tau_R)^M\mathbf{L}(t) \tag{6.27}$$

Some examples of sideband patterns simulated for a selection of different motional models are shown in Fig. 6.7.

Two-dimensional techniques

The other general way of resolving powder patterns from different chemical sites is to generate multidimensional NMR spectra in which the desired powder patterns (or magic-angle spinning sideband patterns) are resolved in one dimension, separated according to (for instance) an isotropic chemical shift in another dimension. Methods for resolving chemical shift anisotropy powder patterns for motional

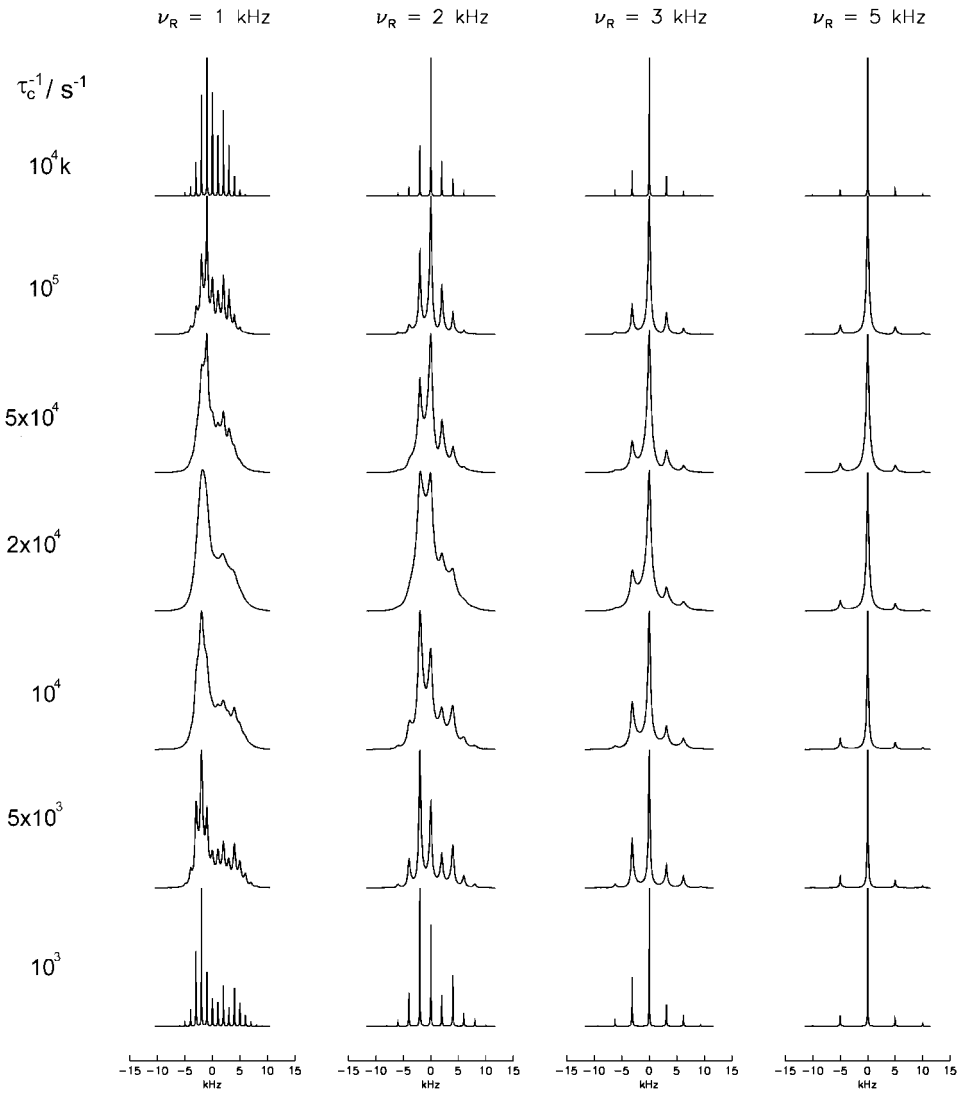

Fig. 6.7 Magic-angle sideband patterns arising from chemical shift anisotropy under conditions of molecular motion for different rates of motion and different spinning speeds. The motional model considered is a two-site hopping, with the shielding tensor principal *z* axis reorienting by 120° and equal populations of the two sites. The shielding tensor is axial with anisotropy (Δ_{cs}) of 10 kHz. For each spinning rate (ν_R), the sideband pattern is calculated for several different motional correlation times, given in the figure as τ_c^{-1}. It should be noted that the degree to which the pattern is distorted by the motion, i.e. the sensitivity of the pattern to the motion, depends upon the spinning rate, as well as τ_c^{-1}/Δ_{cs}, as in the case of static, non-spinning samples.

studies are discussed below. Those for ^{2}H quadrupolar powder patterns are discussed in Section 6.5.

A great many techniques exist for separating chemical shift anisotropy powder patterns. Three of the most used are discussed in Chapter 5 and are the method due to Tycko et al. [3], variable-angle correlation spectroscopy (VACSY) [4] and the

magic-angle turning experiment [**5**]. The first two of these have been adapted for molecular motion studies. However, the magic-angle turning experiment generates the isotropic dimension of the two-dimensional experiment by employing very slow speed spinning (<100 Hz), where it can be assumed that the rotor, and hence the nuclear spins, are effectively stationary for periods of $t_1/3$. Any molecular reorientation during t_1 would invalidate this assumption and lead to a much-broadened spectrum in the corresponding ω_1 dimension of the final two-dimensional spectrum.

The VACSY experiment is a two-dimensional experiment, where FIDs are recorded in successive experiments in which the spinning angle is varied. Subsequent processing of the two-dimensional dataset produces a two-dimensional experiment with an isotropic spectrum in one dimension (ω_2) and chemical shift powder patterns in the other (ω_1); for further details see Section 5.2.2. These powder patterns reflect motional processes in a similar manner to a normal one-dimensional experiment, although the motionally averaged lineshapes are different from those expected from a one-dimensional spectrum of a chemical shift anisotropy powder pattern [**6**]. They can, however, still be simulated to reveal the details of the molecular dynamics. Moreover, the dynamic range of the experiment is different from that of the normal one-dimensional chemical shift anisotropy powder pattern measurement; in particular, the VACSY experiment is sensitive to slower motions than the one-dimensional experiment. To understand this, it is important to remember that powder patterns are sensitive to motions which have τ_c^{-1} of the order of the interaction anisotropy. When spinning the sample about an axis inclined at an angle θ_R to the applied magnetic field, the chemical shift anisotropy is averaged to an effective value of $\frac{1}{2}(3\cos^2\theta_R - 1)$ times the true chemical shift anisotropy, i.e. it is averaged to a smaller value in general (zero if θ_R is the magic angle). In the VACSY experiment, the sample is sequentially spun at different angles, and for every spinning angle (except $\theta = 0$), the effective chemical shift anisotropy is reduced from its true value. Thus, at all spinning angles, the spectrum recorded is sensitive to motions with longer correlation times than is the normal one-dimensional powder pattern.

The chemical shift anisotropy recoupling scheme of Tycko et al. [**3**] is particularly useful for studying molecular motions in complex solids, as its dynamic range can be 'tuned'. In Tycko's experiment, the chemical shift anisotropy is removed with magic-angle spinning, but then reintroduced during the t_1 period by series of $(2n + 2)$, $n = 0, 1, 2, 3, \ldots$ 180° pulses per rotor period; see Section 5.2.1 for further details. The effective chemical shift anisotropy which acts during t_1 is scaled from the true chemical shift anisotropy by an amount which depends on the exact timing of the pulses, with scalings of 0.4 to near zero being possible. The scaled chemical shift powder patterns, which appear in the ω_1 dimension of the final two-dimensional spectrum are sensitive to molecular motions with τ_c^{-1} of the order of the *scaled* chemical shift anisotropy. Thus the experimenter can chose the dynamic range of this experiment to suit the particular motional processes in the sample at the temperature of interest. In the limit of ideal, hard 180° pulses, the motionally-

averaged lineshapes in ω_1 are identical to those that would arise from a one-dimensional static experiment, but where the chemical shift anisotropy is scaled by the particular factor in the two-dimensional experiment. Some examples of simulated ω_1 chemical shift anisotropy powder patterns arising from this experiment are shown in Fig. 6.8, for dimethylsulphone (DMS) for different chemical shift anisotropy scaling factors. Note that the lineshape begins to show distortion due to molecular reorientation when the rate of motion is of the order of the scaled chemical shift anisotropy. The lineshape reaches the fast motion limit once the rate of motion is significantly larger than the scaled chemical shift anisotropy.

6.2.3 Using homonuclear dipolar coupling lineshapes: the WISE experiment

^{1}H–^{1}H dipolar-coupling lineshapes in organic solids are frequently used as a qualitative monitor of motion in a sample. In such samples, the abundance of ^{1}H spins

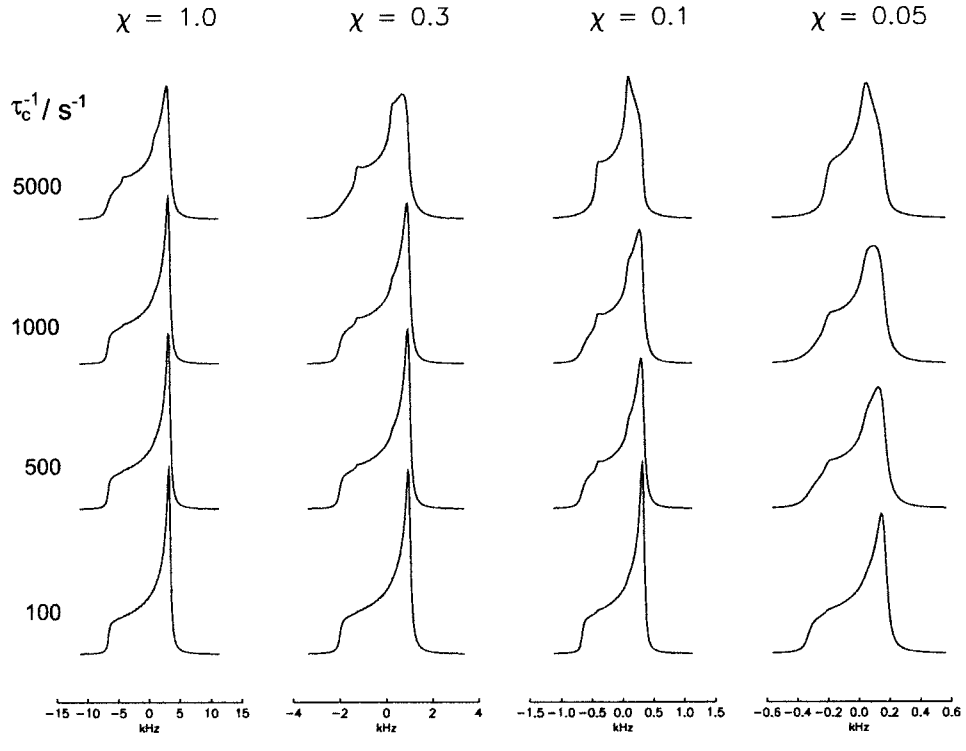

Fig. 6.8 Some simulated f_1 lineshapes arising from the chemical shift anisotropy recoupling experiment due to Tycko et al. [**3**] under conditions of molecular motion. This experiment scales the chemical shift anisotropy, and the resulting f_1 powder lineshapes are sensitive to motions with rates of the order of the *scaled* chemical shift anisotropy. Thus the experiment is excellent for examining slow motions, as the scaling factor can be chosen by the experimenter (see text for details). Note, we use f_1 here to denote a spectral frequency axis in units of Hz, i.e. $\omega_1/2\pi$.

creates a strongly coupled spin network, which gives rise to a ^{1}H NMR spectrum which is simply a broad, gaussian line, usually of the order of several tens of kHz wide. As highlighted in Section 2.2.4, slow-speed magic-angle spinning (significantly slower than the ^{1}H linewidth) has little effect on this and very rapid spinning (>30 kHz in general) is needed to produce a high-resolution spectrum. Intermediate spinning rates create sideband patterns consisting of rather broad sideband lines which are poorly resolved from one another so that the net ^{1}H lineshape is still only slightly different from the static ^{1}H lineshape. However, any molecular motion which averages or partially averages the dipolar coupling on the NMR timescale, i.e. motion with τ_c^{-1} of the order of the ^{1}H linewidth or greater, can significantly reduce the ^{1}H linewidth in static spectra and much sharper sidebands are produced in magic-angle spinning spectra. Of course the problem is that in most organic samples there are several (often many!) different ^{1}H sites and, inevitably, the broad ^{1}H lines from each overlap. Accordingly, the two-dimensional WISE technique [7] has become very popular; here the ^{1}H lineshapes are separated according to the isotropic chemical shifts of the ^{13}C they are bonded to. This is achieved by the pulse sequence shown in Fig. 6.9. Essentially, transverse ^{1}H magnetization is created by an initial ^{1}H 90° pulse. The ^{1}H magnetization is then allowed to evolve during t_1; that remaining at the end of the t_1 period is then transferred to the ^{13}C spins via cross-polarization (see Section 2.5). Finally, the ^{13}C FID is recorded in t_2. The whole experiment is conducted under magic-angle spinning in order to achieve high-resolution in the ^{13}C dimension of the experiment. The cross-polarization step is kept very short (50–100 μs) in order that ^{1}H magnetization is only transferred to those ^{13}C closest to the respective ^{1}H spins, i.e. those directly bonded to ^{1}H in

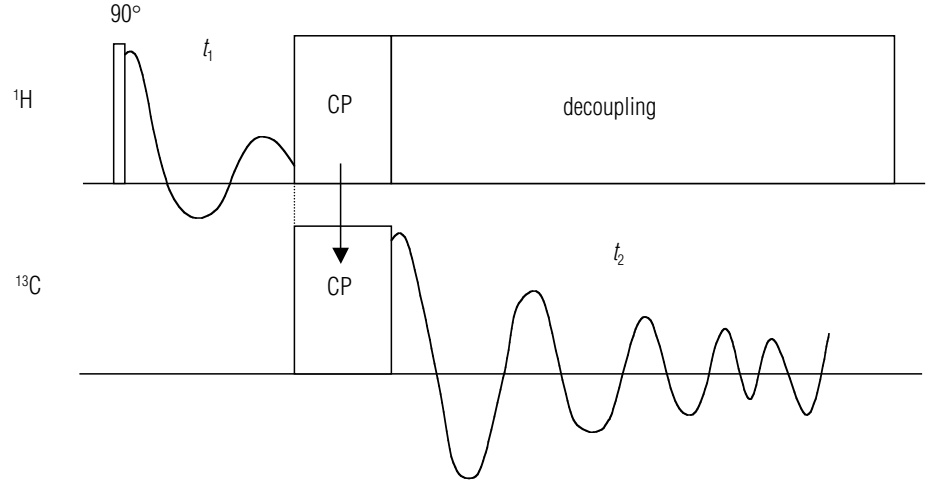

Fig. 6.9 The pulse sequence for the WISE experiment [**7**] which separates ^{1}H wideline spectra according to the isotropic chemical shift of a bonded heteronucleus, in this case ^{13}C.

general. A TOSS sequence (see Section 2.2.3) may be applied prior to acquisition in t_2 to suppress spinning sidebands in the ^{13}C dimension.

There is no need to record two quadrature datasets in order to obtain pure absorption lineshapes in this experiment. In a most samples, the ^1H lineshape can be assumed to be symmetric, providing the chemical shift range of the ^1H spins in the sample is small. In this case, if the ^1H spins are set on resonance, the whole ^1H spectrum is then symmetric about $\omega = 0$, where ω is the offset frequency. Thus, we can record a single two-dimensional dataset and achieve a pure absorption phase two-dimensional frequency spectrum by Fourier transforming with respect to t_2, phasing the resulting ω_2 spectrum as necessary, then zeroing the imaginary part, and finally Fourier transforming with respect to t_1. Zeroing the imaginary part before the final Fourier transformation allows pure absorption two-dimensional lineshapes to be obtained. It also, of course, has the effect of producing a (^1H) spectrum in ω_1 which is necessarily symmetric about $\omega_1 = 0$, but since this is the form we expect in any case for the ^1H spectrum in this dimension, this is not a problem. The ω_1 lineshapes of ^1H spins which are slightly off-resonance can usually still be monitored for signs of molecular motion; the offset from $\omega_1 = 0$ and the symmetrizing in the ^1H dimension does not obscure the intrinsic ^1H linewidth in general.

It should be remembered that the cross-polarization efficiency of mobile sites is in general somewhat less than for static sites. Thus, the ^{13}C (and therefore ^1H) intensities in a WISE spectrum will not in general be quantitative, with the signals from mobile sites being rather less intense than others. Despite this, however, WISE is a very useful and easy-to-implement experiment, for the qualitative detection of motion with correlation times less than about 10^{-4} to 10^{-5} s in solids.

6.3 Relaxation time studies

Relaxation time measurements have long been used to characterize molecular motions in solids. All nuclear spin relaxation processes are mediated by fluctuating nuclear spin interactions, with the fluctuations (generally) arising from molecular motion. Relaxation phenomena are the subject of several entire books; indeed the topic cannot be dealt with properly in much less space. A very brief description of the theoretical basis for understanding relaxation processes is given here simply for completeness and in order to indicate how relaxation time studies may be used to assess molecular motion in solids. For a more detailed description, the reader is referred to reference [8].

Relaxation is the change in time of the density matrix describing the spin system as the system moves back towards equilibrium from some non-equilibrium state imposed, for instance, by a sequence of radio-frequency pulses. Longitudinal relaxation, for example, restores the populations of the Zeeman wavefunctions for a collection of identical spin systems to the equilibrium Boltzmann distribution. It thus

affects the diagonal elements of the density matrix, which describe the populations of the spin system Zeeman wavefunctions. The rate of change of population of any given spin level can be written in terms of the transition rate to that level from all others and vice versa in combination with the populations of those spin levels, in the usual manner for any kinetic process. In turn, the transition rate between two levels i and j is given by the golden rule of quantum mechanics:

$$W_{ij} = \frac{1}{\hbar^2}\int_{-\infty}^{+\infty} \langle \mathrm{Tr}\{\mathbf{H}^*(t+\tau)\}\mathbf{H}^*(t)\rangle \, \mathrm{d}\tau \tag{6.28}$$

where $\mathbf{H}^*(t)$ is the hamiltonian matrix in the Zeeman interaction representation (see Box 2.1 in Chapter 2 for a description of the interaction representation), describing the fluctuating nuclear spin interaction acting on the spin system. In other words, the time dependence of $\mathbf{H}^*(t)$ arises from molecular motions and the intrinsic anisotropy of the nuclear spin interaction. The hamiltonian operator in the Zeeman interaction representation is simply

$$\hat{H}^* = \exp(-i\hat{H}_Z t)\hat{H}\exp(+i\hat{H}_Z t) \tag{6.29}$$

where $\hat{H}_Z$ is the Zeeman hamiltonian operator and $\hat{H}$ is the laboratory frame hamiltonian operator describing the nuclear spin interaction. Equation (6.28) for the transition rate involves the ensemble average over the sample (angle brackets), and the *trace*[1]* of the product of hamiltonian matrices at different times t and $t + \tau$. This latter term is a sum with components of the form $H^*_{ij}(t+\tau)H^*_{ji}(t)$, for all i and j, where H^*_{ij} and H^*_{ji} are hamiltonian matrix elements and i and j refer to elements of the basis set for hamiltonian matrices. To gain some insight into this sum, we restrict ourselves to consideration of relaxation through dipolar coupling and write the dipolar hamiltonian as a sum of spherical tensor operators:

$$\hat{H}(t) = \sum_{m=-2}^{+2}(-1)^M \Lambda_{2M}(t)\hat{T}_{2M} \tag{6.30}$$

where the $\hat{T}_{2M}$ are spherical tensor operators (see Box 3.1 in Chapter 3); a term $\hat{T}_{2M}$ represents an M-quantum term in the dipolar hamiltonian, which links spin levels whose z-quantum numbers differ by M. The $\Lambda_{2M}(t)$ are components of the dipolar-coupling tensor expressed in irreducible tensor form and expressed in the laboratory frame (as in Box 3.1 in Chapter 3). The time-dependence of the hamiltonian due to molecular motion is expressed though the time-varying dipolar-coupling tensor, which changes as the molecule changes orientation through angular motion with respect to the applied magnetic field in the NMR experiment. In the interaction representation, the hamiltonian becomes

* Notes are given on page 279.

$$\begin{aligned}\hat{H}^* &= \exp(-i\hat{H}_Z t)\hat{H}\exp(+i\hat{H}_Z t)\\ &= \sum_{M=-2}^{+2}(-1)^M \Lambda_{2M}(t)\exp(-i\hat{H}_Z t)T_{2M}\exp(+i\hat{H}_Z t)\\ &= \sum_{M=-2}^{+2}(-1)^M \Lambda_{2M}(t)T_{2M}\exp(i\Delta\omega_M)\end{aligned} \tag{6.31}$$

The terms $\Delta\omega_M$ are the differences in the eigenvalues of $\hat{H}_Z$ for eigenfunctions of $\hat{H}_Z$ which differ in z-quantum number by M; thus $\Delta\omega_M$ is simply $M\omega_0$, where ω_0 is the Larmor frequency (see Box 1.3 in Chapter 1). When $\hat{H}^*$ is expressed in this form, it is clear that $\hat{H}^*$ only has non-zero matrix elements between Zeeman spin levels (or product spin levels) whose z-quantum numbers differ by M. The non-zero matrix elements of $\hat{H}^*$ then depend only on the corresponding $\Lambda_{2M}(t)$ and the matrix elements of the T_{2M} operators, which are just numbers. Thus, the integral in Equation (6.28) can be rewritten as a sum of integrals labelled $J_M(\Delta\omega_M)$ where

$$J_M(\Delta\omega_M) = \int_0^\infty \exp(-i\Delta\omega_M t)C_M(t)\,\mathrm{d}t \tag{6.32}$$

in which M is restricted to 0, 1, 2, i.e. $|M|$, and $C_M(t)$ is a correlation function describing the time-dependence of the nuclear spin interaction, i.e. the molecular motion. The function $J_M(\Delta\omega_M)$ is a *spectral density* function. The spectral density is a measure of the amplitude of the M-quantum component of the nuclear spin interaction, in this case the dipolar coupling, oscillating at frequency $\Delta\omega_M = M\omega_0$ as a result of molecular motion.

The correlation function $C_M(t)$ is given by

$$C_M(t) = \langle \Lambda_{2M}(0)\Lambda^*_{2M}(t)\rangle - |\langle \Lambda_{2M}(0)\rangle|^2 \tag{6.33}$$

All relaxation processes can ultimately be described as some linear combination of spectral density functions, $J_M(\Delta\omega_M)$. We have only explicitly considered longitudinal relaxation processes via dipolar coupling here, but a similar case can be made for transverse relaxation, relaxation processes in the rotating frame and cross-relaxation processes, and for other nuclear spin interactions. The spectral densities involved are, in each case, $J_M(\Delta\omega_M)$ where $\Delta\omega_M$ is the frequency of the M-quantum transition involved in the relaxation process under the particular nuclear spin interaction, whatever it may be. In transverse relaxation processes, the transitions involved include zero-quantum transitions and their respective frequencies then appear in the relevant spectral density. In rotating frame relaxation, the transitions involved are those in the rotating frame, and so the corresponding transition frequencies are the nutation frequencies of the relevant nuclei. Hence, rotating frame relaxation processes are sensitive to motions with τ_c^{-1} in the region of the nutation frequency of the particular nuclear spin under a spin-locking pulse, generally tens

to a few hundred kHz. Longitudinal relaxation processes are sensitive to molecular motions with τ_c^{-1} of the order of $M\omega_0$, i.e. the Larmor frequency (generally tens to hundreds of MHz). In contrast, transverse relaxation processes are sensitive to very low frequency motions, of the order of zero-quantum transition frequencies. Thus, a very wide range of motional frequencies may be studied by choosing different relaxation processes to monitor the motion.

In analysing relaxation data, the dominant nuclear spin interaction effecting relaxation must be known and it must exceed the effects of other interactions by at least an order of magnitude, otherwise the data becomes extremely complex to interpret. Accordingly, relaxation times studies are often applied to ^{2}H where the dominant relaxation mechanism is nearly always through quadrupole coupling. In other cases, nuclei with ^{1}H bonded to them often have a dominant mechanism involving dipolar coupling with the ^{1}H, due to the particularly large magnetic moment of ^{1}H (providing that the chemical shift anisotropy associated with the nucleus is small).

Relaxation data is analysed by calculating correlation functions for the nuclear spin interactions acting on the observed spin and likely models of the molecular motion. The correlation functions are then used to calculate the relevant relaxation time. Comparison between experimental and calculated values can then lead to a description of the motion in the system. It should be noted, however, that this type of semiclassical analysis is only valid when the correlation time for the motion is much smaller than the relevant relaxation time. Furthermore, for any motions other than fairly simple ones, the analysis is likely to lead to ambiguities with several motional models calculating similar relaxation times.

6.4 Exchange experiments

Exchange experiments are invaluable for studying slow molecular motions (with correlation times of the order of milliseconds or slower) in solids, and accordingly have seen many applications in polymers for instance, as discussed in Chapter 10. The essential concept of a two-dimensional exchange experiment is straightforward and is illustrated in Fig. 6.10. In this section we deal only with their application to spin-$\frac{1}{2}$ systems; application to spin-1 is dealt with in Section 6.5.4.

Transverse magnetization is created by an initial 90° pulse or cross-polarization step and allowed to evolve during the period t_1 under its characteristic frequency ω_1. This characteristic frequency arises from the nuclear spin interaction which operates during t_1. At the end of t_1, the magnetization is stored along z (the direction of applied magnetic field in the NMR experiment) for a period τ_m, the mixing time, during which molecular dynamical processes may occur. Finally, the magnetization is returned to the transverse plane, where it again evolves under its characteristic frequency, this time ω_2, the evolution being recorded as a FID. If dipolar decoupling is required, e.g. in ^{13}C exchange spectra for organic compounds, it is applied during

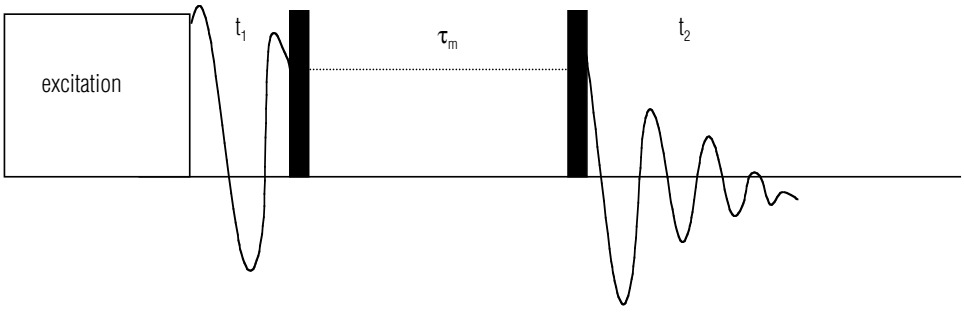

Fig. 6.10 The basic form of a two-dimensional exchange experiment to study molecular motion or chemical exchange; all pulses (black) are 90° pulses. The experiment correlates changes of molecular orientation between the t_1 and t_2 periods. Transverse magnetization is initially excited (via a 90° pulse or cross-polarization, labelled simply 'excitation' in the figure) and allowed to evolve at its characteristic frequency, ω_1, during t_1. The characteristic frequency in static solid samples is dependent on molecular orientation, as the spin interactions acting on the observed spin are anisotropic. At the end of t_1, a second pulse restores the magnetization to z (parallel to $\mathbf{B}_0$) where it is stored for a mixing time τ_m, during which molecular reorientation may occur. Finally, another pulse reconverts the magnetization into observable transverse magnetization whose evolution, this time with offset frequency ω_2, is then recorded in an FID. Subsequent processing of the resulting two-dimensional dataset produces a correlation spectrum which shows how the observed spin's offset frequency changed from ω_1 in t_1 to ω_2 in t_2. Since molecular orientation can be directly correlated with offset frequency, the two-dimensional spectrum represents a map describing the molecular reorientation between t_1 and t_2, i.e. during τ_m.

t_1 and t_2 only. Dipolar decoupling is switched off during the mixing time τ_m to encourage dephasing of unwanted coherences (see Section 6.4.1 below).

Appropriate processing of the resulting two-dimensional time domain datasets yields a two-dimensional frequency correlation spectrum, correlating the characteristic frequency the spin had during t_1 with that it subsequently had in t_2. If molecular reorientation or site exchange has occurred during the mixing time (which happens if the correlation time for the motion, $\tau_c < \tau_m$), the offset frequency after the mixing time, ω_2 is different from the initial offset frequency before molecular reorientation/exchange, ω_1, and so the two-dimensional frequency spectrum contains off-diagonal intensity at (ω_1, ω_2). If there is no exchange during the mixing time, $\omega_1 = \omega_2$ ($\tau_c >> \tau_m$), and spectral intensity appears only along the diagonal of the two-dimensional frequency spectrum. Analysis of the resulting spectrum in terms of molecular motion clearly relies on the offset frequencies ω_1 and ω_2 being constant during the t_1 and t_2 periods respectively, i.e. on there being no molecular motion during these periods. It is for this reason that exchange experiments are only suitable for studying slow molecular motions. By assessing the exchange intensity as a function of mixing time (with $\tau_m >> t_1, t_2$), the correlation time for the motion can be determined; the pattern of exchange intensity in the two-dimensional frequency spectrum allows the geometry the motion to be determined [9]. A key feature here is that motional models are *not* required to extract this latter information in contrast with lineshape analyses and relaxation time studies.

For the most part, exchange experiments in the solid state use either chemical shift anisotropy (for spin-$\frac{1}{2}$) or quadrupole coupling (for spin $> \frac{1}{2}$) under static con-

ditions, i.e. no sample spinning, to generate offset frequencies ω_1 and ω_2 which depend on molecular orientation. The projections onto the two spectral frequency axes are then the corresponding powder patterns resulting from the particular anisotropic spin interaction. The resulting two-dimensional spectrum is in effect, a correlation map between the molecular orientations in t_1 and t_2. Although chemical shift anisotropy and quadrupole coupling are most commonly used in exchange experiments, any anisotropic nuclear spin interaction can be employed. In one example, Schmidt-Rohr and colleagues used the dipolar coupling between isolated pairs of ^{13}C spins in high-density polyethylene to label the frequencies in t_1 and t_2 [**10**].

High-resolution two-dimensional exchange experiments can be performed in the solid state in analogous fashion to solution-state exchange experiments by conducting the experiments (for spin-$\frac{1}{2}$) under rapid magic-angle spinning. These experiments of course monitor only chemical exchange, where the site exchange is accompanied by a change of isotropic chemical shift. Such experiments are generally much simpler to perform and analyse than the static experiments, but obviously their field of application is much smaller. They employ the same basic pulse sequence (Fig. 6.10), with the proviso that the mixing time, τ_m, is an integral number of rotor periods. When this condition is met, the phase of the transverse magnetization at the end of the t_1 period is the same as that at the beginning of t_2; this allows pure absorption lineshapes to be achieved after appropriate processing of the data (see the following section).

Three- and higher-dimensional exchange spectra can be recorded by simple extensions of the basic two-dimensional pulse sequence (Fig. 6.11). The resulting multidimensional frequency spectra then correlate the molecular orientation at three (or more for higher-dimensional spectra) points in time. This allows assessment of the degree to which different motions or molecular jumps are correlated in time.

6.4.1 Achieving pure absorption lineshapes in exchange spectra

There are two basic methods of achieving pure absorption lineshapes in two-dimensional exchange spectra.

(i) *Quadrature detection in* t_1. Two two-dimensional datasets are recorded, one in which the real (or x component) of the t_1 transverse magnetization is measured (indirectly) and one in which the imaginary (or y component) of the t_1 magnetization is measured; x and y here refer to axes in the transverse plane of the rotating frame. In practice, this is done as follows. The initial (t_1) magnetization is excited for both datasets using, say, a 90°_x pulse. Then, for dataset 1, a 90°_{-x} storage pulse at the end of t_1 flips the y component of the t_1 transverse magnetization to z for the mixing time τ_m. This y component of the t_1 magnetization is given by $M_0 \cos \omega_1 t_1$, where M_0 is the initial transverse magnetization

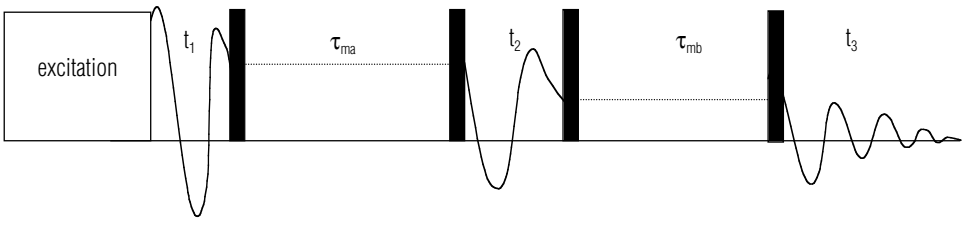

Fig. 6.11 The basic pulse sequence for a three-dimensional exchange experiment; such an experiment correlates changes of molecular orientation between three time periods, t_1, t_2 and t_3 separated by mixing times τ_{ma} and τ_{mb}. All pulses (black) are 90° pulses. The operation of the sequence is similar to that for the two-dimensional exchange experiment (Fig. 6.10) but with the addition of a second mixing time and additional evolution period. Higher-order exchange experiments can be performed by simply adding further mixing and evolution periods.

(along $-y$) at the start of the t_1 period, produced by the 90°_x pulse. $\omega_1 t_1$ is the angle this magnetization has precessed through (about $\mathbf{B}_0/z$) after time t_1. The x component of the t_1 transverse magnetization is unaffected by the 90°_{-x} pulse and so remains in the transverse plane and dephases during the mixing time.[2] The final signal recorded in t_2 is then $M_0 \cos\omega_1 t_1 \exp(i\omega_2 t_2)$. For dataset 2, a 90°_y storage pulse at the end of t_1 stores the x component of the t_1 transverse magnetization ($= M_0 \sin\omega_1 t_1$) along z for the mixing period, while the y component now dephases. The final signal recorded in t_2 is then $M_0 \sin\omega_1 t_1 \exp(i\omega_2 t_2)$. The two datasets are then processed according to the recipe in Fig. 1.21.

(ii) *Off-resonance detection*. One two-dimensional dataset is recorded off-resonance and processed as for the WISE experiment in Section 6.2.3. The resulting two-dimensional spectrum is symmetric about $\omega_1 = 0$, as shown in Fig. 6.12. Clearly, this method is much simpler than the quadrature detection in t_1 method, but exciting broad, off-resonance powder patterns uniformly may not be possible. In practice, then, this method is only suitable for relatively small chemical shift anisotropies of a few kHz.

In order to obtain undistorted, pure phase spectra, it is most important that the spectral data is acquired from t_1, $t_2 = 0$. However, receiver deadtime problems can lead to truncation of the data in t_2. Slightly less of a problem is that finite pulse widths truncate the t_1 data also. Both of these features prevent spectra with t_1 and t_2 truly equal to zero from being recorded. These truncations lead to frequency-dependent phase distortions in the respective spectral dimensions. In principle, these could be corrected by first-order phase corrections, *providing that the loss of information arising from the truncation is not too great*. In practice, for the wider powder lineshapes such corrections are not effective. Instead, datasets from t_1, $t_2 = 0$ are produced by interpolating the experimentally obtained signal and extrapolating back to zero [**11**]. This, however, is not a simple procedure and requires some experience if undistorted spectra are to be obtained. Alternatively, Hahn spin echoes

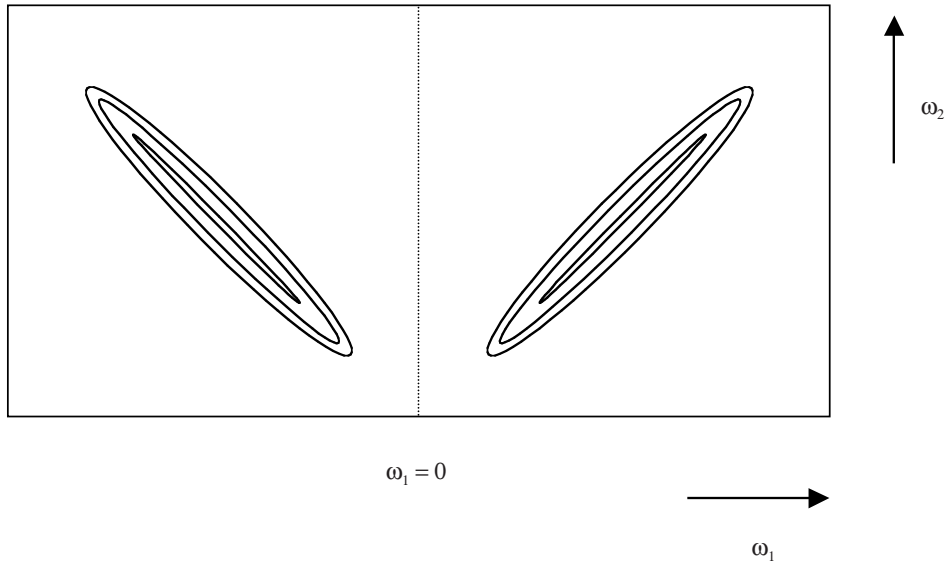

Fig. 6.12 The form of the two-dimensional exchange spectrum which arises if the data is recorded off-resonance in a single experiment. The spectrum is necessarily symmetric about $\omega_1 = 0$, so that either half of the spectrum contains all the data.

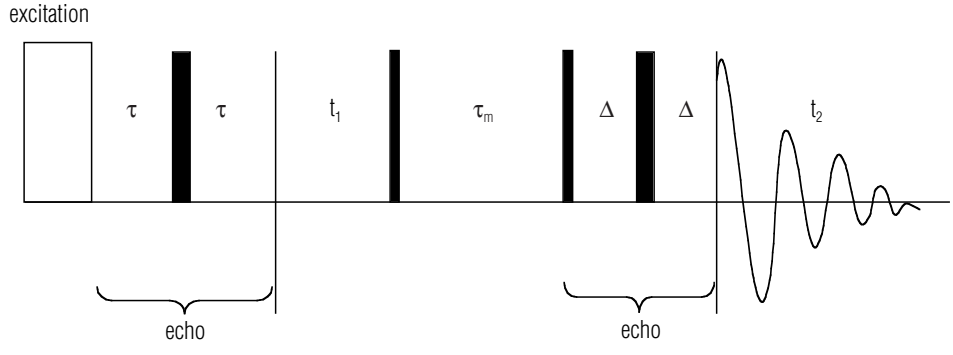

Fig. 6.13 The use of Hahn spin echoes in the recording of two- (and higher) dimensional exchange spectra. Wide pulses (black) are 180° pulses; thin ones (also black) are 90° pulses. Truncation of the time domain data in either t_1 or t_2 leads to gross spectral distortions in the final two-dimensional frequency spectrum in cases where broad powder lineshapes are expected in the corresponding frequency dimensions. Such truncation is usually inevitable due to finite length pulses in the case of t_1 and due to the receiver deadtime in the case of t_2. Using a τ–180°–τ (or Δ–180°–Δ) Hahn echo sequence prior to each t_1 and t_2 allows the respective time domain datasets to be recorded from the true signal maximum and so prevents spectral distortion.

(τ–180°–τ) can be used prior to the t_2 and/or t_1 periods to prevent the truncation of the data in the first place (Fig. 6.13). Then, the acquisition of the FID can be set to begin exactly at $t_2 = 0$, and likewise the pulse which defines the beginning of the mixing period can be set exactly on top of the first echo to acquire a $t_1 = 0$ spectrum. This greatly simplifies data processing. Such steps are essential if pure absorption three-dimensional exchange spectra are to be obtained.

6.4.2 Interpreting two-dimensional exchange spectra

Magic-angle spinning exchange spectra are straightforward to interpret. Off-diagonal peaks correspond to magnetization exchange between the corresponding signals in each dimension, i.e. an off-diagonal peak at (ω_1, ω_2) means that magnetization from the signal at offset ω_1 in the one-dimensional spectrum of the compound exchanges with that at ω_2 during the mixing time. Whether this exchange corresponds to a chemical exchange process or a spin diffusion process then has to be determined. This can be done by recording exchange spectra as a function of temperature; spin diffusion processes are independent of temperature, while chemical exchange processes vary with temperature. However, there may be elements of both processes occurring and this is more difficult to extract.

In two-dimensional static exchange spectra, the intensity at point (ω_1, ω_2) in the two-dimensional frequency spectrum is proportional to the probability that a spin had an offset frequency ω_1 (due to is particular orientation) during t_1 and reoriented such that its offset frequency was ω_2 during t_2. In this manner, model-independent information can be obtained from exchange spectra.

Static two-dimensional exchange spectra can be simulated relatively simply. In the following discussion, we restrict ourselves to the case of discrete N site-hopping motional processes, as defined in Section 6.2 on powder lineshape analysis. If, during t_1, a site has offset frequency ω_1 and then undergoes a reorientation during the mixing time τ_m, the new offset frequency, ω_2, of the site in t_2 can be found using Equation (6.14) in Section 6.2.1.

The time domain signal resulting from the exchange process between sites with frequencies ω_1 and ω_2 is then [**11**]

$$\begin{aligned} s(t_1, t_2; \tau_m) &= \langle \exp(i\omega_1 t_1) \exp(i\omega_2 t_2) \rangle \\ &= \langle \mathbf{1} \cdot \exp(i\omega t_1) \exp(\mathbf{\Pi}\tau_m) \exp(i\omega t_2) \mathbf{p} \cdot 1 \rangle \end{aligned} \tag{6.34}$$

where $\mathbf{\Pi}$ is the kinetic matrix described in Section 6.2.1, $\mathbf{p}$ is an N-dimensional vector whose elements are the populations of each of the N sites and ω a diagonal $N \times N$ matrix whose elements are the offset frequencies of the N sites involved in the hopping process, for a given crystallite orientation in the sample, exactly as described for one-dimensional lineshape analysis. The angle brackets in Equation (6.34) denote 'ensemble average', i.e. that the expression within the brackets should be summed over all possible crystallite orientations. The exponentials of matrices can be evaluated using Equation (6.10) after finding the eigenvectors and eigenvalues of the particular matrix.

Further analysis shows that for axially symmetric interaction tensors, angular reorientation by an angle Θ gives rise to an elliptical ridge in the two-dimensional frequency spectrum which results from Fourier transformation of Equation (6.34). The angle Θ is related to the major and minor axes of the ellipse, a and b, by $\tan \Theta = b/a$. An example is shown in Section 6.5, and further examples are discussed

in Chapter 10. In heterogeneous samples, such as polymers, there is usually a distribution of molecular reorientational angles; two-dimensional exchange patterns can be simulated for different distributions and compared with experiment to reveal this information [**12**].

6.5 ^{2}H NMR

^{2}H is a spin-1 nucleus with a relatively small electric quadrupole moment ($Q = 2.8 \times 10^{-31}\,m^2$) which gives rise to quadrupole coupling constants, χ, in the range 140–220 kHz in organic compounds for instance. Powder NMR spectra of static samples consist of doublet patterns (Fig. 6.14), the doublet arising from the two possible spin transitions: $+1 \leftrightarrow 0$ and $0 \leftrightarrow -1$. These are often called *Pake patterns*; their horns are split by $\frac{3}{4}\chi$, i.e. 105–165 kHz. This moderate width of powder pattern (as compared with other quadrupolar nuclei) makes this nucleus relatively easy to deal with experimentally. Moreover, the powder pattern lineshapes are sensitive to molecular motions with correlation times of the order 10^{-4} to 10^{-6} Hz, which coincidentally corresponds to a range of motional correlation times often found in solids in the temperature range accessible by most commercial NMR spectrometers, i.e. –150°C to 250°C. Because of this, ^{2}H has been extensively used in motional studies, primarily via lineshape analyses, but also through relaxation time measurements and exchange experiments.

^{2}H NMR is also widely used on partially ordered materials, such as liquid crystals, to measure order parameters. This application uses the orientation dependence of the quadrupolar frequency and is discussed in more detail in Chapter 11.

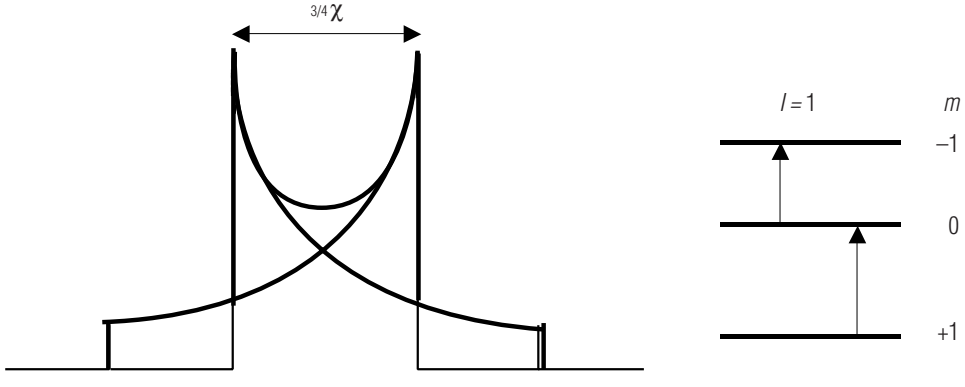

Fig. 6.14 The form of a ^{2}H ($I = 1$) quadrupole powder pattern. The doublet nature of the pattern is due to there being two allowed spin transitions.

6.5.1 Measuring ^{2}H NMR spectra

Quadrupole echo experiment

The width of ^{2}H powder patterns for static samples necessitates the use of echo techniques to record undistorted powder patterns, rather than simple pulse–acquire experiments. As discussed in Section 2.6, the receiver deadtime which must be left after a pulse means that the initial part of the FID in a pulse–acquire experiment is not recorded. This lost data constitutes a significant part of the total FID for broad powder patterns, which have correspondingly short FIDs and lead to severely distorted frequency spectra on Fourier transformation. Accordingly, ^{2}H powder patterns are generally recorded with a *quadrupole echo* or *solid echo* pulse sequence: 90°_x–τ_1–90°_y–τ_2–acquire. The delays τ_1 and τ_2 are approximately equal, but, in practice, τ_2 is adjusted so that the data acquisition begins exactly at the echo maximum. τ_2 (and therefore τ_1) should be at least as long as the receiver deadtime.

There are several practical points to be considered to obtain good results with the quadrupole echo pulse sequence. As already stated, data acquisition must begin exactly at the echo maximum. Finding the echo maximum requires a bit of patience. Firstly, the receiver phase needs to be adjusted so that all the FID intensity appears in the real part of the FID – in other words, so that the frequency spectrum that would arise after Fourier transformation has pure absorption phase. If this is not done, intensity is distributed between the real and imaginary parts of the FID. It is then very difficult to assess the *amplitude* of the FID at any point in time, as the amplitude is the square root of the sum of the squares of the real and imaginary parts. It is therefore very difficult to find the echo maximum (point of maximum amplitude of the FID). If the intensity is all in the real part of the FID, then the magnitude of the real part of the FID is synonymous with the FID amplitude at any point in time.

Having done this, an apparent echo maximum will reveal itself. However, it is important to remember that the FID signal seen on the computer screen is in fact digitized, so only measured at discrete points, despite the continuous line that is drawn between the points in most NMR spectrometer software. Thus it is quite possible (indeed, highly likely) that the true echo maximum actually falls between two recorded FID points. There are several ways of dealing with this.

One is to begin recording the FID well before the apparent echo maximum, i.e. $\tau_2 < \tau_1$. The resulting FID signal is then interpolated between the digitized points in the region of the apparent echo maximum to find the true echo maximum. A new time domain series is then generated, starting from the true echo maximum, via interpolation between the recorded FID points as necessary.

Alternatively, one can change the time points at which FID is recorded, until the true echo maximum is found. This is usually done in practice by keeping τ_2 at a constant value which is much less than τ_1, and varying τ_1 in small amounts in suc-

cessive experiments. The dwell time between recorded FID points is kept constant during this process. Comparing the echo FIDs between the successive experiments will then reveal the true echo maximum. The τ_1 value which produces an FID with the true echo maximum at one of the FID sampling points is then used to record the final FID with the required level of signal averaging.

The method to use is a matter of personal choice. The former method is quicker on spectrometer time, but requires more lengthy processing; the latter uses more spectrometer time, but subsequent processing is straightforward. Where the echo FID is recorded so that the echo maximum appears some way into the FID, the time domain dataset is left-shifted by the appropriate amount prior to Fourier transformation.

Clearly, ^{2}H powder patterns should be symmetric about their isotropic chemical shifts. Experimentally, however, ^{2}H powder patterns often appear distinctly asymmetric due to a variety of factors which should each be attended to as far as possible before the final spectrum is recorded. Firstly, finite pulse widths do not give uniform excitation over the whole powder pattern. In order to get symmetric excitation about the isotropic chemical shift of the ^{2}H powder pattern, it is necessary that the centre of the powder pattern be on resonance. If it is not, it is unlikely that a symmetric powder pattern can ever be recorded. Secondly, the NMR probe response may not be symmetric. This particular feature is governed by the probe electronics and can be altered to some extent on most modern probeheads. Once the ^{2}H powder pattern has been set on resonance, the probe response can be examined. If the powder pattern is unsymmetric at this point in the experiment setup, it is probably the fault of the probe response. The match setting on the probe should be adjusted in small steps until a symmetric ^{2}H powder pattern is obtained.

When recording ^{2}H powder patterns with a quadrupole echo pulse sequence to study molecular motion, it is often useful to record powder patterns for several different echo delay times, τ_1 (and corresponding τ_2). The variation in echo intensity with τ_1 is determined by the transverse relaxation rate (as characterized by T_2). It is the anisotropic T_2 arising from molecular motion which causes the distortion of the ^{2}H powder lineshapes. The variation in echo intensity with τ_1, in combination with the ^{2}H powder lineshapes (also as a function of τ_1), thus gives useful information on the rate and geometry of the molecular motional process. Some simulated ^{2}H powder patterns as a function of τ_1 are shown in Fig. 6.15 for a two-site-hopping molecular motion.

Magic-angle spinning

In principle, magic-angle spinning can remove the effects of first-order quadrupolar linebroadening completely. In practice, this would require spinning at speeds much faster than the ^{2}H quadrupolar powder pattern width. Such spinning

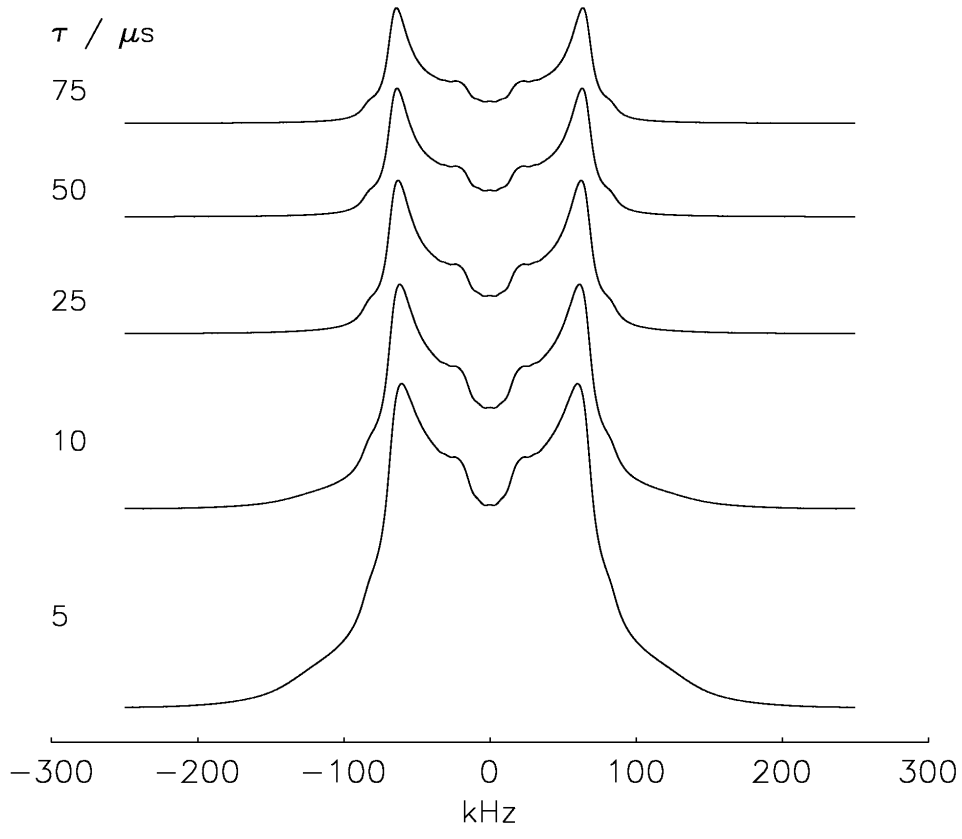

Fig. 6.15 Simulated ^{2}H quadrupole echo spectra for the pulse sequence 90°–τ_1–90°–τ_2–acquire, for different echo delays, $\tau = \tau_1 = \tau_2$. The molecular motion used in the simulations is a two-site hopping which reorients the ^{2}H quadrupole coupling tensor *z* axis by 120°. The motional correlations time is $\tau_c = 10^{-5}$ s for each spectrum.

speeds are unlikely to ever be achievable. At the achievable spinning speeds (up to 50 kHz), the ^{2}H powder pattern breaks up into a series of sharp spinning sidebands. This can be a distinct advantage, as the spectral intensity is then concentrated at discrete points in the frequency spectrum, rather than being smeared out over a wide frequency range in a powder pattern, so the signal-to-noise ratio is much improved.

In principle, ^{2}H magic-angle spinning spectra can be recorded with simple pulse–acquire sequences, rather than echo sequences, as the decay rate of the magic-angle spinning FID is significantly slower than for the static experiment. However, it is still the case that the spectral width required to record the spinning sideband pattern is usually substantial, and so the corresponding dwell time in the FID is small. Thus even a relatively small receiver deadtime before acquisition can correspond to several FID points, resulting in baseline distortions in the Fourier-transformed frequency spectrum. Hence, better quality spectra are often obtained

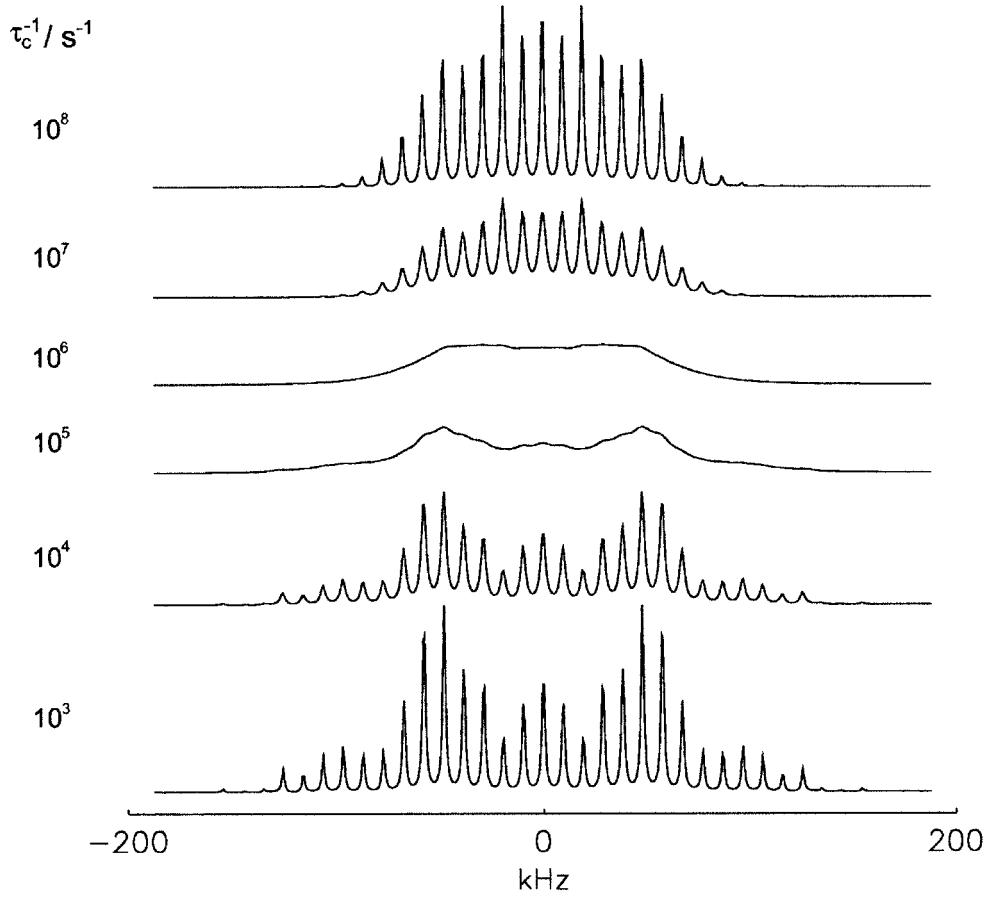

Fig. 6.16 Simulated ^{2}H magic-angle spinning spectra for different hopping rates. The molecular motion used in the simulations is a two-site hopping which reorients the ^{2}H quadrupole coupling tensor *z* axis by 120°. The correlation times for the motions are given as τ_c^{-1} with the spectra.

by using a quadrupole echo pulse sequence even under conditions of magic-angle spinning. The same principles apply in setting up the experiment as in the static case with the added proviso that the echo delay should be an integral number of rotor periods so that rotational echoes are refocused at the start of the FID.

As discussed previously in this chapter, spinning sideband patterns monitor different motional regimes to static powder patterns, the particular range that they are sensitive to depending on the spinning speed as well as the ^{2}H quadrupole-coupling constant. Thus recording ^{2}H spinning sideband patterns at different spinning speeds can give extra information on the motional process. Some simulated ^{2}H spinning sideband patterns for different spinning speeds and a two-site hopping molecular motion are shown in Fig. 6.16.

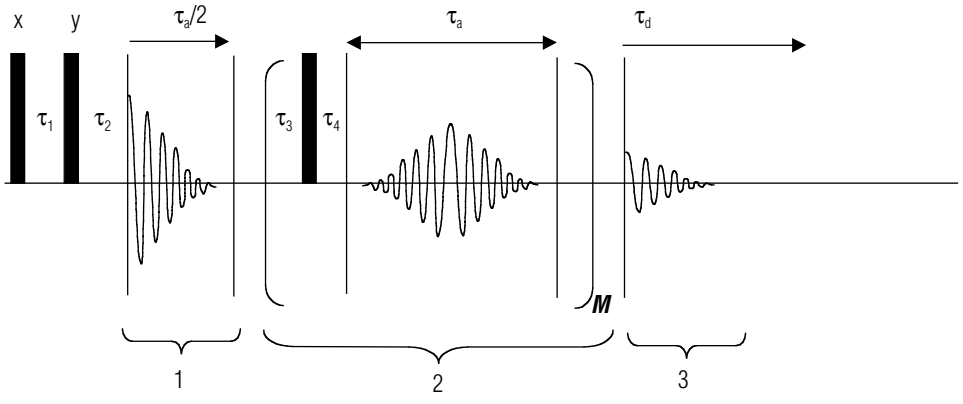

Fig. 6.17 The quadrupolar Carr–Purcell–Meiboom–Gill (QCMPG) pulse sequence [**13**] for recording ^{2}H NMR spectra. Use of this sequence gives ^{2}H spectra which are sensitive to molecular motions over a much wider frequency range than static or magic-angle spinning ^{2}H spectra. The final FID from the experiment is the results from steps 1, 2 and 3 strung together in a single time domain series; the FIDs are collected between the vertical line in the diagram for periods $\tau_a/2$, τ_a and τ_d respectively in steps 1, 2 and 3. All pulses are 90° pulses with the phases given in the diagram. The echo delays τ_1 and τ_2 are approximately equal, with τ_2 being adjusted so that the acquisition in step 1 begins exactly at the echo maximum. Step 2 is repeated *M* times and consists of *M* refocusing 90° pulses with collection of the resulting echo FID after each. τ_3 and τ_4 are short delays designed to protect the receiver from the 90° pulses in step 2.

Quadrupolar Carr–Meiboom–Purcell–Gill pulse sequence

This pulse sequence is shown in Fig. 6.17 [**13**]. It consists of a standard quadrupole echo pulse sequence, after which the echo decay is recorded (step 1). Following this is a series of refocusing 90° pulses, with a complete echo being recorded after each (step 2). Finally, any remaining signal is allowed to decay and is again recorded (step 3). The complete time domain series resulting from the outputs of steps 1, 2 and 3 strung together is then Fourier transformed. This experiment has the effect of splitting the quadrupole echo powder pattern into a manifold of spin-echo sidebands separated by $1/\tau_a$ (see Fig. 6.17 for definition of τ_a). This in itself generates a sensitivity enhancement of an order of magnitude. Moreover, both the envelope of the spin-echo sidebands and their individual lineshapes contain information on molecular motions. It is once again obtained by simulating the spectrum for particular motional models, but the initial study [**14**] shows that the dynamic range of the experiment is at least two orders of magnitude larger than the conventional quadrupole echo experiment. The full dynamic range is 10^2 to 10^8 Hz, i.e. it is sensitive to motions which are both slower and faster than those which the quadrupole echo experiment can monitor. Sideband shapes tend to monitor the lower end of this range, while the overall sideband envelope is sensitive to higher frequency motions. Some example spectra, recorded using this technique, are shown in Fig. 6.18.

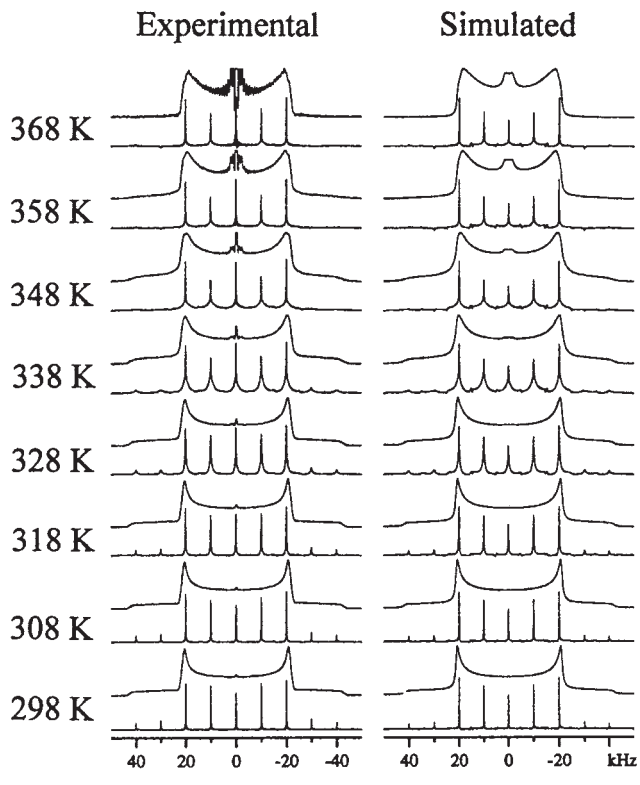

Fig. 6.18 ^{2}H spectra of dimethylsulphone (DMS) recorded with the QCMPG pulse sequence of Fig. 6.17 [**14**] and with the quadrupole echo pulse sequence for comparison. The top spectrum in each pair is the quadrupole echo spectrum; the lower one the QCMPG one. (Taken from Larsen, Jakobsen, Ellis *et al.* (1997).)

6.5.2 ^{2}H lineshape simulations

^{2}H powder patterns and spinning sideband patterns under conditions of molecular motion can be calculated in exactly the same way as for spin-$\frac{1}{2}$ chemical shift anisotropy powder patterns as detailed in Section 6.2.1, except that the shielding tensor needs to be replaced with the electric field gradient tensor ($e\mathbf{q}$) and the chemical shift frequency by the quadrupolar frequency, ω_Q. The quadrupolar frequency is determined by

$$\omega_Q = \frac{eQ}{4I(2I-1)\hbar}\mathbf{b}_0^{PAF} e\mathbf{q}^{PAF}\mathbf{b}_0^{PAF} \tag{6.35}$$

where $\mathbf{b}_0^{PAF}$ is the unit vector in the direction of $\mathbf{B}_0$ in the electric field gradient tensor principal axis frame (PAF) for the particular molecular orientation, in complete analogy with the chemical shift frequency. The electric field gradient tensor principal components are easily derived from the quadrupole-coupling constant and asymmetry, and the fact that this tensor is traceless. The quadrupole coupling constant χ is given by $e^2 q_{zz}^{PAF} Q/\hbar$ where q_{zz}^{PAF} is the z principal value of the electric field

gradient tensor and the asymmetry by $\eta_Q = (q_{yy}^{PAF} - q_{xx}^{PAF})/q_{zz}^{PAF}$. This, plus the fact that $q_{xx}^{PAF} + q_{yy}^{PAF} + q_{zz}^{PAF} = 0$, allows us to write

$$\begin{aligned} eq_{zz}^{PAF} &= (\chi/eQ)\hbar \\ eq_{xx}^{PAF} &= -\frac{1}{2} q_{zz}^{PAF}(1+\eta_Q) \\ eq_{yy}^{PAF} &= -\frac{1}{2} q_{zz}^{PAF}(1-\eta_Q) \end{aligned} \tag{6.36}$$

Using this and the procedure in Section 6.2.1 we can then calculate the static powder pattern or spinning sideband pattern for one of the ^{2}H spin transitions. The powder pattern for the other transition is just the mirror image of this about $\omega = 0$. The sum of the powder patterns for the two transitions is then the final ^{2}H powder/spinning sideband pattern.

6.5.3 Relaxation time studies

The anisotropy (i.e. dependence on molecular orientation) in the relaxation of Zeeman order (as described by the parameter T_{1Z}) and quadrupolar order (as described by the parameter T_{1Q}) has been used with good effect to study fast molecular motions in solids [**15–17**]. A spin system with *quadrupolar order* is described by a density operator proportional to $3\hat{I}_z^2 - I(I+1)$ or $\hat{T}_{20}$ in terms of spherical tensor operators (see Box 3.1 in Chapter 3), while a spin system with *Zeeman order* is described by a density operator proportional to $\hat{I}_z$. For example, the spin state produced by the initial 180° pulse acting on equilibrium magnetization in an inversion recovery experiment is described by a density operator proportional to $-\hat{I}_z$; thus following the decay of this state (or equivalently, recovery of the equilibrium state) enables T_{1Z} to be determined. Quadrupolar order is produced by a 90°_x–τ–45°_y pulse sequence.

T_1 anisotropy for ^{2}H has been used in a two-dimensional experiment [**18**] where the full T_1 anisotropy is displayed in one dimension of the experiment (T_2 anisotropy was similarly dealt with too [**18**]). In this early work, the full two-dimensional spectrum was simulated according to given motional models and motional correlation times, and compared with experiment. However, the fitting of a two-dimensional contour plot or surface plot is notoriously difficult and perhaps it is for this reason that the technique has never been taken up in this form by other spectroscopists. In more recent studies of ^{2}H T_{1Z} and T_{1Q} anisotropy, the approach has been slightly different. The procedure in the analysis of the relaxation rate anisotropy is to calculate the spectral density functions (Equation (6.32)) for given motional models and given molecular jump rates as in the earlier study [**18, 19**]. From the spectral densities, it is then straightforward to calculate the partially relaxed ^{2}H spectral lineshapes for the particular inversion-recovery delays used in the experiment. A good fit of the partially relaxed lineshapes then implies that the motional model and jump

rate are possible descriptions of the true motion in the sample. The effect of molecular motion on T_{1Z} and T_{1Q} is in general different, so it is useful to measure both parameters in order to characterize the motion as fully as possible.

6.5.4 ^{2}H exchange experiments

^{2}H two-dimensional exchange experiments follow much the same format as those for spin-$\frac{1}{2}$ nuclei, except that the storage pulse and reconversion pulses either side of the mixing time τ_m are no longer 90° pulses. The pulse sequence usually used for ^{2}H is shown in Fig. 6.19. Pure absorption spectra are produced by recording two datasets so that there is quadrature detection in t_1; the off-resonance method sometimes used for spin-$\frac{1}{2}$ is not appropriate for ^{2}H because of the difficulty of getting uniform and symmetric excitation of the ^{2}H powder pattern off resonance. Both datasets are recorded using a 90°_x pulse as the initial excitation pulse (pulse 1 in Fig. 6.19). Dataset 1 is recorded using a 54.7°_{-x} pulse as the storage pulse (pulse 2), while dataset 2 is recorded using a 54.7°_y storage pulse. It can be shown that the signals arising from the two experiments are then [9]

$$\begin{aligned} 1: &\quad M_0 \sin\varphi_1 \sin\varphi_2 \sin\varphi_3 \cos\omega_1 t_1 \cdot \cos\omega_2 t_2 \\ 2: &\quad M_0 \cdot \frac{3}{4} \sin\varphi_1 \sin 2\varphi_2 \sin 2\varphi_3 \sin\omega_1 t_1 \cdot \sin\omega_2 t_2 \end{aligned} \tag{6.37}$$

where the φ_i are the flip angles of the various pulses in the sequence. The reason for the 54.7° pulse flip angles now becomes clear; for φ_2 and φ_3 set to 54.7°, the scaling factors for the two datasets become equal. This considerably simplifies the data

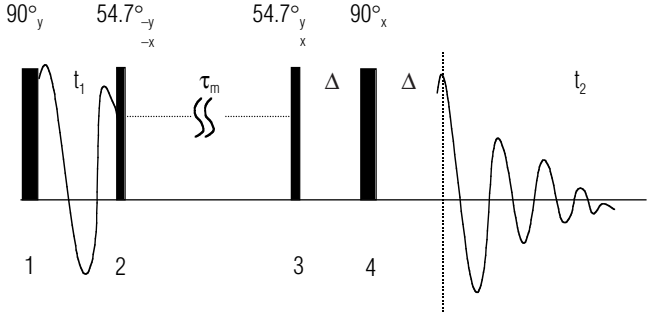

Fig. 6.19 The form of the two-dimensional exchange experiment for ^{2}H (I = 1). It differs from that for the experiment for spin-$\frac{1}{2}$ nuclei (Fig. 6.10) only in the nutation angles of the rf pulses employed. The pulses are numbered as they are discussed in the text. The initial 90°_y pulse excites transverse magnetization which evolves according to its characteristic frequency, ω_1 during t_1. Pulse 2 transfers any transverse magnetization remaining after t_1 to z for storage during the mixing time, τ_m, and pulse 3 then reconverts the magnetization back to transverse magnetization which evolves during t_2. The final Δ–90°_x–Δ sequence is an echo sequence, which allows ^{2}H powder lineshapes to be recorded in t_2 without distortion, which might arise from truncation of the dataset otherwise. Two datasets are recorded so that pure absorption lineshapes are obtained in the final two-dimensional frequency spectrum. For the first dataset, pulse 2 has phase $-y$ and pulse 3, phase y. For the second dataset, these pulses have phase $-x$ and x respectively.

processing. The two datasets are processed in the same way as for the spin-$\frac{1}{2}$ experiment (Fig. 1.21). One point which should be borne in mind is that the two datasets may require scaling relative to each other, as a result of relaxation processes occurring during the mixing time τ_m. The density operator governing the system during τ_m for experiment 1 is proportional to $\hat{I}_z$, and so the system is subject to spin-lattice relaxation as described by the parameter T_{1Z}. However, the density operator during τ_m in experiment 2 is proportional to $(3\hat{I}_z^2 - I(I+1))$ or equivalently, $\hat{T}_{20}$, which corresponds to quadrupolar order, whose relaxation is governed by T_{1Q}. In general, T_{1Z} and T_{1Q} are different, and this can lead to the datasets resulting from the two experiments having different intrinsic amplitudes.

The relatively large widths of ^{2}H powder patterns means that t_1 and t_2 data truncation of the sort described in Section 6.4.1 for spin-$\frac{1}{2}$ systems is nearly always a problem in ^{2}H exchange experiments. Using quadrupolar echoes (–τ–90°–τ–) before both the t_1 and t_2 periods (see Fig. 6.13 and the discussion in Section 6.4.1, but with the Hahn echo replaced with a quadrupole echo) is therefore very advantageous in producing undistorted spectra; an echo step before t_2 is almost essential in ^{2}H exchange experiments. Three-dimensional and reduced four-dimensional ^{2}H exchange experiments have been performed. Details of these can be found in reference [**11**].

A typical two-dimensional ^{2}H exchange spectrum is shown in Fig. 6.20 [**9**].

6.5.5 Resolving ^{2}H powder patterns

Resolution of ^{2}H powder pattern lineshapes can be a problem in uniformly, or multiply-labelled samples. In many cases, ^{2}H labelling of specific sites is near impossible, especially in more complex molecules, or in naturally occurring samples. In other cases, it would be excessively time consuming and expensive to specifically label all sites of interest in a molecule, separately in successive samples. Clearly, some method is needed to resolve ^{2}H signals from different sites. Magic-angle spinning can be useful, although the chemical shift range of ^{2}H is very small, so often MAS is not sufficient to resolve different sites. Two possibilities have been proposed for separating ^{2}H lineshapes in two-dimensional experiments. In the first, ^{2}H spinning sideband patterns (or static-like powder patterns) are separated according to the double-quantum ^{2}H chemical shift (Fig. 6.21) [**20**].

This has the effect of doubling the frequency gap between ^{2}H signals in the double-quantum dimension over what would occur in a single-quantum spectrum, and so improves the resolution over that in a normal one-dimensional MAS spectrum.

In the second, static-type ^{2}H powder patterns are separated according to the ^{13}C chemical shift of the ^{13}C nucleus to which the ^{2}H is bonded [**21**]. The pulse sequence is shown in Fig. 6.22.

Initial ^{13}C transverse magnetization is generated by cross-polarization from ^{1}H. The entire experiment is conducted under magic-angle spinning, which of course

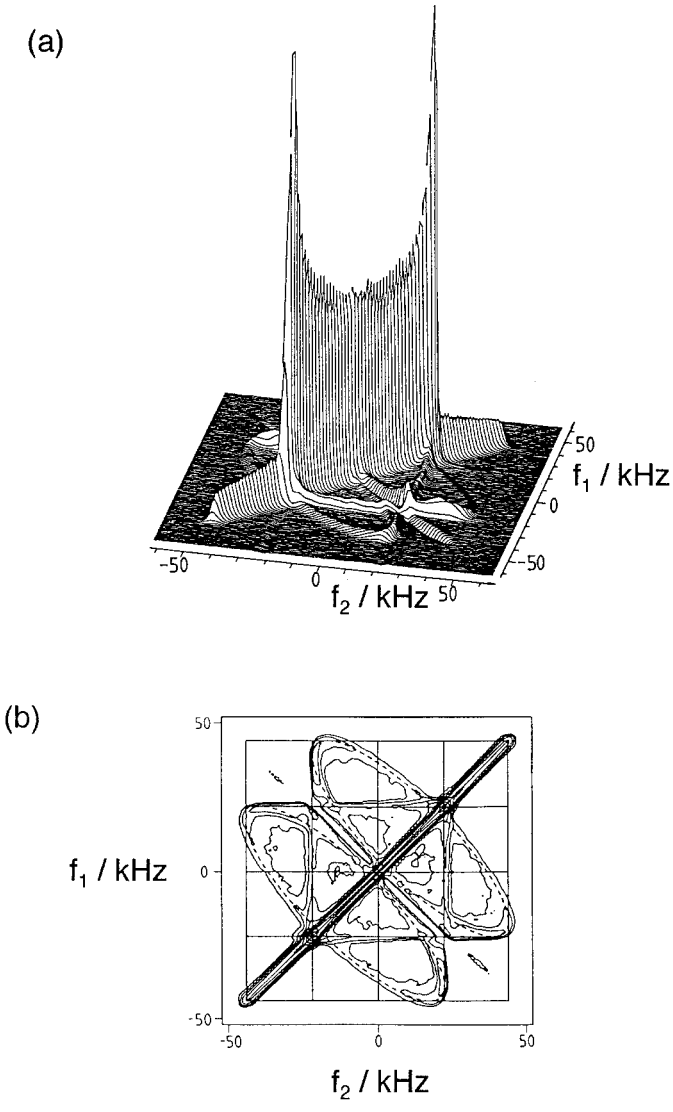

Fig. 6.20 A two-dimensional ^{2}H exchange spectrum for a static sample of DMS [**9**], (a) surface plot and (b) contour plot. As in the spin-$\frac{1}{2}$ case, the geometry of the elliptical ridges seen in the spectrum yields the angle of molecular reorientation occurring during the mixing period of the experiment. (Taken from Schmidt, Blümich and Speiss (1988).)

averages the ^{13}C–^{2}H dipolar coupling to zero. It is reintroduced by a series of rotor-synchronized 180° pulses; $(2N - 2)$ 180° pulses are applied in N rotor periods. Thus multiple-quantum coherences involving the ^{13}C and ^{2}H spins can now be excited via the agency of the ^{13}C–^{2}H dipolar coupling. During the first two rotor periods of the pulse sequence shown in Fig. 6.22, zero- and double-quantum coherences between ^{13}C and ^{2}H spins are excited. In the t_1 period, transverse ^{2}H magnetization is excited and allowed to evolve; in doing so it modulates the zero- and double-quantum coherences, and this is reflected in the final FID recorded in t_2. During the next two rotor cycles, the multiple-quantum coherences are reconverted. A z filter preceding

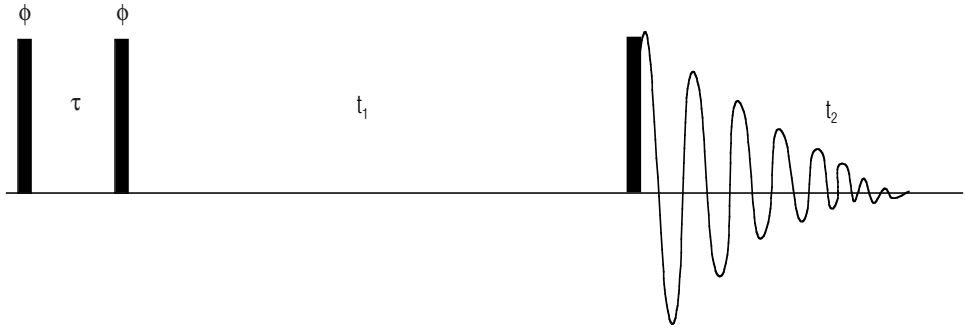

Fig. 6.21 The pulse sequence for the double-quantum ^{2}H experiment [**20**]. This two-dimensional experiment separates ^{2}H spinning sideband patterns (or alternatively, static-like ^{2}H quadrupole powder patterns) according to the ^{2}H double-quantum chemical shift offset, so improving the resolution over a single-quantum experiment. In addition, the double-quantum transition frequency has no contribution from quadrupole coupling (to first order) so the double-quantum spectrum is not complicated by spinning sidebands. ^{2}H double-quantum coherence is excited with the initial 90°_ϕ–τ–90°_ϕ part of the pulse sequence and allowed to evolve in t_1 (double-quantum coherence is selected in t_1 by phase cycling the two 90° excitation pulses). A further 90°_x pulse then transforms the remaining double-quantum coherence into observable single-quantum coherence whose evolution is recorded in a FID in t_2. The entire experiment is conducted under magic-angle spinning. Details of molecular motion are then extracted from the separated ^{2}H spinning sideband patterns by simulation. The τ delay is of the order 10 μs. The t_1 period is rotor-synchronized so that the rotor phase at the start of t_2 is the same for all t_1 datasets. Without this, pure absorption two-dimensional spectra are impossible to produce.

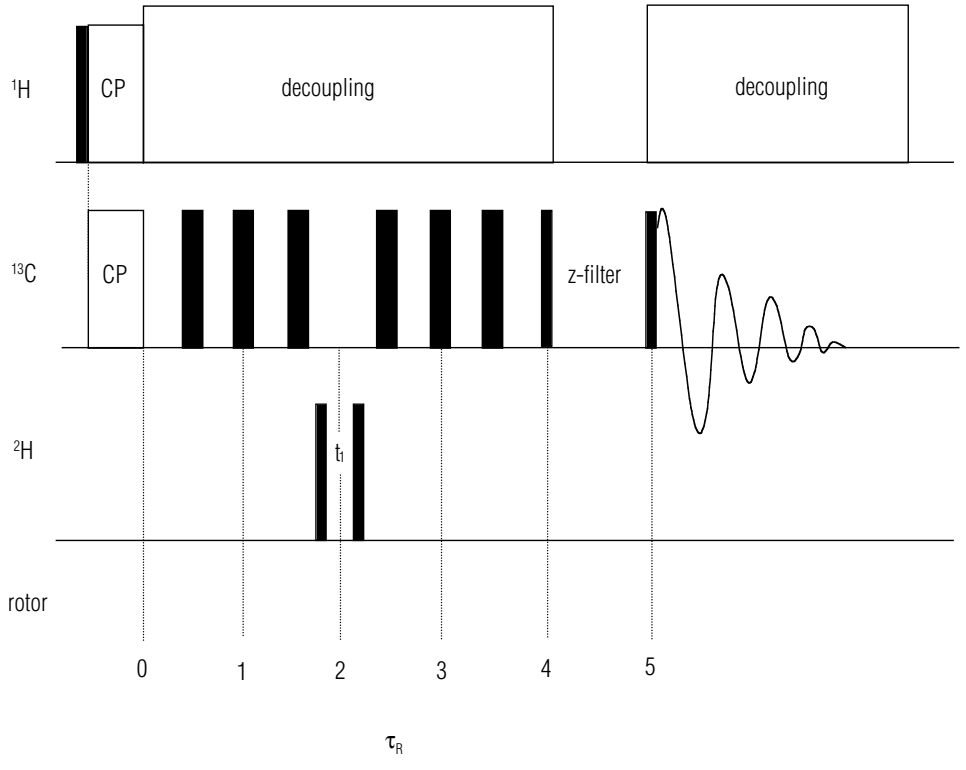

Fig. 6.22 The pulse sequence for a two-dimensional experiment to separate ^{2}H quadrupolar powder patterns according to the isotropic chemical shift of the ^{13}C spin to which the ^{2}H is bonded [**21**] – see text for details.

the detection period ensures a purely absorptive spectrum. Only one dataset needs to be recorded, as it may be assumed that the f_1 spectrum (^{2}H dimension) is symmetric about $\omega_1 = 0$, providing of course that ^{2}H is set on resonance.

Notes

1. The trace of a matrix is the sum of its diagonal elements.
2. If the T_2 relaxation time for the spin under study is very long, the x magnetization may not fully dephase during τ_m, in which case phase cycling needs to be used to remove this component. This can be done by alternating the phase of the storage pulse and receiver together in successive scans.

References

1. A. Abragam, *Principles of Magnetic Resonance*, Clarendon Press, Oxford (1961).
2. M.J. Duer and M.H. Levitt, *Solid-State NMR* **1** (1992) 211.
3. R. Tycko, G. Dabbagh and P.A. Mirau, *J. Magn. Reson. A* **85** (1989) 265.
4. L. Frydman, G.C. Chingas, Y.K. Lee, P.J. Grandinetti, M.A. Eastman, G.A. Barrall and A. Pines, *J. Chem. Phys.* **97** (1992) 4800.
5. Z. Gan, *J. Am. Chem. Soc.* **114** (1992) 8307.
6. L. Frydman, S. Vallabhaneni, Y.K. Lee and L. Emsley, *J. Chem. Phys.* **101** (1994) 111.
7. K. Schmidt-Rohr, J. Clauss and H.W. Spiess, *Macromol.* **25** (1992) 3273.
8. H.W. Spiess, *NMR: Basic Principles and Progress* **15** (1978) 55.
9. C. Schmidt, B. Blümich and H.W. Spiess, *J. Magn. Reson.* **79** (1988) 269.
10. W.-G. Hu, C. Boeffel and K. Schmidt-Rohr, *Macromol.* **32** (1999) 1611.
11. K. Schmidt-Rohr and H.W. Spiess, *Multidimensional Solid-State NMR and Polymers*, Academic Press, London (1994).
12. S. Wefing, S. Kaufmann and H.W. Spiess, *J. Chem. Phys.* **89** (1988) 1234.
13. F.H. Larsen, H.J. Jakobsen, P.D. Ellis and N.C. Nielsen, *J. Phys. Chem. A* **101** (1997) 8597.
14. F.H. Larsen, H.J. Jakobsen, P.D. Ellis and N.C. Nielsen, *Chem. Phys. Lett.* **292** (1998) 467.
15. G.L. Hoatson and R.L. Vold, *NMR: Basic Principles and Progress* **32** (1994).
16. R.L. Vold, G.L. Hoatson and T.Y. Tse, *Chem. Phys. Lett.* **263** (1996) 271.
17. G.L. Hoatson, R.L. Vold and T.Y. Tse, *J. Chem. Phys.* **100** (1994) 4756.
18. A. Scheicher, K. Müller and G. Kothe, *J. Chem. Phys.* **92** (1990) 6432.
19. D.A. Torchia and A. Szabo, *J. Magn. Reson.* **94** (1991) 152.
20. M.J. Duer and E.C. Stourton, *J. Magn. Reson.* **129** (1997) 44.
21. D. Sandström, M. Hong and K. Schmidt-Rohr, *Chem. Phys. Lett.* **300** (1999) 213.

Solid-State NMR Spectroscopy Principles and Applications
Edited by Melinda J. Duer
Copyright © 2002 by Blackwell Science Ltd

Chapter 7
Molecular Structure Determination: Applications in Biology

Oleg N. Antzutkin

7.1 Introduction

Most liquid state NMR spectroscopists with experience of peptide and protein structure determination will be disappointed when they obtain their first solid-state NMR spectrum. They will not see numerous narrow lines in one-dimensional spectra nor sharp cross peaks in two- and three-dimensional spectra. It is quite possible that for some samples, say carbonyl-^{13}C labelled peptides or proteins, one will see a relatively broad (with a linewidth of ca. 3–5 ppm) featureless line in solid-state NMR spectra, even in favourable conditions, i.e. under magic-angle spinning and high-power proton decoupling. For a scientist who has analysed and assigned hundreds or even thousands of lines and crosspeaks in two- and three-dimensional liquid-state NMR spectra, it might be very depressing to see the same broad line in all their protein samples. In most solid-state NMR experiments, the large linewidths expected mean that one can even omit shimming and other routine accessories of liquid-state NMR spectroscopy. For highly crystalline samples, solid-state NMR lines can be relatively sharp (linewidth ca. 0.1 ppm), in cross-polarization/proton-decoupled spectra of polycrystalline samples under magic-angle spinning (MAS) or for single crystals mounted on a goniometer. However, the structure of molecular systems which are easily crystallized, can be elucidated by means of X-ray or neutron diffraction much more easily than with NMR. The most interesting biological cases are transmembrane proteins, large proteins (with a molecular weight larger than 30 kDa) and amyloid peptide fibrils, which are inaccessible to liquid-state NMR and which cannot be crystallized, which makes them impractical for X-ray diffraction studies. This is the area where solid-state NMR can be used for structural investigations and my goal here is to convince the reader that there are numerous solid-state NMR methods already developed for accurate measurements of biologically important macromolecules in disordered solid samples. Nowadays, the most popular solid-state NMR techniques for this purpose are accurate measurements of distances between specifically labelled homonuclear

and/or heteronuclear spins, using rotational resonance, multiple-pulse recoupling, double-quantum spectroscopy or REDOR, as well as determination of torsion angles in various specifically labelled fragments of biopolymers, i.e. $H^{13}C^{13}CH$, $H^{15}N^{13}CH$, $^{15}N^{13}C^{13}C^{15}N$, $O^{13}C^{13}CH$ and $^{13}CO \ldots {}^{13}CO$. Multidimensional correlation spectroscopy on ^{13}C,^{15}N-uniformly labelled single crystals and polycrystalline polypeptides is also a hot topic in solid-state NMR [**1**, **2**]. However, in these experiments, both hetero- and homonuclear dipole–dipole couplings complicate the spectra and therefore broadband heteronuclear as well as selective homonuclear decoupling are needed for successful assignment of signals in multidimensional solid-state NMR spectra.

7.1.1 Useful nuclei in biological solid-state NMR

Most biologically relevant liquid-state NMR studies are based on ^{1}H NMR. This nucleus is abundant (99.8%) and has the largest magnetic moment of all nuclei (with the exception of tritium, ^{3}H, which is, however, radioactive and very low in natural abundance) and therefore has the highest sensitivity. A vast number of ^{1}H multidimensional correlation NMR experiments for the liquid state have been developed for studies of both structure and dynamics of biologically relevant systems (see, for example, classical monographs of references [**3**] and [**4**]). Magnetic Resonance Imaging (MRI), which has found extraordinarily wide applications in medicine, is also based on the detection of protons, since the human body consists mostly of water. Multinuclear multidimensional correlation spectroscopy involving less sensitive nuclei such as ^{13}C and ^{15}N, is also a popular topic in liquid-state NMR nowadays [**4**]. However, in almost all techniques using these nuclei, either the detection of the NMR signal is carried out through the most sensitive nucleus, ^{1}H, or the ^{1}H magnetization is transferred to the less sensitive nuclei, which are then detected, rather than use direct detection of the ^{13}C or ^{15}N.

In contrast, ^{1}H NMR in solids encounters considerable difficulties. In biological solids, such as proteins, DNA or lipids, which contain many hydrogen atoms, ^{1}H spins are coupled in a common network through the dominating dipole–dipole interaction. This gives rise to structureless broad lines in the ^{1}H spectra with widths of the order of 20–50 kHz. Since the whole range of proton chemical shifts in organic compounds is only 10 ppm, such spectra are of limited value. In liquids the ^{1}H dipole–dipole interactions are averaged out by fast rotational motion of molecules. In solids they are not. However, it is possible to 'break' the ^{1}H dipolar-coupled network either by a uniform 99% labelling of biomolecules with another isotope of hydrogen, deuterium (and detecting the remaining 1% of 'isolated' ^{1}H) or by use of a homonuclear dipolar-decoupling pulse sequence, for example, CRAMPS (Combined Rotation And Multiple Pulse Spectroscopy) [**5**, **6**], WIM-12 (Windowless Isotropic Mixing) [**7**], FSLG-2 (Frequency-Switched Lee–Goldberg) [**8**] or MREV-8 [**9**, **10**]. The former strategy has been widely used in studies of liquid crystalline

systems. However, ^{2}H labelling of proteins, DNA or lipids is a rather expensive and difficult procedure. Moreover, such labelled systems might have different biochemical properties, i.e. pK_a, pI, etc., due to isotopic kinetic effects which can be large in the case of the $^{1}H/^{2}H$ substitution. This might affect the path of protein folding, and the whole relevance of structural studies on ^{2}H-labelled systems, as models for the unlabelled systems, will be always in question. Perdeuteration of peptides and proteins is, however, a common practice.

In the second approach, i.e. using homonuclear dipolar-decoupling pulse sequences, ^{1}H lines are still substantially broadened. A large component of this broadening is, however, inhomogeneous broadening due to the variety of chemical environment around the ^{1}H in the sample. However, there are some good examples of the use of ^{1}H CRAMPS in conformational studies of solid peptides, where secondary structures such as α-helix and β-sheet can be distinguished from the ^{1}H chemical shift of the α ^{1}H site in homopolypeptides [**11**].

An alternative to homonuclear decoupling pulse sequencies are experiments under very fast magic-angle spinning (at spinning frequencies up to 40 kHz). As explained in Section 2.2.4, rapid magic-angle spinning can remove homonuclear dipole–dipole interactions. This has been successfully used in studies of polymers [**12**] and biopolymers [**2**]. However, taking into account a vast number of chemically inequivalent ^{1}H sites in a protein, and the natural linewidth of 1–2 ppm of ^{1}H lines, it is unlikely that solid-state ^{1}H NMR of biomolecules will ever reach the 'high-resolution' standards of liquid-state NMR, even in strong magnetic fields and under fast magic-angle spinning.

The high sensitivity of protons is, however, routinely used in the cross-polarization experiments with proton decoupling (see Section 2.5) where ^{1}H magnetization is transferred to less sensitive nuclei such as ^{13}C and ^{15}N, which are then detected while applying ^{1}H decoupling (see Section 2.3). The result of cross-polarization is an enhancement of ^{13}C (or ^{15}N) spin signal by up to the ratio $\gamma(^{1}H)/\gamma(^{13}C)$ (or $\gamma(^{1}H)/\gamma(^{15}N)$). This is a factor of 4 and 10 for carbon-13 and nitrogen-15 spins, respectively. In addition, the time which must be allowed between successive scans in a signal-averaging experiment is determined by the ^{1}H spin-lattice relaxation time, which is relatively short. In contrast, the time between scans for an experiment where ^{13}C or ^{15}N are excited directly by an rf pulse is necessarily long, because of the long relaxation times usually associated with these nuclei. The ^{1}H spin-lattice relaxation time can be additionally shortened by a chemical admixing of minute quantities (ca. 0.1%) of paramagnetic Cu or Mn salts. A slight ramp of the contact pulse applied to one of the nuclei in the cross-polarization experiment is recommended, as this has been found to improve reproducibility of experiments when long-term instabilities of the spectrometer are unavoidable [**13**].

The importance of the high-power proton decoupling in solids is illustrated in Fig. 7.1 [**14**]. ^{13}C resonance lines in non-decoupled spectra are very broad even at high magic-angle spinning frequences.

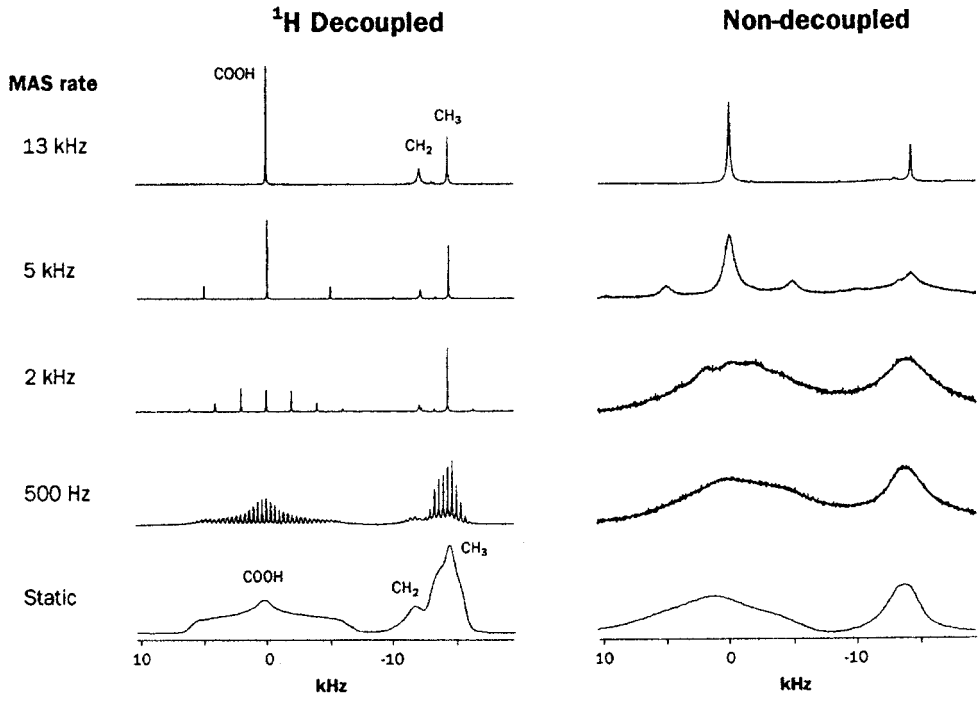

Fig. 7.1 ^{13}C NMR spectra of a powdered mixture of glycine-1-^{13}C, glycine-2-^{13}C and alanine-3-^{13}C showing the effect of magic-angle spinning and ^{1}H-decoupling. The plots are displayed on different vertical scales. Adapted from ref. [**14**].

There are also novel experiments which use indirect detection of less sensitive nuclei. In these, ^{1}H transverse magnetization is created, transferred to the less sensitive nucleus and after transverse magnetization has been allowed to evolve, the remaining transverse magnetization is transferred back to the ^{1}H spins where it is finally detected (Fig. 7.2) [**15**]. The detection at high frequency of the ^{1}H spins gains a factor of 3 in sensitivity for nitrogen-15 nuclei in such an experiment [**15**].

In consequence of the issues addressed above, at the current stage of the development in solid-state NMR, the most popular nuclei in biological applications are not ^{1}H, but ^{13}C and ^{15}N (in peptides and proteins) and in some cases also ^{31}P (in biomembranes, DNA and RNA). ^{13}C and ^{15}N nuclei have NMR Larmor frequencies of $\omega_0(^{13}\mathrm{C}) = 0.2515\ \omega_0(^1\mathrm{H})$ and $\omega_0(^{15}\mathrm{N}) = -0.1014\ \omega_0(^1\mathrm{H})$ respectively, where $\omega_0(^1\mathrm{H})$ is the Larmor frequency for ^{1}H. Natural abundance of carbon-13 and nitrogen-15 isotopes are only 1.108 and 0.37%, respectively, so both carbon-13 and nitrogen-15 spins can be considered as isolated spin systems. Consequently, both homonuclear dipole–dipole and *J*-couplings do not need to be considered in most experiments involving these nuclei. This means that the chemical shifts of both carbon and nitrogen sites can be directly measured from one-dimensional ^{13}C and ^{15}N NMR spectra of unlabelled biomolecular systems.

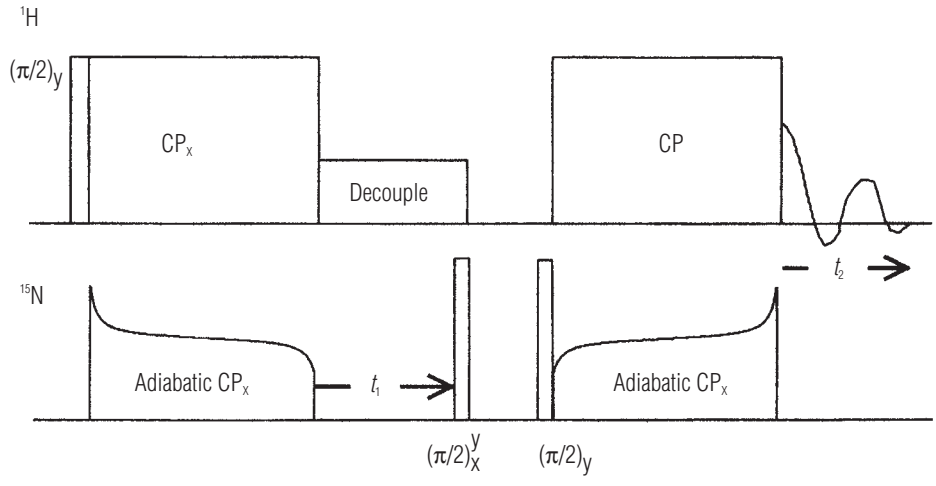

Fig. 7.2 Pulse sequence for ^{1}H-detected two-dimensional ^{1}H/^{15}N correlation spectroscopy (indirect detection of ^{15}N spins). ^{15}N transverse magnetization is prepared with adiabatic cross-polarization using a tangential shaped pulse at the ^{15}N frequency. After the t_1 period, a pair of 90° pulses are applied to select the real or imaginary component of the ^{15}N magnetization, which is then transferred back to ^{1}H spins with the reversed tangential pulse for detection. Adapted from ref. [**15**].

When desired, a specific fragment of a biomolecule can be selectively labelled (usually a pair of the relevant spins is introduced) with either ^{13}C or ^{15}N or both. Specific labelling is a costly procedure, but it is motivated by accurate measurements of structural details of a labelled fragment: interspin distances or specific torsion angles are measured by solid-state NMR in powder samples with errors of only 0.1 Å and 5–10 degrees, respectively. If spin labels are placed in the same molecule, intramolecular structures are tackled. Intermolecular distances can be also measured if labels are placed on different molecular species within the sample. The latter is particularly useful in studies of drug–protein or antibody–protein complexes or even larger assemblies of peptide molecules such as amyloid fibrils. We will discuss these experiments in detail later in this chapter.

The sensitivity of ^{31}P nuclei is relatively high compared with ^{13}C and ^{15}N, since this isotope has a Larmor frequency of $\omega_0(^{31}\mathrm{P}) = 0.4052\ \omega_0(^1\mathrm{H})$, and also 100% natural abundance. ^{31}P NMR has found application in studies of oriented biomembranes [**16–18**] and DNA molecules [**19–23**]. Interesting results on the orientational distribution function of phosphate groups in an oriented fibre of DNA were obtained by means of rotor-synchronized magic-angle spinning experiments. The distribution of chemical shift anisotropy (CSA) tensors in the DNA molecule can be measured and its conformation (or mixture of conformations), namely A-, B-, or C-DNA can be determined. We refer readers to more specialized literature concerning this interesting topic in solid-state NMR [**19–23**].

Other nuclei of interest in biological solid-state NMR, such as ^{2}H ($I = 1$, $\omega_0(^2\mathrm{H}) = 0.1535\ \omega_0(^1\mathrm{H})$, 0.015% natural abundance), ^{14}N ($I = 1$, $\omega_0(^{14}\mathrm{N}) = 0.0723\ \omega_0(^1\mathrm{H})$,

99.64% natural abundance), ^{33}S ($I = \frac{3}{2}$, $\omega_0(^{33}\text{S}) = 0.0768\,\omega_0(^1\text{H})$, 0.76% natural abundance), ^{17}O ($I = \frac{5}{2}$, $\omega_0(^{17}\text{O}) = -0.1356\,\omega_0(^1\text{H})$, 0.037% natural abundance) are quadrupolar nuclei. These encounter difficulties in powder samples because of the broad range (often extremely broad range) of spectral frequencies to be excited due to the large quadrupolar interaction and their dependence on molecular orientation with respect to the external magnetic field (see Chapter 4). However, ^{2}H NMR is routinely used in biological applications of solid-state NMR, in particular for studing both the orientation and motion of structural motifs of membrane proteins incorporated in oriented lipid layers [**16, 18, 24–26**]. An illustrative example of this approach is the uniaxially oriented retinal photoreceptor rhodopsin, in DMPC bilayers, in which the 11-*cis* retinal has been specifically deuterated at the methyl groups at the C19 or C20 positions. Solid-state ^{2}H NMR spectra have provided the orientation and conformation of retinal within the protein binding pocket around the attachment site [**17**].

In metal-binding proteins, some other spin-$\frac{1}{2}$ nuclei such as ^{113}Cd ($I = \frac{1}{2}$, $\omega_0(^{113}\text{Cd}) = -0.2226\,\omega_0(^1\text{H})$, 12.26% natural abundance), can be used as a substitute for other 'native' metals whose nuclei are quadrupolar, such as zinc ($I = \frac{5}{2}$, $\omega_0(^{67}\text{Zn}) = 0.0627\,\omega_0(^1\text{H})$, 4.11% natural abundance) or copper ($I = \frac{3}{2}$, $\omega_0(^{63}\text{Cu}) = 0.2842\,\omega_0(^1\text{H})$, 30.91% natural abundance, $\omega_0(^{65}\text{Cu}) = 0.2653\,\omega_0(^1\text{H})$, 69.09% natural abundance). None of the above mentioned quadrupolar nuclei is commonly used in biological applications of solid-state NMR and therefore are not discussed further in this chapter.

7.1.2 An overview of nuclear spin interactions encountered in biological samples

Let us limit our consideration to just three nuclei which are commonly considered in applications of biological solid-state NMR: ^{1}H, ^{13}C and ^{15}N. All possible interactions between these spins can be summarized in the form of rotating frame hamiltonians as follows:

$$\begin{aligned}\hat{H} = &\left(\hat{H}^{\text{H}} + \hat{H}^{\text{C}}_{\text{iso}} + \hat{H}^{\text{N}}_{\text{iso}} + \hat{H}^{\text{C}}_{\text{CSA}} + \hat{H}^{\text{N}}_{\text{CSA}}\right)\\ &+ \left(\hat{H}^{\text{HH}} + \hat{H}^{\text{CC}} + \hat{H}^{\text{NN}}\right)\\ &+ \left(\hat{H}^{\text{HC}} + \hat{H}^{\text{HN}} + \hat{H}^{\text{CN}}\right)\end{aligned} \tag{7.1}$$

Here terms in the first bracket are hamiltonians describing interactions of the three spins with the external magnetic field (including isotropic chemical shifts, $\hat{H}^{\text{H}}$, $\hat{H}^{\text{C}}_{\text{iso}}$ and $\hat{H}^{\text{N}}_{\text{iso}}$ and chemical shift anisotropy, $\hat{H}^{\text{C}}_{\text{CSA}}$ and $\hat{H}^{\text{N}}_{\text{CSA}}$; the ^{1}H chemical shift anisotropy is small and so is omitted here). The second bracket contains terms describing homonuclear spin–spin interactions, both the direct, dipole–dipole interaction and the indirect, scalar *J*-coupling. Finally, terms in the last bracket of Equation (7.1) describe heteronuclear spin–spin interactions, again both dipole–dipole and *J*-coupling interactions. Note, that the terms $\hat{H}^{\text{CC}}$, $\hat{H}^{\text{NN}}$ and $\hat{H}^{\text{CN}}$

are only relevant in ^{13}C and/or ^{15}N isotopically labelled systems and can be omitted in the case of unlabelled biomolecules.

Each term in Equation (7.1) depends on factors which, if extracted, would contain useful information about the structure of a biomolecule. $\hat{H}^{C}_{iso}$, $\hat{H}^{N}_{iso}$ and $\hat{H}^{C}_{CSA}$, $\hat{H}^{N}_{CSA}$ depend on isotropic chemical shifts and chemical shift anisotropies which are sensitive to the electronic environment around the carbon and nitrogen sites respectively. Chemical shift anisotropies depend on molecular conformation (for example, the secondary or tertiary structure of proteins or peptides) and on the presence of side groups in close vicinity to the nucleus in question. $\hat{H}^{CC}$, $\hat{H}^{NN}$ and $\hat{H}^{HC}$, $\hat{H}^{HN}$ and $\hat{H}^{CN}$ depend on interspin distances. This property is widely used in solid-state NMR for measuring inter- and intramolecular distances.

The main problem in solid-state NMR is that in static solid samples, all the above-mentioned interactions are present simultaneously giving rise to extensively overlapping lines. The resulting spectrum is virtually useless. The state-of-the-art strategy in solid-state NMR is, firstly, to remove all anisotropic interactions and, secondly, to reintroduce desired interactions, in order to obtain reasonably well-resolved one-dimensional or two-dimensional spectra which contain structural information of interest.

The first step in this strategy usually involves magic-angle spinning. Magic-angle spinning removes all anisotropic interactions which behave as second-rank tensors (both the chemical shift anisotropy and the dipole–dipole interactions – see Section 2.2), provided that the rotation frequency, ω_R, is larger than the anisotropy of the interaction to be removed in frequency units. An NMR spectrum of a sample under rapid magic-angle spinning approaches the resolution of a liquid-state NMR spectrum, i.e. only isotropic chemical shifts and *J*-couplings appear in the spectrum. However, it is mechanically difficult to spin a sample faster than the anisotropy associated with the $\hat{H}^{HC}$ and $\hat{H}^{HN}$ terms (^{1}H–^{13}C and ^{1}H–^{15}N dipolar couplings which are 15–25 kHz between directly bonded nuclei). This results in a considerable broadening of lines in ^{13}C and ^{15}N NMR spectra due to interactions of these nuclei with protons. Therefore, ^{1}H decoupling is used in addition in the form of either continuous rf irradiation (see Section 2.3) or by use of a phase-modulated pulse sequence such as TPPM (Two Pulse Phase Modulation) [**27**] or C12 and R24 [**28**].

The second step in the state-of-the-art strategy is to reintroduce (or recouple) the desired interactions. This usually involves specific of pulse sequences which are designed on the basis of a theoretical analysis of spin and space symmetries of the interactions that are to be reintroduced. For example, homonuclear dipole–dipole couplings given by $\hat{H}^{CC}$ and $\hat{H}^{NN}$ terms can be reintroduced under magic-angle spinning by rotational resonance (see Section 3.2.3) [**29–32**], RFDR (Radio-Frequency Driven Recoupling) [**33, 34**], finite pulse (fp)-RFDR designed for use under fast magic-angle spinning [**35**], DRAMA (Dipolar Recovery At the Magic Angle) (see Section 3.2.1) [**36, 37**], MELODRAMA (related to DRAMA) [**38**], DRAWS (a windowless version of DRAMA) [**39**], HORROR [**40**], BABA [**41**], RIL [**42**], C7

[**43**] (see Section 3.2.2) and subsequent variations such as POST-C7 [**44**] and CMR7 [**45**], and the recently developed R-sequences [**28**]. This huge list of pulse sequences all designed for the same purpose or recoupling homonuclear dipolar couplings is motivated by the constant requirement of improved performance of such sequences.

^{13}C–^{15}N heteronuclear dipole–dipole couplings (described by $\hat{H}^{CN}$ in Equation (7.1)) can be reintroduced by the REDOR (ROtational Echo DOuble Resonance) pulse sequence (see Section 3.3.2) [**46**] based on the SEDOR (Spin-Echo DOuble Resonance) technique originally developed for static samples [**47**], and its variant, called TEDOR (Transferred-Echo DOuble Resonance) [**48**]. Three spectrometer channels and triple-resonance NMR probes are needed for these experiments, as pulses are applied to both ^{13}C and ^{15}N spins, and ^{1}H decoupling is additionally required. REDOR experiments allow internuclear distances between specifically labelled carbon and nitrogen sites to be estimated. These distances are important structural constraints for solid peptides, proteins and drug–protein complexes.

Finally, there are the so-called double-quantum heteronuclear local field (2Q-HLF) experiments, such as measurements of torsion angles of specifically labelled fragments, $H^{13}C^{13}CH$ [**49**], $H^{15}N^{13}CH$ [**50**], $^{15}N^{13}C^{13}C^{15}N$ [**51**, **52**], $O^{13}C^{13}CH$ [**53**, **54**] and $^{13}CO \ldots {}^{13}CO$ [**55–57**]. These are more advanced experiments which have been recently developed for static samples or powders under magic-angle spinning. In the first case of this family of methods (measurements of $H^{13}C^{13}CH$ torsion angle under magic-angle spinning), a double-quantum coherence (2QC) between a pair of ^{13}C spins is excited (for example, by a C7 sequence, reintroducing the $\hat{H}^{CC}$ term of Equation (7.1) – see Section 3.2.2 for further discussion of the excitation of double-quantum coherence). The subsequent evolution of the double-quantum coherence is affected by the four ^{1}H–^{13}C dipole–dipole interactions in the $H^{13}C^{13}CH$ fragment (term $\hat{H}^{HC}$ in Equation (7.1)). The evolution of the double-quantum coherence depends on the relative geometry of four ^{1}H–^{13}C dipole–dipole coupling tensors: the effects of the four tensors almost completely cancel each other if the fragment is in the *trans*-conformation ($\theta = 180°$), and add constructively in all other conformations. The success of this experiment relies on the 'local field' condition, i.e. 'breaking up' the infinite net of proton spins in the solid sample, so that the two ^{1}H spins in the $H^{13}C^{13}CH$ fragment are effectively isolated from the rest of the ^{1}H dipolar-coupled network. The local field condition is satisfied by the suppression of the homonuclear proton–proton interaction (term $\hat{H}^{HH}$ in Equation (7.1)) with the aid of a homonuclear decoupling sequence, such as MREV-8 [**9**, **10**] or the Lee–Goldberg decoupling sequence [**58**] or other sequences having the same property [**7**, **8**]. A similar strategy is used for other 2Q-HLF experiments: for measurements of ϕ angles in proteins ($H^{15}N^{13}CH$ torsion angles), heteronuclear ^{15}N–^{13}C double- and zero-quantum coherences are excited (term $\hat{H}^{CN}$ in Equation (7.1)) and evolve in the presence of $\hat{H}^{HC}$ and $\hat{H}^{HN}$ terms in the hamiltonian. ψ angles in proteins ($^{15}N^{13}C^{13}C^{15}N$ torsion angles) are estimated from the evolution of ^{13}C double-quantum coherence affected by two ^{15}N–^{13}C heteronuclear dipole–dipole

interactions which are recoupled by a REDOR train of 180° pulses on the ^{15}N spins. In other experiments of this class, chemical shift tensors of carbonyl carbons are correlated with ^{1}H–^{13}C dipole–dipole coupling tensor ($O^{13}C^{13}CH$ torsion angle) or chemical shift anisotropy tensors of two ^{13}C-labelled carbonyl sites are correlated by means of spin diffusion [**59–61**]. The latter is a method for $^{13}CO \ldots {}^{13}CO$ torsion angle measurements which allows estimations of both ϕ and ψ angles in proteins [**55**, **56**]. The same goal can be reached by assisting the magnetization exchange between the two carbonyl groups with a dipolar recoupling sequence, such as RFDR [**57**]. The latter two experiments are performed under slow magic-angle-spinning. In this regime, spinning sidebands give the required information about chemical shift annisotropy (see Section 2.2.1). Crosspeaks in the two-dimensional correlation spectrum can be quantitatively analysed and compared with calculated spectra, which are functions of corresponding torsion angles. We will consider some of these experiments in detail later in this chapter.

7.2 Chemical shifts

In the following sections of this chapter, structures of a variety of peptides and proteins will be extensively discussed. Basics of the peptide chemistry, nomenclature of amino acids, primary, secondary and tertiary structures of proteins can be found in elementary biochemistry books.

7.2.1 Is a protein in a disordered or in the native well-structured form?

It is widely accepted in the biochemical community that the structure of proteins is highly correlated with their functionality. In some cases intramolecular structural transitions can lead to a dysfunction or even to a deadly disease associated with a protein. A representative example of the latter is the human prion protein which causes the neuronal death in the human brain and leads to a disease known as CJD (Creutzfeldt–Jakob Disease) or GSS (Gerstmann–Sträussler Syndrome) in humans, BSE (Bovine Spongiform Encephalopathy) in cattle, scrapie in sheep or more generally called TSE (Transmissible Spongiform Encephalopathy) [**62**]. Prion diseases are transmissible between species and bring about the slow degeneration of the central nervous system, which inevitably leads to death. A long period of time, 3–10 years, elapses between infection and the appearance of the first clinical syndromes. The structure of a fragment of PrP_C, $PrP_{90–231}$, where PrP_C is, the normal cellular conformation of the human prion protein, has been recently resolved by liquid-state NMR [**63**]. Structure of diseased PrP_{Scr}, the so-called scrapie form, which has the same primary sequence as PrP_C, has also been proposed [**64**]. $PrP_{90–231}$ has been found to adopt a predominantly α-helical structure (Fig. 7.3(a) [**63**]), while PrP_{Scr} is believed to have a structure with four antiparallel β-sheets instead of a pair of

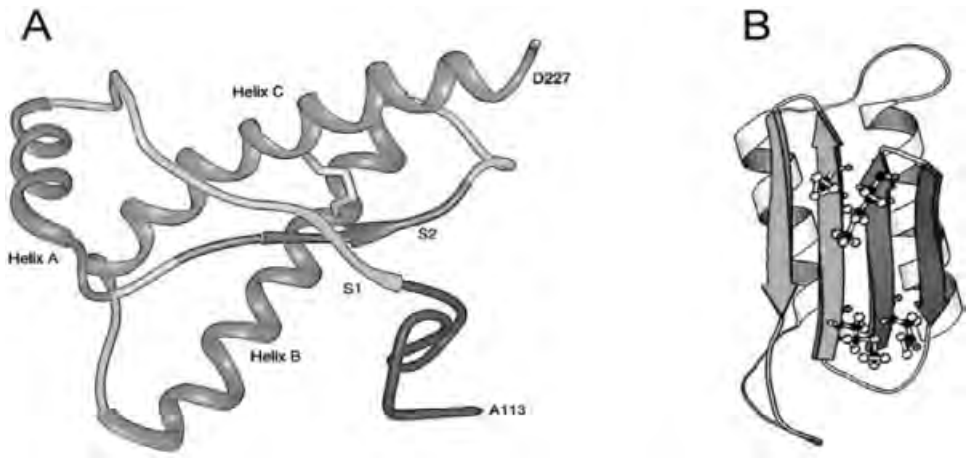

Fig. 7.3 Structures of prion proteins. (a) NMR structure of SHa recombinant (r) PrP_{90-231} [**63**]. Presumably, the structure of the α-helical form of PrP_{90-231} resembles that of PrP_C. (b) Plausible model for the tertiary structure of $HuPrP_{Scr}$ [**64**]. S1 β-strands are the darker arrows; S2 β-strands are the lighter arrows. Four residues implicated in the species barrier are shown in ball-and-stick form (Asn-108, Met-112, Met-129, Ala-133). Adapted from ref. [**62**].

α-helices (Fig. 7.3(b)) [**64**]). It is currently believed that PrP_{Scr} catalyses the transition of PrP_C to the diseased PrP_{Scr} conformation in the course of direct contact between two protein molecules [**62**]. It has also been suggested that a fragment of PrP_{Scr} (PrP_{27-30}) may form oligomers and fibrils due to its high content of β-sheets [**65, 66**]. This in turn might be toxic for neurons. Structures of oligomers and fibrils are certainly an area for solid-state NMR, since fibrillar aggregates are too large for studies by liquid-state NMR and also inaccessible for single-crystal X-ray diffraction studies because of their amorphous nature. Therefore, a pertinent question is: Is it possible, from solid-state NMR experiments, to find out if a protein or a fragment of it is in an α-helix or in a β-sheet secondary conformation?

A simple experiment that can be conducted is the measurement of the isotropic chemical shift offsets of ^{13}C sites in the core of a polypeptide chain. Chemical shifts of C_α and C_β carbons in protein molecules are rather sensitive to the secondary conformation of a protein [**67–71**]: 4–5 ppm is a typical change in the isotropic chemical shift for the α-helix to β-sheet conformational transition. This is a well-known and useful fact in liquid-state NMR [**68**]. There has also been considerable success in the field of quantum-mechanical *ab-initio* calculations of chemical shifts in proteins [**69, 70, 72–79**]. Figure 7.4 depicts both experimental and theoretical histograms showing separation of α-helical and β-sheet chemical shifts for C_α and C_β carbon sites in proteins.

In solids, cross-polarization magic-angle spinning experiments can be performed to measure ^{13}C chemical shifts provided that high power ^1H-decoupling is applied during the acquisition of FID. Here, magic-angle spinning is needed for the removal

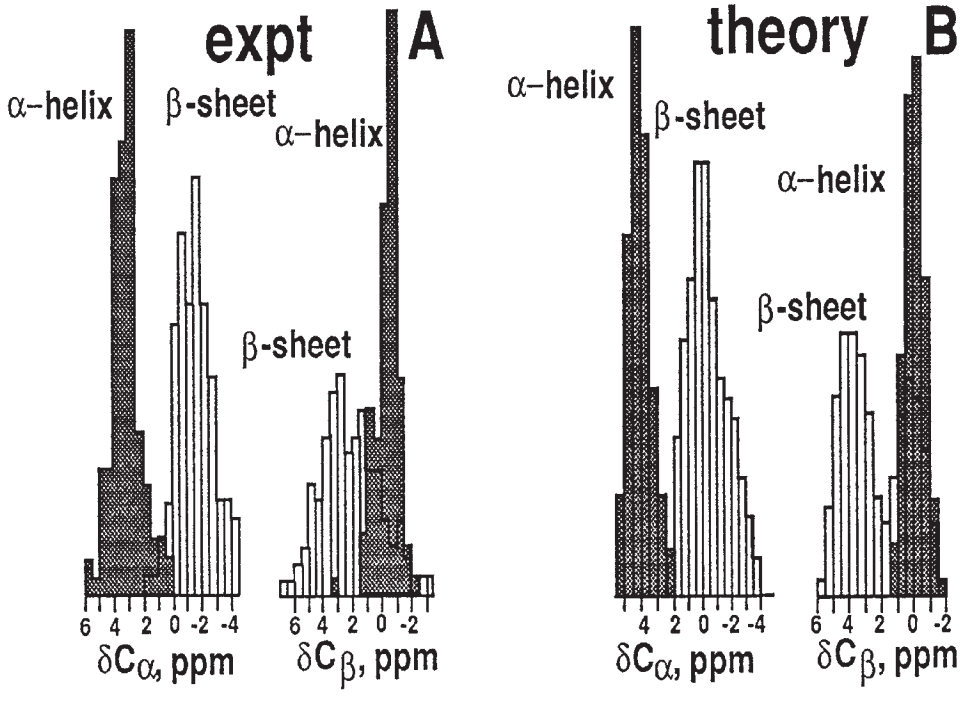

Fig. 7.4 ^{13}C NMR shielding in proteins. (A) Histograms showing separation of α-helical and β-sheet chemical shifts for C_α and C_β sites in proteins (based on global database of Spera and Bax, ref. [**68**]). (B) Histogram showing C_α and C_β shifts for model α-helical and β-sheet (alanine only) fragments, based on *ab-initio* shielding surface calculations [**68**]. Adapted from ref. [**69**].

of ^{13}C chemical shift anisotropy and to assist in removing ^{13}C–^{1}H dipolar couplings. Figure 7.5 shows ^{13}C cross-polarization magic-angle spinning spectra of amyloid-β-protein(1–40) ($A\beta_{1–40}$) which tends to build fibrils, the principal constituent of amyloid plaques in the human brain in the course of Alzheimer's disease. These plaques are believed to trigger inflamatory reactions in the brain tissues, which lead to gradual neurodegeneration [80]. It is known from other types of spectroscopy (IR, Raman and X-ray diffraction on oriented fibrils) that amyloid-β-protein molecules in amyloid fibrils adopt a β-sheet conformation. This can be confirmed by comparing cross-polarization magic-angle spinning NMR spectra of the non-incubated, freshly synthesized and lyophilized $A\beta_{1–40}$–Ala30–$^{13}CH_3$ (Fig. 7.5(a)) which adopts a predominantly random-coil conformation, with the same protein but incubated in aqueous solution at pH = 7.4 and 200 μM for 72 hours (Fig. 7.5(b)). Under these conditions amyloid-β-protein precipitates in the form of long thin (with the diameter of ca. 10 nm) fibrils as clearly seen by transmission electron microscopy (Fig. 7.6). For the purpose of other solid-state NMR experiments which are described later in this chapter, the protein was ^{13}C-labelled at the methyl group of the alanine 30th residue in the protein sequence. Inspecting ^{13}C cross-polarization magic-angle spinning spectra of the protein, one notes that lines in the region of C_α carbons (50–60 ppm) become sharper in the fibrillized sample (see Fig 7.5). This

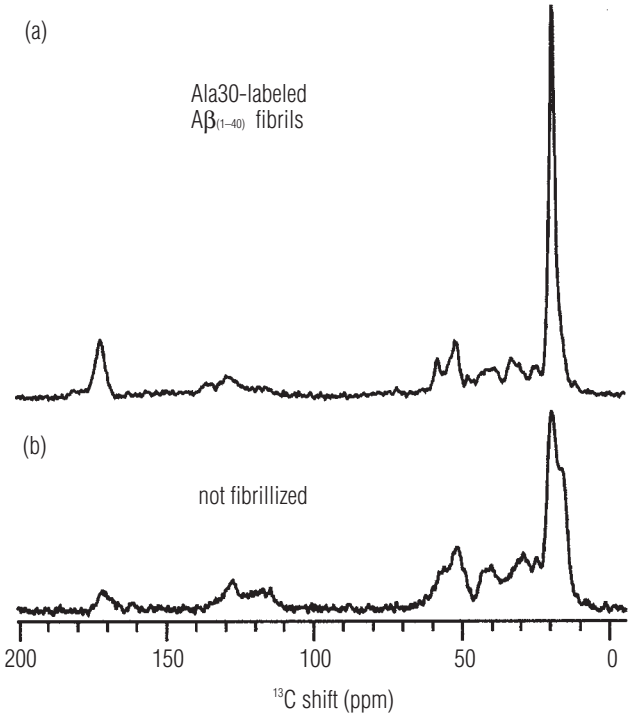

Fig. 7.5 (a) 100.4 MHz ^{13}C cross-polarization magic-angle-spinning (ν_R = 10 kHz) NMR spectra of Alzheimer's amyloid-β-protein(1–40) samples in fibrillized and unfibrillized, lyophilized from, with ^{13}C labels at the methyl carbon of Ala30. (b) Fibrillization produced significant sharpening of the NMR lines, including the methyl ^{13}C line around 20 ppm and natural-abundance ^{13}C lines from carbonyl and aliphatic carbons. Spectra were obtained with proton decoupling at 140 kHz.

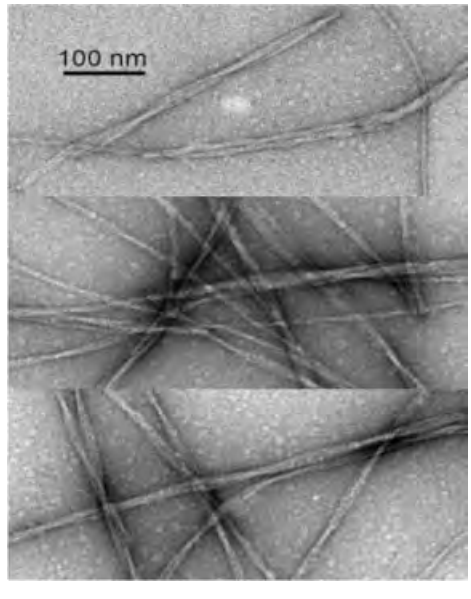

Fig. 7.6 Electron micrographs of negative-stained Alzheimer's amyloid-β-protein(1–40) fibrils adsorbed to carbon films from an amyloid-β-protein(1–40) solution after incubation at 24°C and pH 7.4 for three days. Typical amyloid fibrils are observed, appearing as single filaments or bundles of filaments with overall diameters ranging from 8 to 10 nm and with twist periodicities between 40 and 150 nm. Adapted from ref. [**232**].

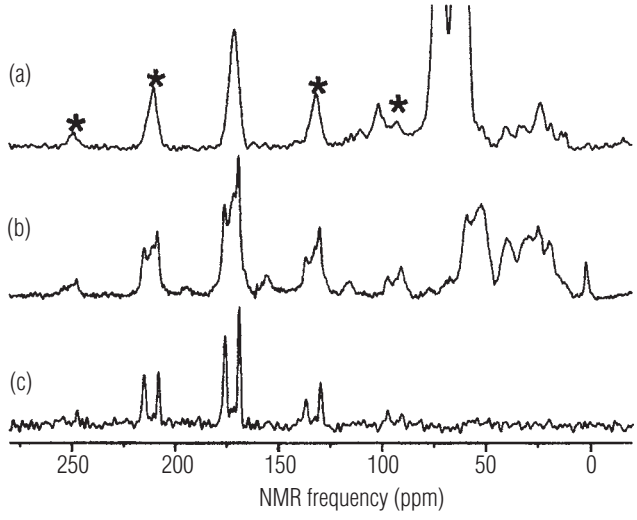

Fig. 7.7 100.4 MHz ^{13}C magic-angle spinning (ν_R = 3.94 kHz) NMR spectra of the gp120 V3 loop peptide RP135, with ^{13}C labels at the carbonyl sites of Pro320 and Gly321. (a) The free peptide in frozen solution (1 : 1 v/v glycerol/H2O, pH 7.2, −125°C). Glycerol was added to suppress crystallization. Asterisks indicate spinning sideband lines. (b) and (c) The complex of the peptide with Fab fragments of the anti-gp120 monoclonical antibody 0.5β (pH 7.0, no glycerol, −125°C, 4 mM peptide and Fab concentrations). Large signals between 55 and 80 ppm in (a) from natural-abundance ^{13}C in glycerol have been cropped. In (b), large natural-abundance ^{13}C NMR signals appear primarily from the Fab. In (c), natural-abundance ^{13}C signals are suppressed by double-quantum filtering, resulting in a clean spectrum of the labelled carbonyl sites of the antibody-bound peptide. Adapted from ref. [**88**].

indicates a well-defined conformation for these sites in the backbone of amyloid-β-protein molecules in fibrils with a shift to larger values of δ, characteristic of the β-sheet conformations.

Another illustrative example concerns solid-state NMR structural studies in the field of another deadly disease, HIV infection and AIDS. It is currently known that the third variable (V3) loop region of the HIV-1 envelope glycoprotein, gp120, is required for viral entry into target T-cells and macrophages [**81**], interacting with chemokine coreceptors on the surface of these cells [**82–84**]. The V3 loop elicits potentially neutralizing antibodies [**85**] and has been a target for AIDS vaccine development [**86**]. HIV is able to escape the host immune response due to the highly variable amino acid sequence of the V3 loop. However, it does contain a conserved central Gly–Pro–Gly–Arg (GPGR) motif of structural and biological significance [**87**]. Figure 7.7 shows cross-polarization, magic-angle spinning ^{13}C NMR spectra [**88**] of a model the V3 loop peptide RP135 [**89**] which is ^{13}C labelled at the carbonyl sites of Pro320 and Gly321. RP135 loop model comprises the central 24 residues of the 40 residue V3 loop of HIV-1 strain IIIB. Figures 7.7(a) and 7.7(b) show cross-polarization, magic-angle spinning ^{13}C NMR spectra of the free unbound RP135 peptide and the same peptide bound to the neutralizing monoclonical anti-gp120 antibody state, respectively. Solid samples were prepared in frozen solution. That the labelled fragment of the RP135 peptide adopts a well-

defined conformation in the RP135–antibody complex (Fig. 7.7(b)) can be seen in the two sharp lines from the ^{13}C-labelled carbonyl sites. Note that for the free peptide which is mostly disordered in solution, carbonyl resonances of the two labelled sites are much broader and heavily overlapped with signals derived from natural abundance ^{13}C spins in this region of the spectrum (see Fig. 7.7(a)). This background signal can be removed by a double-quantum filtering technique [**90, 91**] resulting in a spectrum from the labelled carbonyl sites of the antibody bound peptide only (Fig. 7.7(c)). A few characteristic features of the structure of the RP135–antibody complex in frozen solution have been elucidated in the course of more advanced solid-state NMR experiments discussed later in this chapter [**88**].

7.2.2 Chemical shift anisotropy

Knowledge of the chemical shift tensor (see Section 1.4.1) and its orientation with respect to a molecular axis system has at least two important consequences. First, the chemical shift anisotropy can be related to the distribution of electron density around nuclei which, in turn, can be correlated with the geometry of chemical bonds, i.e. with the structure of a molecular fragment. As already mentioned in the previous section, the full chemical shift tensor can be calculated using *ab-initio* methods for different molecular geometries, allowing correlations between the chemical shift tensor and molecular geometry to be established [**69**]. Secondly, and probably more importantly for applications of solid-state NMR, the principal axes of the chemical shift tensor of some sites are rather conservative parameters and can be fixed relative to a molecular reference frame for a small molecular fragment. Useful examples of this are the chemical shift tensors of carbonyl ^{13}C spins in peptides and proteins. Studies of model peptides indicate that the principal axes of the chemical shift tensor of these sites are 'bound' to the >C═O group and do not vary much (ca. ±5°) in proteins adopting different secondary structures. The principal axis associated with the chemical shift tensor component δ_{33}^{PAF} (see Section 1.4.1) is perpendicular to the carbonyl sp^2 plane, the principal axis associated with δ_{22}^{PAF} component is ca. 10° off the C═O bond and the angles between the δ_{11}^{PAF} principal axis and the C–N bond is approximately 40° [**92**]. Figure 7.8 shows the orientation of the principal axis frame of chemical shift tensor for the carbonyl ^{13}C site in a molecular axis frame of the –HN–C═O fragment. This property of the chemical shift tensor of carbonyl carbons is widely used in various types of two-dimensional correlation experiments, both under static and magic-angle spinning conditions (chemical shift anisotropy/chemical shift anisotropy or chemical shift anisotropy/dipole–dipole correlation spectroscopy), and in torsion and dihedral angle measurements on disordered samples of polymers [**93**] and biopolymers [**55–57**]. As is discussed in Section 7.4.1, in two-dimensional magic-angle spinning exchange NMR spectra, the intensities of the so-called *intersite* cross-peaks reflect the correlations between the anisotropic NMR frequencies of the two ^{13}C-labelled carbonyl sites.

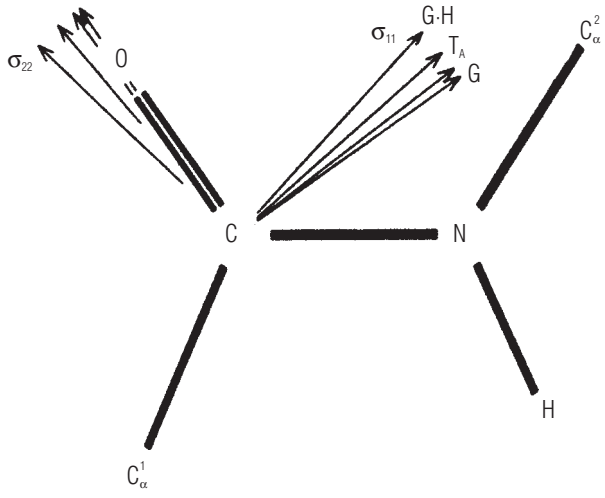

Fig. 7.8 The orientations of principal axes associated with the principal values δ_{11} and δ_{22} of the ^{13}C chemical shift tensor of the glycine carbonyl carbon in four model peptides. The two axes are in the peptide plane, the δ_{33} axis being perpendicular to the plane. The abbreviations refer to the following: A = Ac-Gly-Ala-NH_2, T = Ac-Gly-Tyr-NH_2, G = Ac-Gly-Gly-NH2, G·H = Gly-Gly·HCl. Adapted from ref. [**92**].

These are in turn determined by the relative orientation of the two ^{13}C chemical shift tensors involved [**56, 57**]. The principal values of the chemical shift tensor (δ_{11}^{PAF}, δ_{22}^{PAF}, δ_{33}^{PAF}), needed in the quantitative analysis of the two-dimensional exchange NMR spectrum can be determined from spinning sideband intensities of these sites in one-dimensional magic-angle spinning spectra using either the Herzfeld and Berger method [**94**] or a recently developed *Mathematica* routine [**95**] for the analysis of the chemical shift anisotropy based on direct time-domain calculations [**96, 97**]. In the latter, the χ^2 statistics of the difference between experimental and theoretically calculated spinning sideband intensities is plotted as a function of the chemical shift parameters, the chemical shift anisotropy Δ_{cs} and asymmetry η_{cs}. A minimum occurs around some particular parameter values, and the error limits of the individual chemical shift parameters are also readily estimated, provided that experimental sideband intensities, the experimental spinning frequency, the Larmor frequency and the experimental noise variance are imported into the programme. An example of the χ^2 statistics as a function of the chemical shift parameters for some selected ^{13}C sites of penicillin-V is shown in Fig. 7.9. The *Mathematica* routine for spinning sideband analysis is easy to use and may be downloaded from the world-wide-web site: **/www.fos.su.se/~mhl**.

Let us now return to the first aspect of chemical shift anisotropy discussed above, i.e. the relationship between the structure of a molecule and the chemical shift tensors of its chemical sites. We will use, as examples, two molecules of a biological importance, two β-lactam antibiotics, ampicillin and penicillin-V. Although the underlying reason for the varying pharmacological activity of these antibiotics remains unclear, it is believed that the conformations of the thiazolidine rings and of the side chains are correlated with the biological activity [**98**]. Single-crystal X-ray analyses have shown that the five-membered thiazolidine ring –S1–C2–C3–N4–C5– exists in one of two non-planar conformations. These are

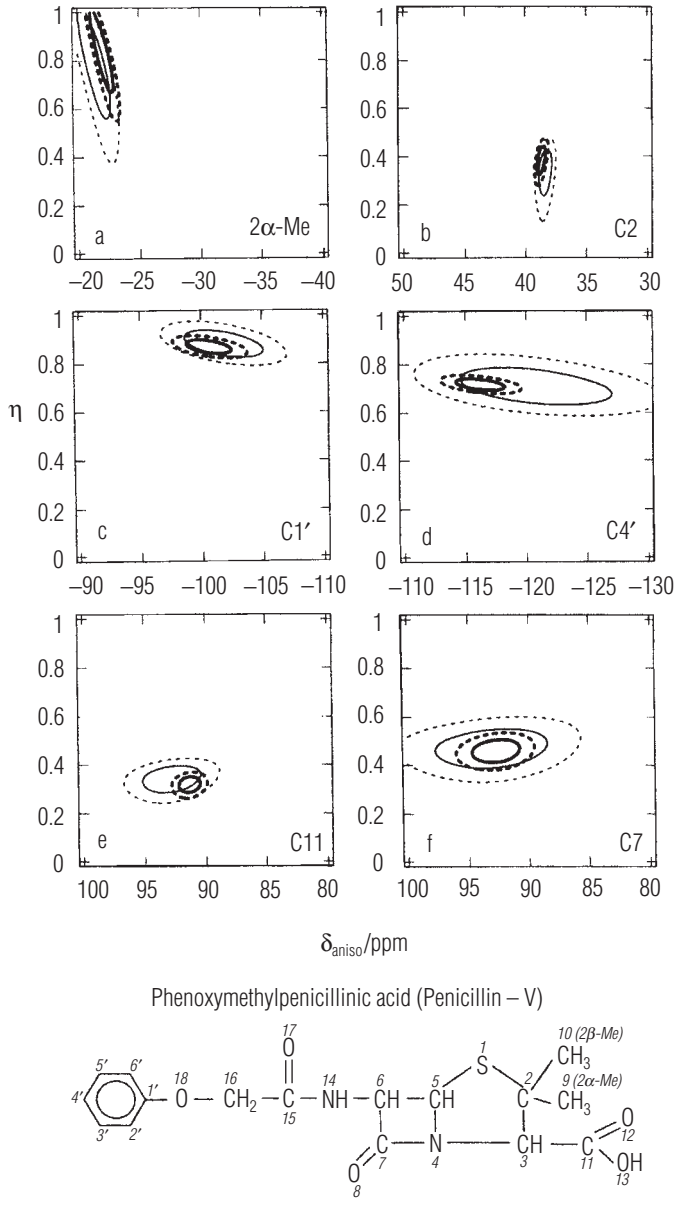

Fig. 7.9 χ^2 statistics as a function of the chemical shift parameters Δ_{σ} and η_{σ} (penicillin-V powder, 2D-PASS experiment, spinning frequencies 1030 (thick lines), and 800 Hz (thin lines). Graphs for six representative ^{13}C sites are presented: (a) 2α-Me, (b) C2, (c) phenyl C1′, (d) phenyl C4′, (e) carboxyl C11, and (f) carbonyl C7. The 68.3% joint confidence limit (solid) and 95.4% joint confidence limit (dashed) for the two CSA parameters are shown. Adapted from ref. [**96**].

termed C-3 or S-1 respectively, indicating that either the carbon C-3 or sulphur S-1 atom is significantly displaced from the plane defined by the other four atoms [**99**]. Penicillin-V is in the C-3 conformation in the solid state [**100**], while ampicillin is in the S-1 conformation [**101**] (see Fig. 7.10). In aqueous solutions, transitions between these two conformations occur. These have been detected from the isotropic chemical shifts of the two methyl groups, side groups of the β-lactam ring [**102**]. However, for different penicillins, fractional populations of C-3 and S-1

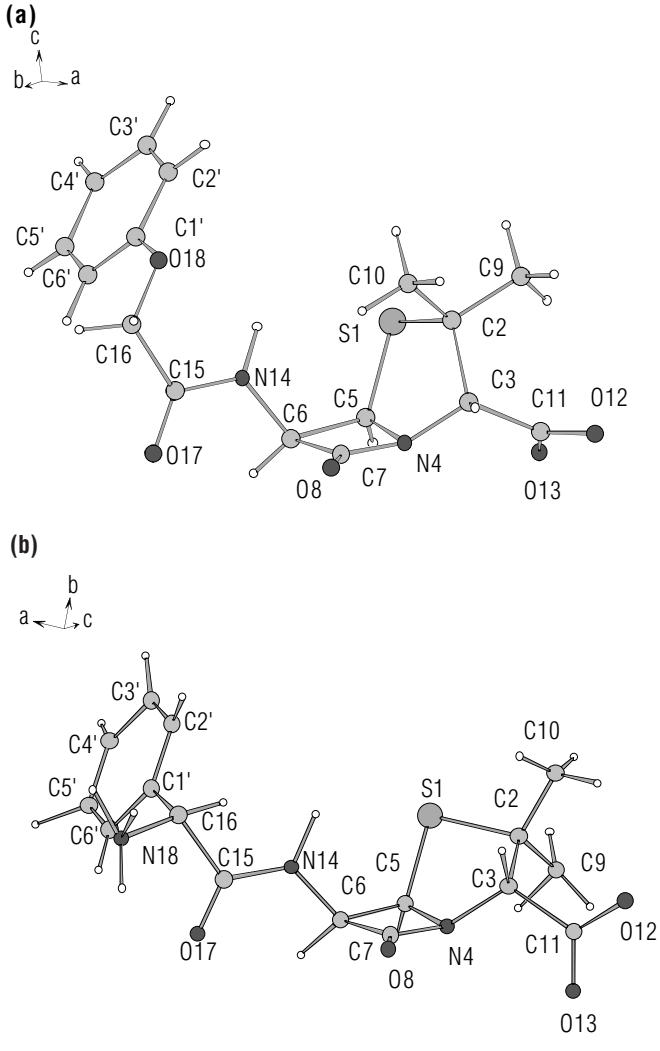

Fig. 7.10 Single-crystal X-ray structures of (a) penicillin-V (C-3 conformer) [**100**] and (b) ampicillin (S-1 conformer) [**101**].

conformations are different, which in turn may be correlated with their pharmacological activity.

Since X-ray structures of both ampicillin and penicillin-V in the solid state are known, it was interesting to investigate how chemical shift tensors of different sites are correlated with the particular geometry of these two molecules. Experimentally, it is not a trivial task to determine chemical shift anisotropies of sixteen ^{13}C sites because of a severe overlap of sixteen powder patterns (in static experiments) or spinning sideband patterns (under magic-angle spinning) (see Fig. 7.11(a)). The 2D-PASS method (see Section 5.2.4) has been employed to separate all spinning sidebands by order [**103**]. The 2D-PASS spectrum of penicillin-V powder is shown in Figs 7.11(b) and 7.11(c) [**96**]. Sideband patterns for each of ^{13}C sites are well

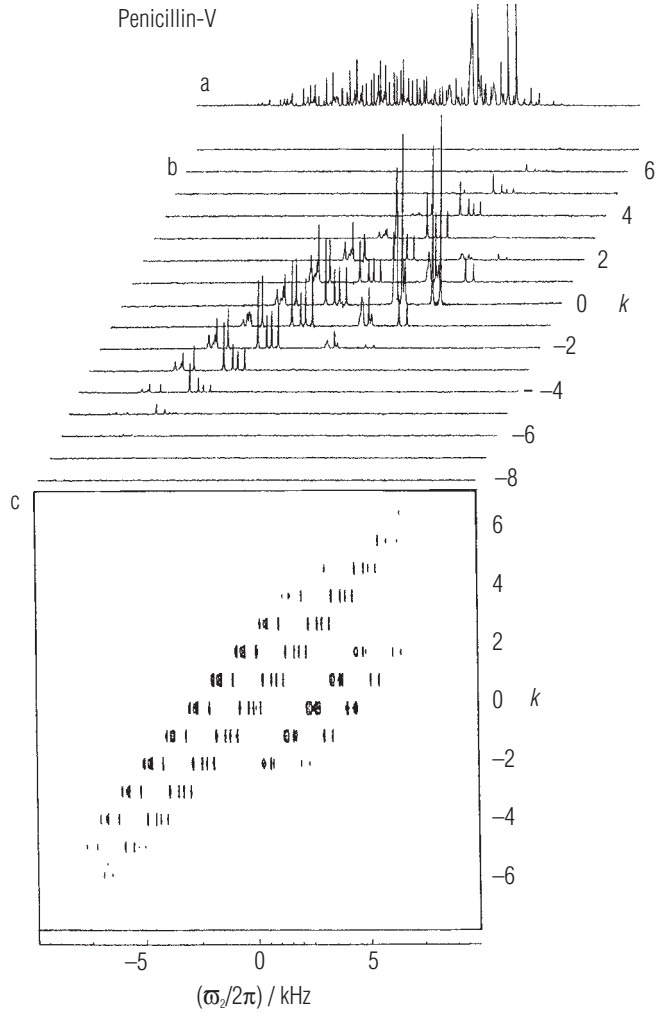

Fig. 7.11 50.3 MHz ^{13}C spectra of penicillin-V powder at a spinning frequency of 1030 Hz. (a) one-dimensional magic-angle-spinning spectrum. (b) 2D-PASS spectrum presented as a stack and (c) a contour plots. Adapted from ref. [**96**].

separated along the diagonals of the two-dimensional spectrum (with the exception of some overlapping sites with similar isotropic shifts and additional broadening or splitting due to ^{13}C–^{14}N dipole-dipole coupling [**104, 105**]). Sideband intensities in each pattern have been analysed with the aid of the *Mathematica* routine discussed above and chemical shift anisotropy values have been estimated [**96**]. χ^2 statistics as functions of the chemical shift parameters, Δ_{cs}^{j} and η_{cs}^{j} (where j denotes the particular ^{13}C site) for penicillin-V powder are shown in Fig. 7.9 for six representative ^{13}C sites. Results of two independent 2D-PASS experiments (performed at spinning frequencies of 800 and 1030 Hz) are shown with areas of both 63.8% and 95.4% joint confidence limits well overlapping for all these sites. This confirms the consistency of both experimental data obtained at two different spinning regimes with calculations embodied in the *Mathematica* routine.

Ab-initio calculations of chemical shift tensors for ^{13}C sites of these two antibiotics were recently performed by A.C. de Dios and co-workers [**106**]. Calculations have been carried out on isolated molecules and therefore no intermolecular interactions including any hydrogen bonding in the solid crystalline state have been taken into account. Two basis sets, restricted Hartree–Fock (RHF) and B3LYP with a 6–31 G** basis set, a hybrid method which makes use of the Becke exchange functional mixed with Hartree–Fock contributions and the correlation functionals of Lee, Yang and Parr, were used in the calculations. Penicillin was given 956 basis functions and ampicillin, 966 basis functions. Both geometry optimization and shielding tensor computation were performed using a parallel version of Gaussian 98 [**107**]. Single crystal structures were taken from the X-ray diffraction data [**100, 101**] and partial geometry of the proton positions was additionally optimized.

Comparing theoretically calculated with experimental principal components of the chemical shift tensor it has been found that the hybrid density functional method, B3LYP, performs better than coupled Hartree–Fock (RHF). Figure 7.12 shows the comparison plot between theoretical, B3LYP/6-311++G-(3d, 2p), shielding tensor components (σ_{ii}) and experimental chemical shift tensor components (δ_{ii})

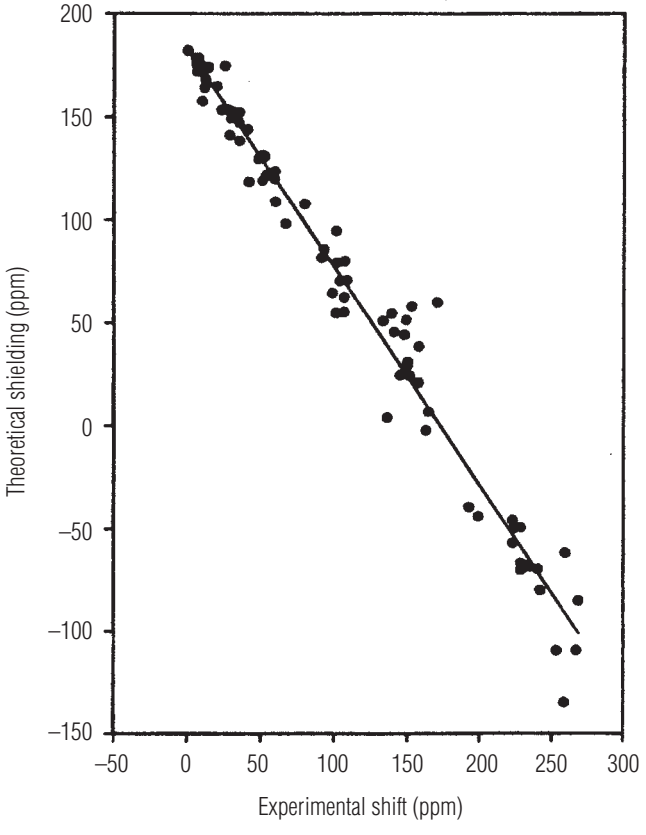

Fig. 7.12 Comparison between theoretical (B3LYP/6-311++G-(3d, 2p)) shielding (σ_{ii}) and experimental chemical shift tensor components (δ_{ii}) for the ^{13}C sites in penicillin-V and ampicillin. Adapted from ref. [**106**].

for the ^{13}C sites in penicillin-V and ampicillin. The slope of the linear regression between theoretical and experimental data is equal to –1.06 (–1.15 in RHF method), the intercept being equal to 183.1 ppm (203.9 ppm in RHF) and the rms deviation, 14.4 ppm (15.9 ppm in RHF). This represents reasonably good agreement between theory and experiment and confirms the reliability of single molecule calculations. Moreover, it gives a basis for seeking correlations between structure and chemical shift tensor components of ^{13}C sites in the two antibiotics. The largest deviation between theoretical and experimental components of the chemical shift tensor were obtained only for the δ_{11} and δ_{22} components of the carboxyl ^{13}C chemical shift tensor and the δ_{22} component for the ^{13}C carbonyl sites. These groups are possibly involved in intermolecular hydrogen bonding which is completely neglected in the calculations. Theoretical studies on the zwitterionic amino acids, L-threnionine and L-tyrosine [**72**] and on the carbonyl carbon sites in model peptides [**108**] show that the above-mentioned components of the ^{13}C chemical shift tensor are the most susceptible to the effects of hydrogen bonding.

The most interesting aspect of the preceding analysis is to find useful correlations between the chemical shift anisotropy of carbon sites and structure. We discuss these correlations in detail below for penicillin-V and ampicillin.

The conformation of the β-lactam ring can be expected to influence the chemical shift tensors of 2α-Me, 2β-Me, C2, C3, C5, C6, C7, C11 and, possibly, even carbonyl C15. ^{13}C chemical shift parameters for some of the sites of the two antibiotics cannot be compared because of overlapping lines their respective spectra. Figure 7.13 shows ^{13}C cross-polarization magic-angle spinning spectra of the two antibiotics spun at 7 kHz. Signals from sites C6 and C16 in ampicillin and C3, C16 and C5 in penicillin-V are overlapped. In this situation, only isotropic chemical shifts can be estimated, while chemical shift tensor parameters cannot be obtained independently for these carbon sites from the experimental sideband patterns. Simulations based on integrated sideband intensities of the overlapping resonances gave poor χ^2 statistics for Δ_{cs} and η_{cs} plots which means that the overlapping sites have rather different chemical shift parameters. In the present analysis, we also omit aromatic carbons which are outside the β-lactam ring. Tables 7.1 and 7.2 show both experimental [**96**] and theoretical (B3LYP) [**106**] chemical shift data for some selected well-resolved ^{13}C sites in the β-lactam ring and other nearby carbons which are in the close neighbourhood to it, in each of the two antibiotics.

The methyl substituents, 2α-Me and 2β-Me, are of great interest since their isotropic chemical shifts display a strong correlation with the conformation of the five-membered heteronuclear ring (see Fig. 7.13 and Tables 7.1 and 7.2). In particular, the isotropic chemical shift of the 2β-Me site changes by +6.4 ppm (–2.3 ppm for the 2α-Me site) in the transition from the S-1 conformer in ampicillin to the C-3 one in penicillin-V. This chemical shift change was attributed by Clayden et al. [**102**] to the influence of the β-lactam carbonyl group (C7). The 2β-Me–C7 separations in the C-3 and S-1 conformers are approximately 3.5 and 4.5 Å, respectively.

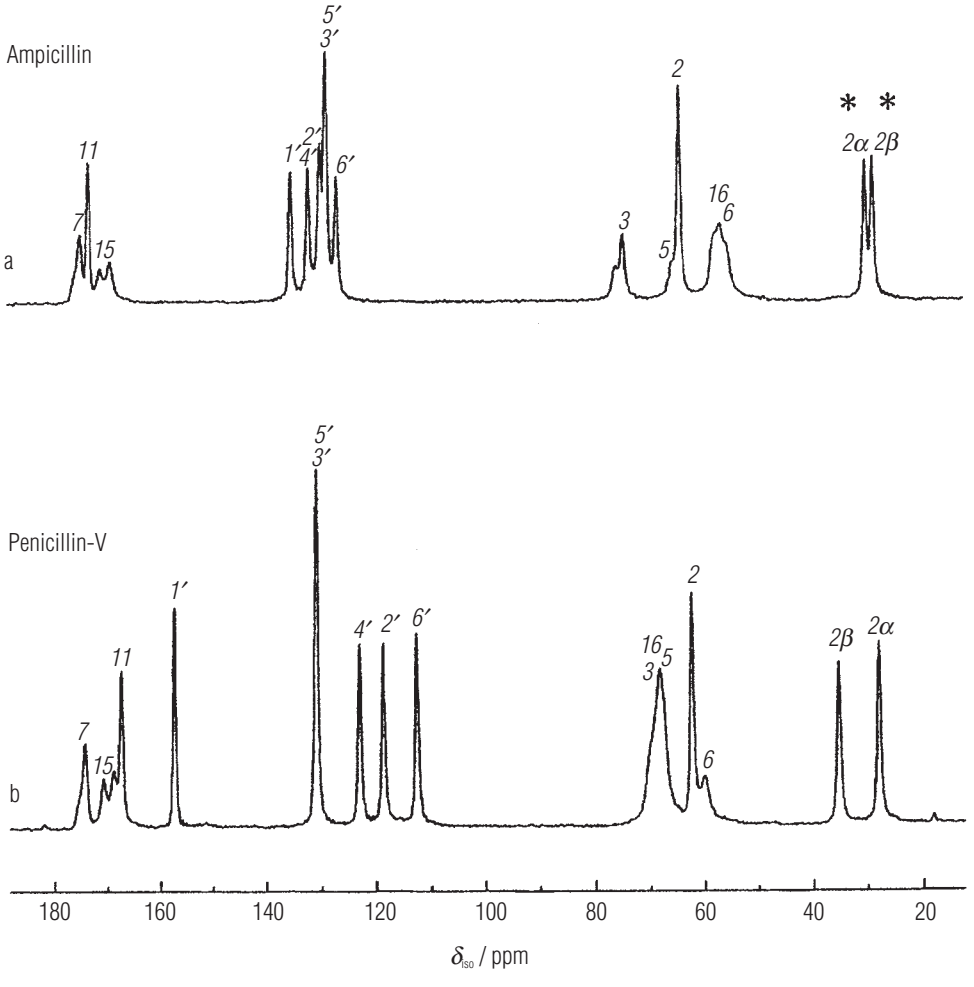

Fig. 7.13 50.3 MHz ^{13}C cross-polarization magic-angle spinning (ν_R = 7.0 kHz) spectra of (a) ampicillin and (b) penicillin-V powder. The assignments of the ^{13}C resonances are taken from ref. [**102**], except for the two ampicillin peaks indicated by asterisks, which have reversed assignments. Adapted from ref. [**96**].

The closer proximity of the carbonyl C7 group to the 2β-Me site in penicillin-V leads to the additional deshielding of this methyl carbon.

In their earlier work on the ^{13}C spectrum of ampicillin, Clayden et al. assigned the resonance at δ_{iso} = 28.9 ppm to the 2α-Me site and the resonance at δ_{iso} = 30.2 ppm to the 2β-Me site [**102**]. These assignments were based on a comparison of solid-state and solution-state NMR spectra [**109**, **110**]. However, the shift differences are small (1.3 ppm) and comparable to shifts which are typically observed when passing from the solution to the solid state. In Table 7.1, a revised assignment is suggested for ampicillin: δ_{iso}(2α-Me) = 30.2 ppm and δ_{iso}(2β-Me) = 28.9 ppm [**96**]. The new assignment, originally based on experimental chemical shift tensor para-

Table 7.1 Calculated[a] and experimental[b] ^{13}C chemical shift tensor parameters for selected carbon sites of ampicillin

carbon site		δ_{iso} (ppm)	Δ_{cs} (ppm)	η_{cs}
2α-Me	expt.	30.2 ± 0.1	–22.9 ± 0.5	0.94 ± 0.06
	calc.	29.0	–24.6	0.88
2β-Me	expt.	28.9 ± 0.1	–28.6 ± 0.5	0.56 ± 0.08
	calc.	27.7	–26.8	0.77
C2	expt.	64.8 ± 0.1	42.0 ± 0.3	0.76 ± 0.02
	calc.	74.8	45.9	0.97
C15	expt.	170.1 ± 0.5[c]	89.1 ± 2.0	0.73 ± 0.04
	calc.[d]	162.3	82.7	0.57
C11	expt.	173.3 ± 0.1	67.1 ± 0.7	0.93 ± 0.02
	calc.[d]	162.8	90.0	0.12
C7	expt.	175.2 ± 0.5[c]	93.2 ± 1.5	0.53 ± 0.04
	calc.[d]	168.7	99.7	0.13

[a] Theoretical components of the shielding tensor (B3LYP calculations) are taken from Rich et al. [**106**] and corrected on the intercept (183.1 ppm) of the linear regression plot: theoretical shielding (σ, ppm) versus experimental shift (δ, ppm).
[b] Experimental data are taken from Antzutkin et al. [**96**].
[c] The signal consists of a ^{13}C–^{14}N doublet [**104**]. The estimated chemical anisotropy and asymmetry are influenced by ^{13}C–^{14}N dipolar couplings.
[d] Intermolecular hydrogen bonding is not taken into account in the calculated values.

Table 7.2 Calculated[a] and experimental[b] ^{13}C chemical shift tensor parameters for selected carbon sites of penicillin-V

Carbon site		δ_{iso} (ppm)	Δ_{cs} (ppm)	η_{cs}
2α-Me	expt.	27.9 ± 0.1	–22.0 ± 0.6	0.84 ± 0.11
	calc.	31.4	–23.8	0.82
2β-Me	expt.	35.3 ± 0.1	–29.6 ± 0.4	0.63 ± 0.06
	calc.	34.2	–29.7	0.68
C2	expt.	62.5 ± 0.1	38.7 ± 0.2	0.40 ± 0.02
	calc.	78.9	49.5	0.39
C15	expt.	169.8 ± 0.5[c]	83.4 ± 1.8	0.88 ± 0.03
	calc.[d]	190.1	102.5	0.73
C11	expt.	167.3 ± 0.2	91.3 ± 0.6	0.32 ± 0.02
	calc.[d]	200.0	117.8	0.65
C7	expt.	174.4 ± 0.5[c]	92.7 ± 1.3	0.46 ± 0.03
	calc.[d]	184.0	108.4	0.04

[a] Theoretical components of the shielding tensor (B3LYP calculations) are taken from Rich et al. [**106**] and corrected on the intercept (183.1 ppm) of the linear regression plot: theoretical shielding (σ, ppm) versus experimental shift (δ, ppm).
[b] Experimental data are taken from Antzutkin et al. [**96**].
[c] The signal consists of a ^{13}C–^{14}N doublet [**104**]. The estimated chemical anisotropy and asymmetry are influenced by ^{13}C–^{14}N dipolar couplings.
[d] Intermolecular hydrogen bonding is not taken into account in the calculated values.

meters, allows the chemical shift anisotropy and the asymmetry parameter of both methyl sites to be roughly preserved when the β-lactam ring conformation is changed. This reassignment has been supported by the theoretical calculations of J.E. Rich et al. [**106**]. Though the chemical shift anisotropy of the methyl groups is smallest, the B3LYP method was able to predict both the isotropic shifts and the chemical shift tensor parameters of 2α-Me and 2β-Me sites in both antibiotics to within 2 ppm or less (which is within about 5% of experimental values, see Tables 7.1 and 7.2). The excellent agreement observed between the calculated and experimental chemical shift tensor components provides confidence in the calculated isotropic chemical shifts. The reassignments of the methyl resonances in the ampicillin spectrum discussed above are also supported by the results of the *ab-initio* calculations. Furthermore, the chemical shift anisotropy parameters are essentially preserved between penicillin-V and ampicillin, which is a remarkable feature, since the isotropic chemical shifts are very sensitive to the structural differences in the thiazolidine ring of these antibiotics.

In contrast to the methyl sites, both δ_{iso} and Δ_{cs} values of the saturated carbon C2 are very similar, while the asymmetry parameter η_{cs} of this site differs significantly in the two antibiotics: $\eta_{cs} = 0.76 \pm 0.02$ in ampicillin and $\eta_{cs} = 0.40 \pm 0.02$ in penicillin-V. This reflects a change of shape for the chemical shift tensor of the C2 carbon from asymmetric in ampicillin towards more axially symmetric in penicillin-V in the course of the conformational transition from the S-1 to C-3 conformer. Though B3LYP theoretical calculations reproduce the trend of η_{cs} rather well, calculated values for Δ_{cs} and absolute values for δ_{iso}, deviate from the experimental values by ca. 15% and 20% in ampicillin and penicillin-V, respectively (see Tables 7.1 and 7.2). However, earlier RHF calculations [**106**], give even larger deviations by an additional 7 ppm from the experimental data for the C2 sites. It can be concluded that both the isotropic chemical shifts and the chemical shift tensor parameters for saturated carbons are sensitive to the inclusion of electron correlation in *ab-initio* calculations. Probably an even better basis set is needed in *ab-initio* calculations in order to reproduce and predict experimental isotropic chemical shifts and chemical shift tensor parameters for saturated carbons. However, although not perfect, *ab-initio* calculations can clearly assist in investigating the effect of the ring conformation on the chemical shift tensors of these sites.

Finally, the experimental chemical shift tensor parameters of the carbonyl site, C7, coincide within error limits for the two compounds suggesting a similar electronic environment in this part of the molecule. This is also true for the carbonyl C15 site. This is to be expected since the S-1 to C-3 transition only involves the reorganization of the β-lactam ring which has little effect on the rigid structure of the four-membered cycle –N4–C5–C6–C7–, or the C15 carbonyl group which is well outside the β-lactam ring. The experimental chemical shift tensors of carboxyl carbon, C11, are very different in the two antibiotics, which may be due to intermolecular hydrogen bonding. However, theoretical calculations cannot assist in this

analysis, since the intermolecular hydrogen bonding was omitted in the calculations. It can be seen in Tables 7.1 and 7.2 that calculated chemical shift tensor parameters for the carbonyl and carboxyl sites deviate considerably from the experimental data. Clearly, more theoretical work has to be done in the future for predicting accurate chemical shift tensors for these groups.

To conclude the discussion on this topic, both isotropic chemical shifts and chemical shift anisotropies can be powerful tools in structural studies of biomolecules. Recently developed solid-state NMR experiments, such as 2D-PASS or others, designed for separating overlapping sideband patterns, can be used to determine chemical shift tensor parameters which can then be compared with those obtained from *ab-initio* theoretical calculations to reveal details of molecular geometry.

7.3 Interspin distance measurements

As discussed in Chapter 3, the through space dipole–dipole coupling is a simple function of the interspin distance. This property is widely used in both liquid and solid-state NMR for measuring intra- and intermolecular distances and hence determination of molecular structures. NOESY is probably the best example of a liquid-state NMR experiment that estimates dipole–dipole couplings. From intensities of crosspeaks in two-dimensional NOESY spectra obtained with different mixing times one can establish constraints on interspin distances. As was mentioned before, these crosspeaks appear due to relaxation mediated by the dipole–dipole interaction.

In spinning solid samples, the dipole–dipole coupling is first removed by magic-angle spinning together with other anisotropic interactions, and then selectively reintroduced by a specific pulse sequence (such as REDOR, RFDR, C7, etc.). As discussed in Chapter 3, the dipole–dipole coupling can be measured either directly from a one-dimensional spectrum or in a two-dimensional fashion, provided that scaling factors of recoupling pulse sequences are evaluated from experiments on model systems with known structure.

Below, we present a few examples of interspin distance measurements using both heteronuclear (such as ^{15}N–^{13}C, ^{31}P–^{13}C, etc.) and the homonuclear (such as ^{13}C–^{13}C) dipole–dipole interactions in powder systems of biological importance.

7.3.1 Heteronuclear distance measurements: the REDOR experiment

Since the introduction of the REDOR technique by Gullion and Schaefer [**46**], it has been widely applied to structural studies of biomolecules. For example, measurements of the heteronuclear ^{15}N-^{13}C distances have allowed the cross-linking of cell walls of microorganisms such as *Bacillus subtilis* [**111**] and *Staphylococcus aureus* [**112**] to be investigated as well as intercatechol cross-linking in sclerotized

cuticle of the insect tobacco hornworm *Manduca sexta* [**113**, **114**]. Structural constraints have been obtained by measuring: (i) ^{15}N–^{13}C distances in [^{15}N ^{13}C]-labelled pentapeptide Leu–enkephalin dihydrate, an endogeneous morphine-like substance [**115**]; (ii) ^{19}F–^{13}C distances in the 143-kDa tetrameric enzyme triptophane synthase [**116**]; (iii) a combination of ^{15}N–^{13}C and ^{19}F–^{13}C distances in ^{13}C and ^{19}F-selectively and ^{15}N-uniformly labelled biomolecular systems such as the complex between 25-kDa glutamine-binding protein (GlnBP) and its ligand, L-glutamine [**117**], as well as in bound factor Xa inhibitors to bovine trypsin [**118**]; (iv) ^{31}P–^{13}C distances in the Rubisco–CABP–CO_2–Mg^{2+} quaternary complex, an important intermediate in photosynthetic reactions [**119**]; (v) ^{15}N–^{31}P distances in a complex of Mg guanosine diphosphate (MgGDP) with uniformly ^{15}N-labelled elongation factor Tu, the 43-kDa bacterial G-protein transporting aminoacyl-tRNAs to the ribosome for protein biosynthesis [**120**]; (vi) both ^{13}C–^{31}P and ^{15}N–^{31}P distances in the 46 kDa enzyme 5-enol-pyruvylshikimate-3-phosphate synthase/shikimate-3-phosphate/phosphoenolpyruvate complex inhibited by ^{13}C-labelled herbicide, N-(phosphomethyl)-glycine, in plants and microorganisms [**121**]; ^{15}N–^{19}F distances in fluorolumazines complexed to the 1 MDa β_{60} capsid of the enzyme luminazine synthase [**122**], and many others.

The detailed theory of REDOR is given in Chapter 3. As mentioned there, there are analytical solutions for REDOR (also SEDOR and TEDOR) dephasing curves, which can be expressed in terms of Bessel functions of the first kind (labelled $J_k(x)$) [**123**]:

$$\frac{\Delta S}{S_0} = 1 - [J_0(\sqrt{2}\lambda_n)]^2 + 2\sum_{k=1}^{\infty} \frac{1}{16k^2 - 1}[J_k(\sqrt{2}\lambda_n)]^2 \tag{7.2}$$

where $\Delta S/S_0$ is the normalized REDOR difference signal, $\lambda_n = nd\tau_R$ is the dimensionless parameter which is the product of the number of dephasing cycles (n), the strength of the dipolar coupling (d), and the rotor period (τ_R). $J_k(x)$ are tabulated solutions to Bessel's equation:

$$x^2 \frac{d^2 J_k(x)}{dx^2} + x \frac{dJ_k(x)}{dx} + (x^2 - k^2) J_k(x) = 0 \tag{7.3}$$

Equation (7.2) allows efficient calculation of a universal REDOR dephasing curve, since the infinite sum in this equation converges rapidly. The series may be safely truncated at $k = 5$ to obtain results within 0.1% of the exact value (see Fig. 7.14) [**123**]. In this way, extensive numerical computations which involve powder averaging can be avoided. Bessel functions, $J_k(x)$, can be found in mathematical packages such as *Mathematica* [**95**]. Note, however, that Equation (7.2) has been derived for an isolated heteronuclear spin pair. For a site surrounded by a cluster of like (heteronuclear) spins, dipole–dipole couplings with all the surrounding spins have to be taken into account in calculations of the REDOR dephasing curve. This can be carried out by numerical computation.

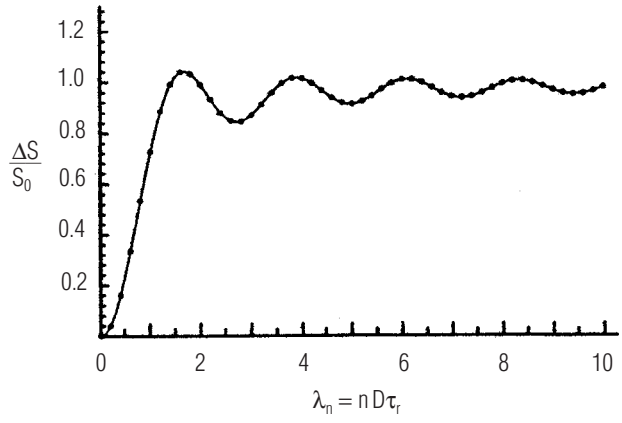

Fig. 7.14 The solid line is a simulation of the REDOR dephasing curve using the Bessel function expansion truncated at $k = 5$. The individual data points (filled dots) are from numerical computations of the integral equation using 1024 × 1024 points in (α, β) space. Adapted from ref. [**123**].

Below we describe one example of REDOR applied to a problem in structural biology: indication of an antiparallel organization of β-sheets in Alzheimer's amyloid $A\beta_{16-22}$ fibrils. Evidence of the β-sheet structure of these fibrils comes from chemical shifts and torsion angle measurements [**124**] which will be described later in this chapter. However, there is a variety of possible supramolecular structures based on β-sheets, for example, either parallel or antiparallel alignment of $A\beta_{16-22}$ molecules in fibrils, as shown in Fig. 7.15.

Other solid-state NMR measurements (such as multiple-quantum experiments on singly-^{13}C–Ala21 labelled $A\beta_{16-22}$) suggest the antiparallel organization of β-sheets in fibrils [**124**]. In order to clarify this issue, REDOR measurements have been performed on two selectively labelled [^{13}C-1-Leu17]–[^{15}N-Ala21]–$A\beta_{16-22}$ and [^{13}C-1-Leu17]–[^{15}N-Phe20]–$A\beta_{16-22}$ samples of lyophilized fibrils. In the case of in-register antiparallel organization of β-sheets in fibrils, hydrogen bonding of Leu17 in one $A\beta_{16-22}$ molecule to Ala21 in the other is expected with a distance of ca. 4.2 Å ($d_{CN} \approx 41$ Hz) between the ^{15}N and ^{13}C labels. This has been proved by REDOR experiments (Fig. 7.16) [**124**]. Distances between ^{13}C-labelled carbonyl carbon of Leu17 and ^{15}N-labelled amide nitrogen of Phe20 in the other sample are expected to be larger, ca. 5.4 Å, which has also been confirmed by the slower build up of the REDOR dephasing curve (see Fig. 7.16). Numerical simulations performed for the two samples took into account a pair of ^{15}N labels from nearby molecules around the ^{13}C-labelled carbon site (whose signal is detected) assuming both an idealized β-sheet geometry and also a slightly distorted one from the idealized case. The latter gave a better agreement with the experimental data, which demonstrates the sensitivity of REDOR data to relatively small changes in molecular geometry. Note, that the build up of REDOR signal shown here corresponds to the region close to $\lambda = 0$ in the universal simulated REDOR dephasing curve shown in Fig. 7.14, since intermolecular heteronuclear ^{15}N–^{13}C dipole–dipole couplings in $A\beta_{16-22}$ fibrils are small.

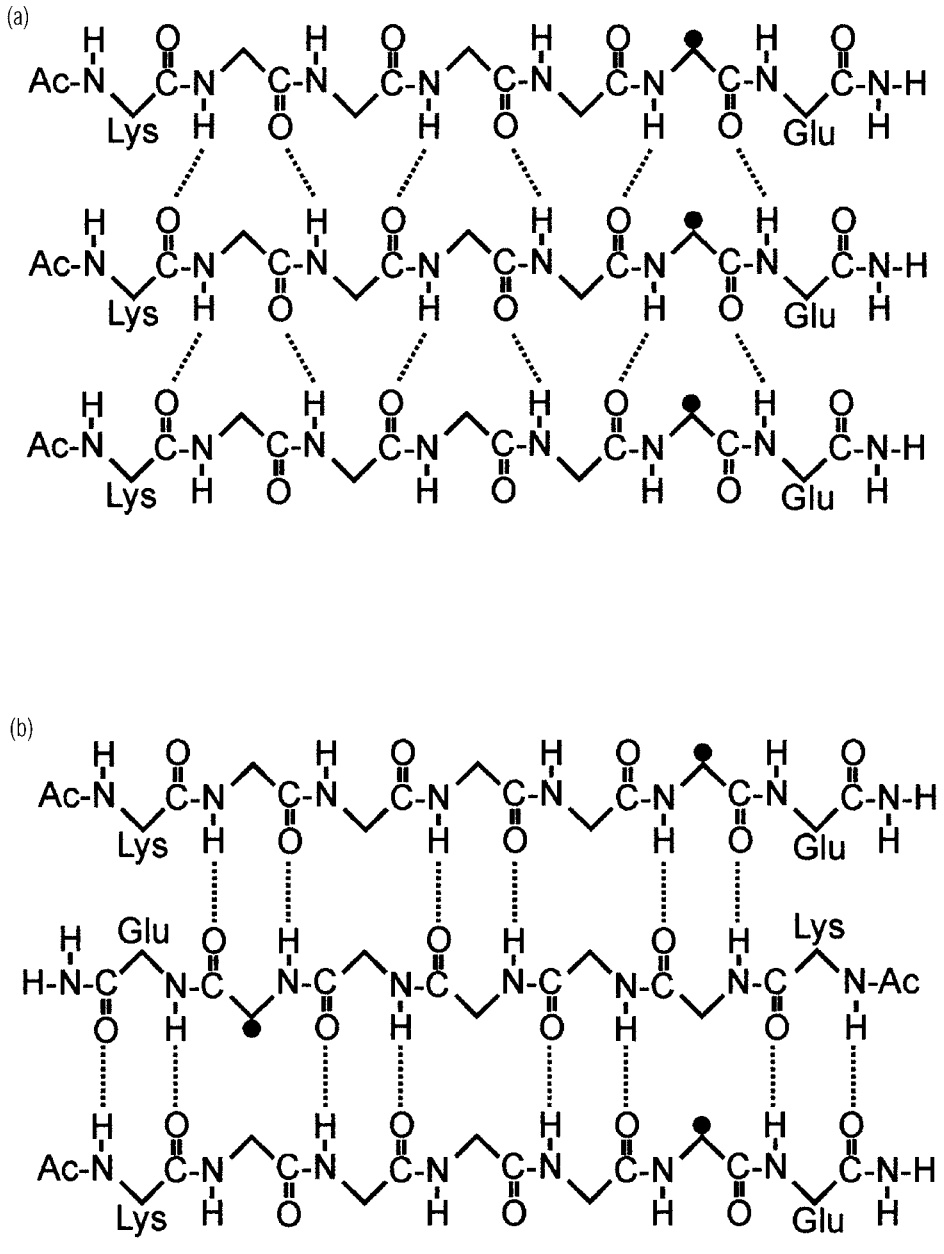

Fig. 7.15 Schematic representations of hypothetical in-register, parallel (a) and in-register, antiparallel (b) β-sheet organizations in Alzheimer's amyloid-β-protein(16–22) fibrils. The peptide sequence is Ac-KLVFFAE-NH_2, i.e. acetylated at the N-terminus and amilated at the C-terminus of the peptide. Dotted lines represent hydrogen bonds. For clarity, black dots indicate the locations of Ala21 methyl carbons.

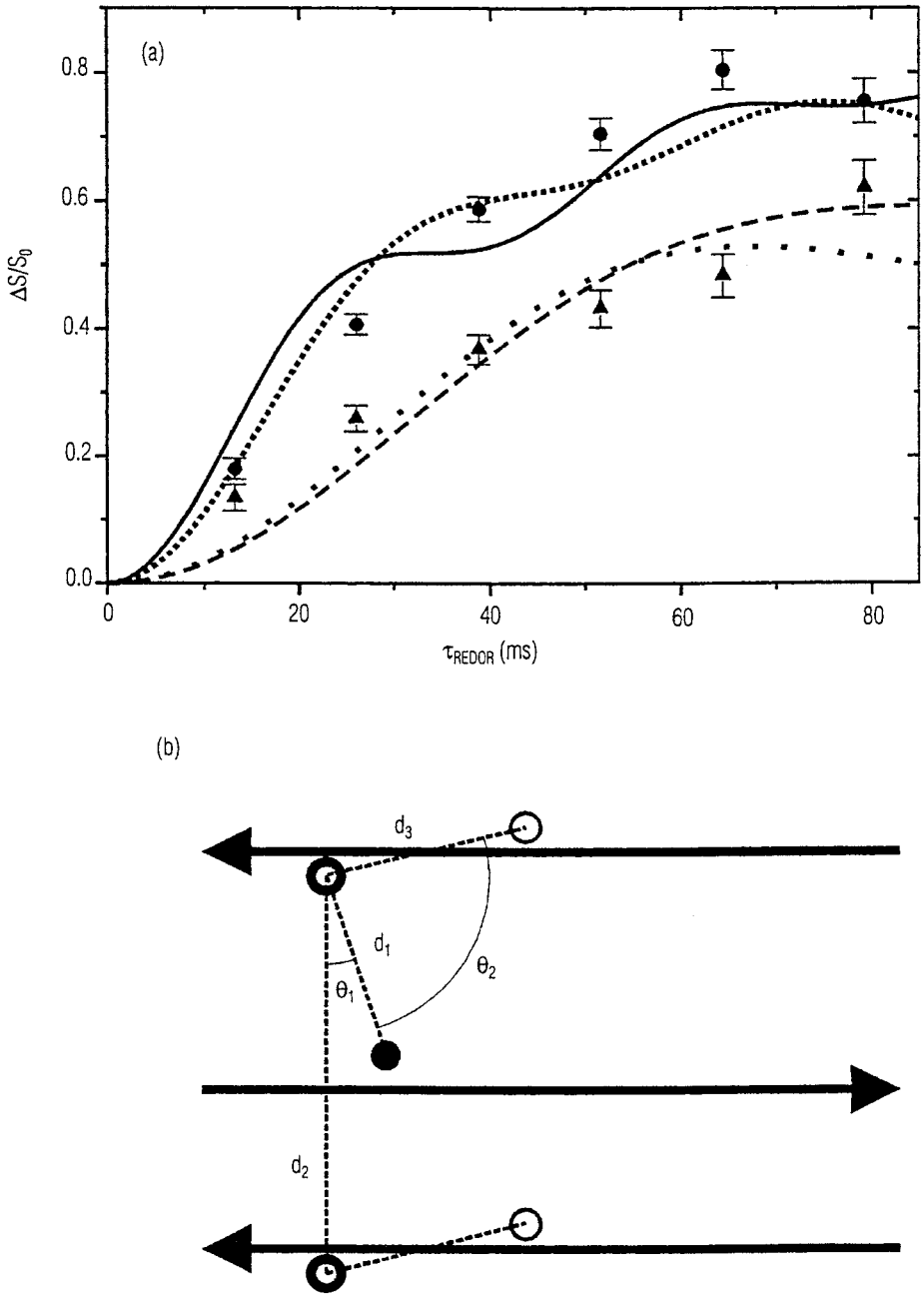

Fig. 7.16 (a) 100.4 MHz ^{13}C-detected $^{13}C/^{15}N$ REDOR measurements on fibrillized Alzheimer's amyloid-β-protein(16–22) samples with ^{13}C labels at the carbonyl carbon of Leu17 and ^{15}N labels at the amide nitrogen of Ala21 (LA sample, black circles) or Phe20 (LF sample, black triangles). The dependence of the normalized REDOR difference signal $\Delta S/S_0$ on the dephasing time τ_{REDOR} is determined by ^{13}C–^{15}N distances and directions. Error bars are determined solely from the rms noise in the experimental spectra. Simulated REDOR curves assume an idealized in-register, antiparallel structure with hydrogen bonding between Leu17 and Ala21 ($d_1 = 4.2$ Å, $d_2 = 9.4$ Å, $d_3 = 3.4$ Å, $\theta_1 = 0°$, $\theta_2 = 90°$ as shown in (b), solid line for the LA sample, dashed line for the LF sample) or a modified geometry that leads to an improved fit to the experimental data ($d_1 = 4.4$ Å, $d_2 = 10.0$ Å, $d_3 = 3.4$ Å, $\theta_1 = 10°$, $\theta_2 = 78°$, closely spaced dotted line for the LA sample, widely spaced dotted line for the LF sample). (b) Antiparallel β-sheet geometry assumed in REDOR simulations. The black circle, thick-walled circles, and thin-walled circles represent a ^{13}C label at the Leu17 carbonyl, ^{15}N labels at the two nearest Ala21 amides, and ^{15}N labels at the two nearest Phe20 amides, respectively.

7.3.2 Homonuclear distance measurements: rotational resonance

In some particular cases, the through-space homonuclear dipole–dipole coupling which is removed by magic-angle spinning, can be reintroduced (and therefore measured) without any specific radio-frequency pulse sequence applied in the detection channel. Assume that one has a sample of isotopically (say, ^{13}C) doubly-labelled biomolecules in which isotropic chemical shift frequencies of the two labelled homonuclear spin sites are ω_{iso}^{k} and ω_{iso}^{j}. If the sample rotation frequency, ω_R, is set to match the condition $\omega_{iso}^{k} - \omega_{iso}^{j} = n\omega_R$, where n is a small integer, the normally narrow spectral lines will broaden or even split into characteristic peakshapes. This broadening is proportional to the dipole–dipole coupling constant, d, and decreases as n increases (Fig. 7.17). The phenomenon is called rotational resonance and its theory is analysed in Chapter 3.

The lineshapes at rotational resonance can be simulated and the homonuclear dipole–dipole constants and hence internuclear distances, can be readily estimated. These are useful measurements in cases where $d > 100$ Hz. For $d < 100$ Hz, the splitting of lines due to the dipole–dipole interaction is small and is usually screened by other effects, such as inhomogeneous broadening. The latter appears due to slight variations of the chemical environment around the observed sites, particularly in biopolymers such as peptides and proteins. However, another experiment, Zeeman magnetization exchange, can be performed at rotational resonance conditions for measuring small dipole–dipole couplings [**31**, **125**]. In this experiment, difference of longitudinal spin magnetizations of the two sites is first prepared by either a weak 180° pulse [**31**] or DANTE sequence [**126**] selectively applied to one of the sites, or by an isotropic rotation sequence [**97**, **127**]. This is allowed to evolve during τ (which is incremented in successive experiments) and finally the signal is observed after the 90° pulse (see Fig. 7.18). The difference of spin magnetizations prepared in this way decays as a function of τ and sometimes acquires oscillations. At rotational resonance, it is the recoupled dipole–dipole interaction which drives Zeeman magnetization exchange. The decay curve can be simulated giving an estimate of d and, therefore, of the interspin distance. Note, however, that for small dipole–dipole couplings and slow spinning, chemical shift tensor parameters (both principal values and orientations) of the two sites as well as the zero-quantum relaxation have to be also included in simulations, which gives uncertainties in distance measurements. For the most frequent double ^{13}C-isotopic labelling scheme in biomolecules, the above-mentioned factors set a limit on measured interspin carbon–carbon distances of 5–6 Å.

We will now discuss an example of the Zeeman magnetization exchange experiment which gives specific conformational information for a small molecule 1,2,3-trimethyl-8-(phenylmethoxy)-imidazo[1,2-a]-pyridinium cation (TMPIP) bound to a large 150-kDa integral membrane protein gastric H^+/K^+-ATPase [**128**].

The nucleotide-driven gastric proton pump maintains the highly acidic milieu of gastric glands and plays an important role in the pathology of peptic ulcer disease

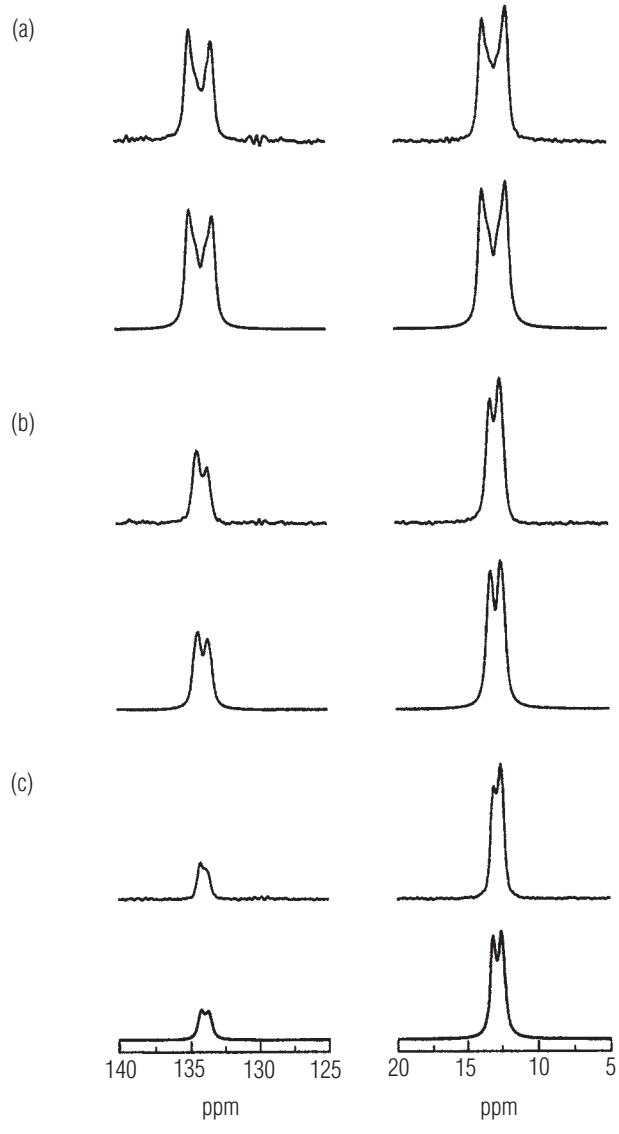

Fig. 7.17 Experimental 50.323 MHz ^{13}C cross-polarization magic-angle-spinning and simulated spectra of 15%-labelled all-*trans*-[11,20-$^{13}C_2$]-retinal. Expanded regions around the isotropic chemical shifts of the C11 (left) and C20 (right) sites at (a) $n = 1$, (b) $n = 2$ and (c) $n = 3$ rotational resonance conditions. For each rotational resonance condition, the upper figures represent experimental spectra (with natural abundance ^{13}C spectra subtracted); the lower figures are simulations. Adapted from ref. [**197**].

[**129**]. TMPIP (Fig. 7.19) is one of its inhibitors and can be considered as a potential drug. The conformation of TMPIP bound to the active site of gastric H^+/K^+-ATPase is a challenge, since it is known that the aromatic group at the 8-position of the imidazopyridine ring is an essential requirement for activity [**130**]. The torsion angle, ϕ_1, can be determined by measuring the distance r_{IS} between the two ^{13}C-labelled carbon sites of TMPIP, C10 and C14 (see Fig. 7.20), using rotational resonance. The other two torsion angles, ϕ_2 and ϕ_3, which describe orientations of the phenyl group relative to the C14 site, cannot be elucidated unambiguously from a single internuclear distance.

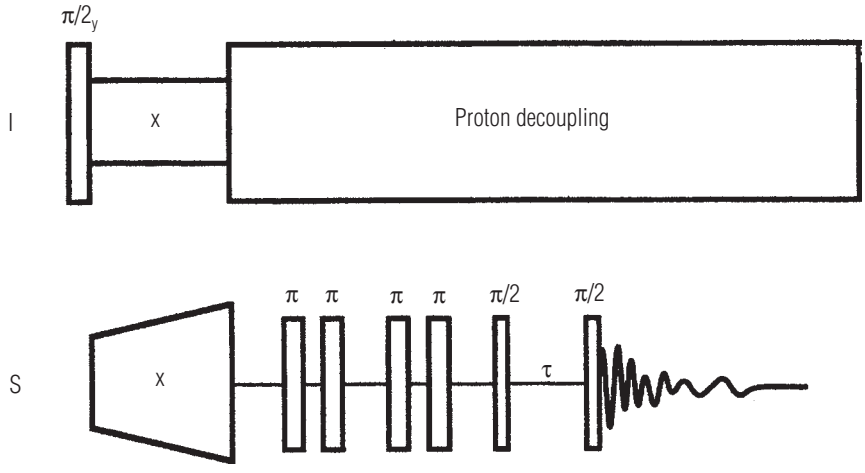

Fig. 7.18 An rf pulse scheme for Zeeman magnetization exchange measurements at rotational resonance. After the ramped cross-polarization pulse applied to *S* spins, an isotropic-rotation sequence of four 180° pulses [**127**] followed by a 90° pulse, prepares a difference of Zeeman magnetizations for a homonuclear spin pair. This is allowed to evolve during the time interval τ and is finally detected after the last 90° pulse. In a simple implementation of the sequence, all phases of 180° pulses are equal to 0°, while those for the two 90° pulses are 90° and 270°, respectively. An extended three-step phase cycle applied to each of the four 180° pulses of the isotropic-rotation sequence (81 steps in total) to remove pulse imperfections can be also implemented. The ramp of the cross-polarization field and switching of the decoupling pulse amplitude are optional. Timings for the 180° pulses of the isotropic-rotation sequence are the solutions of a system of four specific trigonometric equations [**97**]. Adapted from ref. [**197**].

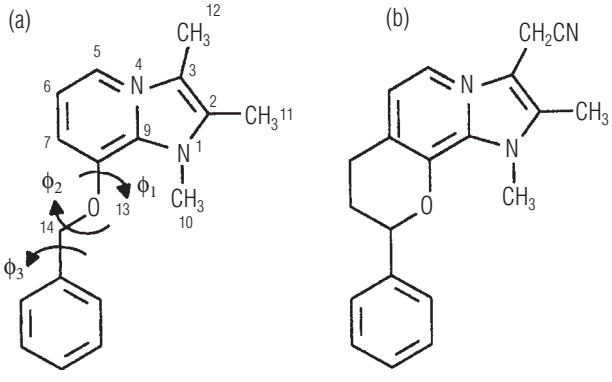

Fig. 7.19 (a) The chemical structure, numbering system and definition of torsion angles, ϕ_1, ϕ_2 and ϕ_3, for the TMPIP (1,2,3-trimethyl-8-(phenylmethoxy)-imidazo[1,2-a]-pyridinium) cation, a potential inhibitor of a protein gastric H^+/K^+-ATPase. (b) Molecular structure of an TMPIP analogue which is chemically restrained in the *syn*-type binding conformation around the C8–O13 chemical bond. Adapted from ref. [**128**].

It is remarkable, that the conformation of TMPIP-$^{13}C_2$ inhibitor bound to H^+/K^+-ATPase has been resolved directly under near-physiological conditions (see Fig. 7.21). The C10–C14 (r_{IS}) distance obtained from simulations of the experimental magnetization exchange curve is 4.3 ± 0.2 Å. This indicates that TMPIP favours a *syn*-type configuration with respect to the torsion angle ϕ_1 when bound to H^+/K^+-ATPase at the high-affinity site. It is worth noting that the inhibitor activity of a similar compound (shown in Fig. 7.19(b)), which is chemically restrained in the *syn*-type binding conformation around the C8–O13 chemical bond, is two orders of

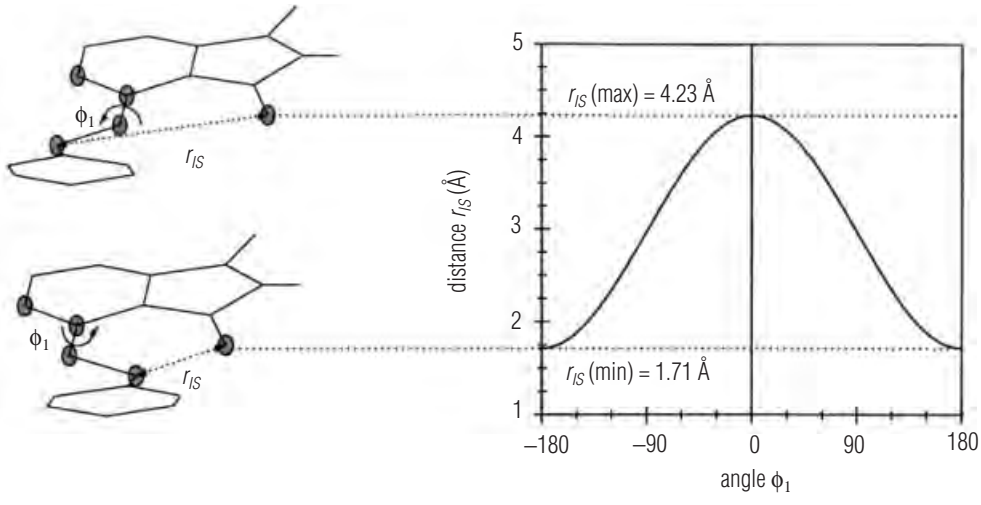

Fig. 7.20 The interrelationship of distance r_{IS}, torsion angle ϕ_1 and molecular conformation of TMPIP. Adapted from ref. [**128**].

magnitude higher than the unrestrained analogues [**128, 130**]. This example provides a rationale for the structure-based design of novel drugs compared with random screening.

Numerous applications of rotational resonance to problems in structural biology involve distance measurements in systems such as retinal in bacteriorhodopsin and rhodopsin [**131–136**], the secondary structure of peptides and phospholipids in biomembranes [**14, 137–142**], a transition state inhibitor of triose phosphate isomerase, phosphoglycolic acid [**143**], amyloid fibrils [**144–146**], a fragment of prion protein [**147**] and others [**148**]. A number of interesting aspects of rotational resonance, such as the dependence of peak shapes on differential transverse relaxation as well as the coherence transfer signals detected in spinning single crystals have been extensively discussed in a number of publications [**32, 149**].

7.3.3 Homonuclear distance measurements: DRAWS, RFDR, (fp)-RFDR

Another approach to recouple homonuclear dipole–dipole interactions is to apply a specific rf pulse sequence to the observed spins. Either double- or zero-quantum coherences, attributes of a coupled spin-$\frac{1}{2}$ pair, are excited by these sequences. A build up or a decay of these multiple-quantum coherences as a function of the excitation time is, generally, a measure of the recoupled dipole–dipole coupling. There are many homonuclear recoupling sequences, two of which, DRAMA [**36**] and C7 [**43, 44**], have been analysed in Chapter 3. In general, the different sequences differ in their robustness to chemical shift anisotropy, rf offset and rf inhomogeneity. These are crucial issues for biological samples where there is only a limited amount of

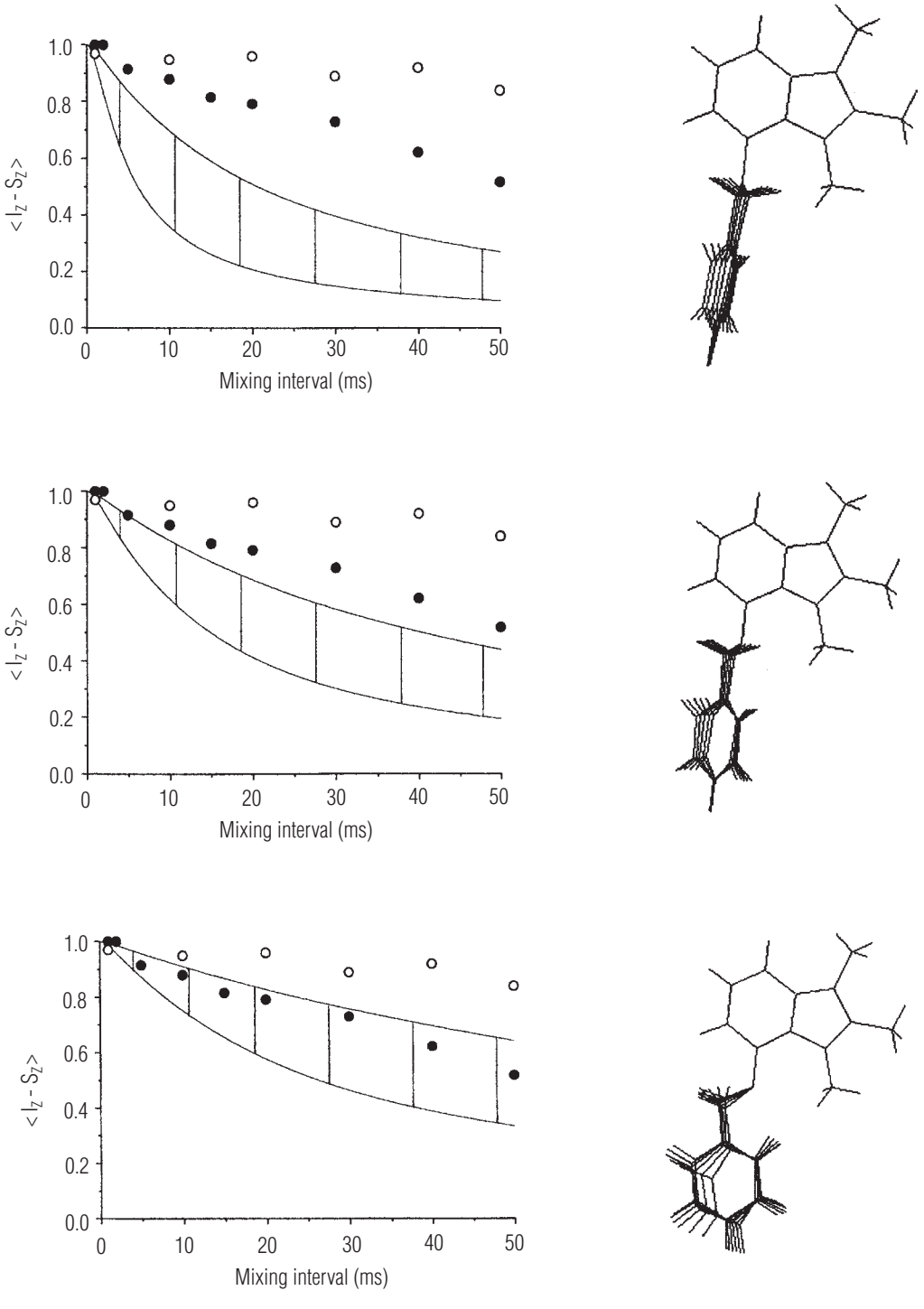

Fig. 7.21 Experimental measurements of magnetization exchange for the proton pump-TMPIP complex at $n = 1$ rotational resonance (sample spinning frequency $\nu_R = 3013$ Hz) between ^{13}C-labelled C10 and C14 carbon sites of TMPIP (black circles) and off-rotational resonance ($\nu_R = 2500$ Hz) (white circles). Simulations of magnetization exchange curves are shown for three interatomic distances as well as tensor orientations. Curves correspond to distance ranges of 3.0–3.4 Å (top graph), 3.5–3.8 Å (middle graph) and 3.9–4.3 Å (bottom graph), where the upper curve corresponds to the longer distance in each case. Molecular conformations of TMPIP corresponding to each distance range are shown alongside each graph. The conformational space traversed by ϕ_1 reflects the r_{IS} ranges bounded by each pair of curves, whereas ϕ_2 and ϕ_3 were obtained by minimum energy calculations. Adapted from ref. [**128**].

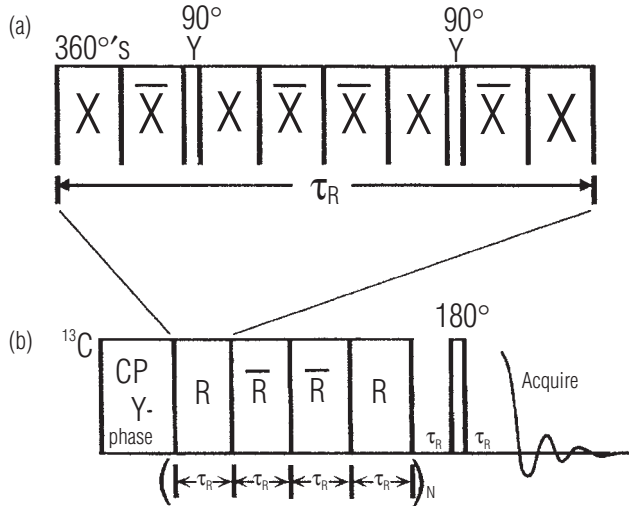

Fig. 7.22 DRAWS pulse sequence: (a) The basic rf sequence for one rotor period; 0°, 180° phase alternating 360° pulses are applied between 90° pulses of phase 90°; (b) the four-rotor supercycle added to compensate for residual offset terms, where R corresponds to the sequence in (a), while $\bar{R}$ represents the same sequence with the phases inverted. A ^{13}C 180° pulse is centered one rotor period after the conclusion of the DRAWS pulse sequence and a Hahn echo is detected one rotor period later. The time span of the $(R\bar{R}\bar{R}R)_N$ DRAWS block corresponds to the mixing time of DRAWS dephasing curves given in Fig. 7.23. Adapted from ref. [**153**].

material. For example, carbonyl carbons in peptides and proteins have a relatively large chemical shift anisotropy (Δ_{cs} ~ 70–80 ppm). If one is interested in measuring a distance between two ^{13}C-labelled carbonyl sites in contiguous amino acid residues in order to obtain an estimate of the peptide torsion angle ϕ, rotational resonance is not suitable because of a very small difference in isotropic chemical shifts of the two sites. DRAMA is also not a good choice for these measurements because this sequence works well only for sites with relatively small chemical shift anisotropy. To improve the performance of DRAMA, chemical shift anisotropy can be refocused by either additional 180° pulses (XY8-DRAMA [**150**]) or by a continuous rf irradiation sequence (MELODRAMA [**38**], DRAWS (Dipolar Recoupling with A Windowless Sequence) [**39**, **151**, **152**]. DRAWS (see Fig. 7.22) has been proved to recouple spin-$\frac{1}{2}$ nuclei over a very broad spectral range and efficiently suppress chemical shift anisotropy and offset effects at moderate rf powers. In addition, DRAWS does not appear to be particularly sensitive to rf inhomogeneity. Also, dipolar recoupling via DRAWS is almost independent of the mutual orientation of the chemical shift tensors of the dipolar-coupled spin pair.

Internuclear ^{13}C–^{13}C distances of up to 6.0 Å can be extracted from experimental data by simulating the evolution of transverse magnetization during DRAWS irradiation. Figure 7.23(a) shows an illustrative example of the DRAWS experiment performed on samples of the truncated Alzheimer's amyloid-β-protein, $A\beta_{10-35}$, one of which was unlabelled (the control sample) while the other two were isotopically ^{13}C labelled at the carbonyl carbons of amino acid residues Val18 and Phe19 [**153**]. One of the labelled samples was prepared as an ether precipitate from trifluoric acid after the peptide had been cleaved from the resin at the final step in the solid phase peptide synthesis. The other labelled sample was fibrillized from aqueous solution at 0.2 mM, pH 5.6, room temperature for 3 days. Simulations of the data clearly

represent different distances: 3.0 ± 0.1 Å for the ether precipitate and 3.5 ± 0.1 Å for the fibrils. The DRAWS curve for the unlabelled fibrillized sample shows a simple exponential decay with a relaxation parameter of the double-quantum coherence, $R_2 = 58\,s^{-1}$. The same value for this relaxation parameter was used in simulations of DRAWS curves obtained for labelled samples. These measurements clearly show a transition from an α-helix to a β-strand secondary structure of the $A\beta_{10-35}$ in the course of fibrillization, since for an α-helix structure, carbonyl–carbonyl distances are in the range 2.9–3.1 Å, while those for a β-strand conformation are in the range 3.3–3.5 Å. This conclusion is also consistent with chemical shifts of the carbonyl carbons in these samples as was discussed previously in this chapter: 175 ppm for the ether precipitate (α-helix) and 170 ppm for fibrils (β-sheet) (see Fig. 7.23(b)). DRAWS has been also used to measure intermolecular carbon–carbon distances in amyloid fibrils prepared from singly ^{13}C-labelled $A\beta_{10-35}$ molecules at different carbonyl positions. These measurements suggest a parallel β-sheet organization of

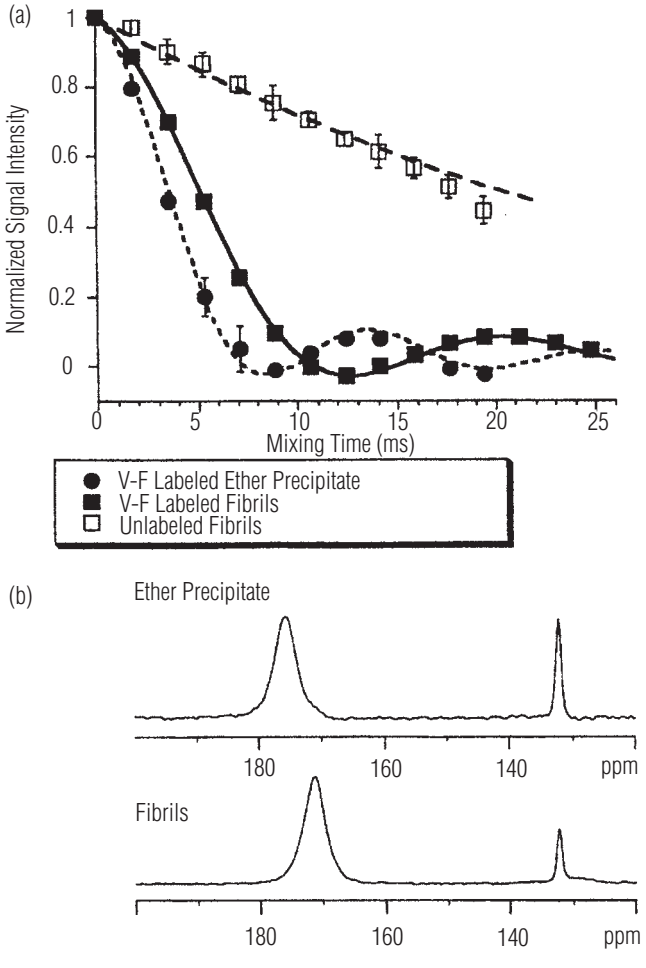

Fig. 7.23 (a) DRAWS data from specifically doubly ^{13}C-labelled Alzheimer's amyloid-β-protein(10–35) samples. Symbols indicate experimental data from [Val18-1-^{13}C]–[Phe19-1-^{13}C]–amyloid-β-protein(10–35) from an ether precipitate (circles), [Val18-1-^{13}C]–[Phe19-1-^{13}C]–amyloid-β-protein(10–35) fibrillized at pH 5.6 (filled squares), and ^{13}C carbonyl signals from unlabelled amyloid-β-protein(10–35) (open squares). Lines result from simulated data using a 3.0 Å distance (short dashes), 3.5 Å distance (solid line), and no dipolar coupling (long dashes). In all simulations a relaxation parameter of $R_2 = 58\,s^{-1}$ was included. (b) Carbonyl region of 50.3 MHz ^{13}C cross-polarization magic-angle spinning NMR spectra for both ether precipitate and fibrillized [Val18-1-^{13}C]–[Phe19-1-^{13}C]–amyloid-β-protein(10–35) samples. The shift of the ^{13}C carbonyl line from 175 ppm for the ether precipitate to 170 ppm for fibrils is consistent with a transition from an α-helix to a β-strand structure. Adapted from ref. [**153**].

$A\beta_{10-35}$ molecules with residues in exact register [**153–155**], in contradiction with the commonly accepted paradigm of the antiparallel cross-β structure of Alzheimer's amyloid fibrils [**153–155**].

One of the drawbacks of DRAWS is the need to include effects from the double-quantum relaxation (T_2^{DQ}) in calculations of DRAWS curves. Although T_2^{DQ} can be measured in a separate experiment (the so-called double-quantum (DQ) DRAWS [**153**] experiment), it is better to avoid this additional parameter in simulations of experimental data. It is also difficult to measure dipolar evolution curves without damping or distortion from effects that cannot be simulated accurately, such as residual effects due to chemical shift anisotropy, especially in high fields, significant rf inhomogeneity and residual couplings to protons. All these factors become increasingly important as the internuclear distances become larger and, so, the dipolar evolution periods become longer.

Tycko and co-workers have suggested an approach, called Constant-Time Double-Quantum-Filtered Dipolar (CTDQFD) dephasing [**91**], which avoids the above-mentioned drawbacks of DRAWS. The CTDQFD scheme (Fig. 7.24) is based on the 'rf-driven recoupling' (RFDR) sequence [**33**, **34**] which generates a non-zero average dipole–dipole coupling under magic-angle spinning by a train of rotor-synchronized 180° pulses, one per rotor period. RFDR is effective when chemical shift anisotropies of the two sites are large and their chemical shift tensors have different relative orientations. RFDR blocks are incorporated into a double-quantum

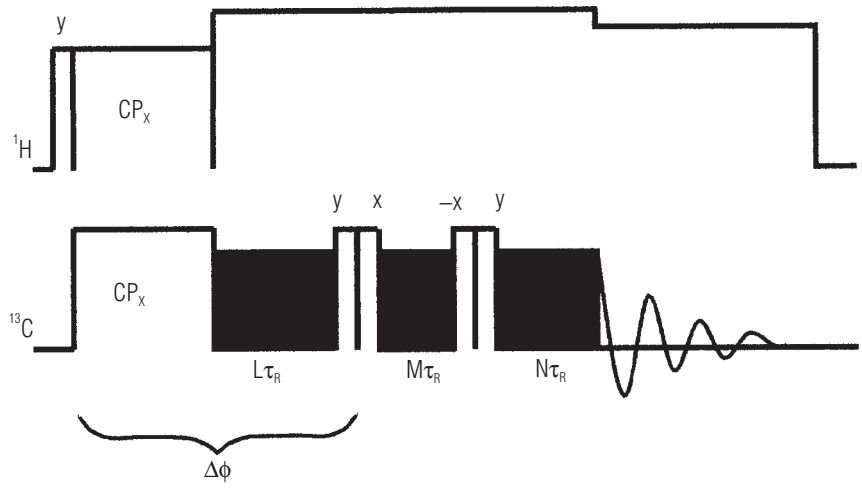

Fig. 7.24 Rf pulse sequence for constant-time double-quantum-filtered dipolar recoupling (CTDQFD) measurements. CP represents Hartmann–Hahn cross-polarization. *x*, *y* and *–x* indicate the phases of 90° pulses. Rf-driven recoupling (RFDR) sequences are applied in the three intervals in black. The double-quantum preparation time is $L\tau_R$. The effective dipolar evolution time is $(M - N)\tau_R$. Double-quantum filtering is accomplished by acquiring signals with overall rf phase shifts $\Delta\phi$ of 0°, 90°, 180° and 270° and alternately adding and subtracting the signals. Adapted from ref. [**124**].

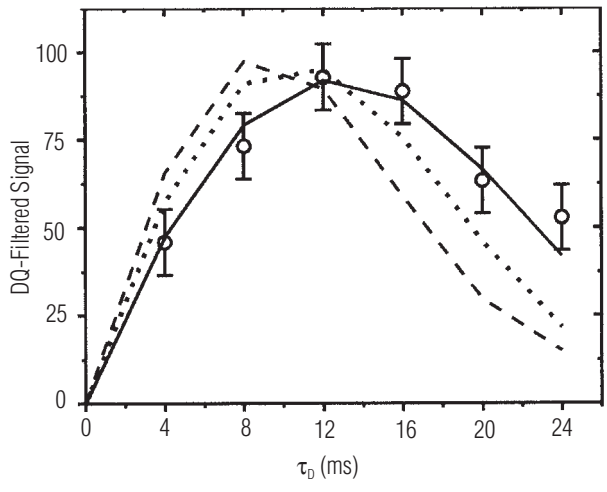

Fig. 7.25 Double-quantum-filtered signal amplitudes (open circles, arbitrary units) for a fibrillized Alzheimer's amyloid-β-protein(16–22) sample in which 20% of the peptide molecules have ^{13}C labels at carbonyl sites of Val18 and Phe19, obtained at 100.4 MHz for ^{13}C under magic angle spinning (ν_R = 4.0 kHz) using the CTDQFD experiment. CTDQFD data were obtained at a double-quantum preparation time $L\tau_R$ of 8 ms, and values of the effective dipolar evolution time $\tau_D = (M - N)\tau_R$ as indicated. Experimental data are compared with simulated CTDQFD curves assuming ϕ and ψ values for Phe19 of –130° and 120° (solid line), –50° and –110° (dotted line), and –60° and –40° (dashed line), respectively. These ϕ and ψ values correspond roughly to the global and local minima in χ^2 in Fig. 7.26(a) and to typical α-helical values and are chosen to illustrate the sensitivity of CTDQFD curves to peptide conformation. Error bars indicate the rms noise in the experimental spectra. Simulated signal amplitudes are scaled for optimal agreement with experimental data. Adapted from ref. [**124**].

filtering sequence [**90**] (discussed in Chapter 3) which is extended to satisfy the *constant-time* condition to:

$$CP_{90+\xi} - (RFDR)_L - 90\hat{\xi} - 90_0 - (RFDR)_M - 90_{180} - 90_{90} - (RFDR)_N - FII$$

Here, CP represents cross-polarization from protons to insensitive nuclei, 90_ξ is a 90° pulse with rf phase ξ, $(RFDR)_L$ represents an RFDR train lasting L rotor periods, FID is the detection period. The double-quantum filtering is achieved by recording FIDs with ξ = 0°, 90°, 180° and 270° which are co-added after multiplication by the factor $\exp(2i\xi)$ (see Chapter 3). The second pair of 90° pulses in the CTDQFD sequence refocuses the dipolar evolution for a pair of coupled spin-$\frac{1}{2}$ nuclei which makes the block $(RFDR)_M$–90_{180}–90_{90}–$(RFDR)_N$ to be ideally equal to $(RFDR)_{M-N}$. This allows the total recoupling period $T = (L + M + N)\tau_R$ to be kept constant throughout an experiment while incrementing the effective dipolar evolution periods by varying L, M and N. Figure 7.25 shows CTDQFD data for the doubly ^{13}C-labelled amyloid [Val18-1-^{13}C,Phe19-1-^{13}C]–$A\beta_{16-22}$ fibrils with a double-quantum preparation time $L\tau_R$ of 8 ms, and the indicated values of the effective dipolar evolution time $\tau_D = (M - N)\tau_R$ which is reached by incrementing M from $M_{max}/2$ to M_{max}, and setting $N = M_{max} - M$. A CTDQFD curve has a shape which is characteristic for a particular secondary structure of the labelled peptide fragment. The build up of the curve is slower for a β-sheet conformation because of a larger carbonyl–carbonyl distance (ca. 3.5 Å) compared with an α-helix conforma-

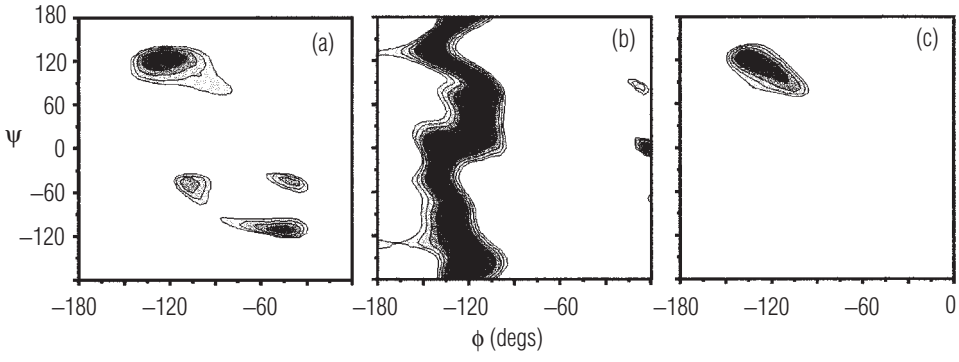

Fig. 7.26 Quantitative analysis of two-dimensional magic-angle-spinning exchange and CTDQFD data (depicted in Figs. 7.29 and 7.25, respectively) for a fibrillized Alzheimer's amyloid-β-protein(16–22) sample in which 20% of the peptide molecules have ^{13}C labels at carbonyl sites of Val18 and Phe19. Contour plots represent the χ^2 deviation between numerical simulations and experimental data as a function of the ϕ and ψ angles of Phe19 assumed in the simulations. χ^2-plots for (a) two-dimensional magic-angle spinning exchange data alone, (b) CTDQFD data alone, (c) the combined data sets. The minimum χ^2 value in (c) occurs with ϕ and ψ values of −130° and 115°, respectively, indicating a β-strand conformation for amyloid-β-protein(16–22) at the central Phe19 residue in the amyloid fibrils. Lowest contour levels (darkest region) are at $\chi^2 = 9$, 2 and 12 in panels (a)–(c), respectively. Higher contours represent increments of 1 unit in panels (a) and (b) and 2 units in panel (c). Adapted from ref. [**124**].

tion (ca. 3.0 Å). It is important to note that CTDQFD curves also depend on the relative orientation of the chemical shift tensors for the two labelled sites. However, this is not an obstacle, since orientations of the chemical shift tensor principal axes of carbonyl carbons are known (at least approximately). Therefore, CTDQFD data can be analysed in terms of the peptide backbone torsion angles, ϕ and ψ (see Fig. 7.26(b)). In most biological applications, it is these angles and not distances which are of importance in structural studies.

Concluding the discussion on distance measurements between homonuclear spins under magic-angle spinning, we would like to mention a pulse sequence which recouples the dipole–dipole interactions even at very fast spinning (up to 30 kHz). Fast spinning is particularly attractive for two-dimensional correlation spectroscopy under magic-angle spinning, since then most anisotropic interactions are removed or strongly suppressed and one approaches the resolution of solution-state NMR. The sequence resembles RFDR in its appearance, but the dipolar recoupling proceeds during the finite 180° pulse which occupies a considerable fraction of the rotor period (up to 0.3) under very fast magic-angle spinning. Therefore, the sequence is called finite-pulse RFDR ((fp)-RFDR) [**35**]. If one uses an ideal infinitely short (δ-functional) 180° pulse, as has been assumed in the theoretical analysis of the original RFDR sequence [**33**], the recoupling efficiency will gradually approach zero with the increase of spinning frequency. The constant-time (CT) version of the (fp)-RFDR experiment for measuring distances between homonuclear spins is shown in Fig. 7.27(a) and the dephasing curve obtained with the CT–(fp)-RFDR sequence for a model sample of 4% diluted doubly labelled [Ala-1-^{13}C]–[Gly-1-^{13}C]–Gly powder is shown in Fig. 7.28. The best fit simulated dephasing curve gives the distance between the labelled carbonyl sites as 3.27 ± 0.05 Å in accord with single crystal X-

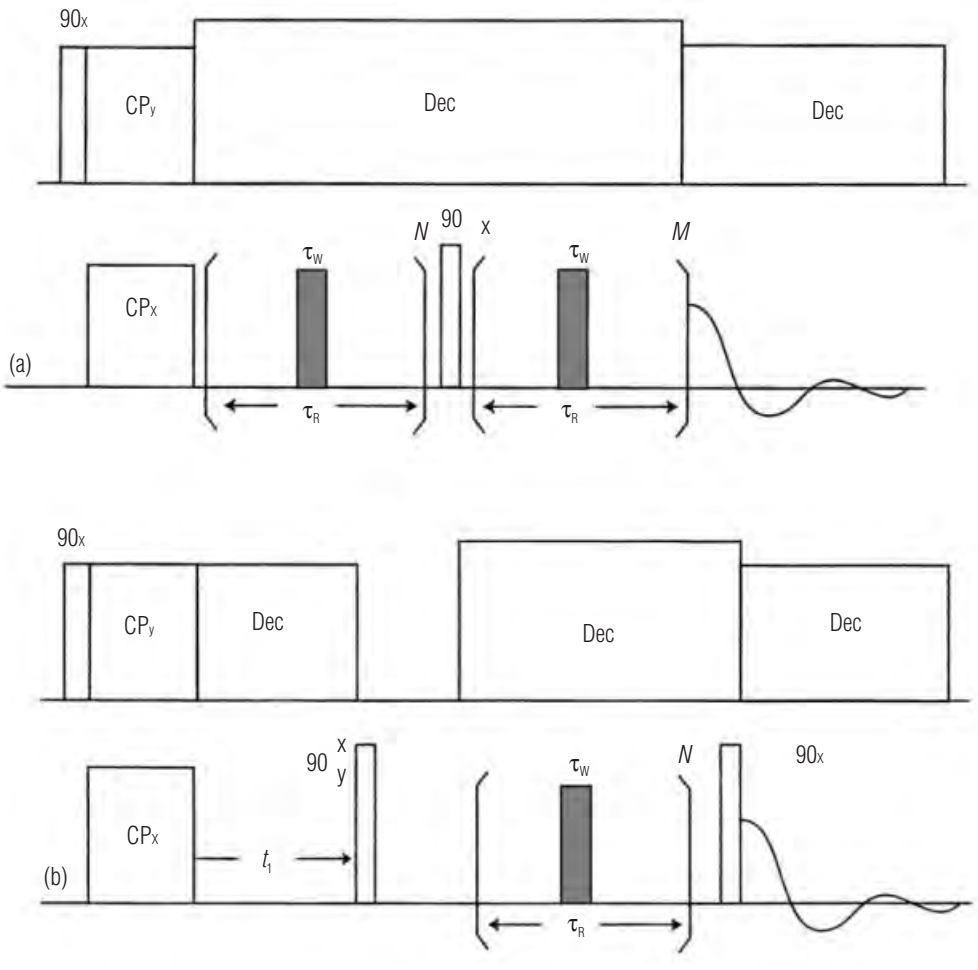

Fig. 7.27 Pulse sequences for (a) constant-time finite-pulse (fp)-RFDR, and (b) two-dimensional $^{13}C/^{13}C$ chemical shift correlation NMR experiments using (fp)-RFDR. In (a) and (b), the top pulse sequence in each case is applied to ^{1}H and the lower one to ^{13}C. In both experiments, ^{13}C transverse magnetization is prepared by Hartmann–Hahn cross-polarization (CP). Time evolution of the spins during the finite pulse width of RFDR 180° pulses (τ_W) applied at the same point in every rotor cycle, τ_R, restores ^{13}C–^{13}C dipole–dipole couplings. In (a), a $90°_x$ pulse is sandwiched by (fp)-RFDR sequences of N and M 180° pulses with the XY-8 phase cycle. N and M must be the number of multiples of the phase cycle. The 90° pulse partly refocuses the dipolar evolution so that the effective dipolar evolution time, τ_m, is proportional to $(N - M)\tau_R$. Therefore, the evolution time dependence of the dipolar dephasing is measured by varying of $N - M$ for a fixed $N + M$ which eliminates the effects of transverse relaxation. In (b), after t_1 evolution due to ^{13}C isotropic chemical shifts, the real or imaginary component is stored along the laboratory z axis while the other component, left in the transverse plane, is dephased during a short period without ^{1}H decoupling. After the mixing block in which ^{13}C–^{13}C dipole–dipole couplings are restored by the (fp)-RFDR sequence, a detection 90° pulse is applied and FID is detected (t_2 period). Adapted from ref. [**2**].

ray diffraction data. (fp)-RFDR can be also implemented as a mixing block in two-dimensional correlation spectroscopy (see Fig. 7.27(b)). A demonstration of the latter on amyloid fibrils of $A\beta_{16–22}$ in which hydrophobic residues from Leu17 through Ala21 are uniformly ^{13}C, ^{15}N-labelled in 10% of the molecules is presented in Fig. 7.29. It is possible to follow one bond carbon–carbon connectivities and

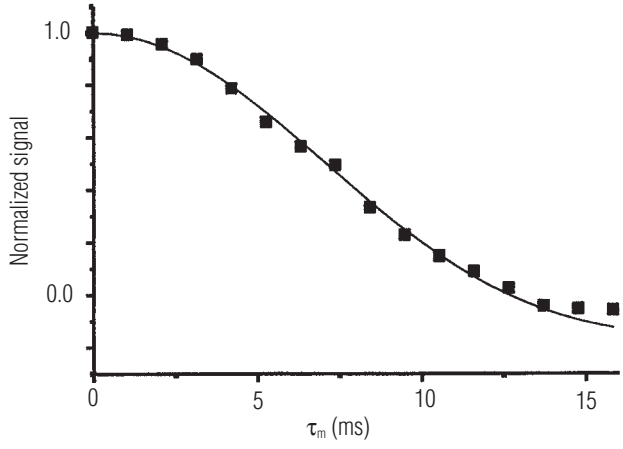

Fig. 7.28 Experimental dephasing curve (filled squares) obtained with the constant time (fp)-RFDR sequence for 4% [Ala-1-^{13}C]–[Gly-1-^{13}C]–Gly in unlabelled Ala–Gly–Gly, together with the best fit simulated dephasing curve (solid line) for an internuclear distance of 3.27 Å. 188.6 MHz ^{13}C CT–(fp)-RFDR spectra were obtained at a magic-angle spinning rate of 30.3 kHz (τ_R = 33.0 μs) with 90° and 180° pulse lengths of 5 and 10 μs, respectively. The total number of CT–(fp)-RFDR cycles, $N + M$, was fixed to 512 while $N - M$ was changed from 0 to 480 so that the effective dipolar evolution time was varied from 0 to 15.8 ms. The experimental dephasing curve is obtained from the average of ^{13}C carbonyl signals from Ala-1 and Gly-2 after subtracting the signals from natural abundance ^{13}C spins. The ^{1}H decoupling field during the detection period is 7 kHz, and no decoupling was applied during the (fp)-RFDR period, since weak ^{1}H–^{13}C dipole–dipole couplings between carbonyl ^{13}C and neighbouring ^{1}H spins are effectively removed by fast magic-angle spinning. Adapted from ref. [**2**].

eventually to assign all NMR lines in a similar manner to the solution-state two-dimensional COSY experiment. As we discussed at the beginning of this chapter, chemical shifts of both C_α and C_β as well as carbonyl carbons can be used in drawing conclusions concerning the secondary structure of peptides and proteins in a ^{13}C-labelled fragment of these molecules.

7.4 Torsion angle measurements

Internuclear distances can be measured using a range of techniques described in Sections 3.2, 3.3 and 7.3. Such measurements are generally most useful for defining rather large-scale structural details, such as the secondary structure of a protein or the docking of a large protein molecule with a small drug molecule. It is possible to use internuclear distances measurements to distinguish between two possible conformations in some cases. A good example of this is the retinal molecule in the protein bacteriorhodopsin; the 6-*cis*- or 6-*trans*-conformations of the retinal can be distinguished by distance measurements between the C-8 and the methyl C-18 carbon sites [**131**]. However, it is often difficult to determine individual structural parameters, such as the torsion angle about a particular bond, on the basis of internuclear distance measurements. The other problem is that it is often problematic to find an isotope labelling scheme which gives spin pairs for which the corresponding internuclear distance is sufficiently sensitive to the interesting angle.

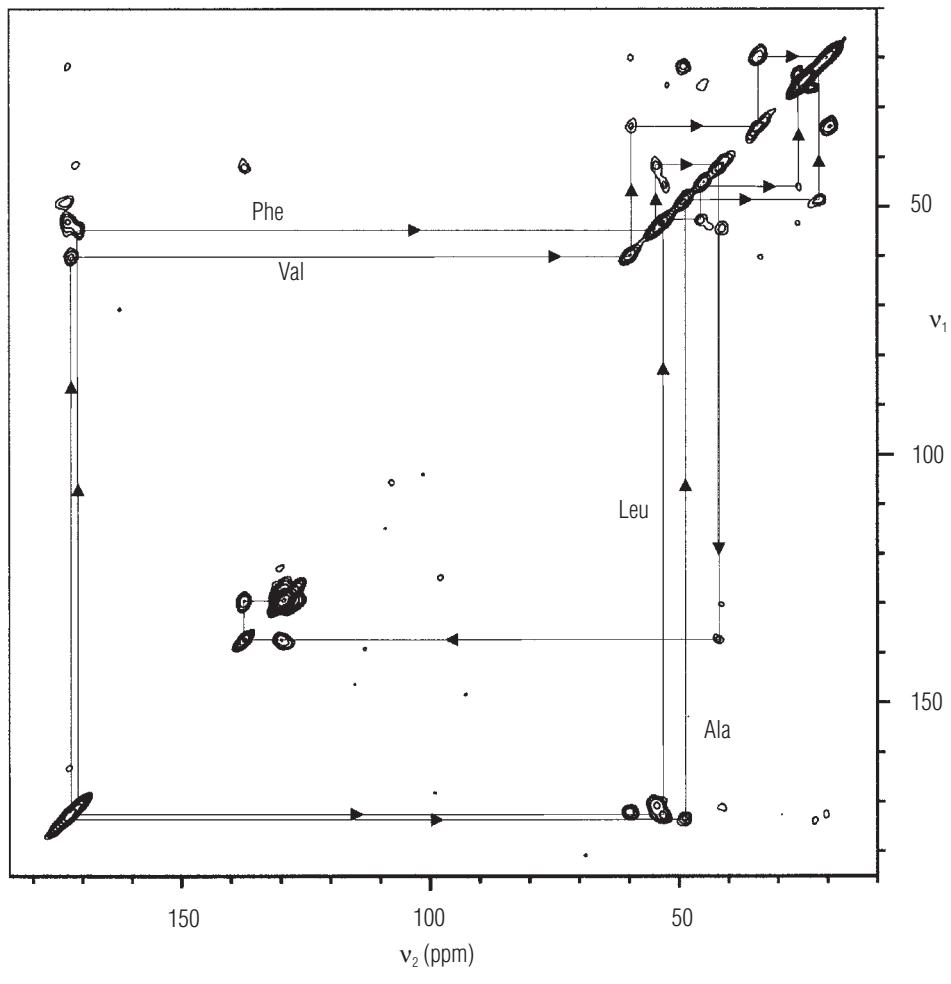

Fig. 7.29 Two-dimensional ^{13}C–^{13}C chemical shift correlation spectrum of a fibrillized Alzheimer's amyloid-β-protein(16–22) sample in which the hydrophobic segment from Leu17 through Ala21 is uniformly ^{13}C- and ^{15}N-labelled in 10% of the molecules. The remaining 90% are unlabelled. The spectrum was acquired at a magic-angle spinning rate of 24 kHz using the two-dimensional exchange pulse sequence described in Fig. 7.27(b). The (fp)-RFDR exchange period was equal to 2.6 ms for selective observation of crosspeaks between directly bonded carbon sites. The two-dimensional assignments of carbonyl, C_α, C_β, C_γ, and C_δ signals for Leu17, Val18, Phe19, Phe20, and Ala21 in amyloid-β-protein(16–22) are indicated by the arrows. Signals from the two phenylalanines are not resolved from one another. Adapted from ref. [**124**].

A different approach is the *direct* measurement of a molecular torsion angle. In solution state, for molecules undergoing fast isotropic motion, torsion angles can be determined from three-bond scalar couplings using the empirical Karplus equations [**156, 157**]. In solids, in which anisotropic spin interactions are not averaged by motion, torsion angles can be extracted by correlating the relative orientations of two interaction tensors, either two chemical shift tensors [**55–57, 59–61, 93, 158–160**] or a chemical shift tensor and a dipole–dipole coupling tensor [**53, 54,**

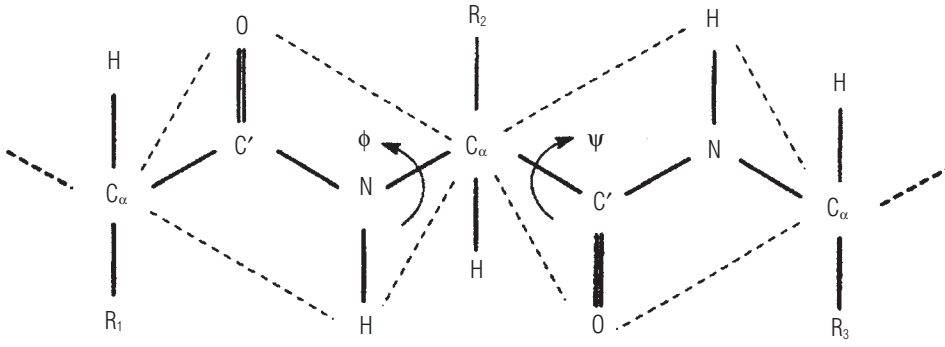

Fig. 7.30 Part of a polypeptide chain where the main chain atoms are represented as rigid peptide units, linked by the C_α carbons. Each unit has two degrees of freedom defined by respective angles ϕ and ψ. Adapted from ref. [**197**].

93, 161, 162], or two dipole–dipole coupling tensors [**49–52, 163, 164**]. These methods have been implemented both in static solids and under magic-angle spinning. For these tensorial interactions to be of use, we must know the orientation of their principal axis frames with respect to some molecular (fragment) frame of reference. The dipolar tensor principal axis frame z axis is always oriented along the internuclear axis between the coupled spins, while the chemical shift tensor orientation and principal values for a particular chemical site (often carbonyl) in the molecular frame is often known (or can be measured) in many systems. The idea of correlating spatially anisotropic spin interactions to extract structural information is not new [**165–168**]. It is the new experimental implementations which have made these methods powerful tools in structural studies of biomolecules.

Figure 7.30 shows the motivation behind these correlation experiments. A peptide fragment illustrates how different tensorial interactions relate to the peptide torsion angles ϕ and ψ. The peptide bond–CO–NH– is rigid and nearly planar because of the sp^2-hybridization of both the carbonyl carbon and the amide nitrogen. Therefore, the only degrees of freedom are rotations around covalent bonds at the C_α atoms bonded to the carbonyl carbon and amide nitrogen. The angle of rotation around the N–C_α bond is defined by convention as ϕ, the torsion angle in the C'_1–N–C_α–C'_2 fragment. It is defined as positive if when viewed along the N–C_α bond, the C'_1 atom must be rotated clockwise to eclipse atom C'_2. The angle of rotation around the C_α–C'_2 bond from the same C_α atom is denoted ψ, i.e. the torsion angle around the N–C_α–C'_2–N fragment. In this way, each peptide unit is associated with two conformational angles ϕ and ψ, and the conformation of the whole main chain of a peptide is completely determined by a set of ϕ and ψ angles for all peptide residues. Moreover, for various secondary structures such as α-helix, 3_{10}-helix, β-sheet, etc., ϕ and ψ angles for amino acid residues adopting these secondary structures, usually fall in a particular region on a ϕ versus ψ plot (the Ramachandran plot [**169**]). For example, in right-handed α-helices (usually the case for L-amino

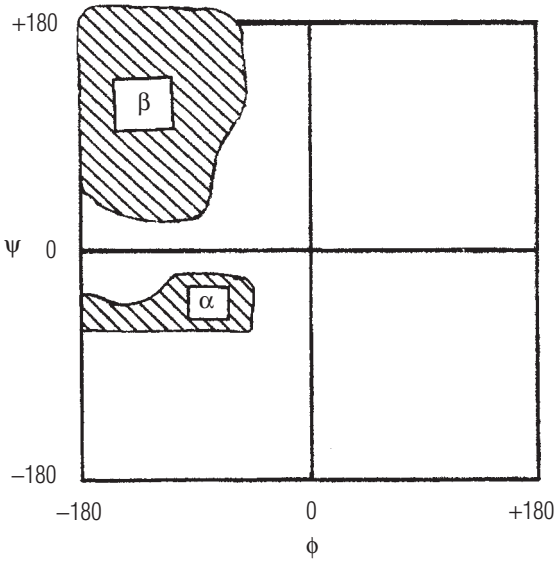

Fig. 7.31 Ramachandran plot showing sterically allowed combinations of angles ϕ and ψ for α-helical and β-sheet secondary structures in proteins. Adapted from ref. [**197**].

acids) consecutive amino acid residues all have ϕ and ψ angles approximately equal to $-60°$ and $-50°$, respectively, while in a β-sheet structure these angles are spread around $\phi = -130°$ and $\psi = +120°$ (Fig. 7.31).

Correlating two tensorial interactions to measure ϕ and ψ torsion angles in solid-state NMR experiments can be done using spin diffusion between the two spins with the tensorial interactions of interest, or by generation of double- or triple-quantum coherence between the spins with the tensorial interactions of interest. We will discuss and compare the three strategies mentioned above, chemical shift–chemical shift, dipolar–chemical shift and dipolar–dipolar tensor correlations, together with a few representative examples of useful applications for some of these methods in biologically relevant systems.

7.4.1 Chemical shift–chemical shift tensor correlation experiments

As already discussed at the beginning of this chapter, the orientation of the principal axis frame of the chemical shift tensor for carbonyl carbons in peptide chains is fairly well conserved with respect to the molecular >C═O fragment. This property allows us to design a number of solid-state NMR experiments in which anisotropic chemical shifts of two ^{13}C-labelled carbonyl carbons are correlated in a two-dimensional NMR experiment, so that the resulting two-dimensional spectrum contains information about the relative orientation of the two chemical shift tensors.

The idea was first realized on static solids by Edzes and Bernards [**59**] and Henrichs and Linder [**60**] and further developed by Tycko et al. [**61**, **93**]. The two-dimensional experiment of this type prepares nuclear spin magnetization on a

molecular fragment M_1, measures its NMR frequency f_1 during t_1, transfers the magnetization to the nearby molecular fragment M_2 by spin diffusion during τ, and measures its NMR frequency f_2 during t_2. If M_2 has the same orientation as M_1, then $f_1 = f_2$ and the two-dimensional exchange spectrum has intensity only along the diagonal. Otherwise, the spectrum has off-diagonal intensity in a pattern that is determined by the relative orientations of the molecular fragments. The orientational correlations specify the conformation of the molecule.

In the static two-dimensional chemical shift–chemical shift tensor exchange spectroscopy applied to systems which are ^{13}C-labelled at two sites, the NMR frequencies are determined by anisotropic chemical shift interactions in both dimensions. The experimental implementation is rather simple and can be expressed by the following sequence of pulses applied to the ^{13}C spins:

$$\mathrm{CP} - t_1 - 90^\circ_{x,-y} - \tau(\text{no decoupling}) - 90^\circ_x - \tau' - 180^\circ_x - \tau' - \mathrm{FID}$$

Spin-diffusion between the two ^{13}C-labelled sites occurs during the period τ. It is driven by ^{13}C–^{13}C dipole–dipole interaction and is also assisted by the ^{1}H–^{13}C and ^{1}H–^{1}H dipole–dipole interactions, since the proton decoupling is off during this time interval. A 90_x–τ'–180_x–τ' Hahn echo block ensures detection of undistorted lineshapes for the broad static powder patterns expected in f_2 (see Section 2.6). Two datasets are recorded with the first (^{1}H) 90° pulse being x and $-y$ respectively in the two experiments. SHR (States–Haberkorn–Ruben) 'hyper-complex' data processing [**170**] is then used to obtain a purely absorptive two-dimensional exchange spectrum.

The two-dimensional chemical shift–chemical shift tensor exchange method has been successfully applied to studies of different forms of solid methanol [**61**], conformations of non-crystalline solid polymers [**93**] and the local structure of dragline silk from the spider *Nephila madagascariensis* [**171**]. The desired information about the conformation or relative orientations of molecules has been extracted by comparing line shapes of the off-diagonal experimental and theoretically calculated intensity patterns. An illustrative example of a two-dimensional chemical shift–chemical shift tensor exchange spectrum of 1-^{13}C glycine labelled *N. madagascariensis* dragline silk is shown in Fig. 7.32. The strong correlation observed between the NMR spectral frequencies of the exchanging groups, which is encoded in the shape of the off-diagonal patterns, arises because the possible relative orientations of the two functional groups are constrained by the bonding geometry of the molecule.

Recently, the two-dimensional chemical shift–chemical shift tensor exchange method has been extended to magic-angle spinning solids and has been applied to conformational studies on biomolecules: a short model tripeptide Ala–Gly–Gly [**55**, **56**], a 17-residue polyalanine-based 3_{10}-helical or α-helical peptide *N*-acetyl-AEAAAKEAAAKEAAA-KA-NH_2 [**172**], an HIV-protein-fragment/antibody complex [**88**] and Alzheimer's amyloid-β-protein(16–22) fibrils [**124**]. Since this method

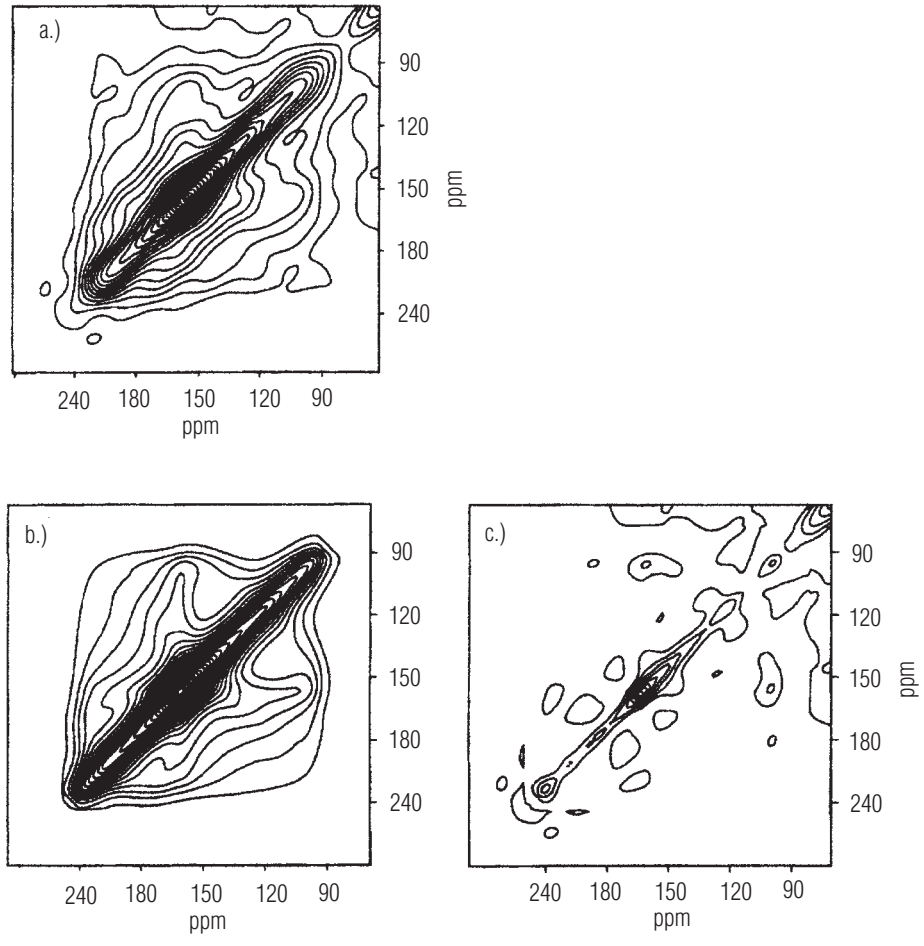

Fig. 7.32 (a) Two-dimensional 125.8 MHz ^{13}C experimental proton-driven spin-diffusion spectrum of glycine-1-^{13}C-labelled *N. madagascariensis* dragline silk at $T = 150$ K. A mixing time of 10 s was used. The spectrum was acquired with 128 transients per data point in t_1 with 96 spectra recorded in the f_1 domain and zero-filled to 256 $\times$ 256 prior to the double Fourier transformation. The resulting two-dimensional spectrum was symmetrized about the diagonal to enhance signal to noise. (b) Best fit of the experimental spectrum to a two-site exchange model with an amorphous background added (14% signal intensity from an isotropic exchange pattern). The conformation represents a $(Gly\text{-}Gly\text{-}X)_m$-$3_1$-helical structure with only two symmetrically inequivalent Gly-1-^{13}C sites. In contrast to the α-helical structures which are stabilized by intrachain hydrogen bonds, 3_1-helices are stabilized by interchain hydrogen bonds (see insert). (c) Difference between the experimental spectrum (a) and fit (b). Adapted from ref. [**171**].

has been shown to be a very useful one in biological applications, we will discuss it in detail.

The basic idea and implementation of the two-dimensional chemical shift–chemical shift tensor exchange method under magic-angle spinning is the same as for the static experiment. The only difference (apart from a more tedious theoretical analysis) is that at moderate spinning frequencies, magic-angle spinning narrows chemical shift anisotropy powder patterns to a set of comparatively sharp spinning

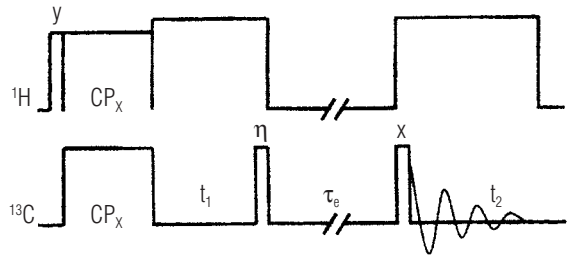

Fig. 7.33 Rf pulse sequence for two-dimensional magic-angle spinning exchange measurements. CP represents Hartmann–Hahn cross-polarization. *x*, *y*, and η indicate the phases of 90° pulses, τ_e is the exchange period. Four complete two-dimensional data sets are acquired, with $\eta = x$ or *y*, and with rf pulses synchronized with magic-angle spinning so that either τ_e or $t_1 + \tau_e$ is a multiple of the rotor period τ_R. Adapted from ref. [**124**].

sidebands. Compared with the nonspinning experiment, rotor-synchronized two-dimensional chemical shift–chemical shift tensor exchange measurements have dramatically improved resolution and sensitivity (by a factor greater than 10) because the off-diagonal signals are concentrated into sharp peaks that connect the spinning sideband frequencies in the f_1 and f_2 dimensions. The increase in sensitivity is the essential issue in biochemical applications where sample quantities are limited and spectra are complex. As with the static experiment, in rotor-synchronized two-dimensional magic-angle spinning exchange spectra, structural information is contained in the off-diagonal region of the two-dimensional spectrum, i.e. in amplitudes of crosspeaks which connect spinning sidebands of the two ^{13}C-labelled sites in a biomolecule.

The pulse sequence for the two-dimensional magic-angle spinning exchange experiment is shown in Fig. 7.33. After the cross-polarization pulse and the evolution period t_1, a 90° pulse of the phase $\phi = x$ or $\phi = -y$ is applied (to store magnetization along *z*) followed by the exchange period τ_e. The intramolecular spin diffusion between the two labelled sites, driven by ^{1}H–^{13}C, ^{1}H–^{1}H and ^{13}C–^{13}C dipole–dipole couplings, is relatively rapid because proton decoupling is not applied during τ. Finally, after the exchange period, a last 90° pulse of phase *x* sets the ^{13}C magnetization to the *x*–*y* plane for detection during t_2.

To obtain purely absorptive two-dimensional magic-angle spinning exchange spectra, the four data sets must be obtained with the pulse sequence synchronized with the sample rotation according to $\tau = n\tau_R$ and $\tau + t_1 = n\tau_R$. The data-processing scheme for two-dimensional rotor-synchronized magic-angle spinning experiments was originally developed by Spiess and co-workers, who applied the two-dimensional magic-angle spinning exchange experiment to studies of slow molecular motion in polymers [**20, 173, 174**]. This more advanced data-processing procedure is needed because of a more complex form of NMR signals obtained under magic-angle spinning as we will see below.

Figure 7.34 shows NMR spectra obtained for a polycrystalline doubly $^{13}C_2$-labelled L-alanylglycylglycine ($^{13}C_2$-AGG) sample spun at a moderate spinning frequency of 2.5 kHz. Two consecutive carbonyl sites in the tripeptide have been ^{13}C-labelled, Ala-1 and Gly-2. Carbonyl labels were used since their ^{13}C chemical shift anisotropy is large and well characterized. The labelled molecules are chemically

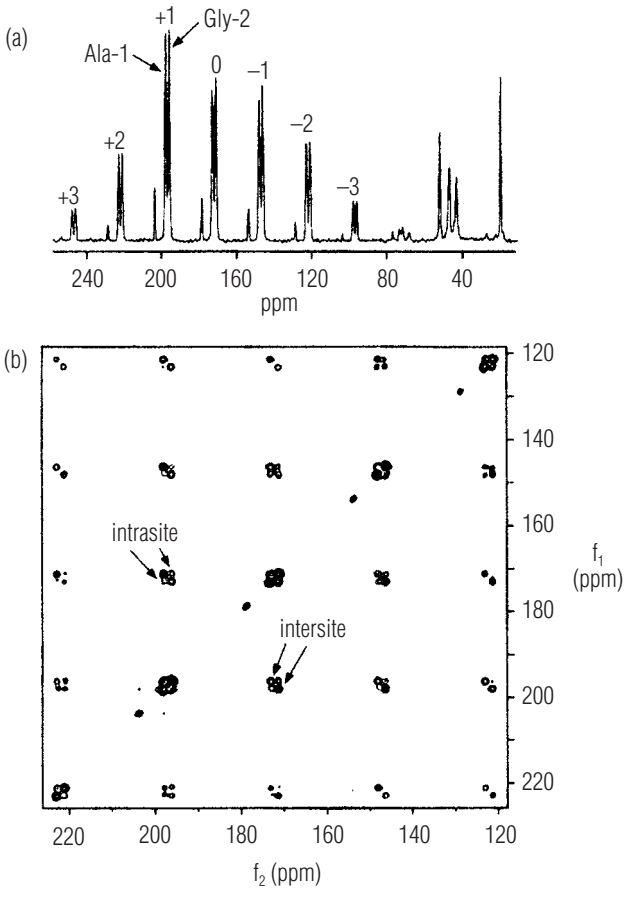

Fig. 7.34 100.4 MHz ^{13}C NMR spectra of polycrystalline 5% [L-alanyl-1-^{13}C]-[glycyl-1-^{13}C]-glycine, recorded with a magic-angle spinning rate of 2.5 kHz. (a) One-dimensional cross-polarization spectrum. Spinning sidebands for the labelled Ala-1 and Gly-2 carbonyl carbons are numbered, with the centerband line defined to be 0. (b) Carbonyl region of the two-dimensional ^{13}C magic-angle spinning NMR exchange spectrum at room temperature. Examples of intersite and intrasite crosspeaks are indicated. Exchange period τ_e = 500 ms plus fractions of τ_R required for synchronization with sample spinning. Maximum t_1 value was equal to 15.3 ms, 256 t_1 increments, 128 signal transients per t_1 value. Adapted from ref. [**55**].

diluted to a quantity of 5% in the unlabelled L-alanylglycylglycine to avoid intermolecular spin diffusion. The latter can obscure torsion angle measurements, since the spin magnetization will diffuse to a number of ^{13}C-labelled sites having different orientations in the crystal unit cell. It is the so-called *intersite* crosspeaks in the two-dimensional exchange spectrum (Fig. 7.34(b)), i.e. peaks between spinning sidebands belonging to the different exchanging sites, which show correlations between the anisotropic NMR frequencies of the two labelled carbonyl sites. Amplitudes of these intersite crosspeaks are, in turn, determined by the relative orientation of the two carbonyl groups within the molecule. The spectrum is obtained with an exchange period of τ = 500 ms, for which the intramolecular diffusion is complete (time constant of the crosspeak build up is $\tau_0 \sim 75$ ms). The other peaks, the so-called *intrasite* crosspeaks, i.e. peaks between sidebands of the same site, appear because of the relaxation of amide ^{14}N nuclei during the exchange period τ. The latter relaxation leads to a change in the net frequency shift anisotropy tensor (which is a sum of the ^{13}C chemical shift tensor and the ^{13}C–^{14}N dipole–dipole coupling

tensor); the effect is to produce crosspeaks similar to those in chemical exchange or slow molecular motions. The influence of amide ^{14}N nuclei on the ^{13}C magnetization during spin exchange is significant and thus, it must be taken into account. However, the complexity of the analysis is compensated by the simple experimental implementation, which is important for biologically relevant samples of small quantities.

The detailed theoretical and computational analysis of the two-dimensional chemical shift–chemical shift tensor exchange data are given in the original work of Tycko et al. [**56**]. Here we will only sketch basic ideas of this analysis, so as to show how the conformational information is encoded in the two-dimensional exchange spectrum. We will also use a different formalism, based on Wigner rotation matrices [**175**] instead of the Cartesian representation of tensors and transformations given in references [**20, 56, 176**].

In the two-dimensional magic-angle spinning exchange experiment for two exchanging sites i and j, the total (integrated over all orientations in a powder sample) spinning sideband crosspeak amplitudes, I^{ij}_{MN}, at frequencies $\omega^i_{\mathrm{iso}} + M\omega_{\mathrm{R}}$ in the first frequency dimension (ω_1) and $\omega^j_{\mathrm{iso}} + N\omega_{\mathrm{R}}$ in the second frequency dimension (ω_2) has been derived in references [**20, 56**]:

$$\begin{aligned} I^{ij}_{MN} &= \frac{1}{8\pi^2}\int_0^{2\pi} \mathrm{d}\alpha \int_0^{\pi} \mathrm{d}\beta \sin\beta \int_0^{2\pi} \mathrm{d}\gamma I^{ij}(\alpha, \beta, \gamma) \\ &= \frac{1}{4\pi}\int_0^{2\pi} \mathrm{d}\alpha \int_0^{\pi} \mathrm{d}\beta \sin\beta (F^i_M)^* F^j_M G^{ij}_{M-N} \end{aligned} \tag{7.4}$$

where $I^{ij}(\alpha, \beta, \gamma)$ is the contribution to the amplitudes of the spinning sideband crosspeaks due to exchange between sites i and j in molecules with orientation characterized by (α, β, γ), the three Euler angles defining the transformation from the molecular to the rotor axis frame, and

$$F^i_N(\alpha, \beta) = \frac{1}{2\pi}\int_0^{2\pi} \mathrm{d}\xi \exp(-iN\xi) f_i(\xi) \tag{7.5}$$

$$G^{ij}_N(\alpha, \beta) = \frac{1}{2\pi}\int_0^{2\pi} \mathrm{d}\xi \exp(-iN\xi) f_i(\xi) f^*_j(\xi) \tag{7.6}$$

The f functions in the last two integrals are extensively used in the theoretical analysis of solid-state NMR experiments under magic-angle spinning [**20, 97**]:

$$f_j(\xi) = f_1(\alpha, \beta, \xi) = \exp\left\{ \sum_{\substack{m=-2 \\ m\neq 0}}^{+2} \frac{\omega^{(m)}_j(\alpha, \beta) \exp(im\xi)}{m\omega_{\mathrm{R}}} \right\} \tag{7.7}$$

where $\omega^{(m)}_j(\alpha, \beta)$ are Fourier harmonics described below and ω_{R} is the sample rotation frequency. If the molecular axis frame is chosen to coincide with the principal axis frame of the chemical shift tensor of the site j (this will minimize the total

number of axis frame transformations), then $\omega_j^{(m)}(\alpha, \beta)$ can be expressed in terms of the second-rank spatial tensor components, A_{2m}^j, of the chemical shift tensor and the Wigner matrix elements, $D_{m'm}^2(\alpha, \beta, \gamma)$ [**175**], which characterize the rotational transformation of a second-rank spherical tensor:

$$\omega_j^{(m)}\left(\alpha_{\mathrm{PR}}^j, \beta_{\mathrm{PR}}^j\right) = \sum_{m'+2}^{+2} A_{2m}^j D_{m'm}^2\left(\alpha_{\mathrm{PR}}^j, \beta_{\mathrm{PR}}^j, 0\right) d_{m0}^2(\beta_{\mathrm{RL}}) + \delta_{m0}\omega_{\mathrm{iso}}^j \tag{7.8}$$

with

$$\begin{aligned} A_{20}^j &= \omega_0\left(\delta_{zz}^j - \delta_{\mathrm{iso}}^j\right) = \omega_0 \Delta_{\mathrm{cs}} \\ A_{2\pm1}^j &= 0 \\ A_{2\pm2}^j &= -\frac{\eta_{\mathrm{cs}}^j}{\sqrt{6}} A_{20}^j \end{aligned} \tag{7.9}$$

$d_{m0}^2(\beta_{\mathrm{RL}})$ is a reduced Wigner rotation matrix element [**175**], $\beta_{\mathrm{RL}} = \arccos(1/\sqrt{3})$ is the magic angle (the second Euler angle in the transformation from the rotor, *R*, to the laboratory, *L*, axis frame). *P* denotes the molecular frame for site *j* so that $(\alpha_{\mathrm{PR}}^j, \beta_{\mathrm{PR}}^j)$ are the Euler angles relating the *j*th molcular frame to the rotor frame, *R*.

The angle parameter, ξ, of the *f*-function in Equation (7.7) has been separated from other angles in Equation (7.7) and is equal to $\gamma_{\mathrm{PR}}^j + \alpha_{\mathrm{RL}}^0 - \omega_{\mathrm{Rt}}$, where α_{RL}^0 is the synchronization angle which defines the rotor position in the laboratory frame at the time point $t = 0$. The exact dependence of ξ on angles γ_{PR}^j and α_{RL}^0 is irrelevant here since ξ is the integration parameter in Equations (7.5) and (7.6).

Note that Equations (7.4)–(7.6) contain functions which depend on the *f* functions of both sites *i* and *j*. On the other hand, Equation (7.8) is written using the transformation from the principal axis frame of the chemical shift tensor of the site *j*, P_j, to the rotor axis frame, *R*. We cannot write the same formulae for $\omega_i^{(m)}$ of the site *i* since, in general, the principal axis frames of chemical shift tensors for sites *i* and *j* are different. Thus, for the site *i*, we first have to perform a rotation from molecular frame P_i to P_j (given by the Euler angles $\Omega^{ij} = (\alpha_{ij}, \beta_{ij}, \gamma_{ij})$ which describes the relative orientation of chemical shift tensors of sites *i* and *j*) and, then apply the transformation from frame P_j to the rotor frame *R* for the final integration in Equation (7.4) over α_{PR}^j and β_{PR}^j. In these transformations we use Wigner rotation matrices because of the following useful property [**175**]:

$$D_{\mathrm{mn}}^2\left(\Omega_{\mathrm{PR}}^i\right) = \sum_{p=-2}^{+2} D_{mp}^2(\Omega^{ij}) D_{pn}^2\left(\Omega_{\mathrm{PR}}^j\right) \tag{7.10}$$

$\omega_i^{(m)}$ for the site *i* now becomes:

$$\omega_j^{(m)}\left(\alpha_{\mathrm{PR}}^j, \beta_{\mathrm{PR}}^j\right) = \sum_{m'=-2}^{+2} \sum_{m''=-2}^{+2} A_{2m'}^j D_{m'm''}^2(\Omega^{ij}) D_{m''m}^2\left(\alpha_{\mathrm{PR}}^j, \beta_{\mathrm{PR}}^j, 0\right) d_{m0}^2(\beta_{\mathrm{RL}}) + \delta_{m0}\omega_{\mathrm{iso}}^j \tag{7.11}$$

with $A^{i}_{2m'}$ given by the chemical shift tensor parameters of the site i as in Equation (7.9).

As can now be seen, the spinning sideband crosspeak amplitudes, I^{ij}_{MN} in Equation (7.4) are functions of the anisotropy and asymmetry parameters of chemical shift tensors of sites i and j, the ratio ω_0/ω_R, and the relative orientation of the principal axis frames of the two chemical shift tensors, Ω^{ij}. It is important to note, that I^{ij}_{MN} vanishes for $M \neq N$, if the exchanging sites have identical chemical shift tensor orientations and principal values, aside from a possible difference in δ_{iso}. I^{ij}_{MN} vanishes for $M \neq N$ since G^{ij}_{N} in Equation (7.6) with $i = j$ will be equal to the following quantity (using the symmetry $\omega_i^{(m)} = (\omega_i^{(-m)})^*$):

$$\begin{aligned} G^{ij}_{M-N}(\alpha,\beta) &= \frac{1}{2\pi}\int_0^{2\pi} d\xi \exp(-i(M-N)\xi)|f_i(\xi)|^2 \\ &= \frac{1}{2\pi}\int_0^{2\pi} d\xi \exp(-i(M-N)\xi) f_i(\xi, \omega_R/2) \\ &= C^{(M-N)}\left(\frac{\omega_R}{2}\right) \end{aligned} \tag{7.12}$$

where $C^{(M-N)}(\omega_R/2)$ are sideband amplitudes at the spinning frequency $\omega_R/2$ in the one-dimensional TOSS experiment [**177, 97**] (see Section 2.2.3). The $C^{(M-N)}(\omega_R/2)$ vanish for $M - N \neq 0$ in powder samples under magic-angle spinning as shown in references [**97, 178**].

$I^{ij}_{MN} \neq 0$ if the exchanging sites have different chemical shift tensor orientations or/and different principal values. Since the latter is roughly conserved between exchanging sites, it is the dependence of the relative orientation of the chemical shift tensor principal axis frames of these sites that makes rotor-synchronized two-dimensional exchange spectroscopy useful for molecular conformation studies. Tycko et al. [**56**] have shown that the amplitudes I^{ij}_{MN} are real numbers, the two-dimensional exchange spectrum is symmetric about its diagonal, i.e. $I^{ij}_{MN} = I^{ij}_{NM}$ and the integral over α in Equation (7.4) needs only be performed over the interval $0 \rightarrow \pi$, saving a factor of two in computation time.

Let us now discuss the geometrical relationships between the peptide torsion angles of interest, ϕ and ψ, and other angles in the transformation between chemical shift tensors of the two ^{13}C-labelled carbonyl sites. This analysis is straightforward if tedious. We express the Euler angles, $\Omega_{12} = (\alpha_{12}, \beta_{12}, \gamma_{12})$ which describes the relative orientation of chemical shift tensors of the exchanging carbonyl sites 1 and 2 in a peptide in terms of torsion angles ϕ and ψ of site 2, dihedral angles (assuming standard geometry of peptide bonds [**179**]) $C^{(1)}$–$N^{(2)}$–$C_\alpha^{(2)}$ ($\pi - \delta_1 \approx 122°$), $N^{(2)}$–$C_\alpha^{(2)}$–$C^{(2)}$ ($\pi - \delta_2 \approx 111°$), $C_\alpha^{(2)}$–$C^{(2)}$–$N^{(3)}$ ($\pi - \delta_3 \approx 116°$) and an angle χ between the y axis of the carbonyl ^{13}C chemical shift tensor (y^{PAF}) and the C–N bond (see Fig. 7.35). As discussed above, y^{PAF} (corresponding to the principal axis δ_{22}) and x^{PAF} (the δ_{11} axis) both lie in the CO–NH peptide plane and are ca. 5–10° and 85–80°

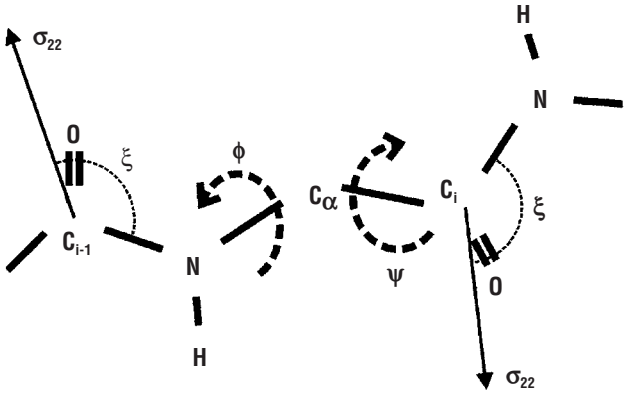

Fig. 7.35 Peptide backbone, illustrating the dihedral angles ϕ and ψ that define the backbone conformation at amino acid residue 2. The principal axis associated with the σ_{22} component of the ^{13}C chemical shielding tensor is also shown for each carbonyl carbon. Adapted from ref. [**56**].

from the CO bond, respectively. Therefore, $\chi \approx 130°$ because of the sp^2 hybridization of the carbonyl carbon, with dihedral angles between bonds equal to 115–120°.

Assuming z^{PAF} (the principal axis associated with the chemical shift tensor component δ_{33}) of the carbonyl ^{13}C chemical shift tensor is oriented perpendicular to the peptide plane, the Euler angles $(\alpha_{12}, \beta_{12}, \gamma_{12})$ can be expressed as [**56**]:

$$\alpha_{12} = \overline{\alpha} + \chi_1 - \delta_1 \tag{7.13}$$

$$\cos\beta_{12} = \sin\phi\sin\psi\cos\delta_2 - \cos\phi\cos\psi \tag{7.14}$$

$$\gamma_{12} = \overline{\gamma} - \chi_2 + \delta_3 \tag{7.15}$$

where χ_1 and χ_2 are the values of χ angles for sites 1 and 2, and $\overline{\alpha}$ and $\overline{\gamma}$ are the following functions of ϕ, ψ and δ_2 with the constraint set by the angle β_{12}:

$$\sin\overline{\alpha}\sin\beta_{12} = \sin\psi\sin\delta_2 \tag{7.16}$$

$$\cos\overline{\alpha}\sin\beta_{12} = -\cos\phi\sin\psi\cos\delta_2 - \sin\phi\cos\psi \tag{7.17}$$

$$\sin\overline{\gamma}\sin\beta_{12} = -\sin\phi\sin\delta_2 \tag{7.18}$$

$$\cos\overline{\gamma}\sin\beta_{12} = -\sin\phi\cos\psi\sin\delta_2 - \cos\phi\sin\psi \tag{7.19}$$

Therefore, for any values of the dihedral angles ϕ and ψ that specify the peptide backbone conformation, the Euler angles Ω_{12} can be calculated, which in turn permits numerical calculations of $\omega_1^{(m)}$ and $f_1(\xi)$, for each pair of integration angles α_{PR}^j and β_{PR}^j (for the site $j = 2$). Crosspeaks in the two-dimensional exchange spectrum of a powder sample which are expressed by integrals given in Equation (7.4) can be obtained by substitution of the integration procedure with a sum which runs over a sufficiently large set of Euler angles α_{PR}^j and β_{PR}^j. Typically, 40 values of $\cos\beta$, 40 values of α and 80 values of ξ which gives a total of 128 000 orientations over a hemisphere, are sufficient for an accuracy within 1% of the amplitude of the strongest crosspeaks in two-dimensional exchange spectra [**56**]. This integration can

be further optimized by adding subspectra calculated for only specific orientations which can be obtained from symmetries of Wigner matrices and an algorithm involving Lebedev's functions [**180, 181**].

It is important to note that due to intrinsic the symmetry of $\omega_i^{(m)}$ and hence of the *f* functions involved in calculations of the crosspeak amplitudes, I_{MN}^{ij}, plus integrations over α and γ (or ξ which is the same as γ), there is an unavoidable conformational degeneracy, i.e. backbone peptide conformations described by either (ϕ, ψ) or ($-\phi$, $-\psi$) give identical two-dimensional exchange spectra. This ambiguity can be resolved by additional solid-state NMR measurements, for example, isotropic chemical shifts or distance measurements.

As already mentioned above, two-dimensional chemical shift–chemical shift tensor magic-angle spinning exchange spectra of peptides are also affected by ^{13}C–^{14}N dipole–dipole coupling from the directly bonded nitrogen. This additional interaction has to be taken into the analysis. At low magnetic fields the effect of residual dipole–dipole splittings in ^{13}C magic-angle spinning spectra due to the effect of the ^{14}N electric quadrupole interaction on the ^{13}C–^{14}N dipolar coupling is well studied [**104, 105**]. In the limit of large external field $\mathbf{B}_{ext}$, the effect of the ^{14}N quadrupole interaction is small ($\sim 1/B_{ext}$), but ^{14}N spins are polarized and produce an additional local dipolar field $\mathbf{B}_{dip}$ at directly bonded ^{13}C sites. This local ^{13}C–^{14}N dipole–dipole field depends on the quantum number $m = -1, 0, 1$ for the component of the ^{14}N spin angular momentum along $\mathbf{B}_{ext}$ and can be written as:

$$\mathbf{B}_{dip} = md_0\left[\mathbf{B}_{ext} - \left(3\frac{\mathbf{r}_{CN}}{r_{CN}}\mathbf{B}_{ext}\right)\frac{\mathbf{r}_{CN}}{r_{CN}}\right] = |D(m)|\mathbf{B}_{ext} \tag{7.20}$$

where $\mathbf{r}_{CN}/r_{CN}$ is a unit vector along the ^{13}C–^{14}N direction and $d_0 = \gamma_N \dfrac{h}{2\pi}\dfrac{1}{|\mathbf{B}_{ext}|r_{CN}^3}$ (γ_N is the ^{14}N gyromagnetic ratio). The total local field due to the chemical shift tensor and the ^{13}C–^{14}N coupling tensor can be expressed in terms of an effective 'local field tensor' which depends on the quantum state *m* of the ^{14}N nuclei: $|\delta'(m)|\mathbf{B}_{ext}$ where $|\delta'(m)| = |\delta| + |D(m)|$.

Thus, each ^{13}C nucleus with a directly bonded ^{14}N nucleus has three possible local field tensors. Therefore, in the two-dimensional exchange experiment between two ^{13}C-labelled carbonyl sites, nine sets of I_{MN}^{ij} values, corresponding to the $3 \times 3 = 9$ possible pairs of local field tensors $|\delta'(m)|$ must be added together to produce a single simulated two-dimensional exchange spectrum. In this analysis, six local field tensors $|\delta_1'(m)|$ and $|\delta_2'(m)|$ ($m, m' = 1, 0, -1$) have to be diagonalized. The diagonalization gives the principal values for the tensors and the principal axes x' and y' in the CO–NH plane, characterized by the values for the angles $\chi'(m)$. For example, in proteins for a C–N bond length of 1.32 Å, $B_{ext} = 9.39$ T, d_0 is 9.9 ppm. Typical principal chemical shift tensor values for carbonyl ^{13}C nuclei in a peptide backbone are 245 ppm, 185 ppm and 90 ppm with $\chi \approx 130°$. Then the calculated principal

values of $|\delta'(m = 1)|$ are 255 ppm, 184.4 ppm and 80.6 ppm, the principal values of $|\delta'(m = -1)|$ are 241.2 ppm, 179.4 ppm and 99.4 ppm, $\chi'(m = 1) = 118.4°$ and $\chi'(m = -1) = 143.4°$. It is clear, then, that the effect of the ^{13}C–^{14}N coupling is significant and has to be taken into account in the analysis of two-dimensional exchange spectra.

The experimental two-dimensional exchange spectrum for $^{13}C_2$-AGG-peptide ^{13}C-labelled at carbonyl sites of both Ala-1 and Gly-2 (shown in Figure 7.34) has been analysed taking into account all the details of the theoretical analysis discussed above [**55**, **56**]. The root-mean-square deviation (RMSD) plot between experimental and calculated crosspeak volumes for a grid of possible ϕ, ψ values has been constructed. The result of this analysis with sideband crosspeaks of the order $-2 \leq n, n' \leq 2$, $n \neq n'$ (in total 40 off-diagonal intersite crosspeaks), shows the global minimum RMSD at $\phi, \psi = -78°, 168°$ in good agreement with the values $\phi, \psi = -83°, 170°$ determined from X-ray diffraction measurements on crystalline AGG [**182**].

Once the method has been tested on a model compound with the known structure, it can be applied to systems of interest to elucidate their structural details. A convincing application of the method has been demonstrated on amyloid fibrils formed by a seven-residue fragment $A\beta_{16–22}$ of the Alzheimer amyloid peptide. It is remarkable that this very short peptide can precipitate from aqueous solutions of neutral pH in a form of long, thin fibrils organized in bundles visible in negatively stained transmission electron micrographs (see Fig. 7.36). The X-ray powder diffraction profile shows two reflections corresponding to 4.7 and 9.9 Å, typical of amyloid fibrils. It is widely believed that 4.7 Å is the distance between amyloid-β-protein molecules organized in antiparallel β-sheets with hydrogen bonds between molecules parallel to the fibril axis. To test this, a two-dimensional chemical shift–chemical shift tensor exchange experiment under magic-angle spinning was performed on a fibrillized $A\beta_{16–22}$ sample in which 20% of the peptide molecules were doubly ^{13}C-labelled at carbonyl sites Val_{18} and Phe_{19} right in the middle region of the peptide molecule. The two-dimensional exchange spectrum (Fig. 7.37) consists of unresolved crosspeaks due to overlapping intersite (between Val_{18} and Phe_{19}) and intrasite (between spinning sidebands of the same site) peaks. It is remarkable that even in this unfavorable situation it is possible to analyse the spectrum [**183**] and the χ^2 plot of deviations between integral amplitudes of sidebands in experimental and calculated spectra (a variant of the RMSD plot), shows a global minimum around $\phi = -130°$ and $\psi = 120°$ (torsion angles of Phe_{19}) (see Fig. 7.26 (a)). The other three local minima around $(\phi, \psi) = (-45°, -110°)$, $(-40°, -50°)$ and $(-110°, -50°)$ have been discarded by an additional CTDQFD experiment (see Section 7.3.3). Combining the two-dimensional exchange and CTDQFD data, a new χ^2 plot shows only one sharp minimum at $(\phi, \psi) = (-130°, 115°)$ which indicate a β-strand conformation for $A\beta_{16–22}$ molecules at the central Phe_{19} residue in the amyloid fibrils.

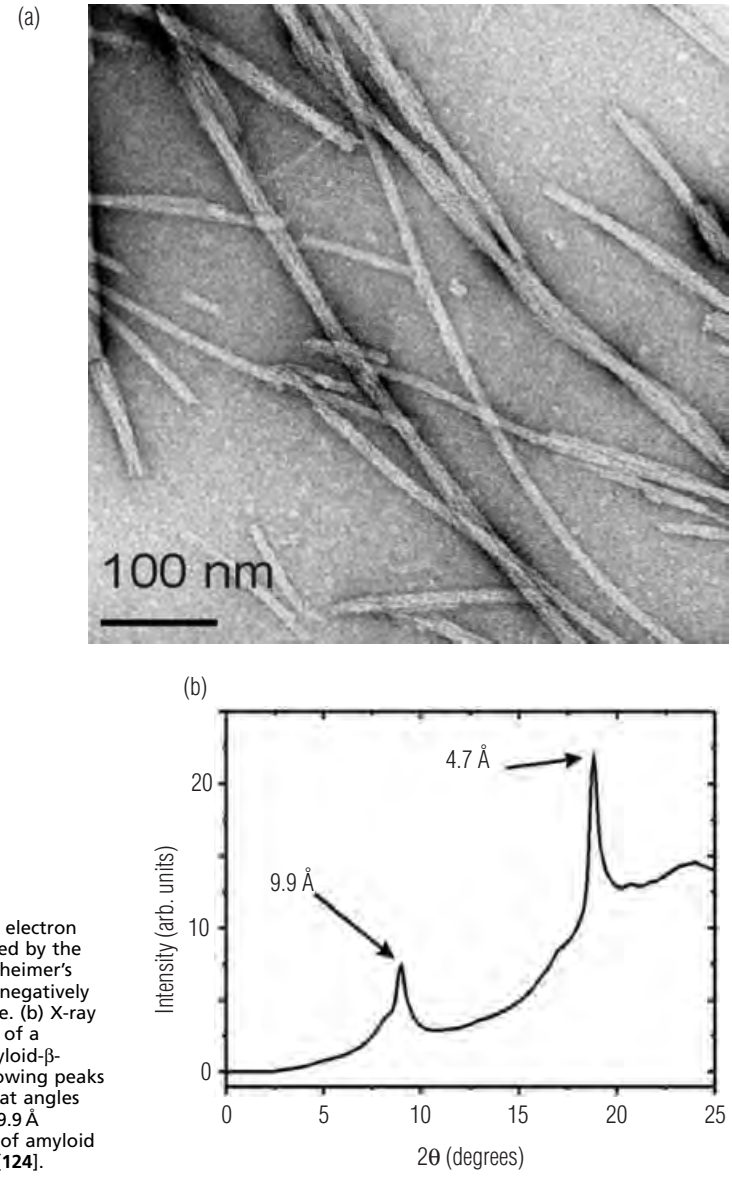

Fig. 7.36 (a) Transmission electron micrograph of fibrils formed by the seven-residue peptide, Alzheimer's amyloid-β-protein(16–22), negatively stained with uranyl acetate. (b) X-ray powder diffraction profile of a fibrillized, lyophylized amyloid-β-protein(16–22) sample, showing peaks in the scattering intensity at angles corresponding to 4.7 and 9.9 Å periodicities characteristic of amyloid fibrils. Adapted from ref. [**124**].

Another variant of the chemical shift–chemical shift tensor correlation experiment under magic-angle spinning has been developed by Blanco and Tycko and is called double-quantum (DQ) chemical shift anisotropy spectroscopy [**57**]. It can be viewed as a magic-angle spinning version of the static DOQSY (DOuble Quantum SpectroscopY) methods developed earlier by Schmidt-Rohr [**158, 184**] and also resembles the DQDRAWS experiment performed under magic-angle spinning by Drobny and co-workers [**185, 186**]. In the DQDRAWS experiment, ^{13}C chemical shift

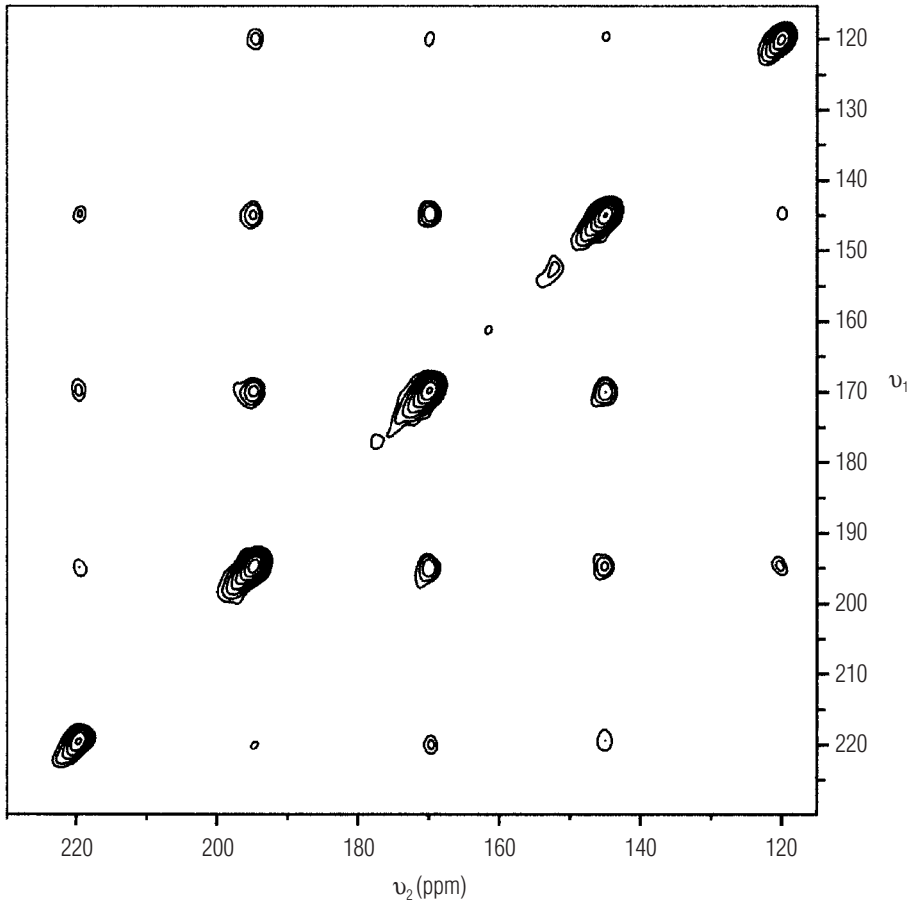

Fig. 7.37 100.4 MHz ^{13}C two-dimensional magic-angle-spinning (ν_R = 2.5 kHz) exchange spectrum of a fibrillized Alzheimer's amyloid-β-protein sample in which 20% of the peptide molecules have ^{13}C labels at carbonyl sites of Val18 and Phe19. The exchange period, τ_e, was equal to 500 ms. Only the carbonyl region of the spectrum is shown (in ppm from TMS for both spectral axes). Signals from the two ^{13}C carbonyl sites are overlapped including the crosspeaks which connect their spinning sidebands. The crosspeak amplitudes are analysed by comparison with numerical simulations to provide constraints on the peptide backbone dihedral angles ϕ and ψ at Phe19, as shown in Fig. 7.26(a).

tensors are correlated through a double-quantum coherence which is prepared using the DRAWS pulse sequence. In the DQCSA experiment of Blanco and Tycko, double-quantum coherences are excited with a radio-frequency driven recoupling (RFDR) sequence [**33**, **34**]. These double-quantum coherences are allowed to evolve during a constant-time t_1 period and then reconverted back by a second RFDR-block and 90° pulse to (−1)-quantum coherence for observation (see Fig. 7.38). A z filter is applied before signal acquisition to remove any unwanted magnetization components [**187**]. In the first variant of the DQCSA experiment (Fig. 7.38(a)), a single 180° pulse at time $t_1 + t_\pi/2$ (t_π is the 180° pulse length) prevents refocusing of the anisotropic chemical shift under magic-angle spinning during the constant

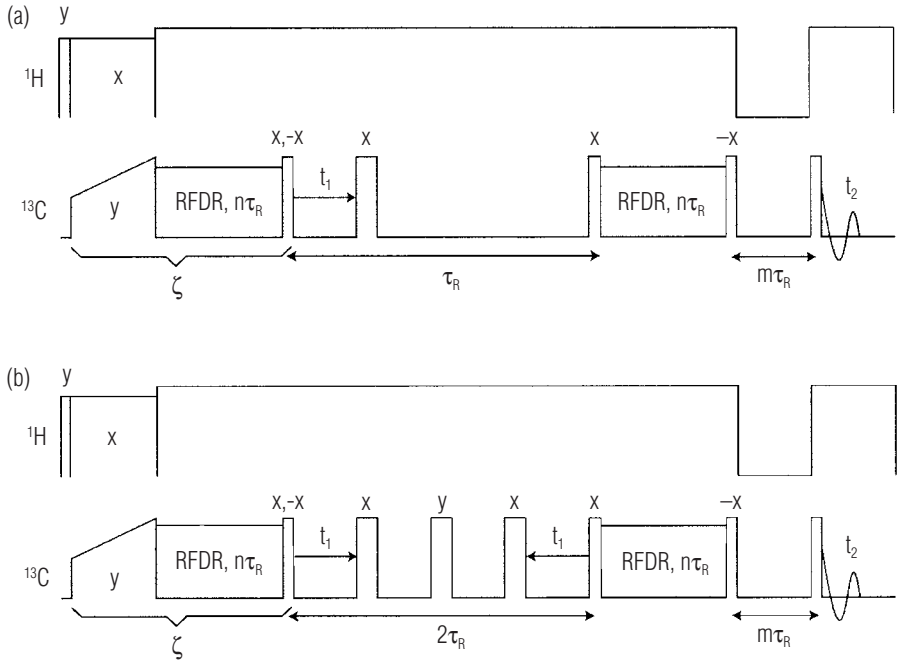

Fig. 7.38 DQCSA pulse sequences. 90° and 180° pulses are indicated by thin and thick open rectangles respectively. ^{13}C magnetization is created by ramped cross-polarization. RFDR sequences for double-quantum preparation and mixing, consisting of a single 180° pulse at the end of each odd-numbered magic-angle spinning rotor period with XY-32 phase cycling, are applied for n rotor periods. Double-quantum filtering is accomplished by application of overall rf phase shifts ζ to the ^{13}C cross-polarization pulse, the first RFDR block, and the first ^{13}C 90° pulse, and multiplication of ^{13}C FID signals by $\exp(2i\zeta)$ before co-addition, with $\zeta = 0°$, 90°, 180°, 270°. (a) Double-quantum evolution period is one rotor period. A single 180° pulse prevents refocusing of anisotropic chemical shifts, leading to t_1-dependent DQCSA signals. (b) Double-quantum evolution period is two rotor periods. Three 180° pulses prevent refocusing of anisotropic chemical shifts and refocus isotropic chemical shifts. Adapted from ref. [**57**].

time period which is one rotation period, τ_R. In the second version of the DQCSA spectroscopy, the constant time period is set to two rotor periods, $2\tau_R$, and three 180° pulses (centred at times $t_1 + t_\pi/2$, τ_R and $2\tau_R - t_1 - t_\pi/2$) are used to prevent refocusing of the anisotropic shifts as well as additionally refocus isotropic shifts (Fig. 7.38(b)). The latter prevents the undesired evolution due to resonance offsets.

A set of double-quantum filtered magic-angle spinning spectra, selected by cycling of an overall rf phase shift ζ of both the cross-polarization pulse and the first RFDR block, is recorded as a function of t_1. The relative orientation of the two chemical shift tensors is encoded in the t_1 dependence of spinning sideband intensities in the double-quantum filtered ^{13}C magic-angle spinning spectrum since double-quantum coherences evolve at the sum of the two anisotropic chemical shifts. The main advantage of this method is that the double-quantum excitation period can be kept short (at the cost of reduced signals), just one or two rotor periods at moderate spinning of ca. 4 kHz, which may be especially useful when analysing

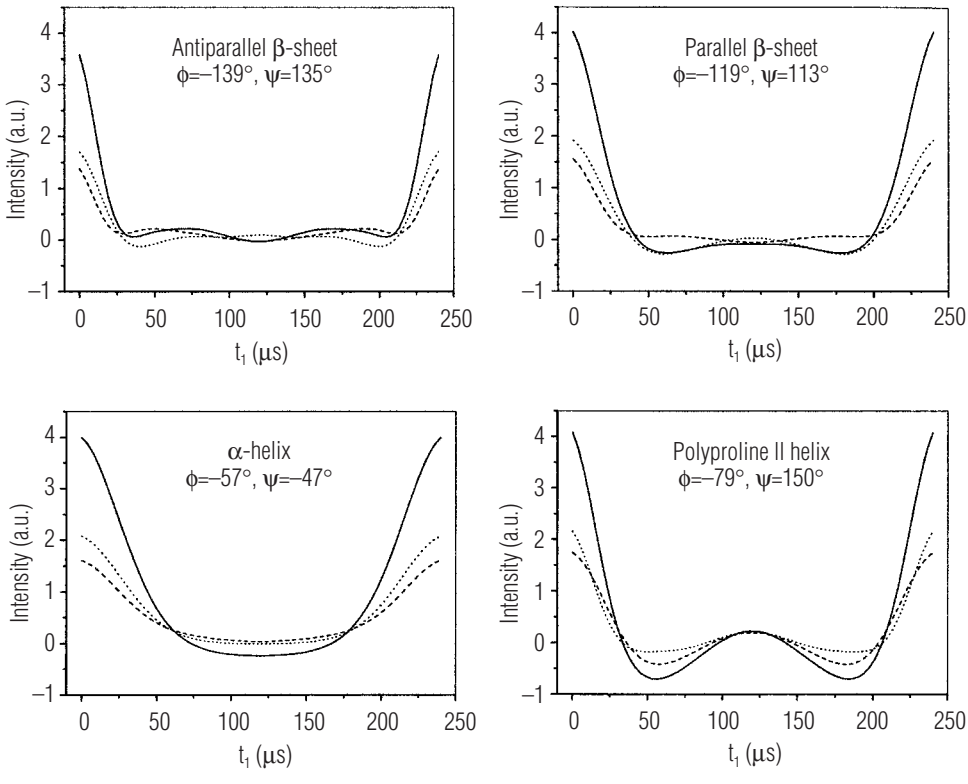

Fig. 7.39 Numerical simulations of DQCSA data, based on the DQCSA pulse sequence in Fig. 7.38(a) and assuming chemical shift tensor parameters as in alanylglycylglycine peptide. Simulated intensities of double-quantum-filtered magic-angle-spinning centerband (solid lines), upfield first-order sideband (dashed lines), and downfield first-order sideband (dotted lines) are shown for dihedral angles which are characteristic of idealized protein secondary structures. Adapted from ref. [**57**].

conformations of peptides at a particular doubly-labelled fragment of the backbone in the presence of additional labelled carbons along the sequence.

Numerical calculations of DQCSA data for a peptide doubly ^{13}C-labelled at the two consecutive carbonyls, based on the pulse sequence in Fig. 7.38(a), are shown in Fig. 7.39 (chemical shift tensor and other parameters are taken to be the same as in the tripeptide alanylglycylglycine). Simulated intensities of double-quantum filtered magic-angle spinning centreband and the two first-order sidebands as functions of t_1 are shown for dihedral angles that are characteristic of idealized secondary structures found in proteins. The double-quantum coherences evolution curves are very different and clearly characteristic for each of the common protein secondary structures.

An example of the DQCSA method applied to the lyophilized powder sample of a 17-residue highly-helical peptide MB(i + 4)EK with the sequence *N*-acetyl-AEAAAKEAAAKEAAAKA-NH_2 (A denotes alanine; K, lysine; E, glutamic acid)

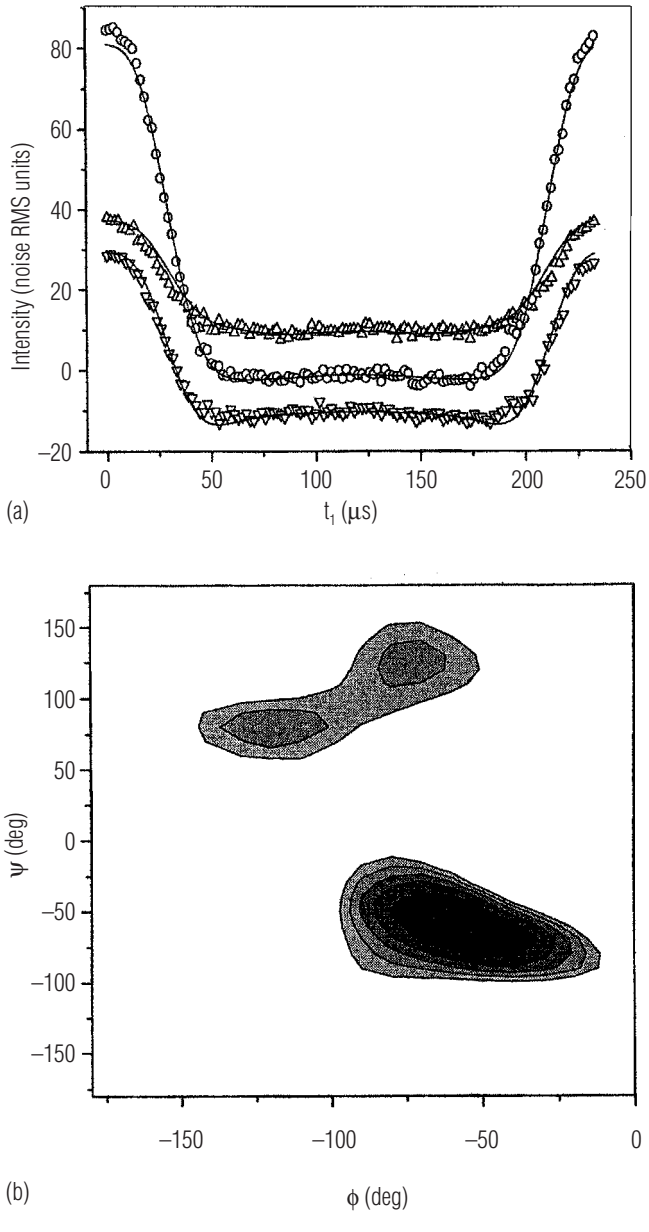

Fig. 7.40 (a) Experimental and simulated 100.8 MHz ^{13}C DQCSA data for the 17-residue helical peptide MB(i + 4)EK in lyophilized form, with ^{13}C labels at six carbonyl sites (30 μmol). Data were obtained with the pulse sequence in Fig. 7.38(b) with $n = 8$ (4 ms recoupling time), $\tau_R = 250$ μs and the total acquisition time of 15.5 hours. The short recoupling time was chosen to minimize signal contributions from non-consecutive carbonyl pairs. ^{1}H decoupling rf field was 85 kHz during RFDR blocks and the t_1 period. Integrated experimental intensities of the centreband (circles), and first-order spinning sidebands (up and down triangles for the upfield and downfield sidebands respectively), are in units of the rms spectral noise, with upfield and downfield first-order sideband intensities shifted vertically for clarity by +10 and −10 units respectively. Simulations assume α-helical dihedral angles ($\phi = -60°$, $\psi = -50°$) for all carbonyl pairs that contribute to the DQCSA signals, because all residues in an α-helix are expected to have approximately the same backbone dihedral angles. (b) Contour plot of the χ^2 deviation between simulated and experimental data, with contour levels incremented in steps of 4000 and with the lowest level at $\chi^2 = 4000$. Adapted from ref. [**57**].

[**172, 188**], which is ^{13}C-labelled at the carbonyl carbons of Ala4, Ala5, Ala8, Ala9, Ala10, and Ala13, is shown in Fig. 7.40. It had been shown previously that the helix content of the peptide in lyophilized form is approximately equal to 85% [**172**]. Data were obtained with the pulse sequence in Fig. 7.38(b) and simulated assuming α-helical dihedral angles $\phi = -60°$, $\psi = -50°$ for all carbonyl pairs that contribute to the DQCSA signal (Fig. 7.40(a)). Simulated intensities were obtained

by numerical calculations of the quantum dynamics of the two-spin system, including finite RFDR 180° pulse amplitudes and summed over molecular orientations. The agreement between experimental and simulated curves is very good for both the centreband and the first-order sidebands. The same data have been also analysed in terms of a χ^2 plot:

$$\chi^2(\phi, \psi) = \frac{1}{\sigma^2} \sum_{i=1}^{N} [E_i - \lambda(\phi, \psi) S_i(\phi, \psi)]^2 \tag{7.21}$$

where the E_i are the experimental intensities of centreband and first-order sidebands in the spectra obtained at different t_1, $S_i(\phi, \psi)$ are the simulated intensities for the assumed values of ϕ and χ (over a grid of ϕ, ψ values with 10° increments), σ is the root-mean-squared noise in experimental spectra, N is the number of intensities analysed ($N = 384$ in this dataset), and $\lambda(\phi, \psi)$ is an overall scaling factor adjusted to minimize χ^2. Figure 7.40(b) shows a contour plot of the $\chi^2(\phi, \psi)$ deviation between simulated and experimental data. The plot shows a global minimum around the α-helical dihedral angles $\phi = -60°$, $\psi = -50°$.

Compared with the two-dimensional magic-angle spinning exchange method, the DQCSA data show fewer false minima in the $\chi^2(\phi, \psi)$ surface and different locations of these minima. ^{14}N relaxation and effects due to the ^{14}N–^{13}C dipole–dipole interaction which are important in the two-dimensional magic-angle spinning exchange spectra, can be ignored in the DQCSA experiments since the t_1 evolution period is made to be very short. On the other hand, a combination of DQCSA, CTDQFD, and two-dimensional magic-angle spinning exchange measurements on the same sample can provide multiple, independent structural constraints that can eliminate ambiguities in dihedral angles due to false local minima in the $\chi^2(\phi, \psi)$ surfaces of any one experimental method.

7.4.2 Dipolar–chemical shift tensor correlation experiments

This class of experiments is based on measurements of correlations between the NMR spectral frequencies of nuclei associated with a functional group (the chemical shift tensor) and a bond (the dipole–dipole coupling tensor) in a single molecule. This provides information about correlations between the relative orientation of the functional group and the bond in a specifically labelled molecule in a powder sample. The NMR spectral frequencies are determined by the chemical shift anisotropy in one dimension and by dipole–dipole interactions in the other dimension.

In almost all dipolar–chemical shift tensor correlation experiments invented so far, a carbonyl or a carboxyl ^{13}C-labelled group has been chosen as the functional group because of its large and well-defined chemical shift tensor [**53**, **54**, **93**, **161**]. The carbonyl ^{13}C chemical shift tensor can be correlated with either homonuclear

^{13}C–^{13}C dipole–dipole interaction [**93**], or with the heteronuclear ^{1}H–^{13}C dipolar tensor [**53, 54**].

In the static experiment of Tycko and co-workers [**93**] polymer molecules were doubly ^{13}C-labelled at one chemical bond and singly ^{13}C-labelled at one functional (carboxyl) group in the same molecule. The pulse sequence on the ^{13}C spins is:

$$\mathrm{CP} - \underbrace{(\tau' - 180^{\circ}_{x} - \tau' - 180^{\circ}_{-x})}_{t_1}\hat{\mathrm{N}} - 90^{\circ}_{x} - \tau(\text{no decoupling}) - 90^{\circ}_{x} - \tau'' - 180^{\circ}_{x} - \tau'' - \mathrm{FID}$$

which differs from the chemical shift–chemical shift tensor correlation pulse sequence discussed in Section 7.4.1, by a Carr–Purcell train of 180° pulses during the t_1 period. The Carr–Purcell train averages out the chemical shifts and chemical shift anisotropy in t_1, leaving the homonuclear dipole–dipole couplings as the only significant interactions in t_1 [**189**]. Purely absorptive, symmetrized two-dimensional dipolar–chemical shift exchange spectra can be obtained by discarding the imaginary part of the complex signal after Fourier transformation with respect to t_2 and phase correction and before Fourier transformation with respect to t_1. Representative two-dimensional dipolar–chemical shift tensor correlation spectra of an epoxy polymer, specifically ^{13}C-labelled at the two directly bonded epoxy carbons and also at the carboxyl carbon, is shown in Figs. 7.41(a) and 7.41(b). The shape of the spectrum is determined by the dipolar splitting of the epoxy carbons in f_1 transferred in part to the carboxyl carbon ridge. It is the intensity pattern of these transferred dipolar splittings that contains the desired conformational information. The intensity pattern is sensitive to the relative orientation of the carboxyl chemical shift tensor and the ^{13}C–^{13}C dipole-dipole tensor as has been shown by numerical calculations (Figs 7.41(c)–7.41(i)). To our knowledge, the method has not yet been applied to structural studies of biomolecules.

In another group of dipolar–chemical shift tensor correlation experiments, the chemical shift tensor of one labelled site is correlated with the heteronuclear ^{1}H–^{13}C dipole–dipole tensor [**53, 54**] of the neighbouring (usually directly bonded) ^{13}C site. In the static method of Schmidt-Rohr [**54, 158, 184**], called Separated-Local-Field DOuble Quantum (SELFIDOQ) NMR, the torsion peptide/protein χ angle is measured by correlating the $^{13}C_{\alpha}$–^{1}H dipolar coupling with the ^{13}C chemical shift tensor of the directly bonded carbonyl carbon through the excited ^{13}C–^{13}C double-quantum coherence. In the static experiment, the anisotropic chemical shift frequency reflects the orientation of the chemical shift tensor principal axis frame with respect to the external magnetic field, $\mathbf{B}_0$, while the $^{13}C_{\alpha}$–^{1}H dipolar splitting encodes the orientation of the C–H chemical bond with respect to $\mathbf{B}_0$. Therefore, the relative orientation of C–H and C═O groups can be determined by correlating the $^{13}C_{\alpha}$–^{1}H dipole–dipole coupling along the first frequency dimension f_1 in a two-dimensional NMR spectrum, and the ^{13}C chemical shift tensor of the carbonyl carbon plus the

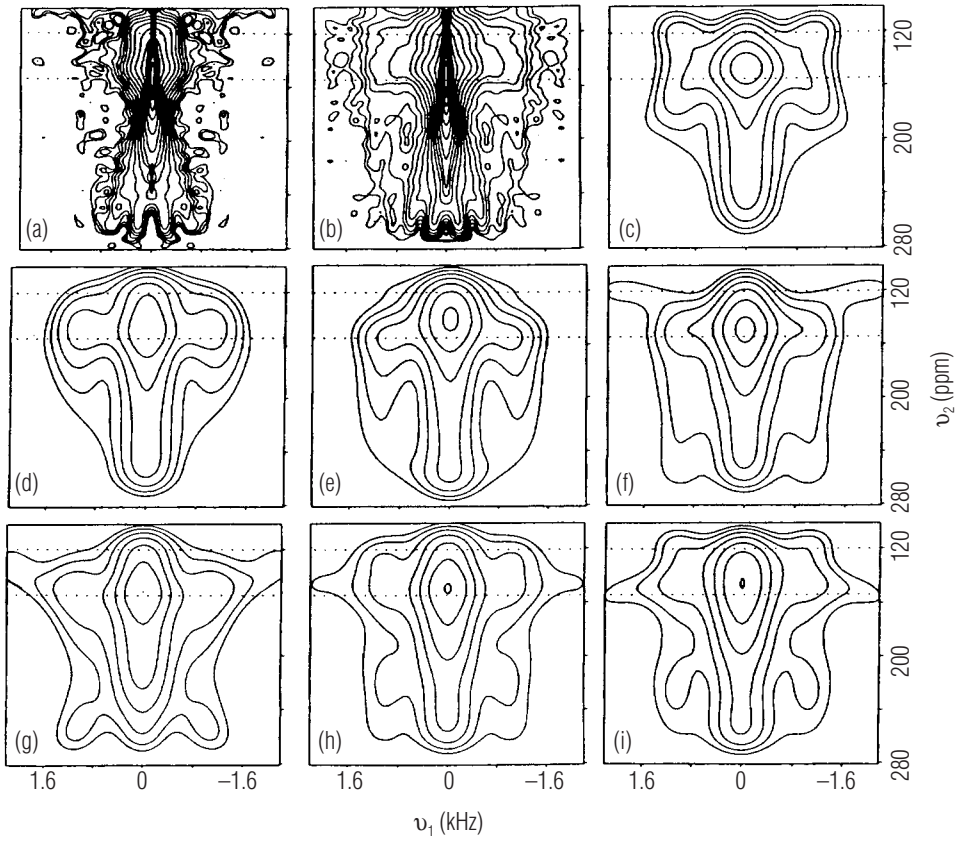

Fig. 7.41 100.47 MHz ^{13}C experimental ((a) and (b)) and simulated ((c)–(i)) two-dimensional dipolar-chemical shift tensor NMR exchange spectra of polymer PEMA (poly(ethyl methacrylate)) polymerized using ca. 4.5 % of ^{13}C-labelled monomers ([$^{13}C_3$]-ethyl methacrylate, selectively ^{13}C-enriched at the carboxyl and at both ethoxy sites) diluted in unlabelled monomers. Dilution of the labelled monomers in unlabelled monomers suppresses carbon–carbon couplings between different monomers, which allows the conformations of individual monomers in the polymer chain to be probed. The exchange period, $\tau = 1$ ms in (a) and $\tau = 0.5$ s in (b). Experimental spectra were obtained at –100°C. In the simulated spectra, the torsion angle χ_2 about the CH_2–O chemical bond has the value 0°, 30°, 60°, 120°, 150°, and 180° in (c)–(i), respectively. The other torsion angle χ_1 (about the CO–O chemical bond) is set to 0°. The fully exchanged spectrum (b) has the high intensity band between $\nu_2 = 120$ ppm and $\nu_2 = 155$ ppm (delineated by dotted lines in all spectra) and is best fitted to the simulated spectrum (c). This suggests a predominantly planar, all-*trans*-conformation of PEMA ($\chi_1 = 0°$, $\chi_2 = 0°$). Adapted from ref. [**93**].

^{13}C–^{13}C dipole–dipole coupling, along the second frequency dimension, f_2. The SELFIDOQ pulse sequence is shown in Fig. 7.42(c). The sequence is comparatively simple, since the experiment is performed on static samples. It consists of the excitation sequence CP_y–τ–180°–τ–$90°_x$ and the reconversion sequence $90°_{-x}$–τ–180°–τ–$90°_{-x}$ blocks on the ^{13}C spins which first excite and then reconvert ^{13}C–^{13}C double-quantum coherences (the 180° pulse in the middle of each block refocuses unwanted heteronuclear ^{13}C–^{14}N and ^{1}H–^{14}N dipole–dipole couplings) and an evolution period t_1 ($t_1/2$–180°–$t_1/2$) between these two blocks. During the t_1 period an MREV-8 sequence [**9**, **10**] (see Section 2.4) is applied to the ^{1}H spins

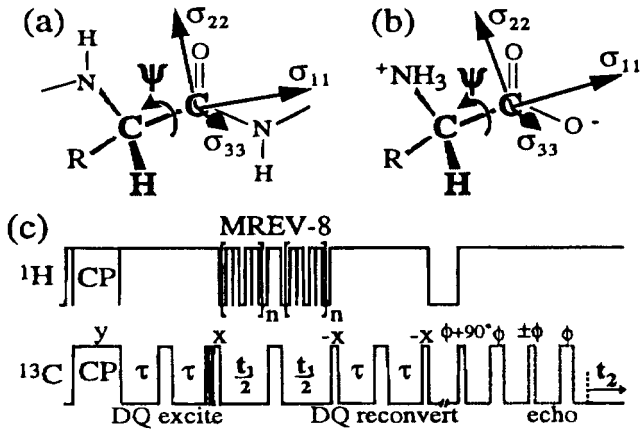

Fig. 7.42 (a) Doubly-^{13}C-labelled amino acid residue in a peptide and (b) doubly-^{13}C-labelled amino acid. The torsion angle ψ determines the orientation of the C_α–H bond relative to the principal axis frame of the ^{13}C chemical shift tensor of the carbonyl carbon. (c) SELFIDOQ pulse sequence for measurements of ψ angle in powder samples, with double-quantum (DQ) excitation (chemical shift evolution is refocused by the 180° pulse), ^{13}C–^{13}C double-quantum evolution under ^{1}H–^{13}C dipolar couplings, double-quantum reconversion, and ^{13}C-detection under ^{13}C chemical shift and ^{13}C–^{13}C dipolar-coupling effects. The two 45° pulses (in black) at the end of the double-quantum excitation period, of phases 90° and 90° or 270°, eliminate spectral artifacts at $f_1 = 0$. Adapted from ref. [**54**].

which effectively removes the homonuclear ^{1}H–^{1}H dipolar couplings and scales the heteronuclear $^{13}C_\alpha$–^{1}H dipole–dipole coupling. Thus, the carbonyl signal in dimension f_2 is modulated by the evolution of the double-quantum coherence under the $^{13}C_\alpha$–^{1}H dipole–dipole coupling in dimension f_1. After a complex Fourier transformation with respect to t_2 and a real Fourier transformation with respect to t_1, a two-dimensional spectrum correlating the $^{13}C_\alpha$–^{1}H dipolar splitting with the anisotropic carbonyl chemical shift is obtained. A representative example of the two-dimensional SELFIDOQ spectrum for polycrystalline $^{13}C_\alpha$–^{13}CO-labelled L-leucine is shown in Fig. 7.43(a) together with a calculated spectrum based on the single-crystal structure of leucine, which exhibits two molecules in the unit cell with different conformations, $\psi = -26°$ and $\psi = -36°$ [**190**] (Fig. 7.43(b)). Simulations demonstrating some possible spectral variations on ψ for a general amino acid residue (except glycine) are shown in Fig. 7.44. The latter illustrates the 'ψ-resolution' of the SELFIDOQ method which can readily distinguish between β-sheet ($\psi = 120°$) and α-helix ($\psi = -60°$) secondary structures. The method, however, suffers from some ambiguities: pairs of angles $\psi = -60° \pm \alpha$ and $120° \pm \beta$, where α and β are arbitrary angles, produce the same spectral patterns because for the two ψ values the C_α–H bond has the same angle with respect to the C–C═O plane and therefore with the principal axis associated with the principal value δ_{33} of the carbonyl chemical shift tensor. Additional solid-state NMR experiments can assist in resolving this ambiguity.

A more sophisticated version of the two-dimensional dipolar–chemical shift tensor correlation experiment under magic-angle spinning is the method invented

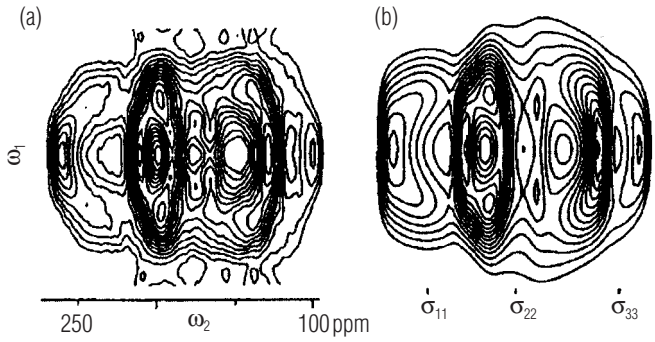

Fig. 7.43 (a) Experimental SELFIDOQ spectrum of doubly-^{13}C-labelled L-leucine. Only the carbonyl chemical-shift region is shown, since the C_α pattern is independent of ψ. (b) Corresponding simulation based on the crystal structure of leucine, which exhibits two molecules with different conformations, $\psi = -26°$ and $\chi = -36°$. An angle of 9° between the principal axis associated with δ_{33} chemical shift tensor component of the carbonyl ^{13}C and the C–C bond, was used in the simulations. Adapted from ref. [**54**].

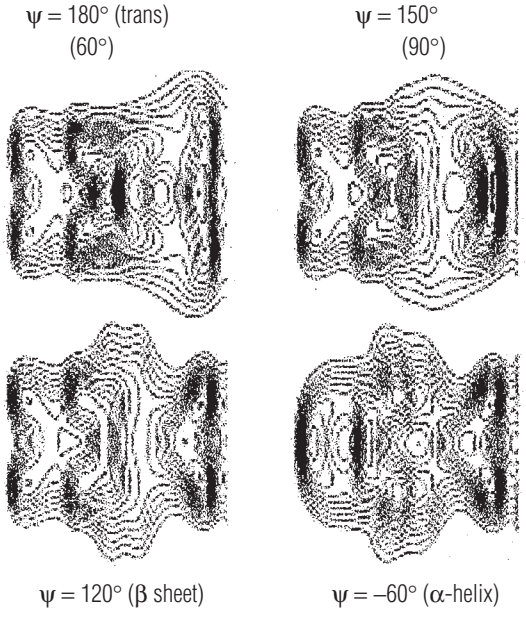

Fig. 7.44 Simulated SELFIDOQ spectra (carbonyl region) for a general amino acid residue (except glycine) in a peptide, for different backbone conformations (*trans*, β-sheet, α-helix) with torsion angles as indicated. Adapted from ref. [**54**].

by Ishii et al. and called RACO (*R*elayed *A*nisotropy *CO*rrelation) [**53**]. This method is an ingenious combination of a few pulse sequence blocks developed for other experiments. The method generates a two-dimensional powder pattern which shows correlations between the ^{13}C chemical shift tensor and the $^{13}C_\alpha$–^{1}H dipolar tensor in the doubly ^{13}C-labelled peptide fragment H–$^{13}C_\alpha$–^{13}CO via a polarization transfer from the carbonyl ^{13}C to the $^{13}C_\alpha$ carbon through the homonuclear ^{13}C–^{13}C dipole–dipole coupling. The ψ peptide angle and the carbonyl ^{13}C chemical shift tensor orientation (principal directions corresponding to the δ_{11} and δ_{22} components)

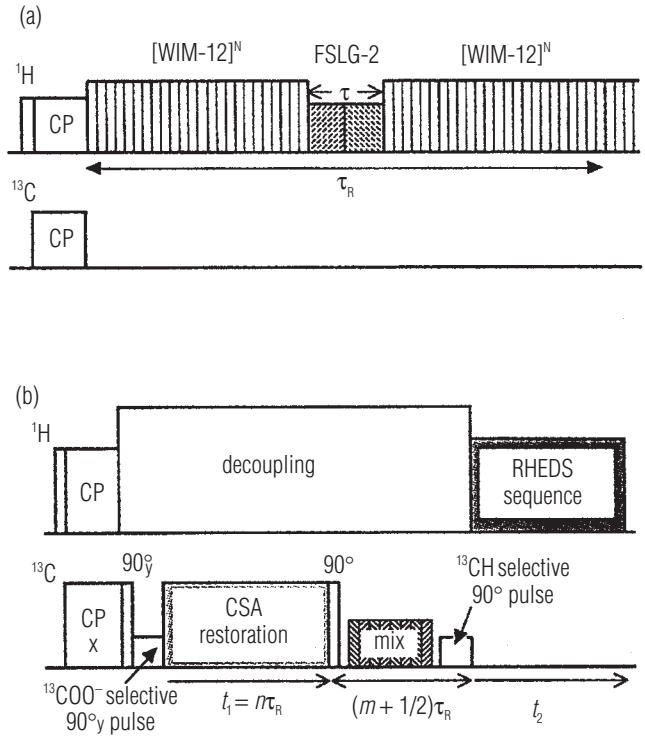

Fig. 7.45 (a) RHEDS pulse sequence for observation of ^{1}H–^{13}C dipolar powder patterns under magic-angle spinning. (b) RACO pulse sequence for measuring the O–$^{13}C_1$–$^{13}C_2$–H torsion angle (see text). Adapted from ref. [**53**].

can be determined by this method assuming that the δ_{33} chemical shift tensor component is oriented perpendicular to the plane of the NH–CO peptide fragment, which is a good assumption for peptides.

The sophistication of the RACO method is in the fact that the experiment runs under magic-angle spinning, and so the anisotropies of all second-rank tensor interactions (both the chemical shift and the dipole–dipole interactions) are averaged out by the sample spinning. Two special blocks of pulses are used for the restoration of these interactions which are then ingeniously correlated by a polarization transfer from the carbonyl ^{13}C carbon site to the C_α one. We will describe this scheme in more detail below.

The chemical shift anisotropy restoration for carbonyl carbons is realized by the rotor synchronized six 180° pulse sequence of Tycko et al. [**191**], while the Rotor-synchronous HEteronuclear Dipolar Switching pulse sequence (called RHEDS, see Fig. 7.45(a)) is used to recouple the ^{13}C–^{1}H dipolar powder pattern under magic-angle spinning. The latter sequence is a combination of the WIM-12 (Windowless Isotropic Mixing) [7] and FSLG-2 (Frequency-Switched Lee–Goldberg) [8] sequences, which is applied to the ^{1}H spins. A part of each rotor period (τ_R–τ) is occupied by the WIM-12 sequence which decouples both the homonuclear ^{1}H–^{1}H and the heteronuclear ^{1}H–^{13}C dipolar interactions.[1]* The rest of the rotor period,

* Notes are given on page 383.

τ, is occupied by the FSLG-2 sequence, which decouples only the ^1H–^1H dipolar interaction leaving the ^{13}C spin evolution to be affected by the heteronuclear ^1H–^{13}C dipole–dipole coupling.[2] The latter interaction will appear in the spectrum as a powder pattern with span proportional to the dipole–dipole coupling constant, d_{HC}, and is scaled depending on a fraction of the rotor period, τ/τ_R, for which the FSLG-2 sequence is active. For small $\tau/\tau_R << 1$, the lineshape of the recoupled dipolar pattern is very close to the static dipolar pattern with the scaling factor $\tau/(\sqrt{3}\tau_R)$, as shown by a theoretical analysis. For details of this analysis we refer readers to the original work [**53**].

The whole RACO sequence is shown in Fig. 7.45(b). After cross-polarization, a 90° pulse returns the prepared carbon magnetization back to the laboratory frame z axis, then a long weak 90° pulse is applied at the resonance frequency of the carbonyl carbons to prepare magnetization of these sites selectively along the laboratory frame x axis. After that, the chemical shift anisotropy restoration block is applied in the t_1 evolution period, which is incremented in successive experiments in multiples of the rotor period, i.e. $t_1 = n\tau_R$. The carbonyl ^{13}C magnetization is then turned back along the z axis and a variant of the rotational resonance experiment (Section 3.2.3) is implemented which recouples the dipole–dipole interaction between the ^{13}C-labelled spins during the mixing time. The spinning frequency of the sample is off the rotational resonance condition during the experiment in order to avoid the recoupling of the ^{13}C–^{13}C dipole–dipole interaction during the other blocks of the pulse sequence and also during the signal acquisition. However, during the mixing time, the rotational resonance condition is fulfilled by a specific frequency switched off-resonance irradiation [**193**]. The length of the mixing period is set to a half-integer of the rotor period to ensure a favourable orientation of the sample at the beginning of the sampling period, when the ^1H–^{13}C dipolar interaction recoupled under magic-angle spinning has the same analytical form (but scaled down) as that for the static sample. Finally, for observation of the ^1H–^{13}C dipolar powder pattern, another selective 90° pulse is applied at the spectral frequency of the C_α sites and the signal in the t_2 domain is sampled at integer multiples of τ_R while the RHEDS sequence is applied to the ^1H spins. This experiment correlates the recoupled chemical shift anisotropy powder pattern in the ω_1 dimension with the recoupled ^1H–^{13}C dipolar powder pattern in the ω_2 dimension. The peculiar shape of the two-dimensional spectrum depends on the relative orientations of the two tensors, namely chemical shift tensor of the carbonyl ^{13}C and the ^1H–^{13}C dipolar coupling tensor. Since the orientation of the principal axes of the chemical shift tensor is well conserved with respect to the molecular frame of the peptide fragment (actually, only conservation of the orientation of the δ_{33} tensorial component is needed), these two-dimensional patterns can be used for determining the peptide angle ψ.

Other experiments can, in principle, give similar information to the RACO experiment. Moreover, many of these are simpler methods from an experimental point of view, because they use either static samples (similar to SELFIDOQ experiment

of Schmidt-Rohr [**54**]), or off-magic-angle spinning, or slow magic-angle spinning so that there is no need to recouple the anisotropic interactions. However, the advantage of the fast magic-angle spinning used in the RACO experiment is that the homonuclear ^{13}C–^{13}C dipole–dipole coupling is removed, and it is, therefore, easy to interpret and simulate the resulting two-dimensional powder patterns even in uniformly ^{13}C-labelled samples. Also, in contrast to the SELFIDOQ experiment [**54**], where the orientation of the chemical shift tensor of the carbonyl ^{13}C site in the molecular frame must be known exactly for the elucidation of the χ angle, RACO is almost released from this demand. Both the dihedral angle χ and the carbonyl ^{13}C chemical shift tensor orientation in the molecular frame can be determined from comparison of the observed two-dimensional RACO spectrum with simulated spectra. Only one assumption is made in the interpretation of a RACO spectrum: the most shielding direction of the chemical shift tensor (the direction of δ_{33}) is assumed to be oriented perpendicular to the C_α–C_1 = O plane. This assumption is reasonable, since the measured deviations from the assumed orientation are only a few degrees for both carboxyl and carbonyl carbons, as discussed previously in this chapter.

The relative orientation between the two tensors described by the two angles λ and μ, as defined in Fig. 7.46(b), can be redefined in terms of the dihedral angle of interest, ψ, and the H–C_α–C_1 angle θ (Fig. 7.46(a)). The latter angle, though not known from any experimental determination, can be safely assumed to be equal to the tetrahedral angle, given the sp^3-hybridization of the C_α carbon. The geometrical transformation between (λ, μ) and (θ, ψ) is worth mentioning here:

$$\lambda = \left(\frac{\sin\theta\cos\psi}{|\sin\theta\cos\psi|}\right)\arccos\left(\frac{\cos\theta}{\sqrt{\cos^2\theta + \sin^2\theta\cos^2\psi}}\right)$$
$$\mu = \arccos(\sin\theta\sin\psi) \qquad (7.22)$$

With these assumptions, the dihedral angle ψ is the unique parameter necessary to determine the H–C_α direction in the molecular frame. One can also calculate the RACO spectrum from a set of (ψ, Λ) angles (where Λ is defined in Fig. 7.46(a)) provided that the principal values of the carbonyl ^{13}C chemical shift tensor and the ^1H–$^{13}C_\alpha$ dipolar-coupling constant are known. Conversely, one can fit the calculated two-dimensional spectrum to the experimental one and estimate both of the dihedral angles ψ and Λ, together with the principal values of the two tensors.

However, there are some limitations of the RACO method: it is impossible to distinguish between the following four mutual tensor orientations: (ψ, Λ), $(-\chi, \Lambda)$, $(\pi - \psi, -\Lambda)$ and $(\pi + \psi, -\Lambda)$ which all give the same two-dimensional spectrum. This comes from the symmetries of the chemical shift and dipolar tensors with respect to reflections in the $x^{mol}y^{mol}$ and $x^{mol}z^{mol}$ planes of the molecular frame.

Figure 7.47 shows calculated RACO spectra for the O–C_1–C_α–H system for different sets of the two angles (ψ, Λ) with $\Lambda = 0$ and $-30°$ and a variety of values for

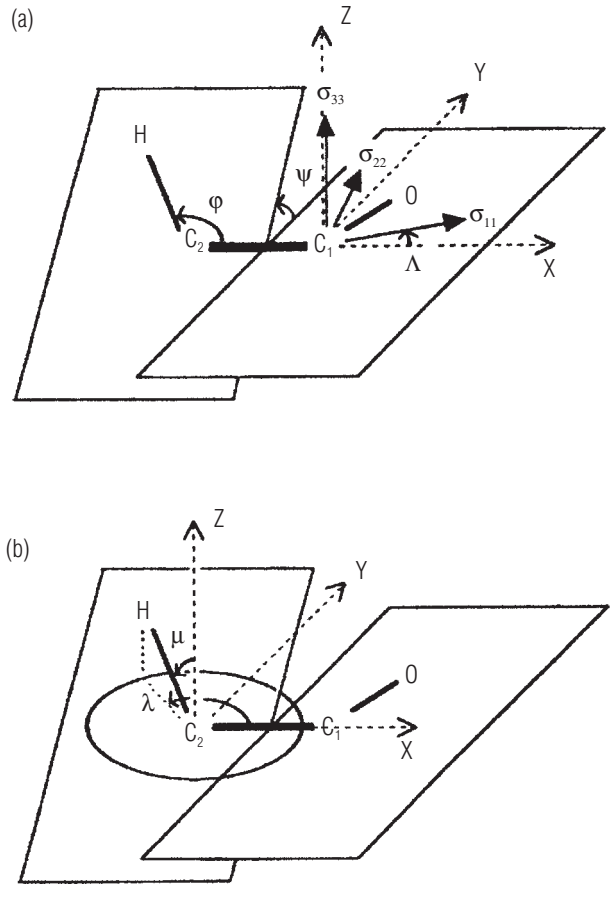

Fig. 7.46 (a) The $^{13}C_1$ chemical shift tensor orientation Λ and the dihedral angle ψ in the O–$^{13}C_1$–$^{13}C_2$–H molecular fragment. (b) The $^{13}C_2$–H bond direction (λ, μ). The *X* and *Z* axes of the molecular frame are parallel to the $^{13}C_2$–$^{13}C_1$ bond and perpendicular to the O–$^{13}C_1$–$^{13}C_2$ plane, respectively. Adapted from ref. [**53**].

the torsion angle ψ. Since Λ ranges only between 0 and –30° in carboxyl carbons, and is around –30° in carbonyl carbons, one can roughly estimate ψ by comparing an experimental spectrum with the map of the calculated spectra. It is quite clear from Fig. 7.47 that the shape of the two-dimensional RACO powder pattern is very sensitive to the both dihedral angles, ψ and Λ.

A convincing comparison between the calculated and experimental RACO spectra of 1,2–$^{13}C_2$–DL-alanine is presented in Fig. 7.48. The torsion angles (χ, Λ) have been determined to be either (137° ± 7°, –6°) or (223° ± 7°, –6°). The former value for ψ is very close to 135.5° obtained from a neutron diffraction study [**194**]. The other two possible sets of angles, (43°, 6°) and (–43°, 6°), which also give the same calculated RACO spectrum, have been discarded on the basis that the δ_{22} direction of the carbonyl ^{13}C chemical shift tensor is known to be oriented towards C═O. All data needed for the calculations of RACO spectra, i.e. chemical shift tensor principal values of the carbonyl ^{13}C carbon site, the C_α–H bond length and the C_1–C_α–H bond angle, were either taken from the literature or measured by the inventors of the RACO method [**53**].

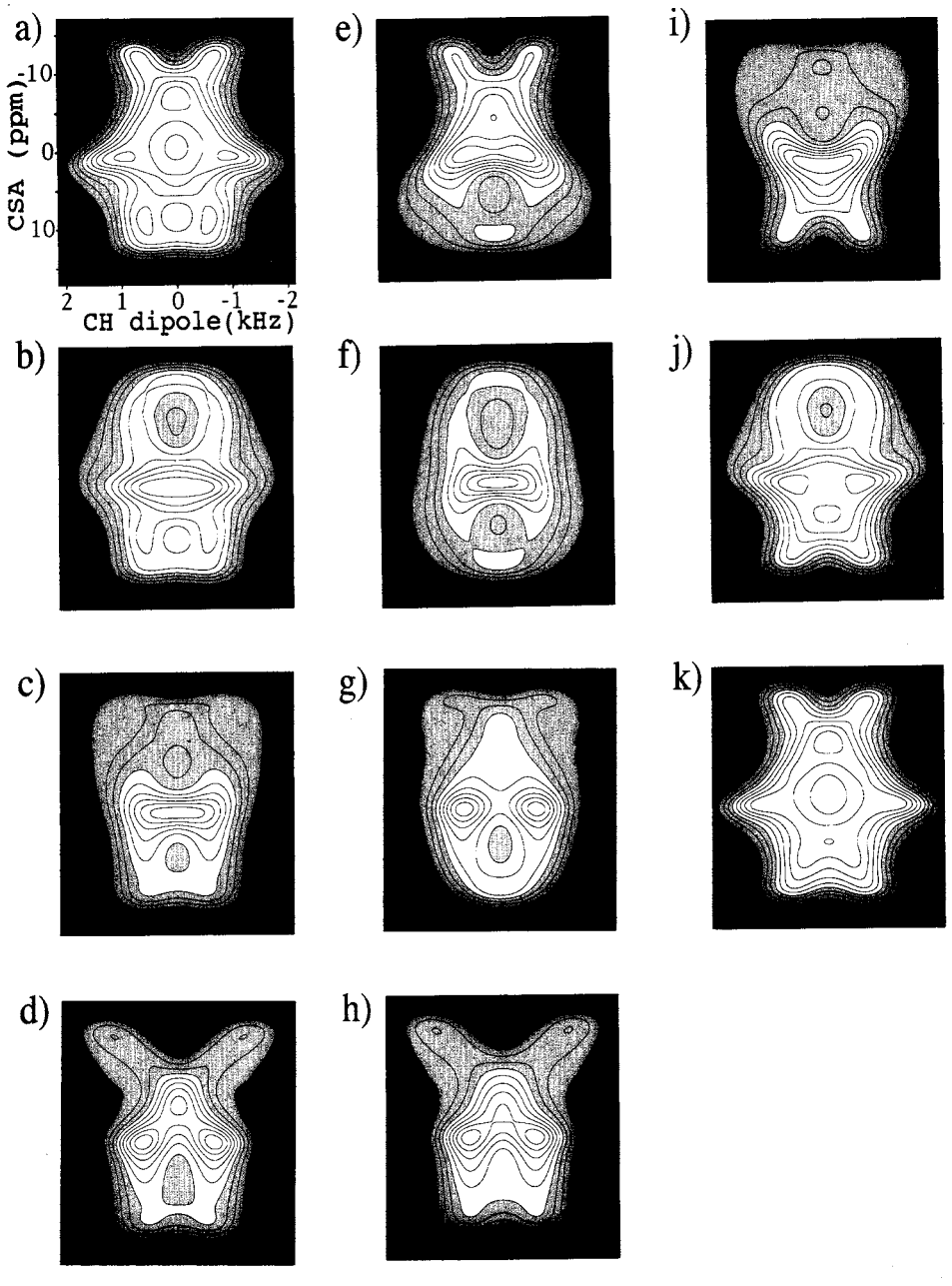

Fig. 7.47 Dihedral angle ψ dependence of simulated RACO spectra for Λ = 0° and –30° and different values for ψ. Simulated spectra were obtained with (ψ, Λ) equal to (a) (0°, 0°), (b) (30°, 0°), (c) (60°, 0°), (d) (90°, 0°), (e) (0°, –30°), (f) (30°, –30°), (g) (60°, –30°), (h) (90°, –30°), (i) (120°, –30°), (j) (150°, –30°), (k) (180°, –30°) and with the following assumptions: direction of the δ_{33} axis is perpendicular to the O–$^{13}C_1$–$^{13}C_2$ plane, the $^{13}C_1$–$^{13}C_2$–H bond angle is 108.55°, the $^{13}C_2$–H bond length is 1.13 Å and the principal values of the carbonyl ^{13}C chemical shift tensor are as in DL-alanine. Adapted from ref. [**53**].

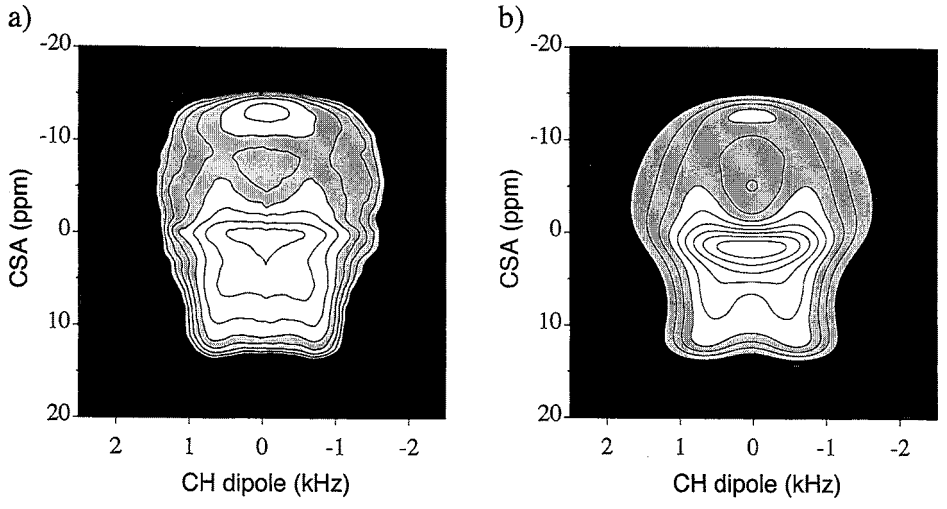

Fig. 7.48 (a) 75.55 MHz ^{13}C magic-angle spinning ($\nu_R = 4060$ Hz) RACO spectrum of DL-alanine-1,2-$^{13}C_2$ obtained using the pulse sequence shown in Fig. 7.45(b). The rf amplitudes of the selective pulses for the C_1 and C_2 carbons were 780 and 710 Hz, respectively. A decoupling field of 90 kHz was applied in the t_1 period and the mixing period. The mixing time is 8 rotation periods (ca. 2 ms). The ratio δ of the FSLG-2 duration in the cycle time is $\frac{1}{7}$. The scaling factors for the f_1 and f_2 dimensions are 0.2 and $1/7\sqrt{3}$, respectively. Other experimental details can be found in ref. [**53**]. (b) Simulated RACO spectrum for DL-alanine-1,2-$^{13}C_2$ with $\psi = 137°$ and $\Lambda = -6°$ and other parameters as given in Fig. 7.47. Adapted from ref. [**53**].

Attractive though the RACO experiment is, it is clear that it has a number of complexities in both the experimental realization and in the simulations of the resulting spectra. In particular, symmetries of the chemical shift and dipolar tensors give a number of uncertainties in the determination of torsion angles.

Finally, it is worth mentioning that the class of dipolar–chemical shift tensor correlation experiments for measuring torsion angles is constantly expanding with new methods. For example, Hong et al. have designed a (^1H–^{13}C dipolar)–(^{15}N chemical shift tensor) correlation experiment for measuring the protein torsion angle ϕ [**195**]. In this experiment, performed under magic-angle spinning, the ^{13}C magnetization evolves rotor synchronously under the ^1H–^{13}C dipolar coupling and the ^{15}N chemical shift interaction during two separately but synchronously incremented t_1 periods (Fig. 7.49). The method, in principle, can distinguish ϕ angles over the full range of 360° when the amide ^{15}N chemical shift tensor is non-axial and does not possess reflection symmetry with respect to the peptide bond. The techique exhibits the highest sensitivity to ϕ torsion angles in the β-sheet structure region as has been demonstrated by simulations and also experimentally on the well-characterized model peptide ^{15}N-acetyl-D,L-valine (solid-state NMR: $\phi = -140°$ [**195**]; X-ray single crystal diffraction: $\phi = -136.5°$ [**196**]).

However, both orientations and principal values of the amide ^{15}N chemical shift tensor are less well conserved in different peptides compared with the carbonyl ^{13}C chemical shift tensor which adds uncertainties in the torsion angle determination.

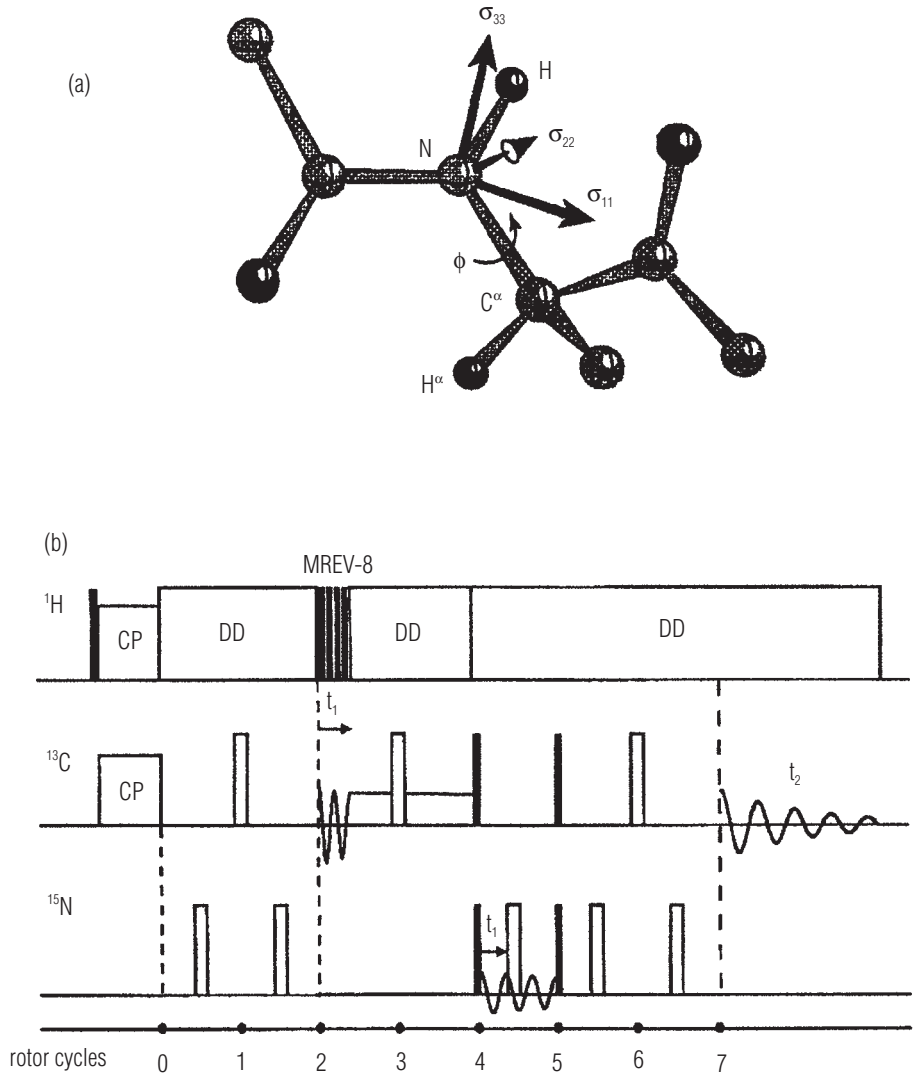

Fig. 7.49 (b) Pulse sequence for measuring the protein ϕ torsion angle (illustrated in (a)) by correlating ^{15}N amide chemical shift tensor and C_α–H_α dipolar-coupling tensor under magic-angle spinning. After the cross-polarization from ^1H to ^{13}C spins, the ^{15}N–$^{13}C_\alpha$ dipolar coupling is recoupled with a REDOR sequence. During the t_1 period, antiphase magnetization terms $\hat{I}_x^C\hat{I}_z^N$ and $\hat{I}_z^C\hat{I}_x^N$ (C and N refer to ^{13}C and ^{15}N spin operators, respectively) evolve under the ^1H–^{13}C dipolar coupling (MREV-8 sequence is applied to ^1H spins) and the doubled ^{15}N chemical shift anisotropy, separately but synchronously. A moving ^{15}N pulse matches the ^{15}N evolution time to the ^1H–^{13}C coupling period as well as doubling the apparent magnitude of the ^{15}N chemical shift anisotropy. This makes the effective strengths of the ^{15}N chemical shift anisotropy and ^1H–^{13}C dipolar coupling comparable, which enhances the spectral variation with respect to the torsion angle ϕ. Finally, another pair of 90° pulses and a REDOR mixing period convert the coherence $\hat{I}_z^C\hat{I}_x^N$ into observable ^{13}C magnetization and the isotropic ^{13}C chemical shifts are detected during t_2 to provide site resolution. Absorptive, sign-sensitive spectra in f_1 are obtained by recording the cosine and sine components of the ^{15}N chemical shift in separate data sets. Adapted from ref. [**195**].

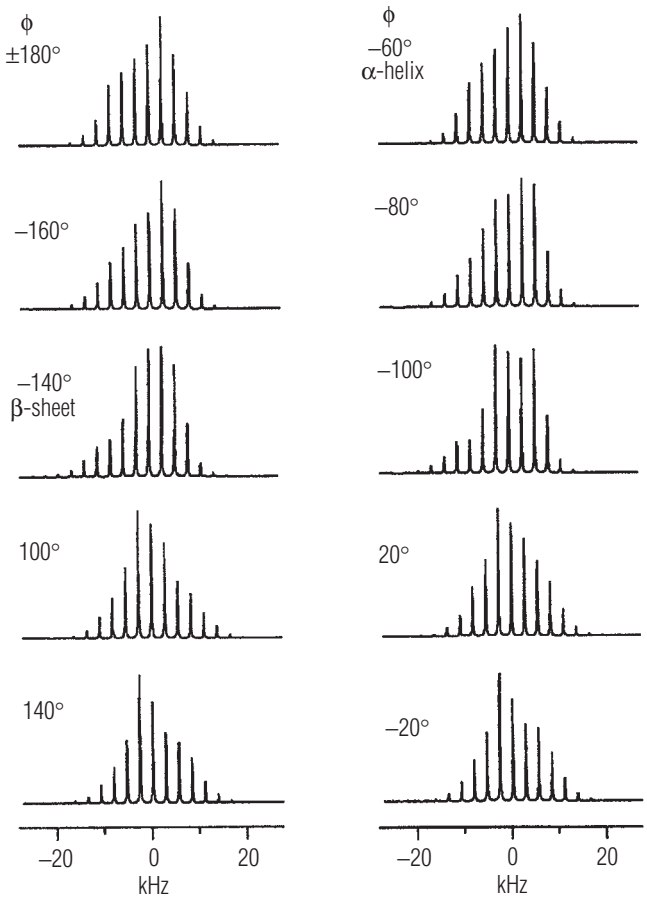

Fig. 7.50 Calculated ($^1H_\alpha$–$^{13}C_\alpha$ dipolar)–(^{15}N chemical shift tensor) magic-angle spinning (ν_R = 2778 Hz) correlation spectra as a function of the torsion angle ϕ with 20° increments. Simulation parameters were: ^{15}N Δ_{cs} = –8512 Hz (–107 ppm at B_0 = 9.4 T), η_{cs} = 0.27, d_{CH} = 10.4 kHz (measured experimentally in the DIPSHIFT experiment); the Euler angles rotating the ^{15}N chemical shift tensor to the ^{15}N–$^{13}C_\alpha$ molecular frame are (α_N, β_N, γ_N) = (–20°, 137°, 240° – ϕ); the corresponding Euler angles for the $^1H_\alpha$–$^{13}C_\alpha$ dipolar-coupling tensor are (0°, 109.5°, 0°). Though spectra ϕ = 120° ± ζ (ζ is an arbitrary angle) are similar, they are different for ϕ = [–180°, 180°]. Adapted from ref. [**195**].

Also, similarities between (^1H–^{13}C dipolar)–(^{15}N chemical shift tensor) correlation spectra with pairs ϕ = 120° ± ζ (ζ is an arbitrary angle) still remain, though spectral differences are visible for some pairs of the complementary ϕ torsion angles (Fig. 7.50). If the orientation of the ^{15}N chemical shift tensor principal axis δ_{11} is not known, the best-fit procedure still provides a good estimate of ϕ, but with a two-fold degeneracy, similar to the RACO experiment of Ishii et al. discussed above [**53**].

7.4.3 Experiments correlating two dipole–dipole coupling tensors

Another class of methods for direct torsion angle measurements uses the effect of two dipolar tensors, on the evolution of either homonuclear or heteronuclear multiple-quantum coherences, zero-, double-quantum (2Q) or triple-quantum (3Q) ones. Dipolar-coupling tensors are of course oriented exactly along the internuclear axis of the dipolar-coupled spins, so the problem of uncertain tensor orientation discussed in the previous section is not an issue here.

The HCCH–2Q-HLF experiment

HCCH–Double-Quantum Heteronuclear Local Field spectroscopy (HCCH–2Q-HLF) [**49**] was invented for estimating the torsion angle in a $^{13}C_2$-labelled $^{1}H–^{13}C–^{13}C–^{1}H$ molecular fragment. The method exploits the evolution of the excited double-quantum coherence between the neighbouring ^{13}C spins in the presence of local heteronuclear $^{1}H–^{13}C$ dipolar fields from the directly bonded ^{1}H spins. The heteronuclear dipolar fields depend on the spin state of protons, and also on the geometric relationship of the two $^{1}H–^{13}C$ coupling tensors. Roughly speaking, in the *trans*-conformation of the H–C–C–H molecular fragment ($\psi = 180°$), the two $^{1}H–^{13}C$ vectors are aligned and, therefore, the four $^{1}H–^{13}C$ dipolar fields cancel each other if the two ^{1}H spins have different spin states. i.e. $|\alpha\beta\rangle$ or $|\beta\alpha\rangle$, where α and β represent the two possible ^{1}H spin states. The $^{13}C_2$ double-quantum coherence is only slightly affected by the local $^{1}H–^{13}C$ dipolar fields from the other two possible spin states of the protons, i.e. $|\alpha\alpha\rangle$ or $|\beta\beta\rangle$. In contrast, for the *cis*-conformation ($\chi = 0$), the two $^{1}H–^{13}C$ bond vectors are not parallel, and so the heteronuclear local fields add constructively for any combination of proton spin states and, therefore, have the largest possible effect on $^{13}C_2$ double-quantum coherence evolution. Other possible relative orientations of the two $^{1}H–^{13}C$ dipolar tensors can also be determined from simulations of the evolution of the double-quantum coherence in the presence of the heteronuclear dipolar fields.

The HCCH–2Q-HLF experiment operates under magic-angle spinning conditions which enforces its sensitivity and resolution. In a rotating sample, the dipolar fields are modulated in time, generating a $^{13}C_2$ double-quantum sideband patterns, the shape of which depends on the H–C–C–H torsion angle.

The pulse sequence for the HCCH–2Q-HLF experiment is shown in Fig. 7.51. After cross-polarization from ^{1}H to ^{13}C with a slight ramp of the ^{13}C rf field to enhance reproducibility [**13**], the ^{13}C transverse magnetization is rotated to the laboratory frame z axis by a 90° pulse of appropriate phase. The C7 pulse sequence (see Section 3.2.2) [**43**] is then applied to create double-quantum coherence between the dipolar-coupled pair of ^{13}C spins. The ^{13}C double-quantum coherences are allowed to evolve for an interval of one rotor period, τ_R, which is divided into two parts:

(1) The first portion is a variable interval t_1, occupied by a homonuclear dipolar decoupling sequence (semiwindowless MREV-8 [**9**, **10**]) applied to the ^{1}H spins. Similar to the FSLG-2 sequence [**8**] used in the RACO experiment of Ishii et al. [**53**] described in Section 7.4.2, MREV-8 effectively suppresses homonuclear dipolar $^{1}H–^{1}H$ couplings while heteronuclear $^{1}H–^{13}C$ dipolar couplings are scaled down by a scaling factor $k < 1$. One cycle of a semiwindowless MREV-8 sequence consists of eight pulses conjoined in pairs with the phases as depicted in Fig. 7.51. Theoretically, these are 90° pulses; in practice pulses of ~106° applied slightly off resonance give a better performance of the

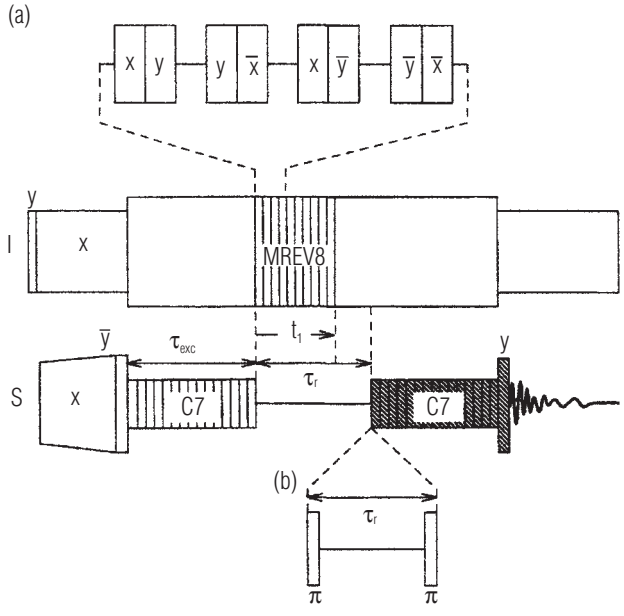

Fig. 7.51 Pulse sequences for determination of ^{1}H–^{13}C–^{13}C–^{1}H torsion angles under magic-angle spinning, through ^{1}H–^{13}C dipolar modulation of the ^{13}C–^{13}C double-quantum coherences. (a) Simplified pulse sequence requiring that the rf carrier is set to the mean of the ^{13}C isotropic shift frequencies of the two ^{13}C-labelled carbon sites. After the ramped cross-polarization pulse and a 90° pulse, the homonuclear recoupling sequence C7 creates double-quantum coherences which evolve under ^{1}H–^{13}C dipolar couplings (MREV-8) for a fraction of a rotation period (t_1). Then double-quantum coherences are reconverted to observable ^{13}C magnetization by a second C7 block and a 90° pulse. Also a standard double-quantum-filtering phase cycle is applied to the shaded part of the sequence. (b) An extra rotor period of unmodulated proton decoupling, bracketed by two 180° pulses, is inserted in order to suppress evolution due to ^{13}C isotropic shifts. Adapted from ref. [**49**].

MREV-8 sequence [8]. The theoretical value for the scaling factor k (scaling of the heteronuclear ^{1}H–^{13}C dipole–dipole couplings) for the MREV-8 sequence, assuming infinitely strong rf pulses, is 0.471.

(2) During the second interval, τ_R–t_1, occupied by ordinary unmodulated high-power proton decoupling, all ^{1}H–^{13}C dipolar couplings are suppressed. Therefore, by incrementing the first part of the interval (t_1), the evolution of the double-quantum coherence is affected by the heteronuclear ^{1}H–^{13}C dipolar interactions between the ^{13}C-labelled carbons and nearby protons, only. In the original version of the HCCH–2Q-HLF experiment, a series of 21 experiments were conducted keeping the total interval for the double-quantum coherence evolution fixed and equal to one rotor period τ_R and incrementing t_1 from 0 to τ_R in steps of $\tau_{MREV}/4$, where τ_{MREV} is adjusted to be $\tau_R/5$. The latter harmonic condition between τ_{MREV} and τ_R is chosen on the basis that the size of the ^{1}H–^{1}H homonuclear dipolar interaction (~20 kHz) which has to be suppressed by the MREV-8 sequence,[3] is approximately five times larger than the spinning frequency of the sample (~4 kHz) at which the experiment is usually performed.

Finally, after the double-quantum coherence evolution period, the modulated double-quantum coherences are reconverted into z magnetization by a second C7 sequence of the same duration as the first. A last 90° pulse converts the z magnetization into observable magnetization. A standard double-quantum filtering phase cycle is applied on the entire reconversion block. This suppresses the background signals from natural abundance ^{13}C spins present in the sample.

The design of the HCCH–2Q-HLF sequence is based on the following theoretical arguments: (i) the anisotropic ^{13}C chemical shifts average to zero over a full rotor period τ_R so by keeping the double-quantum coherences evolution period fixed and equal to τ_R the ^{13}C chemical shift anisotropy has no effect on the double-quantum coherence; (ii) the homonuclear ^{13}C–^{13}C coupling terms may be ignored since double-quantum coherences evolution is independent of the spin–spin couplings; (iii) when the rf carrier is set to the mean of the ^{13}C isotropic shift frequencies of the ^{13}C spin pair, the effect of the isotropic ^{13}C shift on the double-quantum coherence is also removed; (iv) as the heteronuclear ^{1}H–^{13}C dipolar interaction terms of the hamiltonian describing the spin system commute with the other terms in the hamiltonian, they may be considered separately, and are the only terms which actively affect at the dynamics of the $^{13}C_2$ double-quantum coherence during the variable interval t_1.

The HCCH–2Q-HLF experiment has been successfully demonstrated on a number of systems including biologically important ones such as the membrane protein rhodopsin [**163**] and the meta-I photo-intermediate of bovine rhodopsin [**164**].

Results for model systems, polycrystalline ammonium hydrogen 2,2′-$^{13}C_2$-maleate ($^{13}C_2$-AHM) (Fig. 7.52(a)) and diammonium 2,2′-$^{13}C_2$-fumarate ($^{13}C_2$-DAF) (Fig. 7.52(b)) are very convincing [**49**]. In these systems the H–C═C–H moiety is *cis* and *trans*, respectively. The modulations of the double-quantum filtered signal amplitudes for $^{13}C_2$-AHM and $^{13}C_2$-DAF in the HCCH–2Q-HLF experiment are very different (Figs 7.52(c) and 7.52(d) respectively). The modulation amplitude is larger for $^{13}C_2$-AHM as expected, since there is no destructive interference of the local heteronuclear fields for this system. Since the amplitude data have been collected by t_1 increments covering only one rotor period, additional numerous duplication of the dataset with a proper correction on the exponential decay of the double-quantum coherence was needed before Fourier transformation with respect to t_1. Fourier transformation in both dimensions gave rise to the characteristically different spinning sideband patterns (in ω_1) for the two model systems (Figs 7.52(e) and 7.52(f)). The latter reflect genuine modulations of the double-quantum coherences by net heteronuclear local dipolar fields which in turn depends on the relative orientation of the C–H bond vectors. The modulations (and the double-quantum spinning sideband patterns) appeared to be consistent with the *cis*- (±20°) and *trans*- (±10°) conformations for $^{13}C_2$-AHM and $^{13}C_2$-DAF, respectively from simulations (see Figs 7.52 and 7.53 [**49, 197**]). The H–C–C–H torsion angles have been

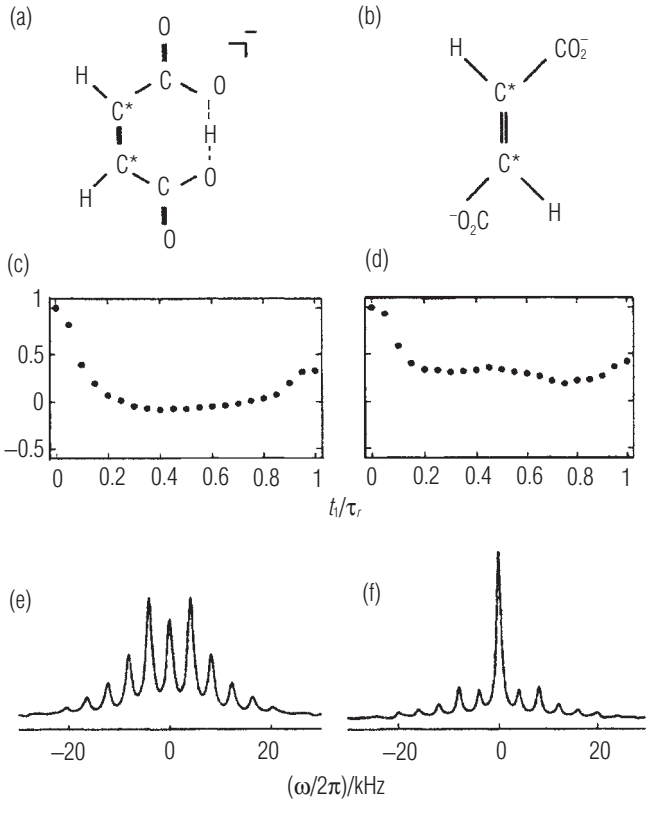

Fig. 7.52 50.323 MHz ^{13}C HCCH–2Q-HFL magic-angle spinning (ν_R = 4056 Hz) experimental results for anions of ammonium hydrogen maleate ($^{13}C_2$-AHM) and diammonium furmarate ($^{13}C_2$-DAF) (structures are shown in (a) and (b), the ammonium cations are not shown). (c) and (d) Modulations of the double-quantum-filtered signal of AHM and DAF respectively, on variation of the homonuclear decoupling period t_1. (e) and (f) Double-quantum spinning sideband patterns obtained by duplication of the s(t_1, f_2) data sets (shown in (c) and (d)) with a correction for the exponential decay of the double-quantum coherence and Fourier transformation with respect to t_1 Adapted from ref. [**49**].

estimated by fitting the experimental amplitudes as a function of the double-quantum evolution interval t_1, $a_{exp}(t_1)$, to theoretical curves of the form:

$$a(t_1) = Af(t_1, k, \mathbf{G})\exp\{-\lambda t_1\} \tag{7.23}$$

where A scales the experimental vertical scale to simulated amplitudes, f is a theoretically calculated function of the evolution period t_1, k is the scaling factor of the MREV-8 pulse sequence, and **G** is the set of geometrical parameters characterizing the positions of the atoms in the H–C–C–H fragment. **G** includes the C–H bond length r_{CH}, the C–C bond length, r_{CC}, the H–C–C bond angles, and the H–C–C–H torsion angle of interest. Finally, λ is a phenomenological damping time constant which takes into account relaxation of the $^{13}C_2$ double-quantum coherence under the ^1H multiple-pulse sequence in t_1. In practice, f may readily be calculated numerically for different molecular geometries [**49**] while λ and A can be determined by least-square fits of $a(t_1)$ to the experimental set of amplitudes $a_{exp}(t_1)$. The details of these simulations can be found either in the original paper [**49**] or in the extended analysis by Feng [**197**]. The results of such simulations for the full range of torsion angles for the double-quantum-filtered signal amplitudes in a HCCH–2Q-HLF experiment for systems with the local bond geometry as in $^{13}C_2$-AHM and $^{13}C_2$-DAF are shown in Fig. 7.54 [**197**]. Note that the simulations reveal ambiguities for

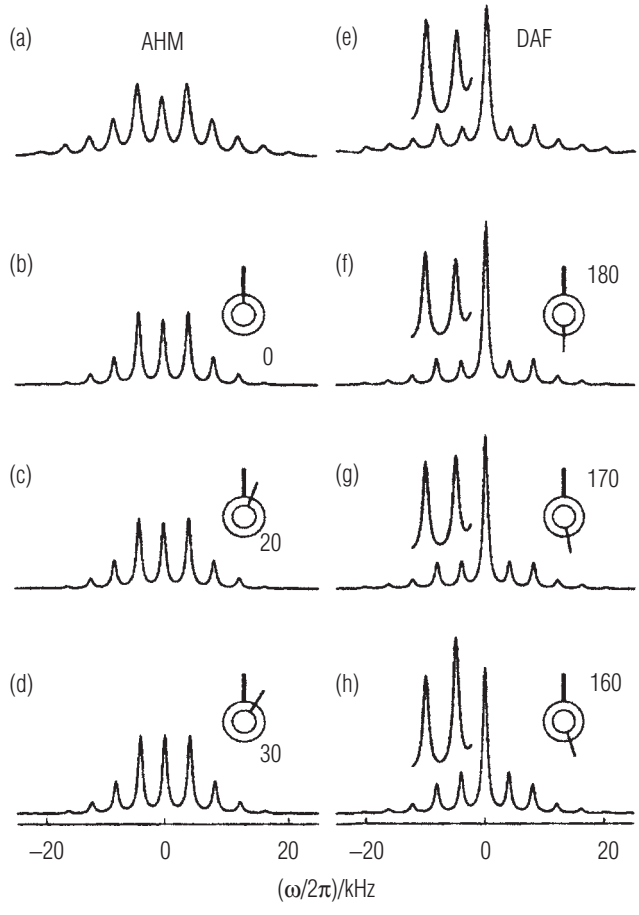

Fig. 7.53 Comparison of HCCH–2Q-HFL experimental results for $^{13}C_2$-AHM and $^{13}C_2$-DAF (given in Fig. 7.52) and simulations. All simulations employed a C–C bond length of 1.33 Å, a C–H bond length of 1.13 Å, a H–C–C dihedral angle of 113.7° and a MREV-8 multiple-pulse scaling factor of $k = 0.43$. The value of ^1H–^{13}C–^{13}C–^1H torsion angle is shown on the plots. (a) Experimental double-quantum sideband pattern for $^{13}C_2$-AHM. (b) Simulations for an exact *cis* geometry. (c) Simulations for a 20° deviation from *cis* geometry. (d) Simulations for a 30° deviation from *cis* geometry. (e) Experimental double-quantum sideband pattern for $^{13}C_2$-DAF. (f) Simulations for an exact *trans* geometry. (g) Simulations for a 10° deviation from *trans* geometry. (h) Simulations for a 20° deviation from *trans* geometry. In the right-hand column, expansions of the first and second sideband regions are also shown. Adapted from ref. [**49**].

torsion angles in the region of 50° to 120° due to the intrinsic symmetry of the dipolar interaction. Moreover, simulations are insensitive to the sign of the torsion angle. In order to resolve such ambiguities, supplementary information must be obtained by other approaches. The method is, however, very angle-sensitive and gives unambiguous results for torsion angles in the range 130° to 180°, i.e. close to the *trans*-conformation.

This method has been applied to biologically important systems which are inaccessible for studies by other methods, such as X-ray crystallography and solution-state NMR: (i) a $^{13}C_2$-labelled sample of the 41 kD integral membrane visual protein rhodopsin [**163**]; (ii) the meta-I photointermediate of bovine rhodopsin [**164**]; in both studies, the H–C10–C11–H torsion angle of this retinylidene chromophore was determined.

Rhodopsin is the light receptor protein responsible for the primary visual response in vertebrate rod cells. It is a transmembrane, seven-helix G-coupled protein, which has a small molecule of the 11-*cis*-retinylidene chromophore covalently bound to

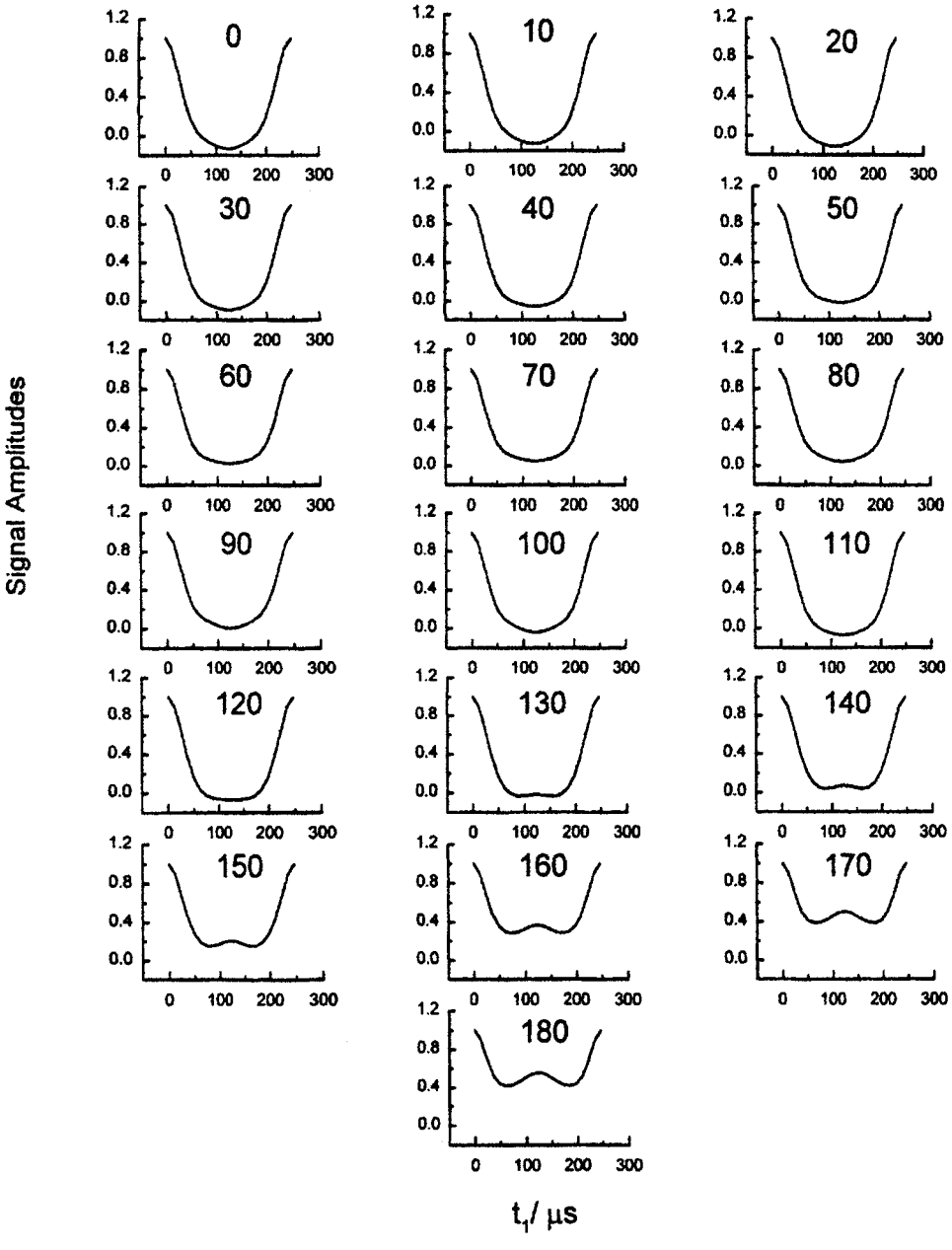

Fig. 7.54 Simulations of the full range of H–C–C–H torsion angles for the double-quantum filtered signal amplitudes in a HCCH–2Q-HLF experiment for systems with the local bond geometry as in AHM and DAF (shown in Fig. 7.52). The torsion angle (in degrees) is indicated in each plot. Adapted from ref. [**197**].

the lysine-296 residue by a protonated Schiff base linkage (see Fig. 7.55 (top)). It is interesting to note that retinal molecules in the all-*trans*-conformation (see Fig. 7.55(a)) have the ability, by simple mixing, to incorporate naturally into the seven-helix 'pro'-rhodopsin protein called opsin. In this bound state the retinylidene chro-

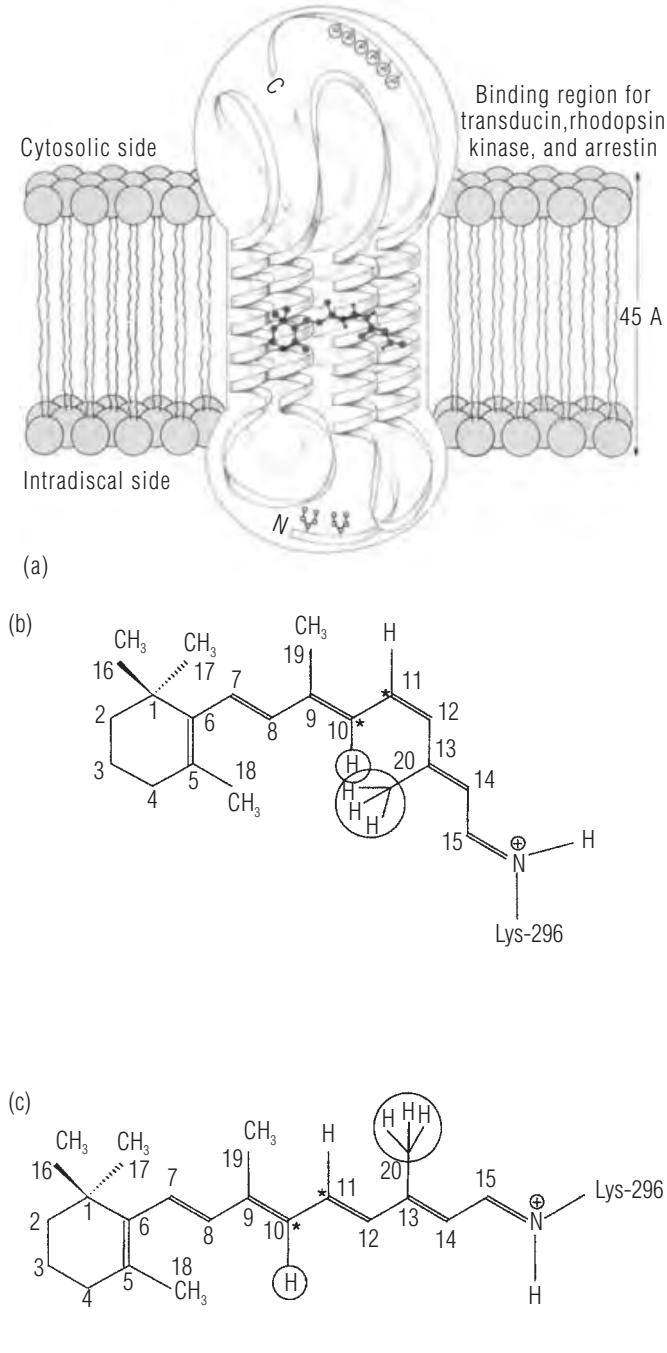

Fig. 7.55 (Top) Model of a transmembrane protein rhodopsin responsible for the primary visual response in vertibrate rod cells. (Reproduced from BIOCHEMISTRY 3/E by Lubert Stryer, 1988.) (Below) Schematic illustration of the molecular structure of the 11-*cis*-retinylidene chromophore in rhodopsin (a), and all-*trans*-retinylidene in photo-intermediate of rhodopsin, metarhodopsin-I, (b). Steric interactions between protons attached to C10 and C20 are shown in both cases. Adapted from ref. [**164**].

mophore in rhodopsin adopts the so-called 11-*cis* conformation shown in Fig. 7.55(b). This geometry of the chromophore with respect to its binding pocket in the protein has been suggested by Smith and co-workers on the basis of ^{13}C isotopic chemical shifts in bovine rhodopsin compared with those in several photointermediates [**198, 199**]. After the absorption of a quantum of light, the retinylidene

isomerizes from 11-*cis* to 11-*trans* [**199**] which leads to the conformational modification of the whole rhodopsin molecule. The latter primary photoproduct is called bathorhodopsin, which gradually passes through a number of other intermediates, including metarhodopsin-I (Fig. 7.56), before the final decomposition to free all-*trans*-retinal and opsin. It is believed that in all these intermediates, the retinylidene chromophore has the extended all-*trans*-conformation. Therefore, the retinal molecule in rhodopsin is a sort of a molecular 'spring' which, after the light absorption, changes its conformation from 11-*cis* to all-*trans* and pushes out the opsin

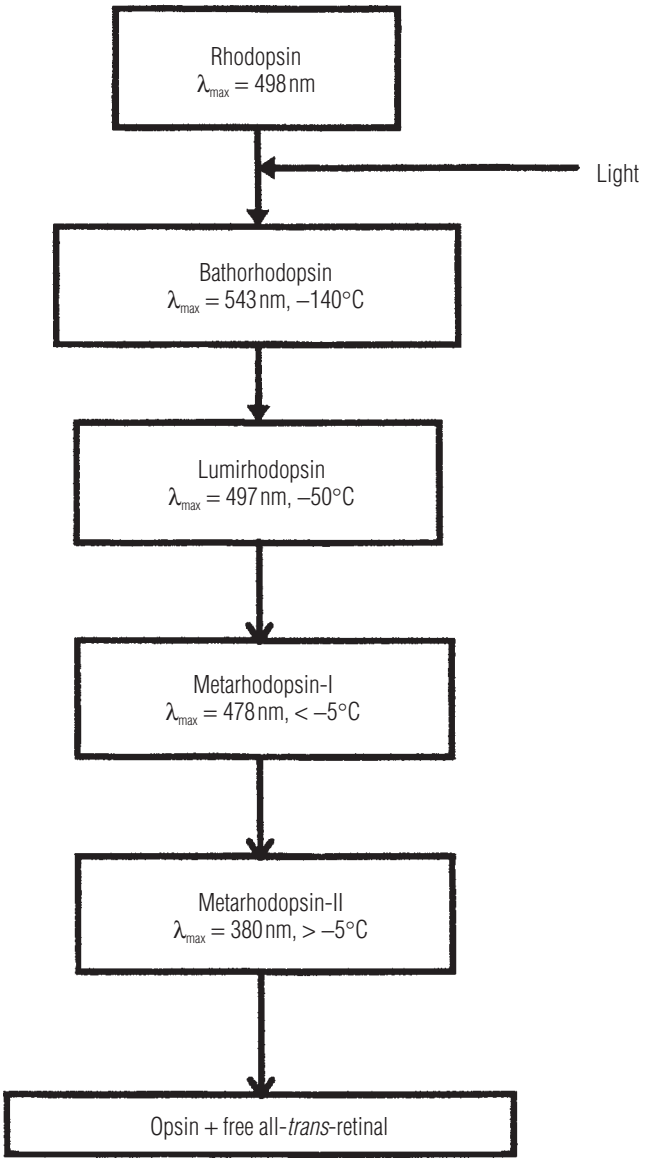

Fig. 7.56 The visual photosequence of bovine rhodopsin. The maximum wavelengths of ultraviolet and visible absorption spectra and the stabilized temperature for each photointermediate are indicated. Adapted from ref. [**164**].

helices. The final modified conformation of rhodopsin triggers the whole cascade of biochemical reactions of vision. The intermediates can be trapped only in the dark (or in far-red light) and at low temperatures.

The photoisomerization process of rhodopsin is extremely fast, lasting only 200 fs [**200**]. This was explained by a steric interaction between the proton attached to C10 and the C20 methyl group (see Fig. 7.55(a)) following a deviation from the planar geometry in the C11–C12 region of the chromophore, which accelerates the isomerization [**201**]. By *ab-initio* Carr–Parrinello calculations the H–C10–C11–H torsion angle in the rhodopsin ground state has been predicted to be close to 165° [**202**].

The system of rhodopsin was ideal for the HCCH–2Q-HLF solid-state NMR experiment. The predicted value of the torsion angle lies in the region of the highest sensitivity of the method, far from regions with ambiguities. The excitation efficiency of the double-quantum coherence is also reasonably high as can be seen in Fig. 7.57(c), which shows the two double-quantum filtered signals from the C10 and C11 ^{13}C-labelled carbon sites of the retinylidene chromophore. The undesired ^{13}C signals from randomly distributed natural ^{13}C spins in the protein and lipid membrane (Fig. 7.57(b)) are completely removed by the double-quantum filtering.

In order to avoid uncertainties associated with the MREV-8 scaling factor k (which depends on the amplitude of the rf pulses, and so deviates from its theoretical value), a polycrystalline sample of all-*trans*-[10,11-$^{13}C_2$]-retinal was used for calibration [**163**]. Single-crystal X-ray diffraction data for this compound confirm the *trans*-conformation of this molecule around the C10–C11 bond, i.e. the H–C10–C11–H torsion angle, ϕ, is very close to 180° [**203**]. The experimental dataset $a_{exp}(t_1)$ (Fig. 7.58(a)) has been successfully fitted to a theoretical curve calculated for $|\phi| = 180°$ and the best fit gave the scaling factor $k = 0.5$. This value was then used in the matching between calculated and experimental data obtained for 10,11-$^{13}C_2$-rhodopsin in the double-quantum heteronuclear local field experiment (Fig. 7.58(b)). The best fit simulations for H–C10–C11–H torsion angle gave a value of $-160° \pm 6°$ as predicted by *ab-initio* calculations [**202**]. The negative sign of ϕ which cannot be determined by the method alone, has been chosen to be consistent with a C11–C12–C13–C14 torsion angle of –140° estimated from the NMR chemical shift data and the known geometry of the chiral binding pocket [**199**].

The other important experiment on the meta-I-photointermediate of bovine rhodopsin confirmed the previously suggested planar *trans*-conformation around the retinylidene H–C10–C11–H bond [**164**]. The method has been also used in conformational studies of some carbohydrates in powder and compared with their structure in aqueous solution [**204**].

Direct determination of the peptide angle ψ, the NCCN–2Q-HLF experiment

The peptide angle ψ is the torsion angle of the N–C_α–C_1–N molecular fragment in the peptide backbone. The ideas of the HCCH–2Q-HLF experiment can be

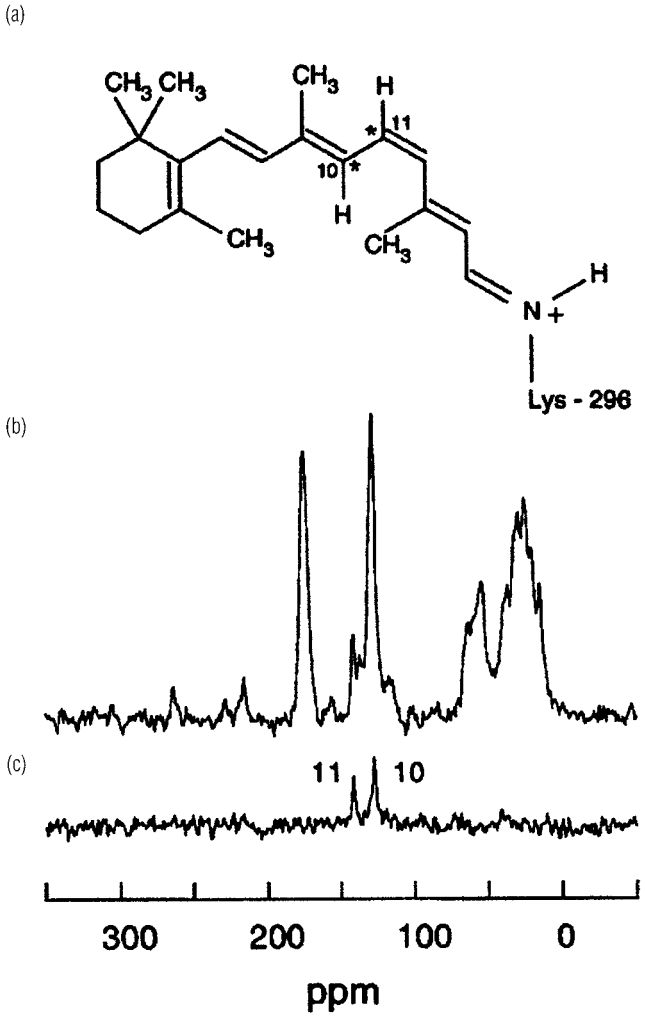

Fig. 7.57 (a) Molecular structure of the retinylidene chromophore in rhodopsin. The ^{13}C labels are indicated by an asterisk. (b) Cross-polarization magic-angle spinning (ν_R = 4430 Hz) 50.323 MHz ^{13}C NMR spectrum of membrane bound bovine rhodopsin (with doubly ^{13}C-labelled retinal-[10,11-$^{13}C_2$] incorporated). The sample contained ~0.5 μM of $^{13}C_2$-labelled rhodopsin packed into a 4 mm zirconiumoxide rotor. (c) Spectrum obtained by $^{13}C_2$ double-quantum filtration using the C7 sequence. The signals from the $^{13}C_2$-labelled retinal chromophore are selected, while the natural abundance background signals are suppressed. The double-quantum excitation interval was τ_{exc} = 452 μs. Adapted from ref. [**163**].

naturally extended to the measurement of this torsion angle provided that the both carbon sites, C_α and C_1 are ^{13}C-labelled. The evolution of the $^{13}C_2$ double-quantum coherence will be now affected by the N–^{13}C heteronuclear dipolar fields instead of ^1H–^{13}C ones. One important point has to be considered: 99.64% of nitrogen atoms are the ^{14}N isotope with the spin $I = 1$ and very low Larmor frequency $\gamma(^{14}N)$ ($\omega_0(^{14}N) = 0.0723\ \omega_0(^1H)$). This leads to at least two difficulties: (i) a rather weak heteronuclear dipolar field associated with the ^{13}C and ^{14}N spin pair which has to be recoupled under magic-angle spinning; (ii) a theoretical analysis for this system is more complex since the quadrupolar interaction acting on the ^{14}N nuclei has to be taken into account. The problem of measuring the angle ψ can be considerably simplified if ^{14}N is substituted by ^{15}N which has $I = \frac{1}{2}$. Such substitution is possible,

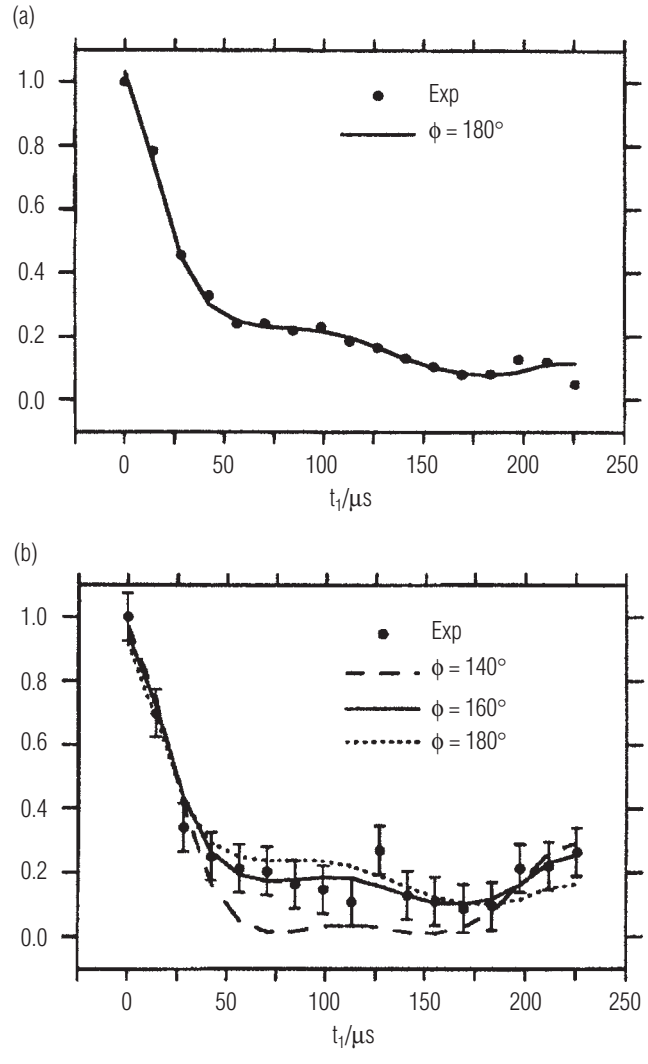

Fig. 7.58 Signal amplitudes for all-*trans*-retinal-[10,11-$^{13}C_2$] (a), and rhodopsin-[10,11-$^{13}C_2$] (b), in a 50.323 MHz ^{13}C HCCH–2Q-HLF NMR experiment. Filled circles: experimental integrated amplitudes as a function of the evolution interval t_1. In (a), solid line: simulation for a ^1H–^{13}C–^{13}C–^1H torsion angle of 180°, H–C–C bond angles of 115°, a C–H bond length of 1.13 Å, a C–C bond length of 1.41 Å, a MREV-8 multiple-pulse scaling factor of $k = 0.50$, and a damping rate constant of $\lambda = 9670\,s^{-1}$. In (b), solid line: simulation for a ^1H–^{13}C–^{13}C–^1H torsion angle of ±160° and damping rate constant $\lambda = 5820\,s^{-1}$. Broken lines: best fit simulations for ^1H–^{13}C–^{13}C–^1H torsion angle of 180° and ±140°. The damping rate constants are $\lambda = 7680\,s^{-1}$ and $5340\,s^{-1}$, respectively. Adapted from ref. [**163**].

for example, by solid-phase peptide synthesis using two selectively labelled amino acids, one with the ^{15}N–$^{13}C_\alpha$–$^{13}C_1$ labelled fragment and the next one in the sequence just ^{15}N-labelled. Nowadays, different ^{13}C and ^{15}N selectively labelled amino acids are readily commercially available.

The first demonstrations of direct measuring of a peptide angle ψ, the so-called NCCN–2Q-HLF experiment, were performed independently by Feng et al. [**51**] and by Costa et al. [**52**]. Alhough the experimental implementations are somewhat different, the idea, theoretical calculations and results on model systems are very similar. The heteronuclear ^{15}N–^{13}C dipole–dipole couplings which are small and removed by a moderate magic-angle spinning rate, are reintroduced by a sequence of recoupling pulses applied to the ^{15}N spins during the evolution of $^{13}C_2$ double-

quantum coherence. As in the HCCH experiment, this evolution depends on the relative orientation of the two ^{15}N–^{13}C dipolar fields. The NCCN–2Q-HLF experiment demands rf irradiation at the Larmor frequencies of the three isotopes, ^{1}H, ^{13}C and ^{15}N, requiring a triply-tuned magic-angle spinning NMR probe and a three-channel NMR spectrometer.

In the experiment of Feng et al. [**51**] (Fig. 7.59) performed at a moderate spinning of ~5 kHz, the rf sequence starts by ramped cross-polarization which is converted into $^{13}C_2$ double-quantum coherence by a 90° pulse followed by a C7 pulse sequence. The $^{13}C_2$ double-quantum coherences then evolve for an interval $t_1 = n\tau_R$, where n is an integer and τ_R is the sample rotation period. During the $^{13}C_2$ double-quantum coherence evolution, strong REDOR 180° pulses are applied to the ^{15}N spins at intervals of $\tau_R/2$, which inhibit the coherent averaging of the ^{15}N–^{13}C dipolar coupling by the magic-angle spinning. The recoupled heteronuclear local fields accelerate the dephasing of the $^{13}C_2$ double-quantum coherences. It is the relative geometry of these local fields around the C_α–C_1 bond which is encoded in the dephasing curve (amplitude of the $^{13}C_2$ double-quantum coherence as a function of t_1). Double-quantum coherences are reconverted into observable ^{13}C magnetization by a second C7 sequence. Double-quantum filtering phase cycling is used (see the shaded pulse

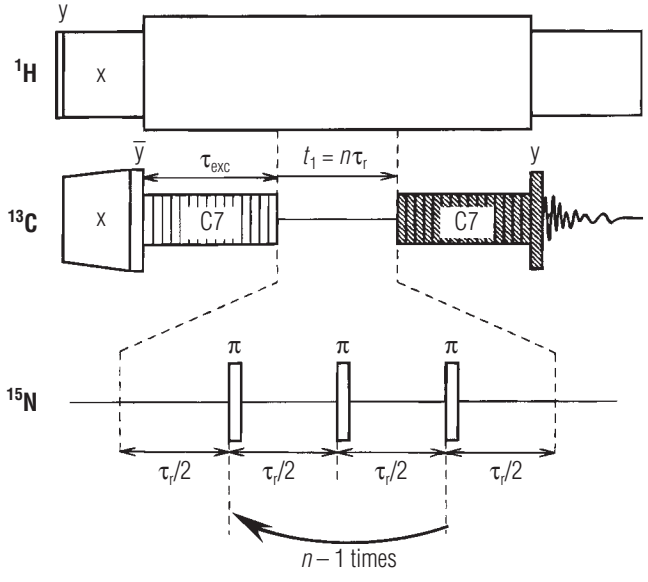

Fig. 7.59 Rf pulse sequence (NCCN–2Q-HLF experiment) for the direct determination of the peptide ψ angle, i.e. the torsion angle of a ^{15}N–^{13}C–^{13}C–^{15}N moiety. After cross-polarization and a 90° pulse, the homonuclear recoupling sequence C7 creates double-quantum coherences which evolve under ^{15}N–^{13}C dipolar couplings (recoupled by REDOR sequence applied to ^{15}N spins) during $t_1 = n\tau_R$. Then double-quantum coherences are reconverted to observable ^{13}C magnetization by a second C7 block and a 90° pulse. Also a standard four-step double-quantum-filtering phase cycle is applied to the shaded part of the sequence. For $n = 0$ ($t_1 = 0$), the evolution period is omitted. The double-quantum decay is calibrated by repeating the pulse sequence with ^{15}N irradiation omitted. Adapted from ref. [**51**].

sequence elements in Fig. 7.59) which eliminates background ^{13}C natural abundance signals. As in REDOR the ^{15}N 180° pulses phase cycled in eight steps according to *XYXY YXYX* [**205**] which minimizes the influence of pulse imperfections. The t_1 evolution period is incremented in steps of τ_R n times. Also, a second set of experiments, without the ^{15}N pulses, is needed to calibrate the relaxation decay of the double-quantum coherences, which is described by the time constant T_2^{2Q}.

In the experiment of Costa et al. [**52**] (Fig. 7.60) performed at the relatively high spinning rate of 14 kHz, the $^{13}C_2$ double-quantum coherences are excited and reconverted by a different recoupling sequence, MELODRAMA-4.5 [**38**] (MD) which requires a rf amplitude of only 4.5 times the spinning speed ($\omega_1 = 4.5\omega_R$), to create $^{13}C_2$ double-quantum coherences, instead of $\omega_1 = 7\omega_R$ in the case of the C7 sequence. Implementations of the C7 sequence at high spinning rates (>10 kHz) are limited because of the large amplitude of rf field applied to ^{13}C spins (>70 kHz) and the unreasonably large amplitude of rf field applied to ^1H spins during any decoupling ($\omega_1(^1H)$ must be larger than $3\omega_1(^{13}C)$) to avoid back cross-polarization from ^{13}C to ^1H during the C7 sequence. The other difference between the two NCCN–2Q-HLF experiments is the application of the synchronous phase inversion rotary resonance recoupling (SPI-R^3) sequence to the ^{15}N spins in the experiment of Costa et al., instead of the REDOR sequence to recouple the ^{13}C–^{15}N dipolar interactions in the t_1 evolution period. R^3-related techniques [**206**] allow heteronuclear dipolar recoupling at low rf power (a radio-frequency amplitude $\omega_1(^{15}N) = \omega_R$) even at high spinning frequencies, when the rotor period shrinks and the finite pulse effects in REDOR sequences of 180° pulses are unavoidable. $X\overline{X}$ phase inversion in the SPI-R^3 sequence has several effects: (i) compensation of the ^{15}N chemical shift anisotropy dependence of the dipolar dynamics; (ii) compensation for ^{15}N isotropic shift offsets, and (iii) compensation for rf inhomogeneity. 180° pulses in the centre of the

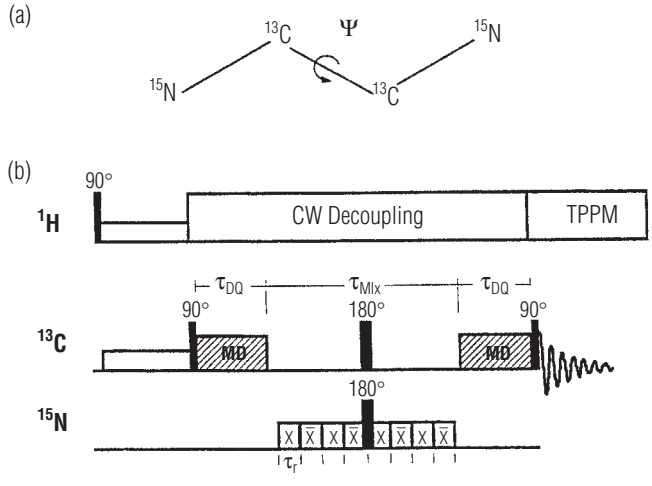

Fig. 7.60 (a) Isotope labelling scheme and (b) pulse sequence for a variant of NCCN–2Q-HLF ψ torsion angle measurement. The sequence differs from that shown in Fig. 7.59 by the use of the MELODRAMA-4.5 (depicted as MD) dipolar-recoupling sequence instead of C7 and by heteronuclear recoupling SPI-R^3 sequence applied to ^{15}N spins instead of REDOR. Adapted from ref. [**52**].

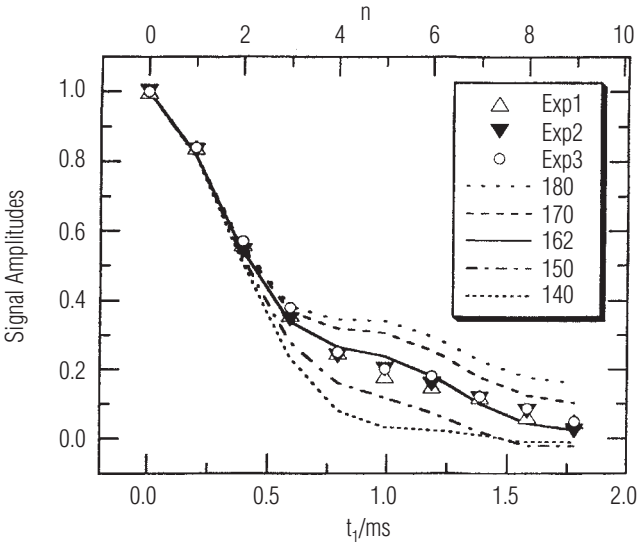

Fig. 7.61 NCCN–2Q-HLF experimental data and simulations for the polycrystalline [^{15}N,$^{13}C_2$-gly]–[^{15}N-gly]–gly•HCl sample. Symbols: experimental signal amplitudes as a function of evolution interval t_1. Three different versions of the ^{15}N 180° pulses were used: well-calibrated 180° pulses (labelled Exp1), misset by 10% 180° pulses (Exp 2) and composite 180° pulses (Exp 3). The experiments were performed at a magnetic field of 9.4 T and under magic-angle spinning with spinning frequency ν_R = 5059 Hz. The double-quantum excitation interval was τ_{exc} = 621 μs. Lines: simulations for torsion angles ψ = ±140°, ±150°, ±160°, ±170° and ±180°, using bond lengths and bond angles from the X-ray structure. Adapted from ref. [**51**].

dephasing period on both ^{13}C and ^{15}N channels refocus ^{13}C chemical shifts while preserving the recoupled ^{15}N–^{13}C dipolar interactions.

The NCCN–2Q-HLF experiment has been demonstrated on [^{15}N,$^{13}C_2$-gly]–[^{15}N-gly]–gly·HCl [**51**] (Fig. 7.61) and [^{15}N,$^{13}C_2$-gly]–[^{15}N-gly]·HCl [**52**] (not shown) polycrystalline samples. The value for the torsion angle of the ^{15}N–^{13}C–^{13}C–^{15}N moiety obtained from single crystal X-ray diffraction is equal to ψ = 164.8° in GGG·HCl [**207**] and ψ = 162.1° in GG·HCl [**208**] corresponding to an extended peptide chain in these polyglycine molecules. The $^{13}C_2$-2Q dephasing curve for the GGG·HCl sample shown in Fig. 7.61 has been simulated and the best fit gave ψ = 162° ± 5° which is in a good agreement with the X-ray data. The simulation parameters were (i) the bond lengths and bond angles of the N–C–C–N moiety, (ii) the N–C–C–N torsion angle ψ and (iii) the decay time constant T_2^{2Q} of the $^{13}C_2$ double-quantum coherence. The bond lengths and bond angles were taken from the X-ray structure. The decay time constant was determined by the calibration experiment (without REDOR 180° pulses applied to the ^{15}N spins). The calculation shows a good result even with the following restrictions: (i) the chemical shift anisotropies are not taken into account; (ii) ^{15}N–^{15}N dipolar couplings (ca. 30 Hz) have been neglected and (iii) ideal 180° pulses are assumed. Note that the torsion angle χ is the only free parameter in the simulations. Also note that the NMR response is insensitive to the sign of ψ due to the symmetry of the interactions around the C–C bond.

The NCCN–2Q-HLF experiment is very sensitive (±5°) to conformation in the region ψ = 120–180° corresponding roughly to the β-sheet structural regime as demonstrated by simulations for a 'standard' peptide backbone geometry (Fig. 7.62(b)). In comparison, a N–C_α REDOR distance measurement (Fig. 7.62(c)) is

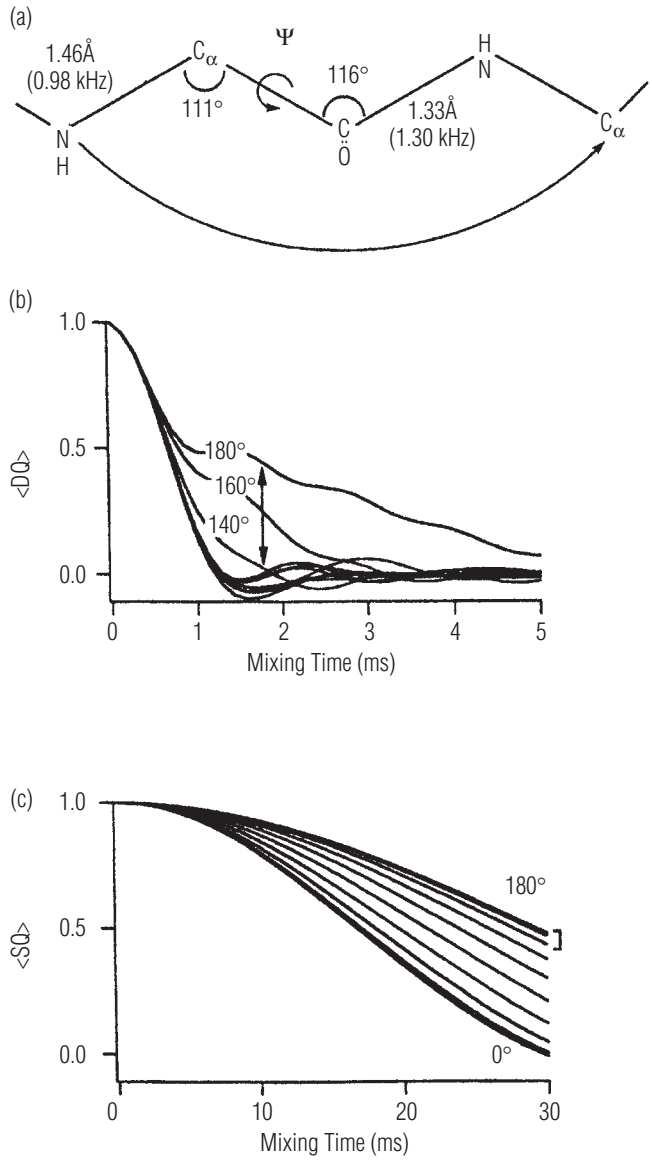

Fig. 7.62 Simulated dephasing curves in the NCCN–2Q-HLF experiment as a function of the ^{15}N–^{13}C–^{13}C–^{15}N torsion angle, ψ. (a) The relevant peptide backbone geometry. (b) Calculated dephasing of double-quantum coherence during mixing as a function of ψ (curves for ψ varying from 0° to 180° in 20° increments are displayed). The method is very sensitive around the *trans*-geometry of the ^{15}N-^{13}C-^{13}C-^{15}N moiety. For comparison, (c) displays the calculated REDOR curves (single-quantum dephasing) for the N–C_α internuclear distance indicated in (a) as a function of χ incremented in steps of 20°. As ψ varies from 180° to 140°, the N–Cα internuclear distance varies by <0.1 Å, corresponding to the spread in single-quantum REDOR dephasing curves indicated by the bracket. Adapted from ref. [**52**].

much less sensitive in this region. As ψ varies from 180° to 140°, the N–C_α internuclear distance varies by less than 0.1 Å, corresponding to the spread in single-quantum REDOR dephasing curves indicated by the bracket in Fig. 7.62(c). Therefore, the sensitivity of the two techniques to ψ in this regime differs by an order of magnitude. However, simulations for the full range of torsion angles measured in the NCCN–2Q-HLF experiment reveal ambiguities in the region of $|\psi| \leq 120°$, as shown in Fig. 7.63 [**197**]. Therefore, the method can be particularly useful in studying β-sheet conformations of peptides.

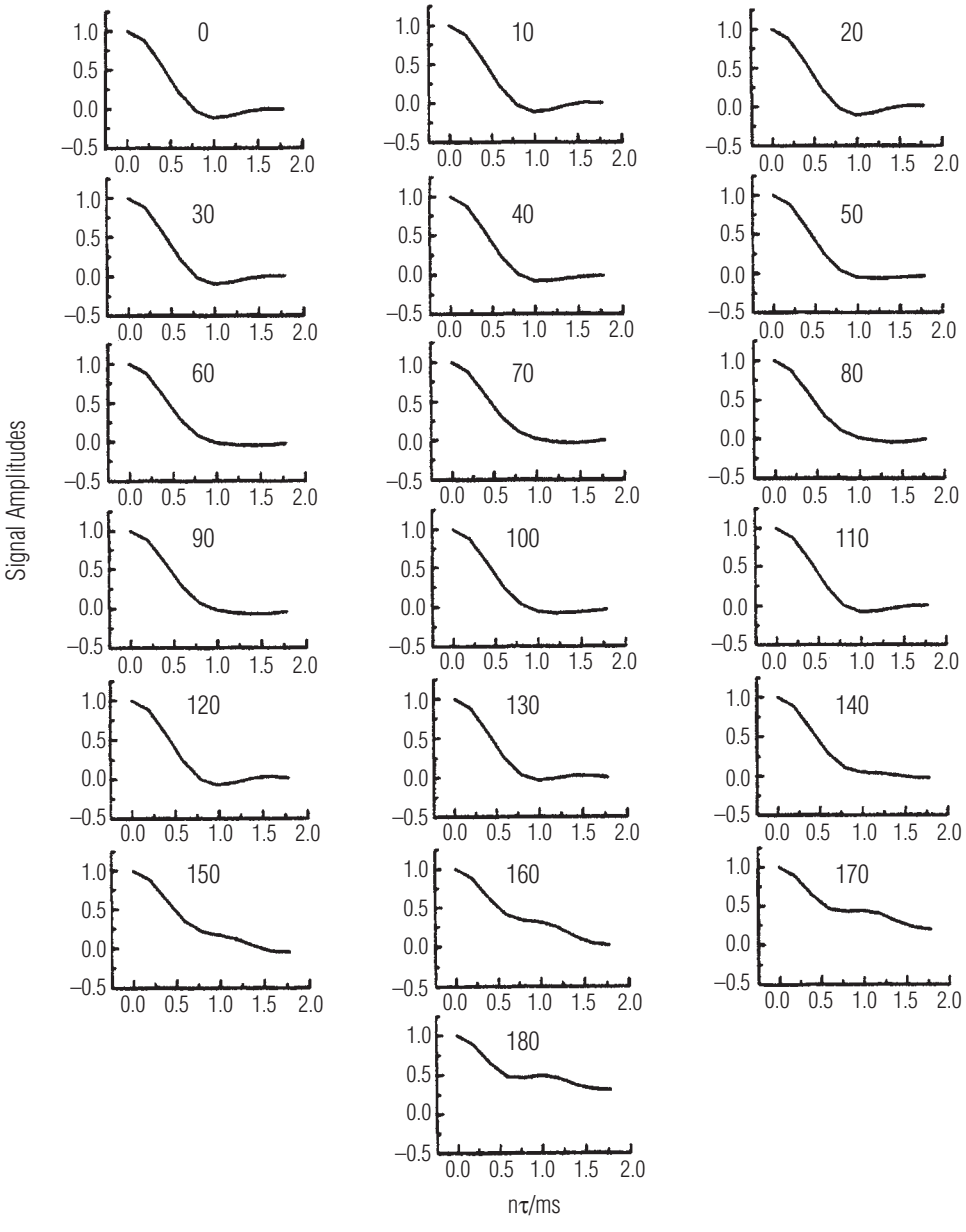

Fig. 7.63 Simulations of the full range of torsion angles for the double-quantum filtered signal amplitudes in a NCCN–2Q-HLF experiment for the 'standard' peptide geometry shown in Fig. 7.62(a). The torsion angle (in degrees) is indicated in each plot. Adapted from ref. [**197**].

Recently, high order multiple-quantum coherences have been tested in peptide ψ torsion angle measurements. The experiment of Levitt and co-workers has been performed on the isotopically labelled tripeptide [^{15}N,$^{13}C_3$-ala]–[^{15}N-gly]–gly monohydrate (AGG) by exciting ^{13}C triple-quantum coherences (3QC) in the $^{13}C_3$-labelled

alanine residue [**209**]. The triple-quantum coherences were allowed to evolve in the presence of REDOR-recoupled heteronuclear ^{15}N–^{13}C dipole–dipole couplings during the constant period to avoid the need to correct for T_2^{3Q} relaxation decay. This experiment is referred to as constant-time NCCN triple-quantum heteronuclear local field spectroscopy (NCCN–3Q-HLF). It has a torsion angle resolution of about ±5° as well as a sufficient sensitivity to discriminate between positive and negative torsion angles. The latter is possible since the four labelled atoms of the N–C(CH_3)–C_α molecular fragment do not lie in the same plane and, thus, the geometry of the C_α–N bond with respect to the four-spin cluster is unique. For this case, the dependence on the sign of ψ persists even after the average over all crystallite orientations of the powder sample, due to the non-symmetric configuration of the entire spin system. However, in spite of this, the experimental triple-quantum coherences evolution curves obtained for polycrystalline AGG were equally well simulated for the two values of $\psi = +161°$ and $-152°$ with the first value being close to the X-ray single crystal value of +160.5° [**210**]. Moreover, the application of the NCCN–3Q-HLF method to structural studies on larger peptide or protein molecules may be rather limited because of the low triple-quantum filtering efficiency of only 6% (theoretically estimated [**211**]) or even less than 2.5% (experimental value [**209**]).

Direct determination of the peptide angle ϕ.HNCH experiments

The other peptide backbone torsion angle ϕ, CO–NH–C_αH(R)–CO, can be obtained from the relative orientation of the NH and C_αH dipolar tensors, which is described by the torsion angle ϕ_H, H–N–C_α–H: $\phi_H = \phi - 60°$ for L-amino acids as illustrated by the Newman projection in Fig. 7.64 ($\phi_H = \phi + 60°$ for D-amino acids). The method of Hong et al. [**50**] for measuring the ϕ torsion angle under magic-angle spinning is a variation of the HCCH–2Q-HLF experiment described above, but it involves the evolution of heteronuclear ^{15}N–^{13}C double- and zero-quantum coherences instead of the homonuclear $^{13}C_2$ double-quantum coherence. The experimental implementation involves ideas from both HCCH and NCCN torsion angle experiments (see Fig. 7.65(a)). Rotor-synchronized REDOR 180° pulses are used to recouple the ^{15}N–^{13}C dipolar interactions (the antiphase term $\hat{I}_y^C \hat{I}_z^N$ in the density operator is prepared, where C and N refer to ^{13}C and ^{15}N spins respectively) followed by a 90° ^{15}N pulse which excites a combination of heteronuclear ^{15}N–^{13}C double- and zero-quantum coherences (expressed by the term $\hat{I}_y^C \hat{I}_x^N$ in the density operator). The latter evolve during t_1 under ^1H–^{13}C and ^1H–^{15}N dipolar interactions, with ^1H–^1H homonuclear couplings removed by the MREV-8 decoupling sequence. After the reconversion of the ^{15}N–^{13}C double- and zero-quantum coherences to ^{13}C (−1) single-quantum coherence, ^{13}C magnetization is detected during t_2. Since the ^1H–^{13}C and ^1H–^{15}N dipolar couplings are scaled down by the MREV-8 sequence by the scaling factor k (which depends on experimental conditions), they have to be directly

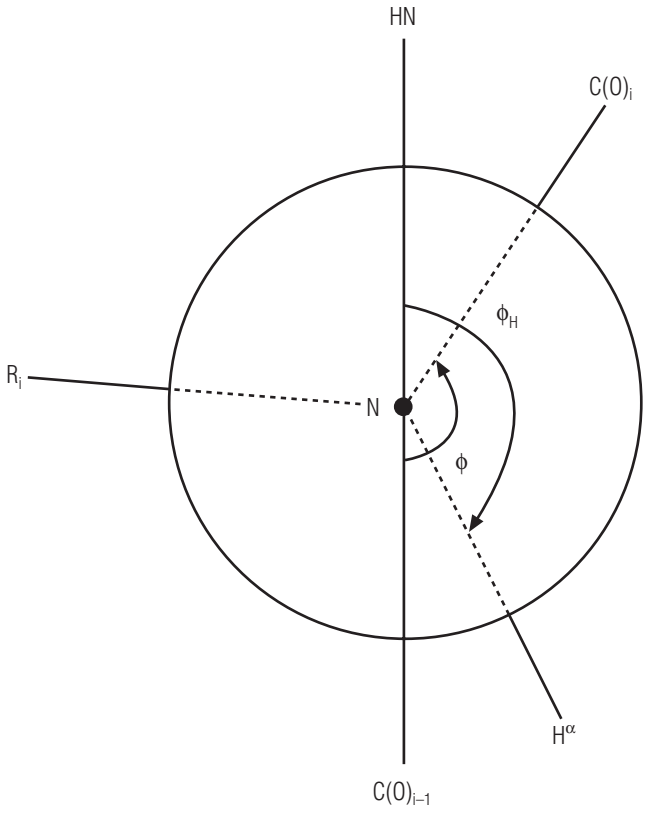

Fig. 7.64 Newman projection of an L-amino acid, viewed along the N–C_α vector (into the plane of the paper). The backbone torsion angle ϕ is defined as $C(O)_{i-1}$–N–C_α–$C(O)_i$, where *i* is the residue (R) number. ϕ is negative as drawn here. The corresponding NMR-measurable torsion angle ϕ_H (H_N–N–C_α–H_α) is related to ϕ by $\phi_H = \phi - 60°$ for L-amino acids. Adapted from ref. [**50**].

measured in additional single-quantum ^{13}C and ^{15}N *DIP*olar-*SHIFT* (DIPSHIFT) correlation experiments under the same conditions as the torsion angle measurements (Fig. 7.65(b)). Such measured scaled dipolar couplings have to be used in the simulations of the ϕ-dependent ^{15}N–^{13}C multiple-quantum spectra. Double Fourier transformation of the resulting two-dimensional time domain signal yields ^{15}N–^{13}C multiple-quantum dipolar sideband patterns in the f_1 dimension,[4] separated according to ^{13}C isotropic chemical shifts in the f_2 dimension.

Simulations of ^{15}N–^{13}C multiple-quantum dipolar sideband spectra for 'standard' peptide bond lengths and dihedral angles (Fig. 7.66) show that the spectra are unique in the range $\phi = [60°, -120°]$ and have the highest angular resolution of ±10° around $\phi = -120° \pm 60°$ when the H–N and H–C bonds are close to being antiparallel ($\phi_H = -180° \pm 60°$). As in other methods for torsion angle measurements, there are unavoidable ambiguities: since $\pm\phi_H$ angles yield the same dipolar sideband spectra, and $\phi_H = \phi - 60°$ for L-amino acids, each simulated spectrum corresponds to two ϕ angles (ϕ_1, ϕ_2) related by $(\phi_1 + \phi_2)/2 = -120°$. Therefore, additional solid-state NMR experiments must be performed in order to resolve these ambiguities. The ϕ torsion angle has been successfully measured by this solid-state NMR method

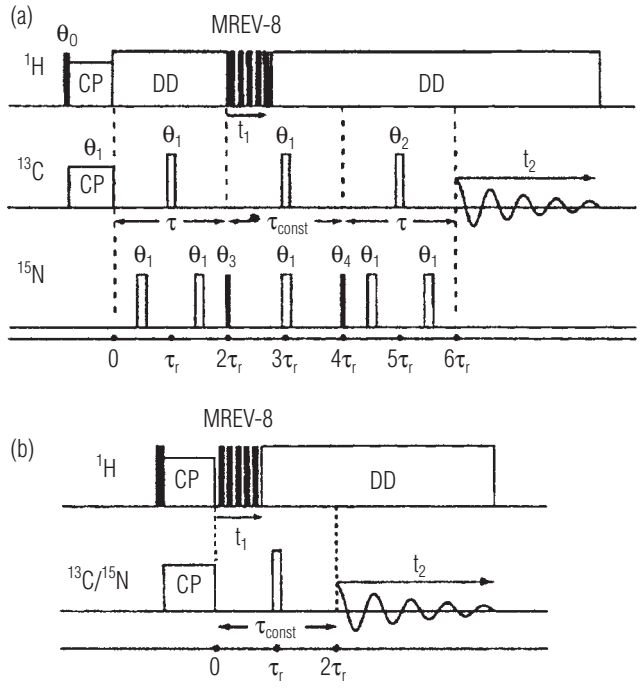

Fig. 7.65 (a) Pulse sequence for HNCH–MQ-HLF experiment. After a Hartmann–Hahn cross-polarization step, the ^{15}N–^{13}C dipolar interaction is recoupled under magic-angle spinning by rotor synchronized ^{15}N and ^{13}C 180° pulses during τ. The excited ^{15}N–^{13}C double- and zero-quantum coherences evolve during t_1 under ^{1}H–^{13}C and ^{1}H–^{15}N dipolar interactions, with ^{1}H homonuclear couplings removed by MREV-8 multiple-pulse decoupling. The evolution period has a maximum length of one rotor period (τ_r), which is half of the constant time period, τ_{const}. A ^{13}C and a ^{15}N 180° pulse are applied in the middle of τ_{const} to refocus ^{13}C and ^{15}N isotropic chemical shifts, respectively. The ^{15}N–^{13}C double- and zero-quantum coherences are then reconverted to single-quantum ^{13}C coherence for the detection of ^{13}C chemical shift during t_2. Details of the phase cycle (θ_0, θ_1, . . . , θ_4) can be found in ref. [**50**]. (b) The DIPSHIFT pulse sequence for measuring ^{1}H–^{13}C and ^{1}H–^{15}N dipolar couplings separated by the ^{13}C and ^{15}N chemical shifts, respectively. The evolution period is the same as that in (a) in order to use the measured ^{1}H–^{13}C and ^{1}H–^{15}N dipolar couplings in the simulations of the ϕ-dependent HNCH–MQ-HLF spectra. Adapted from ref. [**50**].

for singly ^{15}N-labelled N-acetyl-D,L-valine: $\phi = -135°$ [**50**], which agrees remarkably well with the X-ray crystal structure ($\phi = -136.5°$ [**196**]).

An attractive feature of the method is the possibility of separating the ϕ-dependent sideband patterns according to the ^{13}C isotropic chemical shifts, which allows the extraction of ϕ torsion angles in various amino acid residues simultaneously, as long as the C_α isotropic shifts are resolved and the directly bonded nitrogen atoms are labelled with the ^{15}N isotope. In the HNCH experiment combined with an isotropic-anisotropic two-dimensional correlation technique, the ϕ-dependent dipolar patterns are manifested in the f_1 dimension and separated in the f_2 dimension according to the C_α isotropic shifts of the residues. A convincing demonstration of this idea has been presented by Hong on both selectively and extensively (S&E) ^{13}C-labelled and uniformly ^{15}N-labelled ubiquitin (M_r = 8565 g/mol, 76 amino acid residues) expressed by using specifically labelled glucose or glycerol as

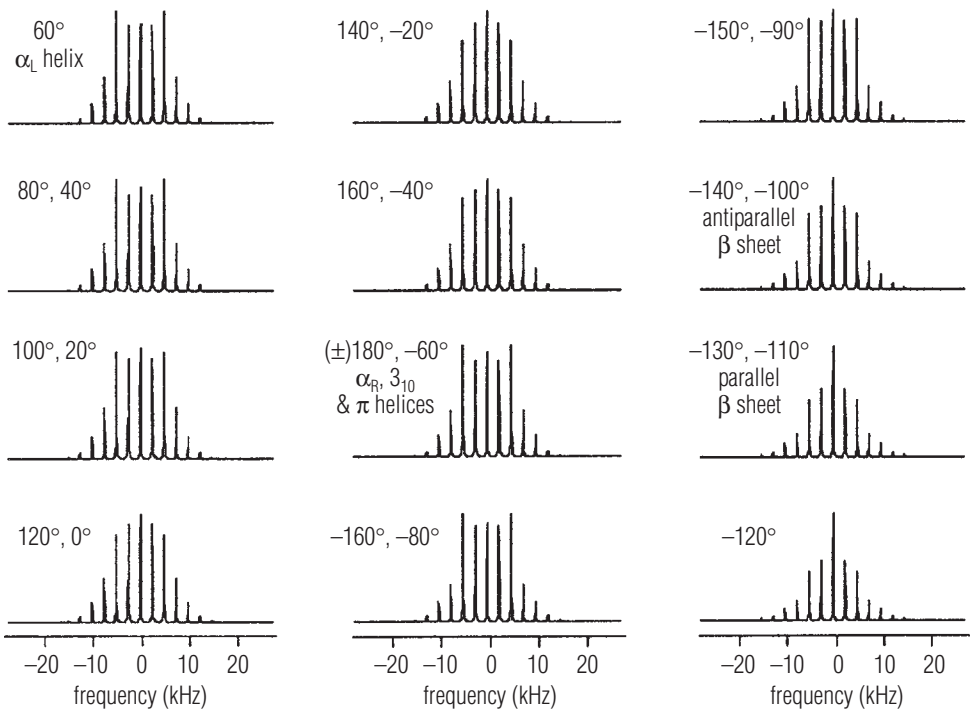

Fig. 7.66 Simulation of HNCH–MQ-HLF dipolar sideband spectra as a function of ϕ for a 'standard' L-configuration peptide geometry. Each spectrum corresponds to two ϕ angles due to the spectral invariance to $\pm\phi_H$. The spectra are unique in the range ϕ = [60°, –120°] and have the highest angular resolution around ϕ = –120°. Input parameters: ^{1}H–^{13}C and ^{1}H–^{15}N dipolar couplings scaled by MREV-8 sequence are 10.9 kHz and –5.2 kHz, respectively; multiple-quantum excitation time, τ = 792 ms; spinning frequency, ν_R = 2525 Hz. Adapted from ref. [**50**].

the sole carbon source in the protein expression media [**212**]: ϕ torsion angles have been measured for Val_{26} (α-helix, –60°), Thr_{12} and Thr_{14} (β-sheet, –135°) and Ala_{46} (β-turn, +20°). Apart from the unavoidable two-fold degeneracies for each of these ϕ angles, these values are in ±10° accord with the single-crystal X-ray diffraction data for ubiquitin [**213**].

An interesting approach based on the HNCH–NMR and called β-sheet filter experiment has been developed by Hong and co-workers [**214**]. This method allows the selection of signals which arise from sites belonging to protein fragments having different secondary structure, either α-helical or β-sheet. Since relative orientations between the H–N and H–C_α vectors are very different in the two conformations (see Fig. 7.67), the evolution of the ^{15}N–^{13}C heteronuclear multiple-quantum coherences differs significantly. Therefore, by choosing the time point (in the evolution t_1 period) corresponding to the largest difference, one can retain the β-sheet signals while removing the α-helical resonances. For suitable spinning speeds, after one-half of a rotation period of the dipolar evolution, β-sheet residues retain significant intensities (20–50%) while α-helical signals almost vanish [**214**]. The β-sheet filter

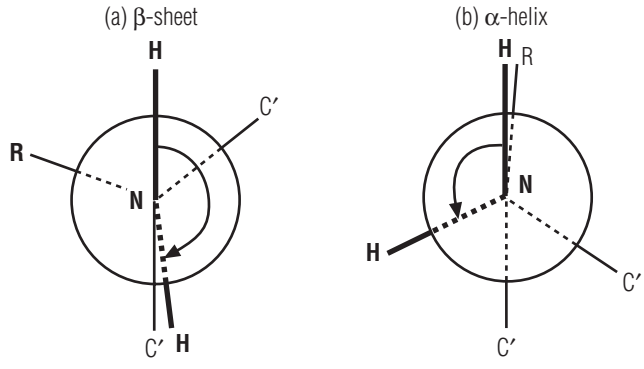

Fig. 7.67 Newman projection of a peptide residue (viewed along the N–C_α bond) showing the different ϕ_H torsion angles for the β-sheet (ϕ_H is about 165–180°) (a) and the α-helical (ϕ_H is about –120°) (b) conformation. Adapted from ref. [**214**].

has been combined with a heteronuclear ^{15}N–^{13}C two-dimensional correlation pulse sequence to better separate overlapping resonances (see Fig. 7.68). This ingenious experiment performed at moderate (4.2 and 6.6 kHz) spinning rates has been successfully demonstrated on 25 mg of both selectively and extensively ^{13}C-labelled and uniformly ^{15}N-labelled solid protein ubiquitin (Fig. 7.69). If desired, the pulse sequence can be converted into a three-dimensional experiment to precisely measure the torsion angles ϕ of different amino acid residues in the protein. This would involve incrementing the HNCH period for one whole rotor period instead of using a constant evolution time of $\tau_R/2$. The third dimension would exhibit dipolar sideband patterns which depend on the torsion angle ϕ.

Another method for measuring the ^1H–^{15}N–^{13}C–^1H peptide torsion angle ϕ is based on the relayed anisotropy correlation (RACO) scheme [**215**]. In this method, the ^1H–^{15}N and the ^1H–^{13}C dipolar tensors are two-dimensionally correlated via polarization transfer from ^{15}N to ^{13}C under magic-angle spinning.

7.5 ^{13}C multiple-quantum NMR spectroscopy

Often we will be interested in the supramolecular structure of biomolecules. For instance, suppose we have a protein of a known primary sequence but for which the secondary structure is not known and is the goal to be tackled. We could do this by measuring all torsion angles along the backbone of the protein using the techniques detailed in the previous section. However, these all rely on specific isotope labelling in selected fragments of the molecule. We would have to synthesize many selectively labelled samples which is impractical in many instances. Let us suppose that, instead of that, we can label all amino acids of one type in the protein, say all the alanines. These will be scattered in the primary sequence of the protein, but they may come close to each other in the folded state of the molecule, forming clusters of labels. The question is then: Is it possible to detect such clusters of spins by a solid-state NMR experiment? An even more interesting application of this strategy

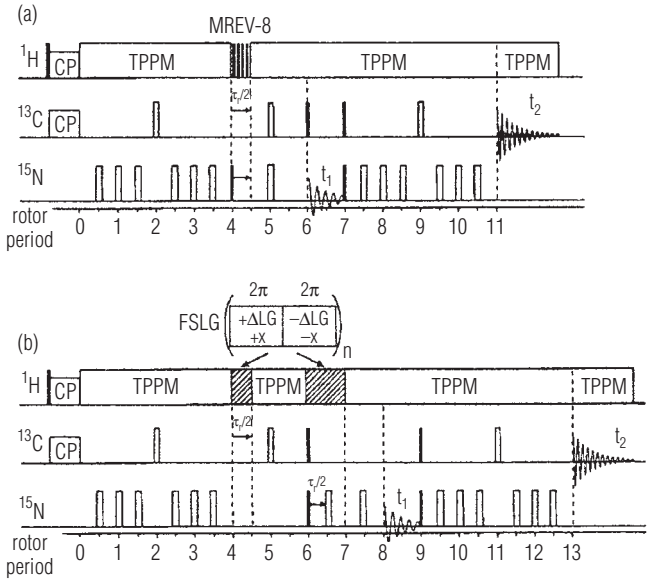

Fig. 7.68 Pulse sequences for the β-sheet filter experiment. (a) The ^{1}H–^{15}N non-doubled version suitable for slow magic-angle spinning of about 5 kHz or less. Filled and open rectangles represent 90° and 180° pulses, respectively. After ^{1}H–^{13}C cross-polarization (CP), the ^{13}C transverse magnetization evolves under the ^{15}N–^{13}C dipolar interaction (recoupled by REDOR) into antiphase coherence of the form $\hat{I}_y^C\hat{I}_z^N$, where C and N refer to ^{13}C and ^{15}N spins, respectively. Then a ^{15}N 90° pulse converts $\hat{I}_y^C\hat{I}_z^N$ into zero- and double-quantum coherences which evolve under the ^{1}H–^{13}C and ^{1}H–^{15}N dipolar couplings simultaneously for one-half of a rotor period, $\tau_R/2$ (homonuclear ^{1}H–^{1}H decoupling is achieved by MREV-8). During this interval β-sheet residues retain significant intensities while α-helical signals almost vanish. After ^{13}C and ^{15}N 180° pulses which refocus the isotropic chemical shift interactions, a 90° ^{13}C pulse converts the zero- and double-quantum coherences into ^{15}N antiphase magnetization $\hat{I}_z^C\hat{I}_y^N$ so that the ^{15}N chemical-shift frequency can be encoded during the evolution period t_1. Finally, the evolved ^{15}N single-quantum coherence is converted back to observable ^{13}C magnetization by a pair of 90° pulses and an identical REDOR period, and ^{13}C isotropic chemical shift signal is acquired during t_2. (b) The ^{1}H–^{15}N doubled version suitable for higher magic-angle spinning rates of about 6–10 kHz. The spin coherence evolves under the ^{1}H–^{13}C and ^{1}H–^{15}N dipolar couplings separately but synchronously. While the ^{1}H–^{1}H FSLG-decoupling is active for one-half of a rotor period for the ^{1}H–^{13}C interaction, it is active for an entire rotor period for the ^{1}H–^{15}N coupling. Combined with a ^{15}N 180° pulse in the middle of the ^{1}H–^{15}N rotor period, the one-rotor-period FSLG decoupling doubles the dynamic phase of the ^{1}H–^{15}N coupling strength. A second ^{15}N 180° pulse refocuses the chemical shift anisotropy, which was recoupled along with the ^{1}H–^{15}N dipolar coupling. Selective doubling of the ^{1}H–^{15}N dipolar coupling makes the magnitudes of the ^{1}H–^{13}C and ^{1}H–^{15}N dipolar couplings comparable which enhances the angular resolution of the technique. Two-pulse phase modulation (TPPM) ^{1}H-decoupling was employed along the sequence. Adapted from ref. [**214**].

is the testing of different putative models of the supramolecular organization of amyloid fibrils, which spontaneously assemble from an aqueous solution of an amyloid protein. Is it possible to distinguish between different arrangements of molecules in β-sheets of fibrils, such as parallel, antiparallel or more complex arrangements such as antiparallel packing of parallel dimers or trimers? For testing of these models one can introduce just one ^{13}C label in a specific amino acid residue which is not in the midpoint of the peptide molecule as has been originally suggested by Benzinger et al. [**154**]. Different arrangements of labelled sites are expected for the aforementioned putative structures (see Fig. 7.70). A parallel, in-register arrangement of the molecules would give an infinite ladder of closely spaced spins; anti-

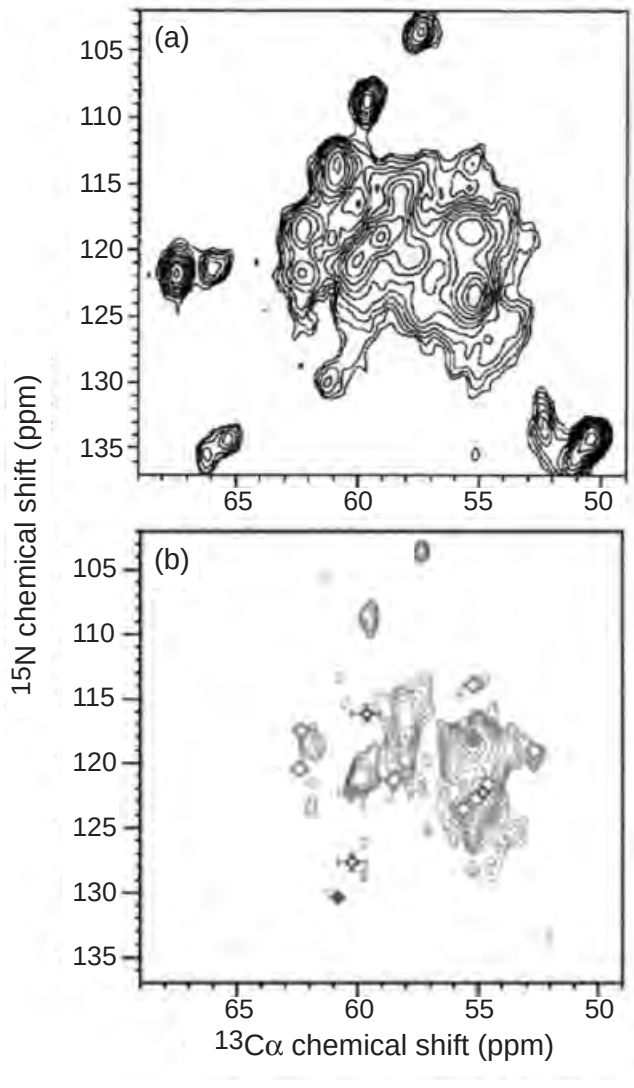

Fig. 7.69 Two-dimensional ^{15}N–^{13}C correlation spectra of ubiquitin (Larmor frequencies are 100.72 MHz for ^{13}C and 40.59 MHz for ^{15}N): (a) without the β-sheet filter (spinning frequency, ν_R = 6600 Hz), (b) ^{1}H–^{15}N non-doubled β-sheet filter (ν_R = 4252 Hz, $\tau = \tau_R/2$ = 117.6 μs). The expected β-sheet spectrum of ubiquitin from X-ray diffraction crystal structure is also shown for comparison: large diamonds, $\phi = -120 \pm 5°$; medium diamonds, $\phi = -110 \pm 5°$; small diamonds, $\phi = -100 \pm 5°$. Adapted from ref. [**214**].

parallel arrangements of the molecules would ensure spins were scattered in the fibril if single molecules were arranged antiparallel or would form clusters of pairs or triples of spins for antiparallel arrangements of dimers and trimers respectively. An NMR method which can, in principle, distinguish between these possible groupings of spins is based on the excitation of multiple-quantum coherences and is called a multiple-quantum NMR spectroscopy or 'spin counting' (see also Section 3.7).

The idea of the method is quite simple and can be explained with the aid of the energy level diagram for a multiple spin system. An ensemble of spin systems consisting of isolated spin-$\frac{1}{2}$ nuclei is usually described by the two spin states $|\alpha\rangle$ and $|\beta\rangle$. It is possible to excite only ±1 quantum coherence for such a spin system, where

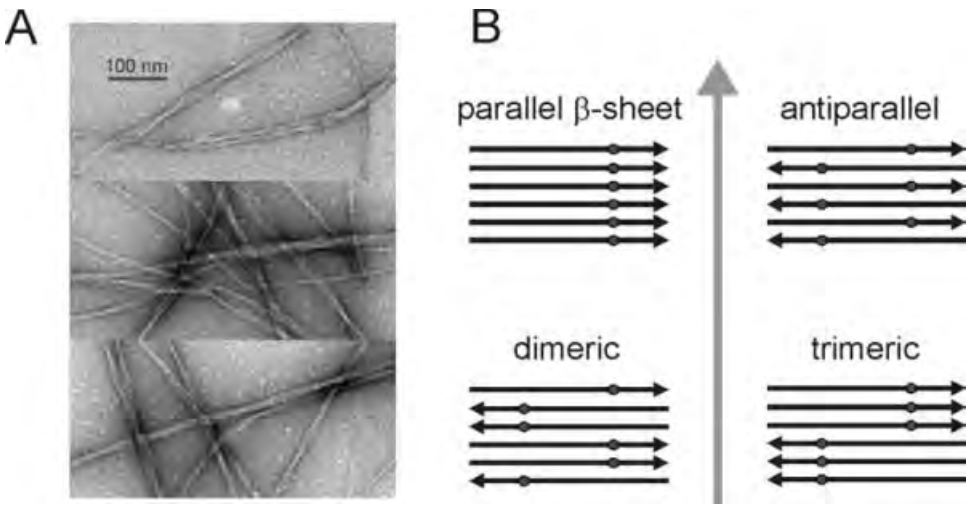

Fig. 7.70 (a) Electron micrographs of negatively stained Alzheimer's-β-protein(1–40) fibrils adsorbed to carbon films. (b) Alzheimer's-β-protein(1–40) fibrils are believed to have a predominantly β-sheet structure with peptide chains (horizontal arrows) approximately perpendicular to the hydrogen bonds which are approximately parallel to the long axis of the fibril (vertical arrow). Four candidates for the supramolecular organization of the fibrils are shown. These can be distinguished experimentally by incorporating ^{13}C labels (dots) at a single site in the peptide and measuring ^{13}C multiple quantum NMR spectra, because observation of an *n*-quantum signal requires that at least *n* ^{13}C nuclei be close enough in space to have significant ^{13}C–^{13}C dipole–dipole couplings. Adapted from ref. [**232**].

(−1)-quantum coherence is the detectable property which gives rise to an FID. For a pair of homonuclear dipolar-coupled spins, there are four eigenstates of the two-spin system: $|\alpha\alpha\rangle$, $|\beta\beta\rangle$ and linear combinations of $|\alpha\beta\rangle$ and $|\beta\alpha\rangle$ states. A number of different coherences in this spin system can be excited such as zero-quantum, ±1- and ±2-quantum coherences. We can proceed from this simple discussion to a cluster of N spins coupled by dipole–dipole interactions. The set of multiple-quantum coherences possible in this spin system, involving all 2^N different energy levels of this system, now extends from order 0 to N; the number of each order expands binomially as the order decreases: one $\pm N$-quantum coherence, $2N$ different $\pm(N-1)$-quantum coherences, and so on up to many different single (±1) and zero-quantum coherences. An *n*-quantum coherence is a coherent quantum mechanical state which involves *n* spins.[5] The main point of the analysis discussed here is that the highest possible coherence order of a coupled spin system is equal to the number of coupled spins in a spin cluster, N. Our discussion now turns to the possibility of excitation and (indirect) detection of high-order multiple-quantum coherences between dipolar-coupled spins.

As discussed in Section 3.7, spin-counting techniques were originally introduced for application to dipolar-coupled ^1H systems [**216, 217**]. This technique has found numerous applications in structural investigations of a wide variety of systems including amorphous silicon hydrate [**218, 219**], diamond film and powder [**220,**

221], doped synthetic polymers [**222–224**], catalyst supports [**225**], chromatographic materials [**226**] and zeolites [**227**].

A basic element of a multiple-quantum excitation pulse sequence consists of a train of 90° pulses with phase $\Delta\phi$ and spacings τ: $90°_{\Delta\phi}$–τ–$90°_{\Delta\phi}$–2τ–$90°_{\Delta\phi}$. Theoretically it is not difficult to show that this sequence generates an effective two-quantum selective hamiltonian [**228**]:

$$\overline{H}_{\text{eff}}(\Delta\phi) = \sum_{i>j} -\frac{d_{ij}}{6}(\hat{I}^i_+\hat{I}^j_+ \exp(-2i\Delta\phi) + \hat{I}^i_-\hat{I}^j_- \exp(2i\Delta\phi)) \qquad (7.24)$$

with a scaling factor proportional to the dipole–dipole couplings between spins. Starting with an initial condition $\hat{I}_z$ ($\hat{I}_x$ or $\hat{I}_y$) all even (odd) order multiple-quantum coherences can be excited by this sequence for an infinitely large spin cluster provided that the excitation time (the length of the pulse train) is longer than the inverse of the effective dipole–dipole coupling between spins. Since only (–1)-quantum coherence is directly detected in NMR, once excited, multiple-quantum coherences must be reconverted back to (–1)-quantum coherence, for detection. This can be done by the same sequence of 90° pulses, but with all 90° phase shifted with respect to the excitation period (see Box 3.3 in Chapter 3). This comes from the dependence of $\overline{H}_{\text{eff}}$ on the phase of pulses in the pulse train (Equation (7.24)). If the excitation (or reconversion) block is specifically phase cycled, one can select any desired order of coherence which was excited during the excitation period. By incrementing the phase $\Delta\phi$ in steps of $360°/2N$, the amplitude of the FID will be modulated. This modulation is due to the interference between multiple-quantum coherences of different orders up to the order N, which were excited during the excitation period. Or in other words, the amplitude of FID as a function of $\Delta\phi$ can be represented as a Fourier series, $\Sigma_n a_n \cos(n\Delta\phi)$, where amplitudes a_n are intensities of multiple-quantum coherences of the corresponding order n. By simulating a set of amplitudes of multiple-quantum coherences as a function of the excitation time, one can fit data to a particular structural model of a spin cluster.

^{1}H multiple-quantum excitation spectroscopy is not really applicable to biomolecules, unless the molecule of interest is heavily deuteriated, since there is a vast number of strongly coupled ^{1}H spins; high-order multiple-quantum coherences will be excited independent of the secondary structure of molecules or their aggregates. It is much more attractive to use ^{13}C spins for this purpose, because there is only a weak background from naturally abundance ^{13}C spins and one can selectively label any desired position of a molecule. However, there are a number of obstacles for ^{13}C multiple-quantum NMR spectroscopy: (i) dipolar couplings between ^{13}C spins are ca. 16 times weaker than for ^{1}H for the same internuclear distance (since $\gamma(^1\text{H})/\gamma(^{13}\text{C}) \sim 4$). Therefore, for ^{13}C spins with internuclear distances of 5–6 Å, rather long multiple-quantum excitation times are needed, and pulse imperfections which will accumulate in the course of the multiple-quantum excitation pulse sequence, will have a destructive effect on the multiple-quantum coherences, particularly on

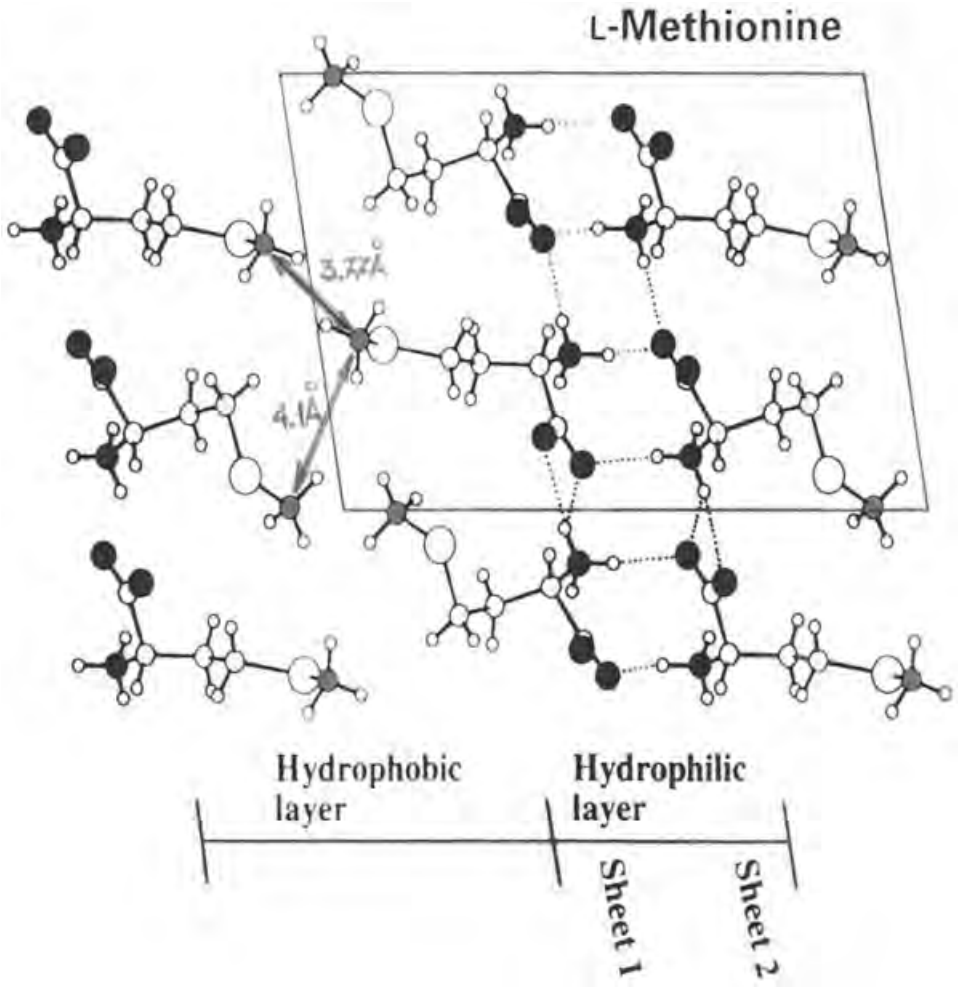

Fig. 7.71 Single crystal structure of L-methionine with the shortest intermolecular distances between methyl carbons (grey circles), 3.77 and 4.1 Å, shown by arrows. Adapted from ref. [**230**].

those of high order. (ii) The chemical shift anisotropy of most carbon sites is 100–1000 larger than that for protons. Therefore, a special modification of the multiple-quantum pulse sequence is needed in order to refocus the undesired evolution of the multiple-quantum coherences due to chemical shift anisotropy, which also has a destructive effect on high-order multiple-quantum coherences.

^{13}C multiple-quantum excitation spectroscopy was first successfully demonstrated on simple model systems of singly labelled amino acids, L-methionine-3-^{13}C and L-alanine-1-^{13}C [**229**]. An infinite net of ^{13}C spins is present in crystals of these compounds with internuclear intermolecular distances of approximately 4 Å (see Fig. 7.71) [**230, 231**]. Pulse sequences for two- and single-quantum selective excitation are shown in Fig. 7.72. Cycles of the excitation and reconversion blocks

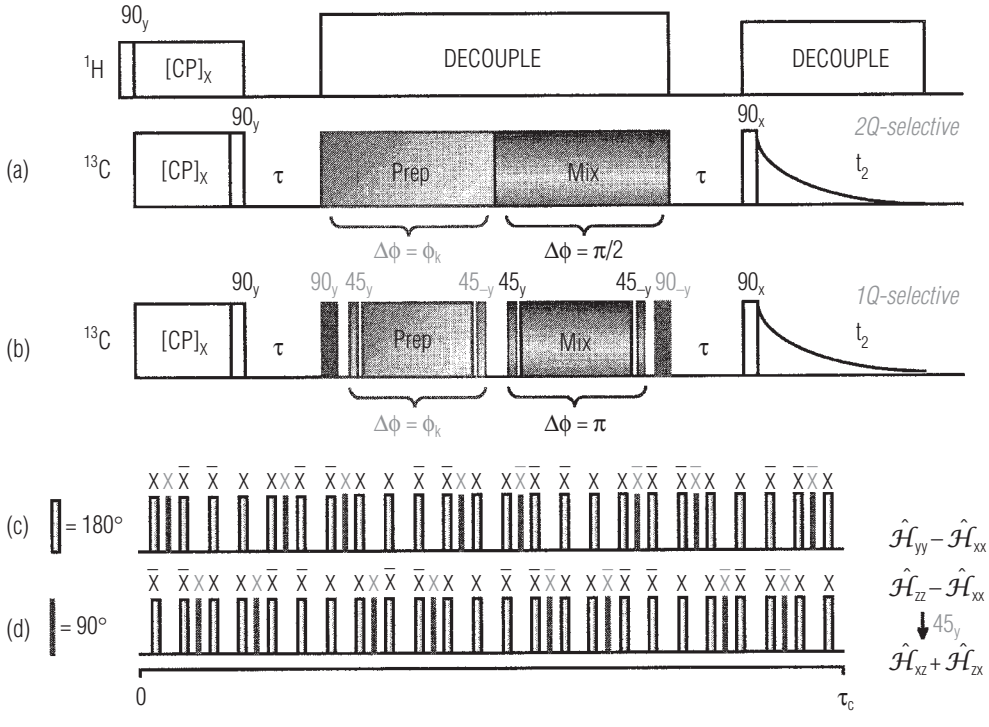

Fig. 7.72 Pulse sequences for double- and single-quantum selective ^{13}C-multiple-quantum-excitation NMR spectroscopy. (a, b) Overall sequences, showing the creation of ^{13}C magnetization by cross-polarization (CP), dephasing periods τ, multiple-quantum preparation (Prep) and mixing (Mix) periods, and signal detection period t_2. (c, d) Multiple pulse cycles used in preparation and mixing periods, with overall phase shifts $\Delta\phi$ which is incremented during the preparation period from 0° to 360° in steps of 360°/2*N*, where *N* is the highest multiple-quantum order among coherences from order 0 to *N* being detected by the sequence. In (c), the double-quantum-selective cycle consists of eight 90° pulses, with the indicated phases, centred about times $\tau_c/24$, $5\tau_c/24$, $7\tau_c/24$, $11\tau_c/24$, $13\tau_c/24$, $17\tau_c/24$, $19\tau_c/24$, and $23\tau_c/24$ as originally designed by Pines and co-worker [**216**]. This sequence coherently averages the homonuclear dipole–dipole coupling hamiltonian $\hat{H}_{dd} = -\Sigma_{i>j} C_{ij} (3\hat{I}_z^i\hat{I}_z^j - \hat{\mathbf{I}}^i \cdot \hat{\mathbf{I}}^j)$ to an effective hamiltonian $\hat{H}_{yy} - \hat{H}_{xx}$ (where $\hat{H}_{\alpha\alpha}$ denotes an operator containing terms of the form $\hat{I}_\alpha^i\hat{I}_\alpha^j$) which is two-quantum selective, so that time reversal is accomplished by the 90° phase shift of the mixing period. In (d), the single-quantum-selective cycle consists of eight 90° pulses, centred about times $2\tau_c/24$, $4\tau_c/24$, $8\tau_c/24$, $10\tau_c/24$, $14\tau_c/24$, $16\tau_c/24$, $20\tau_c/24$ and $22\tau_c/24$, and the preparation and mixing periods are bracketed by two 45° pulses as designed by Suter et al. [**217**], which creates an effective hamiltonian of the form $\hat{H}_{xz} + \hat{H}_{zx}$. The time reversal for the single-quantum-selective sequence is accomplished by the 180° phase shift of the mixing period. The time reversal for the single-quantum-selective sequence is accomplished by the 180° phase shift of the mixing period. Twenty-four 180° pulses, inserted to average out anisotropic chemical shifts on a time scale of $t_c/24$, are centred about times $(2m + 1)t_c/48$, $m = 0, 1, 2, \ldots, 23$.

consist of essentially the same element as the original ^{1}H multiple-quantum experiments either 90°–τ–90°–2τ–90° (for the double-quantum-selective excitation [**216**]) or 90°–2τ–90°–τ–90°, bracketed by two 45° pulses (for the single-quantum selective effective hamiltonian [**217**]), but the chemical shift anisotropy evolution is additionally refocused by a train of 180° pulses evenly spaced along the sequence, such that they form spin echoes at the positions of the 90° pulses (see Fig. 7.72(c) and (d)). Spacings between the 90° pulses are chosen to be of the order of the inverse of the dipole–dipole coupling constant, while that between 180° pulses is of the

order of the inverse of the chemical shift anisotropy in frequency units. Both the cycle time 3τ and the number of 180° pulses in the cycle can be adjusted for each particular system, depending on the ratio between the ^{13}C–^{13}C dipole–dipole coupling constant and ^{13}C chemical shift anisotropy. Too many 180° pulses will lead to signal degradation due to pulse imperfections, while too small a number of them will lead to insufficient suppression of the chemical shift anisotropy and to eventual destruction of the multiple-quantum coherences. Figure 7.73 shows double-quantum selective ^{13}C multiple-quantum excitation spectra for model systems

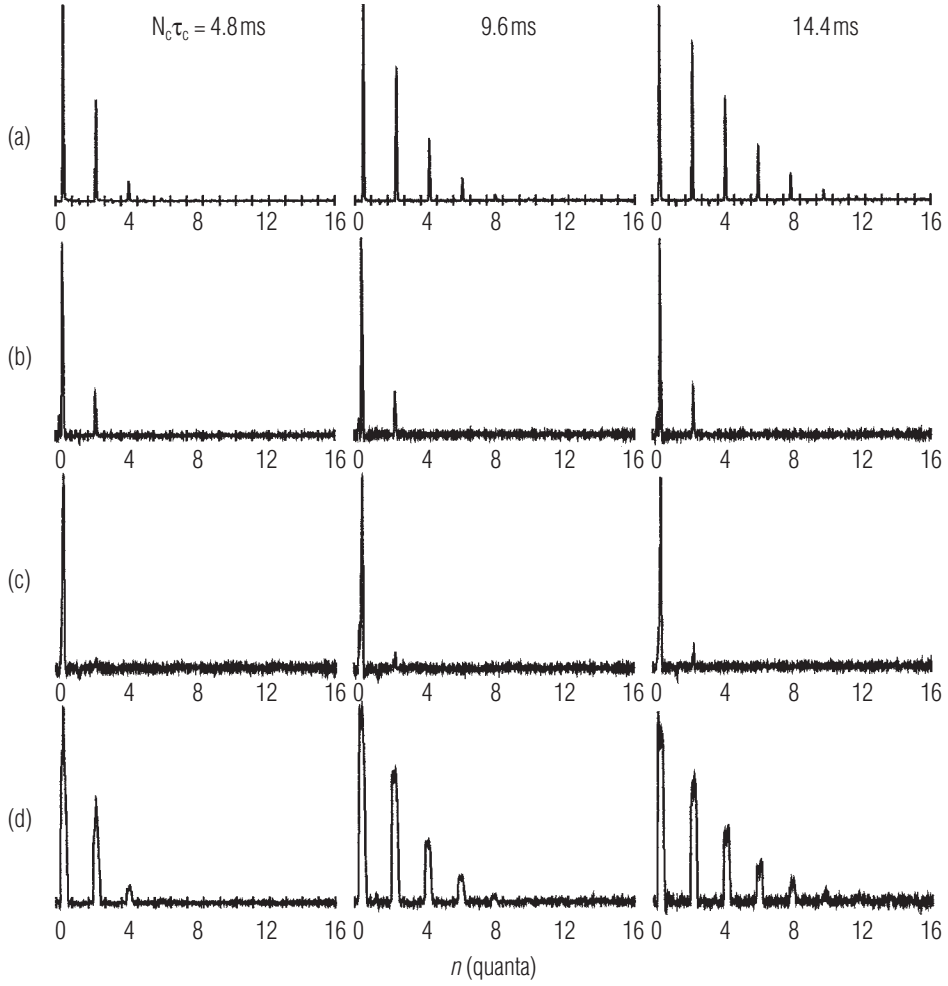

Fig. 7.73 100.8 MHz ^{13}C double-quantum-selective multiple-quantum-excitation NMR spectra of static polycrystalline samples of: (a) L-methionine-*methyl*-^{13}C, (b)5% diluted $(^{13}CH_3)_2C(OH)SO_3Na$, (c) unlabelled L-methionine, and (d) L-alanine-1-^{13}C. Multiple-quantum preparation and mixing times $N_c\tau_c$ are 4.8 ms, 9.6 ms, and 14.4 ms for the first, second, and third columns, respectively. τ_c is 4.8 ms (a, b, c) or 2.4 ms (d). Each trace represents 17 *n*-quantum excitation spectra ($0 \leq n \leq 16$), plotted side-by-side and delineated by vertical tick marks. The range of f_2 in each spectrum is ±5 kHz (a), ±15 kHz (b, d), or ±10 kHz (c). Adapted from ref. [**229**].

obtained at three different excitation times. For methionine-3-^{13}C (Fig. 7.73(a)) and alanine-1-^{13}C (Fig. 7.73(d)), systems in which there is an infinite net of dipolar-coupled ^{13}C spins, high-order multiple-quantum coherences (up to 10-quantum) were excited and detected at the long excitation time of 14.4 ms, while for the control system of 5% diluted ^{13}C doubly-labelled bisulphonic adduct of acetone (BSA-$^{13}C_2$) (Fig. 7.73(b)), only 2-(double)-quantum coherence was detected at all excitation times, as expected for an isolated pair of dipolar-coupled spins. For unlabelled methionine, only a weak double-quantum signal was observed at longer excitation times. This is a background signal from accidental spin pairs of natural abundant ^{13}C spins (1.1%).

It should be emphasized here that the insertion of the refocusing 180° pulses in the original multiple-quantum sequence of Pines and co-workers [**216, 228**] is the essential modification. The modified sequence works well even for carboxyl sites having a large chemical shift anisotropy (ca. 70 ppm) as in alanine-1-^{13}C (see Fig. 7.73(d)). Without these additional 180° pulses, the sequence does not work either for alanine-1-^{13}C or for methionine-3-^{13}C, which has a rather small chemical shift anisotropy of only 7 ppm.

Once the reliability of the ^{13}C multiple-quantum excitation spectroscopy had been tested on the model compounds, it was then successfully applied to a few problems of structural biology. We will give here one example of how this method has been used to probe the β-sheet organization in fibrils formed by the full-length, 40 residue β-amyloid peptide, $A\beta_{1-40}$ [**232**] which is believed to be neurotoxic and is associated with Alzheimer's disease [**233, 234**]. Though an extended β-sheet structure for Aβ fibrils with hydrogen bonds >C=O · · · H–N< parallel to the fibril axis is established from X-ray diffraction measurements on oriented fibril bundles [**235–238**] and also supported by infrared spectroscopy [**235, 239**], the supramolecular organization of the β-sheets is not well established because of the non-crystalline nature of amyloid fibrils. A number of different molecular level structural models for Aβ fibrils has been proposed previously, which used either the commonly accepted paradigm of the energetically more stable cross-β-sheet structure of fibrils [**240**], or the interaction energy optimization of the peptide molecules based on the known primary sequence and the additional two distance constraints of 4.8 and 9.6 Å derived from the two distinct reflections in the X-ray powder diffraction patterns [**241–244**]. Although very different in detail, all of these models invoke an antiparallel β-sheet organization. Below we will show how ^{13}C multiple-quantum NMR experiments indicated an in-register parallel β-sheet organization, and so have ruined all of these theoretically developed structural models of fibrils.

As has been mentioned above, what is known is that amyloid fibrils are composed of Aβ molecules adopting a β-sheet secondary structure and which are perpendicular to the main axis of fibrils. The conceptual basis for multiple-quantum NMR measurements to probe the supramolecular organization of β-sheets within these fibrils is shown in Fig. 7.70 [**232**]. A single ^{13}C label has been introduced into

the peptide molecule as suggested by Benzinger et al. [**154**]. The relative positions of the ^{13}C labels then depend on the β-sheet organization: an infinite chain of the labelled sites with internuclear distances of ca. 4.8 Å is expected only for an in-register, parallel β-sheet while for other models, all labels will be scattered out along the fibril long axis, forming either a zig-zag pattern (antiparallel) or small clusters of labels in groups of two (dimeric structures) or three (trimeric structures) provided that the labelled site is not at the midpoint of the peptide chain. Figure 7.74 shows multiple-quantum NMR spectra of $A\beta P_{1-40}$ fibrillized samples prepared with ^{13}C-methyl-labelled alanine residues at positions 21 and 30 (Ala21 and Ala30) and also one control spectrum of an unfibrillized sample of $[Ala_{30}\text{-}3\text{-}^{13}C]\text{–}A\beta_{1-40}$. The spectra of the two fibrillized samples are very similar and show high-order multiple-quantum signals up to the order of four and even five at long excitation times of 9.6 and 14.4 ms, which indicates ^{13}C spin clusters of at least five for both labelling schemes. Even a cursory inspection of these results favours a parallel structure over

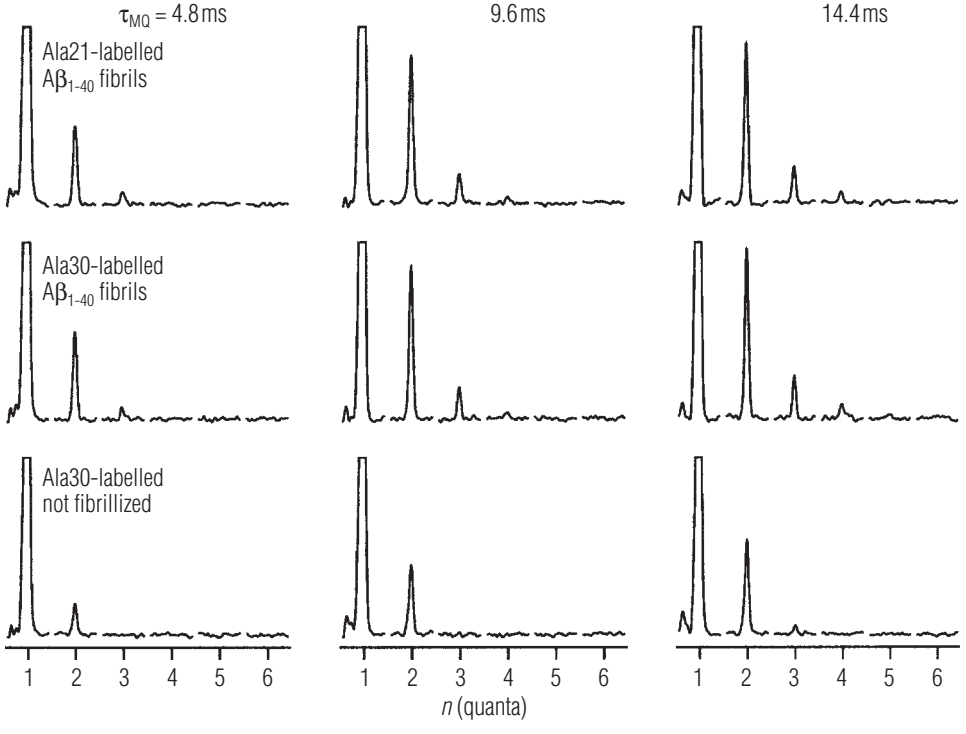

Fig. 7.74 100.8 MHz ^{13}C single-quantum-selective multiple-quantum-excitation NMR spectra of static samples of fibrillized and unfibrillized Alzheimer's amyloid-β-protein(1–40), shown in order of increasing multiple-quantum excitation time τ_{MQ}. Each multiple-quantum-excitation spectrum is displayed as a series of subspectra for multiple-quantum orders from 1 to 6, with a spectral window from –15 kHz to +15 kHz in each subspectrum. Vertical scales are adjusted so that one-quantum peaks are clipped at 25% of their maximum values. In the fibrillized samples (a) and (b), the amplitudes of two- three-, and four-quantum signals increase with increasing τ_{MQ}. Spectra of samples with ^{13}C labels at methyl carbons of Ala21 and Ala30 are nearly identical. In unfibrillized samples (c), the three-quantum amplitude is small and no four-quantum signal is observed. Adapted from ref. [**232**].

the other models. In the unfibrillized sample only a 2-quantum and a very weak 3-quantum signal appear due to dipolar couplings of ^{13}C labels to natural abundance ^{13}C nuclei and couplings among natural abundance ^{13}C nuclei. Multiple-quantum signals of very similar intensities were also obtained for a sample of a simple chemical mixture (dissolved in water and then lyophilized) of all amino acids used in the synthesis of $A\beta_{1-40}$ with one alanine labelled at the methyl position. For this sample, amino acid molecules are uniformly spread through the sample and the 2- and 3-quantum signals detected in this sample are the 'background' signals from the amorphous unstructured material.

In order to prove the above conclusion, one has to perform a quantitative analysis which compares the experimental multiple-quantum signal amplitudes with numerical simulations for different models at the three excitation times of 4.8, 9.6 and 14.4 ms. Simulations have been performed for the four structural models shown in Fig. 7.75 with six nuclear spins placed at appropriate coordinates calculated from the supposed either parallel or antiparallel β-sheet arrangements of the six molecules [**232**]. Natural-abundance ^{13}C nuclei were represented by three additional spins with random coordinates within a rectangular box centred on the labels with a 1.5×10^4 Å^3 volume, based on the estimated density of natural abundance ^{13}C at aliphatic carbon sites. Multiple-quantum NMR signal amplitudes were calculated from a 512×512 density matrix simulation of the quantum-mechanical evolution of a nine-spin system under the effective dipole–dipole coupling hamiltonian ideally created by the rf pulse sequence of Suter et al. [**217**]. Multiple-quantum signal amplitudes were averaged over orientation with respect to the magnetic field and over the random configuration of the natural-abundance ^{13}C spins. The contribution from natural abundance ^{13}C spins which are far from the labels and therefore cannot be included in the simulations, has also been considered in the analysis. Multiple-quantum NMR experiments on unlabelled samples showed only 1- and 2-quantum signals with ratios of signal amplitudes equal to $A_{nat}(1)/A_{nat}(2) \sim 25$, 13 and 9 for excitation times of $\tau_{MQ} = 4.8$, 9.6 and 14.4 ms respectively. Figure 7.75 shows the comparison of the experimental multiple-quantum amplitudes with those calculated for the four models mentioned above. Simulated amplitudes in this figure are $C_{sim}A_{sim}(n) + C_{nat}A_{nat}(n)$, where the coefficients C_{sim} and C_{nat} were adjusted for each model and each τ_{MQ} value to minimize the deviation

$$\chi^2 = \sum_{n=2}^{5} [A_{exp}(n) - C_{sim}A_{sim}(n) + C_{nat}A_{nat}(n)]^2$$

from experimental amplitudes $A_{exp}(n)$. One-quantum amplitudes were not included in χ^2 because of some uncertainties in the natural abundance contribution which can be different for different models. Also, C_{sim} and C_{nat} were constrained to be non-negative, and $A_{nat}(n) = 0$ for $n > 2$. It can be seen in Fig. 7.75 that only simulations for the in-register, parallel β-sheet model adequately describe the experimental multiple-quantum NMR spectra for the two differently labelled fibrillar samples and

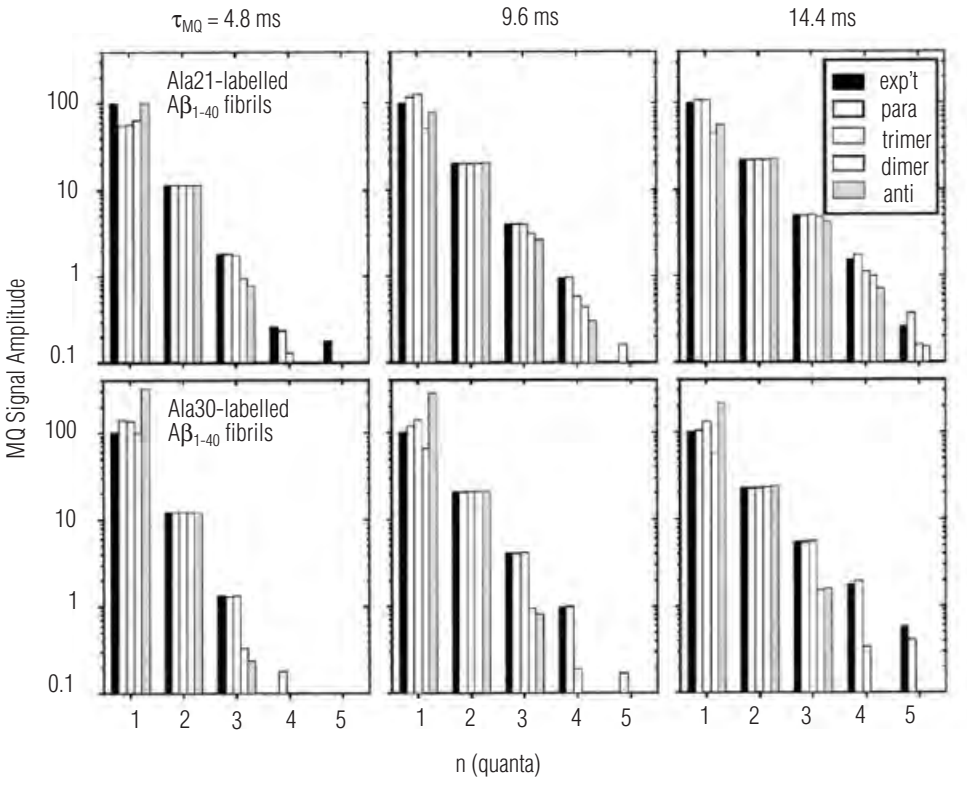

Fig. 7.75 Comparison of experimental ^{13}C single-quantum-selective multiple-quantum-excitation NMR amplitudes (black) with simulations for parallel, trimeric, dimeric, and antiparallel organizations of β-sheets in Alzheimer's amyloid-β-protein(1–40) fibrils, for samples labelled with ^{13}C at methyl carbons of Ala21 and Ala30. Experimental multiple-quantum NMR amplitudes are normalized to a one-quantum amplitude of 100 (logarithmic vertical scale). The parallel β-sheet model fits all of the experimental data most closely. Experimental amplitudes were determined from multiple-quantum NMR spectra in Fig. 7.74 by integrating each subspectrum over the interval from −2 kHz to +3 kHz. Uncertainties in the experimental amplitudes (rms noise integrated over a 5 kHz-wide interval) are ±0.11, ±0.14, and ±0.14 for the Ala21-labelled amyloid-β-protein(1–40) fibril data, and ±0.15, ±0.17 and ±0.24 for the Ala30-labelled amyloid-β-protein(1–40) fibril data, for τ_{MQ} = 4.8 ms, 9.6 ms and 14.4 ms, respectively. Adapted from ref. [**232**].

at all values of the excitation time τ_{MQ}. The other three models, antiparallel, dimeric and trimeric, lead to a significantly poorer fit than the parallel β-sheet model, particularly in the case of Ala30-labelled $A\beta P_{1-40}$ fibrils.

It is important to note that the two main constraints on the supramolecular structure of amyloid-β-protein fibrils obtained from the multiple-quantum NMR experiments cannot exclude alternatives to the in-register, parallel β-sheet model. However, it is absolutely necessary that any such models must place Ala21 and Ala30 methyl carbons in groups of at least five with internuclear distances less than ca. 5.5 Å. In an out-of-register, parallel β-sheet, the internuclear distances would exceed 6.0 Å. Also in a laminated β-sheet structure, the average spacing between laminae is 9.6 Å from X-ray diffraction data [**235**, **245–247**] and therefore one can

omit contributions to experimental multiple-quantum signals from the interlaminae dipole–dipole couplings between labelled spins. Note also that the multiple-quantum NMR experiments, as the first 'cast' to entangle the supramolecular structure, can then be assisted by distance measurements such as REDOR or torsion angle experiments discussed in the previous sections of this chapter. A good example of that can be found for the short 7-mer fragment of the full length amyloid-β-protein, $A\beta P_{16–22}$, discussed previously in this chapter [**124**]. First, multiple-quantum NMR measurements on the singly Ala21 labelled $A\beta P_{16–22}$ showed only a weak 3-quantum and no 4-quantum signals even at the long excitation time of 14.4 ms. This suggested an antiparallel arrangement of molecules in fibrils. To prove that, additional samples have been prepared with both ^{13}C and ^{15}N labels at the sites which are expected to be involved in hydrogen bonding provided that the in-register antiparallel β-sheet structure is formed in fibrils. Indeed, REDOR measurements (see Section 7.3.1) showed contacts with the correct distance of 4.4 Å supporting the in-register antiparallel β-sheet organization [**124**]. This last example proves that various solid-state NMR experiments, if taken in combination, are powerful tools for structural studies on solid systems of biological importance.

Acknowledgements

I thank M.H. Levitt, B.H. Meier, S.J. Opella, E. Oldfield, J. Schaefer, H.W. Spiess, R. Tycko, T. Terao and A. Watts for sending reprints of their recently published papers. I also thank Y. Ishii and R. Tycko for providing material (including figures) on new methods of both distance and torsion angle measurements prior to publication. I am also grateful to J.P. Yesinowski and R. Tycko for useful comments on the manuscript. M. Kritikos is acknowledged for Fig. 7.10. Also support, encouragement and comments from the editor of the book, Melinda J. Duer, during the course of the writing of this chapter are greatly appreciated.

Notes

1. In principle, WIM-12 can be substituted by a simple CW (Continuous-Wave) rf irradiation of sufficiently high amplitude on the ^1H spins. However, WIM-12 gives the same decoupling effect at considerably lower rf amplitudes. Another alternative to WIM-12 could be the TPPM-decoupling sequence suggested by Griffin and co-workers [**27**] or the R24 sequence of Levitt and co-workers [**28**].
2. FSLG-2 is the preferred homonuclear decoupling sequence at higher spinning frequencies due to its shorter cycle time compared with MREV-8 (approximately half), and therefore a better approximation to a constant average hamiltonian during the decoupling cycle [**192**].
3. In the average hamiltonian representation, for the efficient homonuclear decoupling, the cycle time of the MREV-8 sequence, τ_{MREV}, must be of the order of or shorter than the inverse of the effective ^1H–^1H dipolar interaction.

4. As in the HCCH experiment, in order to get the periodic t_1 modulation, the single τ_R signal has to be replicated several times with a proper correction for T_2^{2Q} relaxation prior to Fourier transformation in the first dimension.
5. To be more precise, the density operator describing this state may involve up to N multi-spin operators if there are N coupled spins in the system. $N - n$ of these operators are population operators of the form $\hat{I}_z^i$.

References

1. A. McDermott, T. Polenova, A. Bockmann, K.W. Zilm, E.K. Paulsen, R.W. Martin and G.T. Montelione, *J. Biomol. NMR* **16** (2000) 209.
2. Y. Ishii, *J. Phys. Chem.* (2001) in press.
3. R.R. Ernst, G. Bodenhausen and A. Wokaun, *Principles of Nuclear Magnetic Resonance in One and Two Dimensions*, Oxford University Press, Oxford, UK (1987).
4. K. Wüthrich, *NMR of Proteins and Nuclear Acids*, Wiley, New York (1986), pp. 130–61.
5. R.G. Pembleton, L.M. Ryan and B.C. Gerstein, *Rev. Sci. Instrum.* **48** (1977) 1286.
6. C.E. Bronnimann, B.L. Hawkins, M. Zhang and G.E. Maciel, *Anal. Chem.* **60** (1988) 1743.
7. P. Caravatti, L. Braunschweiler and R.R. Ernst, *Chem. Phys. Lett.* **100** (1983) 305.
8. A. Bielecki, A.C. Kolbert and M.H. Levitt, *Chem. Phys. Lett.* **155** (1989) 341.
9. P. Mansfield, *J. Phys.* **C4** (1971) 1444.
10. W.K. Rhim, D.D. Elleman and R.W. Vaughan, *J. Chem. Phys.* **59** (1973) 3740.
11. A. Shoji, H. Kimura, T. Ozaki, H. Sugisawa and K. Deguchi, *J. Am. Chem. Soc.* **118** (1996) 7604.
12. S.P. Bown, I. Schnell, J.D. Brand, K. Müllen and H.W. Spiess, *Phys. Chem. Chem. Phys.* **2** (2000) 1735.
13. G. Metz, X. Wu and S.O. Smith, *J. Magn. Reson.* **110A** (1994) 219.
14. O.B. Peersen and S.O. Smith, *Concepts Magn. Reson.* **5** (1993) 303.
15. Y. Ishii and R. Tycko, *J. Magn. Reson.* **142** (2000) 199.
16. G.J. Gröbner, A. Taylor, Ph. T.F. Williamson, G. Choi, C. Glaubitz, J.A. Watts, W.J. de Grip and A. Watts, *Anal. Biochem.* **254** (1997) 132.
17. G.J. Gröbner, G. Choi, I.J. Burnett, C. Glaubitz, P.J.E. Verdegem, J. Lugtenburg and A. Watts, *FEBS Lett.* **422** (1998) 201.
18. A.M. Taylor, G. Gröbner, Ph. T.F. Williamson and A. Watts, *Biochemistry* **38** (1999) 11172.
19. G.S. Harbison, V.-D.-Vogt and H.W. Spiess, *J. Chem. Phys.* **86** (1987) 1206.
20. K. Schmidt-Rohr and H.W. Spiess, Multidimensional Solid State NMR and Polymers, Academic Press, London (1994).
21. Z. Song, O.N. Antzutkin, Y.K. Lee, S.C. Shekar, A. Rupprecht and M.H. Levitt, *Biophys. J.* **73** (1997) 1539.
22. Z. Song (1996) *Conformational Transitions and Molecular Order in Wet-Spun Oriented DNA*, PhD thesis, Stockholm.
23. L. van Dam and M.H. Levitt, *J. Mol. Biol.* **304** (2000) 541.
24. J.A.G. Arêas, G.J. Gröbner, L.B. Pellacani, C. Glaubitz and A. Watts, *Magn. Reson. Chem.* **35** (1997) S119.
25. J.A.G. Arêas, G.J. Gröbner, C. Glaubitz and A. Watts, *Biochemistry* **37** (1998) 5582.
26. C. Glaubitz, I.J. Burnett, G. Gröbner, A.J. Mason and A. Watts, *Biochemistry* **121** (1999) 5787.
27. A.E. Bennett, C.M. Rienstra, M. Auger, K.V. Lakshmi and R.G. Griffin, *J. Chem. Phys.* **103** (1998) 6951.
28. M. Carravetta, M. Edén, X, Zhao, A. Brinkmann and M.H. Levitt, *Chem. Phys. Lett.* **321** (2000) 205.
29. E.R. Andrew, A. Bradbury, R.G. Eades and V.T. Wynn, *Phys. Lett.* **4** (1963) 99.
30. E.R. Andrew, S. Clough, L.F. Farnell, T.D. Gledhill and I. Roberts, *Phys. Lett.* **21** (1966) 505.
31. M.H. Levitt, D.P. Raleigh, F. Creuzet and R.G. Griffin, *J. Chem. Phys.* **92** (1990) 6347.

32. M. Helmle, Y.K. Lee, P.J.E. Verdegem, X. Feng, T. Karlsson, J. Lugtenburg, H.J.M. de Groot and M.H. Levitt, *J. Magn. Reson.* **140** (1999) 379 and references therein.
33. A.E. Bennett, J.H. Ok, R.G. Griffin and S. Vega, *J. Chem. Phys.* **96** (1992) 8624.
34. A.E. Bennett, C.M. Rienstra, J.M. Griffiths, W.G. Zhen, P.T. Lansbury and R.G. Griffin, *J. Chem. Phys.* **108** (1998) 9463.
35. Y. Ishii, *J. Chem. Phys.* (2001) in press.
36. R. Tycko and G. Dabbagh, *Chem. Phys. Lett.* **173** (1990) 461.
37. B.H. Meier and W.L. Earl, *J. Chem. Phys.* **85** (1986) 4905.
38. B.-Q. Sun, P.R. Costa, D. Kocisko, P.T. Lansbury, Jr. and R.G. Griffin, *J. Chem. Phys.* **102** (1995) 702.
39. D.M. Gregory, G. Wolfe, T. Jarvie, J. Shiels and G.P. Drobny, *Mol. Phys.* **89** (1996) 1835.
40. N.C. Nielsen, H. Bildsøe, H.J. Jakobsen and M.H. Levitt, *J. Chem. Phys.* **101** (1994) 1805.
41. M. Feike, D.E. Demco, R. Graf, J. Gottwald, S. Hafner and H.W. Spiess, *J. Magn. Reson.* **122A** (1996) 214.
42. M. Baldus, D.G. Geurts and B.H. Meier, *Solid State Nucl. Magn. Reson.* **11** (1998) 157.
43. Y.K. Lee, N.D. Kurur, M. Helmle, O.G. Johannessen, N.C. Nielsen and M.H. Levitt, *Chem. Phys. Lett.* **242** (1995) 304.
44. M. Hohwy, H.J. Jakobsen, M. Edén, M.H. Levitt and N.C. Nielsen, *J. Chem. Phys.* **108** (1998) 2686.
45. C.M. Rienstra, M.E. Hatcher, L.J. Mueller, B.Q. Sun, S.W. Fesik and R.G. Griffin, *J. Am. Chem. Soc.* **120** (1998) 10602.
46. T. Gullion and J. Schaefer, *J. Magn. Reson.* **81** (1989) 196.
47. D.E. Kaplan and E. Hahn, *J. Phys. Radium.* **19** (1958) 821.
48. A.W. Hing, S. Vega and J. Shaefer, *J. Magn. Reson.* **103A** (1993) 151.
49. X. Feng, Y.K. Lee, D. Sandström, M. Edén, H. Maisel, A. Sebald and M.H. Levitt, *Chem. Phys. Lett.* **257** (1996) 314.
50. M. Hong, J. Cross and R.G. Griffin, *J. Phys. Chem.* **101B** (1997) 5869.
51. X. Feng, M. Edén, A. Brinkmann, H. Luthman, L. Eriksson, A. Gräslund, O.N. Antzutkin and M.H. Levitt, *J. Am. Chem. Soc.* **119** (1997) 12006.
52. P.R. Costa, J.D. Gross, M. Hong and R.G. Griffin, *Chem. Phys. Lett.* **280** (1997) 95.
53. Y. Ishii, T. Terao and M. Kainosho, *Chem. Phys. Lett.* **256** (1996) 133.
54. K. Schmidt-Rohr, *J. Am. Chem. Soc.* **118** (1996) 7601.
55. D.P. Weliky and R. Tycko, *J. Am. Chem. Soc.* **118** (1996) 8487.
56. R. Tycko, D.P. Weliky and A.E. Berger, *J. Chem. Phys.* **105** (1996) 7915.
57. F.J. Blanco and R. Tycko, *J. Magn. Reson.* (2001) in press.
58. M. Lee and W.I. Goldberg, *Phys. Rev.* **410A** (1965) 2165.
59. H.T. Edzes and J.P.C. Bernards, *J. Am. Chem. Soc.* **106** (1984) 1515.
60. P.M. Henrichs and M. Linder, *J. Magn. Reson.* **58** (1984) 458.
61. R. Tycko and G. Dabbagh, *J. Am. Chem. Soc.* **113** (1991) 3592.
62. S.B. Prusiner, Nobel lecture, *Proc. Natl. Acad. Sci. USA* **95(23)** (1998) 13363; /www.prionics.ch/prions.html.
63. T.L. James, H. Liu, N.B. Ulyanov, S. Farr-Jones, H. Zhang, D.G. Donne, K. Kaneko, D. Groth, I. Mehlhorn, S.B. Prusiner and F.E. Cohen, *Proc. Natl. Acad. Sci. USA* **94** (1997) 10086.
64. Z. Huang, S.B. Prusiner and F.E. Cohen, *Folding and Design* **1** (1995) 13.
65. S.J. deArmond, M.P. McKinley, R.A. Barry, M.B. Braunfeld, J.R. McColloch and S.B. Prusiner, *Cell* **41** (1985) 221.
66. M.P. McKinley, R. Meyer, L. Kenaga, F. Rahbar, R. Cotter, A. Serban and S.B. Prusiner, *J. Virol.* **65** (1991) 1440.
67. I. Ando, H. Saito, R. Tabeta, A. Shoji and T. Ozaki, *Macromolecules* **17** (1984) 457.
68. S. Spera and A. Bax, *J. Am. Chem. Soc.* **113** (1991) 5490.
69. A.C. deDios and E. Oldfield, *Solid State Nucl. Magn. Reson.* **6** (1996) 101.
70. E. Oldfield, *J. Biomol. NMR* **5** (1995) 217.
71. R. Tycko, *J. Biomol. NMR* **8** (1996) 239.
72. A.C. deDios and E. Oldfield, *J. Am. Chem. Soc.* **116** (1994) 11485.

73. A.C. deDios, D.D. Laws and E. Oldfield, *J. Am. Chem. Soc.* **116** (1994) 7784.
74. A.C. deDios and E. Oldfield, Chemical shifts in biochemical systems, in *Encyclopedia of Nuclear Magnetic Resonance*, Wiley, New York (1996), p. 1330.
75. D.D. Laws, H. Le, A.C. deDios, R.H. Havlin and E. Oldfield, *J. Am. Chem. Soc.* **117** (1995) 9542.
76. J.G. Pearson, J.-F. Wang, J.L. Markley, H.-B. Le and E. Oldfield, *J. Am. Chem. Soc.* **117** (1995) 8823.
77. H.-B. Le and E. Oldfield, *J. Phys. Chem.* **100** (1996) 16423.
78. R.H. Havlin, H.-B. Le, D.D. Laws, A.C. deDios and E. Oldfield, *J. Am. Chem. Soc.* **119** (1997) 11951.
79. J. Heller, D.D. Laws, M. Tomaselli, D.S. King, D.E. Wemmer, A. Pines, R.H. Havlin and E. Oldfield, *J. Am. Chem. Soc.* **119** (1997) 7827.
80. D.J. Selkoe, *J. NIH Res.* **7** (1995) 51.
81. E.O. Freed, D.J. Myers and R. Risser, *J. Virol.* **65** (1991) 190.
82. L. Wu et al., *Nature* **384** (1996) 179.
83. A. Trkola et al., *Nature* **384** (1996) 184–7.
84. E.A. Berger, *AIDS* **11** (Suppl. A) (1997) S3.
85. S. Matsushita et al., *J. Virol.* **62** (1988) 2107.
86. G. Gorse et al., *J. Infect. Dis.* **173** (1996) 330.
87. J.B. Ghiara, E.A. Stura, R.L. Stanfield, A.T. Profy and I.A. Wilson, *Science* **264** (1994) 82.
88. D.P. Weliky, A.E. Bennett, A. Zvi, J. Anglister, P.J. Steinbach and R. Tycko, *Nature Struct. Biol.* **6** (1999) 141.
89. K. Javaherian et al., *Proc. Natl. Acad. Sci. USA* **86** (1989) 6768.
90. R. Tycko and G. Dabbagh, *J. Am. Chem. Soc.* **113** (1991) 9444.
91. A.E. Bennett, D.P. Weliky and R. Tycko, *J. Am. Chem. Soc.* **120** (1998) 4897.
92. T.G. Oas, C.J. Hartzell, T.J. McMahon, G.P. Drobny and F.W. Dahlquist, *J. Am. Chem. Soc.* **109** (1987) 5956.
93. G. Dabbah, D.P. Weliky and R. Tycko, *Macromolecules* **27** (1994) 6183.
94. J. Herzfeld and A.E. Berger, *J. Chem. Phys.* **73** (1980) 6021.
95. S. Wolfram, *The Mathematica Book*, Vol. 3, Wolfram Media/Cambridge University Press, Cambridge, UK, 1996.
96. O.N. Antzutkin, Y.K. Lee and M.H. Levitt, *J. Magn. Reson.* **135** (1998) 144.
97. O.N. Antzutkin, *Progr. Nucl. Magn. Reson. Spectr.* **35** (1999) 203.
98. N.C. Cohen, *J. Med. Chem.* **26** (1983) 259.
99. R.M. Sweet, in *Cephalosporins and Penicillins* (E.H. Flynn, Ed.), Academic Press, New York (1972), p. 281.
100. S. Abrahamson, D.C. Hodgkin and E.N. Maslen, *Biochem. J.* **86** (1963) 514.
101. M.O. Boles and R.J. Girven, *Acta Crystallogr.* **32B** (1976) 2279.
102. N.J. Clayden, C.M. Dobson, L.-Y. Lian and J.M. Twyman, *J. Chem. Soc. Perkin. Trans. II* (1986) 1933.
103. O.N. Antzutkin, S.C. Shekar and M.H. Levitt, *J. Magn. Reson.* **115A** (1995) 7.
104. J.G. Hexem, M.H. Frey and S.J. Opella, *J. Phys. Chem.* **77** (1982) 3847.
105. A.C. Olivieri, *Solid State Nucl. Magn. Reson.* **1** (1992) 345.
106. J.E. Rich, M.N. Manalo and A.C. de Dios, *J. Phys. Chem.* **104A** (2000) 5837.
107. M.J. Frisch et al., Gaussian 98, Revision A7, Inc., Pittsburgh, PA (1998).
108. A.E. Walling, R.E. Pargas and A.C. de Dios, *J. Phys. Chem.* **101A** (1997) 7299.
109. R. Mondelli and P. Vendura, *J. Chem. Soc. Perkin Trans.* **2** (1977) 1749.
110. C. Chang and S.L. Hen, *J. Pharm. Sci.* **68** (1979) 64.
111. Th.M. Forrest, G.E. Wilson, Y. Pan and J. Schaefer, *J. Biol. Chem.* **266** (1991) 24485.
112. G. Tong, Y. Pan, H. Dong, R. Pryor, G.E. Wilson and J. Schaefer, *Biochemistry* **36** (1997) 9859.
113. M.E. Merrit, A.M. Christensen, K.J. Kramer, Th.L. Hopkins and J. Schaefer, *J. Am. Chem. Soc.* **118** (1996) 11278.
114. A.M. Christensen, J. Schaefer, K.J. Kramer, Th.D. Morgan and Th.L. Hopkins, *J. Am. Chem. Soc.* **113** (1991) 6799.

115. K. Nishimura, A. Naito, S. Tuzi, H. Saitô, Ch. Hashimoto and M. Aida, *J. Phys. Chem.* **102B** (1998) 7476.
116. L.M. McDowell, M. Lee, R.A. McKay, K.S. Anderson and J. Schaefer, *Biochemistry* **35** (1996) 3328.
117. Ch. A. Klug, K. Tasaki, N. Tjandra, Ch. Ho and J. Schaefer, *Biochemistry* **36** (1997) 9504.
118. L.M. McDowell, M.A. McCarrick, D.R. Studelska, W.J. Guilford, D. Arnaiz, J.L. Dallas, D.R. Light, M. Whitlow and J. Schaefer, *J. Med. Chem.* **42** (1999) 3910.
119. D.D. Mueller, A. Schmidt, K.L. Pappan, R.A. McKay and J. Schaefer, *Biochemistry* **34** (1995) 5597.
120. L.M. McDowell, D. Barkan, G.E. Wilson and J. Schaefer, *Solid State Nucl. Magn. Reson.* **7** (1996) 203.
121. L.M. McDowell, A. Schmidt, E.R. Cohen, D.R. Studelska and J. Schaefer, *J. Mol. Biol.* **256** (1996) 160.
122. J.M. Goetz, B. Poliks, D.R. Studelska, M. Fischer, K. Kugelbrey, A. Bacher, M. Cushman and J. Schaefer, *J. Am. Chem. Soc.* **121** (1999) 7500.
123. K.T. Mueller, *J. Magn. Reson.* **113A** (1995) 81.
124. J.J. Balbach, Y. Ishii, O.N. Antzutkin, R.D. Leapman, N.W. Rizzo, F. Dyda, J. Reed and R. Tycko, *Biochemistry* **39** (2000) 13748.
125. D.P. Raleigh, M.H. Levitt and R.G. Griffin, *Chem. Phys. Lett.* **146** (1988) 71.
126. P. Caravatti, G. Bodenhausen and R.R. Ernst, *J. Magn. Reson.* **55** (1983) 88.
127. H. Geen, M.H. Levitt and G. Bodenhausen, *Chem. Phys. Lett.* **200** (1992) 350.
128. D.A. Middleton, R. Robins, X. Feng, M.H. Levitt, I.D. Spiers, C.H. Schwalbe, D.G. Reid and A. Watts, *FEBS Lett.* **410** (1997) 269.
129. G. Sachs, *Ann. Rev. Pharmacol. Toxicol.* **28** (1988) 269.
130. J.J. Kaminski et al., *J. Med. Chem.* **34** (1991) 533.
131. F. Creuzet, A. McDermott, R. Gebhard, K. van der Hoff, M.B. Spijker-Assink, J. Herzfeld, M.H. Levitt and R.G. Griffin, *Science* **251** (1991).
132. L.K. Thompson, A.E. McDermott, J. Raap, C.M. van der Wielen, J. Lugtenburg, J. Herzfeld and R.G. Griffin, *Biochemistry* **31** (1992) 7931.
133. A. McDermott, F. Creuzet, R. Gebhard, K. van der Hoef, M.H. Levitt, J. Herzfeld, J. Lugtenburg and R. Griffin, *Biochemistry* **33** (1994) 6129.
134. K.V. Lakshmi, M. Auger, J. Raap, J. Lugtenburg, R.G. Griffin and J. Herzfeld, *J. Am. Chem. Soc.* **115** (1993) 8515.
135. P.J.E. Verdegem, M. Helmle, J. Lugtenburg and H.J.M. de Groot, *J. Am. Chem. Soc.* **119** (1997) 169.
136. P.J.E. Verdegem, *Structure, Function, and Dynamics of the Chromophore of Rhodopsin*, PhD Dissertation, Leiden University (1998).
137. S.O. Smith, *Curr. Opin. Struct. Biol.* **3** (1993) 755.
138. O.B. Peersen, S. Yoshimura, H. Hojo, S. Aimoto and S.O. Smith, *J. Am. Chem. Soc.* **114** (1992) 4332.
139. S.O. Smith, J. Hamilton, A. Salmon and B.J. Bormann, *Biochemistry* **33** (1994) 6327.
140. S.O. Smith, R. Jonas, M. Braiman and B.J. Bormann, *Biochemistry* **33** (1994) 6334.
141. O.B. Peersen, M. Groesbeek, S. Aimoto and S.O. Smith, *J. Am. Chem. Soc.* **117** (1995) 7228.
142. S.O. Smith and B.J. Bormann, *Proc. Natl. Acad. Sci. USA* **92** (1995) 488.
143. Y. Tomita, E.J. O'Connor and A. McDermott, *J. Am. Chem. Soc.* **116** (1994) 8766.
144. P.T. Lansbury, P.R. Costa, J.M. Griffiths, E.J. Simon, M. Auger, K.J. Halverson, D.A. Kocisko, Z.S. Hendsch, T.T. Ashburn, R.G.S. Spencer, B. Tidor and R.G. Griffin, *Nature Struct. Biol.* **2** (1995) 990.
145. J.M. Griffiths, T.T. Ashburn, M. Auger, P.R. Costa, R.G. Griffin and P.T. Lansbury, *J. Am. Chem. Soc.* **117** (1995) 3539.
146. P.R. Costa, D.A. Kocisko, B.Q. Sun, P.T. Lansbury and R.G. Griffin, *J. Am. Chem. Soc.* **119** (1997) 10487.
147. J. Heller, A.C. Kolbert, R. Larsen, M. Ernst, T. Bekker, M. Baldwin, S.B. Prusiner, A. Pines and D. Wemmer, *Protein Sci.* **5** (1996) 1655.

148. J.R. Garbow and C.A. McWherter, *J. Am. Chem. Soc.* **115** (1993) 238.
149. O.N. Antzutkin and M.H. Levitt, *J. Magn. Reson.* **147** (2000) 147.
150. C.A. Klug, W. Zhu, M.E. Merritt and J. Schaefer, *J. Magn. Reson.* **109** (1994) 134.
151. D.M. Gregory, D.J. Mitchell, J.A. Stringer, S. Kiihne, J.C. Shiels, J. Callahan, M.A. Mehta and G.P. Drobny, *Chem. Phys. Lett.* **246** (1995) 654.
152. D.M. Gregory, M.A. Mehta, J.C. Shiels and G.P. Drobny, *J. Chem. Phys.* **107** (1997) 28.
153. D.M. Gregory, T.L.S. Benzinger, T.S. Burkoth, H. Miller-Auer, D.G. Lynn, S.C. Meredith and R.E. Botto, *Solid State Nucl. Magn. Reson.* **13** (1998) 149.
154. T.L.S. Benzinger, D.M. Gregory, T.S. Burkoth, H. Miller-Auer, D.G. Lynn, R.E. Botto and S.C. Meredith, *Proc. Natl. Acad. Sci. USA* **95** (1998) 13407.
155. T.L.S. Benzinger, D.M. Gregory, T.S. Burkoth, H. Miller-Auer, D.G. Lynn, R.E. Botto and S.C. Meredith, *Biochemistry* **39** (2000) 3491.
156. M. Karplus, *J. Phys. Chem.* **30** (1959) 11.
157. A.C. Wang and A. Bax, *J. Am. Chem. Soc.* **118** (1996) 2483.
158. K. Schmidt-Rohr, *Macromolecules* **29** (1996) 3975.
159. D.M. Gregory, M.A. Mehta, J.C. Shiels and G.P. Drobny, *J. Chem. Phys.* **107** (1997) 28.
160. P.V. Bower, N. Oyler, M.A. Mehta, J.R. Long, P.S. Stayton and G.P. Drobny, *J. Am. Chem. Soc.* **121** (1999) 8373.
161. D.P. Weliky, G. Dabbagh and R. Tycko, *J. Magn. Reson.* **104A** (1993) 10.
162. M. Hong, J.D. Gross, W. Hu and R.G. Griffin, *J. Magn. Reson.* **135** (1998) 169.
163. X. Feng, P.J.E. Verdegem, Y.K. Lee, D. Sandström, M. Edén, P. Bovee-Geurts, W.J. de Grip, J. Lugtenburg, H.J.M. de Groot and M.H. Levitt, *J. Am. Chem. Soc.* **119** (1997) 6853.
164. X. Feng, P.J.E. Verdegem, M. Edén, D. Sandström, Y.K. Lee, P. Bovee-Geurts, W.J. de Grip, J. Lugtenburg, H.J.M. de Groot and M.H. Levitt, *J. Biomol. NMR* **16** (2000) 1.
165. R.K. Hester, J.L. Ackermann, B.L. Neff and J.S. Waugh, *Phys. Rev. Lett.* **36** (1976) 1081.
166. M.E. Stoll, A.J. Vega and R.W. Vaughan, *J. Chem. Phys.* **65** (1976) 4093.
167. M. Linder, A. Hohener and R.R. Ernst, *J. Chem. Phys.* **73** (1980) 4959.
168. M.G. Munowitz and R.G. Griffin, *J. Chem. Phys.* **76** (1982) 2848.
169. G.N. Ramachandran and V. Sasisekharan, *Adv. Prot. Chem.* **28** (1968) 283.
170. D.J. States, R.A. Haberkorn and D.J. Ruben, *J. Magn. Reson.* **48** (1982) 286.
171. J. Kümmerlen, J.D. van Beek, F. Vollrath and B.H. Meier, *Macromolecules* **29** (1996) 2920.
172. H.W. Long and R. Tycko, *J. Am. Chem. Soc.* **120** (1998) 7039.
173. A. Hagemeyer, K. Schmidt-Rohr and H.W. Spiess, *Adv. Magn. Reson.* **13** (1989) 85.
174. Z. Luz, H.W. Spiess and J.J. Titman, *Israel J. Chem.* **32** (1992) 145.
175. D.A. Varshalovich, A.N. Moskalev and V.K. Khersonskii, *Quantum Theory of Angular Momentum*, World Scientific, Singapore (1988).
176. A.P.M. Kentgens, E. de Boer and W.S. Veeman, *J. Chem. Phys.* **87** (1987) 6859.
177. W.T. Dixon, *J. Chem. Phys.* **77** (1982) 1800.
178. D.P. Raleigh, E.T. Olejniczak and R.G. Griffin, *J. Chem. Phys.* **89** (1988) 1333.
179. C.R. Cantor and P.R. Schimmel, *The Conformation of Biological Molecules*, W.H. Freeman, New York (1980).
180. V.I. Lebedev and A.L. Skorokhodov, *Sov. Phys. Dokl.* **45** (1992) 587.
181. M. Edén and M.H. Levitt, *J. Magn. Reson.* **132** (1998) 220.
182. E. Subramanian and V. Lalitha, *Biopolymers* **22** (1983) 833.
183. R. Tycko and A.E. Berger, *J. Magn. Reson.* **141** (1999) 141.
184. K. Schmidt-Rohr, W. Hu and N. Zumbulyadis, *Science* **280** (1998) 714.
185. D.M. Gregory, M.A. Mehta, J.C. Shiels and G.P. Drobny, *J. Chem. Phys.* **107** (1997) 28.
186. P.V. Bower, N. Oyler, M.A. Mehta, J.R. Long, P.S. Stayton and G.P. Drobny, *J. Am. Chem. Soc.* **121** (1999) 8373.
187. O.W. Sørensen, M. Rance and R.R. Ernst, *J. Magn. Reson.* **56** (1984) 527–34.
188. S. Marqusee and R.L. Baldwin, *Proc. Natl. Acad. Sci. USA* **84** (1987) 8898–8902.
189. M. Engelsberg and C.S. Yannoni, *J. Magn. Reson.* **88** (1990) 393.
190. M.M. Harding and R.M. Howieson, *Acta Crystallogr.* **32B** (1976) 633–4.
191. R. Tycko, G. Dabbagh and P.A. Mirau, *J. Magn. Reson.* **85** (1989) 265.

192. B.J. VanRossum, C.P. de Groot, V. Ladizhansky, S. Vega and H.J.M. de Groot, *J. Am. Chem. Soc.* **122** (2000) 3465.
193. K. Takegoshi, K. Nomura and T. Terao, *Chem. Phys. Lett.* **232** (1995) 424.
194. M.S. Lehmann, T.F. Koetzle and W.C. Hamilton, *J. Am. Chem. Soc.* **94** (1972) 2657.
195. M. Hong, J.D. Gross, W. Hu and R.G. Griffin, *J. Magn. Reson.* **135** (1998) 169.
196. H. Le and E. Oldfield, *J. Biomol. NMR* **4** (1994) 341.
197. X. Feng, *Estimating Molecular Conformations by Solid-State NMR Spectroscopy*, PhD thesis, Stockholm University (1998).
198. S.O. Smith, J. Courtin, H. de Groot, R. Gebhard and J. Lugtenburg, *Biochemistry* **30** (1991) 7409.
199. M. Han and S.O. Smith, *Biochemistry* **34** (1995) 1425.
200. R.W. Schoenlein, L.A. Peteanu, R.A. Mathies and S.V. Shank, *Science* **254** (1991) 412.
201. R.W. Schoenlein, L.A. Peteanu, Q. Wang, R.A. Mathies and C.V. Shank, *J. Chem. Phys.* **97** (1993) 12087.
202. A. Bifone, H.J.M. de Groot and F.J. Buda, *J. Phys. Chem.* **101B** (1997) 2954.
203. T. Hamanaka, T. Mitsui, T. Ashida and M. Kakudo, *Acta Crystallogr.* **B28** (1972) 214.
204. S. Ravidranathan, X. Feng, T. Karlsson, G. Widmalm and M.H. Levitt, *J. Am. Chem. Soc.* **122** (2000) 1102.
205. T. Gullion, D.B. Baker and M.S. Conradi, *J. Magn. Reson.* **89** (1990) 479–84.
206. T.G. Oas, R.G. Griffin and M.H. Levitt, *J. Chem. Phys.* **89** (1988) 692.
207. V. Lalitha and E. Subramanian, *Cryst. Struct. Commun.* **11** (1982) 561.
208. T.F. Koetzle and W. Hamilton, *Acta Cryst.* **B28** (1972) 2083.
209. M. Edén, A. Brinkmann, H. Luthman, L. Eriksson and M.H. Levitt, *J. Magn. Reson.* **144** (2000) 266.
210. V. Lalitha, E. Subramanian and J. Bordner, *Ind. J. Pure Appl. Phys.* **23** (1985) 506.
211. M. Eden and M.H. Levitt, *Chem. Phys. Lett.* **293** (1998) 173.
212. M. Hong, *J. Magn. Reson.* **139** (1999) 389.
213. S. Vijay-Kumar, C.E. Bugg and W.J. Cook, *J. Mol. Biol.* **194** (1987) 531.
214. D. Huster, S. Yamaguchi and M. Hong, *J. Am. Chem. Soc.* **122** (2000) 11320.
215. Y. Ishii, K. Hirao, T. Terao, Ts. Terauchi, M. Oba, K. Nishiyama and M. Kainosho, *Solid State Nucl. Magn. Reson.* **11** (1998) 169.
216. Y.-S. Yen and A. Pines, *J. Chem. Phys.* **78** (1983) 3579.
217. D. Suter, S.B. Liu, J. Baum and A. Pines, *Chem. Phys.* **114** (1987) 103.
218. J. Baum, K.K. Gleason, A. Pines, A.N. Garroway and J.A. Reimer, *Phys. Rev. Lett.* **55** (1986) 1377.
219. M.A. Petrich, K.K. Gleason and J.A. Reimer, *Phys. Rev.* **B36** (1987) 9722.
220. D.H. Levi and K.K. Gleason, *J. Phys. Chem.* **96** (1992) 8125.
221. B.E. Scruggs and K.K. Gleason, *J. Phys. Chem.* **97** (1993) 9187.
222. B.E. Scruggs and K.K. Gleason, *Macromolecules* **25** (1992) 1864.
223. S.J. Limb, B.E. Scruggs and K.K. Gleason, *Macromolecules* **26** (1993) 3750.
224. G. Buntkowsky, E. Roessler, M. Taupitz and H.M. Vieth, *J. Phys. Chem.* **A101** (1997) 67.
225. S.J. Hwang, D.O. Uner, T.S. King, M. Pruski and B.C. Gerstein, *J. Phys. Chem.* **99** (1995) 3697.
226. W.V. Gerasimowicz, A.N. Garroway, J.B. Miller and L.C. Sander, *J. Phys. Chem.* **96** (1992) 3658.
227. J.G. Pearson, B.F. Chmelka, D.N. Shykind and A. Pines, *J. Phys. Chem.* **96** (1992) 8517.
228. W.S. Warren, D.P. Weitekamp and A. Pines, *J. Chem. Phys.* **73** (1980) 2084.
229. O.N. Antzutkin and R. Tycko, *J. Chem. Phys.* **110** (1999) 2749.
230. B. Dalhus and C.H. Görbitz, *Acta Chem. Scand.* **50** (1996) 544.
231. J.D. Dunitz and R.R. Ryan, *Acta Cryst.* **21** (1966) 617.
232. O.A. Antzutkin, J.J. Balbach, R.D. Leapman, N.W. Rizzo, J. Reed and R. Tycko, *Proc. Natl. Acad. Sci. USA* **97** (2000) 13045.
233. B.A. Yankner, *Neuron* **16** (1996) 921.
234. E. Storey and R. Cappai, *Neuropathol. Appl. Neurobiol.* **25** (1999) 81.
235. P.E. Fraser, J.T. Nguyen, H. Inouye, W.K. Surewicz, D.J. Selkoe, M.B. Podlisny and D.A. Kirschnen, *Biochemistry* **31** (1992) 10716.
236. S.B. Malinchik, H. Inouye, K.E. Szumowski and D.A. Kirschner, *Biophys J.* **74** (1998) 537.
237. H. Inouye, P.E. Fraser and D.A. Kirschner, *Biophys J.* **64** (1993) 502.

238. L.C. Serpell, C.C.F. Blake and P.E. Fraser, *Biochemistry* **39** (2000) 13269.
239. C. Hilbich, B. Kisterswoike, J. Reed, C.L. Masters and K. Beyreuther, *J. Mol. Biol.* **218** (1991) 149.
240. A.J. Geddes, K.D. Parker, E.D.T. Atkins and E. Beighton, *J. Mol. Biol.* **218** (1991) 149.
241. L.O. Tjernberg, D.J.E. Callaway, A. Tjernberg, S. Hahne, C. Lilliehook, L. Terenius, J. Thyberg and Ch. Nordstedt, *J. Biol. Chem.* **274** (1999) 12619.
242. L.P. Li, T.A. Darden, L. Bartolotti, D. Kominos and L.G. Pedersen *Biophys. J.* **76** (1999) 2871.
243. M.O. Chaney, S.D. Webster, Y.M. Kuo and A.E. Roher, *Protein Eng.* **11** (1998) 761.
244. N.D. Lazo and D.T. Downing, *Biochemistry* **37** (1998) 1731.
245. M. Sunde, L.C. Serpell, M. Bartlam, P.E. Fraser, M.B. Pepys and C.C.F. Blake, *J. Mol. Biol.* **273** (1997) 729.
246. M. Sunde and C.C.F. Blake, *Quarterly Reviews of Biophysics* **31** (1998) 1.
247. D.A. Kirschner, H. Inouye, L.K. Duffy, A. Sinclair, M. Lind and D.J. Selkoe, *Proc. Natl. Acad. Sci. USA* **84** (1987) 6953.

Solid-State NMR Spectroscopy Principles and Applications
Edited by Melinda J. Duer
Copyright © 2002 by Blackwell Science Ltd

Chapter 8
NMR Studies of Oxide Glass Structure

Jonathan F. Stebbins

8.1 Introduction

A glass may be defined as a non-crystalline solid produced by disequilibrium cooling of a liquid. Oxide glasses (the subject of this chapter), and their molten precursors, are nearly ubiquitous in industry and in nature. Human uses range from the ancient and the mundane (containers, windows) to the leading edge of new technologies of data processing and transmission (lasers, optical fibre amplifiers, semiconductor devices) and the long-term mission of nuclear waste storage. Potentially glass-forming magmas dominate many heat and mass transfer processes in the earth; the most dangerous of explosive volcanoes erupt products that are largely glassy. To rationalize and predict the macroscopic thermodynamic and transport properties of such materials, a microscopic understanding of their structure and dynamics is required.

The problems posed by glasses and glass-forming liquids are also of considerable fundamental interest. As complex materials lacking the long-range translational order of crystals, they involve such basic issues as geometric and topological description, reduced dimensionality, the nature of configurational entropy, and cooperative dynamics stretching over 15 or more orders of magnitude in time scale. The 'simplest' of glasses such as SiO_2 and B_2O_3 are still the subject of considerable controversy, even after 50 to 60 years of study by all available tools of solid-state physics and chemistry.

Solid-state NMR is particularly useful for studying glasses because NMR observables (chemical shifts, quadrupolar parameters, couplings between nuclides, peak intensities) are element-specific, sensitive to short- and medium-range structure, and (in principle, in many types of experiments) inherently quantitative. The latter aspect often allows inferences from NMR to go beyond those of infrared, Raman, and optical spectroscopy, in which absorption or emission probabilities are inherently matrix- (and thus composition-) dependent. The directional character of many NMR interactions, the commonly observed resolution among locally distinct structural

units, the possibilities of measuring connectivities directly, and sensitivity to dynamics at time scales of seconds to nanoseconds distinguishes the technique from other common approaches such as X-ray and neutron scattering and X-ray absorption spectroscopy.

In some ways NMR may be considered as an 'indirect' method, in that interpretations of spectra of materials of unknown structure generally rely on empirical correlations derived from the study of crystalline materials (or liquids, of course) with known structure. There is need for much more work of this type, to establish and refine correlations between NMR-observables and structural systematics, and to document the effectiveness or accuracy of new techniques. In particular, correlations and 'proximities' that are reported from various two-dimensional experiments could be made quantitatively meaningful by more extended studies of model compounds. Theoretical calculations of NMR parameters and structural correlations [**1–4**] have been very helpful in interpreting spectra of glasses and even in designing experiments, and should continue to grow in importance.

A chapter of this length cannot review all of the extensive literature on NMR of inorganic glasses: previous reviews serve this purpose better [**5–16**]. In particular, I am neglecting a wealth of fascinating NMR studies on 'non-oxidic' glasses, such as those with fluoride, sulphide, selenide, and phosphide as the principle anions and whose range of properties and structural nuances in some ways far exceed those of the silicates, borates, aluminates, germanates and phosphates discussed here (e.g. [**17–22**]) The burgeoning field of metallic glasses will not be addressed at all, as NMR has not yet played a major role in these systems.

The primary NMR observables to be discussed in this chapter are integrated peak intensities, the true isotropic chemical shift δ_{iso} in ppm (which is free of quadrupolar effects and thus frequency-independent) and the quadrupolar coupling constant C_Q in MHz, defined as e^2qQ/h, where e is the charge of the electron, q is the principle component of the electric field gradient tensor, Q is the nuclear quadrupolar moment, and h is Planck's constant. In many experiments, a variable sometimes called the 'quadrupolar product' P_Q is more readily determined, which, if η_Q is the asymmetry parameter for the electric field gradient tensor, is conveniently defined as $P_Q = C_Q[1 + (\eta^2)/3]^{1/2}$. Since $0 \leq \eta \leq 1$, P_Q is greater than C_Q by at most 15.4%.

8.1.1 The 'structure' of a glass

In crystalline solids, the 'structure' is clearly defined by the space group and the positions of a small set of atoms in the unit cell. In principle, the positions of all atoms in at least a hypothetical perfect crystal can be predicted from this information. Glasses and their precursor liquids are fundamentally different, in that lack of long-range translational symmetry implies that we cannot know or predict atomic positions except on a probabilistic basis. In truly molecular systems such as most organic compounds, a fixed set of bonds between a fixed set of atoms *a priori* allows

prediction of many aspects of the short-range structure of a glass. In contrast, most inorganic glass-forming systems have wide available ranges of composition, and are ionic enough so that description in terms of fixed molecules inadequately describes their full complexity. For example, while it is true that the vast majority of silicon atoms in most silicate glasses have four oxygen neighbours in a tetrahedral arrangement with a fairly small range of O–Si–O angles and distances, these groups are interconnected in a disordered fashion that varies with composition, temperature and pressure. To complicate matters, some SiO_5 groups are also present and probably play an important dynamical role, particularly as pressure is increased. At least in normal glass-forming silicate liquids, the lifetime of a typical Si–O bond is similar to the shear relaxation time [**10**, **23**, **24**], implying that 'molecules' cannot be persistent on timescales long relative to 'intermolecular' motions that control viscosity, in obvious contrast to organic polymers.

What, then, is meant by the 'structure' of an inorganic glass? The most common starting point is generally the cation coordination number(s), as exemplified by decades of NMR studies that quantified populations of BO_3 and BO_4 groups in boron-containing glasses [**13**, **14**, **25–27**]. Studies of cation coordination have been more recently extended, using high-resolution NMR, to Li, Na, Mg, Al, Si and others. Here, NMR can in many cases uniquely quantify populations that appear only as an average to other techniques, such as X-ray and neutron scattering. Given that anions (oxide, fluoride, sulphide, etc.) are volumetrically and numerically predominant in most inorganic glasses, description of *anion* coordination is also of key importance. Significant progress has been made recently using NMR to obtain an 'oxygen's-eye-view' of oxide glass structure; future progress can be expected for other anions as NMR techniques improve, particularly for fluoride. For both anions and cations, NMR is in some cases the only technique available to detect relatively low concentrations (a few per cent) of minor species that may play critical roles in kinetic processes because they are relatively high in energy, such as SiO_5 groups and energetically 'disallowed' Al–O–Al linkages.

The first step towards 'medium range' structure can be considered as the way in which structural units link together, which is describable in part by numbers and identities of first cation neighbours to given cations and by bond angles between units. In oxide glasses, one fundamental way of describing such connections, that can often be quantified by NMR, involves 'Q^n' tetrahedral species, where Q designates 'quaternary', and n the number of oxygens connected to other network units, such as SiO_4, BO_4, BO_3, AlO_4 and PO_4 groups. The distinction between bridging oxygens (BO) and non-bridging oxygens (NBO) is complementary. BO are linked between two network-forming cations; NBO are connected only to a single network former. There is some variation in the use of the terms 'network former' and 'network modifier'. Early workers noted that some oxide liquids, such as those rich in SiO_2 and B_2O_3, were highly viscous and had little tendency to crystallize, and hypothesized that these comprised 'networks' of 3-dimensionally interlinked

trigonal or tetrahedral units with a high degree of strong, covalent bonding. 'Network modifying' cations were taken as those that somehow 'broke up' the network, as manifested by reduction in viscosity and increase in the likelihood of crystallization. It is in this sense (chemical and dynamical) that the distinction between 'network former' and 'network modifier', and thus between 'BO' and 'NBO' will be made here. In some systems, cations that clearly 'weaken' the structure and reduce viscosity, such as Li^{+} and Mg^{2+}, may be at least in part four-coordinated, and could be described in a purely geometric sense as 'network formers'. However, this usage could be quite misleading in terms of consequences for liquid and glass properties, and will be avoided here. Ultimately, of course, a continuum of behaviour becomes obvious as more systems are studied, leading to challenges not only in terminology but in terms of connecting spectroscopic observations with properties: for example, should Si^{4+} with five oxygen neighbours, or Pb^{2+} in three or four coordination, be considered a 'former' or 'modifier'? NMR has also begun to yield more direct information on distances between strongly dipolar-coupled cations, both like and unlike, which is fundamental in understanding medium-range ordering.

Structure at a longer range is one of the oldest, most important, but most difficult questions in glass structure, and compositional and structural heterogeneity at scales of several nm and upward is a major topic of discussion. The low spectral resolution inherent in NMR studies of disordered solids has generally limited our ability to obtain data on the kinds of longer-range connectivities that are so elegantly available in liquid-state studies of organic molecules. However, advanced two-dimensional NMR techniques can in some cases give results on connections not only with the first structural unit neighbour but the second as well. A different view of intermediate-range heterogeneity can sometimes be obtained from detailed studies of spin-lattice relaxation, when this is dominated by through-space, and hence long-range, coupling with unpaired electron spins.

8.1.2 The extent of disorder

Glasses are clearly disordered, but how disordered are they? This question must be of fundamental importance in models of glass structure and of thermodynamic and transport properties, but is difficult to address and is rarely measured. NMR, because it is often inherently quantitative, has led to important progress in understanding where on the continuum from random to ordered various aspects of glass structure lie. For spin-$\frac{1}{2}$ nuclides, the low resolution and generally inconveniently broad MAS peaks in glasses may limit the unique interpretation of spectra, but are in themselves meaningful in reflecting some measure of disorder in speciation, bond angles, and/or bond distances. Thus, it was pointed out early on that ^{29}Si MAS peak widths in binary silicate glasses increased systematically with the field strength of the modifier cation, suggesting increasing disorder [**28**], which was later confirmed

by quantitative determination of Q^n species distributions (see below). Experiments that remove quadrupolar broadening, such as DAS and multiple-quantum techniques, may still yield relatively broad peaks for glasses, but these again can be informative as to distributions of parameters that may be linked through a model to the extent of disorder [**29**, **30**]. These and other 2D correlation techniques have been particularly useful in estimating distributions of species and of bond angles.

8.1.3 Liquids vs. glasses

The liquid-state precursors of most inorganic glasses have heat capacities well above the vibrational limit of 3R per gram atom, indicating that their structures change continuously, becoming increasingly disordered, with increasing temperature [**31**, **32**]. The structure observed by spectroscopy on a glass represents (at best) that of the liquid only at its transition temperature (T_g) to the glass. If a resulting structural model is to be used to interpret or even predict properties of the liquid at much higher temperature (for example, viscosity or solid–liquid phase equilibria), then structural changes with temperature cannot be ignored. Important clues about structural changes with temperature can be obtained from studies, at ambient temperature, of glasses prepared with different cooling rates: rapidly cooled samples record the structure at a somewhat higher T_g than do slower cooled or annealed glasses (see section below). Some structural differences attributed to compositional changes may thus be due to variation of T_g instead.

In-situ high-temperature NMR (to temperatures over 2500°C) has made fundamental contributions to this problem, as well as to the related issue of the dynamics of configurational change with temperature in the liquid state. These studies have been reviewed recently [**11**, **33**], and a number of the more recent papers in this area are given in the reference list [**10**, **11**, **23**, **24**, **33–49**]. The dynamics of network modifier cation motion in both glasses and glass-forming melts, of great interest to diffusion and ionic conductivity, has also been studied extensively by NMR, primarily using analyses of spin-lattice relaxation measurements, and has also been discussed recently [**11**, **50–54**].

8.2 NMR techniques for studying glass structure

8.2.1 Static samples

The longest history of NMR studies of glass structure involved collecting spectra on static (non-spinning) samples at relatively low external magnetic fields. What were for a long time probably the most useful, and most quantitative, models of glass structure were developed by Bray and co-workers [**26**, **27**, **55**] from ^{11}B (and ^{10}B) spectra of borate and borosilicate glasses, based on the observation that

trigonal BO_3 groups have large C_Q's and tetrahedral BO_4 groups have small C_Q's. This difference in local structural symmetry leads to large differences in quadrupolar line widths and shapes that allow ready separation and quantitation of their contributions to spectra.

Efforts to exploit such distinctions have occasionally proved to be useful even with modern, high-field, pulsed FT spectrometers. Static spectra may be the only type obtainable in very high (or low) temperature, or in high-pressure experiments. Caution must be used, however, as severe spectral distortions can occur in relatively broad spectra obtained by single-pulse excitation, because of instrumental deadtime (see Section 2.6). Good results can often be obtained with echo techniques (Section 2.6), if care is taken (for quadrupolar nuclides) to adjust pulse power levels to ensure central transition selectivity, as discussed in Chapter 4 [**56**] (satellite transitions are rarely observable is static spectra of glasses). Aside from ^{11}B, static spectra have been useful for ^{17}O in glasses [**57**], where NBO (generally low C_Q) can often be readily distinguished from BO (generally high C_Q) [**10, 58**] (Fig. 8.1). Note that ^{17}O NMR spectra for glasses are invariably collected on samples enriched to about 10 to 40% ^{17}O from the natural abundance of 0.035%, which adds expense and can limit the number of samples studied.

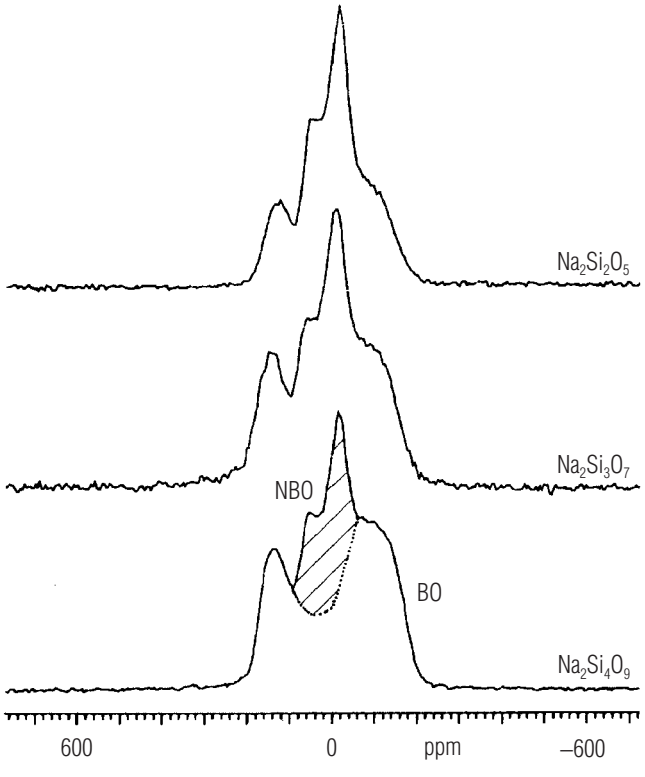

Fig. 8.1 Static (solid echo) ^{17}O NMR spectra for sodium silicate glasses [**58**]. Note increase in ratio of NBO to BO peak areas with increasing Na/Si. Collected at 9.4T on ^{17}O-enriched samples.

Static spectra remain useful for quantifying concentrations of Q^4 groups in silicate glasses that are too small to be well-resolved in MAS spectra [**59–61**] (Fig. 8.2). These are distinct because they have high local symmetry, which in this case is manifested as a chemical shift anisotropy (CSA) much smaller than those of other species that have one or more NBO and hence much lower local symmetry. Although collection of good static spectra can be time-consuming because of their large peak

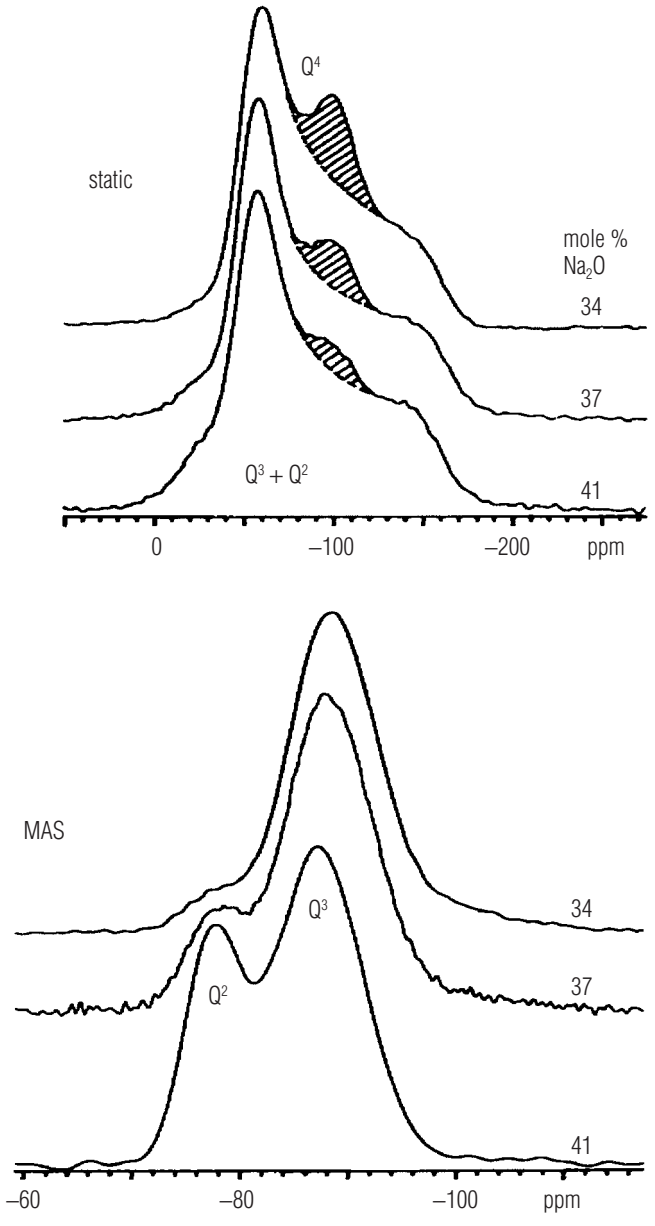

Fig. 8.2 Static and MAS ^{29}Si NMR spectra for sodium silicate glasses [**60**]. In upper spectra, narrow Q^4 peaks are shown by cross-hatching, while Q^3 and Q^2 peaks are not clearly distinguished. In the MAS spectra, Q^n species are partially resolved when they are of relatively high concentration. The presence of Q^4 peaks in all three samples means that a binary distribution of species ($Q^3 + Q^2$ in this composition range) is not adequate to describe the disorder in the glass.

widths, doping with low concentrations (on the order of 0.1%) of paramagnetic impurities such as Gd^{3+} or Co^{2+} (to speed up relaxation times) and isotopic enrichment has been useful.

Classical ^{2}H 'wideline' techniques have been applied to D_2O-containing silicate glasses, providing useful information about the mobility of both molecular D_2O and OD groups [**62**].

In systems with strong homo- or heteronuclear dipolar couplings, static line shapes can be dominated by these couplings. Resolution among distinct sites is generally lost, but the dipolar coupling itself may contain structural information. In glasses, this has been exploited by studies of second moments and spin-echo decay curves, particularly for ^{23}Na and ^{7}Li in silicates [**63**, **64**] and borates [**65**]. Combined with careful studies of crystalline model compounds [**63**], this approach can test models of the homogeneity of cation distributions. Especially for lithium, such studies may have to be done at low temperature to eliminate motional averaging [**64**].

A large number of elements with relatively high atomic number are of major interest in inorganic glasses and have isotopes that are potentially accessible by NMR. However, studies of such nuclides in glasses are made quite challenging by their generally large ranges in chemical shift and corresponding large chemical shift anisotropies (CSA). This 'oversensitivity' to structure means that disorder can lead to peak widths that cannot be narrowed by present (or likely future) MAS experiments. Static spectra may be difficult to observe both because intensity is spread over such a wide range (reducing signal-to-noise ratios) and because of the difficulty of exciting and observing broad peaks by pulsed FT methods (Section 2.6). In such cases, acquisition of a series of spectra for which the observation frequency is progressively offset and echo intensities are summed, can be effective. A good example of this is recent work on ^{207}Pb in silicate glasses, where characteristic 'wideline' peak shapes were used to deduce Pb coordination environments [**66**, **67**] (Fig. 8.3).

An important limitation on the utility of static NMR spectra of glasses is that the anisotropic interactions that are exploited to resolve distinct sites are usually the predominant broadening mechanism, and in general at least partially obscure the effects of disorder. This may be both an advantage and a disadvantage, depending on the structural question being addressed.

8.2.2 Simple MAS spectra

As for other types of materials, MAS spectra with simple, one-pulse acquisition are generally the starting point in NMR studies of inorganic glasses. Both hetero- and homonuclear dipolar broadening can generally be eliminated with fast spinning, as can the CSA, at least for commonly observed nuclides of relatively low atomic number. Resulting spectra often have sufficient resolution to obtain unique and reasonably quantitative populations of structural species.

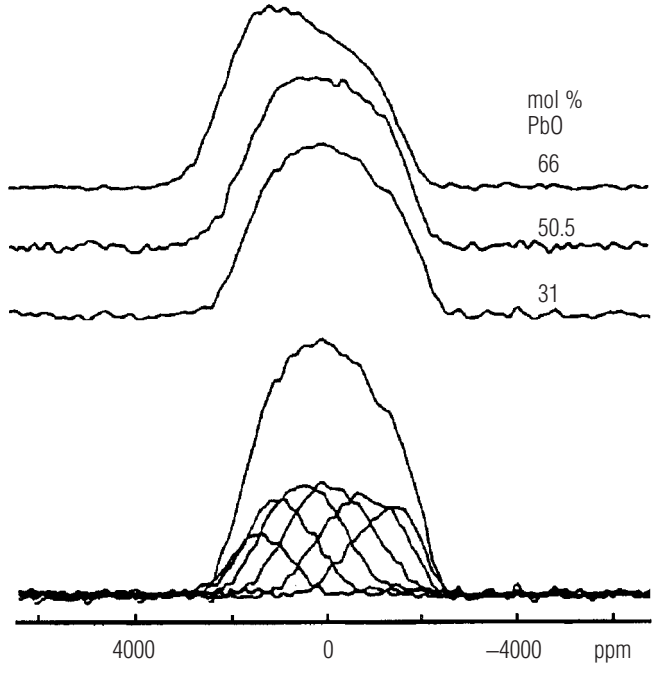

Fig. 8.3 Static whole-echo NMR spectra for ^{207}Pb in a series of Pb–silicate glasses [**66**]. Each is the sum of series of spectra collected with variable transmitter offset, as shown in lower spectrum.

Spin-$\frac{1}{2}$ nuclides

This approach has been extensively applied to ^{29}Si in alkali silicate glasses in order to quantify Q^n species distributions [**61**, **68–73**] (Fig. 8.2). Results are often somewhat dependent on curve fitting of only partially resolved peaks, which generally must be assumed to have symmetrical Gaussian or Gaussian–lorentzian shapes for lack of better constraints. In contrast, in alkaline-earth, aluminosilicate, borosilicate and other multicomponent silicate glasses, ^{29}Si MAS spectra are often completely unresolved because of increased structural disorder and the resulting severe overlap of resonances from different sites [**28**, **74–82**]. In such cases, and even when partial resolution is present, constraints from composition, coupled with simple models of glass structure, can lead to more useful results than unconstrained fitting. A simple example of this, which is surprisingly not always considered, is that in most silicate glasses, the ratio of NBO/BO is fixed by composition alone and, at least in simple systems, can provide an overall constraint on Q^n species populations, increasing the accuracy of spectrum-fitting schemes [**73**]. In cases where observed species populations cannot be reconciled with the expected NBO/BO ratio, the existence of unusual structural species is suggested, such as O^{2-} not bonded to any network cation in La^{3+}-rich [**83**] and Pb^{2+}-rich [**67**] silicate glasses.

Another useful approach is to simultaneously fit even unresolved spectra from a series of glasses with varying composition, with positions and widths of component peaks the same for all and with relative intensities constrained by a model of the

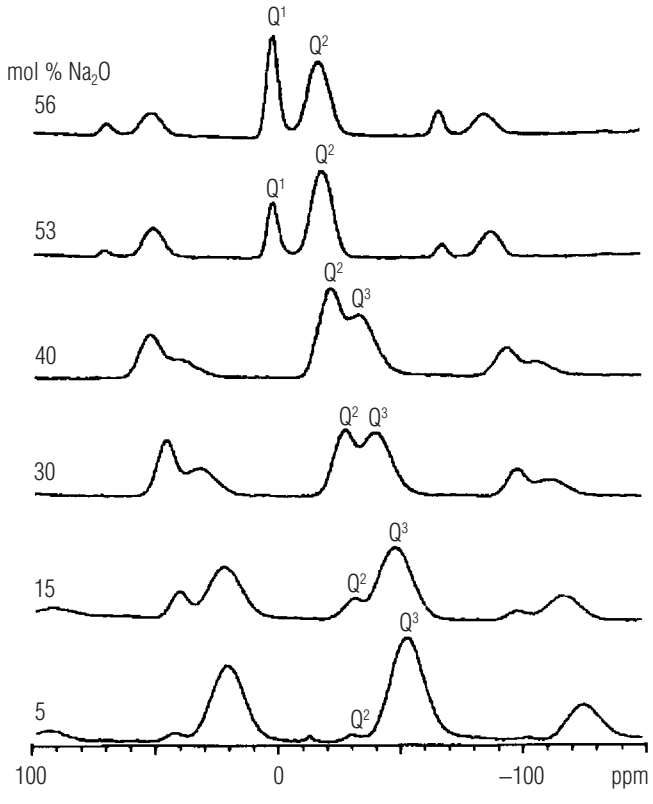

Fig. 8.4 ^{31}P MAS NMR spectra for sodium phosphate glasses, showing Q^n species. In this system, only one or two species (the minimum required by composition) are detected, indicating a relatively ordered distribution [**85**]. Unlabelled peaks are spinning sidebands: note the asymmetry of sideband intensities for the Q^1 and Q^3 sites, consistent with their nearly uniaxial CSA tensors (see section on phosphates).

structure [**84**]. Results will, of course, be model-dependent, but can still serve to test hypotheses and to reach robust qualitative conclusions, such as the relative effects of different modifier cations on the overall ordering state. In any case, the best quantitative results will be obtained if the intensities of spinning sidebands are included in component peak integrals. This may not be strictly necessary if the spinning rate exceeds the width of the CSA (typically about 10 kHz at 9.4 T), or if CSA is small or similar for each site (often the case for Q^4 sites). However, with relatively slow spinning rates it must be kept in mind that because CSA can be quite different from site to site (e.g. Q^3 vs. Q^4), sideband intensities should not be neglected.

Simple MAS spectra have also become a mainstay for ^{31}P NMR of phosphate glasses, although the strong dipolar couplings present for this nuclide have made it amenable to a variety of more sophisticated experiments (see below). As for ^{29}Si, multiple Q^n species can often be observed, often with nearly complete resolution and accompanying accurate quantitation [**85**] (Figs 8.4 and 8.5).

Spin $\frac{3}{2}$ and $\frac{5}{2}$ nuclides

Most NMR studies of quadrupolar nuclides in oxide glasses have been on those with $I = \frac{3}{2}$ (e.g. ^{11}B, ^{23}Na) or $\frac{5}{2}$ (e.g. ^{17}O, ^{25}Mg, ^{27}Al). A few exceptions include ^{6}Li

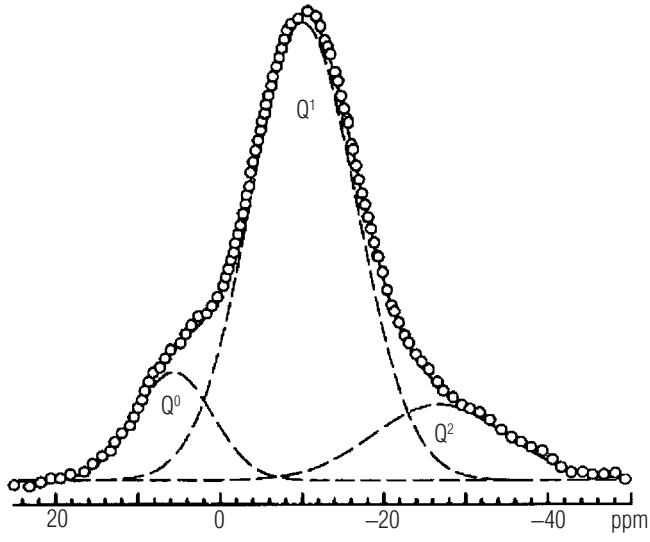

Fig. 8.5 ^{31}P MAS NMR spectrum for a zinc phosphate glass with 67 mol% ZnO [**85**], showing presence of three Q^n species, in contrast with binary distributions in alkali phosphates.

($I = 1$) [**86**] and ^{133}Cs ($I = \frac{7}{2}$) [**65**], both of which have quadrupolar moments small enough to behave effectively as if $I = \frac{1}{2}$ in most systems, and ^{2}H in hydrous glasses [**62**]. Generally, the central ($\frac{1}{2}$ to $-\frac{1}{2}$ transition) is emphasized, but analysis of spinning sidebands for satellite transitions can be useful.

When differences in short-range structure result in large differences in chemical shifts among species, simple MAS spectra for quadrupolar nuclides may be well-enough resolved to address important problems. The most obvious examples involve first-neighbour coordination change, such as the distinction among 4-, 5- and 6-coordinated aluminium in aluminoborates, aluminophosphates and some aluminosilicates [**87–97**] (Fig. 8.6), that between 3- and 4-coordinated boron in borates and borosilicates [**46**, **95**, **98–102**] (Fig. 8.7), and between bridging and non-bridging oxygens in silicates with alkaline earth or trivalent network modifier cations [**97**, **103**, **104**]. High external fields can greatly improve spectra: trigonal and tetrahedral boron sites, for example, are only fully resolved at fields of 14.1 T and above [**95**]. In some cases, however, as for resolution among different coordinations of Al in highly disordered glasses, there seems to be no improvement above 11.7 T, as distributions of chemical shifts begin to dominate the linebroadening. Fast spinning speeds (12–15 kHz at 9.4 T; correspondingly higher at higher fields) are often essential, both to avoid sideband overlap with central peaks and to ensure full orientational averaging. Small rf tip angles ($\pi/6$ or less for the solid) must be chosen to assure quantitative results in systems with wide variations of C_Q from one type of site to another (e.g. ^{11}B and ^{17}O), or, correspondingly, larger tip angles can be chosen to accentuate low concentrations of species with small C_Q's.

In many cases, however, second-order quadrupolar broadening severely hampers resolution among sites known to be present in glasses: obvious examples are Q^n

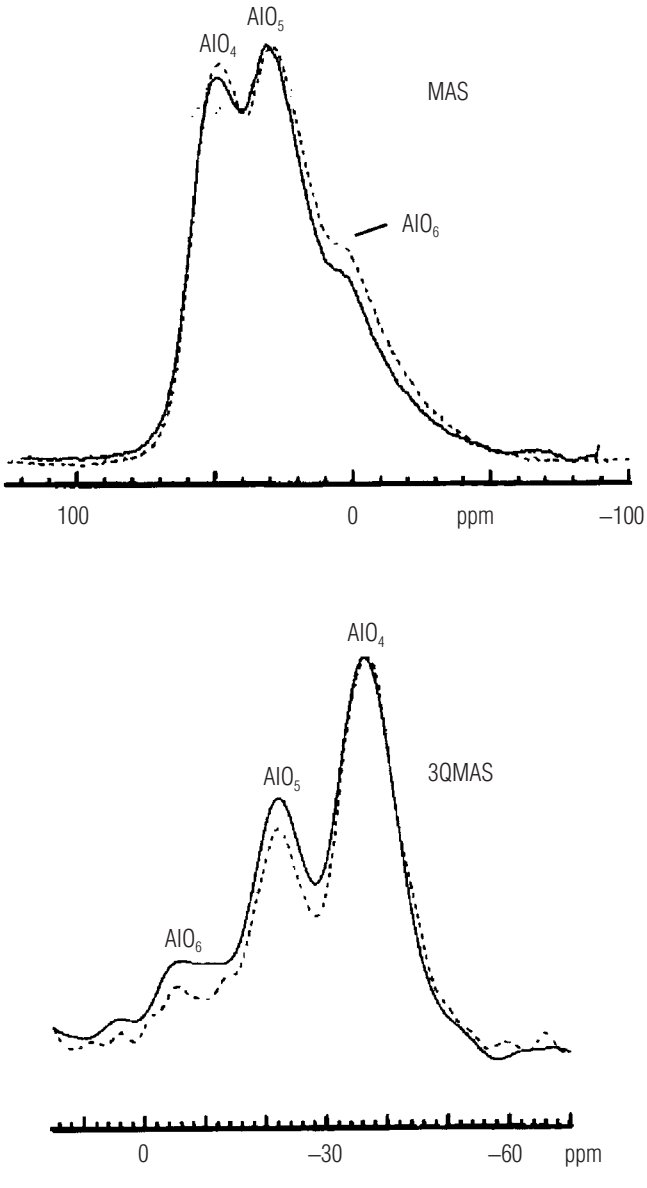

Fig. 8.6 ^{27}Al MAS and isotropic projection of 3QMAS NMR spectra for a glass with 10 mol% Li_2O, 15% Al_2O_3, and 75% B_2O_3, collected at 9.4 T [**95**]. Dashed curves are for fast-quenched (higher glass transition temperature); solid curves for slow-cooled (lower T_g). Spectra are normalized to the height of the AlO_4 peak, and show decrease in mean coordination number with higher T_g. Note narrower, more symmetrical peaks, and better resolution, in 3QMAS spectra.

species for AlO_4 groups, and BO vs. NBO for some alkali silicates. Even in more favourable cases (e.g. Al coordination), quadrupolar broadening can combine with distributions of parameters (C_Q, δ_{iso}) to make quantitation difficult. Major improvements have been demonstrated in such cases by new techniques that eliminate such broadening (see below).

Even for completely unresolved spectra, too broadened by disorder to be fitted to quadrupolar line shapes, useful information can be obtained by collecting spectra

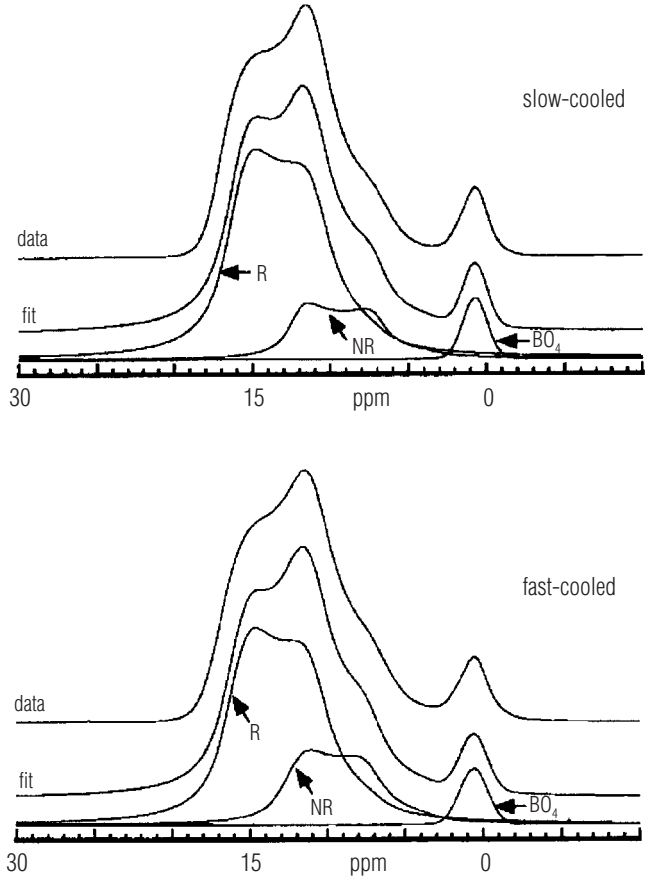

Fig. 8.7 ^{11}B MAS NMR spectra, collected at 14.1 T, for a glass with 5 mol% Na_2O, 95% B_2O_3 [**95**]. Simulations, based in part on previous wideline NMR studies, show BO_3 groups presumed to be in three-membered boroxyl rings ('R') and in non-ring ('NR') sites. Note increase in the proportion of the latter at higher T_g (fast-cooled); note also the complete resolution of BO_3 and BO_4 sites.

at two or more different external fields which provide two or more values of the Larmor frequency ν_0. For nuclear spin I, the observed MAS centre of gravity δ_{MAS} of each transition ($m \rightarrow m - 1$, generally $m = \frac{1}{2}$ for this application) is offset from the true isotropic chemical shift δ_{iso} by the isotropic quadrupolar shift δ_Q, with

$$\delta_{MAS} = \delta_{iso} + \delta_Q \tag{8.1}$$

$$\delta_Q = 10^6 (P_Q / \nu_0)^2 k \tag{8.2}$$

$$k = -\frac{3}{40} \frac{I(I+1) - 9m(m-1) - 3}{I^2(2I-1)^2} \times 10^6 \tag{8.3}$$

For $I = \frac{3}{2}$, k is –25 000 for the central ($m = \frac{1}{2}$) transition; for $I = \frac{5}{2}$ the value is –6000. Thus, with two or more values of δ_{obs} at two or more ν_0's, at least mean values of δ_{iso} and P_Q can be estimated. Analyses of this sort have provided important new structural information on effects of composition on Na and Li coordination in silicate and borate glasses [**65, 105–108**].

Analysis of spinning sidebands

Fitting of spinning sideband intensities to derive CSA tensors has been attempted for ^{29}Si in glasses, but is made difficult by overlapping ranges of δ_{iso} for each component species [**109**]. ^{31}P is more promising in this respect [**110**]. For $I = \frac{3}{2}$ and $\frac{5}{2}$, analysis of satellite transition sidebands in glasses has proved to be very useful. A simple approach relies on the fact that the offset of the centre of gravity of the $\pm\frac{1}{2}$ to $\pm\frac{3}{2}$ sideband manifold from δ_{iso} scales differently from that for the central transition. As can be seen from Equations (8.1) to (8.3), this offset is substantially lower for the $m = \frac{3}{2}$ satellite transition than for the central transition for $I = \frac{5}{2}$ (i.e. $k = 750$ vs. -6000). If true centres of gravity (not peak maxima) are used, and if satellite sidebands can be accurately observed (not always feasible for large C_Q's or low Larmor frequencies), combination of results from sidebands and central peaks can yield estimates of both δ_{iso} and P_Q [**102, 111**]. Such analyses have been particularly useful in showing changes in δ_{iso} for ^{27}Al with quench rate [**112**] and from glass to high-temperature liquids [**45**]. Other analyses rely on simulation of the entire spinning sideband manifold [**113**]. Also for $I = \frac{5}{2}$, the quadrupolar broadening of the $\pm\frac{1}{2}$ to $\pm\frac{3}{2}$ transition is considerably less than that for the central transition, in some cases (particularly for ^{27}Al) leading to better resolution and quantitation of site populations, even to analyses of distributions in parameters [**111, 114, 115**] (Fig. 8.8).

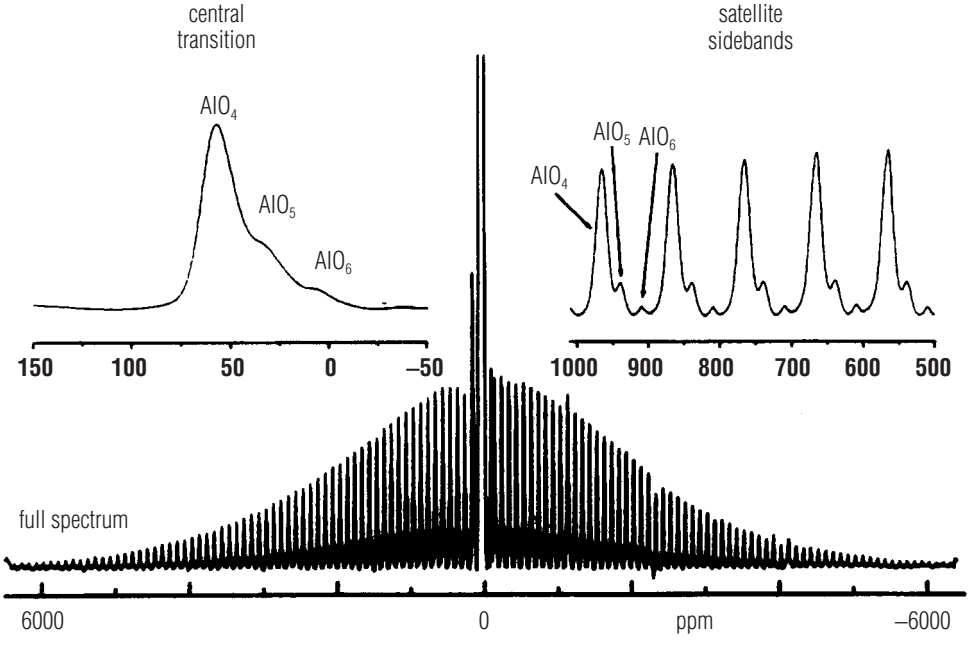

Fig. 8.8 ^{27}Al MAS NMR spectra for a glass with 20 mol% Na_2O, 30% Al_2O_3, and 50% B_2O_3, collected at 11.7 T [**111**]. Note improved resolution in $\pm\frac{1}{2}$ to $\pm\frac{3}{2}$ sidebands, and characteristic shape of sideband manifold.

For $I = \frac{3}{2}$, the second-order quadrupolar shift is larger for the $\pm\frac{1}{2}$ to $\pm\frac{3}{2}$ transitions than for the central transition (i.e. k in Equation (8.3) is 50 000 instead of 25 000). In the special case when different sites have very different C_Q values (as for BO_3 and BO_4 sites in borates), this effect may actually increase the separation in frequency of the two resonances and thus enhance resolution [**102**, **114**, **116**, **117**]. With or without actual resolution of multiple sites, analysis of the shape of the entire spinning sideband manifold can yield data for quadrupolar parameters and, in some cases, for their range of values in disordered glasses [**116**, **117**].

8.2.3 Techniques for observing ^{1}H and ^{19}F in glasses

^{1}H and ^{19}F deserve special mention in that they are both important in some oxide glass systems (e.g. volcanic glasses and optical materials, and glasses undergoing corrosion by water or water vapour), but unusually strong homonuclear dipolar couplings and correspondingly severe linebroadening have limited the information obtainable. Particularly with the advent of very fast spinning (>25 kHz) MAS probes, this situation is rapidly changing, as described in Chapter 2.

The CRAMPS technique has proved useful for both nuclides in oxide glasses when they were abundant enough to be 'non-dilute', i.e. to have high probabilities of having at least one strongly coupled neighbour [**118**, **119**]. For ^{1}H, the narrow range of δ_{iso} means that fast MAS may produce spectra of comparable quality. The presence of numerous spinning sidebands may complicate analyses, but also may help to distinguish among different H-bearing species with differing dipolar couplings [**120**, **121**]. In dilute systems, ^{1}H–^{1}H dipolar coupling may be insignificant, yielding narrow spectra with conventional MAS techniques [**122**] (Fig. 8.9), although the probe background signal can be severe unless a specially fabricated probe is used.

Exploration of ^{19}F with high-resolution NMR techniques has only begun in a few oxide glass systems [**118**]. While it is clear that MAS at 20 to 25 kHz can give well-resolved spectra in inorganic crystalline fluorides even with closest-packed F^- ions

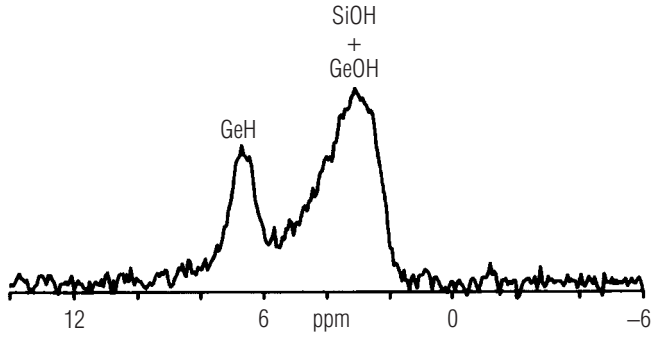

Fig. 8.9 ^{1}H MAS NMR spectrum (spinning rate of about 10 kHz, at field strength 9.4 T) for a GeO_2-doped silica glass, loaded with H_2 and UV-irradiated, after subtraction of intense background signal [**122**]. Sample contains about 8×10^{19} H atoms per cm^3 of glass, equivalent to about 500 ppm by weight of H_2O.

and strong hetero- and homonuclear dipolar interactions, the chemical shift ranges of F sites in glasses may pose resolution difficulties [**123**, **124**].

8.2.4 Cross-polarization techniques

Unlike the situation for organic solids, CPMAS has been applied to inorganic glasses only in special cases, for example to test for proximity of Si, Al, P or O sites to hydrogen- or fluoride-containing species [**118**, **119**, **125–130**]. In these examples, a change in shape or in relative intensity of the low-frequency nuclide spectrum from CP to non-CP conditions was sought. Although complicated by the possibility of dynamical effects such as H^+ or F^- ion mobility that can inhibit cross-polarization, such studies are useful for deducing qualitative effects of composition on structure, in particular in determining the relative proximity of H^+ or F^- to different network sites (Fig. 8.10).

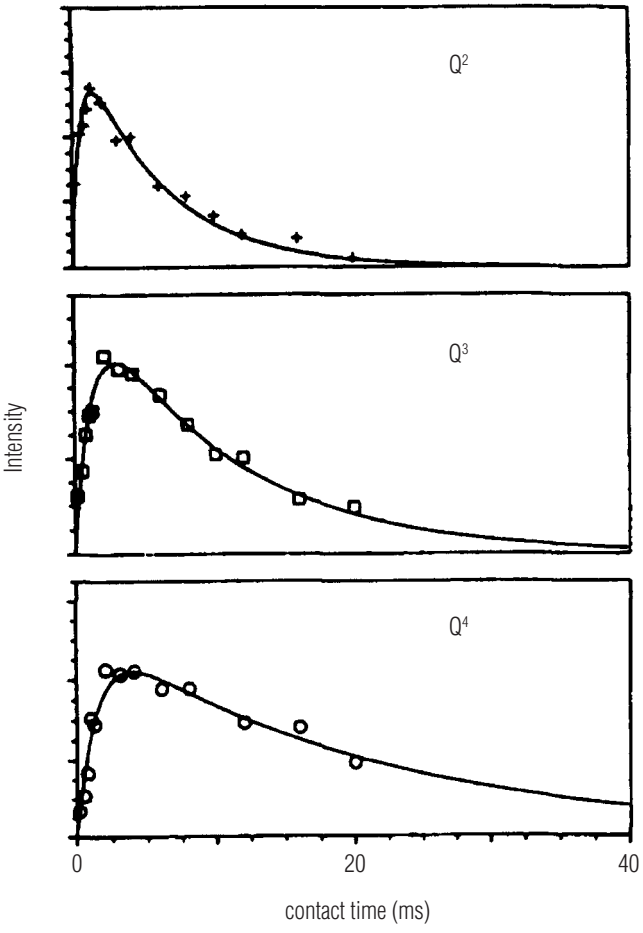

Fig. 8.10 ^{1}H–^{29}Si CPMAS intensity as a function of contact time for different sites in a $Na_2Si_4O_9$ glass with 9.1 wt% H_2O [**130**]. Note slower rate of cross-polarization (less steep initial curve) for the Q^4 site, which does not have non-bridging oxygens.

With the development of wide-range double- or triple-tuned probes and broad-banded multichannel spectrometers, cross-polarization from nuclides other than ^{1}H and ^{19}F has begun to be explored in glasses. Such efforts have begun to yield important new data on order/disorder among cations with strong dipolar couplings, e.g. ^{11}B–^{27}Al in oxide glasses [**131, 132**] (see next section). Particularly in systems involving quadrupolar nuclides, spin-locking dynamics can be quite complex and needs to be optimized carefully as well as tested on crystalline model compounds.

8.2.5 Other double resonance experiments

The Spin Echo DOuble Resonance (SEDOR) experiment (see Chapter 3) has been extensively applied to glasses that contain multiple cations with strong dipolar interactions, for example ^{23}Na and ^{7}Li in silicates [**107**]. The basic strategy of this experiment is to record a spin echo as a function of a delay time for one nuclide (e.g. ^{23}Na), in the presence of all dipolar couplings (thus a static sample) and compare it with a similar experiment in which defocusing due to the heteronuclear coupling (e.g. ^{7}Li) is suppressed. The evolution of the resulting curve depends on the relative distributions in space of the two nuclides. Although interpretation for quadrupolar nuclides can be complex, careful studies of crystalline model compounds can allow useful data on cation distributions to be obtained from glasses [**133**]. In general, results seem to be most consistent with relatively homogeneous modifier cation distributions, although other models including like–like clustering cannot be completely ruled out. Pairing of 'unlike' cations is generally not supported by these results (Fig. 8.11).

Rotational Echo DOuble Resonance (REDOR) has also provided information about alkali cation clustering (or, the lack thereof) in silicate glasses [**133**]. In these

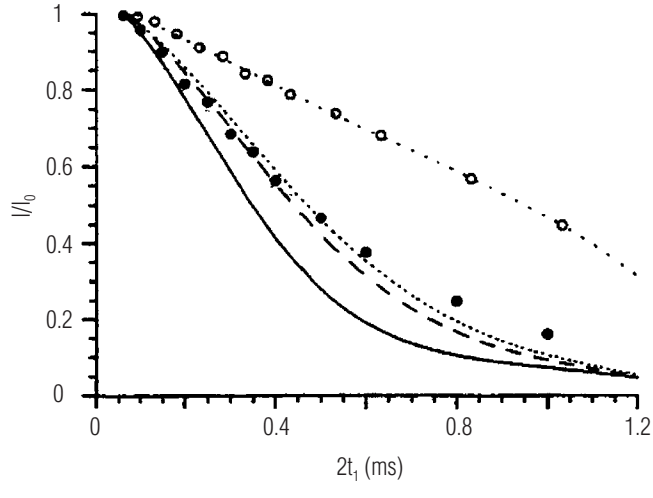

Fig. 8.11 SEDOR NMR data for a mixed-alkali silicate glass with 10.6 mol% Li_2O, 28.2% Na_2O [**107**]. The relative intensity vs. echo delay is plotted. Open circles and fitted line show ^{23}Na spin-echo results without ^{7}Li defocusing pulses; solid circles show data collected with defocusing pulses. The lower dotted and dashed curves show predicted behaviour for two scenarios with alkali cations distributed with uniform spatial separation; the lower solid curve shows that predicted for a more random distribution with some relatively close inter-cation distances (and hence rapid dephasing).

experiments, ^{29}Si MAS spectra, which resolve distinct Q^n sites, were recorded with and without rotor-synchronized inversion of ^{23}Na or ^{7}Li spins. Difference spectra thus are affected by the extent of dipolar coupling, and hence cation proximity. Interpretations are again somewhat complex, but again are consistent with a lack of cation clustering. ^{29}Si–^{31}P and ^{29}Si–^{7}Li SEDOR experiments have also shown that SiO_6 sites in phosphosilicate glasses tend to be closer to both P and Li cations than are the SiO_4 sites, an observation consistent with the chemical shifts of the latter, which indicate that they are primarily Q^4 groups [**134**] (Fig. 8.12). ^{11}B–^{27}Al REDOR, like the CPMAS experiments mentioned above, indicate a high degree of mixing of B and Al sites in aluminoborate glasses [**134**].

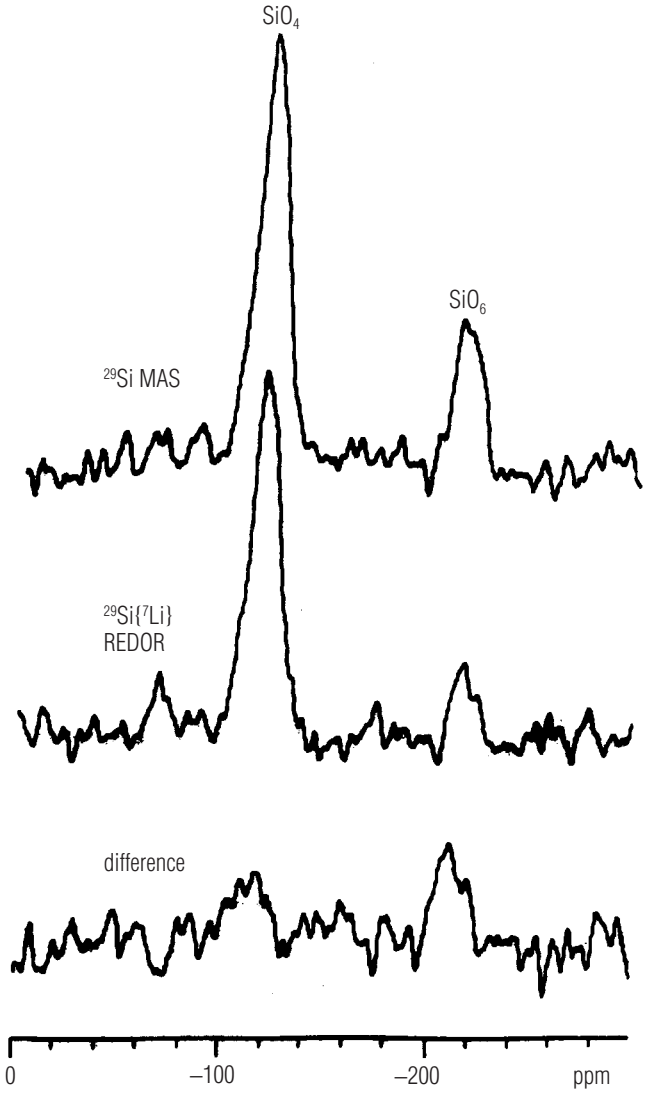

Fig. 8.12 ^{29}Si–{^{7}Li} REDOR results for a glass with 17 mol% Li_2O, 33% SiO_2, 50% P_2O_5 [**134**]. Top spectrum is simple spin-echo data; middle spectrum is with ^{7}Li inversion pulses; lower spectrum is difference. Note higher relative intensity of the SiO_6 in the latter.

TRAnsfer of Population in DOuble Resonance (TRAPDOR) (see Chapter 3) is a related experiment, in which difference spectra with and without dipolar dephasing by a second nuclide can reveal at least relative proximity, and has been exploited to study interactions between ^{31}P and ^{23}Na and ^{27}Al in phosphates [**135**] (see below).

8.2.6 Two-dimensional correlation experiments

As in liquid-state NMR studies, important information can sometimes be extracted from two-dimensional correlation spectra of glasses, even for systems with incompletely resolved 1-D spectra. For example, an early two-dimensional correlation experiment for ^{29}Si in silicate glasses showed extensive mixing between structural units [**136**], while a pulse sequence that results in a two-dimensional spectrum correlating static CSA patterns with MAS frequencies allowed Q^n speciation to be deduced in a $Na_2Si_2O_5$ glass [**137**]. In an experiment seeking a similar type of correlation, which required a special 'angle flipping' probe as for DAS (see Chapter 4), as well as costly isotopic enrichment to obtain adequate signal-to-noise ratios, ^{29}Si MAS spectra for silicate glasses spinning at the magic angle were correlated with those of the sample spinning on an axis perpendicular to the external field [**138**, **139**] (Fig. 8.13). The latter contains CSA information, which was used to fit and quantify the sub-spectra of the Q^4, Q^3, Q^2, Q^1 and Q^0 species. In a related

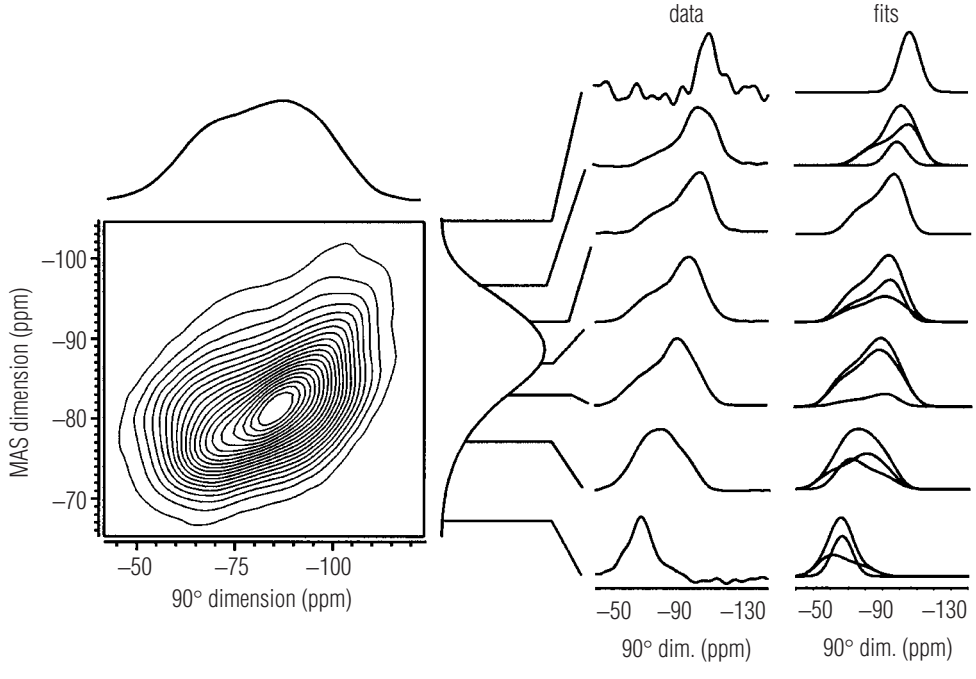

Fig. 8.13 ^{29}Si magic-angle flipping correlation NMR spectrum for ^{29}Si-enriched $CaSiO_3$ glass, showing slices at various positions in the MAS dimension, with fits using CSA patterns for various Q^n species [**138**].

experiment, Variable Angle Correlation SpectroscopY (VACSY) data are sampled at a set of different spinning angles, then processed to again obtain a two-dimensional spectrum with δ_{iso} on one axis and the correlated CSA's on the other. This approach has been applied successfully to phosphate glasses [**140**].

A related problem is the lack of resolution in extremely broad ^{207}Pb spectra of glasses. A modified, shifted-echo version of the PASS sequence was applied to a lead phosphate glass to obtain correlations between isotropic chemical shift and chemical shift anisotropy, which were interpreted in light of extensive data on CSA's of crystalline lead compounds [**141**].

In the Radio-Frequency Dipolar Recoupling (RFDR) experiment (see Chapter 3 for discussion of dipolar-recoupling experiments), strong homonuclear dipolar couplings, which are averaged away by fast MAS, are restored by rotor-synchronized pulses. In the resulting two-dimensional spectra, off-diagonal peaks grow in with increasing mixing time as the result of exchange between nearby spins. At least qualitative measures of proximity may thus be obtained. In glasses, this approach has proved most useful in phosphates where ^{31}P–^{31}P interactions are sampled, revealing intermediate-range connectivity among PO_4 groups [**110, 142, 143**] (see section on phosphates below). A more recently developed two-dimensional double-quantum method has also demonstrated phosphate group linkages in glasses [**144, 145**] (Fig. 8.14), and has begun to offer intriguing possibilities for silicate unit proximities in ^{29}Si-enriched silicates [**146**].

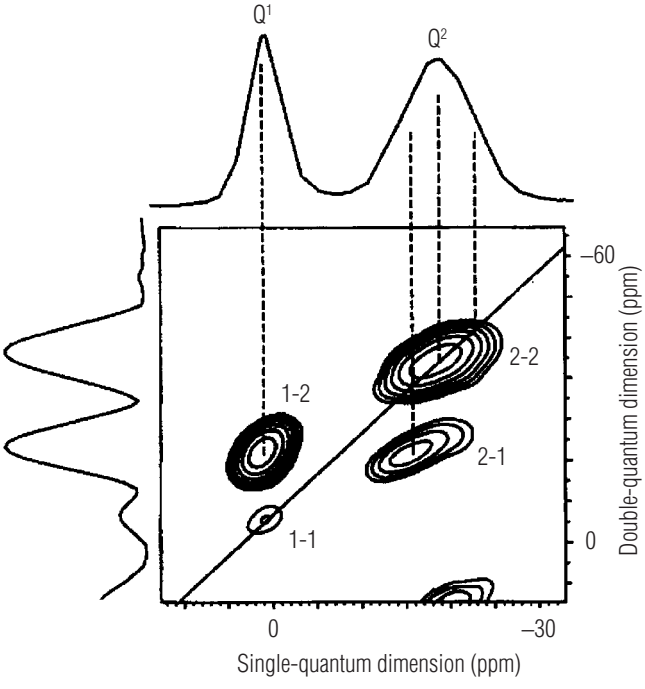

Fig. 8.14 ^{31}P double-quantum NMR spectrum of a glass with 58 mol% Na_2O and 32% P_2O_5 [**145**]. The numbers on the two-dimensional plot show proximities of various Q^n pairs.

A variety of heteronuclear correlation experiments are possible among strongly dipolar-coupled cations in oxide glasses. For example, ^{1}H–^{31}P heteronuclear correlation spectroscopy (HETCOR) has helped to specify the sites in phosphate glasses that interact with water during corrosion [**125**], and ^{11}B–^{27}Al HETCOR has shown correlations between sites with different Al coordination and sites with different B coordination [**132**] (see section on boron-containing glasses). DAS has been combined with cross-polarization to yield correlation spectra between isotropic line shapes for ^{23}Na and phosphate sites in mixed-alkali phosphates [**147**].

8.2.7 Techniques that eliminate second-order quadrupolar broadening (DOR, DAS, MQMAS)

Over the last ten years, three families of techniques have greatly extended the utility of solid state NMR on spin-$\frac{3}{2}$ and $\frac{5}{2}$ in glasses. All three of these can eliminate second-order quadrupolar broadening from NMR spectra and are discussed in detail in Chapter 4. For some nuclides, this may substantially increase resolution, allowing detection of previously unseen structural species. Especially significant in glasses is the fact that residual peak widths (sometimes surprisingly large) are controlled only by distributions of parameters, which can potentially be mapped into distributions of real structural variables and hence to the state of order/disorder.

Double rotation (DOR) NMR

The principle of DOR is simple and elegant, involving the rotation of the sample simultaneously about two carefully selected angles with respect to the external field [**148**, **149**]. Unfortunately, the mechanical difficulty of this approach, resulting in relatively low spinning rates and closely spaced spinning sidebands, has limited its application to disordered materials with large distributions of chemical shifts. If DOR technology can be improved, it could hold great promise: the 1-D character of the experiment could be particularly useful if signal-to-noise is insufficient for a two-dimensional experiment, as for samples that are very small or have very long spin-lattice relaxation times.

Dynamic angle spinning (DAS) NMR

The major advantages of DAS [**150–152**] for glasses seem to be the highly quantitative lineshapes and relative intensities that can result (in contrast, for example, to multiple-quantum MAS, below), as well as much greater excitation efficiency. DAS NMR has produced a number of important new structural findings in oxide glasses. ^{23}Na DAS has helped to refine changes with composition in Na^{+} coordination in

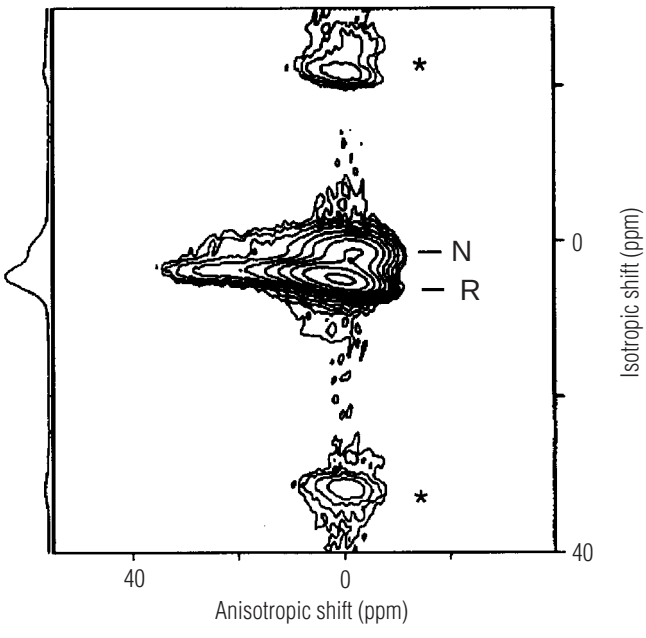

Fig. 8.15 ^{11}B DAS spectrum of B_2O_3 glass (97% ^{10}B) collected at 8.4 T [**154**]. Note two distinct peaks visible in both two-dimensional spectrum and in isotropic dimension projection (left), assigned as boroxyl ring (R) and non-ring (NR) sites. The asterisk (*) marks spinning sidebands.

telluride glasses [**153**]. ^{11}B DAS has confirmed the presence of two types of boron sites in B_2O_3 and alkali borate glasses, interpreted as those in three-membered 'boroxyl' rings and those not in rings – a subject of long investigation and considerable controversy [**154–156**] (Fig. 8.15). An early study of ^{17}O in K, Mg silicate glasses showed a surprising degree of ordering in modifier cation distributions around NBO's [**30**]; later DAS spectra of K, Na glasses indicated random mixtures of cations next to NBO's, consistent with the greater similarity of size and field strength than for the K, Mg pair [**29**] (Fig. 8.16). Anisotropic-dimension ^{17}O DAS lineshapes for BO sites have also been analysed, using known correlations between the Si–O–Si angle and C_Q, to yield the first accurate bond angle distribution for a two-component glass [**30**].

Multiple quantum MAS (MQMAS) NMR

Multiple quantum MAS NMR, particularly the triple-quantum experiment (3QMAS), has been an exciting breakthrough for glass studies. It can be carried out with an ordinary MAS probe, and thus is generally easier to implement than DOR or DAS, although the best spectra seem to be obtained with the very high rf pulse powers reachable only in probes with small-diameter rotors and coils (4 mm and below). Several variations of 3QMAS have been applied to glasses, but all share the significant disadvantage that both excitation and reconversion efficiencies depend on the C_Q [**157–160**]. This means that peak shapes may be somewhat distorted, and

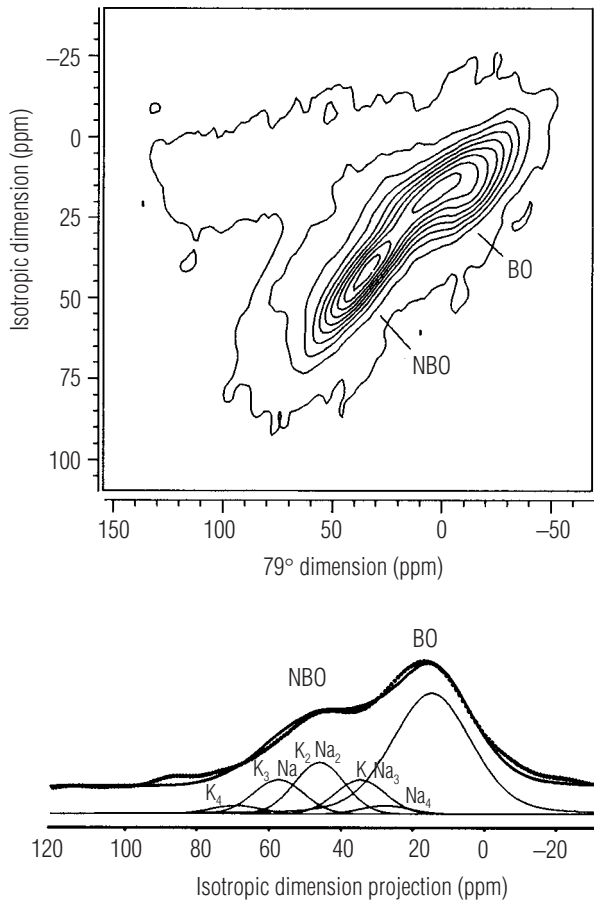

Fig. 8.16 ^{17}O DAS NMR spectrum for a glass of $NaKSi_2O_5$ composition, collected at 9.4 T. Lower plot shows the total isotropic projection. Individual gaussian peaks show bridging oxygen (BO) peak and a model for the non-bridging oxygen peak (NBO). The latter is based on the positions and widths of the NBO peaks in the pure-K and pure-Na end members and an assumption of random mixing of K and Na around NBO's [**29**].

relative intensities of peaks for sites with different C_Q's may be inaccurate. However, relative intensities can be calculated from a knowledge of the C_Q's, and also quantitative intensities derived from experimental data. In some cases, T_2 values can be short enough to make difficult 3QMAS pulse sequences with a third, echo pulse (see Chapter 4). Nonetheless, important constraints have been obtained on glass structure using 3QMAS for ^{11}B [**95**, **161**], ^{17}O, ^{23}Na [**143**, **162**] and ^{27}Al. For the latter, 3QMAS seems to be the best technique available for resolving small concentrations of AlO_5 and AlO_6 groups from predominant AlO_4 sites [**87**, **97**, **111**] (Fig. 8.5), or showing their absence. For ^{17}O, 3QMAS has allowed clear resolution of distinct types of bridging oxygen sites (e.g. Si–O–Si, Si–O–Al, B–O–B, Si–O–B, Al–O–Al) in glasses, leading to significant revisions of conventional views of connectivity and disorder [**129**, **163–166**] (Fig. 8.17). Non-bridging oxygen environments have also been characterized [**97**, **103**, **104**, **163**].

Several variations of the 3QMAS experiment have been applied to glasses, including the originally proposed two-pulse sequence [**157**], and including those that use

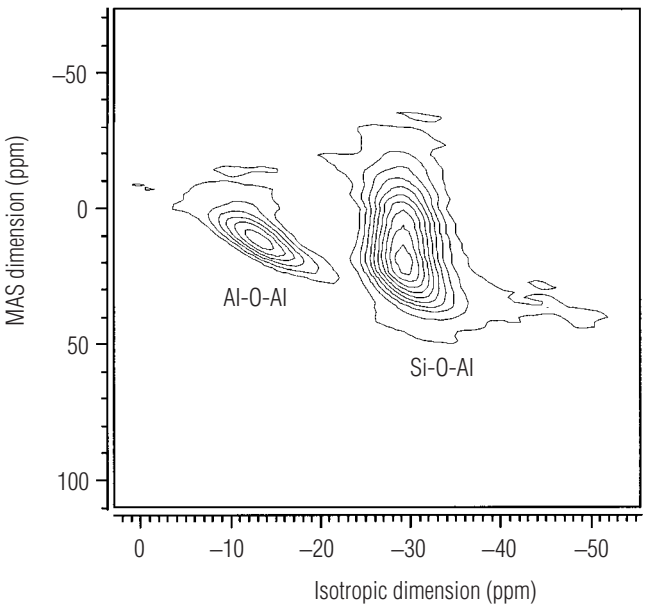

Fig. 8.17 ^{17}O 3QMAS NMR spectrum (9.4 T) for a glass on the $NaAlO_2$–SiO_2 join with Si/Al = 0.7 [**166**]. Note complete resolution of the two main peaks in the two-dimensional plot and complete overlap in the MAS dimension.

a third pulse to generate an echo and in some cases allow 'pure phase' spectra (Chapter 4) [**160**]. The latter can have advantages of improved signal-to-noise ratio and easier phase correction; the former may be advantageous when short T_2's, common in glasses, make signal loss during an echo delay significant. For $I = \frac{5}{2}$, with the second-order isotropic quadrupolar shift δ_Q as defined in Equations (8.1) to (8.3), the centre of gravity in the isotopic, multiple-quantum dimension taken as 3QMAS, and the centre of gravity in the single-quantum MAS dimension as δ_{MAS},

$$\delta_Q = 17/27\,\delta_{MAS} + 31/27\,\delta_{3QMAS} \tag{8.4}$$

$$\delta_{iso} = 10/27\,\delta_{MAS} - 31/27\,\delta_{3QMAS} \tag{8.5}$$

P_Q can then be calculated from δ_Q. Projections or slices in the MAS dimension, although often somewhat distorted from true MAS lineshapes, can be fitted to estimate η_Q and thus derive C_Q from P_Q. In such spectra ($I = \frac{5}{2}$), peaks elongated along trends of slope = –31/17 are caused by variation in δ_{iso} with little change in P_Q, as is often observed for NBO sites in ^{17}O 3QMAS spectra [**97, 103**]. Trends of constant δ_{iso} with varying P_Q would display slopes of +31/10.

8.2.8 Spin-lattice relaxation and structure

Spin-lattice relaxation studies in glasses have generally focused on the dynamics of diffusive motion of alkali cations elevated temperatures. Much has been learned from such work (see citations in introduction), but the focus here is on their static structure.

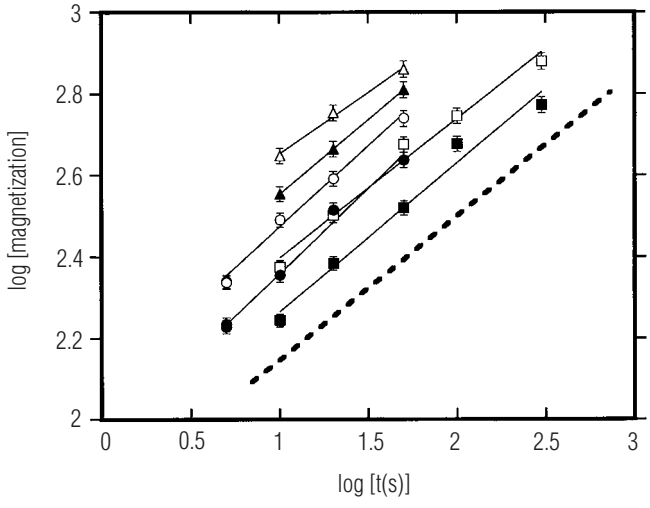

Fig. 8.18 ^{29}Si magnetization recovery after saturation, vs. $\log_{10}$ of delay time, for a $Li_2Si_4O_9$ glass doped with Gd_2O_3 as a paramagnetic relaxation agent [**168**]. Open symbols are for Q^3 sites, solid symbols for Q^4 sites. Glasses with 2000, 1000 and 500 ppm dopant are shown by triangles, circles and squares, respectively. Only the early, power law relaxation is shown. The dashed line has a slope of 0.35, an average value for all of the data. The dimensionality of the distribution of pairs of Si and Gd sites is expected to be 6 times this slope, yielding a value of 2.1, well below the value of 3 for a conventional solid and indicating a fractal character to the intermediate-range structure [**168**].

In solids, where spin-lattice relaxation is dominated by through-space dipolar coupling between nuclear spins and those of unpaired electrons (as opposed to spin diffusion), magnetization recovery after saturation should initially follow a power law, not an exponential behaviour [**167, 168**]. ^{29}Si in at least SiO_2 and alkali silicate glasses seems to be such a system. Pragmatically speaking, this can make it difficult to obtain 'fully relaxed' spectra of silicates with slow relaxation (very low contents of paramagnetic impurities), but detailed study of relaxation may also provide useful information on spatial heterogeneity both of silicate species and of the paramagnetic centres themselves. For example, a reduced power law slope for relaxation in $Li_2Si_4O_9$ glasses indicated reduced dimensionality and a fractal character to Q^n species distribution, consistent with a submicroscopic phase separation [**168**] (Fig. 8.18); study of the compositional dependence of relaxation rate on the concentration of rare earth cations in SiO_2 glass suggested clustering that is significant to fluorescence lifetimes critical in optical amplifiers [**167**]. One conclusion from these studies is significant to any NMR work on glasses: if differential relaxation among components of a spectrum is noted, it is likely to indicate at least medium-range heterogeneity, which is of central importance in models of glass energetics (Fig. 8.19). It may also be a sign of phase separation (either crystalline or glassy) that can complicate the interpretation of data.

8.3 Applications to specific glass systems

In this section I discuss further selected examples of the types of scientific questions that have been addressed, and in some cases even answered, by NMR studies of glass. Again, space does not allow a comprehensive review, but I hope that this kind of introduction will be useful in stimulating and guiding future NMR studies, as

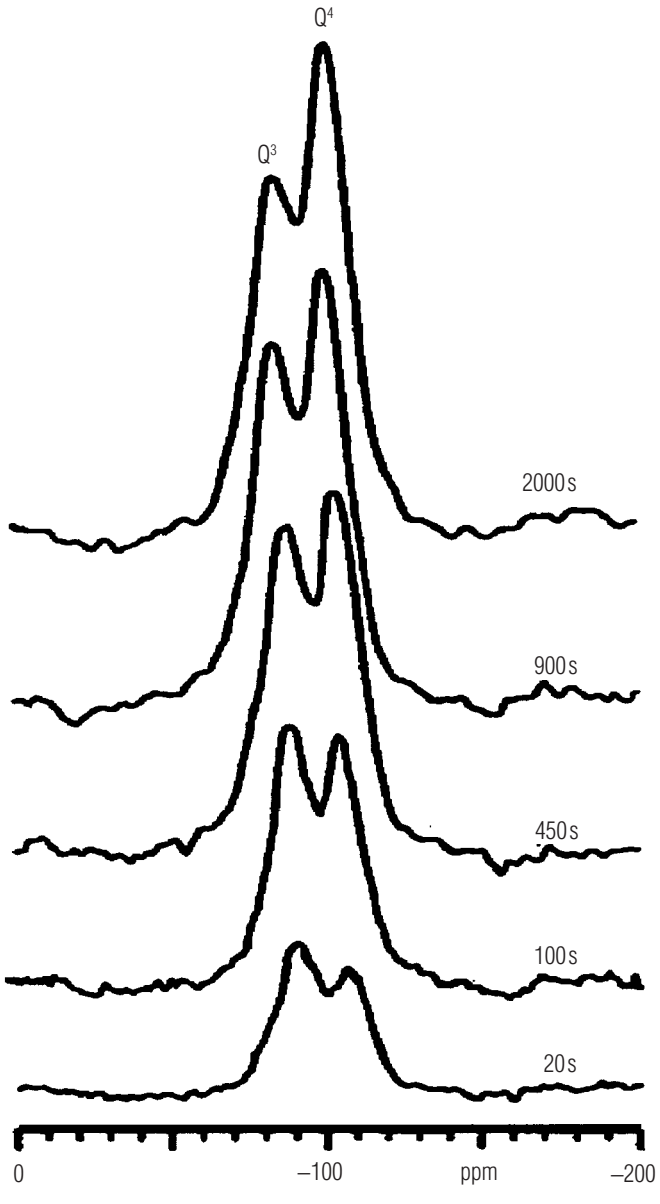

Fig. 8.19 ^{29}Si MAS NMR spectra for $Li_2Si_4O_9$ glass with 500 ppm Gd_2O_3, source of some of the data in Fig. 8.17 [**168**], showing differential relaxation between Q^3 and Q^4 peaks as a function of delay time after saturation. Sample was homogeneous on a optical scale (100's of nm), but heterogeneous on a smaller scale (on the order of a few nm).

well as bringing together somewhat disparate threads for those looking at larger issues of structure and dynamics.

8.3.1 Boron-containing oxide glasses

Boron-containing glasses have widespread use in corrosion-resistant containers, tank linings, and piping in laboratories and the chemical industry, are the most

common fibre reinforcement in glass-polymer composites, and are common in optical components. They also offer a wealth of possibilities for structural studies by NMR.

Network structure

The fact that boron in oxide glasses can readily adopt either three- or four-coordination gives boron-containing glasses and glass-forming liquids unique properties, some of which are strongly dependent upon and, to some extent, adjustable by varying composition and network coordination. The ready quantifiability of BO_3 and BO_4 concentrations by low-field, 'wideline' methods lead to the development of detailed structural models of borate and borosilicate glass structure that have been extensively reviewed [**6**, **7**, **13**, **14**, **26**, **27**]. Analysis of quadrupolar lineshapes of high field ^{11}B MAS spectra often takes advantage of such early determinations of C_Q and η_Q, and supplies new information on chemical shifts [**46**, **79**, **95**, **100**, **101**, **156**, **169**] (Fig. 8.7). High resolution ^{27}Al MAS NMR, including spinning sideband analysis [**114**, **117**] and 3QMAS, have demonstrated the importance of unusual, five- and six-coordinated aluminium sites in aluminoborate glasses, particularly those with alkaline earth modifier cations [**87**, **89**, **111**] (Figs 8.6 and 8.8). Increasing the field strength of the network modifier cation systematically increases the mean Al coordination number [**89**, **95**].

Early wideline NMR work on ^{11}B, ^{10}B and NQR studies also distinguished BO_3 sites with one or two NBO's ('asymmetric' sites), which are characterized by relatively large values of η_Q because of the loss of axial symmetry, from BO_3 sites with no NBO's ('symmetric' sites) [**14**, **170**]. High-resolution ^{11}B NMR has begun to partially resolve such sites [**95**, **111**, **169**] (Fig. 8.20), as well as distinctions among 'ring' and 'non-ring' BO_3 groups [**95**, **154–156**] (Figs 8.7 and 8.15). Satellite transition sidebands for ^{11}B at some fields may improve separation of trigonal and tetrahedral boron sites, and sideband manifolds have been analysed to suggest not only multiple BO_3 sites but also multiple BO_4 sites [**116**, **117**].

Analysis of ^{29}Si MAS data can help to determine the partitioning of NBO's among BO_3 groups and SiO_4 groups [**95**, **169**], but, except in glasses with relatively low B contents, ^{29}Si spectra are often poorly resolved because of the disorder and ensuing range of chemical shifts. Nonetheless, detailed modelling of mean ^{29}Si chemical shifts in alkali borosilicate glasses, using ranges derived from crystalline silicates, has led to the conclusion that NBO's are approximately equally distributed among Si and B sites, which is not entirely in agreement with earlier models based only on wideline ^{11}B studies [**80–82**].

^{17}O NMR holds considerable promise for testing and refining well-established models of borate and borosilicate glasses. A systematic study using ^{11}B, ^{17}O and ^{29}Si NMR, for example, attempted to produce a complete structural view of a series of alkali borosilicates [**169**]; work that combined ^{17}O DOR and ^{11}B DAS [**149**]

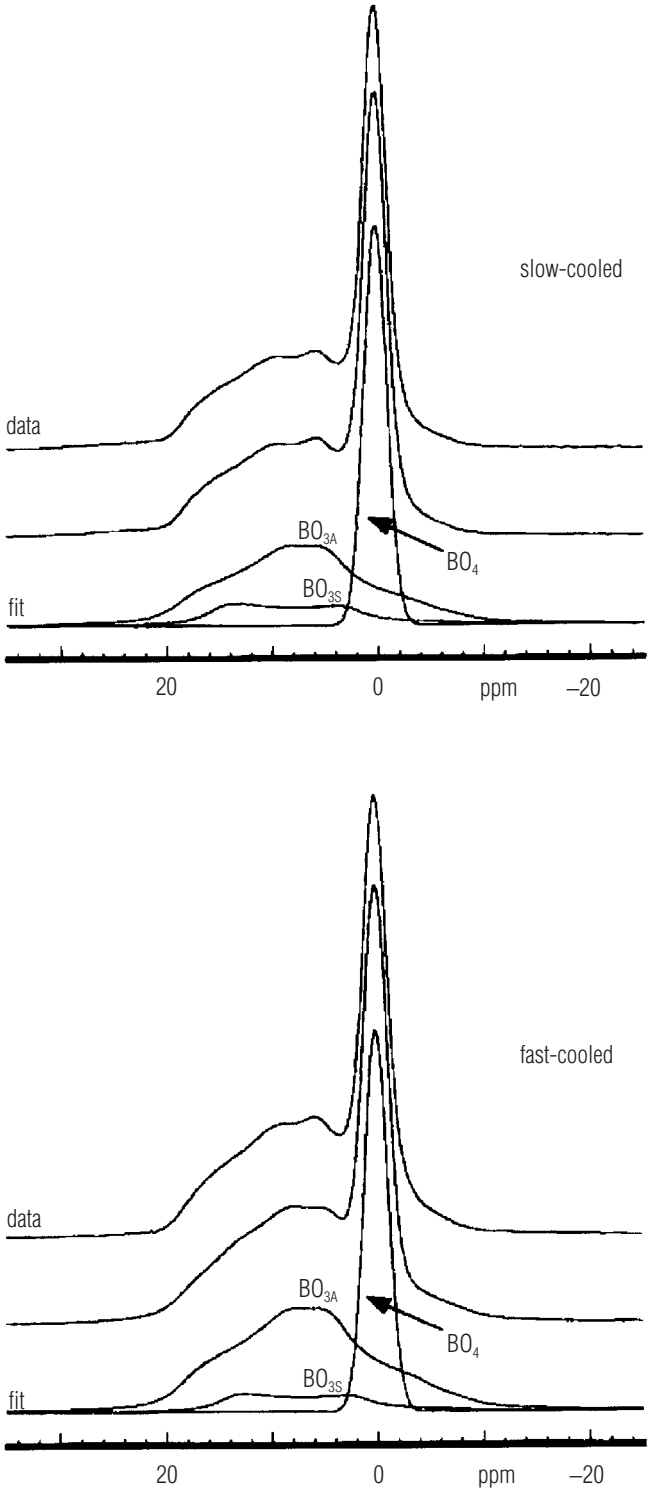

Fig. 8.20 ^{11}B MAS NMR spectra (9.4 T) for a glass with approximately 44.5 mol% Na_2O, 11.0% B_2O_3 and 44.5% SiO_2 [**95**], showing fits for BO_3 groups with no NBO (BO_{3A}), those with one or two NBO's (BO_{3S}) and BO_4 groups. Note increased relative proportion of BO_3 sites in fast-cooled (higher T_g) sample.

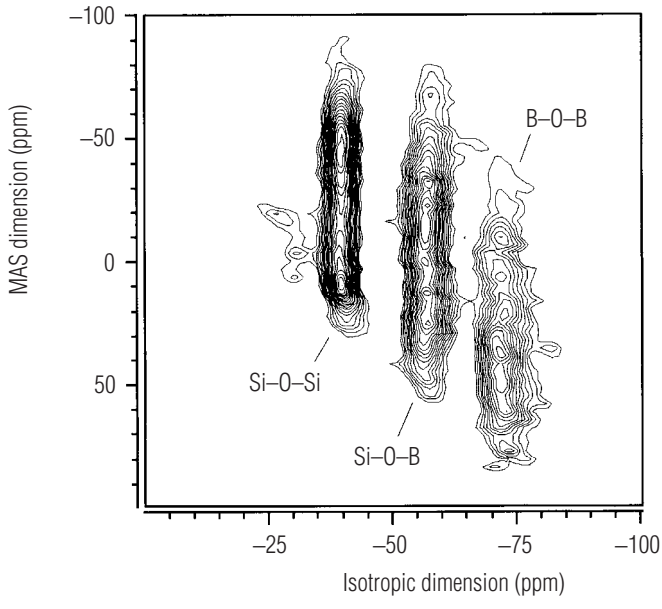

Fig. 8.21 ^{17}O 3QMAS NMR spectrum (9.4 T) for a glass with 40 mol% B_2O_3 and 60% SiO_2 [**164**].

attempted to observe and quantify all B and O sites in B_2O_3 glass, which could again lead to an unusually complete structural picture. However, characterization of oxygen sites was in the first case hindered by the low resolution of the static spectra used; in the second case results may have been affected by complex spinning sideband patterns. More recent 3QMAS results show excellent resolution among many of the possible O sites in boron-containing glasses [**163**, **164**]. In particular, high concentrations of B–O–Si sites in binary B_2O_3–SiO_2 glasses (Fig. 8.21), as well as relatively low concentrations of B–O–B sites in some ternary glasses, demonstrate that borate and silicate components mix more completely than had been surmised by earlier models, and thus have important implications for both thermodynamic and transport properties. ^{17}O 3QMAS has resolved NBO sites, probably on SiO_4 groups, in alkali borosilicate glasses [**163**], and NBO's connected to boron sites in several binary borate glasses [**171**].

Another view of connectivity among network cations may be obtained from a variety of experiments that rely on strong dipolar coupling to estimate at least relative proximities. In aluminoborate glasses, an obvious opportunity is provided by the high natural abundances and Larmor frequencies of ^{11}B and ^{27}Al. CPMAS and REDOR experiments on these nuclides both suggest that B and Al sites are highly mixed, in that most B sites have Al neighbours and vice versa, as permitted by composition [**131**, **132**, **134**]. An elegant ^{11}B–^{27}Al CPMAS HETCOR experiment in a magnesium aluminoborate glass demonstrated significant correlations between all combinations of boron sites (BO_3, BO_4) and aluminium sites (AlO_4, AlO_5, AlO_6), although that between the two tetrahedral sites seemed to be lower than expected

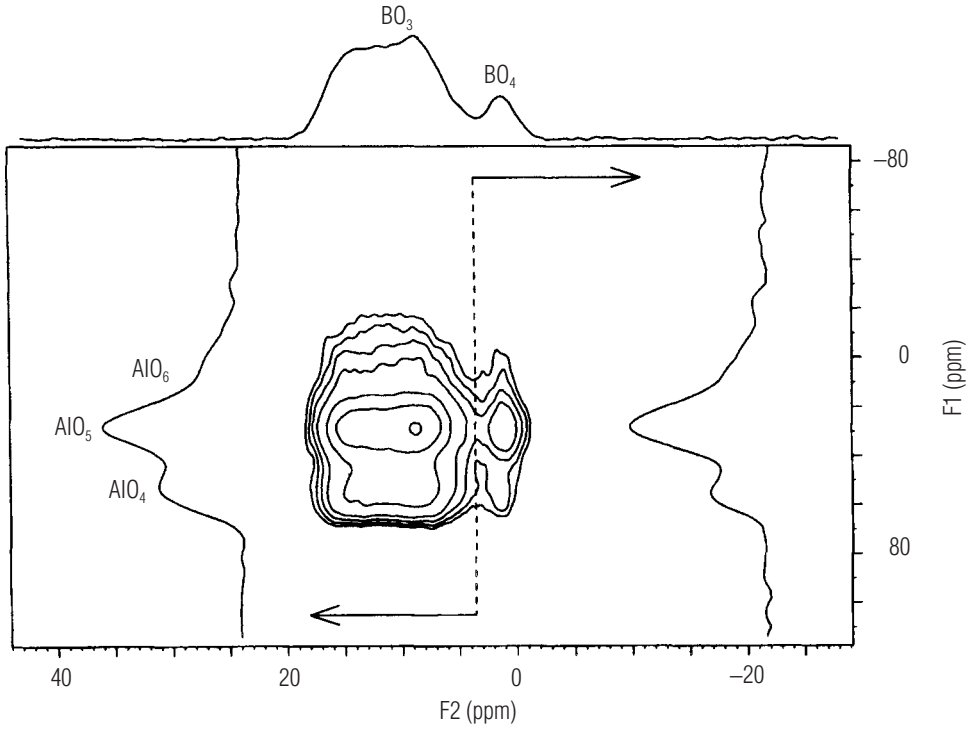

Fig. 8.22 ^{11}B–{^{27}Al} CP-HETCOR NMR spectrum of a glass with 25 mol% MgO, 30% Al_2O_3 and 45% B_2O_3 [**132**]. Projection to the left shows correlations with BO_3 subspectrum; projection to the right shows that for the BO_4 subspectrum. The latter has been normalized in intensity to match the maximum peak height for the former. Note the relatively low intensity of the BO_4–AlO_4 correlation.

from random mixing, possibly for bond-valence reasons [**132**] (Fig. 8.22). An oxygen connected only to two tetrahedra of trivalent cations would be severely underbonded, but this could be compensated by increased bonding to Mg^{2+}. This last observation highlights the key need for future applications of such studies, which is to distinguish among models in which cation pairing (like or unlike) is greater, less than, or indistinguishable from that predicted by structural models, whether they are based on random mixing or on a more sophisticated statistical thermodynamical approach [**84**].

Alkali sites

^{6}Li, ^{7}Li, ^{23}Na and ^{133}Cs static and MAS NMR spectra for borate (and silicate) glasses, although relatively easy to observe, are generally featureless and broad enough to make unique interpretation difficult. However, detailed studies at multiple external fields can be analysed to obtain mean values of isotropic shift and C_Q. In Li, Na, K borate and silicate glasses, such data show systematic effects of both silica content

and of the ratio of one modifier cation to another [**65**, **133**]. Interpretation in light of empirical chemical shift 'calibrations' [**86**, **172**, **173**] indicates that partial substitution of a smaller cation for a larger actually *increases* the mean site size of the latter, and vice versa, because of competition for available NBO's, a process that must be considered in models of the *mixed alkali effect* on transport properties [**108**]. This effect is also seen in ^{133}Cs spectra of borate glasses [**27**] and by *in situ*, high-temperature NMR measurements of isotropic chemical shifts [**53**]. It is important in such analyses that appropriate chemical shift correlations are used. For ^{23}Na, within groups of structures with the same ligand (e.g. borates, silicates, germanates, carbonates, fluorides), increase in mean Na–first neighbour bond distance (and associated increase in coordination number) systematically decreases δ_{iso} to lower frequency [**108**], although correlations for each group lie on somewhat different curves. This trend is qualitatively similar to those observed for ^{6}Li, ^{11}B, ^{25}Mg, ^{27}Al, ^{29}Si [**108**] and even ^{43}Ca [**174**], but is opposite to that predicted from a simultaneous fit to data for a wide range of ligands [**175**].

The extent of homogeneity of distribution of Li, Na and Cs sites in silicate and borate glasses has been extensively tested by spin-echo decay, SEDOR and REDOR techniques in silicates and borates [**63**, **65**, **107**, **133**, **176**]. Although interpretations of these results are somewhat complex, they seem to be most consistent with models that have uniform (i.e. non-clustered) cation distributions. This places important constraints on models that emphasize spatial heterogeneity, such as the *modified random network model* [**177**, **178**].

8.3.2 Silicate, aluminosilicate and germanate glasses

Silicates and aluminosilicates are the most common 'low tech' industrial glasses (containers, windows, etc.) as well as having more sophisticated applications in electronic and optical systems; aluminosilicate glass-forming melts are by far the most common natural magmas.

Short-range structure

As for boron-containing glasses, perhaps the most clear and definitive applications of NMR to silicate glasses involve the first-neighbour coordination environment. SiO_6 and SiO_5 groups have been observed in glasses quenched from melts at high pressure [**73**, **179**, **180**, **181**] (Fig. 8.23), and the latter are even present in small concentrations in alkali silicate glasses formed at ambient pressure [**180**, **182**]. Both can be quite abundant in phosphosilicates [**90**, **183–185**], where the high charge and electronegativity of the phosphorus cation allows it to 'out compete' Si for short, tetrahedral bonds to oxygen (Fig. 8.12).

Aluminium coordination in aluminosilicate glasses has long been an interesting and controversial subject, because of the hypothesized role of AlO_6 in

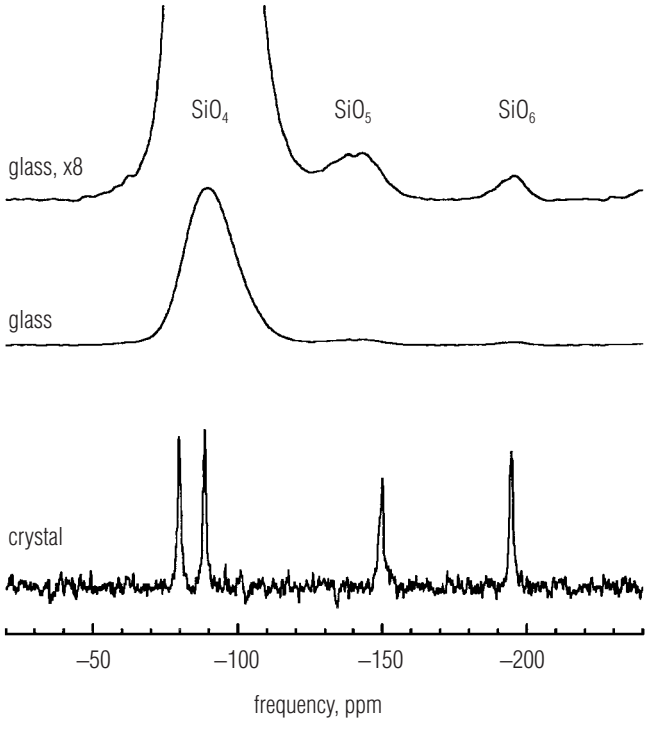

Fig. 8.23 ^{29}Si MAS NMR spectra (14.1 T) for $CaSi_2O_5$ glass (isotopically enriched) quenched from a melt at 10 GPa pressure, and corresponding crystalline high-pressure phase (normal isotopes) [**178**].

thermodynamic properties, particularly in aluminium-rich systems. It is clear that ^{27}Al MAS NMR at relatively high fields can readily detect both AlO_5 and AlO_6 groups, although quantitation can be difficult because of overlapped quadrupolar lineshapes and the possibility of missing signal for sites with very large values (>10 MHz) of C_Q. Significant concentrations of high-coordinate Al have been observed in a variety of systems, including Mg-, Y- and La-aluminosilicates [**91**, **92**, **97**] and high-pressure glasses [**96**]. 3QMAS seems to give considerably better resolution than MAS, and is probably the best technique for detecting low concentrations of these species [**87**]. As in aluminoborate glasses (see above), higher field-strength modifier cations promote the conversion of AlO_4 to AlO_5 and AlO_6, again because of competition for small, low-coordinate environments.

As mentioned above for borates, at least the relative effects of composition on Na and Li site size in alkali (and mixed-alkali) silicate glasses can be observed by analysing data from multiple fields [**108**, **133**]. This approach has also been successfully applied to determine the relative effects of water content on Na sites in aluminosilicates [**105**, **106**].

Bridging and non-bridging oxygens can often be distinguished in static or MAS ^{17}O spectra of silicate glasses. The network modifier(s) that coordinate the NBO has a large effect on chemical shift, leading in some systems (e.g. Na silicates) to severe peak overlap in MAS spectra [**58**], but in others (e.g. Ba and Ca silicates) to enhanced

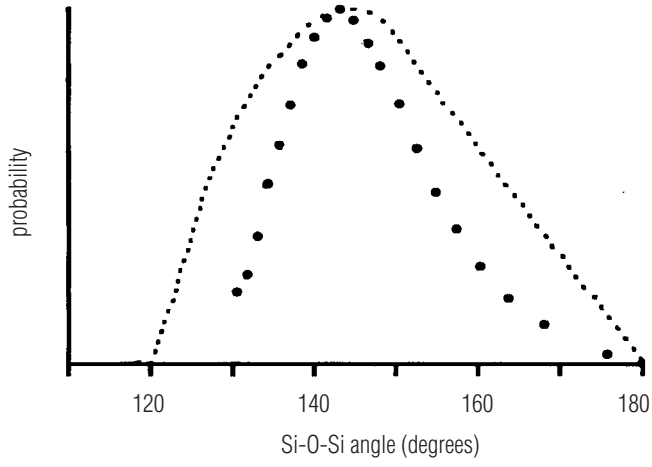

Fig. 8.24 Si–O–Si bond angle distribution in $K_2Si_4O_9$ glass deduced from bridging oxygen peak shape in 3QMAS spectrum combined with correlation between angle and C_Q [**30**]. The fine dotted line shows distribution derived previously for SiO_2 glass from X-ray scattering data.

resolution [**103**]. DAS or 3QMAS may yield much higher resolution [**29, 30, 103**]. In favourable cases (e.g. Ca aluminosilicates), even small concentrations of NBO can be detected by MAS or 3QMAS, even in systems that should, by conventional models, contain all Q^4 and thus only BO sites [**104**].

Disorder in first-neighbour coordination, for both cations and anions, can be a significant part of the overall disorder in a glass. This includes the obvious configurational disorder added if network species of different coordinations mix randomly. From the viewpoint of oxygen sites, the distribution of modifier cations around NBO's can be investigated at least qualitatively by isotropic peak widths in DAS or 3QMAS spectra [**29, 30, 103**] (Fig. 8.16). The random cation mixing that is observed, at least when two modifiers are present that have the same charge and sizes that are not too different, seems to be consistent with results from SEDOR and REDOR studies of mixed-alkali glasses [**133, 176**] (Fig. 8.11). However, significant ordering was suggested from DAS studies of a mixed K, Mg glass [**30**] and in earlier ^{17}O MAS studies of Ca, Mg glasses [**77**], perhaps because the small size and high charge of the Mg^{2+} cation allows it to occupy unique sites in the structure.

Distributions in bond angles have long been discussed as a major contribution to the overall disorder of glasses [**31**]. The average and range of Si–O–Si angles have been estimated from the ^{29}Si lineshape of SiO_2 glass [**186, 187**] and from ^{17}O DAS spectra of $K_2Si_4O_9$ glass [**30**], the latter relying on correlations between C_Q and angle [**1, 188**] (Fig. 8.24). Similar correlations were used to estimate the much narrower Ge–O–Ge angle distribution in GeO_2 glass, by fitting of MAS and static ^{17}O spectra [**189**].

Intermediate-range structure

The distribution of second neighbours can be considered the beginning of intermediate-range structure (or the longer-range part of short-range structure). In

silicates, NMR has made major contributions to the quantification of Q^n species, which is determined by second-neighbour (or first cation neighbour) ordering around SiO_4 sites. As described in the first section, both static and MAS (Fig. 8.2), as well as two-dimensional correlation techniques have proved useful (Fig. 8.13). An important conclusion from such studies has been that for equilibria among species such as the following:

$$2Q^3 = Q^2 + Q^4 \tag{8.6}$$

higher field strength modifier cations (higher charge, smaller radius) systematically shift the reaction to the right [**12**, **28**, **59**, **61**, **138**], with perhaps the most extreme values resulting from Pb^{2+} [**67**]. In the compositional ranges studied, this leads to a greater contribution to the overall configurational entropy, if it is assumed that the species mix randomly. However, this disorder apparently does not reach the limit of a fully random distribution of BO and NBO, leaving room for increased disorder as temperature is increased, which has been detected in several studies [**48**, **59**, **190**]. Q^n speciation, as determined by NMR, has been incorporated into thermodynamic models of solid–liquid phase equilibria [**191**] and has been used to 'calibrate' the relative intensities of vibrational bands in Raman spectra [**192**, **193**], which can be particularly useful in interpreting data from challenging *in situ* high-temperature and pressure Raman measurements on melt and glass structure.

At longer range, two-dimensional correlation experiments have provided some of the first data on the connectivity among silicate units [**146**], which will be of key importance in testing models, such as the *modified random network*, that incorporate significant medium-range compositional heterogeneity.

By analogy with high-temperature crystalline aluminosilicates, the distribution of Al and Si on tetrahedral sites in glasses and melts has generally been assumed to be random, with perhaps some 'aluminium avoidance', in which energetically unfavourable Al–O–Al linkages are minimized. This question is an important part of models of thermodynamics of glass-forming aluminosilicate liquids. Systematic decreases in liquid-state heat capacity with decreasing temperature [**31**, **194**] have suggested the possibility of some ordering. NMR is again one of the few approaches that can address this issue directly. Early ^{29}Si MAS data suggested at least some Al-avoidance, as peak widths were observed to decrease as Si/Al approached [**128**]. More recently, ^{29}Si MAS NMR spectra have been analysed quantitatively using a statistical mechanical model of ordering, and has noted considerable, but incomplete, Al-avoidance [**84**]. As expected from cation field strengths and known effects in crystals, higher field strength cations (Ca^{2+} vs. Na^+) tend to promote disorder. The finding of some Al–O–Al sites (instead of only the more stable mixture of Si–O–Si plus Si–O–Al) in aluminosilicate glasses by ^{17}O 3QMAS [**166**] (Fig. 8.17) is thus an important step in quantifying an old but unresolved question.

8.3.3 Hydrogen-containing species in oxide glasses

Hydrogen-bearing species can have huge effects on thermodynamic and transport properties of glass-forming oxide liquids, and thus have great importance to both geological and technological processes. For example, the addition of a fraction of a per cent of H_2O to a high-silica glass melt may lower its viscosity by orders of magnitude. OH concentrations of a part per million or less can cause sufficient infrared absorption to be detrimental to long-range data transmission in silica glass communications fibres, but deliberate addition of 100's of ppm of H-bearing species may be desirable in augmenting non-linear optical properties useful in more complex optical components [**122**].

In relatively oxidized systems (probably including most natural magmas), all H is bonded to O and can thus be considered part of an OH group or H_2O molecule. At low concentrations, most or all is present as the former; at concentrations above a few wt%, H_2O the molecular species becomes predominant, at least in well-studied aluminosilicates [**195**]. ^{1}H MAS NMR showed that isolated OH groups produced spectra with few spinning sidebands, because of the relative lack of homonuclear dipolar broadening; in contrast, H_2O sites produced extensive sideband manifolds that could be simulated to estimate the relative abundances of the two species, which were consistent with infrared data [**121**]. A potential advantage of NMR in this instance is that in contrast to IR, quantification of not only relative concentrations of species but of absolute concentrations is in principle independent of the glassy matrix composition. ^{1}H CRAMPS, as well as MAS in ^{1}H-dilute systems, can produce usable chemical shift data, despite the narrow total range for this nuclide [**119**, **120**, **130**], and has been useful in estimating the extent of hydrogen bonding [**121**].

A recent innovation in optical materials has involved loading SiO_2 and SiO_2–GeO_2 glasses with H_2 at near-ambient temperature, followed by ultraviolet irradiation to create permanent refractive index changes that may be used to form optical Bragg gratings, holograms, etc. ^{1}H MAS NMR has proved useful in distinguishing and quantifying the H-bearing species that are produced by these processes, which can include Si–H and Ge–H [**122**] (Fig. 8.9).

The effect of H_2O addition, and hence OH group formation, on the network structure of aluminosilicate glasses is a long and controversial issue that can only be touched upon here. From a spectroscopic viewpoint, the key issue is what cation(s) the OH groups are bonded to. If Si or Al, the implication is that dissolution of water 'breaks up' the anionic network, making rationalization of effects on viscosity relatively straightforward. If OH is bonded only to network modifiers, then the situation becomes more complex, as the interaction of H^+ and even of molecular H_2O with bridging oxygens (thus weakening, if not breaking, the network bonds) needs to be considered.

In binary alkali silicates, it is clear from ^{29}Si NMR and other techniques that dissolution of water does indeed systematically increase the content of NBO [**130**, **196**,

197]. The interpretation of ^{17}O NMR on such glasses is complicated by the disordered nature of the NBO's produced, and the apparently large C_Q's of the OH species themselves [**129**, **198**, **199**]. In H_2O-bearing aluminosilicate glasses, extensive studies of ^{29}Si, ^{27}Al and ^{23}Na MAS and CPMAS NMR have suggested that the primary interactions of OH groups are with Na, and not with the network species [**105**, **106**, **126**, **127**], although particularly for Al, definitive interpretation of results is hampered by the limited number of available model compounds. Evidence for this conclusion includes relatively small changes in ^{29}Si and ^{27}Al spectra from dry to hydrated samples, the apparent constancy of ^{27}Al chemical shifts, and the relatively large changes in ^{23}Na spectra on hydration. ^{17}O MAS and 3QMAS spectra are similar in anhydrous and hydrous aluminosilicate glasses, although some subtle differences may be present [**129**]. This puzzling result again implies that O bonded directly to H in these systems may be difficult to observe, either because of large C_Q values or, possibly, for dynamical reasons.

8.3.4 Phosphate glasses

Phosphate ions readily link together to form stable, strongly-bonded network liquids. The resulting glasses have relatively low transition temperatures, large thermal expansivities, and optical properties that make them interesting for a variety of technological applications, from glass-to-metal seals to laser systems. Some phosphate-based glasses can be slowly assimilated and replaced during growth of bone tissue in living organisms, making them ideal for human bone implants. The high natural abundance, wide chemical shift range, and strong (but not overwhelming) homonuclear dipolar coupling of ^{31}P also make phosphate glasses ideal for applying NMR to answer fundamental questions of network glass structure. NMR (and other) studies of phosphate and phosphate-containing glasses have been reviewed at length [**85**, **162**].

Short-range structure

When fully oxidized to the 5+ state, phosphorus is four-coordinated by oxygen in oxide glasses, at least in the ambient-pressure materials that have been explored so far. It differs from other common network formers (B, Al, Si) in that at least one oxygen always seems to be non-bridging, including the double-bonded oxygen that forms the apex of the PO_4 tetrahedron in crystalline and glassy P_2O_5. The high charge and electronegativity of the phosphorus ion, however, has large effects on other normally tetrahedral network formers, and can force Al and even Si into five- and six-coordination at ambient pressure, as discovered in glasses by MAS NMR [**85**, **90**, **183**, **185**] (Fig. 8.12). In high alkali content glasses with a high P/Al ratio, for example, nearly all Al is present as AlO_6 [**200**] and presumably acts primarily as a network modifying cation.

Network speciation

As for ^{29}Si, ^{31}P in crystalline and glassy phosphates has distinct ranges of δ_{iso} for Q^n species, where $0 \leq n \leq 3$. Separation of peaks for different species is often distinct, resulting in relatively straightforward determination of relative abundances and modelling of equilibria among them [**201**, **202**]. At least in alkali phosphate glasses, disproportionation reactions (e.g. $2Q^2 = Q^3 + Q^1$) seem to be less important than in silicates, so that binary Q^n species distributions predominate (Fig. 8.4). It is not yet clear whether this greater degree of ordering in phosphates is a chemical/bonding effect, or results in part from their low glass transition temperatures. For higher field strength modifiers, e.g. Zn^{2+} [**203**] and possibly alkaline earth systems [**204**], three phosphate anionic species are present (Fig. 8.5), more similar to silicates. Chemical shift values for individual types of Q^n sites in phosphates vary strongly with the field strength of the modifier cation, opening the possibility for detailed studies of cation disorder [**205**].

As for ^{29}Si, phosphate Q^n species have distinctive CSA patterns, that can be useful in their characterization in both static 1-D spectra and in more complex two-dimensional experiments, such as VACSY results on silver iodide–silver phosphate glasses [**140**]. The orthophosphate unit (Q^0), with four nearly equivalent NBO's, tends to have a very small CSA, while Q^1 and Q^3 phosphate groups have large, near axial CSA's consistent with their single BO or single NBO [**6**, **110**, **140**] (Fig. 8.4).

In silicate glasses with relatively low concentrations of P_2O_5, NMR and other types of spectroscopy have shown that P and Si are not randomly distributed, but that regions rich in phosphate and NBO's form, reducing the share of NBO's on Si sites [**99**, **206**]. In ternary potassium aluminosilicate liquids with added P_2O_5 (and B_2O_3) that are analogous to natural granitic magmas, this sort of competition for NBO's has significant effects on the thermodynamic activity of silica and hence on crystal-liquid phase equilibria. The solubility of apatite, a minor but important calcium phosphate mineral in many silicic magmas, is also controlled by these effects, forming one of the more convincing links between NMR of glasses and large-scale geological processes [**206**].

Connectivities among structural units

The dipolar couplings between ^{31}P nuclei in phosphorus-rich glasses can be fully averaged by even moderate MAS spinning rates, but are strong enough to carry significant distance and connectivity information when they are recoupled using rotor-synchronized radiofrequency pulses in 2D exchange experiments (RFDR) [**142**, **143**]. Off-diagonal peaks in the spectra give qualitative views of the average proximity of various Q^n sites, but are somewhat difficult to quantify because the rate of magnetization transfer depends not only on distance but on energy difference between the site types, and hence on their relative orientations [**144**].

Nonetheless, choosing reasonable approximations, this approach has been used in a detailed study of Li-phosphate glasses to show that the intermediate-range structure is consistent with a random model, probably ruling out strongly clustered alternatives [**110**]. A more recently developed approach is the double-quantum (DQ) MAS experiment, which reveals direct coupling between spin pairs [**144**]. This approach may represent a real breakthrough in its ability to measure connections not only between, for example, Q^1 and Q^2 sites, but also between different kinds of Q^1 or Q^2 sites, distinguished by bond angles or other local structural differences [**145**] (Fig. 8.14). This permits a longer-range view of anionic structure than previously obtainable, such as the lengths of phosphate chains [**207**].

The proximity of different phosphate units to sodium and aluminium cations in aluminosilicate glasses has been explored by several NMR approaches, including spin diffusion [**208**] and TRAPDOR studies [**135**]. In particular, the latter showed that ^{23}Na–^{31}P and ^{27}Al–^{31}P dipolar couplings varied from site to site. The results suggested that some phosphate groups were connected to aluminate groups, supporting a model with significant mixing of tetrahedral units [**135**].

8.3.5 Thermal history effects

Thermal history effects on glass structure are often viewed as a minor experimental inconvenience. This may be the case for some reports: all that we know about rapidity of structural relaxation well above T_g indicates that glass structure should be independent of initial, high-temperature melting conditions or time [**209**], unless the process involves a compositional change such as loss of water, CO_2, or alkalis, all of which are common problems in glass making. For example, differences in ^{11}B DAS spectra of B_2O_3 as a function of melting time were sensibly attributed to progressive devolatilization, not to slow structural rearrangement [**154**]. In contrast, studies of samples deliberately prepared with different cooling rates or different annealing steps near to T_g may provide significant insights into the effect of temperature on the structure of the liquid, which is crucial to the understanding of both thermodynamic and transport properties [**10**].

Unfortunately, available laboratory cooling rates generally cannot change T_g by more than 100 to 200°C, so that resulting structural changes may be relatively small, requiring careful work for their detection. Among the fastest cooling rates are those for rapidly pulled glass fibres. A definitive early wideline NMR study showed, for example, that a multicomponent commercial boro-aluminosilicate glass in original fibre form had a significantly lower concentration of BO_4 groups than its annealed equivalent [**210**], consistent with thermodynamic models of these materials [**211**, **212**] which suggest that the enthalpy of the following type of reaction is positive, favouring the right-hand side at higher temperature:

$$BO_4 = BO_3 + NBO \tag{8.7}$$

This effect has been confirmed by several high-resolution ^{11}B NMR studies for some compositions, but not others, suggesting that the enthalpy may be composition dependent [**46, 95**] (Fig. 8.20). ^{29}Si MAS NMR has also been applied to study simultaneously the effects of cooling rate on Si and B sites, and hence the location of the NBO's in the structure [**95**], and ^{27}Al has shown the effects of temperature on the fraction of AlO_5 and AlO_6 groups in aluminoborate [**95**] (Fig. 8.6). The enthalpies estimated for such reactions generally indicate that they are not the predominant cause of measured configurational heat capacities, except for the case of the temperature effects on the boroxyl ring to non-ring ratio (Fig. 8.7), which may play a major energetic role [**95**]. In borosilicates, ^{17}O 3QMAS has also demonstrated thermal history effects on NBO contents directly [**163**].

In silicate glasses, ^{29}Si MAS NMR studies of Q^n concentrations as functions of thermal history have shown the enthalpies of reactions such as (8.6) are also positive, leading to wider distributions of species at higher temperature and thus higher configurational entropy [**59, 190**], consistent with *in situ* NMR studies [**48**] and high-temperature Raman spectroscopy [**193, 213**]. This same approach showed that the small concentrations of SiO_5 sites in alkali silicate glasses at ambient pressure increase with higher T_g [**180, 182**] (Fig. 8.25), but that large concentrations of SiO_6 sites in phosphosilicates seem to be lower in fast-quenched samples [**90, 185**]. In binary SiO_2–Al_2O_3 glasses, in which AlO_5 and AlO_6 groups were first seen by NMR [**214**], cooling rate has a large effect on speciation [**93, 94**], possibly because of small-scale phase separation. In binary CaO–Al_2O_3 glasses, which often contain AlO_4, AlO_5 and AlO_6 groups, cooling rate was shown to affect chemical shifts, as determined by analysis of spinning sidebands [**112**].

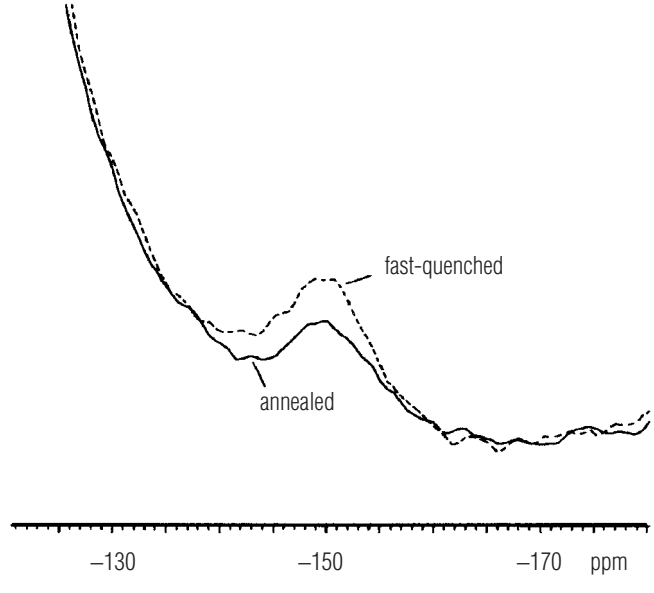

Fig. 8.25 ^{29}Si MAS NMR spectrum of isotopically enriched $K_2Si_4O_9$ glass synthesized at ambient pressure and containing about 0.1% SiO_5 groups giving a peak at –150 ppm [**181**]. Note the increase in intensity of this peak in the sample with the faster quench rate (higher T_g).

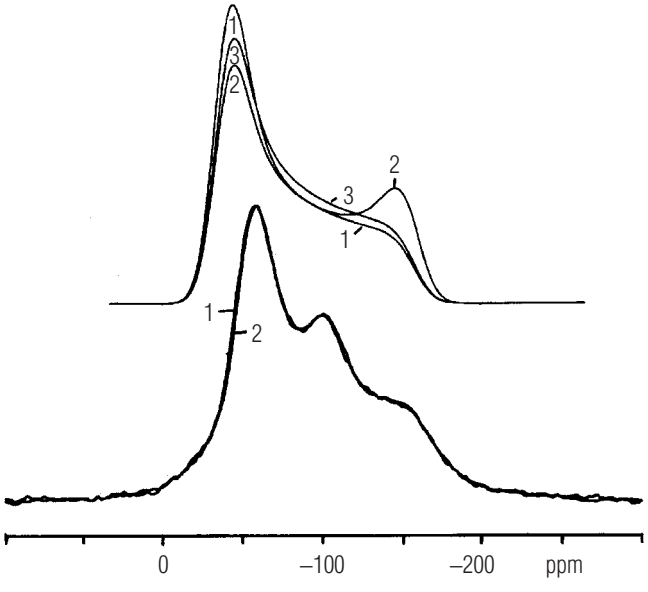

Fig. 8.26 Static ^{29}Si NMR spectra for $Na_2Si_2O_5$ glass, designed to test for alignment of structural units during flow [**214**]. Upper spectra are simulations for Q^3 groups. Curves 1 and 2 include a small fraction of groups with non-random orientation, with 'sheets' parallel to external field axis (1) and perpendicular (2). Curve 3 is for the normal random powder distribution. Experimental data (below) are for rapidly sheared sheets of glass, oriented parallel (1) and perpendicular (2) to field: the two curves are indistinguishable.

8.3.6 Long-range structural anisotropy

In organic polymer and macromolecular liquids, large-scale alignment of molecules is expected during flow, resulting in significant mechanical and optical anisotropies in their quenched, glassy equivalents. The same effect might be expected in inorganic glass-formers, if chain- or sheet-like 'molecules' are persistent at the timescale of viscous transport. NMR of nuclides with large responses to local structural anisotropy can be extremely sensitive to non-random alignments of structural units, particularly where C_Q is large (e.g. ^{11}B in BO_3 groups) or when CSA is large (e.g. ^{29}Si or ^{31}P in Q^3 and Q^2 sites). In a study of a number of borosilicate fibres and borate and silicate glass films and sheets, no differences were detected between static NMR spectra with varying orientation of the sample with respect to the external field [**215**], indicating that local structural rearrangement occurs at a timescale similar to the shear viscosity relaxation time (Fig. 8.26). (In other words, the timescales of network bond breaking and of shear transport of structural groups relative to each other are similar.) In contrast, some orientational effects seemed to be present in ^{31}P NMR spectra of an extruded sodium metaphosphate glass [**216**], suggesting the possibility of persistent, 'molecular' bonding in phosphate chains at the relatively low glass transition temperatures of these systems.

Acknowledgements

I would like to thank all of my colleagues who provided preprints and reprints of their recent studies in an attempt to keep this chapter as timely as possible, and

apologize to them if for reasons of length (or poor taste?) I have neglected to include some of their results. I am also grateful to the editor, Melinda Duer, for taking on the task of preparing this useful book.

References

1. P.J. Grandinetti, J.H. Baltisberger, I. Farnan, Stebbins, J.F., U. Werner and A. Pines, *J. Phys. Chem.* **99** (1995) 12341.
2. J.A. Tossell, *J. Non-Cryst. Solids* **120** (1990) 13.
3. J.A. Tossell, *Am. Mineral.* **78** (1993) 911.
4. J.A. Tossell and G. Saghi-Szabo, *Geochim. Cosmochim. Acta* **61** (1997) 1171.
5. G. Engelhardt and D. Michel, *High-Resolution Solid-State NMR of Silicates and Zeolites*, Wiley, New York (1987) 485 pp.
6. H. Eckert, in B. Blümich (Eds.), *Solid-State NMR IV. Methods and Applications of Solid-State NMR*, Springer-Verlag, Berlin (1994), p. 127.
7. H. Eckert, *Prog. Nucl. Mag. Reson.* **24** (1992) 159.
8. H. Eckert, *Ber. Bunsenges Phys. Chem.* **94** (1990) 1062.
9. R.J. Kirkpatrick, in F.C. Hawthorne (Eds.), *Spectroscopic Methods in Mineralogy and Geology*, Mineralogical Society of America, Washington, D.C. (1988), p. 341.
10. J.F. Stebbins, S. Sen and A.M. George, *J. Non-Cryst. Solids* **192 & 193** (1995) 298.
11. J.F. Stebbins, in J.F. Stebbins, P.F. McMillan and D.B. Dingwell (Eds.), *Structure, Dynamics, and Properties of Silicate Melts*, Mineralogical Society of America, Washington, D.C. (1995), p. 191.
12. J.F. Stebbins, in T.J. Ahrens (Eds.), *Handbook of Physical Constants*, American Geophysical Union, Washington, D.C. (1995), p. 303.
13. P.J. Bray and M.L. Liu, in G.E. Walrafen and A.G. Revesz (Eds.), *Structure and Bonding in Non-crystalline Solids*, Plenum Press, New York (1986), p. 285.
14. P.J. Bray and G.L. Petersen, *Z. Naturforsch.* **53a** (1998) 273.
15. P.J. Bray, *J. Non-Cryst. Solids* **73** (1985) 19.
16. R. Dupree, S.C. Kohn, M.G. Mortuza and D. Holland, in L.D. Pye, W.C. La Course and H.J. Stevens (Eds.), *Physics of Non-Crystalline Solids*, Taylor & Francis, London (1992), p. 718.
17. J.A. Sill, S.W. Martin and D.R. Torgesson, *J. Non-Cryst. Solids* **168** (1994) 86.
18. A. Pradel, G. Taillades, M. Ribes and H. Eckert, *J. Non-Cryst. Solids* **188** (1995) 75.
19. R. Maxwell, D. Lathrop and H. Eckert, *J. Non-Cryst. Solids* **180** (1995) 244.
20. S.J. Hwang, C. Fernandez, J.P. Amoureux, J.W. Han, J. Cho, S.W. Martin and M. Pruski, *J. Am. Chem. Soc.* **120** (1998) 7337.
21. C. Hudalla, B. Weber and H. Eckert, *J. Non-Cryst. Solids* **224** (1998) 69.
22. B. Gee, H. Eckert, A. Pradel, G. Taillades and M. Ribes, *J. Non-Cryst. Solids* **215** (1997) 32.
23. J.F. Stebbins, S. Sen and I. Farnan, *Am. Mineral.* **80** (1995) 861.
24. I. Farnan and J.F. Stebbins, *J. Am. Chem. Soc.* **112** (1990) 32.
25. P.J. Bray and J.G. O'Keefe, *Phys. Chem. Glasses* **4** (1963) 37.
26. W.J. Dell, P.J. Bray and S.Z. Xiao, *J. Non-Cryst. Solids* **58** (1983) 1.
27. J. Zhong and P.J. Bray, *J. Non-Cryst. Solids* **111** (1989) 67.
28. J.B. Murdoch, J.F. Stebbins and I.S.E. Carmichael, *Am. Mineral.* **70** (1985) 332.
29. P. Florian, K.E. Vermillion, P.J. Grandinetti, I. Farnan and J.F. Stebbins, *J. Am. Chem. Soc.* **118** (1996) 3493.
30. I. Farnan, P.J. Grandinetti, J.H. Baltisberger, J.F. Stebbins, U. Werner, M.A. Eastman and A. Pines, *Nature* **358** (1992) 31.
31. P. Richet and D.R. Neuville, in S.K. Saxena (Ed.), *Thermodynamic Data*, Springer-Verlag, New York (1992), p. 132.
32. P. Richet, *Geochim. Cosmochim. Acta* **48** (1984) 471.

33. J.F. Stebbins and S. Sen, in A.C. Wright, S.A. Feller and A.C. Hannon (Eds.), *Borate Glasses, Crystals and Melts*, Society of Glass Technology, Sheffield, UK (1997), p. 34.
34. R.J. Kirkpatrick, R.K. Sato, J. Haase, R.K. Brow, D. Sidebottom and F. Green, *Am. Ceram. Soc. Ann. Mtg. Abs.* **97** (1995) 21.
35. P. Florian, D. Massiot, B. Poe, I. Farnan and J.P. Coutures, *Solid-State NMR* **5** (1995) 233.
36. D. Massiot, D. Trumeau, B. Touzo, I. Farnan, J.C. Rifflet, A. Douy and J.P. Coutures, *J. Phys. Chem.* **99** (1995) 16455.
37. B.T. Poe, P.F. McMillan, B. Coté, D. Massiot and J. Coutures, *J. Phys. Chem.* **96** (1992) 8220.
38. B.T. Poe, P.F. McMillan, B. Coté, D. Massiot and J.P. Coutures, *Science* **259** (1993) 786.
39. B.T. Poe, P.F. McMillan, B. Coté, D. Massiot and J.P. Coutures, *J. Am. Ceram. Soc.* **77** (1994) 1832.
40. B. Coté, D. Massiot, B.T. Poe, P.F. McMillan and J.P. Coutures, *Rev. Staz. Speri. Vetro* **23** (1993) 451.
41. I. Farnan and J.F. Stebbins, *J. Non-Cryst. Solids* **124** (1990) 207.
42. I. Farnan and J.F. Stebbins, *Science* **265** (1994) 1206.
43. A.M. George and J.F. Stebbins, *Am. Mineral.* **83** (1998) 1022.
44. J.F. Stebbins, I. Farnan and X. Xue, *Chem. Geol.* **96** (1992) 371.
45. J.F. Stebbins and I. Farnan, *Science* **255** (1992) 586.
46. J.F. Stebbins and S.E. Ellsworth, *J. Am. Ceram. Soc.* **79** (1996) 2247.
47. J.F. Stebbins and S. Sen, *J. Non-Cryst. Solids* **224** (1997) 80.
48. H. Maekawa and T. Yokokawa, *Geochim. Cosmochim. Acta* **61** (1997) 2569.
49. F. Taulelle, J.P. Coutures. D. Massiot and J.P. Rifflet, *Bull. Magn. Reson.* **11** (1989) 318.
50. H. Jain, O. Kanert and K.L. Ngai, *Defect Diffus. Forum* **75** (1991) 163.
51. O. Kanert, J. Steinert, H. Jain and K.L. Ngai, *J. Non-Cryst. Solids* **131** (1991) 1001.
52. S. Sen and J.F. Stebbins, *Phys. Rev.* **55B** (1997) 3512.
53. A.M. George and J.F. Stebbins, *Phys. Chem. Mineral.* **23** (1996) 526.
54. J.F. Stebbins, *Chem. Rev.* **91** (1991) 1353.
55. G.E. Jellison, Jr. and P.J. Bray, *Journal of Non-Crystalline Solids* **29** (1978) 187.
56. Z. Xu and J.F. Stebbins, *Solid-State NMR* **11** (1998) 243.
57. G.E. Jellison, L.W. Panek, P.J. Bray and J.G.B. Rouse, *J. Chem. Phys.* **66** (1977) 802.
58. X. Xue, J.F. Stebbins and M. Kanzaki, *Am. Mineral.* **79** (1994) 31.
59. J.F. Stebbins, *J. Non-Cryst. Solids* **106** (1988) 359.
60. J.F. Stebbins, *Nature* **330** (1987) 465.
61. H. Maekawa, T. Maekawa, K. Kawamura and T. Yokokawa, *J. Non-Cryst. Solids* **127** (1991) 53.
62. H. Eckert, J.P. Yesinowski, E.M. Stolper, T.R. Stanton and J. Holloway, *J. Non-Cryst. Solids* **93** (1987) 93.
63. B. Gee and H. Eckert, *Solid-State NMR* **5** (1995) 113.
64. A.T.W. Yap and S.R. Elliott, *J. Non-Cryst. Solids* **193** (1995) 207.
65. E. Ratai, M. Janssen and H. Eckert, *Solid-State Ionics* **105** (1998) 25.
66. F. Fayon, C. Landron, K. Sakurai, C. Bessada and D. Massiot, *J. Non-Cryst. Solids* **243** (1999) 39.
67. F. Fayon, C. Bessada, D. Massiot, I. Farnan and J.P. Coutures, *J. Non-Cryst. Solids* **234** (1998) 403.
68. R. Dupree, D. Holland, P.W. McMillan and R.F. Pettifer, *J. Non-Cryst. Solids* **68** (1984) 399.
69. R. Dupree, D. Holland and D.S. Williams, *J. Non-Cryst. Solids* **81** (1986) 185.
70. R. Dupree, D. Holland and M.G. Mortuza, *J. Non-Cryst. Solids* **116** (1990) 148.
71. W. Hater, W. Müller-Warmuth, M. Meier and G.H. Frischat, *J. Non-Cryst. Solids* **113** (1989) 210.
72. J.F. Emerson, P.E. Stallworth and P.J. Bray, *J. Non-Cryst. Solids* **113** (1989) 253.
73. X. Xue, J.F. Stebbins, M. Kanzaki and R.G. Tronnes, *Science* **245** (1989) 962.
74. G. Libourel, C. Geiger, L. Merwin and A. Sebald, *Chem. Geol.* **96** (1991) 387.
75. C.I. Merzbacher, B.L. Sherriff, J.S. Hartman and W.B. White, *J. Non-Cryst. Solids* **124** (1990) 194.
76. R. Oestrike, W.H. Yang, R.J. Kirkpatrick, R.L. Hervig, A. Navrotsky and B. Montez, *Geochim. Cosmochim. Acta* **51** (1987) 2199.

77. R.J. Kirkpatrick, T. Dunn. S. Schramm, K.A. Smith, R. Oestrike and G. Turner, in G.E. Walrafen and A.G. Revesz (Eds.), *Structure and Bonding in Noncrystalline Solids*, Plenum Press, New York (1986), p. 302.
78. R.J. Kirkpatrick, R. Oestrike, J.C.A. Weiss, K.A. Smith and E. Oldfield, *Am. Mineral.* **71** (1986) 705.
79. K.L. Geisinger, R. Oestrike, A. Navrotsky, G.L. Turner and R.J. Kirkpatrick, *Geochim. Cosmochim. Acta* **52** (1988) 2405.
80. S.W. Martin, D. Bain, K. Budhwani and S. Feller, *J. Am. Ceram. Soc.* **75** (1992) 1117.
81. S.W. Martin, A. Bhatnagar, C. Parameswar, S. Feller and J. MacKenzie, *J. Am. Ceram. Soc.* **78** (1995) 952.
82. S.W. Martin, J.W. Mackenzie, A. Bhatnagar, S. Bhowmik and S.A. Feller, *Phys. Chem. Glasses* **36** (1995) 82.
83. T. Schaller, J.F. Stebbins and M. Wilding, *J. Non-Cryst. Solids* **243** (1999) 146.
84. S.K. Lee and J.F. Stebbins, *Am. Mineral.* **84** (1999) 937.
85. R.J. Kirkpatrick and R.K. Brow, *Solid-State NMR* **5** (1995) 9.
86. Z. Xu and J.F. Stebbins, *Solid-State NMR* **5** (1995) 103.
87. J.H. Baltisberger, Z. Xu, J.F. Stebbins, S. Wang and A. Pines, *J. Am. Chem. Soc.* **118** (1996) 7209.
88. R.K. Brow, R.J. Kirkpatrick and G.L. Turner, *J. Am. Ceram. Soc.* **76** (1993) 919.
89. B.C. Bunker, R.J. Kirkpatrick, R.K. Brow, G.L. Turner and C. Nelson, *J. Am. Ceram. Soc.* **74** (1991) 1430.
90. R. Dupree, D. Holland, M.G. Mortuza, J.A. Collins and M.W.G. Lockyer, *J. Non-Cryst. Solids* **112** (1989) 111.
91. J.T. Kohli, J.E. Shelby and J.S. Frye, *Phys. Chem. Glasses* **33** (1992) 73.
92. P.F. McMillan and R.J. Kirkpatrick, *Am. Mineral.* **77** (1992) 898.
93. B.T. Poe, P.F. McMillan, C.A. Angell and R.K. Sato, *Chem. Geol.* **96** (1992) 241.
94. R.K. Sato, P.F. McMillan, P. Dennison and R. Dupree, *J. Phys. Chem* **95** (1991) 4484.
95. S. Sen, Z. Xu and J.F. Stebbins, *J. Non-Cryst. Solids* **226** (1998) 29.
96. J.L. Yarger, K.H. Smith, R.A. Nieman, J. Diefenbacher, G.H. Wolf, B.T. Poe and P.F. McMillan, *Science* **270** (1995) 1964.
97. T. Schaller and J.F. Stebbins, *J. Phys. Chem.* **102B** (1998) 10690.
98. G. El-Damrawi, W. Muller-Warmuth, H. Doweidar and I.A. Gohar, *Phys. Chem. Glasses* **34** (1993) 52.
99. H. Gan, P.C. Hess and R.J. Kirkpatrick, *Geochem. Cosmochim. Acta* **58** (1994) 4663.
100. S. Schramm and E. Oldfield, *J. Chem. Soc., Chem. Commun.* (1982) 980.
101. G.L. Turner, K.A. Smith, R.J. Kirkpatrick and E. Oldfield, *J. Mag. Reson.* **67** (1986) 544.
102. L. van Wüllen and W. Müller-Warmuth, *Solid-State NMR* **2** (1993) 279.
103. J.F. Stebbins, J.V. Oglesby and Z. Xu, *Am. Mineral.* **82** (1997) 1116.
104. J.F. Stebbins and Z. Xu, *Nature* **390** (1997) 60.
105. B.C. Schmidt, T. Riemer, S.C. Kohn, H. Behrens and R. Dupree, *Geochim. Cosmochim. Acta* (in press, 1999).
106. S.C. Kohn, M.E. Smith, P.J. Dirken, E.R.H. van Eck, A.P.M. Kentgens and R. Dupree, *Geochim. Cosmochim. Acta* **62** (1998) 79.
107. B. Gee and H. Eckert, *J. Phys. Chem.* **100** (1996) 3705.
108. J.F. Stebbins, *Solid-State Ionics* **112** (1998) 137.
109. E. Schneider, J.F. Stebbins and A. Pines, *J. Non-Cryst. Solids* **89** (1987) 371.
110. T.M. Alam and R.K. Brow, *J. Non-Cryst. Solids* **223** (1998) 1.
111. L. Zürchner, J.C.C. Chan, W. Müller-Warmuth and H. Eckert, *J. Phys. Chem.* **102B** (1998) 4495.
112. P.F. McMillan, W.T. Petuskey, B. Coté, D. Massiot, C. Landon and J.P. Coutures, *J. Non-Cryst. Solids* **195** (1996) 261.
113. C. Mundus and W. Müller-Warmuth, *Solid-State NMR* **5** (1995) 79.
114. C. Jäger, W. Müller-Warmuth, C. Mundus and L. van Wüllen, *J. Non-Cryst. Solids* **149** (1992) 209.
115. C. Jäger, G. Kunath, P. Losso and G. Scheler, *Solid-State NMR* **2** (1993) 73.

116. C. Jäger, K. Herzog, B. Thomas, M. Feike and G. Kunath-Fandrei, *Solid-State NMR* **5** (1995) 51.
117. G. Kunath-Fandrei, D. Ehrt and C. Jäger, *Z. Naturforsch.* **50A** (1995) 413.
118. T. Schaller, D.B. Dingwell, H. Keppler, W. Knöller, L. Merwin and A. Sebald, *Geochim. Cosmochim. Acta* **56** (1992) 701.
119. T. Schaller and A. Sebald, *Solid-State NMR* **5** (1995) 89.
120. S.C. Kohn, R. Dupree and M.E. Smith, *Nature* **337** (1989) 539.
121. H. Eckert, J.P. Yesinowski, L.A. Silver and E.M. Stolper, *J. Phys. Chem.* **92** (1988) 2055.
122. Q. Zeng, J.F. Stebbins, A.D. Heaney and T. Erdogan, *J. Non-Cryst. Solids* (in press, 1999).
123. L.S. Du, F. Wang and C.P. Grey, *J. Sol. State Chem.* **140** (1998) 285.
124. F. Wang and C.P. Grey, *Chem. Mater.* **9** (1997) 1068.
125. R.M. Wenslow and K.T. Mueller, *J. Phys. Chem.* **102** (1998) 9033.
126. S.C. Kohn, R. Dupree and M.G. Mortuza, *Chem. Geol.* **96** (1992) 399.
127. S.C. Kohn, R. Dupree and M.E. Smith, *Geochim. Cosmochim. Acta* **53** (1989) 2925.
128. I. Farnan, S.C. Kohn and R. Dupree, *Geochim. Cosmochim. Acta* **51** (1987) 2869.
129. Z. Xu, H. Maekawa, J.V. Oglesby and J.F. Stebbins, *J. Am. Chem. Soc.* **120** (1998) 9894.
130. J. Kümmerlen, L.H. Merwin, A. Sebald and H. Keppler, *J. Phys. Chem.* **96** (1992) 6405.
131. L. van Wüllen, L. Züchner, W. Müller-Warmuth and H. Eckert, *Solid-State NMR* **6** (1996) 203.
132. J.C.C. Chan, M. Bertmer and H. Eckert, *Chem. Phys. Let.* **292** (1998) 154.
133. B. Gee, M. Janssen and H. Eckert, *J. Non-Cryst. Solids* **215** (1997) 41.
134. L. van Wüllen, B. Gee, L. Zuchner, M. Bertmer and H. Eckert, *Ber. Bunsen-Gesell. Phys. Chem.* **100** (1996) 1539.
135. T. Schaller, C. Rong, M.J. Toplis and H. Cho, *J. Non-Cryst. Solids* **248** (1999) 19.
136. C.T.G. Knight, R.J. Kirkpatrick and E. Oldfield, *J. Non-Cryst. Solids* **116** (1990) 140.
137. M.J. Duer, S.R. Elliott and L.F. Gladden, *J. Non-Cryst. Solids* **189** (1995) 107.
138. P. Zhang, P.J. Grandinetti and J.F. Stebbins, *J. Phys. Chem.* **101** (1997) 4004.
139. P. Zhang, C. Dunlap, P. Florian, P.J. Grandinetti, I. Farnan and J.F. Stebbins, *J. Non-Cryst. Solids* **204** (1996) 294.
140. J.W. Zwanziger, K.K. Olsen and S.L. Tagg, *Phys. Rev.* **47B** (1993) 14618.
141. F. Fayon, C. Bessada, A. Douy and D. Massiot, *J. Magn. Reson.* (in press, 1999).
142. C. Jäger, M. Feike, R. Born and H.W. Spiess, *J. Non-Cryst. Solids* **180** (1994) 91.
143. C. Jäger, P. Hartmann, G. Kunath-Fandrei, O. Hirsch, P. Rehak, J. Vogel, M. Feike, H.W. Spiess, K. Herzog and B. Thomas, *Ber. Bunsen-Gesell. Phys. Chem.* **100** (1996) 1560.
144. K.K. Olsen, J.W. Zwanziger, P. Hartmann and C. Jäger, *J. Non-Cryst. Solids* **222** (1997) 199.
145. M. Feike, C. Jäger and H.W. Speiss, *J. Non-Cryst. Solids* **223** (1998) 200.
146. K. Glock, O. Hirsch, P. Rehak, B. Thomas and C. Jäger, *J. Non-Cryst. Solids* **232–234** (1998) 113.
147. R.M. Wenslow and K.T. Mueller, *J. Non-Cryst. Solids* **231** (1998) 78.
148. K.T. Mueller, Y. Wu, B.F. Chmelka, J. Stebbins and A. Pines, *J. Am. Chem. Soc.* **113** (1990) 32.
149. R.E. Youngman, S.T. Haubrich, J.W. Zwanziger, M.T. Janicke and B.F. Chmelka, *Science* **269** (1995) 1416.
150. K.T. Mueller, J.H. Baltisberger, E.W. Wooten and A. Pines, *J. Phys. Chem.* **96** (1992) 7001.
151. P.J. Grandinetti, in D.M. Grant and R.K. Harris (Eds.), *Encyclopedia of Nuclear Magnetic Resonance*, John Wiley & Sons, New York (1995), p. 1768.
152. P.J. Grandinetti, J.H. Baltisberger, A. Llor, Y.K. Lee, U. Werner, M.A. Eastman and A. Pines, *J. Magn. Reson.* **103A** (1993) 72.
153. S.L. Tagg, R.E. Youngmann and J.W. Zwanziger, *J. Phys. Chem.* **99** (1995) 5111.
154. R.E. Youngman and J.W. Zwanziger, *J. Non-Cryst Solids* **168** (1994) 293.
155. R.E. Youngman and J.W. Zwanziger, *J. Am. Chem. Soc.* **117** (1995) 1397.
156. R.E. Youngman and J.W. Zwanziger, *J. Phys. Chem.* **100** (1996) 16720.
157. L. Frydman and J.S. Harwood, *J. Am. Chem. Soc.* **117** (1995) 5367.
158. A. Samoson, *Chem. Phys. Lett.* **247** (1995) 203.
159. J.P. Amoureux, C. Fernandez and L. Frydman, *Chem. Phys. Lett.* **259** (1996) 347.
160. D. Massiot, *J. Magn. Reson.* **122A** (1996) 240.
161. S.J. Hwang, C. Fernandez, J.P. Amoureux, J. Cho, S.W. Martin and M. Pruski, *Solid-State NMR* **8** (1997) 109.

162. R.K. Brow, T.M. Alam, D.R. Tallant and R.J. Kirkpatrick, *Mat. Res. Bull.* **23** (1998) 63.
163. S. Wang and J.F. Stebbins, *J. Am. Ceram. Soc.* (in press, 1999).
164. S. Wang and J.F. Stebbins, *J. Non-Cryst. Solids* **231** (1998) 286.
165. P.J. Dirken, S.C. Kohn, M.E. Smith and E.R.H. van Eck, *Chem. Phys. Lett.* **266** (1997) 568.
166. J.F. Stebbins, S.K. Lee and J.V. Oglesby, *Am. Mineral.* **84** (1999) 983.
167. S. Sen and J.F. Stebbins, *J. Non-Cryst. Solids* **188** (1995) 54.
168. S. Sen and J.F. Stebbins, *Phys. Rev.* **50** (1994) 822.
169. B.C. Bunker, D.R. Tallant, R.J. Kirkpatrick and G.L. Turner, *Phys. Chem. Glass.* **31** (1990) 30.
170. J.F. Stebbins, P. Zhao and S. Kroeker, *Sol. St. NMR* (submitted).
171. G.E. Jellison and P.J. Bray, *Solid-State Commun.* **19** (1976) 517.
172. A.M. George and J.F. Stebbins, *Am. Mineral.* **80** (1995) 878.
173. A.M. George, S. Sen and J.F. Stebbins, *Solid-State NMR* **10** (1997) 9.
174. R. Dupree, A.P. Howes and S.C. Kohn, *Chem. Phys. Lett.* **276** (1997) 399.
175. H. Koller, G. Engelhardt, A.P.M. Kentgens and J. Sauer, *J. Phys. Chem.* **98** (1994) 1544.
176. B. Gee and H. Eckert, *Ber. Bunsen-Gesell. Phys. Chem.* **100** (1996) 1610.
177. G.N. Greaves et al., *Phil. Mag.* **64A** (1991) 1059.
178. G.N. Greaves and K.L. Ngai, *J. Non-Cryst. Solids* **172** (1994) 1378.
179. J.F. Stebbins and B.T. Poe, *Geophys. Res. Lett.* (in press, 1999).
180. J.F. Stebbins and P. McMillan, *J. Non-Cryst. Solids* **160** (1993) 116.
181. X. Xue, J.F. Stebbins, M. Kanzaki, P.F. McMillan and B. Poe, *Am. Mineral.* **76** (1991) 8.
182. J.F. Stebbins, *Nature* **351** (1991) 638.
183. R. Dupree, D. Holland and M.G. Mortuza, *Nature* **328** (1987) 416.
184. S. Prabakar, K.J. Rao and C.N.R. Rao, *Mat. Res. Bull.* **26** (1991) 285.
185. M. Nogami, K. Miyamura, Y. Kawasaki and Y. Abe, *J. Non-Cryst. Solids* **211** (1997) 208.
186. R. Dupree and R.F. Pettifer, *Nature* **308** (1984).
187. L.F. Gladden, T.A. Carpenter and S.R. Elliot, *Phil. Mag.* **53B** (1986) L81.
188. H. Maekawa, P. Florian, D. Massiot, H. Kiyono and M. Nakamura, *J. Phys. Chem.* **100** (1996) 5525.
189. R. Hussin, R. Dupree and D. Holland, *J. Non-Cryst. Solids* **246** (1999) 159.
190. M.E. Brandriss and J.F. Stebbins, *Geochim. Cosmochim. Acta* **52** (1988) 2659.
191. S.J. Gurman, *J. Non-Cryst. Sol.* **125** (1990) 151.
192. B.O. Mysen and J.D. Frantz, *Am. Mineral.* **78** (1993) 699.
193. B.O. Mysen and J.D. Frantz, *Chem. Geol.* **96** (1992) 321.
194. P. Richet, R.A. Robie, J. Rogez, B.S. Hemingway, P. Courtial and C. Téqui, *Phys. Chem. Min.* **17** (1990) 385.
195. E. Stolper, *Contrib. Mineral. Petrol.* **81** (1982) 1.
196. J.F. Stebbins, *Mat. Res. Bull.* **17** (1992) 45.
197. N. Zotov and H. Keppler, *Am. Mineral.* **83** (1998) 823.
198. H. Maekawa, T. Saito and T. Yokokawa, *J. Phys. Chem. B* (in press, 1998).
199. X. Xue and M. Kanzaki, *Phys. Chem. Mineral.* **26** (1998) 14.
200. R.K. Brow, R.J. Kirkpatrick and G.L. Turner, *J. Am. Ceram. Soc.* **76** (1993) 919.
201. R.K. Brow, R.J. Kirkpatrick and G.L. Turner, *J. Non-Cryst. Solids* **116** (1990) 39.
202. R.K. Brow, D.R. Tallant, J.J. Hudgens, S.W. Martin and A.D. Irwin, *J. Non-Cryst. Solids* **177** (1994) 221.
203. R.K. Brow, D.R. Tallant, S.T. Myers and C.C. Phifer, *J. Non-Cryst. Solids* **191** (1995) 45.
204. J.P. Fletcher, R.J. Kirkpatrick, D. Howell and S.H. Risbud, *J. Chem. Soc. Faraday Trans.* **89** (1993) 3297.
205. R.K. Brow, C.C. Phifer, G.L. Turner and R.J. Kirkpatrick, *J. Am. Ceram. Soc.* **74** (1991) 1287.
206. H. Gan and P.C. Hess, *Am. Mineral.* **77** (1992) 495.
207. R. Witter, P. Hartmann, J. Vogel and C. Jäger, *Solid-State NMR* 1460 (1998) 189.
208. M.J. Toplis and T. Schaller, *J. Non-Cryst. Solids* **224** (1998) 57.
209. D.B. Dingwell and S.L. Webb, *Eur. J. Mineral.* **2** (1990) 427.
210. P.K. Gupta, M.L. Lui and P.J. Bray, *J. Am. Ceram. Soc.* **68** (1985) C82.
211. R.J. Araujo, *J. Non-Cryst. Solids* **58** (1983) 201.

212. R. Araujo, in G.E. Walrafen and A.G. Revesz (Eds.), *Structure and Bonding in Noncrystalline Solids*, Plenum Press, New York (1986), p. 13.
213. P.F. McMillan, G.H. Wolf and B.T. Poe, *Chem. Geol.* **96** (1992) 351.
214. S.H. Risbud, R.J. Kirkpatrick, A.P. Taglialavore and B. Montez, *J. Am. Ceram. Soc.* **70** (1987) C10.
215. J.F. Stebbins, D.R. Spearing and I. Farnan, *J. Non-Cryst. Solids* **110** (1989) 1.
216. M. Braun, Y. Yue, C. Rüssel and C. Jäger, *J. Non-Cryst. Solids* **241** (1998) 204.

Solid-State NMR Spectroscopy Principles and Applications
Edited by Melinda J. Duer
Copyright © 2002 by Blackwell Science Ltd

Chapter 9
Porous Materials

Jacek Klinowski

9.1 Introduction

Although NMR is widely used in materials research for the study of structure and dynamics, its inherently low sensitivity makes it useful primarily for the study of bulk phenomena and materials with extensive internal surfaces. Porous materials such as silica gel, activated carbon, synthetic zeolites, pillared clays and layered materials are invariably amorphous or poorly crystalline, with pores irregularly spaced and broadly distributed in size. Such materials are very difficult to study by conventional methods of structural elucidation, but can be profitably examined by solid-state NMR. This chapter surveys the main areas in which the technique has been shown to be successful. I do not intend to give a thorough review of the field (which would be the subject of a separate book), but rather to describe the potential of NMR for the study of porous materials.

9.2 Zeolites

Porous materials are conventionally divided into three categories according to pore diameter: microporous (pores smaller than 20 Å); mesoporous (20–5000 Å pores); and macroporous (pores larger than 5000 Å). Molecular sieves are a large class of *microporous* open-framework solids, which includes aluminosilicates (zeolites), aluminophosphates and related materials of diverse structures, as well as the newer family of *mesoporous* silicate sieves. Zeolites are built from corner-sharing SiO_4^{4-} and AlO_4^{5-} tetrahedra and contain regular systems of intracrystalline cavities and channels of molecular dimensions [**1–6**]. The negative charge of the framework, equal to the number of the constituent aluminium atoms, is balanced by exchangeable cations, M^{n+}, typically sodium, located in the channels which normally also contain water. The name 'zeolite' (from the Greek ζεω = to boil and λιθοσ = stone) was coined by Cronstedt [7] in 1756 to describe the behaviour

of the mineral stilbite which, when heated, rapidly loses water and thus seems to boil.

The general formula of a zeolite is

$$M_{x/n}(AlO_2)_x(SiO_2)_y \cdot mH_2O$$

with $y \geq x$. Aluminate tetrahedra cannot be neighbours in the frameworks of hydrothermally prepared zeolites, i.e. Al–O–Al linkages are forbidden, a requirement known as the Loewenstein rule [**8**]. There are at present ca. 40 identified species of zeolite minerals (with $1 \leq y/x \leq 5$) as well as many synthetic species giving a total of 121 recognized structure types [**1**]. Other elements, such as Ga, Ge, B, V, Fe and P can substitute for Si and Al in the framework. Some zeolite structures are shown in Fig. 9.1.

The most important properties of zeolites are the ability to sorb organic and inorganic substances, to act as cation exchangers and to catalyse a wide variety of reactions. The zeolitic channel systems, which may be one-, two- or three-dimensional and may occupy more than 50% of the crystal volume, are normally filled with water. When water is removed, other species such as gaseous elements, ammonia, alkali metal vapours, hydrocarbons, alcohols and many others may be accommodated in the intracrystalline space. Depending on pore diameter and on molecular dimensions, this process is often highly selective. Thus zeolitic sorption is a powerful method for the resolution of mixtures by 'molecular sieving'.

Cations neutralizing the electrical charge of the aluminosilicate framework can be exchanged for other cations from solutions. Zeolites possess ion-exchange selectivities for certain cations, and this is used for the isolation and concentration of these cations. The molecule-sieving properties of zeolites can be further modified by ion exchange. Thus zeolite Na-A sorbs both N_2 and O_2 while Ca-A sorbs nitrogen preferentially to oxygen.

However, the ability to catalyse reactions such as cracking, hydrocracking, oxidation and isomerization of hydrocarbons, by far overshadows all other applications of zeolites. Rare-earth exchanged and hydrogen forms of some zeolites, such as zeolite Y, mordenite, gmelinite and chabazite, have a cracking activity orders of magnitude greater than that of conventional silica/alumina catalysts. Zeolite-based catalysis was discovered [**9**] in 1960 and, soon after, cracking catalysts based on zeolite Y were introduced. The highly siliceous synthetic zeolite ZSM-5, introduced in 1972 [**10**], is a particularly powerful catalyst.

9.3 Aluminophosphate molecular sieves

Aluminophosphate molecular sieves [**11**], designated as $AlPO_4$, formally the porous crystalline equivalents of aluminium phosphate, are built from alternating AlO_4^{4-} and PO_4^{4-} tetrahedra. Many such structures have been prepared, including a number

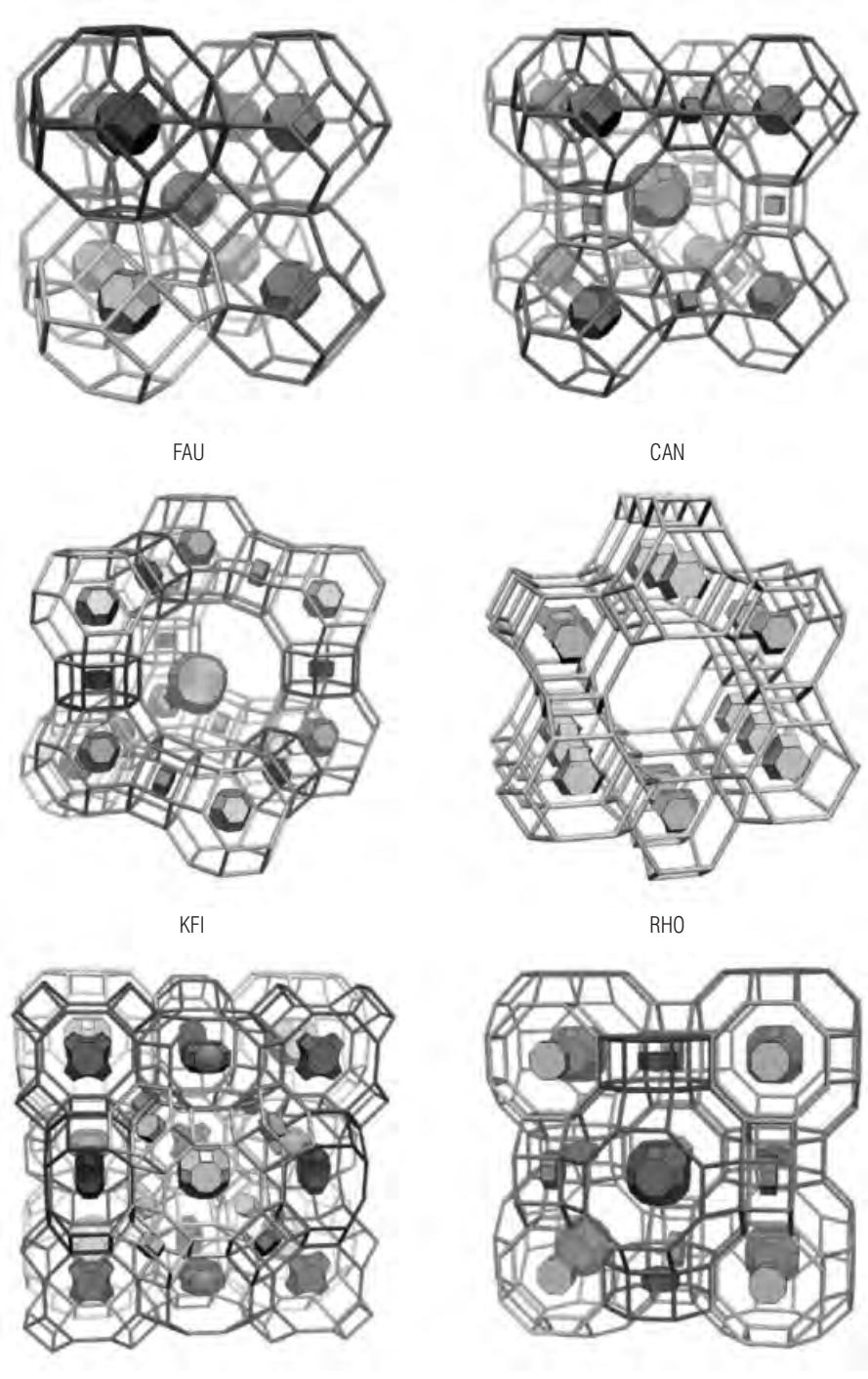

Fig. 9.1 Framework structures of zeolites of structure types SOD (sodalite), LTA (zeolite A), FAU (faujasite), CAN (cancrinite), KFI (zeolite ZK-5) and RHO (zeolite Rho). The positions of tetrahedral atoms are at the crossings of the straight lines which symbolize T–T linkages. Oxygen atoms (not shown) lie approximately half-way between the T atoms. The types of cages involved in each structure are represented by polyhedra which have been shrunk towards their centres. Sodalite is formed by direct face-sharing of 4-membered rings in the neighbouring truncated octahedra, more correctly described as tetrakaidodecahedra (also known as 'sodalite cages' or 'β-cages'). Zeolite A is formed by linking the sodalite cages through double 4-membered rings. Faujasite is formed by linking the sodalite cages through double six-membered rings. Cancrinite is formed by direct linking of 11-hedra ('ε-cages' or 'cancrinite cages'). Other polyhedra are also present: the 'α-cage' (26-hedron of type I); double 8-membered ring; double 6-membered ring (hexagonal prism) and the 18-hedron ('γ-cage'). Exchangeable non-framework cations are not shown for clarity.

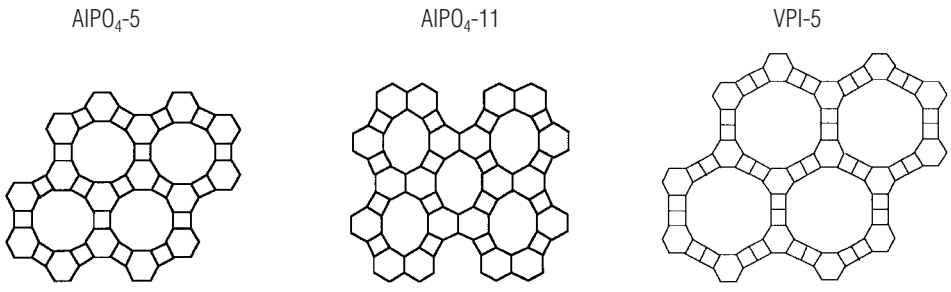

Fig. 9.2 Framework projections of $AlPO_4$-5 along [001], $AlPO_4$-11 along [100] and VPI-5 along [001]. Aluminium and phosphorous atoms are located at the apices of the polygons.

which do not have analogues among conventional zeolites, such as $AlPO_4$-5 [**12**], $AlPO_4$-11 and VPI-5, a remarkable material with 18-membered rings (see Fig. 9.2) [**13**, **14**]. The large channel diameter gives VPI-5 potential for the separation of large molecules, and for catalytic cracking of the heavy fractions of petroleum. Cloverite [**15**], a gallophosphate molecular sieve with 20-membered rings, is the most porous molecular sieve prepared so far. Incorporation of silicon in the aluminophosphate framework gives silicoaluminophosphates, SAPO, and the incorporation of a metal into $AlPO_4$ and SAPO gives the MeAPO and MeAPSO sieves, respectively [**16**].

9.4 Mesoporous molecular sieves

Chemical processes involving bulky molecules require materials with channel openings larger than in zeolites and aluminophosphate molecular sieves, and there has been increasing demand for materials with pore diameters in the *mesopore* range. The synthesis of the M41S family of mesoporous sieves, using aggregates of an amphicillic surfactant as the template, has responded to this need by extending the realm of molecular sieves into the very-large-pore regime [**17**, **18**]. The new materials exhibit remarkable features: (i) well-defined pore size (16–100 Å in diameter) and shape; (ii) very large surface area (ca. 990 m^2/g) and pore volume (ca. 0.74 cm^3/g); (iii) the possibility of fine 'tuning' of the pore aperture; (iv) high thermal and hydrolytic stability (up to 950°C); (v) very high degree of pore ordering over micrometer length scales; and (vi) excellent thermal insulation and sound-proofing properties. There are prospects of using them in the chemical and petroleum industries (catalysis, hydrocracking, treatment of heavier oil feeds, production of fine organics), separation of macromolecules and very large cations, pharmaceutical industry (purification and slow release of drugs) and the manufacture of nanoelectronic devices. Heteroatoms such as Al, Ga and B have been introduced into the mesoporous structure in order to generate Brønsted acidity and thus catalytic activ-

ity [**19**]. However, the silicate network of the mesoporous sieves is amorphous, and their ^{29}Si NMR spectra are essentially those of silica (see Chapter 8). NMR has been used to monitor the concentration of silanol groups and the insertion of heteroatoms (such as Al) into the structure.

9.5 Spectroscopic considerations

Synthetic molecular sieves are usually microcrystalline and furthermore typically contain *four* formally 10-electron atomic species (Si^{4+}, Al^{3+}, O^{2-} and Na^{+}) which makes them difficult to study by conventional techniques of structural elucidation. The development of high-resolution solid-state NMR techniques, such as magic-angle spinning (MAS), gave zeolite chemistry a powerful structural tool to monitor all elemental components of such frameworks.

^{29}Si, ^{27}Al, ^{31}P and ^{17}O have been observed in the frameworks of molecular sieves using MAS NMR. In particular, ^{29}Si NMR has provided many new insights into the structure and chemistry of zeolites. Lines originating from crystallographically inequivalent silicon atoms can now be resolved and related to structural parameters.

The full range of ^{29}Si chemical shifts is over 500 ppm wide, but most shifts are found in a narrower range of ca. 120 ppm. Pioneering studies in high-resolution solid-state ^{29}Si NMR spectroscopy were performed by Lippmaa et al. [**20**], who carried out the first comprehensive investigation of a variety of silicates.

With 100% natural abundance, and with a chemical shift range of about 450 ppm, ^{27}Al is in principle a very favourable nucleus for NMR. However, its quadrupole interaction is usually large, which broadens and shifts the resonance lines. As discussed in Chapter 4, with quadrupolar nuclei of non-integer spin, the central transition, the only one which is normally observed, is independent of the quadrupolar interaction to first order, but is affected by second-order effects which are inversely proportional to the magnetic field strength. Chapter 4 details how to deal with such nuclei, but to summarize, the best spectra are obtained at very high magnetic fields (which reduces the magnitude of the quadrupole coupling) and with fast magic-angle spinning (to reduce the quadrupole-coupling broadening and eliminate dipolar and chemical shift anisotropy effects). It is essential to use strong radiofrequency pulses with small flip angles to obtain quantitatively reliable results [**20–22**].

The difficulties involved in the detection and quantification of aluminium in solids by NMR have hindered NMR studies of the $AlPO_4$ molecular sieves, which apart from large quadrupolar effects, show strong interactions with water and other adsorbates. The development of double-rotation (DOR), dynamic-angle spinning (DAS) and multiple-quantum MAS (MQ-MAS) NMR (see Chapter 4) was thus a major advance in the study of quadrupolar nuclei.

High-resolution ^{1}H MAS NMR can be used for the measurement of zeolitic acidity. In general, the difficulties involved in high-resolution ^{1}H work in the solid state are the strong dipolar interactions (see Chapter 3) and the narrow range of ^{1}H chemical shifts. The consequence of this is that only a limited number of NMR lines can be resolved. Fortunately, the protons in dehydrated zeolites are usually relatively far apart, which considerably reduces the dipolar interaction, enabling information on the chemical status of hydroxyl groups in zeolites to be obtained [**23**].

^{15}N NMR work on molecules sorbed on zeolites has shown the usefulness of the technique for the study of zeolitic acidity and other surface phenomena. The nitrogen atom in molecules such as ammonia and pyridine has a lone pair of electrons and binds directly to the surface site. One is therefore observing large effects on a nucleus with a wide (over 1000 ppm) range of chemical shifts [**24**].

The atomic diameter of xenon is 4.6 Å, comparable to the diameter of zeolitic channels, and ^{129}Xe NMR is useful for investigating microporous materials. ^{129}Xe has spin $I = \frac{1}{2}$, a natural abundance of 26.44% and a large gyromagnetic ratio. The T_1 for xenon adsorbed inside solids is fairly short, typically in the range of 10 ms to a few seconds. Xenon is non-reactive and easily detectable by NMR; its chemical shift varies within an enormous range (over 6000 ppm) and is very sensitive to physical environment, as shown by its strong dependence on density in the pure phases: the liquid at 224 K resonates 161 ppm downfield from the gas at zero density, while the solid at 161 K resonates at −74 ppm [**25**].

9.6 Monitoring the composition of the aluminosilicate framework of zeolites

Framework Si in zeolites is tetrahedrally coordinated, and there are thus five different possible environments for a silicon atom, denoted as Si(nAl), where n (≤4) signifies the number of aluminium atoms connected, via oxygens, to a silicon. Each type of Si(nAl) building block corresponds to a definite range of ^{29}Si chemical shift. When a ^{29}Si MAS NMR spectrum of a zeolite (a) contains more than one line; and (b) is correctly assigned in terms of Si(nAl) units, the Si/Al ratio in the zeolitic framework may be calculated from the spectrum alone. This method is valid because in the absence of Al–O–Al linkages the environment of every Al atom is Al(4Si). Therefore, each Si–O–Al linkage in an Si(nAl) unit incorporates 0.25 Al atoms, and the whole unit 0.25 nAl atoms. The Si/Al ratio in the aluminosilicate framework may be calculated directly from the ^{29}Si MAS NMR spectrum using the formula [**26**].

$$(\mathrm{Si/Al})_{\mathrm{NMR}} = \frac{I_4 + I_3 + I_2 + I_1 + I_0}{I_4 + 0.75I_3 + 0.5I_2 + 0.25I_1} \tag{9.1}$$

where I_n denotes the intensity (peak area) of the NMR line corresponding to the Si(nAl) building unit. By comparing $(Si/Al)_{NMR}$ values with the results of chemical analysis, which gives *bulk* composition, the amount of extra-framework aluminium can be calculated, which is important when dealing with chemically modified zeolites.

Equation (9.1) is independent of structure and applies to all zeolites provided the assumptions made in its derivation are justified. It can, by implication, serve as a test for the correctness of spectral assignment. Its validity has been tested in the case of zeolites X and Y and their gallosilicate equivalents, which can be synthesized in a range of compositions. The spectra can be deconvoluted using Gaussian peak shapes, and the areas of the individual deconvoluted lines used in Equation (9.1). Very good agreement was found between the Si/Al ratios obtained by chemical analysis and those calculated from the spectra. Equation (9.1) works well with materials which have framework Si/Al ratios less than about 10. However, it cannot be directly applied to spectra containing overlapping lines from Si(nAl) units of crystallographically inequivalent Si atoms [**27**, **28**].

9.7 Ordering of atoms in tetrahedral frameworks

^{29}Si NMR enables us to determine the *ordering* of Si and Al atoms in the zeolitic framework. The areas under the peaks in the deconvoluted spectra of zeolites X and Y are directly proportional to the populations of the respective structural units in the sample. It is therefore possible to estimate these from the spectra (Fig. 9.3) and to compare them with the relative numbers of such units contained in models involving different Si, Al ordering schemes. For most Si/Al ratios, more than one ordering scheme is compatible with the Si(nAl) intensities determined by ^{29}Si MAS NMR [**26**, **29**, **30**]. The choice between the *various* schemes is made on the basis of (a) the degree of agreement between the actual spectral intensities and those required by the given model; (b) compliance with crystal symmetry requirements; and (c) minimum electrostatic repulsion within the aluminosilicate framework. Figure 9.4 shows the preferred ordering schemes for Si/Al = 1.67. The ordering of tetrahedral atoms in natural and synthetic ultramarine [**31**] and synthetic mazzite (zeolite omega) [**27**] have been determined using the same approach.

The ^{29}Si chemical shift is also correlated with the T–O–T angles in zeolitic frameworks and is very useful for structural determination. Chemical shifts in the framework silicates cristobalite, quartz, albite and natrolite have been correlated with the mean Si–O bond *distances*, and relationships involving θ, $\cos\theta/(\cos\theta - 1)$, $\sin(\theta/2)$ and $\sec\theta$ have been developed, which are in good agreement with the results of semi-empirical calculations of chemical shift [**6**]. Similar correlations are found in silicate glasses (see Chapter 8). The original correlations were between the

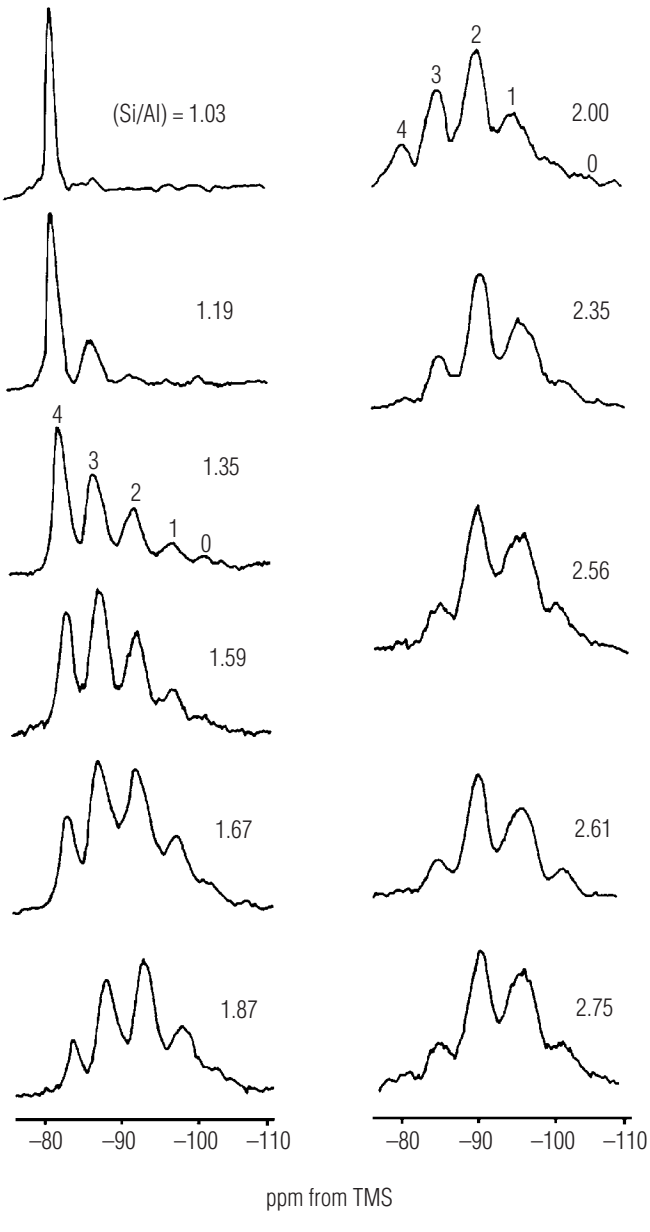

Fig. 9.3 High-resolution ^{29}Si MAS NMR spectra of synthetic zeolites Na-X and Na-Y [**29**]. Si(*n*Al) lines are identified by the *n* above the peaks

chemical shift of the Si(4Si) peak and the magnitude of the T–O–T angle. These arguments were extended to *all five* Si(*n*Al) peaks, and an approximately linear semi-empirical relationship was given between δ of an Si(*n*Al) peak and the total (non-bonded) Si . . . T distance (T = Si or Al) calculated from the T–O–T angle [**32**]. The apparent ^{27}Al 'chemical shift' in zeolites is affected by the second-order quadrupole interaction and is strongly field-dependent. The chemical shift corrected for the

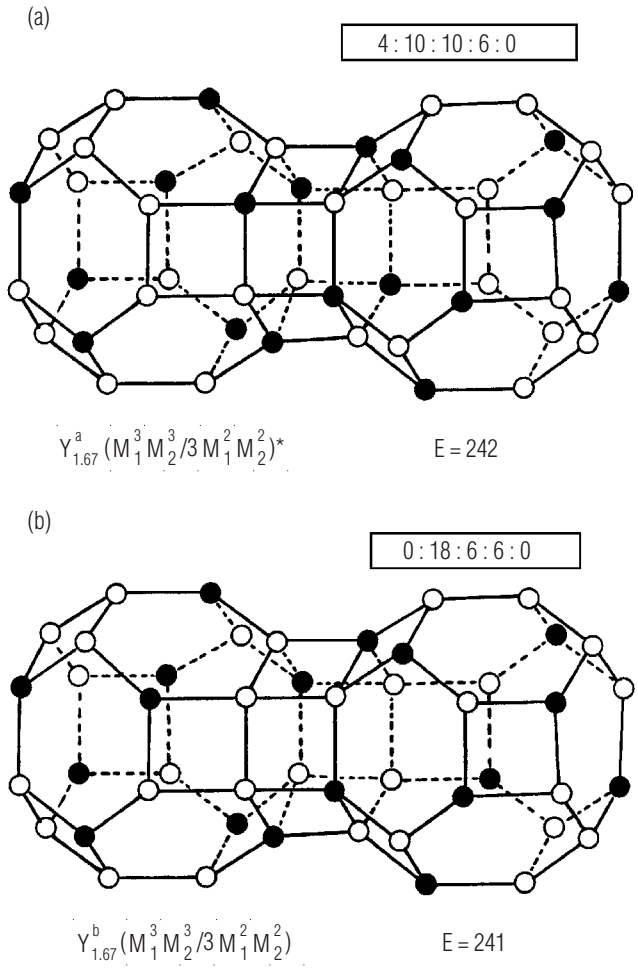

Fig. 9.4 Two of the possible Si, Al ordering schemes for zeolite Y with Si/Al = 1.67 [**29**]. Open circles denote Si atoms, closed circles Al atoms. The ratio of intensities S(4Al) : Si(3Al) : Si(2Al) : Si(1Al) : Si(0Al) corresponding to each scheme is given in the upper right-hand corner. *E* is the calculated electrostatic energy for the double cage in units of $(qe)^2/a$, where *a* is the T–O–T distance. The asterisk denotes the preferred scheme.

quadrupole interaction is related to structural parameters in a similar fashion to ^{29}Si chemical shifts.

9.8 Resolving crystallographically inequivalent tetrahedral sites

In naturally occurring zeolites the Si/Al ratio is less than ca. 5, but materials with much lower Al contents can be synthesized. One of them, known as ZSM-5, has an Si/Al ratio between 20 and many thousand, and possesses remarkable catalytic properties. A crystalline microporous material called silicalite, isostructural with ZSM-5 but containing only traces of Al, has also been prepared.

A highly siliceous zeolite may be expected to give an uncomplicated ^{29}Si MAS NMR spectrum, consisting only of the Si(4Al) line. The spectrum of as-prepared

ZSM-5 is indeed almost featureless. However, the spectrum of a sample of silicalite with a particularly low Al content shows considerable fine structure [**33**, **34**]. As many as 20 individual lines can be separately resolved and the linewidth of the narrowest line is ca. 5 Hz. The chemical shifts of *all* the peaks are characteristic of Si(4Si) groupings in highly siliceous materials. The multiplicity arises from the crystallographically inequivalent tetrahedral environments of the Si(4Si) sites. The spectrum may be simulated by 20 Gaussian lines, and the total intensity of the spectrum is 24 times greater than the intensity of the smallest line. This indicates that the space group of silicalite contains 24 inequivalent sites in the unit cell. X-ray diffraction (XRD) shows that silicalite can exist in the monoclinic and the orthorhombic forms, and that the slight changes of symmetry involved are related to the residual aluminium content. The same structural transformation was also found to be reversibly temperature-induced, the 'low' temperature form being monoclinic and the 'high' temperature form, orthorhombic. ^{29}Si MAS NMR detects much more subtle changes in the structure of silicalite: minute variations in atomic position [**34–36**] which do not involve symmetry changes detectable by XRD. Spectra measured in the range 153–403 K are sensitive even to small temperature changes and reveal that structural transformations continue over the entire range. By contrast, the changes in the XRD pattern are slight. This demonstrates the remarkable sensitivity with which NMR can monitor relatively minor modifications in atomic positions. The addition of very small amounts of adsorbed organic molecules to dehydrated silicalite induces similar phase transitions and similar, but not identical, changes in the ^{29}Si NMR spectra [**37–39**].

Two-dimensional solid-state NMR techniques have also been used to assign the individual NMR peaks to specific crystallographic sites [**33**, **40–46**]. In particular, two-dimensional homonuclear correlation spectroscopy (COSY) is feasible with ^{29}Si in zeolites, particularly when isotopically enriched in ^{29}Si [**41**, **42**]. ^{29}Si 2D INADEQUATE and double-quantum filtered COSY experiments on highly siliceous zeolites have also been performed [**46**, **47**].

J-scaled COSY can provide useful information about zeolitic frameworks. The technique *scales up* the scalar splittings between the crosspeak components, thereby enhancing crosspeak intensities and consequently improving spectral resolution between adjacent diagonal and crosspeaks. ^{29}Si *J*-scaled COSY at natural isotopic abundance allowed the spectrum of highly siliceous mordenite to be assigned [**47**]. The conventional ^{29}Si MAS NMR spectrum of the sample (Fig. 9.5) consists of three peaks in the intensity ratio of 2 : 1 : 3. This may be explained in terms of the known structure of mordenite, which contains four distinct tetrahedral crystallographic sites in the intensity ratio T1 : T2 : T3 : T4 = 2 : 2 : 1 : 1 (Fig. 9.6), with two of the peaks overlapping. The correlation between ^{29}Si chemical shifts and the mean Si–O–Si bond angles permits the immediate assignment of the downfield peak to the T1 site and shows that the T2 site is a component of the strongest peak (Table 9.1). However, the ⟨T3–O–T⟩ and ⟨T4–O–T⟩ bond angles are similar, so that the two pos-

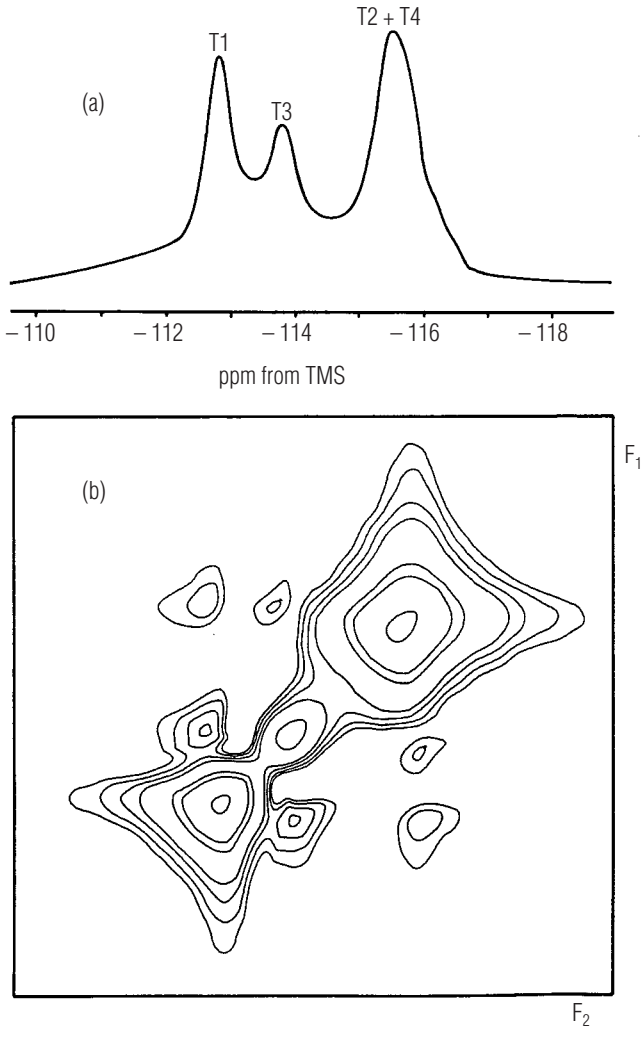

Fig. 9.5 (a) ^{29}Si MAS NMR spectrum of highly siliceous mordenite; (b) *J*-scaled COSY spectrum [**47**].

Table 9.1 The connectivities and typical mean T–O–T bond angles of the mordenite structure (see Fig. 9.6)

T-site	No. per unit cell	Neighbouring sites	Mean T–O–T bond angle
T1	16	T1, T1, T2, T3	150.4°
T2	16	T1, T2, T2, T4	158.1°
T3	8	T1, T1, T3, T4	153.9°
T4	8	T2, T2, T3, T4	152.3°

sible assignments of the three peaks in the spectrum are to T1 : T4 : T2 + T3 or to T1 : T3 : T2 + T4 crystallographic sites.

The 2D *J*-scaled COSY spectrum (Fig. 9.6) reveals three crosspeaks. On the basis of the known connectivities of the mordenite structure (Table 9.1), only two cross-

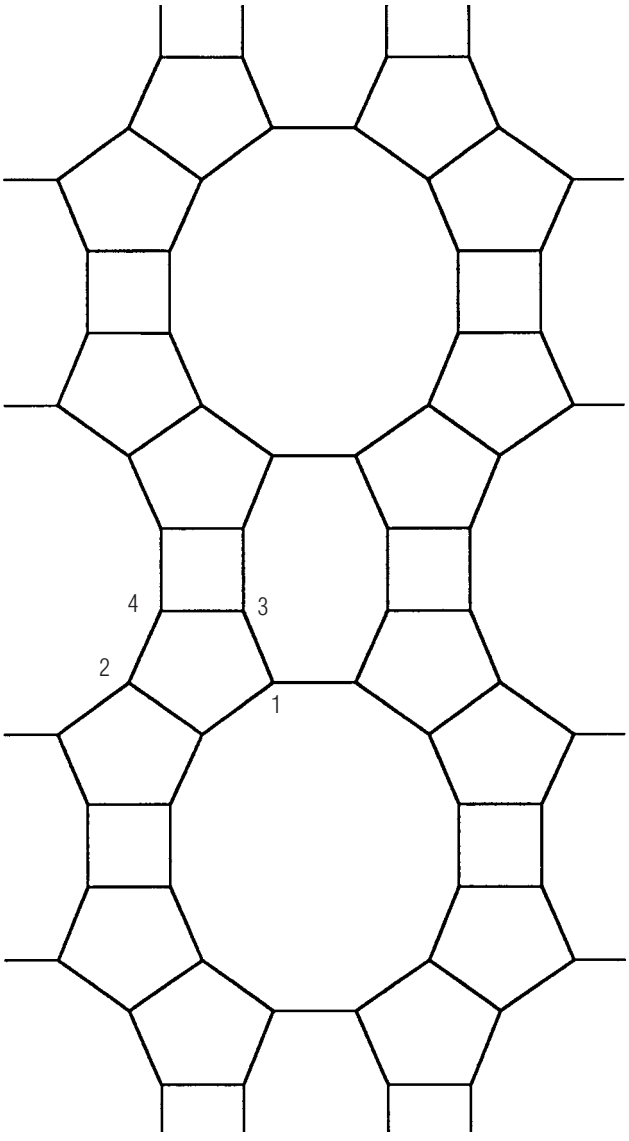

Fig. 9.6 The structure of mordenite viewed along [001]. The relative populations of the four kinds of crystallographic sites (16:16:8:8 per unit cell) are not reflected in this projection.

peaks are predicted for the T1:T4:T2 + T3 assignment, while the T1:T3:T2 + T4 assignment implies that three should be observed. Thus the detection of three cross-peaks shows that the correct interpretation is T1:T3:T2 + T4.

9.9 Spectral resolution, lineshape and relaxation

The resolution of ^{29}Si MAS NMR spectra of zeolites increases until a field of about 4.70 T is reached, and no further improvement is observed above this value. Dipolar

^{29}Si–^{29}Si coupling is unlikely to be responsible, in view of the magnetic dilution of the ^{29}Si nucleus; the weakness of such coupling, which is in any case removable by MAS; and the fact that dipolar interactions are field-independent. Melchior [**48**] suggested that the likely cause is the ^{29}Si–^{27}Al dipole–quadrupole interaction. Such interaction gives rise to splitting and broadening of ^{13}C MAS NMR spectra of α-carbon atoms in amino acids [**49**].

The removal of aluminium from the zeolitic framework leads to very marked narrowing of NMR lines. When no Al is present, the Si(4Si) lines from silicalite/ZSM-5 are very narrow indeed. Fyfe *et al.* [**34**, **39**] studied the effect of dealumination on linewidths of Si(4Si) lines in several zeolites, to find that substantial line narrowing occurs at Si/Al > 100. However, since it was shown [**50**] that an *aluminated* sample with Si–Al distance of only 5.0 Å gives highly resolved spectra, it is likely that improved spectral resolution is due to a process, such as healing of structural defects, which occurs in parallel with dealumination during hydrothermal treatment.

^{29}Si spin-lattice relaxation times, T_1, in zeolites are 5–30 s. Also, for a given zeolite, T_1 of a silicon atom in an Si(nAl) unit varies little with n, and is also insensitive to a change in the Si/Al ratio. This indicates that relaxation is not affected by the presence of ^{27}Al and also explains why the short recycle times used by most workers (typically 5 s, i.e. much shorter than $5T_1$) still give quantitatively reliable spectra.

It had often been assumed that spin-lattice relaxation in zeolites is controlled by spin diffusion from paramagnetic centres. However, this mechanism is likely to be inefficient in view of the large distance between neighbouring silicons, the relatively low abundance of ^{29}Si, and the 'detuning' influence of ^{27}Al. Also, the 'impurity' hypothesis cannot explain why T_1 for synthetic zeolites with very low levels of paramagnetics remains short, nor why, upon rendering a zeolite amorphous, T_1 increases by orders of magnitude while the concentration of the paramagnetic component remains constant. Measurements [**51**] of the T_1 relaxation times of a number of zeolites contained in sealed capsules under oxygen and argon atmospheres reveal that the effect of oxygen is dramatic, while water and paramagnetic impurities play a secondary role. For dealuminated mordenite, T_1 is reduced by three orders of magnitude in comparison with the value under argon. Furthermore, relaxation times of crystallographically inequivalent Si atoms often differ within the same sample. These results explain why T_1 increases so dramatically when the zeolite is made amorphous and why relaxation in compact silicates (such as quartz) and glasses is so slow. It is simply that most Si atoms in such samples are inaccessible to oxygen. The significant lengthening of T_1 upon addition to zeolites of various organic materials is due to the displacement of oxygen from the intracrystalline space by the guest molecules. Reports of a major influence of dehydration of the zeolite on the T_1 of ^{29}Si stem from the failure to separate the effects of *dehydration* and *evacuation*. The results of reference [**51**] (a) offer a means of rapid acquisition of ^{29}Si NMR spectra of zeolites; (b) suggest a new, quantitatively reliable method for the study of

surfaces of amorphous silicas, silica-aluminas and silicate glasses; and (c) provide a method for obtaining site-selective spectra *via* careful control of the partial pressure of oxygen.

Spin-lattice relaxation times of ^{27}Al in zeolitic frameworks (0.3–70 ms depending on temperature) are governed by the electric quadrupole interaction with the crystal electric field gradients modulated by translational motion of *polar sorbate molecules* and charge-compensating cations [**52**]. Relaxation times in zeolite Na-X are unchanged upon replacing two-thirds of intracrystalline H_2O by D_2O with the same overall pore-filling factor. Since ^1H and ^2H have very different gyromagnetic constants, relaxation of ^{27}Al cannot be caused by the magnetic dipole interaction with ^1H of the water molecules. Furthermore, T_1 dramatically increases upon dehydration of the sample, which demonstrates that the controlling mechanism in hydrated samples must be the *quadrupolar* interaction of ^{27}Al with the crystal electric field gradient produced by the very similar electric dipole moments of the H_2O and D_2O molecules. Dipolar interactions with paramagnetic impurities become significant as a ^{27}Al relaxation mechanism only at very low temperatures.

9.10 Dealumination and realumination of zeolites

Solid-state ^{27}Al MAS NMR spectra of as-prepared zeolites generally contain a single peak corresponding to tetrahedrally coordinated Al, and are thus much simpler than their ^{29}Si counterparts. This is a direct consequence of the fact that while five types of Si(*n*Al) environments are possible for the silicon atom, only one possibility, Al(4Si), exists for the aluminium. However, while the coordination of Si in zeolites is always four-fold, Al can be 4- or 6-coordinate, and ^{27}Al MAS NMR is very sensitive to coordination. In aluminophosphate molecular sieves, 5-coordinate Al is often present.

Early work indicated that the amount of 6-coordinate (extra-framework) Al calculated from the difference between the result of chemical analysis and the quantity of *framework* Al measured from ^{29}Si spectra did not agree with the results of ^{27}Al MAS NMR: extra-framework Al was always underestimated by the latter. The problem was resolved when it was shown that quantitatively reliable ^{27}Al spectra can only be obtained at very high magnetic fields, with fast MAS, and using strong radiofrequency pulses with small flip angles.

Since Brønsted acid groups in zeolites are associated with 4-coordinated framework aluminium, their catalytic activity strongly depends on the concentration and location of Al in the structure. Upon hydrothermal treatment of zeolite NH_4-Y, a process known as 'ultrastabilization' [**53**, **54**], part of the aluminium is ejected from the framework into the intracrystalline space, and the vacancies are reoccupied by silicon from other parts of the crystal. As a result, thermal stability of the zeolite is greatly increased, so that the product retains crystallinity at temperatures in excess

of 1000°C. Samples subjected to different types of treatment have been examined by ^{29}Si and ^{27}Al solid-state NMR [**55–59**], while the Si/Al ratios were determined from spectral intensities using Equation (9.1). ^{29}Si NMR clearly shows that Al is removed from the framework, and that the resulting vacancies are subsequently reoccupied by silicon, which comes not only from the surface or from amorphous parts of the sample but also from its bulk, which may involve the elimination of entire fragments of the framework. Chemical analysis shows no change in composition: the 'missing' Al is now in 6-coordination, and there is a consequent loss of ion-exchange capacity. ^{27}Al MAS NMR shows how 6-coordinate non-framework Al species (Al^{NF}) build up at the expense of the 4-coordinated framework Al (Al^{F}) as the calcination temperature is increased.

In order to elucidate the nature of Al^{NF}, ^{1}H–^{27}Al MAS NMR spectra, with cross-polarization (CP) of the dealuminated samples, were recorded [**60–62**]. Figure 9.7 clearly shows that the intensity of the peaks at 0 and 30 ppm increases relative to the peak at 60 ppm. This indicates that the 30 ppm peak is a separate ^{27}Al resonance, possibly due to 5-coordinate Al. Furthermore, the position of NMR peaks in ^{27}Al MAS NMR spectra reported in reference [**60**], recorded at the higher field of 11.7 T (as opposed to 9.4 T in reference [**62**]), is the same at 0, 30 and 60 ppm. As the second-order quadrupole interaction is inversely proportional to the magnetic field, components of a quadrupolar lineshape must shift to high frequency when the magnetic field is increased. Since the distance between peaks is unchanged, they must correspond to independent resonances.

The process of ultrastabilization can be completely reversed by a simple hydrothermal treatment with aqueous solutions of strong bases [**63**, **64**]. The reaction can be profitably studied by NMR, which indicates that aluminium atoms hydrothermally eliminated from the framework of zeolite Y can be subsequently reinserted into the framework. Sample crystallinity is largely retained in the process, and is strongly dependent upon the residual sodium content of the parent material, the concentration of the base and the temperature.

^{29}Si MAS NMR spectra [**151**] of dealuminated samples (middle traces in Fig. 9.8) indicate the removal of framework aluminium from the parent sample (top trace). However, the spectra of samples treated with KOH (lower traces) are very different. The intensities of the Si(0Al) peaks are greatly reduced, and the intensities of the Si(1Al), Si(2Al), Si(3Al) and Si(4Al) peaks correspondingly increased, signifying that a considerable amount of aluminium has entered the framework. Using values of $(Si/Al)_{NMR}$ calculated from Equation (9.1) in conjunction with the values of the *overall* Si/Al ratio we can calculate the number of framework and non-framework atoms per unit cell. The results show that all extra-framework Al atoms in samples 2, 4 and 6 have re-entered the framework to give realuminated samples 3, 5 and 7, respectively. Furthermore, the spectra of the realuminated samples are very different from that of the parent sample 1 despite the fact that the composition of all four samples is similar. This shows that although the overall structure of the crystal

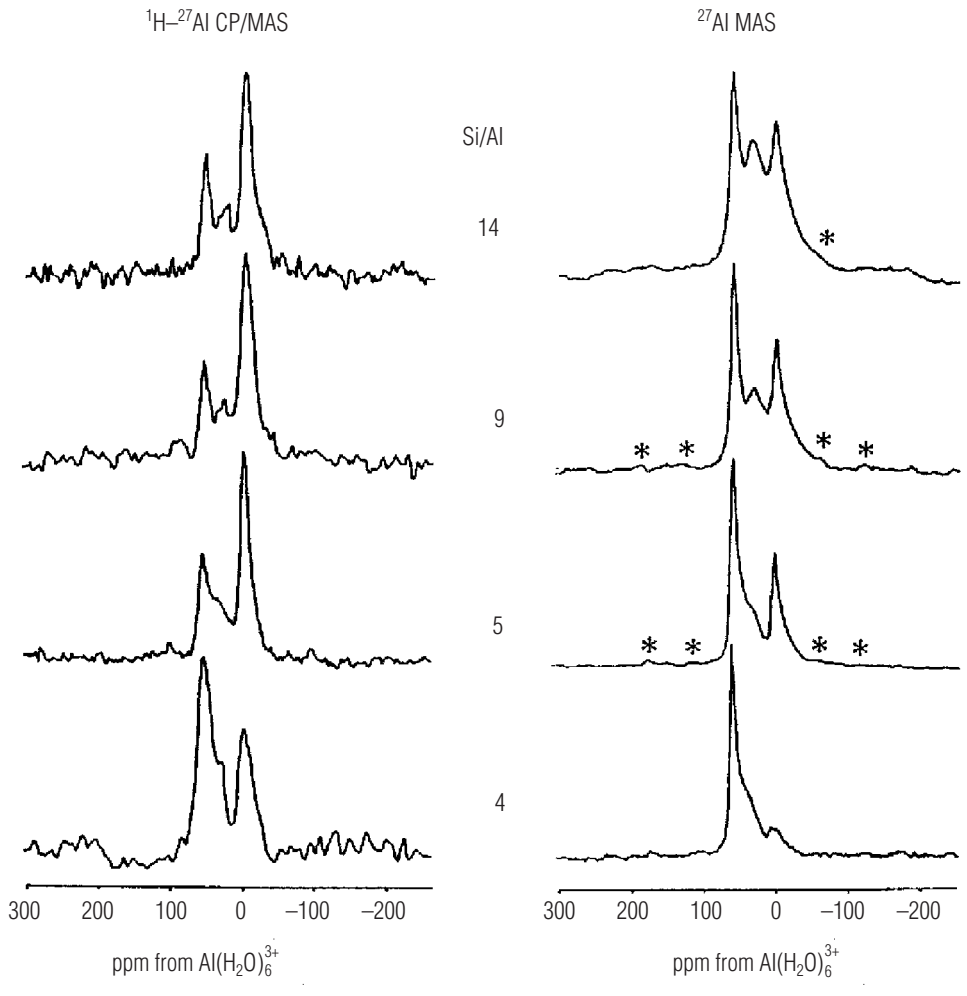

Fig. 9.7 ^{27}Al MAS and ^{1}H–^{27}Al CP/MAS NMR spectra of increasingly dealuminated zeolite H-Y [**61**]. The Si/Al ratios calculated from ^{29}Si MAS NMR spectra are indicated. *denotes spinning sidebands.

is known exactly, the Si, Al *distribution* among the tetrahedral sites is different in each case.

Freude et al. [**65**] measured the relative amounts of 4- and 6-coordinate Al in thermally treated zeolite Y, to find that loss of ^{27}Al line intensity takes place in treated zeolites in comparison with the parent material, evidently due to extra-framework Al being in an environment of low symmetry. The 'invisible' aluminium could be present as $Al(OH)_3$, $Al(OH)_2^+$, $Al(OH)^{2+}$, Al_2O_3 or some polymeric aluminous species. The hydroxide is unlikely to be present in stabilized zeolites, which are strong solid acids, as it is not favoured in acidic aqueous solutions. The 'low symmetry environment' may be the surface of the crystallites or the secondary pore system. Indeed, Lohse and Mildebrath [**66**] found Al_2O_3 clusters inside the meso-

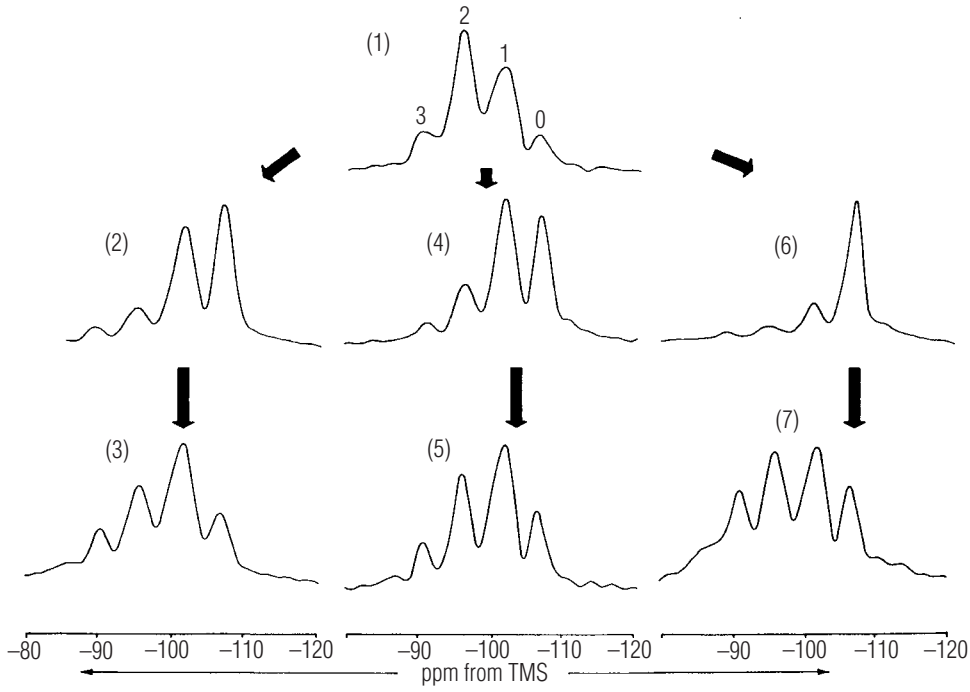

Fig. 9.8 ^{29}Si MAS NMR spectra of ultrastabilized and hydrothermally realuminated zeolites for the single ultrastabilization/realumination cycle [**151**]. Sample 1 (Si/Al = 2.56) is the parent for samples 2, 4 and 6 (Si/Al ratios 4.96, 4.26 and 7.98 respectively), which upon treatment with KOH solution give rise to samples 3, 5 and 7 (Si/Al ratios of 2.44, 2.70 and 2.09), respectively. Numbers above individual peaks give the *n* in Si(*n*Al).

pore system formed as a result of a proposed 'condensation of lattice defects' during thermal treatment, while Dwyer et al. [**67, 68**] and Ward and Lunsford [**69**] reported an enrichment in Al at the external surface of the particles of ultrastable zeolite Y.

^{27}Al quadrupole nutation NMR [**70**] (see Chapter 4 for details) offers insights into the dealumination–realumination process. The technique permits ^{27}Al sites with different quadrupole coupling constants to be resolved along F_1.

The nutation spectrum of the parent sample 1 (Fig. 9.9) consists of two peaks, both with the same linewidth and both corresponding to framework (F) aluminium. The presence of *two* peaks is due to the fact that the quadrupole interaction characteristic of framework ^{27}Al is of the same order of magnitude as the strength of the radiofrequency pulse. Sample D-1 has been mildly and sample D-2 strongly, dealuminated. Figure 9.9 clearly shows that the amount of framework aluminium decreases in the process. Similarly, the nutation spectra of realuminated samples R-3 and R-4 demonstrate that the aluminium does go back into the framework. As realumination progresses, the F peak increases at the expense of the other peaks.

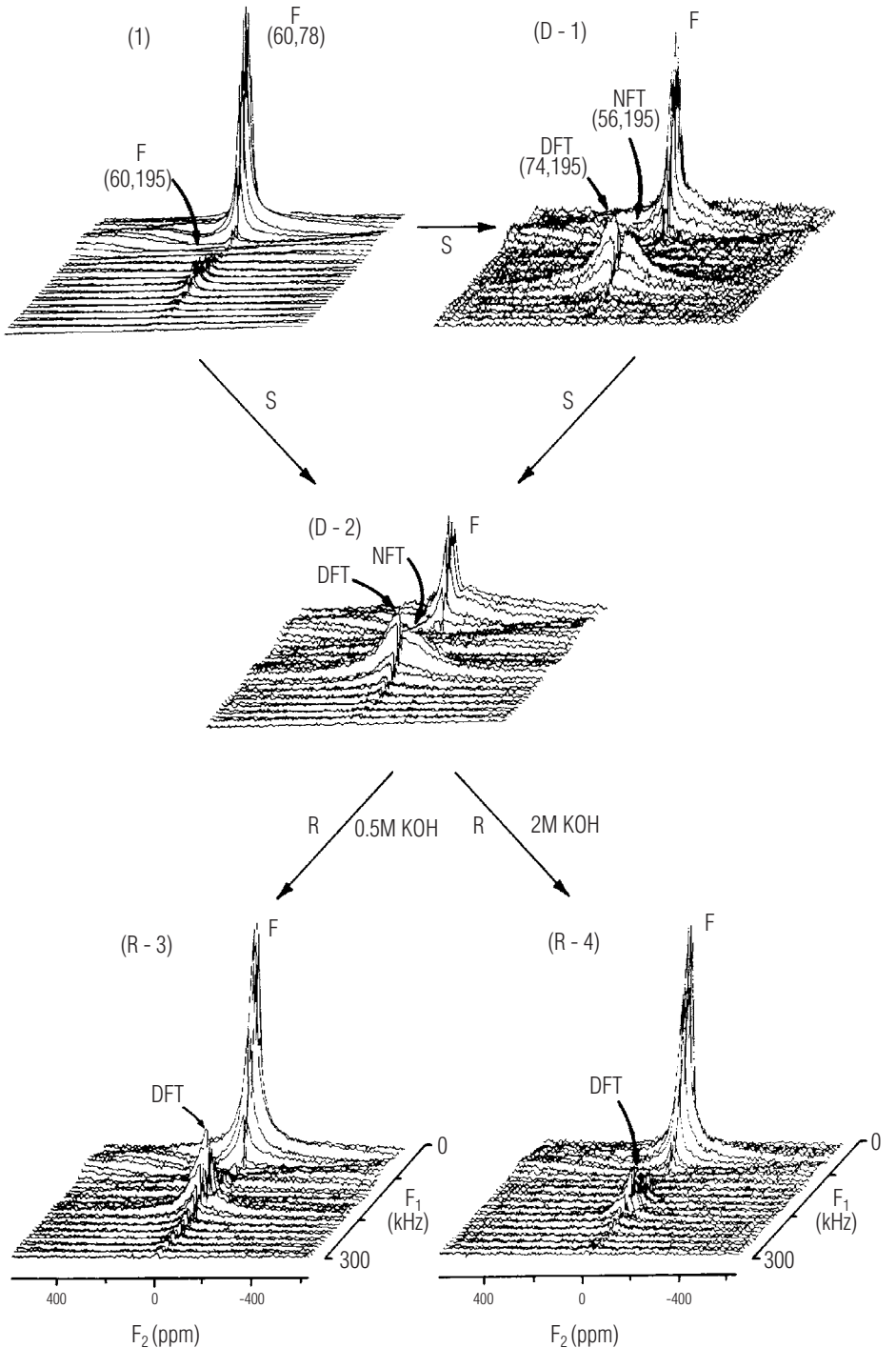

Fig. 9.9 ^{27}Al quadrupole nutation spectra of hydrothermal dealumination–realumination [**63**]. Parent sample 1 has been steamed (S) for various lengths of time to give dealuminated samples D-1 and D-2 (framework Si/Al ratios of 3.10 and 4.91). Sample D-2 has been realuminated (R) with KOH to give samples R-3 and R-4 (Si/Al ratios of 2.59 and 1.54).

9.11 NMR studies of Brønsted acid sites

Study of acidic surface sites capable of donating protons to adsorbed molecules is crucial to heterogeneous catalysis. It is vital to know the concentration, strength and accessibility of the Brønsted and Lewis acid sites, and the details of their interaction with the adsorbed organics. The Brønsted acidity of zeolites arises from the presence of accessible hydroxyl groups associated with framework aluminium ('structural hydroxyls'). While all the tetrahedral sites in synthetic faujasites (zeolites X and Y) are crystallographically equivalent, there are four distinct kinds of inequivalent framework oxygens, denoted as O_1, O_2, O_3 and O_4 [**1**]. Extensive ^{1}H MAS NMR measurements have led to the assignment of the various proton resonances as follows [**71, 72**]:

Line 'a' at 1.3–2.3 ppm from tetramethylsilane (TMS), due to non-acidic (silanol) hydroxyls on the surface of zeolite crystallites and crystal defects sites;
Line 'b' at 3.8–4.4 ppm from bridging OH groups involving O_1 oxygen atoms and pointing towards the zeolitic supercages (see Fig. 9.1);
Line 'c' at ca. 5 ppm from protons on O_3 atoms and pointing towards the other oxygens in the sodalite cages;
Line 'd' at 6.5–7.0 ppm, due to residual NH_4^+ cations;
Line 'e' at 2.6–3.6 ppm, due to Al–OH groups attached to non-framework Al.

^{1}H NMR of static samples can readily probe the geometry of the Brønsted acid site [**73, 74**]. It is a convenient tool for the determination of the Al–H distance, because the second moment of the broad-line proton spectra, which is inversely proportional to the sixth power of the distance between the dipole-coupled nuclei, is dominated by the ^{1}H–^{27}Al interaction. Spectra are obtained by Fourier transformation of the FID following the $\pi/2$–τ–π pulse sequence. An argument based on van Vleck's formula [**75**] has been used [**76**] to calculate the aluminium–proton distance, $r_{Al–H}$, from the second moment. ^{1}H NMR studies of zeolites H-Y and H-ZSM-5 have given $r_{H–Al} = 2.38 \pm 0.04$ Å and 2.48 ± 0.04 Å, respectively, for isolated bridging hydroxyl groups [**73, 74**]. The structure of the active site in zeolite H-ZSM-5 is shown in Fig. 9.10. The Al–H distance is larger than in zeolite H-Y because of the smaller T–O–T angles in a framework composed mostly of 5-membered rings.

The spectra of ammonia, trimethylamine, pyridine and acetonitrile isotopically enriched with ^{15}N and adsorbed on various zeolites [**77–79**] show that resonance shifts depend strongly on the interactions of sorbate molecules with cations, and Brønsted and Lewis acid sites. The ^{15}N chemical shift changes by 18.5 ppm as the pore-filling factor θ of $^{15}NH_3$ on zeolites Na-X, Na-Y, Na-mordenite and Na-Y

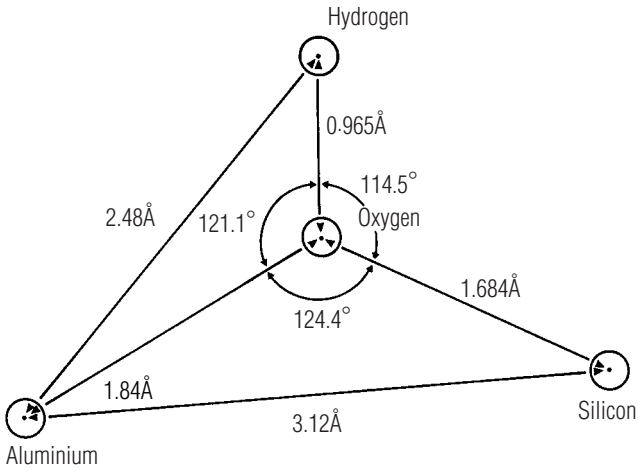

Fig. 9.10 The geometry of the Brønsted acid site in zeolite H-ZSM-5 [**73, 74**]. Atomic radii are not to scale.

varies between 0 and 1. In sodium forms, the resonance shift is mainly due to intermolecular interactions. For ultrastable zeolite Y, the ^{15}N resonance of ammonia does not change between $\theta = 0.2$ and 0.72, and is approximately equal to that measured for liquid ammonia. It was concluded [**77, 78**] that at higher θ the ammonia molecules are packed so closely that their resonance shift becomes liquid-like. In ultrastabilized samples a strong association of ammonia molecules occurs even at low coverages, leading to a constant chemical shift. At low coverages, the resonance shift of $^{15}NH_3$ on zeolite H-Y remains constant, and is close to that for NH_4^+ solutions. This shows that all ammonia molecules are converted into ammonium cations through interaction with structural hydroxyl groups. Consideration of the equilibrium between the surface sites and the sorbate allows the resonance shifts for the surface complexes to be obtained. The formation of pyridinium ions in ultrastable zeolites has been followed, leading to direct determination of the number of interacting hydroxyl groups. ^{15}N NMR is far superior to ^{13}C NMR for this purpose. Acetonitrile can be conveniently used for characterization of the interactions with the exchangeable cations and Lewis acid sites [**77–79**]. The electron acceptor strength of ultrastable zeolites increases with increased temperature of activation, the rise being particularly drastic in the region 300–400°C.

Trimethylphosphine has also been used [**80, 81**] as a probe in ^{31}P MAS NMR studies of zeolite H-Y. When a sample is activated at 400°C, the spectrum is dominated by the resonance due to $(CH_3)_3PH^+$ complexes, formed by chemisorption of the probe molecule on Brønsted acid sites. At least two types of such complexes were detected: an immobilized complex coordinated to hydroxyl protons, and a highly mobile one which is desorbed at 300°C.

9.12 Chemical status of guest organics in the intracrystalline space

The declining oil reserves have stimulated considerable efforts towards the exploitation of alternative sources of energy and organic chemicals. One solution is to use the abundant supply of coal as a source of synthesis gas ($CO + H_2$), which is readily converted to methanol (MeOH). MeOH can then be transformed into higher molecular weight hydrocarbons (olefins, aliphatics and aromatics) over shape-selective zeolite catalysts such as H-ZSM-5 [**10**]. The high silica content (Si/Al ratio is typically 30) gives ZSM-5 high thermal stability, while the channel diameter is very convenient for many applications, particularly in the petroleum industry. H-ZSM-5 is capable of converting MeOH to hydrocarbons up to C_{10}, which is the basis of several important reactions, such as the MTG (methanol-to-gasoline) process. The mechanism of the reaction, particularly as concerns the formation of the first C–C bond and the nature of the interactions between the CH_3OH molecules and the zeolitic framework, has been the subject of controversy [**82, 83**]. ^{1}H NMR has been used [**84–86**] to study the chemistry of methanol adsorbed on H-ZSM-5.

Samples for MAS NMR [**85, 86**] were contained inside capsules [87] which could be spun inside the MAS NMR probehead at rates of up to 3 kHz. The design of the capsule allowed the samples to be dehydrated at 400°C under a pressure of 10^{-5} mbar before adsorption of the organic material. Capsules were then sealed while keeping the sample at liquid nitrogen temperature, in order to prevent the onset of chemical reactions, and high-resolution ^{1}H MAS NMR spectra were recorded.

Hydrogen bonding causes downfield chemical shifts in alcohols because of the deshielding of the proton as a result of the electrostatic polarization of the OH bond. In liquid CH_3OH, hydrogen bonding causes a downfield shift of 3.1 ppm relative to CH_3OH in CCl_3D, where there is no hydrogen bonding. The ^{1}H MAS NMR spectrum of CH_3OH adsorbed on zeolite H-ZSM-5 (Fig. 9.11) [**86, 88**] contains a line at 4.1 ppm, corresponding to the methyl protons. and another at 9.1 ppm, corresponding to the hydroxyl protons. When CD_3OH is adsorbed, only the 9.1 ppm line is observed, which demonstrates that all hydroxyls resonate at the same chemical shift. When six molecules of CD_3OH are adsorbed per Brønsted site, one line corresponding to the hydroxyl groups is found at 9.1 ppm. By contrast, when CH_3OD is adsorbed, apart from the line at 4.1 ppm corresponding to the methyl groups, there is a small resonance at *ca*. 9.4 ppm. Adsorption of CD_3OD demonstrates that this latter line originates initially from the framework Brønsted acid sites.

The large downfield shift of the hydroxyl resonance of the CH_3OH upon adsorption on H-ZMS-5 must be caused by very strong hydrogen bonding and/or direct protonation of the alcohol. Note that all hydroxyl groups in the spectrum in Fig. 9.11 resonate at the same chemical shift, which indicates that all protons are equivalent on the timescale of the NMR experiment. It appears that each molecule of methanol is formally identical to a methoxonium ion. The charged cluster, a supercation, may rotate in the intracrystalline space so that different hydroxyl protons

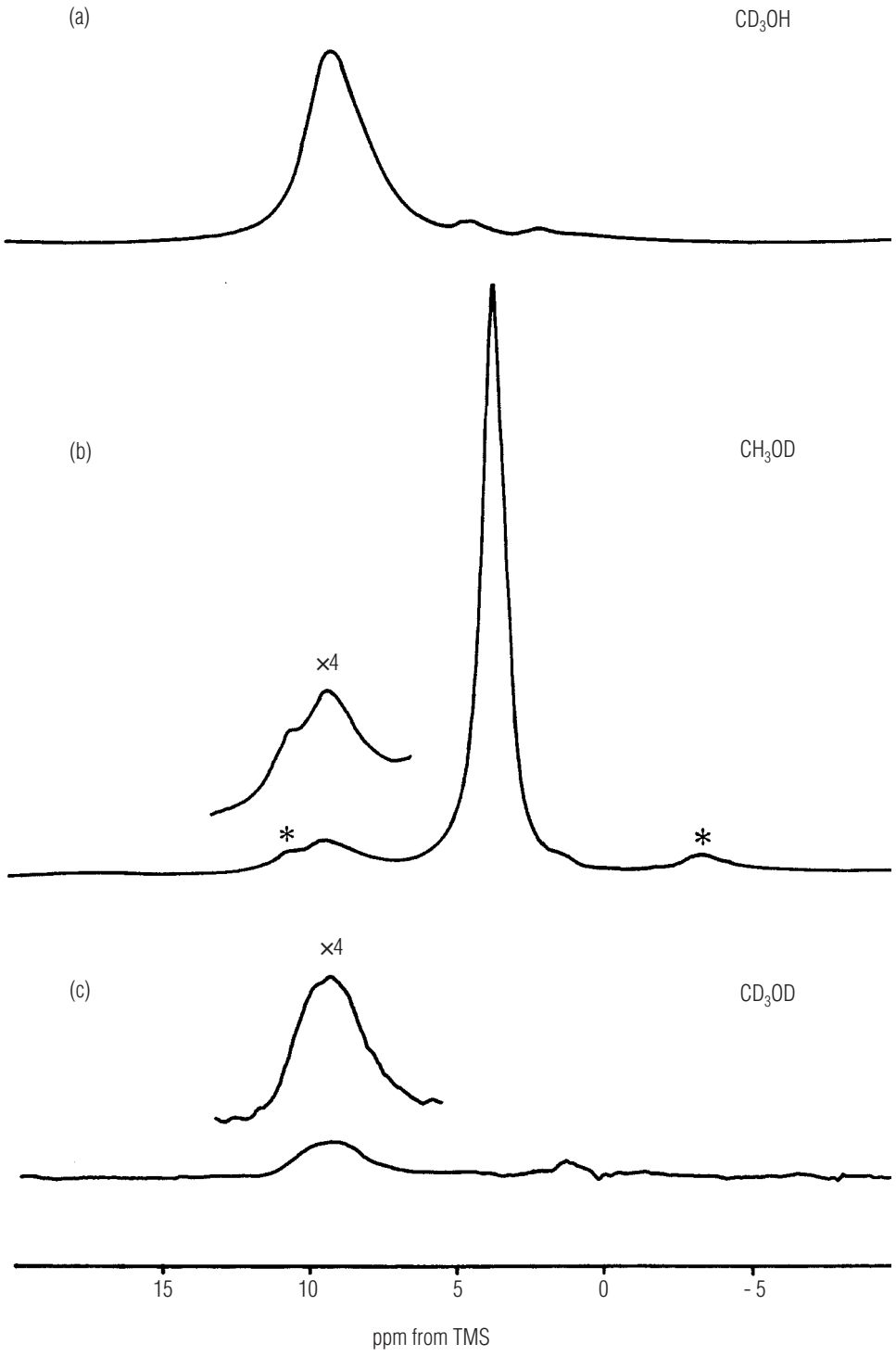

Fig. 9.11 ^{1}H MAS NMR spectra of (a) CD_3OH; (b) CH_3OD; (c) and CD_3OD adsorbed on zeolite H-ZSM-5 [**86**]. *denote spinning sidebands.

approach the bridging framework oxygen in turn, thus becoming equivalent on the NMR timescale. At the lower coverage of two molecules per Brønsted acid site, the hydroxyl line moves from 9.1 ppm in Fig. 9.11(a) to 10.5 ppm, indicating the presence of fast exchange between the proton of the zeolitic acid site and the OD group of the adsorbed methanol.

9.13 *In situ* studies of catalytic reactions

Shape selectivity of zeolites [**9**, **89–92**] arises from the fact that the probabilities of forming various products in the narrow intracrystalline cavities and channels are largely determined by molecular dimension and configuration.

^{13}C MAS NMR can probe directly the role of the active site in shape-selective catalytic reactions on zeolites *in situ*. The kind and quantity of chemical species present inside the particle can now be directly monitored [**88**, **93–99**]. This information, not forthcoming from other techniques, is usefully compared with the composition of the gaseous products to give new insights into reaction pathways on molecular sieves and to assist in the design of new shape-selective catalysts. These experiments have: (i) identified 29 different organic species *in the adsorbed phase* and monitored their fate during the course of the reaction; (ii) observed directly different kinds of shape selectivity in a zeolite; (iii) unequivocally distinguished between mobile and bound species.

^{13}C MAS NMR spectra of sealed H-ZSM-5 are well resolved. The spectrum of a sample with adsorbed MeOH, maintained at room temperature, contains a single resonance due to MeOH. After heating the sample to 150°C, the spectrum is composed of two lines corresponding to MeOH and dimethylether (DME) respectively. Figure 9.12 shows that in a sample treated at 300°C for 35 min, MeOH and DME have been completely converted to a mixture of aliphatics and aromatics. The various ^{13}C NMR resonances can be reliably assigned to different hydrocarbon species [**100–103**]. In addition to chemical shift information, and the monitoring of the number and relative intensity of the various ^{13}C NMR lines, two-dimensional ^{13}C spectra have been used [**101**, **102**] to determine the connectivity of carbons, the number of protons attached to each carbon atom in the various organics and the details of ^{13}C–^{1}H J couplings, enabling firm assignments for a number of resonances to be made.

A well-resolved two-dimensional J-coupled spectrum [**101**], measured using no decoupling during part of the evolution period while synchronizing the time increment and the rotation period of the MAS spinner, is given in Fig. 9.13. Multiplicities of the lines confirm that the assignments based on conventional one-dimensional spectra are correct. For example, the resonance centred at −10.7 ppm is split into five components with a requisite intensity ratio in the 2D spectrum, which confirms

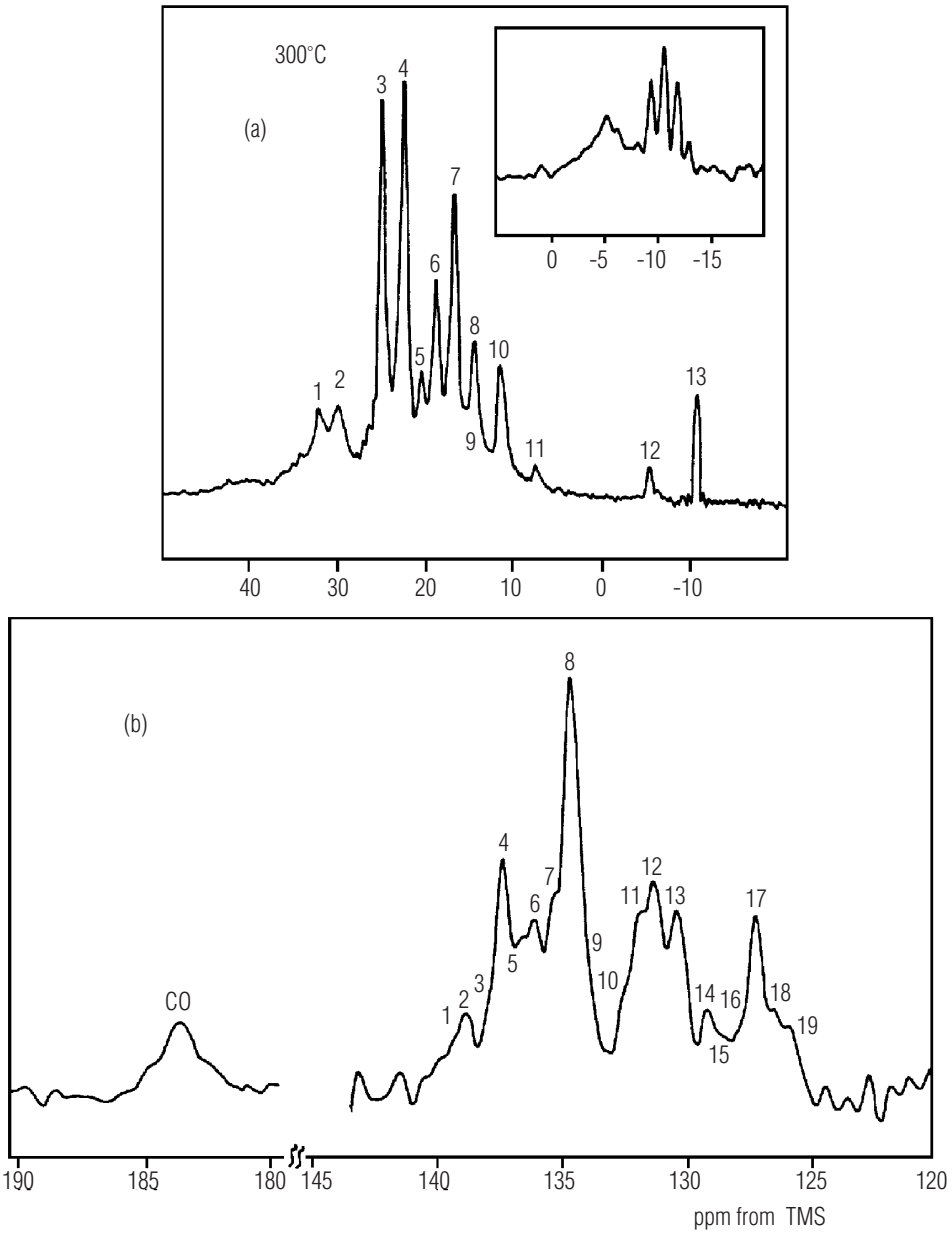

Fig. 9.12 ^{13}C MAS NMR spectra of H-ZSM-5 with 50 torr of adsorbed MeOH heated to 300°C for 35 mins and recorded with proton decoupling only (a) aliphatic region; (b) aromatic and CO region [**93**]. Intensities in (a) and (b) are not on the same scale. The inset shows *J*-coupling of methane and cyclopropane carbons (recorded without decoupling). Spectral assignments are as follows [peak numbers and intensities (s = strong, m = medium, w = weak) are in brackets, { } for aliphatic and ( ) for aromatic]: *i*-butane {3, s}; propane {7, s}; *n*-butane {3, 9, m}; *n*-hexane {1, 4, 8, m}; *i*-pentane {1, 2, 4, 10, m}; *n*-heptane {1, 2, 4, 8, m}; methane {13, m}; ethane {11, w}; cyclopropane {12, w}; *o*-xylene (4, 12, 17, s){5}; *p*-xylene (7, 13, s){6}; *m*-xylene (2, 12, 15, 17, w){5}; toluene (2, 13, 14, 18, w){5}; 1,2,4-trimethylbenzene (4, 6, 8, 11, 13, 16, m){5, 6}; 1,3,5-trimethylbenzene (3, 16, w){5}; 1,2,3-trimethylbenzene (5, 7, 16, 19, w){5, 8}; 1,2,4,5-tetramethylbenzene (8, 11, s){6}; 1,2,3,5-tetramethylbenzene (5, 7, 10, 13, m){5, 8}; 1,2,3,4-tetramethylbenzene (7, 9, 16, w){5, 8}. Because of the different Overhauser enhancements of different carbons, peak intensities give only an approximate concentration of the various species.

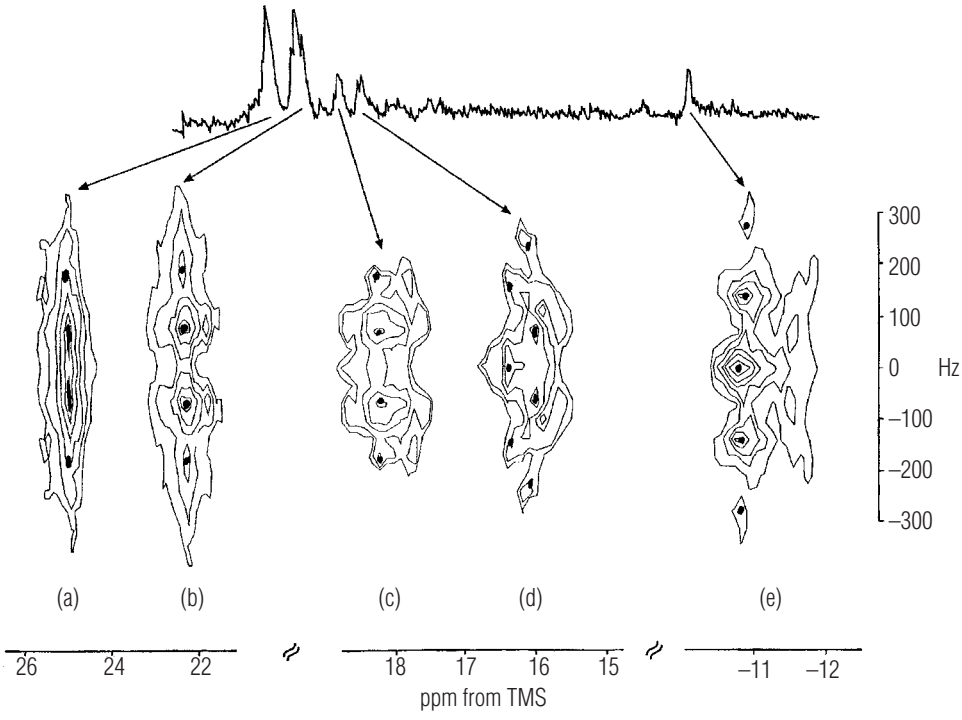

Fig. 9.13 Heteronuclear two-dimensional *J*-resolved ^{13}C MAS NMR spectrum of zeolite H-ZSM-5 with adsorbed methanol treated at 300°C for 30 min [**101**].

that it must be due to adsorbed methane. Similarly, the quartet (methyl) and triplet (methylene) multiplets clearly indicate the presence of propane adsorbed in the intracrystalline space.

The 2D spin diffusion ^{13}C NMR experiment allows us to examine further the spectral assigments obtained from the 1D and the 2D *J*-resolved experiments [**102**]. It also provides new details concerning distribution of hydrocarbons in zeolite ZSM-5. The rate of spin diffusion is very strongly dependent on the internuclear separation, so that magnetization exchange occurs only between nuclei in adjacent functional groups within the same molecule (the intramolecular case) or between nuclei in neighbouring molecules mixed on a microscopic level (the intermolecular case).

Figure 9.14 shows the 2D spin-diffusion spectrum of aliphatic hydrocarbons trapped in the zeolite. The 1D spectrum, corresponding to the diagonal peaks in the 2D spectrum, have been assigned previously [**93**, **94**], but the assigment of line **b** has been questioned [**102**]. It is clear that *n*-hexane and *n*-heptane are present, since line **e** comes exclusively from their CH_3 groups. Therefore, considering the chemical shift of CH_2 groups of *n*-hexane and *n*-heptane, both hydrocarbons must contribute to line **b**. In the *J*-resolved experiment this line was not split into a triplet,

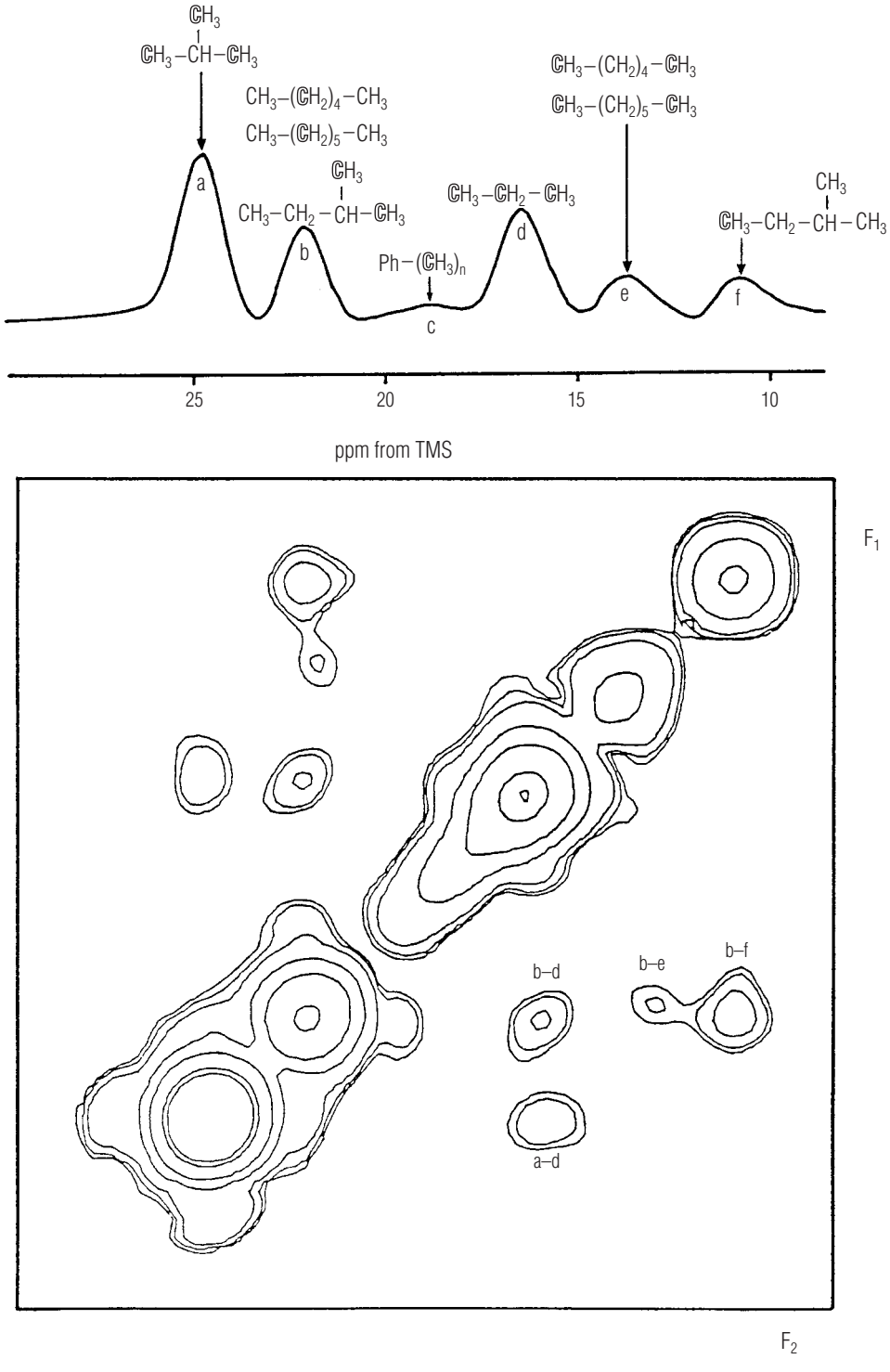

Fig. 9.14 ^{13}C NMR spin diffusion spectrum of products of methanol conversion into gasoline over zeolite ZSM-5, with the projection onto the F_2 axis (corresponding to a conventional spectrum) at the top [**102**]. Carbon atoms to which individual resonances are assigned are highlighted. For line assignment see Table 9.2.

Table 9.2 Assignment of the 2D ^{13}C NMR spin-diffusion spectrum in Fig. 9.14

DIAGONAL PEAKS			
Signal	Chemical shift (ppm)	Group	Assignment
a	24.7	CH_3	isobutane
b	22.3	$CH_3CH_2CH(CH_3)_2$	isopentane
		CH_2	*n*-hexane + *n*-heptane
c	18.7	CH_3	methyl-substituted benzenes
d	16.7	$CH_3 + CH_2$	propane
e	14.3	CH_3	*n*-hexane + *n*-heptane
f	11.2	$CH_3CH_2CH(CH_3)_2$	isopentane

CROSSPEAKS		
Signals	Assignment	Type of spin diffusion
a–d	isobutane – propane	intermolecular
b–d	isopentane – propane	intermolecular
b–e	*n*-hexane	intramolecular
	n-heptane	intramolecular
b–f	isopentane	intramolecular

because no homonuclear proton decoupling was applied during the first half of the evolution period, so that any splitting was obscured by substantial dipolar broadening. By contrast, CH_3 groups of isobutane undergo free rotation, which reduces the dipolar interaction and allows the quartet splitting of line **b** to be observed in the spin-diffusion spectrum. We note that lines of *n*-butane in the spin-diffusion spectrum are missing. Cross-polarization is very inefficient for lines of mobile products, so that only those which are present in high concentration, such as propane, appear in the spectrum with any significant intensity. The assignments of the various lines are given in Table 9.2.

Munson et al. [**99**] disproved the suggestion [**93**] that, since CO is observed prior to hydrocarbon formation, it is an intermediate in the reaction. Methanol-^{13}C and formic acid-^{13}C were first coadsorbed on the H-ZSM-5 catalyst, and an *in situ* NMR experiment was performed. The conversion rate of methanol was not affected by large quantities of CO. Spectra of a sample containing formic acid-^{13}C and unlabelled methanol were then measured. ^{13}CO was not incorporated in the reaction product. The conclusion is that CO is neither an intermediate nor a catalyst in MTG chemistry.

9.14 Direct observation of shape selectivity

The *distribution* of adsorbed species in the sample of zeolite with adsorbed methanol treated at 300°C is very different from that observed in the reaction products as monitored outside the zeolite [**93**, **94**]. The principal aromatics expected to be

present are *m*- and *p*-xylene, 1,2,4-trimethylbenzene and toluene. However, the main species actually found in the adsorbed phase are *o*- and *p*-xylene and 1,2,4,5-tetramethylbenzene, with smaller amounts of 1,2,4-trimethylbenzene and 1,2,3,5-tetramethylbenzene. The other xylenes, tri- and tetramethylbenzenes are also found but in smaller amounts. The distribution of the three trimethylbenzenes in the adsorbed phases is very different from the thermodynamic equilibrium distribution. The fact that 1,2,3- or 1,3,5-trimethylbenzenes (with kinetic diameters of 6.4 and 6.7 Å, respectively) are not found among the products outside the zeolite, but are present in the adsorbed phase, while the smaller 1,2,4-trimethylbenzene (6.1 Å) is found in both, clearly demonstrates the reality of the concept of product selectivity. The channel dimensions of ZSM-5 are 5.6 × 5.3 Å, but more space is available at the intersection of the straight and zig-zag channels. While a greater amplitude of thermal vibrations of the framework, increases the maximum effective size of the channels, and allows the smaller isomer to diffuse out of the crystal, the two larger isomers, although formed, are unable to diffuse out at 300°C and must isomerize to 1,2,4-trimethylbenzene before they can diffuse out of the framework.

The distribution of the tetramethylbenzenes in the intracrystalline space is also most unexpected. None of them has ever been reported in the products of the reaction at 300°C and yet all three are clearly present in the adsorbed phase. Because of the restricted intracrystalline space they can only form at channel intersections, but (unlike the trimethylbenzenes) are not generated in the thermodynamic equilibrium distribution. 1,2,3,5-tetramethylbenzene (6.7 Å) should be the dominant species on thermodynamic grounds; in fact it is 1,2,4,5-tetramethylbenzene (6.1 Å) which dominates. The thermodynamicallly least favoured isomer, 1,2,3,4-tetramethylbenzene (6.4 Å), is found in small quantities. The fact that tetramethylbenzenes are not found in the products again demonstrates product shape selectivity. Their *relative abundance* in the adsorbed phase, on the other hand, shows that an additional kind of shape selectivity occurs within the intracrystalline space. It does not rely on the ability of species to enter or to leave the crystal nor on the size of the transition state: isomerisation is sterically restricted within the crystallite at the active site itself.

9.15 Aluminophosphate molecular sieves

The $AlPO_4$ are a challenge to multinuclear solid-state NMR, given the wide variety of new crystal structures, the fact that they contain two different kinds of 100% abundant nuclei (^{31}P and ^{27}Al) in close proximity and aluminium in 4-, 5- and 6-coordination with respect to oxygen. Blackwell and Patton [**104**] were the first to take up the challenge when they recorded the spectra of $AlPO_4$-5, $AlPO_4$-11, $AlPO_4$-17 and $AlPO_4$-31, and compared them with some non-microporous materials, such

as $AlPO_4$-quartz, metavariscite and $AlPO_4$-tridimite. The spectra were generally consistent with known framework structures, but the ^{27}Al chemical shift range was wide (from –18.7 to 44.9 ppm) and quadrupolar effects were very much in evidence. The template molecules present in as-synthesized $AlPO_4$ also affect the ^{31}P NMR chemical shifts. The ^{29}Si chemical shifts in SAPOs are similar to those found in zeolites: –92 ppm in SAPO-5 and –90.2 ppm in SAPO-37, a material with the faujasite structure. ^{11}B in BAPO-5 resonates at –1.1 ppm and ^{31}P at –29 ppm.

The ordering of tetrahedral atoms (Al, P and Mg) in MgAPO-20, the magnesium aluminophosphate with the framework structure of sodalite, have been determined using arguments similar to those used for the ordering of Si and Al in zeolites (see above) [**105**]. The ^{27}Al MAS NMR spectrum of MgAPO-20 containing 15% magnesium (Fig. 9.15) shows a single $Al(OP)_4$ environment, while the ^{31}P spectrum consists of two major peaks at –21.1 and –28.0 ppm, due to $P(OAl)_2(OMg)_2$ and $P(OAl)_3(OMg)$ units in the 1:2 intensity ratio. The additional weak lines are from $P(OAl)(OMg)_3$ and $P(OAl)_4$ units. The spectra confirm that the magnesium is present exclusively on aluminium sites, allowing us to calculate the framework composition from the relative intensities of the NMR peaks (Fig. 9.16), and enabling us to distinguish between alternative ordering schemes for the framework elements.

Kolodziejski et al. [**106**] carried out a 2-D ^{31}P NMR study of spin diffusion in aluminophosphate VPI-5. XRD refinement of the structure of the as-prepared material leaves a large difference between the observed and calculated patterns. Also, the ^{31}P and ^{27}Al MAS NMR spectra are difficult to reconcile with the proposed structure. First, the space group $P6_3cm$ calls for two crystallographically distinct phosphorous positions with relative occupancies 2:1, while the room-temperature ^{31}P MAS NMR spectrum contains *three* resonances in an intensity ratio of 1:1:1. Second, the ^{27}Al MAS NMR spectrum contains peaks from 4- and 6-coordinate aluminium, but the latter cannot be accounted for in this model. Finally, the structure of VPI-5 was refined in the $P6_3$ space group (see Fig. 9.17 and reference [**152**]), which is fully consistent with the NMR results. Variable-temperature studies assigned the peaks at –23 ppm (1) and –27 ppm (2) to phosphorous atoms in 6-4 sites (P2 and P3) and the peak at –33 ppm (3) in Fig. 9.18 to phosphorous atoms in 4-4 sites (P1). However, it is was not known how peaks 1 and 2 are to be assigned to *particular* P2 and P3 sites.

The 2-D ^{31}P NMR spin-diffusion spectra of this material have a remarkably high signal-to-noise ratio (Fig. 9.19) and each pair of peaks gives rise to crosspeaks. Figure 9.19 shows that spin diffusion can be slowed down by fast MAS, so that only the strongest ^{31}P–^{31}P dipolar interactions survive under fast MAS, which must be reflected in the dependence of the crosspeaks intensities on the MAS rate. A comparison of the strongest ^{31}P–^{31}P dipolar interactions calculated from the XRD structure, P2–P3 (192 Hz) < P1–P2 (281 Hz) < P1–P3 (304 Hz), with the MAS rates (in brackets), 1–2 (5.91 kHz) < 1–3 (6.03 kHz) < 2–3 (8.07 kHz), showed that peaks 1, 2 and 3 should be assigned to sites P2, P3 and P1, respectively.

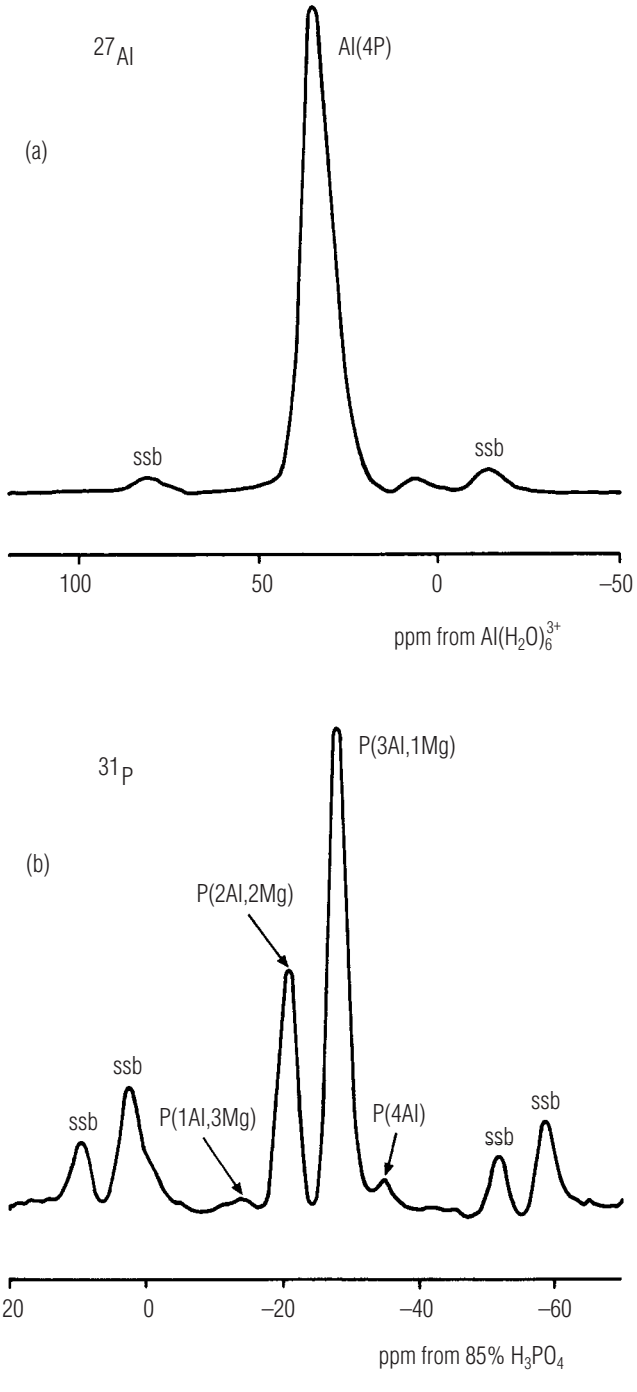

Fig. 9.15 ^{27}Al (a) and ^{31}P (b) MAS NMR spectra of MgAPO-20 [**105**]. 'ssb' denotes spinning sidebands.

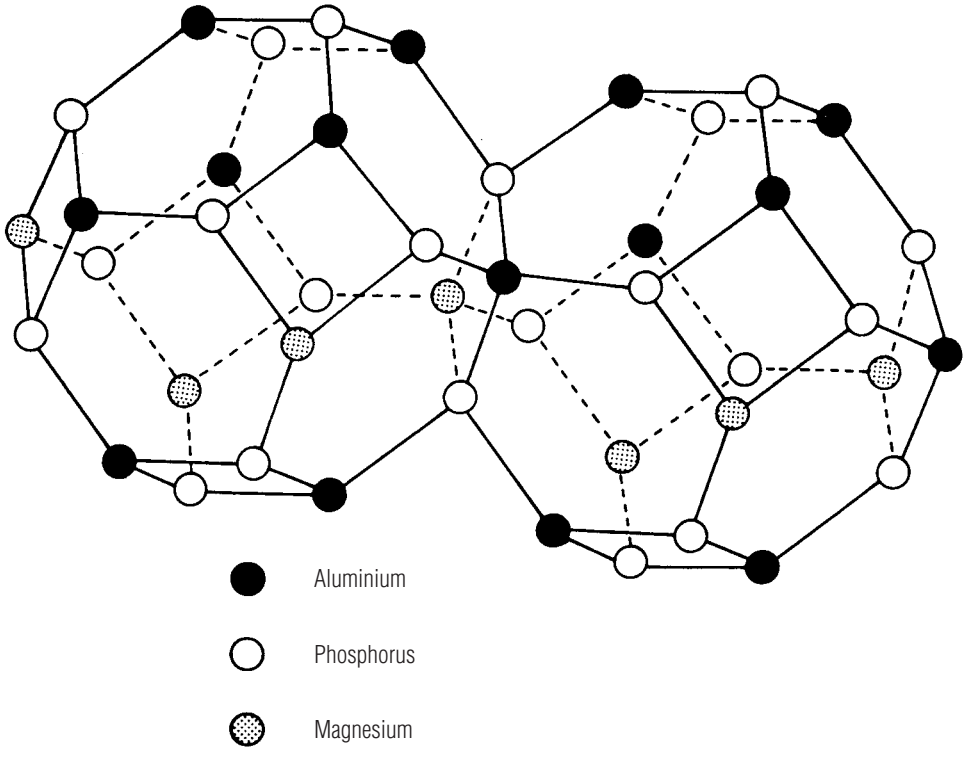

Fig. 9.16 Proposed ordering of Al, P and Mg in the framework of MgAPO-20 [**105**]. The 14-hedral sodalite cage (a truncated octahedron) is built of eight 6-membered and six 4-membered rings. Tetrahedral aluminium, phosphorus and magnesium atoms, represented by circles, are linked through oxygen atoms (not shown for clarity).

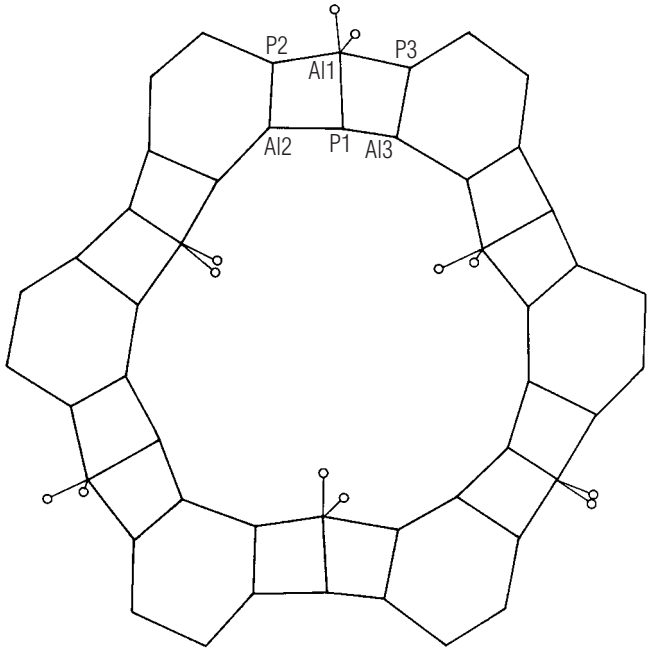

Fig. 9.17 One layer of the framework structure of hydrated VPI-5 along the [001] direction showing the deviation from $P6_3cm$ symmetry [**152**]. Aluminium and phosphorous atoms, linked via oxygen atoms (not shown for clarity) are located at the apices of the polygons. Sites located between two fused 4-membered rings are known as 4-4 sites; those located between 6-membered and 4-membered rings are known as 6-4 sites. P2 and P3, and Al2 and Al3 sites are inequivalent as a result of the distortion. The Al1 site is 6-coordinated as a result of bonding to four bridging oxygens and two 'framework' water molecules (their oxygen atoms are shown by open circles). Other intracrystalline water is not shown.

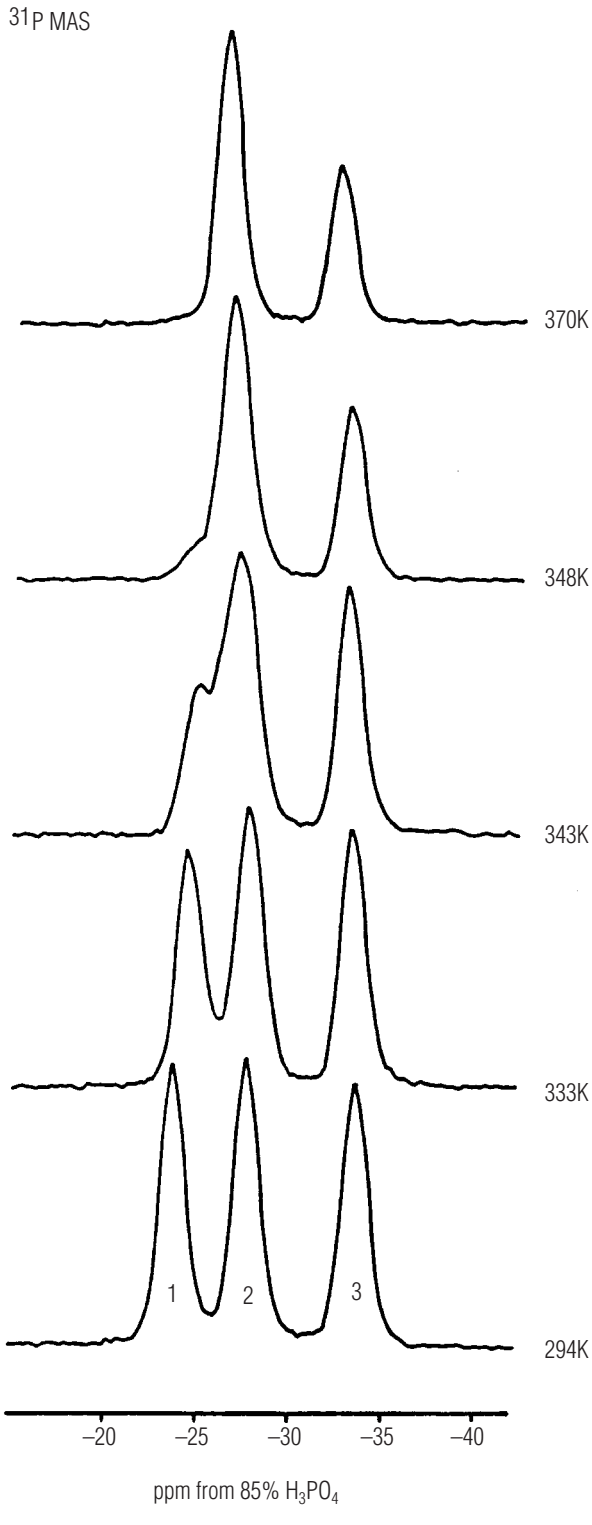

Fig. 9.18 ^{31}P MAS NMR spectra of VPI-5 at various temperatures [**106**].

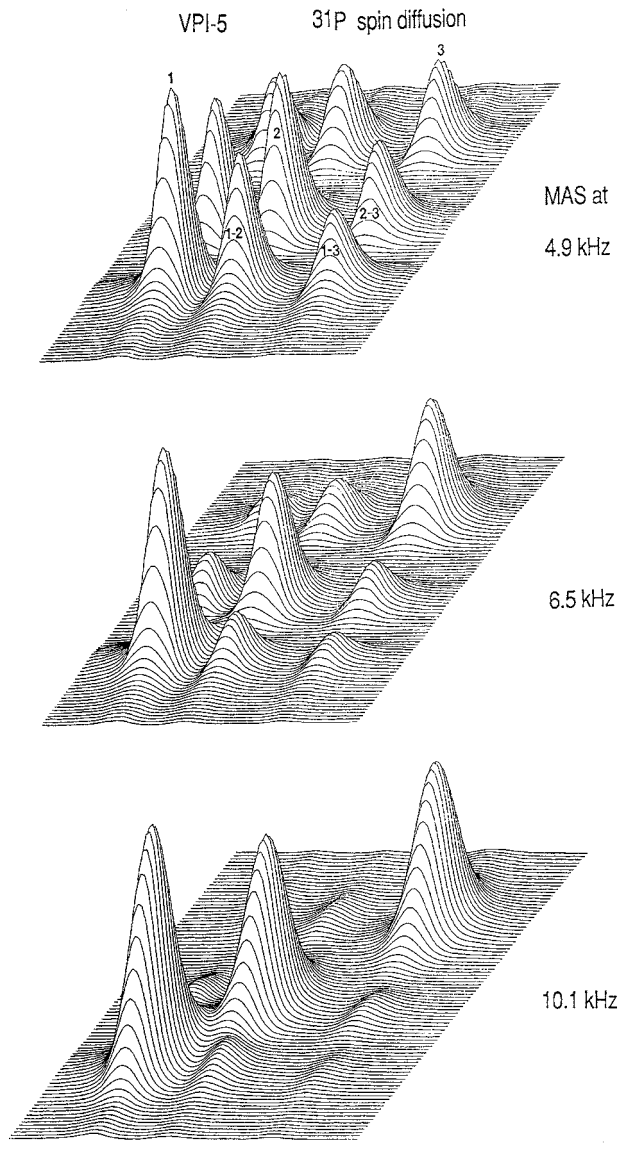

Fig. 9.19 Experimental 2D ^{31}P NMR spin-diffusion spectra of hydrated VPI-5 recorded at various MAS speeds [**106**]. (a) 4.9 kHz; (b) 6.5 kHz and (c) 10.1 kHz. The three spectra are not on the same intensity scale, so that only the relative intensities within each can be compared.

9.16 Multinuclear studies of sorbed species

Diffusional behaviour of sorbed species is studied by NMR using one of three main approaches: the van Vleck method of moments [**75**]; relaxation measurements and the pulsed field gradient method [**107**].

The pulsed field gradient method [**107**], in which spin-echoes are measured in the presence of a time-dependent magnetic field gradient, can be used to determine

effective diffusion coefficients, D_{eff}, in powdered zeolites. The spin-echo amplitude is [**108**]

$$\ln \psi(\sigma g) = \ln \psi(0) - \gamma^2 \sigma^2 g^2 \Delta t \left[D^* + \frac{p D_g^*}{\gamma^2 \sigma^2 g^2 \tau p D_g^* + 1} \right] \tag{9.2}$$

where σ and g are, respectively, the width and amplitude of the gradient pulses at intervals Δt, p is the fraction of the sorbate molecules in the intercrystalline space and D^*, D_g^* are respectively the intra- and intercrystalline self-diffusion coefficients. D_{eff}, the quantity in the square bracket, is approximately equal to $\langle d^2 \rangle / 6\Delta t$ where $\langle d^2 \rangle$ is the mean square displacement of the molecule over the interval Δt.

There are two limiting situations:

(i) $\tau >> \Delta t$, i.e. $\langle d^2 \rangle^{1/2} <<$ crystal radius; in this case $D_{\text{eff}} = D^*$
(ii) $\tau << \Delta t$, i.e. $\langle d^2 \rangle^{1/2} >>$ crystal radius; in this case $D_{\text{eff}} = pD_g^*$.

Pulsed field gradient studies of methane sorbed on zeolite (Ca, Na)-A, and *n*-butane and *n*-heptane on zeolite Na-X, under the conditions of case (i) showed [**109**] that D_{eff} decreases with increasing hydrocarbon chain length and with the fractional saturation of crystals, θ. At room temperature the values of D_{eff} (= D^*) are similar to those measured in bulk liquids.

An intriguing aspect of these measurements is that the values of D^*, determined from NMR, and from conventional sorption kinetics, used to differ by several orders of magnitude: the values from NMR were always larger and similar to those measured in bulk liquids. The discrepancy, far greater than the uncertainty of either method, was resolved when it was shown that the actual sorption rates are not determined by intracrystalline diffusion, but by diffusion outside the zeolite particles, surface barriers and/or by the rate of dissipation of the heat of sorption. NMR-derived results are therefore vindicated. Large diffusion coefficients (of the order of $10^{-6}\,\text{cm}^2\,\text{s}^{-1}$) can be reliably measured by sorption kinetics only in large crystals of natural zeolites. NMR has demonstrated [**110**] that surface barriers are indeed present in zeolite powders.

The very small quadrupole interactions of ^{2}H ($I = 1$) makes it particularly useful in chemical studies. As a consequence of the presence of two ($m = 1 \leftrightarrow m = 0$ and $m = 0 \leftrightarrow m = -1$) spin transitions, the spectrum of a deuterated organic in a solid is a doublet, the peak separation of which is related to the orientation of the ^{2}H–^{13}C bond in the external magnetic field (see Chapters 1 and 4). Dipolar interactions of ^{2}H manifest themselves as spectral broadening. Since the quadrupolar interactions of ^{2}H are sensitive to molecular motion, the nucleus is very useful for chemical studies of molecular motion at a wide range of frequencies. ^{2}H NMR is a convenient tool for the study of molecular ordering and the molecular motion of adsorbed probe molecules (see Chapter 6), and may become an important complementary technique for the study of interface systems in general, and liquid crystals in par-

ticular (see Chapter 10). ^{2}H NMR is not a *direct* technique of spectral interpretation, but one which relies on the agreement between the experimental spectra and those calculated from a particular model. Experiments are performed with *static* samples, and dynamic information is extracted by comparing spectra measured at different temperatures with model computer simulations involving a number of adjustable parameters. An great amount of ^{2}H work in solids has been reported (see Chapter 6) but, surprisingly, there are not many recent papers which are directly relevant to molecular sieves.

Eckman and Vega [**111**] investigated the dynamics of small organic molecules, such as methanol, benzene, toluene and *p*-xylene, adsorbed on a series of zeolites in a range of temperatures. They obtained information on the dynamics of the filling of the intracrystalline space, the motion of the adsorbed species and site-selective adsorption. Kustanovich et al. [**112**] interpreted the ^{2}H spectra of two deuteriated species of *p*-xylene, $CH_3C_6D_4CH_3$ and $CD_3C_6H_4CD_3$, on zeolite Na-ZSM-5, in terms of possible dynamic states and sorption sites of the guest molecules. Five dynamic states were identified, with relative populations varying with the level of loading and the temperature. Deuterium NMR results on *p*-xylene-d_6, toluene-d_3 and benzene-d_6 sorbed on H-ZSM-5 [**113**], as well as on mono-, di- and trimethylamine adsorbed on zeolites ZK-5 and Y [**114**] have been reported, in all cases yielding a wealth of dynamic information.

Duer et al. [**115**] re-examined the dynamic behaviour of water in the channels of VPI-5 and arrived at a motional model which applies throughout the 225–348 K temperature range. There are at least two sites for the intracrystalline water: one is bound to framework aluminium, and undergoes rotational motion about the Al–OH_2 bond, the other is a free site within the VPI-5 channels. The motion at the latter site is approximately isotropic, with increasing tumbling rate with temperature. The results, discussed with reference to a six-site motional model, show interesting dynamic behaviour in the 261–297 K temperature range.

9.17 ^{129}Xe NMR

Ito and Fraissard [**116**] suggested that the chemical shift of ^{129}Xe adsorbed inside a zeolite is the sum of the terms corresponding to the various perturbations affecting the xenon

$$\delta = \delta_0 + \delta_S + \delta_{Xe\text{-}Xe} \cdot \rho_{Xe} + \delta_E (+\delta_M) \tag{9.3}$$

where δ_0 is the reference; δ_S arises from collisions between xenon and the surface of the zeolitic channels and cavities; $\delta_{Xe\text{–}Xe} \cdot \rho_{Xe}$ arises from Xe–Xe collisions, and is expected to vary linearly with Xe density; δ_E takes account of an 'electric field' effect due to the exchangeable cations; and δ_M accounts for the presence of paramagnetic species. They were the first to take advantage of the properties of ^{129}Xe for the study

of xenon on zeolites Ca-A, Na-X, Na-Y, H-Y and Ca-Y. The observed chemical shift/density gradients were interpreted in terms of collisions between Xe atoms and between Xe and the cavity walls. Zeolites L, ZSM-5, ZSM-11 and ZK-4 show an approximately linear increase in chemical shift with the concentration of adsorbed xenon [**116**, **117**]. The values of δ_S obtained by extrapolation back to zero concentration show a large dependence on the zeolitic structure, ranging from 58 ppm for zeolite Y to 110 ppm for ZSM-5 (Fig. 9.20). Thus ^{129}Xe NMR is very sensitive to pore dimensions, a potentially invaluable tool in characterizing unknown molecular sieve structures. Equation (9.3) implies that the chemical shift of ^{129}Xe is affected by the size and shape of the pores, by xenon–xenon collisions, by the presence of strong adsorption sites, by the presence of paramagnetic species, adsorbed molecules and phase transitions. De Menorval et al. [**118**] studied xenon adsorbed on zeolite Y containing particulate platinum. They concluded that chemisorption of hydrogen occurs homogeneously on all particles of similar size and determined the mean size of the platinum particles from their results. Ripmeester [**119**] showed that lines from liquid, solid, gaseous and sorbed xenon could be distinguished in zeolite Na-X containing excess sorbate. For H-mordenite at 240 K two broad ^{129}Xe resonances are observed, one attributed to xenon in side pockets in the structure and the other to xenon in the main channels. It also appears that ^{129}Xe NMR can determine directly the surface area of zeolite samples, which may be of considerable practical importance. While the initial hopes of predicting pore dimensions of unknown structures from ^{129}Xe NMR are still unfulfilled, the technique does provide valuable information, particularly where structural data are absent.

Multiple-quantum NMR [**120**] is an ingenious 'spin counting' tool for characterizing homonuclear spin clusters in the solid state. The technique, which is particularly well suited for studies of species adsorbed in the voids of molecular sieves [**121**, **122**], employs a 2D NMR pulse sequence [**123**], which forces nuclear spins to act collectively via their dipolar couplings, thus creating multiple quantum (MQ) coherences, which are observed after conversion into observable single-quantum coherences.

The collective behaviour of spins can be understood as a simultaneous flip of two (double-quantum coherence), three or more spins (triple and higher-order multiple-quantum coherences). Thus the spin system coherently exchanges two, three or ΔM photons, respectively, with the resonant radiation. This can occur only if the preparation time τ is sufficient to establish communication, via pairwise dipolar interactions, within the group of spins intended to be excited. Dipolar interaction renders two spins correlated after a time period which is roughly proportional to the cube of their separation. It follows that multiple-quantum coherences develop at a rate determined by the spatial distribution of spins in the sample. For a uniform distribution the MQ transition order ΔM grows monotonically with increasing τ. If the system constitutes a collection of diluted, isolated clusters, the MQ count will reach a plateau, corresponding to ΔM, equal to the number of spins in the cluster.

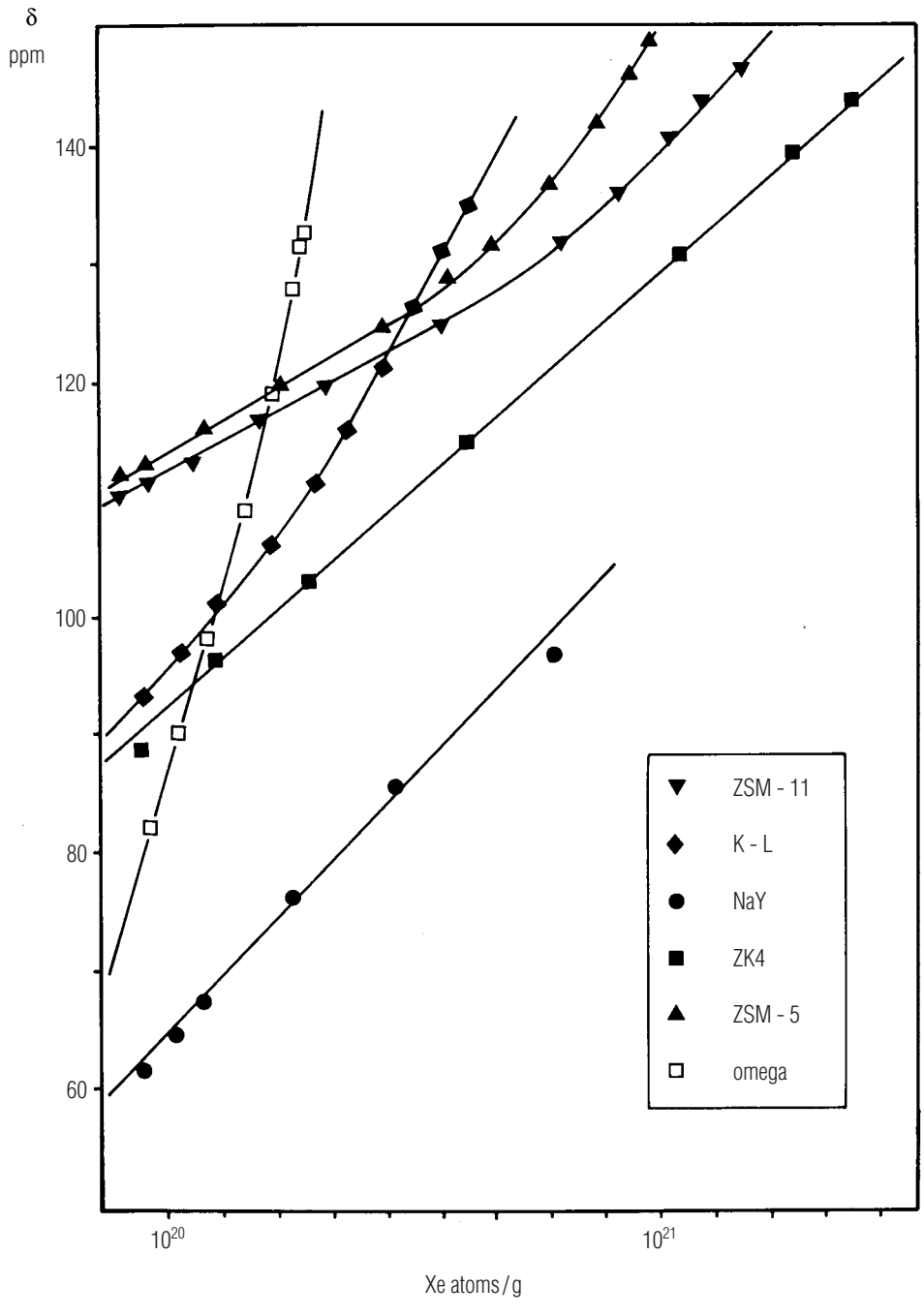

Fig. 9.20 ^{129}Xe chemical shift versus the total number of xenon atoms adsorbed per gram of sample for various zeolites [**117**].

Local and macroscopic distributions of adsorbed benzene, 1,3,5-trimethylbenzene, and hexamethylbenzene (HMB) molecules in zeolite Na-Y have been investigated by ^{129}Xe and ^{1}H multiple-quantum NMR [**122**]. Samples containing organic guests adsorbed at temperatures near the melting point of the bulk species produce multiple or broad xenon lines characteristic of interparticle adsorbate concentration gradients. After heat treatment of the samples, the ^{129}Xe NMR spectrum collapses to a single sharp line, consistent with a uniform xenon distribution. 'Counting' hydrogen clusters by multiple-quantum NMR reveals intraparticle HMB distributions consistent with one molecule per cavity at low loadings and two molecules per cavity at higher loadings (Fig. 9.21).

^{129}Xe NMR studies of adsorbed films were performed on high surface-area materials such as graphitized carbon black or exfoliated graphite. Raftery et al. [**124**] observed NMR of ^{129}Xe in thin films of xenon frozen onto the surfaces of glass. The ^{129}Xe polarization was enhanced by optical pumping, and the xenon was then

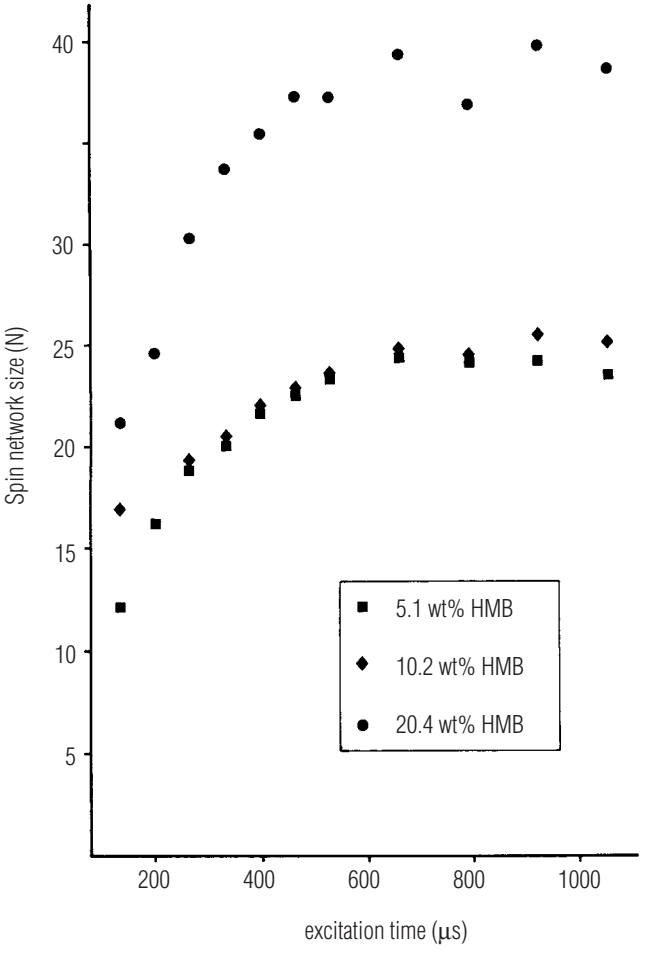

Fig. 9.21 Results of ^{1}H MQ NMR experiments for hexamethylbenzene (HMB) adsorbed at 573 K on dehydrated zeolite Na-Y [**122**]. The HMB molecule contains 18 hydrogens, so the spin cluster size is 18 per one molecule. At lower loadings (5.1 and 10.2 wt%) the plateau corresponds to about one HMB molecule per supercage and at higher loading (20.4 wt%) the plateau reflects an occupancy of two HMB guests per supercage.

transferred to a high-field NMR spectrometer allowing the observation of strong signals from xenon films only ca. 1 μm thick. Given that most heterogeneous catalytic reactions take place on the gas/solid interface, optical pumping is an exciting development for increasing the sensitivity of the NMR experiment.

9.18 New NMR techniques for the study of molecular sieves

Spin-Echo Double Resonance (SEDOR) [**125**] is capable of measuring local heteronuclear dipolar interactions between selected (by the spectroscopist) nuclei of different species *I* and *S*, from which the relative spatial disposition of spins *I* and *S* can be deduced.

A very useful feature of SEDOR is that, by measuring the dipolar coupling between selected nuclei, it probes only their immediate vicinity. This is because the dipolar interaction is inversely proportional to the cube of the internuclear distance, so that it falls off very quickly with internuclear separation. ^{27}Al–^{31}P SEDOR has been used to measure Al–P distances in aluminophosphate molecular sieves [**126**]. Such information can provide valuable insight into their local structure. For example, framework and extra-framework Al in zeolites can be distinguished.

Double resonance techniques may be tailored to study the defocusing process on rotational echoes generated by MAS rather than on static spin echoes. Rotational Spin-echo Double Resonance (REDOR) [**127**], Rotary Resonance Recoupling (RRR) [**128**] and Transferred-Echo Double Resonance (TEDOR) [**129**] can selectively measure individual heteronuclear dipolar couplings in crystalline solids, which give rise to multiple-peak MAS NMR spectra. Fyfe et al. [**130**] used dipolar-dephasing MAS NMR for the study of mixed pairs of quadrupolar and spin-$\frac{1}{2}$ nuclei in VPI-5. Dipolar connectivities were examined in both directions between ^{31}P and ^{27}Al, REDOR and TEDOR experiments performed, as well as a two-dimensional extension of the TEDOR experiment. Such experiments partially restore the heteronuclear dipolar coupling under MAS via a train of radiofrequency pulses, thereby providing information about connectivities and distances between coupled nuclei. These techniques clearly have considerable potential for structural elucidation.

The second-order quadrupolar interaction, which affects all quadrupolar nuclei, is reduced, but not removed, by magic-angle spinning. Its completete removal is the most important current problem in solid-state NMR. Three different techniques have been proposed to achieve this aim: DOuble-Rotation (DOR), Dynamic-Angle Spinning (DAS) [**131**, **132**] and Multiple-Quantum MAS (MQ-MAS) [**133–136**].

Wu et al. [**137**] showed that ^{27}Al DOR is capable of resolving discrete framework aluminium sites in VPI-5, permitting quantitative investigation of site-specific adsorbate interactions (typically H_2O interactions) with the framework. Figure 9.22(a)

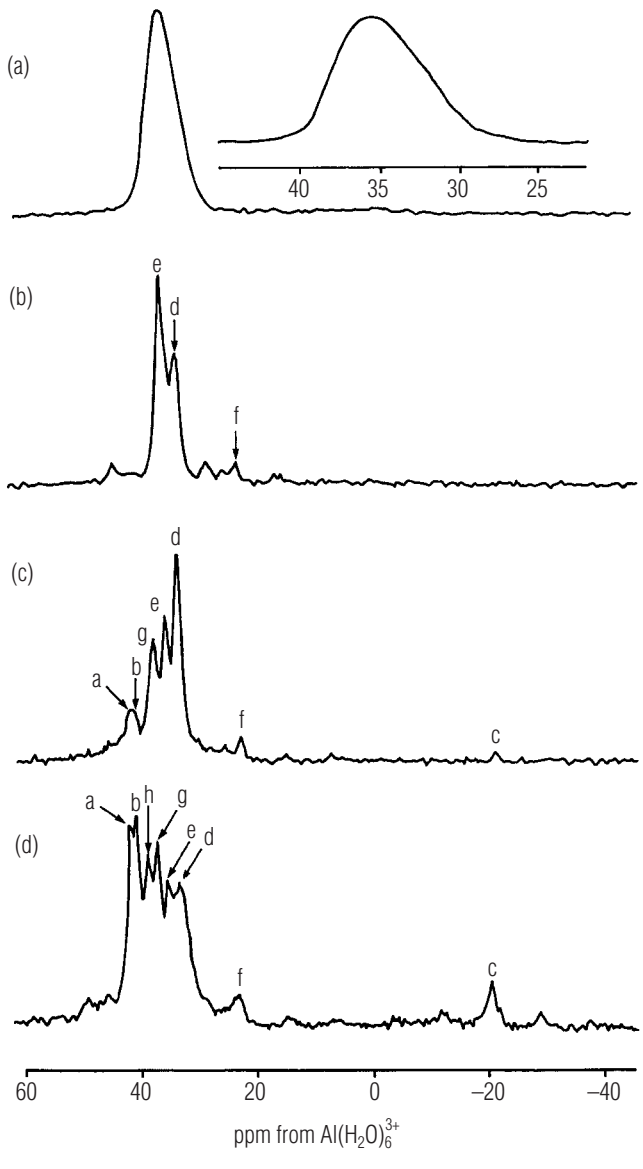

Fig. 9.22 Application of ^{27}Al DOR NMR to VPI-5 [**137**]. (a) MAS spectrum of dehydrated VPI-5; (b) DOR spectrum of dehydrated VPI-5; (c) DOR spectrum after 2 days of rehydration; (d) DOR spectrum after 23 days of rehydration.

shows the ^{27}Al MAS spectrum of dehydrated VPI-5 and Fig. 9.22(b), the DOR spectrum of the same sample. Two peaks unresolved in the MAS spectrum, **d** at 33.3 ppm and **e** at 35.9 ppm, are observed in the DOR spectrum. From the 1:2 intensity ratio of these two peaks, peak **d** is assigned to Al1 sites and peak **e** to Al2 sites in Fig. 9.17. During dehydration, 6-coordinated Al sites are converted to 4-coordinated sites, consistent with the disappearance of peak **c** at –18.4 ppm. Fur-

thermore, in hydrated VPI-5, ^{27}Al tetrahedral sites (peaks **a** and **b**) are altered by dehydration to yield different ^{27}Al tetrahedral environments (peaks **d** and **e**). Two sharp lines which emerge upon slow rehydration, **g** at 37.3 ppm and **h** at 38.8 ppm, arise from Al2 species influenced by adsorbed water molecules.

^{27}Al DOR distinguishes the extremely distorted 5-coordinated aluminium sites in the molecular sieve precursor $AlPO_4$-21 [**138**]. Upon calcination, $AlPO_4$-21 transforms to $AlPO_4$-25, which has two 4-coordinated aluminium sites with similar isotropic chemical shifts which cannot be resolved in an 11.7 T field. However, the two tetrahedral environments have different quadrupole coupling constants and are distinguished by DOR at 4.2 T. DOR was used [**139**] to monitor the nature of the phase transition of $AlPO_4$-11 observed when water is adsorbed. In the hydrated material, water is strongly attached to approximately one-fifth of the framework aluminium, producing 6-coordinated Al. All five suggested crystallographic sites are hydrated to an equal extent. Because of this, the ^{27}Al NMR peak due to the 6-coordinate species does not completely narrow upon DOR.

Although the optimal conditions for MQ-MAS are difficult to establish and the interpretation of the spectra is indirect (and often difficult), the technique is being increasingly used for the study of quadrupolar nuclei of half-integer spin, such as ^{17}O, ^{27}Al, ^{85}Rb, ^{23}Na, ^{11}B and ^{93}Nb [**140–150**].

Quintuple-quantum MQ-MAS (5Q-MAS) discriminates between the different ^{27}Al sites in $AlPO_4$-11, VPI-5 [**140**], chabazite-related precursor of $AlPO_4$-34 [**141**] and $AlPO_4$-14 [**146**] more sensitively than DOR or DAS, and allows the direct determination of the number of different species and of their real chemical shifts and quadrupolar parameters. The various sites cannot be differentiated by MAS. 5Q-MAS distinguishes at least two inequivalent aluminium sites in H-ZSM-5, establishes a correlation between ^{27}Al, ^{29}Si and ^{1}H NMR results and provides information about the distribution and siting of aluminium in the framework [**145**].

While impressive in their resolution, the MQ-MAS spectra described above often simply confirm information available from other techniques of structural elucidation: the method is still under development. However, there are prospects of using it to monitor ^{17}O (oxygen is the most abundant element in the Earth's crust) and to measure interatomic connectivities and dipolar interactions between quadrupolar nuclei, which amounts to direct determination of interatomic distances. Thus MQ-MAS combined with REDOR has been used to establish the interatomic connectivities between quadrupolar and spin-$\frac{1}{2}$ nuclei [**147**], such as ^{1}H–^{27}Al and ^{19}F–^{27}Al spin pairs in fluorinated and hydrated aluminophosphates [**150**].

^{17}O MQ-MAS spectra measured in the high field of 17.6 T show good resolution between the lines from Si–O–Si and Si–O–Al fragments and enable a correlation between the isotropic value of the chemical shift and the Si–O–Al bond angle to be obtained [**148**, **149**]. A change of the bridging Si–O–Si angle by 13.4° gives rise to a 5.7 ppm change in the isotropic ^{17}O chemical shift.

9.19 Conclusions

The future of NMR in the study of porous materials looks bright. The structure of the porous solid itself can now be probed using various two-dimensional NMR techniques, and further developments are in the pipeline. Multi-dimensional NMR of solids clearly has considerable prospects. Quadrupole nutation NMR can probe the environment of nuclei in rigid solid catalysts, rotational resonance measures accurately the distance between specific sites, and surface-sensitive techniques, such as SEDOR with its modifications and ^{2}H NMR, overcome the traditional limitations of nuclear magnetic resonance. *In situ* techniques can identify the intermediates and products of catalytic reactions, and elucidate their mechanism. Multiple-quantum NMR can count molecules present in porous solids. Finally, DOR, DAS and MQ-MAS effectively average second-order quadrupolar interactions. Applications of most of these techniques have hardly begun. At the same time, high magnetic fields and constant advances in NMR hardware have made it possible to monitor virtually all chemical elements in solids. There is no doubt that the next few years will witness many exciting new experiments.

References

1. W.M. Meier, D.H. Olson and C. Baerlocher, *Atlas of Zeolite Structure Types (updates on http://kristall.erdw.ethz.ch/IZA-SC/)*, Elsevier, London (1996).
2. D.W. Breck, *Zeolite Molecular Sieves: Structure, Chemistry and Use*, John Wiley, London (1974).
3. R.M. Barrer, *Zeolites and Clay Minerals as Sorbents and Molecular Sieves*, Academic Press, London (1978).
4. R.M. Barrer, *Hydrothermal Chemistry of Zeolites*, Academic Press, London (1982).
5. R. Szostak, *Molecular Sieves: Principles of Synthesis and Identification*, Van Nostrand Reinhold, New York (1989).
6. G. Engelhardt and D. Michel, *High Resolution Solid-State NMR of Silicates and Zeolites*, John Wiley, Chichester (1987).
7. A.F. Cronstedt, *Kongl. Vetenskaps Acad. Handl. Stockholm* **17** (1756) 120.
8. W. Loewenstein, *Am. Mineral.* **39** (1954) 92.
9. P.B. Weisz and V.J. Frilette, *J. Phys. Chem.* **64** (1960) 382.
10. R.J. Argauer and G.R. Landolt, *U.S. Patent No. 3,702,886* (1972).
11. S.T. Wilson, B.M. Lok, C.A. Messina, T.R. Cannan and E.M. Flanigen, *J. Am. Chem. Soc.* **104** (1982) 1146.
12. J.M. Bennett, J.P. Cohen, E.M. Flanigen, J.J. Pluth and J.V. Smith, Crystal structure of tetrapropylammonium hydroxide-aluminum phosphate number 5, in G.D. Stucky and F.G. Dwyer (Eds.), *Intrazeolite Chemistry, ACS Symposium Series No. 218*, Vol. 218, American Chemical Society, Washington, DC (1983), p. 109.
13. M.E. Davis, C. Saldarriaga, C. Montes, J. Garces and C. Crowder, *Zeolites* **8** (1988) 362.
14. M.E. Davis, C. Saldarriaga, C. Montes, J. Garces and C. Crowder, *Nature* **331** (1988) 698.
15. M. Estermann, L.B. McCusker, C. Bärlocher, A. Merrouche and H. Kessler, *Nature* **352** (1991) 320.
16. E.M. Flanigen, B.M. Lok, R.L. Patton and S.T. Wilson, *Pure Appl. Chem.* **58** (1986) 1351.
17. J.S. Beck, J.C. Vartuli, W.J. Roth, M.E. Leonowicz, C.T. Kresge, K.D. Schmitt, C.T.W. Chu,

D.H. Olson, E.W. Sheppard, S.B. McCullen, J.B. Higgins and J.L. Schlenker, *J. Am. Chem. Soc.* **114** (1992) 10834.
18. C.T. Kresge, M.E. Leonowicz, W.J. Roth, J.C. Vartuli and J.S. Beck, *Nature* **359** (1992) 710.
19. J.S. Beck and J.C. Vartuli, *Current Opinion in Solid State and Materials Science* **1** (1996) 76.
20. E. Lippmaa, M. Mägi, A. Samoson, G. Engelhardt and A.-R. Grimmer, *J. Am. Chem. Soc.* **102** (1980) 4889.
21. A. Samoson and E. Lippmaa, *Phys. Rev.* **B28** (1983) 6567.
22. P.P. Man, J. Klinowski, A. Trokiner, H. Zanni and P. Papon, *Chem. Phys. Lett.* **151** (1988) 143.
23. H. Pfeifer, NMR of solid surfaces, in P. Diehl, E. Fluck, H. Günther, R. Kosfeld and J. Seelig (Eds.), *Solid-State NMR II: Inorganic Matter*, NMR: Basic Principles and Progress, Vol. 31, Springer-Verlag, New York (1994), p. 31.
24. J. Mason, Nitrogen, in J. Mason (Ed.), *Multinuclear NMR*, Plenum Press, New York (1987), p. 335.
25. D. Raftery and B.F. Chmelka, Xenon NMR Spectroscopy, in P. Diehl, E. Fluck, H. Günther, R. Kosfeld and J. Seelig (Eds.), *Solid-State NMR I: Methods*, NMR: Basic Principles and Progress, Vol. 30, Springer-Verlag, New York (1994), p. 111.
26. G. Engelhardt, U. Lohse, E. Lippmaa, M. Tarmak and M. Mägi, *Z. Anorg. Allg. Chem.* **482** (1981) 49.
27. J. Klinowski and M.W. Anderson, *J. Chem. Soc., Faraday Trans. I* **82** (1986) 569.
28. R.H. Jarman, A.J. Jacobson and M.T. Melchior, *J. Phys. Chem.* **88** (1984) 5748.
29. J. Klinowski, S. Ramdas, J.M. Thomas, C.A. Fyfe and J.S. Hartman, *J. Chem. Soc., Faraday Trans. II* **78** (1982) 1025.
30. M.T. Melchior, D.E.W. Vaughan and A.J. Jacobson, *J. Am. Chem. Soc.* **104** (1982) 4859.
31. J. Klinowski, S.W. Carr, S.E. Tarling and P. Barnes, *Nature* **330** (1987) 56.
32. S. Ramdas and J. Klinowski, *Nature* **308** (1984) 521.
33. C.A. Fyfe, G.C. Gobbi, J. Klinowski, J.M. Thomas and S. Ramdas, *Nature* **296** (1982) 530.
34. C.A. Fyfe, J.H. O'Brien and H. Strobl, *Nature* **326** (1987) 281.
35. J. Klinowski, T.A. Carpenter and L.F. Gladden, *Zeolites* **7** (1987) 73.
36. H. Strobl, C.A. Fyfe, G.T. Kokotailo, C.T. Pasztor and D.M. Bibby, *J. Am. Chem. Soc.* **109** (1987) 4733.
37. G.W. West, *Aust. J. Chem.* **37** (1984) 455.
38. C.A. Fyfe, G.J. Kennedy, C.T. DeSchutter and G.T. Kokotailo, *J. Chem. Soc., Chem. Commun.* (1984) 541.
39. C.A. Fyfe, G.C. Gobbi, G.J. Kennedy, J.D. Graham, R.S. Ozubko, W.J. Murphy, A. Bothner-By, J. Dadok and A.S. Chesnick, *Zeolites* **5** (1985) 179.
40. C.A. Fyfe, H. Gies, Y. Feng and G.T. Kokotailo, *Nature* **341** (1989) 223.
41. C.A. Fyfe, H. Gies and Y. Feng, *J. Am. Chem. Soc.* **111** (1989) 7702.
42. C.A. Fyfe, H. Gies and Y. Feng, *J. Chem. Soc., Chem. Commun.* (1989) 1240.
43. C.A. Fyfe, Y. Feng, H. Gies, H. Grondey and G.T. Kokotailo, *J. Am. Chem. Soc.* **112** (1990) 3264.
44. C.A. Fyfe, H. Grondey, Y. Feng and G.T. Kokotailo, *J. Am. Chem. Soc.* **112** (1990) 8812.
45. C.A. Fyfe, H. Gies, Y. Feng and H. Grondey, *Zeolites* **10** (1990) 278.
46. C.A. Fyfe, H. Grondey, Y. Feng and G.T. Kokotailo, *Chem. Phys. Lett.* **173** (1990) 211.
47. W. Kolodziejski, P.J. Barrie, H.Y. He and J. Klinowski, *J. Chem. Soc., Chem. Commun.* (1991) 961.
48. M.T. Melchior, Silicon and aluminum ordering of zeolites: interpretation of Si-29 NMR data for faujasite and ZK-4, *ACS Symposium Series*, Vol. 218, American Chemical Society, Wahington, DC (1983), p. 243.
49. J.G. Hexem, M.H. Frey and S.J. Opella, *J. Am. Chem. Soc.* **103** (1981) 224.
50. H. Hamdan and J. Klinowski, *Chem. Phys. Lett.* **139** (1987) 576.
51. J. Klinowski, T.A. Carpenter and J.M. Thomas, *J. Chem. Soc., Chem. Commun.* (1986) 956.
52. J. Haase, H. Pfeifer, W. Oehme and J. Klinowski, *Chem. Phys. Lett.* **150** (1988) 189.
53. C.V. McDaniel and P.K. Maher, New ultra-stable form of faujasite, *Molecular Sieves*, Society of Chemical Industry, London (1968), p. 186.
54. C.V. McDaniel and P.K. Maher, Zeolite stability and ultrastable zeolites, in J.A. Rabo (Ed.), *Zeolite*

Chemistry and Catalysis, ACS Monograph 171, American Chemical Society, Washington, DC (1976), p. 285.
55. J. Klinowski, J.M. Thomas, C.A. Fyfe and G.C. Gobbi, *Nature* **296** (1982) 533.
56. I.E. Maxwell, W.A. van Erp, G.R. Hays, T. Couperus, R. Huis and A.D.H. Clague, *J. Chem. Soc., Chem. Commun.* (1982) 523.
57. G. Engelhardt, U. Lohse, A. Samoson, M. Mägi, M. Tarmak and E. Lippmaa, *Zeolites* **2** (1982) 59.
58. G. Engelhardt, U. Lohse, V. Patzelová, M. Mägi and E. Lippmaa, *Zeolites* **3** (1983) 233.
59. G. Engelhardt, U. Lohse, V. Patzelová, M. Mägi and E. Lippmaa, *Zeolites* **3** (1983) 239.
60. L. Kellberg, M. Linsten and H.J. Jakobsen, *Chem. Phys. Lett.* **182** (1991) 120.
61. J. Rocha and J. Klinowski, *J. Chem. Soc., Chem. Commun.* (1991) 1121.
62. J. Rocha, S.W. Carr and J. Klinowski, *Chem. Phys. Lett.* **187** (1991) 401.
63. H. Hamdan, B. Sulikowski and J. Klinowski, *J. Phys. Chem.* **93** (1989) 350.
64. P.J. Barrie, L.F. Gladden and J. Klinowski, *J. Chem. Soc., Chem. Commun.* (1991) 592.
65. D. Freude, T. Fröhlich, H. Pfeifer and G. Scheler, *Zeolites* **3** (1983) 171.
66. U. Lohse and M. Mildebrath, *Z. Anorg. Allg. Chem.* **476** (1981) 126.
67. J. Dwyer, F.R. Fitch, F. Machado, G. Qin, S.M. Smyth and J.C. Vickerman, *J. Chem. Soc., Chem. Commun.* (1981) 422.
68. J. Dwyer, F.R. Fitch, G. Qin and J.C. Vickerman, *J. Phys. Chem.* **86** (1982) 4574.
69. M.B. Ward and J.H. Lunsford, *J. Catal.* **87** (1984) 524.
70. A. Samoson, E. Lippmaa, G. Engelhardt, U. Lohse and H.G. Jerschkewitz, *Chem. Phys. Lett.* **134** (1987) 589.
71. D. Freude, M. Hunger and H. Pfeifer, *Chem. Phys. Lett.* **91** (1982) 307.
72. D. Freude, M. Hunger, H. Pfeifer and W. Schwieger, *Chem. Phys. Lett.* **128** (1986) 62.
73. D. Freude and J. Klinowski, *J. Chem. Soc., Chem. Commun.* (1988) 1411.
74. D. Freude, J. Klinowski and H. Hamdan, *Chem. Phys. Lett.* **149** (1988) 355.
75. J.H. van Vleck, *Phys. Rev.* **74** (1948) 1168.
76. D. Freude, *Adv. Colloid Interface Sci.* **23** (1985) 21.
77. D. Michel, A. Germanus, D. Scheler and B. Thomas, *Z. Phys. Chem. (Leipzig)* **262** (1981) 113.
78. D. Michel, A. Germanus and H. Pfeifer, *J. Chem. Soc., Faraday Trans. I* **78** (1982) 237.
79. I. Jünger, W. Meiler and H. Pfeifer, *Zeolites* **2** (1982) 310.
80. W.P. Rothwell, X.S. Wen and J.H. Lunsford, *J. Am. Chem. Soc.* **106** (1984) 2452.
81. J.H. Lunsford, W.P. Rothwell and W. Shen, *J. Am. Chem. Soc.* **107** (1985) 1540.
82. C.D. Chang, *Catal. Rev. Sci. Eng.* **25** (1983) 1.
83. G. Winde, A.V. Volkov, A.V. Kiselev and V.I. Lygin, *Russian J. Phys. Chem.* **49** (1975) 1716.
84. Z. Luz and A.J. Vega, *J. Phys. Chem.* **91** (1987) 374.
85. G. Mirth, J.A. Lercher, M.W. Anderson and J. Klinowski, *J. Chem. Soc., Faraday Trans.* **86** (1990) 3039.
86. M.W. Anderson, P.J. Barrie and J. Klinowski, *J. Phys. Chem.* **95** (1991) 235.
87. T.A. Carpenter, J. Klinowski, D.T.B. Tennakoon, C.J. Smith and D.C. Edwards, *J. Magn. Reson.* **68** (1986) 561.
88. M.W. Anderson, M.L. Occelli and J. Klinowski, *J. Phys. Chem.* **96** (1992) 388.
89. S.M. Csicsery, Shape-selective catalysis, in J.A. Rabo (Ed.), *Zeolite Chemistry and Catalysis, ACS Monograph 171*, American Chemical Society, Washington, DC (1976), p. 680.
90. N.Y. Chen, W.W. Kaeding and F.G. Dwyer, *J. Am. Chem. Soc.* **101** (1979) 6783.
91. W.W. Kaeding, *U.S. Patent No. 4,029,716* (1977).
92. W.O. Haag and D.H. Olson, *U.S. Patent No. 4,097,543* (1978).
93. M.W. Anderson and J. Klinowski, *J. Am. Chem. Soc.* **112** (1990) 10.
94. M.W. Anderson and J. Klinowski, *Nature* **339** (1989) 200.
95. B.R. Richardson, N.D. Lazo, P.D. Schettler, J.L. White and J.F. Haw, *J. Am. Chem. Soc.* **112** (1990) 2886.
96. N.D. Lazo, J.L. White, E.J. Munson, M. Lambregts and J.F. Haw, *J. Am. Chem. Soc.* **112** (1990) 4050.
97. J.L. White, N.D. Lazo, B.R. Richardson and J.F. Haw, *J. Catal.* **125** (1990) 260.

98. E.J. Munson and J.F. Haw, *Anal. Chem.* **62** (1990) 2532.
99. E.J. Munson, N.D. Lazo, M.E. Moellenhoff and J.F. Haw, *J. Am. Chem. Soc.* **113** (1991) 2783.
100. J.B. Stothers, *Carbon-13 NMR Spectroscopy*, Academic Press, New York (1972).
101. M.W. Anderson and J. Klinowski, *Chem. Phys. Lett.* **172** (1990) 275.
102. W. Kolodziejski and J. Klinowski, *Appl. Catal.* **A81** (1992) 133.
103. M.T. Aronson, R.J. Gorte, W.E. Farneth and D. White, *J. Am. Chem. Soc.* **111** (1989) 840.
104. C.S. Blackwell and R.L. Patton, *J. Phys. Chem.* **88** (1984) 6135.
105. P.J. Barrie and J. Klinowski, *J. Phys. Chem.* **93** (1989) 5972.
106. W. Kolodziejski, H.Y. He and J. Klinowski, *Chem. Phys. Lett.* **191** (1992) 117.
107. E.O. Stejskal and J.E. Tanner, *J. Chem. Phys.* **42** (1965) 288.
108. J. Kärger, *Z. Phys. Chem. (Leipzig)* **248** (1971) 27.
109. J. Caro, J. Kärger, H. Pfeifer and R. Schöllner, *Z. Phys. Chem. (Leipzig)* **256** (1975) 698.
110. J. Kärger, W. Heink, H. Pfeifer, M. Rauscher and J. Hoffmann, *Zeolites* **2** (1982) 275.
111. R.R. Eckman and A.J. Vega, *J. Phys. Chem.* **90** (1986) 4679.
112. I. Kustanovich, D. Fraenkel, Z. Luz, S. Vega and H. Zimmermann, *J. Phys. Chem.* **92** (1988) 4134.
113. I. Kustanovich, H.M. Vieth, Z. Luz and S. Vega, *J. Phys. Chem.* **93** (1989) 7427.
114. I. Kustanovich, Z. Luz, S. Vega and A.J. Vega, *J. Phys. Chem.* **94** (1990) 3138.
115. M.J. Duer, H.Y. He, W. Kolodziejski and J. Klinowski, *J. Phys. Chem.* **98** (1994) 1198.
116. T. Ito and J. Fraissard, *J. Chem. Phys.* **76** (1982) 5225.
117. J. Fraissard and T. Ito, *Zeolites* **8** (1988) 350.
118. L.C. de Menorval, J. Fraissard and T. Ito, *J. Chem. Soc., Faraday Trans. I* **78** (1982) 403.
119. J.A. Ripmeester, *J. Am. Chem. Soc.* **104** (1982) 289.
120. M. Munowitz and A. Pines, *Science* **233** (1986) 525.
121. R. Ryoo, S.B. Liu, L.C. Demenorval, K. Takegoshi, B. Chmelka, M. Trecoske and A. Pines, *J. Phys. Chem.* **91** (1987) 6575.
122. B.F. Chmelka, J.G. Pearson, S.B. Liu, R. Ryoo, L.C. de Menorval and A. Pines, *J. Phys. Chem.* **95** (1991) 303.
123. J. Baum, M. Munowitz, A.N. Garroway and A. Pines, *J. Chem. Phys.* **83** (1985) 2015.
124. D. Raftery, H. Long, L. Reven, P. Tang and A. Pines, *Chem. Phys. Lett.* **191** (1992) 385.
125. D.E. Kaplan and E.L. Hahn, *J. Phys. Radium* **19** (1958) 821.
126. E.R.H. van Eck and W.S. Veeman, *Solid State NMR* **1** (1992) 1.
127. T. Gullion and J. Schaefer, *J. Magn. Reson.* **81** (1989) 196.
128. T.G. Oas, R.G. Griffin and M.H. Levitt, *J. Chem. Phys.* **89** (1988) 692.
129. A.W. Hing, S. Vega and J. Schaefer, *J. Magn. Reson.* **96** (1992) 205.
130. C.A. Fyfe, K.T. Mueller, H. Grondey and K.C. Wong-Moon, *Chem. Phys. Lett.* **199** (1992) 198.
131. A. Samoson, E. Lippmaa and A. Pines, *Mol. Phys.* **65** (1988) 1013.
132. A. Llor and J. Virlet, *Chem. Phys. Lett.* **152** (1988) 248.
133. M.J. Duer and C. Stourton, *35th Experimental NMR Conference (ENC), Poster No. WP221* (1994).
134. L. Frydman and J.S. Harwood, *J. Am. Chem. Soc.* **117** (1995) 5367.
135. A. Medek, J.S. Harwood and L. Frydman, *J. Am. Chem. Soc.* **117** (1995) 12779.
136. J.P. Amoureux, C. Fernandez and L. Frydman, *Chem. Phys. Lett.* **259** (1996) 347.
137. Y. Wu, B.F. Chmelka, A. Pines, M.E. Davis, P.J. Grobet and P.A. Jacobs, *Nature* **346** (1990) 550.
138. R. Jelinek, B.F. Chmelka, Y. Wu, P.J. Grandinetti, A. Pines, P.J. Barrie and J. Klinowski, *J. Am. Chem. Soc.* **113** (1991) 4097.
139. P.J. Barrie, M.E. Smith and J. Klinowski, *Chem. Phys. Lett.* **180** (1991) 6.
140. C. Fernandez and J.P. Amoureux, *Chem. Phys. Lett.* **242** (1995) 449.
141. C. Fernandez, J.P. Amoureux, L. Delmotte and H. Kessler, *Microporous Materials* **6** (1996) 125.
142. C. Fernandez and J.P. Amoureux, *Solid State NMR* **5** (1996) 315.
143. J. Rocha, Z. Lin, C. Fernandez and J.P. Amoureux, *J. Chem. Soc., Chem. Commun.* (1996) 2513.
144. J. Rocha, A.P. Esculcas, C. Fernandez and J.P. Amoureux, *J. Phys. Chem.* **100** (1996) 17889.
145. P. Sarv, C. Fernandez, J.P. Amoureux and K. Keskinen, *J. Phys. Chem.* **100** (1996) 19223.
146. C. Fernandez, J.P. Amoureux, J.M. Chézeau, L. Delmotte and H. Kessler, *Microporous Materials* **6** (1996) 331.

147. C. Fernandez, D.P. Lang, J.P. Amoureux and M. Pruski, *J. Am. Chem. Soc.* **120** (1998) 2672.
148. J.P. Amoureux, F. Bauer, H. Ernst, C. Fernandez, D. Freude, D. Michel and U.T. Pingel, *Chem. Phys. Lett.* **285** (1998) 10.
149. U.T. Pingel, J.P. Amoureux, T. Anupold, F. Bauer, H. Ernst, C. Fernandez, D. Freude and A. Samoson, *Chem. Phys. Lett.* **294** (1998) 345.
150. M. Pruski, C. Fernandez, D.P. Lang and J.P. Amoureux, *Catalysis Today* **49** (1999) 401.
151. H. Hamdan and J. Klinowski, Secondary synthesis of faujasitic catalysts, in M.H. Occelli and H.E. Robson (Eds.), *ACS Symposium Series*, Vol. 398, American Chemical Society No. 398, Washington, DC (1989), p. 448.
152. L.B. McCusker, C. Bärlocher, E. Jahn and M. Bülow, *Zeolites* **11** (1991) 308.

Solid-State NMR Spectroscopy Principles and Applications
Edited by Melinda J. Duer
Copyright © 2002 by Blackwell Science Ltd

Chapter 10
Solid Polymers

Ulrich Scheler

10.1 Introduction

Polymer materials play an important role for the use as mass, low-cost materials as well as for 'high-tech' materials, tailor-made for special applications. The possibility of producing polymeric materials for specific applications relies on an understanding of so-called structure–property relationships. The macroscopic properties of synthetic polymers depend on their molecular structure and on their organization, i.e. morphology, molecular order and molecular dynamics. Processing a polymer after its initial synthesis can modify these properties as well [**1**, **2**]. High-resolution NMR is the most powerful tool for structural elucidation in polymers currently available. Because the majority of polymers are used as solid materials, there is considerable interest in studying their solid-state properties. Furthermore a number of high-performance polymers are insoluble in most organic solvents, which does not permit frequent solution-state studies. Advanced solid-state NMR techniques have been developed and used to characterize special properties of solid polymers [**3**, **4**].

Polymers are macromolecules which are formed from a sequence of repeat units. A variety of chemical reactions, such as condensation, ring-opening, polyaddition and radical reactions, are used to link monomers into the polymeric structure. The repeat units can be either of the same type (homopolymers) or of different types (copolymers). In the latter case the sequential arrangement of the different types of repeat units has a strong influence on the properties of the resulting polymer. The combination of different monomers in a copolymer can result in an average of the properties arising from the individual monomers or can give new and totally different ones. The latter is most often the desired outcome. However, when monomers whose homopolymers have totally different properties are combined, there is a certain probability that they do not mix, but instead form separate phases. Another way of combining the properties of different polymers is by mixing different homopolymers. Depending on the miscibility, polymer alloys or blends are formed.

In blends, the miscibility is low and the homopolymers have a tendency to phase separate; special processing steps are required if this is to be avoided. The properties of the final material are strongly influenced by the degree of phase separation and by the domain sizes of each polymer in the blend.

Most polymers are long-chain linear molecules, but ones with various degrees of branching also exist. The density of branches strongly influences macroscopic properties. In addition, highly branched and hyperbranched species are found and, more recently, perfectly branched star-like polymers (so-called dendrimers) [**5**]. This latter development has potential for interesting applications such as contrast agents for MRI or as carriers for gene-transfer systems, where the active species is contained in the core of the dendrimer.

A special group of branched polymers are crosslinked polymers. These are mostly linear polymers that have links between the chains. In soft materials (i.e. low modulus), the existence of crosslinks leads to elastic properties. A material being soft means that the polymer chains can be displaced with respect to each other. The crosslinks, however, restrict the degree of displacement and prevent continuous translation of molecules with respect to each other or cold flow. As a result, materials with elastic properties are formed, the so-called elastomers.

The majority of polymers are amorphous and, when the molecular weight exceeds a critical value, usually form a coiled shape. However, some polymers can arrange themselves with a three-dimensional periodic order and so form crystals. The chain structure in most cases prevents the formation of large single crystals, as the chain conformation must be properly ordered all the way along the chain. Entropy does not favour such an ordering and this feature effectively restricts the crystal growth. Therefore, most polymers that can form crystallites are semicrystalline with amorphous regions between the crystallites, as sketched in Fig. 10.1. The order in the crystalline part requires a certain conformation of the polymer chain, so that it can fit into the three-dimensional ordered structure. This conformational order results in restrictions of the molecular mobility, which reveals itself macroscopically as better mechanical stability. The crystalline part of the polymer due to the restricted motional degrees of freedom is usually is stiffer, which implies it can become brittle. Commonly, the crystallites take the form of lamellae, but spherulites are also found, especially for small crystallites.

The stereoscopic arrangement of the different polymer units can have a strong influence on the resulting properties of the material. Only stereoregular materials can crystallize. Although stereoregularity is most conveniently studied in high-resolution, solution-state NMR, it can be studied in the solid state via NMR as well. One of the advantages of solid-state NMR is that the dynamics associated with changes in the relevant orientations can also be studied. Importantly, the rate range which can be probed by solid-state NMR is that which is important for materials applications. A prominent example of the effect of stereoregularity is seen in polypropylene, where the methyl sidegroup can be arranged in different positions.

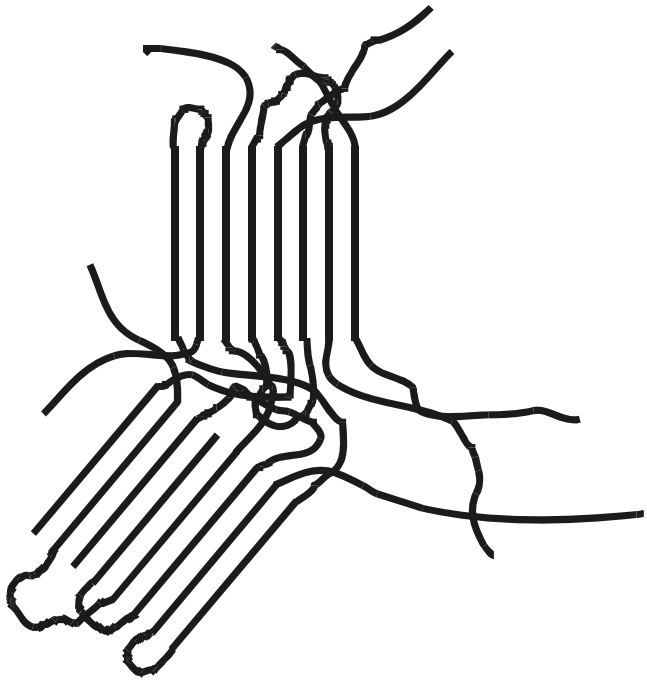

Fig. 10.1 Schematic of a typical semicrystalline polymer. Crystalline lamellae alternate with disordered amorphous regions. A single polymer chain can extend from the crystalline to the amorphous part or into the next crystallite.

As depicted in Fig. 10.2, the ^{13}C cross-polarization, magic-angle spinning NMR spectrum is strongly affected by the *tacticity* [**6**, **7**, **8**] of the material (see Fig. 10.2 for definition of tacticity). The properties differ as well, because only isotactic and syndiotactic propylene can crystallize with a degree of crystallinity around 70%. Atactic polypropylene, which ideally has no stereoregularity, is purely amorphous and forms a more rubber-like material.

An interesting combination of properties is found in liquid-crystalline materials (see also Chapter 11), where anisotropic properties under external fields (electric, magnetic, shear) lead to self-organization in the liquid-crystalline phase. This self-organized structure can be conserved under a transition from the oriented liquid-crystalline phase to the solid phase in the presence of the external field. The possibility of combining liquid-crystalline properties with polymer materials has led to an interesting combination of materials properties.

10.2 Structure of polymers

As pointed out in the introduction, the most powerful tool of structural elucidation currently available for polymers is probably high-resolution, solution-state NMR. However, structural information is available using solid-state NMR as well.

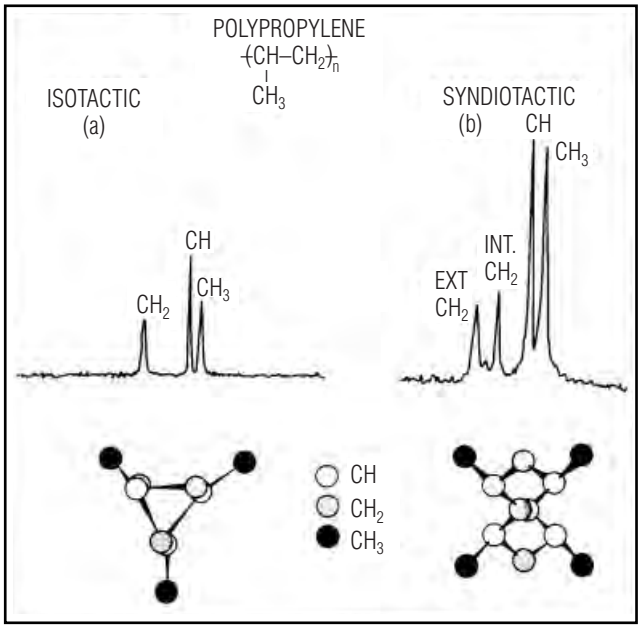

Fig. 10.2 Stereoregularity in poly(propylene) and its signature in the ^{13}C solid-state spectrum (a) isotactic and (b) syndiotactic. (From A.E. Tonelli, *NMR Spectroscopy and Polymer Microstructure: The Conformational Connection*, Reprinted by permission of John Wiley & Sons Inc., New York.)

Although it has been rarely applied, at least to date, for the elucidation of polymer chain structures, solid-state NMR can be very useful. In particular, the correlation of different NMR interactions in a multidimensional experiment can result in high selectivity and resolution for different structural/dynamical regions of the polymer material. This is perhaps the major advantage of NMR for the characterization of solid polymers [**4**].

Because indirect, *J*-, coupling is usually not resolved in solid-state NMR spectra of polymers, the major information about the polymer structure in solid-state NMR is gained from the ^{13}C chemical shift. The isotropic chemical shift allows different chain conformations to be identified. The conformation of the polymer chain influences the spectrum through the so-called *gamma-gauche* effect. This effect means that the isotropic chemical shift of a ^{13}C spin depends on the conformation in neighbouring parts of the polymer chain. This effect has been studied widely and has been applied to the assignment of conformations of polymer chains. Knowledge of the changes of the isotropic chemical shift with the conformation is the basis of experiments studying the dynamics of the conformational changes. In addition, packing effects which affect chain conformations can show up in solid-state NMR spectra. The chemical shift anisotropy can be used to probe orientations of molecular segments with respect to $\mathbf{B}_0$, the external magnetic field. This is exploited in experiments which characterize molecular order or study the dynamics of reorientations (see below). When this information can be resolved for different isotropic shifts, an assignment of order or dynamical behaviour to different chemical sites is

possible. The *gamma-gauche* effect is most commonly exploited in ^{13}C NMR but is by no means restricted to that nucleus. The effect is detectable for any nucleus which exhibits a large chemical shift range like ^{31}P or ^{19}F.

The high-resolution one-dimensional solid-state NMR spectra (magic-angle spinning ^{13}C or ^{1}H with Combined Rotation and Multiple-Pulse Sequence (CRAMPS), i.e. magic-angle spinning plus multiple-pulse sequence, such as MREV-8 for the removal of ^{1}H–^{1}H dipolar couplings) of polymers are generally inhomogeneously broadened, compared with spectra from crystalline, molecular compounds. This broadening is due to a distribution of chemical shifts resulting from different conformations and different sequences of repeat units in copolymers. Recent developments in *ab-initio* calculations of NMR spectra provide a route for calculating chemical shift distributions for different (calculated) models of copolymer structure or conformational distribution, and different sequences of repeat units in the polymer chain. Comparison of the calculated spectra with experimental observations [**9**] allows the structural model for the polymer to be tested.

Proton chemical shifts can be used to reveal structural information providing high-resolution solid-state NMR techniques like CRAMPS [**10**, **11**] or high-rate magic-angle spinning are applied. However, these techniques are not routinely available as yet, and so ^{1}H magnetization tends to be used as part of more complicated, multidimensional experiments. The major advantage here is in the sensitivity especially in complicated experiments. An intriguing application is the so-called chemical shift filter which as been applied as a selection step in spin-diffusion experiments [**30**]. Under the application of a multiple-pulse sequence, i.e. MREV-8, the homonuclear dipolar coupling is suppressed (see Section 2.4). The chemical shift is preserved, but scaled by a constant factor. Under the multiple-pulse sequence, the magnetization from different structures exhibits different Larmor frequencies, and so precesses at different rates around the effective field for the multiple-pulse sequence (see Section 2.4), which for the example of MREV-8 is the (1, 0, 1) direction in the rotating frame. After a suitable time, one isochromate will be along the z axis while the others will be at or near the x–y plane, as a result of the different precession rates. If the multiple-pulse sequence is terminated in this situation, the isochromates in or near the x–y plane will dephase rapidly under proton–proton dipolar coupling, while the component along the z direction is preserved. This latter component can be put into the transverse plane subsequently by a 90° pulse and an FID recorded. Thus selection of magnetization based on structure using the differences in proton chemical shifts has been achieved.

Recent developments in high-rate magic-angle spinning systems make the application of proton NMR for structural elucidation in polymers a real possibility [**12**]. The tentative area of application is in the elucidation of secondary structure rather than in structural assignment along the chain. One way forward has been in the use of double-quantum spectroscopy (see Section 3.2.2). Double-quantum coherences

do not lead to any directly observable signal, but may be monitored indirectly as part of a two-dimensional NMR experiment. In the resulting spectrum, the directly detected (single-quantum) dimension (f_2) is the single-quantum chemical shift dimension as in a normal one-dimensional experiment; the indirectly detected double-quantum dimension (f_1) shows the sum of the chemical shifts of coupled spins. Distinct patterns are observed in the two-dimensional frequency spectrum, similar to those in an INADEQUATE experiment in high-resolution NMR [**13**]. This double-quantum coherence is the simultaneous evolution of two coupled spins. In the solid state, the coupling usually is provided by the direct dipolar coupling, which is distance-dependent. The existence of a double-quantum coherence is therefore a signature for spatial proximity. Fitting of theoretical spectra, especially spinning sideband patterns in the double-quantum dimension, to the experimental observations can be exploited for the quantitative analysis of internuclear distances [**14**]. A similar approach is valid for the investigation of polymer dynamics probed indirectly via the variation of the internuclear arrangement. This technique has in recent years triggered a large interest in the use of protons as a probe nucleus for NMR which yields high receptivity without the need for isotopic labelling. This technique has so far only limited application to polymeric systems due to their inherent disorder. It has widely been applied to study organic molecules of various sizes, preferentially crystalline ones. In principle there is no limitation to smaller molecular weight, and with an appropriate selection there would be even the possibility to study semicrystalline materials. A heteronuclear version of this approach based on a REDOR-type heteronuclear recoupling pulse sequence has been applied to poly(carbonate) [**15**]. This experiment is applied to probe spatial proximity of nuclei. Because it appears to be limited to strong couplings, it can only probe the nearest neighbours. The advantage for future applications is seen in the pronounced sensitivity to the relative orientations of the chemical shift tensors of the nuclei involved in the coupling, which could be further exploited to study the spatial arrangement of the atoms in the macromolecule.

10.3 Polymer dynamics

One of the key issues in polymers is the molecular dynamics, which can be studied by NMR methods over several orders of correlation times. The internal molecular dynamics controls the mechanical properties of the materials. In rigid materials with restricted molecular mobility, the ability to dissipate energy is limited. Such polymers are usually mechanically strong but often brittle. For this reason, special materials have been developed in which a soft segment in the polymer chain can be utilized for shock absorption to dissipate the energy. The combination of two materials, of which one is hard and one is softer, can yield a mechanically strong material which also holds the possibility of shock absorption.

10.3.1 NMR methods for studying polymer dynamics

As has been pointed out in Chapter 6, all relaxation phenomena are coupled to molecular motion. Thus any relaxation rate that can be accessed experimentally depends on the correlation times of molecular motions. Different relaxation processes, especially spin-lattice (T_1), transverse (T_2) and rotating-frame spin-lattice ($T_{1\rho}$) thus probe different rates of molecular motion. T_1 depends mainly on the spectral density of the motion at the Larmor frequency ω_0 and the dependence of the spin-lattice relaxation rates on the strength of the static magnetic field provides an important insight into the molecular dynamics with τ_c^{-1} (where τ_c is the correlation time for the motion) around ω_0. Insight into the nature of motional processes governing relaxation is gained from the temperature dependence of the relaxation rates. In thermally activated processes, the activation energy can easily be determined from the slope of the relaxation time as a function of the inverse of temperature, the so-called Arrhenius plot.

Given the Larmor frequencies in modern high-field instruments, the spin-lattice relaxation rate is generally determined by high-frequency motions in the order of tens or hundreds of MHz; such motions are usually vibrational or librational motions of small molecular segments or atoms. Motional rates in the order of tens or hundreds of kHz are typical for motions of polymer segments. T_2 and $T_{1\rho}$ are very sensitive to these types of motions and so measurements of both these parameters are widely applied in conjunction with different experiments for the investigation of crosslinking and ageing of elastomeric materials. $T_{1\rho}$ in particular has been extensively applied to the study of crosslinking in elastomers. The existence of crosslinks has in most cases been determined from studies of the molecular mobility [**16**].

In addition, filtered relaxation experiments play an important role. In these types of NMR experiments, a filter pulse sequence is implemented prior the relaxation measurement part of the experiment, so that only magnetization from spins fulfilling the filter criterion is used in the subsequent relaxation experiment. A filter can select magnetization only from certain spatial regions or can create a spatial gradient in the magnetization. This gradient can be based on any NMR criterion, which could be differences in relaxation times, for instance. This concept is widely used in NMR imaging. $T_{1\rho}$ in particular has the advantage that it acts as a band-stop filter, which selectively suppresses magnetization from spins which undergo motions of rates comparable to the locking field strength.

This type of filtered relaxation experiment has been applied to semicrystalline samples in which well-defined helical jumps are observed in the crystalline part of the polymer. Relaxation time measurements have been used to study these motions by performing experiments in which magnetization from the crystalline regions of the polymer only is selected in a first step. The selection in these cases is conveniently achieved for ^{13}C using cross-polarization (from ^{1}H) with a short contact time.

This method utilizes the fact that the heteronuclear dipolar coupling in the mobile amorphous regions of the polymer is partially averaged out by molecular motion resulting in negligible cross-polarization intensity from these regions for short contact times. An alternative method is the so-called delayed contact experiment. In this experiment the excitation of the proton magnetization is followed by a spin-lock pulse. After a delay to be adjusted according to the sample properties, the Hartmann–Hahn contact pulse on the X nucleus is applied. Depending on the differences in $T_{1\rho}$ only components with a long proton $T_{1\rho}$ contribute to the cross-polarization signal [**55**].

Another important application of the filtering concept is in studies of spin diffusion in heterogeneous polymers. A spatial gradient in the magnetization is generated by a suitable selection criterion and the return to equilibrium of the spin magnetization is monitored subsequently. For instance, magnetization can be created according to the mobility of the molecules in a particular region of the polymer, by various methods. Rigid regions are generally the crystalline parts of the polymer, while mobile regions are associated with the amorphous parts. The return to equilibrium is then synonymous with the 'flow' of magnetization between rigid (crystalline) and mobile (amorphous) regions, and so studying this process leads to a determination of the crystalline and amorphous domain sizes. Applications of this approach and technical principles will be discussed in Section 10.4.

The macroscopic mechanical properties of polymer materials are particularly governed by slow motions. For these slower motions, two-dimensional exchange experiments are most appropriate (see Section 6.4). In these experiments, the anisotropy of the chemical shift is used to provide a measure of the relative orientation of molecular segments to the static magnetic field. After the excitation of initial transverse magnetization, using appropriate filtering selections if needed, the orientation-dependent frequency is measured for two periods of time, t_1 and t_2. These two times are separated by a mixing time during which molecular reorientation may take place. In the resulting two-dimensional frequency spectrum, any intensity along the diagonal is a signal from spins which did not change their frequency during the mixing time, meaning they did not change their orientation during this period. The interesting part of the spectrum is any off-diagonal intensity. The specific quantity measured in such an experiment is a two-time correlation function. The orientation of molecular segments relative to the external magnetic field is probed during the evolution (t_1) and detection (t_2) periods of the experiment. These times are typically short compared to the mixing time during which molecular reorientation takes place. Therefore the probing times can be considered as points in time, and the molecular orientations at these two times are correlated to a two-dimensional exchange spectrum. Once the principle of the two-dimensional exchange experiment is established, it can in principle easily be extended to two and more mixing times, resulting in a three- (or more) time correlation function.

Variation of the mixing time in an exchange experiment yields the time depen-

dence of the molecular reorientations. In this way, different types of correlation time distributions can in principle be distinguished. However, for long mixing times, the quantitative analysis is complicated by multiple exchange processes involving more than two sites.

To prevent any ambiguities in the interpretation of exchange spectra, the orientation of the chemical shift tensor with respect to a molecular frame of reference should be known. Because the dipolar-coupling tensor is always oriented with the unique principal axis along the internuclear vector between the coupled spins, the relative orientation of the chemical shift tensor to the dipolar tensor provides that orientation. In a separated local field experiment, this relative orientation can be measured. Depending on the problem under study, either the orientation of the chemical shift tensor with respect to the heteronuclear ^{1}H–^{13}C dipolar-coupling tensor [**17**] or to the homonuclear ^{13}C–^{13}C dipolar-coupling tensor [**18**] can be measured, though the latter method generally requires ^{13}C-enriched samples.

In a spectrum dominated by the chemical shift anisotropy, there is a clear relation between the spectral frequency and the orientation of the chemical shift tensor related to a certain molecular segment (see Equation (1.90) in Chapter 1). Thus any molecular reorientation leads to a change in spectral frequency. If reorientations by a fixed angle occur, only certain spectral frequency changes occur. In the two-dimensional exchange spectrum this leads to distinct elliptical patterns, as discussed in Section 6.4. From the shapes of the ellipses, i.e. from the ratio between the two axes of the ellipse, the jump angle involved in the molecular reorientation can be determined directly. A typical example for such well-defined changes in molecular orientation are the helical jumps of polymer chains in crystalline domains, as shown in Fig. 10.3. These are combined motions of rotation and translation, with the rotational jump angle defined by crystal lattice. Because polymers like poly(ethylene) are semicrystalline with amorphous phases between the crystallites, these jump motions combined with a translation in the crystal lattice finally lead to the movement of polymer segments out of the crystalline domain and into the amorphous domain. In two-dimensional exchange experiments under magic-angle spinning, an exchange between the isotropic chemical shifts of the all-*trans* conformation, that is found in the crystalline part, and the chemical shift of the *gauche*-containing conformers is observed for long mixing times in accordance with this [**19**]. In order to observe exchange in both directions, i.e. into and out of the crystalline region, single-pulse excitation must be used. If cross-polarization is used instead, there is a tendency to underestimate the signal from the amorphous part of the polymer, as cross-polarization efficiency is reduced in this region due to the molecular motion which occurs here. In order to change from an all-*trans* conformation in the crystallite to any *gauche*-containing conformation, the chain segment under study has to leave the crystallite. However, as *trans*-conformers are present in the amorphous part as well, not all exchange intensity arising from *gauche*- to *trans*-conformer exchange is proof that chains enter the crystallites as well as leave. It is perhaps

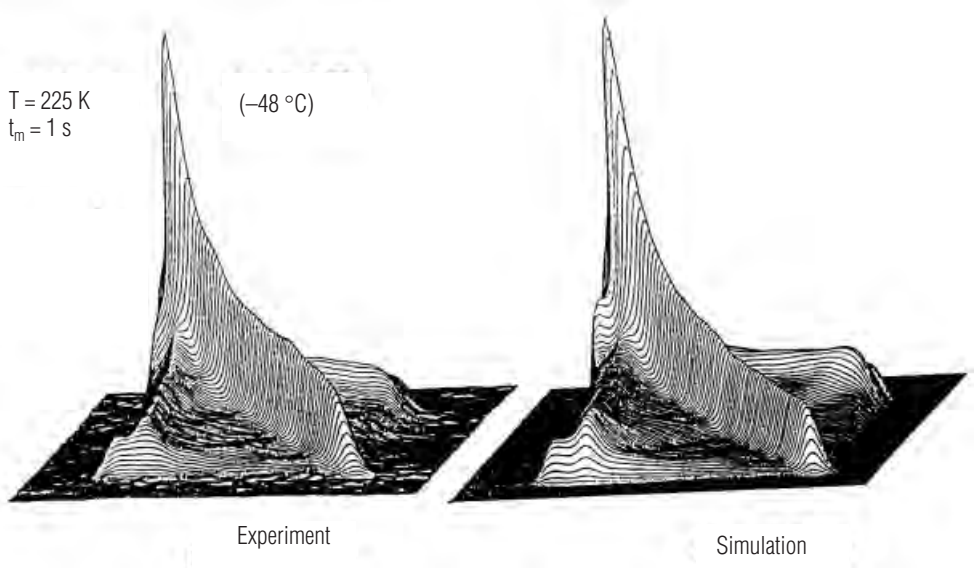

Fig. 10.3 Static two-dimensional exchange spectrum for poly(ethyleneoxide) PEO. The experimental spectrum on the left clearly shows the characteristic ridges for a well-defined jump angle associated with the 7_1 helical structure of this polymer. (From K. Schmidt-Rohr and H.W. Spiess, *Multidimensional Solid-State NMR and Polymers*. Reproduced by permission of Academic Press, London.)

difficult to imagine a polymer chain end being able to find its way back into a crystalline region from the amorphous part, although there is a finite probability for that process. The movement of polymer chains out of crystalline regions and not returning would, over long periods of time, lead to a deterioration of mechanical properties. In commercial materials, the introduction of branches in the polymer chain slows this process down significantly.

Extending the exchange experiment to three or more dimensions, permits the study of sequences of motions. For instance, it can be demonstrated that after a jump in one direction there is a higher probability that the polymer chain will jump back to its original position rather than jump a further step in the original direction. This occurs because any rotation of a helical polymer requires a simultaneous translational motion of the polymer chain to preserve the local crystal symmetry. After a jump there are only two possibilities for a further jump (while retaining the crystal symmetry): a jump in the same direction or a return jump. The fact that a well-defined translation is needed to conduct a helical jump is the source of an additional interaction which places restrictions on the possibilities for multiple jumps in one direction, as each additional jump stretches the polymer chain further from its equilibrium position within the crystalline region. As a result, after a jump in one direction there is a higher probability for a return jump than for an additional jump in the same direction. The most prominent examples are PVAc (polyvinylacetate) which shows no helical jumps and PEO (polyethyleneoxide) which exhibits one of the best examples of helical jumps. Due to the 3_1 helix in PEO, a jump by 120°

requires a translation by one polymer repeat unit. A three-dimensional exchange experiment has been conducted on PEO [**4**] to investigate the chain motion in the crystalline regions. The question in the terms of this NMR experiment is whether a non-vanishing intensity is found in the plane of $\omega_1 = \omega_3$ of the three-dimensional spectum. If there is, it means that a spin representing a molecular segment, moved out of its starting orientation defined by resonance frequency ω_1 to another orientation (leading to a signal at ω_2 during t_2) and then returned to its original orientation, resulting in a signal at $\omega_3 = \omega_1$. In Fig. 10.4, two three-dimensional ^{13}C exchange spectra are depicted for PEO and PVAc. In the case of PEO, a clear ridge for $\omega_3 = \omega_1$ is visible while it is missing in the case of the disordered PVAc, showing that well-ordered jumps occur for PEO, but not for PVAc.

This type of 'memory effect' observed in the molecular motions of PEO through three-dimensional exchange spectroscopy can also be studied through measurements of correlation times for the motion. A purely random process, a process in which every jump has the same probability, is described by an exponential loss of correlation. Therefore any non-exponential loss of correlation is a sign of a type of memory effect, where motions occurring at a time t are correlated to jumps that have occurred at a time $(t - \tau)$. Reduced versions of the three- and four-dimensional exchange experiments have been applied to study the time evolution of correlation times for this purpose [**20, 21**]. The source of the non-exponential loss of correlation is one of the big open questions in polymer physics. Does it arise because the system is spatially heterogeneous, so that the net correlation function for the motion

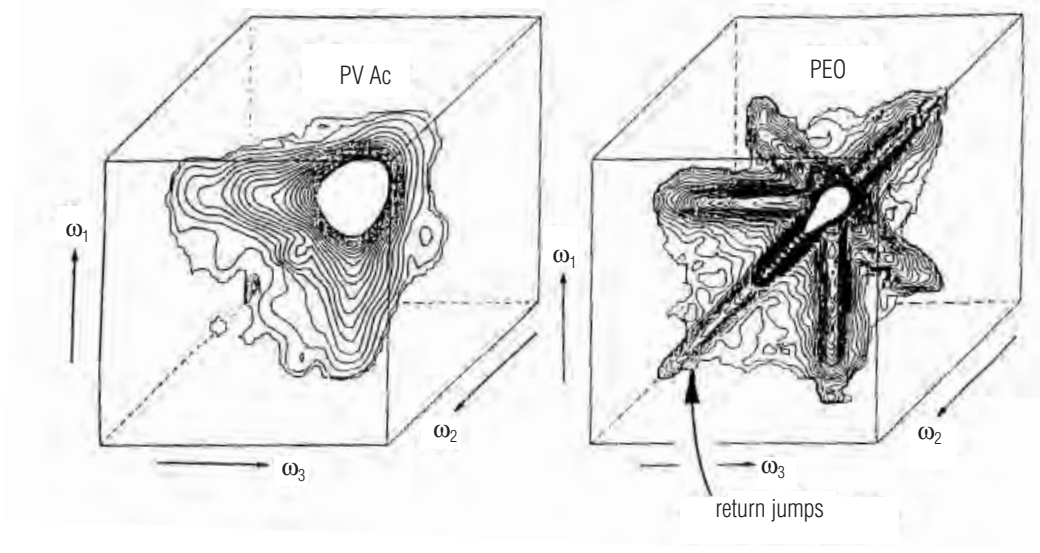

Fig. 10.4 Three-dimensional static ^{13}C exchange spectra of poly(ethyleneoxide) and poly(vinylacetate). (From K. Schmidt-Rohr and H.W. Spiess, *Multidimensional Solid-State NMR and Polymers*. Reproduced by permission of Academic Press, London.)

is a superposition of exponential functions, or is the correlation function intrinsically non-exponential, but spatially homogeneous?

In recent years, the application of double-quantum spectroscopy has provided additional ways to enhance resolution in multidimensional spectra. Multiple-quantum coherences cannot be observed directly, as discussed in Section 3.2.2. However, it is possible to indirectly detect their evolution in a two-dimensional experiment. Double- or, in general, multiple-quantum coherence is excited during the preparation period of the experiment. It then evolves during the evolution time, t_1. The remaining coherence is then converted during a mixing period into observable single-quantum coherence which is detected during t_2. Depending on the nature of the mixing period, exchange patterns for different types of molecular reorientation can be detected and analysed. Although the analysis is not as straightforward as for the exchange experiments described above, multiple-quantum experiments provide the same information with the additional advantage that no equivalent of the diagonal signal from non-exchanging spins is observed [**22**, **23**]. In an application to poly(butadiene) rubbers [**24**] the residual dipolar couplings in highly mobile elastomers have been used to determine local order parameters in these polymers. These local order parameters have been compared with predictions from theories of polymer dynamics.

10.4 Phase separation of polymers

Many polymers in practical applications are multi-component systems. The heterogeneities in polymers can be of a chemical or physical nature. Chemical hetereogeneities are found in copolymers, polymer blends and polymer composites. Copolymers consist of two or more types of repeat units along the polymer chain. These can have an alternating arrangement or form block structures. The length of the respective blocks strongly influences the properties of the polymer material, and so it is important to be able to study the structures of these materials. A block structure or *phase separation* is common when the equivalent homopolymers would not themselves mix. Processing parameters, such as temperature, pressure and rate of supply of reactants during the polymerization of copolymers, can influence and to some extent control the degree of phase separation.

Polymer composites contain filler material which usually consists of inorganic particles. These are used for the enhancement of mechanical properties such as tensile strength and stiffness. Physical heterogeneities in polymer materials usually result from differences in the molecular mobility between the different domains of semicrystalline polymers. Fillers in polymer composites can also be seen as causing heterogeous regions in the material in a similar way.

A simple but clear example of physical heterogeneity is poly(ethylene), perhaps the simplest possible polymer with a repeat unit of [~CH_2–CH_2~]. Because the bond

angle of the C–C bond is not 180° but about 105°, the repeat units cannot arrange in a linear manner. The polymer chains can be either in an all-*trans* conformation or in various combinations of *trans* and *gauche* conformations. These can be distinguished on a ^{13}C NMR spectrum because of the so-called *gamma-gauche* effect. This results in the carbons in the all-*trans* conformation giving a signal at 32 ppm while the different *gauche* conformations result in signals around 30 ppm, which can easily be distinguished in the ^{13}C NMR spectrum as depicted in Fig. 10.5. Only the all-*trans* conformation can form the crystalline structure. This implies a second possibility for the spectroscopic separation of the crystalline and the amorphous phase.

Because of the high mobility in the amorphous phase above the glass transition temperature, the dipolar coupling between the protons is partially averaged. This results in a two-component proton signal. As the chemical shift in proton spectra can be neglected, information is derived from the linewidth, as shown in Fig. 10.6(a).

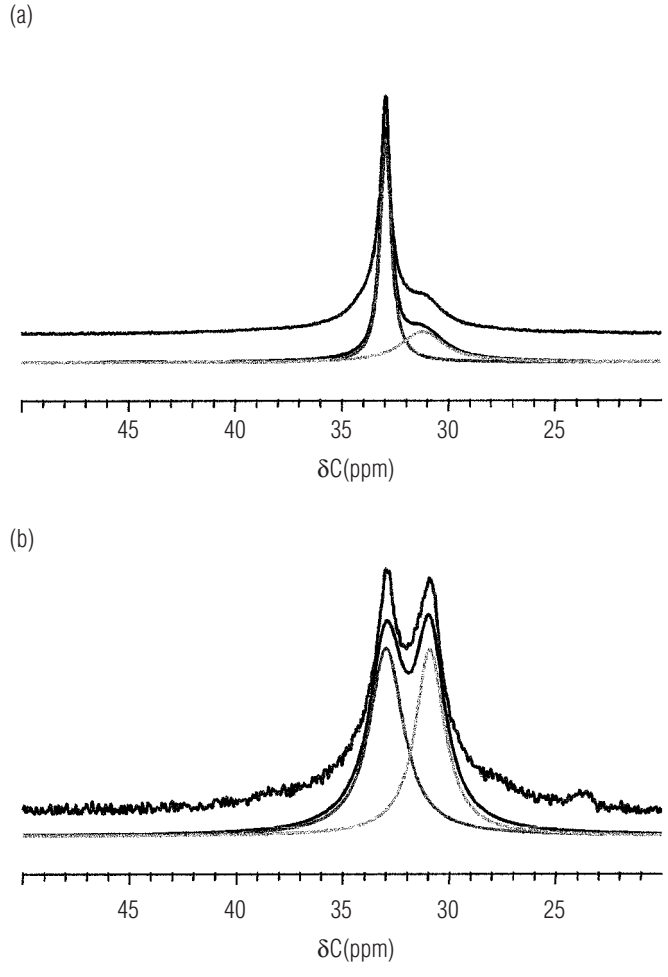

Fig. 10.5 ^{13}C spectra of poly(ethylene). (a) Acquired with cross-polarization from ^{1}H to ^{13}C which due to the partially motional averaging of the heteronuclear dipolar coupling in the amorphous part overestimates the crystalline part. (b) Direct ^{13}C polarization where the signal intensities are a measure of the relative content.

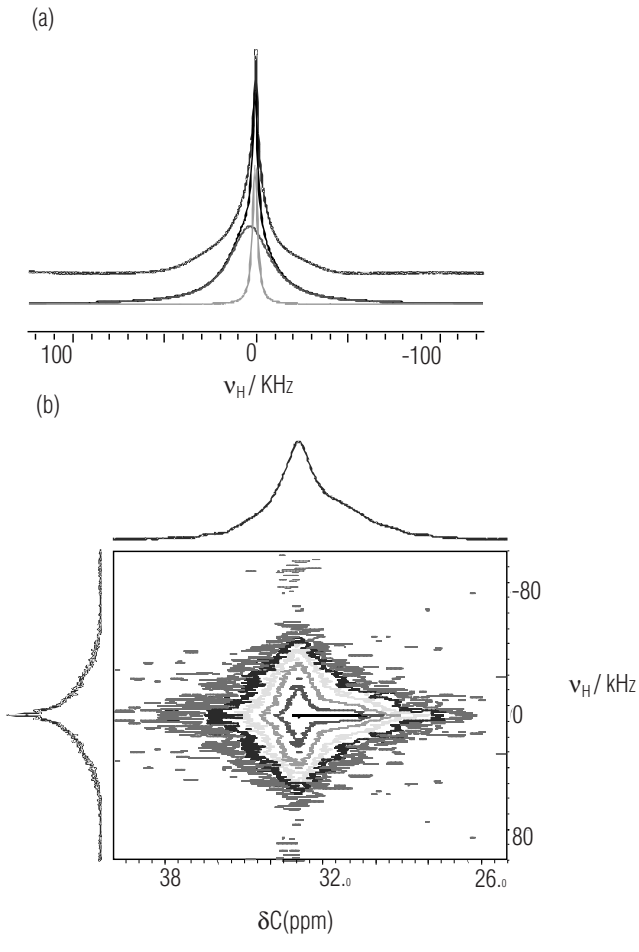

Fig. 10.6 (a) ^{1}H spectrum of poly(ethylene) with a decomposition into two subspectra for the crystalline and the amorphous portion respectively. (b) Wideline separation (WISE) spectrum of polyethylene which illustrates the correlation of information about conformation as obtained from the ^{13}C spectrum with the information on mobility as obtained from the ^{1}H spectrum.

The WISE experiment (WIdeline SEparation) is one of the simplest two-dimensional experiments (see Section 6.2.3). In this experiment, the ^{1}H lines are separated according to the chemical shift of the adjacent ^{13}C spins. A WISE spectrum for poly(ethylene) is shown in Fig. 10.6(b).

An alternative to the ^{1}H–^{13}C cross-polarization step in the WISE experiment is the application of Lee–Goldburg cross-polarization, which arranges for ^{1}H spin-lock to be at the magic angle in the rotating frame [**25**]. Under this condition, the heteronuclear ^{1}H–^{13}C dipolar coupling is retained and rapid magnetization transfer is facilitated. The advantage of the scheme is that the ^{1}H homonuclear dipolar coupling is suppressed under spin lock at the magic angle. Therefore, as a ^{1}H spin transfers its magnetization to a nearby ^{13}C spin, the ^{1}H spin magnetization is not 'topped up' by magnetization from the other surrounding ^{1}H, as it would be under normal spin-locking conditions. Under normal spin-locking conditions in the WISE experi-

ment, the ^{1}H–^{13}C cross-polarization contact time has to be kept short to ensure that the ^{13}C spins only receive magnetization from the directly bonded ^{1}H. This leads to only low cross-polarization intensities and so poor signal-to-noise ratios. However, with Lee–Goldburg cross-polarization, high selectivity is retained even at long contact times, which enhances the sensitivity [**26**].

A polymer blend is usually described as being miscible when it has a single glass transition temperature T_g. However, a single T_g does not exclude phase separation on a length scale in the order of 10 nm. It is therefore important to investigate the domain sizes present in any sample. Depending on composition and domain sizes, different NMR experiments are chosen for the determination of the domain sizes.

In favourable cases of phase separation, an NMR-sensitive nucleus is present in only one of the phases. Then polarization transfer experiments can be used to establish a measure of distance and thus of phase separation and domain sizes. One intriguing example is a blend of PVDF (poly(vinylidenefluoride)) and PMMA (poly(methylmethacrylate)), one of the rare examples where a fluoropolymer is miscible with a protonated polymer. In this case, the length scale being probed is rather low and cross-polarization and multiple cross-polarization techniques have been used to study the system. Because ^{19}F is only present in the PVDF part, any magnetization transfer from ^{19}F to ^{13}C spins of the PMMA is a signature of the proximity of the two materials [**27**, **28**] on a length scale of a few nanometres, as cross-polarization over greater distances is highly inefficient. A detailed quantitative analysis of the time evolution of the magnetization under cross-polarization can provide quantitative distance information [**29**]. In addition, double cross-polarization and depolarization experiments as depicted in Fig. 10.7 have been used to support this finding.

The most common technique to study heterogeneities in polymers is spin diffusion. Spin diffusion is the diffusion of coherent magnetization without diffusion of matter. It occurs among abundant spins (i.e. ^{1}H in polymers) via the agency of the dipolar coupling between homonuclear spins. Dipolar coupling is discussed in Section 1.4.2; as presented there, the dipolar hamiltonian for a homonuclear spin pair can be approximated as (in angular frequency units, rad s^{-1}):

$$\hat{H}_{\mathrm{dd}}^{\mathrm{homo}} = -\left(\frac{\mu_0}{4\pi}\right)\frac{\gamma^2\hbar}{r^3}(A + B) \tag{10.1}$$

where the terms A and B are defined in Section 1.4.2, Equation (1.108); r is the internuclear distance.

The interesting term here is the B term, containing the so-called flip-flop term between the two coupled spins, I and S:

$$B = -\frac{1}{4}[\hat{I}_+\hat{S}_- + \hat{I}_-\hat{S}_+](3\cos^2\theta - 1) \tag{10.2}$$

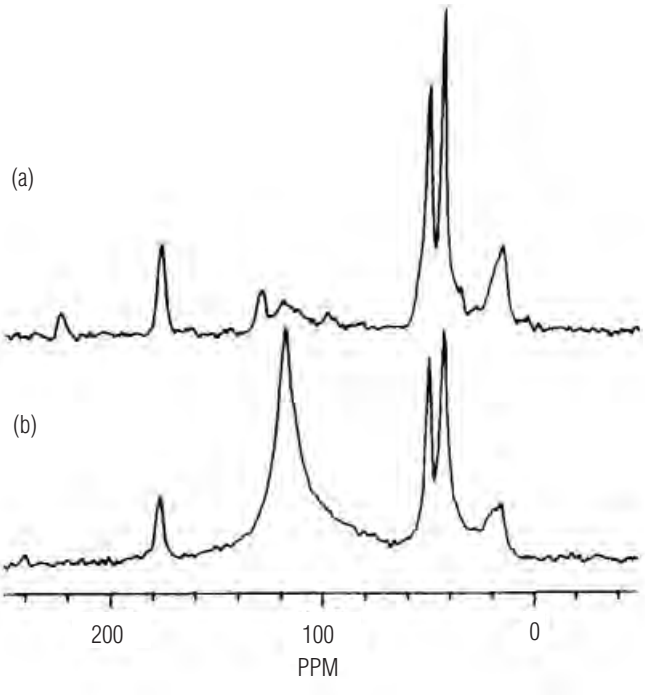

Fig. 10.7 Double cross-polarization experiments applied to a blend of poly(methylmethacrylate) (PMMA) and poly(vinylidenefluoride) (PVDF). (a) ^{19}F–^{13}C cross-polarization, magic-angle spinning (CPMAS) spectrum of 60/40 PMMA/PVDF blend. (b) ^{19}F–^{1}H–^{13}C double cross-polarization spectrum with a short 400 μs ^{19}F–^{1}H contact time to select the protons in the vicinity of fluorine. (Reprinted with permission of Maas et al., *J. Chem. Phys.* **95** (1991) 4698–4708; © 1991 American Institute of Physics.)

If the two spins have opposite spin orientation, both spins simultaneously change their orientations under the action of term B (a so-called *flip-flop*) and thus conserve the net magnetization. For a spin pair, this actually leads to an oscillation of the coherent magnetization between the two spins. In the case of a multispin system, after the first flip-flop process between a spin pair, there are then possibilities of further flip-flop processes between the same spin pair *or* between one of those two spins and another spin. This leads to the coherent magnetization being smeared out as depicted schematically in Fig. 10.8. Because the time evolution of the spatial distribution of the magnetization at short times can be described by a diffusion equation, this process is called spin diffusion. It is described by

$$\frac{\partial M(r,t)}{\partial t} = D\frac{\partial^2 M(r,t)}{\partial^2 t} \tag{10.3}$$

D denotes the spin diffusion constant. This constant in principle can be derived from the strength of the dipolar coupling. However, molecular motion lowers the effective dipolar coupling and thus the spin diffusion constant. This is particularly problematic in systems where one component is rigid and one is mobile, as spin diffusion can be severely restricted in the mobile component. The generally accepted value for the spin diffusion constant for ^{1}H is the one found experimentally by Spiess et al. [30] in a series of block copolymers of poly(styrol) and poly(methyl-

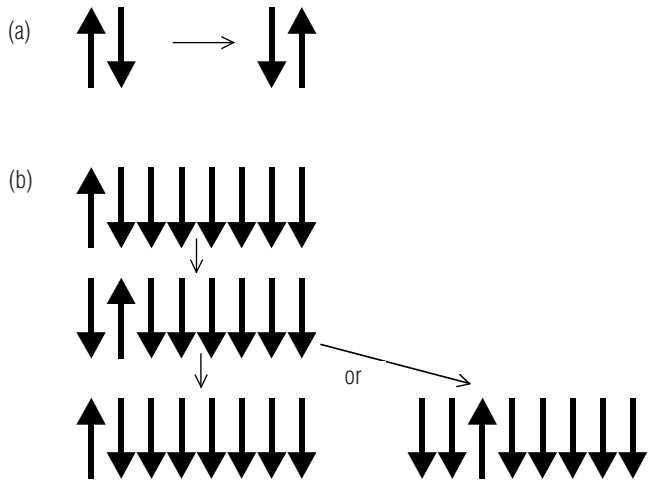

Fig. 10.8 Schematic of the principle of spin diffusion. (a) In a two-spin system the flip-flop term in the dipolar hamiltonian leads to a periodic exchange of magnetization between the coupled spins. (b) In a multispin system (here shown in one dimension for clarity) after the first flip-flop there are two possibilities for magnetization exchange. In three dimensions, this type of process leads to an incoherent exchange of magnetization.

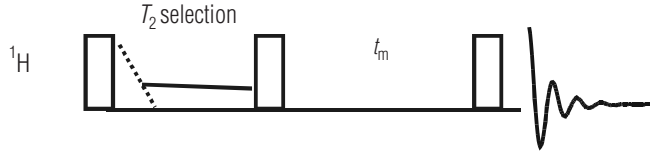

Fig. 10.9 Pulse sequence of the Goldman–Shen experiment. The first pulse selects magnetization based on T_2, contributions with a short T_2 decay before storage of the selected magnetization along $\mathbf{B}_0$ by the second pulse. During the time between the second and third pulses, spin diffusion takes place.

methacrylate) by a comparison with electron microscopy and small-angle X-ray scattering, with a value of $0.8\,\mathrm{nm^2\,ms^{-1}}$.

Spin diffusion is a phenomenon that is also common in liquid systems, but is much more pronounced in solids, particularly for ^{1}H spins in organic systems, due to much stronger effective dipolar coupling. It is often the source of experimental problems, because it leads to a smearing out of magnetization profiles created by special excitation techniques. However, this effect can be put to use in polymers for the determination of domain sizes. The basic idea is illustrated in the so-called Goldman–Shen experiment as depicted in Fig. 10.9. Although there are more elaborate versions for special applications, the basic features are common in all. In a first step, a ^{1}H magnetization gradient is established due to some criterion that allows the different phases or domains to be distinguished. In the second step, the return to an equilibrium magnetization profile is monitored indirectly, via a series of spectra detected during a third period of the experiment after different mixing times. From the time dependence of the build up of the equilibrium magnetization, information about the domain sizes can be extracted. The shape of the build-up curve contains information on the phase structure, i.e. the basic shape of the different domains. In the case of lamellar phases, the spin diffusion can only take place

in one dimension, while in a case where spherical domains are embedded in a matrix, the diffusion of the magnetization occurs in three dimensions simultaneously and is thus faster. To take these geometrical considerations into account, a constant factor describing the dimensionality of the diffusion process is introduced into Equation (10.3).

In simple cases, where the system consists of just two phases, the initial, linear, rate of magnetization build up in the initially demagnetized phase can be used to determine domain sizes. A more accurate determination is derived from simulations of the build up. This simplified approach breaks down if the system contains an interfacial region. Then, the initial part of the magnetization build up deviates from the simplified diffusion law represented by Equation (10.3). A third phase has to be taken into account in the simulation of the magnetization equilibration curve, and the results can be used to estimate the thickness of this interface. A good example where this occurs is semicrystalline poly(ethylene), where the selection of the mobile amorphous part can be achieved by the dipolar filter. The resulting build up in the crystalline part is monitored via cross-polarization to ^{13}C where the crystalline and amorphous parts are easily distinguished by their respective chemical shifts. The magnetization built up strongly deviates from a linear initial rate behaviour due to the presence of an interfacial region.

The principle of high-resolution solid-state NMR detection for spin diffusion experiments has been used in a two-dimensional experiment involving CRAMPS (Combined Rotation and Multiple-Pulse Sequence) [**31**]. Crosspeaks in this experiment indicate spin exchange, spin diffusion and therefore proximity. For a quantitative analysis a variation of the mixing time in the experiment is necessary. This experiment uses the same principle as the radio-frequency driven recoupling (RFDR) experiment [**32**].

Further developments of the Goldman–Shen experiment include more elaborate filter techniques for establishing the initial magnetization gradient and high-resolution solid-state NMR detection methods, most often via the detection of a ^{13}C magic-angle spinning spectrum after cross-polarization from ^{1}H to ^{13}C [**30**], but CRAMPS detection of ^{1}H has been used as well [**33**]. For the filtering, either structural or mobility criteria can be used. In the original Goldman–Shen experiment, the magnetization gradient is established based on the differences in the proton line width, or decay times of the proton FID. A similar method is applied in the so-called dipolar filter, which is basically a multiple-pulse sequence averaging dipolar coupling and chemical shift anisotropy for the ^{1}H spins to zero. Such a sequence is effective only if it is applied with a cycle time that is short compared to the inverse of the linewidth; for longer cycle times, all magnetization is destroyed. In a polymer system, the mobile regions have relatively narrow ^{1}H linewidths due to the partial averaging of the dipolar coupling by molecular motion, while the rigid component has a much larger ^{1}H linewidth. Thus to select the mobile component of a polymer system, the multiple-pulse sequence recycle time is adjusted so that magnetization

from the rigid component is destroyed, while that from mobile regions is retained. Therefore, efficient averaging and line narrowing is achieved for the mobile part, while the magnetization of the rigid part is suppressed. Other selection techniques are based on the differences in the proton chemical shift [**34**]. Because of the small distribution of proton chemical shift, high-resolution solid-state NMR has to be applied in these experiments. Based on CRAMPS in the rotating frame, a situation is generated where the magnetization of one component is along the z axis while the magnetization from other components are in or near the x–y plane. If the multiple-pulse irradiation is terminated at this point, the magnetization in the x–y plane will rapidly decay away under the strong proton–proton dipolar coupling. A subsequent 90° pulse then allows the z magnetization to be 'read'. The selection can be further facilitated by appropriate phase cycling of the read pulse to ensure that only the z magnetization component contributes to the final signal. Other modifications to the basic experiment include high-resolution detection via CRAMPS. The most efficient way uses ^{13}C cross-polarization, magic-angle spinning in the detection. In the ^{13}C cross-polarization, magic-angle spinning spectrum, the different phase components can easily be distinguished and the magnetization build up can be monitored for the different components separately, much more easily than in the ^{1}H-detected experiment. An application to polyethylene is shown in Fig. 10.10. An initial ^{1}H magnetization gradient is created using a dipolar filter adjusted so that only magnetization in the mobile amorphous regions remains. The ^{1}H magnetization then diffuses during a mixing time and is finally transferred via cross-

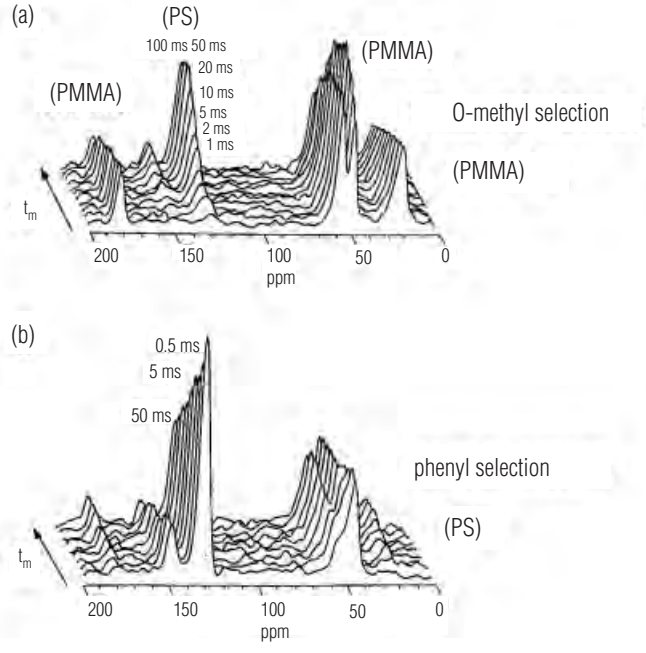

Fig. 10.10 Example of spin diffusion in a block copolymer of poly(methylmethacrylate) PMMA and poly(styrol) PS. The initial magnetization gradient is achieved by a ^{1}H chemical shift filter with (a) selection of the protons in the methoxy group in PMMA and (b) of the phenyl proton in PS. In both cases after the spin diffusion period, the remaining magnetization is transferred to ^{13}C via cross-polarization and detected under magic-angle spinning and TOSS (see Section 2.2).

polarization to the ^{13}C magnetization that is detected. The experiment is repeated for several mixing times to generate a detailed picture of the ^{1}H spin diffusion process. The data so measured can be analysed in the time domain or, equivalently, in the frequency domain. The time domain analysis has advantages in data handling, because the effect of the noise is under better control [**35**, **36**]. However, in many cases, it appears simpler to fit the intensities of the signals in the frequency domain. This is especially true in cases where there are well-resolved spectra. Alternatively, a multi-component time domain analysis can be applied.

Finally, it should be mentioned that the effect of T_1 during any spin diffusion measurement should be taken into account [**37**]. In systems where T_1 of the two components does not differ too much, the T_1 decay during the spin diffusion period can be monitored in a control experiment. In the case of larger differences of T_1 between the respective components, the difference of the decay rates of the components could lead to contributions to the spin diffusion curves which have a similar form to spin diffusion. In these cases more elaborate experimental schemes have to be applied, in which the Goldman–Shen experiment is performed so as to monitor separately the evolution of magnetization stored in the z and $-z$ directions. In the case of longitudinal (T_1) relaxation, the time evolution of these two magnetizations is different and this allows the separation of T_1 and spin diffusion effects [**38**].

10.5 Oriented polymers

Most polymers have a long chain structure which disposes them to have different properties in the chain direction and in the directions perpendicular to the chain. Macroscopic orientation is induced in many polymers as a result of the polymer processing. The large tensile strength of fibres along the chain is a result of parallel orientation of the polymer chains along the fibre axis. Extrusion-moulded polymers carry preferential molecular orientations as well. In many cases this is undesirable because at high degrees of molecular orientation, the polymers become brittle in directions perpendicular to the orientation.

Liquid-crystalline polymers contain mesogenic groups either in sidechains or in the main chain [**39**]. Such polymers provide the possibility of achieving molecular alignment through either electric or magnetic fields or through the application of mechanical forces in the liquid-crystalline phase. The order generated in the liquid-crystalline phase can be retained in the solid material, for instance, after cooling into the solid phase after orienting in the nematic phase for thermotropic liquid crystallites. This gives the extra possibility of adjusting the orientations of polymers either during the synthesis of the polymer or in subsequent processing. Liquid-crystalline polymers that have mesogenic groups in a sidechain have the particular advantage that the polymer main chain can be decoupled from the oriented mesogenic groups by means of a flexible spacer [**40**]. This 'decoupling' allows the full

orientational ordering of the mesogenic groups in the external field without interference of long-chain effects like entanglement of the polymer.

While scattering techniques like X-ray diffraction are the most appropriate techniques to characterize highly oriented systems, NMR seems to be the appropriate way to characterize weakly oriented ones. In perfectly ordered systems, the dipolar splitting in ^{1}H NMR spectra can be used to characterize the molecular orientation. However, perfect alignment in all structural elements is rarely feasible. Therefore, a spectroscopic separation of the oriented structures from non-oriented ones is needed.

Where selective deuteration of the functional groups of interest is possible, ^{2}H NMR provides an effective way for the selective study of the oriented part of the macromolecules (see Chapter 11). This is effective and provides detailed information about orientation distributions with respect to one single angle [**41**]. The same information is accessible through selective ^{13}C enrichment. In this case, the spectrum is dominated by a single ^{13}C chemical shift tensor. The position of the line in the ^{13}C NMR spectrum directly yields the orientation of the ^{13}C chemical shift tensor with respect to $\mathbf{B}_0$. However it should be remembered that isotropic labelling requires a molecular change which might result in changes in the material's properties.

In order to interpret the results from these experiments in terms of molecular orientations, one has to relate the principal axis frame of the nuclear spin interaction to some macroscopic sample frame. A molecular frame of reference is described by the *director* axis defining the molecular orientation. The principal axis frame of the nuclear spin interaction tensor (^{13}C chemical shift or ^{2}H quadrupole coupling) does not in general coincide with this frame. A sample frame is chosen to represent the sample orientation. Finally the NMR experiment is carried out in the laboratory frame, possibly under sample spinning, which adds a time-dependence to the molecular orientation. All this means that several coordinate transformations have to be taken into account for simulation of spectra (see Chapter 11 for further details).

For quantitative treatment, the distribution of molecular orientations is expanded in terms of Legendre polynomials [**42**]. For each Legendre polynomial, a subspectrum can be calculated. Fitting a weighted sum of such subspectra to the experimental spectrum finally yields the expansion of the orientation distribution in terms of Legendre polynomials.

^{13}C cross-polarization, magic-angle spinning (CPMAS) experiments have been employed in many structural studies because of the resolution in terms of structural elements that can be achieved. In conjunction with other experimental techniques which provide sensitivity to orientation, ^{13}C CPMAS spectra can provide the selectivity and thus enable the site-selective measurement of orientations. In magic-angle spinning experiments, the sample rotation introduces an additional time-dependence in molecular orientation relative to the static magnetic field $\mathbf{B}_0$, providing the sample

is placed in the rotor in such a way that the molecular orientation axis is not aligned with the rotor axis. As discussed in Section 2.2, sample spinning at a rate lower than the chemical shift anisotropy results in a set of spinning sidebands separated by the sample rotation frequency, ν_R, in the spectrum. These spinning sidebands are in phase when the sample is isotropic or if the molecular orientation distribution is such that there are equal populations of orientations with $\pm\gamma$, where γ is the azimuthal angle describing the molecular orientation (or, more precisely, the orientation of the nuclear spin interaction principal axis frame) with respect to the rotor axis frame (see Section 2.2) for details). This condition is not fulfilled in the case of an oriented sample where the director orientation axis is not parallel to the rotor axis. In this case, the observed spectrum varies with initial phase of the rotor during the detection of the signal. This can be conveniently probed when the experiment is triggered with the optical signal from the black-and-white marking on a rotor, usually used to determine the sample rotation frequency as depicted schematically in Fig. 10.11. A series of such spectra is depicted in Fig. 10.12. As already mentioned, such spectra require an optical trigger to indicate a particular point in the rotor rotation cycle. Following the trigger, a variable evolution period is inserted prior the excitation, which is incremented to one rotor period. The spectra depicted in Fig. 10.12 are taken from one such series. A clear phase modulation can be observed However, a simultaneous quantitative analysis of the phase modulations for different peaks in the spectrum, given they represent different degrees of orientation, appears to be impossible. The method of choice for the analysis is the a

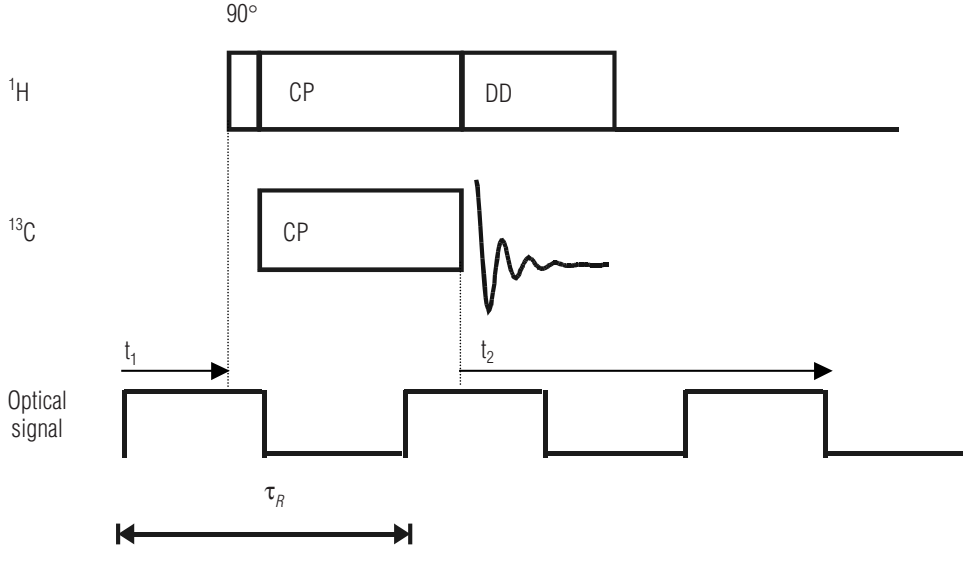

Fig. 10.11 Pulse sequence for the rotor-synchronized two-dimensional experiment to probe molecular orientations. An evolution time prior to the first pulse allows the rotor position to reach a certain point prior to acquisition of the FID.

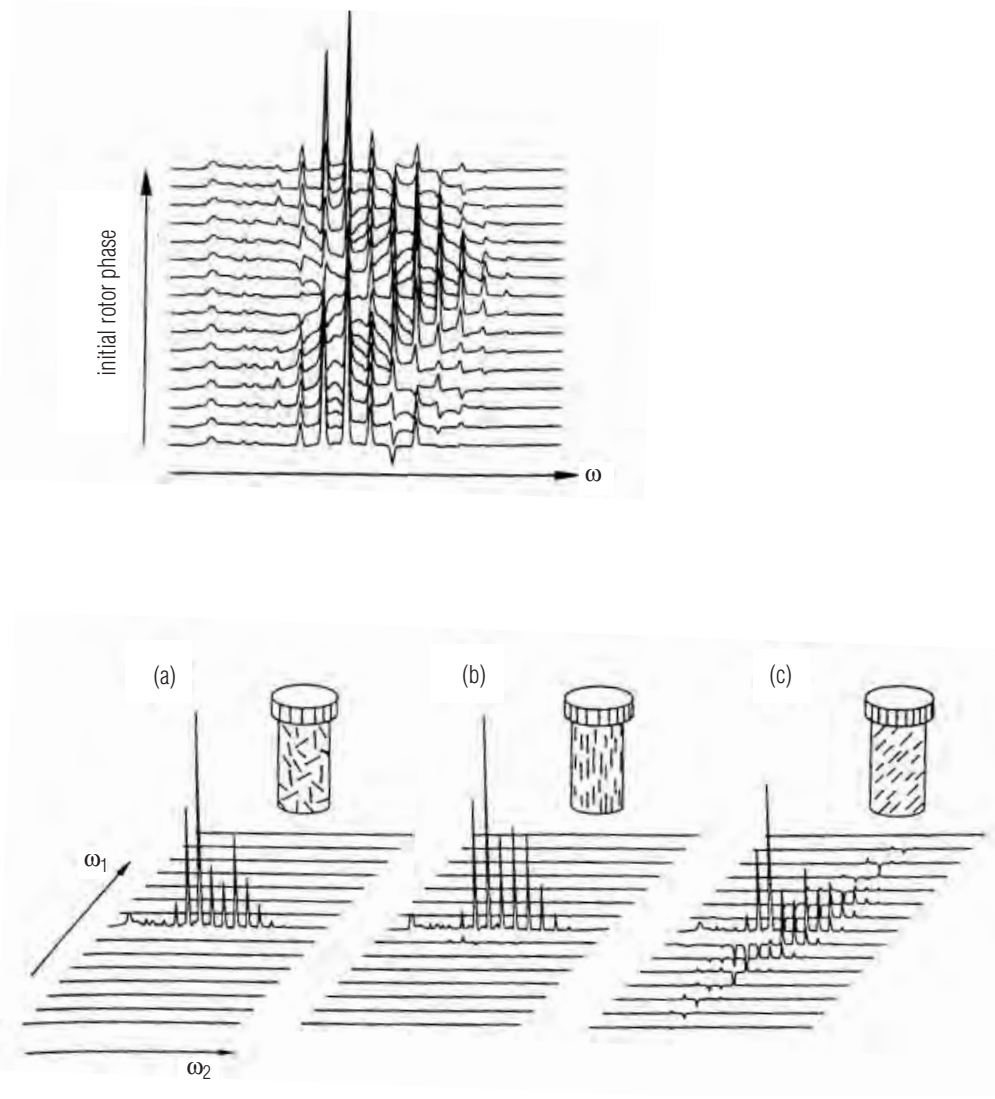

Fig. 10.12 Top: Series of rotor-synchronized ^{13}C spectra of highly uniaxially oriented fibres for different rotor phases (t_1). Below are examples of two-dimensional sideband patterns obtained after Fourier transformation along t_1 of datasets such as that at the top of the figure: (a) for an isotropic mixture of fibres; (b) for fibres uniaxially oriented parallel to the rotor axis; and (c) for an orientation of about 45° with respect to the rotor axis. (From K. Schmidt-Rohr and H.W. Spiess, *Multidimensional Solid-State NMR and Polymers*. Reproduced by permission of Academic Press, London.)

second Fourier transformation with respect to the evolution time t_1. After this Fourier transformation a two-dimensional sideband pattern is observed, shown in Fig. 10.12. Because there is no decay of the signal in t_1, the linewidth in the f_1 dimension of the two-dimensional spectrum vanishes. A simple argument can be used to understand the signature of molecular orientation in such a two-dimensional spectrum. For an isotropic sample, there would be no difference in the observed spectra

collected for different t_1. Thus following the second Fourier transformation in t_1, intensity would be observed only at $\omega_1 = 0$. In contrast, for an oriented sample, the spectra for different t_1 differ with respect to the initial rotor phase. As a result, after the second Fourier transformation intensity is observed for $\omega_1 \neq 0$ as well [**43**]. The intensity off the centre slice (at $\omega_1 = 0$) is a measure of the molecular orientation. This experiment can be combined with a technique to separate the spinning sidebands by sideband order for better resolution. This leads to a three-dimensional experiment which has been applied to a liquid-crystalline sidechain polymer to elucidate the order parameter for each individual functional group [**44**, **45**]. Although this experiment requires an experiment time of nearly three days, it is efficient because all order parameters can be measured simultaneously. Figure 10.13 shows a three-dimensional spectrum for a liquid-crystalline sidechain polymer. The data reveal a gradient of orientation (a lowering of the order parameters) along the spacer from the mesogenic group to the main chain.

In addition to the above-described uniaxial molecular orientations, polymers may acquire biaxial orientation, as a result of processing like extrusion moulding. To probe such orientations, a two-dimensional exchange experiment has been developed, in which a macroscopic reorientation of the whole sample is performed during the mixing time [**46**]. The full orientation distribution has been mapped for an industrial sample, drawn PET (poly(ethylene terephthalate) film, using a three-dimensional version of this experiment. While the chain orientations with respect to the film plane are confined to 15° FWHM (full width at half maximum), the orientation distribution in the plane is much wider with a FWHM of 90°. This implies that the drawing results in a biaxial orientation distribution function with different degrees of orientation [**47**].

In a recent development, the orienting process has been studied for liquid-crystalline polymers [**48**]. The electric field that causes the orienting is supplied synchronously with the NMR experiment. For a reversible process, where molecular orienting can be repeated continuously, indirect detection as in a two-dimensional experiment is possible. This means that the orientation process is repeated and a series of NMR spectra are detected with an incremented delay between the start of the orientation process and the beginning of the NMR experiment. From such a series of spectra, the time development of the orientation process can be deduced, even when the process of orientation is faster than the time taken to record a FID.

10.6 Fluoropolymers

Fluoropolymers are a special group of polymers because of their unique combination of properties. These properties include high-temperature stability, chemical resistivity, particular dielectric properties and low friction coefficient. The chemistry

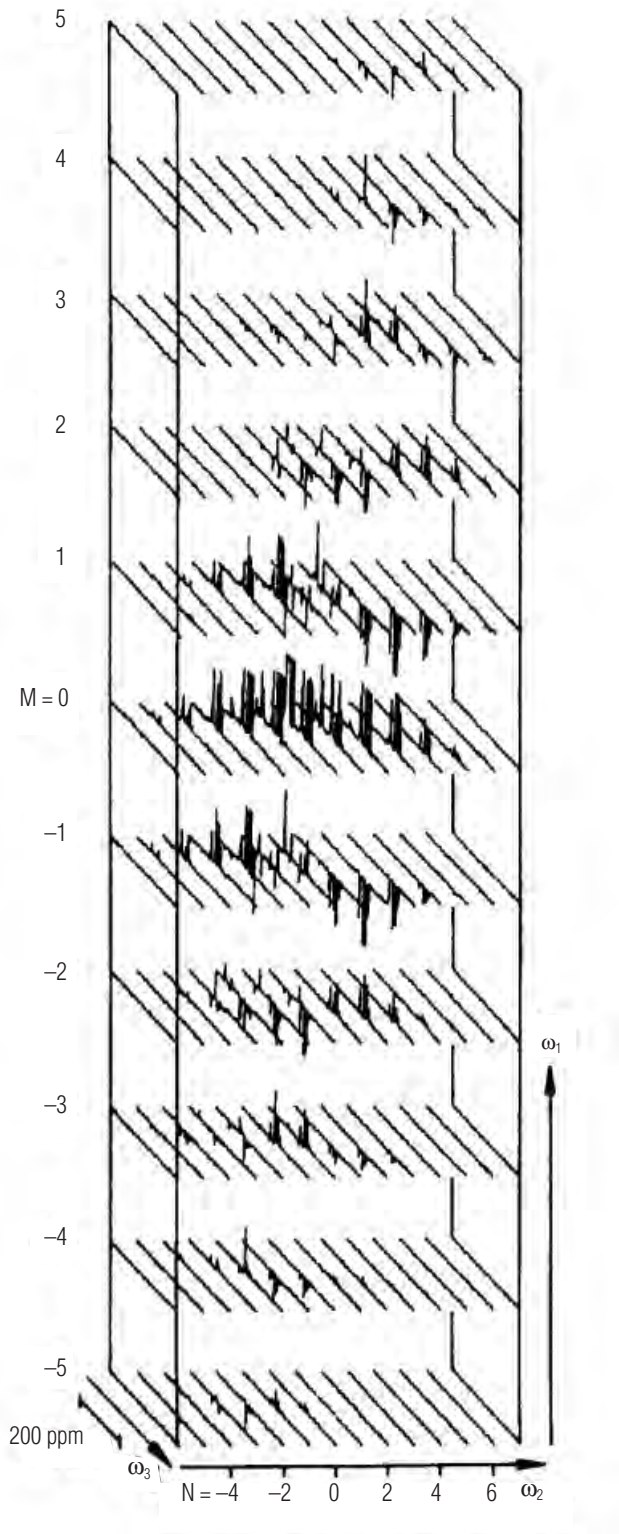

Fig. 10.13 Three-dimensional rotor-synchronized magic-angle spinning spectrum of a liquid crystalline sidegroup polymer which separates the spinning sidebands by their order in one dimension, by orientation in the second and chemical shift in a third dimension. (Reprinted with permission of Titman et al., *J. Chem. Phys.* **98** (1993) 3816–26; © 1993 American Institute of Physics.)

involved in the synthesis of fluoropolymers is somewhat unique as well. The most common fluoropolymer is PTFE (polytetrafluoroethylene); its surface properties lead to a variety of applications. Limitations arise from its mechanical properties and the fact that it cannot be melt processed. To overcome these limitations, copolymers are synthesized.

There are unique possibilities for NMR characterization of these polymers because they naturally contain ^{19}F, which appears to be the ideal probe nucleus for NMR. A natural abundance of the NMR-active isotope of 100% and a high magnetogyric ratio leads to a receptivity second only to that of the proton. In addition, ^{19}F has a large distribution of chemical shifts (2000 ppm in total, about 400 ppm for organic fluorinated materials). This implies a high sensitivity of the spectrum to the chemical environment of the nucleus under study. ^{19}F NMR combines the possibilities of chemical shift anisotropy as utilized in ^{13}C spectra and the strong dipolar coupling as utilized in ^{1}H spectra for the characterization of fluoropolymers. This, on the other hand, means that both effects have to be taken into account in the experimental setup. If this is done carefully, all the techniques described previously for ^{1}H and ^{13}C can be applied to ^{19}F NMR for the characterization of fluoropolymers as well.

Using high-rate magic-angle spinning in conjunction with increased molecular motion from sample heating permits a sequence analysis in fluorinated copolymers via the ^{19}F chemical shift [**49**, **50**]. Although *J*-coupling in the spectra of the polymers is invisible, the sensitivity of the ^{19}F chemical shift provides a detailed insight into the polymeric structure from which a sequential assignment is possible.

For the study of semicrystalline fluoropolymers, static multiple pulse experiments which average the dipolar coupling and scale chemical shift have proved to be suitable. Above the glass transition temperature of the amorphous region, molecular motion leads to averaging of the chemical shift anisotropy, a narrow line is observed. The motion is hindered in the crystalline part, and so a chemical shift powder pattern is observed in the ^{19}F multiple-pulse experiment. A comparison with simulated spectra permits the determination of the degree of crystallinity in the samples [**51**]. A temperature-dependent study provides the possibility of assigning different relaxation processes known from other studies to specific molecular motions.

One of the interests in fluoropolymers originates from their dielectric properties. A partially fluorinated polymer of wide practical application is PVDF (poly(vinylidenefluoride)), which is probably the simplest polymer that contains protons and fluorine. It exists in two basic modifications, the helical β form and the α form, which has an all-*trans* conformation. In this form, the polymer chain carries a resulting dipole moment which can be used for macroscopically poling the sample. In order to achieve high-resolution ^{19}F spectra from samples containing abundant protons, both the homonuclear and the heteronuclear dipolar coupling has to be averaged out [**52**, **53**].

The isotropic ^{19}F chemical shift strongly depends on packing and conformation within the polymer material. This provides an effective means of studying conformations, as depicted in Fig. 10.14, where four signals can be assigned to ^{19}F nuclei in a CF_2 environment. Molecular motion in the amorphous part leads to an averaged chemical shift in the signal at –92 ppm. The signals at –82 ppm and –99 ppm originate from fluorine in the crystalline part of the polymer. The *gamma-gauche* effect [**6**] leads to two separate signals for the inequivalent fluorine nuclei. The signal at –115 ppm originates from so-called head-to-head polymerization, two adjacent CF_2 groups. Two-dimensional spin exchange experiments [**32**] on PVDF result in strong crosspeaks between the two signals of the crystalline part and between the signals from the amorphous part and the head-to head polymerizations. No spin exchange is observed between the head-to-head polymerizations and the crystalline part, which proves that the imperfections are located in the amorphous part of the polymer [**54**]. On the other hand, ^{19}F relaxation times strongly depend on molecular mobility which provides the possibility of studying structure and mobility simultaneously [**55**]. In a similar manner to the correlation of mobility information from proton spectra with structural data from ^{13}C spectra, there is the possibility of applying the same approach to ^{19}F [**56**].

To overcome the problems associated with the low compatibility of PTFE with other material modification, procedures like plasma treatment and radiation modification are carried out. As opposed to polyethylene, which under irradiation exhibits a strong tendency of crosslinking [**57**], the dominant process in fluoropolymers under irradiation is chain scission. However, under inert conditions in the melt, PTFE forms crosslinks as well. Recent NMR investigations on such materials provide evidence for the formation of crosslinks [**58**, **59**]. The content of branching points is significantly higher than the content of possible end groups, a finding that can only be explained by the existence of crosslinks, i.e. branches that connect two main chains. In this case the existence of crosslinks has been proved directly from structural data rather than indirectly from changes in the molecular mobility.

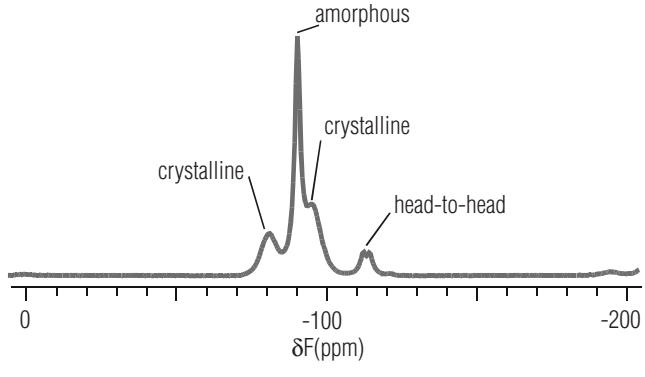

Fig. 10.14 ^{19}F spectrum of PVDF acquired under magic-angle spinning at a rate of 32 kHz. The signals at –88 ppm and –99 ppm originate from the crystalline part of the polymer. Because PVDF in this β-form forms a helix, one of the fluorines in the CF_2 group has the next CF_2 group in a *trans* position and the other one has the next CF_2 group in a *gauche* position. The signal at –92 ppm originates from the amorphous part and the one at –115 ppm from head-to-head polymerizations, two neighbouring CF_2.

References

1. P.J. Flory, *Principles of Polymer Chemistry*, Cornell University Press, Ithaca (1953).
2. J. Brandrup and E.H. Immergut (Eds.), *Polymer Handbook* (3rd edn.), John Wiley & Sons, New York–Chichester–Brisbane (1989).
3. R.R. Ernst, G. Bodenhausen and A. Wokaun, *Principles of Nuclear Magnetic Resonance in One and Two Dimensions*, Oxford University Press, Oxford (1987).
4. K. Schmidt-Rohr and H.W. Spiess, *Multidimensional Solid-State NMR and Polymers*, Academic Press, London (1994).
5. G. Newkome, C.N. Moorefield and F Vögtle, *Dendritic Molecules – Concepts, Syntheses, Perspective*, VCH, Weinheim (1996).
6. A.E. Tonelli and F.C. Schilling, *Acc. Chem. Res.* **14** (1981) 233.
7. V.J. McBriety and K.J. Packer, *Nuclear Magnetic Resonance of Solid Polymers*, Cambridge University Press, Cambridge (1993).
8. F.A. Bovey, *Chain Structure and Conformation of Macromolecules*, Academic Press, New York (1982).
9. R. Born, H.W. Spiess, W. Kutzelnigg, U. Fleischer and M. Schindler, *Macromol.* **27** (1994) 1500.
10. U. Haeberlen, *High-resolution NMR in Solids*, supplement 1 in *Advances in Magnetic Resonance*, Academic Press, New York, San Francisco, London (1976).
11. B.C. Gerstein and C.R. Dybovski, *Transient Techniques in NMR of Solids*, Academic Press, London (1985).
12. S. Hafner and H.W. Spiess, *Concepts Magn. Reson.* **10** (1998) 99.
13. A. Bax, R. Freeman and T.A. Frenkiel, *J. Am. Chem. Soc.* **103** (1981) 2102.
14. I. Schnell, S.P. Brown, H.Y. Low, H. Ishida and H.W. Spiess, *J. Am. Chem. Soc.* **120** (1998) 11784.
15. K. Saalwächter, R. Graf, D.E. Demco and H.W. Spiess, *J. Magn. Reson.* **139** (1999) 287.
16. R. Kimmich, *NMR Tomography, Diffusometry, Relaxometry*, Springer, Berlin (1997).
17. M. Lindner, A. Höhener and R.R. Ernst, *J. Chem. Phys.* **73** (1980) 4959.
18. M.G. Munnowitz and R.G. Griffin, *J. Chem. Phys.* **76** (1982) 2848.
19. K. Schmidt-Rohr and H.W. Spiess, *Macromol.* **24** (1991) 5288.
20. U. Tracht, A. Heuer, S.A. Reinsberg and H.W. Spiess, *Appl. Magn. Reson.* **17** (1999) 227.
21. U. Tracht, M. Wilhelm, A. Heuer and H.W. Spiess, *J. Magn. Reson.* **140A** (1999) 460.
22. K. Schmidt-Rohr, W. Hu and C. Boeffel, *Macromol.* **32** (1999) 1611.
23. H. Kaji and K. Schmidt-Rohr, *Macromol.* **33** (2000) 5169.
24. R. Graf, D.E. Demco, S. Hafner and H.W. Spiess, *Solid-State NMR* **12** (1998) 139.
25. M. Lee and W.I. Goldburg, *Phys. Rev.* **140A** (1965) 1261.
26. S. Ray, V. Ladizanski and S. Vega, *J. Magn. Reson.* **135** (1998) 427.
27. C.H. Klein, W.E.R. Maas, W.S. Veemann, G.H. Werumens Bunning and J.M.J. Vankan, *Macromol.* **23** (1990) 406.
28. W.E.J.R. Maas, W.A.C. van der Heijden and W.S. Veeman, *J. Chem. Phys.* **95** (1991) 4698.
29. D.E. Demco, J. Tegenfeld and J.S. Waugh, *Phys. Rev.* **11B** (1975) 4133.
30. J. Clauss, K. Schmidt-Rohr and H.W. Spiess, *Acta Polymer.* **44** (1993) 1.
31. P. Caravatti, P. Neuenschwander and R.R. Ernst, *Macromol.* **18** (1985) 119.
32. A.E. Bennett, J.H. Ok and R.G. Griffin, *J. Chem. Phys.* **96** (1992) 8624.
33. P. Caravatti, P. Neuenschwander and R.R. Ernst, *Macromol.* **19** (1986) 1889.
34. K. Schmidt-Rohr, J. Clauss and H.W. Spiess, *Magn. Reson. Chem.* **28** (1990) 3.
35. A.M. Kenwright and B.J. Say, *Solid-State NMR* **7** (1996) 85.
36. B.J. Say and A.M. Kenwright, in R.N. Ibbett (Ed.), *NMR Spectroscopy of Polymers*, Blackie, Glasgow (1993).
37. K.J. Packer, I.J.F. Poplett and M.J. Taylor, *J. Chem. Soc. Faraday Trans.* 1, **84** (1988) 3581.
38. M. Geppi, R.K. Harris, A.M. Kenwright and B.J. Say, *Solid-State NMR* **12** (1998) 15.
39. A. Ciferri (Ed.), *Liquid Crystallinity in Polymers, Principles and Fundamental Properties*, VCH, Weinheim (1991).
40. C.B. McArdle (Ed.), *Liquid Crystalline Side Group Polymers*, Blackie, Glasgow (1988).

41. H.W. Spiess, in *Developments in Oriented Polymers* (ed. I.M. Ward), Applied Science, London (1987).
42. V. McBriety, *J. Chem. Phys.* **61** (1974) 872.
43. G.S. Harbison and H.W. Spiess, *Chem. Phys. Lett.* **124** (1986) 1206.
44. J.J. Titman, S. Féaux de Lacroix and H.W. Spiess, *J. Chem. Phys.* **98** (1993) 3816.
45. Titman, J.J., D.-L. Tzou, S. Féaux de Lacroix, C. Böffel and H.W. Spiess, *Acta Polym.* **45** (1994) 204.
46. K. Schmidt-Rohr, M. Hehn, D. Schaefer and H.W. Spiess, *J. Chem. Phys.* **97** (1992) 2247.
47. B.F. Chmelka, K. Schmidt-Rohr and H.W. Spiess, *Macromol.* **26** (1993) 2282.
48. P. Holstein, J. Rauchfuss, M. Winkler, G. Klotzsche and D. Geschke, *Solid-State NMR* **10** (1998) 225.
49. P.K. Isbester, T.A. Kestner and E.J. Munson, *Macromol.* **30** (1997) 280.
50. A.D. English and O.T. Garza, *Macromol.* **12** (1979) 351.
51. A.J. Vega and A.D. English, *Macromol.* **13** (1980) 1635.
52. U. Scheler and R.K. Harris, *Chem. Phys. Lett.* **262** (1996) 137.
53. S.A. Carss, U. Scheler, R.K. Harris, P. Holstein and R.A. Fletton, *Magn. Reson. Chem.* **34** (1996) 63.
54. U. Scheler, *Bull. Magn. Reson.* **19** (1999) 52.
55. P. Holstein, U. Scheler and R.K. Harris, *Polymer* **39** (1998) 4937.
56. U. Scheler and R.K. Harris, *Solid-State NMR* **7** (1996) 11.
57. H.W. Beckham and H.W. Spiess, *Macromol. Chem. Phys.* **195** (1994) 1471.
58. E. Katoh, H. Sugisawa, A. Oshima, Y. Tabata, T. Seguchi and T. Yamazaki, *Radiation Physics and Chemistry* **54** (1999) 165.
59. B. Fuchs and U. Scheler, *Macromol.* **33** (2000) 120.

Solid-State NMR Spectroscopy Principles and Applications
Edited by Melinda J. Duer
Copyright © 2002 by Blackwell Science Ltd

Chapter 11
Liquid-Crystalline Materials

James W. Emsley

Liquid-crystalline phases are intermediate between solids and the ordinary, isotropic liquid phase, and their NMR spectra have similarities with both these extremes. The most important aspect of liquid-crystalline phases is that they are liquids. The molecules are rotating and diffusing at rates similar to those in isotropic liquids.

The rotational motion of the molecules is rapid, but not random. The rapidity of the motion is such that usually the nuclear spin interactions are averaged, but the non-randomness means that the averages are different to those in an isotropic liquid. This has the very important consequence that the anisotropic parts of the nucelar spin interaction tensors (discussed in Part I) have non-zero averages. Thus, the spectra will be affected by partially averaged dipolar interactions, and also quadrupolar splittings if $I > \frac{1}{2}$. These two interactions produce spectra which are much richer in detail than those of isotropic liquids, and in this respect resemble those from solids. The dipolar interaction between nuclei in different molecules are averaged to zero in liquid-crystalline samples, unlike the case of solids, and this gives the possibility of having truly high-resolution spectra. The anisotropic contribution to the shielding tensor is also non-zero, and this will affect the spectrum, but, as we shall see, it is often possible to prepare a sample in such a way that the effect of this is simply to shift the lines and not to introduce extra complicating features.

The ability to obtain the partially averaged dipolar and quadrupolar interactions from the spectra means that NMR is a very useful method for studying liquid-crystalline samples. We shall see that it is possible to obtain structural information, conformational distributions, and an insight into the nature of the non-random rotational motion of the molecules. It is very important to note that this is true both of the molecules which form the liquid-crystalline phase, and for any other molecules present in the sample.

11.1 The liquid-crystalline state

A single component system might exist as a crystalline solid at low temperature, and on raising the temperature it may undergo a transition at a precise temperature, T_{CLC}, to a liquid-crystalline phase. On raising the temperature further the sample would eventually undergo a transition at T_{LCI} to an isotropic liquid phase. A phase diagram for such a sample is shown in Fig. 11.1. This progression of phases with temperature is because there is a decrease in order on going from the solid to the liquid crystal, and from the liquid crystal to the isotropic liquid. In the solid crystal, the molecules reside on a lattice which extends throughout the sample, which we describe as infinite spatial order. For non-spherical molecules there will also be orientational order, which will also be infinite in extent. When the solid melts to a liquid-crystalline phase, the lattice breaks down and the spatial order may be completely lost, but some orientational order always remains, but is not of infinite extent. This orientational order is referred to as being long-range to distinguish it from the short-range orientational order which exists between neighbouring molecules of anisotropic shape in an isotropic liquid. The phases which have only orientational order are known as nematics. There are liquid-crystalline phases which also have some long-range spatial order, and these are given various names which reflect other important properties of the phases. Thus, if the sample is a single component, so that at fixed pressure a change in phase can occur only by changing temperature, then they are known as smectics, or discotics depending on the shapes of the molecules forming the phases. For multicomponent systems these terms are also used when the macroscopic order can be understood in terms of the interactions between the individual molecules. Quite different kinds of liquid-crystalline phases are formed when groups of molecules aggregate together and it is the large, anisotropic aggregates which then arrange themselves to produce the long-range

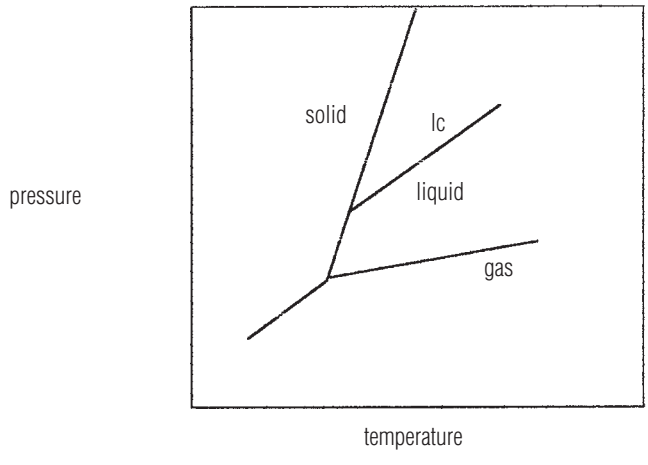

Fig. 11.1 Phase diagram for a system showing a liquid-crystalline phase.

order. The most common of these systems are those consisting of amphiphillic molecules such as the soaps, mixed with water. These systems are often referred to as lyotropic (solvent-loving) liquid crystals, although the term micellar is perhaps more appropriate since it emphasizes the importance of the aggregation of the molecules. Indeed there are phases in which the presence of a solvent is necessary, but which do not have micelle formation. An example is the phase formed when poly-γ-benzyl-L-glutamate is dissolved in organic solvents, such as chloroform. There are in fact a very large number of different types of liquid-crystalline phases, and not all of them can be described here. The interested reader should consult the introductory text by Collings and Hird [**1**] or the *Handbook of Liquid Crystals* [**2**].

11.2 Orientational order

The description of the orientation of a molecule in a solid crystal is simply a question of specifying the angles that a reference frame fixed in the molecule, x^{mol}, y^{mol}, z^{mol}, makes with a laboratory-fixed frame, x, y, z. Clearly this is not sufficient to describe the orientation of a molecule in a liquid crystal where the molecule is rotating and diffusing. The first step in achieving this aim is to define the *director reference frame*, x^{d}, y^{d}, z^{d}, which has axes pointing along the directions of most probable orientations of the molecules at a point in the sample. Another way of defining these orientations is in terms of unit vectors, $\mathbf{n}_x$, $\mathbf{n}_y$ and $\mathbf{n}_z$ which are defined with respect to the fixed laboratory frame (where z is along $\mathbf{B}_0$) either by Euler angles (see Box 1.2, Chapter 1), α_{dB}, β_{dB} and γ_{dB}, or by θ_{dx}, θ_{dy} and θ_{dz}, the angles between the x, y and z axes of the two frames. Note that here, α_{dB}, β_{dB} and γ_{dB} define the rotation from the *laboratory frame to the director reference frame*. Elsewhere in this book, we have used (α, β, γ) to describe rotation from some reference frame into the laboratory frame, i.e. the opposite rotation. As will become apparent later, the laboratory → director frame definition is a more natural one in this work.

The orientation of the director frame varies continuously throughout a sample which is not subject to an external constraint. This means that if we were to undertake a random walk through the sample at one instant in time, the director orientations would be changing spatially in a random manner, and there would be no net, overall orientation of the sample. If we focus on one point in the sample, the orientation of the director at this point will fluctuate in time. This time-dependence of director orientation can make an appreciable, or even dominant contribution to spin relaxation, and in this context it is necessary to differentiate between an *instantaneous director*, for which $\mathbf{n}_x$, $\mathbf{n}_y$ and $\mathbf{n}_z$ will be time-dependent, and the time-averaged, *average director*. When equilibrium spectral parameters other than relaxation rates are being considered, it is not necessary to differentiate between these two director frames, and so the term *director* is used rather than the more accurate *average director*.

11.2.1 Phase symmetry

The nature of the distribution of the orientations of the molecules about the director at one point in a sample can be used to place liquid crystals into a broad symmetry classification. Thus, the highest orientational symmetry this distribution can have is $D_{\infty h}$, that is, there is uniaxial, or cylindrical symmetry about one direction, chosen to be z^{d}, and reflection symmetry about the plane $x^{\mathrm{d}}y^{\mathrm{d}}$. The uniaxial symmetry means that the orientational distribution about x^{d} and y^{d} are identical. The reflection plane is lost if the molecules are chiral, thus reducing the symmetry to being D_{∞}. Phases in which the orientational distributions of the molecules are unequal about x^{d} and y^{d} are known as biaxial. As we will see, NMR can be a useful way of deciding whether a phase is uniaxial or biaxial.

11.2.2 Molecular orientational order

Now that we have defined the director it is possible to quantify the non-random nature of the motion of the molecules in liquid-crystalline phases. We will confine the discussion here to uniaxial, non-chiral phases. More general treatments can be found in the articles by Zannoni [**3**] and Merlet et al. [**4**]. For uniaxial phases the director is completely specified by a unit vector, $\mathbf{n}_z$, which we will simplify to **n**. Consider one molecule, which will at first be taken to be rigid, at one instant in time, and fix within it a reference frame, x^{mol}, y^{mol}, z^{mol}. The director will make Euler angles α_{md}, β_{md}, γ_{md} in this frame, but the uniaxial symmetry about the director renders α_{md} redundant; the two remaining angles are illustrated in Fig. 11.2. As the molecule moves through the phase it takes the reference frame with it, and the Euler angles become time-dependent. All the molecules in the sample of a particular kind

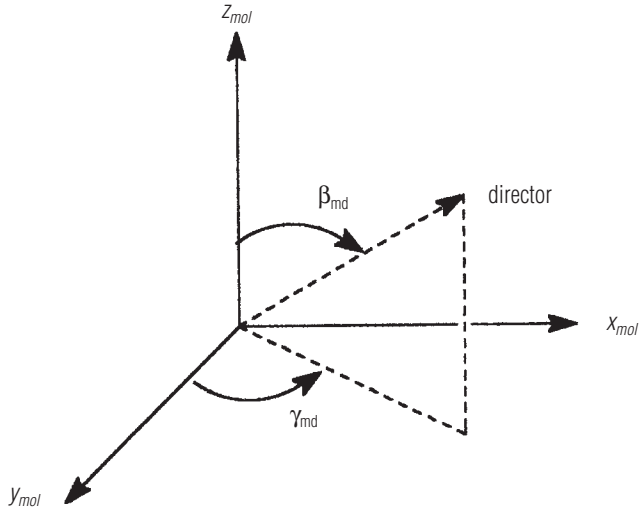

Fig. 11.2 The Euler angles for the director in a molecular frame for a uniaxial phase.

will be behaving in the same way, so that when the system is at thermal equilibrium the probability density, $P_{LC}(\beta_{md}(i), \gamma_{md}(i))$ that any single molecule of species i has an orientation relative to **n** such that the Euler angles are in the ranges $\beta_{md}(i) + d\beta_{md}(i)$ and $\gamma_{md}(i) + d\gamma_{md}(i)$ will be a stationary function. A knowledge of this *singlet orientational probability density* allows us to calculate the average of any property of the system which depends upon the orientation of single molecules. Note the careful wording here: the function $P_{LC}(\beta_{md}(i), \gamma_{md}(i))$ is only a partial description of the orientational order in the phase since it does not reveal anything about the probabilities of pairs, triples, etc., of molecules being simultaneously at particular orientations. Fortunately, for most purposes in NMR we do not require to know these higher-order probability distribution functions.

11.3 The general, time-independent NMR hamiltonian for liquid-crystalline samples

The hamiltonian describing the nuclear spin interactions in a liquid-crystalline sample is identical with that for a solid, except that the strength of the interactions are averaged by the rapid motion relative to the director. It is convenient when discussing how rotational motion averages the hamiltonian to use the irreducible, spherical tensor notation (see Box 3.1, Chapter 3), so that, in general,

$$\hat{H} = \sum_{\lambda} \sum_{q} (-1)^{q} \Lambda_{kq}(\lambda) \hat{T}_{k-q}(\lambda) \tag{11.1}$$

where $\Lambda_{kq}(\lambda)$ is the qth component of the kth rank irreducible tensor representing the λth interaction, and $\hat{T}_{k-q}(\lambda)$ is the $-q$th component of the nuclear spin operator. Equation (11.1) is expressed in the laboratory frame with the applied magnetic field, $\mathbf{B}_0$ along z. In general k is either 2 or 0 and q takes the integer values between k and $-k$, but, as noted in Section 1.1, most NMR experiments are done in a static magnetic field of sufficient intensity that the spectra depend only on the terms with $q = 0$, corresponding to the components of the nuclear spin interactions along $\mathbf{B}_0$, thus Equation (11.1) simplifies to

$$\hat{H} = \sum_{\lambda} \Lambda_{00}(\lambda) \hat{T}_{00}(\lambda) + \Lambda_{20}(\lambda) \hat{T}_{20}(\lambda) \tag{11.2}$$

The timescale of molecular motion in liquid-crystalline phases ($\sim 10^{-9}$ s), and the magnitude of the anisotropic interactions, such as dipolar couplings, quadrupolar be averaged over this motion. The spin operators are independent of the molecular orientation, and so the averaging affects only the components $\Lambda_{k0}(\lambda)$. The component $\Lambda_{00}(\lambda)$ is a scalar and is independent of molecular orientation. Thus, denoting averages over molecular orientation by $\langle\ \rangle$:

$$\hat{H} = \sum_{\lambda} \Lambda_{00}(\lambda)\hat{T}_{00}(\lambda) + \langle \Lambda_{20}(\lambda)\hat{T}_{20}(\lambda)\rangle \tag{11.3}$$

Note that this hamiltonian is of the same form as that for solid samples, and so the spectra will be essentially the same. The differences in the form of the spectra that do arise lie in the differences in macroscopic order in the two kinds of phase. The averaging of the anisotropic terms $\langle\Lambda_{20}(\lambda)\rangle$ over the molecular motion leads to a scaling of the magnitudes of the interactions. An NMR spectrum of a liquid-crystalline spectrum, therefore, may yield values of $\Lambda_{00}(\lambda)$ and $\langle\Lambda_{20}(\lambda)\rangle$. The anisotropic term, $\langle\Lambda_{20}(\lambda)\rangle$ is the one of most interest: the scalar term is usually close in value to its counterpart obtained either from a solid or isotropic liquid sample.

The primary interest is in how $\langle\Lambda_{20}(\lambda)\rangle$ is related to components $\langle\Lambda_{2n}^{\text{mol}}(\lambda)\rangle$ of the interactions in a molecule-fixed frame. For a molecule-fixed in space relative to $\mathbf{B}_0$ the component with $k = 2$ depends on molecular orientation via

$$\Lambda_{20}(\lambda) = \sum_{n} D_{0n}^{2*}(0, \beta_{mB}, \gamma_{mB})\Lambda_{2n}^{\text{mol}} \tag{11.4}$$

$\Lambda_{2n}^{\text{mol}}(\lambda)$ is a component in a molecule-fixed frame, whose orientation with respect to $\mathbf{B}_0$ is described by the complex conjugate of the Wigner function $D_{0n}^{2*}(0, \beta_{mB}, \gamma_{mB})$, and β_{mB} and γ_{mB} are the Euler angles of the field direction in this frame. Note that we need to use the complex conjugate Wigner rotation matrix in Equation (11.4). The complex conjugate transpose of a Wigner rotation matrix is the inverse rotation matrix and we must use this, as the Euler angles β_{md}, γ_{md} describe the rotation from the laboratory frame to the director frame. In Equation (11.4), we wish to transform the frame of reference in the opposite direction to this, i.e. from the director to the laboratory frame, and so must use the inverse rotation matrix, whose components appear in Equation (11.4). It is more useful to express the transform between the field-fixed and molecular-fixed frames in two steps. First a transformation from the molecular to the director fixed frame,

$$\Lambda_{2p}^{d}(\lambda) = \sum_{n} D_{pn}^{2*}(0, \beta_{md}, \gamma_{md})\Lambda_{2n}^{\text{mol}} \tag{11.5}$$

For a uniaxial phase the rotational symmetry about the director means that p is restricted to being zero, and rapid rotational motion of the molecules means that the Wigner function in Equation (11.5) is replaced by its average, $\langle D_{0n}^{2*}\rangle$, giving

$$\Lambda_{20}^{d}(\lambda) = \sum_{n} \langle D_{0n}^{2*}\rangle \Lambda_{2n}^{\text{mol}} \tag{11.6}$$

The second transformation is from the director to the field-fixed frame, giving

$$\Lambda_{20}(\lambda) = \frac{1}{2}(3\cos^2\beta_{dB} - 1)\sum_{n} \langle D_{0n}^{2*}\rangle \Lambda_{2n}^{\text{mol}} \tag{11.7}$$

Remember that Equation (11.7) is for the case of cylindrical symmetry about both the field and the director. The more general case of biaxial phases is discussed in reference [5].

Comparing Equations (11.3) and (11.7), it is apparent that NMR spectra may be used to obtain values of $\langle D_{0n}^{2*}\rangle\Lambda_{2n}^{\mathrm{mol}}$. We will see that in favourable cases it is possible to obtain separately both $\Lambda_{2n}^{\mathrm{mol}}$, which will give information on molecular properties such as geometry and conformation, and $\langle D_{0n}^{2*}\rangle$, which is related to the orientational order of the molecules.

11.4 Molecular order parameters

The averages $\langle D_{0n}^{2*}\rangle$ are known as second-rank molecular order parameters. Their values depend on the location within the molecule chosen for x^{mol}, y^{mol}, z^{mol}. This is particularly important when the molecules are flexible, and we will return to this complication later. At the moment it is sufficient to note that the axes must be fixed in a rigid subsection of the molecules. In fact, to simplify the discussion we will at first consider the molecules to be entirely rigid.

The $\langle D_{0n}^{2*}\rangle$ depend upon the non-random character of the molecular rotational motion, but they are not a complete description of the orientational order of the molecules. It is useful to see the connection that order parameters have with the *singlet probability density function*, $P_{\mathrm{LC}}(\beta_{md}, \gamma_{md})$, which although it gives a more detailed picture is still not a complete description of orientational order. Thus, the average of any function of the orientation of single, rigid molecules, such as $D_{pn}^{2*}(0, \beta_{md}, \gamma_{md})$, is given by

$$\begin{aligned}\langle D_{0n}^{2*}(0, \beta_{md}, \gamma_{md})\rangle &= \langle D_{0n}^{2*}\rangle \\ &= \int D_{0n}^{2*}(0, \beta_{md}, \gamma_{md}) P_{\mathrm{LC}}(\beta_{md}, \gamma_{md}) \sin\beta_{md}\,\mathrm{d}\beta_{md}\,\mathrm{d}\gamma_{md}\end{aligned} \tag{11.8}$$

This shows us that obtaining values of the order parameters from NMR experiments may allow us to test models for $P_{\mathrm{LC}}(\beta_{md}, \gamma_{md})$. NMR is in fact one of the best methods for doing this.

Another way of connecting $P_{\mathrm{LC}}(\beta_{md}, \gamma_{md})$ to $\langle D_{0n}^{2*}\rangle$ is to note that since the singlet orientational distribution function is a continuous, well-behaved function of the angles β_{md} and γ_{md}, then it can be expanded as a linear combination of the similarly well-behaved kth rank Wigner functions $D_{pn}^{k}(0, \beta_{md}, \gamma_{md})$,

$$P_{\mathrm{LC}}(\beta_{md}, \gamma_{md}) = \sum_{k,n} f_{kn} D_{0n}^{k}(0, \beta_{md}, \gamma_{md}) \tag{11.9}$$

The expansion coefficients are obtained by multiplying both sides of Equation (11.9) by $D_{0n}^{k*}(0, \beta_{md}, \gamma_{md})$ and integrating to give

$$\int D_{0n}^{k*}(0,\beta_{md},\gamma_{md})P_{\mathrm{LC}}(\beta_{md},\gamma_{md})\sin\beta_{md}\mathrm{d}\beta_{md}\mathrm{d}\gamma_{md}$$
$$= \int f_{kn}D_{0n}^{k*}(0,\beta_{md},\gamma_{md})D_{0n}^{k}(0,\beta_{md},\gamma_{md})\sin\beta_{md}\mathrm{d}\beta_{md}\mathrm{d}\gamma_{md} \qquad (11.10)$$

The LHS above is simply $\langle D_{0n}^{k*}\rangle$, while the RHS can be simplified by using the orthogonality of the Wigner functions, and their normalization, to give

$$f_{kn} = [(2k+1)/4\pi^2]\langle D_{0n}^{k*}\rangle \qquad (11.11)$$

The summation in Equation (11.9) extends over all even values of k from 0 to ∞, and so the terms having $k = 2$ – that is, involving the five order parameters $\langle D_{0n}^{2*}\rangle$ with $n = 0, \pm1, \pm2$ – form only a small part of an infinite series. The series does converge rapidly when the molecules are only weakly ordered, and in this case the values of the second-rank order parameters largely determine the form of $P_{\mathrm{LC}}(\beta_{md}, \gamma_{md})$. At the other extreme, all the order parameters $\langle D_{0n}^{k*}\rangle$ with $n \neq 0$ approach zero, while those with $n = 0$ converge on unity, and the series does not converge.

11.4.1 Different representations of the order parameters

The use of $\langle D_{0n}^{2*}\rangle$ to describe the second-rank order parameters follows logically from the use of irreducible tensors to describe the terms in the hamiltonian, and this notation also allows us to see how to generalize to the cases when there is lower symmetry about either the director (common) or the field (unusual). However, it is more usual to express the order parameters as averages of functions involving the angles, θ_{xn}, θ_{yn}, θ_{zn} between the director, **n**, and the molecule-fixed axes, x^{mol}, y^{mol}, z^{mol}. These are usually referred to as Saupe order parameters, and are defined as:

$$S_{\alpha\beta} = \left\langle \frac{1}{2}(3\cos\theta_{\alpha n}\cos\theta_{\beta n} - \delta_{\alpha\beta}) \right\rangle \qquad (11.12)$$

where $\delta_{\alpha\beta} = 1$ if $\alpha = \beta$, and zero otherwise. The relationship between the $\langle D_{0n}^{2*}\rangle$ and the $S_{\alpha\beta}$ is given in Table 11.1.

Table 11.1 The relationship between the two representations of the molecular order parameters

$S_{\alpha\beta}$	$\langle D_{0n}^{2*}\rangle$	S_{xy}	$i\sqrt{\frac{3}{8}}[\langle D_{22}^{2*}\rangle - \langle D_{2\text{-}2}^{2*}\rangle]$
S_{zz}	$\langle D_{00}^{2*}\rangle$	S_{xz}	$-\sqrt{\frac{3}{8}}[\langle D_{0\text{-}1}^{2*}\rangle + \langle D_{01}^{2*}\rangle]$
S_{xx}–S_{yy}	$\sqrt{\frac{3}{2}}[\langle D_{02}^{2*}\rangle + \langle D_{0\text{-}2}^{2*}\rangle]$	S_{yz}	$i\sqrt{\frac{3}{8}}[\langle D_{01}^{2*}\rangle - \langle D_{0\text{-}1}^{2*}\rangle]$

11.4.2 Molecular order parameters and the symmetry of rigid molecules

We have already used the axial symmetry about the director to restrict the order parameters to the set with $p = 0$. Equation (11.8) shows that the effect of symmetry is contained in the distribution function $P_{\mathrm{LC}}(\beta_{md}, \gamma_{md})$, but except for chiral systems there is an equivalence between the symmetry of this function and that of the molecules in the phase. A full account of the orientational order in chiral systems is given by Merlet et al. [**4**], and we will defer a discussion of this phenomenon until later.

We start our discussion by noting that for a rigid molecule there are at most just five independent second-rank order parameters, corresponding to the five values which can be taken by n in $\langle D^{2*}_{0n} \rangle$. It is easier perhaps to appreciate this by observing that in the equivalent definition, the 3×3 matrix formed by the complete set of second-rank Saupe order parameters is real and symmetric in the sense that $S_{\alpha\beta} = S_{\beta\alpha}$. This reduces the independent set to being S_{xx}, S_{yy}, S_{zz}, $S_{xy} = S_{yx}$, $S_{xz} = S_{zx}$ and $S_{yz} = S_{zy}$. The reduction to five occurs because the sum of the diagonal elements is zero for any choice of axes, so that two of the diagonal elements can be replaced by their difference. It is conventional to choose z as the most ordered axis, and to choose x and y such that $S_{xx} - S_{yy}$ is positive.

For rigid molecules, which in practice means solutes since all mesogenic molecules have some degree of flexibility, there is just one order matrix, and there is always one set of axes, the principal axes, for which the off-diagonal elements are all zero. The principal order parameters are therefore just two in number, S_{zz} and $S_{xx} - S_{yy}$. The role of symmetry is to guide us in choosing the location of the axes which produces the smallest set of independent order parameters. Thus, consider a molecule like the 1,2-dichlorocyclopropane shown in Fig. 11.3. The two-fold axis,

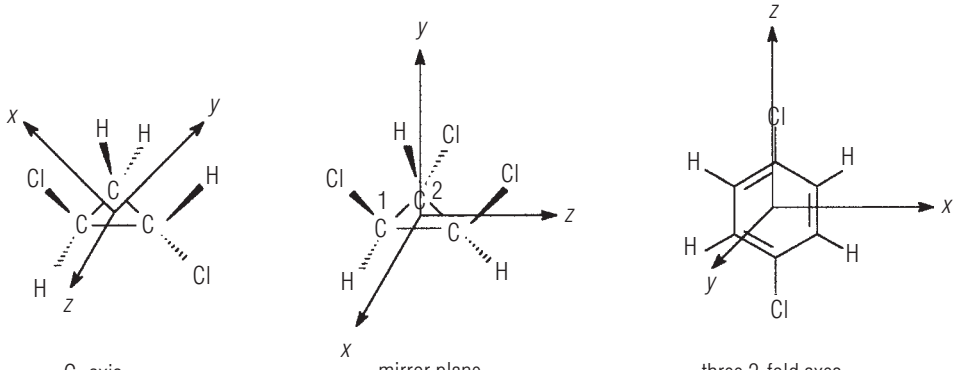

Fig. 11.3 Location of the principal axes *xyz* of the Saupe order matrix for some rigid molecules with different elements of symmetry dissolved in a uniaxial liquid-crystalline phase.

z, is a principal axis for **S**, and all that is known about x and y is that they must be located in the plane perpendicular to the symmetry axis. All three principal axes are fixed if the molecule has two orthogonal two-fold axes, such as in 1,4-dichlorobenzene (see Fig. 11.3). A molecular mirror plane has the same simplifying effect, so that in the tri-substituted cyclopropane shown in Fig. 11.3 the normal, z, to the molecular mirror plane is a principal axis.

If a molecule has a three-fold axis of symmetry, or higher, then this axis is a principal axis, for example, in methyl chloride. The other two principal axes must lie in the plane perpendicular to the three-fold axis. However, for this symmetry $S_{xx} = S_{yy}$, so that the location within the plane of these axes need not be specified.

11.5 Director alignment

The NMR spectra observed for liquid-crystalline samples depend critically on whether there is a distribution of the directors or whether they are uniformly aligned. The directors may in principle be aligned by applying a constraint such as surface forces (using glass plates), an electric field, or a magnetic field. The latter may be unavoidable since most NMR experiments take place with a static magnetic field applied. To understand how magnetic field alignment occurs we start by considering the effect of a field on individual molecules in a sample. The general principles can be understood by restricting the discussion to rigid molecules with cylindrical symmetry.

Rigid, cylindrically symmetric molecules of anisotropic shape have a contribution to their free energy in a magnetic field given by

$$F_{\text{mag}} = -\frac{1}{3} N_A \Delta\kappa_{\text{mol}} \left(\frac{3}{2} \cos^2 \beta_{mB} - \frac{1}{2} \right) \frac{B_0^2}{\mu_0} \tag{11.13}$$

where

$$\Delta\kappa_{\text{mol}} = \kappa_{\text{mol}\parallel} - \kappa_{\text{mol}\perp} \tag{11.14}$$

is the anisotropy in the magnetic susceptibility of a single molecule, N_A is Avogadro's number, and μ_0 is the permeability of free space and has the value $4\pi \times 10^{-7}\,\text{H m}^{-1}$. This energy is a minimum when $\beta_{mB} = 0$ when $\Delta\kappa_{\text{mol}}$ is positive, and so the molecules try to adopt this orientation. This is opposed by the randomizing effect of molecular collisions. The alignment produced is quantified by calculating the average

$$S_{\text{mol}} = \left\langle \left(\frac{3}{2} \cos^2 \beta_{mB} - \frac{1}{2} \right) \right\rangle = \frac{\Delta\kappa_{\text{mol}} B_0^2}{15 \mu_0 k_B T} \tag{11.15}$$

which is an order parameter for magnetic field induced order. For an isotropic liquid in which there is no molecular aggregation, then S_{mol} is ~10^{-5} for molecules with a large value of $\Delta\kappa_{\text{mol}}$ and $B_0 > 9T$. In fact, this field-induced alignment has been exploited to obtain structural information [**6**].

In a liquid crystal, the tendency of the molecules to be aligned by a magnetic field is aided by the anisotropic, intermolecular forces which produce the long-range orientational order. It is now useful to express $(\frac{3}{2}\cos^2\beta_{mB} - \frac{1}{2})$ as

$$\left(\frac{3}{2}\cos^2\beta_{mB} - \frac{1}{2}\right) = \left(\frac{3}{2}\cos^2\beta_{md} - \frac{1}{2}\right)\left(\frac{3}{2}\cos^2\beta_{\text{d}B} - \frac{1}{2}\right) \tag{11.16}$$

Only the function $(\frac{3}{2}\cos^2\beta_{md} - \frac{1}{2})$ is averaged by the molecular motion, and is replaced by S_{zz}, where z is the symmetry axis of the molecular magnetic susceptibility tensor. The result is that

$$F_{\text{mag,LC}} = -\frac{1}{3}N_{\text{A}}\Delta\kappa_{\text{mol}}\left(\frac{3}{2}\cos^2\beta_{\text{d}B} - \frac{1}{2}\right)\frac{S_{zz}B_0^2}{\mu_0} \tag{11.17}$$

A typical value of S_{zz} is 0.5, so that the torque on the liquid crystal directors is about 10^6 larger than that on individual molecules in an isotropic liquid. It is sufficient in fact for quite modest fields (~0.1T) to essentially completely align the directors (not the molecules!) for uniaxial nematic samples. The alignment is parallel to $\mathbf{B}_0$ when $\Delta\kappa$ is positive, and perpendicular when it is negative.

A sample in which the directors are not aligned will give spectra similar to those from polycrystalline, or non-crystalline solids, that is, a broad, unresolved lineshape spread over many kHz. Alignment of the directors produces spectra similar to those from solid single crystals, that is a set of narrow lines (Hz to ~100 Hz).

The rate at which the directors align in nematic samples depends on the viscosity and elastic constants of the sample. The rate of the alignment process is fast in low molar mass samples (<1 s) while polymeric samples might take up to several hours to completely align.

Thermotropic smectic liquid crystals may also be aligned by magnetic fields, but the process is hindered by the need for the directors to form into layers. It is not easy to predict whether a particular smectic sample will align in the field of an NMR spectrometer. It is usually possible to align smectic A samples if they have a nematic phase at a higher temperature. Cooling a sample slowly in the field from the nematic phase into the smectic A leads to preservation of the director alignment.

Discotic samples other than the nematic discotics, usually do not align in NMR fields, and this is true also of lyotropic amphiphillics, such as the lamellar and hexagonal phases formed by soap solutions. In these cases it is possible to align the directors using surface forces. This is achieved by containing the sample between glass plates with a separation of <100 μm.

11.6 Dipolar couplings between nuclei in rigid molecules in liquid-crystalline phases

Dipolar coupling has exactly the same effect on liquid-crystalline samples as it does on that of a solid. The only difference being that the coupling in a liquid-crystalline sample is averaged over the rapid molecular motion. The dipolar tensor is totally anisotropic, that is, the scalar part is zero, so that the hamiltonian, $\hat{H}_{\mathrm{dd}}$, in the Cartesian representation and in angular frequency units, has the form (see Section 3.1)

$$\hat{H}_{dd} = -2\sum_{i>j} C_{ij}\left[\hat{I}_z^i\hat{I}_z^j - \frac{1}{4}\left(\hat{I}_+^i\hat{I}_-^j + \hat{I}_-^i\hat{I}_+^j\right)\right] \tag{11.18}$$

The dipolar interaction is also cylindrically symmetric about the direction of $\mathbf{r}_{ij}$, the vector connecting the two coupled nuclei. Transforming to a molecular frame with one axis a along $\mathbf{r}_{ij}$ gives

$$C_{ij} = \frac{1}{2}(3\cos^2\beta_{\mathrm{dB}} - 1)\left(\frac{\mu_0}{4\pi}\right)\frac{\gamma_i\gamma_j}{r_{ij}^3}\hbar S_{ij} \tag{11.19}$$

Equation (11.19) tells us that each measured value of C_{ij} for a rigid molecule gives directly the ratio S_{ij}/r_{ij}^3. If r_{ij}^3 is known then one order parameter is obtained for each observed C_{ij}. The geometry of the molecule might be known from some other experimental technique, such as X-ray or neutron diffraction, or microwave spectroscopy. However, note that molecules are never wholly rigid, there being always zero-point vibrational motion. This has interesting effects on dipolar couplings, which we will return to later, and for the moment we will still consider the molecule as truly rigid. In passing, the complications introduced by vibrational motion will restrict the precision of the measurement of S_{ij} from Equation (11.19) to being $\leq$~5%.

If a set of S_{ij} values has been obtained it is more informative to relate each of them to order parameters in a common molecular frame, *abc*. This is done by utilizing the transformation properties of second-rank tensors, such as **S** (Equation (11.3)) to give:

$$\begin{aligned} S_{ij} = {} & S_{aa}\cos^2\theta_{ija} + S_{bb}\cos^2\theta_{ijb} + S_{cc}\cos^2\theta_{ijc} \\ & + 2S_{ab}\cos\theta_{ija}\cos\theta_{ijb} + 2S_{ac}\cos\theta_{ija}\cos\theta_{ijc} + 2S_{bc}\cos\theta_{ijb}\cos\theta_{ijc} \end{aligned} \tag{11.20}$$

Combining Equations (11.19) and (11.20), and using the property

$$S_{aa} + S_{bb} + S_{cc} = 0 \tag{11.21}$$

which is true for any set of axes, gives:

$$\begin{aligned} C_{ij} = {} & -\frac{1}{2}(3\cos^2\beta_{\mathrm{dB}} - 1)\left(\frac{\mu_0}{4\pi}\right)\frac{\gamma_i\gamma_j}{r_{ij}^3}\frac{\hbar}{2} \\ & \times[S_{aa}(3\cos^2\theta_{ija} - 1) + (S_{bb} - S_{cc})(\cos^2\theta_{ijb} - \cos^2\theta_{ijc}) \\ & + 4S_{ab}\cos\theta_{ija}\cos\theta_{ijb} + 4S_{ac}\cos\theta_{ija}\cos\theta_{ijc} + 4S_{bc}\cos\theta_{ijb}\cos\theta_{ijc}] \end{aligned} \tag{11.22}$$

Table 11.2 Location of the principal axes *abc* of the second rank orientational order parameters $\langle D^2_{mm} \rangle$ for molecules of different point group symmetries dissolved in non-chiral uniaxial phases

Molecular point group	Location of axes *abc*	Independent order parameters (in term of Wigner elements)	Independent order parameters (in term of Saupe elements)
C_1, C_i	Not defined by symmetry	$\langle D^2_{00} \rangle$, $\langle D^2_{01} \rangle$, $\langle D^2_{0-1} \rangle$ $\langle D^2_{02} \rangle$, $\langle D^2_{0-2} \rangle$	S_{aa}, $S_{bb} - S_{cc}$, S_{bc}, S_{ab}, S_{ac}
C_s, C_2, C_{2h}	*a* normal to the plane or parallel to the 2-fold axis	$\langle D^2_{00} \rangle$, $\langle D^2_{02} \rangle$, $\langle D^2_{0-2} \rangle$	S_{aa}, $S_{bb} - S_{cc}$, S_{bc}
C_{2v}	*a* parallel to the 2-fold axis *b* normal to the mirror plane	$\langle D^2_{00} \rangle$, $\langle D^2_{02} \rangle$	S_{aa}, S_{bb}–S_{cc}
D_2, D_{2h}	*a,b,c* parallel to the 2-fold axes		
D_{2d}, C_3, C_{3v}, C_{3h}, D_3, D_{3h}, D_{3d}, C_4, C_{4v}, C_{4h}, D_4, D_{4h}, D_{4d}, S_4, C_5, C_{5h}, C_{5v}, D_5, D_{5h}, D_{5d}, C_6, C_{6h}, C_{6v}, D_6, D_{6h}, D_{6d}, S_6, C_∞, $C_{\infty v}$, $C_{\infty h}$, $D_{\infty h}$	*a* parallel to the *p-fold* axis or intersection of mirror planes	$\langle D^2_{00} \rangle$	S_{aa}

Choosing *abc* to reflect the point group symmetry of the molecule will reduce the number of terms, in accord with the rules in Table 11.2.

11.6.1 Geometry of rigid molecules from dipolar couplings

Clearly from Equation (11.19), if the values of the S_{ij} are known then a set of values of the internuclear distances can be obtained. As we shall see, this may be possible by using measured values of quadrupolar splittings. However, this is not very useful for rigid molecules, simply because it is more accurate to guess the values of the geometrical parameters from comparison with similar structures, or to calculate them by molecular orbital methods. It is more useful to use Equation (11.22) to obtain both the order parameters and the geometrical information. To do this it is only necessary to assume the value of one distance between the interacting nuclei. For this reason the dipolar couplings give the shape of a set of interacting nuclei but not the absolute size. This is not a serious difficulty since a distance can usually be assumed with a high degree of precision.

As noted already, molecules are never rigid, and accurate values of r_{ij} can be obtained from liquid crystal NMR (LCNMR) only by allowing for vibrational motion, and this is true also for distances obtained by other methods. We will not go into the details of how to correct for vibrational motion, these can be found in

the article by Diehl [7]. It is instructive, however, to note that the averaging process involves both the orientational order as well as the internuclear distances. This is clearly revealed by noting that truly rigid molecules with tetrahedral symmetry should not show dipolar, or other anisotropic interactions, when in a liquid-crystalline medium. This is because the orientational order parameters for such a symmetry are all zero. In practice, molecules such as methane do show dipolar splittings in their spectra. This is because the individual vibrational modes, except for the totally symmetric stretching vibration have lower symmetries and non-zero orientation order parameters associated with them.

11.7 Deuterium quadrupolar splittings for rigid molecules in liquid-crystalline phases

Deuterium, which has $I = 1$, is by far the most important quadrupolar nucleus used to study liquid-crystalline samples. The magnitudes of the components of the quadrupolar tensor for deuterium are of the order of 100–200 kHz, which is usually much smaller than the Zeeman interaction. This means that the spectra depend only on χ_{zz}^{lab} the component along $\mathbf{B}_0$ (see Chapter 4), and the hamiltonian, $\hat{H}_{\text{Q}}$ for $I = 1$ is

$$\hat{H}_{\text{Q}} = \frac{1}{4}\chi_{zz}^{\text{lab}}(3\hat{I}_z^2 - 2) \tag{11.23}$$

The spectrum for a single deuterium without any dipolar coupling to other nuclei is a doublet with a splitting, $\Delta\nu_i$, given by

$$\Delta\nu_i = \frac{3}{2}\chi_{zz}^{\text{lab}} \tag{11.24}$$

The relationship between line positions in groups of equivalent deuterons is more complex, but values of χ_{zz}^{lab} can be obtained directly from the spectrum in the case of CD_2 or CD_3 groups. More complex cases require the use of a spectral analysis programme.

The quadrupolar interaction is also totally anisotropic and so we need to consider only how $\chi_{zz,i}^{\text{lab}}$ for a deuterium at a site i in a molecule is related to components of the quadrupolar tensor, χ^{mol}, expressed in a molecular frame a, b, c:

$$\chi_{zz,i}^{\text{lab}} = \frac{1}{2}(3\cos^2\beta_{\text{dB}} - 1)\Big[\chi_{aa,i}S_{aa} + \frac{1}{3}(\chi_{bb,i} - \chi_{cc,i})(S_{bb} - S_{cc}) + \frac{4}{3}\chi_{ab,i}S_{ab} + \frac{4}{3}\chi_{ac,i}S_{ab} + \frac{4}{3}\chi_{bc,i}S_{ab}\Big] \tag{11.25}$$

For deuterium in C–D bonds the principal axes of χ^{mol} can to a good approximation be assumed to have a along the bond direction, corresponding to χ_{aa}^{mol} having

the largest magnitude. When the molecular frame corresponds to the principal axis frame of the quadrupole coupling tensor, the terms involving off-diagonal elements of χ^{mol} in Equation (11.25) vanish, to give

$$\chi_{zz,i}^{\text{lab}} = \frac{1}{2}(3\cos^2\beta_{dB} - 1)\left[\chi_{aa,i}^{\text{PAF}}\left(S_{aa} + \frac{1}{3}\eta_{Q,i}(S_{bb} - S_{cc})\right)\right] \tag{11.26}$$

where

$$\eta_{Q,i} = \frac{\chi_{bb,i}^{\text{PAF}} - \chi_{cc,i}^{\text{PAF}}}{\chi_{aa,i}^{\text{PAF}}} \tag{11.27}$$

Locating the principal axes b and c is a problem if the site symmetry is low, but this problem is often circumvented by assuming that $\eta_{Q,i} = 0$. Measurements of the magnitude and location of the deuterium quadrupolar tensors have been made on aromatic compounds and here it is found that b is approximately in the ring plane, and that $\eta_{Q,i}$ is ~0.05. If η_i is assumed to be zero, then Equation (11.26) has the simple form

$$\chi_{zz,i}^{\text{lab}} = \frac{1}{2}(3\cos^2\beta_{dB} - 1)\chi_{aa,i}^{\text{PAF}}S_{aa} = \frac{1}{2}(3\cos^2\beta_{dB} - 1)\chi_{CDi}S_{CDi} \tag{11.28}$$

χ_{CDi} is known as the deuterium quadrupolar-coupling constant, and has values in the ranges shown in Table 11.3.

Equation (11.28) is often used to determine the C–D bond order parameters, S_{CDi}, by assuming a value for χ_{CDi}. The uncertainty in the assumed value for χ_{CDi}, plus the assumption that $\eta_i = 0$ produces a systematic error in the S_{CDi} of typically 5–10%.

One of the main reasons for measuring values of S_{CDi} for rigid molecules is to determine from them the order parameters for the molecule in some common frame, x, y, z. In general this requires measuring at least five values of $\chi_{zz,i}$, deriving five S_{CDi}, and then to use

$$\begin{aligned} S_{CDi} = {} & S_{zz}\frac{1}{2}(3\cos^2\theta_{CDz,i} - 1) + \frac{1}{2}(S_{xx} - S_{yy})(\cos^2\theta_{CDx,i} - \cos^2\theta_{CDy,i}) \\ & + 2S_{xy}\cos\theta_{CDx,i}\cos\theta_{CDy,i} + 2S_{xz}\cos\theta_{CDx,i}\cos\theta_{CDz,i} \\ & + 2S_{yz}\cos\theta_{CDy,i}\cos\theta_{CDz,i} \end{aligned} \tag{11.29}$$

where the angles $\theta_{CD\alpha,i}$ are between the ith C–D bond and the axis α.

Table 11.3 Average values of quadrupolar-coupling constants, χ_{CD}, for deuterium nuclei in C–D bonds

Bond type	χ_{CD} (kHz)
sp^3	170
sp^2	185
sp	180

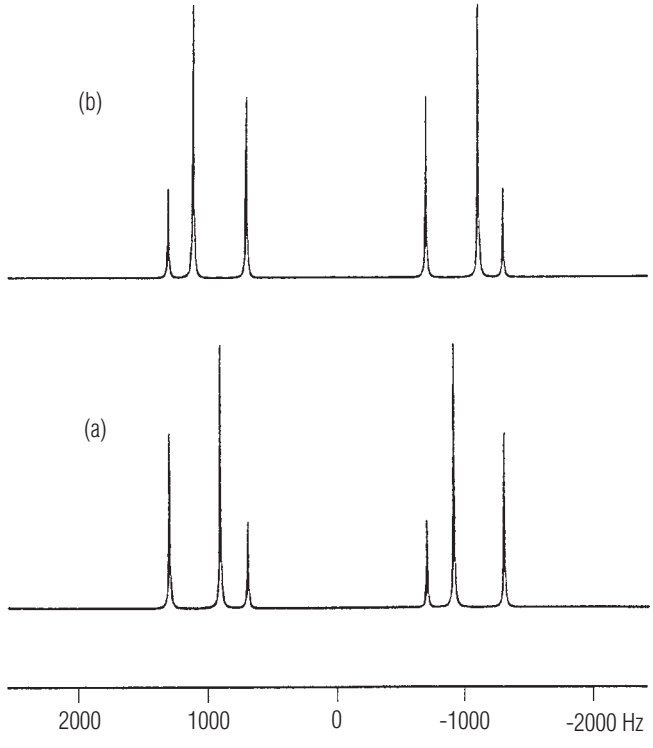

Fig. 11.4 ^{2}H spectra for a pair of symmetrically equivalent deuterium nuclei with the ratio, ω_Q/d, of the quadrupolar splitting to the dipolar coupling (a) positive and (b) negative.

11.7.1 Signs of quadrupolar splittings

The $\chi_{zz,i}$ may be positive or negative, and the sign is not always revealed by the experimental spectrum. If a group of deuteriums have a spectrum showing resolved inter-deuteron dipolar couplings, C_{ij}, then the intensity distributions of the lines may reveal the relative signs of $\Delta\nu_i/C_{ij}$. A common example is the spectrum given by CD_2 groups, as shown in Fig. 11.4. For more complex examples it is necessary to simulate the spectra for different sign combinations of $\Delta\nu_i$ and C_{ij}.

11.8 Chemical shift anisotropy for rigid molecules in liquid crystalline phases

The chemical shift contribution to the spectral frequency for a single, uncoupled (or decoupled) nucleus is given by

$$\omega_{\mathrm{cs},i} = \gamma_i B_0 \sigma^{\mathrm{lab}}_{zz,i} \tag{11.30}$$

where $\sigma^{\mathrm{lab}}_{zz,i}$ is the component along $\mathbf{B}_0$ of the nuclear shielding tensor (see Section 1.4.1). The shielding tensor has both a scalar, $\sigma_{\mathrm{iso},i}$, and an anisotropic part, $\boldsymbol{\sigma}^{\mathrm{lab}}_{\mathrm{aniso},i}$. Both these terms are dependent on the electronic structure of the molecule, but

note that there are also contributions to both terms from the bulk magnetic susceptibility.

The dependence of $\sigma^{\text{lab}}_{zz,i}$ on the director orientation is

$$\sigma^{\text{lab}}_{zz,i} = \sigma_{\text{iso},i} + \sigma^{\text{d}}_{\text{aniso},zz,i}\frac{1}{2}(3\cos^2\beta_{\text{d}B} - 1) \tag{11.31}$$

so that observation of how the spectral frequency depends on $\beta_{\text{d}B}$ allows $\sigma^{\text{d}}_{\text{aniso},zz,i}$ to be separated from $\sigma_{\text{iso},i}$. Note that the presence of the scalar term is an advantage in that it allows the absolute sign of $\sigma^{\text{d}}_{\text{aniso},zz,i}$ to be determined.

One way of separating $\sigma^{\text{d}}_{\text{aniso},zz,i}$ from $\sigma_{\text{iso},i}$ for a sample in a uniaxial phase is to record the spectrum of a sample which has the directors in some known distribution, for example a uniform distribution in three dimensions. The broad, powder pattern for a single spin-$\frac{1}{2}$ nucleus, with no spin–spin coupling, will be one of two possible shapes, as shown in Fig. 11.5. These shapes are similar to those observed for solid samples, but with the difference that they depend on the symmetry of the phase, rather than the site symmetry of the nucleus. The disadvantages of this method are principally that of overlap of the powder patterns when there is more than one nucleus contributing to the spectrum.

The angle $\beta_{\text{d}B}$ can be changed for some uniaxial smectic phases by first aligning the directors uniformly along $\mathbf{B}_0$, and then turning the sample in the field. In very viscous smectic phases, such as smectic *B*, this is easily achieved.

Two other methods for separating isotropic from anisotropic NMR parameters, sample rotation and the use of a mixed solvent of liquid crystals with opposite signs of $\Delta\kappa$, will be deferred until later.

The relationship between $\sigma^{\text{d}}_{\text{aniso},zz,i}$ and components in a molecular frame, *a*, *b*, *c*, is

$$\begin{aligned}\sigma^{\text{lab}}_{\text{aniso},zz,i} = \frac{1}{2}(3\cos^2\beta_{\text{d}B} - 1)\Bigg[&\frac{2}{3}S_{aa}\left(\sigma^{\text{mol}}_{aa,i} - \frac{1}{2}(\sigma^{\text{mol}}_{bb,i} + \sigma^{\text{mol}}_{cc,i})\right)\\ &+ \frac{1}{3}(S_{bb} - S_{cc})(\sigma^{\text{mol}}_{bb,i} - \sigma^{\text{mol}}_{cc,i})\\ &+ \frac{4}{3}(S_{ab}\sigma^{\text{mol}}_{ab,i} + S_{ac}\sigma^{\text{mol}}_{ac,i} + S_{bc}\sigma^{\text{mol}}_{bc,i})\Bigg]\end{aligned} \tag{11.32}$$

If the molecular frame (labelled 'mol') coincides with the principal axis frame for the shielding tensor, then the off-diagonal terms of Equation (11.32) vanish, but this still means that Equation (11.32) contains five unknowns. The order parameters may be obtained, for example, from measurements of dipolar couplings between nuclei in the same molecules, at the same temperature, and this reduces to three the number of unknown elements of $\boldsymbol{\sigma}^{\text{mol}}_i$. In principle, measurements on samples with

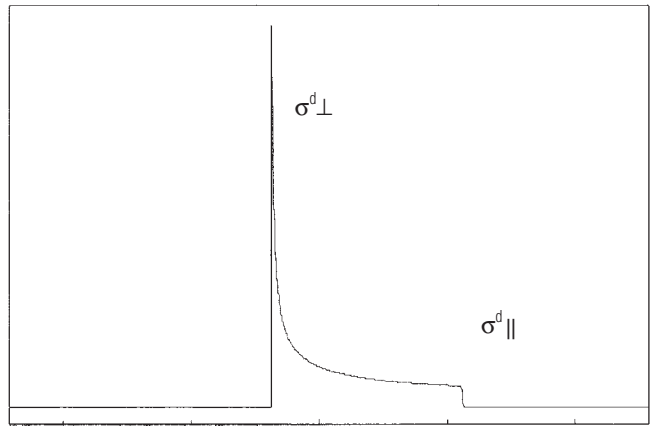

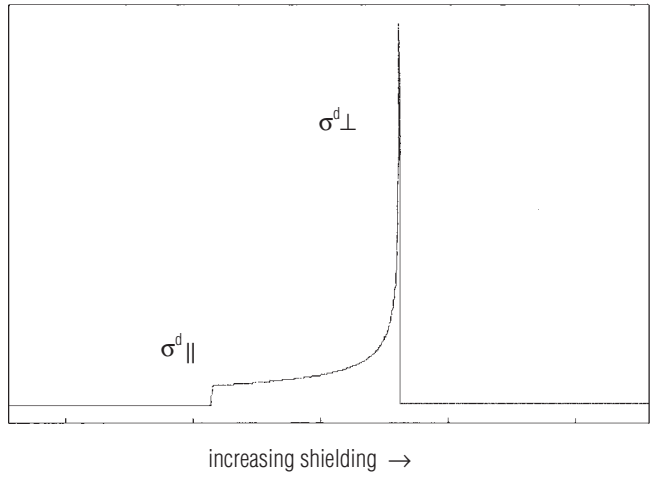

Fig. 11.5 Spectra from spin-$\frac{1}{2}$ nuclei in samples with a random distribution of the directors with respect to $\mathbf{B}_0$ when the sign of $\sigma^{d}_{aniso,zz,i}$ is (a) positive and (b) negative.

different order parameters could give the individual elements $\sigma^{mol}_{aa,i}$, $\sigma^{mol}_{bb,i}$, and $\sigma^{mol}_{cc,i}$, but in practice it is difficult to obtain samples which have the order parameters sufficiently different from being linearly dependent for this to be a viable technique in general.

11.9 Electron-mediated spin–spin coupling in liquid-crystalline samples

The spin–spin coupling between two spins i and j, J_{ij}, encountered in the spectra of samples in isotropic liquids also affects the spectra of both solids and liquid-crystalline samples. For solids, J_{ij} often has only a minor influence on the spectrum, but it is more important for liquid-crystalline samples and indeed in some cases can be larger than C_{ij}. J_{ij} is the scalar contribution to the electron mediated spin–spin

coupling, and there is also an anisotropic contribution, $J^{\text{lab}}_{\text{aniso},zz,ij}$. This usually has a smaller effect on spectra of anisotropic samples than the dipolar coupling, and indeed when the proton is one of the coupled nuclei can safely be ignored. For other pairs, the effects of this anisotropic coupling cannot be ignored. The hamiltonian for this interaction is

$$\hat{H}_J = \sum_{i>j} J_{ij}\left[\hat{I}^i_z\hat{I}^j_z + \frac{1}{2}\left(\hat{I}^i_+\hat{I}^j_- + \hat{I}^i_-\hat{I}^j_+\right)\right] + J^{\text{lab}}_{\text{aniso},zz,ij}\left[\hat{I}^i_z\hat{I}^j_z - \frac{1}{4}\left(\hat{I}^i_+\hat{I}^j_- + \hat{I}^i_-\hat{I}^j_+\right)\right] \quad (11.33)$$

The term in $\hat{H}_J$ involving $J^{\text{lab}}_{\text{aniso},zz,ij}$ has the same operators as the dipolar interaction, and so affects the spectrum in an identical way. This means that $J^{\text{lab}}_{\text{aniso},zz,ij}$ cannot be obtained from the spectrum except in combination with C_{ij}, and for this reason it is sometimes referred to as pseudo-dipolar coupling.

Spectral analysis yields values of $T^{\text{lab}}_{zz,ij}$, the component along $\mathbf{B}_0$ of a total spin–spin coupling tensor, given by

$$T^{\text{lab}}_{zz,ij} = 2C_{ij} + J^{\text{lab}}_{\text{aniso},zz,ij} \quad (11.34)$$

The relative importance of $J^{\text{lab}}_{\text{aniso},zz,ij}$ and C_{ij} can sometimes be obtained. To understand how, let us first note that $J^{\text{lab}}_{\text{aniso},zz,ij}$ is related to components in a molecular frame a, b, c by

$$\begin{aligned} J^{\text{lab}}_{\text{aniso},zz,i} = \frac{1}{2}(3\cos^2\beta_{dB} - 1)\Bigg[&\frac{2}{3}S_{aa}\left(J^{\text{mol}}_{\text{aniso},aa,ij} - \frac{1}{2}\left(J^{\text{mol}}_{\text{aniso},bb,ij} + J^{\text{mol}}_{\text{aniso},cc,ij}\right)\right) \\ &+ \frac{1}{3}(S_{bb} - S_{cc})\left(J^{\text{mol}}_{\text{aniso},bb,ij} - J^{\text{mol}}_{\text{aniso},cc,ij}\right) \\ &+ \frac{4}{3}\left(S_{ab}J^{\text{mol}}_{\text{aniso},ab,ij} + S_{ac}J^{\text{mol}}_{\text{aniso},ac,ij} + S_{bc}J^{\text{mol}}_{\text{aniso},\boldsymbol{bc},ij}\right)\Bigg] \end{aligned} \quad (11.35)$$

Consider a molecule which has a symmetry axis C_n with $n > 2$. Choosing a to lie on this axis means that all the dipolar interactions in the molecule are given by $C_{ij} = 2S_{aa}/r^3_{ij}$. The ratios of the C_{ij} therefore are independent of S_{aa}, and should be determined only by the geometry. If the geometry is known, then the experimental ratios of the $T^{\text{lab}}_{zz,ij}$ can be compared with values calculated from the known r_{ij}. Note that it is important to correct the values of r^3_{ij} for the effects of vibrational motion. If this is done, then a deviation from the expected ratios can be attributed to contributions from the $J^{\text{lab}}_{\text{aniso},aa,ij}$. A good example of using this technique is for the molecules benzene and hexafluorobenzene. Both have a 6-fold axis, and the ratios of the three C_{HH} or C_{FF} are fixed. Thus C_{12}, C_{13} and C_{14} are in the ratios 1.0000 : 0.1924 : 0.1250 and so if the $J^{\text{mol}}_{\text{aniso},aa,ij}$ are all negligibly small, the observed $T^{\text{lab}}_{zz,ij}$ should also be in these ratios, and should be independent of temperature and the choice of liquid-crystalline solvent. For benzene this is true to a good precision, thus it can be concluded that the $J^{\text{lab}}_{\text{aniso},zz,\text{HH}}$ are all negligibly small. But the measured values of $T^{\text{lab}}_{zz,\text{FF}}$ for hexafluorobenzene show deviations from this behaviour [8], thus for one

solvent the ratios were found to be 1.0000 : 0.1870 ± 0.0016 : 0.1337 ± 0.0016. These deviations are small (<6%), but they are larger than the effects of vibrational motion, and are attributal to significant contributions to $T^{\text{lab}}_{zz,\text{FF}}$.

The conclusion from studies on these and other compounds is that $J^{\text{lab}}_{\text{aniso},zz,ij}$ is small enough to be neglected when at least one of the coupled nuclei is a proton. The magnitude of $J^{\text{lab}}_{\text{aniso},zz,ij}$ is expected to rise with the atomic number of the coupled nuclei.

11.9.1 The determination of the structure, orientational order and conformations of flexible molecules in liquid-crystalline samples

Internal motion in molecules affects the NMR spectra of samples in all states of matter in similar ways and leads to averages of the spectral parameters. This type of motion has a profound effect on the orientational order of molecules in liquid-crystalline phases, and therefore influences the relationships between the measured, averaged NMR interactions and the structure and conformations of the molecules. In fact, the molecules which form liquid-crystalline phases are flexible, and so the measurement of their orientational order is not so straightforward as that described for rigid molecules.

The effect that internal motion has on the NMR spectra depends upon the inverse of its correlation time, τ_c^{-1} (see Chapter 6), relative to the magnitude of the change, $\delta\Lambda_{k0}$, it produces on the magnetic interactions. When $\tau_c^{-1} > \delta\Lambda_{k0}$, there will usually be a change in the permutation symmetry of the interacting spins, and this may change the chemical and magnetic equivalencies of nuclei in the molecules. This affects the spin part of the hamiltonian, and in this respect liquid-crystalline samples are similar to solids.

11.9.2 Molecular orientational order for flexible molecules

Fast motion also averages the magnitudes of the magnetic interactions. Thus, the scalar terms, $\Lambda_{00}(\lambda)$, in Equation (11.2) are averaged in the same way that they are in isotropic liquids, but this is not true of the anisotropic terms, $\Lambda_{20}(\lambda)$. To deal with this averaging we first introduce local order parameters $\langle D^{2*}_{0n}\rangle(j)$ and $S_{\alpha\beta}(j)$. Thus, transforming $\Lambda(\lambda')$ to a frame fixed in the jth rigid molecular subunit gives

$$\Lambda_{20}(\lambda') = \frac{1}{2}(3\cos^2\beta_{dB} - 1)\sum_n \Lambda^{\text{mol}}_{2n}(\lambda')\langle D^{2*}_{0n}\rangle(j) \tag{11.36}$$

where λ' refers only to interactions involving nuclei within the jth group. The expressions which use Saupe order parameters for the dipolar couplings (Equation (11.23)), the deuterium quadrupolar interaction (Equation (11.25)), the chemical shift anisotropy (Equation (11.32)), and the anisotropy in spin–spin coupling

(Equation (11.35)) all remain of the same form except the $S_{\alpha\beta}$ are replaced by $S_{\alpha\beta}(j)$.

To illustrate the use of local order parameters consider the molecule 4-pentylbenzonitrile (Fig. 11.6(a)). Rotation about the bonds in the alkyl chain generates conformational states described by the set of five angles ϕ_l. The dipolar couplings between the four protons in the ring will vary as the molecule changes conformation. For example, consider the molecule to be in just two conformations, as shown in Fig. 11.6(b).

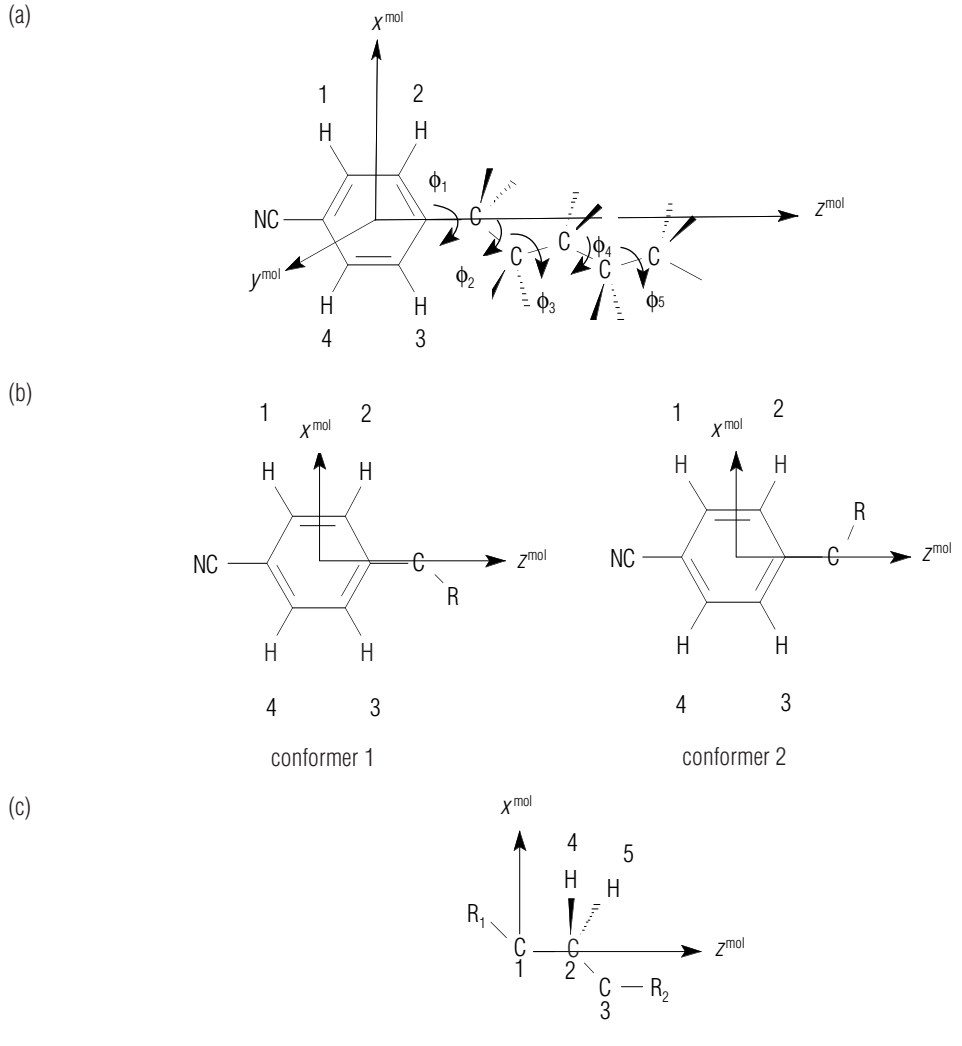

Fig. 11.6 (a) 4-pentylbenzonitrile; the frame shown is the molecular axis frame. (b) Two different conformations of 4-pentylbenzonitrile within the same frame. (c) A fragment of the alkyl chain of 4-pentylbenzonitrile, again in the same axis frame.

R represents the rest of the chain, and the two conformers are related by reflection in the y^{mol}–z^{mol} plane, where y^{mol} and z^{mol} are defined in Fig. 11.6. If the molecule is in a liquid-crystalline solvent with the directors aligned along $\mathbf{B}_0$, the dipolar couplings in conformer 1 depend on local order parameters $S_{\alpha\beta}(1)$, and those in conformer 2 depend on $S_{\alpha\beta}(2)$. Thus $C_{13}(1)$ and $C_{13}(2)$ are

$$\begin{aligned} C_{13}(1) = -\frac{1}{2}\left(\frac{\mu_0}{4\pi}\right)\frac{\gamma_H^2}{r_{13}(1)^3}\hbar[&S_{zz}(1)(3\cos^2\theta_{13z}(1) - 1) \\ &+ (S_{xx}(1) - S_{yy}(1))(\cos^2\theta_{13x}(1) - \cos^2\theta_{13y}(1)) \\ &+ 4S_{xz}(1)\cos\theta_{13x}(1)\cos\theta_{13z}(1)] \end{aligned} \tag{11.37}$$

$$\begin{aligned} C_{13}(2) = -\frac{1}{2}\left(\frac{\mu_0}{4\pi}\right)\frac{\gamma_H^2}{r_{13}(2)^3}\hbar[&S_{zz}(2)(3\cos^2\theta_{13z}(2) - 1) \\ &+ (S_{xx}(2) - S_{yy}(2))(\cos^2\theta_{13x}(2) - \cos^2\theta_{13y}(2)) \\ &+ 4S_{xz}(2)\cos\theta_{13x}(2)\cos\theta_{13z}(2)] \end{aligned} \tag{11.38}$$

where x, y, z refer to the molecular frame.

The local order parameters are related by:

$$S_{zz}(1) = S_{zz}(2) = S_{zz}(\text{ring})$$

$$S_{xx}(1) - S_{yy}(1) = S_{xx}(2) - S_{yy}(2) = S_{xx}(\text{ring}) - S_{yy}(\text{ring})$$

$$S_{xz}(1) = -S_{xz}(2).$$

If the bond lengths and angles are identical in the two conformers, then the geometrical terms in the two conformers are equal, that is $r_{13}(1) = r_{13}(2) = r_{13}$, and $\theta_{13\alpha}(1) = \theta_{13\alpha}(1) = \theta_{13\alpha}$. When the two conformers interconvert rapidly the averaged coupling is given by

$$\begin{aligned} \langle C_{13}\rangle = -\frac{1}{2}\left(\frac{\mu_0}{4\pi}\right)\frac{\gamma_H^2}{r_{13}^3}\hbar[&S_{zz}(\text{ring})(3\cos^2\theta_{13z} - 1) \\ &+ (S_{xx}(\text{ring}) - S_{yy}(\text{ring}))(\cos^2\theta_{13x} - \cos^2\theta_{13y})] \end{aligned} \tag{11.39}$$

where the $S_{\alpha\alpha}(\text{ring})$ are local order parameters for the ring. Extending the averaging to be over all the possible chain conformations leads to the conclusion that Equation (11.39) still holds because all the conformations are related by the symmetry of the rotational potentials about the bonds. Thus, the number of non-zero local order parameters used to describe interactions within a rigid subgroup is determined by the symmetry of the subgroup combined with the symmetry of the rotational potentials.

It is important to note that although the dipolar couplings between nuclei within the ring do not depend on off-diagonal elements $S_{\alpha\beta}$(ring), these elements are not zero.

Now let us consider a rigid subgroup in the chain (Fig. 11.6(c)).

The two protons lie above and below the x^{mol}–y^{mol} plane, and R_1 and R_2 represent the rest of the alkyl chain. The dipolar couplings between nuclei 1–5 within this fragment, labelled 'cf' for chain fragment, averaged over all the molecular conformations depend on local order parameters S_{zz}(cf), S_{xx}(cf) – S_{yy}(cf), and S_{xz}(cf). Measurement of all these couplings would enable these three elements to be obtained, but again note that the other off-diagonal elements are not zero, but they cannot be determined from the dipolar couplings. If the two protons are replaced by deuteriums, then measurement of their quadrupolar splitting $\Delta\nu_4 = \Delta\nu_5 = 3\chi_{\mathrm{CD}}/2$, gives just $S_{\mathrm{CD}}(4) = S_{\mathrm{CD}}(5)$, which are local order parameters expressed in a frame with one of the axes along the C–D bond direction. These are related to the $S_{\alpha\beta}$(cf) by Equation (11.30).

11.9.3 Conformationally dependent order parameters

How are the local order parameters for different rigid subgroups within a flexible molecule related to one another? To answer this question a conformationally dependent singlet orientational probability density, $P_{\mathrm{LC}}(\beta_{md}, \gamma_{md}, \phi_l)$ is defined, which is the probability that the molecule is at an orientation in the liquid-crystalline phase when in a conformation specified by a set of bond rotational angles ϕ_l. A straightforward extension of Equations (11.7) and (11.8) then allows us to define order parameters, $\langle D^{2*}_{0n}\rangle(\phi_l)$, which depend on the conformational state of the molecule (or equivalently, $S_{\alpha\beta}(\phi_l)$):

$$\begin{aligned}\langle D^{2*}_{0n}(0, \beta_{md}, \gamma_{md})\rangle(\phi_l) &= \langle D^{2*}_{0n}\rangle(\phi_l) \\ &= \int D^{2*}_{0n}(0, \beta_{md}, \gamma_{md}) P_{\mathrm{LC}}(\beta_{md}, \gamma_{md}, (\phi_l)) \sin\beta_{md} \mathrm{d}\beta_{md} \mathrm{d}\gamma_{md}\end{aligned} \tag{11.40}$$

Local order parameters, $\langle D^{2*}_{0n}\rangle(j)$, are obtained by integrating over all the angular variables:

$$\begin{aligned}\langle D^{2*}_{0n}(0, \beta_{md}, \gamma_{md})\rangle(j) &= \langle D^{2*}_{0n}\rangle(j) \\ &= \int D^{2*}_{0n}(0, \beta_{md}, \gamma_{md}) P_{\mathrm{LC}}(\beta_{md}, \gamma_{md}, (\phi_l)) \sin\beta_{md} \,\mathrm{d}\beta_{md} \mathrm{d}\gamma_{md} \mathrm{d}\phi_l\end{aligned} \tag{11.41}$$

To obtain the $\langle D^{2*}_{0n}\rangle(\phi_l)$ from experimental data it is necessary to propose a model for $P_{\mathrm{LC}}(\beta_{md}, \gamma_{md}, (\phi_l))$, while values of the local order parameters $\langle D^{2*}_{0n}\rangle(j)$ may be obtained directly from partially averaged dipolar or quadrupolar splittings.

11.10 Determination of the conformationally dependent orientational order parameters and the conformational distributions of molecules in liquid-crystalline phases from NMR parameters

Equation (11.40) shows that the conformationally dependent order parameters, $\langle D^{2*}_{0n}\rangle(\phi_l)$, or equivalently $S_{\alpha\beta}(\phi_l)$, can be obtained if $P_{LC}(\beta_{md}, \gamma_{md}, (\phi_l))$ is known. It is also possible to obtain the conformational distribution $P_{LC}(\phi_l)$ from this function by integration over β_{md} and γ_{md}:

$$P_{LC}(\phi_l) = \int P_{LC}(\beta_{md}, \gamma_{md}, (\phi_l))\sin\beta_{md}\,d\beta_{md}\,d\gamma_{md} \tag{11.42}$$

The function $P_{LC}(\beta_{md}, \gamma_{md}, (\phi_l))$ is characterized from the averaged dipolar couplings or deuterium quadrupolar splittings. Both depend on $P_{LC}(\beta_{md}, \gamma_{md}, (\phi_l))$ via the conformationally dependent order parameters, $S_{\alpha\beta}(\phi_l)$ and $P_{LC}(\phi_l)$. Thus,

$$\langle C_{ij}\rangle_{\phi} = \int C_{ij}(\phi_l)P_{LC}(\phi_l)\,d\phi_l \tag{11.43}$$

where

$$\begin{aligned} C_{ij}(\phi_l) = -\frac{1}{2}(3\cos^2\beta_{dB} - 1)\left(\frac{\mu_0}{4\pi}\right)\frac{\gamma_i\gamma_j}{r_{ij}(\phi_l)^3}\frac{\hbar}{2} \\ [S_{aa}(\phi_l)(3\cos^2\theta_{ija}(\phi_l) - 1) \\ + (S_{bb}(\phi_l) - S_{cc}(\phi_l))(\cos^2\theta_{ijb}(\phi_l) - \cos^2\theta_{ijc}(\phi_l)) \\ + 4S_{ab}(\phi_l)\cos\theta_{ija}(\phi_l)\cos\theta_{ijb}(\phi_l) \\ + 4S_{ac}(\phi_l)\cos\theta_{ija}(\phi_l)\cos\theta_{ijc}(\phi_l) \\ + 4S_{bc}(\phi_l)\cos\theta_{ijb}(\phi_l)\cos\theta_{ijc}(\phi_l)] \end{aligned} \tag{11.44}$$

The quadrupolar interaction is similarly

$$\langle\chi^{lab}_{zz,i}\rangle_{\phi} = \int \chi^{lab}_{zz,i}P_{LC}(\phi_l)d(\phi_l) \tag{11.45}$$

with

$$\chi^{lab}_{zz,i}(\phi_l) = \frac{1}{2}(3\cos^2\beta_{dB} - 1)\left[\chi^{PAF}_{aa,i}\left(S_{aa}(\phi_l) + \frac{1}{3}\eta_{Q,i}(S_{bb}(\phi_l) - S_{cc}(\phi_l))\right)\right] \tag{11.46}$$

Here it is assumed that the components $X^{PAF}_{aa,i}$, etc. do not depend on ϕ_l.

The general procedure is to assume a form for $P_{LC}(\beta_{md}, \gamma_{md}, (\phi_l))$, and to use it to calculate values of $\langle C_{ij}\rangle_{\phi}$ and/or $\langle X^{lab}_{zz,i}\rangle_{\phi}$ and to compare these with those observed. The calculated and observed values are then brought in to best agreement by minimizing the target function

$$F = \frac{\left(\sum_{i<j} \left[\langle C_{ij} \rangle_{\phi}(\text{observed}) - \langle C_{ij} \rangle_{\phi}(\text{calculated}) \right]^2 \right)^{\frac{1}{2}}}{N_{\text{f}}} \tag{11.47}$$

with respect to adjustable parameters in the model function $P_{\text{LC}}(\beta_{md}, \gamma_{md}, (\phi_l))$; N_{f} is the number of degrees of freedom.

11.10.1 Theoretical models for $P_{\text{LC}}(\beta_{md}, \gamma_{md}, (\phi_l))$

Let us examine now the general principles which can be used to guide a choice for a model of $P_{\text{LC}}(\beta_{md}, \gamma_{md}, (\phi_l))$. It is useful to define a potential $U_{\text{LC}}(\beta_{md}, \gamma_{md}, (\phi_l))$, which is related to $P_{\text{LC}}(\beta_{md}, \gamma_{md}, (\phi_l))$ by

$$P_{\text{LC}}(\beta_{md}, \gamma_{md}, (\phi_l)) = Z^{-1} \exp[-U_{\text{LC}}(\beta_{md}, \gamma_{md}, (\phi_l))/k_{\text{B}}T] \tag{11.48}$$

with

$$Z = \int \exp[-U_{\text{LC}}(\beta_{md}, \gamma_{md}, (\phi_l))/k_{\text{B}}T] \sin\beta_{md} \mathrm{d}\beta_{md} \mathrm{d}\gamma_{md} \mathrm{d}(\phi_l) \tag{11.49}$$

This effective potential can then be conveniently subdivided into a part, $U_{\text{iso}}((\phi_l))$, which can be regarded as being intrinsic to the molecules, and which contributes to the potential in both liquid-crystalline and isotropic phases, and a part, $U_{\text{ext}}(\beta_{md}, \gamma_{md}, (\phi_l))$, which contributes to the potential only in the liquid-crystalline phase. The term $U_{\text{iso}}((\phi_l))$ can be regarded as the potential for intramolecular motions. If these are rotations about bonds then $U_{\text{iso}}((\phi_l))$ is often written generally as

$$U_{\text{iso}}((\phi_l)) = \sum_l \sum_n V_{nl} \cos(n\theta) + U_{ij}^{\text{steric}} \tag{11.50}$$

The term U_{ij}^{steric} allows for short-range repulsion between atoms i and j. Note that the V_{nl} are specific to each bond rotation and so the first term in Equation (11.50) does not allow for any cooperativity in the intramolecular motions.

The anisotropic effective potential, $U_{\text{ext}}(\beta_{md}, \gamma_{md}, (\phi_l))$, can be expressed generally as the infinite series

$$U_{\text{ext}}(\beta_{md}, \gamma_{md}, (\phi_l)) = \sum_k \sum_n \varepsilon_{kn}(\phi_l) \mathcal{C}_{kn}(\beta_{md}, \gamma_{md}) \tag{11.51}$$

The $\mathcal{C}_{kn}(\beta_{md}, \gamma_{md})$ are modified spherical harmonics and are appropriate for uniaxial liquid-crystalline phases. For biaxial phases the Wigner functions $D^k_{n'n}(\alpha_{md}, \beta_{md}, \gamma_{md})$ must be used, but we will restrict the discussion to uniaxial phases.

Computer simulation studies have shown that drastically truncating the series in Equation (11.51) to just those terms with $k = 2$ is a reasonably good approximation, which leaves just five terms corresponding to $n = 0, \pm1, \pm2$.

The expansion coefficients $\varepsilon_{2n}(\phi_l)$ could also be expanded in a general series, such as a Fourier series

$$\varepsilon_{2n}(\phi_l) = \sum_q a_{ql} \cos(q\phi_l) + b_{ql} \sin(q\phi_l) \tag{11.52}$$

In fact, this expansion has not been used to model real data. Simpler, approximate models have been found to be quite successful. Thus, the Additive Potential methods [**9**] assign an interaction tensor, $\varepsilon_{2n}(j)$ to each rigid subunit, j, in the molecules, which do not depend on the ϕ_l. The $\varepsilon_{2n}(\phi_l)$ and $\varepsilon_{2p}(j)$ are related by

$$\varepsilon_{2n}(\phi_l) = \sum_j \sum_p \varepsilon_{2p}(j) D^2_{pn}(\alpha_j, \beta_j, \gamma_j) \tag{11.53}$$

The Euler angles $(\alpha_j, \beta_j, \gamma_j)$ give the orientation of the j fragment in the reference axes used to calculate the $\varepsilon_{2n}(\phi_l)$, and they vary as the molecule changes conformation. The number of non-zero, independent values of $\varepsilon_{2p}(j)$ depends on the local, effective symmetry of the jth fragment. As an example [**10**], consider the nematogen I35 (Fig. 11.7(a)).

The benzene ring A has effective symmetry C_{2v} and so the fragment tensor has principal axes x_A, y_A, z_A (Fig. 11.7(b)).

The independent, non-zero components of ε(ring A) are ε_{zz}(ring A) and ε_{xx}(ring A) – ε_{yy}(ring A). Ring B (Fig. 11.7(c)) has only a plane of symmetry so only y_B, the plane normal, is a principal axis and the non-zero components of ε(ring B) are

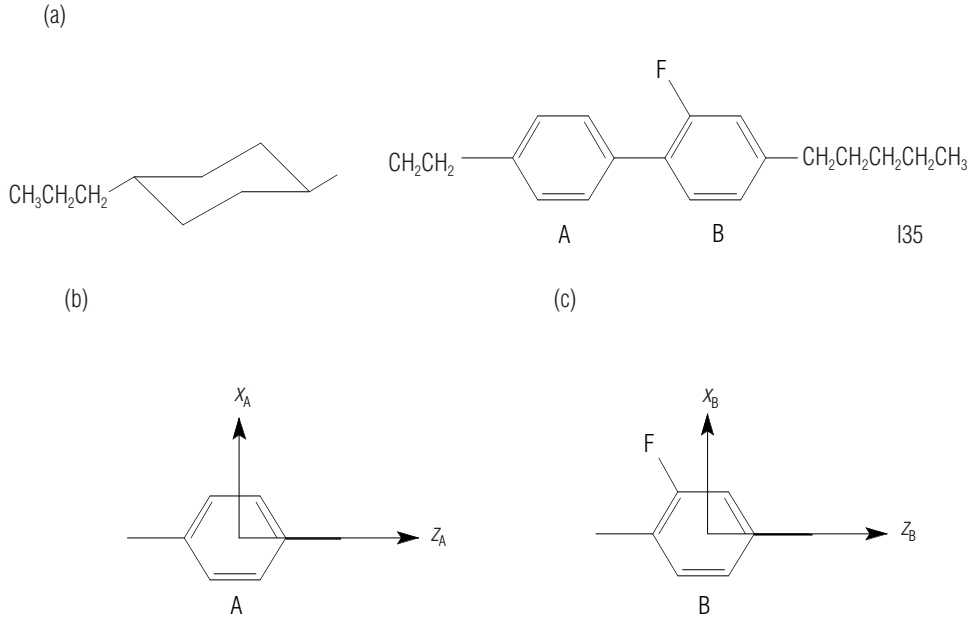

Fig. 11.7 (a) The nematogen I35. (b) Benzene ring A of I35 with a local axis frame. (c) Benzene ring B of I35 with a local axis frame.

ε_{zz}(ring B) and ε_{xx}(ring B) – ε_{yy}(ring B) and ε_{xz}(ring B) = ε_{zx}(ring B). In fact, because z_A and z_B are parallel then ε_{zz}(ring A) = ε_{zz}(ring B). The two rings are not coplanar and so ε_{xx}(ring A) – ε_{yy}(ring A) ≠ ε_{xx}(ring B) – ε_{yy}(ring B).

In the simplest model all the C–C bonds in the rest of the molecule are assumed to be cylindrically symmetric and assigned an identical ε_{zz}(C–C). An additional refinement would be to add a contribution ε_{zz}(C–H) for each C–H bond but, in practice, including this did not reduce the error function further.

This simple fragment additivity is easy to apply to complex molecules, but it does have flaws. The principal flaw is that the total interaction tensor $\varepsilon(\phi_l)$ for the *l*th conformation does not always reflect the overall shape correctly, as it should if, as expected, this is the most important factor determining how the $\varepsilon(\phi_l)$ change with conformation. An obvious way of correcting this flaw would be to make the $\varepsilon(\phi_l)$ directly proportional to the shape, and indeed this has been implemented. However, it proves to be expensive in terms of computer time.

Another general way of modelling the $\varepsilon(\phi_l)$ is to invoke the maximum entropy principle of information theory. This leads to the result

$$U_{\text{ext}}(\beta_{md}, \gamma_{md}, (\phi_l)) = \sum_{\lambda} A_\lambda \Lambda_{20}^{(\lambda)}(\beta_{md}, \gamma_{md}, (\phi_l)) \tag{11.54}$$

where $\Lambda_{20}^{(\lambda)}(\beta_{md}, \gamma_{md}, (\phi_l))$ is the λth measured anisotropic NMR parameter, usually a dipolar coupling or a quadrupolar splitting. The coefficients A_λ are varied to bring observed and calculated data sets into best agreement. In the first implementations of the maximum entropy method the contribution of $U_{\text{int}}((\phi_l))$ was not included. The result of doing this is that the $P_{\text{LC}}(\beta_{md}, \gamma_{md}, (\phi_l))$ obtained is 'unbiased'. It starts from being completely flat if there are no experimental values of $\Lambda_{20}^{(\lambda)}$, and develops features which grow in intensity as the $\Lambda_{20}^{(\lambda)}$ values increase in magnitude. Including $U_{\text{int}}((\phi_l))$ with an assumed form [**11–13**] introduces bias, and the $P_{\text{LC}}((\phi_l))$ will be close to $P_{\text{iso}}((\phi_l))$, the conformational distribution in the isotropic phase, if the $\Lambda_{20}^{(\lambda)}$ are all small, and may deviate considerably from the isotropic distribution if the $\Lambda_{20}^{(\lambda)}$ are large. This behaviour is also found for the distributions derived by the Additive Potential methods, and is consistent with results obtained by computer simulations.

The use of NMR to obtain the conformational distribution of a mesogen is illustrated by the case of the nematogen 4-pentyl-4′-cyanobiphenyl (5CB) which was partially deuteriated as shown in Fig. 11.8. The deuterium spectrum is shown in Fig. 11.9 and this was analysed to yield six quadrupolar splittings, $\Delta\nu_i$. The conformations which the alkyl chain can adopt were simplified by using the rotational isomeric state (RIS) model. This assumes that for each of the three different fragments C_{i-1}–C_i–C_{i+1}–C_{i+2} (i = 2, 3 and 4) there are just three rotational states, *trans*, *gauche*$^+$ and *gauche*$^-$ (Fig. 11.10).

In this simple model there are fourteen conformers generated by rotations about the C–C bonds in the alkyl chain. Figure 11.11 shows the probabilities of these

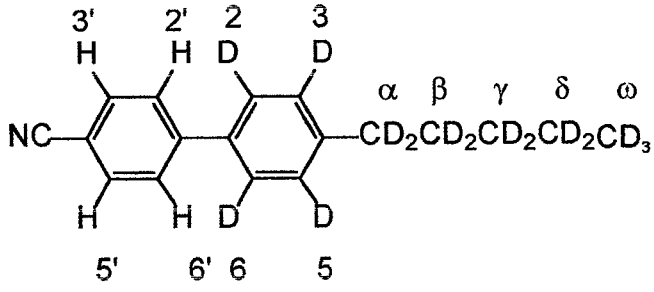

Fig. 11.8 Partially-deuteriated 5CB-d_{15}.

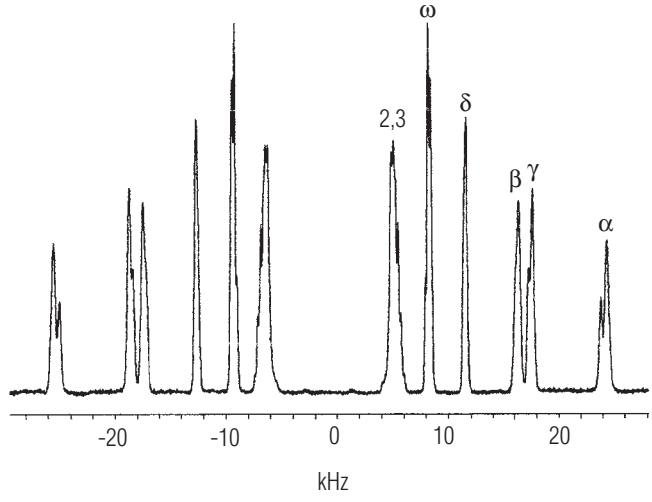

Fig. 11.9 30.7 MHz deuterium spectrum of 5CB-d_{15}.

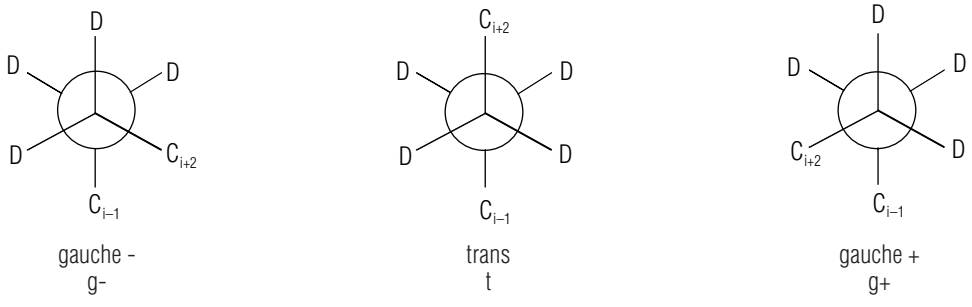

Fig. 11.10 Rotational states of an alkyl chain considered in the discussion of 5CB (Fig. 11.8).

conformers obtained by the Additive Potential method by fitting calculated to observed quadrupolar splittings. For this molecule the differences between $P_{LC}(\phi_1, \phi_2, \phi_3)$ and $P_{iso}(\phi_1, \phi_2, \phi_3)$ are large, being about 30% for the rotamer *ttt*. One should note that NMR is unique in providing experimental evidence of how the molecular conformational distribution is changed by the formation of a liquid-crystalline phase.

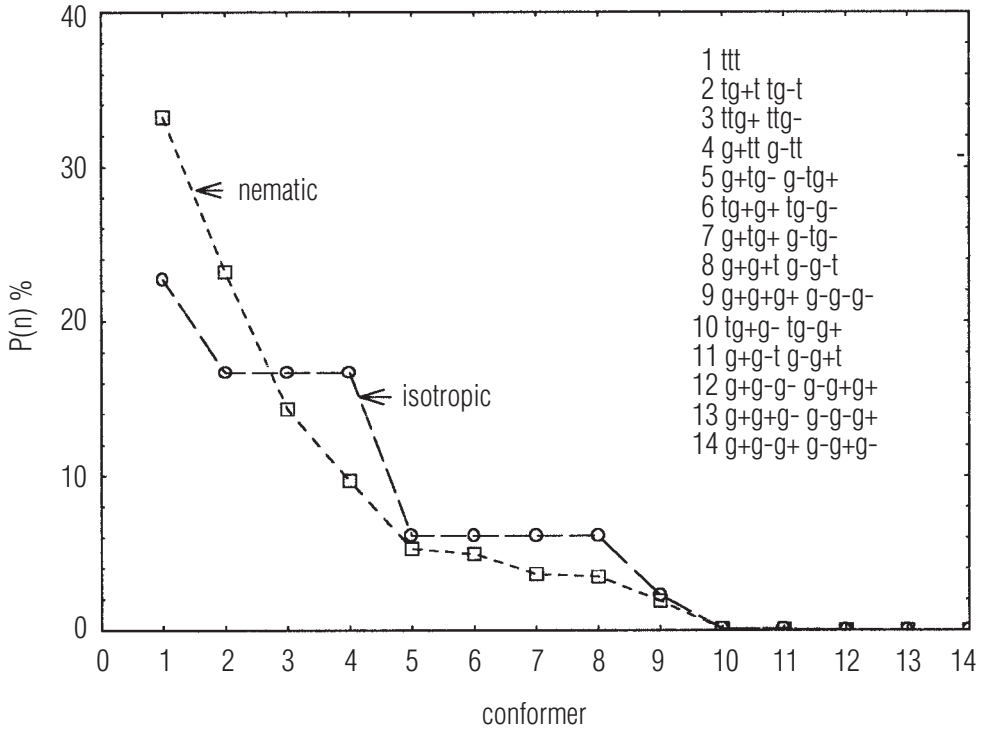

Fig. 11.11 Probabilities, *P*(*n*) of the conformers of 5CB (Fig. 11.8) in nematic and isotropic phases as obtained from an analysis of the deuterium quadrupolar splittings by the Additive Potential method.

11.11 NMR experiments for liquid-crystalline samples

Most of the NMR experiments which are used to study liquid-crystalline samples are straightforward applications of methods developed for solid or isotropic liquid samples. There are some techniques, however, which are particularly useful for liquid-crystalline samples.

11.11.1 Simplification of proton spectra by partial deuteriation plus deuterium decoupling

The spectra given by groups of protons become increasingly complex as the number of interacting protons increases. A limit is reached when there is more than about eleven protons, when the spectrum becomes a broad, unresolved resonance. Even below this limit the spectra may be resolved, but be virtually impossible to analyse in isolation. The most general method for obtaining the dipolar couplings from such intractable spectra is to reduce the number of interacting protons by replacing some of them by deuterium. This in itself is not usually sufficient to produce an analysable

spectrum, and the crucial step is to decouple the ^1H–^2H spin–spin interactions. The decoupling is best achieved by irradiating at the centre of the deuterium spectrum with a single frequency, that is without any modulation. Good results have been obtained by using a single, double-tuned solenoid coil with a diameter of about 8 mm. The sample is contained in a 5 mm o.d. tube of about 20 mm length, with the sample prevented from running out of the horizontally held tube by a vortex plug, as shown in Fig. 11.12. The free induction decays are acquired while irradiating the deuteriums with about 10 W of rf power. The decoupling power will heat the sample and this has a large effect on the magnitude of the dipolar couplings and leads to very broad lines. This heating is avoided by having the power on only while acquiring the FID and having a period between pulses of several (typically 5–10 s) seconds to allow the heat to dissipate. The acquisition time is restricted to being less than about 0.1 s. Figure 11.13 shows the ^1H–$\{^2H\}$ spectrum obtained for the four protons in the molecule shown in Fig. 11.8. It is an AA′BB′ spectrum and is easily analysed to yield the dipolar couplings d_{AB}, $d_{AB'}$, and $(d_{AA'} + d_{BB'})$.

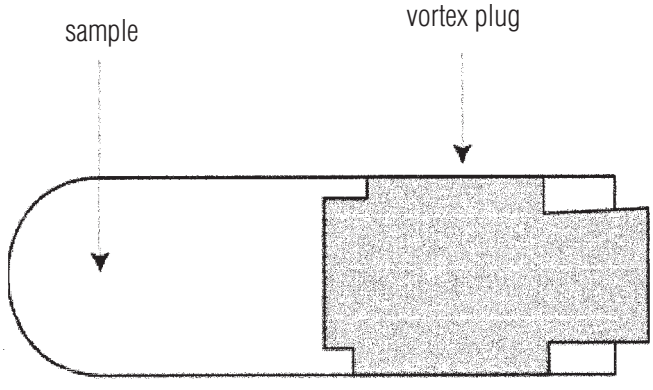

Fig. 11.12 Sample tube for ^1H–$\{^2H\}$ experiments on liquid-crystalline samples.

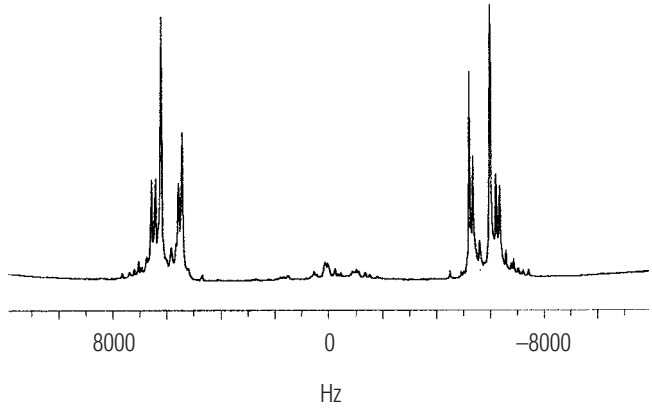

Fig. 11.13 200 MHz ^1H–$\{^2H\}$ spectrum of 5CB-d_{15}.

11.11.2 Multiple-quantum spectra

Multiple-quantum coherences are difficult to observe directly in NMR, but can be detected indirectly by a two-dimensional experiment, such as that using the pulse sequence shown in Fig. 11.14. The density matrix after the second 90° pulse contains coherences of all orders. Their relative intensities depend upon the interval τ and they all evolve during t_1 under the full hamiltonian of the spin system. The third 90° pulse converts unobservable multiple-quantum coherences into observable single-quantum coherence, whose decay is monitored during t_2. The three-pulse sequence produces all the possible nQ transitions, where n is the multiple-quantum order, and a selection is achieved by either phase cycling, as in Fig. 11.14(a), or by applying field gradient pulses as in Fig. 11.14(b). The value of τ is chosen experimentally to optimize the intensity of the desired multiple-quantum spectra. Note that the nQ spectra with $n < N$ cannot be phased and so the spectra are presented in magnitude mode. Another method utilizes the TPPI technique for obtaining all the nQ spectra simultaneously, but with each spectrum shifted so as to prevent their overlap. The TPPI method is to increment the phase by $2\pi/N$, where N is the total number of spins, at each value of Δt_1, the increment in the evolution period. This produces a shift in frequency of the nth order spectrum by $2n\pi/N\Delta t_1$. Figure 11.15 shows an example of the TPPI method applied to obtain all the nQ proton spectra of benzene dissolved in a nematic solvent [**14**].

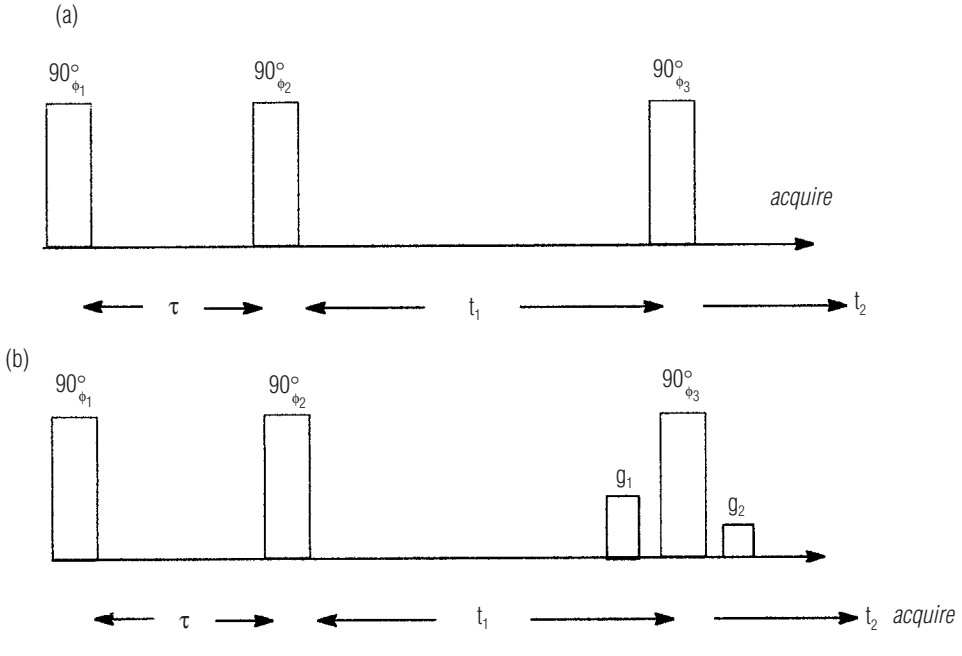

Fig. 11.14 Pulse sequence for the two-dimensional multiple-quantum experiment using order selection by (a) phase cycling, and (b) field gradients.

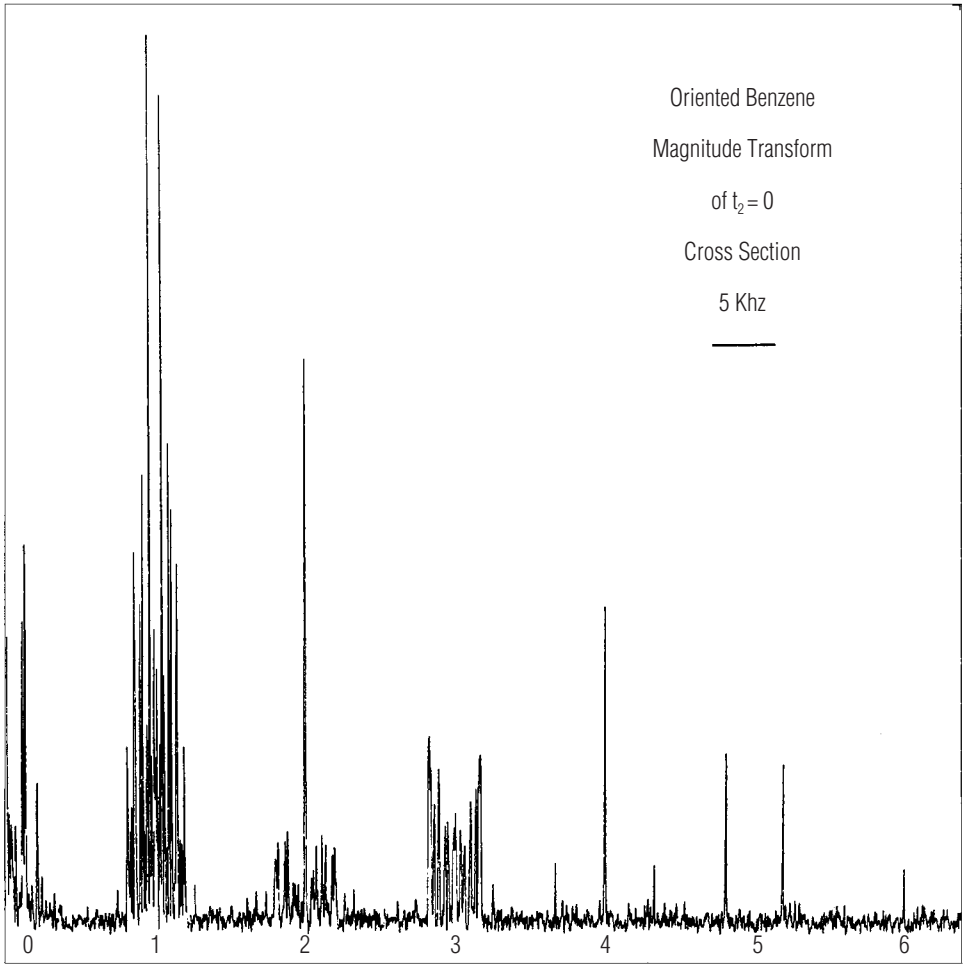

Fig. 11.15 Multiple-quantum spectra of benzene dissolved in a nematic solvent obtained by the TPPI method [**14**]. The coherence orders (*n*) giving rise to each component of the spectrum are shown below the spectrum.

The great advantage of multiple-quantum spectra is their simplicity. Thus, the *N*Q spectrum is always a single line. The number of lines increases as *n* decreases, as can clearly be seen in Fig. 11.15. It should be noted that multiple-quantum spectroscopy does not increase the size of a spin system that could in theory be analysed. This is because it is still necessary to simulate the *n*Q spectra with the full hamiltonian for a spin system. The advantage of multiple-quantum spectroscopy is to facilitate the analysis of spectra which are too complex to analyse by conventional techniques. A good illustration of this point is provided by the case of the proton spectrum of ethylbenzene (Fig. 11.16) dissolved in nematic solvents [**15**]. There are ten protons in the molecule and the spectrum is very complicated, as shown in Fig. 11.17, and defied many attempts at analysis. The spectrum was finally analysed by combining multiple-quantum spectroscopy, and partial deuteriation plus spin-

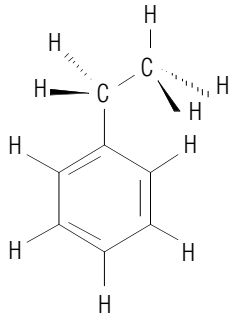

Fig. 11.16 Ethylbenzene.

echo refocusing to simplify the spectra. Thus Fig. 11.18(a) shows a 9Q spectrum of ethylbenzene obtained with the pulse sequence shown in Fig. 11.14(a), while Fig. 11.18(b) shows the 6RQ (the R denoting refocused) spectrum obtained from a sample of ethylbenzene-β,β,β-d_3 using the pulse sequence shown in Fig. 11.19. The 180° pulse in the centre of the t_1 period has the effect of refocusing the spin–spin interactions with a non-resonant nucleus, in this case deuterium, and also of refocusing the chemical shift differences in the proton spectrum. A systematic method of analysing a succession of nQ spectra has been developed [**16**].

11.11.3 Symmetry selection by multiple-quantum filtering

Single-quantum spectra of spin systems with some elements of permutation symmetry can be simplified by subjecting them to a multiple-quantum filter. The basic idea is that coherences can only be generated between states which belong to the same symmetry class of the permutation symmetry group of the spin system. The way that this can be exploited in order to simplify spectra is illustrated by a four spin-$\frac{1}{2}$ system in Fig. 11.20. There is only one transition with a change in the total magnetic quantum number of $\Delta M = 4$, and several with $\Delta M = 3$, but to simplify the diagram only two of these are shown. If the spins have some permutation symmetry, then the spin states $\alpha\alpha\alpha\alpha$ or $\beta\beta\beta\beta$ must belong to the highest symmetry class of the nuclear spin permutation group. The idea is to create the NQ or $(N - 1)$Q coherences, in this case $N = 4$, destroying all others either by phase cycling or gradient selection, and to transfer this coherence into single-quantum coherence by the pulse sequence in Fig. 11.14. The experiment is done with τ fixed at a value chosen to give a maximum intensity, and t_1 is fixed to the minimum value possible for the spectrometer hardware. The 1Q spectrum obtained by Fourier transforming with respect to t_2 contains transitions which are only between states belonging to the highest symmetry class of the spin permutation group. Figure 11.21 shows the ordinary, non-selected, and the 6Q selected spectra given by the ^{19}F nuclei in a sample of fluorobenzene dissolved in a nematic solvent [**17**]. The much simpler symmetry-selected spectrum reflects the high permutation symmetry in this spin system. Note

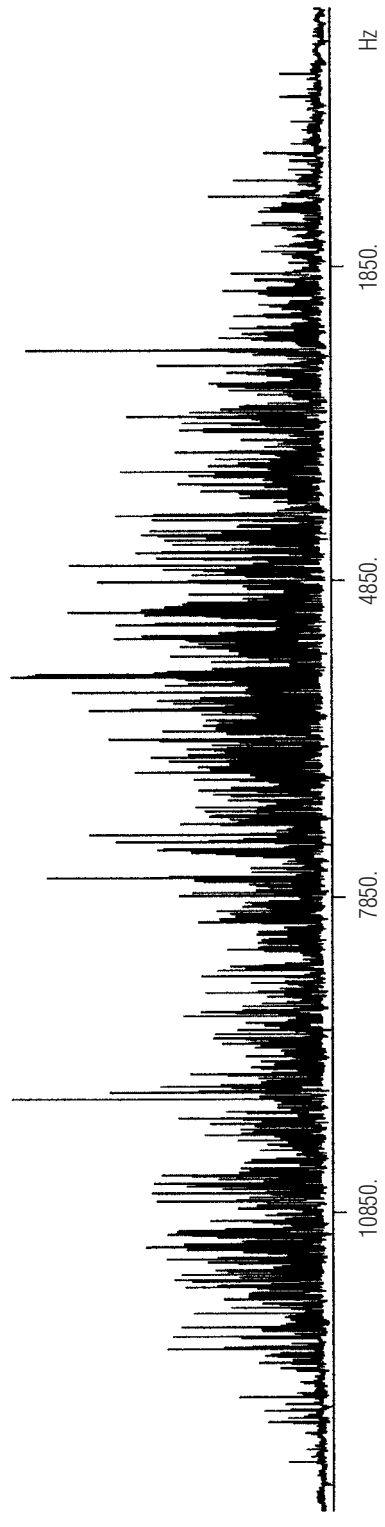

Fig. 11.17 300 MHz ^{1}H spectrum of ethylbenzene dissolved in a nematic solvent [**15**].

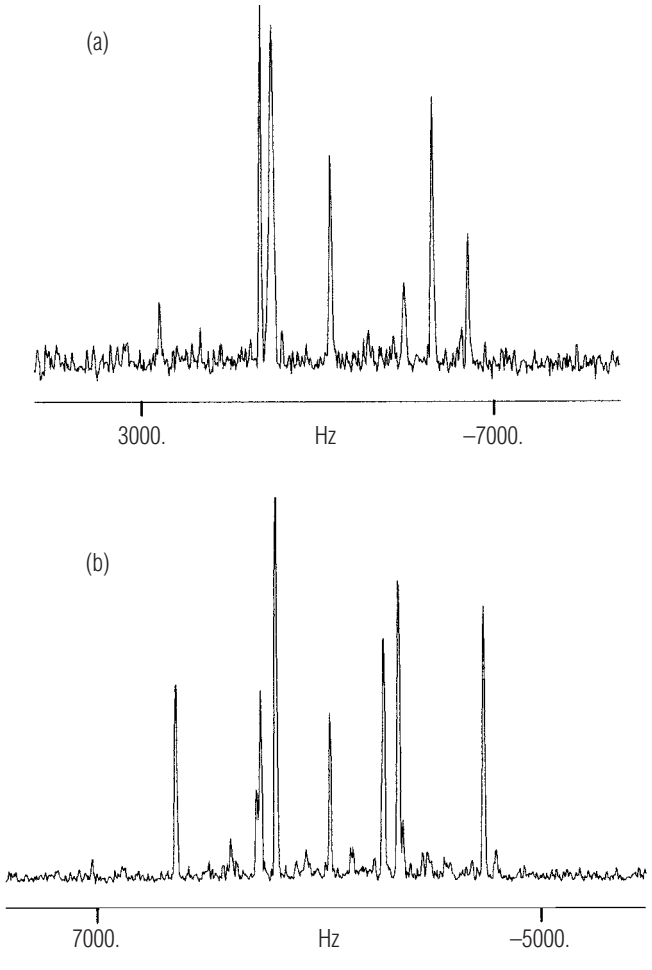

Fig. 11.18 300 MHz ^{1}H multiple-quantum spectra of a sample of (a) ethylbenzene, and (b) ethylbenzene-β,β,β-d_3 dissolved in a nematic solvent. The 9Q spectrum shown in (a) was obtained with the pulse sequence shown in Fig. 11.14(a), and the 6RQ spectrum in (b) was obtained with the sequence shown in Fig. 11.19.

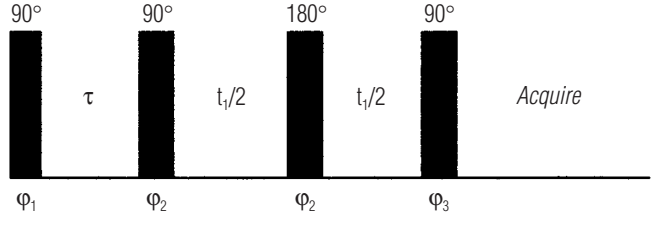

Fig. 11.19 Pulse sequence used to obtain n^lRQ spectra which have coupling to a non-resonant nucleus refocused.

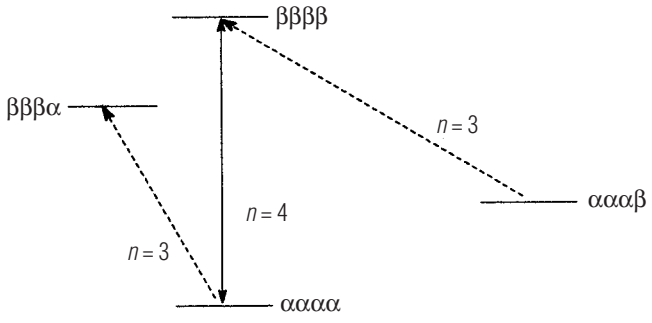

Fig. 11.20 Examples of transitions in a system of four spin-$\frac{1}{2}$ nuclei with changes in total magnetic quantum number, M, of 3 and 4. For the sake of clarity only two of the possible spin states with total magnetic quantum number $M = 1$ are shown.

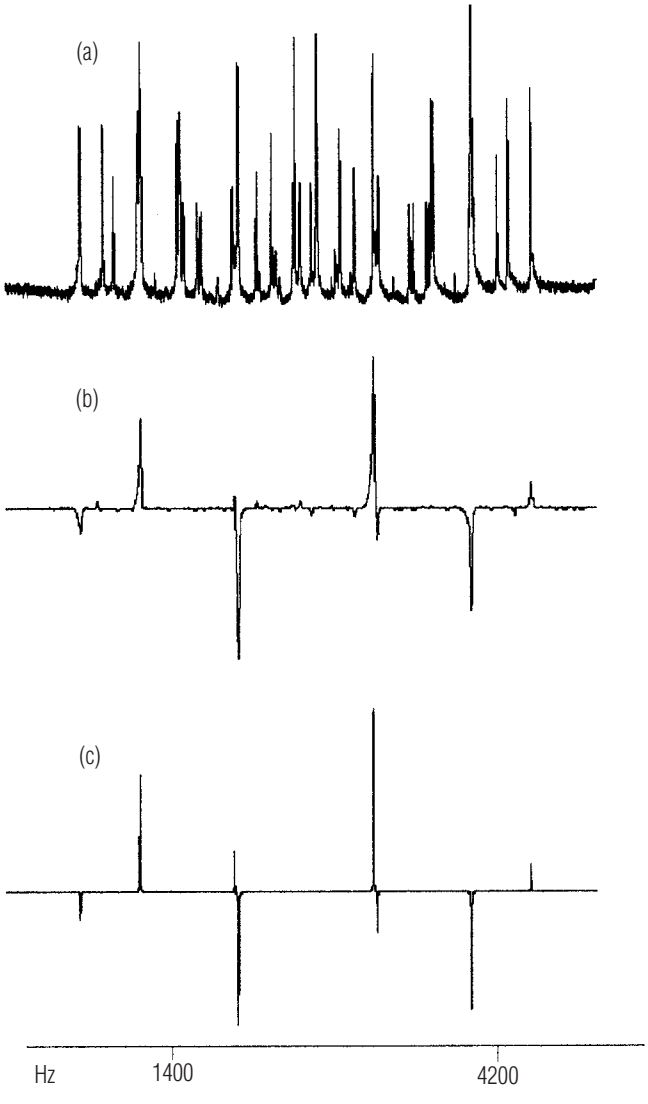

Fig. 11.21 188.3 MHz ^{19}F spectra of a sample of hexafluorobenzene dissolved in a nematic liquid-crystalline solvent. (a) The normal, non-selected, (b) a 6Q selected spectrum obtained with the pulse sequence shown in Fig. 11.14(b), and (c) a spectrum simulated with the parameters obtained by analysis of (a).

that *N*Q, but not (*N* – 1)Q, selected spectra can be phased, and that there is a division of the lines into two groups differing by a 180° phase shift.

11.11.4 Rotation of liquid-crystalline samples

The effect of rotating a liquid-crystalline sample about an axis β to B_0 is identical to that for solids when the directors cannot be aligned directly by the spectrometer field. This applies to many, if not most, phases other than the nematics. Nematic phases behave in a radically different way. Thus, nematic samples with a positive anisotropy, Δκ, in the magnetic susceptibility align parallel with B_0 when β is < 54.7° and the spinning rate, ν_R, exceeds a threshold frequency, ν_{th}. The value of ν_{th} depends upon the rotational viscosity and on B_0^2, and is typically ~ 200 Hz at 4.7 T. The effect on the NMR spectrum is that all the anisotropic terms are scaled by a reduction factor,

$$R(\beta) = \frac{1}{2}(3\cos^2\beta - 1) \tag{11.55}$$

When β > 54.7° the directors are distributed in the plane perpendicular to the rotation axis. The anisotropic interactions become averaged by the spinning, but there are also spinning sidebands produced at intervals of $2\nu_R$, whose intensities are dependent on the magnitude of the anisotropic interactions.

At the magic angle, the director is free to adopt a completely random orientation, and spinning now has the same effect as on a polycrystalline solid, that is the spectrum is dispersed over spinning sidebands at intervals of ν_R.

Samples with Δκ negative have their directors aligned when β > 54.7° are distributed in the plane perpendicular to the rotation axis when β < 54.7°, and show the same behaviour as samples with Δκ positive.

Figures 11.22 and 11.23 show the effect of rotating a sample of fluorobenzene [**18**] dissolved in the nematic liquid-crystalline solvent manufactured by Merck and known as ZLI 1167. It is a mixture of three compounds (Fig. 11.24).

This liquid crystal has Δκ negative, and also does not contain any aromatic groups. The proton spectra of the fluorobenzene dissolved in ZLI 1167 are dependent on dipolar and scalar spin–spin couplings and are strongly second order. Their analysis is, however, quite straightforward, using an iterative computer program. The dipolar couplings are scaled by the reduction factor $R(\beta)$, and can be used to determine $R(\beta)$ with high precision. The ^{13}C–{^1H} spectra are much simpler and comprise a doublet for each group of equivalent ^{13}C nuclei. The doublet structure is because of spin–spin coupling to the fluorine.

The centre of each doublet is the chemical shift, $\delta_i(\beta)$, which is determined by the chemical shift anisotropy, Δ_{cs} (see Section 1.4.1), and the isotropic chemical shift, $\delta_{iso,i}$:

$$\delta_i(\beta) = R(\beta)\Delta_{cs,i} + \delta_{iso,i} \tag{11.56}$$

Figure 11.25 shows a plot of ^{13}C chemical shift, $\delta_{Ci}(\beta)$ against $R(\beta)$, which yields $\Delta_{cs,i}$ from the slopes and $\delta_{C.iso,i}$ as the intercepts.

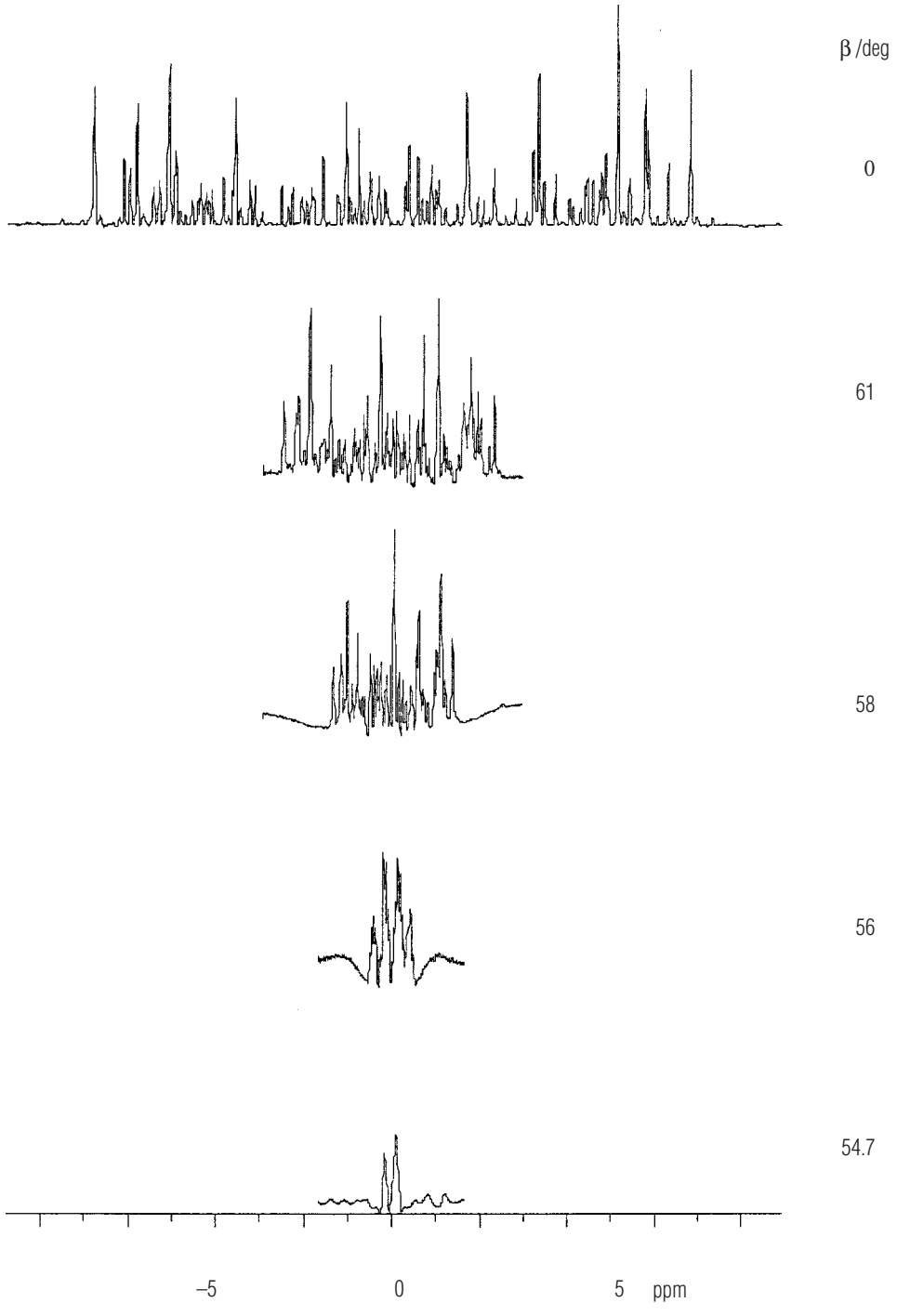

Fig. 11.22 200 MHz ^{1}H spectra of a sample of fluorobenzene dissolved in a nematic liquid-crystalline solvent and rotated at different angles, β, to the magnetic field. The values of β are shown against each spectrum.

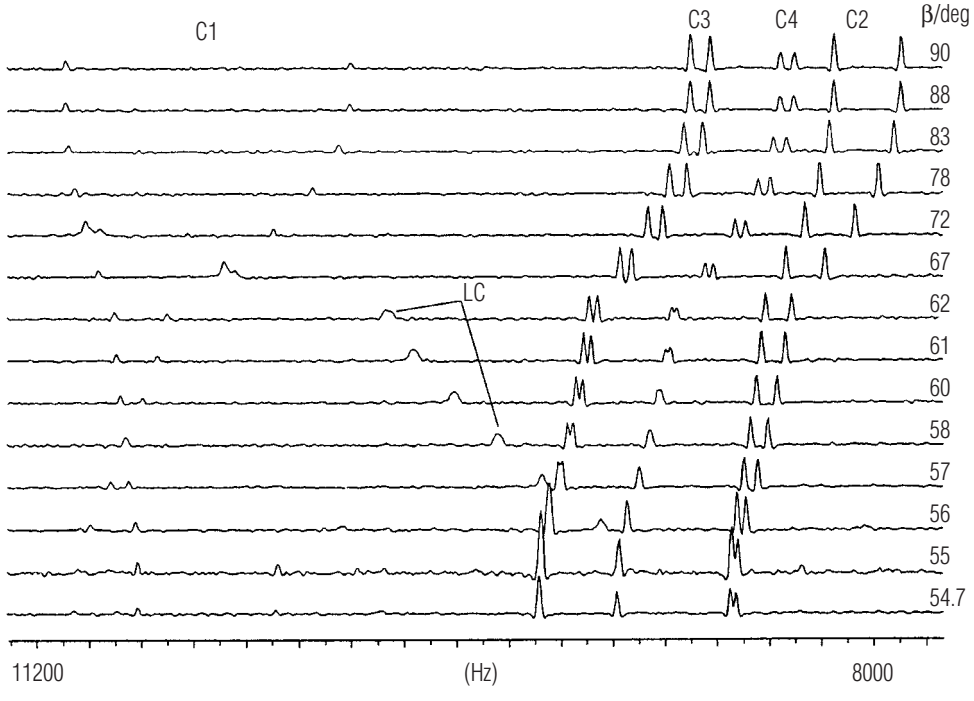

Fig. 11.23 50.3 MHz ^{13}C–{^1H} spectra of a sample of fluorobenzene dissolved in a nematic liquid-crystalline solvent and rotated at different angles, β, to the magnetic field. The values of β are shown against each spectrum.

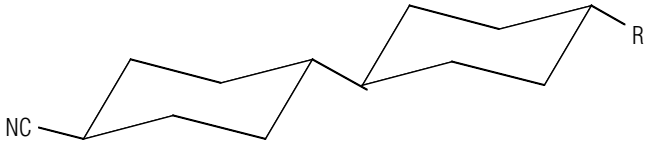

ZLI 1167 R = C_3H_7, C_5H_{11}, C_7H_{15}

Fig. 11.24 The nematic liquid-crystal solvent, ZLI 1167.

The doublet separations are equal to the magnitude of T_{CF} which depends on β through

$$T_{CF}(\beta) = R(\beta)(2C_{CF} + J_{aniso,CF}) + J_{CF} \qquad (11.57)$$

The relative signs of $(2C_{CF} + J_{aniso,CF})$ and J_{CF} are obtained by noting how $|T_{CF}(\beta)|$ varies with $R(\beta)$. Thus, it is very clear from the spectra in Fig. 11.23 that for C_1, $(2C_{CF} + J_{aniso,CF})$ and J_{CF} are of opposite sign when $\beta < 58°$. For this carbon the coupling $^1J_{CF}$ is known to be negative, and so the absolute sign of $(2C_{CF} + J_{aniso,CF})$ is obtained. The values of $J_{aniso,CF}$ in fluorobenzene are thought to be << C_{CF} and so the absolute sign of this dipolar coupling is derived. This in turn determines the sign of S_{zz} and from the proton spectra the sign of $S_{xx} - S_{yy}$. These order parameters can

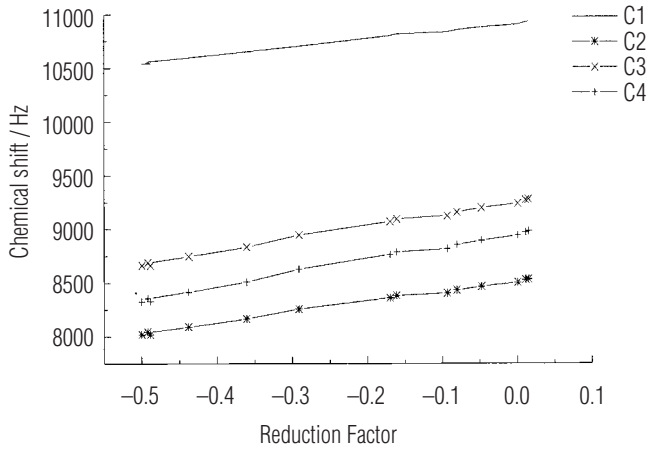

Fig. 11.25 Chemical shifts of the ^{13}C nuclei in a sample of fluorobenzene dissolved in a nematic solvent as a function of the reduction factor, $R(\beta)$ produced by sample rotation. C1–C4 refer to the different ^{13}C sites.

then be used to calculate the signs of the C_{CF} at the other positions, and then the absolute signs of the J_{CF} follow from the variation of the $T_{CF}(\beta)$ with $R(\beta)$.

The example of fluorobenzene illustrates the way in which sample rotation can be used to obtain the signs and the assignment of dipolar couplings between ^{13}C, a dilute spin, and ^{19}F, a single abundant spin. The method has also been used to obtain dipolar couplings between a group of abundant protons and single, diluted protons in the partially deuteriated liquid crystal shown in Fig. 11.8. Figure 11.13 shows the deuterium-decoupled proton spectrum. The four abundant protons give the ten intense lines, but the sample was 98% deuteriated and weak lines occur from the species shown in Fig. 11.26 containing a single proton in addition to the four abundant protons.

The weak lines at the base of the left-hand side set of strong lines, and the lines in the centre of the spectrum, come from molecules 1 and 2 in Fig. 11.26, and these are shown on an expanded scale in Fig. 11.27. The lines from the molecules 3–8 are mainly hidden under the strong lines at the right-hand side of Fig. 11.13. They can be revealed by rotating the sample at different angles, β, of the rotation axis to B_0, as shown by the spectra in Fig. 11.28. The experiments revealed the dipolar couplings between the single dilute protons and the four abundant aromatic protons [**19**].

11.11.5 Liquid-crystalline mixed solvents consisting of two components of opposite sign of the anisotropy in their magnetic susceptibility

The directors of a nematic liquid crystal with a positive anisotropy, $\Delta\kappa$, in the magnetic susceptibility will orient parallel to $\mathbf{B}_0$, while they orient at 90° when $\Delta\kappa$ is negative. Mixing two such nematogenic solvents in proportions such that $\Delta\kappa$ is approximately zero produces a solvent in which the directors will switch from being parallel to perpendicular to $\mathbf{B}_0$ as the temperature is changed, and over a small range both director orientations coexist. These mixed solvents can be very useful in giving

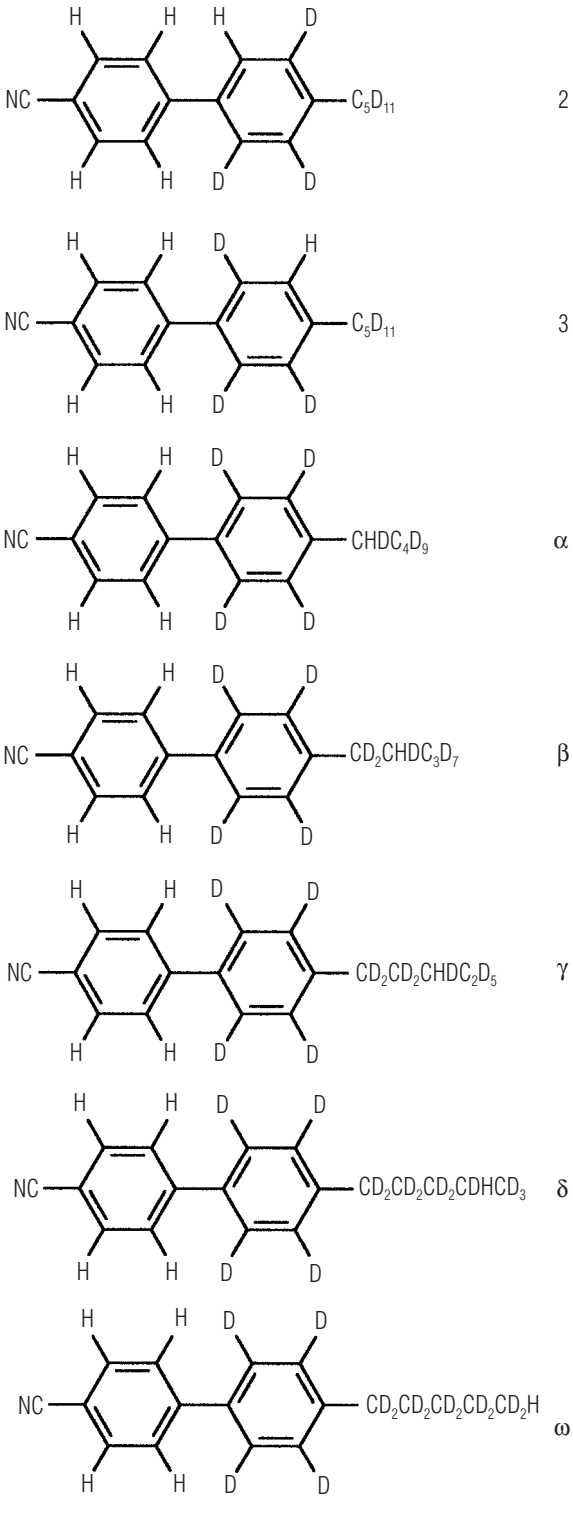

Fig. 11.26 Isotopomers of 98% deuteriated 5CB-d_{15} containing five protons.

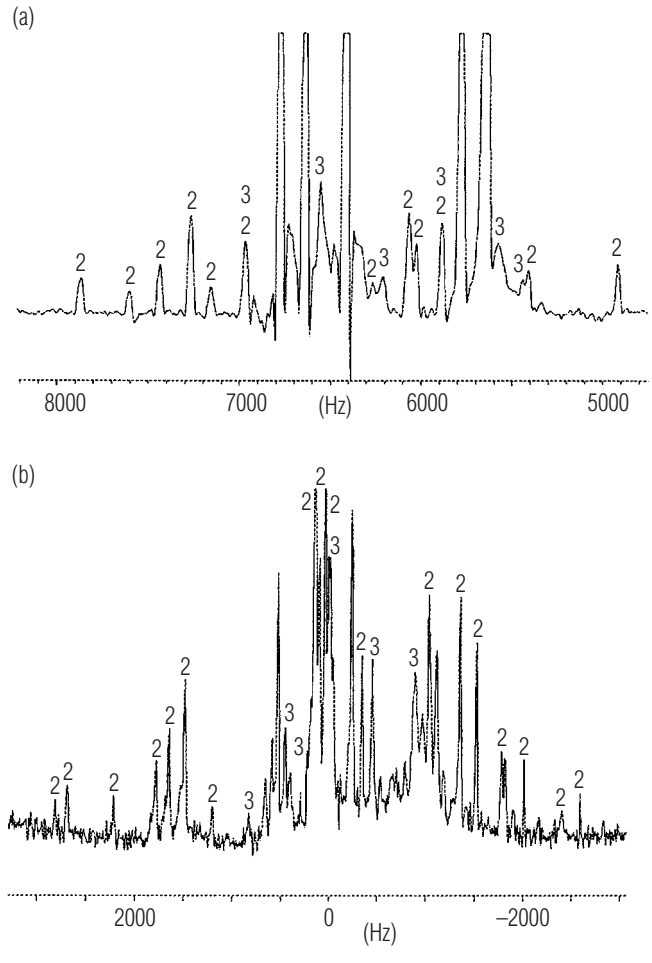

Fig. 11.27 Expansions of the 200 MHz ^{1}H–{^{2}H} spectra of 5CB-d_{15} shown in Fig. 11.13. (a) The left outer part, and (b) the centre part. The peaks are labelled with the site of the fifth, dilute proton in the isotopomer (see Fig. 11.26).

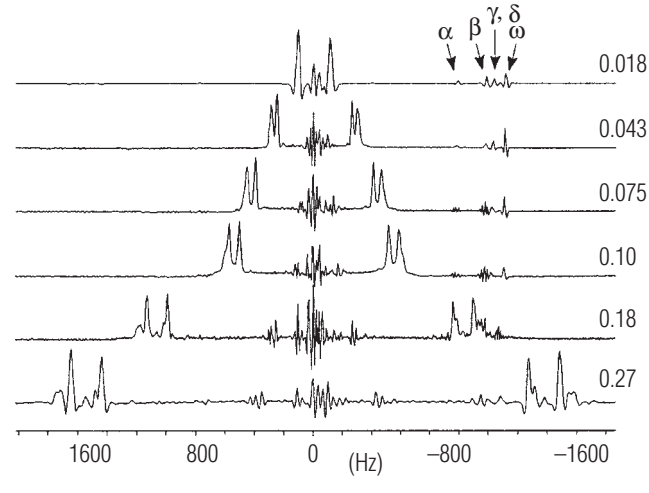

Fig. 11.28 200 MHz ^{1}H–{^{2}H} spectra of 5CB-d_{15} obtained on a sample rotated about an axis making different angles, β, to the magnetic field. The reduction factors, $R(\beta)$ are shown against each spectrum.

spectra of solute molecules at the two director orientations, and therefore providing a means for separating scalar from anisotropic contributions to the chemical shift and spin–spin coupling.

Thus Equation (11.31) gives

$$\sigma^{\text{lab}}_{zz,i}(\text{parallel}) = \sigma_{\text{iso},i} + \sigma^{\text{lab}}_{\text{aniso},zz,i}$$

when the director is parallel to $\mathbf{B}_0$, and

$$\sigma^{\text{lab}}_{zz,i}(\text{perpendicular}) = \sigma_{\text{iso},i} - \frac{1}{2}\sigma^{\text{lab}}_{\text{aniso},zz,i}$$

when it is perpendicular. So that

$$\sigma_{\text{iso},i} = \frac{1}{3}(\sigma^{\text{lab}}_{zz,i}(\text{parallel}) + 2\sigma^{\text{lab}}_{zz,i}(\text{perpendicular}))$$

and

$$\sigma^{\text{lab}}_{\text{aniso},zz,i} = \frac{2}{3}(\sigma^{\text{lab}}_{zz,i}(\text{parallel}) - \sigma^{\text{lab}}_{zz,i}(\text{perpendicular}))$$

Note that this method does not separate out the contributions to $\sigma_{\text{iso},i}$ and $\sigma^{\text{lab}}_{\text{aniso},zz,i}$ from the electronic structure of the solute molecules and the bulk magnetic susceptibility of the sample.

For spin–spin coupling the most important result that can be obtained by recording spectra in a mixed solvent is the determination of the signs of the coupling constants, and in this sense it is giving the same information as the variable spinning experiment.

11.11.6 The separated local field experiment

This is a two-dimensional experiment which was initially applied to solid samples, but it has found particular uses for liquid-crystalline samples. It has usually been applied to obtain dipolar couplings between ^{13}C and ^{1}H nuclei, and the general nature of the simplest such experiments are illustrated in Fig. 11.29. In the t_1 interval the protons are subjected to a sequence, which effectively removes the dipolar coupling between the protons, so that carbon magnetization evolves under an effective hamiltonian, which in average hamiltonian theory, taken to *zero*th order has the general form

$$\hat{H}_{\text{eff}} = K_{\text{cs}}(\hat{H}^I_{\text{Z}} + \hat{H}^{IS}_{\text{dd}} + \hat{H}^{IS}_J) + K_{\text{dd}}\hat{H}^{II}_{\text{dd}} + \hat{H}^{II}_J + \hat{H}^S_{\text{Z}} + \hat{H}^{SS}_{\text{dd}} + \hat{H}^{SS}_J \qquad (11.59)$$

$\hat{H}^I_{\text{Z}}$ and $\hat{H}^S_{\text{Z}}$ are the Zeeman terms for the unobserved, labelled I, and observed, labelled S, nuclei. The terms $\hat{H}^{II}_{\text{dd}}$, $\hat{H}^{IS}_{\text{dd}}$ and $\hat{H}^{SS}_{\text{dd}}$ are forms of $\hat{H}_{\text{dd}}$ (see Equation (11.18)), and, $\hat{H}^{II}_J$, $\hat{H}^{IS}_J$ and $\hat{H}^{IS}_J$ are similarly forms of $\hat{H}_J$ (see Equation (11.34)). The terms K_{cs} and K_{dd} are reduction factors whose values depend upon the dipolar refocusing sequence. For an ideal refocusing sequence K_{dd} would be zero. The value

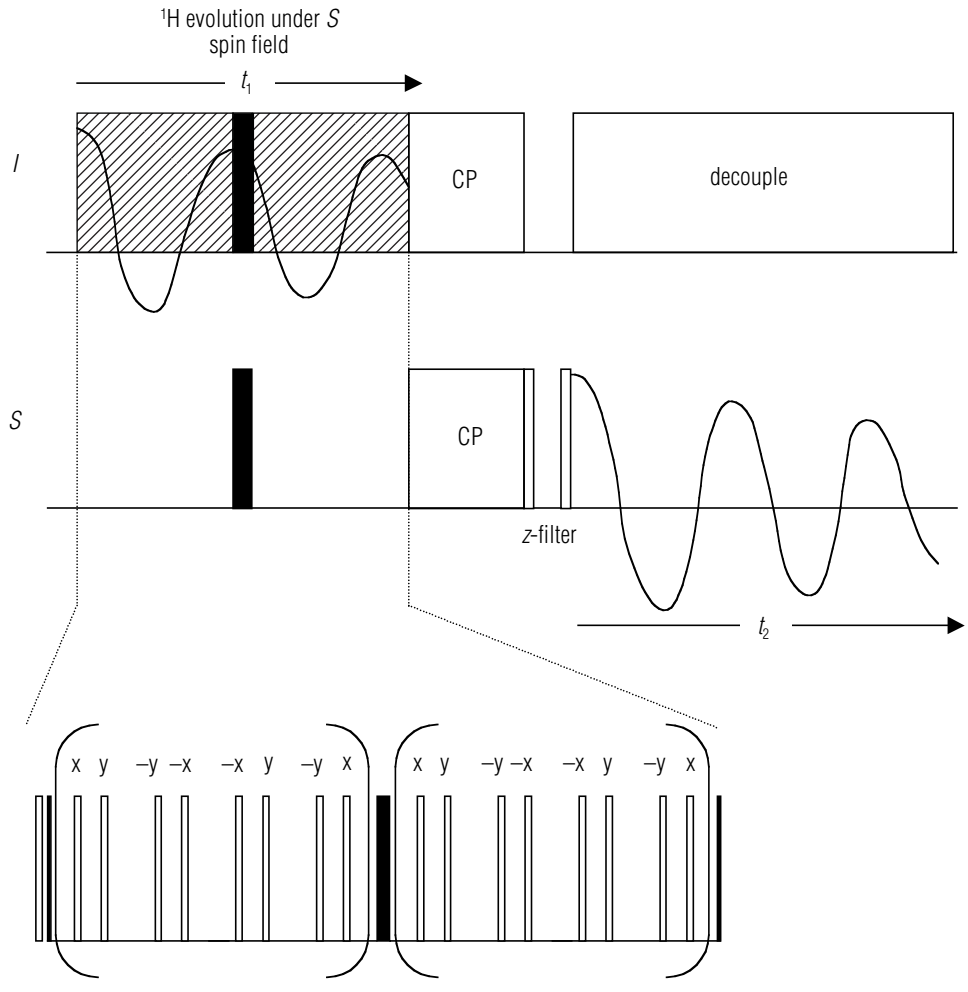

Fig. 11.29 The separated local field (SLF) experiment. Broad black lines are 180° pulses; narrow ones are 45° pulses; the rest are 90° pulses. The bracketed pulse sequences are MREV-8 sequences which remove homonuclear dipolar coupling between the *I* spins. Simultaneous 180° pulses on the *I* and *S* spins in the middle of the t_1 period remove the *I* spin chemical shift, while retaining the *I–S* dipolar coupling.

of K_{cs} for the MREV-8 sequence, as an example of a commonly used refocusing sequence, is predicted theoretically by average hamiltonian theory taken to zeroth order to be 0.471, provided the pulses are of infinitely short duration. In practice K_{cs} can be expected to deviate from this value depending upon the experimental realization of the pulses, and on the nature of the spin system. Since the aim of the experiment is to determine the dipolar couplings d_{IS}, the uncertainty in K_{cs} gives a systematic error in their determination.

The basic experiment to determine dipolar couplings between natural abundance ^{13}C and ^{1}H nuclei is very considerably improved by using ^{1}H rather than ^{13}C detection [**20, 21**]. A pulse sequence to obtain proton detected local field, PDLF, spectra is shown in Fig. 11.30(a). The advantage of PDLF is not only in sensitivity, which

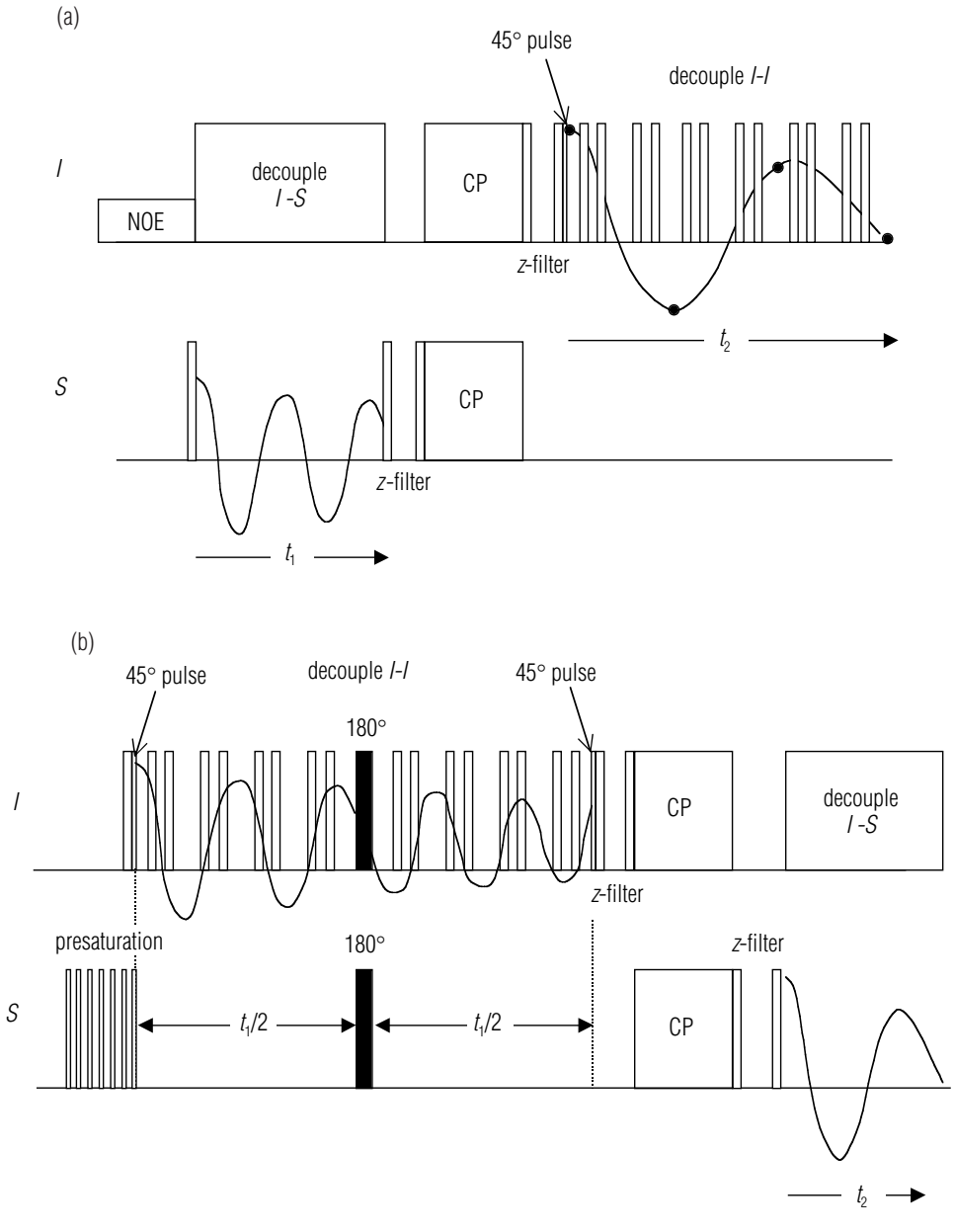

Fig. 11.30 Pulse sequence used to obtain (a) proton-detected local field (PDLF) and (b) proton-encoded local field (PELF) ^{13}C spectra. In the diagrams, narrow pulses are 90° pulses except for the 45° pulse indicated. In (a), a homonuclear dipolar decoupling sequence is used in t_2 to remove *I–I* dipolar coupling. The FID is therefore sampled at the points indicated (black dots) within the pulse cycles. In (b), the homonuclear dipolar decoupling sequence of length t_d is applied in t_1, which is therefore incremented in units of t_d [**20**].

is considerable, but also that the proton spectra are simpler. Simultaneous dipolar refocusing and detection is difficult, and an alternative is to use the pulse sequence shown in Fig. 11.30(b). In the t_1 period the proton magnetization evolves with inter-proton dipolar refocusing, and this is detected by observing the ^{13}C signal in t_2. The advantages of this proton-encoded local field experiment (PELF) are illustrated in Fig. 11.31, which shows the simulated spectra for an oriented sample of benzene. The SLF spectrum of the benzene comprises 36 lines. This is because the single ^{13}C isotopomers (Fig. 11.32) each contain six protons and the ^{13}C is coupled simultaneously to each of them, giving a doublet by H(1), a triplet by the protons H(2), a triplet by H(3), and a doublet by H(4). In contrast, the six protons couple only to a single ^{13}C, giving a doublet from one-bond coupling, $^1T_{CH}$, of relative intensity 1, a doublet from $^2T_{CH}$ of intensity 2, a doublet from $^3T_{CH}$ of intensity 2, and a doublet from $^4T_{CH}$, of intensity 1. In more complex molecules the effect of long-range coupling is to broaden all the lines in SLF spectra, while in PDLF or PELF it leads to a build up of an unresolved central line, but does not affect the widths of the larger split lines from short-range coupling. This is illustrated by the predicted spectra for the methyl carbon in 5CB shown in Fig. 11.31(b).

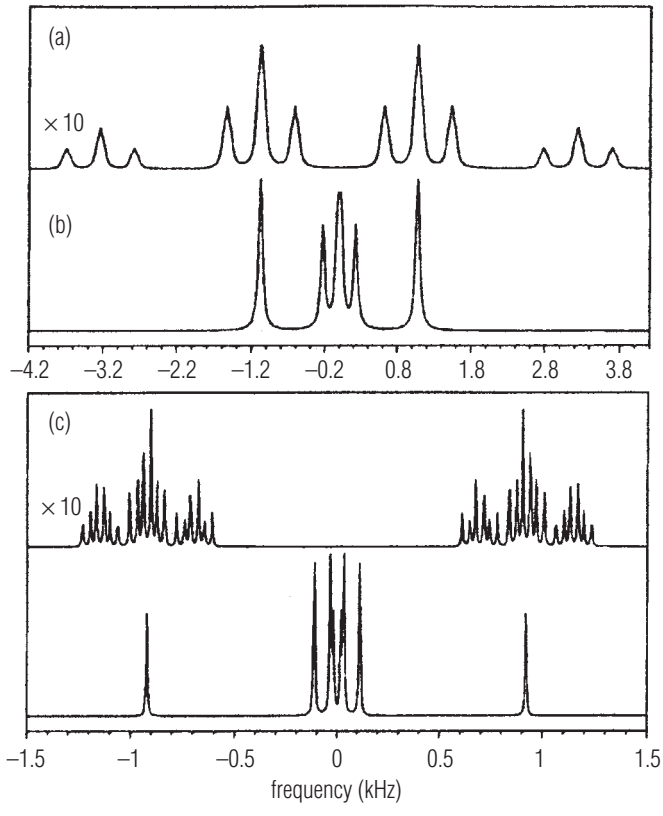

Fig. 11.31 Simulated SLF (a) and PDLF (b) spectra for oriented benzene, and (c) for the methyl group in 5CB (Fig. 11.8) [**21**].

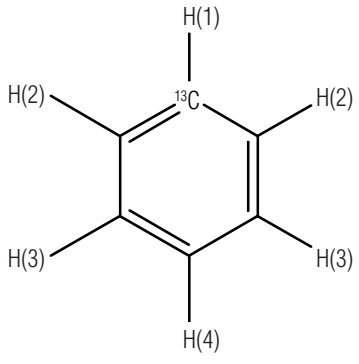

Fig. 11.32 The labelling scheme used in the discussion of the benzene molecule in text.

In practice, for mesogenic molecules the decoupling in the t_2 interval, and the efficiency of the refocusing in t_1 are both difficult to achieve because of the large magnitudes of the dipolar couplings. This situation can be improved by spinning the sample about an angle close to the magic angle. This leads to a reduction of all the anisotropic interactions and makes decoupling and refocusing more efficient. This combined technique is known as off-magic-angle spinning, OMAS. An example of an OMAS-PDLF spectrum of 5CB is shown in Fig. 11.33.

11.12 Spectra of chiral and prochiral molecules in chiral liquid-crystalline phases

The two R and S enantiomers of a molecule containing a single chiral centre when dissolved in a non-chiral liquid-crystalline phase will have identical NMR spectra. But, when in a chiral phase they will in principle have different spectra. This phenomenon can be used to measure the ratio of the concentrations of the two enantiomers, the enantiomeric excess. A very good chiral nematic phase for this purpose consists of a synthetic polypeptide dissolved in an organic solvent. The most used to date has been poly-(γ-benzyl-L-glutamate) (PBLG), whose structure is shown in Fig. 11.34, dissolved in organic solvents such as chloroform, methylene dichloride, and dimethylformamide. PBLG can be obtained commercially with different degrees of polymerization (DP), and good results are obtained when this is in the range 350–600. The chiral compound to be investigated is dissolved in the PBLG/solvent mixture, and thoroughly mixed by repeated centrifugation while in the NMR tube. The spectra differ because the order matrices S_R and S_S differ in both the magnitude of the principal elements, and the orientation of the principal axes. This difference manifests itself in principle as differences in all the partially averaged anisotropic NMR interactions, but some are more sensitive than others [**22**].

Deuterium spectra tend to be the most sensitive to differences in the orientational order of the enantiomers. The orientational order parameters for solutes in PBLG

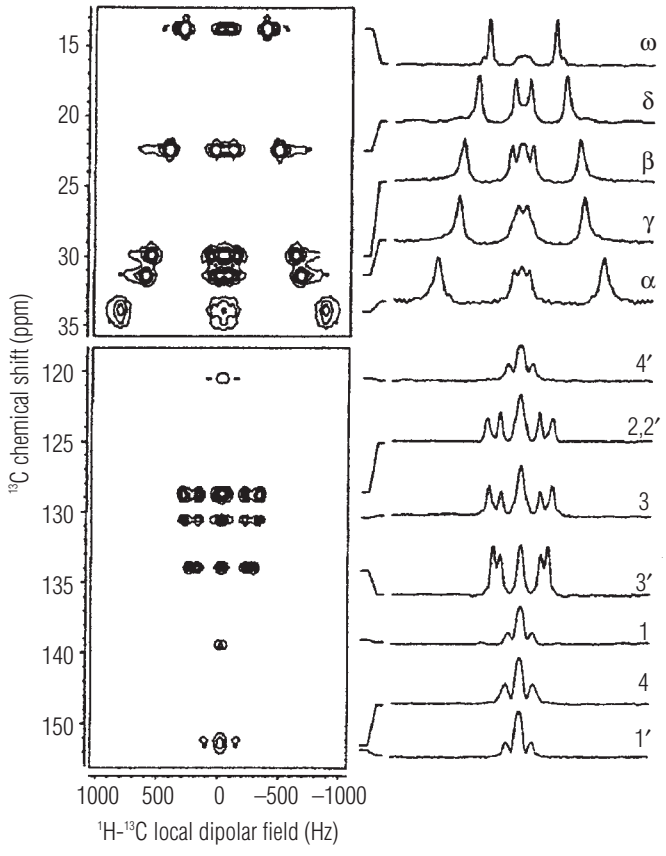

Fig. 11.33 Off-magic-angle (OMAS) spinning PDLF spectrum of 5CB (Fig. 11.8) [**21**].

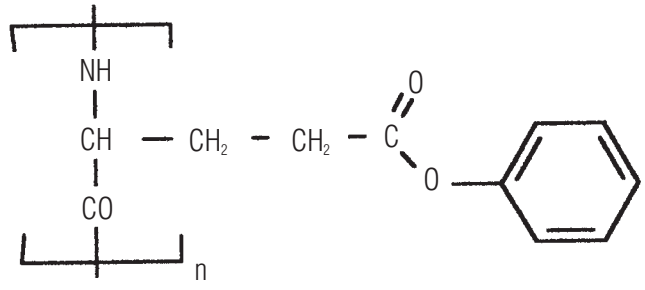

Fig. 11.34 Structure of poly-γ-benzyl-L-glutamate.

are very small, typically 10^{-3} to 10^{-4}, and so the quadrupolar splittings are <1 kHz, however, the widths of the lines are of the order of a few Hertz, and so the quadrupolar doublets from different enantiomers may easily be resolved. One very important development has been the ability to obtain ^{2}H–{^{1}H} spectra of deuterons at natural abundance [**23**]. Figure 11.35 shows an example [**22**] of the natural abundance ^{2}H–{^{1}H} spectrum of racemic 3-butyne-2-ol dissolved in PBLG/CHCl3.

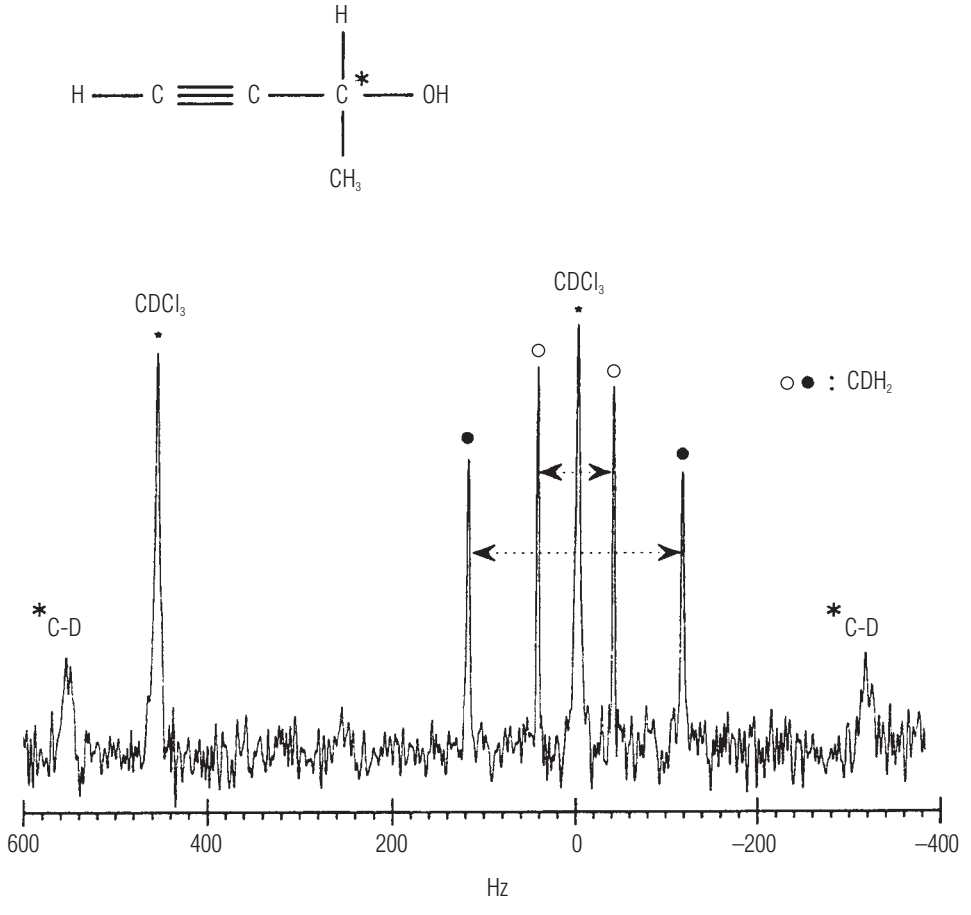

Fig. 11.35 38.4 MHz ^2H–{^1H} spectrum of racemic 3-butyne-2-ol dissolved in PBLG/$CHCl_3$ [**21**].

The spectra of enantiomers may also differ because of differences in chemical shift anisotropy or dipolar couplings. A study has been reported which compares the possible NMR methods of discriminating between enantiomers using PBLG/solvent as a chiral liquid-crystalline solvent [**22**].

A very interesting effect may be observed when prochiral molecules are dissolved in chiral liquid-crystalline solvents. For example, the spectrum from the two deuterium nuclei in CH_3CD_2OH as a solute in nematic solvent is a doublet. This is because the molecule has a mirror plane which makes the two C–D bonds equivalent, and so their order parameters, S_{CD}, are equal. When this molecule is a solute in PBLG/$CHCl_3$ the spectrum is two pairs of quadrupolar split doublets. The molecule appears to have lost the mirror plane symmetry. This is a general phenomenon and is not because the molecules are being distorted by their surroundings, but is a consequence of a reduction in symmetry of the chiral phase. A phase containing chiral molecules cannot, in principle, have reflection symmetry about the

Table 11.4 The changes from molecular point groups, G'_M to effective point groups, G_M which produce a change in the NMR spectra of molecules in chiral liquid-crystalline phases [**4**]

G'_M	G_M
C_s	C_1
C_{2v}	C_2
S_4	C_2
D_{2d}	D_2

plane perpendicular to the director, so that a chiral nematic phase has symmetry D_∞. This means that the distribution function $P_{LC}(\alpha, \beta, \gamma)$ cannot be invariant to reflection in the plane perpendicular to the director. The consequences for the order matrices of molecules in a chiral phase can be considered by introducing the idea of an effective molecular point group, G_M, which may differ from the point group of the isolated molecule, G'_M. It was noted earlier that the principal axes of S may be located by considering the point group symmetry. For chiral phases the effective point group is used. For the four G'_M given in Table 11.4 there is a reduction of symmetry to G_M when the liquid-crystalline phase is chiral, which affects both the rules for locating the principal axes of S, and the permutation symmetry of the nuclear spins [**4**].

For ethanol, the reduction of symmetry from C_s to C_1 means that it is not possible to locate any of the principal axes of the order matrix from symmetry, and that the two C–D (or C–H) bond directions in the molecule have different order parameters.

Note that a phase is chiral if any of the molecules dissolved in it are chiral. In practice the magnitude of the effects produced by the reduction of effective symmetry will depend on how many molecules in the phase are chiral, and on the strength of the chiral, intermolecular, anisotropic forces. Thus, not all chiral phases show measurable effects on NMR spectra from the change in effective symmetry of molecules dissolved in them.

References

1. P.J. Collings and M. Hird, *Introduction to Liquid Crystals*, Taylor & Francis, London (1997).
2. D. Demus, J.W. Goodby, G.W. Gray, H. Spiess and V. Vill (Eds.), *Handbook of Liquid Crystals*, Springer-Verlag.
3. C. Zannoni, in *NMR of Liquid Crystals* (Ed. J.W. Emsley), Riedel, Dordrecht (1984).
4. D. Merlet, J.W. Emsley, P. Lesot and J. Courtieu, *J. Chem. Phys.* **111** (1999) 6890.
5. J.W. Emsley, in *Encyclopedia of NMR* (Eds. D.M. Grant and R.K. Harris), John Wiley & Sons, Chichester (1995), p. 2788.
6. A.A. Bothner-By, in *Encyclopedia of NMR* (Eds. D.M. Grant and R.K. Harris), John Wiley & Sons, Chichester (1995), p. 2932.

7. P. Diehl, in *NMR of Liquid Crystals* (Ed. J.W. Emsley), Reidel, Dordrecht (1985).
8. J. Gerritsen and C. MacLean, *Rec. Trav. Chim.* **91** (1972) 1393.
9. J.W. Emsley, in *Encyclopedia of NMR* (Eds. D.M. Grant and R.K. Harris), John Wiley & Sons, Chichester (1995), p. 2781.
10. E. Ciampi, M.I.C. Furby, L. Brennan, J.W. Emsley, A. Lesage and L. Emsley, *Liquid Crystals* **26** (1999) 109.
11. R. Berardi, F. Spinozzi and C. Zannoni, *Chem. Phys. Lett.* **260** (1996) 633.
12. D. Catalano, J.W. Emsley, G. La Penna and C.A. Veracini, *J. Chem. Phys.* **105** (1996) 10595.
13. R. Berardi, F. Spinozzi and C. Zannoni, *J. Chem. Phys.* **109** (1998) 3742.
14. G. Drobny, in *NMR of Liquid Crystals* (Ed. J.W. Emsley), Reidel, Dordrecht (1985).
15. C. Algieri, F. Castiglione, G. Celebre, G. De Luca, M. Longeri and J.W. Emsley, *Phys. Chem. Chem. Phys.* **2** (2000) 3405.
16. F. Castiglione, G. Celebre, G. De Luca and M. Longeri, *J. Magn. Reson.* **142** (2000) 216.
17. M. Carravetta, F. Castiglione, G. De Luca, M. Edgar, J.W. Emsley, R.D. Farrant, E.K. Foord, J.C. Lindon, M. Longeri, W.E. Palke and D.L. Turner, *J. Magn. Reson.* **135** (1998) 298.
18. M.I.C. Furby, Ph.D thesis, University of Southampton (1998).
19. E. Ciampi, G. De Luca and J.W. Emsley, *J. Magn. Reson.* **129** (1997) 207.
20. K. Schmidt-Rohr, D. Nanz, L. Emsley and A. Pines, *J. Phys. Chem.* **98** (1994) 6668.
21. S. Caldarelli, M. Hong, L. Emsley and A. Pines, *J. Phys. Chem.* **100** (1996) 18696.
22. M. Sarfati, P. Lesot, D. Merlet and J. Coutieu, *J. Chem. Soc. Chem. Comm.* (in press, 2000).
23. P. Lesot, D. Merlet, A. Loewenstein and J. Courtieu, *Tetrahedron: Asymmetry* **9** (1998) 1871.

Solid-State NMR Spectroscopy Principles and Applications
Edited by Melinda J. Duer
Copyright © 2002 by Blackwell Science Ltd

Index

2D exchange, see two-dimensional exchange
2D-Phase-Adjusted Spinning Sidebands (PASS) experiment, 232–4
  application to ampicillin and penicillin V, 296–7
^{2}H NMR, 267–79, 503, 521–7
  ^{2}H-^{13}C dipolar recoupling, 276–8
  CMPG sequence, 272–3
  double-quantum NMR, 276, 278
  exchange experiments, 275–6
  lineshape simulations, 273–4
  magic-angle spinning, 269–71
  measuring spectra, 268–73
  powder patterns in, 267, 269
  quadrupole echo experiment, 268–9
  relaxation time studies, 274–6
  resolving powder patterns in, 276–9
^{2}H quadrupole coupling constant, 267, 526
3D exchange, see three-dimensional exchange

absorption lineshape, 66–7
active rotation, 20–24
adiabaticity parameter, 164
aluminophosphate molecular sieves, 438–40
aluminosilicate glasses, 421–5
autocorrelation function, 241
average hamiltonian theory, 88–97
average hamiltonian, 89–90
  for C7 sequence, 148
  for double-quantum excitation, 138–40
  for DRAMA sequence, 126–30
  for REDOR, 157
  for rotational resonance, 152, 153
  for WAHUHA sequence, 95, 97

basis function, 12
  for multi-spin systems, 51
biomolecular NMR
  2D-PASS (on ampicillin, penicillin V), 296–7
  chemical shift anisotropy, 293–303
    dependence on molecular geometry, 293, 299
    of ^{13}C sites in ampicillin and penicillin V, 296–7
    of carbonyl ^{13}C in peptides, 293–4
  chemical shift dependence on molecular conformation, 289–93
  commonly used nuclei, 281–5
  double-quantum heteronuclear local field experiments, 287–8
  local field condition, 287
  measurement of molecular torsional angles, 287–8
  prion proteins, 288–93
  spinning sidebands (analysis of), 294
Boltzmann distribution, 14–15
boron-containing oxide glasses, 416–21

C7, 133–5, 286
  analysis of pulse sequence, 145–8
  average hamiltonian, 148
carrier frequency, 66, 70
chemical shift anisotropy, 46
  measurement, 222–34
  recoupling pulse sequence, 222–5
  variable-angle spinning experiments for measuring (VACSY), 225–8
  magic-angle turning experiment for measuring, 228–31
  separation of spinning sidebands for measuring, 231–4
chemical shift asymmetry, 46
chemical shift filter, 487
chemical shift frequency, 41–3
chemical shift anisotropy recoupling pulse sequences, 222–5
chemical shift tensor, 46
chemical shift
  definition, 46
  dependence on molecular conformation in proteins, 289–93
  gamma-gauche effect, 289–93, 486–71, 495, 509
chemical shift-chemical shift tensor correlation experiments, 322–38

conformational degeneracy in, 331
DQ chemical shift (DQCSA) spectroscopy, 333–8
DQ-DRAWS experiment, 333–4
under magic-angle spinning, 325–38
CMPG sequence (for quadrupolar nuclei), 206
coherence order pathway, 63–5
coherence, 30–33, 62
commutator, 10
constant-time double-quantum (DQ) filtered dipolar (CTDQFD) dephasing, 315–17
correlation time, 241
coupling tensor, general, 37
C_Q, definition, 392
CRAMPS, 487
cross polarization, 97–107
dynamics, 102
experimental details, 102–3
Hartman-Hahn match condition, 99
quadrupolar nuclei, 209–11
ramped contact pulses, 103
sideband match condition, 107
theory, 98–102
under magic-angle spinning, 103, 104–7

density matrix, 30–32
density operator
defined, 29–30
at thermal equilibrium, 33
time evolution of, 33–6
dephasing, 140, 154, 155, 158
diamagnetic contribution to shielding, 38
dipolar decoupling sequences, 86–97
FSLG-2, 343
high-power (continuous wave), 85–6
MREV-8, 87, 555
multiple-pulse sequences, 86–7
WAHUHA, 87–97
WIM-12, 343
dipolar filter, 500–501
dipolar hamiltonian, see *dipole coupling hamiltonian*
dipolar recoupling pulse sequences
application to biomolecules, 311–19
heteronuclear
REAPDOR, 164–5
REDOR, 154–60, 287
Rotor-synchronous HEteronuclear Dipolar Switching (RHEDS), 343
SEDOR, 148, 153–4, 287
Synchronous Phase-Inversion Rotary Resonance Recoupling, 363
TEDOR, 287
TRAPDOR, 161–4
homonuclear
C7, 133–5, 145, 286
DRAMA, 123–5, 133, 138–9, 142–3, 286
DRAWS, 313
finite-pulse (fp)-RFDR, 315
RFDR, 286, 313, 500
rotational resonance, 135–7, 149–53
dipole – chemical shift tensor correlation experiments, 338–50
^{15}N-^{13}C correlation experiment, 348–50
DIPSHIFT experiment, 368
Relayed Anisotropy Correlation (RACO) experiment, 342–8, 371
Separated Local Field DQ (SELFIDOQ) experiment, 339–41
static homonuclear experiment, 339
dipole coupling constant, 48, 123
dipole coupling hamiltonian, 47–8
heteronuclear, 55
homonuclear, 50
under magic-angle spinning, 120
in terms of spherical tensor operators, 117–18
dipole coupling, 46–56, 112
dipole coupling tensor, 48–9, 116–19
under magic-angle spinning, 119–20, 129
dipole-dipole tensor correlation experiments, 350–71
HCCH-DQ-Heteronuclear Local Field (HCCH-DQ-HLF), 351–9
NCCN-DQ-Heteronuclear Local Field (NCCN-DQ-HLF), 359–67
NCCN-3Q-Heteronuclear Local Field (NCCN-3Q-HLF), 366–7
HNCH-DQ-Heteronuclear Local Field (HNCH-DQ-HLF), 367–70
β-sheet filter experiment, 370–71
dipole-dipole coupling, see *dipole coupling interaction*
Dirac bra/ket notation, 12
dispersion lineshape, 66–7
double rotation (DOR), 191–3
application to glasses, 411, 417
application to porous materials, 475–7
double-quantum (DQ) spectroscopy, 132–5, 138, 140–45, 145–8, 166–9, 276, 278, 311–19, 487–8
analysis of (for dipolar-coupled systems), 138–44
double-quantum heteronuclear local field experiments, 287–8
DRAMA, 123–5, 133, 138–9, 142–3, 286
analysis of pulse sequence, 126–30
average hamiltonian for sequence, 130
simulating lineshapes from, 130–31
DRAWS, 313
dynamic-angle spinning (DAS), 193–5
applications to glasses, 411–12, 417, 423, 428
recording 2D datasets, 200–3
phase cycling, 201

eigenstate of spin system, 7
electric field gradient tensor, 58, 179
electric quadrupole moment, 56–7, 179
ensemble average, 7, 15, 30, 61–2, 213
Euler angles, 25–7
relating CSA tensors in terms of torsion angles, 329–30
exchange experiments
2D pulse sequences, 262, 265

^{2}H, 275–6
3D pulse sequence, 264
achieving absorption lineshapes, 263–5
use of Hahn spin echoes in, 264–5
interpretation of, 266–7
expectation value, 8
exponential operators, 20

frequency offset, 61
FSLG-2, 343

gamma gauche effect, 289–93, 486–71, 495, 509
germanate glasses, 421–5
glasses (oxide)
^{17}O NMR, 417, 422, 423, 424, 426
2D-correlation experiments, 409–11, 423
2D-exchange experiments, 427–8
2D-PASS, 410
analysis of spinning sidebands, 404–5
CRAMPS, 405–6, 425
cross polarization, 406–7
deconvolving magic-angle spinning spectra, 399–400
double rotation, 411, 417
double-quantum spectroscopy, 410, 428
dynamic-angle spinning, 411–12, 417, 423, 428
HETCOR experiments, 411, 419
homomgeneity of cation distribution, 398
magic-angle spinning, 398–405
MQMAS, 412–14, 417, 419, 422, 423, 424, 426, 429
recording spectra with very broad lines, 398
REDOR, 407–8, 419, 421, 423
SEDOR, 407, 421, 423
spin-lattice relaxation, 414–15
TRAPDOR, 409, 428
VACSY, 410, 427
wideline (static) techniques, 395–6, 428, 430
golden rule of quantum mechanics, 259
Goldman-Shen experiment, 499–500

hamiltonian
dipole coupling, 47–8, 50, 55, 111, 116, 117, 120
general spin interaction, 36–7
quadrupole coupling, 57–8, 179, 180, 181, 183–4
shielding, 38, 41
Zeeman, 14
see also, *average hamiltonian*
Hartman-Hahn match condition, 99
heteronuclear dipolar coupling, 54–6
homonuclear dipolar coupling, 49–54
homonuclear dipolar decoupling sequences, see *dipolar decoupling sequences*
hydrogen-containing oxide glasses, 425–6
hypercomplex data processing, 68–9, 131, 323

inhomogeneous interaction, 41
interaction representation, 93
intermediate frequency (IF), 70, 71
isotropic chemical shift frequency, 43–4
isotropic quadrupolar shift, 182
isotropic shielding, 40

Larmor frequency, 5
Lee-Goldburg cross-polarization, 496–7
lineshape simulation, 59–61
^{2}H powder patterns, 273–4
with magic-angle spinning, 76–8
with molecular motion, 243–9
liquid-crystal phases
^{2}H quadrupole splittings in, 525–7
Additive Potential (AP) method, 537, 539–40
chemical shift anisotropy in, 527–9
chiral phases, 558–61
dipole couplings in, 523–5
director alignment in, 521–2
molecular order parameters, 518–21, 535–40
molecular orientational order in, 515–16, 531–4
multiple-quantum NMR experiments in, 542–8
NMR experiments for, 540–58
nuclear spin interaction hamiltonian for, 516–18
orientational order in, 514
phase symmetry, 515
rotational isomeric state (RIS) model, 538
Saupe order parameters, 519
scalar coupling in, 529–31
separated local field experiments, 554–8
local field condition, 287
lowering operator, 13

magic-angle spinning, 73–5
effect on homonuclear dipole coupling, 83–5
see also, *spinning sidebands*
Magic-Angle Turning (MAT) experiment, 228–31
magnetization, 4
effect of rf pulses on, 5–7
expectation value of, 15–16, 32, 35
Magnus expansion, 89, 174
Markov process, 243, 247, 250
matrices (of spin operators), 12–13
measurement of molecular torsional angles, 287–8, 319–71
mesoporous molecular sieves, 440–41
molecular motion
^{2}H NMR, 267–79
effect of magic-angle spinning on powder lineshapes, 251–3
effect on anisotropic spin interactions, 240
exchange experiments, 261–7
limitations of lineshape analysis, 249–50
lineshapes in the limit of fast motion, 248–9
powder lineshape analysis, 242–50
relaxation times for studying, 258–61
resolving powder lineshapes in the study of, 250–56
simulating powder lineshapes, 243–8
spinning sideband patterns under, 254
MREV-8, 555
multidimensional NMR, 61–3

multiple-quantum magic-angle spinning (MQMAS), 195–200
absorption mode spectrum, 200, 201, 203
adiabatic transfer methods, 200
antiecho, 201
cross polarization with, 210
echo formation, 200, 201, 202
fast amplitude-modulated (FAM) pulses, 200
HETCOR experiments with, 210–11
multiple-quantum – single-quantum conversion, 199–200
multiple-quantum excitation, 199
phase cycling, 199, 203, 205
recording 2D datasets, 200–203
shifted echo, 202–3
z-filter in, 202
multiple-quantum spectroscopy for spectral assignment, 542–8
multiple-quantum spin counting experiments, 171–7, 472–4
^{13}C under magic-angle spinning, 371–83

nuclear magnetic moment, 4
nutation frequency, 5
quadrupolar nuclei, 209, 210
nutation spectrum, 206, 208

off-magic-angle spinning, 558
offset, 61
optical pumping, 474–5

Pake patterns, 267
paramagnetic contribution to shielding, 38
passive rotation, 24–8
perturbation theory, 37
phase cycling, 63–6
phase of rf pulse, 5
phase-twisted lineshape, 67
phasing, 67
phosphate glasses, 426–8
2D exchange experiments, 427–8
polymers
^{19}F NMR, 508–9
cross-polarization in, 489–90, 497
dipolar filter, 500–501
double-quantum spectroscopy, 487–8, 494
dynamics in, 489–94
fluoropolymers, 506–9
oriented, 502–6
phase separation in, 494–502
relaxation in, 489
separated local field experiments, 491
spin diffusion in, 490, 497–502
structure of, 485–8
three-dimensional exchange experiments, 492–3
two-dimensional exchange experiments, 490–92, 494, 506, 509
WISE, 495–6
porous materials
^{129}Xe NMR, 442, 471–2, 474
^{15}N NMR, 442, 455, 456
^{1}H NMR, 442, 455, 456
^{27}Al NMR, 441, 444, 450, 451, 465
^{27}Al T_1 relaxation times in, 450
^{29}Si NMR, 441, 442, 443–4, 446, 448–9, 451, 465
^{29}Si T_1 relaxation times in, 449
2D-J spectroscopy, 459–61
2D-spin diffusion experiments, 461–2, 465
^{2}H NMR, 470
^{31}P NMR, 457
adsorbed organic species, 459–63
COSY, 446
double rotation, 475–7
INADEQUATE, 446
J-scaled COSY, 446
MQMAS, 477
multiple-quantum spin counting experiments, 472–4
pulsed field gradient studies, 470
quadrupole nutation, 453
REDOR/SEDOR, 475
study of Brønsted acid sites, 455–8
powder pattern, 43, 45, 56
simulating, 59–61, 243–50
P_Q, definition, 392
principal axis frame, 40, 42
prion proteins, 288–93

quadrature detection, 63, 66–9
quadrupolar coupling, see *quadrupole coupling*
quadrupolar order, 274, 276
quadrupole coupling, 56–9, 179–84
first-order energy correction, 182
isotropic shift, 182
magic-angle spinning, 189–91
and rf pulses, 184–8
second-order energy correction, 182
quadrupole coupling asymmetry parameter, 179, 208
quadrupole coupling constant, 58, 180, 208
quadrupole coupling hamiltonian, 57–8, 179, 180
full, 181
secular terms, to second order, 183
quadrupole coupling tensor, 180
quadrupole echo pulse sequence, 108–9, 268–9
quadrupole nutation, 206–8
quadrupole splitting, 185

Radio-Frequency Driven recoupling (RFDR), 286, 313, 500
raising operator, 13
Ramachandran plot, 321–2
REAPDOR, 164–5
receiver phase, 64–5, 66
reconversion pulse sequence (multiple-quantum experiments), 133, 139, 140, 142
REDOR, 154–60, 287
analytical solution to dephasing curves, 160, 304
application to biomolecules, 303–7
application to glasses, 407–8, 419, 421, 423

application to porous materials, 475
refocussing (of transverse magnetization), 153, 154, 158, 162, 164
quadrupolar effects, 193, 195
relaxation times
^{2}H motional studies, 274–6
in studies of molecular motion, 258–61
relaxation, 489
anisotropy of, 274
rotating frame, 5–6, 17
rotation of
axis frames, 24–8
operators, 20–24
vectors, 20–24
wavefunctions, 20–24
rotation operators, 21–3
rotation echoes, 79–80
rotational resonance, 135–7, 286
application to gastric H^+/K^+ ATPase, 308–11
Rotor-synchronous HEteronuclear Dipolar Switching (RHEDS), 343

satellite transition spectroscopy, 191
satellite transitions (quadrupolar nuclei), 185
Schrödinger's equation, 8
secular terms (in hamiltonian), 37
SEDOR, 148, 153–4, 287
application to glasses, 407, 421, 423
separated local field experiment, 554–8
see also *dipolar–chemical shift tensor correlation experiments, chemical shift–chemical shift tensor correlation experiments, dipolar–dipolar tensor correlation experiments*
shielding anisotropy, 40, 43
shielding asymmetry, 40
shielding interaction, 38–46
shielding hamiltonian, 38, 41
shielding tensor, 38–42, 216
dependence on bonding, 219–21
diamagnetic part, 38, 216
in ethene, 218
paramagnetic part, 38, 216
silicate glasses, 421–5
solid-echo pulse sequence, 108–9
spectral density function, 260
spherical tensor operators, 113–15, 516
rotation of, 114
spin counting, see *multiple-quantum spin counting experiments*
spin diffusion, 497–502
effect of ^{14}N on ^{13}C spin diffusion, 326–7
spin locking
in cross polarization, 98
quadrupolar nuclei, 211, 212–14
spin operators, 9–11
spin system, definition, 7
spinning sidebands, 75–9
2D-PASS, 232–4
24 separation of, 231–4
for homonuclear dipole coupling, 84
removing, 80–83
simulating, 76–8, 251–3
superposition state, 18
symmetry-derived recoupling sequences, see *C7*
Synchronous Phase-Inversion Rotary Resonance Recoupling SPRI-R^3), 363

T_1 anisotropy, 274
T_2 anisotropy, 274
TEDOR, 287
three-dimensional exchange, 492–3
time reversal, 140, 142, 176
toggling frame, 90–95, 127–8, 138–9, 145–6, 150, 156
torsion angle measurements in biomolecules, 319–71
torsion angles in peptide chains, definitions of, 321
TOtal Suppression of Spinning sidebands (TOSS), 81–3, 231
TRAPDOR, 161–4
application to glasses, 409, 428
two-dimensional exchange spectroscopy, 261–7
^{2}H, 275–6
achieving absorption lineshapes in, 263–5
applications to polymers, 490–92, 494, 506, 509
interpretation of spectra, 266–7
use of echoes in, 265

Variable-Angle Correlation SpectroscopY (VACSY), 227–8
to study molecular motion, 254–5
vector model of NMR, 3–7

WIdeline SpEctroscopy (WISE), 256–8
application to polymers, 495–7
pulse sequence, 257
WIM-12, 343

Zeeman basis, 14–15, 52
Zeeman hamiltonian, 14
Zeeman interaction, 37
Zeeman order, 274, 276
zeolites, 437–8
zero crossing, 163
z-filter, 69, 202